ISSN 1949-8470 (online)

World Journal of *Radiology*

World J Radiol 2022 January 28; 14(1): 1-29

Published by Baishideng Publishing Group Inc

World Journal of Radiology

Contents

Monthly Volume 14 Number 1 January 28, 2022

MINIREVIEWS

ORIGINAL ARTICLE

Retrospective Cohort Study

World Journal of Radiology

Monthly Volume 14 Number 1 January 28, 2022

Contents

ABOUT COVER

Peer Reviewer of *World Journal of Radiology*, Fabiana Perrone, MD, Doctor, Medical Oncology Unit, University Hospital of Parma, Parma 43126, Italy. fabiana.perrone89@libero.it.

AIMS AND SCOPE

The primary aim of *World Journal of Radiology* (*WJR*, *World J Radiol*) is to provide scholars and readers from various fields of radiology with a platform to publish high-quality basic and clinical research articles and communicate their research findings online.

WJR mainly publishes articles reporting research results and findings obtained in the field of radiology and covering a wide range of topics including state of the art information on cardiopulmonary imaging, gastrointestinal imaging, genitourinary imaging, musculoskeletal imaging, neuroradiology/head and neck imaging, nuclear medicine and molecular imaging, pediatric imaging, vascular and interventional radiology, and women's imaging.

INDEXING/ABSTRACTING

The *WJR* is now abstracted and indexed in Emerging Sources Citation Index (Web of Science), PubMed, PubMed Central, China National Knowledge Infrastructure (CNKI), China Science and Technology Journal Database (CSTJ), and Superstar Journals Database. The 2021 edition of Journal Citation Reports® cites the 2020 Journal Citation Indicator (JCI) for *WJR* as 0.51.

RESPONSIBLE EDITORS FOR THIS ISSUE

NAME OF JOURNAL
World Journal of Radiology

ISSN
ISSN 1949-8470 (online)

LAUNCH DATE
January 31, 2009

FREQUENCY
Monthly

EDITORS-IN-CHIEF
Thomas J Vogl

EDITORIAL BOARD MEMBERS
https://www.wjgnet.com/1949-8470/editorialboard.htm

PUBLICATION DATE
January 28, 2022

INSTRUCTIONS TO AUTHORS
https://www.wjgnet.com/bpg/gerinfo/204

GUIDELINES FOR ETHICS DOCUMENTS
https://www.wjgnet.com/bpg/GerInfo/287

GUIDELINES FOR NON-NATIVE SPEAKERS OF ENGLISH
https://www.wjgnet.com/bpg/gerinfo/240

PUBLICATION ETHICS
https://www.wjgnet.com/bpg/GerInfo/288

PUBLICATION MISCONDUCT
https://www.wjgnet.com/bpg/gerinfo/208

ARTICLE PROCESSING CHARGE
https://www.wjgnet.com/bpg/gerinfo/242

STEPS FOR SUBMITTING MANUSCRIPTS
https://www.wjgnet.com/bpg/GerInfo/239

ONLINE SUBMISSION
https://www.f6publishing.com

World Journal of Radiology

Submit a Manuscript: https://www.f6publishing.com

World J Radiol 2022 January 28; 14(1): 1-12

DOI: 10.4329/wjr.v14.i1.1

ISSN 1949-8470 (online)

MINIREVIEWS

Incidental radiological findings suggestive of COVID-19 in asymptomatic patients

Marwa Romeih, Mary R Mahrous, Mohamed El Kassas

ORCID number: Marwa Romeih 0000-0003-2099-0577; Mary R. Mahrous 0000-0002-1038-8372; Mohamed El Kassas 0000-0002-3396-6894.

Author contributions: All authors equally contributed to this paper with conception and design of the work, literature review, drafting and critical revision, editing, and final approval of the final version of the manuscript.

Conflict-of-interest statement: The authors declares no relevant conflict-of-interest to this work.

Country/Territory of origin: Egypt

Specialty type: Radiology, nuclear medicine and medical imaging

Provenance and peer review: Invited article; Externally peer reviewed.

Peer-review model: Single blind

Peer-review report's scientific quality classification

Grade A (Excellent): A
Grade B (Very good): B
Grade C (Good): 0
Grade D (Fair): 0
Grade E (Poor): 0

Marwa Romeih, Department of Radiodiagnosis, Faculty of Medicine, Helwan University, Cairo 11795, Egypt

Mary R Mahrous, Department of Radiodiagnosis, National Heart institute, Cairo 11795, Egypt

Mohamed El Kassas, Department of Endemic Medicine, Faculty of Medicine, Helwan University, Cairo 11795, Egypt

Corresponding author: Mohamed El Kassas, MD, MSc, PhD, Associate Professor, Department of Endemic Medicine, Faculty of Medicine, Helwan University, Helwan, Cairo 11795, Egypt. m_elkassas@hq.helwan.edu.eg

Abstract

Despite routine screening of patients for coronavirus disease 2019 (COVID-19) symptoms and signs at hospital entrances, patients may slip between the cracks and be incidentally discovered to have lung findings that could indicate COVID-19 infection on imaging obtained for other reasons. Multiple case reports and case series have been published to identify the pattern of this highly infectious disease. This article addresses the radiographic findings in different imaging modalities that may be incidentally seen in asymptomatic patients who carry COVID-19. In general, findings of COVID-19 infection may appear in computed tomography (CT), magnetic resonance imaging, positron emission tomography-CT, ultrasound, or plain X-rays that show lung or only apical or basal cuts. The identification of these characteristics by radiologists and clinicians is crucial because this would help in the early recognition of cases so that a rapid treatment protocol can be established, the immediate isolation to reduce community transmission, and the organization of close monitoring. Thus, it is important to both the patient and the physician that these findings are highlighted and reported.

Key Words: Incidental; Asymptomatic COVID-19; Chest computed tomography; Positron emission tomography-computed tomography; Magnetic resonance imaging; Ultrasound; Oncology patients

Received: February 1, 2021
Peer-review started: February 1, 2021
First decision: September 2, 2021
Revised: September 9, 2021
Accepted: December 23, 2021
Article in press: December 23, 2021
Published online: January 28, 2022

P-Reviewer: Delgado-Gallegos JL, Rodriguez-Pla A
S-Editor: Ma YJ
L-Editor: A
P-Editor: Ma YJ

Core Tip: Nowadays, the world is confronting a coronavirus disease 2019 (COVID-19) pandemic that has a major global influence on health, social, and economic issues. COVID-19 shows many different presentations with a wide range of severity. Because it is considered the most significant major health epidemic since that of the Spanish flu 100 years ago, the identification of all patterns of disease is extremely critical to protect the community and healthcare workers from such a highly contagious disease. Radiologists must be alert to recognize the different radiographic findings that suggest COVID-19, even in asymptomatic cases, in different imaging modalities.

Citation: Romeih M, Mahrous MR, El Kassas M. Incidental radiological findings suggestive of COVID-19 in asymptomatic patients. *World J Radiol* 2022; 14(1): 1-12
URL: https://www.wjgnet.com/1949-8470/full/v14/i1/1.htm
DOI: https://dx.doi.org/10.4329/wjr.v14.i1.1

INTRODUCTION

The coronavirus disease 2019 (COVID-19) pandemic is caused by severe acute respiratory syndrome coronavirus 2 (SARS-CoV-2). Infection has a major global influence on social, health, and economic issues. COVID-19 is considered the most significant major health epidemic since the Spanish flu 100 years ago[1]. It first appeared in Wuhan, China, in December 2019 and was officially declared a pandemic by the World Health Organization (WHO) on March 11, 2020, extending rapidly worldwide thereafter and becoming an outbreak. By the end of 2020, more than 78 million people were infected, leading to over 1.7 million deaths[2]. Unlike infections with other coronaviruses, asymptomatic COVID-19 patients are infectious, leading to the rapid spread of infection worldwide[1,3]. The most common modes of transmission of the virus are person-to-person spreading during intimate contact with an infected person (or asymptomatic infected carriers), inhalation of respiratory droplets, and contact with surfaces contaminated with respiratory droplets or aerosols, which can penetrate the lungs through the nose or mouth[2,4,5]. SARS-CoV-2 virus uses the angiotensin-converting enzyme 2 (ACE2) receptor for cell entry. ACE2 receptors are present in high amounts on epithelial cells, which are more predominant in oral mucosa and lungs, than in heart, blood vessels, brain, and other organs, leading to a diversity in the disease presentation[5-8]. The clinical presentation of COVID-19 ranges from asymptomatic to critically ill, and the most common manifestations are mild to moderate respiratory illness, where recovery occurs without requiring special treatment[6-8]. However, many nonspecific symptoms, such as fever, fatigue, shivering, anorexia, headache, olfactory dysfunction and loss of taste, shortness of breath, cough with or without expectoration, dyspnea, chest tightness, diarrhea, nausea, vomiting, abdominal pain, and muscle soreness, overlap with other viral infections[2,5-12]. Despite most patients with COVID-19 complaining of mild symptoms, the death rate is considerable, ranging from 0.3%–13.1%, with more susceptibility to severe forms of the disease in older patients, especially those with underlying disease, such as diabetes mellitus, cardiovascular disease, respiratory disease, hyperlipidemia, obesity, and chronic renal and hepatic disease[4,10,11].

COVID-19 DIAGNOSIS

A confirmed case of coronavirus disease 2019 (COVID-19) is defined by World Health Organisation as a patient with a positive reverse transcription-polymerase chain reaction (RT-PCR) test, irrespective of clinical signs and symptoms[12]. This test directly assesses the viral load from a nasopharyngeal swab, sputum, or endotracheal lavage[13]. It has impressive specificity of up to 100% owing to its specificity to the severe acute respiratory syndrome coronavirus 2 (SARS-CoV-2) genome sequence, but has imperfect sensitivity of 89% (95%CI: 81%–94%)[14]. A positive result denotes the presence of viable virus only, and a negative result does do not rule out COVID-19 infection[13,15]. False-negative RT-PCR results may occur if the test is performed too early or late in infection course, the viral load is insufficient, or the specimen is of poor

quality and also due to technical errors or inappropriate handling and shipping of the specimen. False-positive results may occasionally occur due to technical errors or reagent contamination[14,16,17]. The turnaround time for an RT-PCR test ranges from 50 min to 4 h for semi- to fully automated, walk-away assays and 6–14 h for manually performed assays[12,13,18].

More than 50% of patients with a positive RT-PCR test may be asymptomatic at the time of testing only or throughout the entire duration of the disease, leading to more spread of the virus. Accordingly, it is essential to detect COVID-19 infection at the early stage to immediately isolate the infected person from the healthy population[14,19]. The need for a simple, rapid method to identify asymptomatic patients who need urgent medical or surgical intervention in an emergency and in oncology patients, patients in the intensive care unit, or those who need hospital admission is crucial to prevent the spread of infection. In cases where RT-PCR test results take some time to be available and because this test has imperfect sensitivity, chest radiography is appropriate[8,9,20-23].

CLASSICAL IMAGING CRITERIA OF COVID-19

To prevent the spread of infection in hospital patients or healthcare workers, chest radiography is considered the first-line imaging modality to be performed in patients with suspected coronavirus disease 2019 (COVID-19) or to exclude the presence of COVID-19 infection in patients who need to receive medical or surgical treatment[10,13,17,18,24-29]. Most radiological imaging modalities are beneficial in characterizing COVID-19 infection.

Chest X-ray

Chest X-ray (CXR) findings in COVID-19 patients usually appear at 10–12 d from symptom onset as bilateral lower zone consolidation patches or diffuse airspace opacities with peripheral distribution[10,11,30]. The CXR may be normal in up to 63% of cases, particularly in the early stages[28], and it has a great value in patients with moderate to severe disease who have acute respiratory distress syndrome, showing bilateral diffuse alveolar consolidation that may progress to white lung with or without mild pleural effusion[26,31-33].

Yasin *et al*[7] studied the association of COVID-19 severity and X-ray findings among 350 positive COVID-19 patients. Of them, 62.9% had an abnormal baseline CXR, and the most common findings were consolidation opacities (81.3%), followed by reticular interstitial thickening (39.9%) and ground glass opacities (GGOs) (32.5%). An example of CXR findings in a patient with COVID-19 is presented in Figure 1.

Chest computed tomography

Chest computed tomography (CT) plays a pivotal role in the early detection of COVID-19 pneumonia and has better sensitivity (98%) compared with RT-PCR (89%), particularly in the early course of the disease. However, it also has low specificity (25%) due to the overlap between COVID-19 pneumonia and other types of viral pneumonia[5,8,30,31]. Radiologists must be familiar with the different imaging findings of COVID-19 pneumonia to differentiate it from other types of pneumonia[11,13,30]. Early COVID-19 chest CT findings include bilateral multiple GGOs with a peripheral, subpleural, and posterior distribution, with or without consolidation. In the late phase, the consolidation patches, linear opacities, "crazy-paving" pattern, reversed halo sign, and vascular enlargement become more common[5,9,10,18,32]. The pulmonary histologic findings of COVID-19 resemble those of other coronavirus infections, such as severe acute respiratory syndrome coronavirus 1 (SARS-CoV-1) and Middle East respiratory syndrome coronavirus (MERS-CoV)[4], which also shows similarities in chest CT findings[23,33,34]. Great variability is observed in chest CT findings in COVID-19 patients according to the stage and severity of the disease[6,9,15,24,25,35,36]. The Radiological Society of North America classifies the chest CT findings into four categories related to COVID-19 diagnosis: (1) Compatible with viral pneumonia; (2) Indeterminate; (3) Atypical (suggestive of other diagnoses); and (4) No evidence of pneumonia[37].

The Fleischner Society[38] recommends performing a chest CT in moderate to severe infections presenting with hypoxemia and moderate to severe dyspnea, regardless of the RT-PCR test result [39], while RT-PCR is indicated if incidental findings on CT suggest the presence of viral pneumonia[14,19,34,38,39]. Chest abnormalities associated with COVID-19 may be incidentally detected in the visualized lung

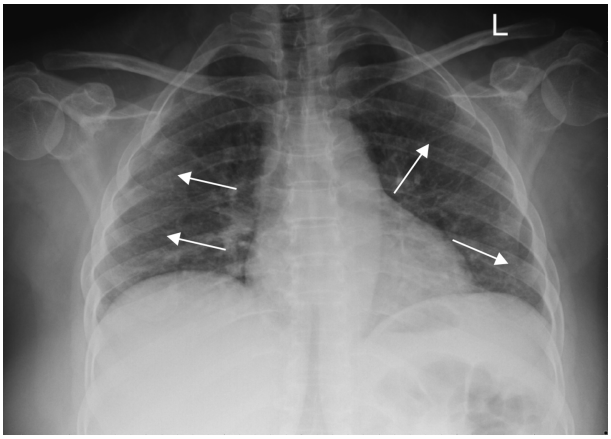

Figure 1 Postero-anterior chest X-RAY in one asymptomatic patient with coronavirus disease 2019 pneumonia from our institution. It shows Interstitial infiltrates and ill-defined, patchy, peripheral opacities in bilateral lung fields.

parenchyma in CT examinations of other body regions, such as in the lower lung base in abdominal CT (Figure 2), the lung apex in head and neck CT studies (Figure 3), and the lung tissues seen in dorso-lumbar spine CT[18,40]. Several studies have been published reporting incidental chest CT findings of COVID-19 in the visualized lung parenchyma in patients with acute abdomen without respiratory manifestation who undergo abdominal CT in the scenario of an acute pandemic[41-47](Table 1).

Lung ultrasound

A lung ultrasound (US) in COVID-19 pneumonia is usually performed using a portable US machine at the bedside to minimize the spread of infection to other patients and healthcare workers[48]. The classical appearance is bilateral irregular pleural lines, subpleural consolidation, areas of thick white lung tissue, and thick irregular vertical artifacts suggesting interstitial alveolar damage[48-50]. In the pediatric age group, lung US has an advantage over CT because it does not use ionizing radiation. Vertical artifacts (70%) and pleural irregularities (60%) were the most common abnormalities detected in 10 symptomatic pediatric patients with confirmed COVID-19 who underwent a chest US while awaiting RT-PCR results Notably, pleural effusions were absent in all 10 patients[44,50,51]. The follow-up of lung US findings to monitor pulmonary involvement in symptomatic COVID-19 patients is preferable to the use of repeated CT scans, especially in critically ill patients or patients on a ventilator, owing to the difficulty in transporting such patients to the CT equipment[5,8,50]. Additionally, US can detect pneumothorax and other complications. However, a major disadvantage is the prolonged close exposure of the operator to the infection and also the need for careful sterilization of the device and the use of transducer and keyboard covers[10]. No reports about incidental lung US findings are available because this is not a routine examination, and it is only performed in certain circumstances.

Magnetic resonance imaging

Although magnetic resonance imaging (MRI) plays no role in the diagnosis of COVID-19 pneumonia, there are many reports of the detection of incidental COVID-19 in MRIs performed for other diagnostic purposes in asymptomatic patients[8,40,42]. After an extensive review of the literature, we found many cases of reported COVID-19 findings in upper lung cuts that appear in brain, neck, and cervico-dorsal spine MRIs and in lower cuts in abdomen and liver MRI studies[4,52-55]. COVID-19 infection appears as peripheral areas of high signal on T2-weighted short tau inversion recovery imaging caused by edema or alveolar opacities. A high T1 signal is observed due to higher tissue density, and partial alveolar collapse with focal areas of restricted diffusion is observed on diffusion-weighted imaging because of increased cell density from the inflammatory reaction. Partial collapse with a heterogeneous enhancement pattern is observed after contrast administration. Thus, radiologists should be alert and look carefully for these findings[34,42,54-56]. Figure 4 shows an example of cardiac MRI findings in a COVID-19 patient. Ates *et al*[52] studied thorax CT and MRI findings in 32 COVID-19 patients who underwent chest CT and then MRI within 24 h after the chest CT. They reported that MRI had a sensitivity of 91.67% and a specificity

Table 1 Summary of incidental asymptomatic COVID-19 studies

Ref.	Imaging modality used	Number of incidental asymptomatic COVID-19 cases/total number of cases	Setting
Ali *et al*[41]	^{18}F-FDG PET-CT	87/764; only 3 of which were RT-PCR negative	Asymptomatic oncology patient
Ferrando-Castagnetto *et al*[47]	^{18}F-FDG PET-CT	1	COVID-19 asymptomatic cancer patient for routine oncological indication
Pallardy *et al*[44]	^{18}F-FDG PET-CT	20/529	COVID-19 asymptomatic cancer patients for routine oncological indication
Wakfie-Corieh *et al*[68]	^{18}F-FDG PET-CT	23/1079, only 14 of which were RT-PCR positive	COVID-19 asymptomatic cancer patients for routine oncological indication
Mo *et al*[66]	^{18}F-FDG PET-CT	1	COVID-19 asymptomatic cancer patients for routine oncological indication
Franceschi *et al*[67]	^{18}F-FDG PET-CT	1	Asymptomatic diffuse large B-cell lymphoma patient
Setti *et al*[64]	^{18}F-FDG PET-CT	5/13	COVID-19 asymptomatic cancer patients
Albano *et al*[65]	^{18}F-FDG PET-CT	6/65 patients	COVID-19 asymptomatic oncology patient
	SPECT-CT	1/12 patients	Asymptomatic patient with treated differentiated thyroid carcinoma
Angelini *et al*[42]	Whole-body MRI	1	COVID-19 asymptomatic multiple myeloma patient under follow-up
Deen *et al*[57]	Liver MRI (basal chest cuts)	1	Emergency patient with hepatic focal lesion
Di Girolamo *et al*[43]	MRI of the abdomen	1	COVID-19 asymptomatic cancer patient for routine oncological indication
Ap Dafydd *et al*[22]	Chest CT	9/240 of CTs were reported as abnormal, only one of which was RT-PCR positive.	Asymptomatic patients prior to major thoracic or abdominal surgery
Siegel *et al*[59]	CT of the abdomen and pelvis (basal chest cuts)	3	Patients presented to emergency department with abdominal pain
Ali *et al*[26]	Chest CT (for other causes)	44	COVID-19 asymptomatic cases
Hyne *et al*[60]	Cerebral angiography	1	Patient presented to emergency department with neurological manifestations

COVID-19: Coronavirus disease 2019; FDG-PET/CT: Fluorodeoxyglucose-positron emission tomography-computed tomography; SPECT/CT: Single photon emission computed tomography; MRI: Magnetic resonance imaging.

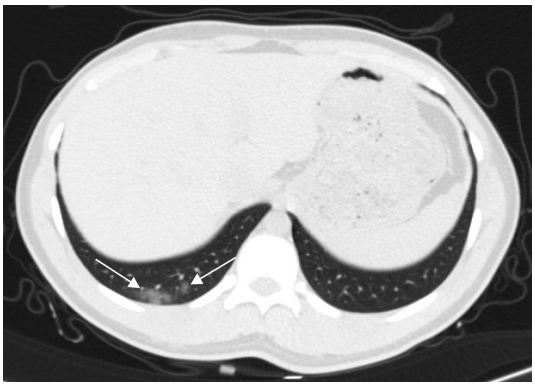

Figure 2 Axial-basal chest cut in urinary tract computed tomography in a patient presenting with renal colic at our institution who was diagnosed with asymptomatic coronavirus disease 2019 due to the presence of peripheral small focal areas of ground glass veiling.

of 100%. Furthermore, rapid limited study using a T2-weighted spin echo sequence, which is widely available in all scanners and can detect GGOs or consolidative patches with no exposure to radiation, was suggested. Angelini *et al*[42] reported a case of incidental COVID-19 pneumonia in a 60-year-old male with multiple myeloma and negative respiratory symptoms who underwent whole-body MRI as routine follow-

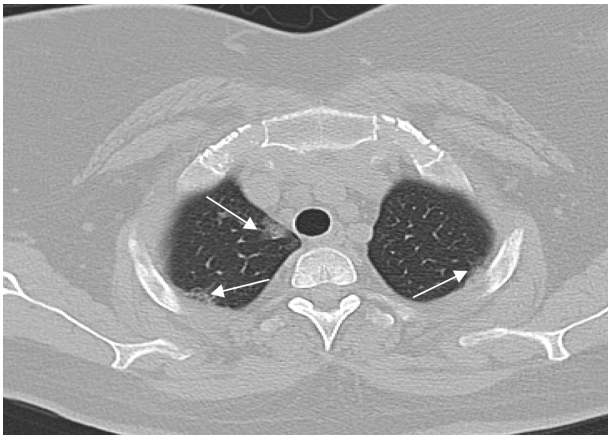

Figure 3 Axial-apical chest cut in brain computed tomography in a patient presenting with head trauma at our institution who was diagnosed with asymptomatic coronavirus disease 2019 due to the bilateral presence of multiple peripheral small foci of ground glass veiling with mild interstitial thickening.

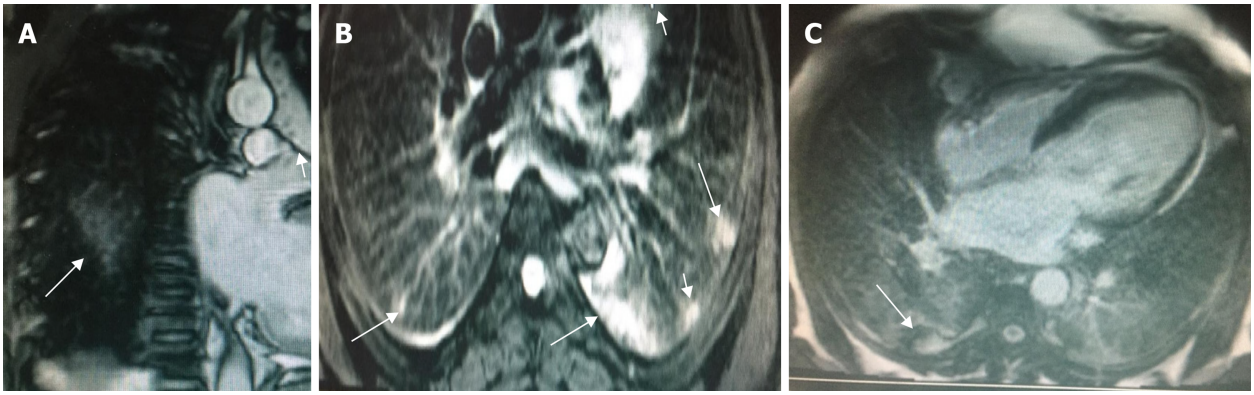

Figure 4 Cardiac magnetic resonance images of a patient with coronavirus disease 2019 who presented to our institute for a viability study showing multifocal peripheral areas of abnormal signal in both lungs that appear as high signal intensity areas localized in the coronal plane (A), high T2 signals (B), and faint heterogenous enhancement in post-contrast sequences (C).

up. The COVID-19 pneumonia presented as peripheral posterior GGOs in the lung in T2-weighted sequences. Deen *et al*[57] reported the detection of incidental basal lung lesions on liver MRI in a 49-year-old woman with a negative RT-PCR result for COVID-19 who presented at the emergency department with vague symptoms. An abdominal US revealed a liver mass, and subsequent MRI examination identified it as a hemangioma, while the scanned lung base showed peripheral high T2-weighted focal areas with restricted diffusion in the left lower lobe. Consequently, the patient underwent a chest CT that confirmed presence of bilateral multiple GGOs. Di Girolamo *et al*[43] reported a 71-year-old woman with T4a colorectal cancer who underwent an abdominal MRI for routine follow-up of hepatic metastasis that led to the incidental detection of bilateral lower lobe GGOs in the scanned lung. Thereafter, the patient underwent RT-PCR, which confirmed that they were positive for COVID-19. MRI can help in the early recognition of cases so that a rapid treatment protocol can be established, the immediate isolation to reduce community transmission, and the organization of close monitoring. Thus, it is important to both the patient and the physician that these findings are highlighted and reported.

ASYMPTOMATIC COVID-19 PATIENTS IN ELECTIVE AND EMERGENCY SURGERIES

On April 15, 2020, the Royal College of Surgeons and Royal College of Radiologists published guidelines on the use of preoperative reverse transcription-polymerase chain reaction (RT-PCR) and chest computed tomography (CT) during the coronavirus

disease 2019 (COVID-19) pandemic to exclude COVID-19 infection before elective surgery. These guidelines aim to eliminate the risk of COVID-19-related complications after elective surgery and prevent the transmission of COVID-19 to other patients and healthcare workers[22]. The major obstacle in the management of acute surgical conditions in both urgent and elective surgery is the increased risk of nosocomial transmission. Chetan *et al*[58] evaluated chest CT screening for COVID-19 in a total of 439 elective and emergency surgical patients. The elective surgical cohort included 156 patients who underwent preoperative low-dose unenhanced chest CT, and the emergency surgical cohort included 283 patients with abdominal emergencies where the preoperative abdominal CT was extended cranially to include the lungs from below the carina. Of the 432 patients, 32 (7%) showed potential COVID-19-related lung changes[58]. These findings changed surgical management in the elective surgical cohort only and not in the acute abdominal emergency cohort requiring surgery. On the other hand, Ap Dafydd *et al*[22] assessed the role of chest CT in screening for asymptomatic COVID-19 infection in self-isolating patients before elective oncological surgery. They concluded that preoperative chest CT was unhelpful and might introduce an unnecessary delay. Siegel reported suspected incidental COVID-19 findings in the lung bases in abdominal CT, which raised the possibility of the transmission COVID-19 to the clinician[59]. Thus, direct communication between the radiologist and the referring physician is the first step to protect both patients and healthcare workers against the spread of infection. Furthermore, the authors documented the possibility of viral pneumonia being used as a broad term that helps in decision-making. Hynes *et al*[60] detected incidental peripheral GGOs in the upper lobes of both lungs, which were characteristic of COVID-19 pneumonia, in a 97-year-old female patient who presented with stroke. She underwent arch-to-vertex CT angiography, which was negative for acute stroke. Sun *et al*[8] performed a systematic review and meta-analysis of chest imaging findings in patients with COVID-19. They concluded that chest CT had a low specificity in differentiating COVID-19 pneumonia from other types of pneumonia and recommended that COVID-19 diagnosis be confirmed by clinical and laboratory examinations. Dedeilia *et al*[61] reported that COVID-19 had a major effect on pediatric surgery, because children with COVID-19 are usually asymptomatic or have mild symptoms. Furthermore, many upper respiratory infections in children, such as influenza virus, rhinovirus, and others, present the same symptoms as COVID-19, and coinfection of SARS-CoV-2 may also occur[4,28,62]. Thus, the surgical committee must follow established guidelines to facilitate the workflow and prevent virus transmission, and every patient should be tested by RT-PCR. However, if rapid intervention is crucial in an emergency and RT-PCR results are not available soon enough, the assessment can be based on clinical conditions and/or chest imaging findings [7,22,60].

The guidelines for preoperative COVID-19 testing for elective cancer surgery of 15 April, 2020, were updated on May 14, 2020, to document accumulating evidence that preoperative chest CT screening does not add to the detection of COVID-19 in asymptomatic, isolated, and tested patients and is not recommended for screening before elective cancer surgery[58]. Thus, chest CT should only be considered for screening in preoperative planning in asymptomatic patients who are not isolated when RT-PCR test results are unavailable.

ASYMPTOMATIC COVID-19 ONCOLOGY PATIENTS

Oncology patients are a very special group of because of their high vulnerability to infections caused by risk factors due to their impaired immune systems, such as leukopenia, long-lasting immunosuppression (steroids, antibodies), or low immunoglobulin levels[63]. Oncology patients infected with COVID-19 may present as asymptomatic or with nonspecific symptoms, like fever, cough, dyspnea, fatigue, myalgia, and headache[49,64]. Also, because oncology patients need to continue their treatment, especially in newly discovered cases or patients receiving their treatment as chemotherapy, radiotherapy, or other forms, the benefit: risk ratio of cancer treatment may need to be reconsidered in certain patients[49,65,66]. Some reports are describing the accidentally discovered COVID-19 signs in different imaging modalities performed within the context of following cancer patients. However, the most attractive data was related to the use of fluorodeoxyglucose (FDG) positron emission tomography-CT (PET-CT) imaging, which demonstrates the increased uptake across a variety of pathological etiologies, including infections, inflammatory processes, and neoplasms. Thus, FDG PET-CT imaging plays a role in localizing foci of infection and inflam-

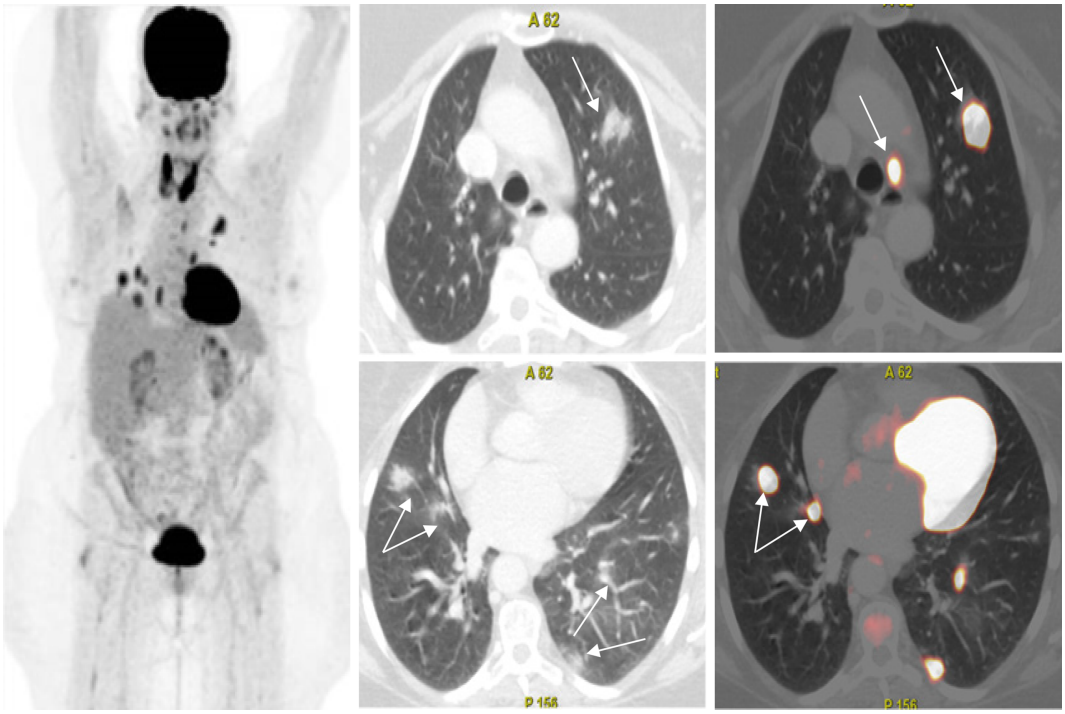

Figure 5 Axial fused thoracic ^{18}Fluorodeoxyglucose-positron emission tomography-computed tomography showing multiple variable-sized metabolically active and mainly subpleural subsegmental consolidative lesions with an SUV_{max} of up to 10.9 as well as metabolically active lymph node seen in the aorto-pulmonary window in a patient with thyroid cancer and asymptomatic coronavirus 2019.

mation in cases of fever of unknown origin. PET-CT permits detailed evaluation of both functional and anatomical/pathological processes[58,44]. Albano *et al*[65] reported a case series performed in the nuclear medicine units in Northern Italy from March 16–24, 2020. This included 65 asymptomatic patients referred for PET-CT with no suspicion of COVID-19 infection. Of them, six (9%) showed ^{18}F-FDG-avid interstitial pneumonia, suggesting COVID-19 infection. The study also included 12 patients who were admitted for whole-body ^{131}I scintigraphy followed by single photon emission CT 3–4 d after radioiodine administration, and 1 of these patients showed peripheral GGOs, suggesting COVID-19 infection, but not an increase in radioiodine uptake. All of the patients with findings suggestive of COVID-19 infection were confirmed positive upon further workup. Mo *et al*[66] reported similar findings in another asymptomatic 60-year oncology patient in the United States with human papillomavirus, and Franceschi *et al*[67] reported a similar scenario in an asymptomatic 61-year-old patient with treated primary diffuse large B-cell lymphoma. Wakfie-Corieh *et al*[68] retrospectively reviewed 1079 oncologic ^{18}F-FDG PET-CT scans performed between February 2 and May 18, 2020 to identify lung and extraparenchymal lung involvement in asymptomatic cancer patients with COVID-19. The authors concluded that FDG PET-CT-positive findings were usually limited to thoracic structures, and silent, distant involvement was infrequent. An example of PET-CT findings in COVID-19 infection is shown in Figure 5. Another retrospective review discussed the incidental findings suggestive of COVID-19 in asymptomatic cancer patients in France who underwent ^{18}F-FDG PET-CT from January 1 to February 21, 2020, in the era before COVID-19 (n = 867 PET-CT scans) and from March 16 to April 17, 2020, in the era of socially spread COVID-19 (n = 529 PET-CT). They noticed a 1.6% increase in parenchymal lung changes during the COVID-19 era[44].

Infection with COVID-19 may remain asymptomatic and appears as incidental findings in nuclear imaging procedures performed for standard oncologic indications [63-67]. PET-CT findings are considered sensitive for the detection of early COVID-19 infection, even before its detection as nasal viral carriage[41,55,66]. It appears in ^{18}F-FDG PET-CT as multiple areas of GGOs showing increased FDG uptake (SUV_{max} is usually around 5.5)[41,55,66]. Some theories explain the FDG activity detected in COVID-19 pulmonary lesions is the result of viral replication after the viral particles penetrate the cells. This replication starts to overwhelm the cellular structure, inciting a proinflammatory state that disrupts the infected and adjacent endothelium, leading

to increased FDG uptake[67].

Landete *et al*[28] reported some correlation between the degree of FDG uptake in pulmonary lesions and COVID-19 infection, which may be used as a predictor for the recovery time because the patients with pulmonary lesions had a higher SVU_{max} and took longer to recover. However, a larger sample size is necessary to confirm the predictive value. Many authors did not recommend the use of PET-CT as a primary diagnostic modality for investigating cases of suspected COVID-19 in the emergency setting because PET is an expensive imaging modality associated with prolonged acquisition times and increased radiation burden in comparison with conventional CXR and chest CT[18,44,56].

Nuclear medicine has no primary role in the diagnosis of COVID-19, yet awareness of the pattern of COVID-19 in this type of patient who is either asymptomatic or in the early stage of the disease before manifestations may have great implications in the further management of oncology patients with underlying immunosuppression, either by malignancy or oncologic therapeutics, because the virus is highly contagious and PET requires a much lengthier time in the unit than most other investigations.

CONCLUSION

In some asymptomatic patients with coronavirus disease 2019 (COVID-19) pneumonia on different radiological tools, reverse transcription-polymerase chain reaction, the definitive test for COVID-19, may be false negative. As community transmission of the COVID-19 increases and isolation restrictions are lifted, incidental findings highly suspicious of COVID-19 pneumonia on imaging modalities of asymptomatic patients may become more common. It is crucial to be aware of such appearances and the difficulties that come with them. Radiologists must be alert to signs of COVID-19 infection in various imaging modalities because many asymptomatic patients present to the radiology department for other reasons and could be already infected with COVID. If it remains unrecognized, these patients can transmit COVID-19 to the community and to healthcare workers.

REFERENCES

1 **Pitlik SD**. COVID-19 Compared to Other Pandemic Diseases. *Rambam Maimonides Med J* 2020; **11** [PMID: 32792043 DOI: 10.5041/RMMJ.10418]

2 **Shereen MA**, Khan S, Kazmi A, Bashir N, Siddique R. COVID-19 infection: Origin, transmission, and characteristics of human coronaviruses. *J Adv Res* 2020; **24**: 91-98 [PMID: 32257431 DOI: 10.1016/j.jare.2020.03.005]

3 **Choi H**, Qi X, Yoon SH, Park SJ, Lee KH, Kim JY, Lee YK, Ko H, Kim KH, Park CM, Kim YH, Lei J, Hong JH, Kim H, Hwang EJ, Yoo SJ, Nam JG, Lee CH, Goo JM. Erratum: Extension of Coronavirus Disease 2019 (COVID-19) on Chest CT and Implications for Chest Radiograph Interpretation. *Radiol Cardiothorac Imaging* 2020; **2**: e204001 [PMID: 33779627 DOI: 10.1148/ryct.2020204001]

4 **Singhal T**. A Review of Coronavirus Disease-2019 (COVID-19). *Indian J Pediatr* 2020; **87**: 281-286 [PMID: 32166607 DOI: 10.1007/s12098-020-03263-6]

5 **Revzin MV**, Raza S, Warshawsky R, D'Agostino C, Srivastava NC, Bader AS, Malhotra A, Patel RD, Chen K, Kyriakakos C, Pellerito JS. Multisystem Imaging Manifestations of COVID-19, Part 1: Viral Pathogenesis and Pulmonary and Vascular System Complications. *Radiographics* 2020; **40**: 1574-1599 [PMID: 33001783 DOI: 10.1148/rg.2020200149]

6 **Pham TD**. Classification of COVID-19 chest X-rays with deep learning: new models or fine tuning? *Health Inf Sci Syst* 2021; **9**: 2 [PMID: 33235710 DOI: 10.1007/s13755-020-00135-3]

7 **Yasin R**, Gouda W. Chest X-ray findings monitoring COVID-19 disease course and severity. *Egypt J Radiol Nucl Med* 2020; **51**: 193 [DOI: 10.1186/s43055-020-00296-x]

8 **Sun Z**, Zhang N, Li Y, Xu X. A systematic review of chest imaging findings in COVID-19. *Quant Imaging Med Surg* 2020; **10**: 1058-1079 [PMID: 32489929 DOI: 10.21037/qims-20-564]

9 **Lomoro P**, Verde F, Zerboni F, Simonetti I, Borghi C, Fachinetti C, Natalizi A, Martegani A. COVID-19 pneumonia manifestations at the admission on chest ultrasound, radiographs, and CT: single-center study and comprehensive radiologic literature review. *Eur J Radiol Open* 2020; **7**: 100231 [PMID: 32289051 DOI: 10.1016/j.ejro.2020.100231]

10 **Kwee TC**, Kwee RM. Chest CT in COVID-19: What the Radiologist Needs to Know. *Radiographics* 2020; **40**: 1848-1865 [PMID: 33095680 DOI: 10.1148/rg.2020200159]

11 **Yuki K**, Fujiogi M, Koutsogiannaki S. COVID-19 pathophysiology: A review. *Clin Immunol* 2020; **215**: 108427 [PMID: 32325252 DOI: 10.1016/j.clim.2020.108427]

12 **World Health Organization**. WHO Interim guidance 20 March 2020 - Global Surveillance for

COVID-19 disease caused by human infection with novel coronavirus (COVID-19). Who 2020; 1–4. Available from: https://www.who.int/publications-detail/global-surveillance-for-human-infection-with-novel-coronavirus-(2019-ncov)

13 **Sethuraman N**, Jeremiah SS, Ryo A. Interpreting Diagnostic Tests for SARS-CoV-2. *JAMA* 2020; **323**: 2249-2251 [PMID: 32374370 DOI: 10.1001/jama.2020.8259]

14 **Kim H**, Hong H, Yoon SH. Diagnostic Performance of CT and Reverse Transcriptase Polymerase Chain Reaction for Coronavirus Disease 2019: A Meta-Analysis. *Radiology* 2020; **296**: E145-E155 [PMID: 32301646 DOI: 10.1148/radiol.2020201343]

15 **Xie X**, Zhong Z, Zhao W, Zheng C, Wang F, Liu J. Chest CT for Typical Coronavirus Disease 2019 (COVID-19) Pneumonia: Relationship to Negative RT-PCR Testing. *Radiology* 2020; **296**: E41-E45 [PMID: 32049601 DOI: 10.1148/radiol.2020200343]

16 **Wölfel R**, Corman VM, Guggemos W, Seilmaier M, Zange S, Müller MA, Niemeyer D, Jones TC, Vollmar P, Rothe C, Hoelscher M, Bleicker T, Brünink S, Schneider J, Ehmann R, Zwirglmaier K, Drosten C, Wendtner C. Virological assessment of hospitalized patients with COVID-2019. *Nature* 2020; **581**: 465-469 [PMID: 32235945 DOI: 10.1038/s41586-020-2196-x]

17 **Pu J**, Leader JK, Bandos A, Ke S, Wang J, Shi J, Du P, Guo Y, Wenzel SE, Fuhrman CR, Wilson DO, Sciurba FC, Jin C. Automated quantification of COVID-19 severity and progression using chest CT images. *Eur Radiol* 2021; **31**: 436-446 [PMID: 32789756 DOI: 10.1007/s00330-020-07156-2]

18 **D'Andrea A**, Radmilovic J, Carbone A, Forni A, Tagliamonte E, Riegler L, Liccardo B, Crescibene F, Sirignano C, Esposito G, Bossone E. Multimodality imaging in COVID-19 patients: A key role from diagnosis to prognosis. *World J Radiol* 2020; **12**: 261-271 [PMID: 33362917 DOI: 10.4329/wjr.v12.i11.261]

19 **Döhla M**, Boesecke C, Schulte B, Diegmann C, Sib E, Richter E, Eschbach-Bludau M, Aldabbagh S, Marx B, Eis-Hübinger AM, Schmithausen RM, Streeck H. Rapid point-of-care testing for SARS-CoV-2 in a community screening setting shows low sensitivity. *Public Health* 2020; **182**: 170-172 [PMID: 32334183 DOI: 10.1016/j.puhe.2020.04.009]

20 **Cleverley J**, Piper J, Jones MM. The role of chest radiography in confirming covid-19 pneumonia. *BMJ* 2020; **370**: m2426 [PMID: 32675083 DOI: 10.1136/bmj.m2426]

21 **European Society of Radiology (ESR)**. The identity and role of the radiologist in 2020: a survey among ESR full radiologist members. *Insights Imaging* 2020; **11**: 130 [PMID: 33270175 DOI: 10.1186/s13244-020-00945-9]

22 **Ap Dafydd D**, O'Mahony M, Jhanji S, Devaraj A, Allum W, Nicol D, Blunt DM, Riddell AM. The role of CT chest in screening for asymptomatic COVID-19 infection in self-isolating patients prior to elective oncological surgery: findings from a UK Cancer Hub. *Br J Radiol* 2021; **94**: 20200994 [PMID: 33242245 DOI: 10.1259/bjr.20200994]

23 **Wong HYF**, Lam HYS, Fong AH, Leung ST, Chin TW, Lo CSY, Lui MM, Lee JCY, Chiu KW, Chung TW, Lee EYP, Wan EYF, Hung IFN, Lam TPW, Kuo MD, Ng MY. Frequency and Distribution of Chest Radiographic Findings in Patients Positive for COVID-19. *Radiology* 2020; **296**: E72-E78 [PMID: 32216717 DOI: 10.1148/radiol.2020201160]

24 **World Health Organization**. Use of chest imaging in COVID-19. 2020; 1–56. Available from: https://www.who.int/publications/i/item/use-of-chest-imaging-in-covid-19

25 **Carotti M**, Salaffi F, Sarzi-Puttini P, Agostini A, Borgheresi A, Minorati D, Galli M, Marotto D, Giovagnoni A. Chest CT features of coronavirus disease 2019 (COVID-19) pneumonia: key points for radiologists. *Radiol Med* 2020; **125**: 636-646 [PMID: 32500509 DOI: 10.1007/s11547-020-01237-4]

26 **Ali RMM**, Ghonimy MBI. Radiological findings spectrum of asymptomatic coronavirus (COVID-19) patients. *Egypt J Radiol Nucl Med* 2020; **51**: 0-5 [DOI: 10.1186/s43055-020-00266-3]

27 **Kaufman AE**, Naidu S, Ramachandran S, Kaufman DS, Fayad ZA, Mani V. Review of radiographic findings in COVID-19. *World J Radiol* 2020; **12**: 142-155 [PMID: 32913561 DOI: 10.4329/wjr.v12.i8.142]

28 **Landete P**, Quezada Loaiza CA, Aldave-Orzaiz B, Muñiz SH, Maldonado A, Zamora E, Sam Cerna AC, Del Cerro E, Alonso RC, Couñago F. Clinical features and radiological manifestations of COVID-19 disease. *World J Radiol* 2020; **12**: 247-260 [PMID: 33362916 DOI: 10.4329/wjr.v12.i11.247]

29 **Zhang HW**, Yu J, Xu HJ, Lei Y, Pu ZH, Dai WC, Lin F, Wang YL, Wu XL, Liu LH, Li M, Mo YQ, Zhang H, Luo SP, Chen H, Lyu GW, Zhou ZG, Liu WM, Liu XL, Song HY, Chen FZ, Zeng L, Zhong H, Guo TT, Hu YQ, Yang XX, Liu PN, Li DF. Corona Virus International Public Health Emergencies: Implications for Radiology Management. *Acad Radiol* 2020; **27**: 463-467 [PMID: 32113880 DOI: 10.1016/j.acra.2020.02.003]

30 **Inui S**, Kurokawa R, Nakai Y, Watanabe Y, Kurokawa M, Sakurai K, Fujikawa A, Sugiura H, Kawahara T, Yoon SH, Uwabe Y, Uchida Y, Gonoi W, Abe O. Comparison of Chest CT Grading Systems in Coronavirus Disease 2019 (COVID-19) Pneumonia. *Radiol Cardiothorac Imaging* 2020; **2**: e200492 [PMID: 33778648 DOI: 10.1148/ryct.2020200492]

31 **Ai T**, Yang Z, Hou H, Zhan C, Chen C, Lv W, Tao Q, Sun Z, Xia L. Correlation of Chest CT and RT-PCR Testing for Coronavirus Disease 2019 (COVID-19) in China: A Report of 1014 Cases. *Radiology* 2020; **296**: E32-E40 [PMID: 32101510 DOI: 10.1148/radiol.2020200642]

32 **Mathew RP**, Jose M, Jayaram V, Joy P, George D, Joseph M, Sleeba T, Toms A. Current status quo on COVID-19 including chest imaging. *World J Radiol* 2020; **12**: 272-288 [PMID: 33510852 DOI: 10.4329/wjr.v12.i12.272]

33 **Revzin MV**, Raza S, Srivastava NC, Warshawsky R, D'Agostino C, Malhotra A, Bader AS, Patel RD, Chen K, Kyriakakos C, Pellerito JS. Multisystem Imaging Manifestations of COVID-19, Part 2: From Cardiac Complications to Pediatric Manifestations. *Radiographics* 2020; **40**: 1866-1892 [PMID: 33136488 DOI: 10.1148/rg.2020200195]

34 **Ng MY**, Lee EYP, Yang J, Yang F, Li X, Wang H, Lui MM, Lo CS, Leung B, Khong PL, Hui CK, Yuen KY, Kuo MD. Imaging Profile of the COVID-19 Infection: Radiologic Findings and Literature Review. *Radiol Cardiothorac Imaging* 2020; **2**: e200034 [PMID: 33778547 DOI: 10.1148/ryct.2020200034]

35 **Hameed S**, Elbaaly H, Reid CEL, Santos RMF, Shivamurthy V, Wong J, Jogeesvaran KH. Spectrum of Imaging Findings at Chest Radiography, US, CT, and MRI in Multisystem Inflammatory Syndrome in Children Associated with COVID-19. *Radiology* 2021; **298**: E1-E10 [PMID: 32584166 DOI: 10.1148/radiol.2020202543]

36 **Baratella E**, Crivelli P, Marrocchio C, Bozzato AM, Vito A, Madeddu G, Saderi L, Confalonieri M, Tenaglia L, Cova MA. Severity of lung involvement on chest X-rays in SARS-coronavirus-2 infected patients as a possible tool to predict clinical progression: an observational retrospective analysis of the relationship between radiological, clinical, and laboratory data. *J Bras Pneumol* 2020; **46**: e20200226 [PMID: 32965310 DOI: 10.36416/1806-3756/e20200226]

37 **de Jaegere TMH**, Krdzalic J, Fasen BACM, Kwee RM; COVID-19 CT Investigators South-East Netherlands (CISEN) study group. Radiological Society of North America Chest CT Classification System for Reporting COVID-19 Pneumonia: Interobserver Variability and Correlation with Reverse-Transcription Polymerase Chain Reaction. *Radiol Cardiothorac Imaging* 2020; **2**: e200213 [PMID: 33778589 DOI: 10.1148/ryct.2020200213]

38 **Or Caspi**, Michael J. Smart RBN. The Role of Chest Imaging in Patient Management During the COVID-19 Pandemic A Multinational Consensus Statement From the Fleischner Society. *Ann Oncol* 2020; 19-21

39 **Rubin GD**, Ryerson CJ, Haramati LB, Sverzellati N, Kanne JP, Raoof S, Schluger NW, Volpi A, Yim JJ, Martin IBK, Anderson DJ, Kong C, Altes T, Bush A, Desai SR, Goldin J, Goo JM, Humbert M, Inoue Y, Kauczor HU, Luo F, Mazzone PJ, Prokop M, Remy-Jardin M, Richeldi L, Schaefer-Prokop CM, Tomiyama N, Wells AU, Leung AN. The Role of Chest Imaging in Patient Management During the COVID-19 Pandemic: A Multinational Consensus Statement From the Fleischner Society. *Chest* 2020; **158**: 106-116 [PMID: 32275978 DOI: 10.1016/j.chest.2020.04.003]

40 **Palmucci S**, Mauro LA, Messina M, Russo B, Failla G, Milone P, Berretta M, Ettorre GC. Diffusion-weighted MRI in a liver protocol: its role in focal lesion detection. *World J Radiol* 2012; **4**: 302-310 [PMID: 22900131 DOI: 10.4329/wjr.v4.i7.302]

41 **Ali SA**, Abdelkawi MM. Incidentally recognized COVID-19 pneumonia in routine oncologic 18F-FDG PET/CT examinations: a local experience during pandemic era. *Egypt J Radiol Nucl Med* 2020; **51** [DOI: 10.1186/s43055-020-00333-9]

42 **Angelini V**, Villanacci A, Belotti A, Castagnoli F, Frittoli B, Corvino A, Brunetti A, Grazioli L. Incidental whole-body MRI evidence of COVID-19 in an asymptomatic patient in a high prevalence region. *Egypt J Radiol Nucl Med* 2020; **51** [DOI: 10.1186/s43055-020-00288-x]

43 **Di Girolamo M**, Muscogiuri E, Zucchelli A, Laghi A. An Incidental Diagnosis of SARS-CoV-2 Pneumonia With Magnetic Resonance Imaging. *Cureus* 2020; **12**: e12115 [PMID: 33489530 DOI: 10.7759/cureus.12115]

44 **Pallardy A**, Rousseau C, Labbe C, Liberge R, Bodet-Milin C, Kraeber-Bodere F, Fleury V. Incidental findings suggestive of COVID-19 in asymptomatic cancer patients undergoing 18F-FDG PET/CT in a low prevalence region. *Eur J Nucl Med Mol Imaging* 2021; **48**: 287-292 [PMID: 32860074 DOI: 10.1007/s00259-020-05014-3]

45 **Barrios-López JM**, Rego-García I, Muñoz Martínez C, Romero-Fábrega JC, Rivero Rodríguez M, Ruiz Giménez JA, Escamilla-Sevilla F, Mínguez-Castellanos A, Fernández Pérez MD. Ischaemic stroke and SARS-CoV-2 infection: a causal or incidental association? *Neurología* 2020; **35**: 295-302 [DOI: 10.1016/j.nrleng.2020.05.008]

46 **Tulchinsky M**, Fotos JS, Slonimsky E. Incidental CT Findings Suspicious for COVID-19-Associated Pneumonia on Nuclear Medicine Examinations: Recognition and Management Plan. *Clin Nucl Med* 2020; **45**: 531-533 [PMID: 32502091 DOI: 10.1097/RLU.0000000000003100]

47 **Ferrando-Castagnetto F**, Wakfie-Corieh CG, García AMB, García-Esquinas MG, Caro RMC, Delgado JLC. Incidental and simultaneous finding of pulmonary thrombus and COVID-19 pneumonia in a cancer patient derived to ^{18}F-FDG PET/CT. New pathophysiological insights from hybrid imaging. *Radiol Case Rep* 2020; **15**: 1803-1805 [PMID: 32788944 DOI: 10.1016/j.radcr.2020.07.032]

48 **Alrifai A**, El-Raey FM, Yousef AM, Zaky S. Ultrasound in Suspected Pneumonic COVID-19: Our Experience. *Int J Med Arts* 2020; **2**: 682-689 [DOI: 10.21608/ijma.2020.43493.1176]

49 **Iqbal M**, Shahbaz M, Qadeer O Bin, Nazir K, Naeem M, Afzal MS, Imran MB. Nuclear medicine practices during the COVID-19 pandemic—review of some recently published protocols. *Egypt J Radiol Nucl Med* 2020; **51**: 1-8 [DOI: 10.1186/s43055-020-00349-1]

50 **Jackson K**, Butler R, Aujayeb A. Lung ultrasound in the COVID-19 pandemic. *Postgrad Med J* 2021; **97**: 34-39 [PMID: 32895294 DOI: 10.1136/postgradmedj-2020-138137]

51 **Haft JW**, Atluri P, Ailawadi G, Engelman DT, Grant MC, Hassan A, Legare JF, Whitman GJR, Arora RC; Society of Thoracic Surgeons COVID-19 Task Force and the Workforce for Adult Cardiac and Vascular Surgery. Adult Cardiac Surgery During the COVID-19 Pandemic: A Tiered Patient Triage Guidance Statement. *Ann Thorac Surg* 2020; **110**: 697-700 [PMID: 32305286 DOI:

10.1016/j.athoracsur.2020.04.003]
52 **Ates OF**, Taydas O, Dheir H. Thorax Magnetic Resonance Imaging Findings in Patients with Coronavirus Disease (COVID-19). *Acad Radiol* 2020; **27**: 1373-1378 [PMID: 32830031 DOI: 10.1016/j.acra.2020.08.009]
53 **Kaiser Ururahy Nunes Fonseca E**, Chate RC, Neto RS, Ishikawa WY, Silva MMA, Yokoo P, Szarf G. Pulmonary Findings of COVID-19 Identified at Cardiac MRI. *Radiol Cardiothorac Imaging* 2020; **2**: e200193 [PMID: 33778575 DOI: 10.1148/ryct.2020200193]
54 **Langenbach MC**, Hokamp NG, Persigehl T, Bratke G. MRI appearance of COVID-19 infection. *Diagn Interv Radiol* 2020; **26**: 377-378 [PMID: 32352920 DOI: 10.5152/dir.2020.20152]
55 **Torkian P**, Rajebi H, Zamani T, Ramezani N, Kiani P, Akhlaghpoor S. Magnetic resonance imaging features of coronavirus disease 2019 (COVID-19) pneumonia: The first preliminary case series. *Clin Imaging* 2021; **69**: 261-265 [PMID: 33002753 DOI: 10.1016/j.clinimag.2020.09.002]
56 **Fields BKK**, Demirjian NL, Dadgar H, Gholamrezanezhad A. Imaging of COVID-19: CT, MRI, and PET. *Semin Nucl Med* 2021; **51**: 312-320 [PMID: 33288215 DOI: 10.1053/j.semnuclmed.2020.11.003]
57 **Deen SS**, Wetscherek M, Karia S, Godfrey EM. Diagnostic challenges of incidental lung lesions on liver MRI during the COVID-19 pandemic. *BMJ Case Rep* 2020; **13** [PMID: 32690573 DOI: 10.1136/bcr-2020-237430]
58 **Chetan MR**, Tsakok MT, Shaw R, Xie C, Watson RA, Wing L, Peschl H, Benamore R, MacLeod F, Gleeson FV. Chest CT screening for COVID-19 in elective and emergency surgical patients: experience from a UK tertiary centre. *Clin Radiol* 2020; **75**: 599-605 [PMID: 32593409 DOI: 10.1016/j.crad.2020.06.006]
59 **Siegel A**, Chang PJ, Jarou ZJ, Paushter DM, Harmath CB, Arevalo J Ben, Dachman A. Lung base findings of coronavirus disease (COVID-19) on abdominal CT in patients with predominant gastrointestinal symptoms. *Am J Roentgenol* 2020; **215**: 607-609 [DOI: 10.2214/ajr.20.23232]
60 **Hynes JP**, Moore P, Murray JG. Coronavirus Disease (COVID-19) Detected at the Lung Apices During CT Angiography in Acute Stroke Assessment. *AJR Am J Roentgenol* 2020; **215**: W40 [PMID: 32538694 DOI: 10.2214/AJR.20.23484]
61 **Dedeilia A**, Esagian SM, Ziogas IA, Giannis D, Katsaros I, Tsoulfas G. Pediatric surgery during the COVID-19 pandemic. *World J Clin Pediatr* 2020; **9**: 7-16 [PMID: 33014718 DOI: 10.5409/wjcp.v9.i2.7]
62 **Dong Y**, Mo X, Hu Y, Qi X, Jiang F, Jiang Z, Tong S. Epidemiology of COVID-19 Among Children in China. *Pediatrics* 2020; **145** [PMID: 32179660 DOI: 10.1542/peds.2020-0702]
63 **Gosain R**, Abdou Y, Singh A, Rana N, Puzanov I, Ernstoff MS. COVID-19 and Cancer: a Comprehensive Review. *Curr Oncol Rep* 2020; **22**: 53 [PMID: 32385672 DOI: 10.1007/s11912-020-00934-7]
64 **Setti L**, Kirienko M, Dalto SC, Bonacina M, Bombardieri E. FDG-PET/CT findings highly suspicious for COVID-19 in an Italian case series of asymptomatic patients. *Eur J Nucl Med Mol Imaging* 2020; **47**: 1649-1656 [PMID: 32342191 DOI: 10.1007/s00259-020-04819-6]
65 **Albano D**, Bertagna F, Bertoli M, Bosio G, Lucchini S, Motta F, Panarotto MB, Peli A, Camoni L, Bengel FM, Giubbini R. Incidental Findings Suggestive of COVID-19 in Asymptomatic Patients Undergoing Nuclear Medicine Procedures in a High-Prevalence Region. *J Nucl Med* 2020; **61**: 632-636 [PMID: 32238429 DOI: 10.2967/jnumed.120.246256]
66 **Mo A**, Brodin NP, Tomé WA, Garg MK, Kabarriti R. COVID-19 Incidentally Detected on PET/CT During Work-up for Locally Advanced Head and Neck Cancer. *In Vivo* 2020; **34**: 1681-1684 [PMID: 32503829 DOI: 10.21873/invivo.11961]
67 **Franceschi AM**, Clifton M, Ahmed O, Matthews R, Franceschi D. Incidental PET/CT Findings of Suspected COVID-19 in a Region of High Prevalence. *Cureus* 2020; **12**: e9716 [PMID: 32944437 DOI: 10.7759/cureus.9716]
68 **Wakfie-Corieh CG**, Blanes García AM, Ferrando-Castagnetto F, Valhondo-Rama R, Ortega Candil A, Rodríguez Rey C, Cabrera Martín MN, García-Esquinas MG, Couto Caro RM, Pedrera Canal M, Carreras Delgado JL. Assessment of extra-parenchymal lung involvement in asymptomatic cancer patients with COVID-19 pneumonia detected on ^{18}F-FDG PET-CT studies. *Eur J Nucl Med Mol Imaging* 2021; **48**: 768-776 [PMID: 32901353 DOI: 10.1007/s00259-020-05019-y]

World Journal of Radiology

Submit a Manuscript: https://www.f6publishing.com

World J Radiol 2022 January 28; 14(1): 13-18

DOI: 10.4329/wjr.v14.i1.13

ISSN 1949-8470 (online)

MINIREVIEWS

Chest radiological finding of COVID-19 in patients with and without diabetes mellitus: Differences in imaging finding

Sunay Gangadharan, Storm Parker, Fahad Wali Ahmed

ORCID number: Sunay Gangadharan 0000-0002-5491-142X; Storm Parker 0000-0001-9654-5221; Fahad Wali Ahmed 0000-0003-4100-1571.

Author contributions: Gangadharan S and Parker S contributed to writing the manuscript substantially; Ahmed FW conceived the idea of this article and contributed to writing, design and editing of the manuscript.

Conflict-of-interest statement: The authors declare that they have no competing or conflicts of interests.

Country/Territory of origin: United Kingdom

Specialty type: Radiology, nuclear medicine and medical imaging

Provenance and peer review: Invited article; Externally peer reviewed.

Peer-review model: Single blind

Peer-review report's scientific quality classification

Grade A (Excellent): A
Grade B (Very good): B
Grade C (Good): 0
Grade D (Fair): 0
Grade E (Poor): 0

Open-Access: This article is an open-access article that was

Sunay Gangadharan, Storm Parker, Department of Radiology, University Hospitals Sussex NHS Foundation Trust, Brighton BN2 5BE, United Kingdom

Fahad Wali Ahmed, Department of Medical Oncology, King Faisal Specialist Hospital and Research Centre, Madinah 42522, Saudi Arabia

Corresponding author: Fahad Wali Ahmed, FRCP, MBBS, PhD, Consultant Physician-Scientist, Department of Medical Oncology, King Faisal Specialist Hospital and Research Centre, 7345, Madinah 42522, Saudi Arabia. fahadwali@yahoo.com

Abstract

The pandemic of novel coronavirus disease 2019 (COVID-19) is caused by severe acute respiratory syndrome coronavirus 2 (SARS-CoV-2). Diabetes mellitus is a risk factor for developing severe illness and a leading cause of death in patients with COVID-19. Diabetes can precipitate hyperglycaemic emergencies and cause prolonged hospital admissions. Insulin resistance is thought to cause endothelial dysfunction, alveolar capillary micro-angiopathy and interstitial lung fibrosis through pro-inflammatory pathways. Autopsy studies have also demonstrated the presence of microvascular thrombi in affected sections of lung, which may be associated with diabetes. Chest imaging using x-ray (CXR) and computed tomography (CT) of chest is used to diagnose, assess disease progression and severity in COVID-19. This article reviews current literature regarding chest imaging findings in patients with diabetes affected by COVID-19. A literature search was performed on PubMed. Patients with diabetes infected with SARS-CoV-2 are likely to have more severe infective changes on CXR and CT chest imaging. Severity of airspace consolidation on CXR is associated with higher mortality, particularly in the presence of co-morbidities such as ischaemic heart disease. Poorly controlled diabetes is associated with more severe acute lung injury on CT. However, no association has been identified between poorly-controlled diabetes and the incidence of pulmonary thromboembolism in patients with COVID-19.

Key Words: Diabetes mellitus; COVID-19; Chest X-Ray; Chest imaging using x-ray; Computed tomography of chest

Received: March 30, 2021
Peer-review started: March 30, 2021
First decision: October 17, 2021
Revised: November 16, 2021
Accepted: December 28, 2021
Article in press: December 28, 2021
Published online: January 28, 2022

P-Reviewer: Liu D
S-Editor: Wang LL
L-Editor: A
P-Editor: Wang LL

Core Tip: COVID-19 infection can present as multifocal peripheral airspace changes on chest imaging using x-ray (CXR). Ground-glass opacities are the most common computed tomography finding in coronavirus disease 2019 (COVID-19). Post admission daily bloody glucose readings are a strong predictor for COVID-19 CXR changes that indicate poorer outcomes. Poorly controlled diabetes is associated with increased volumes of ground-glass opacity and consolidation. Diabetes is also linked with endothelial dysfunction and hypercoagulability, which may result in the formation of microvascular thrombi in peripheral segments of lung.

Citation: Gangadharan S, Parker S, Ahmed FW. Chest radiological finding of COVID-19 in patients with and without diabetes mellitus: Differences in imaging finding. *World J Radiol* 2022; 14(1): 13-18
URL: https://www.wjgnet.com/1949-8470/full/v14/i1/13.htm
DOI: https://dx.doi.org/10.4329/wjr.v14.i1.13

INTRODUCTION

The world is currently undergoing a significant healthcare crisis due to the severe acute respiratory syndrome coronavirus 2 (SARS-CoV-2) pandemic. In March 2020, World Health Organisation declared a pandemic caused by SARs-CoV-2. SARS-CoV-2 was named novel coronavirus disease 2019 (COVID-19). Hospitals in different countries have been overwhelmed with patients suffering from COVID-19. So far, 2.78 million people have died as of 29th March 2021[1].

Diabetes mellitus (DM) is a risk factor associated with severe illness in SARS-CoV-2 infection, precipitating hyperglycaemic emergencies such as diabetic ketoacidosis (DKA) and hyperosmolar hyperglycaemic state (HHS)[2]. A third of deaths in England up to May 2020 related to COVID-19 occurred in people with DM[3]. Patients with DM are more likely to stay longer in hospital[4]. DM can cause a deregulated immune system predisposing to infection; the endothelial angiotensin-converting enzyme 2 (ACE2) receptor responsible for SARS-CoV-2 invasion in human cells has reduced expression in patients of DM, possibly due to glycosylation[5]. Insulin resistance and altered glucose homeostasis have been thought to cause alveolar capillary micro-angiopathy and interstitial fibrosis *via* over-inflammation[6].

A normal chest radiograph does not exclude COVID-19 pneumonia, and no single feature on a radiograph is diagnostic[7]. However, a combination of multifocal peripheral airspace changes often found bilaterally may be present in COVID-19. Due to limited PCR testing capacity in the early d of the pandemic, in addition to its low sensitivity and waiting period of up to 2 d, many clinicians turned to chest computed tomography (CT) for early detection of COVID-19.

Studies have reported the negative predictive value of using CT to be above 90%[8, 9]. Chest CT was used to detect subtle radiological changes consistent with COVID-19 in patients where the chest radiograph was reported to be normal or indeterminate. Typical CT findings seen in patients with COVID-19 include peripheral ground-glass opacities (GGO), which progresses to consolidation and interstitial thickening within GGO areas known as 'crazy paving pattern'[10,11]. These non-specific imaging findings of acute lung injury are indistinguishable from other types of viral pneumonia or interstitial lung diseases, thereby limiting the use of CT as a confirmatory diagnostic test in COVID-19.

This article reviews current literature regarding chest imaging changes in patients with DM affected by COVID-19.

LITERATURE SEARCH

A literature search was conducted on PubMed using the keywords of COVID-19 or Coronavirus; CXR or x-ray or radiograph; CT chest; CTPA or pulmonary embolism or PE; and diabetes mellitus or diabetes within the title or abstract.

Chest Radiography

Studies have shown chest radiographs of patients with DM to have increased bilateral airspace consolidation compared to patients without DM[12,13]. The severity of chest radiograph changes in patients with DM has indicated a significant correlation with mortality, as evidenced in multivariate analysis by Cellina *et al*[14]. Patients with bilateral peripheral alveolar disease (Figure 1) often present at a later stage and have a worse outcome. However, some patients with COVID-19 have preserved lung compliance despite being acutely hypoxaemic, suggesting poorer outcomes result from processes other than alveolar damage[15].

In some studies, DM alone was not associated with an increased risk of intensive care unit admission or death. Still, it was associated with cardiovascular disease as a driver of poorer outcomes. Izzi-Engbeaya *et al*[16] studied 889 patients admitted to London hospitals with COVID-19, and their outcomes found patients with DM were found to have a 33% increased risk of death or ICU admission if they also have ischaemic heart disease. Surprisingly, a similar severity of CXR changes was demonstrated for patients with and without DM. Mozzini *et al*[17] (2021) studied 50 Italian patients with COVID-19, 32% of which had DM. Patients with hypertension or DM had 8 times greater risk of having more severe CXR changes.

COVID-19 infection in patients with DM leads to hyperglycaemia, and in some cases leads to DKA and/or HHS[2]. It has been shown that there is a positive correlation between daily average blood glucose readings and CXR findings. Similarly, post-admission day-1 hyperglycaemia was found to be the strongest independent predictor for COVID-19 CXR changes. This was a stronger predictor than age, body mass index, and temperature[18].

Chest computed tomography

Earlier studies employed semi-quantitative methods to analyse chest computed tomography (CT) findings (Figure 2) in patients with COVID-19[19,20]. This involved a single, or multiple experienced radiologists blinded to clinical parameters and assigning a score based on the severity of findings. Higher chest CT scores have been found in patients with DM, suggesting more severe COVID-19 pneumonia when compared with patients without DM[19]. Findings by Iacobellis *et al*[18] suggested day-1 hyperglycaemia as a predictor of COVID-19 severity on CXR were confirmed on CT.

Patients with poorly-controlled DM are likely to have more severe COVID-19 pneumonia. A recent study by Lu *et al*[21] using a quantitative artificial intelligence algorithm found parameters including the percentage of ground glass volume (PGV) and percentage of consolidation volume (PCV), positively correlated with fasting blood glucose and HbA1c. Unlike semi-quantitative methods, results using this approach were not affected by inter- and intra-observer variability. Raoufi *et al*[20] used a semi-quantitative method to study 117 patients with DM in Iran and found no significant difference in patients with well-controlled (defined as maintaining glycaemic variability between 3.9-10 mmol/L) and poorly-controlled DM. However, the poorly-controlled group contained almost 4 times the number of patients (93 *vs* 24). Furthermore, the median age of patients in the well-controlled group were older (75 *vs* 62 years) which may have been a confounding factor for this negative result[20].

Studies have shown mortality rates to be higher among patients with poorly-controlled DM and COVID-19 than the general population with COVID-19[22,23]. In particular, high HbA1c levels have been linked with inflammation and hypercoagulability, resulting in an increased mortality rate in patients with DM suffering from COVID-19[24]. However, the accuracy of these results may be influenced by other co-morbidities such as ischaemic heart disease and stroke. No large-scale studies have yet shown an association between worse CT findings and mortality in DM.

A high incidence of venous and arterial thrombotic complications in critically ill patients with COVID-19 has been reported previously[25]. Recent literature based on autopsy studies shows that the origin of thrombotic lesions in COVID-19 is largely unknown. Lung histopathological analysis found multiple thrombi in small to medium pulmonary arteries giving rise to the theory of COVID-19 associated immunothrombosis, contrary to the conventional thromboembolic pathomechanism of PE [26,27]. In situ microvascular thrombosis or immunothrombosis occurs due to alveolar injury, inflammatory storm and disruption of the thromboprotective pulmonary vascular endothelium. COVID-19 clinical outcomes are worse in patients with diseases associated with endothelial dysfunction such as systemic hypertension, DM and obesity[28].

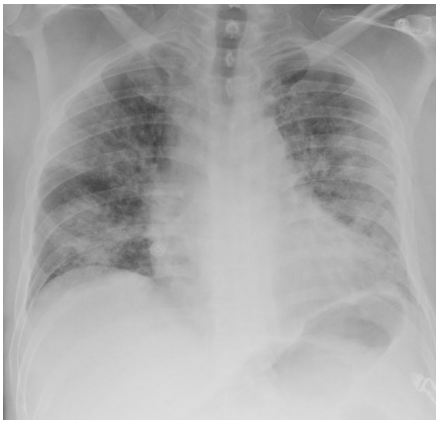

Figure 1 The Chest X-Ray demonstrates multiple bilateral peripheral predominant airspace opacities. There is no pleural effusion.

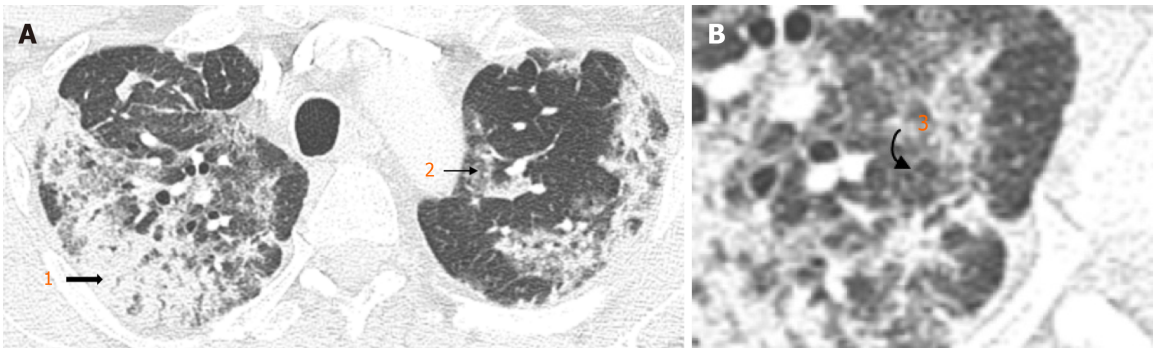

Figure 2 Chest X-Ray. A: Typical appearances of COVID-19 infection: Bilateral peripheral consolidation (1. block arrow), multifocal groundglass opacities (2. straight arrow); B: Some areas of smooth intralobular septal thickening (3. curved arrow).

The radiological finding of subsegmental or segmental thrombi in peripheral segments of lung affected by acute lung injury and the absence of deep vein thrombosis (DVT) in patients with COVID-19 infection, assumes the theory of immunothrombosis[27]. Monfardini *et al*[29] found 76% of patients with a moderate-high pre-test probability of PE and positive D-dimer level (a fibrin degradation product measured to help diagnose thrombosis), had positive CTPA findings. Nevertheless, only 15% of these patients were associated with ultrasound detected lower limb DVT[29], suggesting the remainder probably represented immunothrombosis. A meta-analysis of twenty-seven studies by Suh *et al*[30] revealed DVT was only found in 42% of patients with PE.

As yet, no large-scale studies have reported a link between pulmonary thromboembolism and DM in patients with COVID-19. Kaminetzky *et al*[31] found patients with DM were significantly less frequently observed to have CTPA examinations. Of 23 patients identified to have PE in this study, only 3 had DM; however, this finding may be attributed to the small sample size.

CONCLUSION

DM predisposes to immune deregulation and reduced expression of the ACE2 receptor, leading to severe acute lung injury[5,6]. Studies have proven a link between DM and more severe airspace consolidation based on chest x-ray findings[12,13]. Furthermore, CXR evidence suggests DM is associated with higher mortality in COVID-19. The exact pathogenesis of this is unclear but may be related to microvascular immunothrombosis[26,28].

There is now quantitative evidence to suggest poorly controlled DM is associated with more severe lung injury on CT[21]. However, no large-scale studies have investigated a direct link between CT findings and mortality in DM. Although the incidence of PE is greater in critically ill patients with COVID-19[25], no link has been established between poorly controlled DM and the risk of PE.

As new research into COVID-19 is produced and evidence emerges from autopsy studies, the understanding of pathobiology of the disease has evolved. However, there remains scope for future research; particularly whether small pulmonary thromboses represent venous thromboembolism, immunothrombosis, or a combination of both. Furthermore, a direct link between DM and immunothrombosis may help to guide future management strategies.

ACKNOWLEDGEMENT

We will like to thank Kirresh OZ for providing radiographs.

REFERENCES

1 **CCSE Dashboard [Internet]**. COVID-19 Dashboard by the Center for Systems Science and Engineering (CSSE) at Johns Hopkins University (JHU). [cited 20 February 2021]. Available from: https://www.arcgis.com/apps/opsdashboard/index.html#/bda7594740fd40299423467b48e9ecf6

2 **Rafique S**, Ahmed FW. A Case of Combined Diabetic Ketoacidosis and Hyperosmolar Hyperglycemic State in a Patient With COVID-19. *Cureus* 2020; **12**: e8965 [PMID: 32766007 DOI: 10.7759/cureus.8965]

3 **Barron E**, Bakhai C, Kar P, Weaver A, Bradley D, Ismail H, Knighton P, Holman N, Khunti K, Sattar N, Wareham NJ, Young B, Valabhji J. Associations of type 1 and type 2 diabetes with COVID-19-related mortality in England: a whole-population study. *Lancet Diabetes Endocrinol* 2020; **8**: 813-822 [PMID: 32798472 DOI: 10.1016/S2213-8587(20)30272-2]

4 **Ahmed FW**, Kirresh OZ, Robinson AV. A Retrospective Study Assessing the Effect of Diabetes on Mortality in Patients With COVID-19 at a Teaching Hospital in the United Kingdom [Internet]. 2021. [cited 20 February 2021]. Available from: https://www.cureus.com/articles/54241

5 **Sartore G**, Ragazzi E, Faccin L, Lapolla A. A role of glycation and methylation for SARS-CoV-2 infection in diabetes? *Med Hypotheses* 2020; **144**: 110247 [PMID: 33254553 DOI: 10.1016/j.mehy.2020.110247]

6 **Sardu C**, Gargiulo G, Esposito G, Paolisso G, Marfella R. Impact of diabetes mellitus on clinical outcomes in patients affected by Covid-19. *Cardiovasc Diabetol* 2020; **19**: 76 [PMID: 32527257 DOI: 10.1186/s12933-020-01047-y]

7 **Cleverley J**, Piper J, Jones MM. The role of chest radiography in confirming covid-19 pneumonia. *BMJ* 2020; **370**: m2426 [PMID: 32675083 DOI: 10.1136/bmj.m2426]

8 **Ai T**, Yang Z, Hou H, Zhan C, Chen C, Lv W, Tao Q, Sun Z, Xia L. Correlation of Chest CT and RT-PCR Testing for Coronavirus Disease 2019 (COVID-19) in China: A Report of 1014 Cases. *Radiology* 2020; **296**: E32-E40 [PMID: 32101510 DOI: 10.1148/radiol.2020200642]

9 **Herpe G**, Lederlin M, Naudin M, Ohana M, Chaumoitre K, Gregory J, Vilgrain V, Freitag CA, De Margerie-Mellon C, Flory V, Ludwig M, Mondot L, Fitton I, Jacquier ARR, Ardilouze P, Petit I, Gervaise A, Bayle O, Crombe A, Mekuko Sokeng M, Thomas C, Henry G, Bliah V, Le Tat T, Guillot MS, Gendrin P, Garetier M, Bertolle E, Montagne C, Langlet B, Kalaaji A, Kayayan H, Desmots F, Dhaene B, Saulnier PJ, Guillevin R, Bartoli JM, Beregi JP, Tasu JP. Efficacy of Chest CT for COVID-19 Pneumonia Diagnosis in France. *Radiology* 2021; **298**: E81-E87 [PMID: 32870139 DOI: 10.1148/radiol.2020202568]

10 **Ufuk F**, Savaş R. Chest CT features of the novel coronavirus disease (COVID-19). *Turk J Med Sci* 2020; **50**: 664-678 [PMID: 32394687 DOI: 10.3906/sag-2004-331]

11 **Ye Z**, Zhang Y, Wang Y, Huang Z, Song B. Chest CT manifestations of new coronavirus disease 2019 (COVID-19): a pictorial review. *Eur Radiol* 2020; **30**: 4381-4389 [PMID: 32193638 DOI: 10.1007/s00330-020-06801-0]

12 **Elemam NM**, Hannawi H, Salmi IA, Naeem KB, Alokaily F, Hannawi S. Diabetes mellitus as a comorbidity in COVID-19 infection in the United Arab Emirates. *Saudi Med J* 2021; **42**: 170-180 [PMID: 33563736 DOI: 10.15537/smj.2021.2.25700]

13 **Bhandari S**, Rankawat G, Singh A, Gupta V, Kakkar S. Impact of glycemic control in diabetes mellitus on management of COVID-19 infection. *Int J Diabetes Dev Ctries* 2020; 1-6 [PMID: 32905072 DOI: 10.1007/s13410-020-00868-7]

14 **Cellina M**, Gibelli D, Valenti Pittino C, Toluian T, Marino P, Oliva G. Risk Factors of Fatal Outcome in Patients With COVID-19 Pneumonia. *Disaster Med Public Health Prep* 2020; 1-8 [PMID: 32907676 DOI: 10.1017/dmp.2020.346]

15 **Gattinoni L**, Coppola S, Cressoni M, Busana M, Rossi S, Chiumello D. COVID-19 Does Not Lead to a "Typical" Acute Respiratory Distress Syndrome. *Am J Respir Crit Care Med* 2020; **201**: 1299-1300 [PMID: 32228035 DOI: 10.1164/rccm.202003-0817LE]

16 **Izzi-Engbeaya C**, Distaso W, Amin A, Yang W, Idowu O, Kenkre JS, Shah RJ, Woin E, Shi C, Alavi N, Bedri H, Brady N, Blackburn S, Leczycka M, Patel S, Sokol E, Toke-Bjolgerud E, Qayum A, Abdel-Malek M, Hope DCD, Oliver NS, Bravis V, Misra S, Tan TM, Hill NE, Salem V. Adverse outcomes in COVID-19 and diabetes: a retrospective cohort study from three London teaching

hospitals. *BMJ Open Diabetes Res Care* 2021; **9** [PMID: 33408084 DOI: 10.1136/bmjdrc-2020-001858]

17 **Mozzini C**, Cicco S, Setti A, Racanelli V, Vacca A, Calciano L, Pesce G, Girelli D. Spotlight on Cardiovascular Scoring Systems in Covid-19: Severity Correlations in Real-world Setting. *Curr Probl Cardiol* 2021; **46**: 100819 [PMID: 33631706 DOI: 10.1016/j.cpcardiol.2021.100819]

18 **Iacobellis G**, Penaherrera CA, Bermudez LE, Bernal Mizrachi E. Admission hyperglycemia and radiological findings of SARS-CoV2 in patients with and without diabetes. *Diabetes Res Clin Pract* 2020; **164**: 108185 [PMID: 32360710 DOI: 10.1016/j.diabres.2020.108185]

19 **Guo W**, Li M, Dong Y, Zhou H, Zhang Z, Tian C, Qin R, Wang H, Shen Y, Du K, Zhao L, Fan H, Luo S, Hu D. Diabetes is a risk factor for the progression and prognosis of COVID-19. *Diabetes Metab Res Rev* 2020; e3319 [PMID: 32233013 DOI: 10.1002/dmrr.3319]

20 **Raoufi M**, Khalili S, Mansouri M, Mahdavi A, Khalili N. Well-controlled *vs* poorly-controlled diabetes in patients with COVID-19: Are there any differences in outcomes and imaging findings? *Diabetes Res Clin Pract* 2020; **166**: 108286 [PMID: 32592836 DOI: 10.1016/j.diabres.2020.108286]

21 **Lu X**, Cui Z, Pan F, Li L, Liang B, Yang L, Zheng C. Glycemic status affects the severity of coronavirus disease 2019 in patients with diabetes mellitus: an observational study of CT radiological manifestations using an artificial intelligence algorithm. *Acta Diabetol* 2021; **58**: 575-586 [PMID: 33420614 DOI: 10.1007/s00592-020-01654-x]

22 **Wu ZH**, Tang Y, Cheng Q. Diabetes increases the mortality of patients with COVID-19: a meta-analysis. *Acta Diabetol* 2021; **58**: 139-144 [PMID: 32583078 DOI: 10.1007/s00592-020-01546-0]

23 **Zhu L**, She ZG, Cheng X, Qin JJ, Zhang XJ, Cai J, Lei F, Wang H, Xie J, Wang W, Li H, Zhang P, Song X, Chen X, Xiang M, Zhang C, Bai L, Xiang D, Chen MM, Liu Y, Yan Y, Liu M, Mao W, Zou J, Liu L, Chen G, Luo P, Xiao B, Zhang Z, Lu Z, Wang J, Lu H, Xia X, Wang D, Liao X, Peng G, Ye P, Yang J, Yuan Y, Huang X, Guo J, Zhang BH. Association of Blood Glucose Control and Outcomes in Patients with COVID-19 and Pre-existing Type 2 Diabetes. *Cell Metab* 2020; **31**: 1068-1077.e3 [PMID: 32369736 DOI: 10.1016/j.cmet.2020.04.021]

24 **Wang Z**, Du Z, Zhu F. Glycosylated hemoglobin is associated with systemic inflammation, hypercoagulability, and prognosis of COVID-19 patients. *Diabetes Res Clin Pract* 2020; **164**: 108214 [PMID: 32416121 DOI: 10.1016/j.diabres.2020.108214]

25 **Klok FA**, Kruip MJHA, van der Meer NJM, Arbous MS, Gommers D, Kant KM, Kaptein FHJ, van Paassen J, Stals MAM, Huisman MV, Endeman H. Confirmation of the high cumulative incidence of thrombotic complications in critically ill ICU patients with COVID-19: An updated analysis. *Thromb Res* 2020; **191**: 148-150 [PMID: 32381264 DOI: 10.1016/j.thromres.2020.04.041]

26 **Patel BV**, Arachchillage DJ, Ridge CA, Bianchi P, Doyle JF, Garfield B, Ledot S, Morgan C, Passariello M, Price S, Singh S, Thakuria L, Trenfield S, Trimlett R, Weaver C, Wort SJ, Xu T, Padley SPG, Devaraj A, Desai SR. Pulmonary Angiopathy in Severe COVID-19: Physiologic, Imaging, and Hematologic Observations. *Am J Respir Crit Care Med* 2020; **202**: 690-699 [PMID: 32667207]

27 **van Dam LF**, Kroft LJM, van der Wal LI, Cannegieter SC, Eikenboom J, de Jonge E, Huisman MV, Klok FA. Clinical and computed tomography characteristics of COVID-19 associated acute pulmonary embolism: A different phenotype of thrombotic disease? *Thromb Res* 2020; **193**: 86-89 [PMID: 32531548]

28 **Loo J**, Spittle DA, Newnham M. COVID-19, immunothrombosis and venous thromboembolism: biological mechanisms. *Thorax* 2021; **76**: 412-420 [PMID: 33408195 DOI: 10.1136/thoraxjnl-2020-216243]

29 **Monfardini L**, Morassi M, Botti P, Stellini R, Bettari L, Pezzotti S, Alì M, Monaco CG, Magni V, Cozzi A, Schiaffino S, Bnà C. Pulmonary thromboembolism in hospitalised COVID-19 patients at moderate to high risk by Wells score: a report from Lombardy, Italy. *Br J Radiol* 2020; **93**: 20200407 [PMID: 32735448 DOI: 10.1259/bjr.20200407]

30 **Suh YJ**, Hong H, Ohana M, Bompard F, Revel MP, Valle C, Gervaise A, Poissy J, Susen S, Hékimian G, Artifoni M, Periard D, Contou D, Delaloye J, Sanchez B, Fang C, Garzillo G, Robbie H, Yoon SH. Pulmonary Embolism and Deep Vein Thrombosis in COVID-19: A Systematic Review and Meta-Analysis. *Radiology* 2021; **298**: E70-E80 [PMID: 33320063 DOI: 10.1148/radiol.2020203557]

31 **Kaminetzky M**, Moore W, Fansiwala K, Babb JS, Kaminetzky D, Horwitz LI, McGuinness G, Knoll A, Ko JP. Pulmonary Embolism at CT Pulmonary Angiography in Patients with COVID-19. *Radiol Cardiothorac Imaging* 2020; **2**: e200308 [PMID: 33778610 DOI: 10.1148/ryct.2020200308]

World Journal of Radiology

Submit a Manuscript: https://www.f6publishing.com

World J Radiol 2022 January 28; 14(1): 19-29

DOI: 10.4329/wjr.v14.i1.19

ISSN 1949-8470 (online)

ORIGINAL ARTICLE

Retrospective Cohort Study

Effect of training on resident inter-reader agreement with American College of Radiology Thyroid Imaging Reporting and Data System

Yang Du, Meredith Bara, Prayash Katlariwala, Roger Croutze, Katrin Resch, Jonathan Porter, Medica Sam, Mitchell P Wilson, Gavin Low

ORCID number: Yang Du 0000-0002-9150-2932; Meredith Bara 0000-0002-0565-050X; Prayash Katlariwala 0000-0002-5822-1071; Roger Croutze 0000-0002-0060-2170; Katrin Resch 0000-0001-6654-3153; Jonathan Porter 0000-0002-8067-1722; Medica Sam 0000-0002-3962-633X; Mitchell P Wilson 0000-0002-1630-5138; Gavin Low 0000-0002-4959-8934.

Author contributions: Du Y, Bara M and Low G designed the study; Du Y, Bara M, Croutze R, Resch K, Porter J, Sam M, Wilson MP and Low G performed the research; Du Y, Bara M, Katlariwala P, Low G and Wilson MP analyzed the data and wrote the manuscript; all authors have read and approved the final manuscript.

Institutional review board statement: This retrospective, single-institution observational study was approved by the institutional Health Research Ethics Board (Pro 00104708).

Informed consent statement: This study was exempted from obtaining informed consent.

Conflict-of-interest statement: The authors have no conflict of interest to declare.

Data sharing statement: The raw

Yang Du, Meredith Bara, Prayash Katlariwala, Roger Croutze, Katrin Resch, Jonathan Porter, Medica Sam, Mitchell P Wilson, Gavin Low, Department of Radiology and Diagnostic Imaging, University of Alberta, Edmonton T6G 2B7, Alberta, Canada

Corresponding author: Yang Du, BSc, FRCPC, MD, Doctor, Staff Physician, Department of Radiology and Diagnostic Imaging, University of Alberta, 2A2.41 WMC, 8440-112 St NW, Edmonton T6G 2B7, Alberta, Canada. yang.du@usask.ca

Abstract

BACKGROUND

The American College of Radiology Thyroid Imaging Reporting and Data System (ACR TI-RADS) was introduced to standardize the ultrasound characterization of thyroid nodules. Studies have shown that ACR-TIRADS reduces unnecessary biopsies and improves consistency of imaging recommendations. Despite its widespread adoption, there are few studies to date assessing the inter-reader agreement amongst radiology trainees with limited ultrasound experience. We hypothesize that in PGY-4 radiology residents with no prior exposure to ACR TI-RADS, a statistically significant improvement in inter-reader reliability can be achieved with a one hour training session.

AIM

To evaluate the inter-reader agreement of radiology residents in using ACR TI-RADS before and after training.

METHODS

A single center retrospective cohort study evaluating 50 thyroid nodules in 40 patients of varying TI-RADS levels was performed. Reference standard TI-RADS scores were established through a consensus panel of three fellowship-trained staff radiologists with between 1 and 14 years of clinical experience each. Three PGY-4 radiology residents (trainees) were selected as blinded readers for this study. Each trainee had between 4 to 5 mo of designated ultrasound training. No trainee had received specialized TI-RADS training prior to this study. Each of the readers independently reviewed the 50 testing cases and assigned a TI-RADS score to each case before and after TI-RADS training performed 6 wk apart. Fleiss kappa was used to measure the pooled inter-reader agreement. The relative diagnostic performance of readers, pre- and post-training, when compared

dataset is available from the corresponding author at yang.du@usask.ca. Consent for data sharing was not obtained but the presented data are anonymized and risk of identification is low.

STROBE statement: Guidelines of the STROBE statement have been adopted.

Country/Territory of origin: Canada

Specialty type: Radiology, nuclear medicine and medical imaging

Provenance and peer review: Unsolicited article; Externally peer reviewed.

Peer-review model: Single blind

Peer-review report's scientific quality classification
Grade A (Excellent): A, A
Grade B (Very good): B
Grade C (Good): 0
Grade D (Fair): 0
Grade E (Poor): 0

Received: October 12, 2021
Peer-review started: October 12, 2021
First decision: December 9, 2021
Revised: December 21, 2021
Accepted: January 11, 2022
Article in press: January 11, 2022
Published online: January 28, 2022

P-Reviewer: Beck-Razi N, Lee KS, Naganuma H
S-Editor: Wang LL
L-Editor: A
P-Editor: Wang LL

against the reference standard.

RESULTS
There were 33 females and 7 males with a mean age of 56.6 ± 13.6 years. The mean nodule size was 19 ± 14 mm (range from 5 to 63 mm). A statistically significant superior inter-reader agreement was found on the post-training assessment compared to the pre-training assessment for the following variables: 1. "Shape" (k of 0.09 [slight] pre-training *vs* 0.67 [substantial] post-training, $P < 0.001$), 2. "Echogenic foci" (k of 0.28 [fair] pre-training *vs* 0.45 [moderate] post-training, $P = 0.004$), 3. 'TI-RADS level' (k of 0.14 [slight] pre-training *vs* 0.36 [fair] post-training, $P < 0.001$) and 4. 'Recommendations' (k of 0.36 [fair] pre-training *vs* 0.50 [moderate] post-training, $P = 0.02$). No significant differences between the pre- and post-training assessments were found for the variables 'composition', 'echogenicity' and 'margins'. There was a general trend towards improved pooled sensitivity with TI-RADS levels 1 to 4 for the post-training assessment while the pooled specificity was relatively high (76.6%-96.8%) for all TI-RADS level.

CONCLUSION
Statistically significant improvement in inter-reader agreement in the assigning TI-RADS level and recommendations after training is observed. Our study supports the use of dedicated ACR TI-RADS training in radiology residents.

Key Words: Thyroid; Thyroid nodule; American College of Radiology Thyroid Imaging Reporting and Data System; Inter-reader agreement; Ultrasound

Core Tip: There is a statistically significant improvement in inter-reader agreement among radiology trainees with limited ultrasound experience using the American College of Radiology Thyroid Imaging Reporting and Data System (TI-RADS) after training for TI-RADS grading and recommendations. This study demonstrates the learnability of TI-RADS in radiology trainees.

Citation: Du Y, Bara M, Katlariwala P, Croutze R, Resch K, Porter J, Sam M, Wilson MP, Low G. Effect of training on resident inter-reader agreement with American College of Radiology Thyroid Imaging Reporting and Data System. *World J Radiol* 2022; 14(1): 19-29
URL: https://www.wjgnet.com/1949-8470/full/v14/i1/19.htm
DOI: https://dx.doi.org/10.4329/wjr.v14.i1.19

INTRODUCTION

Thyroid nodules are detected in more than 50% of healthy individuals with approximately 95% representing asymptomatic incidental nodules[1-3]. Moreover, an increasing number of thyroid nodules are being detected in recent years on account of improved quality and increased frequency of medical imaging[4]. Although most thyroid nodules are benign and do not require treatment, adequate characterization is necessary in order to identify potentially malignant nodules[1-3]. The American College of Radiology Thyroid Imaging Reporting and Data System (ACR TI-RADS) was therefore introduced to standardize the ultrasound characterization of thyroid nodules based on 5 morphologic categories (composition, echogenicity, shape, margins, and echogenic foci). A TI-RADS score is obtained to represent the level of suspicion for cancer and further direct the need for follow-up and/or tissue sampling [5]. First published in 2017, ACR TI-RADS has been widely adopted by many centers worldwide. Studies have shown that ACR-TIRADS reduces unnecessary biopsies and improves consistency of imaging recommendations[6,7].

Despite its widespread adoption, there are few studies available to date assessing the inter-reader reliability of TI-RADS amongst radiology trainees with limited ultrasound experience. A single-institutional study performed in China by Teng *et al* [8] evaluated three trainees with less than three months of ultrasound experience,

demonstrating fair to almost perfect agreement amongst readers for TI-RADS categorization, with improved agreement and diagnostic accuracy after training. To our knowledge, no similar inter-reader agreement studies have been performed in North American trainees. The purpose of this study is to evaluate the inter-reader reliability amongst radiology trainees before and after designated TI-RADS training in a North American institution.

MATERIALS AND METHODS

This retrospective, single-institution observational study was approved by the institutional Health Research Ethics Board (Pro 00104708). This study was exempted from obtaining informed consent. A retrospective review of the local Picture Archiving and Communication System (PACS) was performed to identify thyroid ultrasound studies containing thyroid nodules between July 1, 2019 to July 31, 2020. Included cases required at least 1 thyroid nodule (minimal dimension of 5 mm) with both transverse and sagittal still images and cine video recording in at least 1 plane. Nodules with non-diagnostic image quality, incomplete nodule visualization, and absence of a cine clip covering the entirety of the nodule were excluded. The type of ultrasound make, model, or platform were not considered in the selection process.

Eighty consecutive thyroid nodules meeting eligibility criteria were selected by 2 authors (YD, 6 years clinical experience; MB, 3 years clinical experience) from the eligible ultrasound examinations. A single case could include more than one nodule if sufficient imaging was available to meet inclusion criteria for multiple nodules. Still images of each nodule in both transverse and sagittal planes as well as at least 1 cine video clip of the nodule were saved in a teaching file hosted on our institutional Picture Archiving and Communication System. Each nodule and its representative images/cine clips were saved separately. If a single patient had two nodules, the relevant images and cine clips for each nodule were saved as separate case numbers. Of these, 50 cases were allocated into the "testing" group and 30 cases into the "training" group. Non-random group selection was performed to allow an approximately even distribution of TI-RADS categories within each group and to prevent under-representation of any category. A steering committee consisting of 2 authors including the principal investigator (YD, MB) attempted to evenly divide cases of differentiating difficulty equally between "testing" and "training" groups. This variable approach was selected over a pathological gold standard in an attempt to reduce referral bias in the "testing" group, a situation likely encountered by Teng *et al* [8] where 61% (245/400) of included nodules were pathologically malignant. The trainees were blinded to the distribution approach of the "testing" group.

All patient identifiers were removed apart from age and gender. All cases were evaluated by a consensus review of 3 independent fellowship-trained board-certified staff radiologists with between 1 and 14 years of clinical experience each (GL, MW, MS). Any disagreement on the scoring of nodules for the ACR TI-RADS level was resolved by re-review and consensus discussion. Findings on the consensus review were recorded and set as the standard of reference. This approach has been used in other recent inter-reader reliability studies assessing ACR Reporting and Data Systems [9].

Three PGY-4 radiology residents (trainees) were selected as blinded readers for this study. Each trainee had between 4 to 5 mo of designated ultrasound training, in addition to non-designated ultrasound training on other rotations throughout their training. No trainee had received specialized TI-RADS training prior to this study. Each of the readers independently reviewed the 50 testing cases and assigned TI-RADS score to each case. The readers were provided with a summary chart detailing the ACR TI-RADS classification as described in the ACR TI-RADS White Paper and had access to an online TI-RADS calculator (https://tiradscalculator.com) at the time of independent review[5]. The readers were instructed to assign TI-RADS points for each category including composition, echogenicity, shape, margins, echogenic foci, and to determine the TI-RADS level and ACR TI-RADS recommendations. The pre-training responses were entered into an online survey generated *via* Google Forms. Four weeks after the readers had completed the pre-training assessment; a one hour-long teaching session including a Microsoft PowerPoint presentation illustrating important features of ACR TI-RADS was provided to the readers along with a Microsoft Word document summarizing common areas of disagreement in nodule characterization[5]. The teaching session provided a step-by-step review of the 5 main sonographic features used for nodule scoring in ACR TI-RADS: (1) Composition; (2)

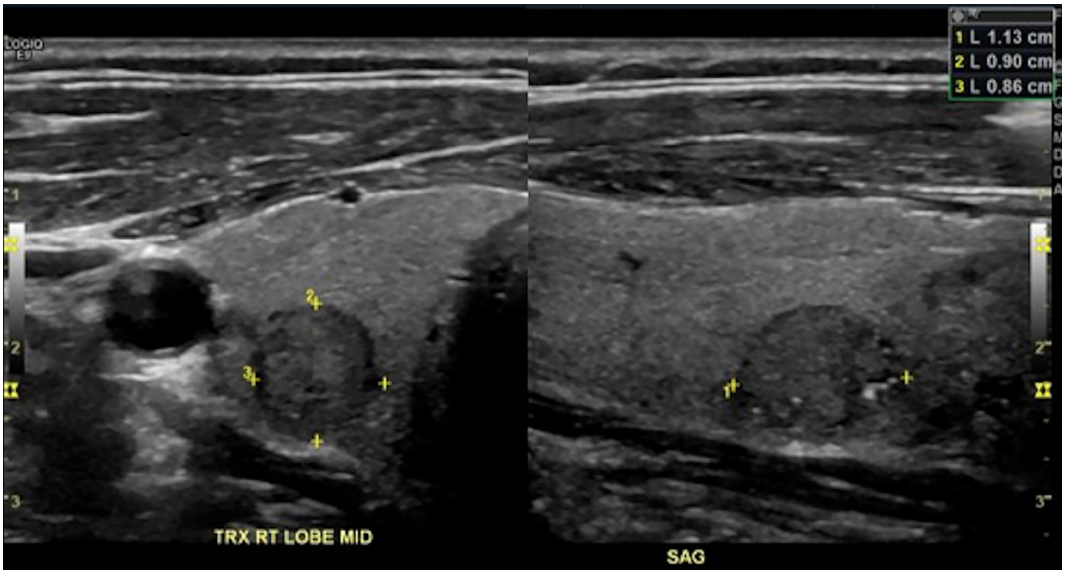

Figure 1 A 51-year-old female with a 1.1 cm × 0.9 cm × 0.9 cm right mid pole thyroid nodule. This nodule was classified correctly with perfect concordance by all 3 readers as solid (+ 2 points), hypoechoic (+ 2 points), taller-than-wide (+ 3 points), smooth margins (+ 0 points), and with punctate echogenic foci (+ 3 points). This had a total points of 10 and a Thyroid Imaging Reporting and Data System level of TR5.

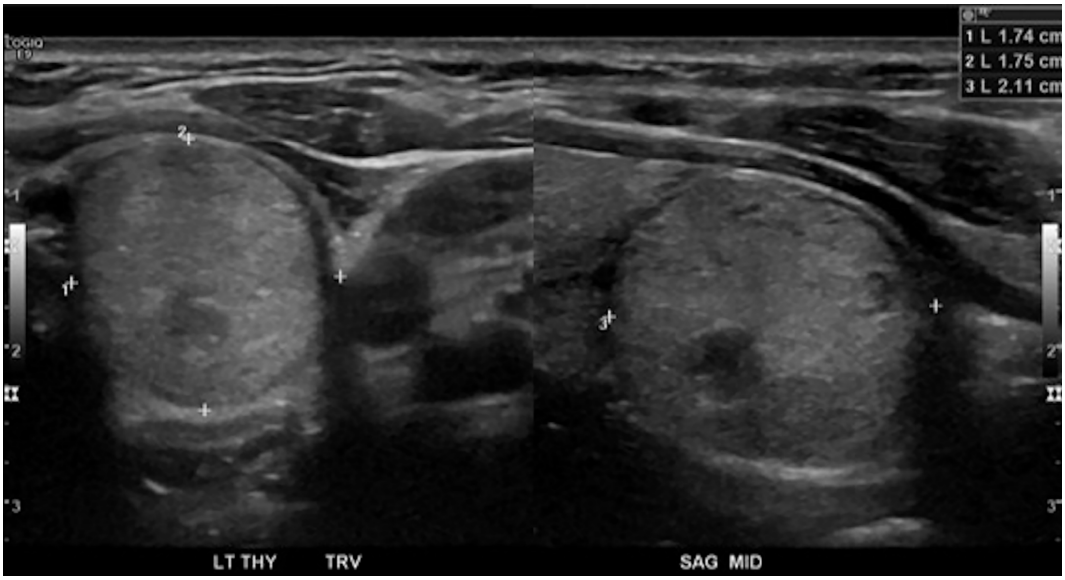

Figure 2 A 45-year-old female with a 1.7 cm × 1.8 cm × 2.1 cm left mid pole thyroid nodule. This nodule was classified by first two readers as Thyroid Imaging Reporting and Data System (TI-RADS) level TR4 and by the third reader as TI-RADS level TR5. The first two readers classified the nodule as solid (+ 2 points), isoechoic (+ 2 points), taller-than-wide (+ 3 points), smooth margins (+ 0 points) and with no echogenic foci (+ 0 points) for a total points of 6 and a TI-RAD level of TR4. For the third reader, a single discrepancy in the scoring of echogenicity as hypoechoic (+ 2 points) rather than isoechoic (+ 1 point) as in the other 2 readers, resulted in a total points of 7 and a TI-RADS level of TR5. As can be seen in the images, the nodule has mixed echogenicity although most of the nodule is isoechoic making this the preferred option.

Echogenicity; (3) Shape; (4) Margin; and (5) Echogenic foci. Each feature's description and interpretation was discussed and illustrated by examples. The readers were given ample opportunity to ask questions, and the consensus panel provided focused clarification to readers in areas of reader uncertainty. Additionally, the trainees were instructed to review the training file that contained the 30 training cases on PACS and corresponding answers were provided for each case. Two weeks after the training session (six weeks after the pre-training assessment), the 50 anonymized cases from the ''testing'' group were re-sent to the readers for independent review. Readers were instructed to re-score the 50 cases and the post-training responses were entered into an online survey generated *via* Google Forms.

Statistical analysis

Categorical variables were expressed as values and percentages. Continuous variables were expressed as the mean ± SD. The following statistical tests were used:

Fleiss kappa (overall agreement) was used to calculate the pooled inter-reader agreement. The kappa (K) value interpretation as suggested by Cohen was used: ≤ 0.20 (slight agreement), 0.21–0.40 (fair agreement), 0.41–0.60 (moderate agreement), 0.61–0.80 (substantial agreement), and 0.81–1.00 (almost perfect agreement)[10].

Paired *t*-test was used to evaluate for significant difference between agreement coefficients[11].

Using the consensus panel as the reference standard, the relative diagnostic parameters (sensitivity, specificity, positive predictive value and negative predictive value) per TI-RADS level were calculated for individual readers and on a pooled basis.

RESULTS

The testing cases comprised of 50 nodules in 40 patients. There were 33 (82.5%) females and 7 males. The mean patient age was 56.6 ± 13.6 years with an age range from 29 to 80 years. Of the 50 nodules, 31 (62%) were located in the right lobe, 18 (36%) in the left lobe and 1 (2%) in the isthmus. The mean nodule size was 19 ± 14 mm with a range from 5 to 63 mm. According to the reference standard that consisted of a consensus panel of 3 fellowship trained staff radiologists, there were 11 (22%) TI-RADS level 1 nodules, 9 (18%) TI-RADS level 2 nodules, 9 (18%) TI-RADS level 3 nodules, 13 (26%) TI-RADS level 3 nodules, and 8 (16%) TI-RADS level 5 nodules.

The pooled inter-reader agreement with the reference standard, pre- and post-training, is listed in Table 1. A statistically significant improvement in reader agreement was demonstrated in post-training inter-reader agreement for nodule shape ($P < 0.001$), presence of echogenic foci ($P = 0.004$), TI-RADS level ($P < 0.001$) and overall recommendation ($P = 0.02$). Each of these categories improved at least one category of agreement. Only margin characterization remained at slight agreement after training. Similarly, the percentage reader agreement with the reference standard for sonographic features (Table 2), TI-RADS levels (Table 3) and recommendations (Table 4) are also included. Figure 1 provides an illustrated example of complete reader concordance for nodule scoring using ACR TI-RADS. In contrast, Figure 2 provides an illustrated example where there is discordance in reader scoring using ACR TI-RADS.

Finally, the relative diagnostic performance of readers, pre- and post-training, when compared against the reference standard is included in Table 5 and Table 6, respectively. Pre-training pooled sensitivities ranged from 22.3%-66.7% and pooled specificity ranged from 72.2%-95.1%, dependent on TI-RADS category. Post-training pooled sensitivities ranged from 40.7%-63% and pooled specificity ranged from 76.6%-96.8%, dependent on TI-RADS category.

DISCUSSION

The overall inter-reader agreement for ACR TI-RADS should take into account the inter-reader agreement of its two major outcome variables – '*TI-RADS level*' and '*ACR TI-RADS recommendations*'. In our study, the inter-reader agreement for *'TI-RADS level'* showed a significant improvement with training ($k = 0.14$ (slight) on the pre-training assessment *vs* $k = 0.36$ (fair) on the post-training assessment)[12]. Our inter-reader agreement for *'ACR TI-RADS recommendations'* also showed a significant improvement with training ($k = 0.36$ (fair) on the pre-training assessment *vs* $k = 0.50$ (moderate) on the post-training assessment [P = 0.02]). Our findings suggest that even a single didactic training session can significantly improve the overall inter-reader agreement in radiology residents. Our findings compare favorably with other inter-reader agreement studies involving ACR TI-RADS. A study by Hoang *et al*[7] involving 8 board certified radiologists (2 from academic centers with subspecialty training in US and 6 from private practice with no subspecialty training in US) found a fair ($k = 0.35$) inter-reader agreement for *'TI-RADS level'*, and moderate ($k = 051$) inter-reader agreement for *'ACR TI-RADS recommendations'*[7]. Teng *et al*[8] assessed the learnability and reproducibility of ACR TI-RADS in post-graduate freshmen. The study included 3 readers with < 3 mo ultrasound experience and 3 experts with > 15 years ultrasound experience each. The readers independently evaluated 4 groups of nodules

Table 1 Pooled inter-reader agreement with the reference standard

	Pre-training, *k*	Post-training, *k*	*P* value of the difference
Composition	0.46 (95%CI: 0.37 to 0.54), moderate	0.52 (95%CI: 0.44 to 0.61), moderate	0.32
Echogenicity	0.36 (95%CI: 0.29 to 0.44), fair	0.44 (95%CI: 0.37 to 0.52), moderate	0.30
Shape	0.09 (95%CI: 0.02 to 0.21), slight	0.67 (95%CI: 0.56 to 0.78), substantial	< 0.001
Margins	0.03 (95%CI: -0.14 to 0.08), slight	0.05 (95%CI: -0.05 to 0.15), slight	0.71
Echogenic Foci	0.28 (95%CI: 0.19 to 0.37), fair	0.45 (95%CI: 0.36 to 0.53), moderate	0.004
TI-RADS Level	0.14 (95%CI: 0.08 to 0.20), slight	0.36 (95%CI: 0.30 to 0.42), fair	< 0.001
Recommendations	0.36 (95%CI: 0.27 to 0.45), fair	0.50 (95%CI: 0.41 to 0.59), moderate	0.02

Table 2 Percentage reader agreement with the reference standard for sonographic features

Sonographic feature	RS	$R1_{pre}$	$R1_{post}$	$R2_{pre}$	$R2_{post}$	$R3_{pre}$	$R3_{post}$
Composition	*n*	*n* (%)					
Spongiform	4	0 (0)	1 (25)	1 (25)	1 (25)	3 (75)	4 (100)
Cystic or almost completely cystic	11	3 (27.3)	5 (45.5)	7 (63.6)	8 (72.7)	10(90.9)	10(90.9)
Mixed cystic and solid	12	9 (75)	6 (50)	5 (41.7)	7 (58.3)	5 (58.3)	6 (50)
Solid	27	26 (96.3)	26 (96.3)	25 (92.6)	26 (96.3)	18 (66.7)	19 (70.4)
Echogenicity							
Anechoic	11	3 (27.3)	5 (45.5)	5 (45.5)	5 (45.5)	9 (81.8)	8 (72.7)
Hyperechoic or isoechoic	27	23 (85.2)	23 (85.2)	19 (70.4)	21 (77.8)	19 (70.4)	20 (74.1)
Hypoechoic	12	2 (16.7)	4 (33.3)	9 (75)	8 (66.7)	4 (33.3)	4 (33.3)
Shape							
Wilder than tall	42	38 (90.5)	39 (92.9)	7 (16.7)	39 (92.9)	41 (97.6)	40 (95.2)
Taller than wide	8	7 (87.5)	7 (87.5)	7 (87.5)	7 (87.5)	6 (75)	4 (50)
Margins							
Smooth or ill defined	47	36 (76.6)	35 (74.5)	35 (74.5)	33 (70.2)	43 (91.5)	45 (95.7)
Lobulated or irregular	3	1 (33.3)	2 (66.7)	1 (33.3)	2 (66.7)	0 (0)	0 (0)
Echogenic foci							
None or large comet tail artifact	41	20 (48.8)	36 (87.8)	29 (70.7)	39 (95.1)	29 (70.7)	29 (70.7)
Macrocalcification	3	1 (33.3)	1 (33.3)	0 (0)	2 (66.7)	2 (66.7)	2 (66.7)
Punctate echogenic foci	6	5 (83.3)	4 (66.7)	2 (33.3)	5 (83.3)	3 (50)	3 (50)

RS: Reference standard; R1: Reader 1; R2: Reader 2; R3: Reader 3.

with 50 nodules per group. After evaluating each group, a post-group training session was carried out for the freshman. The study found that the inter-reader agreement improved with training. Chung *et al*[13] performed a study evaluating the impact of radiologist's experience on ACR TI-RADS. Six fellowship-trained radiologists were divided into two groups (experienced *vs* less experienced) with the experienced group having at least 20 years of post-fellowship experience each and the less experienced group having 1 year or less of post-fellowship experience each. The study found no significant differences for inter-reader agreement between experienced *vs* less experienced readers for *'TI-RADS level'* or *'ACR TI-RADS recommendations'*. The inter-reader agreement was moderate for both experienced and less experienced groups for '*TI-RADS level*' and moderate to substantial (experienced *vs* less experienced, respectively) for '*ACR TI-RADS recommendations*'. Seifert *et al*[14] evaluated the inter-reader agreement and efficacy of consensus reading for several thyroid imaging risk stratification systems including ACR TI-RADS. The study involved 4 experienced

Table 3 Percentage reader agreement with the reference standard for American College of Radiology Thyroid Imaging Reporting and Data System levels

ACR TI-RADS level	RS, *n*	R1 $_{pre}$, *n* (%)	R1 $_{post}$, *n* (%)	R2 $_{pre}$, *n* (%)	R2 $_{post}$, *n* (%)	R3 $_{pre}$, *n* (%)	R3 $_{post}$, *n* (%)
1	11	1 (9.1)	5 (45.5)	1 (9.1)	7 (63.6)	10 (90.9)	8 (72.7)
2	9	3 (33.3)	4 (44.4)	0 (0)	4 (44.4)	3 (33.3)	3 (33.3)
3	9	4 (44.4)	5 (55.5)	1 (11.1)	6 (66.7)	4 (44.4)	6 (66.7)
4	13	4 (30.8)	5 (38.5)	5 (38.5)	9 (69.2)	5 (38.5)	5 (38.5)
5	8	7 (87.5)	4 (50)	6 (75)	5 (62.5)	3 (37.5)	3 (37.5)

ACR TI-RADS: American College of Radiology Thyroid Imaging Reporting and Data System; RS: Reference standard; R1: Reader 1; R2: Reader 2; R3: Reader 3.

Table 4 Percentage reader agreement with the reference standard for American College of Radiology Thyroid Imaging Reporting and Data System recommendations

Recommendations	RS, *n*	R1 $_{pre}$, *n* (%)	R1 $_{post}$, *n* (%)	R2 $_{pre}$, *n* (%)	R2 $_{post}$, *n* (%)	R3 $_{pre}$, *n* (%)	R3 $_{post}$, *n* (%)
No follow up	25	13 (52)	17 (68)	10 (40)	19 (76)	21 (84)	22 (88)
Follow up	5	3 (60)	1 (20)	1 (20)	3 (60)	3 (60)	3 (60)
FNA	20	17 (85)	15 (75)	18 (90)	17 (85)	11 (55)	13 (65)

RS: Reference standard; R1: Reader 1; R2: Reader 2; R3: Reader 3; FNA: Fine needle aspiration.

specialist readers with more than 5 years of clinical experience each. The readers independently scored 40 thyroid image datasets in session 1 followed by a joint consensus read (C1). After this, the process was repeated with independent scoring of 40 new image datasets in session 2, followed by another consensus read (C2). For ACR TI-RADS, the study found a significantly higher inter-reader agreement for session 2 (k = 0.57, moderate) *vs* session 1 (k = 0.32, fair) [$P < 0.01$], indicating that the addition of a consensus read had an impact in improving the inter-reader agreement.

Our study also evaluated the inter-reader agreement of individual sonographic features including composition, echogenicity, shape, margins, and echogenic foci. Our findings showed a significant improvement in inter-reader agreement with training for features such as '*shape*' (k = 0.09, slight $_{pre\text{-}training}$ versus k = 0.67, substantial $_{post\text{-}training}$, $P <$ 0.001) and '*echogenic foci*' (k = 0.28, fair $_{pre\text{-}training}$ versus k = 0.45, moderate $_{post\text{-}training}$, P = 0.004) but not for the others. The features with the strongest inter-reader agreement in our study were '*shape*' (k = 0.67 $_{post\text{-}training}$, substantial) and 'composition' (k = 0.52 $_{post\text{-}training}$, moderate). Hoang *et al*[7] also found similar findings in their study with 'shape' (k = 0.61, substantial) and 'composition' (k = 0.58, moderate) having the strongest inter-reader agreement amongst the 5 principal sonographic features. The feature with the poorest inter-reader agreement in our study was margins (k = 0.05 $_{post\text{-}training}$, slight). Similarly, Hoang *et al* [7] also found that 'margins' had the poorest inter-reader agreement (k = 0.25, fair) in their study. The poor inter-reader agreement for 'margins' is not surprising as accurate assessment requires a thorough review of the entire cine clip, rather than review of the still images only. Margins may also be harder to interpret through ultrasound artifacts. Finally, two of the available answer options for 'margins' in ACR TI-RADS are 'ill defined' (TI-RADS + 0 points) and 'irregular' (TI-RADS + 2 points). However, both options share innate conceptual similarities in interpretation and can lead to overlap. The poorest and strongest inter-reader agreement were also matched with the same features identified by Hoang's board-certified radiologists, indicating that the limitation may be inherent to the reporting and data system rather than trainee experience.

We also evaluated the relative sensitivity and specificity of the radiology residents in assigning TI-RADS levels compared to consensus reference standard before and after training. There was a general trend towards improved pooled sensitivity with TI-RADS levels 1 to 4 for the post-training assessment while the pooled specificity was relatively high (76.6-96.8%) for all TI-RADS level. Overall findings suggest that a single didactic training session improves the detection of benign (TI-RADS 1-3) lesions while

Table 5 The relative sensitivity, specificity, positive predictive value, and negative predictive value per Thyroid Imaging Reporting and Data System Level on the pre-training assessment compared to the reference standard

Pre-training, Statistics	TI-RADS 1, %	TI-RADS 2, %	TI-RADS 3, %	TI-RADS 4, %	TI-RADS 5, %
Sensitivity					
R1	9.1 (0.2-41.3)	33.3 (7.5-70.1)	44.4 (13.7-78.8)	30.8 (9.1-61.4)	87.5 (47.4-99.7)
R2	9.1 (0.2-41.3)	0 (0-33.6)	11.1 (0.3-48.3)	38.5 (13.9-68.4)	75 (34.9-96.8)
R3	90.9 (58.7-99.8)	33.3 (7.5-70.1)	44.4 (13.7-78.8)	38.5 (13.9-68.4)	37.5 (8.5-75.5)
Pooled	36.4 (20.4-54.9)	22.2 (8.6-42.3)	33.3 (16.5-54)	35.9 (21.2-52.8)	66.7 (44.7-84.4)
Specificity					
R1	100 (91.0-100)	90.2 (76.9-97.3)	92.7 (80.1-98.5)	62.2 (44.8-77.5)	76.2 (60.6-88)
R2	100 (91-100)	97.6 (87.1-99.9)	80.5 (65.1-91.2)	81.1 (64.8-92)	50 (34.2-65.8)
R3	66.7 (49.8-80.9)	97.6 (87.1-99.9)	95.1 (83.5-99.4)	89.2 (74.6-97)	90.5 (77.4-97.3)
Pooled	88.9 (81.8-94)	95.1 (89.7-98.2)	89.4 (82.6-94.3)	76.6 (67.6-84.1)	72.2 (63.5-79.8)
Positive predictive value					
R1	100	42.9 (16.8-73.6)	57.1 (26.4-83.2)	22.2 (10.3-41.6)	41.2 (27.7-56.1)
R2	100	0	11.1 (1.8-46.8)	41.7 (21.5-65.1)	22.2 (14.8-32.1)
R3	43.5 (32.2-55.5)	75 (26-96.2)	66.7 (30.1-90.3)	55.6 (28.3-79.8)	42.9 (17.1-73.2)
Pooled	48 (31.8-64.6)	50 (25.9-74.1)	40.9 (24.8-59.2)	35 (23.9-48)	31.4 (23.5-40.5)
Negative predictive value					
R1	79.6 (76.4-82.5)	86.1 (79.4-90.8)	88.4 (80.8-93.2)	71.9 (62.2-79.9)	97 (83.5-99.5)
R2	79.6 (76.4-82.5)	81.6 (80.9-82.4)	80.5 (75.8-84.5)	79 (70.4-85.6)	91.3 (75.3-97.3)
R3	96.3 (79.8-99.4)	87 (80.7-91.4)	88.6 (81.2-93.4)	80.5 (72.6-86.5)	88.4 (81.5-92.9)
Pooled	83.2 (79.2-86.6)	84.8 (81.9-87.3)	85.9 (82.3-88.9)	77.3 (72.5-81.5)	91.9 (86.5-95.3)

TI-RADS: Thyroid Imaging Reporting and Data System; RS: Reference standard; R1: Reader 1; R2: Reader 2; R3: Reader 3.

retaining high specificity in radiology residents. Improved identification of benign lesions is critical in avoiding unnecessary biopsies and interventions, a major aim of the ACR TI-RADS system.

The current study has several limitations. One limitation is the lack of a pathological reference standard. The reference standard was an expert consensus review by 3 board certified radiologists with Body Imaging fellowship and 1-14 years of clinical experience. However, it should be noted that this study is designed primarily to evaluate inter-reader reliability of radiology residents, and not the inherent performance of the ACR TI-RADS itself. As such, an expert consensus panel was deemed a practical reference standard, and one that simulates 'real world' clinical practice[9]. Another limitation is the relatively small number of cases used. However, even with this limited number of cases, we were able to show statistically significant improvements in inter-reader agreement for the two major outcome variables (TI-RADS level and ACR TI-RADS recommendations). While there is a relatively even distribution of TI-RADS levels among the test cases *via* non-random selection, there is uneven distribution of individual ultrasound features within the group. Of the 50 test cases, only 3 nodules demonstrated 'lobulated or irregular' margins (TI-RADS points +2), while the remaining 47 are 'smooth' or 'ill-defined' (TI-RADS points +0). A larger sample size can improve this and lead to more representative analysis of individual ultrasound features. Finally, training retention over time was not evaluated in this study, with the post-training testing performed two weeks after didactic and training case review.

Table 6 The relative sensitivity, specificity, positive predictive value, and negative predictive value per Thyroid Imaging Reporting and Data System Level on the post-training assessment compared to the reference standard

Post-training, Statistics	TI-RADS 1, %	TI-RADS 2, %	TI-RADS 3, %	TI-RADS 4, %	TI-RADS 5, %
Sensitivity					
R1	45.5 (16.8-76.6)	44.4 (13.7-78.8)	55.6 (21.2-86.3)	38.5 (13.9-68.4)	50 (15.7-84.3)
R2	63.6 (30.8-89.1)	44.4 (13.7-78.8)	66.7 (29.9-92.5)	69.2 (38.6-90.9)	62.5 (24.5-91.5)
R3	72.7 (39-94)	33.3 (7.5-70.1)	66.7 (29.9-92.5)	38.5 (13.9-68.4)	37.5 (8.5-75.5)
Pooled	60.6 (42.1-77.1)	40.7 (22.4-61.2)	63 (42.4-80.6)	48.7 (32.4-65.2)	50 (29.1-70.9)
Specificity					
R1	92.3 (79.1-98.4)	97.6 (87.1-99.9)	90.2 (76.9-97.3)	70.3 (53-84.1)	81 (65.9-91.4)
R2	94.9 (82.7-99.4)	97.6 (87.1-99.9)	95.1 (83.5-99.4)	73 (38.6-90.9)	90.5 (77.4-97.3)
R3	66.7 (49.8-80.9)	95.1 (83.5-99.4)	97.6 (87.1-99.9)	86.5 (71.2-95.5)	90.5 (77.4-97.3)
Pooled	84.6 (76.8-90.6)	96.8 (91.9-99.1)	94.3 (88.6-97.7)	76.6 (67.6-84.1)	87.3 (80.2-92.6)
Positive predictive value					
R1	62.5 (32-85.5)	80 (33.6-96.9)	55.6 (29.4-79)	31.3 (16.3-51.5)	33.3 (16.5-56)
R2	77.8 (45.8-93.6)	80 (33.6-96.9)	75 (41.8-92.6)	47.4 (32.2-63.1)	55.6 (29.9-78.6)
R3	38.1 (25.8-52.2)	60 (22.6-88.5)	85.7 (45.1-97.8)	50 (25.6-74.4)	42.9 (17.1-73.2)
Pooled	52.6 (40.1-64.8)	73.3 (48.6-88.9)	70.8 (52.8-84.1)	42.2 (31.5-53.8)	42.9 (29-57.9)
Negative predictive value					
R1	85.7 (77.6-91.2)	88.9 (81.7-93.5)	90.2 (81.6-95.1)	76.5 (66.8-84)	89.5 (80.7-94.5)
R2	90.2 (80.8-95.3)	88.9 (81.7-93.5)	92.9 (83.7-97)	87.1 (74.5-94)	92.7 (83.7-96.9)
R3	89.7 (76.3-95.9)	86.7 (80.3-91.2)	93 (84.1-97.1)	80 (71.9-86.2)	88.4 (81.5-92.9)
Pooled	88.4 (83.2-92.1)	88.2 (84.5-91.1)	92.1 (87.6-95)	81 (75.5-85.4)	90.2 (85.9-93.2)

TI-RADS: Thyroid Imaging Reporting and Data System; RS: Reference standard; R1: Reader 1; R2: Reader 2; R3: Reader 3.

CONCLUSION

Overall, the current study demonstrates a statistically significant improvement in inter-reader agreement among radiology residents, with no prior ACR TI-RADS experience, in the assignment of TI-RADS level and recommendations after a single didactic teaching session compared to expert consensus. Our study demonstrates the learnability of the ACR TI-RADS system and supports the use of dedicated training in radiology residents. Future studies can also be directed to evaluate the effect of additional training sessions with focus on areas/features demonstrating lower inter-rater agreement such as "margins" and retention of training over time.

ARTICLE HIGHLIGHTS

Research background

Thyroid nodules are common and often incidental. The American College of Radiology Thyroid Imaging Reporting and Data System (ACR TI-RADS) standardizes the use of ultrasound for thyroid nodule risk stratification.

Research motivation

Despite the widespread usage of this system, the learnability of TI-RADS has not been proven in radiology trainees.

Research objectives

To evaluate the inter-reader reliability amongst radiology trainees before and after TI-

RADS training.

Research methods

Three PGY-4 radiology residents were evaluated for inter-reader reliability with a 50 thyroid nodule data set before and after a 1-hour didactic teaching session and review of a training data set, with assessment performed 6 wk apart. Performance was compared to a consensus panel reference standard of three fellowship trained radiologists.

Research results

After one session of dedicated TI-RADS training, the radiology residents demonstrated statistically significant improvement in inter-reader agreement in subcategories of "shape", "echogenic foci", "TI-RADS level", and "recommendations" when compared with expert panel consensus. A trend towards higher pooled sensitivity for TI-RADS level 1-4 is also observed.

Research conclusions

Resident trainees demonstrated a statistically significant improvement in inter-reader agreement for both TI-RADS level and recommendations after training. This study demonstrates the learnability of the ACR TI-RADS.

Research perspectives

A multi-institutional and multi-national assessment of radiology resident diagnostic accuracy and inter-reader reliability of ACR TI-RADS classification and recommendations before and after training would improve the generalizability of these results.

REFERENCES

1 **Gharib H**, Papini E, Garber JR, Duick DS, Harrell RM, Hegedüs L, Paschke R, Valcavi R, Vitti P; AACE/ACE/AME Task Force on Thyroid Nodules. American association of clinical endocrinologists, american college of endocrinology, and associazione medici endocrinologi medical guidelines for clinical practice for the diagnosis and management of thyroid nodules--2016 update. *Endocr Pract* 2016; **22**: 622-639 [PMID: 27167915 DOI: 10.4158/EP161208.GL]

2 **Grani G**, Lamartina L, Cantisani V, Maranghi M, Lucia P, Durante C. Interobserver agreement of various thyroid imaging reporting and data systems. *Endocr Connect* 2018; **7**: 1-7 [PMID: 29196301 DOI: 10.1530/EC-17-0336]

3 **Smith-Bindman R**, Lebda P, Feldstein VA, Sellami D, Goldstein RB, Brasic N, Jin C, Kornak J. Risk of thyroid cancer based on thyroid ultrasound imaging characteristics: results of a population-based study. *JAMA Intern Med* 2013; **173**: 1788-1796 [PMID: 23978950 DOI: 10.1001/jamainternmed.2013.9245]

4 **Lim H**, Devesa SS, Sosa JA, Check D, Kitahara CM. Trends in Thyroid Cancer Incidence and Mortality in the United States, 1974-2013. *JAMA* 2017; **317**: 1338-1348 [PMID: 28362912 DOI: 10.1001/jama.2017.2719]

5 **Tessler FN**, Middleton WD, Grant EG, Hoang JK, Berland LL, Teefey SA, Cronan JJ, Beland MD, Desser TS, Frates MC, Hammers LW, Hamper UM, Langer JE, Reading CC, Scoutt LM, Stavros AT. ACR Thyroid Imaging, Reporting and Data System (TI-RADS): White Paper of the ACR TI-RADS Committee. *J Am Coll Radiol* 2017; **14**: 587-595 [PMID: 28372962 DOI: 10.1016/j.jacr.2017.01.046]

6 **Ha EJ**, Na DG, Baek JH, Sung JY, Kim JH, Kang SY. US Fine-Needle Aspiration Biopsy for Thyroid Malignancy: Diagnostic Performance of Seven Society Guidelines Applied to 2000 Thyroid Nodules. *Radiology* 2018; **287**: 893-900 [PMID: 29465333 DOI: 10.1148/radiol.2018171074]

7 **Hoang JK**, Middleton WD, Farjat AE, Teefey SA, Abinanti N, Boschini FJ, Bronner AJ, Dahiya N, Hertzberg BS, Newman JR, Scanga D, Vogler RC, Tessler FN. Interobserver Variability of Sonographic Features Used in the American College of Radiology Thyroid Imaging Reporting and Data System. *AJR Am J Roentgenol* 2018; **211**: 162-167 [PMID: 29702015 DOI: 10.2214/AJR.17.19192]

8 **Teng D**, Fu P, Li W, Guo F, Wang H. Learnability and reproducibility of ACR Thyroid Imaging, Reporting and Data System (TI-RADS) in postgraduate freshmen. *Endocrine* 2020; **67**: 643-650 [PMID: 31919768 DOI: 10.1007/s12020-019-02161-y]

9 **Pi Y**, Wilson MP, Katlariwala P, Sam M, Ackerman T, Paskar L, Patel V, Low G. Diagnostic accuracy and inter-observer reliability of the O-RADS scoring system among staff radiologists in a North American academic clinical setting. *Abdom Radiol (NY)* 2021; **46**: 4967-4973 [PMID: 34185128 DOI: 10.1007/s00261-021-03193-7]

10 **McHugh ML**. Interrater reliability: the kappa statistic. *Biochem Med (Zagreb)* 2012; **22**: 276-282 [PMID: 23092060 DOI: 10.11613/BM.2012.031]

11 **Gwet KL**. Testing the Difference of Correlated Agreement Coefficients for Statistical Significance. *Educ Psychol Meas* 2016; **76**: 609-637 [PMID: 29795880 DOI: 10.1177/0013164415596420]

12 **Li W**, Wang Y, Wen J, Zhang L, Sun Y. Diagnostic Performance of American College of Radiology TI-RADS: A Systematic Review and Meta-Analysis. *AJR Am J Roentgenol* 2021; **216**: 38-47 [PMID: 32603229 DOI: 10.2214/AJR.19.22691]

13 **Chung R**, Rosenkrantz AB, Bennett GL, Dane B, Jacobs JE, Slywotzky C, Smereka PN, Tong A, Sheth S. Interreader Concordance of the TI-RADS: Impact of Radiologist Experience. *AJR Am J Roentgenol* 2020; **214**: 1152-1157 [PMID: 32097031 DOI: 10.2214/AJR.19.21913]

14 **Seifert P**, Görges R, Zimny M, Kreissl MC, Schenke S. Interobserver agreement and efficacy of consensus reading in Kwak-, EU-, and ACR-thyroid imaging recording and data systems and ATA guidelines for the ultrasound risk stratification of thyroid nodules. *Endocrine* 2020; **67**: 143-154 [PMID: 31741167 DOI: 10.1007/s12020-019-02134-1]

Published by **Baishideng Publishing Group Inc**
7041 Koll Center Parkway, Suite 160, Pleasanton, CA 94566, USA
Telephone: +1-925-3991568
E-mail: bpgoffice@wjgnet.com
Help Desk: https://www.f6publishing.com/helpdesk
https://www.wjgnet.com

ISSN 1949-8470 (online)

World Journal of *Radiology*

World J Radiol 2022 February 28; 14(2): 30-54

Published by Baishideng Publishing Group Inc

World Journal of Radiology

Contents

Monthly Volume 14 Number 2 February 28, 2022

MINIREVIEWS

LETTER TO THE EDITOR

World Journal of Radiology

Monthly Volume 14 Number 2 February 28, 2022

Contents

ABOUT COVER

Associate Editor of *World Journal of Radiology*, Matteo Bauckneht, MD, PhD, Assistant Professor, Department of Health Sciences, University of Genova and IRCCS Ospedale Policlinico San Martino, Genova 16132, Italy. matteo.bauckneht@hsanmartino.it

AIMS AND SCOPE

The primary aim of *World Journal of Radiology* (*WJR*, *World J Radiol*) is to provide scholars and readers from various fields of radiology with a platform to publish high-quality basic and clinical research articles and communicate their research findings online.

WJR mainly publishes articles reporting research results and findings obtained in the field of radiology and covering a wide range of topics including state of the art information on cardiopulmonary imaging, gastrointestinal imaging, genitourinary imaging, musculoskeletal imaging, neuroradiology/head and neck imaging, nuclear medicine and molecular imaging, pediatric imaging, vascular and interventional radiology, and women's imaging.

INDEXING/ABSTRACTING

The *WJR* is now abstracted and indexed in Emerging Sources Citation Index (Web of Science), PubMed, PubMed Central, China National Knowledge Infrastructure (CNKI), China Science and Technology Journal Database (CSTJ), and Superstar Journals Database. The 2021 edition of Journal Citation Reports® cites the 2020 Journal Citation Indicator (JCI) for *WJR* as 0.51.

RESPONSIBLE EDITORS FOR THIS ISSUE

Production Editor: *Ying-Yi Yuan*; **Production Department Director:** *Xu Guo*; **Editorial Office Director:** *Jia-Ping Yan*.

NAME OF JOURNAL
World Journal of Radiology

ISSN
ISSN 1949-8470 (online)

LAUNCH DATE
January 31, 2009

FREQUENCY
Monthly

EDITORS-IN-CHIEF
Thomas J Vogl

EDITORIAL BOARD MEMBERS
https://www.wjgnet.com/1949-8470/editorialboard.htm

PUBLICATION DATE
February 28, 2022

INSTRUCTIONS TO AUTHORS
https://www.wjgnet.com/bpg/gerinfo/204

GUIDELINES FOR ETHICS DOCUMENTS
https://www.wjgnet.com/bpg/GerInfo/287

GUIDELINES FOR NON-NATIVE SPEAKERS OF ENGLISH
https://www.wjgnet.com/bpg/gerinfo/240

PUBLICATION ETHICS
https://www.wjgnet.com/bpg/GerInfo/288

PUBLICATION MISCONDUCT
https://www.wjgnet.com/bpg/gerinfo/208

ARTICLE PROCESSING CHARGE
https://www.wjgnet.com/bpg/gerinfo/242

STEPS FOR SUBMITTING MANUSCRIPTS
https://www.wjgnet.com/bpg/GerInfo/239

ONLINE SUBMISSION
https://www.f6publishing.com

World Journal of Radiology

Submit a Manuscript: https://www.f6publishing.com

World J Radiol 2022 February 28; 14(2): 30-46

DOI: 10.4329/wjr.v14.i2.30

ISSN 1949-8470 (online)

MINIREVIEWS

Acute coronary syndrome on non-electrocardiogram-gated contrast-enhanced computed tomography

Shu Yoshihara

Specialty type: Radiology, Nuclear Medicine and Medical Imaging

Provenance and peer review: Invited article; externally peer reviewed.

Peer-review model: Single blind

Peer-review report's scientific quality classification

Grade A (Excellent): 0
Grade B (Very good): B
Grade C (Good): 0
Grade D (Fair): 0
Grade E (Poor): 0

P-Reviewer: Apiratwarakul K

Received: October 18, 2021
Peer-review started: October 18, 2021
First decision: December 10, 2021
Revised: December 14, 2021
Accepted: February 15, 2022
Article in press: February 15, 2022
Published online: February 28, 2022

Shu Yoshihara, Department of Diagnostic Radiology, Iwata City Hospital, Iwata 438-8550, Japan

Corresponding author: Shu Yoshihara, MD, PhD, Doctor, Department of Diagnostic Radiology, Iwata City Hospital, 512-3 Ookubo, Iwata 438-8550, Japan. shuy@hospital.iwata.shizuoka.jp

Abstract

It is not rare for acute coronary syndrome (ACS) patients to present with symptoms that are atypical, rather than chest pain. It is sometimes difficult to achieve a definitive diagnosis of ACS for such patients who present with atypical symptoms, normal initial biomarkers of myocardial necrosis, and normal or nondiagnostic electrocardiograms (ECGs). Although cardiac CT allows for assessments of coronary artery stenosis as well as myocardial perfusion defect in patients with suspected ACS, it requires ECG gating and is usually performed with high-performance multislice CT for highly probable ACS patients. However, several recent reports have stated that ACS is detectable by myocardial perfusion defects even on routine non-ECG-gated contrast-enhanced CT. A growing number of contrast-enhanced CT scans are now being performed in emergency departments in search of pathologies responsible for a patient's presenting symptoms. In order to avoid inappropriate management for this life-threatening event, clinicians should be aware that myocardial perfusion defect is more commonly detectable even on routine non-ECG-gated contrast-enhanced CT performed in search of other pathologies.

Key Words: Acute coronary syndrome; Non-ECG-gated CT; Computed tomography; Myocardial perfusion defect; Emergency department

Core Tip: Definitive diagnosis of acute coronary syndrome (ACS) is sometimes difficult to achieve, especially in patients who present with atypical symptoms, normal initial biomarkers of myocardial necrosis, and normal or nondiagnostic electrocardiograms (ECGs). In order to avoid inappropriate management for this life-threatening event, clinicians should be aware that myocardial perfusion defect is more commonly detectable even on routine non-ECG-gated contrast-enhanced computed tomography performed in search of other pathologies. In this review, several essential points of image interpretation in diagnosing ACS on non-ECG-gated contrast-enhanced computed tomography has been described.

Citation: Yoshihara S. Acute coronary syndrome on non-electrocardiogram-gated contrast-enhanced computed tomography. *World J Radiol* 2022; 14(2): 30-46
URL: https://www.wjgnet.com/1949-8470/full/v14/i2/30.htm
DOI: https://dx.doi.org/10.4329/wjr.v14.i2.30

INTRODUCTION

Acute coronary syndrome (ACS) is a term used to refer to a range of conditions associated with acute myocardial ischemia and/or infarction, which are usually due to an abrupt reduction in the coronary blood flow[1]. Chest pain characteristics, specific associated symptoms, electrocardiogram (ECG) abnormalities, and the levels of serum biomarkers of myocardial necrosis are essential for a diagnosis of ACS[1]. However, rather than chest pain, some ACS patients present with atypical symptoms[2-4]. A review of over 430,000 patients from the National Registry of Myocardial Infarction II with confirmed acute myocardial infarction (AMI) showed that one-third presented at the hospital with no chest pain [2]. Patients such as these often present with symptoms including dyspnea alone, weakness, nausea and/or vomiting, palpitations, syncope, or cardiac arrest. The implications of absence of chest pain are important in terms of therapy and prognosis. The Registry report revealed that patients without chest pain were less likely to receive a diagnosis of a confirmed MI on admission, and were also less likely to receive thrombolytic therapy or primary percutaneous coronary intervention, and to undergo treatment with appropriate medical therapy. It is unsurprising that these differences were associated with increased in-hospital mortality[2]. Therefore, it is sometimes difficult to achieve a definitive diagnosis of ACS, especially for patients who present with atypical symptoms, normal initial biomarkers of myocardial necrosis, and normal or nondiagnostic ECGs. Even in the presence of acute coronary ischemia, women, diabetics, and the elderly are more likely to present with atypical symptoms, and caution is required in evaluating possible ACS[2,3]. The use of computed tomography (CT) in the emergency department (ED) has increased at a consistent exponential rate[5]. Due to their greater temporal and spatial resolution, current multi-slice computed tomography (MSCT) systems are capable of rapid scanning that renders non-ECG-gated images with fewer cardiac motion artifacts. Although imaging of various cardiac diseases is superior with ECG-gated MSCT images, typically there is sufficient information provided in non-ECG-gated MSCT images of the thorax or abdomen to identify a number of incidental cardiac abnormalities like myocardial perfusion defect (MPD) of the left ventricle which may be related to the patient's presenting symptoms[6]. Consequently, clinically unrecognized ACS cases identified on CT performed for the indication of other diseases are increasing, especially in the ED. In this article, we present clinically unrecognized several ACS cases detected on routine non-ECG-gated contrast-enhanced CT performed in the ED for discriminating other pathologies. Non-ECG-gated contrast-enhanced CT was performed using an 80-row MSCT scanner (Aquilion Prime, Toshiba Medical Systems, Tochigi, Japan). The scanning parameters were as follows: tube voltage, 120 kV; tube current, mA modulation technique with a noise index of 12 (maximum 500 mA); gantry rotation time, 350 ms; reconstruction slice thickness, 1mm. An intravenous bolus of nonionic contrast medium (55 kg < body weight; iopamidol 300 mg iodine/mL, 55 kg ≥ body weight; iopamidol 370 mg iodine/ml) was delivered through a vein in the arm with a flow rate of 3.3 mL/s. The dose of contrast medium was appropriately 600 mg I/kg of body weight, to a maximum of 100 mL. The scanning delay was calculated by monitoring the contrast values that increased to 150 Hounsfield units in the descending aorta as the region of interest (25-30 s after injection). A second scan was performed 120 s after injection. When focal decrease of the left ventricular myocardial enhancement was visually found, a region of interest was manually set to measure CT attenuation values of the normal and hypoperfused myocardium. MPD was defined as a decrease of 20 or more Hounsfield units compared with the adjacent normal enhanced myocardium.

CARDIAC COMPUTED TOMOGRAPHY AND ACS

Progress in the technical development of cardiac CT enables rapid, accurate imaging of the cardiovascular system. With cardiac CT, it is necessary to use either prospective or retrospective ECG gating to synchronize the CT image with the ECG. In both methods, the waveform of the ECG is used to coordinate image reconstruction with the heart's position in the chest[7]. Recently, a large body of evidence has been published supporting early assessment of coronary artery stenosis by cardiac CT as an accurate, safe, and efficient rapid diagnostic strategy for ED patients with low-intermediate risk acute chest pain[8-11]. As a result, the appropriate use criteria for cardiac CT designated detection of coronary artery stenosis by cardiac CT as appropriate for use in acute chest pain patients for whom the likelihood of ACS is low or intermediate[12]. Moreover, identification of regional subendocardial or transmural hypoattenuation of the myocardium in cardiac CT provides incremental diagnostic value to detect ACS [13]. Based on this novel evidence, the updated SCCT guidelines for the interpretation and reporting of coronary CT angiography have newly designated that myocardial CT enhancement patterns should be assessed during performance of cardiac CT[14].

NON-ELECTROCARDIOGRAM-GATED CONTRAST-ENHANCED CT AND ACS

Recently, several reports have been published that suggest non-ECG-gated contrast-enhanced CT can detect ACS with high diagnostic accuracy (Table 1)[15-19]. Mano *et al*[17] evaluated the frequency of MPD on non-ECG-gated contrast-enhanced CT performed with a 64-slice CT scanner, which was done to assess aortic dissection or pulmonary embolism in 154 patients who had been admitted to the ED with acute chest pain and/or back pain. MPD was detected in 43 patients, 26 (60%) of whom were ultimately diagnosed with AMI. In the remaining 111 patients without MPD, only 2 (2%) were ultimately diagnosed with AMI. They showed good diagnostic performance for MPD on non-ECG-gated contrast-enhanced CT in predicting AMI with a sensitivity of 93% and a specificity of 87%. Watanabe *et al*[18] evaluated the presence of MPD on non-ECG-gated contrast-enhanced CT using a 64-slice CT scanner in 23 patients who had been admitted to the ED with acute-onset chest pain and underwent emergent invasive coronary angiography. Of the 23 patients, 13 were diagnosed with ACS and the remaining 10 were diagnosed with other conditions. MPD was detected in 11 (85%) of the 13 ACS patients. They showed good diagnostic performance for MPD on non-ECG-gated contrast-enhanced CT in predicting ACS with a sensitivity of 85% and a specificity of 90%. In comparison with the other studies using non-ECG-gated contrast-enhanced arterial phase CT imaging for detecting ACS, Yamazaki *et al*[19] evaluated the ACS detection capability of using non-ECG-gated contrast-enhanced parenchymal phase CT imaging acquired with a 100-s scan delay. They showed good diagnostic performance for MPD visualized on non-ECG-gated contrast-enhanced CT during the parenchymal phase in predicting ACS with a sensitivity of 91% and a specificity of 93%. In non-ECG-gated contrast-enhanced CT, the normal myocardium is usually blurry because reconstructed images are a mixture of the systolic and diastolic phases. Indeed, cardiac motion artifacts are recognized to be the most important factor to degrade diagnostic performance on non-ECG-gated contrast-enhanced CT[19]. However, the frequency of false positive cases who were misjudged to have MPD without myocardial ischemia mainly due to cardiac motion artifacts was only 15%-20% in the previous reports[17,18]. In cases with ACS, decreased regional myocardial wall motion due to acute myocardial ischemia will contribute to reduced motion artifacts and sharp visualization of the myocardial border.

IMPORTANT POINTS OF IMAGE INTERPRETATION IN DETECTING ACS ON NON-ELECTROCARDIOGRAM-GATED CONTRAST-ENHANCED CT

Vascular territories of the coronary artery

CT images are usually oriented and displayed using transaxial views, but these images do not cleanly transect the ventricle, atria, or myocardial regions supplied by the major coronary arteries. The American Heart Association (AHA) showed the cardiac plane definition and display for tomographic image modalities[20]. Essentially, it has been suggested that, using any noninvasive method, the displays for evaluation of cardiac structures are presented in three orthogonal cardiac planes: horizontal long axis, vertical long axis, and short axis (Figure 1). Therefore, it is important to evaluate a suspicious findings of MPD detected in transaxial images by multiplanar reformatted cardiac plane images. To identify a culprit coronary artery and likely location of flow-limiting coronary stenosis, knowledge of the distribution of coronary blood flow in the AHA 17-segment model of the left ventricle is also important. Figure 2 shows the general assignment of the 17 myocardial segments to one of the three major coronary arteries[20]. The apex, segment 17, which can be supplied by any of the three arterie, is where the greatest variability in myocardial blood supply occurs. Segments 1, 2, 7, 8, 13, 14, and 17 are assigned to the left anterior descending artery (LAD) distribution, and segments 3, 4, 9, 10, and 15 to the

Table 1 Studies investigating the ability of non-ECG-gated contrast-enhanced computed tomography to detect acute coronary syndrome

Ref.	Type of CT	CT phase	No. of Patients	No. of ACS	No. of positive MPD	True Positive	False Positive	True Negative	False Negative	Sensitivity (%)	Specificity (%)	PPV (%)	NPV (%)
Gosalia *et al*[15], 2004	SD	Arterial	37	18	16	15	1	18	3	83	95	94	86
Moore *et al*[16], 2006	16-slice	Arterial	87	11	10	6	4	72	5	55	95	60	94
Mano *et al* [17], 2015	64-slice	Arterial	154	28	43	26	17	109	2	93	87	60	98
Watanabe *et al*[18], 2016	64-slice	Arterial	23	13	12	11	1	9	2	85	90	92	82
Yamazaki *et al*[19], 2016	16/64-slice	Parenchymal	47	32	30	29	1	14	3	91	93	97	82

ACS: Acute coronary syndrome, MPD: Myocardial perfusion defect, PPV: Positive predictive value, NPV: Negative predictive value, SD: Single detector.

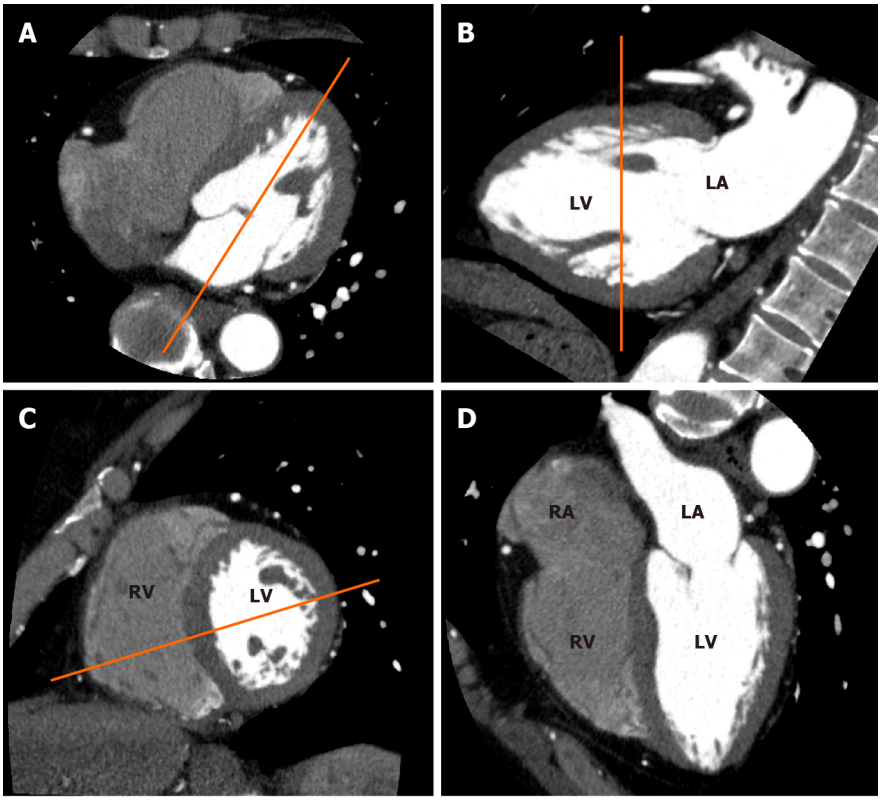

DOI: 10.4329/wjr.v14.i2.30

Figure 1 Electrocardiogram-gated cardiac computed tomography (CT)-based sequential approach to CT imaging of cardiac planes. A: From an axial CT data set at the level of the mitral valve, a longitudinal plane bisecting the mitral valve and the left ventricular apex is used to create a vertical long axis view; B: From the vertical long axis view, a slice parallel to the mitral annulus at the mid ventricular level is used to obtain a short axis view; C: From the short axis view, a slice bisecting the center of the left ventricle (LV) and the intersection between the junction of the free wall and diaphragmatic wall of the right ventricle (RV) are used to obtain a horizontal long axis view. (D) Horizontal long axis view showing the left atrium, LV, right atrium and RV.

right coronary artery (RCA) when it is dominant. Generally, segments 5, 6, 11, 12, and 16 are assigned to the left circumflex coronary artery (LCX). However, it should be noted that the coronary artery blood supply to the myocardial segments is variable. Coronary dominance is determined by the artery supplying the posterior descending artery (Figure 3). Among the general population, approximately

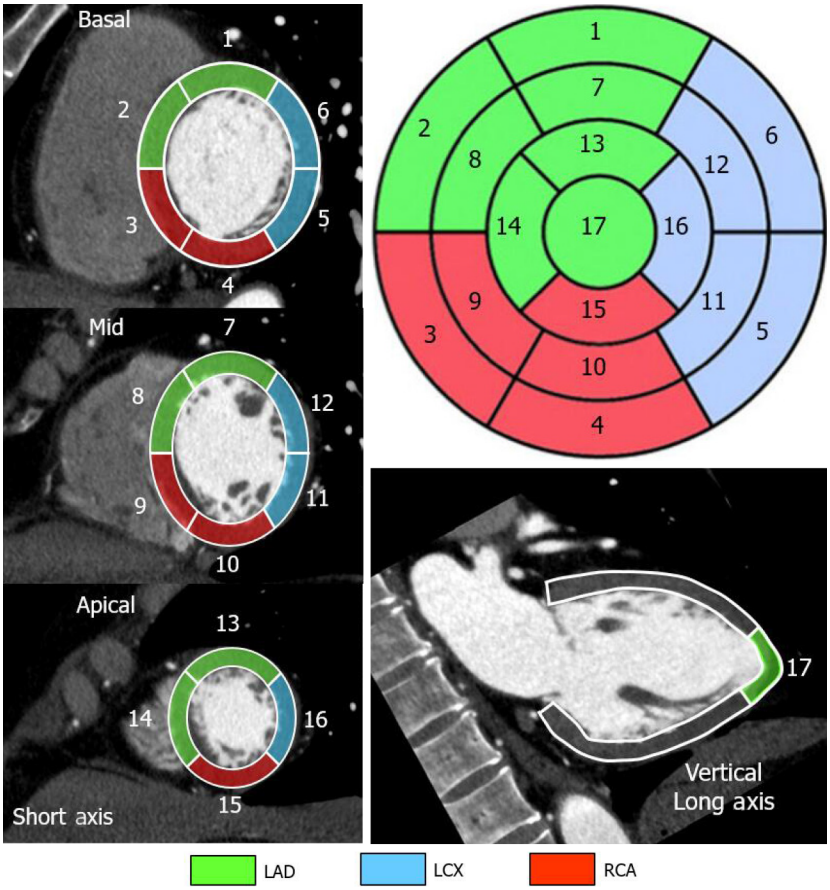

DOI: 10.4329/wjr.v14.i2.30

Figure 2 Standard segmental myocardial display in a 17-segment model. Electrocardiogram-gated cardiac computed tomography-based individual assignment of left ventricular segmentation following the American Heart Association 17-segment model with corresponding color-coded coronary artery perfusion territories for a right-dominant coronary system. LAD: Left anterior descending artery in green; LCX: Left circumflex coronary artery in blue; RCA: Right coronary artery in red.

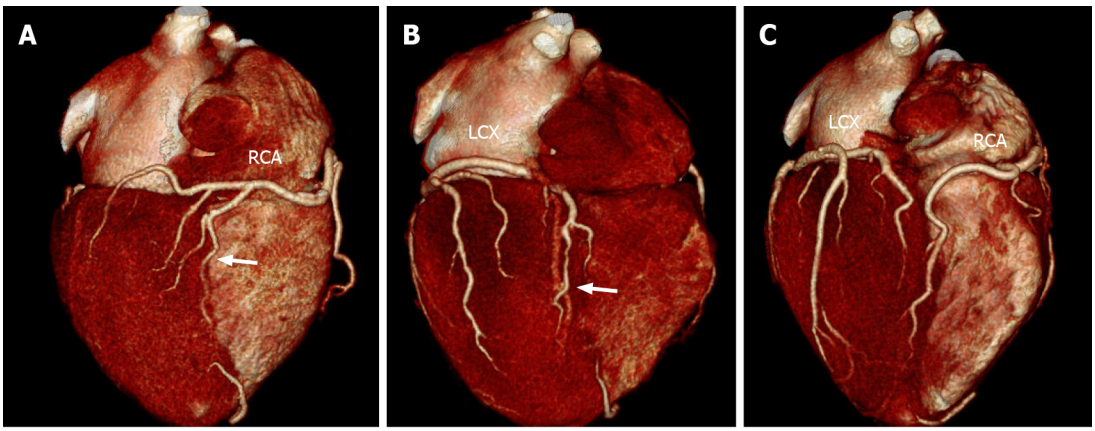

DOI: 10.4329/wjr.v14.i2.30

Figure 3 Variability in the coronary artery blood supply to the myocardium. Three-dimensional volume-rendered electrocardiogram-gated cardiac computed tomography images showing the inferior surface of the heart representing different coronary anatomy variants; A: Standard, right-dominant circulation. Right coronary artery (RCA) supplies posterior descending branch (arrow). Left circumflex coronary artery (LCX) supplies only inferolateral left ventricular myocardium; B: Left-dominant circulation. LCX supplies posterior descending branch (arrow). RCA supplies only right ventricular myocardium; C: Codominant circulation. Inferior myocardium is supplied both RCA and LCX.

70%-80% is right-dominant (supplied by the RCA), 5%-10% is left-dominant (supplied by the LCX), and 10%-20% is co-dominant (supplied by both the RCA and LCX)[21]. In our experience, MPD territories demonstrated on non-ECG-gated contrast-enhanced CT agree with the results of invasive coronary angiography, radionuclide myocardial perfusion imaging, and cardiac magnetic resonance imaging

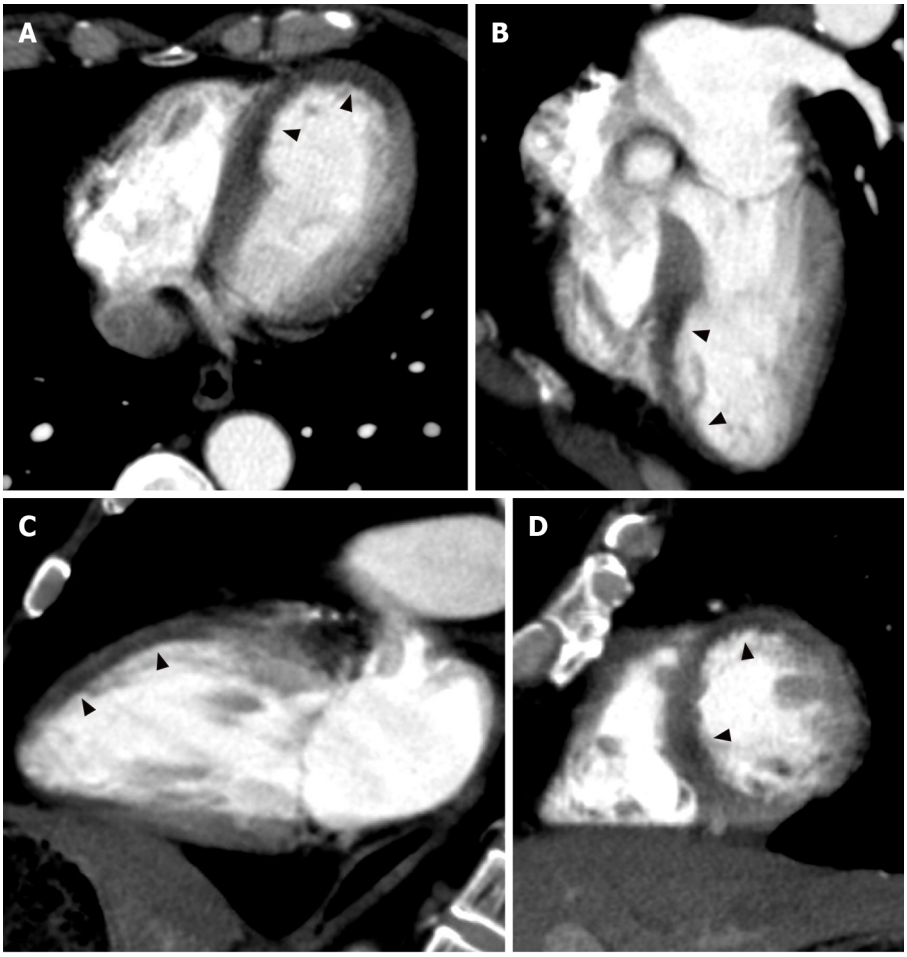

DOI: 10.4329/wjr.v14.i2.30

Figure 4 Non-electrocardiogram-gated contrast-enhanced computed tomography images in acute coronary syndrome of left anterior descending artery. A 64-year-old man with chest pain underwent non-electrocardiogram (ECG)-gated contrast-enhanced computed tomography (CECT) in search of aortic dissection. Axial (A), horizontal long axis (B), vertical long axis (C), and short axis (D) reformatted non-ECG-gated CECT images acquired 29 s after contrast injection showed decreased myocardial enhancement in the mid to apical anterior wall to the septum and apex of the left ventricle (arrowheads).

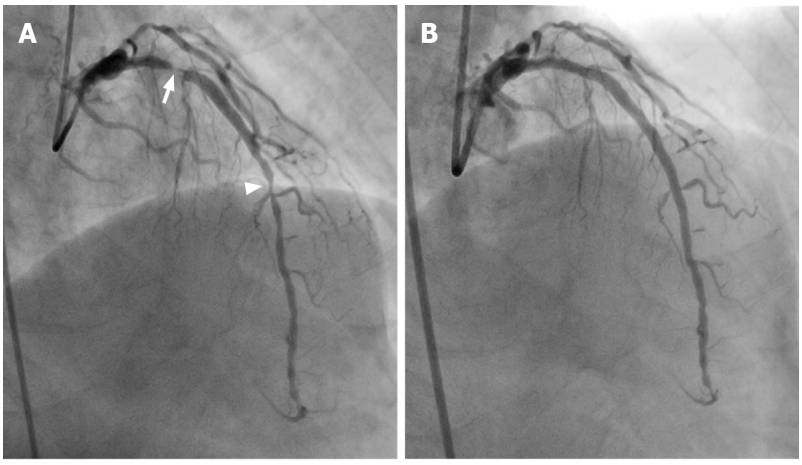

DOI: 10.4329/wjr.v14.i2.30

Figure 5 Corresponding invasive coronary angiography in acute coronary syndrome of left anterior descending artery. A: Same patient as Figure 4. Invasive coronary angiography showed 90% and 75% stenosis in the proximal (arrow) and mid (arrowhead) site of the left anterior descending artery; B: Subsequent percutaneous coronary intervention was performed by balloon angioplasty and stent implantation. His laboratory examination showed no elevation of cardiac biomarkers.

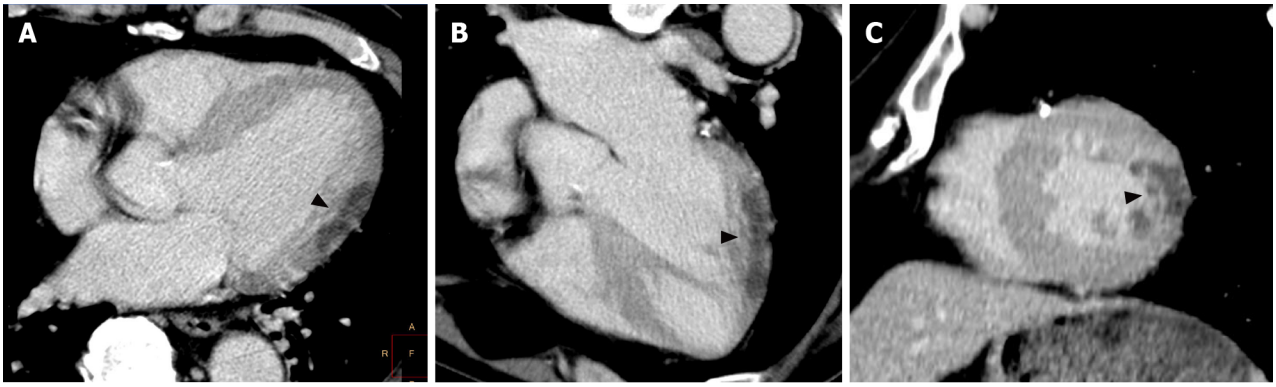

DOI: 10.4329/wjr.v14.i2.30

Figure 6 Non-electrocardiogram-gated contrast-enhanced computed tomography images in acute coronary syndrome of left circumflex coronary artery. A 65-year-old man with epigastralgia underwent non-electrocardiogram (ECG)-gated contrast-enhanced computed tomography (CECT) in search of aortic dissection. Axial (A), horizontal long axis (B), and short axis (C) reformatted non-ECG-gated CECT images acquired 120 s after contrast injection showed decreased myocardial enhancement in the mid lateral wall of the left ventricle (arrowheads).

with high accuracy (LAD: Figures 4 and 5, LCX: Figures 6 and 7, RCA: Figures 8 and 9).

Global myocardial ischemia

In a study that evaluated the presence of MPD on non-ECG-gated contrast-enhanced CT, Watanabe *et al* [18] described a patient with AMI of the left main trunk who did not show MPD. In our experience, broad MPD induced by the occlusion of the left main trunk highlights the normally perfused myocardial enhancement in the RCA territory (Figures 10 and 11). Balanced ischemia is a well-known limitation of stress radionuclide myocardial perfusion imaging[22]. MPD seen in radionuclide myocardial perfusion imaging results from the relative difference in radiotracer uptake of the left ventricular myocardium normalized to the most normal area with the highest radiotracer uptake. Therefore, in patients with ischemia that is relatively balanced among the three major vascular territories, this potentially results in a homogeneous radiotracer distribution in the myocardium, thus underestimating the severity of ischemia or even indicating a falsely normal result. MPD demonstrated on contrast-enhanced CT also reflects the relative difference in left ventricular myocardial contrast enhancement. Hence, it may be difficult to detect global myocardial ischemia as focal MPD on non-ECG-gated contrast-enhanced CT even in a rest condition.

Hemopericardium

Common causes of pericardial effusion include heart failure, renal failure, neoplasm, infection, and injury, including trauma and myocardial infarction[23]. Pericardial fluid characteristics are reflected in the CT attenuation value. It is likely that a value closer to the value of water (0 Hounsfield units) is a simple effusion. A value greater than that of water density can be observed in conditions including malignancy, purulent exudate, and hemopericardium[23]. Hemopericardium is induced by cardiac rupture, ruptured ascending aortic dissection, trauma, neoplasm, and as a consequence of cardiac surgery (iatrogenic)[24,25]. Left ventricular free wall rupture is one of the complications of AMI that is often fatal. Acute rupture is usually fatal, but some patients with a small ventricular tear, which may be sealed temporarily by a clot or fibrinous pericardial adhesions, may progress to a subacute form allowing late survival. In cases with hemopericardium, the presence of MPD on contrast-enhanced CT is a finding highly suspicious of left ventricular free wall rupture and should be carefully checked. Accompanying myocardial defects are also detected even in non-ECG-gated contrast-enhanced CT (Figures 12 and 13).

Papillary muscle

The papillary muscles are one of the components of the mitral valve apparatus[26]. Two papillary muscles arise from the area between the apical and middle thirds of the left ventricular wall. Both the anterior and posterior mitral valve leaflets are attached *via* primary, secondary, and tertiary chordae to both anterolateral and posteromedial papillary muscles. The anterolateral papillary muscle is often composed of a single major muscle group, whereas the posteromedial papillary muscle usually comprises two or three major muscle groups (Figure 14). Left ventricular papillary muscles are particularly vulnerable to ischemia because they are perfused by the terminal portion of the coronary vascular bed. The anterolateral papillary muscle is supplied by the diagonal branches of the LAD and often by marginal branches from the LCX. In contrast, the supply to the posteromedial papillary muscle is *via* the posterior descending branch of the LCX or RCA (depending on dominance)[27]. Necrosis of a papillary muscle is a frequent complication of MI and it should be recognized because it may lead to papillary

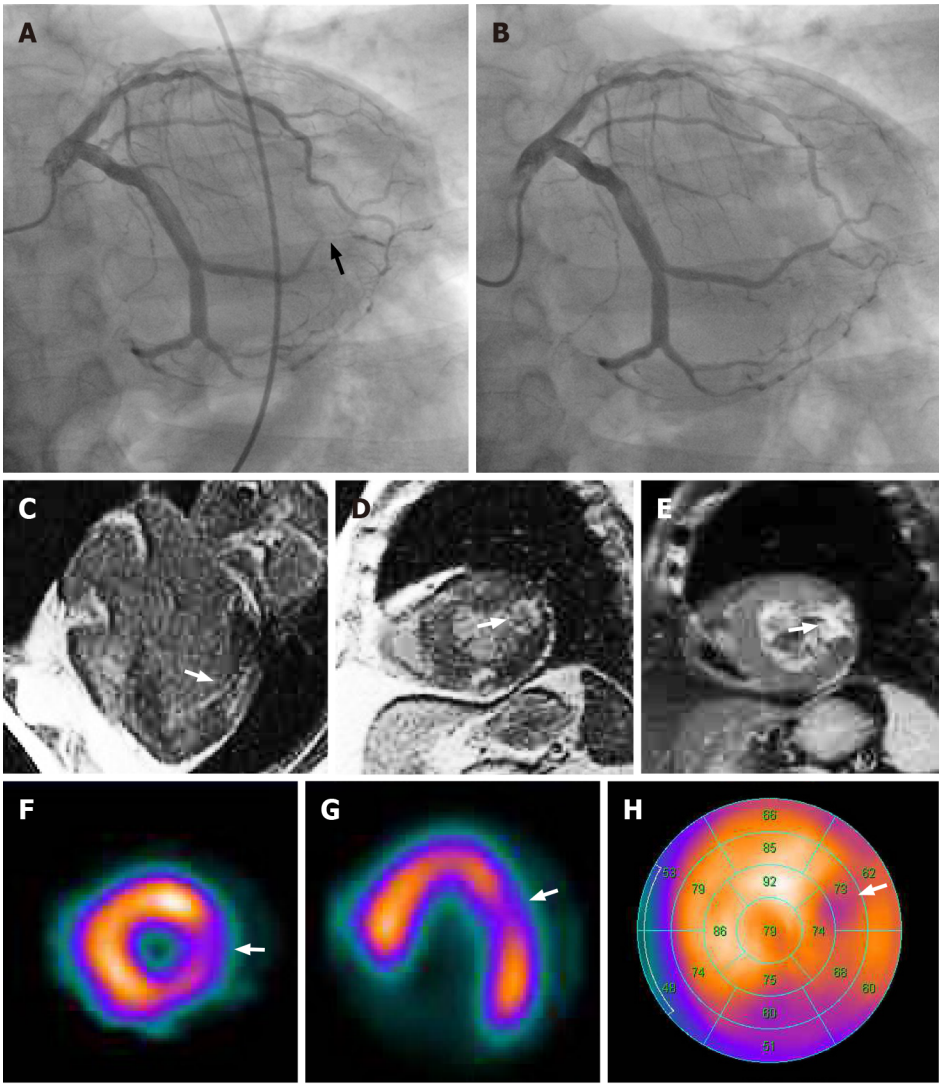

DOI: 10.4329/wjr.v14.i2.30

Figure 7 Corresponding invasive coronary angiography, cardiac magnetic resonance imaging and tetrofosmin single-photon emission computed tomography in acute coronary syndrome of left circumflex coronary artery. Same patient as Figure 6. A: Invasive coronary angiography showed 99% stenosis in the posterolateral branch of the left circumflex coronary artery (arrow). B: Subsequent percutaneous coronary intervention was performed by balloon angioplasty and stent implantation. His laboratory data showed elevation of cardiac biomarkers (creatine kinase 1620 IU/L, creatine kinase MB 120 IU/L). Horizontal long axis (C) and short axis (D) views of the contrast-enhanced cardiac magnetic resonance imaging (MRI) showed late gadolinium enhancement in the mid lateral wall of the left ventricle (arrow). A short axis view of the T2-weighted cardiac MRI showed high signal intensity in the mid lateral wall of the left ventricle (E, arrow). Short axis (F) and horizontal long axis (G) views and a bull's eye polar plot (H) of rest technetium-99m tetrofosmin single-photon emission computed tomography myocardial perfusion imaging showed hypoperfusion in the mid lateral wall of the left ventricle (arrows).

muscle rupture, which is a rare but often-fatal mechanical complication. The posteromedial papillary muscle is particularly vulnerable to myocardial ischemia because of its single system of blood supply (Figure 15). The presence of MPD of the papillary muscle on contrast-enhanced CT is a finding suspicious of papillary muscle ischemia or necrosis, and detectable even in non-ECG-gated contrast-enhanced CT (Figure 16).

Myocardial fat

CT attenuation values are quantitative, and they can be used to define a structure's density or the iodine content after administration of iodinated contrast media. In a cardiac CT study, Nieman *et al*[28] showed that CT attenuation values found in patients with long-standing (over 1 year) MI (-13 ± 37 HU) were significantly lower than in patients with acute (within 1 wk) MI (26 ± 26 HU) and normal hearts (73 ± 14 HU). Histologic analyses showed that myocardial fat at the site of a healed MI is common with a prevalence of 68%-84%[29,30]. The presence of myocardial fat can be identified at the macroscopic level by CT, although a small amount of microscopic myocardial fat may be undetectable[31]. Myocardial fat at the site of a MI is frequently observed as a subendocardial low attenuation in the distribution of the culprit coronary artery on both non-contrast and contrast-enhanced CT even in non-ECG-gated CT (Figure 17). Concomitant regional myocardial wall motion reduction in areas of old MI may support the

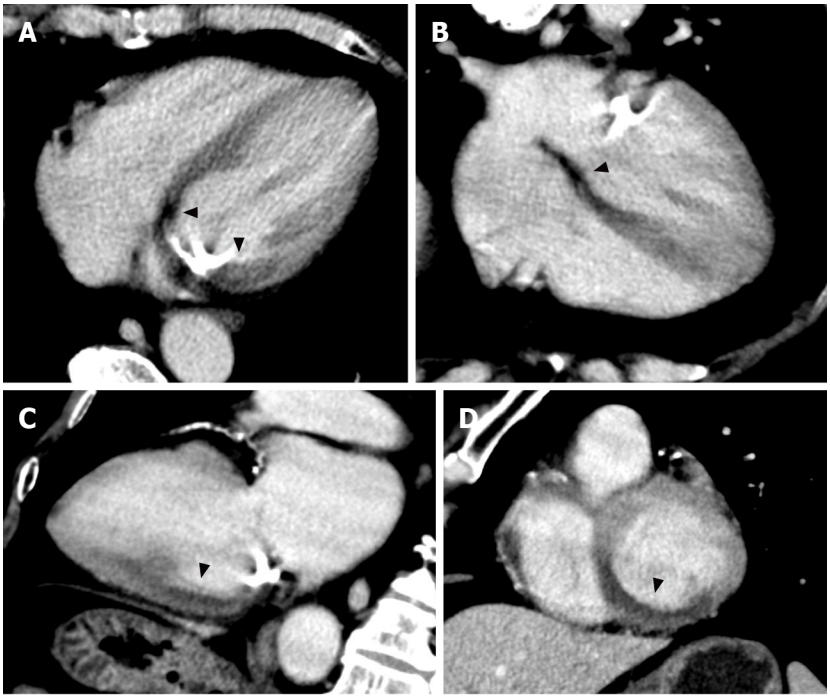

DOI: 10.4329/wjr.v14.i2.30

Figure 8 Non-electrocardiogram-gated contrast-enhanced computed tomography images in acute coronary syndrome of right coronary artery. A 67-year-old man with chest pain underwent non-electrocardiogram (ECG)-gated contrast-enhanced computed tomography (CECT) in search of aortic dissection. Axial (A), horizontal long axis (B), vertical long axis (C), and short axis (D) reformatted non-ECG-gated CECT images acquired 120 s after contrast injection showed decreased myocardial enhancement in the basal to mid inferior, inferolateral, and inferoseptal wall of the left ventricle (arrowheads).

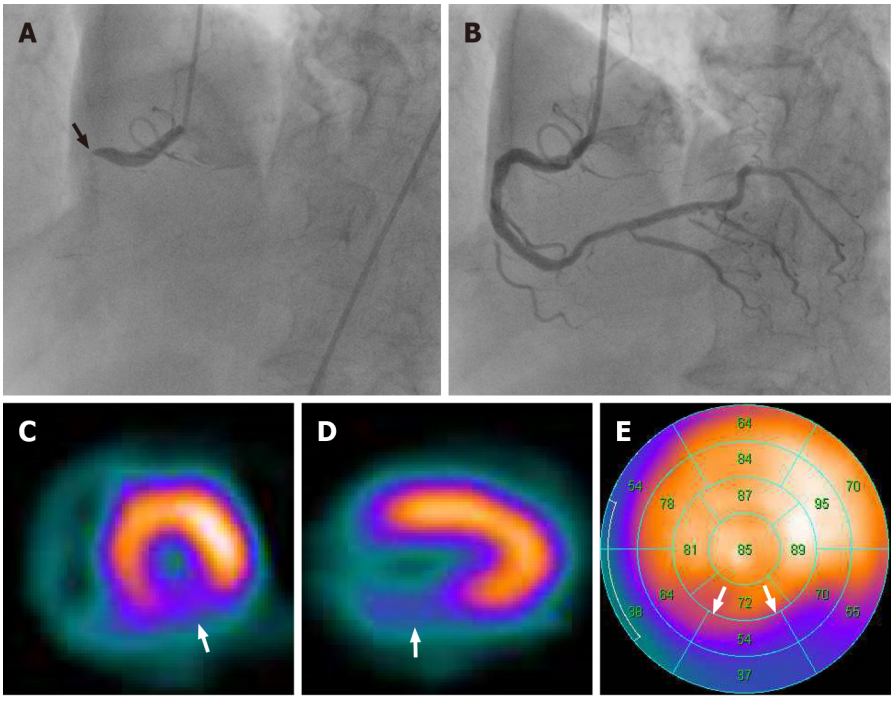

DOI: 10.4329/wjr.v14.i2.30

Figure 9 Corresponding invasive coronary angiography and sestamibi single-photon emission computed tomography in acute coronary syndrome of right coronary artery. Same patient as Figure 8. A: Invasive coronary angiography showed total occlusion in the proximal site of the right coronary artery (arrow); B: Subsequent percutaneous coronary intervention was performed by balloon angioplasty and stent implantation. His laboratory data showed elevation of cardiac biomarkers (creatine kinase 1620 IU/L, creatine kinase MB 239 IU/L). Short axis (C) and vertical long axis (D) views and a bull's eye polar plot (E) of rest technetium-99m sestamibi single-photon emission computed tomography myocardial perfusion imaging showed perfusion defect in the basal to mid inferior, inferolateral and inferoseptal wall of the left ventricle (arrows).

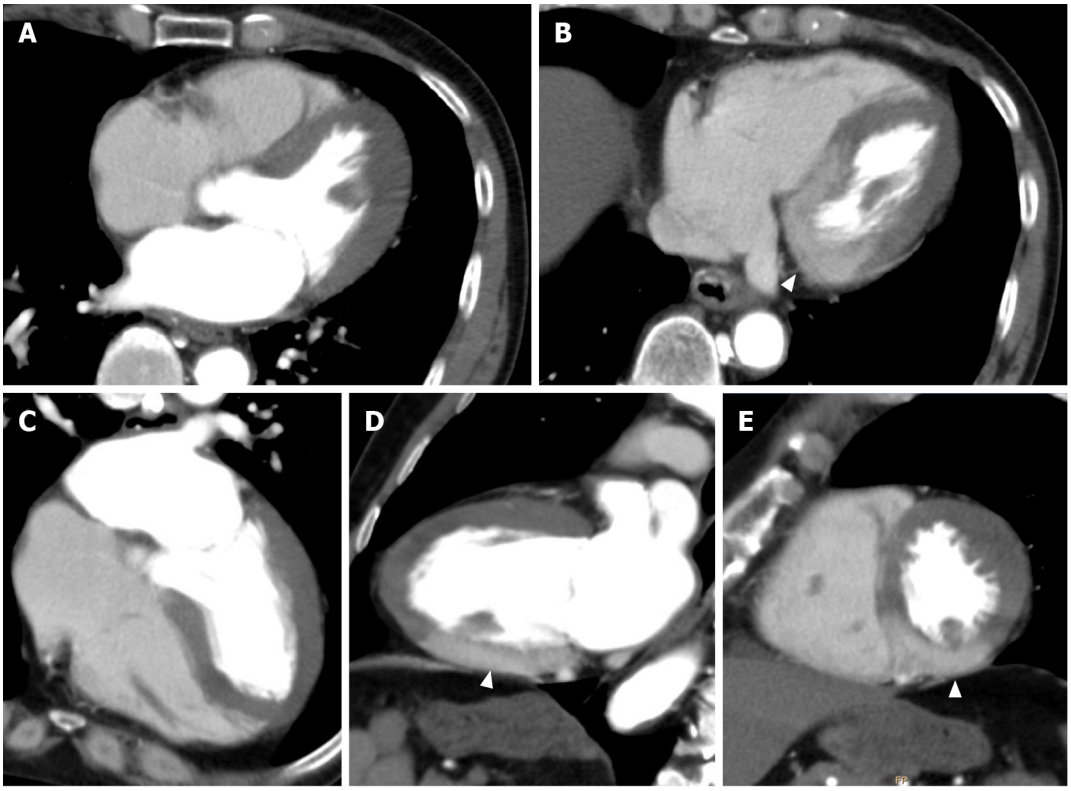

DOI: 10.4329/wjr.v14.i2.30

Figure 10 Non-electrocardiogram-gated contrast-enhanced computed tomography images in acute coronary syndrome of left main trunk. A 70-year-old man with severe dyspnea underwent non-electrocardiogram (ECG)-gated contrast-enhanced computed tomography (CECT) for discriminating acute pulmonary thromboembolism. Axial (A, B), horizontal long axis (C), vertical long axis (D), and short axis (E) reformatted non-ECG-gated CECT images acquired 120 s after contrast injection showed localized myocardial enhancement only in the basal to mid inferior wall of the left ventricle (arrowheads).

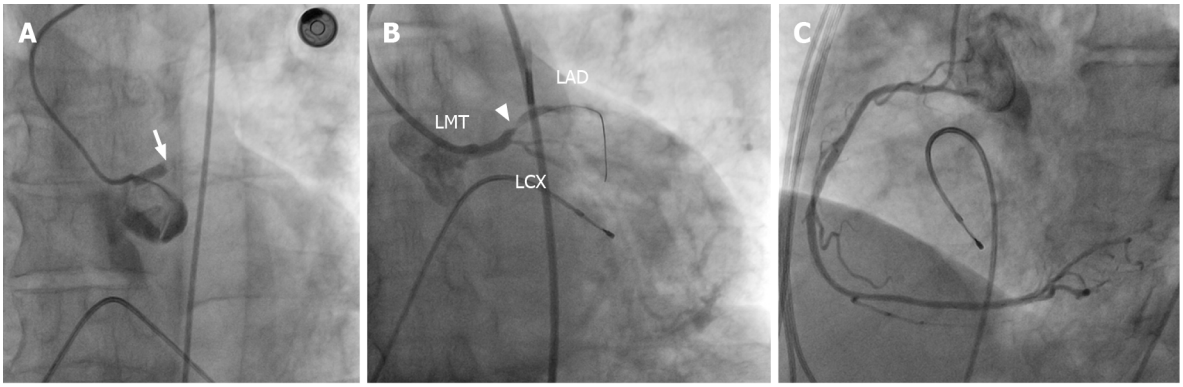

DOI: 10.4329/wjr.v14.i2.30

Figure 11 Corresponding invasive coronary angiography in acute coronary syndrome of left main trunk. Same patient as Figure 10. A: Invasive coronary angiography showed thrombotic occlusion in the left main trunk (arrow). Subsequent percutaneous coronary intervention (PCI) was tried. B: After guidewire was crossed to the left anterior descending artery, there was minimal improvement in flow and 99% stenosis in the proximal site of the left anterior descending artery appeared (arrowhead); C: The right coronary artery showed no significant stenosis. The patient died during PCI because of uncontrollable ventricular fibrillation. LMT: Left main trunk; LAD: Left anterior descending artery; LCX: Left circumflex coronary artery.

clear visualization of the myocardial fat. The prevalence of left ventricular myocardial fat detected by CT increases as the infarct age becomes higher[32]. Because it is important to differentiate ACS from OMI, in cases who present MPD on contrast-enhanced CT, CT-detectable myocardial fat associated with old MI should be excluded by comparison with non-contrast CT. In our experience, AMI of the RCA complicated with old MI of the diagonal branch was successfully distinguished by comparison with non-contrast CT in a non-ECG-gated CT examination (Figures 17-19). However, because OMI does not always show myocardial fat, it is difficult to differentiate ACS from OMI without CT-detectable myocardial fat only with usual contrast-enhanced computed tomography.

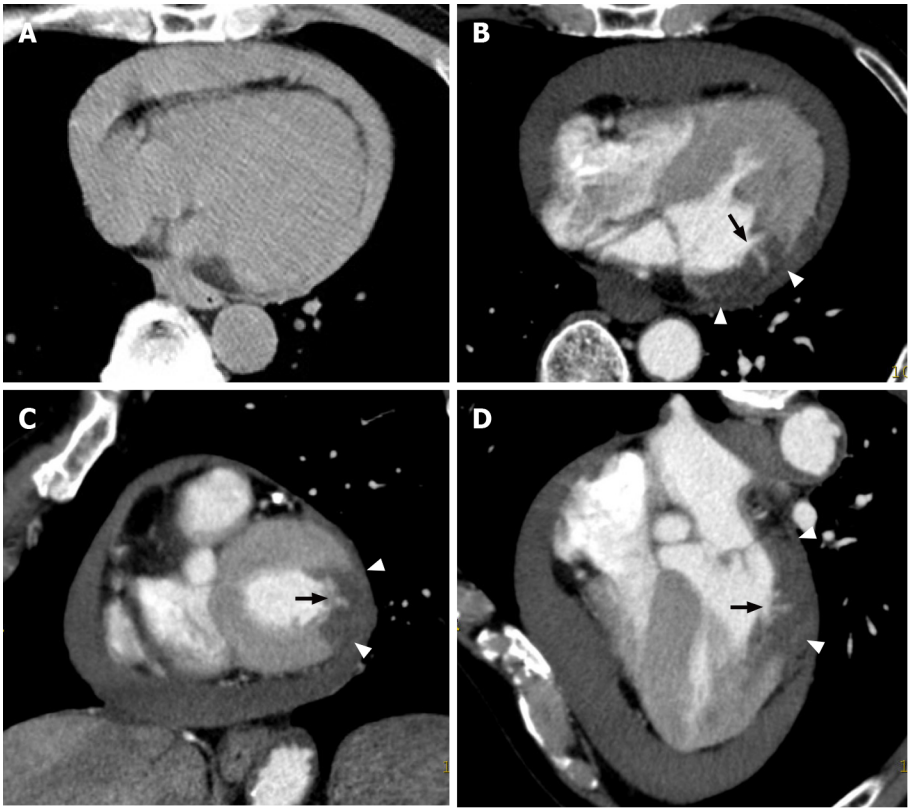

DOI: 10.4329/wjr.v14.i2.30

Figure 12 Non-electrocardiogram-gated contrast-enhanced computed tomography images in postinfarct cardiac free wall rupture. A: An 81-year-old man with syncope first underwent non-electrocardiogram (ECG)-gated non-contrast whole body computed tomography (CT), and moderate pericardial effusion was found. The attenuation value of the pericardial effusion was about 50 Hounsfield units. Subsequently, non-ECG-gated contrast-enhanced CT (CECT) was performed in search of ascending aortic dissection. Axial (B), short axis (C), and horizontal long axis (D) reformatted non-ECG-gated CECT images acquired 120 s after contrast injection showed decreased myocardial enhancement in the basal to mid lateral wall of the left ventricle (arrowheads) and a small myocardial defect (arrow).

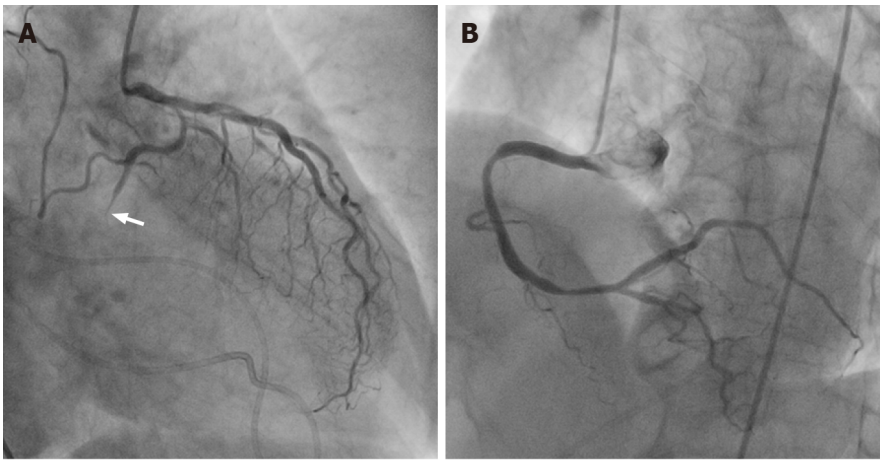

DOI: 10.4329/wjr.v14.i2.30

Figure 13 Corresponding invasive coronary angiography in postinfarct cardiac free wall rupture. Same patient as Figure 12. A: Invasive coronary angiography showed total occlusion in the distal site of the left circumflex coronary artery (arrow); B: The right coronary artery showed no significant stenosis. The patient subsequently underwent a surgical operation. After removal of the large clot within the pericardium, a small perforation was found in the lateral wall of the left ventricle, confirming a definitive diagnosis of left ventricular free wall rupture.

CONCLUSION

Definitive diagnosis of ACS is sometimes difficult to achieve, especially in patients who present with atypical symptoms, normal initial biomarkers of myocardial necrosis, and normal or nondiagnostic ECGs. In order to avoid inappropriate management for this life-threatening event, clinicians should be

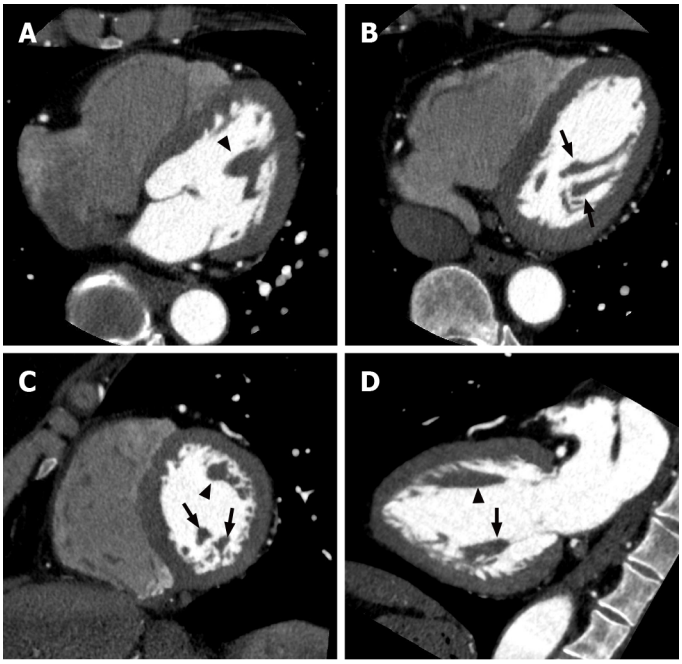

DOI: 10.4329/wjr.v14.i2.30

Figure 14 Left ventricular papillary muscles. Axial (A, B), short axis (C), and vertical long axis (D) reformatted electrocardiogram-gated cardiac CT images showing the anatomy of the left ventricular chamber of the normal heart. The anterolateral (arrowheads) and posteromedial (arrows) papillary muscles manifest as filling defects within the contrast-filled left ventricular lumen.

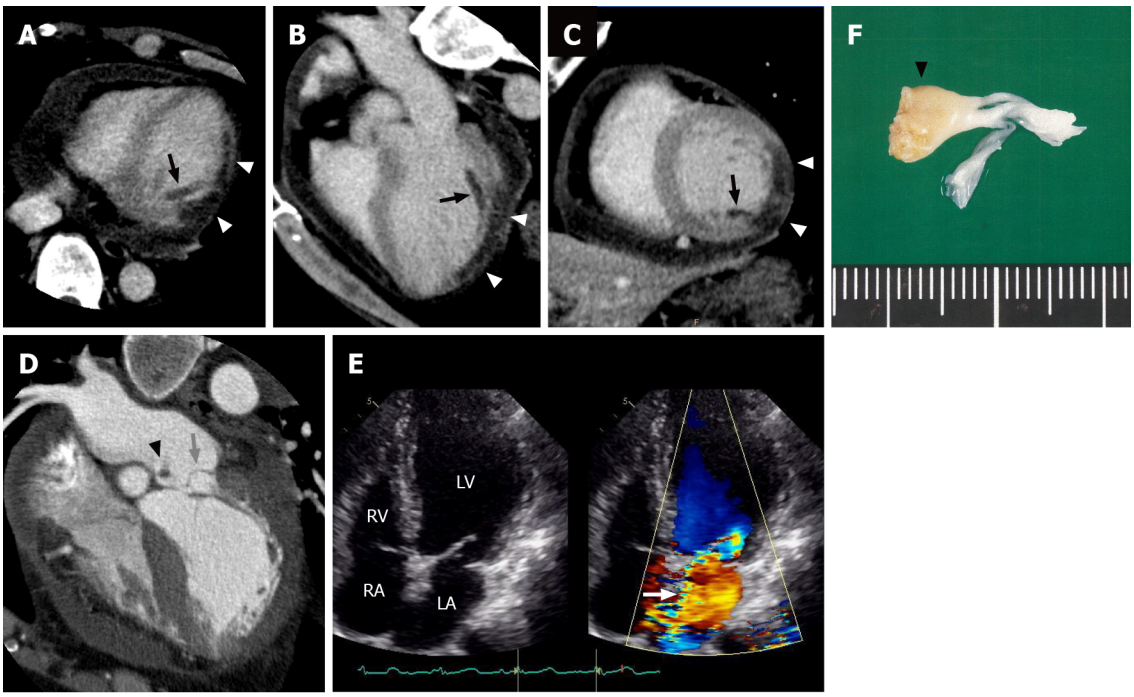

DOI: 10.4329/wjr.v14.i2.30

Figure 15 Postinfarct left ventricular papillary muscle rupture. Electrocardiogram-gated cardiac CT images from a 61-year-old man with posteromedial papillary muscle rupture complicated by acute ST elevation myocardial infarction due to total occlusion of the left circumflex coronary artery. Axial (A), three-chamber (B), and short axis (C) reformatted cardiac CT images showed decreased myocardial enhancement in the inferolateral wall (white arrowheads) and posteromedial papillary muscle (black arrows) of the left ventricle. A horizontal long axis image (D) showed severe prolapse of the posterior mitral valve leaflet into the left atrium (grey arrow) with discernible papillary muscle attachment (black arrowhead). An apical four-chamber color Doppler image of the transthoracic echocardiogram showed severe mitral regurgitation during ventricular systole extending to the posterior left atrial wall (E, white arrow). The patient subsequently underwent a mitral valve replacement. Surgical specimen showed posteromedial papillary muscle attached to the resected posterior mitral leaflet (F, black arrowhead). LV: Left ventricle; LA: Left atrium; RV: Right ventricle; RA: Right atrium.

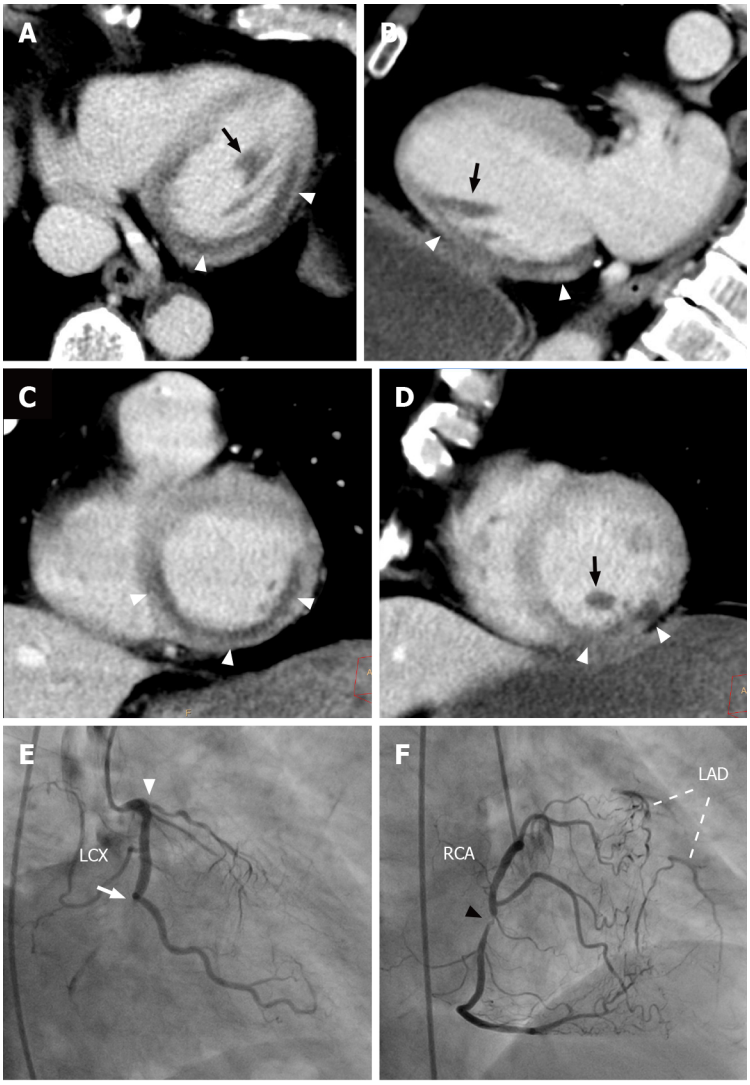

DOI: 10.4329/wjr.v14.i2.30

Figure 16 Myocardial perfusion defect of the posteromedial papillary muscle on non-electrocardiogram-gated contrast-enhanced computed tomography. A 68-year-old man with right anterior chest pain underwent non-electrocardiogram (ECG)-gated contrast-enhanced computed tomography (CECT) in search of aortic dissection. Axial (A), vertical long axis (B), and short axis (C, D) reformatted non-ECG-gated CECT images acquired 120 s after contrast injection showed decreased myocardial enhancement in the basal to mid inferior, inferolateral, and inferoseptal walls of the left ventricle (arrowheads). Decreased myocardial enhancement was also recognized in the posteromedial papillary muscle (arrows). Invasive coronary angiography showed total occlusion in the distal site of the left circumflex coronary artery (E, arrow), total occlusion in the proximal site of the left anterior descending artery (E, arrowhead), and 90% stenosis in the mid site of the right coronary artery (F, arrowhead), which provides abundant collateral flow to the left anterior descending artery. The patient subsequently underwent an emergent coronary artery bypass grafting. LAD: Left anterior descending artery; LCX: Left circumflex coronary artery; RCA: Right coronary artery.

aware that MPD is more commonly detectable even on routine non-ECG-gated contrast-enhanced CT performed in search of other pathologies.

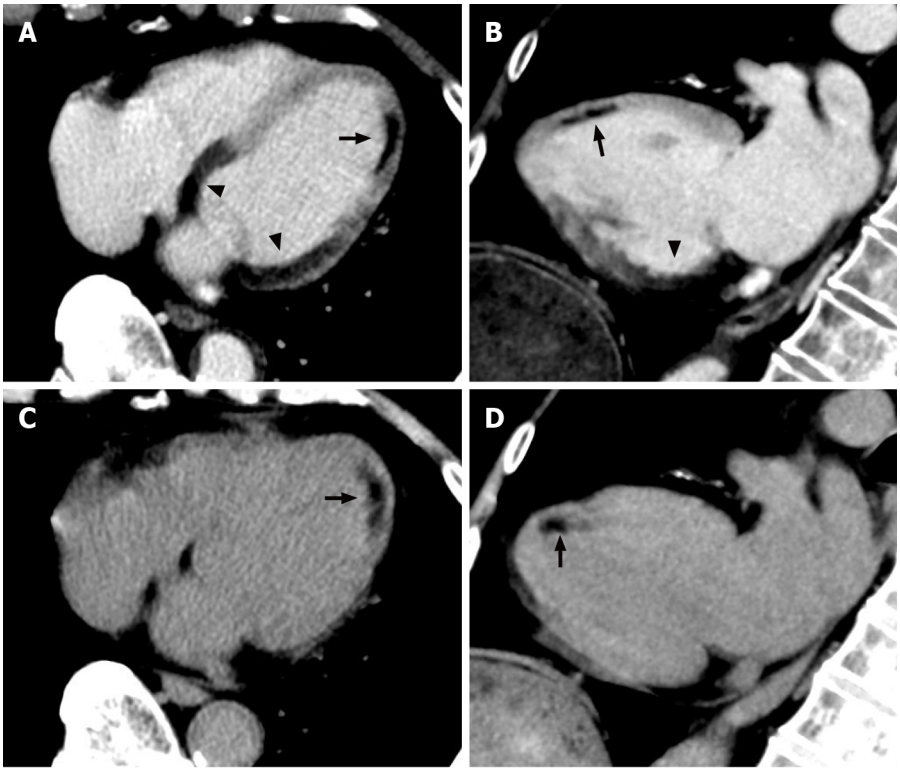

DOI: 10.4329/wjr.v14.i2.30

Figure 17 Non-electrocardiogram-gated contrast-enhanced computed tomography images in acute coronary syndrome of right coronary artery complicated with anterior old myocardial infarction. An 82-year-old man with back pain underwent non-electrocardiogram (ECG)-gated contrast-enhanced computed tomography (CECT) in search of aortic dissection. Axial (A) and vertical long axis (B) reformatted non-ECG-gated CECT images acquired 120 s after contrast injection showed decreased myocardial enhancement in the basal to mid inferior, inferolateral, and inferoseptal walls of the left ventricle (arrowheads). Non-ECG-gated CECT images also showed decreased myocardial enhancement in the mid anterior wall of the left ventricle apart from the above-mentioned area (arrow). Axial (C) and vertical long axis (D) reformatted non-ECG-gated non-contrast CT images showed subendocardial low attenuation less than 0 Hounsfield units only in the mid anterior wall of the left ventricle, which is consistent with myocardial fatty degeneration associated with the old myocardial infarction (arrow).

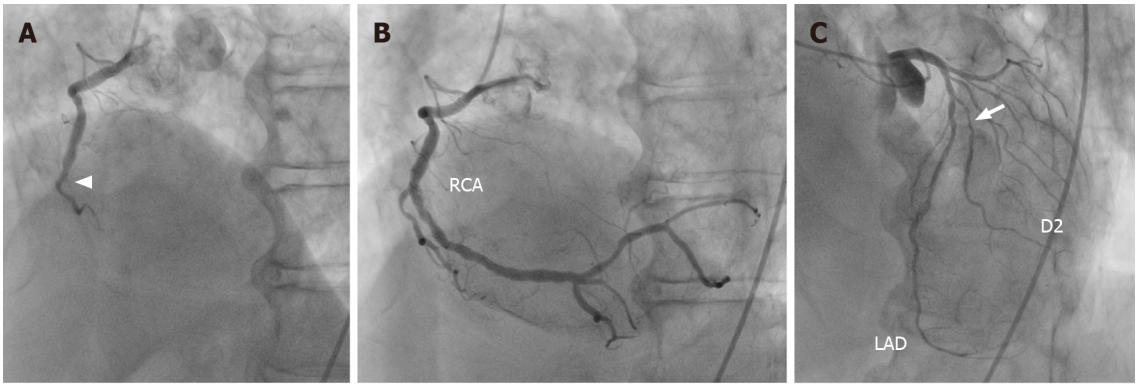

DOI: 10.4329/wjr.v14.i2.30

Figure 18 Corresponding invasive coronary angiography in acute coronary syndrome of right coronary artery complicated with anterior old myocardial infarction. Same patient as Figure 17. A: Invasive coronary angiography showed total occlusion in the mid site of the right coronary artery (arrowhead); B: Subsequent percutaneous coronary intervention was performed by balloon angioplasty and stent implantation. C: Invasive coronary angiography also showed 75% stenosis in the proximal site of the second diagonal branch (arrow). RCA: Right coronary artery; LAD: Left anterior descending artery; D2: Second diagonal branch.

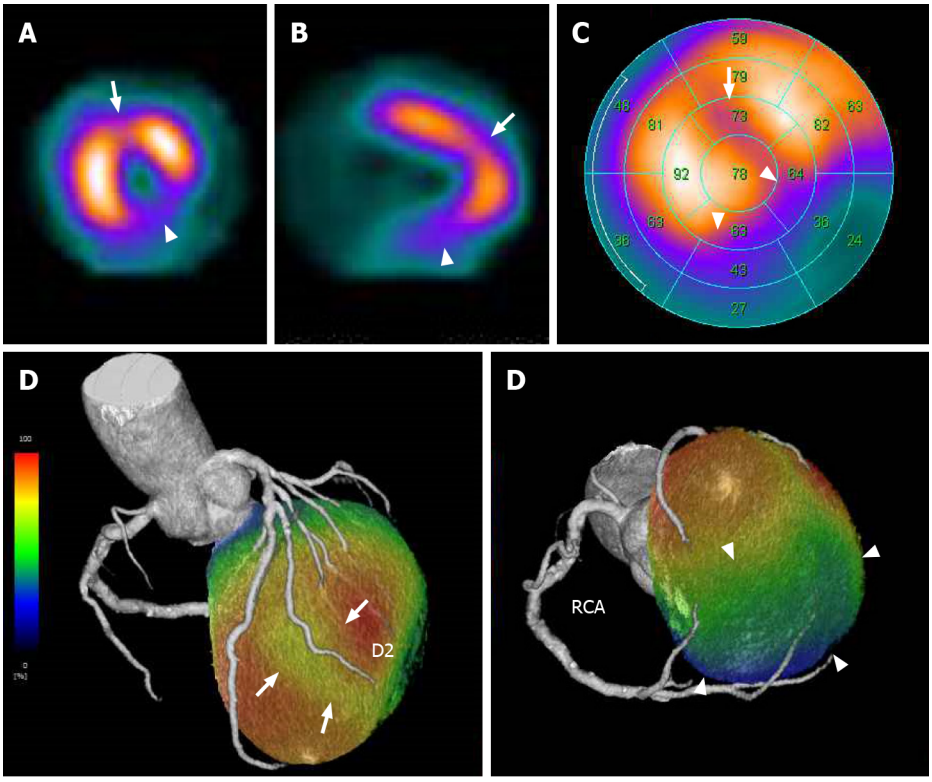

DOI: 10.4329/wjr.v14.i2.30

Figure 19 Corresponding sestamibi single-photon emission computed tomography in acute coronary syndrome of right coronary artery complicated with anterior old myocardial infarction. Same patient as Figures 17 and 18. Rest technetium-99m sestamibi single-photon emission computed tomography (SPECT) myocardial perfusion imaging (MPI) are shown. Short axis (A) and vertical long axis (B) views and a bull's eye polar plot (C) of rest technetium-99m sestamibi SPECT MPI showed perfusion defects in the basal to mid inferior, inferolateral, and inferoseptal walls of the left ventricle (arrowheads). In addition, SPECT MPI also showed hypoperfusion in the mid anterior wall of the left ventricle (arrows). The volume-rendered, coregistered SPECT MPI, and cardiac CT images demonstrated that hypoperfusion in the mid anterior wall of the left ventricle seen on the SPECT MPI corresponded with the territory of the second diagonal branch (D, arrows), whereas the perfusion defects in the basal to mid inferior, inferolateral, and inferoseptal walls of the left ventricle seen on the SPECT MPI corresponded with the territory of the right coronary artery (D, arrowheads). LAD: Left anterior descending artery, D2: Second diagonal branch; RCA: Right coronary artery.

FOOTNOTES

Author contributions: Yoshihara S designed and performed all of this study and wrote the all of the revised manuscript.

Conflict-of-interest statement: The authors declare that they have no conflicts of interest.

Country/Territory of origin: Japan

ORCID number: Shu Yoshihara 0000-0001-9294-3767.

S-Editor: Liu JH
L-Editor: A
P-Editor: Liu JH

REFERENCES

1 **Amsterdam EA**, Wenger NK, Brindis RG, Casey DE Jr, Ganiats TG, Holmes DR Jr, Jaffe AS, Jneid H, Kelly RF, Kontos MC, Levine GN, Liebson PR, Mukherjee D, Peterson ED, Sabatine MS, Smalling RW, Zieman SJ; ACC/AHA Task Force Members. 2014 AHA/ACC guideline for the management of patients with non-ST-elevation acute coronary syndromes: a

report of the American College of Cardiology/American Heart Association Task Force on Practice Guidelines. *Circulation* 2014; **130**: e344-e426 [PMID: 25249585 DOI: 10.1161/CIR.0000000000000134]

2 **Canto JG**, Shlipak MG, Rogers WJ, Malmgren JA, Frederick PD, Lambrew CT, Ornato JP, Barron HV, Kiefe CI. Prevalence, clinical characteristics, and mortality among patients with myocardial infarction presenting without chest pain. *JAMA* 2000; **283**: 3223-3229 [PMID: 10866870 DOI: 10.1001/jama.283.24.3223]

3 **Kosuge M**, Kimura K, Ishikawa T, Ebina T, Hibi K, Tsukahara K, Kanna M, Iwahashi N, Okuda J, Nozawa N, Ozaki H, Yano H, Nakati T, Kusama I, Umemura S. Differences between men and women in terms of clinical features of ST-segment elevation acute myocardial infarction. *Circ J* 2006; **70**: 222-226 [PMID: 16501283 DOI: 10.1253/circj.70.222]

4 **Body R**, Carley S, Wibberley C, McDowell G, Ferguson J, Mackway-Jones K. The value of symptoms and signs in the emergent diagnosis of acute coronary syndromes. *Resuscitation* 2010; **81**: 281-286 [PMID: 20036454 DOI: 10.1016/j.resuscitation.2009.11.014]

5 **Larson DB**, Johnson LW, Schnell BM, Salisbury SR, Forman HP. National trends in CT use in the emergency department: 1995-2007. *Radiology* 2011; **258**: 164-173 [PMID: 21115875 DOI: 10.1148/radiol.10100640]

6 **Shriki JE**, Shinbane J, Lee C, Khan AR, Burns N, Hindoyan A, Wilcox A. Incidental myocardial infarct on conventional nongated CT: a review of the spectrum of findings with gated CT and cardiac MRI correlation. *AJR Am J Roentgenol* 2012; **198**: 496-504 [PMID: 22357988 DOI: 10.2214/AJR.11.7683]

7 **American College of Cardiology Foundation Task Force on Expert Consensus Documents**, Mark DB, Berman DS, Budoff MJ, Carr JJ, Gerber TC, Hecht HS, Hlatky MA, Hodgson JM, Lauer MS, Miller JM, Morin RL, Mukherjee D, Poon M, Rubin GD, Schwartz RS. ACCF/ACR/AHA/NASCI/SAIP/SCAI/SCCT 2010 expert consensus document on coronary computed tomographic angiography: a report of the American College of Cardiology Foundation Task Force on Expert Consensus Documents. *J Am Coll Cardiol* 2010; **55**: 2663-2699 [PMID: 20513611 DOI: 10.1016/j.jacc.2009.11.013]

8 **Goldstein JA**, Chinnaiyan KM, Abidov A, Achenbach S, Berman DS, Hayes SW, Hoffmann U, Lesser JR, Mikati IA, O'Neil BJ, Shaw LJ, Shen MY, Valeti US, Raff GL; CT-STAT Investigators. The CT-STAT (Coronary Computed Tomographic Angiography for Systematic Triage of Acute Chest Pain Patients to Treatment) trial. *J Am Coll Cardiol* 2011; **58**: 1414-1422 [PMID: 21939822 DOI: 10.1016/j.jacc.2011.03.068]

9 **Hoffmann U**, Truong QA, Schoenfeld DA, Chou ET, Woodard PK, Nagurney JT, Pope JH, Hauser TH, White CS, Weiner SG, Kalanjian S, Mullins ME, Mikati I, Peacock WF, Zakroysky P, Hayden D, Goehler A, Lee H, Gazelle GS, Wiviott SD, Fleg JL, Udelson JE; ROMICAT-II Investigators. Coronary CT angiography *vs* standard evaluation in acute chest pain. *N Engl J Med* 2012; **367**: 299-308 [PMID: 22830462 DOI: 10.1056/NEJMoa1201161]

10 **Litt HI**, Gatsonis C, Snyder B, Singh H, Miller CD, Entrikin DW, Leaming JM, Gavin LJ, Pacella CB, Hollander JE. CT angiography for safe discharge of patients with possible acute coronary syndromes. *N Engl J Med* 2012; **366**: 1393-1403 [PMID: 22449295 DOI: 10.1056/NEJMoa1201163]

11 **Cury RC**, Feuchtner GM, Batlle JC, Peña CS, Janowitz W, Katzen BT, Ziffer JA. Triage of patients presenting with chest pain to the emergency department: implementation of coronary CT angiography in a large urban health care system. *AJR Am J Roentgenol* 2013; **200**: 57-65 [PMID: 23255742 DOI: 10.2214/AJR.12.8808]

12 **Taylor AJ**, Cerqueira M, Hodgson JM, Mark D, Min J, O'Gara P, Rubin GD; American College of Cardiology Foundation Appropriate Use Criteria Task Force; Society of Cardiovascular Computed Tomography; American College of Radiology; American Heart Association; American Society of Echocardiography; American Society of Nuclear Cardiology; North American Society for Cardiovascular Imaging; Society for Cardiovascular Angiography and Interventions; Society for Cardiovascular Magnetic Resonance, Kramer CM, Berman D, Brown A, Chaudhry FA, Cury RC, Desai MY, Einstein AJ, Gomes AS, Harrington R, Hoffmann U, Khare R, Lesser J, McGann C, Rosenberg A, Schwartz R, Shelton M, Smetana GW, Smith SC Jr. ACCF/SCCT/ACR/AHA/ASE/ASNC/NASCI/SCAI/SCMR 2010 appropriate use criteria for cardiac computed tomography. A report of the American College of Cardiology Foundation Appropriate Use Criteria Task Force, the Society of Cardiovascular Computed Tomography, the American College of Radiology, the American Heart Association, the American Society of Echocardiography, the American Society of Nuclear Cardiology, the North American Society for Cardiovascular Imaging, the Society for Cardiovascular Angiography and Interventions, and the Society for Cardiovascular Magnetic Resonance. *J Am Coll Cardiol* 2010; **56**: 1864-1894 [PMID: 21087721 DOI: 10.1016/j.jacc.2010.07.005]

13 **Pursnani A**, Lee AM, Mayrhofer T, Ahmed W, Uthamalingam S, Ferencik M, Puchner SB, Bamberg F, Schlett CL, Udelson J, Hoffmann U, Ghoshhajra BB. Early resting myocardial computed tomography perfusion for the detection of acute coronary syndrome in patients with coronary artery disease. *Circ Cardiovasc Imaging* 2015; **8**: e002404 [PMID: 25752898 DOI: 10.1161/CIRCIMAGING.114.002404]

14 **Leipsic J**, Abbara S, Achenbach S, Cury R, Earls JP, Mancini GJ, Nieman K, Pontone G, Raff GL. SCCT guidelines for the interpretation and reporting of coronary CT angiography: a report of the Society of Cardiovascular Computed Tomography Guidelines Committee. *J Cardiovasc Comput Tomogr* 2014; **8**: 342-358 [PMID: 25301040 DOI: 10.1016/j.jcct.2014.07.003]

15 **Gosalia A**, Haramati LB, Sheth MP, Spindola-Franco H. CT detection of acute myocardial infarction. *AJR Am J Roentgenol* 2004; **182**: 1563-1566 [PMID: 15150010 DOI: 10.2214/ajr.182.6.1821563]

16 **Moore W**, Fields J, Mieczkowski B. Multidetector computed tomography pulmonary angiogram in the assessment of myocardial infarction. *J Comput Assist Tomogr* 2006; **30**: 800-803 [PMID: 16954933 DOI: 10.1097/01.rct.0000230001.15650.05]

17 **Mano Y**, Anzai T, Yoshizawa A, Itabashi Y, Ohki T. Role of non-electrocardiogram-gated contrast-enhanced computed tomography in the diagnosis of acute coronary syndrome. *Heart Vessels* 2015; **30**: 1-8 [PMID: 24221182 DOI: 10.1007/s00380-013-0437-8]

18 **Watanabe T**, Furuse Y, Ohta Y, Kato M, Ogawa T, Yamamoto K. The Effectiveness of Non-ECG-Gated Contrast-Enhanced Computed Tomography for the Diagnosis of Non-ST Segment Elevation Acute Coronary Syndrome. *Int Heart J* 2016; **57**: 558-564 [PMID: 27593539 DOI: 10.1536/ihj.16-072]

19 **Yamazaki M**, Higuchi T, Shimokoshi T, Kiguchi T, Horii Y, Yoshimura N, Aoyama H. Acute coronary syndrome: evaluation of detection capability using non-electrocardiogram-gated parenchymal phase CT imaging. *Jpn J Radiol* 2016;

34: 331-338 [PMID: 26883335 DOI: 10.1007/s11604-016-0527-5]

20 **Cerqueira MD**, Weissman NJ, Dilsizian V, Jacobs AK, Kaul S, Laskey WK, Pennell DJ, Rumberger JA, Ryan T, Verani MS; American Heart Association Writing Group on Myocardial Segmentation and Registration for Cardiac Imaging. Standardized myocardial segmentation and nomenclature for tomographic imaging of the heart. A statement for healthcare professionals from the Cardiac Imaging Committee of the Council on Clinical Cardiology of the American Heart Association. *Circulation* 2002; **105**: 539-542 [PMID: 11815441 DOI: 10.1161/hc0402.102975]

21 **Angelini P**. Coronary artery anomalies--current clinical issues: definitions, classification, incidence, clinical relevance, and treatment guidelines. *Tex Heart Inst J* 2002; **29**: 271-278 [PMID: 12484611]

22 **Berman DS**, Kang X, Slomka PJ, Gerlach J, de Yang L, Hayes SW, Friedman JD, Thomson LE, Germano G. Underestimation of extent of ischemia by gated SPECT myocardial perfusion imaging in patients with left main coronary artery disease. *J Nucl Cardiol* 2007; **14**: 521-528 [PMID: 17679060 DOI: 10.1016/j.nuclcard.2007.05.008]

23 **Wang ZJ**, Reddy GP, Gotway MB, Yeh BM, Hetts SW, Higgins CB. CT and MR imaging of pericardial disease. *Radiographics* 2003; **23** Spec No: S167-S180 [PMID: 14557510 DOI: 10.1148/rg.23si035504]

24 **Haddadin S**, Milano AD, Faggian G, Morjan M, Patelli F, Golia G, Franchi P, Mazzucco A. Surgical treatment of postinfarction left ventricular free wall rupture. *J Card Surg* 2009; **24**: 624-631 [PMID: 20078707 DOI: 10.1111/j.1540-8191.2009.00896.x]

25 **Restrepo CS**, Gutierrez FR, Marmol-Velez JA, Ocazionez D, Martinez-Jimenez S. Imaging patients with cardiac trauma. *Radiographics* 2012; **32**: 633-649 [PMID: 22582351 DOI: 10.1148/rg.323115123]

26 **Otto CM**. Clinical practice. Evaluation and management of chronic mitral regurgitation. *N Engl J Med* 2001; **345**: 740-746 [PMID: 11547744 DOI: 10.1056/NEJMcp003331]

27 **Voci P**, Bilotta F, Caretta Q, Mercanti C, Marino B. Papillary muscle perfusion pattern. A hypothesis for ischemic papillary muscle dysfunction. *Circulation* 1995; **91**: 1714-1718 [PMID: 7882478 DOI: 10.1161/01.cir.91.6.1714]

28 **Nieman K**, Cury RC, Ferencik M, Nomura CH, Abbara S, Hoffmann U, Gold HK, Jang IK, Brady TJ. Differentiation of recent and chronic myocardial infarction by cardiac computed tomography. *Am J Cardiol* 2006; **98**: 303-308 [PMID: 16860013 DOI: 10.1016/j.amjcard.2006.01.101]

29 **Baroldi G**, Silver MD, De Maria R, Parodi O, Pellegrini A. Lipomatous metaplasia in left ventricular scar. *Can J Cardiol* 1997; **13**: 65-71 [PMID: 9039067]

30 **Su L**, Siegel JE, Fishbein MC. Adipose tissue in myocardial infarction. *Cardiovasc Pathol* 2004; **13**: 98-102 [PMID: 15033159 DOI: 10.1016/S1054-8807(03)00134-0]

31 **Kimura F**, Matsuo Y, Nakajima T, Nishikawa T, Kawamura S, Sannohe S, Hagiwara N, Sakai F. Myocardial fat at cardiac imaging: how can we differentiate pathologic from physiologic fatty infiltration? *Radiographics* 2010; **30**: 1587-1602 [PMID: 21071377 DOI: 10.1148/rg.306105519]

32 **Ichikawa Y**, Kitagawa K, Chino S, Ishida M, Matsuoka K, Tanigawa T, Nakamura T, Hirano T, Takeda K, Sakuma H. Adipose tissue detected by multislice computed tomography in patients after myocardial infarction. *JACC Cardiovasc Imaging* 2009; **2**: 548-555 [PMID: 19442939 DOI: 10.1016/j.jcmg.2009.01.010]

World Journal of Radiology

Submit a Manuscript: https://www.f6publishing.com

World J Radiol 2022 February 28; 14(2): 47-49

DOI: 10.4329/wjr.v14.i2.47

ISSN 1949-8470 (online)

LETTER TO THE EDITOR

Diagnostic accuracy of thoracic imaging modalities for the detection of COVID-19

Haben Dawit, Marissa Absi, Nayaar Islam, Sanam Ebrahimzadeh, Matthew D F McInnes

Specialty type: Radiology, nuclear medicine and medical imaging

Provenance and peer review: Unsolicited article; Externally peer reviewed.

Peer-review model: Single blind

Peer-review report's scientific quality classification

Grade A (Excellent): A
Grade B (Very good): 0
Grade C (Good): 0
Grade D (Fair): 0
Grade E (Poor): 0

P-Reviewer: Sageena G

Received: August 7, 2021
Peer-review started: August 7, 2021
First decision: November 11, 2021
Revised: November 11, 2021
Accepted: February 19, 2022
Article in press: February 19, 2022
Published online: February 28, 2022

Haben Dawit, Marissa Absi, Nayaar Islam, Sanam Ebrahimzadeh, Clinical Epidemiology Program, Ottawa Hospital Research Institute, Ottawa K1E4M9, ON, Canada

Matthew D F McInnes, Department of Radiology, The Ottawa Hospital Research Institute Clinical Epidemiology Program, Ottawa K1H8L6, ON, Canada

Corresponding author: Matthew D F McInnes, MD, PhD, Professor, Department of Radiology, The Ottawa Hospital Research Institute Clinical Epidemiology Program, 451 Smyth Road, Ottawa K1H8L6, ON, Canada. mmcinnes@toh.ca

Abstract

The ongoing coronavirus disease 2019 (COVID-19) pandemic continues to present diagnostic challenges. The use of thoracic radiography has been studied as a method to improve the diagnostic accuracy of COVID-19. The 'Living' Cochrane Systematic Review on the diagnostic accuracy of imaging tests for COVID-19 is continuously updated as new information becomes available for study. In the most recent version, published in March 2021, a meta-analysis was done to determine the pooled sensitivity and specificity of chest X-ray (CXR) and lung ultrasound (LUS) for the diagnosis of COVID-19. CXR gave a sensitivity of 80.6% (95%CI: 69.1-88.6) and a specificity of 71.5% (95%CI: 59.8-80.8). LUS gave a sensitivity rate of 86.4% (95%CI: 72.7-93.9) and specificity of 54.6% (95%CI: 35.3-72.6). These results differed from the findings reported in the recent article in this journal where they cited the previous versions of the study in which a meta-analysis for CXR and LUS could not be performed. Additionally, the article states that COVID-19 could not be distinguished, using chest computed tomography (CT), from other respiratory diseases. However, the latest review version identifies chest CT as having a specificity of 80.0% (95%CI: 74.9-84.3), which is much higher than the previous version which indicated a specificity of 61.1% (95%CI: 42.3-77.1). Therefore, CXR, chest CT and LUS have the potential to be used in conjunction with other methods in the diagnosis of COVID-19.

Key Words: COVID-19; Chest x-ray; Computed tomography; Lung ultrasound; Specificity and sensitivity; Diagnostic accuracy

Core Tip: The global coronavirus disease 2019 (COVID-19) outbreak has greatly impacted the world, with almost 200 million cases worldwide and more than 4 million deaths (as of July 21, 2021). Reverse transcriptase polymerase chain reaction is the current gold-standard for diagnosing COVID-19, but due to a diagnostic error rate greater than 10%, alternate modes of diagnosis are needed. Our review demonstrates that chest X-ray, chest computed tomography and lung ultrasound may have the potential to aid healthcare workers in the diagnosis of COVID-19.

Citation: Dawit H, Absi M, Islam N, Ebrahimzadeh S, McInnes MDF. Diagnostic accuracy of thoracic imaging modalities for the detection of COVID-19. *World J Radiol* 2022; 14(2): 47-49
URL: https://www.wjgnet.com/1949-8470/full/v14/i2/47.htm
DOI: https://dx.doi.org/10.4329/wjr.v14.i2.47

TO THE EDITOR

We appreciate Kumar *et al*[1] consideration of our study in their paper on the discrepancies in the clinical and radiological profiles of coronavirus disease 2019 (COVID-19)[1]. In this paper, the use of chest computed tomography (CT), chest X-ray (CXR), and lung ultrasound (LUS) as possible diagnostic tools for the COVID-19 is discussed. The authors cite the findings from two versions of the Cochrane Review titled "Thoracic imaging tests for the diagnosis of COVID-19." As more information becomes available, this systematic review has aimed to keep pace with the new data. The most recent version of the review, published in March 2021, has shown differences in the sensitivities and specificities of these three image modalities compared to the findings in prior versions reported in the article by Kumar *et al*[1].

Firstly, the authors cited the initial review by Salameh *et al*[2], which determined that CXR had a pooled sensitivity of CXR is 82.1% (95%CI: 62.5-92.7)[1,2] in patients who had COVID-19. The second version of the review, by Islam *et al*[3], determined that CXR had a sensitivity ranging from 56.9% to 89.0% and specificity ranging from 11.1% to 88.9%[1,3] in patients with COVID-19. As opposed to the first two versions, in the third and most recent version, there was a sufficient number of studies, evaluating the diagnostic accuracy of CXR, to perform a meta-analysis. The updated version of the review conducted a meta-analysis with 9 studies and 3694 participants for CXR. The following imaging modality had sensitivity and specificity of 80.6% (95%CI: 69.1-88.6) and 71.5% (95%CI: 59.8-80.8)[4], respectively. These findings demonstrate that CXR is moderately sensitive and moderately specific to COVID-19, and may have the potential to be used as a secondary method for diagnosis, however, due to the limited number of studies, accuracy estimates must be carefully interpreted[4]. In the upcoming fourth version of the systematic review, additional studies evaluating CXR have been included. In this review, additional analyses have been done to support our conclusion, and potential sources of variabilities in CXR accuracy estimates will be discussed.

Secondly, the article by Kumar *et al*[1] states that chest CT may not be capable of discriminating COIVD-19 from other respiratory diseases[1]. The review by Salameh *et al*[2] obtained a pooled specificity of 18.1% (95%CI: 3.71-55.8)[2] for chest CT, in cases where CT scans were used as the primary diagnostic test, which was subsequently updated to 61.1% (95%CI: 42.3-77.1) in the subsequent edition [3]. The third and most recent version identified that the specificity of chest CT has increased substantially to 80.0% (95%CI: 74.9-84.3), based on 41 studies with 16133 patients[4]. The improved specificity could be due to the stricter inclusion criteria for this version. In the most recent version, studies that published index test findings without clearly defining the images as positive or negative[4] for COVID-19, were excluded. An alternate explanation for the improved specificity could be the increase in studies that use well-developed definitions for index test positivity (*e.g.* Co-RADS)[4]. Furthermore, studies from the later stage of the pandemic were included with each review version which affected our specificity values through improved knowledge about the indications of COVID-19 in imaging results [4].

Lastly, the most recent version of the 'Living' Cochrane Systematic Review observed that in patients suspected of having COVID-19, LUS had a sensitivity and specificity rate of 86.4% (95%CI: 72.7-93.9) and 54.6% (95%CI: 35.3-72.6)[4], respectively. The accuracy estimates were produced through a meta-analysis including 5 studies with 446 patients[4]. These findings differ from the second review version cited by Kumar *et al*[1], which reported a sensitivity of 96.8% and sensitivity of 62.3% for LUS[1,3]. The second version of the review was based off of one study, therefore a meta-analysis was not completed[1, 3]. The increase in studies in the most recent version reduced the role of chance in our results, and provided a better picture of the diagnostic accuracy of LUS; however, the number of studies remains small and all data should be carefully interpreted.

In summary, the most recent version of the 'Living' Cochrane Systematic Review was able to perform further analyses on the diagnostic accuracy of CXR and LUS. The data demonstrates that CXR is moderately specific and moderately sensitive, while LUS is sensitive, but not specific for the diagnosis

of COVID-19. Additionally, the review demonstrated that chest CT is moderately specific for the diagnosis of COVID-19. We hope that future studies will be more rigorous and transparent when designing and reporting the findings of their study. We admire the continued interest in our systematic review and will update our review as more information on the diagnostic accuracy of these imaging modalities becomes available.

FOOTNOTES

Author contributions: All authors contributed to writing and editing this work.

Conflict-of-interest statement: There was no conflict of interest present in the production of this letter.

Country/Territory of origin: Canada

ORCID number: Haben Dawit 0000-0002-8052-4124; Marissa Absi 0000-0003-4581-9629; Nayaar Islam 0000-0002-1159-7629; Sanam Ebrahimzadeh 0000-0003-3890-1683; Matthew D F McInnes 0000-0001-8404-4075.

S-Editor: Fan JR
L-Editor: A
P-Editor: Fan JR

REFERENCES

1 **Kumar H**, Fernandez CJ, Kolpattil S, Munavvar M, Pappachan JM. Discrepancies in the clinical and radiological profiles of COVID-19: A case-based discussion and review of literature. *World J Radiol* 2021; **13**: 75-93 [PMID: 33968311 DOI: 10.4329/wjr.v13.i4.75]

2 **Salameh JP**, Leeflang MM, Hooft L, Islam N, McGrath TA, van der Pol CB, Frank RA, Prager R, Hare SS, Dennie C, Spijker R, Deeks JJ, Dinnes J, Jenniskens K, Korevaar DA, Cohen JF, Van den Bruel A, Takwoingi Y, van de Wijgert J, Damen JA, Wang J; Cochrane COVID-19 Diagnostic Test Accuracy Group, McInnes MD. Thoracic imaging tests for the diagnosis of COVID-19. *Cochrane Database Syst Rev* 2020; **9**: CD013639 [PMID: 32997361 DOI: 10.1002/14651858.CD013639.pub2]

3 **Islam N**, Salameh JP, Leeflang MM, Hooft L, McGrath TA, van der Pol CB, Frank RA, Kazi S, Prager R, Hare SS, Dennie C, Spijker R, Deeks JJ, Dinnes J, Jenniskens K, Korevaar DA, Cohen JF, Van den Bruel A, Takwoingi Y, van de Wijgert J, Wang J, McInnes MD; Cochrane COVID-19 Diagnostic Test Accuracy Group. Thoracic imaging tests for the diagnosis of COVID-19. *Cochrane Database Syst Rev* 2020; **11**: CD013639 [PMID: 33242342 DOI: 10.1002/14651858.CD013639.pub3]

4 **Islam N**, Ebrahimzadeh S, Salameh JP, Kazi S, Fabiano N, Treanor L, Absi M, Hallgrimson Z, Leeflang MM, Hooft L, van der Pol CB, Prager R, Hare SS, Dennie C, Spijker R, Deeks JJ, Dinnes J, Jenniskens K, Korevaar DA, Cohen JF, Van den Bruel A, Takwoingi Y, van de Wijgert J, Damen JA, Wang J, McInnes MD; Cochrane COVID-19 Diagnostic Test Accuracy Group. Thoracic imaging tests for the diagnosis of COVID-19. *Cochrane Database Syst Rev* 2021; **3**: CD013639 [PMID: 33724443 DOI: 10.1002/14651858.CD013639.pub4]

World Journal of Radiology

Submit a Manuscript: https://www.f6publishing.com

World J Radiol 2022 February 28; 14(2): 50-54

DOI: 10.4329/wjr.v14.i2.50

ISSN 1949-8470 (online)

LETTER TO THE EDITOR

Comments on "Review of the role of diagnostic modalities and imaging findings in the COVID-19 pandemic"

Sai Swarupa R Vulasala, Dheeraj R Gopireddy, Priya Bhosale, Mayur K Virarkar

Specialty type: Radiology, nuclear medicine and medical imaging

Provenance and peer review: Invited article; Externally peer reviewed.

Peer-review model: Single blind

Peer-review report's scientific quality classification

Grade A (Excellent): 0
Grade B (Very good): B, B, B
Grade C (Good): 0
Grade D (Fair): 0
Grade E (Poor): 0

P-Reviewer: Al-Ani RM, Samadder S, Shariati MBH

Received: November 6, 2021
Peer-review started: November 6, 2021
First decision: December 10, 2021
Revised: December 11, 2021
Accepted: February 15, 2022
Article in press: February 15, 2022
Published online: February 28, 2022

Sai Swarupa R Vulasala, Dheeraj R Gopireddy, Mayur K Virarkar, Department of Radiology, University of Florida College of Medicine, Jacksonville, FL 32209, United States

Priya Bhosale, Department of Diagnostic Radiology, UT MD Anderson Cancer Center, Houston, TX 77030, United States

Corresponding author: Sai Swarupa R Vulasala, MBBS, Research Assistant, Radiology, University of Florida College of Medicine, No. 655 West 8th Street, C90 2nd Floor, Clinical Center, Jacksonville, FL 32209, United States. vulasalaswarupa@gmail.com

Abstract

The present letter to the editor corresponds to the article entitled "Comprehensive literature review on the radiographic findings, imaging modalities, and the role of radiology in the coronavirus disease 2019 (COVID-19) pandemic" by Pal *et al*, published in *World J Radiol*. 2021; 13(9): 258-282. With zero to unknown prevalence, COVID-19 has created a heterogeneous and unforeseen situation across the world. Healthcare providers encountered new challenges in image interpretation, characterization, and prognostication of the disease. Pal *et al* delineated the radiological findings, which would guide the radiologists to identify the early signs of severe infection.

Key Words: COVID-19; Computed tomography; Lung ultrasound; COVID-19 scoring systems

Core Tip: Besides reverse transcriptase-polymerase chain reaction being the most standard test, chest X-ray, computed tomography, and lung ultrasound play a supportive role for Coronavirus disease 2019 (COVID-19) diagnosis. The main focus of this letter is to emphasize the importance of imaging in the COVID-19 pandemic. The various imaging characteristics aid in determining the severity of the disease and prognosis. The implementation of scoring systems further improves diagnostic efficiency. In addition, Pal *et al* discussed their COVID-19 first wave experience and recommended a few strategies for overcoming the second wave.

Citation: Vulasala SSR, Gopireddy DR, Bhosale P, Virarkar MK. Comments on "Review of the role of diagnostic modalities and imaging findings in the COVID-19 pandemic". *World J Radiol* 2022; 14(2): 50-54
URL: https://www.wjgnet.com/1949-8470/full/v14/i2/50.htm
DOI: https://dx.doi.org/10.4329/wjr.v14.i2.50

TO THE EDITOR

We read with interest the article published in the World Journal of Radiology by Pal *et al*[1] on the depiction of radiological findings in identifying and predicting coronavirus disease 2019 (COVID-19) patient patterns. We would like to commend the authors for this vital article encompassing the pathophysiology and evidence-based review of COVID-19 severity scoring systems on chest X-ray (CXR), computed tomography (CT), and lung ultrasound (LUS). The authors outlined the artificial intelligence (AI) aspect of the diagnostic process and its importance in supporting human resources during the pandemic.

Although reverse transcriptase-polymerase chain reaction (RT-PCR) is the standard work-up for a specific diagnosis, it is limited by sample quality, laboratory errors, ribonucleic acid (RNA) stability, and variable sensitivity[2]. RT-PCR involves two steps: (1) Reverse transcription; and (2) Quantitative real time polymerase chain reaction. It can detect RNA by using either RNA or deoxyribonucleic acid (DNA) as positive controls. Most of the commercial kits adopt DNA as control in fear of RNA degradation by ribonucleases (RNases). However, DNA kits cannot report failed reverse transcriptase step, thus resulting in high false negative rates (40%) and variable sensitivity[3]. To avoid this concern, appropriate controls are necessary for viral RNA detection. Also, a negative RT-PCR requires repetition of the test in cases of clinical suspicion[4]. In contrast, imaging is a rapid and reliable procedure to evaluate suspicion of COVID-19 in individuals presenting with cough, dyspnea, and fatigue. At the beginning of the pandemic, there was a distinct and contentious discussion on the role and importance of radiology as part of the clinical management of COVID-19.

CXR is a readily accessible and inexpensive modality in the majority of clinical settings. It is helpful for triage among suspected COVID-19 individuals in the emergency department[5]. Peripheral predominant hazy opacification, bilateral lower lobe consolidation, and air space opacities similar to acute respiratory distress syndrome are the characteristic findings of COVID-19 on CXR. Pleural effusion, nodules, and pneumothorax are also unusual findings that can be discerned in COVID-19 patients[6].

Radiological assessment of lung edema (RALE) (Table 1) and Brixia score (Table 2) are the CXR-based grading systems in practice to predict the severity and prognosis of COVID-19 disease. According to a study by Au-Yong *et al*[7], RALE and Brixia scores have correlations of 0.87 and 0.86, respectively, in predicting patient outcomes. Individuals with high scores (RALE > 25 and Brixia > 11) have increased chances of intensive care unit admission or death within 60 days after diagnosis. As acknowledged by Pal *et al*[1] the usage of CXR has been limited by lower sensitivity (56%) and specificity (60%).

CT imaging is the preferred diagnostic modality, given its high sensitivity (94%)[1]. However, the specificity of CT ranges from 25% to 80%[1]. Lateralized, bilateral, multifocal, basilar and peripheral predominance and peripheral ground-glass opacities are the classical CT findings of COVID-19 pneumonia. Non-classical features include subsegmental vessel engorgement, “atoll sign,” reticular opacifications, subpleural curvilinear opacifications, and bilateral hilar lymphadenopathy. All these findings are well illustrated by Pal *et al*[1].

COVID-19 reporting and data system (CO-RADS) (Table 3) and MuLBSTA (multilobular infiltration, hypo-lymphocytosis, bacterial coinfection, smoking history, hypertension, and age) (Table 4) scoring systems aid in the identification of the lung involvement and prognosis in suspected COVID-19 patients. Pal *et al*[1] described that CO-RADS and MuLBSTA have a sensitivity of 61% and 65.1%, and specificity of 81% and 95.4%, respectively. The main drawbacks of CT in clinical setting are: radiation exposure, the need to transfer the patient to the imaging room, and availability.

Lung ultrasound (LUS) may assist physicians in assessing the disease severity with sensitivity and specificity of 65%-76.9% and 72.7%-77.1%, respectively[1]. It identifies subtle lung findings in the periphery which remain hidden in majority of CXR[8]. In addition, the findings of COVID-19 pneumonia on LUS correlate well with CT findings[9,10]. Hence LUS can be employed in the common and standard practice. LUS is advantageous as it eliminates the radiation risk and resource consumption of CXR and CT, if the patients require daily monitoring of lung status. It also overcomes the limitations of CT by its portability and accessibility at bedside with great learning curve. B-line artifacts, subpleural consolidations, pleural irregularities, and patchy opacities can be seen on the LUS of COVID-19-infected patients. The presence of B-lines indicates parenchymal involvement, and they increase proportionately with the disease, resulting in “white lungs”[2]. With recuperation from illness, B-lines are replaced with A-lines, which represent normal lung surface. Subpleural consolidation specifies the inflammatory changes; however, these findings may last for several weeks after recovery.

Table 1 Radiological assessment of lung edema classification[13]

Consolidation	
Score	Extent of alveolar opacities in each lung quadrant.
0	0%
1	0-25%
2	25-50%
3	50-75%
4	> 75%
If consolidation is ≥ 1, then score density	
1	Hazy
2	Moderate
3	Dense
Final RALE scoring	
Right lung	**Left lung**
Upper quadrant, Cons × Density= Q1	Upper quadrant, Cons × Density= Q3
Lower quadrant, Cons × Density= Q2	Lower quadrant, Cons × Density= Q4
Total RALE: Q1+Q2+Q3+Q4	

RALE: Radiological assessment of lung edema.

Table 2 Brixia score

Score	Findings on CXR in three divided zones of each lung
0	No abnormal findings
1	Interstitial infiltrates
2	Interstitial > Alveolar infiltrates
3	Alveolar > Interstitial infiltrates

CXR: Chest X-ray.

A 12-zone scoring system is used to quantify and predict the severity of lung involvement. Individuals are classified as normal, mild, moderate, and severely infected, with scores of 0, 1-5, 6-14, and ≥ 15, respectively. A cutoff score of 8 of 36 is 91% sensitive in predicting COVID-19 diagnosis. Hence LUS may be used as a screening tool, but in conjunction with other imaging modalities due to its ineffective differentiation between acute ongoing infection and recovery[1,2].

Although the role of magnetic resonance imaging, Fluorodeoxyglucose positron emission tomography, CT pulmonary angiography, and point-of-care echocardiography is limited in COVID-19, they may help detect complications such as myocarditis, cardiomyopathy, right ventricular dilatation, and pulmonary embolism and monitor the treatment response. AI is an algorithm-based entity that allows rapid diagnosis and enhances a health system's capability. AI COVID-19 algorithm has a sensitivity, specificity, and accuracy of 84%, 93%, and 90.8%, respectively. AI-based deep learning technology has detected COVID-19 on CT with an area under the receiver operating characteristic curve of 0.96 and sensitivity and specificity of 90% and 96%, respectively[11]. Wehbe *et al*[12] compared the performance of AI and radiologists and reported similar diagnostic accuracy of 82% and 81%, respectively. Hence, AI has the ability to assist radiologists in prompt diagnosis and to improve workflow efficiency.

Familiarity with the COVID-19 imaging findings was essential for radiologists working during the pandemic. Even though the disease spread is controlled currently, the discovery of newer virus strains highlights the importance of strategies such as increasing work capacity and imaging capabilities that might be helpful during a future unanticipated outbreak.

Table 3 Coronavirus disease 2019 reporting and data system classification.

Category	Level of COVID-19 suspicion	Findings
0	Non-interpretable	Technically insufficient scan to assign a score
1	Very low	Normal lung
2	Low	Typical of infection other than COVID-19
3	Equivalent/unsure	Non-specific findings to COVID-19 and other infections
4	High	Suspicious of COVID-19
5	Very high	Typical COVID-19 findings
6	Proven	Positive RT-PCR for COVID-19

COVID-19: Coronavirus disease 2019; RT-PCR: Reverse transcriptase- polymerase chain reaction.

Table 4 Multilobular infiltration, hypo-lymphocytosis, bacterial coinfection, smoking history, hypertension, and age scoring system

Parameter	Yes	No
Multi-lobar involvement	+ 5	0
Lymphopenia (≤ 0.8 $\times 10^9$/L)	+ 4	0
Bacterial co-infection in blood or sputum	+ 4	0
Smoking history	Active smoker: + 3; Prior Smoker: + 2	0
Hypertension	+ 2	0
Age ≥ 60 yr	+ 2	0

FOOTNOTES

Author contributions: Vulasala SSR, Gopireddy DR, Bhosale P, Virarkar MK have equal contributions; all authors have read and approved the final manuscript.

Conflict-of-interest statement: The authors declare they have no conflicts of interest.

Country/Territory of origin: United States

ORCID number: Sai Swarupa R Vulasala 0000-0002-9387-3673; Dheeraj R Gopireddy 0000-0001-8441-7804; Priya Bhosale 0000-0003-4014-4941; Mayur K Virarkar 0000-0002-5825-3102.

S-Editor: Xing YX
L-Editor: A
P-Editor: Xing YX

REFERENCES

1 **Pal A**, Ali A, Young TR, Oostenbrink J, Prabhakar A, Deacon N, Arnold A, Eltayeb A, Yap C, Young DM, Tang A, Lakshmanan S, Lim YY, Pokarowski M, Kakodkar P. Comprehensive literature review on the radiographic findings, imaging modalities, and the role of radiology in the COVID-19 pandemic. *World J Radiol* 2021; **13**: 258-282 [PMID: 34630913 DOI: 10.4329/wjr.v13.i9.258]
2 **Skoczyński S**, Buda N, Mendrala K, Górecki T, Kucewicz-Czech E, Krzych Ł, Koszutski T, Darocha T. Lung ultrasound may improve COVID-19 safety protocols. *J Thorac Dis* 2021; **13**: 2698-2704 [PMID: 34164162 DOI: 10.21037/jtd-21-295]
3 **Luo G**, Zhang J, Zhang S, Hu B, Hu L, Huang Z. High-quality RT-PCR with chemically modified RNA controls. *Talanta* 2021; **224**: 121850 [PMID: 33379066 DOI: 10.1016/j.talanta.2020.121850]

4 **Arevalo-Rodriguez I**, Buitrago-Garcia D, Simancas-Racines D, Zambrano-Achig P, Del Campo R, Ciapponi A, Sued O, Martinez-García L, Rutjes AW, Low N, Bossuyt PM, Perez-Molina JA, Zamora J. False-negative results of initial RT-PCR assays for COVID-19: A systematic review. *PLoS One* 2020; **15**: e0242958 [PMID: 33301459 DOI: 10.1371/journal.pone.0242958]

5 **Reeves RA**, Pomeranz C, Gomella AA, Gulati A, Metra B, Hage AN, Lange S, Parekh M, Donuru A, Lakhani P, Sundaram B. Performance of a Severity Score on Admission Chest Radiography in Predicting Clinical Outcomes in Hospitalized Patients With Coronavirus Disease (COVID-19). *AJR Am J Roentgenol* 2021; **217**: 623-632 [PMID: 33112201 DOI: 10.2214/AJR.20.24801]

6 **Jacobi A**, Chung M, Bernheim A, Eber C. Portable chest X-ray in coronavirus disease-19 (COVID-19): A pictorial review. *Clin Imaging* 2020; **64**: 35-42 [PMID: 32302927 DOI: 10.1016/j.clinimag.2020.04.001]

7 **Au-Yong I**, Higashi Y, Giannotti E, Fogarty A, Morling JR, Grainge M, Race A, Juurlink I, Simmonds M, Briggs S, Cruikshank S, Hammond-Pears S, West J, Crooks CJ, Card T. Chest Radiograph Scoring Alone or Combined with Other Risk Scores for Predicting Outcomes in COVID-19. *Radiology* 2021; 210986 [PMID: 34519573 DOI: 10.1148/radiol.2021210986]

8 **Boero E**, Schreiber A, Rovida S, Vetrugno L, Blaivas M. The role of lung ultrasonography in COVID-19 disease management. *J Am Coll Emerg Physicians Open* 2020 [PMID: 32838389 DOI: 10.1002/emp2.12194]

9 **Skopljanac I**, Ivelja MP, Barcot O, Brdar I, Dolic K, Polasek O, Radic M. Role of Lung Ultrasound in Predicting Clinical Severity and Fatality in COVID-19 Pneumonia. *J Pers Med* 2021; **11** [PMID: 34442401 DOI: 10.3390/jpm11080757]

10 **Lieveld AWE**, Kok B, Azijli K, Schuit FH, van de Ven PM, de Korte CL, Nijveldt R, van den Heuvel FMA, Teunissen BP, Hoefsloot W, Nanayakkara PWB, Bosch FH. Assessing COVID-19 pneumonia-Clinical extension and risk with point-of-care ultrasound: A multicenter, prospective, observational study. *J Am Coll Emerg Physicians Open* 2021; **2**: e12429 [PMID: 33969350 DOI: 10.1002/emp2.12429]

11 **Szabó IV**, Simon J, Nardocci C, Kardos AS, Nagy N, Abdelrahman RH, Zsarnóczay E, Fejér B, Futácsi B, Müller V, Merkely B, Maurovich-Horvat P. The Predictive Role of Artificial Intelligence-Based Chest CT Quantification in Patients with COVID-19 Pneumonia. *Tomography* 2021; **7**: 697-710 [PMID: 34842822 DOI: 10.3390/tomography7040058]

12 **Wehbe RM**, Sheng J, Dutta S, Chai S, Dravid A, Barutcu S, Wu Y, Cantrell DR, Xiao N, Allen BD, MacNealy GA, Savas H, Agrawal R, Parekh N, Katsaggelos AK. DeepCOVID-XR: An Artificial Intelligence Algorithm to Detect COVID-19 on Chest Radiographs Trained and Tested on a Large U.S. Clinical Data Set. *Radiology* 2021; **299**: E167-E176 [PMID: 33231531 DOI: 10.1148/radiol.2020203511]

13 **Warren MA**, Zhao Z, Koyama T, Bastarache JA, Shaver CM, Semler MW, Rice TW, Matthay MA, Calfee CS, Ware LB. Severity scoring of lung oedema on the chest radiograph is associated with clinical outcomes in ARDS. *Thorax* 2018; **73**: 840-846 [PMID: 29903755 DOI: 10.1136/thoraxjnl-2017-211280]

Published by **Baishideng Publishing Group Inc**
7041 Koll Center Parkway, Suite 160, Pleasanton, CA 94566, USA
Telephone: +1-925-3991568
E-mail: bpgoffice@wjgnet.com
Help Desk: https://www.f6publishing.com/helpdesk
https://www.wjgnet.com

ISSN 1949-8470 (online)

World Journal of *Radiology*

World J Radiol 2022 March 28; 14(3): 55-69

Published by Baishideng Publishing Group Inc

World Journal of Radiology

Contents

Monthly Volume 14 Number 3 March 28, 2022

EDITORIAL

SYSTEMATIC REVIEWS

World Journal of Radiology

Monthly Volume 14 Number 3 March 28, 2022

Contents

NAME OF JOURNAL

World Journal of Radiology

ISSN

ISSN 1949-8470 (online)

LAUNCH DATE

January 31, 2009

FREQUENCY

Monthly

EDITORS-IN-CHIEF

Thomas J Vogl

EDITORIAL BOARD MEMBERS

https://www.wjgnet.com/1949-8470/editorialboard.htm

PUBLICATION DATE

March 28, 2022

INSTRUCTIONS TO AUTHORS

https://www.wjgnet.com/bpg/gerinfo/204

GUIDELINES FOR ETHICS DOCUMENTS

https://www.wjgnet.com/bpg/GerInfo/287

GUIDELINES FOR NON-NATIVE SPEAKERS OF ENGLISH

https://www.wjgnet.com/bpg/gerinfo/240

PUBLICATION ETHICS

https://www.wjgnet.com/bpg/GerInfo/288

PUBLICATION MISCONDUCT

https://www.wjgnet.com/bpg/gerinfo/208

ARTICLE PROCESSING CHARGE

https://www.wjgnet.com/bpg/gerinfo/242

STEPS FOR SUBMITTING MANUSCRIPTS

https://www.wjgnet.com/bpg/GerInfo/239

ONLINE SUBMISSION

https://www.f6publishing.com

E-mail: bpgoffice@wjgnet.com https://www.wjgnet.com

World Journal of Radiology

Submit a Manuscript: https://www.f6publishing.com

World J Radiol 2022 March 28; 14(3): 55-59

DOI: 10.4329/wjr.v14.i3.55

ISSN 1949-8470 (online)

EDITORIAL

Artificial intelligence in dentomaxillofacial radiology

Seyide Tugce Gokdeniz, Kıvanç Kamburoğlu

Specialty type: Radiology, nuclear medicine and medical imaging

Provenance and peer review: Invited article; Externally peer reviewed.

Peer-review model: Single blind

Peer-review report's scientific quality classification

Grade A (Excellent): 0
Grade B (Very good): 0
Grade C (Good): C
Grade D (Fair): 0
Grade E (Poor): 0

P-Reviewer: Fakhradiyev I

Received: March 20, 2021
Peer-review started: March 20, 2021
First decision: July 18, 2021
Revised: September 5, 2021
Accepted: February 22, 2022
Article in press: February 22, 2022
Published online: March 28, 2022

Seyide Tugce Gokdeniz, Kıvanç Kamburoğlu, Department of Dentomaxillofacial Radiology, Ankara University Faculty of Dentistry, Ankara 06500, Turkey

Corresponding author: Kıvanç Kamburoğlu, DDS, MSc, PhD, Professor, Department of Dentomaxillofacial Radiology, Ankara University Faculty of Dentistry, Besevler, Ankara 06500, Turkey. dtkivo@yahoo.com

Abstract

Artificial intelligence (AI) has the potential to revolutionize healthcare and dentistry. Recently, there has been much interest in the development of AI applications. Dentomaxillofacial radiology (DMFR) is within the scope of these applications due to its compatibility with image processing methods. Classification and segmentation of teeth, automatic marking of anatomical structures and cephalometric analysis, determination of early dental diseases, gingival, periodontal diseases and evaluation of risk groups, diagnosis of certain diseases, such as; osteoporosis that can be detected in jaw radiographs are among studies conducted by using radiological images. Further research in the field of AI will make great contributions to DMFR. We aim to discuss most recent AI-based studies in the field of DMFR.

Key Words: Artificial intelligence; Diagnostic imaging; Radiology; Dentistry

Core Tip: Scientists are enthusiastic about conducting artificial intelligence (AI) research related to dentomaxillofacial radiology (DMFR). Image and patient recognition are important in DMFR, however initial investment costs are still high and misdiagnosis may occur in real clinical situations. Up until now, DMFR related AI studies revealed successful results to some extent, however human physiological system is so complex that AI can be a supplementary method but not a substitution for human knowledge, capability and decision-making ability.

Citation: Gokdeniz ST, Kamburoğlu K. Artificial intelligence in dentomaxillofacial radiology. *World J Radiol* 2022; 14(3): 55-59
URL: https://www.wjgnet.com/1949-8470/full/v14/i3/55.htm
DOI: https://dx.doi.org/10.4329/wjr.v14.i3.55

INTRODUCTION

In recent times, technical developments and innovation have become integral parts of clinical dentistry. Owing to recent developments in the field of artificial intelligence (AI), significant improvements may be expected in dentistry and dentomaxillofacial radiology (DMFR). AI is defined as the way, method, tool, and algorithm, that is developed for the intelligent solution of the issues encountered with computer application of intelligent thinking. They contain elements which are able to imitate human thinking, understanding, comprehension, interpretation and learning characteristics utilized for problem solving[1]. Numerous studies have been carried out in order to find solutions that utilize the latest technology to solve dental field-related issues. These studies are comprised of a wide range of objectives, including the diagnosis of caries; assessment of various pathologies; orthodontic treatment of crowded teeth and dental implant placement *via* robotic surgery[2-5]. In DMFR studies, this technology has come to the forefront due to its compatibility with image processing methods. Current topical examples of studies conducted on radiological images are: Classification and segmentation of teeth; automatic marking of anatomical structures and cephalometric analysis; early detection of dental diseases; gingival-periodontal diseases and evaluation of risk groups and the diagnosis of certain diseases such as osteoporosis that can be detected in jaw radiographs[6]. In dental radiology there are both theoretical and practical application examples of these specific tasks. The output gained from artificial learning is expected to reduce the daily workload of physicians as well as the rate of both false diagnosis and underdiagnosis in dental practice.

According to the radiological diagnosis tool used, we aim to present the current studies in the field of DMFR under two main headings. Current AI studies in the field of DMFR are given in Figure 1. The main study topics in DMFR related to AI are given in Table 1.

Some of the current AI studies using panoramic radiography devices

The most widely used radiological diagnostic tool in dentistry is the panoramic radiograph. It provides two-dimensional image and related information regarding major mandibular and maxillary jaw bones, all existing teeth and surrounding supporting tissues. Two-dimensional imaging of this region, which has a complex anatomy, causes superposition of various tissues on each other. Therefore, it is possible that panoramic radiographs can be interpreted incorrectly or incompletely in certain cases. Critical assessment of dental images is an essential portion of the diagnostic procedure in daily clinical scenarios. General evaluation by a specialist is based on tooth detection and numbering[7]. A study verified the assumption that a convolutional neural network-CNN-based method could be skilled to analyze and score tooth on panoramic images for automated dental charting objectives. The suggested method targeted at assisting dentists during their diagnostic procedures. The system's performance level was found to be similar to the specialists' level, which meant that the radiology specialist could use the finding gained from the technique for automated charting when solely assessment and subtle adjustments were necessary as an alternative to manual data insertion[7].

Several different studies are published on the automatic detection of odontogenic cysts and tumors[8-10]. Odontogenic cysts and tumors do not demonstrate their distinctive radiographic features until they extend to a significant dimension. The early radiographic findings of odontogenic cysts and tumors are so similar that even well trained DMFR experts cannot always accurately conduct their diagnosis. In addition, they may not reveal symptoms in advanced levels[11,12]. Because of such characteristics of odontogenic cysts and tumors, commonly observed cysts such as dentigerous cysts and odontogenic keratocytes may threaten the patient's quality of life if they are large or subsequently cause pathological fractures[13,14]. However, *You Only Look Once* (*YOLO*)-a state-of-the-art, real-time object detection system could not be only responsible for the wrong negative diagnosis in one research, which consisted of radiologically indeterminate initial pathologies and maxillary entities that even trained clinicians find difficult to accurately diagnose. As noted, some pathologies in the maxilla are hindered by low bone density and several related anatomical structures that cross with the superpositions of the panoramic image. Odontogenic keratocytes on the maxilla were not detected by both YOLO and two-thirds of clinicians, including experts and general practitioners. Surprisingly, however, there were few instances where YOLO diagnosed and accurately distinguished pathologies that clinicians could not detect[15]. The CNN YOLO detector demonstrated diagnostic effectiveness at least comparable to that of trained dentists in assessing odontogenic cysts and tumors[15]. A number of components affecting clinician ability need to be assessed in future research. It is possible that implementation of CNNs in oral and maxillofacial diagnostic imaging may reveal favorable results for clinicians[15].

Ameloblastomas and keratocystic odontogenic tumors (KCOTs) are among the most commonly observed odontogenic tumors of the jaws. Preoperative definitive detection of these lesions may help dental surgeons in treatment planning[16,17]. In another study, a CNN was created for the evaluation of ameloblastomas and KCOTs[3]. The accuracy of the CNN developed in this study was close to the accuracy of dental experts in detecting ameloblastoma and KCOTs. CNN can help reduce the workload of oral and maxillofacial surgeons by detecting ameloblastomas and KCOTs in a very short time. More research needs to be done in order to clarify and define CNN before it may be widely used in diagnostic imaging purposes[3].

Table 1 Main study topics in dentomaxillofacial radiology related to artificial intelligence

No.	Main study topics
1	Localization/measurement of cephalometric landmarks
2	Diagnosis of osteoporosis
3	Classification of the maxillofacial cysts and/or tumors
4	Identification of alveolar bone resorption
5	Classification of periapical lesions
6	Diagnosis of multiple dental diseases
7	Classification of tooth types
8	Detection of dental caries
9	Classification of the stage of the lower third molar

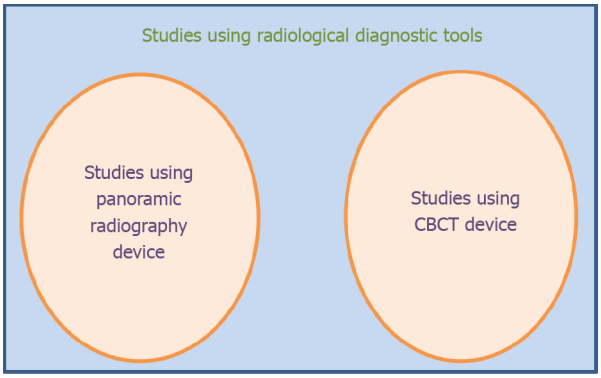

DOI: 10.4329/wjr.v14.i3.55

Figure 1 Current artificial intelligence studies in the field of dentomaxillofacial radiology. CBCT: Cone beam computed tomography.

In previous studies, the determination of the relationship with osteoporosis from dental panoramic radiographs was investigated by AI algorithms. In one study, 680 patients were simultaneously subjected to skeletal bone mineral density (BMD) examinations and digital panoramic radiography evaluations, and the results showed that the deep learning-based evaluation of digital panoramic radiography images could be useful and reliable in the automated screening of osteoporosis patients [18]. In another study on this subject, the effectiveness of a deep convolutional neural network (DCNN) based computer aided diagnosis (CAD) technique in osteoporosis detection on panoramic imaging was evaluated. As a result, the DCNN-based CAD technique was found to demonstrate a high level of consistency with dental radiology experts experienced in clinical osteoporosis assessment[19]. The authors suggested that a DCNN-based CAD system could provide dentists with information regarding initial diagnosis of osteoporosis and patients with asymptomatic osteoporosis may be sent to convenient medical referral for further evaluation[18,19].

In a study, a caries detection technique that used deep learning algorithms was proposed for the assessment of dental carious lesions[2]. Although the model exhibits high effectiveness in the detection of caries for both maxillary premolars and molars, this caries evaluation technique has some drawbacks. Since the study was conducted by using two dimensional images, solely interproximal and occlusal carious lesions could be detected, however; lingual and buccal carious lesions could not be detected[2].

Some of the current AI studies using cone beam computed tomography devices

Since the beginning of 2000s, cone beam computed tomography (CBCT) as a 3D imaging method has become widely used in cases where clinical examination and conventional radiographs were insufficient to reveal necessary information[20]. A CNN algorithm was created to detect periapical lesions on CBCT images. The system, which identified and enumerated teeth in volumetric data, was succeeded in diagnosing periapical lesions with 92.8% accuracy. In another study, automatic mandibular canal segmentation was performed on CBCT images with CNN developed[21]. Another area for AI is the detection of oral diseases. In a study, researchers aimed to identify and distinguish lichen planus and leukoplakia lesions with an artificial neural network trained with intraoral photographs and found promising results[22].

A 2011 study suggested that an AI technique could be useful in the automatical localization of a key landmark on CBCT images[23]. The ability to make 3D measurements for cephalometric analysis on CBCT images is an important advantage, however; the performance of automatic localization in current technique is not sufficient and effective in the clinical scenario[23]. Therefore, known techniques can be suggested for using preliminary localization of cephalometric landmarks, but manual correction is still required before further cephalometric analysis.

Limitations and future aspects

Future studies that critically assess certain issues and their clinical potential are essential. In spite of the promising performance results obtained from current AI techniques, it is mandatory to confirm the effectivenes and consistency of these techniques by using appropriate external data from new patients or collected from other dental institutions[24]. In its future goals, it can be expected not only to strengthen the effectiveness of AI techniques on par with specialists, but also to diagnose initial pathologies that are invisible to the human eye.

CONCLUSION

AI has the potential to revolutionize healthcare and dentistry. Owing to recent developments in the field of AI, scientists have become increasingly enthusiastic about conducting AI research. Image and patient recognition are important in DMFR. However, initial investment costs are currently high, and inappropriate assumptions may be made in a real-life clinical scenarios. Hitherto, DMFR-related AI studies revealed a certain degree of successful results. However, the human physiological system is exceedingly complex. As such, AI is acceptable as a supplementary method, but it cannot be seen a substitution for human knowledge, capabilities, and decision-making abilities. Additionally, the diagnostic performance of AI models may differ depending on the algorithms that are used. It is essential to validate the consistency and effectiveness of these techniques by using accurate representative images from different sources before implementing and applying these techniques to real clinical situations. With that said, further research in the field of AI has the potential to make great contributions to DMFR.

FOOTNOTES

Author contributions: Gökdeniz ST and Kamburoğlu K have made substantial contributions to conception and writing of the paper and revising it critically for important intellectual content; both have approved the final version to be published and assume full responsibility for its content; all authors have agreed to the order of authorship prior to submission.

Conflict-of-interest statement: Authors declare no conflict of interests for this article.

Country/Territory of origin: Turkey

ORCID number: Seyide Tugce Gokdeniz 0000-0001-9756-8265; Kıvanç Kamburoğlu 0000-0002-4134-5756.

S-Editor: Fan JR
L-Editor: A
P-Editor: Fan JR

REFERENCES

1 **Wong SH**, Al-Hasani H, Alam Z, Alam A. Artificial intelligence in radiology: how will we be affected? *Eur Radiol* 2019; **29**: 141-143 [PMID: 30027407 DOI: 10.1007/s00330-018-5644-3]
2 **Lee JH**, Kim DH, Jeong SN, Choi SH. Detection and diagnosis of dental caries using a deep learning-based convolutional neural network algorithm. *J Dent* 2018; **77**: 106-111 [PMID: 30056118 DOI: 10.1016/j.jdent.2018.07.015]
3 **Poedjiastoeti W**, Suebnukarn S. Application of Convolutional Neural Network in the Diagnosis of Jaw Tumors. *Healthc Inform Res* 2018; **24**: 236-241 [PMID: 30109156 DOI: 10.4258/hir.2018.24.3.236]
4 **Faber J**, Faber C, Faber P. Artificial intelligence in orthodontics. *APOS Trends Orthod* 2019; **9**: 201-205 [DOI: 10.25259/APOS_123_2019]

5 **Woo SY**, Lee SJ, Yoo JY, Han JJ, Hwang SJ, Huh KH, Lee SS, Heo MS, Choi SC, Yi WJ. Autonomous bone reposition around anatomical landmark for robot-assisted orthognathic surgery. *J Craniomaxillofac Surg* 2017; **45**: 1980-1988 [PMID: 29042168 DOI: 10.1016/j.jcms.2017.09.001]

6 **Hwang JJ**, Jung YH, Cho BH, Heo MS. An overview of deep learning in the field of dentistry. *Imaging Sci Dent* 2019; **49**: 1-7 [PMID: 30941282 DOI: 10.5624/isd.2019.49.1.1]

7 **Tuzoff DV**, Tuzova LN, Bornstein MM, Krasnov AS, Kharchenko MA, Nikolenko SI, Sveshnikov MM, Bednenko GB. Tooth detection and numbering in panoramic radiographs using convolutional neural networks. *Dentomaxillofac Radiol* 2019; **48**: 20180051 [PMID: 30835551 DOI: 10.1259/dmfr.20180051]

8 **Ariji Y**, Yanashita Y, Kutsuna S, Muramatsu C, Fukuda M, Kise Y, Nozawa M, Kuwada C, Fujita H, Katsumata A, Ariji E. Automatic detection and classification of radiolucent lesions in the mandible on panoramic radiographs using a deep learning object detection technique. *Oral Surg Oral Med Oral Pathol Oral Radiol* 2019; **128**: 424-430 [PMID: 31320299 DOI: 10.1016/j.oooo.2019.05.014]

9 **Lee JH**, Kim DH, Jeong SN. Diagnosis of cystic lesions using panoramic and cone beam computed tomographic images based on deep learning neural network. *Oral Dis* 2020; **26**: 152-158 [PMID: 31677205 DOI: 10.1111/odi.13223]

10 **Cattoni F**, Teté G, Calloni AM, Manazza F, Gastaldi G, Capparè P. Milled *vs* moulded mock-ups based on the superimposition of 3D meshes from digital oral impressions: a comparative *in vitro* study in the aesthetic area. *BMC Oral Health* 2019; **19**: 230 [PMID: 31664999 DOI: 10.1186/s12903-019-0922-2]

11 **Diwan A**, Bhagavaldas MC, Bagga V, Shetty A. Multidisciplinary Approach in Management of a Large Cystic Lesion in Anterior Maxilla - A Case Report. *J Clin Diagn Res* 2015; **9**: ZD41-ZD43 [PMID: 26155589 DOI: 10.7860/JCDR/2015/13540.5992]

12 **Vincent SD**, Deahl ST, Johnson DL. An asymptomatic radiolucency of the posterior maxilla. *J Oral Maxillofac Surg* 1991; **49**: 1109-1115 [PMID: 1716304 DOI: 10.1016/0278-2391(91)90147-e]

13 **Montoro JRDMC**, Tavares MG, Melo DH, Franco RDL, De Mello-Filho FV, Xavier SP, Trivellato AE, Lucas AS. Ameloblastoma mandibular tratado por ressecção óssea e reconstrução imediata. *Braz J Otorhinolaryngol* 2008; **74**: 155-157 [DOI: 10.1590/s0034-72992008000100026]

14 **Ruslin M**, Hendra FN, Vojdani A, Hardjosantoso D, Gazali M, Tajrin A, Wolff J, Forouzanfar T. The Epidemiology, treatment, and complication of ameloblastoma in East-Indonesia: 6 years retrospective study. *Med Oral Patol Oral Cir Bucal* 2018; **23**: e54-e58 [PMID: 29274152 DOI: 10.4317/medoral.22185]

15 **Yang H**, Jo E, Kim HJ, Cha IH, Jung YS, Nam W, Kim JY, Kim JK, Kim YH, Oh TG, Han SS, Kim H, Kim D. Deep Learning for Automated Detection of Cyst and Tumors of the Jaw in Panoramic Radiographs. *J Clin Med* 2020; **9** [PMID: 32545602 DOI: 10.3390/jcm9061839]

16 **Apajalahti S**, Kelppe J, Kontio R, Hagström J. Imaging characteristics of ameloblastomas and diagnostic value of computed tomography and magnetic resonance imaging in a series of 26 patients. *Oral Surg Oral Med Oral Pathol Oral Radiol* 2015; **120**: e118-e130 [PMID: 26166034 DOI: 10.1016/j.oooo.2015.05.002]

17 **Jaeger F**, de Noronha MS, Silva ML, Amaral MB, Grossmann SM, Horta MC, de Souza PE, de Aguiar MC, Mesquita RA. Prevalence profile of odontogenic cysts and tumors on Brazilian sample after the reclassification of odontogenic keratocyst. *J Craniomaxillofac Surg* 2017; **45**: 267-270 [PMID: 28089087 DOI: 10.1016/j.jcms.2016.12.011]

18 **Lee KS**, Jung SK, Ryu JJ, Shin SW, Choi J. Evaluation of Transfer Learning with Deep Convolutional Neural Networks for Screening Osteoporosis in Dental Panoramic Radiographs. *J Clin Med* 2020; **9** [PMID: 32024114 DOI: 10.3390/jcm9020392]

19 **Lee JS**, Adhikari S, Liu L, Jeong HG, Kim H, Yoon SJ. Osteoporosis detection in panoramic radiographs using a deep convolutional neural network-based computer-assisted diagnosis system: a preliminary study. *Dentomaxillofac Radiol* 2019; **48**: 20170344 [PMID: 30004241 DOI: 10.1259/dmfr.20170344]

20 **Orhan K**, Bayrakdar IS, Ezhov M, Kravtsov A, Özyürek T. Evaluation of artificial intelligence for detecting periapical pathosis on cone-beam computed tomography scans. *Int Endod J* 2020; **53**: 680-689 [PMID: 31922612 DOI: 10.1111/iej.13265]

21 **Jaskari J**, Sahlsten J, Järnstedt J, Mehtonen H, Karhu K, Sundqvist O, Hietanen A, Varjonen V, Mattila V, Kaski K. Deep Learning Method for Mandibular Canal Segmentation in Dental Cone Beam Computed Tomography Volumes. *Sci Rep* 2020; **10**: 5842 [PMID: 32245989 DOI: 10.1038/s41598-020-62321-3]

22 **Jurczyszyn K**, Kozakiewicz M. Differential diagnosis of leukoplakia *vs* lichen planus of the oral mucosa based on digital texture analysis in intraoral photography. *Adv Clin Exp Med* 2019; **28**: 1469-1476 [PMID: 30916899 DOI: 10.17219/acem/104524]

23 **Cheng E**, Chen J, Yang J, Deng H, Wu Y, Megalooikonomou V, Gable B, Ling H. Automatic Dent-landmark detection in 3-D CBCT dental volumes. *Annu Int Conf IEEE Eng Med Biol Soc* 2011; **2011**: 6204-6207 [PMID: 22255756 DOI: 10.1109/IEMBS.2011.6091532]

24 **Steyerberg EW**. Validation of prediction models: Steyerberg E. W, Clinical Prediction Models: A Practical Approach to Development, Validation, and Updating. New York: Springer; 2010: 299–310

World Journal of Radiology

Submit a Manuscript: https://www.f6publishing.com

World J Radiol 2022 March 28; 14(3): 60-69

DOI: 10.4329/wjr.v14.i3.60

ISSN 1949-8470 (online)

SYSTEMATIC REVIEWS

Immunosuppressive treatment and radiotherapy in kidney transplant patients: A systematic review

Valentina Lancellotta, Andrea D'Aviero, Bruno Fionda, Calogero Casà, Ilaria Esposito, Francesco Preziosi, Anna Acampora, Fabio Marazzi, György Kovács, Barbara Alicja Jereczek-Fossa, Alessio Giuseppe Morganti, Vincenzo Valentini, Maria Antonietta Gambacorta, Jacopo Romagnoli, Luca Tagliaferri

Specialty type: Radiology, nuclear medicine and medical imaging

Provenance and peer review: Invited article; Externally peer reviewed.

Peer-review model: Single blind

Peer-review report's scientific quality classification

Grade A (Excellent): 0
Grade B (Very good): 0
Grade C (Good): C, C
Grade D (Fair): D
Grade E (Poor): 0

P-Reviewer: Chan WYK, China; Ryckman JM, United States

Received: October 11, 2021
Peer-review started: October 11, 2021
First decision: December 10, 2021
Revised: December 20, 2021
Accepted: March 15, 2022
Article in press: March 15, 2022
Published online: March 28, 2022

Valentina Lancellotta, Andrea D'Aviero, Bruno Fionda, Calogero Casà, Ilaria Esposito, Francesco Preziosi, Fabio Marazzi, Vincenzo Valentini, Maria Antonietta Gambacorta, UOC Radioterapia Oncologica, Dipartimento di Diagnostica per Immagini, Radioterapia Oncologica ed Ematologia, Fondazione Policlinico Universitario A. Gemelli IRCCS, Rome 00168, Rome, Italy

Anna Acampora, Sezione di Igiene, Dipartimento Universitario di Scienze della Vita e Sanità Pubblica, Università Cattolica del Sacro Cuore, Rome 00168, Rome, Italy

György Kovács, Università Cattolica del Sacro Cuore, Gemelli-INTERACTS, Rome, 00168 Rome, Italy

Barbara Alicja Jereczek-Fossa, Department of Oncology and Hemato-oncology, European Institute of Oncology, University of Milan, Milan 20141, Italy

Alessio Giuseppe Morganti, Radiotherapy Center, IRCCS Azienda Ospedaliero-Universitaria di Bologna, Bologna 40121, Italy

Jacopo Romagnoli, Luca Tagliaferri, Renal Transplant Unit, Fondazione Policlinico Universitario A. Gemelli IRCCS, Rome 00168, Rome, Italy

Corresponding author: Bruno Fionda, MD, Doctor, UOC Radioterapia Oncologica, Dipartimento di Diagnostica per Immagini, Radioterapia Oncologica ed Ematologia, Fondazione Policlinico Universitario A. Gemelli IRCCS, Largo Agostino Gemelli 8, Romre 00168, Rome, Italy. bruno.fionda@yahoo.it

Abstract

BACKGROUND

Immunosuppression (IS) therapy may contribute to cancer development. Some authors have proposed to reduce immunosuppression drugs dose in case of viral infections, in immunosuppression-related diseases, and in patients undergoing radiotherapy. The present analysis reports the results of a systematic review on kidney transplant recipients undergoing immunosuppression and radiotherapy.

AIM

To define if it is necessary reduce immunosuppression drugs during radiotherapy.

METHODS
The literature search was based on three electronic databases (Pubmed, Scopus, and Web of Science) using selected keywords linked through the "AND" and "OR" Boolean operators to build specific strings for each electronic search engine. Two researchers independently screened the citations, and disagreement was resolved by discussion or through the intervention of a third author. The review was conducted and reported according to the PRISMA statement. Extracted data were narratively synthesized, and, where possible, frequencies, percentages, and ranges were calculated.

RESULTS
The literature search resulted in 147 citations. After abstracts screening, 21 records were selected for full-text evaluation. Fifteen of these were excluded, leaving six papers considered suitable for analysis. There is still no clear evidence that withdrawing antimetabolites and/or calcineurin inhibitors and/or mammalian target of rapamycin-inhibitors, as opposed to continuing maintenance IS, improves patient survival in kidney transplant recipients with cancer undergoing radiotherapy. Only few retrospective studies on small cancer patient cohorts are available in this setting, but without comparison of different immunosuppression treatments. Even where immunosuppression therapy was described, patient survival seemed to be correlated only with cancer stage and type.

CONCLUSION
The results of this systematic review do not support the reduction of immunosuppression dose in patients undergoing radiotherapy.

Key Words: Renal transplant patients; Graft rejection; Immunosuppression; Radiotherapy; Survival

Core Tip: This systematic review aimed to define the need of immunosuppressive therapy modulation during radiotherapy. There is still no clear evidence that withdrawing antimetabolites and/or calcineurin inhibitors and/or mammalian target of rapamycin-inhibitors improves patient survival in kidney transplant recipients with cancer undergoing radiotherapy. Even where immunosuppression therapy was described, patient survival seemed to be correlated only with cancer stage and type. The results of this systematic review do not support the reduction of immunosuppression dose in patients undergoing radiotherapy.

Citation: Lancellotta V, D'Aviero A, Fionda B, Casà C, Esposito I, Preziosi F, Acampora A, Marazzi F, Kovács G, Jereczek-Fossa BA, Morganti AG, Valentini V, Gambacorta MA, Romagnoli J, Tagliaferri L. Immunosuppressive treatment and radiotherapy in kidney transplant patients: A systematic review. *World J Radiol* 2022; 14(3): 60-69
URL: https://www.wjgnet.com/1949-8470/full/v14/i3/60.htm
DOI: https://dx.doi.org/10.4329/wjr.v14.i3.60

INTRODUCTION

Renal transplant patients have an increased risk of developing *de novo* cancers, with an incidence up to four times higher than the general population[1-3]. Recipients of transplanted organs have variable risk of cancer development. In fact, the risk of developing malignancies depends on transplanted organ, exposure to lymphocyte-depleting antibody-based therapies, immune status of the donor/recipient, and type of immunosuppressive therapy[4,5]. Current immunosuppressive regimens involved in carcinogenesis after organ transplantation are based on a combination of T-cell depleting or inhibiting agents, such as calcineurin inhibitors, monoclonal and polyclonal antibodies, cell cycle inhibitors, antimetabolites, and corticosteroids[6]. As for other oncological settings, radiotherapy (RT) may play a significant role in the treatment of cancer in transplanted patients[7]. However, RT may also have adverse effects in these patients and in particular an increased immunosuppressive effect induced by anti-rejection drugs[8,9]. This effect depends on several factors such as total dose, treatment technique, dose/fractionation, and irradiated volume. Treatment techniques are external beam RT (EBRT) or interventional RT (IRT), also known as brachytherapy[10-12].

Despite the "fragility" of transplanted kidneys, RT seems to be feasible also in this patient population [13-22]. Moreover, modern and high-precision RT techniques can deliver the dose only to the macroscopic tumor while sparing immune cells in the surrounding tissues with consequent reduction of

the suppressive effect on the immune system[23,24]. On the other hand, in kidney-transplanted patients, immunosuppressive regimens may counteracts the RT immunostimulatory effect. More generally, considering the immunosuppressive effect of RT due to bone marrow toxicity, and therefore the possible increased effect of anti-rejection drugs, a relevant problem in these patients concerns the need to modulate immunosuppressive therapy during and after RT. However, clear evidence regarding this topic is lacking in literature. Furthermore, guidelines on the management of immunosuppressive therapy in patients undergoing RT are also missing. Indeed, only a few studies have addressed this issue and literature reviews on this topic are missing. Based on this background, this systematic review aimed to define the need of immunosuppressive therapy modulation during RT.

MATERIALS AND METHODS

Development of clinical question

The clinical question was developed based on the Population, Intervention, Comparison, and Outcomes (PICO). The clinical question was: (P) In kidney transplant recipients with cancer undergoing RT, maintaining antimetabolites and/or calcineurin inhibitors and/or mammalian target of rapamycin (mTOR) inhibitors (I) is superior when compared to withdrawal of antimetabolites and/or calcineurin inhibitors and/or mTOR inhibitors (C), in relation to the outcomes (O) of benefit and harm (Table 1)? and reports the development of Grades of Recommendation, Assessment, Development, and Evaluation (GRADE) Recommendation.

Search strategy and selection of evidence

The systematic review was conducted in accordance with the PRISMA guidelines[25]. We performed a comprehensive literature search using PubMed, Scopus, and Web of Science (up to July 2019) using selected keywords linked through the Boolean operators "AND" and "OR" to build specific strings for each electronic search engine (Table 2 and Figure 1). ClinicalTrials.gov was searched for ongoing or recently completed trials, and PROSPERO was searched for ongoing or recently completed systematic reviews. Electronic search was supplemented by manually searching the references of included studies and review articles. The search was restricted to papers published in English. In order to avoid the missing of relevant studies, we chose this strategy burdened by high sensitivity and low specificity. Conference papers, surveys, letters, editorials, book chapters, case reports, and reviews were excluded. Time restriction (2010-July 2019) of the publication was considered. Studies were identified through a search process performed by three independent reviewers (LT, VL, AA), and uncertainty regarding eligibility was resolved by a multidisciplinary committee (JR-transplant surgeon, FM-radiation and medical oncology, FP-radiation oncologist, CC-radiation oncologist, IE-dermatologist). Eligible citations were retrieved for full-text review. An external expert committee defined the outcomes of benefit and harm (GK, BJF, AGM). A multidisciplinary master board (VV, MAG, LT, JR) coordinated the project and performed the final independent check and the definitive approval of the review. The GRADEpro Guideline Development Tool (McMaster University, 2015) was used to create summary of findings tables in Cochrane systematic reviews. The quality assessment showed high clinical and methodological heterogeneity and risks of bias in the included studies, making quantitative synthesis inappropriate. Therefore, meta-analysis outcomes were not reported.

Inclusion criteria

(1) Kidney transplant recipients with cancer undergoing RT; (2) Reporting patients overall survival (OS), progression free survival, graft survival, toxicity, and local control; (3) Published in English language as original articles; (4) Time restriction (2010-2019).

Exclusion criteria

Conference papers, surveys, letters, editorials, book chapters, and literature reviews.

Identification of Outcomes

The external expert committee identified the following outcomes of benefit: OS (defined as the time from baseline to death from any cause or last follow-up), graft survival (defined as time from transplant to graft failure), progression free survival (PFS, defined as time from baseline to clinical or radiological progression), and local control (LC, defined as time from baseline to cancer detected in the treated site at any time after initial treatment). The identified outcome of harm included acute and late toxicity. All these outcomes were considered as “critical” for the decision-making process.

Quality of evidence evaluation

Certainty of evidence for all selected outcomes was performed according to the GRADE approach, considering study limitations, imprecision, indirectness, inconsistency, and publication biases. Certainty level started at higher pre-specified level for randomized controlled trials, but levels of certainty could

Table 1 Population, Intervention, Comparison, and Outcomes model

PICO	
Patients	Kidney transplant recipients with cancer undergoing radiotherapy
Intervention	Withdraw antimetabolites and/or calcineurin inhibitors and/or mTOR inhibitors
Comparator	Maintain antimetabolites and/or calcineurin inhibitors and/or mTOR inhibitors
Outcome	Core outcome sets
Time frame	2010-2019
Study type	RCTs, meta-analysis of RCT; observational analytical studies

mTOR: Mammalian target of rapamycin; PICO: Population, Intervention, Comparison, and Outcomes; RCT: Randomized controlled trial.

Table 2 Search strategy

Electronic engineer	Search string
Pubmed	((“Renal transplant” OR “kidney transplant” OR “kidney transplantation” OR “renal transplantation”) AND (metastasis OR metastatic OR metastases OR “cancer” OR neoplasm OR “tumour” OR “cancers” OR “tumours” OR “tumor” OR “tumors” OR neoplasms OR melanoma OR PTLD OR lymphoma) AND (radiotherapy OR “radiation therapy”)) AND (“calcineurin inhibitors” OR “calcineurin inhibitor” OR CNI OR tacrolimus OR cyclosporine OR everolimus OR sirolimus OR “mTOR inhibitors” OR “mTOR-inhibitors” OR antimetabolites OR “antimetabolite”)
Web of Science	ALL=(((Renal transplant) OR (kidney transplant) OR (kidney transplantation) OR (renal transplantation)) AND (metastasis OR metastatic OR metastases OR cancer OR neoplasm OR tumour OR cancers OR tumours OR tumor OR tumors OR neoplasms OR melanoma OR PTLD OR lymphoma) AND (radiotherapy OR (radiation therapy)) AND ((calcineurin inhibitors) OR (calcineurin inhibitor) OR CNI OR tacrolimus OR cyclosporine OR everolimus OR sirolimus OR (mTOR inhibitors) OR (mTOR-inhibitors) OR antimetabolites OR antimetabolite))
Scopus	((“Renal transplant” OR “kidney transplant” OR “kidney transplantation” OR “renal transplantation”) AND (metastasis OR metastatic OR metastases OR “cancer” OR neoplasm OR “tumour” OR “cancers” OR “tumours” OR “tumor” OR “tumors” OR neoplasms OR melanoma OR PTLD OR lymphoma) AND (radiotherapy OR “radiation therapy”)) AND (“calcineurin inhibitors” OR “calcineurin inhibitor” OR CNI OR tacrolimus OR cyclosporine OR everolimus OR sirolimus OR “mTOR inhibitors” OR “mTOR-inhibitors” OR antimetabolites OR “antimetabolite”)AND (LIMIT-TO (PUBYEAR, 2019) OR LIMIT-TO (PUBYEAR, 2018) OR LIMIT-TO (PUBYEAR, 2017) OR LIMIT-TO (PUBYEAR, 2016) OR LIMIT-TO (PUBYEAR, 2015) OR LIMIT-TO (PUBYEAR, 2014) OR LIMIT-TO (PUBYEAR, 2013) OR LIMIT-TO (PUBYEAR, 2012) OR LIMIT-TO (PUBYEAR, 2011) OR LIMIT-TO (PUBYEAR, 2010) OR LIMIT-TO (PUBYEAR, 2009)) AND (LIMIT-TO (LANGUAGE, "English"))

CNI: Calcineurin inhibitor; mTOR: Mammalian target of rapamycin.

be downgraded if limitations in one of the above-mentioned domains were detected. Evidence was classified as having high, moderate, low, and very low level of certainty.

Benefit/harm balance and clinical recommendation

Based on the summary of evidence, the following judgments about the benefit-to-risk ratio between intervention and comparison were stated: Favorable, uncertain/favorable, uncertain, uncertain/unfavorable, and unfavorable (both for intervention or comparison). The strength of the recommendation was considered as strong positive, conditional positive, uncertain, conditional negative, or strong negative.

RESULTS

The flowchart of the study selection process is shown in Figure 1. The literature search resulted in 147 single citations. After literature screening, 21 records were identified for full-text evaluation. Out of these, 15 were excluded, and the reasons for exclusion are reported in Figure 1. Six full text papers were considered eligible and were included in the final analysis.

Characteristics of the included studies

All studies were retrospective and included a total of 65 kidney transplant patients with subsequent cancer diagnosis. Regarding the type of cancer, five studies included prostate cancer (PCa) patients while one study reported on subjects with lymphoma. No direct comparisons between different treatment approaches in terms of immunosuppressive therapy modulation was performed. The main

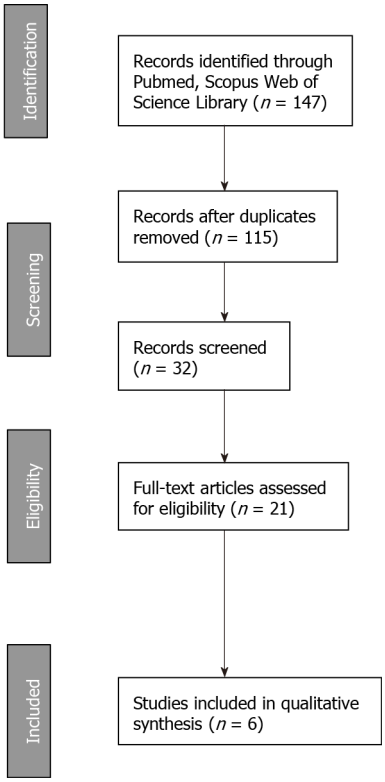

DOI: 10.4329/wjr.v14.i3.60

Figure 1 PRISMA flow-chart for outcomes and toxicity.

characteristics of included studies are shown in Table 3 (first author, objective, treatment features, and main results).

Literature review

Antunes *et al*[13] analyzed the incidence of urologic malignancies in renal transplant recipients and reported on their treatment and outcomes. Twenty-nine PCa patients were included in the study with a mean age of 62.6 ± 6.1 years (range: 50-73 years). EBRT was performed in 5 patients. Although the authors did not find a statistically significant difference between type of immunosuppressive drugs and PCa development, they emphasized that 13 out of 29 patients (44.8%) received azathioprine. No statistically significant impact of duration or type of immunosuppression on *de novo* development of urologic malignancies or OS was recorded. No patient undergoing RT had allograft failure. Follow-up duration after PCa treatment ranged from 3 mo to 96 mo. One-, five-, and ten-year OS rates after PCa diagnosis were 86.2%, 86.2%, and 79.3%, respectively. Only 1 patient died of PCa. The remaining patients died of PCa-independent reasons (cardiac failure or infection)[13].

Binsaleh *et al*[15] retrospectively analyzed treatment and outcome of 9 renal transplant patients with subsequent PCa. Median age at PCa diagnosis was 63.6 years. One patient was treated with androgen deprivation therapy alone, 4 patients with RT alone, and 4 patients with a combination of androgen deprivation therapy and EBRT (60-66 Gy). Immunosuppressive therapy was as follows: 4 patients were on cyclosporine, azathioprine, and steroids regimen; 3 patients received cyclosporine, mycophenolate, and steroids (then changed to a sirolimus-based therapy); 1 patient was on tacrolimus, azathioprine, and steroids regimen; 1 patient received tacrolimus, mycophenolate mofetil, and steroids. Three out of the 9 patients had their immunosuppressive regimen changed from cyclosporine, mycophenolate, and steroids to a sirolimus-based therapy, and 6 had "judicious reductions" in their calcineurin inhibitor dosages. Four transplanted kidneys showed renal failure, and 3 out of 4 of them were treated with RT: 1 patient was on tacrolimus, azathioprine, and steroids therapy and was treated with EBRT alone (60 Gy); 1 patient was on tacrolimus, mycophenolate mofetil, and steroids and was treated with androgen deprivation therapy plus EBRT (60 Gy); 1 patient was on cyclosporine, azathioprine, and steroids and was treated with androgen deprivation plus EBRT (60 Gy); finally, 1 patient was on cyclosporine, azathioprine, and steroids and was treated with androgen deprivation therapy alone. The authors concluded that a combination of RT with androgen deprivation therapy provides good control of the disease while preserving renal function. The comparative long-term follow-up of patients with reduced doses of calcineurin-inhibitor-based immunosuppression or sirolimus-based treatments is not known [15].

Table 3 Characteristics of included studies

Ref.	Study design	Patients (*n*)	Mean age	Type of cancer	Intervention	Patient survival	Graft survival
Binsaleh *et al*[15], 2011	Retrospective	9	55 (range: 40-72)	PCa	RT (60-66 Gy); 3 patients had their immunosuppressive regimen changed to a sirolimus-based therapy, while 6 had "judicious" reductions of CNI dosages	NR	4/9 failure; 5/9 good
Pettenati *et al*[20], 2016	Retrospective	6	63.5 yr (± 7.2)	PCa	RT (EBRT: 76 Gy; IRT: 145 Gy) +Immunosuppressive therapy [2 pts: CNI + AZA + steroids; 19 pts: CNI + MMF + Steroids; 2 pts: MMF, mTORI + Steroids]	1 patient died of PCa	No graft loss nor change in renal function due to PCa treatment
Antunes *et al*[13], 2018	Retrospective	29	53.4 (±10,7)	PCa	RT in 5 patients (details not reported)	1-yr: 86.2%5-yr: 86.2%10-yr: 79.3%	No patient undergoing RT had allograft failure
Oh *et al* [26], 2019	Retrospective	13	66 (range: 42-80)	PCa	RT (EBRT: 78 Gy; IRT: 144 Gy) + Immunosuppressive therapy [CIA (*n* = 8), MMF (*n* = 13), AZA (*n* = 3), tacrolimus (*n* = 12), sirolimus (*n* = 9), and/or prednisone (*n* = 20)]	3 yr: 93.8%	NR
Tasaki *et al* [21], 2019	Retrospective	3	65 (range: 60-67)	PCa	RT (IRT: 145 Gy) + Immunosuppressive therapy [2 pts: CIA + MMF + MP; 1 pt: tacrolimus + MMF +MP]	NR	2 pts good graft function; 1 pt declined graft function after 2 yr
Velvet *et al* [27], 2019	Retrospective	3	59.5	Lymphoma	RT (details not reported) + reduced immunosuppressive regimen	6 mo: 66.6%	NR

CNI: Calcineurin inhibitor; mTOR: Mammalian target of rapamycin; NR: Not reported; PCa: Prostate cancer; RT: Radiotherapy; EBRT: External beam RT; IRT: Interventional RT.

Pettenati *et al*[20] published the results of their retrospective single center study. A control population of non-organ transplant and non-end-stage renal disease patients with PCa was used to compare tumor features and oncological outcome with 24 renal-transplanted patients (PCa incidence in all patients was 1.5%). Mean follow-up was 47 mo. PCa was mostly localized (*n* = 21, 87.5%) and treated with radical prostatectomy (*n* = 16, 76.2%), LDR-IRT (*n* = 3, 14.3%, 145 Gy), EBRT (*n* = 1, 4.7%), or active surveillance (*n* = 1, 4.7%). On the contrary, 3 patients had locally advanced PCa and were treated with EBRT combined with androgen deprivation therapy. Two patients were on a regimen of calcineurin inhibitors plus azathioprine plus steroids; 19 patients were on calcineurin inhibitors plus mycophenolate mofetil plus steroids; 2 patients were on mycophenolate mofetil plus mTOR inhibitors plus steroids. No graft failure due to PCa treatment was reported. Nineteen renal-transplant patients with localized PCa (90.5%) were free from biochemical recurrence at last follow-up. Considering the radical prostatectomy subset, no difference in PCa characteristics at diagnosis and biochemical recurrence rate was found between renal-transplant patients (*n* = 16) and control patients (*n* = 64). The authors concluded that localized PCa following renal transplantation was not associated with adverse features as compared to non-transplant patients. Standard treatments could be proposed to renal-transplanted patients with satisfying results both on oncological outcome and graft function[20].

Tasaki *et al*[21] retrospectively analyzed safety and efficacy of IRT in 3 patients with PCa after renal transplantation. The clinical stage was cT1N0M0 in all patients. The median age at diagnosis was 65 years (range: 60-67 years). Immunosuppressive regimens were cyclosporine A plus mycophenolate mofetil plus methylprednisolone in 2 patients and tacrolimus plus mycophenolate mofetil plus methylprednisolone in 1 patient. The median time between transplantation and IRT was 7 years (range: 4-10 years). Two patients received low dose-rate IRT (dose, 145 Gy), and one patient was treated with high dose-rate IRT (dose, 19 Gy in 2 fractions) combined with external beam irradiation (EBRT, 39 Gy in 13 fractions). Median follow-up after IRT was 44 mo (range: 34-50 mo). No patient developed biochemical or clinical progression and no clinically significant RT-induced adverse events were reported. Two patients maintained a good graft function while one patient had a decline of graft function 2 years after IRT. The authors concluded that low dose-rate IRT and high dose-rate IRT of PCa seem feasible and safe in renal-transplanted recipient with oncological outcomes similar to those recorded in the general population[21].

Oh *et al*[26] reported on biochemical disease-free survival, distant metastasis free, OS, and toxicity in 28 patients with renal transplant who were subsequently treated with definitive RT for PCa. The median age was 66 years, and median follow-up time was 30 mo. Twenty-four patients (86%) were treated with IRT (144 Gy), and 4 patients (14%) were treated with external-beam RT (78 Gy). Immunosuppressive regimens were cyclosporine (*n* = 8), mycophenolate mofetil (*n* = 13), azathioprine (*n* = 3), tacrolimus (*n* = 12), sirolimus (*n* = 9), and/or prednisone (*n* = 20). At last follow-up, 2 patients had died, 1 from

metastatic PCa and 1 from other reasons. Three-year biochemical relapse-free survival, distant metastasis-free, and OS were 95.8%, 93.1%, and 93.8%, respectively. One patient developed grade 3 gastrointestinal late toxicity. The authors concluded that organ transplant recipient with PCa and treated with RT have excellent 3-year outcomes[26].

Velvet *et al*[27] conducted a single center retrospective study on management and outcomes of central nervous system lymphomas in 6 kidney transplant patients. During the lymphoma treatment, immunosuppressive therapy was reduced in all patients. Mycophenolate mofetil and prednisolone without calcineurin inhibitor were prescribed to 5 out of 6 patients. Three out of six patients underwent RT: one patient was also treated with chemotherapy and four cycles of cytotoxic T lymphocytes (alive at last follow-up); one patient was also treated with craniotomy and rituximab (graft failure and then death for acute left ventricular failure); one patient was also treated with chemotherapy (unknown cause of death). RT total dose and technique were not reported and 6-mo OS was 66.6%. This study supports observational data suggesting that patients treated with mycophenolate mofetil and without calcineurin inhibitor may have increased risk of cancer after transplantation[27].

Data synthesis

No study showed that withdrawing antimetabolites and/or calcineurin inhibitor and/or mammalian target of rapamycin-inhibitors as opposed to continuing maintenance immunosuppression improves patient survival in kidney transplant recipients with cancer undergoing RT.

DISCUSSION

The present systematic review showed that in kidney transplant recipients developing cancer and undergoing RT, clear evidence on improved function of the graft and/or of patients survival after modulating or withdrawing immunosuppressive therapy, as opposed to continuing maintenance immunosuppression, is lacking; conversely, only few retrospective studies on small RT-treated cancer cohorts are available, mainly including PCa patients, without comparison between different immunosuppressive strategies[26,27]. RT appears to be a feasible therapeutic option also in this setting, with oncological outcomes not clearly different from the general patient population[28].

In fact, while no studies compared different immunosuppressive treatments, when immunosuppressive drugs were reported, patients' survival seemed to be correlated only with cancer stage or type. Due to lack of evidence, it seems reasonable to entrust the clinical management of these patients to a multi-disciplinary team including nephrologists, cancer surgeons, medical and radiation oncologists, pathologists, and radiologists. In fact, discussion of clinical cases in a multidisciplinary expert team could allow a more homogeneous treatment approach and improvement of clinical outcomes. This evaluation needs to consider the clinical specificities beyond tumor burden, such as comorbidities, compliance to treatment, general performance status, and history of the disease to select the best approach for the individual patient following the principles of personalized medicine. Furthermore, for clinical and deontological reasons, it is also mandatory to discuss all possible implications with the patient to define the therapeutic strategy and obtain a detailed informed consent.

Moreover, due to the lack of available results from prospective trials, studies with this design should be promoted. However, considering the rarity of patients undergoing renal transplantation and requiring RT, and therefore the difficulty in carrying out prospective trials, an alternative aimed at generating evidence in this field could be to share retrospective data from different centers in order to create pooled analyses[29,30].

This study has several limitations. Only six studies were included in the analysis, totaling only 65 patients. Furthermore, all studies have been lacking in reporting important data such as details of RT, radiation-induced toxicity, a complete assessment of renal function, and the impact of RT on immune function. These limitations prevent clear conclusions from being drawn on the question of this review and, in particular, on the need to suspend or modulate immunosuppressive therapy in patients undergoing renal transplantation and subsequent RT.

CONCLUSION

There is no evidence that immunosuppressive therapy should be modulated in kidney transplant patients undergoing RT. Prospective studies or pooled analyses are needed to define the proper treatment for this very selected group of patients.

ARTICLE HIGHLIGHTS

Research background

Cancer is the second most common cause of mortality and morbidity in kidney transplant recipients. Immunosuppression can influence the efficacy of cancer treatment and modification of the immunosuppressive regimen may restore anti-neoplastic immune responses improving oncologic prognosis. However, patients are usually reluctant to modify their immunosuppression, fearing rejection and potential graft loss.

Research motivation

To develop reference points for guiding the transplant professionals in the clinical decision-making process and to improve the management of kidney transplant recipients with cancer.

Research objectives

Little evidence is available on radiotherapy management of cancer in kidney transplant recipients; in certain instances (*e.g.*, in case of pelvic cancer or cancer of the transplanted kidney) it is also unclear which could be the best loco-regional treatment option, among the full range of ablative devices/techniques, to be used as an alternative to nephron sparing surgery, currently the preferred option.

Research methods

The overall process included: (1) The formulation of one specific question based on the Population, Intervention, Comparison, and Outcomes methodology; (2) Systematic literature review and summary for experts for each question; and (3) Extracted data were narratively synthesized and, where possible, frequencies, percentages, and ranges were calculated.

Research results

There is still no clear evidence that withdrawing anti-metabolites and/or calcineurin inhibitor and/or mammalian target of rapamycin inhibitors as opposed to continuing maintenance immunosuppression might improve patient survival in kidney transplant recipients with cancer undergoing radiotherapy. There are few retrospective studies on small cancer cohorts undergoing radiotherapy, especially prostate, without comparison of different immunosuppressive treatments. The radiation therapy can be performed with excellent oncological outcomes. No studies have compared different immunosuppressive treatment, and, when the immunosuppressive drugs are reported, patients' survival seems to be correlated only with cancer stage or type. In addition, there are no data on the eventual effects of immunosuppressive drugs, especially mammalian target of rapamycin inhibitors, on the healing of radiotherapy-induced skin toxicity.

Research conclusions

Although all the statements of the consensus are not methodologically evidence-based and their strength might therefore be questionable, they represent a starting point to orient transplant physicians in their everyday practice, and, above all, these statements clearly indicate the points that need to be addressed in the clinical research in this setting.

Research perspectives

Prospective studies or pooled analyses are needed to define the proper treatment for this very selected group of patients.

FOOTNOTES

Author contributions: Valentini V, Morganti AG, Tagliaferri L, and Romagnoli J contributed to scientific committee; Acampora A, Lancellotta V, and Tagliaferri L contributed to working group performing literature review and summary for experts; Romagnoli J, Marazzi F, Preziosi F, Casà C, and Esposito I contributed to resolve uncertainty regarding eligibility; Kovács G, Jereczek-Fossa A, and Gambacorta MA contributed to revise the manuscript.

Conflict-of-interest statement: the authors reported no potential competing interest.

PRISMA 2009 Checklist statement: The authors have read the PRISMA 2009 Checklist, and the manuscript was prepared and revised according to the PRISMA 2009 Checklist.

Country/Territory of origin: Italy

ORCID number: Valentina Lancellotta 0000-0003-3507-7051; Andrea D'Aviero 0000-0002-9194-620X; Bruno Fionda 0000-0003-3368-1810; Calogero Casà 0000-0001-5785-0549; Ilaria Esposito 0000-0002-2047-6140; Francesco Preziosi 0000-0001-6780-6621; Anna Acampora 0000-0001-5363-403X; Fabio Marazzi 0000-0003-0977-0143; György Kovács 0000-0001-5149-9831; Barbara Alicja Jereczek-Fossa 0000-0001-8151-3673; Alessio Giuseppe Morganti 0000-0001-9793-3410; Vincenzo Valentini 0000-0003-4637-6487; Maria Antonietta Gambacorta 0000-0001-5455-8737; Jacopo Romagnoli 0000-0002-7153-0346; Luca Tagliaferri 0000-0003-2308-0982.

S-Editor: Wang LL
L-Editor: Filipodia
P-Editor: Wang LL

REFERENCES

1 **Agraharkar ML**, Cinclair RD, Kuo YF, Daller JA, Shahinian VB. Risk of malignancy with long-term immunosuppression in renal transplant recipients. *Kidney Int* 2004; **66**: 383-389 [PMID: 15200447 DOI: 10.1111/j.1523-1755.2004.00741.x]
2 **Bosmans JL**, Verpooten GA. Malignancy after kidney transplantation: still a challenge. *Kidney Int* 2007; **71**: 1197-1199 [DOI: 10.1038/sj.ki.5002306]
3 **Engels EA**. Epidemiologic perspectives on immunosuppressed populations and the immunosurveillance and immunocontainment of cancer. *Am J Transplant* 2019; **19**: 3223-3232 [PMID: 31206226 DOI: 10.1111/ajt.15495]
4 **Acuna SA**. Etiology of increased cancer incidence after solid organ transplantation. *Transplant Rev (Orlando)* 2018; **32**: 218-224 [PMID: 30017342 DOI: 10.1016/j.trre.2018.07.001]
5 **Collett D**, Mumford L, Banner NR, Neuberger J, Watson C. Comparison of the incidence of malignancy in recipients of different types of organ: a UK Registry audit. *Am J Transplant* 2010; **10**: 1889-1896 [PMID: 20659094 DOI: 10.1111/j.1600-6143.2010.03181.x]
6 **Gallo A**, Miele M, Badami E, Conaldi PG. Molecular and cellular interplay in virus-induced tumors in solid organ recipients. *Cell Immunol* 2019; **343**: 103770 [PMID: 29523417 DOI: 10.1016/j.cellimm.2018.02.010]
7 **Bosacki C**, Vallard A, Jmour O, Ben Mrad M, Lahmamssi C, Bousarsar A. Radiotherapy and immune suppression: A short review. *Bull Cancer* 2020; **107**: 84-101 [DOI: 10.1016/j.bulcan.2019.09.010]
8 **Schaue D**. A Century of Radiation Therapy and Adaptive Immunity. *Front Immunol* 2017; **8**: 431 [PMID: 28443099 DOI: 10.3389/fimmu.2017.00431]
9 **Postow MA**, Callahan MK, Barker CA, Yamada Y, Yuan J, Kitano S, et al. Immunologic correlates of the abscopal effect in a patient with melanoma. *N Engl J Med* 2012; **366**: 925-931 [DOI: 10.1056/nejmoa1112824]
10 **Massaccesi M**, Cusumano D, Boldrini L, Dinapoli N, Fionda B, Teodoli S, et al. A new frontier of image guidance: Organs at risk avoidance with MRI-guided respiratory-gated intensity modulated radiotherapy: Technical note and report of a case. *J Appl Clin Med Phys* 2019; **20**: 194-198 [DOI: 10.1002/acm2.12575]
11 **Lancellotta V**, Cellini F, Fionda B, De Sanctis V, Vidali C, Fusco V, Barbera F, Gambacorta MA, Corvò R, Magrini SM, Tagliaferri L. The role of palliative interventional radiotherapy (brachytherapy) in esophageal cancer: An AIRO (Italian Association of Radiotherapy and Clinical Oncology) systematic review focused on dysphagia-free survival. *Brachytherapy* 2020; **19**: 104-110 [PMID: 31636025 DOI: 10.1016/j.brachy.2019.09.005]
12 **Tagliaferri L**, Fionda B, Bussu F, Parrilla C, Lancellotta V, Deodato F, Cammelli S, Boldrini L, Gambacorta MA, Morganti AG, Valentini V, Paludetti G, Peris K, Kovacs G. Interventional radiotherapy (brachytherapy) for squamous cell carcinoma of the nasal vestibule: a multidisciplinary systematic review. *Eur J Dermatol* 2019; **29**: 417-421 [PMID: 31486400 DOI: 10.1684/ejd.2019.3599]
13 **Antunes H**, Tavares-da-Silva E, Oliveira R, Carvalho J, Parada B, Bastos C, Figueiredo A. De Novo Urologic Malignancies in Renal Transplant Recipients. *Transplant Proc* 2018; **50**: 1348-1354 [PMID: 29753463 DOI: 10.1016/j.transproceed.2018.02.086]
14 **Beydoun N**, Bucci J, Malouf D. Iodine-125 prostate seed brachytherapy in renal transplant recipients: an analysis of oncological outcomes and toxicity profile. *J Contemp Brachytherapy* 2014; **6**: 15-20 [PMID: 24790617 DOI: 10.5114/jcb.2014.40769]
15 **Binsaleh S**. Diagnosis and treatment of prostate cancer in renal-transplant recipients. *Int Urol Nephrol* 2012; **44**: 149-155 [PMID: 21614508 DOI: 10.1007/s11255-011-9988-8]
16 **Dahlke S**, Schwarz A, Bruns F, Bremer M, Miemietz M, Christiansen H, Meyer A. Pelvic radiotherapy after renal transplantation. *Anticancer Res* 2012; **32**: 5083-5086 [PMID: 23155284]
17 **Elkentaoui H**, Robert G, Pasticier G, Bernhard JC, Couzi L, Merville P, Ravaud A, Ballanger P, Ferrière JM, Wallerand H. Therapeutic management of de novo urological malignancy in renal transplant recipients: the experience of the French Department of Urology and Kidney Transplantation from Bordeaux. *Urology* 2010; **75**: 126-132 [PMID: 19864001 DOI: 10.1016/j.urology.2009.06.106]
18 **Haroon UH**, Davis NF, Mohan P, Little DM, Smyth G, Forde JC, Power RE. Incidence, Management, and Clinical Outcomes of Prostate Cancer in Kidney Transplant Recipients. *Exp Clin Transplant* 2019; **17**: 298-303 [PMID: 30602361 DOI: 10.6002/ect.2018.0048]
19 **Hevia V**, Gómez V, Díez Nicolás V, Alvarez S, Gómez Del Cañizo C, Galeano C, Gomis A, García-Sagredo JM, Marcen R, Burgos FJ. Development of urologic de novo malignancies after renal transplantation. *Transplant Proc* 2014; **46**: 170-

175 [PMID: 24507046 DOI: 10.1016/j.transproceed.2013.12.004]

20 **Pettenati C**, Jannot AS, Hurel S, Verkarre V, Kreis H, Housset M, Legendre C, Méjean A, Timsit MO. Prostate cancer characteristics and outcome in renal transplant recipients: results from a contemporary single center study. *Clin Transplant* 2016; **30**: 964-971 [PMID: 27251769 DOI: 10.1111/ctr.12773]

21 **Tasaki M**, Kasahara T, Kaidu M, Kawaguchi G, Hara N, Yamana K, Maruyama R, Takizawa I, Ishizaki F, Saito K, Nakagawa Y, Ikeda M, Umezu H, Nishiyama T, Aoyama H, Tomita Y. Low-Dose-Rate and High-Dose-Rate Brachytherapy for Localized Prostate Cancer in ABO-Incompatible Renal Transplant Recipients. *Transplant Proc* 2019; **51**: 774-778 [PMID: 30979463 DOI: 10.1016/j.transproceed.2018.10.027]

22 **Iizuka J**, Hashimoto Y, Kondo T, Takagi T, Nozaki T, et al. Efficacy and Feasibility of Intensity-Modulated Radiation Therapy for Prostate Cancer in Renal Transplant Recipients. *Transplant Proc* 2016; **48**: 914-917

23 **Fionda B**, Massaccesi M, Tagliaferri L, Dinapoli N, Iezzi R, Boldrini L. Abscopal effect and interventional oncology: state of art and future perspectives. *Eur Rev Med Pharmacol Sci* 2020; **24**: 773-776 [PMID: 32016981 DOI: 10.26355/eurrev_202001_20058]

24 **Mazzola R**, Jereczek-Fossa BA, Franceschini D, Tubin S, Filippi AR, Tolia M, Lancia A, Minniti G, Corradini S, Arcangeli S, Scorsetti M, Alongi F. Oligometastasis and local ablation in the era of systemic targeted and immunotherapy. *Radiat Oncol* 2020; **15**: 92 [PMID: 32366258 DOI: 10.1186/s13014-020-01544-0]

25 **Moher D**, Liberati A, Tetzlaff J, Altman DG; PRISMA Group. Preferred reporting items for systematic reviews and meta-analyses: the PRISMA statement. *PLoS Med* 2009; **6**: e1000097

26 **Oh SC**, Tariq MB, Reddy CA, Ciezki JP, Stephans KL, Tendulkar RD. Outcomes in Organ Transplant Recipients With Prostate Cancer Treated With Radiotherapy. *Clin Genitourin Cancer* 2019; **17**: e162-e166 [PMID: 30446400 DOI: 10.1016/j.clgc.2018.10.005]

27 **Velvet AJJ**, Bhutani S, Papachristos S, Dwivedi R, Picton M, Augustine T, Morton M. A single-center experience of post-transplant lymphomas involving the central nervous system with a review of current literature. *Oncotarget* 2019; **10**: 437-448 [PMID: 30728897 DOI: 10.18632/oncotarget.26522]

28 **Mazzola R**, Cuccia F, Bertani A, Tubin S, Conaldi PG, Corradini S, Tolia M, Guba M, Alongi F. The role of radiotherapy in patients with solid tumours after solid organ transplantation: a systematic review. *Lancet Oncol* 2021; **22**: e93-e104 [PMID: 33662300 DOI: 10.1016/S1470-2045(20)30590-8]

29 **Lancellotta V**, Guinot JL, Fionda B, Rembielak A, Di Stefani A, Gentileschi S. SKIN-COBRA (Consortium for Brachytherapy data Analysis) ontology: The first step towards interdisciplinary standardized data collection for personalized oncology in skin cancer. *J Contemp Brachytherapy* 2020; **12**: 105-110 [DOI: 10.5114/jcb.2020.94579]

30 **Tagliaferri L**, Budrukkar A, Lenkowicz J, Cambeiro M, Bussu F, Guinot JL, Hildebrandt G, Johansson B, Meyer JE, Niehoff P, Rovirosa A, Takácsi-Nagy Z, Boldrini L, Dinapoli N, Lanzotti V, Damiani A, Gatta R, Fionda B, Lancellotta V, Soror T, Monge RM, Valentini V, Kovács G. ENT COBRA ONTOLOGY: the covariates classification system proposed by the Head & Neck and Skin GEC-ESTRO Working Group for interdisciplinary standardized data collection in head and neck patient cohorts treated with interventional radiotherapy (brachytherapy). *J Contemp Brachytherapy* 2018; **10**: 260-266 [PMID: 30038647 DOI: 10.5114/jcb.2018.76982]

Published by **Baishideng Publishing Group Inc**
7041 Koll Center Parkway, Suite 160, Pleasanton, CA 94566, USA
Telephone: +1-925-3991568
E-mail: bpgoffice@wjgnet.com
Help Desk: https://www.f6publishing.com/helpdesk
https://www.wjgnet.com

ISSN 1949-8470 (online)

World Journal of *Radiology*

World J Radiol 2022 April 28; 14(4): 70-106

Published by Baishideng Publishing Group Inc

World Journal of Radiology

Contents

Monthly Volume 14 Number 4 April 28, 2022

MINIREVIEWS

ORIGINAL ARTICLE

Retrospective Cohort Study

Retrospective Study

LETTER TO THE EDITOR

World Journal of Radiology

Monthly Volume 14 Number 4 April 28, 2022

Contents

NAME OF JOURNAL
World Journal of Radiology

ISSN
ISSN 1949-8470 (online)

LAUNCH DATE
January 31, 2009

FREQUENCY
Monthly

EDITORS-IN-CHIEF
Thomas J Vogl

EDITORIAL BOARD MEMBERS
https://www.wjgnet.com/1949-8470/editorialboard.htm

PUBLICATION DATE
April 28, 2022

INSTRUCTIONS TO AUTHORS
https://www.wjgnet.com/bpg/gerinfo/204

GUIDELINES FOR ETHICS DOCUMENTS
https://www.wjgnet.com/bpg/GerInfo/287

GUIDELINES FOR NON-NATIVE SPEAKERS OF ENGLISH
https://www.wjgnet.com/bpg/gerinfo/240

PUBLICATION ETHICS
https://www.wjgnet.com/bpg/GerInfo/288

PUBLICATION MISCONDUCT
https://www.wjgnet.com/bpg/gerinfo/208

ARTICLE PROCESSING CHARGE
https://www.wjgnet.com/bpg/gerinfo/242

STEPS FOR SUBMITTING MANUSCRIPTS
https://www.wjgnet.com/bpg/GerInfo/239

ONLINE SUBMISSION
https://www.f6publishing.com

World Journal of Radiology

Submit a Manuscript: https://www.f6publishing.com

World J Radiol 2022 April 28; 14(4): 70-81

DOI: 10.4329/wjr.v14.i4.70

ISSN 1949-8470 (online)

MINIREVIEWS

Focal liver lesions in cirrhosis: Role of contrast-enhanced ultrasonography

Tommaso Vincenzo Bartolotta, Angelo Randazzo, Eleonora Bruno, Adele Taibbi

Specialty type: Radiology, nuclear medicine and medical imaging

Provenance and peer review: Invited article; Externally peer reviewed.

Peer-review model: Single blind

Peer-review report's scientific quality classification

Grade A (Excellent): 0
Grade B (Very good): 0
Grade C (Good): 0
Grade D (Fair): D
Grade E (Poor): 0

P-Reviewer: Ren J, China

Received: February 25, 2021
Peer-review started: February 25, 2021
First decision: May 3, 2021
Revised: May 16, 2021
Accepted: April 8, 2022
Article in press: April 8, 2022
Published online: April 28, 2022

Tommaso Vincenzo Bartolotta, Angelo Randazzo, Eleonora Bruno, Adele Taibbi, Department of Radiology, University Hospital "Paolo Giaccone", Palermo 90127, Italy

Tommaso Vincenzo Bartolotta, Department of Radiology, Fondazione Istituto G. Giglio Hospital, Cefalù 90015, Italy

Corresponding author: Tommaso Vincenzo Bartolotta, MD, PhD, Associate Professor, Department of Radiology, University Hospital "Paolo Giaccone", Section of Radiology, Department BiND, Palermo 90127, Italy. tommasovincenzo.bartolotta@unipa.it

Abstract

Contrast-enhanced ultrasound (CEUS) represents a great innovation for the evaluation of focal liver lesions (FLLs). The main advantage of CEUS is the real-time imaging examination and the very low toxicity in patients with renal failure. Liver cirrhosis has been recognized as a major risk factor for the onset of hepatocellular carcinoma (HCC) and intrahepatic cholangiocarcinoma (ICC). HCC in liver cirrhosis develops as the last step of a complex that leads to the gradual transformation from regenerative nodule through dysplastic nodule to HCC. In patients with liver cirrhosis, a surveillance program is recommended consisting of ultrasound (US) for detecting small focal lesions. A wide spectrum of benign and malignant lesions other than HCC may be found in the cirrhotic liver and their differentiation is important to avoid errors in staging diseases that may preclude potentially curative therapies. Several published studies have explored the value of CEUS in liver cirrhosis and they have been shown to have excellent diagnostic and prognostic performances for the evaluation of non-invasive and efficient diagnosis of FLLs in patients at high risk for liver malignancies. The purpose of this article is to describe and discuss CEUS imaging findings of FLLs including HCC and ICC, all of which occur in cirrhotic livers with varying prevalence.

Key Words: Ultrasonography; Contrast-enhanced ultrasound; Liver cirrhosis; Liver neoplasms; Hepatocellular carcinoma; Focal liver lesions

Core Tip: Contrast-enhanced ultrasound (CEUS) represents a breakthrough in the evaluation of focal liver lesions (FLLs). Currently, CEUS is included as a part of the suggested diagnostic work-up of FLLs in cirrhotic patients and in their follow-up for an accurate assessment of therapeutic response. After a brief description of the basis of different CEUS techniques, several liver lesions that can be found in the cirrhotic liver including benign, malignant or pseudo-lesions, will be described and discussed on the basis of our experience and literature data.

Citation: Bartolotta TV, Randazzo A, Bruno E, Taibbi A. Focal liver lesions in cirrhosis: Role of contrast-enhanced ultrasonography. *World J Radiol* 2022; 14(4): 70-81
URL: https://www.wjgnet.com/1949-8470/full/v14/i4/70.htm
DOI: https://dx.doi.org/10.4329/wjr.v14.i4.70

INTRODUCTION

Liver cirrhosis

Liver cirrhosis represents the final stage of chronic inflammation through the establishment of necrosis and fibrogenesis up to a total subversion of the hepatic parenchyma and it has systemic repercussions and a fatal outcome in the absence of a liver transplant. Liver cirrhosis is the 14th most common cause of death worldwide[1].

Etiologically, liver cirrhosis recognizes infectious causes (hepatitis B, hepatitis C, schistosoma japonicum), autoimmune (primary biliary cirrhosis, autoimmune hepatitis, primary sclerosing cholangitis), alcohol abuse, metabolic causes (Wilson disease, hemochromatosis) and vascular or cryptogenic causes[2]. The combination of imaging and serological investigation (transaminases and cholestasis indices) is often sufficient for the diagnosis; however, the gold standard remains the liver biopsy which also allows physicians to identify the noxa that led to the stage of cirrhosis[1]. In the clinical setting, ultrasound (US) allows a morphological assessment of the liver and portal circulation. US also plays a major role as the recommended tool for surveillance every 6 mo at early detection of small hepatocellular carcinoma (HCC)[3].

Imaging characterization of focal lesions in cirrhosis is crucial for appropriate patient management[4, 5]. To this end, US is a non-specific technique used to characterize focal liver lesions (FLLs).

Contrast-enhanced ultrasound

At the end of the 1990s, the introduction of contrast agents based on intravenous microbubbles to contrast-specific gray-scale US techniques has enabled contrast-enhanced ultrasonography (CEUS) to represent macro-vascularity and also microcirculation (vessels up to 40 μm). Starting in the 2000s, the advent of low-solubility gas bubbles (like sulfur hexafluoride) with phospholipid shells for their flexibility has led to a full real time CEUS examination[6].

CEUS, throughout the vascular phase with its blood-pool contrast agent, allows real-time recording with non-invasive assessment of liver perfusion without resorting to expensive and not very common equipment such as Computed Tomography (CT) or Magnetic Resonance Imaging (MRI) that require the use of ionizing radiation or nephrotoxic contrast agents. OF note, when gas microbubbles are injected into the vein, they remain in the intravascular space (blood-pool agents), Only one of marketed contras agents shows a late phase with uptake by hepatic Kupffer cells (Table 1)[7].

CEUS is safe and well tolerated: Renal or pulmonary diseases do not present contraindications for this use and no blood tests are needed to check kidney function. In a study of about 23000 patients, less than 0.01% of the patient population reported a serious adverse event with no death events[8].

Actually, CEUS is included in the diagnostic work-up of FLLs detected in the healthy population and to study metastases in patients with cancer and to identify HCC in cirrhotic patients, allowing for better management of the disease with effective and advantageous therapies[9-10]. A recent meta-analysis showed that specificity and sensitivity for CEUS in the characterization of FLLs were respectively 87% and 92%[10]. CEUS is gaining an increasing role in the imaging work-up of HCC and many international guidelines are now considering CEUS as a diagnostic tool for HCC as well as CT and MRI with encouraging results and is positive in terms of the cost-benefit analysis[11-12]. Based on literature data and our experience in our center, the recent innovations in the CEUS of FLLs in cirrhotic patients will be presented and discussed.

TECHNICAL NOTE

The US cases illustrated in this article are acquired through various ultrasound equipment provided

Table 1 Characteristics of contrast agents SonoVue and Sonazoid for contrast-enhanced ultrasound

Agent	SonoVue	Sonazoid
Gas	Sulfurhexafluoride (SF_6)	Perfluorobutane (C_4F_{10})
Envelope	Monolayer of phospholipid (DSPC, DPPG-Na)	Monolayer of phospholipid (Hydrogenated egg phosphatidyl serine Na)
MI	Low MI (< 0.1)	Intermediate MI (> 0.2)
Mean size	1.5-2.5 μm	2.3-2.9 μm
Distribution after injection	Pure blood pool agent	Blood pool agent with uptake by hepatic Kupffer cells after 1 min by injection

DSPC: 1,2-distearoyl-sn-glycero-3-phosphocholine; DPPG-Na: 1,2-dipalmitoyl-sn-glycero-3-phospho-rac-glycerol sodium; MI: Mechanical index.

with multifrequency convex array probes and contrast-specific imaging software: MyLab Twice (Esaote, Genova, Italy), RS80A and RS85A (Samsung Medison, Co. Ltd., Seoul, Korea) and iU22 unit (Philips Ultrasound, Bothell, WA, USA). Before the injection of bolus contrast, a standard exam together with color/power and pulsed Doppler valuation was always performed to optimize lesion images and define the best plane for its visualization. The contrast agent used was composed of gas microbubbles filled with sulfur hexafluoride (SonoVue, Bracco, Milan, Italy) that was injected using a 20- or 22-gauge needle in a cubital vein and a 2.4-mL bolus with a 5-10 ml of saline flush. Low mechanical index (MI) from 0.05 to 0.08 and low frame rate (5 Hz) were used for real-time imaging to avoid microbubble breakdown. The level of the lesion was the focus of examination and the duration of each exam was about 5 min after contrast agent injection.

The digital cine-loops were acquired before and after performing the contrast at different times in the arterial phase (from 10 s to 35 s after the injection), portal phase (from 55 s to 80 s after the injection) and delayed phase (from 235 s to 260 s after the injection).

Basal echogenicity and the dynamic modality of enhancement of each lesion in all vascular phases and among the near liver parenchyma were compared.

CIRRHOTIC NODULES

Liver cirrhosis has been recognized as a major risk factor for the onset of HCC and intrahepatic cholangiocarcinoma (ICC) compared to the non-cirrhotic population, of 30 and 20 times, respectively[13]. In the management of hepatic nodules in liver cirrhosis, early diagnosis and treatment is mandatory. HCC in liver cirrhosis develops as the last step of a complex, multi-step hepatocarcinogenesis process during several molecular and tissue alterations leading to the gradual transformation from regenerative nodule (RN) through low- and high-grade dysplastic nodule (DN) to HCC[14]. Changes of intranodular blood supply is the main transformation for imaging diagnosis: RN show similar blood supply to a normal liver. As a consequence, RNs are typically non-hypervascular. They can be seen as numerous tiny hypoechoic or hyperechoic nodules throughout the liver on grayscale US whereas at CEUS they usually are iso-enhancing to the adjacent liver parenchyma throughout the vascular phase, even if they may show transient hypo-vascularity in the arterial phase[4] (Figure 1).

DN are the next step towards HCC. Often multiple, DNs are classified as low or high grade according to the presence of cytological atypia. These borderline lesions show wide variations of blood supply with overlaps of vascular supply between DN and well-differentiated HCC, with the vast majority of RN and DN being isoechoic to the adjacent liver parenchyma in portal venous and late phase at CEUS [15].

Of note, in a study encompassing 215 FLLs in cirrhotic patients and comparing the CEUS features of RN and DN, 95.1% of RN lesions showed delayed or simultaneous enhancement in the arterial phase in comparison to surrounding liver parenchyma. On the other hand, DN lesions resembled this contrast-enhancement pattern only partially, due to the presence of intralesional areas of arterial enhancement followed by a wash out in the late phase. In pathology, these areas of arterial contrast-enhancement within the DN have proven to be early HCC[16]. Hence, any enhancement in the arterial phase within a nodule should be regarded as suspicious for HCC, resembling a "nodule in a nodule" appearance.

MALIGNANT LESIONS

Hepatocellular carcinoma

HCC is the fifth most common cancer in men and the ninth in women showing a greater incidence in developing countries where over 80% of all estimated new cases worldwide occurred in 2012[17].

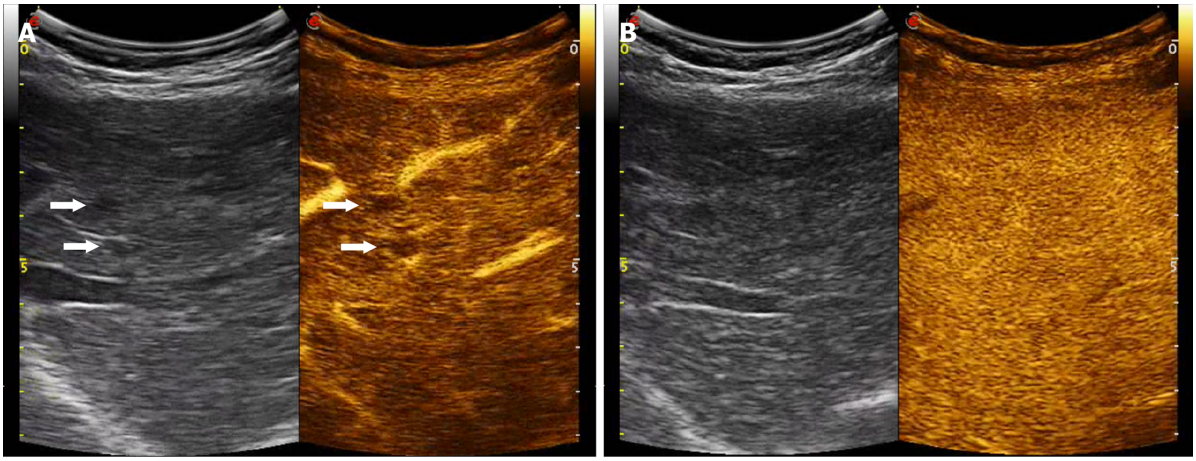

DOI: 10.4329/wjr.v14.i4.70

Figure 1 Regenerative nodule. A: Contrast-enhanced ultrasound examination in the arterial phase (29 s after the i.v. injection of contrast agent) shows two millimetric hypoechoic nodules, showing lack of contrast enhancement (right, arrows); B: In the late phase (142 s after the injection) both nodules are isoechoic to the adjacent liver parenchyma.

Almost 90% of HCCs originate through a stepway progression from RN to HCC which may take place in a quite variable period, even though it may take only a few months[18]. On the other hand, the estimated doubling time of HCC ranges between 4 and 6 mo[19].

At CEUS, the typical enhancement pattern of HCC is hyperenhancement in the arterial phase followed by gradual and mild wash-out in the portal venous and/or late phases[10] (Figure 2). Washout is represented as a relatively hypoechoic aspect compared to healthy liver parenchyma in the later stages of the study with any type of contrast-enhancement in the arterial phase. In general, at CEUS, the presence of the wash-out sign is highly suggestive of malignancy. In HCC, washout begins over 60-90 s after injection of contrast agent, whereas metastases or intrahepatic cholangiocarcinoma usually show a rapid washout (< 60 s) (Table 2) (Figure 3)[20]. Therefore, in CEUS, an observation period of up to approximately 5 min is required to easily visualize the typically subtle and late (> 1 min) washout of HCC (Figure 2).

Noteworthy, a study showed that arterial enhancement patterns of HCC at CEUS are related to the degree of histologic differentiation: moderately differentiated HCC exhibits a classic behavior after contrast agent injection compared to well-differentiated HCC. Extended observation in the portal phase is important for reporting late washout that in HCC occurs more frequently later than in the portal venous phase[21]. As a caveat, well-differentiated HCC may appear iso-enhancing in the portal-venous or late phase[9].

On the other hand, in a study by Tada *et al*[22], 63 of 68 (92.6%) small HCCs (< 3 cm in size) showed a mainly diffuse and homogeneous enhancement in the arterial-phase whereas large HCCs presented a heterogeneous arterial-phase enhancement pattern mainly related to non-enhancing areas of fibrosis, necrosis or internal hemorrhage.

In general, thanks to the real-time nature of CEUS, its high spatial and temporal resolution, the sensitivity of CEUS in the detection of hypervascularization of cirrhotic nodules was found to be higher compared to CT/MRI[23].

Overall, CEUS showed a sensitivity of 88.8%, a specificity of 89.2% and a PPV of 91.3% in the characterization of HCC[24].

Although it is still a matter of debate, several international guidelines are now endorsing the use of CEUS as a first or second-line diagnostic tool for the diagnosis of HCC[12,25]. In 2016, the American College of Radiology included CEUS in its comprehensive Liver Imaging Reporting and Data System (LI-RADS): a unique scoring system for CEUS examinations in patients with increased risk of HCC. A systematic review comparing the cost-effectiveness of CEUS with CT and MRI confirmed that CEUS is cost-effective in the surveillance of patients with liver cirrhosis[11].

Table 3 shows the main recommendations on the use of CEUS in cirrhotic patients according to the World Federation for Ultrasound in Medicine & Biology[26].

CEUS has shown high sensitivity for the evaluation of portal vein patency and in the differential diagnosis between benign and malignant portal vein thrombosis, this latter occurring in cirrhotic patients at various stages[27]. A thrombus showing hypervascularity in the arterial phase, irrespective of the presence of subsequent washout, is deemed to be malignant[10].

CEUS can also be used with valid results in guidance, response and detection of complications of interventional procedures[28] (Figure 4). CEUS may be of help during or after the interventional procedure[29]. Intraprocedural use of CEUS showed a relevant clinical impact, reducing the number of re-treatments and the related costs per patient[30].

Table 2 Imaging enhancement pattern of cirrhotic nodules and malignant focal liver lesions on Contrast-enhanced ultrasound

Lesion	Arterial phase	Portal venous phase	Late phase	Post-vascular phase
RN	Hypo-enhance	Iso-enhance	Iso-enhance	Iso-enhance
DN	Hypo-enhance or partial hyper-enhanced within lesion (early-HCC)	Iso-enhance	Iso-enhance	Iso-enhance
HCC	Hyper-enhance	Hypo-enhance or iso-enhance	Hypo-enhance or iso-enhance[1]	Hypo-enhance (mild and late washout) or iso-enhance[1]
ICC	Rim-enhance or Hyper-enhance with early washout (< 60 seconds)	Hypo-enhance	Hypo-enhance	Hypo-enhance
Metastasis	Rim-enhance or Hyper-enhance with early washout (< 60 seconds)	Hypo-enhance	Hypo-enhance	Hypo-enhance

[1]Well differentiated hepatocellular carcinoma. RN: Regenerative nodules; DN: Dysplastic nodules; HCC: Hepatocellular carcinoma; ICC: Intrahepatic cholangiocarcinoma.

Table 3 Recommendations contrast-enhanced ultrasound in cirrhotic liver

Recommendations	Notes
Characterization FLLs found in patients with liver cirrhosis to establish a diagnosis of malignancy	CT or MR imaging is required for a complete staging
In nodules not suitable for biopsy	When CT or MR are inconclusive
Selection of FLLs with different contrast pattern in a cirrhotic liver to be biopsied	
Monitoring changes in enhancement patterns in FLLs in cirrhotic liver requiring follow-up	
Guiding percutaneous biopsies to increase the diagnostic outcome	To compare to B-mode US

FLLs: Focal liver lesions; CT: Computed tomography; MR: Magnetic resonance; US: Ultrasounds.

The three-dimensional evaluation through the CEUS of the tumor lesion allows more accurate planning and the treatment with locoregional therapies[31,32] (Figure 5).

Intrahepatic cholangiocarcinoma

Intrahepatic peripheral cholangiocarcinoma (ICC) constitutes the second most common primary liver malignant tumor in cirrhotic patients and accounts for 1%–3% of newly developed tumors[32,33]. Differentiating ICC from HCC is of clinical relevance since liver transplantation is contraindicated in patients with ICC given poorly reported outcomes[34].

At CEUS, ICC shows heterogeneous contrast enhancement in the arterial phase with a substantially hypoechoic appearance in the extended portal-venous phase[35]. A rim-like contrast-enhancement has been reported but with a quite variable range (8-51% of cases)[9]. The presence and the quantity of fibrotic tissue and necrotic areas may strongly influence the CEUS appearance of ICC. This latter may present at CEUS overlapping features with HCC[36]. At CEUS, a clue suggestive for ICC is the presence of a wash out occurring earlier than 60 s, whereas HCC usually washes out later on (Figure 6)[37,38]. The same temporal difference in wash-out between HCC and other malignancies, including ICC, is also used by the CEUS LI-RADS lexicon for the diagnosis of ICC[10].

In a multicenter study of 1,006 nodules from 848 patients, the use of CEUS LI-RADS criteria for HCC - namely, arterial phase hyperenhancement and late washout (onset ≥ 60 s after contrast injection) of mild degree - was 98.5% predictive of HCC with no risk of misdiagnosis for pure cholangiocarcinoma[39]. To this purpose, contrast-enhanced CT and MRI may provide useful information due to the different contrast agent kinetic. Microbubbles are essentially blood pool agents and remain confined to the vascular space, whereas iodinated contrast agent and gadolinium chelates are essentially extra-cellular contrast agents and progressively accumulate in the fibrotic spaces of ICC[39].

The presence of both ICC and HCC components in the same lesion can make the lesion even more difficult and biopsy may be eventually needed in equivocal cases.

Metastasis

Metastatic liver deposits are relatively uncommon in the cirrhotic liver. This finding may probably be due to alteration of hemodynamics and the microstructural environment in the liver[40]. In particular, the hepatofugal portal venous flow may prevent neoplastic cells from seeding and flourishing in the liver[41]. Liver metastases from colorectal carcinoma are infrequently reported to spread to the cirrhotic

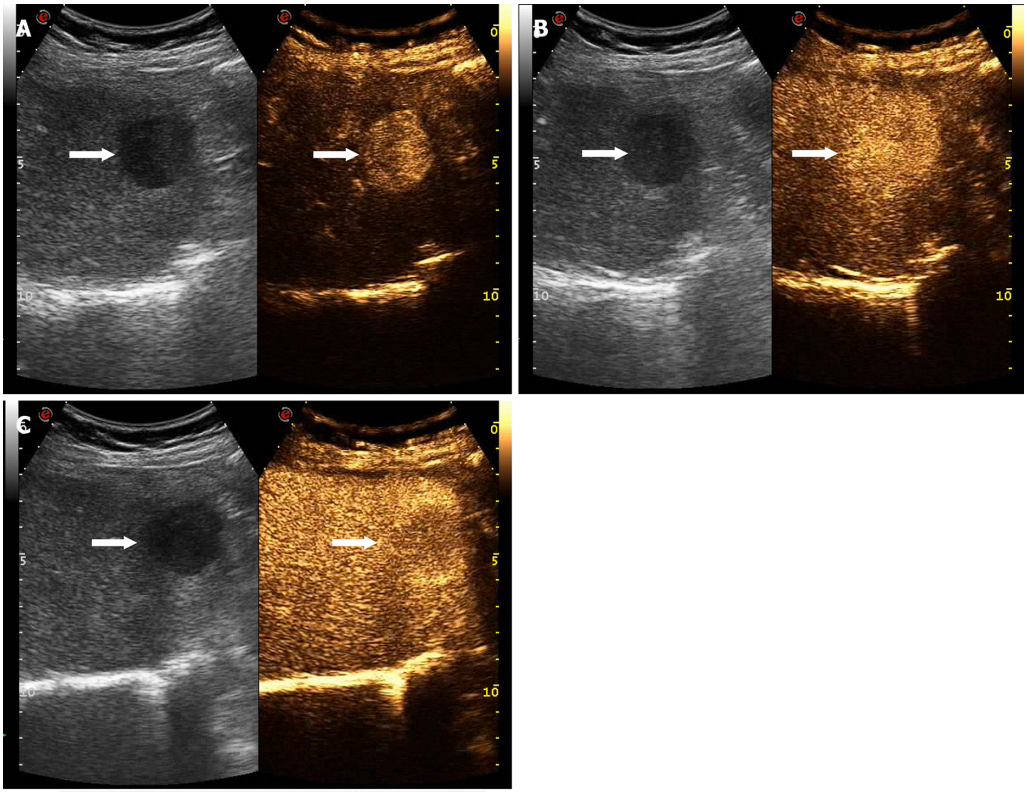

DOI: 10.4329/wjr.v14.i4.70

Figure 2 Hepatocellular carcinoma. A: Contrast-enhanced ultrasound examination in the arterial phase (30 s after the i.v. injection of contrast agent) shows a 3 cm sized hypoechoic nodule, showing a marked contrast enhancement (right, arrow); B: In the portal phase (70 s after the injection) the lesion is still hyper-enhancing in comparison to the adjacent liver parenchyma (arrows); C: Only waiting for the extended portal phase (*i.e.* 122 s after the injection) the lesion shows a mild and late wash-out and appears moderately hypoechoic (arrows).

liver[42]. Metastases from non-Hodgkin B-cell lymphoma may also involve the liver in patients with hepatitis C virus and typically consist of multiple small nodules[43].

On CEUS, liver metastases show a sharp and early washout within 60 s of contrast administration, irrespective of the contrast enhancement type in the arterial phase (Figure 3)[44]. This latter may present various patterns, such as rim-like, dotted, heterogeneous or even homogeneous, depending on the size and the grade of cellularity, vascularity, fibrosis and necrosis accompanying the development of the lesion.

BENIGN LESIONS

A wide spectrum of benign lesions may arise in a cirrhotic liver. Hence, it is crucial to avoid the misdiagnosis of benign liver lesions as HCC (*i.e.* minimize false positives) because this diagnostic interpretation may incorrectly increase the tumor burden[43].

Generally, at CEUS, a benign lesion presents a progressive and sustained enhancement in all phases of the study[45] (Table 4, Figures 7 and 8). Although tumor lesions may have similar characteristics, a clinical context of oncological or cirrhotic pathology allows differentiating the nature of the lesions[21]. Further aspects that are decisive for the diagnosis are detected by observing the arterial phase[4].

Hemangioma

Hemangioma is seen less frequently in cirrhotic patients than in the general population. In general, imaging features remain similar to those of hemangiomas observed in non-cirrhotic patients[46].

At CEUS, hemangioma has a characteristic globular, progressive, peripheral and discontinuous enhancement (Figure 7). However, with progressive cirrhosis, hemangiomas are likely to decrease in size, become more fibrotic and may appear as a hypo vascular lesion with a lack of peripheral globular contrast-enhancement[47,48]. Furthermore, flash filling hemangiomas may pose a diagnostic dilemma with well-differentiated HCC not showing wash-out, thus needing further radiological workup with CT or MRI for the final diagnosis.

Table 4 Imaging enhancement pattern of benign focal liver lesions on contrast-enhanced ultrasound

Lesion	Arterial phase	Portal venous phase	Late phase	Post-vascular phase
Hepatic cysts	Non-enhance	Non-enhance	Non-enhance	Non-enhance
Cystic hydatid disease	Non-enhance cysts and septa	Non-enhance cysts and septa	Non-enhance cysts and septa	Non-enhance cysts and septa
Abscess	Rim-enhance with enhanced septa; no central enhancement	Rim-enhance with enhanced septa; no central enhancement	Hypo-enhance rim; no central enhancement	Hypo-enhance rim; no central enhancement
Hemangioma	Peripheral, discontinuous and globular hyper-enhance	Peripheral, globular iso enhance and fill-in	Iso-enhance or hypo-enhance	Iso-enhance or hypo-enhance
FNH	Hyper-enhance from the center to peripheral region spoke-wheel vascularity	Hyper-enhance with/without un-enhanced central scar	Iso-enhance or hyper-enhance with/without un-enhanced central scar	Iso-enhance or hypo-enhance
HA	Hyper-enhance	Iso-enhance	Iso-enhance	Iso-enhance or hypo-enhance
Pseudo lesions	Hyper-enhance	Hyper-enhance or iso-enhance	Iso-enhance	Iso-enhance

FNH: Focal nodular hyperplasia; HA: Hepatocellular adenoma.

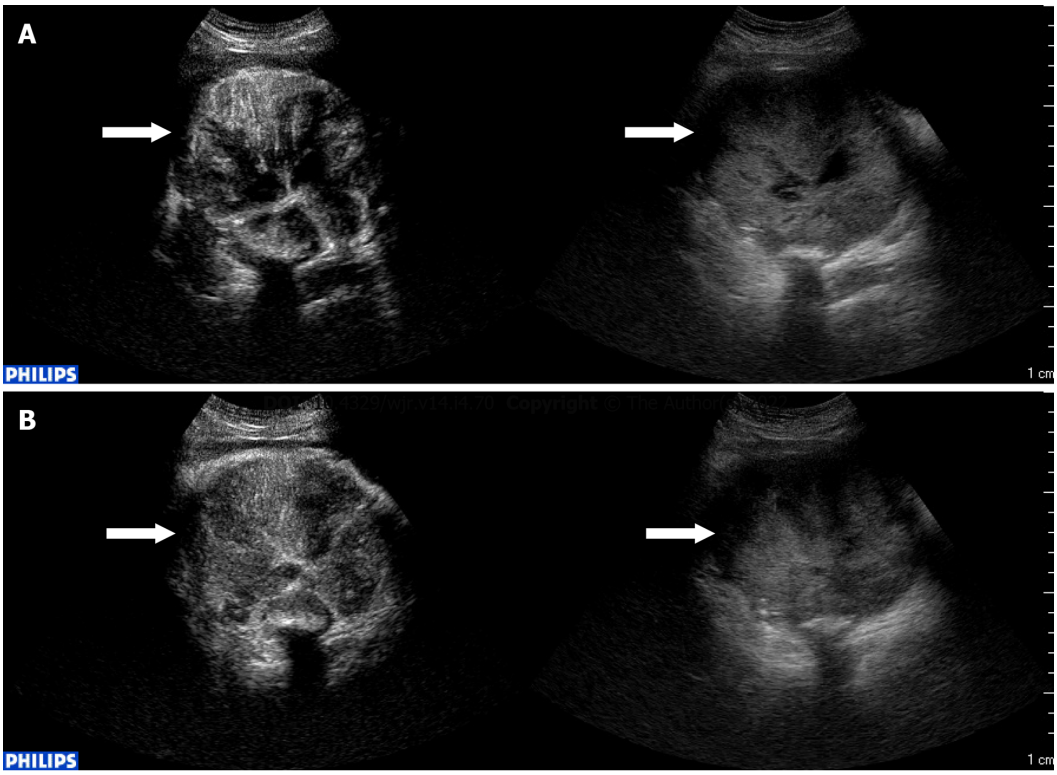

DOI: 10.4329/wjr.v14.i4.70

Figure 3 Liver metastasis from gastrointestinal stromal tumor. A: Contrast-enhanced ultrasound examination in the arterial phase (10 s after the i.v. injection of contrast agent) shows a large (11 cm) mass, showing heterogeneous contrast enhancement (left, arrow); B: Still in the arterial phase (40 s after the injection) the mass shows early wash-out.

Focal nodular hyperplasia

Although Focal nodular hyperplasia (FNH) is the second most common benign liver tumor after hemangioma, the report of FNH-like nodules in the cirrhotic liver is only sporadic and imaging appearance is similar to FNH arising in the non-cirrhotic liver[43,49].

At CEUS, the typical findings of FNH are a centrifugal contrast-enhancement pattern with a spoke-wheel appearance in the arterial phase followed by sustained contrast-enhancement and iso or hyperechoic appearance in portal-venous and late phase[50] (Figure 8). A central avascular area in the arterial phase is often appreciable in FNH larger than 3 cm with a hypoechoic appearance.

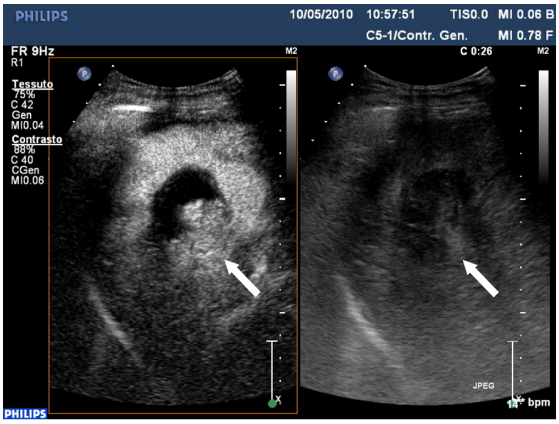

DOI: 10.4329/wjr.v14.i4.70

Figure 4 One-month post-procedural assessment of hepatocellular carcinoma after TACE. Contrast-enhanced ultrasound examination in the arterial phase (26 s after the i.v. injection of contrast agent) shows a clear cut intralesional area of contrast-enhancement indicating still viable tumor.

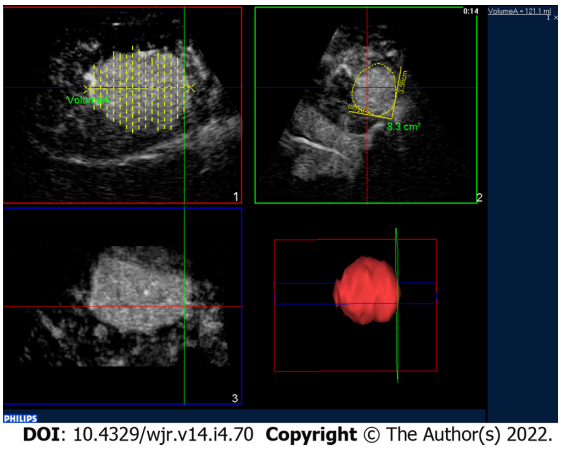

DOI: 10.4329/wjr.v14.i4.70

Figure 5 Contrast-enhanced ultrasound 3D. Contrast-enhanced ultrasound of a hepatocellular carcinoma in the arterial phase: Three-dimensional rendering and volume calculation.

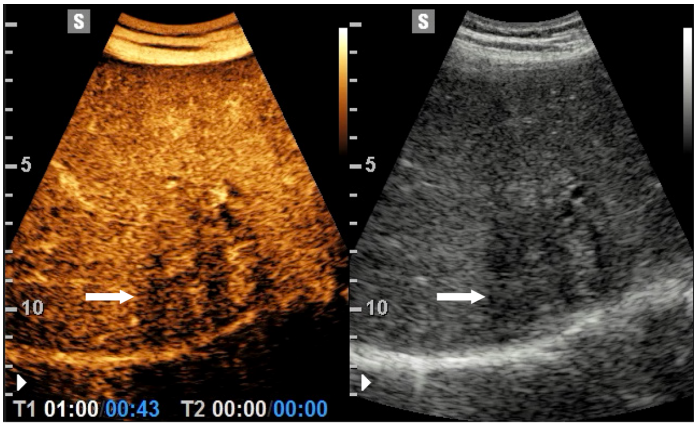

DOI: 10.4329/wjr.v14.i4.70

Figure 6 Intrahepatic cholangiocarcinoma. Contrast-enhanced ultrasound examination in the arterial phase (43 s after the i.v. injection of contrast agent) shows an ill-defined lesion showing heterogeneous washout (left, arrow).

Hepatocellular adenoma

The incidence of hepatocellular adenoma (HA) in the cirrhotic liver is exceedingly rare with a few reports in the literature[51].

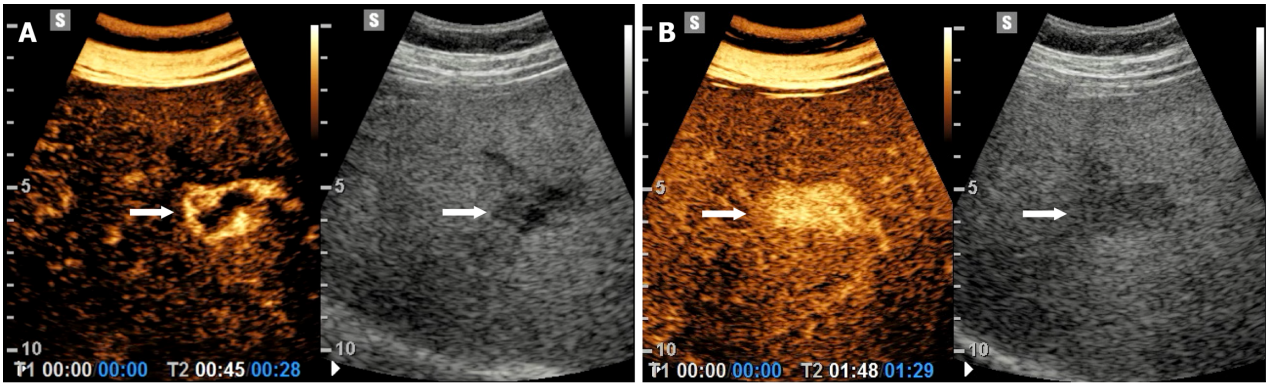

DOI: 10.4329/wjr.v14.i4.70

Figure 7 Hemangioma. A: Contrast-enhanced ultrasound examination in the arterial phase (28 s after the i.v. injection of contrast agent) shows a peripheral globular contrast-enhancement pattern (left, arrow); B: In the portal venous phase (89 s after the injection) a centripetal and complete fill-in is appreciable.

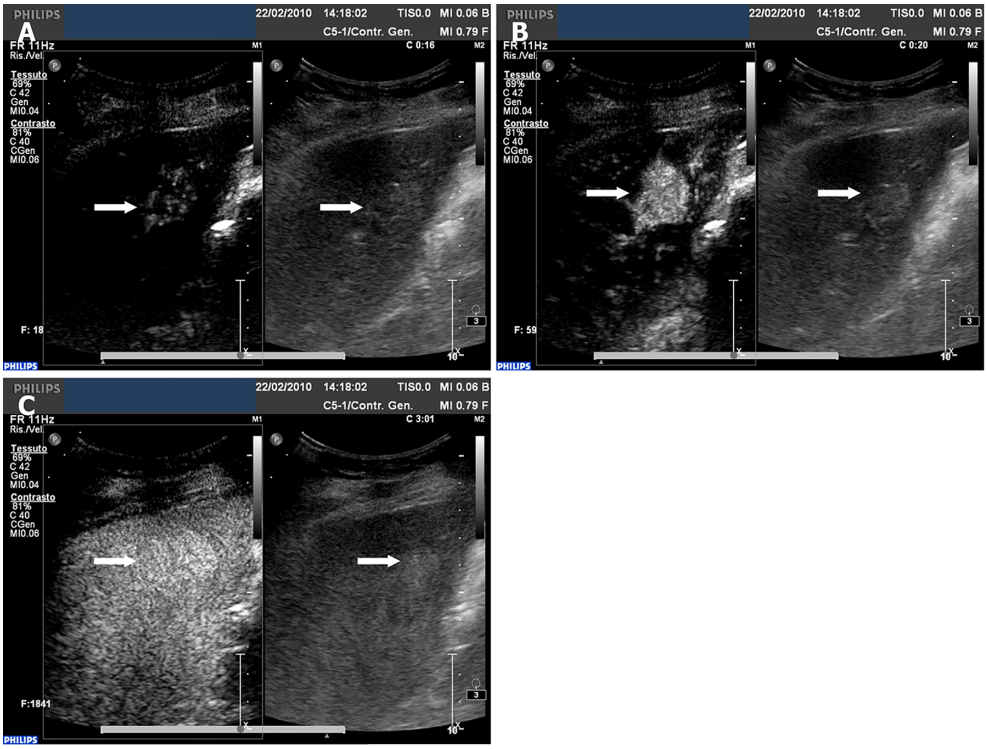

DOI: 10.4329/wjr.v14.i4.70

Figure 8 Focal nodular hyperplasia. A: Contrast-enhanced ultrasound examination in the early arterial phase (16 s after the i.v. injection of contrast agent) shows a spoke-wheel appearance (left, arrow); B: Four seconds later, still in the arterial phase the lesion is homogeneously and strongly enhancing (left, arrow); C: In the late phase (180 s after the injection) the lesion is still slightly hyperechoic to the adjacent liver parenchyma.

At CEUS, a peripheral enhancement with centripetal filling and sustained hypervascularization, suggests the diagnosis of HA[10,52]. However, as a warning, HA may show a hypoechoic appearance in the portal-venous and late phase[52].

Cystic lesions

Simple biliary and peribiliary cysts have similar features in cirrhotic and noncirrhotic livers. They present a homogenous anechoic appearance, a very thin wall and through transmission with posterior acoustic enhancement and no contrast enhancement at CEUS[43]. CEUS may be a problem-solving technique in diagnosing complicated non-anechoic cyst or a rare form of *Co*-existence of hepatocellular carcinoma and cystic echinococcosis[53]. Usually, CEUS shows a lack of enhancement of septa separating daughter cysts[54].

Hepatic abscesses, pyogenic, fungal and amebic have similar CEUS features in cirrhotic and non-cirrhotic livers. Abscesses do not have a significant internal enhancement after contrast ultrasound administration but septations within the lesion may enhance as well as an irregular peripheral rim[55].

Pseudo lesions

Focal fatty changes or confluent hepatic fibrosis can mimic malignancies. Focal fatty changes are an increase or decrease in fat content in a focal area of the liver parenchyma owing to an aberrant portal-venous vascularization[55].

Confluent hepatic fibrosis is usually shown in patients with alcohol-related cirrhosis. It involves peripheral parenchymal replacement by thick fibrotic bands that appear as focal wedge-shaped areas with thick fibrotic bands causing retraction of the overlying capsule; the presence of inflammation can lead to inhomogeneous arterial phase hyperenhancement[40].

At CEUS, these pseudo lesions present isoenhanced in comparison with the surrounding liver parenchyma during the extended portal-venous phase[55], furthermore, fibrosis is usually seen in a typical position (medial segment of the left lobe or anterior segment of the right lobe)[40].

CONCLUSION

A wide spectrum of benign and malignant lesions other than HCC may be found in the cirrhotic liver. More than several years after its release, CEUS is being used for safe diagnostic imaging which enables real-time recognition of enhancement characteristics of focal liver lesions arising in cirrhotic patients. Currently, CEUS is increasingly being performed on a routine basis and is included as a part of the recommended diagnostic work-up of HCC as well as in the follow-up.

FOOTNOTES

Author contributions: Bartolotta TV, Randazzo A, Bruno E and Taibbi A contributed equally to this work; All authors have read and approved the final manuscript.

Conflict-of-interest statement: Tommaso Vincenzo Bartolotta: Lecturer for Samsung.

Country/Territory of origin: Italy

ORCID number: Tommaso Vincenzo Bartolotta 0000-0002-8808-379X; Angelo Randazzo 0000-0001-9558-5248; Eleonora Bruno 0000-0001-6876-2587; Adele Taibbi 0000-0001-6442-744X.

S-Editor: Wang LL
L-Editor: Filipodia
P-Editor: Wang LL

REFERENCES

1 **Tsochatzis EA**, Bosch J, Burroughs AK. Liver cirrhosis. *Lancet* 2014; **383**: 1749-1761 [PMID: 24480518 DOI: 10.1016/S0140-6736(14)60121-5]
2 **Blachier M**, Leleu H, Peck-Radosavljevic M, Valla DC, Roudot-Thoraval F. The burden of liver disease in Europe: a review of available epidemiological data. *J Hepatol* 2013; **58**: 593-608 [PMID: 23419824 DOI: 10.1016/j.jhep.2012.12.005]
3 **Taibbi A**, Petta S, Matranga D, Caruana G, Cannella R, Busè G, Marco VD, Midiri M, Bartolotta TV. Liver stiffness quantification in biopsyproven nonalcoholic fatty liver disease patients using shear wave elastography in comparison with transient elastography. *Ultrasonography* 2020; **40**: 407-416 [PMID: 33561928 DOI: 10.14366/usg.20147]
4 **Ronot M**, Dioguardi Burgio M, Purcell Y, Pommier R, Brancatelli G, Vilgrain V. Focal lesions in cirrhosis: Not always HCC. *Eur J Radiol* 2017; **93**: 157-168 [PMID: 28668410 DOI: 10.1016/j.ejrad.2017.05.040]
5 **Kim MJ**, Lee S, An C. Problematic lesions in cirrhotic liver mimicking hepatocellular carcinoma. *Eur Radiol* 2019; **29**: 5101-5110 [PMID: 30788586 DOI: 10.1007/s00330-019-06030-0]
6 **Quaia E**. Microbubble ultrasound contrast agents: an update. *Eur Radiol* 2007; **17**: 1995-2008 [PMID: 17351779 DOI: 10.1007/s00330-007-0623-0]
7 **Barr RG**, Huang P, Luo Y, Xie X, Zheng R, Yan K, Jing X, Xu H, Fei X, Lee JM. Contrast-enhanced ultrasound imaging of the liver: a review of the clinical evidence for SonoVue and Sonazoid. *Abdom Radiol (NY)* 2020; **45**: 3779-3788 [PMID: 32424608 DOI: 10.1007/s00261-020-02573-9]
8 **Piscaglia F**, Bolondi L; Italian Society for Ultrasound in Medicine and Biology (SIUMB) Study Group on Ultrasound

Contrast Agents. The safety of Sonovue in abdominal applications: retrospective analysis of 23188 investigations. *Ultrasound Med Biol* 2006; **32**: 1369-1375 [PMID: 16965977 DOI: 10.1016/j.ultrasmedbio.2006.05.031]

9 **Durot I**, Wilson SR, Willmann JK. Contrast-enhanced ultrasound of malignant liver lesions. *Abdom Radiol (NY)* 2018; **43**: 819-847 [PMID: 29094174 DOI: 10.1007/s00261-017-1360-8]

10 **Bartolotta TV**, Vernuccio F, Taibbi A, Lagalla R. Contrast-Enhanced Ultrasound in Focal Liver Lesions: Where Do We Stand? *Semin Ultrasound CT MR* 2016; **37**: 573-586 [PMID: 27986175 DOI: 10.1053/j.sult.2016.10.003]

11 **Westwood M**, Joore M, Grutters J, Redekop K, Armstrong N, Lee K, Gloy V, Raatz H, Misso K, Severens J, Kleijnen J. Contrast-enhanced ultrasound using SonoVue® (sulphur hexafluoride microbubbles) compared with contrast-enhanced computed tomography and contrast-enhanced magnetic resonance imaging for the characterisation of focal liver lesions and detection of liver metastases: a systematic review and cost-effectiveness analysis. *Health Technol Assess* 2013; **17**: 1-243 [PMID: 23611316 DOI: 10.3310/hta17160]

12 **Cassinotto C**, Aubé C, Dohan A. Diagnosis of hepatocellular carcinoma: An update on international guidelines. *Diagn Interv Imaging* 2017; **98**: 379-391 [PMID: 28395852 DOI: 10.1016/j.diii.2017.01.014]

13 **Forner A**, Llovet JM, Bruix J. Hepatocellular carcinoma. *Lancet* 2012; **379**: 1245-1255 [PMID: 22353262 DOI: 10.1016/S0140-6736(11)61347-0]

14 **Choi JY**, Lee JM, Sirlin CB. CT and MR imaging diagnosis and staging of hepatocellular carcinoma: part I. Development, growth, and spread: key pathologic and imaging aspects. *Radiology* 2014; **272**: 635-654 [PMID: 25153274 DOI: 10.1148/radiol.14132361]

15 **Kim TK**, Lee KH, Khalili K, Jang HJ. Hepatocellular nodules in liver cirrhosis: contrast-enhanced ultrasound. *Abdom Imaging* 2011; **36**: 244-263 [PMID: 21253723 DOI: 10.1007/s00261-011-9686-0]

16 **Wu W**, Chen M, Yan K, Dai Y, Yin S, Yang W, Fan Z. Evaluation of contrast-enhanced ultrasound for diagnosis of dysplastic nodules with a focus of hepatocellular carcinoma in liver cirrhosis patients. *Chin J Cancer Res* 2015; **27**: 83-89 [PMID: 25717230 DOI: 10.3978/j.issn.1000-9604.2015.02.06]

17 **Ferlay J**, Soerjomataram I, Dikshit R, Eser S, Mathers C, Rebelo M, Parkin DM, Forman D, Bray F. Cancer incidence and mortality worldwide: sources, methods and major patterns in GLOBOCAN 2012. *Int J Cancer* 2015; **136**: E359-E386 [PMID: 25220842 DOI: 10.1002/ijc.29210]

18 **Sato T**, Kondo F, Ebara M, Sugiura N, Okabe S, Sunaga M, Yoshikawa M, Suzuki E, Ogasawara S, Shinozaki Y, Ooka Y, Chiba T, Kanai F, Kishimoto T, Nakatani Y, Fukusato T, Yokosuka O. Natural history of large regenerative nodules and dysplastic nodules in liver cirrhosis: 28-year follow-up study. *Hepatol Int* 2015; **9**: 330-336 [PMID: 25788204 DOI: 10.1007/s12072-015-9620-6]

19 **An C**, Choi YA, Choi D, Paik YH, Ahn SH, Kim MJ, Paik SW, Han KH, Park MS. Growth rate of early-stage hepatocellular carcinoma in patients with chronic liver disease. *Clin Mol Hepatol* 2015; **21**: 279-286 [PMID: 26523271 DOI: 10.3350/cmh.2015.21.3.279]

20 **Bhayana D**, Kim TK, Jang HJ, Burns PN, Wilson SR. Hypervascular liver masses on contrast-enhanced ultrasound: the importance of washout. *AJR Am J Roentgenol* 2010; **194**: 977-983 [PMID: 20308500 DOI: 10.2214/AJR.09.3375]

21 **Jang HJ**, Kim TK, Burns PN, Wilson SR. Enhancement patterns of hepatocellular carcinoma at contrast-enhanced US: comparison with histologic differentiation. *Radiology* 2007; **244**: 898-906 [PMID: 17709836 DOI: 10.1148/radiol.2443061520]

22 **Tada T**, Kumada T, Toyoda H, Ito T, Sone Y, Kaneoka Y, Maeda A, Okuda S, Otobe K, Takahashi K. Utility of Contrast-enhanced Ultrasonography with Perflubutane for Determining Histologic Grade in Hepatocellular Carcinoma. *Ultrasound Med Biol* 2015; **41**: 3070-3078 [PMID: 26360976 DOI: 10.1016/j.ultrasmedbio.2015.07.023]

23 **Maruyama H**, Takahashi M, Ishibashi H, Yoshikawa M, Yokosuka O. Contrast-enhanced ultrasound for characterization of hepatic lesions appearing non-hypervascular on CT in chronic liver diseases. *Br J Radiol* 2012; **85**: 351-357 [PMID: 21224305 DOI: 10.1259/bjr/20440141]

24 **Zheng SG**, Xu HX, Liu LN. Management of hepatocellular carcinoma: The role of contrast-enhanced ultrasound. *World J Radiol* 2014; **6**: 7-14 [PMID: 24578787 DOI: 10.4329/wjr.v6.i1.7]

25 **Kang HJ**, Lee JM, Yoon JH, Han JK. Role of Contrast-Enhanced Ultrasound as a Second-Line Diagnostic Modality in Noninvasive Diagnostic Algorithms for Hepatocellular Carcinoma. *Korean J Radiol* 2021; **22**: 354-365 [PMID: 33236540 DOI: 10.3348/kjr.2020.0973]

26 **Dietrich CF**, Nolsøe CP, Barr RG, Berzigotti A, Burns PN, Cantisani V, Chammas MC, Chaubal N, Choi BI, Clevert DA, Cui X, Dong Y, D'Onofrio M, Fowlkes JB, Gilja OH, Huang P, Ignee A, Jenssen C, Kono Y, Kudo M, Lassau N, Lee WJ, Lee JY, Liang P, Lim A, Lyshchik A, Meloni MF, Correas JM, Minami Y, Moriyasu F, Nicolau C, Piscaglia F, Saftoiu A, Sidhu PS, Sporea I, Torzilli G, Xie X, Zheng R. Guidelines and Good Clinical Practice Recommendations for Contrast-Enhanced Ultrasound (CEUS) in the Liver-Update 2020 WFUMB in Cooperation with EFSUMB, AFSUMB, AIUM, and FLAUS. *Ultrasound Med Biol* 2020; **46**: 2579-2604 [PMID: 32713788 DOI: 10.1016/j.ultrasmedbio.2020.04.030]

27 **Tarantino L**, Ambrosino P, Di Minno MN. Contrast-enhanced ultrasound in differentiating malignant from benign portal vein thrombosis in hepatocellular carcinoma. *World J Gastroenterol* 2015; **21**: 9457-9460 [PMID: 26327753 DOI: 10.3748/wjg.v21.i32.9457]

28 **Francica G**, Meloni MF, Riccardi L, Giangregorio F, Caturelli E, Terracciano F, de Sio I. Role of Contrast-Enhanced Ultrasound in the Detection of Complications After Ultrasound-Guided Liver Interventional Procedures. *J Ultrasound Med* 2020; **40**: 1665-1673 [PMID: 33085814 DOI: 10.1002/jum.15540]

29 **Ferraioli G**, Meloni MF. Contrast-enhanced ultrasonography of the liver using SonoVue. *Ultrasonography* 2018; **37**: 25-35 [PMID: 28830058 DOI: 10.14366/usg.17037]

30 **Mauri G**, Porazzi E, Cova L, Restelli U, Tondolo T, Bonfanti M, Cerri A, Ierace T, Croce D, Solbiati L. Intraprocedural contrast-enhanced ultrasound (CEUS) in liver percutaneous radiofrequency ablation: clinical impact and health technology assessment. *Insights Imaging* 2014; **5**: 209-216 [PMID: 24563244 DOI: 10.1007/s13244-014-0315-7]

31 **Bartolotta TV**, Taibbi A, Matranga D, Midiri M, Lagalla R. 3D vs 2D contrast-enhanced sonography in the evaluation of therapeutic response of hepatocellular carcinoma after locoregional therapies: preliminary findings. *Radiol Med* 2015; **120**: 695-704 [DOI: 10.1007/s11547-015-0514-4]

32 **Rimola J**, Forner A, Tremosini S, Reig M, Vilana R, Bianchi L, Rodríguez-Lope C, Solé M, Ayuso C, Bruix J. Non-invasive diagnosis of hepatocellular carcinoma ≤ 2 cm in cirrhosis. Diagnostic accuracy assessing fat, capsule and signal intensity at dynamic MRI. *J Hepatol* 2012; **56**: 1317-1323 [PMID: 22314420 DOI: 10.1016/j.jhep.2012.01.004]

33 **Sersté T**, Barrau V, Ozenne V, Vullierme MP, Bedossa P, Farges O, Valla DC, Vilgrain V, Paradis V, Degos F. Accuracy and disagreement of computed tomography and magnetic resonance imaging for the diagnosis of small hepatocellular carcinoma and dysplastic nodules: role of biopsy. *Hepatology* 2012; **55**: 800-806 [PMID: 22006503 DOI: 10.1002/hep.24746]

34 **Sapisochín G**, Fernández de Sevilla E, Echeverri J, Charco R. Liver transplantation for cholangiocarcinoma: Current status and new insights. *World J Hepatol* 2015; **7**: 2396-2403 [PMID: 26464755 DOI: 10.4254/wjh.v7.i22.2396]

35 **Loria F**, Loria G, Basile S, Crea G, Frosina L, Di Carlo I. Contrast-enhanced ultrasound appearances of enhancement patterns of intrahepatic cholangiocarcinoma: correlation with pathological findings. *Updates Surg* 2014; **66**: 135-143 [PMID: 24802031 DOI: 10.1007/s13304-014-0251-6]

36 **Vilana R**, Forner A, Bianchi L, García-Criado A, Rimola J, de Lope CR, Reig M, Ayuso C, Brú C, Bruix J. Intrahepatic peripheral cholangiocarcinoma in cirrhosis patients may display a vascular pattern similar to hepatocellular carcinoma on contrast-enhanced ultrasound. *Hepatology* 2010; **51**: 2020-2029 [PMID: 20512990 DOI: 10.1002/hep.23600]

37 **Li R**, Yuan MX, Ma KS, Li XW, Tang CL, Zhang XH, Guo DY, Yan XC. Detailed analysis of temporal features on contrast enhanced ultrasound may help differentiate intrahepatic cholangiocarcinoma from hepatocellular carcinoma in cirrhosis. *PLoS One* 2014; **9**: e98612 [PMID: 24874413 DOI: 10.1371/journal.pone.0098612]

38 **Wildner D**, Bernatik T, Greis C, Seitz K, Neurath MF, Strobel D. CEUS in hepatocellular carcinoma and intrahepatic cholangiocellular carcinoma in 320 patients - early or late washout matters: a subanalysis of the DEGUM multicenter trial. *Ultraschall Med* 2015; **36**: 132-139 [PMID: 25812115 DOI: 10.1055/s-0034-1399147]

39 **Terzi E**, Iavarone M, Pompili M, Veronese L, Cabibbo G, Fraquelli M, Riccardi L, De Bonis L, Sangiovanni A, Leoni S, Zocco MA, Rossi S, Alessi N, Wilson SR, Piscaglia F; CEUS LI-RADS Italy study group collaborators:. Contrast ultrasound LI-RADS LR-5 identifies hepatocellular carcinoma in cirrhosis in a multicenter restropective study of 1,006 nodules. *J Hepatol* 2018; **68**: 485-492 [PMID: 29133247 DOI: 10.1016/j.jhep.2017.11.007]

40 **Elsayes KM**, Chernyak V, Morshid AI, Tang A, Kielar AZ, Bashir MR, Sirlin CB. The spectrum of Pitfalls, Pseudolesions, and Potential Misdiagnoses in Cirrhosis. *AJR Am J Roentgenol* 2018; **211**: 87-96 [PMID: 29932761 DOI: 10.2214/AJR.18.19781]

41 **Seymour K**, Charnley RM. Evidence that metastasis is less common in cirrhotic than normal liver: a systematic review of post-mortem case-control studies. *Br J Surg* 1999; **86**: 1237-1242 [PMID: 10540123 DOI: 10.1046/j.1365-2168.1999.01228.x]

42 **Gervaz P**, Pak-art R, Nivatvongs S, Wolff BG, Larson D, Ringel S. Colorectal adenocarcinoma in cirrhotic patients. *J Am Coll Surg* 2003; **196**: 874-879 [PMID: 12788423 DOI: 10.1016/S1072-7515(03)00117-0]

43 **Galia M**, Taibbi A, Marin D, Furlan A, Dioguardi Burgio M, Agnello F, Cabibbo G, Van Beers BE, Bartolotta TV, Midiri M, Lagalla R, Brancatelli G. Focal lesions in cirrhotic liver: what else beyond hepatocellular carcinoma? *Diagn Interv Radiol* 2014; **20**: 222-228 [PMID: 24509186 DOI: 10.5152/dir.2014.13184]

44 **Bartolotta TV**, Taibbi A, Picone D, Anastasi A, Midiri M, Lagalla R. Detection of liver metastases in cancer patients with geographic fatty infiltration of the liver: the added value of contrast-enhanced sonography. *Ultrasonography* 2017; **36**: 160-169 [PMID: 28145108 DOI: 10.14366/usg.16041]

45 **Zarzour JG**, Porter KK, Tchelepi H, Robbin ML. Contrast-enhanced ultrasound of benign liver lesions. *Abdom Radiol (NY)* 2018; **43**: 848-860 [PMID: 29167944 DOI: 10.1007/s00261-017-1402-2]

46 **Duran R**, Ronot M, Di Renzo S, Gregoli B, Van Beers BE, Vilgrain V. Is magnetic resonance imaging of hepatic hemangioma any different in liver fibrosis and cirrhosis compared to normal liver? *Eur J Radiol* 2015; **84**: 816-822 [PMID: 25703650 DOI: 10.1016/j.ejrad.2015.01.016]

47 **Brancatelli G**, Federle MP, Blachar A, Grazioli L. Hemangioma in the cirrhotic liver: diagnosis and natural history. *Radiology* 2001; **219**: 69-74 [PMID: 11274536 DOI: 10.1148/radiology.219.1.r01ap3269]

48 **Wu XF**, Bai XM, Yang W, Sun Y, Wang H, Wu W, Chen MH, Yan K. Differentiation of atypical hepatic hemangioma from liver metastases: Diagnostic performance of a novel type of color contrast enhanced ultrasound. *World J Gastroenterol* 2020; **26**: 960-972 [PMID: 32206006 DOI: 10.3748/wjg.v26.i9.960]

49 **Lee YH**, Kim SH, Cho MY, Shim KY, Kim MS. Focal nodular hyperplasia-like nodules in alcoholic liver cirrhosis: radiologic-pathologic correlation. *AJR Am J Roentgenol* 2007; **188**: W459-W463 [PMID: 17449744 DOI: 10.2214/AJR.05.1998]

50 **Giambelluca D**, Taibbi A, Midiri M, Bartolotta TV. The "spoke wheel" sign in hepatic focal nodular hyperplasia. *Abdom Radiol (NY)* 2019; **44**: 1183-1184 [PMID: 30488100 DOI: 10.1007/s00261-018-1852-1]

51 **Seo JM**, Lee SJ, Kim SH, Park CK, Ha SY. Hepatocellular carcinoma arising from hepatocellular adenoma in a hepatitis B virus-associated cirrhotic liver. *Clin Radiol* 2012; **67**: 329-333 [PMID: 22079485 DOI: 10.1016/j.crad.2011.09.003]

52 **Garcovich M**, Faccia M, Meloni F, Bertolini E, de Sio I, Calabria G, Francica G, Vidili G, Riccardi L, Zocco MA, Ainora ME, Ponziani FR, De Gaetano AM, Gasbarrini A, Rapaccini GL, Pompili M. Contrast-enhanced ultrasound patterns of hepatocellular adenoma: an Italian multicenter experience. *J Ultrasound* 2019; **22**: 157-165 [PMID: 30306412 DOI: 10.1007/s40477-018-0322-5]

53 **Bo R**, Yasen A, Shao Y, Zhang W, Lin R, Jiang T, Wen H, Xiao H, Aji T. Co-existence of hepatocellular carcinoma and cystic echinococcosis. *Infect Agent Cancer* 2020; **15**: 5 [PMID: 32010203 DOI: 10.1186/s13027-020-0275-0]

54 **Pakala T**, Molina M, Wu GY. Hepatic Echinococcal Cysts: A Review. *J Clin Transl Hepatol* 2016; **4**: 39-46 [PMID: 27047771 DOI: 10.14218/JCTH.2015.00036]

55 **Selkoe DJ**, Hardy J. The amyloid hypothesis of Alzheimer's disease at 25 years. *EMBO Mol Med* 2016; **8**: 595-608 [PMID: 27025652 DOI: 10.15252/emmm.201606210]

World Journal of Radiology

Submit a Manuscript: https://www.f6publishing.com

World J Radiol 2022 April 28; 14(4): 82-90

DOI: 10.4329/wjr.v14.i4.82

ISSN 1949-8470 (online)

ORIGINAL ARTICLE

Retrospective Cohort Study

Decreased cross-sectional muscle area in male patients with clear cell renal cell carcinoma and peritumoral collateral vessels

Federico Greco, Bruno Beomonte Zobel, Carlo Augusto Mallio

Specialty type: Radiology, nuclear medicine and medical imaging

Provenance and peer review: Invited article; Externally peer reviewed.

Peer-review model: Single blind

Peer-review report's scientific quality classification

Grade A (Excellent): 0
Grade B (Very good): 0
Grade C (Good): C, C
Grade D (Fair): 0
Grade E (Poor): E

P-Reviewer: Iida H, Japan; Lin X, China; Sato H, Japan

Received: October 24, 2021
Peer-review started: October 24, 2021
First decision: December 10, 2021
Revised: December 15, 2021
Accepted: March 25, 2022
Article in press: March 25, 2022
Published online: April 28, 2022

Federico Greco, Unità Operativa Complessa Diagnostica per Immagini Territoriale Aziendale, Cittadella della Salute Azienda Sanitaria Locale di Lecce, Lecce 73100, Italy

Bruno Beomonte Zobel, Carlo Augusto Mallio, Unit of Diagnostic Imaging, Università Campus Bio-Medico di Roma, Rome 00128, Italy

Corresponding author: Federico Greco, MD, Doctor, Unità Operativa Complessa Diagnostica per Immagini Territoriale Aziendale, Cittadella della Salute Azienda Sanitaria Locale di Lecce, Piazza Filippo Bottazzi, Lecce 73100, Italy. federicogreco@outlook.com

Abstract

BACKGROUND

Sarcopenia is the loss of skeletal muscle mass (SMM) and is a sign of cancer cachexia. Patients with advanced renal cell carcinoma (RCC) may show cachexia.

AIM

To evaluate the amount of SMM in male clear cell RCC (ccRCC) patients with and without collateral vessels.

METHODS

In this study, we included a total of 124 male Caucasian patients divided into two groups: ccRCCa group without collateral vessels (n = 54) and ccRCCp group with collateral vessels (n = 70). Total abdominal muscle area (TAMA) was measured in both groups using a computed tomography imaging-based approach. TAMA measures were also corrected for age in order to rule out age-related effects.

RESULTS

There was a statistically significant difference between the two groups in terms of TAMA ($P < 0.05$) driven by a reduction in patients with peritumoral collateral vessels. The result was confirmed by repeating the analysis with values corrected for age ($P < 0.05$), indicating no age effect on our findings.

CONCLUSION

This study showed a decreased TAMA in ccRCC patients with peritumoral collateral vessels. The presence of peritumoral collateral vessels adjacent to ccRCC might be a fine diagnostic clue to sarcopenia.

Key Words: Cancer cachexia; Body composition; Clear cell renal cell carcinoma;

Collateral vessels; Kidney cancer; Sarcopenia

Core Tip: Clear cell renal cell carcinoma (ccRCC) can be detected with or without peritumoral collateral vessels. These vessels have been defined as enlarged capsular veins, stimulated by tumor-related effects. The presence of peritumoral collateral vessels around ccRCC is a poorly investigated phenomenon, with unclear clinical meaning. Here, we reported a novel association between peritumoral collateral vessels and loss of skeletal muscle in patients with ccRCC. The effect was not influenced by age, supporting the concept that peritumoral collateral vessels adjacent to ccRCC should drive clinicians' attention towards cancer cachexia.

Citation: Greco F, Beomonte Zobel B, Mallio CA. Decreased cross-sectional muscle area in male patients with clear cell renal cell carcinoma and peritumoral collateral vessels. *World J Radiol* 2022; 14(4): 82-90
URL: https://www.wjgnet.com/1949-8470/full/v14/i4/82.htm
DOI: https://dx.doi.org/10.4329/wjr.v14.i4.82

INTRODUCTION

Cancer cachexia is the reduction of adipose tissue and skeletal muscle (SM) which cannot be fully compensated with nutrition, resulting in progressive functional impairment[1]. This condition is due to energy disbalance during growth of the neoplasm[2]. Advanced neoplastic diseases can lead to loss of up to 85% of adipose and SM tissues[3]. Cancer cachexia and weight loss influence prognosis and response to therapy[4,5]. Renal cell carcinoma (RCC) patients with an advanced and metastatic disease are susceptible to cachexia. RCC patients have a relatively high prevalence of sarcopenia, the term for loss of SM mass (SMM)[4,6]. For example, sarcopenia was detected in up to 47% of patients with localised RCC and 29%-68% of patients with metastatic RCC[7-9]. Sarcopenic RCC patients have a worse overall survival than RCC patients without sarcopenia[10].

SM is not only part of the locomotor system but also produces and releases cytokines and myokines through the contraction of muscle fibres and thus has endocrine activity[11]. By releasing myokines into the circulation, SM can communicate with other organs such as adipose tissue, bone, the liver, and the brain, underlining the importance of this organ for regulating endocrine balance and decreasing risk of various diseases[12].

Body mass index (BMI) is an indicator used for obesity classification but does not convey information about body composition nor does it provide details about the quantity and distribution of different tissues such as SM and abdominal adipose tissue compartments. For this, computed tomography (CT) and magnetic resonance imaging (MRI) are gold standard methods for quantitative assessment and non-invasive tissue characterisation[13-19].

Peritumoural collateral vessels in RCC result from enlargement of capsular renal veins[19]. Gonadal vein recruitment can be present, especially in RCCs located at the lower renal pole[19]. Conversely, lesions located at the upper renal pole have different drainage routes including the adrenal and lower phrenic veins[19]. A study performed on 58 RCC patients reported 28 patients with peritumoural collateral vessels, of which 18 presented with gonadal vein recruitment[19]. Peritumoural collateral vessels with gonadal vein outflow were detected only in RCCs greater than 5 cm in diameter[19].

It is reasonable to speculate that increased blood demand due to tumour hypercellularity and neovascularisation, in possible association with main renal vein thrombosis, are factors contributing to the development of peritumoural collateral vessels in RCC patients. Hypercellularity could influence changes in cellular architecture leading to alternative routes of venous outflow that can become macroscopically evident as peritumoural collateral vessels with CT and MRI imaging (Figure 1). The presence of collateral vessels adjacent to RCC is considered a sign of locally advanced disease (*i.e.*, pT stage > T3a)[20]. However, these vessels can also be present in early stages of RCC.

The direct comparison of SMM in clear cell RCC (ccRCC) patients with and without peritumoural collateral vessels has not been performed to date. Evaluating the relationship between peritumoural collateral vessels in ccRCC patients and reductions of SMM would be of clinical interest for prognostic implications. We hypothesised that ccRCC patients would have a decreased cross-sectional total abdominal muscle area (TAMA) and peritumoural collateral vessels as a metabolic systemic consequence of locally advanced disease. To address this question, we evaluated SMM in male ccRCC patients with and without peritumoural collateral vessels using a CT imaging-based approach.

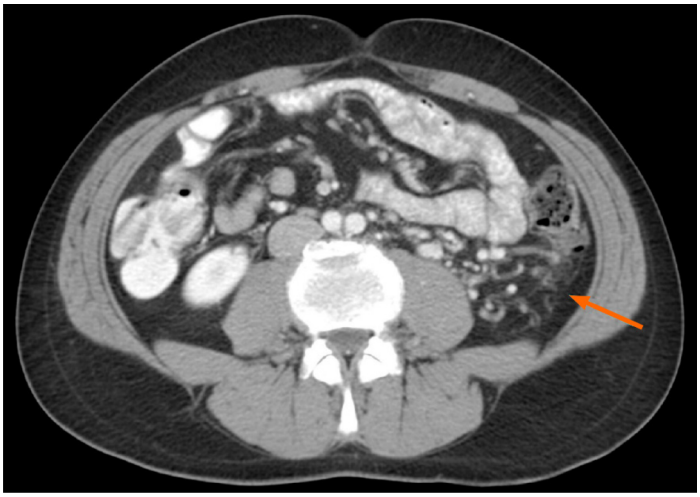

DOI: 10.4329/wjr.v14.i4.82

Figure 1 Axial computed tomography image shows the presence of clear cell renal cell carcinoma collateral vessels with the typical tortuous course located in the retroperitoneal space (arrow).

MATERIALS AND METHODS

This observational retrospective study was conducted in accordance with the Declaration of Helsinki. CT images and data from ccRCC patients with and without peritumoural collateral vessels were downloaded from the Cancer Imaging Archive (TCIA)[21-23]. This data collection received approval from our Institutional Review Board. The subsequent analysis contained publicly available and anonymised data which did not require further review due to previous protections implemented by TCIA. All enrolled subjects signed a written informed consent agreement.

A total of 267 patients with a histologically proven diagnosis of ccRCC were evaluated and selected by examining medical histories and CT images. The exclusion criteria for this study were: Female patients, patients with non-Caucasian ethnicity, patients who had undergone MRI examination only, patients who had undergone chest CT only, heminephrectomised and nephrectomised patients, patients with previous renal ablation, cirrhotic patients with collateral vessels, and patients with a congenital solitary kidney. The selected ccRCC patients were divided into two groups: Absence and presence of collateral vessels (ccRCCa and ccRCCp, respectively).

CT analysis

All ccRCC patients underwent CT examination. Horos v.4.0.0 RC2 software was used for acquisition of TAMA measurements with a semi-automatic function that allowed identification of SM tissue attenuation values (*i.e.*, range 10-40 Hounsfield units)[16]. TAMA (cm^2) was defined as the sum of the areas of the abdominal muscles visible on an axial image located 3 cm above the lower margin of L3 [16]. This area was measured by selecting a region of interest (ROI) on the following muscles: The rectus abdominis, transversus abdominis, external oblique, quadratus lumborum, iliocostalis lumborum, longissimus thoracis, spinalis thoracis, and psoas major[13]. All ROIs were independently drawn by two radiologists (F.G., 5 years of experience; C.A.M., 9 years of experience) who were blinded to the clinical data. The mean of the two measurements was utilised as the value for each subject.

Statistical analysis

Data distribution normality was assessed by the Shapiro-Wilk test. Comparison of TAMA between the ccRCCa and ccRCCp groups was performed using the Student's *t*-test. To rule out age-related effects, TAMA values were corrected by dividing individual values of TAMA by the age of each subject. Sub-analyses for TAMA assessment were performed by Student's *t*-tests between ccRCC patients with low (I/II) or high (III/IV) Fuhrman grade and between patients that were alive or deceased at the time of data collection. To evaluate the reliability of measurements by the two radiologists, the intraclass correlation coefficient for the TAMA measurements was calculated using Cronbach's alpha (also known as coefficient alpha). Finally, Kaplan-Meier curves were included to assess survival of the ccRCCa and ccRCCp groups. The threshold of statistical significance was established at $P < 0.05$.

RESULTS

A total of 124 male Caucasian ccRCC patients were selected according to the exclusion criteria. The two groups were composed as follows: ccRCCa (n = 54; mean age: 57, range: 26-83) and ccRCCp (n = 70; mean age: 59.8, range: 34-84). The staging of ccRCCa group patients were as follows: 1 T1N0M0, 8 T1aN0M0, 21 T1aNxM0, 6 T1bN0M0, 7 T1bNxM0, 1 T1bNxM1, 3 T2N0M0, 1 T2NxM0, 2 T3aN0M0, 2 T3aN0M1, 1 T3bN0M0, and 1 T3bNxM0. The staging of ccRCCp group patients were as follows: 10 T1aNxM0, 1 T1aNxM0, 1 T1aN1M0, 2 T1bN0M0, 8 T1bNxM0, 5 T2N0M0, 1 T2N0M1, 4 T2NxM0, 2 T2aNxM0, 1 T2bN0M0, 9 T3aN0M0, 1 T3aN0M1, 5 T3aNxM0, 1 T3aN0M1, 8 T3aNxM1, 1 T3aN1M1, 3 T3bN0M0, 4 T3bNxM0, 1 T3bNxM1, 1 T4NxM0, and 1 T4N1M1.

Only three (2.41%) of 124 patients had renal vein thrombosis and these three were included in the ccRCCp group (4.28% of ccRCCp patients). No patients had segmental renal vein thrombosis. All patients of the ccRCCp group (n = 70; 100%) showed an exophytic growth pattern. In addition, 31.42% of ccRCCp patients had T1 stage (n = 22), 18.57% T2 (n = 13), 47.14% T3 (n = 33), and 2.85% T4 (n = 2). A total of 28 patients had a history of previous malignancy and 11 patients received a neoadjuvant treatment.

No significant difference was detected in the ages of the two groups (P = 0.21). A statistically significant difference between the ccRCCa and ccRCCp groups was obtained for TAMA (P < 0.05). These results are summarised in Table 1 and represented in Figure 2. Examples of CT cases showing the observed effect are shown in Figure 3. Statistically significant differences between the ccRCCa and ccRCCp groups were confirmed after TAMA values were corrected for age (P < 0.05) (Table 1).

No statistically significant differences (P = 0.66) were found between ccRCC patients with low (n = 44; 1 grade I and 43 grade II) and high (n = 80; 61 grade III and 19 grade IV) Fuhrman grades. These results are summarised in Table 2. Patients who were deceased (n = 33) at the time of data collection demonstrated a statistically significant reduction (P < 0.001) of TAMA in comparison to those that were still alive (n = 90) (Table 3). Cronbach's alpha of the two tracers was 0.913, indicating excellent reliability. No significant differences in survival between the two groups (available data for 54 of 54 ccRCCa patients and 69 of 70 ccRCCp patients) were found based on the Kaplan-Meier method (log-rank test: Z = 1.88, P = 0.06) (Figure 4).

DISCUSSION

This study showed a significant decrease of SMM in the ccRCCp patient group compared to the ccRCCa group. Although SMM is expected to decrease with age, we did not find a significant difference between the ccRCCa and ccRCCp groups in terms of age. This finding was supported by analysis of age-corrected TAMA values. Since differences in SMM can segregate according to gender and ethnicity, only male Caucasian patients were included in the present study to eliminate these potentially confounding factors[24,25].

It has been hypothesised that contraction of myofibres can affect metabolism by triggering the release of humoral/exercise factors from SM which signal for an increase in glucose demand from distant organs[26]. The concept of humoral factors has been progressively developed since cytokine interleukin 6 (IL-6) was found to increase in response to physical exercise causing both autocrine and endocrine effects[27,28].

The cytokines and other peptides produced, expressed, and secreted by SM are called myokines. This term, suggested by Pederson *et al*[29], derives from the Greek words for "muscle" and "motion" and refers to such molecules that exert an endocrine effect on the human body. The physiological consequences of autocrine and paracrine action of myokines includes regulation of muscle growth and lipid metabolism. For example, the myokines produced during exercise, including IL-6, IL-7, IL-15, irisin, and leukaemia inhibitory factor, determine muscle growth by stimulating protein synthesis and hypertrophy. Conversely, myostatin, a member of the transforming growth factor β (TGF-β) superfamily, causes muscle atrophy[30,31]. Activin A, another member of TGF-β superfamily, reproduces the same action of myostatin on SM[30]. Increased blood levels of activin A is known to reduce muscle strength and has been positively correlated with cachexia in cancer patients[32].

Factors that can distort tumour extension such as peritumoural inflammation or the presence of a secondary pseudocapsule can reduce the effectiveness of CT in distinguishing T1 and T2 stages from T3a[19,33]. Incorrect staging, in fact, was detected in 27 of 94 tumours in a study of RCC patients using cross-sectional imaging[19]. Peritumoural collateral vessels in RCC patients showed a specificity of 94% and positive predictive value of 88% in staging of locally advance disease by cross-sectional CT imaging [19].

In our study, 100% of the patients from the ccRCCp group exhibited an exophytic growth pattern. This novel finding suggests a link between peritumour collateral vessels and the RCC growth pattern. Body composition imaging has gained an important role in the assessment of oncological risk, pathogenesis, and development of RCC[14-17]. CT imaging features of the tumour can also provide indications about the patient's body composition. In the present study, the peritumoural collateral

Table 1 Total abdominal muscle area and total abdominal muscle area corrected for age in the two groups

	TAMA (cm²)	TAMA_C (cm²)
ccRCCa group (mean, range, and SD)	164.02 (91, 233.5 ± 31.86)	3.08 (1.29, 5.83 ± 1.06)
ccRCCp group (mean, range, and standard deviation)	150.91 (76.3, 218.3 ± 30.34)	2.67 (1, 4.67 ± 0.91)
P	0.02	0.02

TAMA: Total abdominal muscle area; TAMA_C: Total abdominal muscle area corrected for age; ccRCC: Clear cell renal cell carcinoma.

Table 2 Total abdominal muscle area of clear cell renal cell carcinoma patients with low Fuhrman grade (I/II) and high Fuhrman grade (III/IV)

	TAMA (cm²)
ccRCC patients with low fuhrman grade (I/II) (mean, range, and standard deviation)	158.27 (83.2-233.5), 35.41
ccRCC patients with high Fuhrman grade (III/IV) (mean, range, and standard deviation)	155.71 (76.3-219.2), 29.44
P	0.66

TAMA: Total abdominal muscle area; ccRCC: Clear cell renal cell carcinoma.

Table 3 Total abdominal muscle area of alive and dead clear cell renal cell carcinoma patients

	TAMA (cm²)
Alive ccRCC patients	162.02
(mean, range, and standard deviation)	91, 233.5 ± 28.42
Dead ccRCC patients	150.91
(mean, range, and standard deviation)	76.3, 219.2 ± 34.84
P	0.0008

TAMA: Total abdominal muscle area; ccRCC: Clear cell renal cell carcinoma.

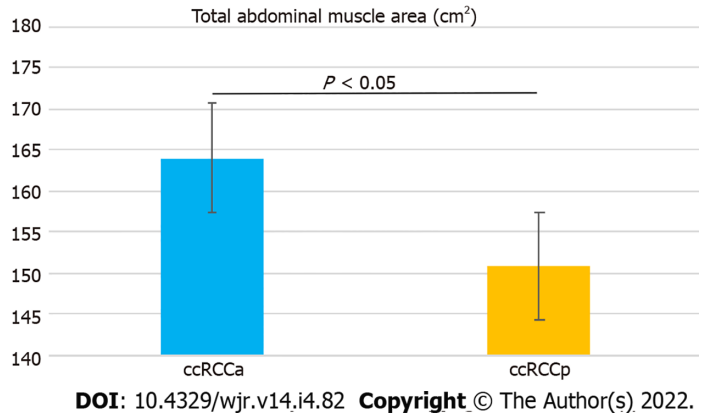

DOI: 10.4329/wjr.v14.i4.82

Figure 2 Bar chart with error bars showing a significant difference in mean values of total abdominal muscle area between the two groups. ccRCC: Clear cell renal cell carcinoma.

vessels adjacent to the ccRCC was associated with a reduction of SMM, a possible sign of sarcopenia. Most likely, in ccRCCp patients, locally advanced disease determines muscle trophism loss as compared to ccRCCa patients. The progressive SMM reduction assessed by CT could be considered a sign of sarcopenia, and therefore of cancer cachexia, with potential prognostic implication for patients. Indeed, deceased ccRCC patients demonstrated a statistically significant reduction of TAMA relative to live

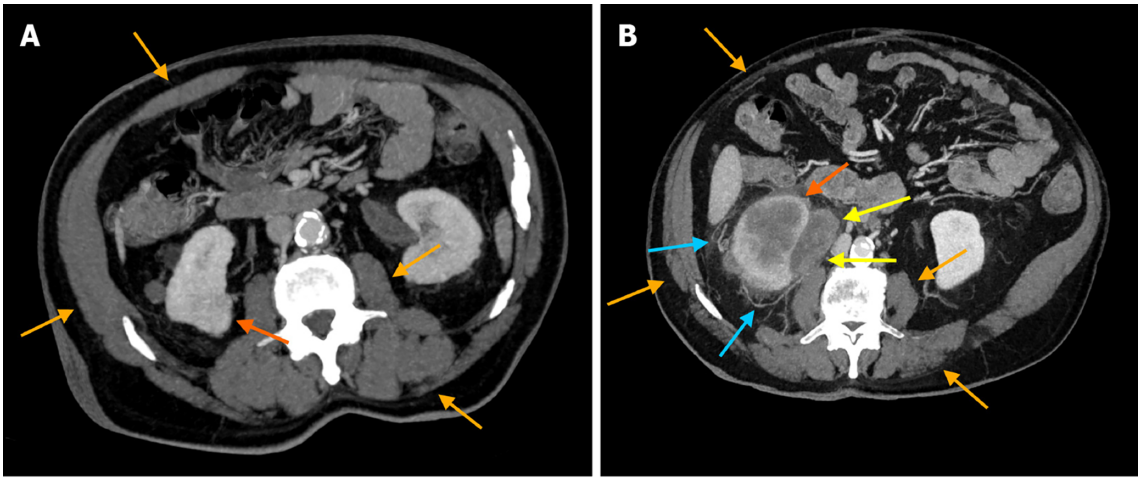

DOI: 10.4329/wjr.v14.i4.82 **Copyright** © The Author(s) 2022.

Figure 3 Axial computed tomography images with maximum intensity projection reconstruction of an 84-year-old male clear cell renal cell carcinoma patient without collateral vessels and an 82-year-old male clear cell renal cell carcinoma patient with collateral vessels. These images show skeletal muscle masses (SMMs) and tumors in a clear cell renal cell carcinoma patient without collateral vessels (ccRCCa) (A) and a clear cell renal cell carcinoma patient with collateral vessels (ccRCCp) (B) (orange and dark orange arrows in A and B, respectively), as well as collateral vessels adjacent to the tumor in the ccRCCp patient (light blue arrows in B) and nodal metastasis infiltrating the ureter (yellow arrows in B). Please note the decrease of SMM clearly evident in the ccRCCp patient (B) compared to the ccRCCa patient (A).

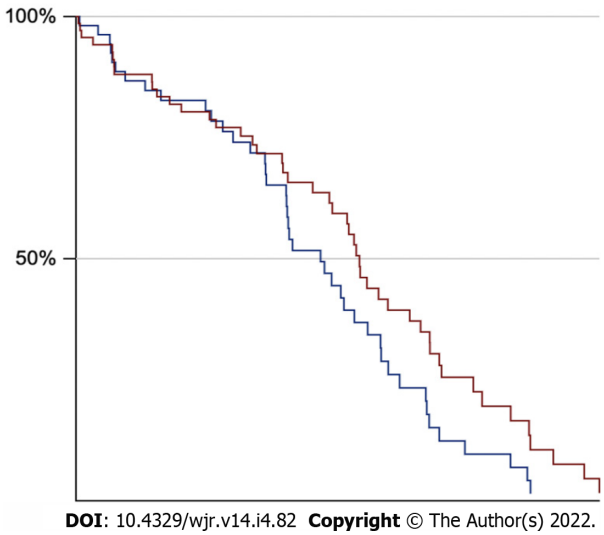

DOI: 10.4329/wjr.v14.i4.82 **Copyright** © The Author(s) 2022.

Figure 4 Kaplan-Meier curves showing no statistically significant difference of survival between the two groups (ccRCCa group is depicted as blue curve and ccRCCb group is depicted as red curve).

patients, suggesting a link between sarcopenia and survival in our sample. However, Kaplan-Maier curves showed a difference just above the statistical threshold between the ccRCCa and ccRCCp patient groups.

The results of this study are supported by recent evidence showing a significant reduction of subcutaneous adipose tissue in ccRCC patients with peritumoural collateral vessels[17]. The limitations of this study include the retrospective study design which did not allow us to assess detailed clinical and anamnestic data including occupation, BMI, hormone blood levels, disease-free survival, timing of CT imaging, performing status, therapies, and CT follow-up after treatment. For instance, testosterone deficiency is known to be associated with an increase in proinflammatory cytokines. Inclusion of hormonal data, such as testosterone levels, could help better understand the cytokine cascade that is associated with pathogenesis and changes in body composition[34,35]. Similarly, CT follow-up after treatment (*e.g.*, surgery or chemotherapy/targeted immunotherapy) would have been helpful to understand changes in the sarcopenia index and the relationship with peritumoural collateral vessels after treatment. The vendor, model, and acquisition parameters (such as slice thickness) of the CT imaging used in this study were also unavailable. Images from the open-source TCIA were often acquired heterogeneously at multiple centres as part of clinical routine. A larger sample size would have

strengthened our multivariate assessment of whether collateral vessels are an independent predictor of sarcopenia as well as the potential impact of other variables such as staging[36-38].

Further studies are needed to evaluate sarcopenia index changes after treatment to add robustness to the role of peritumoural collateral vessels as a prognostic biomarker for ccRCC patients. Such studies should consider abdominal circumference and patients' occupation, which is a factor that can influence SMM (for example, people who are engaged in heavy physical labour would be expected to have significantly more muscle mass compared to office workers)[39]. Finally, SMM content of other subtypes of kidney cancer (*e.g.*, chromophobe and papillary) or other categories of cancer patients should be evaluated to assess the impact of SMM trophism on a patient's health status and prognosis.

CONCLUSION

This study showed a reduction of SMM in ccRCC patients with peritumoural collateral vessels. The presence of peritumoural collateral vessels adjacent to ccRCC is a good candidate biomarker for sarcopenia and therefore of cancer cachexia.

ARTICLE HIGHLIGHTS

Research background

Sarcopenia is the loss of skeletal muscle mass (SMM) and is part of cancer cachexia in which there is a decrease of adipose tissue and SM. Peritumoral collateral vessels adjacent to renal cell carcinoma (RCC) are indicative of locally advanced disease.

Research motivation

Metabolic systemic consequence related to a locally advanced disease might be linked to a decrease of SSM in clear cell RCC (ccRCC) patients with peritumoral collateral vessels, possibly providing clinically relevant information.

Research objectives

The aim of this study was to evaluate the amount of SMM in male ccRCC patients with and without peritumoral collateral vessels, in order to understand a possible relationship between sarcopenia and collateral vessels.

Research methods

In this study, we included a total of 124 male Caucasian patients divided into two groups: ccRCCa (n = 54) and ccRCCp (n = 70) groups, respectively, without and with collateral vessels. Computed tomography imaging-based approach was used for total abdominal muscle area (TAMA) measurements.

Research results

There was a statistically significant difference between the two groups for TAMA ($P < 0.05$).

Research conclusions

This study showed a reduction of TAMA in male ccRCC patients with peritumoral collateral vessels.

Research perspectives

Further studies, on larger sample size and with longitudinal data, will shed light on collateral vessels adjacent to RCC as a possible biomarker of cachexia and sarcopenia.

FOOTNOTES

Author contributions: Greco F and Mallio CA contributed equally to this work; Greco F and Mallio CA designed the research; Greco F and Mallio CA performed the research; Greco F and Mallio CA analyzed the data; Greco F, Beomonte Zobel B, and Mallio CA validated the research; Greco F and Mallio CA wrote the paper; Greco F, Beomonte Zobel B, and Mallio CA supervised the research.

Institutional review board statement: All the procedures were retrospective and agreed with the Declaration of Helsinki. CT images and data of ccRCC patients were retrieved from The Cancer Imaging Archive (TCIA). The TCIA project received approval of the Institutional Review Board. This subsequent retrospective analysis was on the publicly available, anonymized data and did not require further review due to previous protections implemented by

TCIA.

Conflict-of-interest statement: The authors declare that they have no conflict of interest to disclose.

Data sharing statement: The data presented in this study are openly available in The Cancer Imaging Archive (https://wiki.cancerimagingarchive.net/display/Public/TCGA-KIRC, accessed on 1 November 2019).

STROBE statement: The authors have read the STROBE Statement—checklist of items, and the manuscript was prepared and revised according to the STROBE Statement—checklist of items.

Country/Territory of origin: Italy

ORCID number: Federico Greco 0000-0002-9477-0238; Bruno Beomonte Zobel 0000-0001-9227-5535; Carlo Augusto Mallio 0000-0002-0149-0801.

S-Editor: Ma YJ
L-Editor: Wang TQ
P-Editor: Ma YJ

REFERENCES

1 **Tisdale MJ**. Mechanisms of cancer cachexia. *Physiol Rev* 2009; **89**: 381-410 [PMID: 19342610 DOI: 10.1152/physrev.00016.2008]
2 **Daas SI**, Rizeq BR, Nasrallah GK. Adipose tissue dysfunction in cancer cachexia. *J Cell Physiol* 2018; **234**: 13-22 [PMID: 30078199 DOI: 10.1002/jcp.26811]
3 **Murphy RA**, Wilke MS, Perrine M, Pawlowicz M, Mourtzakis M, Lieffers JR, Maneshgar M, Bruera E, Clandinin MT, Baracos VE, Mazurak VC. Loss of adipose tissue and plasma phospholipids: relationship to survival in advanced cancer patients. *Clin Nutr* 2010; **29**: 482-487 [PMID: 19959263 DOI: 10.1016/j.clnu.2009.11.006]
4 **Semeniuk-Wojtaś A**, Lubas A, Stec R, Syryło T, Niemczyk S, Szczylik C. Neutrophil-to-lymphocyte Ratio, Platelet-to-lymphocyte Ratio, and C-reactive Protein as New and Simple Prognostic Factors in Patients With Metastatic Renal Cell Cancer Treated With Tyrosine Kinase Inhibitors: A Systemic Review and Meta-analysis. *Clin Genitourin Cancer* 2018; **16**: e685-e693 [PMID: 29454639 DOI: 10.1016/j.clgc.2018.01.010]
5 **Blum D**, Stene GB, Solheim TS, Fayers P, Hjermstad MJ, Baracos VE, Fearon K, Strasser F, Kaasa S; Euro-Impact. Validation of the Consensus-Definition for Cancer Cachexia and evaluation of a classification model--a study based on data from an international multicentre project (EPCRC-CSA). *Ann Oncol* 2014; **25**: 1635-1642 [PMID: 24562443 DOI: 10.1093/annonc/mdu086]
6 **Martin L**, Birdsell L, Macdonald N, Reiman T, Clandinin MT, McCargar LJ, Murphy R, Ghosh S, Sawyer MB, Baracos VE. Cancer cachexia in the age of obesity: skeletal muscle depletion is a powerful prognostic factor, independent of body mass index. *J Clin Oncol* 2013; **31**: 1539-1547 [PMID: 23530101 DOI: 10.1200/JCO.2012.45.2722]
7 **Psutka SP**, Boorjian SA, Moynagh MR, Schmit GD, Costello BA, Thompson RH, Stewart-Merrill SB, Lohse CM, Cheville JC, Leibovich BC, Tollefson MK. Decreased Skeletal Muscle Mass is Associated with an Increased Risk of Mortality after Radical Nephrectomy for Localized Renal Cell Cancer. *J Urol* 2016; **195**: 270-276 [PMID: 26292038 DOI: 10.1016/j.juro.2015.08.072]
8 **Sharma P**, Zargar-Shoshtari K, Caracciolo JT, Fishman M, Poch MA, Pow-Sang J, Sexton WJ, Spiess PE. Sarcopenia as a predictor of overall survival after cytoreductive nephrectomy for metastatic renal cell carcinoma. *Urol Oncol* 2015; **33**: 339.e17-339.e23 [PMID: 26094169 DOI: 10.1016/j.urolonc.2015.01.011]
9 **Fukushima H**, Nakanishi Y, Kataoka M, Tobisu K, Koga F. Prognostic Significance of Sarcopenia in Patients with Metastatic Renal Cell Carcinoma. *J Urol* 2016; **195**: 26-32 [PMID: 26292042 DOI: 10.1016/j.juro.2015.08.071]
10 **Hu X**, Liao DW, Yang ZQ, Yang WX, Xiong SC, Li X. Sarcopenia predicts prognosis of patients with renal cell carcinoma: A systematic review and meta-analysis. *Int Braz J Urol* 2020; **46**: 705-715 [PMID: 32213202 DOI: 10.1590/S1677-5538.IBJU.2019.0636]
11 **Pedersen BK**. Muscle as a secretory organ. *Compr Physiol* 2013; **3**: 1337-1362 [PMID: 23897689 DOI: 10.1002/cphy.c120033]
12 **Pedersen L**, Hojman P. Muscle-to-organ cross talk mediated by myokines. *Adipocyte* 2012; **1**: 164-167 [PMID: 23700527 DOI: 10.4161/adip.20344]
13 **Prado CM**, Heymsfield SB. Lean tissue imaging: a new era for nutritional assessment and intervention. *JPEN J Parenter Enteral Nutr* 2014; **38**: 940-953 [PMID: 25239112 DOI: 10.1177/0148607114550189]
14 **Greco F**, Mallio CA, Grippo R, Messina L, Vallese S, Rabitti C, Quarta LG, Grasso RF, Beomonte Zobel B. Increased visceral adipose tissue in male patients with non-clear cell renal cell carcinoma. *Radiol Med* 2020; **125**: 538-543 [PMID: 32067162 DOI: 10.1007/s11547-020-01146-6]

15 **Greco F**, Quarta LG, Grasso RF, Beomonte Zobel B, Mallio CA. Increased visceral adipose tissue in clear cell renal cell carcinoma with and without peritumoral collateral vessels. *Br J Radiol* 2020; **93**: 20200334 [PMID: 32516557 DOI: 10.1259/bjr.20200334]

16 **Greco F**, Mallio CA. Relationship between visceral adipose tissue and genetic mutations (VHL and KDM5C) in clear cell renal cell carcinoma. *Radiol Med* 2021; **126**: 645-651 [PMID: 33400184 DOI: 10.1007/s11547-020-01310-y]

17 **Greco F**, Quarta LG, Carnevale A, Giganti M, Grasso RF, Beomonte Zobel B, Mallio CA. Subcutaneous Adipose Tissue Reduction in Patients with Clear Cell Renal Cell Carcinoma and Peritumoral Collateral Vessels: A Retrospective Observational Study. *Appl Sci* 2021; **11**: 6076

18 **Greco F**, Faiella E, Santucci D, Mallio CA, Nezzo M, Quattrocchi CC, Beomonte Zobel B, Grasso RF. Imaging of Renal Medullary Carcinoma. J Kidney Cancer VHL. 2017 4:1-7 [PMID: 28405543 DOI: 10.15586/jkcvhl.2017.62]

19 **Murphy BL**, Gaa J, Papanicolaou N, Lee MJ. Gonadal vein recruitment in renal cell carcinoma: incidence, pathogenesis and clinical significance. *Clin Radiol* 1996; **51**: 797-800 [PMID: 8937323 DOI: 10.1016/s0009-9260(96)80008-0]

20 **Bradley AJ**, MacDonald L, Whiteside S, Johnson RJ, Ramani VA. Accuracy of preoperative CT T staging of renal cell carcinoma: which features predict advanced stage? *Clin Radiol* 2015; **70**: 822-829 [PMID: 25953656 DOI: 10.1016/j.crad.2015.03.013]

21 **NIH National Cancer Institute**. Available from: https://cancergenome.nih.gov/

22 **Akin O**, Elnajjar P, Heller M, Jarosz R, Erickson B, Kirk S, Lineham M, Gautam R, Vikram R, Garcia KM, Roche C, Bonaccio E, Filippini J. Radiology Data from The Cancer Genome Atlas Kidney Renal Clear Cell Carcinoma [TCGA-KIRC] collection. The Cancer Imaging Archive 2016

23 **Clark K**, Vendt B, Smith K, Freymann J, Kirby J, Koppel P, Moore S, Phillips S, Maffitt D, Pringle M, Tarbox L, Prior F. The Cancer Imaging Archive (TCIA): maintaining and operating a public information repository. *J Digit Imaging* 2013; **26**: 1045-1057 [PMID: 23884657 DOI: 10.1007/s10278-013-9622-7]

24 **Janssen I**, Heymsfield SB, Wang ZM, Ross R. Skeletal muscle mass and distribution in 468 men and women aged 18-88 yr. *J Appl Physiol (1985)* 2000; **89**: 81-88 [PMID: 10904038 DOI: 10.1152/jappl.2000.89.1.81]

25 **Silva AM**, Shen W, Heo M, Gallagher D, Wang Z, Sardinha LB, Heymsfield SB. Ethnicity-related skeletal muscle differences across the lifespan. *Am J Hum Biol* 2010; **22**: 76-82 [PMID: 19533617 DOI: 10.1002/ajhb.20956]

26 **Goldstein MS**. Humoral nature of the hypoglycemic factor of muscular work. *Diabetes* 1961; **10**: 232-234 [PMID: 13706674 DOI: 10.2337/diab.10.3.232]

27 **Ostrowski K**, Rohde T, Zacho M, Asp S, Pedersen BK. Evidence that interleukin-6 is produced in human skeletal muscle during prolonged running. *J Physiol* 1998; **508** (Pt 3): 949-953 [PMID: 9518745 DOI: 10.1111/j.1469-7793.1998.949bp.x]

28 **Steensberg A**, van Hall G, Osada T, Sacchetti M, Saltin B, Klarlund Pedersen B. Production of interleukin-6 in contracting human skeletal muscles can account for the exercise-induced increase in plasma interleukin-6. *J Physiol* 2000; **529**: 237-242 [PMID: 11080265 DOI: 10.1111/j.1469-7793.2000.00237.x]

29 **Pedersen BK**, Steensberg A, Fischer C, Keller C, Keller P, Plomgaard P, Febbraio M, Saltin B. Searching for the exercise factor: is IL-6 a candidate? *J Muscle Res Cell Motil* 2003; **24**: 113-119 [PMID: 14609022 DOI: 10.1023/a:1026070911202]

30 **Deshmukh AS**, Cox J, Jensen LJ, Meissner F, Mann M. Secretome Analysis of Lipid-Induced Insulin Resistance in Skeletal Muscle Cells by a Combined Experimental and Bioinformatics Workflow. *J Proteome Res* 2015; **14**: 4885-4895 [PMID: 26457550 DOI: 10.1021/acs.jproteome.5b00720]

31 **Grube L**, Dellen R, Kruse F, Schwender H, Stühler K, Poschmann G. Mining the Secretome of C2C12 Muscle Cells: Data Dependent Experimental Approach To Analyze Protein Secretion Using Label-Free Quantification and Peptide Based Analysis. *J Proteome Res* 2018; **17**: 879-890 [PMID: 29322779 DOI: 10.1021/acs.jproteome.7b00684]

32 **Loumaye A**, de Barsy M, Nachit M, Lause P, Frateur L, van Maanen A, Trefois P, Gruson D, Thissen JP. Role of Activin A and myostatin in human cancer cachexia. *J Clin Endocrinol Metab* 2015; **100**: 2030-2038 [PMID: 25751105 DOI: 10.1210/jc.2014-4318]

33 **Frank I**, Blute ML, Cheville JC, Lohse CM, Weaver AL, Zincke H. An outcome prediction model for patients with clear cell renal cell carcinoma treated with radical nephrectomy based on tumor stage, size, grade and necrosis: the SSIGN score. *J Urol* 2002; **168**: 2395-2400 [PMID: 12441925 DOI: 10.1097/01.ju.0000035885.91935.d5]

34 **Ficarra V**, Galfano A, Mancini M, Martignoni G, Artibani W. TNM staging system for renal-cell carcinoma: current status and future perspectives. *Lancet Oncol* 2007; **8**: 554-558 [PMID: 17540307 DOI: 10.1016/S1470-2045(07)70173-0]

35 **Mohamad NV**, Wong SK, Wan Hasan WN, Jolly JJ, Nur-Farhana MF, Ima-Nirwana S, Chin KY. The relationship between circulating testosterone and inflammatory cytokines in men. *Aging Male* 2019; **22**: 129-140 [PMID: 29925283 DOI: 10.1080/13685538.2018.1482487]

36 **Gu W**, Wu J, Liu X, Zhang H, Shi G, Zhu Y, Ye D. Early skeletal muscle loss during target therapy is a prognostic biomarker in metastatic renal cell carcinoma patients. *Sci Rep* 2017; **7**: 7587 [PMID: 28790354 DOI: 10.1038/s41598-017-07955-6]

37 **Choi Y**, Oh DY, Kim TY, Lee KH, Han SW, Im SA, Bang YJ. Skeletal Muscle Depletion Predicts the Prognosis of Patients with Advanced Pancreatic Cancer Undergoing Palliative Chemotherapy, Independent of Body Mass Index. *PLoS One* 2015; **10**: e0139749 [PMID: 26437072 DOI: 10.1371/journal.pone.0139749]

38 **Sato H**, Goto T, Hayashi A, Kawabata H, Okada T, Takauji S, Sasajima J, Enomoto K, Fujiya M, Oyama K, Ono Y, Sugitani A, Mizukami Y, Okumura T. Prognostic significance of skeletal muscle decrease in unresectable pancreatic cancer: Survival analysis using the Weibull exponential distribution model. *Pancreatology* 2021; **21**: 892-902 [PMID: 33722506 DOI: 10.1016/j.pan.2021.03.002]

39 **Fang H**, Berg E, Cheng X, Shen W. How to best assess abdominal obesity. *Curr Opin Clin Nutr Metab Care* 2018; **21**: 360-365 [PMID: 29916924 DOI: 10.1097/MCO.0000000000000485]

World Journal of Radiology

Submit a Manuscript: https://www.f6publishing.com

World J Radiol 2022 April 28; 14(4): 91-103

DOI: 10.4329/wjr.v14.i4.91

ISSN 1949-8470 (online)

ORIGINAL ARTICLE

Retrospective Study

Outcome of percutaneous drainage for septic complications coexisted with COVID-19

Mohamed A Deif, Ahmad M Mounir, Sherif A Abo-Hedibah, Ahmed M Abdel Khalek, Ali H Elmokadem

Specialty type: Radiology, nuclear medicine and medical imaging

Provenance and peer review: Invited article; Externally peer reviewed.

Peer-review model: Single blind

Peer-review report's scientific quality classification

Grade A (Excellent): 0
Grade B (Very good): B, B
Grade C (Good): 0
Grade D (Fair): 0
Grade E (Poor): 0

P-Reviewer: Wang CY, Taiwan; Wang D, Thailand

Received: December 29, 2021
Peer-review started: December 29, 2021
First decision: February 21, 2022
Revised: March 13, 2022
Accepted: April 9, 2022
Article in press: April 9, 2022
Published online: April 28, 2022

Mohamed A Deif, Department of Radiology, National Liver Institute, Menoufia University, Shibin Al Kawm 32521, Egypt

Ahmad M Mounir, Ahmed M Abdel Khalek, Ali H Elmokadem, Department of Radiology, Mansoura University, Mansoura 35516, Egypt

Sherif A Abo-Hedibah, Department of Radiology, Cairo university, Cairo 12613, Egypt

Corresponding author: Ali H Elmokadem, MD, PhD, Associate Professor, Department of Radiology, Mansoura University, Elgomhoria St, Mansoura 35516, Egypt.
mokadem83@yahoo.com

Abstract

BACKGROUND

The resulting tissue hypoxia and increased inflammation secondary to severe coronavirus disease 2019 (COVID-19) combined with viral load, and other baseline risk factors contribute to an increased risk of severe sepsis or co-existed septic condition exaggeration.

AIM

To describe the clinical, radiological, and laboratory characteristics of a small cohort of patients infected by severe acute respiratory syndrome coronavirus 2 who underwent percutaneous drainage for septic complications and their post-procedural outcomes.

METHODS

This retrospective study consisted of 11 patients who were confirmed to have COVID-19 by RT-PCR test and required drain placement for septic complications. The mean age ± SD of the patients was 48.5 ± 14 years (range 30-72 years). Three patients underwent cholecystostomy for acute acalculous cholecystitis. Percutaneous drainage was performed in seven patients; two peripancreatic collections; two infected leaks after hepatic resection; one recurrent hepatic abscess, one psoas abscess and one lumbar abscess. One patient underwent a percutaneous nephrostomy for acute pyelonephritis.

RESULTS

Technical success was achieved in 100% of patients, while clinical success was achieved in 4 out of 11 patients (36.3%). Six patients (54.5%) died despite proper

percutaneous drainage and adequate antibiotic coverage. One patient (9%) needed operative intervention. Two patients (18.2%) had two drainage procedures to drain multiple fluid collections. Two patients (18.2%) had repeat drainage procedures due to recurrent fluid collections. The average volume of the drained fluid immediately after tube insertion was 85 mL. Follow-up scans show a reduction of the retained content and associated inflammatory changes after tube insertion in all patients. There was no significant statistical difference (P = 0.6 and 0.4) between the mean of WBCs and neutrophils count before drainage and seven days after drainage. The lymphocyte count shows significant increased seven days after drainage (P = 0.03).

CONCLUSION

In this study, patients having septic complications associated with COVID-19 showed relatively poor clinical outcomes despite technically successful percutaneous drainage.

Key Words: COVID-19; SARS-CoV-2; Coronavirus; Sepsis; Drainage; Abscess

Core Tip: This article highlights the relationship between coronavirus disease 2019 (COVID-19) and sepsis. COVID-19 is associated with high risk of severe sepsis or exaggeration of co-existed septic condition. Percutaneous drainage of septic complications co-existed with COVID-19 associated with relatively poor clinical outcomes despite technically successful procedures.

Citation: Deif MA, Mounir AM, Abo-Hedibah SA, Abdel Khalek AM, Elmokadem AH. Outcome of percutaneous drainage for septic complications coexisted with COVID-19. *World J Radiol* 2022; 14(4): 91-103
URL: https://www.wjgnet.com/1949-8470/full/v14/i4/91.htm
DOI: https://dx.doi.org/10.4329/wjr.v14.i4.91

INTRODUCTION

Sepsis is defined as a life-threatening organ dysfunction that happens due to dysregulated host response to an infection[1]. In the bacterial type of sepsis, which is the most frequent etiology, early and rapid therapy by the appropriate antibiotic is essential to reduce the incidence of complications and mortality rates. Most patients infected by severe acute respiratory syndrome coronavirus 2 (SARS-CoV-2) present no severe symptomatology, but almost 5% of patients show severe lung injury or even multiple organ dysfunction syndrome, with mortality at the ICUs between 8% and 38% depending on the country[2,3]. Patients admitted to ICU showed a dysregulated host response in the form of hyperinflammation, changes in the coagulation profile, and dysregulation in the immune response[4], similar to what happens in bacterial sepsis[5,6]. The body's adaptive protection mechanism is formed by a moderate inflammatory response and immune suppression, and if any of them become excessive or uncontrolled, this protective compensation will transform into destructive and decompensated status, then sepsis develops[7-9]. Accordingly, most deaths in critically ill coronavirus disease 2019 (COVID-19) patients are caused by sepsis[10,11].

Hematological examinations for COVID-19 patients show elevated cytokines, C-reactive protein (CRP), abnormal liver and myocardial enzymes decreased lymphocytes, declined platelets, and increased D-dimmer[12]. These findings are similar to sepsis caused by bacterial infections. So, severe COVID-19 could be a sepsis-induced by viral infection causing severe systemic inflammatory response (so-called inflammatory storm)[13,14]. Inflammatory storms are not unique to COVID-19 but also happen in other respiratory viral infections that mimic COVID-19[15,16], such as influenza, SARS, avian influenza, swine flu, and MERS[17-19]. Additionally, specimen cultures in about 80% of COVID-19 patients with septic complications show no bacterial or fungal infection, and the viral infection seems to be the only cause for sepsis[20,21]. Accordingly, sepsis is expected to be responsible for worsening the clinical conditions of these critically ill COVID-19 patients. Our objective was to describe the clinical, radiological, and laboratory characteristics of a small cohort of patients infected by SARS-CoV-2 who underwent percutaneous drainage and their post-procedural outcomes. We hypothesized that septic complication associated with severe COVID-19 has a poor outcome despite adequate percutaneous drainage and antibiotic therapy.

MATERIALS AND METHODS

Patient selection

A local institutional review board approved this retrospective study, and waivers of consent of medical record review were received. COVID-19 patients who underwent image-guided percutaneous drainage for suspected septic complications were identified. Patient demographics and clinical and radiological reports were obtained through electronic medical records and picture archiving and communication system (PACS). The severity of the pulmonary parenchymal involvement and distribution of the pulmonary lesions secondary to COVID-19 was assessed by chest X-ray in 4 patients and chest CT in 7 patients. Flow chart of the study is shown in Figure 1.

Patients demographics

Eleven patients (10 males and 1 female) who were confirmed to have COVID-19 by RT-PCR test required drain placement for septic complications. The mean age ± SD of the patients was 48.5 ± 14 years (range 30-72 years). Three patients underwent cholecystostomy for acute acalculous cholecystitis (Figure 2). Percutaneous drainage was performed in seven patients; two peripancreatic collections (Figure 3); two infected bile leaks in hepatic donor and after resection of hepatic hemangioma; one recurrent hepatic abscess after eight days of surgical evacuation (Figure 4), one psoas abscess (Figure 5) and one lumbar abscess. One patient underwent percutaneous nephrostomy for acute pyelonephritis (Figure 6).

Study outcomes

The primary outcome measures were technical and clinical success. The technical success was achieved by completion of the procedure without procedural complications, while the definition of clinical success was the resolution of symptoms without the subsequent need for operative drainage or patient mortality secondary to related sepsis. Secondary outcomes included the amount of drained fluid, microbial analysis of drained fluid, the period of tube drainage, and changes in laboratory findings before and after drainage.

Percutaneous drainage procedures

Septic complications were diagnosed by ultrasonography, computed tomography, or magnetic resonance imaging. Two interventional radiologists at two institutions with 10 and 13 years of experience performed all percutaneous drainage procedures. All procedures were done after administration of local anesthesia. Percutaneous access into the collections, inflamed gall bladder, or kidney was achieved under sonographic guidance with an 18- or 21-gauge needle. Using the Seldinger technique and micro-puncture set, following serial dilatations, a drainage catheter was placed. The drainage catheters used ranged from 8-French to 10-French. In all cases, no immediate complications were noted.

Antibiotic therapy was started once the symptoms of septic complications presented on the patients. The antibiotics regimen was readjusted according to the drained fluid culture results. The drained fluid for each patient was analyzed regarding its character and maximum possible volume when the tubes were initially placed. Then a fluid sample was sent for bacterial culture and gram stain evaluation. Patients were observed for any major complications requiring surgical intervention till the last date of follow-up.

Statistical analysis

Data were analyzed with SPSS® V. 21 (IBM Corp., New York, NY, United States; formerly SPSS Inc., Chicago, IL, United States). The normality of data was first tested with the Shapiro test. Qualitative data were described using numbers and percentages. Continuous variables were presented as mean ± SD for parametric data and median (range) for non-parametric data. Finally, the laboratory findings were compared with Wilcoxon test.

RESULTS

Fever and abdominal pain were the most common presenting symptoms, and acute kidney injury (AKI) was the most frequent comorbidity. Technical success was achieved in 100% of patients, while clinical success was achieved only in 4 of 11 patients (36.4%). Despite percutaneous drainage, one patient (9%) needed exploratory laparotomy five days after drainage that revealed perforated sigmoid colon, which was managed by resection followed by patient improvement and discharge after 18 d. Six other patients (54.5%) died within a month after proper percutaneous drainage and adequate antibiotic coverage, all of them were admitted to ICU and put under mechanical ventilation. The cause of death was overlapped between COVID-19 related respiratory failure and sepsis. One patient needed cystogasterostomy for peripancreatic collection after 21 d of tube insertion. Two patients (18.2%) had two drainage procedures to drain multiple fluid collections. Two patients (18.2%) had recurrent fluid collections and repeated

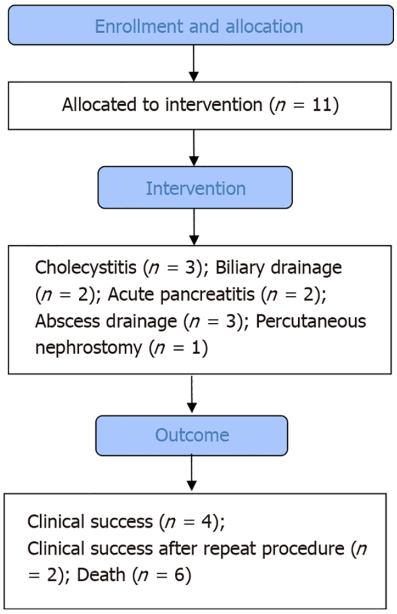

DOI: 10.4329/wjr.v14.i4.91

Figure 1 Flow chart of the study.

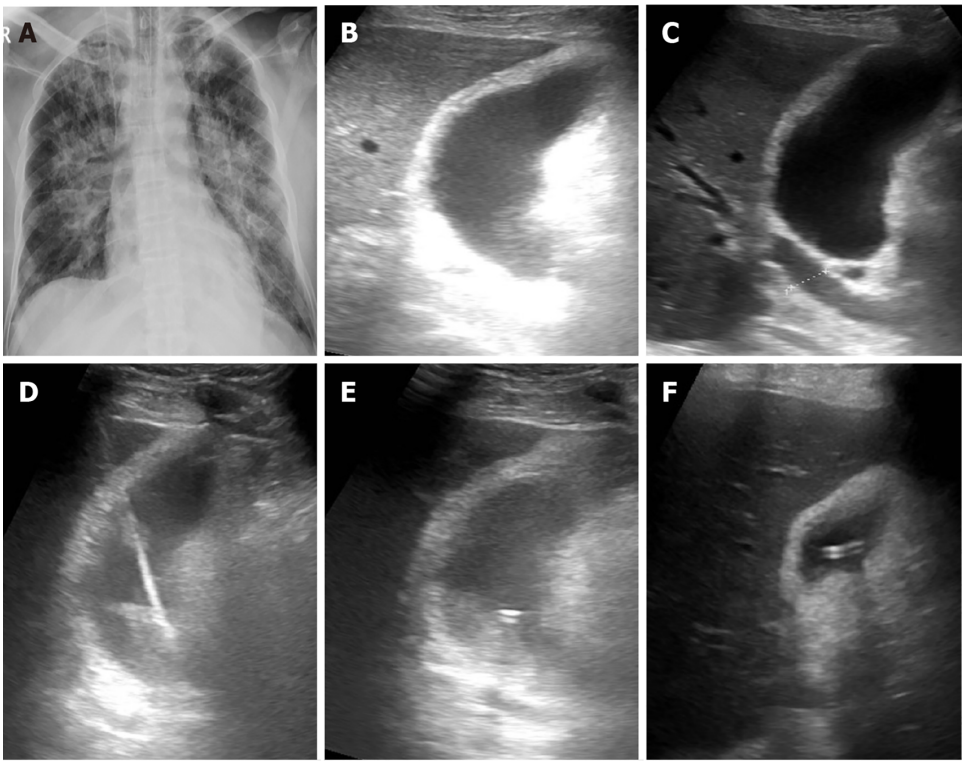

DOI: 10.4329/wjr.v14.i4.91

Figure 2 Cholecystostomy in a 72-yr-old male presented by acute cholecystitis. A: Frontal chest X-ray shows opacities involving both lungs with central predominance; B and C: B-mode ultrasound images show distended thick-walled gall bladder with biliary dilatation; D: B-mode ultrasound image show puncture needle through the gall bladder; E: B-mode ultrasound image tube inside the gall bladder; F: B-mode ultrasound image of the gall bladder after drainage.

percutaneous drainage procedures. The average volume of the drained fluid immediately after tube insertion was 85 mL. The average duration of drainage was 16 d. Follow-up scans showed a reduction of the retained content and associated inflammatory changes after tube insertion in all patients. Patient demographics, comorbidities, and outcomes are listed in Table 1.

The nature of drained fluid was reported in all cases. The fluid was reported as "dark green" or "pus" in cholecystostomy cases, "serosanguinous" and "infected bile" in complicated hepatic resection cases, "brownish" in the peripancreatic collection, "clotted blood" in the hepatic abscess, and "pus" in the

Table 1 Patients' demographics, comorbidities and outcome

	Cause of sepsis	Procedures	Age (yr)	Sex	Presentation	Co-morbidities	Ventilator	Tracheostomy	Outcome
Patient 1	Acute cholecystitis	Cholecystostomy	72	Male	Fever	IHD. AKI	40 d before drain	20 d before drain	Died 8 d post drain
Patient 2	Cholangitis and cholecystitis	Cholecystostomy	61	Male	Fever	Jaundice. AKI (on dialysis)	1 d before drain	12 d post drain	Died 16 d post drain
Patient 3	Acute cholecystitis	Cholecystostomy	55	Male	Abdominal pain	DM	No	No	Discharged 4 d post drain.
Patient 4	Post-operative biliary leakage resection of hemangioma	U/S guided drain	48	Female	Fever	DM. Septic shock	10 d post drain	No	Died 12 d post drain
Patient 5	Post-operative biliary leakage after liver resection for transplant	U/S guided drain	30	Male	Fever	No	No	No	Discharged 18 d post drain
Patient 6	Acute pancreatitis	CT-guided drain and EUS cystogast-rostomy	43	Male	Abdominal pain	HTN. Hyperlip-idemia	27 d post drain	No	Died 28 d post drain
Patient 7	Acute pancreatitis	U/S guided drain	41	Male	Abdominal pain	GB stones. Biliary obst. AKI	No	No	Discharged 10 d post drain
Patient 8	Recurrent hepatic abscess after surgical evacuation	U/S guided drain (2 tubes)	63	Male	Abdominal pain	DM. AKI	1 d before drain	1 d before drain	Died 19 d post drain
Patient 9	Right ilio-psoas and perivetebral abscesses	CT-guided drain then tube upsizing	60	Male	Abdominal pain	HTN. DM, AKI	3 d before drain	7 d post drain	Died 13 d post drain
Patient 10	Left lumbar region abscess and unhealthy sigmoid colon	CT-guided drainage. Sigmoid resection	31	Male	Abdominal pain and distension	Crohn's disease. Achalasia. GJ. Esophageal dilatation	No	No	Clinical failure after 18 d followed by another tube insertion and sigmoid resection. Discharged 48 d
Patient 11	Right pyelonephritis	Rt PCN	30	Male	Abdominal pain	Right hemicolectomy	No	No	Discharged 9 d post drain. Recurrence after 39 d and managed by tube exchange

U/S: Ultrasonography; EUS: Endoscopic ultrasound; PCN: Percutaneous nephrostomy; IHD: Ischemic heart disease; AKI: Acute kidney injury; DM: Diabetes mellitus; HTN: Hypertension; GB: Gall bladder; GJ: Gastrojejunostomy.

other collections. After all procedures, samples from drained fluid samples were sent for microbial analysis. Peripheral blood culture was performed for 9 out of 11 patients. In three cases (27.3%), fluid culture results were negative for bacterial growth; however, in one of them, the peripheral blood culture was positive for *Klebsiella* pneumonia. Eight cases (72.7%) were found to have positive fluid culture, with Escherichia coli being the most common isolated pathogen followed by *Klebsiella* pneumonia.

Only three patients had imaging features of severe pulmonary parenchymal disease attributed to COVID-19 at drainage tome, nevertheless three other patients were admitted to ICU and put under ventilator due to progression of respiratory symptoms. The parenchymal lesions were ground-glass opacities and consolidations with the basal and peripheral predominant distribution. In addition, pleural effusion was reported in three patients. The median time between confirmed diagnosis of COVID-19 by RT-PCR test and drainage of septic complications (time to drainage) was 8 d (range 0 d to 48 d). Table 2 shows data of drainage procedure, drained fluid, outcome, and chest imaging.

The mean WBCs and neutrophil counts show reduction 1 d and 7 d after drainage however there was no significant statistical difference (P = 0.6) between the mean of WBCs count before drainage (15.4 × 10^9/L) and seven days after drainage (12.1 × 10^9/L) and between the mean count of neutrophil (P = 0.4) before drainage (82.8 × 10^9/L) and seven days after drainage (70.9 × 10^9/L). The lymphocyte count

Table 2 Data of drainage procedure, drained fluid, and chest imaging

	IR procedure	Drain	Guide	Puncture	Drained fluid	Culture		Chest imaging	COVID-19 severity	Lesion distribution	Time between PCR test and drainage
						Drain	Peripheral blood				
Patient 1	Cholecystostomy	1 (8 Fr)	U/S	18G needle	Dark green	-ve	MDR (*Klebsiella*)	X-ray	Severe	Bilateral consolidation	48 d
Patient 2	Cholecystostomy	1 (8 Fr)	U/S	18G needle	Dark green	*E.coli* and *Klebsiella* pneumoniae	-ve	CT	Mild	Bilateral basal GGO with minimal effusion	3 d
Patient 3	Cholecystostomy	1 (8 Fr)	U/S	18G needle	Pus	*P. aeruginoa*. MRSA. *E.coli*	-ve	X-ray	Normal	Normal	5 d
Patient 4	Percutaneous drainage	1 (10 Fr)	U/S	18G needle	Infected bile	*E.coli*	-ve	CT	Sever	Bilateral consolidation with mild effusion	8 d
Patient 5	Percutaneous drainage	1 (8 Fr)	U/S	18G needle	Sero-sanginous	-ve	-ve	CT	Mild	Mild right pleural effusion	3 d
Patient 6	Percutaneous drainage	1 (10 Fr)	CT	21G needle	Brownish	*E.coli* and *Klebsiella* pneumoniae	-ve	CT	Mild	Left minimal effusion and basal GGO	17 d
Patient 7	Percutaneous drainage	1 (8 Fr)	CT	18G needle	Brownish	*E.coli*	-ve	CT	Mild	Bilateral basal GGO	2 d
Patient 8	Percutaneous drainage	2 (8 Fr)	U/S	18G needle	Clotted blood	-ve	-ve	X-ray	Normal	Mild right side pleural effusion	9 d
Patient 9	Percutaneous drainage	1 (10 Fr). 1 (8 Fr)	CT and US	21G needle	Pus	MRSA and staph aureus	-ve	CT	Severe	Bilateral GGO and consolidations	15 d
Patient 10	Percutaneous drainage	2 (8 Fr)	CT	21G needle	Pus	*E.coli* and *Ent. Foecalis*	NA	CT	Mild	Right side GGO	0 d
Patient 11	Right PCN	2 (8 Fr)	U/S and fluoro	21G needle	Pus	*Klebsiella* pneumoniae	-ve	X-ray	Normal	Normal	12 d

CT: Computed tomography; U/S: Ultrasonography; GGO: Ground-glass opacity; NA: Not available.

shows significant increased seven days after drainage (P = 0.03). Five patients had AKI manifested by elevation of the serum creatinine and urea levels. Total bilirubin level was elevated in eight patients and showed no significant reduction after drainage (P = 0.2). The CRP values were not significantly different (P = 0.06) before (182.0 mg/dL) and one week after tube insertion (133.0 mg/dL). Other inflammatory markers as D-dimer, procalcitonin and LDH were elevated in all patients before drainage and showed variable degree of non-statistically reduction and increase after drainage. The laboratory findings are listed in Table 3.

DISCUSSION

This study presents the clinical, radiological, and laboratory data for patients who underwent percutaneous drainage to manage septic complications associated with COVID-19 infection. The main finding is that patients with suspected septic complications associated with COVID-19 show relatively poor outcomes with 36.4% clinical success of percutaneous drainage despite 100% technical success. This finding was confirmed by the insignificant difference between the inflammatory markers before and after tube drainage insertion. Severe sepsis related to COVID-19 viral infection may be related to a decrease in mitochondrial efficiency and dysfunction of the respiratory chain[22,23]. In addition, autopsies have confirmed hyperinflammatory state with organ fibrosis, especially in high metabolic cells with high mitochondrial volume such as pneumocytes, endothelial cells, hepatocytes, and renal cells[24]. The resulting tissue hypoxia and increased inflammation, viral load, and other baseline risk factors contribute to an increased risk of severe sepsis or co-existed septic condition exaggeration.

Table 3 Median (inter-quartile range) for laboratory findings before drainage, 1 d and 7 d after drainage

	Pre drain	D1	D7	*P* value
WBCs × 10^9/L	15.4 (12.50-17.40)	18.8 (10.6-22.1)	12.1 (10.3-21.8)	0.656
Neutrophil × 10^9/L	82.8 (72.3-91.8)	86.6 (70.4-94.2)	70.9 (60.9-92.3)	0.091
Lymphocyte × 10^9/L	6.8 (3.7-9.9)	7.10 (2.8-11.2)	10.9 (2.9-19.2)	0.032[a]
CRP (mg/L)	182.0 (91.0-368.0)	166.0 (32.0-80.0)	133.0 (26.0-170.0)	0.061
Creatinine (μmol/L)	122.0 (70.0-353.0)	109.0 (54.0-426.0)	97.0 (56.0-364.0)	0.789
Urea (mmol/L)	9.2 (5.8-19.7)	8.6 (3.6-22.4)	9.1 (2.8-28.2)	0.574
Bilirubin (μmol/L)	19.1 (15.0-28.4)	14.4 (29.9-12.4)	15.5 (12.5-21.8)	0.247
D-Dimer (ng/mL)	1441.0 (620.0-3340.0)	1363.0 (460.0-2780.0)	1413.0 (380.0-3560.0)	0.373
Procalcitonin (ng/mL)	1.5 (1.1-3.0)	1.87 (0.85-3.56)	1.5800 (0.31-3.11)	0.398
LDH (IU/L)	359.0 (194.0-750.0)	397.0 (155.0-768.0)	438.0 (144.0-798.0)	0.929

[a]$P < 0.05$.

CRP: C-reactive protein; WBC: White blood cell; LDH: Lactate dehydrogenase.

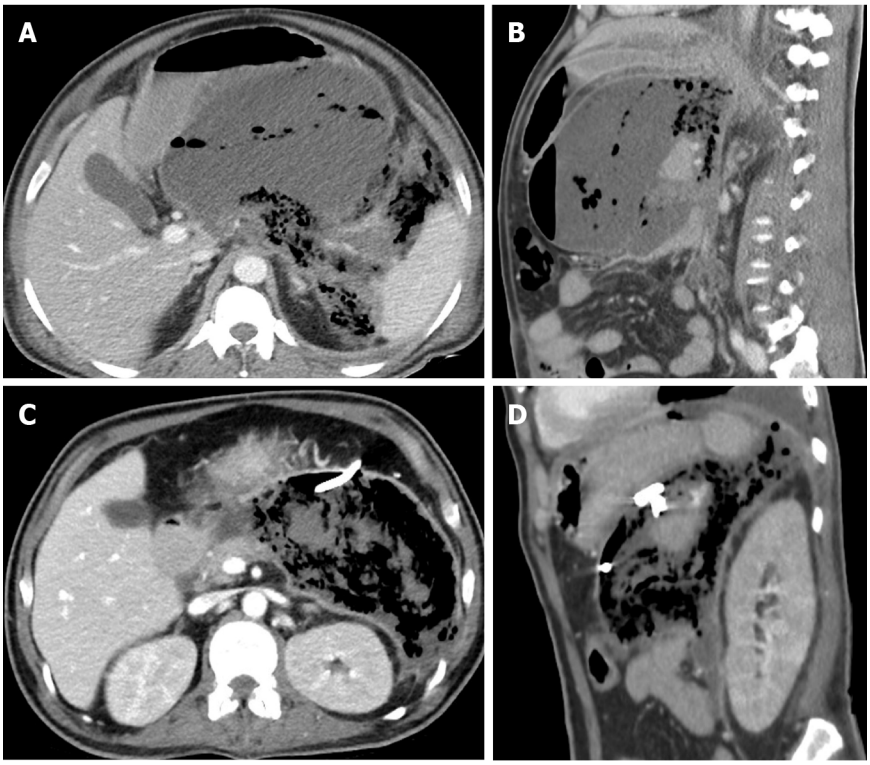

DOI: 10.4329/wjr.v14.i4.91

Figure 3 Percutaneous drainage of peripancreatic collection in a 43-yr-old male presented by acute pancreatitis. A and B: Axial and sagittal contrast enhanced computed tomography (CT) images show large peripancreatic collection/walled-off necrosis. The collection is mixed with pockets of gas inside and there is extension of the gas density into the retroperitoneal and perisplenic spaces; C and D: Axial and sagittal contrast enhanced CT images 22 d after tube insertion show reduction of the collection size with increased amount of gas within the collection.

This study included different types of septic complications as acute acalculous cholecystitis, acute pancreatitis, post-operative infection, abscesses in different locations, and acute pyelonephritis. Several reports described acute acalculous cholecystitis in COVID-19 patients[25-30] and raised the possibility of underlying dysregulated immune response or presence of viral RNA within the gall bladder wall as a culprit factor[28-30]. Percutaneous cholecystostomy for COVID-19 patients is recommended by multi-society position statement in case of surgical contraindication and after the failure of conservative therapy with antibiotics[31]. It is generally a preferred non-surgical procedure due to its relative safety, simplicity of execution, and reduced costs. Mattone *et al*[25] reported clinical failure of percutaneous

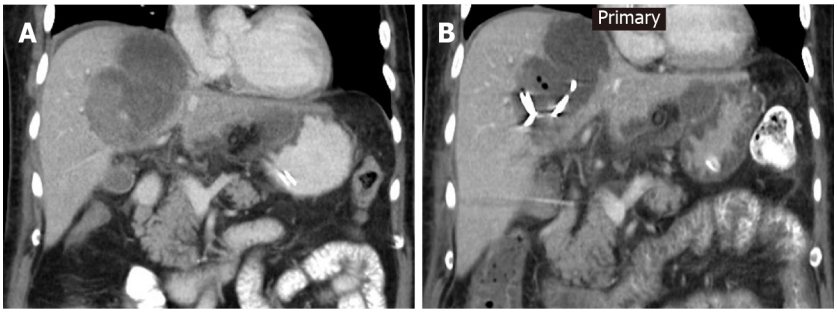

DOI: 10.4329/wjr.v14.i4.91

Figure 4 Percutaneous drainage of hepatic abscess in a 63-yr-old male. A: Coronal contrast enhanced computed tomography (CT) image shows thick-walled hepatic abscess with dependent high density inside secondary to clotted blood, a rim of perihepatic fluid is also noted; B: Coronal contrast enhanced CT image 6 d after tube insertion show reduction of the abscess size with few foci of gas density.

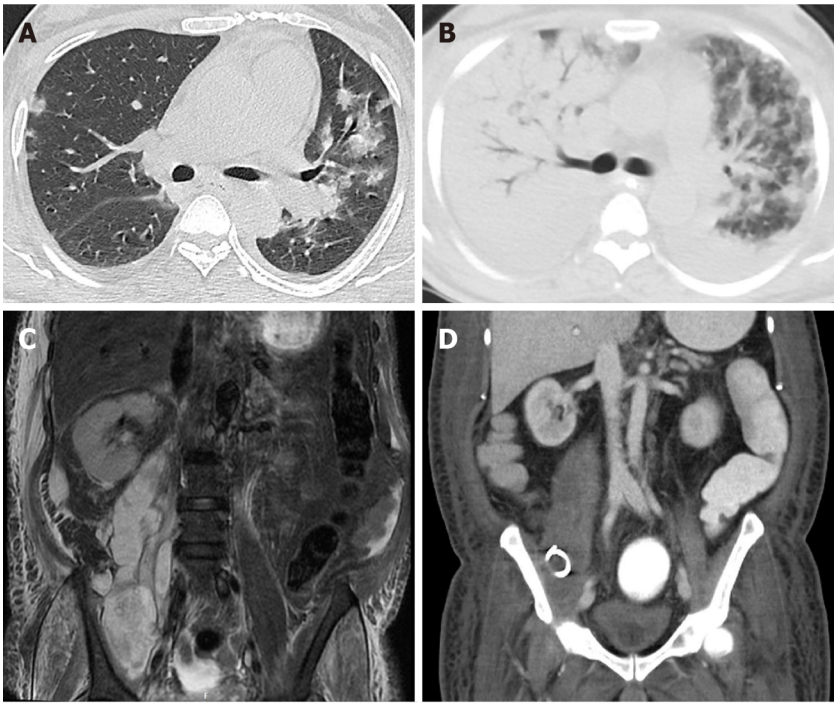

DOI: 10.4329/wjr.v14.i4.91

Figure 5 Percutaneous drainage of right psoas major abscess in a 60-yr-old male. A: Axial chest computed tomography (CT) image in pulmonary window shows bilateral ground-glass opacities (GGOs) and minimal bilateral pleural effusion; B: Axial chest CT image in pulmonary window 11 d after initial CT shows bilateral consolidation involving most of the right lung and GGOs in the remaining left lung parenchyma; C: Coronal T2 FAT SAT image shows large multi-locular psoas major abscess associated with muscular and subcutaneous soft tissue edema; D: Coronal contrast enhanced CT images 8 d after tube insertion show reduction of the collection size with regression of the associated soft tissue edema.

cholecystostomy after 3-d from tube insertion; the patient was shifted to surgery that revealed gangrenous cholecystitis. In this study, clinical success was reported only in one of three patients had cholecystostomy drainage of acute cholecystitis. Contrary to this result, cholecystostomy improved the clinical status of patients presented by acute acalculous cholecystitis co-existed with COVID-19[26,27]; however, the period of hospitalization was prolonged (25-67 d) compared to the mean hospitalization period in non-COVID-19 patients (10.5 d)[32].

COVID-19 associated pancreatic injury and acute pancreatitis are thought to be a result of direct cytopathic effect mediated by local viral replication or indirect mechanism related to either a systemic response to a harmful immune response or respiratory failure induced by the SARS-CoV-2[33]. COVID-19 patients with acute pancreatitis are more likely to experience admission to the ICU, peripancreatic fluid collections, pancreatic necrosis, persistent organ failure, prolonged hospital stay, and higher than usually reported 30-d mortality[34]. We encountered two cases of pancreatitis in the current study, one of them died 28 days after drainage.

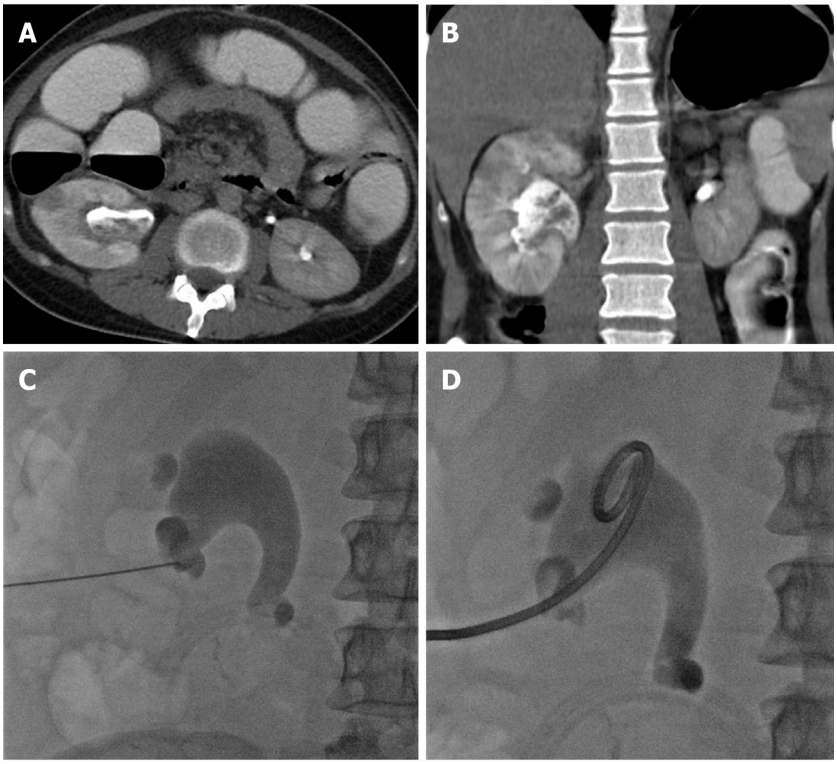

DOI: 10.4329/wjr.v14.i4.91

Figure 6 Percutaneous nephrostomy in a 30-yr-old male presented with acute pyelonephritis. A and B: Axial and coronal computed tomography images in excretory phase show characteristic features of acute pyelonephritis in the form of focal hypoenhnacing areas (striated nephrogram) and debris in dilated renal pelvis; C and D: Frontal fluoroscopic images show puncture needle in the lower calyces and successful insertion of nephrostomy tube.

In a meta-analysis performed by Abate *et al*[35], twenty-three articles with 2947 participants were included. The meta-analysis showed a very high global rate of postoperative mortality among COVID-19 patients of 20%. Percutaneous drainage was performed for two patients after complicated hepatic resection for hemangioma and liver donor, only the second patient survived and was discharged 18 days after drainage. The good outcome in this patient is attributed to the non-inflammatory nature of the drained fluid, lower inflammatory marker and less severity of COVID-19 as compared to the other patient.

Hepatic abscesses have been described in association with COVID-19[36,37]. While García Virosta *et al*[36] reported clinically successful percutaneous drainage for hepatic abscess and patient discharge after ten days from tube insertion, Elliot *et al*[37] reported a rapidly progressive severe acute respiratory distress syndrome, which was complicated by multiorgan failure and severe sepsis that ended by death after percutaneous drainage of hepatic abscess in a patient with COVID-19. One patient in this study presented with a large lumbar region abscess secondary to sigmoid colon perforation as proved by laparotomy. Bowel perforation secondary to COVID-19 has been attributed to microcirculation thrombosis[38] or direct insult to the colonic cells by the SARS-CoV-2 itself[39].

There is scanty literature on the association between COVID-19 and acute pyelonephritis. van 't Hof *et al*[40] described an unusual course of acute pyelonephritis in a young female with persistent fever and multiple blood clotting and hemorrhagic events one week after recovery from COVID-19. Similar to our results, pyelonephritis was managed successfully by percutaneous nephrostomy. More frequently, AKI is encountered among critically ill patients with COVID-19, affecting approximately 20%-40% of patients admitted to the hospital and particularly to the ICU[41]. AKI was the most frequent comorbidity (5/11) in this study. A significantly higher in-hospital death rate for patients with kidney abnormalities and AKI was reported by a study consisting of 701 SARS-CoV-2 positive patients[42].

COVID-19 requires a multidisciplinary approach to treatment with interventional radiology procedures that have contributed to worldwide patient care. In a study consisting of 92 patients who underwent 124 interventional procedures[43] [abscess drainage (12), percutaneous cholecystostomy (8), and nephrostomy tube (4)], the mortality rate in this study was 16.3 % (15/92). However, there was no specific data as regards clinical, laboratory, and radiological data of the included patients or correlation between specific IR procedures and mortality. In this study the poor outcome was related to the combined burden of severe COVID-19 pneumonia, presence of other co-morbidities and extent of sepsis.

This study has several limitations. First, our study cohort is small. Second, this study was retrospective in nature. Third, our results were not compared to a negative SARS-CoV-2 group with matched age, complication, and comorbidities; this may have overestimated the poor outcome of percutaneous drainage in this study group.

CONCLUSION

The current study demonstrates relatively poor clinical outcomes for patients having suspected septic complications associated with COVID-19 despite technically successful tube drainage and adequate antibiotic therapy. This study emphasizes the need for a large-scale comparative study on the relationship between septic complications, COVID-19, and comorbidities that might lead to poor clinical outcomes and clarifies the necessary precautions for percutaneous drainage in such patients.

ARTICLE HIGHLIGHTS

Research background

The resulting tissue hypoxia and increased inflammation secondary to severe coronavirus disease 2019 (COVID-19) combined with viral load, and other baseline risk factors contribute to an increased risk of severe sepsis or co-existed septic condition exaggeration.

Research motivation

We performed percutaneous drainage for septic complications of COVID-19 and wanted to report our experience.

Research objectives

To describe the clinical, radiological, and laboratory characteristics of a small cohort of patients infected by severe acute respiratory syndrome coronavirus 2 who underwent percutaneous drainage for septic complications and their post-procedural outcomes.

Research methods

This retrospective study consisted of 11 patients who were confirmed to have COVID-19 by RT-PCR test and required drain placement for septic complications. The mean age ± SD of the patients was 48.5 ± 14 years (range 30-72 years). Three patients underwent cholecystostomy for acute acalculous cholecystitis. Percutaneous drainage was performed in seven patients; two peripancreatic collections; two infected leaks after hepatic resection; one recurrent hepatic abscess, one psoas abscess and one lumbar abscess. One patient underwent a percutaneous nephrostomy for acute pyelonephritis.

Research results

Technical success was achieved in 100% of patients, while clinical success was achieved in 4 out of 11 patients (36.3%). Six patients (54.5%) died despite proper percutaneous drainage and adequate antibiotic coverage. One patient (9%) needed operative intervention. Two patients (18.2%) had two drainage procedures to drain multiple fluid collections. Two patients (18.2%) had repeat drainage procedures due to recurrent fluid collections. The average volume of the drained fluid immediately after tube insertion was 85 mL. Follow-up scans show a reduction of the retained content and associated inflammatory changes after tube insertion in all patients. There was no significant statistical difference (P = 0.6 and 0.4) between the mean of WBCs and neutrophils count before drainage and seven days after drainage. The lymphocyte count shows significant increased seven days after drainage (P = 0.03).

Research conclusions

In this study, patients having septic complications associated with COVID-19 showed relatively poor clinical outcomes despite technically successful percutaneous drainage.

Research perspectives

Prospective, larger multicentric study is needed to validate our results.

FOOTNOTES

Author contributions: Deif MA and Elmokadem AH designed the research study; Deif MA and Mounir AM performed the research; Elmokadem AH, Abo-Hedibah SA and Abdel Khalek AM analyzed the data and wrote the manuscript; all authors have read and approved the final manuscript.

Institutional review board statement: The study was reviewed and approved by the Mansoura university Institutional Review Board (R.21.12-1545).

Informed consent statement: A local institutional review board approved this retrospective study, and waivers of consent of medical record review were received.

Conflict-of-interest statement: All authors declare no conflict of interest.

Data sharing statement: Technical appendix, statistical code, and dataset available from the corresponding author at mokadem83@yahoo.com.

Country/Territory of origin: Egypt

ORCID number: Mohamed A Deif 0000-0002-8486-2622; Ahmad M Mounir 0000-0002-3322-7960; Sherif A Abo-Hedibah 0000-0002-1863-9828; Ahmed M Abdel Khalek 0000-0002-7751-7660; Ali H Elmokadem 0000-0001-5119-9548.

S-Editor: Gao CC
L-Editor: A
P-Editor: Gao CC

REFERENCES

1 **Singer M**, Deutschman CS, Seymour CW, Shankar-Hari M, Annane D, Bauer M, Bellomo R, Bernard GR, Chiche JD, Coopersmith CM, Hotchkiss RS, Levy MM, Marshall JC, Martin GS, Opal SM, Rubenfeld GD, van der Poll T, Vincent JL, Angus DC. The Third International Consensus Definitions for Sepsis and Septic Shock (Sepsis-3). *JAMA* 2016; **315**: 801-810 [PMID: 26903338 DOI: 10.1001/jama.2016.0287]

2 **Carter C**, Notter J. COVID-19 disease: a critical care perspective. *Clin Integr Care* 2020; **1**: 100003

3 **Quah P**, Li A, Phua J. Mortality rates of patients with COVID-19 in the intensive care unit: a systematic review of the emerging literature. *Crit Care* 2020; **24**: 285 [PMID: 32498689 DOI: 10.1186/s13054-020-03006-1]

4 **Mehta P**, McAuley DF, Brown M, Sanchez E, Tattersall RS, Manson JJ; HLH Across Speciality Collaboration, UK. COVID-19: consider cytokine storm syndromes and immunosuppression. *Lancet* 2020; **395**: 1033-1034 [PMID: 32192578 DOI: 10.1016/S0140-6736(20)30628-0]

5 **Ding R**, Meng Y, Ma X. The Central Role of the Inflammatory Response in Understanding the Heterogeneity of Sepsis-3. *Biomed Res Int* 2018; **2018**: 5086516 [PMID: 29977913 DOI: 10.1155/2018/5086516]

6 **Nedeva C**, Menassa J, Puthalakath H. Sepsis: Inflammation Is a Necessary Evil. *Front Cell Dev Biol* 2019; **7**: 108 [PMID: 31281814 DOI: 10.3389/fcell.2019.00108]

7 **Gentile LF**, Cuenca AG, Efron PA, Ang D, Bihorac A, McKinley BA, Moldawer LL, Moore FA. Persistent inflammation and immunosuppression: a common syndrome and new horizon for surgical intensive care. *J Trauma Acute Care Surg* 2012; **72**: 1491-1501 [PMID: 22695412 DOI: 10.1097/TA.0b013e318256e000]

8 **Rosenthal MD**, Kamel AY, Rosenthal CM, Brakenridge S, Croft CA, Moore FA. Chronic Critical Illness: Application of What We Know. *Nutr Clin Pract* 2018; **33**: 39-45 [PMID: 29323761 DOI: 10.1002/ncp.10024]

9 **Liu Y**, Mao B, Liang S, Yang JW, Lu HW, Chai YH, Wang L, Zhang L, Li QH, Zhao L, He Y, Gu XL, Ji XB, Li L, Jie ZJ, Li Q, Li XY, Lu HZ, Zhang WH, Song YL, Qu JM, Xu JF; Shanghai Clinical Treatment Experts Group for COVID-19. Association between age and clinical characteristics and outcomes of COVID-19. *Eur Respir J* 2020; **55** [PMID: 32312864 DOI: 10.1183/13993003.01112-2020]

10 **Thomas-Rüddel D**, Winning J, Dickmann P, Ouart D, Kortgen A, Janssens U, Bauer M. [Coronavirus disease 2019 (COVID-19): update for anesthesiologists and intensivists March 2020]. *Anaesthesist* 2020; **69**: 225-235 [PMID: 32189015 DOI: 10.1007/s00101-020-00758-x]

11 **Alhazzani W**, Møller MH, Arabi YM, Loeb M, Gong MN, Fan E, Oczkowski S, Levy MM, Derde L, Dzierba A, Du B, Aboodi M, Wunsch H, Cecconi M, Koh Y, Chertow DS, Maitland K, Alshamsi F, Belley-Cote E, Greco M, Laundy M, Morgan JS, Kesecioglu J, McGeer A, Mermel L, Mammen MJ, Alexander PE, Arrington A, Centofanti JE, Citerio G, Baw B, Memish ZA, Hammond N, Hayden FG, Evans L, Rhodes A. Surviving Sepsis Campaign: guidelines on the management of critically ill adults with Coronavirus Disease 2019 (COVID-19). *Intensive Care Med* 2020; **46**: 854-887 [PMID: 32222812 DOI: 10.1007/s00134-020-06022-5]

12 **Guan WJ**, Ni ZY, Hu Y, Liang WH, Ou CQ, He JX, Liu L, Shan H, Lei CL, Hui DSC, Du B, Li LJ, Zeng G, Yuen KY, Chen RC, Tang CL, Wang T, Chen PY, Xiang J, Li SY, Wang JL, Liang ZJ, Peng YX, Wei L, Liu Y, Hu YH, Peng P, Wang JM, Liu JY, Chen Z, Li G, Zheng ZJ, Qiu SQ, Luo J, Ye CJ, Zhu SY, Zhong NS; China Medical Treatment Expert Group for Covid-19. Clinical Characteristics of Coronavirus Disease 2019 in China. *N Engl J Med* 2020; **382**: 1708-1720 [PMID: 32109013 DOI: 10.1056/NEJMoa2002032]

13 **Huang C**, Wang Y, Li X, Ren L, Zhao J, Hu Y, Zhang L, Fan G, Xu J, Gu X, Cheng Z, Yu T, Xia J, Wei Y, Wu W, Xie X, Yin W, Li H, Liu M, Xiao Y, Gao H, Guo L, Xie J, Wang G, Jiang R, Gao Z, Jin Q, Wang J, Cao B. Clinical features of patients infected with 2019 novel coronavirus in Wuhan, China. *Lancet* 2020; **395**: 497-506 [PMID: 31986264 DOI: 10.1016/S0140-6736(20)30183-5]

14 **Wu Z**, McGoogan JM. Characteristics of and Important Lessons From the Coronavirus Disease 2019 (COVID-19) Outbreak in China: Summary of a Report of 72 314 Cases From the Chinese Center for Disease Control and Prevention. *JAMA* 2020; **323**: 1239-1242 [PMID: 32091533 DOI: 10.1001/jama.2020.2648]

15 **Elmokadem AH**, Batouty NM, Bayoumi D, Gadelhak BN, Abdel-Wahab RM, Zaky M, Abo-Hedibah SA, Ehab A, El-Morsy A. Mimickers of novel coronavirus disease 2019 (COVID-19) on chest CT: spectrum of CT and clinical features. *Insights Imaging* 2021; **12**: 12 [PMID: 33533965 DOI: 10.1186/s13244-020-00956-6]

16 **Elmokadem AH**, Bayoumi D, Abo-Hedibah SA, El-Morsy A. Diagnostic performance of chest CT in differentiating COVID-19 from other causes of ground-glass opacities. *EJRN* 2021; **52**: 1-10 [DOI: 10.1186/s43055-020-00398-6]

17 **Penn R**, David-Sanchez RY, Long J, Barclay W. Aberrant RNA replication products of highly pathogenic avian influenza viruses and its impact in the mammalian associated cytokine storm. *Access Microbiol* 2019; **1** [DOI: 10.1099/acmi.ac2019.po0457]

18 **Spencer JV**, Religa P, Lehmann MH. Editorial: Cytokine-Mediated Organ Dysfunction and Tissue Damage Induced by Viruses. *Front Immunol* 2020; **11**: 2 [PMID: 32038654 DOI: 10.3389/fimmu.2020.00002]

19 **Boomer JS**, To K, Chang KC, Takasu O, Osborne DF, Walton AH, Bricker TL, Jarman SD 2nd, Kreisel D, Krupnick AS, Srivastava A, Swanson PE, Green JM, Hotchkiss RS. Immunosuppression in patients who die of sepsis and multiple organ failure. *JAMA* 2011; **306**: 2594-2605 [PMID: 22187279 DOI: 10.1001/jama.2011.1829]

20 **Zhou F**, Yu T, Du R, Fan G, Liu Y, Liu Z, Xiang J, Wang Y, Song B, Gu X, Guan L, Wei Y, Li H, Wu X, Xu J, Tu S, Zhang Y, Chen H, Cao B. Clinical course and risk factors for mortality of adult inpatients with COVID-19 in Wuhan, China: a retrospective cohort study. *Lancet* 2020; **395**: 1054-1062 [PMID: 32171076 DOI: 10.1016/S0140-6736(20)30566-3]

21 **Abo-Hedibah SA**, Tharwat N, Elmokadem AH. Is chest X-ray severity scoring for COVID-19 pneumonia reliable? *Pol J Radiol* 2021; **86**: e432-e439 [PMID: 34429790 DOI: 10.5114/pjr.2021.108172]

22 **Brealey D**, Brand M, Hargreaves I, Heales S, Land J, Smolenski R, Davies NA, Cooper CE, Singer M. Association between mitochondrial dysfunction and severity and outcome of septic shock. *Lancet* 2002; **360**: 219-223 [PMID: 12133657 DOI: 10.1016/S0140-6736(02)09459-X]

23 **Singer M**. The role of mitochondrial dysfunction in sepsis-induced multi-organ failure. *Virulence* 2014; **5**: 66-72 [PMID: 24185508 DOI: 10.4161/viru.26907]

24 **Shenoy S**. Coronavirus (Covid-19) sepsis: revisiting mitochondrial dysfunction in pathogenesis, aging, inflammation, and mortality. *Inflamm Res* 2020; **69**: 1077-1085 [PMID: 32767095 DOI: 10.1007/s00011-020-01389-z]

25 **Mattone E**, Sofia M, Schembari E, Palumbo V, Bonaccorso R, Randazzo V, La Greca G, Iacobello C, Russello D, Latteri S. Acute acalculous cholecystitis on a COVID-19 patient: a case report. *Ann Med Surg (Lond)* 2020; **58**: 73-75 [PMID: 32895611 DOI: 10.1016/j.amsu.2020.08.027]

26 **Ying M**, Lu B, Pan J, Lu G, Zhou S, Wang D, Li L, Shen J, Shu J; From the COVID-19 Investigating and Research Team. COVID-19 with acute cholecystitis: a case report. *BMC Infect Dis* 2020; **20**: 437 [PMID: 32571224 DOI: 10.1186/s12879-020-05164-7]

27 **Wahid N**, Bhardwaj T, Borinsky C, Tavakkoli M, Wan D, Wong T. Acute Acalculous Cholecystitis During Severe COVID-19 Hospitalizations. *Am J Gastroenterol* 2020; **115**: S794 [DOI: 10.14309/01.ajg.0000708300.51603.f0]

28 **Alhassan SM**, Iqbal P, Fikrey L, Mohamed Ibrahim MI, Qamar MS, Chaponda M, Munir W. Post COVID 19 acute acalculous cholecystitis raising the possibility of underlying dysregulated immune response, a case report. *Ann Med Surg (Lond)* 2020; **60**: 434-437 [PMID: 33224493 DOI: 10.1016/j.amsu.2020.11.031]

29 **Bruni A**, Garofalo E, Zuccalà V, Currò G, Torti C, Navarra G, De Sarro G, Navalesi P, Longhini F, Ammendola M. Histopathological findings in a COVID-19 patient affected by ischemic gangrenous cholecystitis. *World J Emerg Surg* 2020; **15**: 43 [PMID: 32615987 DOI: 10.1186/s13017-020-00320-5]

30 **Balaphas A**, Gkoufa K, Meyer J, Peloso A, Bornand A, McKee TA, Toso C, Popeskou SG. COVID-19 can mimic acute cholecystitis and is associated with the presence of viral RNA in the gallbladder wall. *J Hepatol* 2020; **73**: 1566-1568 [PMID: 32890595 DOI: 10.1016/j.jhep.2020.08.020]

31 **Campanile FC**, Podda M, Arezzo A, Botteri E, Sartori A, Guerrieri M, Cassinotti E, Muttillo I, Pisano M, Brachet Contul R, D'Ambrosio G, Cuccurullo D, Bergamini C, Allaix ME, Caracino V, Petz WL, Milone M, Silecchia G, Anania G, Agrusa A, Di Saverio S, Casarano S, Cicala C, Narilli P, Federici S, Carlini M, Paganini A, Bianchi PP, Salaj A, Mazzari A, Meniconi RL, Puzziello A, Terrosu G, De Simone B, Coccolini F, Catena F, Agresta F. Acute cholecystitis during COVID-19 pandemic: a multisocietary position statement. *World J Emerg Surg* 2020; **15**: 38 [PMID: 32513287 DOI: 10.1186/s13017-020-00317-0]

32 **Popowicz A**, Lundell L, Gerber P, Gustafsson U, Pieniowski E, Sinabulya H, Sjödahl K, Tsekrekos A, Sandblom G. Cholecystostomy as Bridge to Surgery and as Definitive Treatment or Acute Cholecystectomy in Patients with Acute Cholecystitis. *Gastroenterol Res Pract* 2016; **2016**: 3672416 [PMID: 26839538 DOI: 10.1155/2016/3672416]

33 **Wang F**, Wang H, Fan J, Zhang Y, Zhao Q. Pancreatic Injury Patterns in Patients With Coronavirus Disease 19 Pneumonia. *Gastroenterology* 2020; **159**: 367-370 [PMID: 32247022 DOI: 10.1053/j.gastro.2020.03.055]

34 **Pandanaboyana S**, Moir J, Leeds JS, Oppong K, Kanwar A, Marzouk A, Belgaumkar A, Gupta A, Siriwardena AK, Haque AR, Awan A, Balakrishnan A, Rawashdeh A, Ivanov B, Parmar C, M Halloran C, Caruana C, Borg CM, Gomez D, Damaskos D, Karavias D, Finch G, Ebied H, K Pine J, R A Skipworth J, Milburn J, Latif J, Ratnam Apollos J, El Kafsi J, Windsor JA, Roberts K, Wang K, Ravi K, V Coats M, Hollyman M, Phillips M, Okocha M, Sj Wilson M, A Ameer N, Kumar N, Shah N, Lapolla P, Magee C, Al-Sarireh B, Lunevicius R, Benhmida R, Singhal R, Balachandra S, Demirli Atıcı S, Jaunoo S, Dwerryhouse S, Boyce T, Charalampakis V, Kanakala V, Abbas Z, Nayar M; COVID PAN collaborative group. SARS-CoV-2 infection in acute pancreatitis increases disease severity and 30-day mortality: COVID PAN collaborative study. *Gut* 2021; **70**: 1061-1069 [PMID: 33547182 DOI: 10.1136/gutjnl-2020-323364]

35 **Abate SM**, Mantefardo B, Basu B. Postoperative mortality among surgical patients with COVID-19: a systematic review and meta-analysis. *Patient Saf Surg* 2020; **14**: 37 [PMID: 33062056 DOI: 10.1186/s13037-020-00262-6]

36 **García Virosta M**, Ortega I, Ferrero E, Picardo AL. Diagnostic Delay During the COVID-19 Pandemic: Liver Abscess Secondary to Acute Lithiasic Cholecystitis. *Cir Esp (Engl Ed)* 2020; **98**: 409 [PMID: 32408994 DOI: 10.1016/j.ciresp.2020.04.010]

37 **Elliott R**, Ohene Baah N, Grossman VA, Sharma AK. COVID-19 Related Mortality During Management of a Hepatic Abscess. *J Radiol Nurs* 2020; **39**: 271-274 [PMID: 32982611 DOI: 10.1016/j.jradnu.2020.09.001]

38 **Nahas SC**, Meira-JÚnior JD, Sobrado LF, Sorbello M, Segatelli V, Abdala E, Ribeiro-JÚnior U, Cecconello I. Intestinal perforation caused by COVID-19. *Arq Bras Cir Dig* 2020; **33**: e1515 [PMID: 33237160 DOI: 10.1590/0102-672020190001e1515]

39 **De Nardi P**, Parolini DC, Ripa M, Racca S, Rosati R. Bowel perforation in a Covid-19 patient: case report. *Int J Colorectal Dis* 2020; **35**: 1797-1800 [PMID: 32458395 DOI: 10.1007/s00384-020-03627-6]

40 **van 't Hof LJ**, Pellikaan L, Soonawala D, Roshani H. An Unusual Presentation of Pyelonephritis: Is It COVID-19 Related? *SN Compr Clin Med* 2021; 1-6 [PMID: 33937632 DOI: 10.1007/s42399-021-00909-0]

41 **Revzin MV**, Raza S, Srivastava NC, Warshawsky R, D'Agostino C, Malhotra A, Bader AS, Patel RD, Chen K, Kyriakakos C, Pellerito JS. Multisystem Imaging Manifestations of COVID-19, Part 2: From Cardiac Complications to Pediatric Manifestations. *Radiographics* 2020; **40**: 1866-1892 [PMID: 33136488 DOI: 10.1148/rg.2020200195]

42 **Cheng Y**, Luo R, Wang K, Zhang M, Wang Z, Dong L, Li J, Yao Y, Ge S, Xu G. Kidney disease is associated with in-hospital death of patients with COVID-19. *Kidney Int* 2020; **97**: 829-838 [PMID: 32247631 DOI: 10.1016/j.kint.2020.03.005]

43 **Lee KS**, Talenfeld AD, Browne WF, Holzwanger DJ, Harnain C, Kesselman A, Pua BB. Role of interventional radiology in the treatment of COVID-19 patients: Early experience from an epicenter. *Clin Imaging* 2021; **71**: 143-146 [PMID: 33259979 DOI: 10.1016/j.clinimag.2020.10.048]

World Journal of Radiology

Submit a Manuscript: https://www.f6publishing.com

World J Radiol 2022 April 28; 14(4): 104-106

DOI: 10.4329/wjr.v14.i4.104

ISSN 1949-8470 (online)

LETTER TO THE EDITOR

Follow-up computed tomography scan in post-COVID-19 pneumonia

Asad Chohan, Saiara Choudhury, Rahul Dadhwal, Abhay P Vakil, Rene Franco, Pahnwat Tonya Taweesedt

Specialty type: Radiology, nuclear medicine and medical imaging

Provenance and peer review: Unsolicited article; Externally peer reviewed.

Peer-review model: Single blind

Peer-review report's scientific quality classification

Grade A (Excellent): A
Grade B (Very good): B
Grade C (Good): C
Grade D (Fair): 0
Grade E (Poor): 0

P-Reviewer: Arteaga-Livias K, Peru; Naswhan AJ, Qatar; Valencia GA, Peru

Received: December 17, 2021
Peer-review started: December 17, 2021
First decision: February 21, 2022
Revised: February 24, 2022
Accepted: March 26, 2022
Article in press: March 26, 2022
Published online: April 28, 2022

Asad Chohan, Saiara Choudhury, Rahul Dadhwal, Abhay P Vakil, Rene Franco, Pahnwat Tonya Taweesedt, Pulmonary Medicine, Corpus Christi Medical Center, Corpus Christi, TX 78411, United States

Corresponding author: Pahnwat Tonya Taweesedt, MD, Academic Fellow, Pulmonary Medicine, Corpus Christi Medical Center, 3315 S Alameda St, Corpus Christi, TX 78411, United States. pahnwatt@gmail.com

Abstract

The coronavirus disease 2019 (COVID-19) global pandemic can be a severe illness that leads to morbidity and mortality. With the increasing number of COVID-19 pneumonia survivors, several long-term changes may persist, including abnormal imaging of lung parenchyma. In addition to the clinical course, it is vital to follow up on pulmonary imaging during the post-infectious period, which is not routinely required in other common pulmonary diagnoses. Computed tomography (CT) scan of the chest is an effective and diagnostic tool for pneumonia which gives an insight into structural abnormalities within the lungs, complications, and possible progression of the disease. Several studies have monitored COVID-19 pneumonia and its complications using serial CT chest imaging from the initial phase of infection, hospitalization, and post-discharge. Nonetheless, long-term follow-up imaging data in post-COVID-19 is still limited. We have summarized the findings utilizing a systematic review of the literature regarding COVID-19 pneumonia imaging, including long-term follow-up.

Key Words: COVID-19; Pneumonia; Computed tomography; Evolution; Progression

Core Tip: Changes seen in computed tomography imaging related to coronavirus disease 2019 (COVID-19) pneumonia appear to progress and peak around two weeks post-hospitalization. Overall improvement and complete resolution of COVID-19 pneumonia-related changes imaging can be seen in the majority of the patients with long-term follow-up. We have summarized the findings utilizing a systematic review of the literature regarding COVID-19 pneumonia imaging, including long-term follow-up.

Citation: Chohan A, Choudhury S, Dadhwal R, Vakil AP, Franco R, Taweesedt PT. Follow-up computed tomography scan in post-COVID-19 pneumonia. *World J Radiol* 2022; 14(4): 104-106
URL: https://www.wjgnet.com/1949-8470/full/v14/i4/104.htm
DOI: https://dx.doi.org/10.4329/wjr.v14.i4.104

TO THE EDITOR

We read the article titled "Review on radiological evolution of COVID-19 pneumonia using computed tomography" by Casartelli *et al*[1] with keen interest. A chest computed tomography (CT) scan can be a useful diagnostic tool in a high-prevalence or pandemic situation, especially with clinical correlation. Risk stratification and assessing the progression of disease are also effective uses of CT chest imaging in coronavirus disease 2019 (COVID-19) patients. Given the global spread of COVID-19 and the magnitude of both direct and indirect effects of the disease, a CT scan of the chest can help in long-term prognostication in patients who survive.

Multiple studies have concluded that with disease progression, certain initial CT findings in COVID-19 can evolve with a specific pattern and regularity. COVID-19 pneumonia-related changes seen on CT chest imaging typically progress rapidly, plateau, and subsequently start to resolve thereafter. Changes in CT imaging vary widely from six to seventeen days but typically stabilize within the first two weeks of COVID-19 pneumonia. In the short term, some of the features seem to recur, with scans mostly showing consolidations and ground-glass opacities (GGO). Besides GGO, chest CT characteristics that indicate the reparation, including subpleural, linear opacities, and fibrotic changes, were also reported. A sign termed "fishing net on trees" has also been reported. Some reports have also mentioned interseptal thickening and fibrous streaks[1,2]. Three weeks post-discharge, GGO and fibrous stripes have been seen, while after four weeks, mostly linear opacities remained. The "tinted" sign and bronchovascular bundle distortion have also been mentioned. The bronchovascular bundle distortion could possibly be a result of inflammatory destruction or subsegmental atelectasis. The latter two signs mentioned above may signify the gradual resolution of inflammation with re-expansion of alveoli based on previous reports. This review included reports with follow-up durations of up to four months[1].

In a study conducted by Pan *et al*[3], two hundred nine patients with COVID-19 infection, who had been admitted to the hospital, undertook serial chest CT at three, seven, and twelve months. One-year CT chest follow-up revealed residual linear lesions, multiple areas of reticular opacities/cysts, and complete resolution in 12%, 13%, and 75%, respectively[3]. In another study conducted by Guan *et al*[4], CT results of 69 patients who had COVID-19 infection were assessed in three different phases: Initial CT, peak CT, and CT prior to discharge. Peak CT in this study was the highest attenuation of the density without alteration in size during COVID-19 progression or the maximal size of lesion on CT which is the most common pattern. The intervals were closely correlated to lobe scores and CT appearances; the higher the lobe score, the longer the intervals. The lobe score was calculated according to the percentage of the lesion in one lobe with the zero equals to no lesion, one equals more than 0% to less than 25%, two equals 25% to less than 50%, three equals 50% to less than 75%, and four equals to 75% or more. While the utilization of lobe score may be beneficial, further studies are necessary to assess its effectiveness on a larger scale.

The duration of initial interval is inversely correlated with the amount of consolidations, air bronchograms, and irregular lines[3]. The intervals will be longer if irregular and reticular lines are seen on the peak CT and pre-discharge CT. After that, COVID-19 pneumonia lesions on the CT chest may resolve completely, while GGO, irregular and reticular lines may remain[3]. In a similar study conducted by Chen *et al*[5], 41 patients were followed with chest CT during the hospital stay and at two weeks, one month, three months, six months, and one year after discharge. The study concluded that patients showed continuous improvement on lung CT scans during the 1-year follow-up time; however residual lesions (GGO and reticular patterns) may still be found, which are associated with lung volume parameters and risk of developing lung opacities[5]. Liu *et al*[6] retrospectively evaluated chest CT follow-ups on 51 patients with COVID-19 performed on the day prior to discharge, two weeks post-discharge, and four weeks post-discharge. The results of this study indicated that changes seen were significantly reduced, including density reduction on follow-up scans as compared to the scans done at the time of discharge.

Unlike the systematic review by Casartelli *et al*[1], these results showed that 64.7% of discharged patients progressed to complete resolution of previously seen lung lesions at 4-wk follow-up, indicating that damaged lung tissue could heal in patients with COVID-19 pneumonia[5]. In another study conducted by Liu *et al*[7], 41 patients diagnosed with COVID-19 were followed up after seven months with chest CT and cardiopulmonary exercise testing. The predominant chest CT patterns at seven months included parenchymal bands (41%), interlobular septal thickening (32%), and traction bronchiectasis (29%). Sixty-one percent of the patients achieved complete radiological resolution, while 29% went on to develop pulmonary fibrosis. Those patients who went on to develop fibrotic lung disease appeared to have an increased risk due to older age and comorbid conditions[7].

While CT scan of the chest is an effective tool in COVID-19 patients, the side effects to patients of repeat irradiation need to be kept in mind and the use of low dose CT to follow up these patients can be considered. In conclusion, CT scans of the chest are an effective diagnostic tool which can provide insight into the structural pathology of pulmonary disease, its progression, and its association with long-term effects. Future studies should be utilized to define its utility in determining long-term progression in patients with COVID-19 pneumonia.

FOOTNOTES

Author contributions: Chohan A and Taweesedt PT wrote the letter; Choudhury S wrote the letter; Franco R, Dadhwal R, Vakil AP and Taweesedt PT revised the letter.

Conflict-of-interest statement: All authors declare no conflicts-of-interest related to this article.

Country/Territory of origin: United States

ORCID number: Asad Chohan 0000-0002-1801-9792; Saiara Choudhury 0000-0001-7225-4905; Rahul Dadhwal 0000-0001-6963-1466; Abhay P Vakil 0000-0003-4947-0233; Rene Franco 0000-0002-0684-7734; Pahnwat Tonya Taweesedt 0000-0002-5791-6920.

S-Editor: Wang JJ
L-Editor: A
P-Editor: Wang JJ

REFERENCES

1 **Casartelli C**, Perrone F, Balbi M, Alfieri V, Milanese G, Buti S, Silva M, Sverzellati N, Bersanelli M. Review on radiological evolution of COVID-19 pneumonia using computed tomography. *World J Radiol* 2021; **13**: 294-306 [PMID: 34630915 DOI: 10.4329/wjr.v13.i9.294]

2 **Mejía-Zambrano H**. Radiological and functional pulmonary complications in patients recovered from COVID-19. *Microb Infect Chemother* 2021 [DOI: 10.54034/mic.e1217]

3 **Pan F**, Yang L, Liang B, Ye T, Li L, Liu D, Wang J, Hesketh RL, Zheng C. Chest CT Patterns from Diagnosis to 1 Year of Follow-up in Patients with COVID-19. *Radiology* 2022; **302**: 709-719 [PMID: 34609153 DOI: 10.1148/radiol.2021211199]

4 **Guan CS**, Lv ZB, Li JJ, Du YN, Chen H, Cui T, Guo N, Chen BD, Xie RM. CT appearances, patterns of progression, and follow-up of COVID-19: evaluation on thin-section CT. *Insights Imaging* 2021; **12**: 73 [PMID: 34110540 DOI: 10.1186/s13244-021-01019-0]

5 **Chen Y**, Ding C, Yu L, Guo W, Feng X, Su J, Xu T, Ren C, Shi D, Wu W, Yi P, Liu J, Tao J, Lang G, Li Y, Xu M, Sheng J, Li L, Xu K. One-year follow-up of chest CT findings in patients after SARS-CoV-2 infection. *BMC Med* 2021; **19**: 191 [PMID: 34365975 DOI: 10.1186/s12916-021-02056-8]

6 **Liu C**, Ye L, Xia R, Zheng X, Yuan C, Wang Z, Lin R, Shi D, Gao Y, Yao J, Sun Q, Wang X, Jin M. Chest Computed Tomography and Clinical Follow-Up of Discharged Patients with COVID-19 in Wenzhou City, Zhejiang, China. *Ann Am Thorac Soc* 2020; **17**: 1231-1237 [PMID: 32692945 DOI: 10.1513/AnnalsATS.202004-324OC]

7 **Liu M**, Lv F, Huang Y, Xiao K. Follow-Up Study of the Chest CT Characteristics of COVID-19 Survivors Seven Months After Recovery. *Front Med (Lausanne)* 2021; **8**: 636298 [PMID: 33732719 DOI: 10.3389/fmed.2021.636298]

Published by **Baishideng Publishing Group Inc**
7041 Koll Center Parkway, Suite 160, Pleasanton, CA 94566, USA
Telephone: +1-925-3991568
E-mail: bpgoffice@wjgnet.com
Help Desk: https://www.f6publishing.com/helpdesk
https://www.wjgnet.com

ISSN 1949-8470 (online)

World Journal of *Radiology*

World J Radiol 2022 May 28; 14(5): 107-113

Published by Baishideng Publishing Group Inc

World Journal of Radiology

Contents

Monthly Volume 14 Number 5 May 28, 2022

ORIGINAL ARTICLE

Retrospective Study

World Journal of Radiology

Monthly Volume 14 Number 5 May 28, 2022

Contents

ABOUT COVER

Editorial Board Member of *World Journal of Radiology*, Ertan Şahin, MD, Associate Professor, Department of Nuclear Medicine, Faculty of Medicine, University of Gaziantep, Gaziantep 27100, Turkey. er_ahin@yahoo.com

AIMS AND SCOPE

The primary aim of *World Journal of Radiology* (*WJR*, *World J Radiol*) is to provide scholars and readers from various fields of radiology with a platform to publish high-quality basic and clinical research articles and communicate their research findings online.

WJR mainly publishes articles reporting research results and findings obtained in the field of radiology and covering a wide range of topics including state of the art information on cardiopulmonary imaging, gastrointestinal imaging, genitourinary imaging, musculoskeletal imaging, neuroradiology/head and neck imaging, nuclear medicine and molecular imaging, pediatric imaging, vascular and interventional radiology, and women's imaging.

INDEXING/ABSTRACTING

The *WJR* is now abstracted and indexed in Emerging Sources Citation Index (Web of Science), PubMed, PubMed Central, Reference Citation Analysis, China National Knowledge Infrastructure, China Science and Technology Journal Database, and Superstar Journals Database. The 2021 edition of Journal Citation Reports® cites the 2020 Journal Citation Indicator (JCI) for *WJR* as 0.51.

RESPONSIBLE EDITORS FOR THIS ISSUE

Production Editor: *Wen-Wen Qi*; **Production Department Director:** *Xu Guo*; **Editorial Office Director:** *Jia-Ping Yan*.

NAME OF JOURNAL
World Journal of Radiology

ISSN
ISSN 1949-8470 (online)

LAUNCH DATE
January 31, 2009

FREQUENCY
Monthly

EDITORS-IN-CHIEF
Thomas J Vogl

EDITORIAL BOARD MEMBERS
https://www.wjgnet.com/1949-8470/editorialboard.htm

PUBLICATION DATE
May 28, 2022

INSTRUCTIONS TO AUTHORS
https://www.wjgnet.com/bpg/gerinfo/204

GUIDELINES FOR ETHICS DOCUMENTS
https://www.wjgnet.com/bpg/GerInfo/287

GUIDELINES FOR NON-NATIVE SPEAKERS OF ENGLISH
https://www.wjgnet.com/bpg/gerinfo/240

PUBLICATION ETHICS
https://www.wjgnet.com/bpg/GerInfo/288

PUBLICATION MISCONDUCT
https://www.wjgnet.com/bpg/gerinfo/208

ARTICLE PROCESSING CHARGE
https://www.wjgnet.com/bpg/gerinfo/242

STEPS FOR SUBMITTING MANUSCRIPTS
https://www.wjgnet.com/bpg/GerInfo/239

ONLINE SUBMISSION
https://www.f6publishing.com

World Journal of Radiology

Submit a Manuscript: https://www.f6publishing.com

World J Radiol 2022 May 28; 14(5): 107-113

DOI: 10.4329/wjr.v14.i5.107

ISSN 1949-8470 (online)

ORIGINAL ARTICLE

Retrospective Study

Investigation of coronoid process hyperplasia using Levandoski analysis on panoramic radiographs

Sule Erdem, Suheda Erdem

Specialty type: Radiology, nuclear medicine and medical imaging

Provenance and peer review: Invited article; Externally peer reviewed.

Peer-review model: Single blind

Peer-review report's scientific quality classification

Grade A (Excellent): 0
Grade B (Very good): 0
Grade C (Good): C, C
Grade D (Fair): D
Grade E (Poor): 0

P-Reviewer: Naganuma H, Japan; Tao Q, China

Received: January 19, 2022
Peer-review started: January 19, 2022
First decision: March 24, 2022
Revised: April 2, 2022
Accepted: April 27, 2022
Article in press: April 27, 2022
Published online: May 28, 2022

Sule Erdem, Suheda Erdem, Department of Oral and Maxillofacial Radiology, Giresun University, Giresun 28200, Turkey

Corresponding author: Sule Erdem, DDS, Assistant Professor, Department of Oral and Maxillofacial Radiology, Giresun University, Teyyareduzu, Giresun 28200, Turkey.
suledelil92@gmail.com

Abstract

BACKGROUND

The diagnosis of coronoid process hyperplasia (CPH) is usually based on symptoms and radiological imaging. Because of its similar symptoms, it can be confused with temporomandibular joint diseases. Therefore, an objective and reproducible way of diagnosis should be determined.

AIM

To investigate CPH using Levandoski analysis on panoramic radiographs to determine its prevalence.

METHODS

A total of 300 panoramic radiograph images (600 coronoid processes) were examined. Having measured the Condyle-Gonion (Cd-Go) and Coronoid-Gonion (Cor-Go) distances, the Cor-Go:Cd-Go ratio was calculated for the left and right sides of each image.

RESULTS

There was a statistically significant difference in Cd-Go and Cor-Go distances between male and female participants ($P < 0.001$). There was no statistically significant relationship between Cor-Go:Cd-Go ratios and gender ($P > 0.05$).

CONCLUSION

Cd-Go and Cor-Go distances were statistically significantly increased in males on both the left and right sides. The ratio of Cor-Go:Cd-Go was preserved in both genders. The prevalence of CPH was found to be 0.3%.

Key Words: Coronoid process; Hyperplasia; Prevalence; Levandoski analysis; Panoramic radiograph

Core Tip: Coronoid process hyperplasia (CPH) is an abnormal bone elongation. It is usually seen with a mouth-opening limitation. There are various disorders in which limited mouth opening is seen in the differential diagnosis. Therefore, an objective and reproducible radiological method should be used in the diagnosis. Levandoski analysis is a method frequently used for the diagnosis of mandibular and facial asymmetries on panoramic radiographs. However, its use in the diagnosis of CPH is not very common and is not well-known by physicians. One of the aims of this study is to raise the awareness of physicians about Levandoski analysis and CPH.

Citation: Erdem S, Erdem S. Investigation of coronoid process hyperplasia using Levandoski analysis on panoramic radiographs. *World J Radiol* 2022; 14(5): 107-113
URL: https://www.wjgnet.com/1949-8470/full/v14/i5/107.htm
DOI: https://dx.doi.org/10.4329/wjr.v14.i5.107

INTRODUCTION

Coronoid process hyperplasia (CPH) was first described by the German surgeon Bernhard Von Langenbeck in 1853[1]. CPH is an abnormal bone elongation that commonly occurs bilaterally. As it a rare condition, no epidemiological studies have been reported[2]. It is predominantly seen during the second decade of life, mostly among the male population[3] and may develop asymptomatically, presenting with late symptoms[4]. However, CPH is usually noticed with a progressive mouth opening limitation, which is thought to be caused by interference with the zygomatic bone[3]. Thus, it becomes necessary to explain the morphometric relationship between the coronoid processes and condyles because limited mouth opening is not always caused by CPH. Additionally, visual diagnosis of CPH without using an analysis system is not an accurate and reproducible way[5].

Computed tomography (CT) and cone-beam computed tomography (CBCT) have been reported to be useful methods, providing three-dimensional images in the diagnosis of CPH[6]. However, CT and CBCT are not used in routine radiological examinations. Panoramic radiography is the simplest radiological method that can be used in the diagnosis of CPH and has a low radiation dose[5]. In addition, the majority of CPH cases reported to date have used panoramic graphy as a diagnostic method[3].

To date, no morphometric or prevalence study has been performed on a large sample group using Levandoski analysis. The purpose of this article is to investigate the coronoid process morphometrically and determine the prevalence of CPH in a sample subpopulation using Levandoski analysis with panoramic radiographs.

MATERIALS AND METHODS

The present study followed the principles of the Helsinki Declaration. Approval was granted by the Ethics Committee of University Ordu (No: 2021/231).

The images of the participants who underwent panoramic graphy were analysed retrospectively. The study was performed on images without artefacts that could adversely affect the evaluation. The participants included in this study were in the second decade and older. The participants with trauma, pathological formations and anomalies in condyle or coronoid process regions, musculoskeletal anomalies and congenital bone dysplasia were not included. In addition, the images where the condyle and coronoid tips and the gonion point could not be clearly distinguished, and the images with any artifacts were not included. The patients gave their consent for their radiographic images and information to be used in scientific studies.

Image analysis

The images were obtained with a panoramic X-ray unit (Orthopos XG 3, Sirona Dental Systems, Bensheim, Germany) operating at 60-90 kVp and 3-16 mAs. When the scans were being taken, the patients were in an upright position, with their heads and necks in a neutral position and the Frankfort plane parallel to the floor. All examinations and measurements were performed on a 27-inch colour LCD screen (BE27AQLB, Asus Computer GmBH, Ratingen, Germany) with a resolution of 2560 × 1440 pixels.

A total of 300 panoramic graphs (600 coronoid processes) were examined using Levandoski analysis by a maxillofacial radiologist with five years of experience in a dimly-lit room. The ages and genders of participants were recorded using to the software database system. When Condyle (Cd)-Gonion (Go) and Coronoid (Cor)-Go distances were measured, the Cor-Go: Cd-Go ratio was calculated for the left and right side of each image (Figure 1). Line 1 is the maxillary vertical midline, which passes through the nasal septum. Lines 2, 3 and 4 are perpendicular to line 1 and are tangent to the lower border of the symphysis mandible, the tip of the condyle and the tip of the coronoid process, respectively.

To examine the intra-observer agreement, the images were reassessed by the same observer two weeks later.

Cd: Tip of the condyle.

Cor: Tip of the coronoid process.

Go: The most outward point of the mandibular angle.

Cd-Go: Distances between the Cd and Go points.

Cor-Go: Distances between the Cor and Go points.

Cor-Go: Cd-Go: Ratio diagnosed of CPH when above 1.15 (Kubota *et al*[5]).

Statistical analysis

The data were transferred to the Statistical Package for Social Sciences 20.0 for Windows. Mann-Whitney U test was used for the variables with two categories that do not have a normal distribution. The Student t-test was used to compare the means of the data in two independent groups with normal distribution.

Since the relationship between two continuous variables without normal distribution was examined, the Spearman's rho correlation test was used to evaluate the intra-observer agreement.

All statistical tests were conducted at the 95% confidence level; the findings were considered statistically significant at the significance level of 0.05.

RESULTS

The present study was performed retrospectively using 300 panoramic radiographs (126 males and 174 females). CPH was encountered in only one female out of 300 participants; the prevalence of CPH was found to be 0.3% in the sample subpopulation.

The Cd-Go and Cor-Go distances by gender are displayed in Table 1. There was a statistically significant difference in the Cd-Go and Cor-Go distances between male and female participants ($P < 0.001$). The Cd-Go and Cor-Go distances are statistically significantly increased in males on both left and right sides. Table 2 displays the Cor-Go: Cd-Go ratios according to gender. There was no statistically significant relationship between the Cor-Go: Cd-Go ratios and gender ($P > 0.05$).

Based on the Spearman's rho analysis, the statistically significant ($P < 0.01$) perfect agreement was found between the Cor-Go:Cd-Go ratios calculated at two-week intervals (the rho value for the left side equals 0.987, for the right side 0.978).

CPH was detected in only one patient. The measurements of the patient were as follows: Cor-Go/Cd-Go 76.6/63.6 mm for the right side, 69.1/54.8 mm for the left side, Cor-Go:Cd-Go 1.20 for the right side and 1.26 for the left side.

DISCUSSION

CPH, also known as an elongated mandibular coronoid process, is a rare condition characterised by elongation of the process. In the case of clinical suspicion of CPH, the diagnosis can be made radiologically. The cephalometric analysis has been reported to be a reliable method in the diagnosis of CPH [5]. However, based on this method, only the measurements and evaluations of the right coronoid process can be made, leaving the left side of the radiograph unclear. Therefore, a simple radiographic method, such as panoramic radiography that allows bilateral examination, is required[5]. Displaying anatomical structures in true dimensions without magnification and superimposition, CT is a useful diagnostic method in CPH[7,8]. However, CT is an imaging method involving a high radiation dose; therefore, it cannot be used for routine examination. Four-dimensional CT (4DCT) is a new imaging method that can display the mandibular movement as well as the surrounding soft tissue mobility. The 4DCT assessment has the potential to understand the mechanisms underlying the symptoms in CPH patients[9]. Panoramic radiography is a simple and useful method to diagnose patients with CPH[5]; therefore, it is the most frequently used imaging method to diagnose CPH[3].

Table 1 Condyle-gonion and coronoid-gonion distances according to gender

Total, *n* = 300	Right Cd-Go, Min-Max, mean ± SD	Right Cor-Go, Min-Max, mean ± SD	Left Cd-Go, Min-Max, mean ± SD	Left Cor-Go, Min-Max, mean ± SD
Male, *n* = 126	49.6-93.0; 72.56 ± 7.34	47.5-82.7; 67.75 ± 7.57	49.9-92.0; 72.26 ± 7.41	47.5-83.10; 67.03 ± 7.69
Female, *n* = 174	47.9-82.3; 65.45 ± 5.87	45.8-77.6; 61.07 ± 5.99	43.3-78.9; 65.33 ± 6.03	42.30-78.2; 60.69 ± 5.94
P value	< 0.001[a]	< 0.001[a]	< 0.001[a]	< 0.001[a]

[a]Statistically significant. Measurements are in mm; Cd-Go: Distances between the tip of the condyle and gonion point; Cor-Go: Distances between the tip of the coronoid process and gonion point. SD: Standard deviation.

Table 2 Coronoid-gonion:condyle-gonion ratios according to gender

Total, *n* = 300	Right Cor-Go:Cd-Go, Min-Max, mean ± SD	Left Cor-Go:Cd-Go, Min-Max, mean ± SD
Male, *n* = 126	0.76-1.14; 0.93 ± 0.07	0.76-1.13; 0.93 ± 0.07
Female, *n* = 174	0.78-1.20; 0.93 ± 0.07	0.78-1.26; 0.93 ± 0.07
P value	0.929	0.859

Cd-Go: Distances between the tip of the condyle and gonion point; Cor-Go: Distances between the tip of the coronoid process and gonion point. SD: Standard deviation.

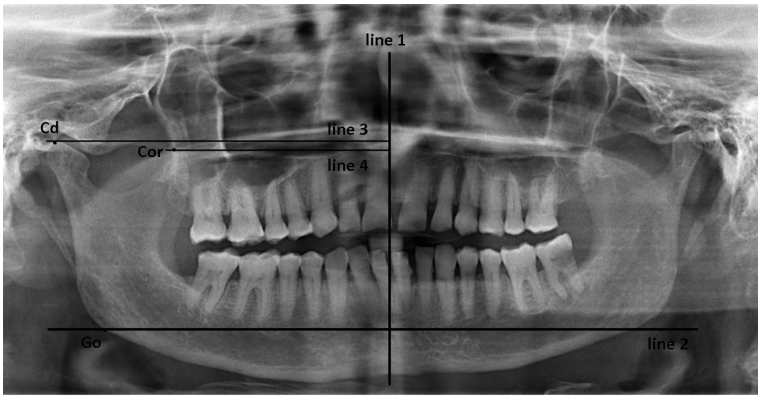

DOI: 10.4329/wjr.v14.i5.107

Figure 1 The Cor-Go:Cd-Go ratio was calculated for the left and right side of each image.

The etiology of CPH is not well described, and many theories have been put forward, such as genetic inheritance[10], hormonal stimulus[11], facial injuries and trauma[12] and temporal muscle activity[13]. According to a review that included 115 cases and was published by Goh *et al*[3] in 2020, CPH is predominantly seen bilaterally, mostly in males, during the second decade of life. In the present study of 300 patients, bilateral CPH was found in a 50-year-old female patient.

Although CPH is known to be a rare condition, its prevalence is unknown. Izumi *et al*[18] encountered CPH in 17 of 1665 patients whose data had been examined. However, this is not a prevalence study but a case-control study conducted with database records of a clinic where only patients with temporomandibular joint findings were admitted. In the present study, the Cor-Go:Cd-Go ratio was measured applying Levandoski analysis, which is a useful and reproducible way to diagnose CPH, on the panoramic radiographs of each participant. CPH was encountered in only one out of 300 participants, and the prevalence of CPH was found to be 0.3% in the sample subpopulation.

Levandoski developed his analysis for examining panoramic radiographs and adapted it for temporomandibular joint evaluation[14]. This analysis has been used in the diagnosis of facial and dental asymmetries and CPH in later years. There has been reported a good correlation between standard face photographs and Levandoski analysis[15]. Various studies have supported the applicability of the analysis in diagnosing facial and dental asymmetries[15,16].

Kubota *et al*[5] used Levandoski analysis on panoramic radiographs for the diagnosis of CPH. They compared three patients with CT-confirmed CPH and a control group of 56 participants to verify the

reliability of the analysis in the diagnosis of CPH. They reported that the Cor-Go and Cor-Go: Cd-Go values were significantly higher in the patients than in the control group. They reported the Cor-Go: Cd-Go value as the maximum of 1.07 for the control group and the minimum of 1.15 for the patient group. At the same time, they compared the Cor-Go: Cd-Go value with cephalometric and panoramic radiographs only for the right side in all participants (n = 59) and found a stable correlation. They did not report a statistically significant difference in the Cor-Go: Cd-Go values based on gender. In the current study consisting of 300 participants, there was no significant difference in the Cor-Go:Cd-Go values between males and females, similar to the study of Kubota *et al* However, the Cd-Go and Cor-Go distances for both left and right sides increased statistically significantly in males (P < 0.001).

An Anatolian skull with CPH was examined by Çorumlu *et al* using Levandoski analysis on panoramic radiographs[17]. They reported that the Cor-Go and Cd-Go measurements were 95.10 mm and 79.03 mm on the right side and 97.53 mm and 87.80 mm on the left side; the Cor-Go: Cd-Go value was 1.20 on the right side. In the case they reported, the Cor-Go: Cd-Go value for the left side was below the 1.15 required for CPH but above the normal value of 1.07. For this reason, they interpreted their case bilaterally. In the present study, CPH was detected in only one patient. The measurements of the patient were as follows: Cor-Go and Cd-Go are 76.6 and 63.6 mm, respectively, for the right side and 69.1 and 54.8 mm for the left side; the Cor-Go: Cd-Go ratio is 1.20 for the right side and 1.26 for the left side.

Izumi *et al*[18] retrospectively analysed the data of 1,665 patients who visited the temporomandibular joint (TMJ) centre to contribute to a case-control study. They determined criteria to rule out the conditions other than CPH that cause limitation in mouth opening: (1) Limitation of the mouth opening that does not heal for a year or more; (2) The impossibility of forced mouth opening; (3) The absence of any symptoms, such as pain or sound, when opening the mouth in the TMJ area; (4) The absence of abnormal disc position and osteoarthritic condylar changes on magnetic resonance images; and (5) The absence of a history of mandibular trauma and inflammation. Seventeen of the 18 patients who satisfied the criteria agreed to undergo CT and participate in the study. CPH without interference with the zygomatic bone was detected in 13 out of 17 patients, and CPH with interference with the zygomatic bone was diagnosed in four patients. Moreover, the configurations and height levels of coronoid processes were examined. An angular shape was seen in only four cases with the zygomatic bone interference. The height of the coronoid process was reported to be significantly higher in the case group than in the control group.

In another study in which 16 patients with CPH (eight congenital, eight induced) were examined with cephalometric graphs together with a control group of 16 participants, no difference in the height of the condylar process was reported between the groups; however, the height of the coronoid process was reported to be significantly greater in the patient group[19].

Stopa *et al*[20] used the coronoid-condylar index (CCI) on CT images to diagnose CPH. They included in their study 13 participants with CPH and 13 participants without mandibular disease and reported that the CCI value, obtained using the measurement method they recommended, in the patients without CPH was approximately 1. They claimed that in the presence of CPH, the CCI increased to 1.25 and supposed that if the value rose above 1.15, there was a coronoid-condylar derangement.

In the study conducted by Tavassol *et al*[21], CT images of 41 patients, consisting of 40 healthy individuals and 1 with CPH, were examined. The condyle and coronoid lengths and Cor: Cd ratio were measured with reference to the tangent point that passed through the sigmoid notch. The mean ratio for the healthy group of the participants was 0.78. The values were calculated for only one patient with bilateral CPH: the ratio was 2.1 for the left side and 1.87 for the right side. The accuracy of the results of this study is questionable, as the reference tangent line is determined arbitrarily.

CONCLUSION

The Cd-Go and Cor-Go distances were statistically significantly increased in males on both the left and right sides. The evidence that these values were predominant in males may be related to the fact that the anatomical dimensions of males are larger than those of females. Although the Cd-Go and Cor-Go distances were higher in males, the ratio of Cor-Go: Cd-Go was preserved for both genders.

According to the results of this study using the Levandoski analysis, the prevalence of CPH was found to be 0.3%. In the present study, the images were re-evaluated after two weeks, and intra-observer agreement was found perfect. According to this result, can be say that Levandoski analysis is a reproducible method for diagnosis of CPH. This method is very simple and can be used in the diagnosis of CPH by measuring with any radiology software.

Present study was not conducted with a large sample group and only one case of CPH was found. in order to reliably obtain the prevalence of CPH, studies with larger sample groups and different ethnic populations are necessary.

ARTICLE HIGHLIGHTS

Research background

The images of the participants who underwent panoramic graphy were analysed retrospectively. The radiographs taken in the last 1 year retrospectively from the date of the study were used.

Research motivation

The fact that there are few studies on Coronoid Process Hyperplasia was the main motivation of this research.

Research objectives

To detect coronoid process hyperplasia by making repeatable measurements on panoramic radiographs.

Research methods

When Condyle (Cd)-Gonion (Go) and Coronoid (Cor)-Go distances were measured, the Cor-Go:Cd-Go ratio was calculated for the left and right side of each image. Line 1 is the maxillary vertical midline, which passes through the nasal septum. Lines 2, 3 and 4 are perpendicular to line 1 and are tangent to the lower border of the symphysis mandible, the tip of the condyle and the tip of the coronoid process, respectively.

Research results

Coronoid Process Hyperplasia was encountered in only one female out of 300 participants; the prevalence of CPH was found to be 0.3% in the sample subpopulation.

Research conclusions

The Cd-Go and Cor-Go distances were statistically significantly increased in males on both the left and right sides. The evidence that these values were predominant in males may be related to the fact that the anatomical dimensions of males are larger than those of females. Although the Cd-Go and Cor-Go distances were higher in males, the ratio of Cor-Go:Cd-Go was preserved for both genders.

Research perspectives

Present study was not conducted with a large sample group and only one case of CPH was found. in order to reliably obtain the prevalence of CPH, studies with larger sample groups and different ethnic populations are necessary.

FOOTNOTES

Author contributions: Erdem S developed the protocol and wrote manuscript, collected data and edited manuscript; both authors analysed data, have read and approve the final manuscript.

Institutional review board statement: Approval was granted by the Ethics Committee of University Ordu (No: 2021/231).

Conflict-of-interest statement: The authors declare that there is no conflict of interest.

Data sharing statement: Since the retrospective study was conducted, informed consent was not obtained from the patients. No data other than age and gender were recorded.

Country/Territory of origin: Turkey

ORCID number: Sule Erdem 0000-0002-8670-9947; Suheda Erdem 0000-0002-3214-7272.

S-Editor: Wang LL
L-Editor: A
P-Editor: Wang LL

REFERENCES

1 **Von Langenbeck B**. Angeborene kleinheit der unterkiefer. *Langenbeck's Archiv* 1861; **1**: 451-455
2 **Mulder CH**, Kalaykova SI, Gortzak RA. Coronoid process hyperplasia: a systematic review of the literature from 1995. *Int J Oral Maxillofac Surg* 2012; **41**: 1483-1489 [PMID: 22608198 DOI: 10.1016/j.ijom.2012.03.029]
3 **Goh YC**, Tan CC, Lim D. Coronoid hyperplasia: A review. *J Stomatol Oral Maxillofac Surg* 2020; **121**: 397-403 [PMID: 31904534 DOI: 10.1016/j.jormas.2019.12.019]
4 **Farronato M**, Lucchina AG, Mortellaro C, Fama A, Galbiati G, Farronato G, Maspero C. Bilateral Hyperplasia of the Coronoid Process in Pediatric Patients: What is the Gold Standard for Treatment? *J Craniofac Surg* 2019; **30**: 1058-1063 [PMID: 30339589 DOI: 10.1097/SCS.0000000000004768]
5 **Kubota Y**, Takenoshita Y, Takamori K, Kanamoto M, Shirasuna K. Levandoski panographic analysis in the diagnosis of hyperplasia of the coronoid process. *Br J Oral Maxillofac Surg* 1999; **37**: 409-411 [PMID: 10577758 DOI: 10.1054/bjom.1999.0159]
6 **Ghazizadeh M**, Sheikhi M, Salehi MM, Khaleghi A. Bilateral coronoid hyperplasia causing painless limitation of mandibular movement. *Radiol Case Rep* 2018; **13**: 112-117 [PMID: 29487645 DOI: 10.1016/j.radcr.2017.11.001]
7 **Alias A**, Ibrahim ANM, Bakar SNA. Morphometric Analysis of Coronoid Process of Mandible by CT in the Malaysian Population: An Important Step for Determination of Sex. *J Dent Sci Res Ther* 2018; **5**: 1-8 [DOI: 10.29199/2637-7055/dsrt.101015]
8 **Fukumori T**, Tagawa T, Inui M. Bilateral coronoid process hyperplasia and short stature. A case report. *Int J Oral Maxillofac Surg* 1993; **22**: 139-144 [PMID: 8340622 DOI: 10.1016/s0901-5027(05)80237-1]
9 **Huang W**, Akashi M, Nishio T, Negi N, Kimoto A, Hasegawa T. Can four-dimensional computed tomography support diagnosis and treatment planning? *Oral Maxillofac Surg* 2020; **24**: 515-520 [PMID: 32621034 DOI: 10.1007/s10006-020-00876-1]
10 **Leonardi R**, Caltabiano M, Lo Muzio L, Gorlin RJ, Bucci P, Pannone G, Canfora M, Sorge G. Bilateral hyperplasia of the mandibular coronoid processes in patients with nevoid basal cell carcinoma syndrome: an undescribed sign. *Am J Med Genet* 2002; **110**: 400-403 [PMID: 12116218 DOI: 10.1002/ajmg.10432]
11 **Rowe NL**. Bilateral developmental hyperplasia of the mandibular coronoid process. a report of two cases. *Br J Oral Surg* 1963; **1**: 90-104 [PMID: 14089492 DOI: 10.1016/s0007-117x(63)80056-6]
12 **Bayar GR**, Akcam T, Gulses A, Sencimen M, Gunhan O. An excessive coronoid hyperplasia with suspected traumatic etiology resulting in mandibular hypomobility. *Cranio* 2012; **30**: 144-149 [PMID: 22606859 DOI: 10.1179/crn.2012.021]
13 **Sarnat BG**, Engel MB. A serial study of mandibular growth after removal of the condyle in the Macaca rhesus monkey. *Plast Reconstr Surg (1946)* 1951; **7**: 364-380 [PMID: 14833933 DOI: 10.1097/00006534-195105000-00002]
14 **Levandoski RR**. Mandibular whiplash. Part II. An extension flexion injury of the temporomandibular joints. *Funct Orthod* 1993; **10**: 45-51 [PMID: 8359749]
15 **Piedra I**. The Levandoski Panoramic Analysis in the diagnosis of facial and dental asymmetries. *J Clin Pediatr Dent* 1995; **20**: 15-21 [PMID: 8634190]
16 **Biagi R**, Craparo A, Trovato F, Butti AC, Salvato A. Diagnosis of dental and mandibular asymmetries in children according to Levandoski Panoramic Analysis. *Eur J Paediatr Dent* 2012; **13**: 297-300 [PMID: 23270287]
17 **Lee JC**. Retraction notice to "Therapeutic effect of prostaglandin E1 in monocrotaline-induced pulmonary arterial hypertension rats" by Lee JC (Anat Cell Biol 2017;50:60-8). *Anat Cell Biol* 2017; **50**: 245 [PMID: 29043105 DOI: 10.5115/acb.2017.50.3.245]
18 **Izumi M**, Isobe M, Toyama M, Ariji Y, Gotoh M, Naitoh M, Kurita K, Ariji E. Computed tomographic features of bilateral coronoid process hyperplasia with special emphasis on patients without interference between the process and the zygomatic bone. *Oral Surg Oral Med Oral Pathol Oral Radiol Endod* 2005; **99**: 93-100 [PMID: 15599354 DOI: 10.1016/j.tripleo.2004.04.013]
19 **Isberg A**, Eliasson S. A cephalometric analysis of patients with coronoid process enlargement and locking. *Am J Orthod Dentofacial Orthop* 1990; **97**: 35-40 [PMID: 2296941 DOI: 10.1016/S0889-5406(05)81706-8]
20 **Stopa Z**, Wanyura H, Kowalczyk P. Coronoid-condylar index in assessing of mandibular coronoid hyperplasia. Preliminary results. *Adv Med Sci* 2013; **58**: 429-433 [PMID: 24327533 DOI: 10.2478/ams-2013-0005]
21 **Tavassol F**, Spalthoff S, Essig H, Bredt M, Gellrich NC, Kokemüller H. Elongated coronoid process: CT-based quantitative analysis of the coronoid process and review of literature. *Int J Oral Maxillofac Surg* 2012; **41**: 331-338 [PMID: 22192388 DOI: 10.1016/j.ijom.2011.10.033]

Published by **Baishideng Publishing Group Inc**
7041 Koll Center Parkway, Suite 160, Pleasanton, CA 94566, USA
Telephone: +1-925-3991568
E-mail: bpgoffice@wjgnet.com
Help Desk: https://www.f6publishing.com/helpdesk
https://www.wjgnet.com

ISSN 1949-8470 (online)

World Journal of *Radiology*

World J Radiol 2022 June 28; 14(6): 114-179

Published by Baishideng Publishing Group Inc

World Journal of Radiology

Contents

Monthly Volume 14 Number 6 June 28, 2022

World Journal of Radiology

Monthly Volume 14 Number 6 June 28, 2022

Contents

ABOUT COVER

Editorial Board Member of *World Journal of Radiology*, Jaber S Alqahtani, MSc, PhD, Academic Research, Assistant Professor, Research Scientist, Department of Respiratory Care, Prince Sultan Military College of Health Sciences, Dammam 34313, Saudi Arabia. Alqahtani-Jaber@hotmail.com

AIMS AND SCOPE

The primary aim of *World Journal of Radiology* (*WJR*, *World J Radiol*) is to provide scholars and readers from various fields of radiology with a platform to publish high-quality basic and clinical research articles and communicate their research findings online.

WJR mainly publishes articles reporting research results and findings obtained in the field of radiology and covering a wide range of topics including state of the art information on cardiopulmonary imaging, gastrointestinal imaging, genitourinary imaging, musculoskeletal imaging, neuroradiology/head and neck imaging, nuclear medicine and molecular imaging, pediatric imaging, vascular and interventional radiology, and women's imaging.

INDEXING/ABSTRACTING

The *WJR* is now abstracted and indexed in Emerging Sources Citation Index (Web of Science), PubMed, PubMed Central, Reference Citation Analysis, China National Knowledge Infrastructure, China Science and Technology Journal Database, and Superstar Journals Database. The 2021 edition of Journal Citation Reports® cites the 2020 Journal Citation Indicator (JCI) for *WJR* as 0.51.

RESPONSIBLE EDITORS FOR THIS ISSUE

NAME OF JOURNAL
World Journal of Radiology

ISSN
ISSN 1949-8470 (online)

LAUNCH DATE
January 31, 2009

FREQUENCY
Monthly

EDITORS-IN-CHIEF
Thomas J Vogl

EDITORIAL BOARD MEMBERS
https://www.wjgnet.com/1949-8470/editorialboard.htm

PUBLICATION DATE
June 28, 2022

INSTRUCTIONS TO AUTHORS
https://www.wjgnet.com/bpg/gerinfo/204

GUIDELINES FOR ETHICS DOCUMENTS
https://www.wjgnet.com/bpg/GerInfo/287

GUIDELINES FOR NON-NATIVE SPEAKERS OF ENGLISH
https://www.wjgnet.com/bpg/gerinfo/240

PUBLICATION ETHICS
https://www.wjgnet.com/bpg/GerInfo/288

PUBLICATION MISCONDUCT
https://www.wjgnet.com/bpg/gerinfo/208

ARTICLE PROCESSING CHARGE
https://www.wjgnet.com/bpg/gerinfo/242

STEPS FOR SUBMITTING MANUSCRIPTS
https://www.wjgnet.com/bpg/GerInfo/239

ONLINE SUBMISSION
https://www.f6publishing.com

World Journal of Radiology

Submit a Manuscript: https://www.f6publishing.com

World J Radiol 2022 June 28; 14(6): 114-136

DOI: 10.4329/wjr.v14.i6.114

ISSN 1949-8470 (online)

REVIEW

Tuberculosis conundrum - current and future scenarios: A proposed comprehensive approach combining laboratory, imaging, and computing advances

Suleman Adam Merchant, Mohd Javed Saifullah Shaikh, Prakash Nadkarni

Specialty type: Radiology, nuclear medicine and medical imaging

Provenance and peer review: Invited article; Externally peer reviewed.

Peer-review model: Single blind

Peer-review report's scientific quality classification

Grade A (Excellent): A
Grade B (Very good): B
Grade C (Good): C, C
Grade D (Fair): 0
Grade E (Poor): 0

P-Reviewer: Barbosa OA, Brazil; Phan LMT, South Korea; Primadhi RA, Indonesia

A-Editor: Zhu JQ, United States

Received: January 17, 2022
Peer-review started: January 17, 2022
First decision: March 16, 2022
Revised: April 17, 2022
Accepted: May 27, 2022
Article in press: May 27, 2022
Published online: June 28, 2022

Suleman Adam Merchant, Lokmanya Tilak Municipal Medical College and General Hospital, Mumbai 400022, Maharashtra, India

Mohd Javed Saifullah Shaikh, Department of Radiology, North Bengal Neuro Centre, Jupiter magnetic resonance imaging, Diagnostic Centre, Siliguri 734003, West Bengal, India

Prakash Nadkarni, College of Nursing, University of Iowa, Iowa 52242, IA, United States

Corresponding author: Suleman Adam Merchant, MBBS, MD, Former Dean, Professor & Head (Radiology), Lokmanya Tilak Municipal Medical College and General Hospital, Sion Hospital, Mumbai 400022, Maharashtra, India. suleman.a.merchant@gmail.com

Abstract

Tuberculosis (TB) remains a global threat, with the rise of multiple and extensively drug resistant TB posing additional challenges. The International health community has set various 5-yearly targets for TB elimination: mathematical modelling suggests that a 2050 target is feasible with a strategy combining better diagnostics, drugs, and vaccines to detect and treat both latent and active infection. The availability of rapid and highly sensitive diagnostic tools (GeneXpert, TB-Quick) will vastly facilitate population-level identification of TB (including rifampicin resistance and through it, multi-drug-resistant TB). Basic-research advances have illuminated molecular mechanisms in TB, including the protective role of Vitamin D. Also, Mycobacterium tuberculosis impairs the host immune response through epigenetic mechanisms (histone-binding modulation). Imaging will continue to be key, both for initial diagnosis and follow-up. We discuss advances in multiple imaging modalities to evaluate TB tissue changes, such as molecular imaging techniques (including pathogen-specific positron emission tomography imaging agents), non-invasive temporal monitoring, and computing enhancements to improve data acquisition and reduce scan times. Big data analysis and Artificial Intelligence (AI) algorithms, notably in the AI subfield called "Deep Learning", can potentially increase the speed and accuracy of diagnosis. Additionally, Federated learning makes multi-institutional/multi-city AI-based collaborations possible without sharing identifiable patient data. More powerful hardware designs - *e.g.*, Edge and Quantum Computing- will facilitate the role of computing applications in TB. However, "Artificial Intelligence needs real Intelligence to guide it!" To have maximal impact, AI must use a holistic

approach that incorporates time tested human wisdom gained over decades from the full gamut of TB, *i.e.*, key imaging and clinical parameters, including prognostic indicators, plus bacterial and epidemiologic data. We propose a similar holistic approach at the level of national/international policy formulation and implementation, to enable effective culmination of TB's endgame, summarizing it with the acronym "TB - REVISITED".

Key Words: Tuberculosis; Radiology; GenXpert; Artificial intelligence; Molecular imaging; Quantum computing

Core Tip: A Holistic (comprehensive) approach is suggested to achieve tuberculosis (TB) elimination goals. Early diagnosis especially for Multi-Drug Resistant TB. Utility of Modern Rapid Diagnostic Tools. The role of Imaging in TB and key radiological signs. Comprehensive Artificial Intelligence(AI) algorithms incorporating key Imaging and clinical signs. The role of Vitamin D supplementation in complementing the TB drug regimen. Molecular Imaging. Quantum Computing and other perspectives in TB strategies to help achieve the various targets set for elimination of TB. A unified Global approach with edge computing/ dashboards and other technological innovations.

Citation: Merchant SA, Shaikh MJS, Nadkarni P. Tuberculosis conundrum - current and future scenarios: A proposed comprehensive approach combining laboratory, imaging, and computing advances. *World J Radiol* 2022; 14(6): 114-136
URL: https://www.wjgnet.com/1949-8470/full/v14/i6/114.htm
DOI: https://dx.doi.org/10.4329/wjr.v14.i6.114

INTRODUCTION

Nearly 1.5 centuries after Robert Koch discovered *Mycobacterium tuberculosis* (MTB) in 1882, tuberculosis (TB) remains a global threat and a deadly human pathogen, ubiquitous enough to comprise an occupational hazard for medical personnel in many locales. Its high prevalence in both immunocompetent and immunocompromised individuals historically made TB a top-10 cause of death worldwide and the leading cause of death from a single infectious agent, though it fell to 13th after being overtaken by COVID-19 in 2021[1]. 95% of cases and deaths occur in developing countries. About one-quarter of the world's population has a TB infection, though most are not (yet) symptomatic and contagious[2]. Because people with active TB can infect 5-15 other people through close contact over a single year, the consequence of delayed/missed diagnosis cascade[2]. However, TB is curable and preventable[2].

The incessant rise of Multidrug-resistant TB (MDR-TB) and extensively drug-resistant (XDR) TB, either primary or acquired, pose an additional challenge[3,4]. Incidence of either varies in different studies: More concerning, only 1/3rd of such individuals accessed treatment in 2020[2].

The three countries with the largest share of the global burden in 2019 were India (27%, 2.8 million cases annually, 150,000 MDR-TB cases every year), China (14%), and the Russian Federation (8%)[5,6]. In 2020, an estimated 10 million people fell ill with TB worldwide. The largest number of new TB cases occurred in the WHO South-East Asian Region (43%), African Region (25%), and Western Pacific (18%)[2]. In descending case-count order, eight countries account for two thirds of the total: India, China, Indonesia, the Philippines, Pakistan, Nigeria, Bangladesh, and South Africa[2].

Ending the TB epidemic by 2030 is among the health targets of the United Nations Sustainable Development Goals[2]. The End TB Strategy defines five-yearly milestones/targets for reducing TB cases and deaths. The targets for 2030 are a 90% reduction in TB deaths and an 80% reduction in new cases per year, compared with levels in 2015, with a reduction in new cases to < 1 per million population annually by 2050[7,8].

DIAGNOSIS OF TB

MDR-TB: Advances in laboratory diagnosis

MDR-TB is defined as an infection with MTB strains non-responsive to isoniazid (INH) and rifampicin (RIF), the 2 most effective first-line anti-TB drugs. Mutations in the INH and RIF resistance gene confers high competitive fitness, favoring their spread: >90% of RIF-resistant strains are also INH-resistant[9-11]. Most people develop MDR-TB because of delayed or incomplete treatment, increasing subsequent

healthcare costs dramatically[12]. MDR-TB is curable with second-line drugs: In 2018, the treatment success rate of MDR-TB patients was 59% worldwide. The earlier treatment regimens for up to 2 years have been superseded by WHO's updated (2021) recommendation for shorter (9-11 mo) and fully oral regimens, which increase compliance greatly[2,13,14]. Previously laboratory confirmation of TB by culture required 6-8 wk: Diagnosing MDR-TB, which used to be exclusively clinical, involved delays of up to 4 mo to identify therapeutic response failure; coupled with persistently positive sputum smears after 4 mo of regular treatment with a first-line DOTS (Directly Observed Treatment, Short-course Regimen)[15-17]. Such therapeutic setbacks especially impacted impoverished or illiterate patients psychologically: after expecting a treatment duration of 7-9 mo only, to be informed halfway through that a new regimen was necessary, they often stopped treatment and were lost to follow-up, eventually spreading MDR-TB to others, exponentially. The spread of MDR-TB was also worsened by policies of using the much cheaper 'regular TB' drug regimen empirically: Treating MDR-TB is 5-200 times more expensive than treating nondrug resistant TB[18].

However, PCR based technologies such as cartridge based nucleic acid amplification techniques [CBNAAT] (GeneXpert®, Cepheid United States, introduced in 2010), can now rapidly detect both MTB genetic material from sputum samples and RIF resistance within 2 h using the current generation of technology, without requiring special technicians/rooms and barely occupying the space of a computer printer, at a cost of $5/test[19,12]. This has been called the most exciting innovation in TB diagnostics in over a century[12]. It is recommended by WHO, which developed policies/guidelines and monitoring frameworks for its use to support developing countries' Ministries of Health (MOHs) in their implementation[12,20]. The latest GeneXpert technology (MTB/RIF Ultra) has a ten-fold improvement in the lower limit of TB detection, and improves differentiation of certain silent mutations, RIF resistance detection in mixed infections (in 3-7 d), increased specificity in detecting RIF resistance in paucibacillary specimens, and better sensitivity in both pulmonary samples and extrapulmonary samples such as pleural/ascitic fluid and biopsied material such as lymph nodes[12,19,21-23]. Our group were amongst the first to successfully use it for lymph nodes and also to recommend the same being used to detect MDR TB upfront.

TB-QUICK is a recent ultrasensitive MTB detection platform which combines loop-mediated isothermal amplification and clustered regularly interspaced short palindromic repeats (CRISPR)-Cas12b reaction for M TB detection. It is highly sensitive (with a near single-copy sensitivity), requires less sample input and offers even a shorter turnaround time than Gene-Xpert for RIF resistance[24].

In South Africa, national screening of high-risk groups [*e.g.*, human immunodeficiency virus (HIV)-infected individuals), deployment of Gene-Xpert machines, treating latent TB, and using quality MTB drugs with shorter regimens led to a decline in TB[25]. We suggest that an identical approach be deployed elsewhere to control the spread of this dreaded scourge.

Overall, TB, either incident or prevalent, is found in 4.1% of the MDR-TB contacts, which is higher than the corresponding prevalence rates of 1.9% and 1.7% reported among household contacts of drug-susceptible TB in the same locality[26,27]. In a study it was shown that RFLP analysis confirmed the transmission of MDR-TB among household contacts while regression analysis showed XDR-TB had an even higher risk of household transmission among all MDR-TB cases[28]. We have successfully used CBNAAT to diagnose extrapulmonary TB, and feel this has tremendous potential to revolutionize TB, especially MDR-TB early diagnosis, treatment, and further management. Piatek *et al*[12] and Mechal *et al*[23] have independently reported the same.

National TB control programs are working to eliminate TB mainly by intensifying efforts to find and cure patients with active disease. Mathematical models developed by Dye and Williams[29] suggest that, while most TB patients can be cured with present drug regimens, the 2050 target is far more likely to be achieved with a synergistic combination of diagnostics, drugs, and vaccines to detect and treat both latent infection and active disease.

IMAGING METHODS IN TUBERCULOSIS

Note: While interventional radiology plays a major role in TB treatment, we deliberately limit this review's scope to diagnostic/prognostic imaging.

TB has a known propensity for dissemination from its primary site and can affect virtually any organ system in the body. It therefore demonstrates a variety of clinical and radiologic findings and can mimic numerous other diseases[30]. Hence, the role of imaging in TB has grown exponentially. The possibility of TB is often first suggested on an imaging study, particularly in relatively inaccessible sites.

In a known case of TB, imaging is often requested to assess the extent of disease, evaluate response to therapy, or detect residual infection after completion of anti-TB therapy. Imaging is also vital in guiding aspiration biopsies, therapeutic drainage of collections of pathological fluid *etc*[31]. Hence, Radiologists will continue to play a vital role in eliminating TB.

Imaging findings in TB depend upon the extent of the disease process. Familiarity with various imaging features permits early diagnosis and prompt management, thereby reducing patient morbidity [30].

In this section, we will also refer to various techniques that fall into the category of "Molecular Imaging Technology" (MIT). MIT visualizes molecules of relevance to a disease at both microscopic levels and in living subjects. For the latter, it provides 3D spatial characterization (often using existing imaging modalities) and non-invasive, temporal monitoring within the same subject[32]. MIT may augment TB research by advancing fundamental knowledge and accelerating the development of novel diagnostics, biomarkers, and therapeutics[32].

Conventional Chest radiography

While radiology training has moved away from conventional radiology, most of the developing world's population cannot access tomographic (cross sectional) imaging readily for logistic or financial reasons. Therefore, the time-tested signs/patterns of TB in conventional chest X-ray (CXR) cannot be forgotten. There is no excuse for missing a Ghon's focus/complex or lamellar effusion of childhood TB in a CXR taken for a different purpose (Figure 1). CXR has high sensitivity but limited specificity for detecting pulmonary TB. As recommended by WHO's guidelines, it is very suitable for TB screening and triaging, to stratify for risk, assess asymptomatic active disease, and for follow-up[33]. Stability of radiographic findings for 6 mo distinguishes inactive from active disease. Where CT is unavailable, lordotic view and penetrated (high kV) views improve depiction of the lung apices and mediastinal/carinal nodes, respectively[34]. Dual-energy radiography with bone subtraction, has also been used to improve depiction of the lung apices[34].

Ultrasonography

Ultrasonography (US) is one of the commonest recommended examinations for TB, including in the evaluation of suspected/affected lymph nodes and for guiding biopsies for the same. Basic details are well known and beyond the scope of this manuscript. It is a very useful non-invasive examination method in children including those with cervical lymphadenitis (across age groups). The US signs of hilar absence, short to long axis (S/L) ratio ≥ 0.5, an unclear edge, necrosis, an echogenic thin layer, strong echoes and capsular or peripheral vascularity; may aid in the diagnosis of cervical tuberculous lymphadenitis[35]. Endobronchial US-guided fine-needle aspiration biopsy for intrathoracic TB lymphadenopathy is valuable when bronchoalveolar lavage and sputum culture are ambiguous[36].

US elastography: [Strain/shear wave] is useful for further evaluation of lymph nodes and the detection of complications such as fibrosis[37,38]. US elastography (USE) techniques are classified by the type of excitation applied: (1) Strain elastography; and (2) Shear wave elastography. Strain elastography includes constant force-induced displacement (static/quasi-static imaging) or acoustic energy-induced physiologic motion. Shear wave elastography is sub-classified as: Transient elastography, point shear wave elastography (pSWE), two-dimensional SWE (2D-SWE), and three-dimensional SWE. Shear wave USE has clear advantages over strain USE by virtue of being quantitative and user independent. However, shear wave measurements are effective only till 3 cm depth from the skin surface, as the shear wave signal tends to attenuate rapidly beyond this depth. This though is an ideal depth for evaluating most cervical TB lymph nodes. On the color elastogram, red represents the softest and blue represents the hardest areas, while intermediate stiffness is indicated by green. These colors represent the relative hardness of tissues on the elastogram (Figure 2A-C). The units of measurement are kilopascal (kPA) or Velocity (V) in meters/sec (m/s) - [1 KPa = 3 × V^2(m/s)][39].

Cervical, axillary, and inguinal lymph nodes are easily evaluated by standard USE; and USE has the potential to non-invasively differentiate tuberculous from metastatic lymph nodes because of the latter's greater stiffness[40,41]. On strain USE a cut-off value of 3.0 (strain ratio) has been suggested for determining if a mass/tissue is benign or malignant[42-44]. Shehata *et al*[43] stated that the best shear wave elasticity ratio cut-off value that allows significant differentiation between benign and malignant mass groups was > 4.9. USE also has great potential for marking biopsy sites in a lymph node for collecting samples for confirmation of the disease, as well as for drug sensitivity purposes, especially in drug resistant TB (Figure 2D). The samples collected should also be run through CBNAAT techniques such as GenXpert. This will enable MDR TB to be detected upfront (refer 'diagnosis of TB section).

These non-invasive techniques will be useful both for initial diagnosis and follow-up, including treatment - response assessment and monitoring of sequelae; *e.g.*, post TB medication Liver fibrosis (Figure 3); where avoiding a liver biopsy would be a great boon[38]. Shear wave Elastography features while assessing liver tissue stiffness are as follows: (1) Normal: 1.37 m/s, Metavir F0-F1; (2) Mild Fibrosis: 1.37 - 1.55 m/s, Metavir F2; (3) Advanced Fibrosis: 1.55 - 1.8 m/s, Metavir F3; and (4) Cirrhosis: > 1.8 m/sec, F4[39]. Metavir is an acronym for "meta-analysis of histological data in viral hepatitis".

EUS: EUS elastography has proven to be useful for the evaluation of mediastinal and abdominal lymph nodes and can provide additional information about the structure and pathology of mediastinal and abdominal lymph nodes. It is an excellent method for targeting different areas of the lymph node to avoid unnecessary needle passes in EUS guided biopsies[40].

Multimodal ultrasound imaging: Multimodal ultrasound imaging combines several US modalities simultaneously: Color Doppler US, US elastography, and contrast-enhanced ultrasound (discussed

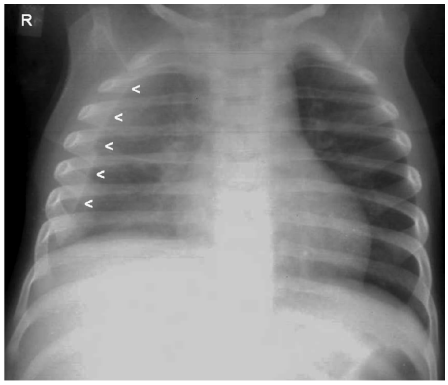

DOI: 10.4329/wjr.v14.i6.114

Figure 1 Lamellar pleural effusion. Frontal chest radiograph of an 18-mo-old child with Pulmonary tuberculosis (primary complex) reveals a lamellar pleural effusion- (homogeneous increased radio-opacity along lateral aspect of right lung field with blunting of the right costophrenic angle- mimicking the appearance of pleural thickening) - [arrowheads]. Image courtesy – Department of Radiology, KEM Hospital, Mumbai.

shortly). It differentiates tuberculous from non-tuberculosis superficial tuberculous lymphadenitis with 100.00% sensitivity and a 94.12% positive predictive value[45].

Micro-Bubbles in diagnosis and theragnostics: "Theragnostics" combines disease diagnosis with therapy[46,47]. Micrometer-sized gas bubbles "micro-bubbles (MB)" allow for intravenous contrast-enhanced US: MBs oscillate resonantly when subjected to high-frequency US, which they reflect intensely[48].

The utility of the same in diagnostic radiology, especially for the urinary tract, is well established[49]. They can readily be utilized for US assessment of vesico-ureteric reflux in patulous golf-hole ureterovesical junctions seen in TB, circumventing the use of ionizing radiation. Kiessling *et al*[50] discuss conjugation of antibodies to the MB surface and incorporation of various molecules inside or onto the MB shell.

MBs have potential for targeted therapies. High-intensity US (HIUS) temporarily disrupts the blood-brain barrier, allowing medications contained in MBs, which HIUS also disrupts, to treat CNS cancers and intracranial TB[50]. Additionally, MBs can deliver medications to TB lymph nodes, as well as gene therapy to tissues exhibiting congenital disease phenotypes[51].

Ultra-high-frequency US and Ultrasound biomicroscopy: Ultrasound biomicroscopy (UBM) is a superb tool to assess superficial TB lesions such as skin TB (lupus vulgaris), both in their diagnosis, as well as during follow up (Figure 4). This is safe and easily repeatable and avoids the use of repeated biopsies. Ma *et al*[48] have designed a small-aperture (0.6 mm × 3 mm) IVUS probe optimized for high-frequency contrast imaging. Their design utilizes a dual-frequency (6.5 MHz/30 MHz) transducer for exciting microbubbles at low frequencies (near their resonance) and detecting their broadband harmonics at high frequencies. Fei *et al*[52] have developed broadband lithium niobate single element ultrasonic transducers in the range of 100-300 MHz for high resolution imaging. They claim a performance comparable to optical resolution and state that availability of ultrahigh frequency transducers will make Ultrasound Biomicroscopy (UBM) a promising tool to study fine biological structures. Future applications of CEUS and UBM could be expected in TB too.

Dark Field Radiography

X-ray dark-field radiography relies on ultra-small-angle scattering (diffraction) of X-rays at the material interfaces within the tissue under investigation[53]. "Dark field", when applied to visible light, refers to the bright appearance of scattering objects on a dark background. Healthy lung tissue, with numerous air/parenchyma interfaces in the alveoli, produces a relatively high signal[54,55]. Introduced experimentally in 2008, Dark field radiography may increase sensitivity for early detection of varied lung pathologies involving the alveoli, including tuberculosis.

Computed Tomography

Computed tomography (CT) enables non-invasive diagnosis of TB in patients with negative sputum examination or no sputum production (as occurs in the follow-up of patients on anti-tuberculosis therapy (ATT) or at presentation) non-invasively: it permits empirical ATT initiation until culture results are obtained[56]. Contrast-enhanced CT is the investigation of choice for evaluating mediastinal LNs and identifying pleural enhancement in empyema (Figure 5). High-resolution CT (HRCT) reconstructions are especially useful to detect miliary and centrilobular nodules, ground-glass opacities,

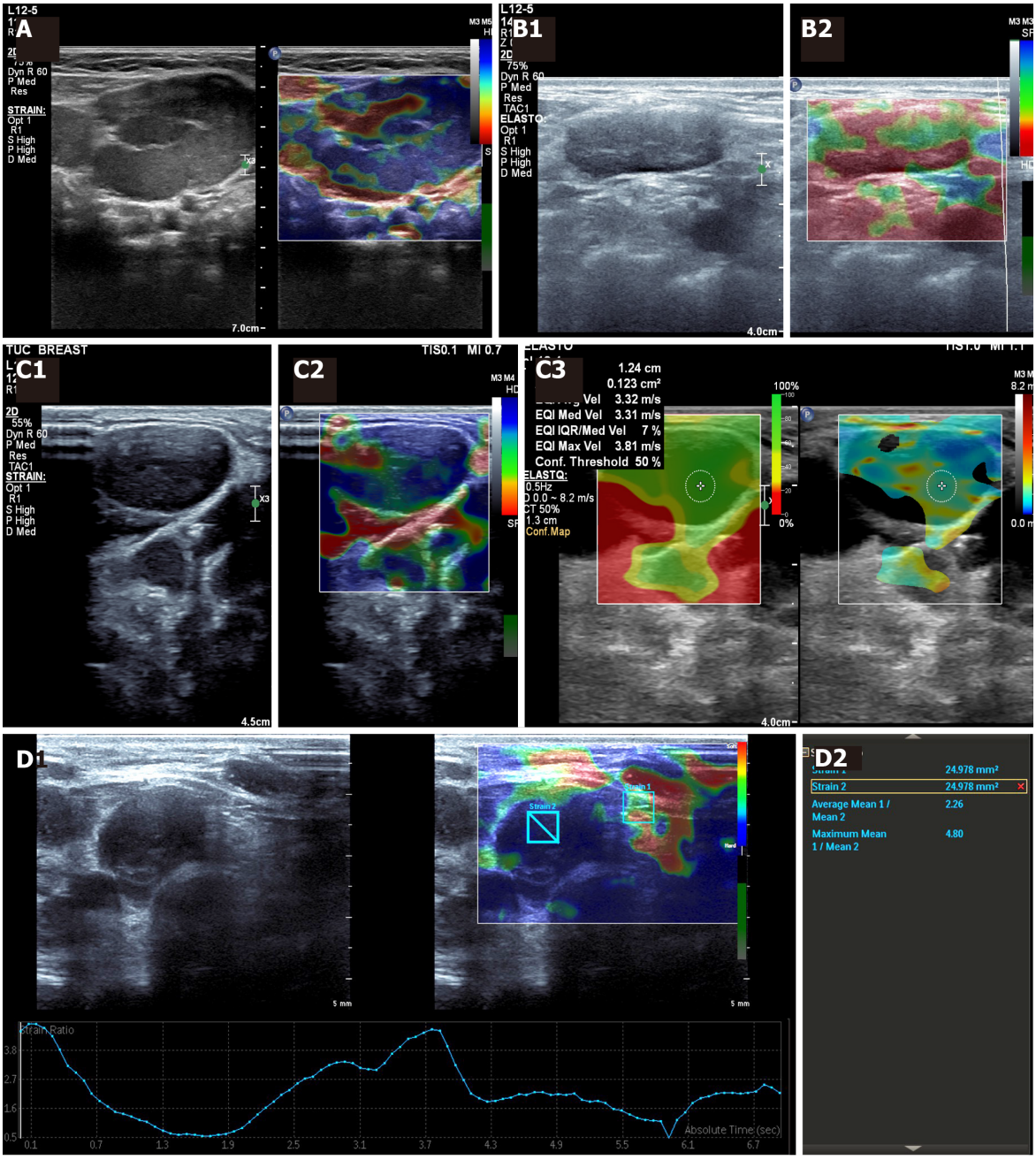

DOI: 10.4329/wjr.v14.i6.114

Figure 2 Cervical tuberculosis lymph node. A: Cervical tuberculosis lymph node: Ultrasonography (US) elastography - central necrotic area appears soft (red); B: Tuberculous lymphadenopathy: A 16-year-old female with fever and neck swelling; B1: Grey scale B-mode image: shows an enlarged lymph node with diffusely hypoechoic echotexture and loss of fatty hilum; B2: Strain US Elastography: Showing a mixed pattern, predominantly soft (red); C: Tuberculous lymphadenopathy: 35-year-old male with neck swelling and history of weight loss; C1: Grey scale image: shows an enlarged lymph node with diffusely hypoechoic echotexture and loss of fatty hilum; C2: Strain US elastography: Showing soft areas within (red areas) s/o necrosis / liquefaction; C3: Shear wave US elastography: Shows relatively low shear wave values; D: Tuberculous lymphadenopathy: Neck US of a 14-year-old female (known case of drug resistant tuberculosis); D1: Grey scale B-mode image: enlarged lymph nodes with diffusely hypoechoic echotexture and loss of fatty hilum; D2: Strain US Elastography: The strain elastography reveals a low strain ratio (2.26). Elastography details are noted on the elastography graph too. Trucut biopsy was done - results awaited. Images courtesy Dr. Chaubal N, Thane Ultrasound Centre, India.

and air-trapping (Figure 6).

Multi-detector CT and its volumetric capability enables earlier and more accurate diagnosis of pulmonary lesions: detection of radiographically occult disease; assessment of disease activity, parenchymal lesions (including miliary TB), mediastinal lymph nodes (LNs), and visualized bones. It also helps evaluate complications like bronchiectasis, cavitation, associated fungal balls, LN necrosis, and pleural/airway/diaphragmatic pathology (Figure 7).

Spectral imaging on CT (dual-/tri-/quad-energy), when it becomes widely available, should further enhance radiologists' diagnostic armamentarium[38]. Khan *et al*[57] concluded that dual energy CT is superior to high-resolution CT for assessing pulmonary TB. Recent CT iterative reconstructions allow

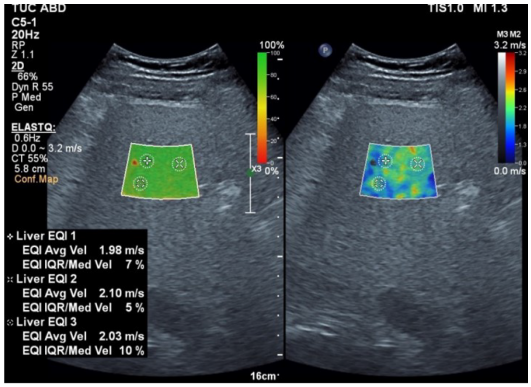

DOI: 10.4329/wjr.v14.i6.114

Figure 3 Shear wave ultrasonography elastography of Liver: 28-year male, on tuberculosis medications for 8 mo, with altered liver functions. Stiffness median - 1.76 metres/sec -- Metavir F3: indicative of Enhanced liver fibrosis. Images courtesy Dr. Chaubal N, Thane Ultrasound Centre, India.

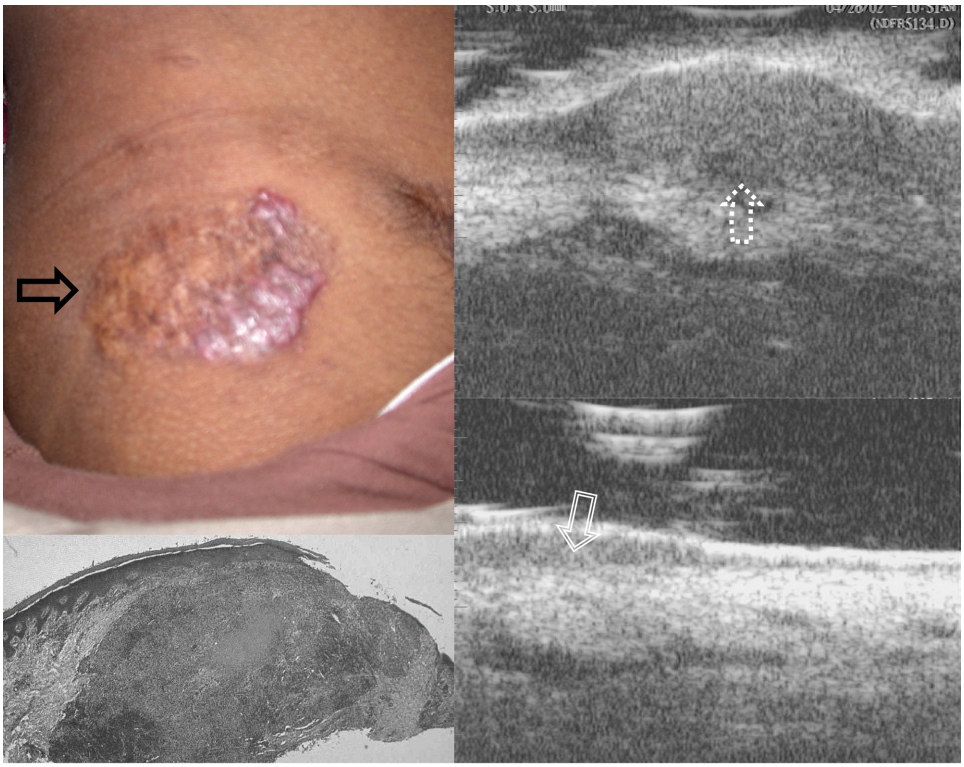

DOI: 10.4329/wjr.v14.i6.114

Figure 4 Ultrasound Biomicroscopy scanned at 50 MHz - Skin tuberculosis - lupus vulgaris. A well-defined reddish-brown plaque with papulo-nodular borders is seen on the skin (black arrow), Ultrasound biomicroscopy (UBM) shows a well-defined heterogenous mass lesion in the dermis (up arrow-dotted), Histopathology shows a well-defined tuberculous granuloma in the dermis (white filled arrow), Follow up UBM after 6 mo of AKT shows marked decrease in the size of granuloma in the dermis (down arrow- dashed). Images Courtesy Dr. Bhatt K, UBM Institute & Sonography Centre, Mumbai.

significant X-ray dose reduction and improved image quality over conventional filtered back-projection reconstruction methods[58]. These advantages would enable greater use of CT in Molecular Imaging.

Magnetic Resonance Imaging

Magnetic resonance imaging (MRI) yields high soft tissue contrast and resolution with high sensitivity for detection of tissue necrosis, as occurs in TB[59]. While MRI lacks the ionizing-radiation hazard, it usually requires longer acquisition times. However, more recently, short-sequence lung MRI (such as HASTE T2, BLADE T2, TRUFI T2 and VIBE T1) have been used for pulmonary imaging in TB patients [60]. Cardiac MRI has made rapid progress too and is the ideal modality for diagnosing Cardiac TB.

Cardiac TB can take the form of Pericarditis, Peri-Myocarditis or a Pancarditis. Pericardial TB is the commonest manifestation of Cardiac TB (Figure 8A and B). In its early form it is seen as pericardial thickening. In advanced cases, pericardial effusion and septations are seen. Accompanying para-spinal

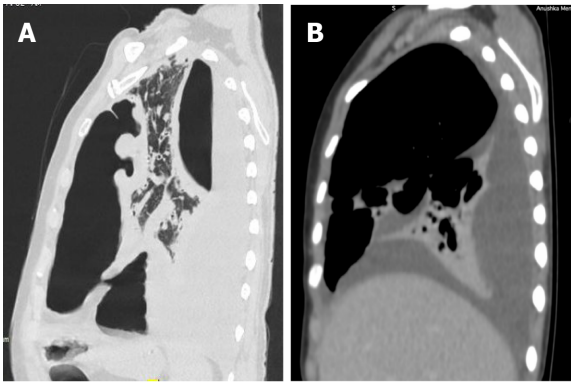

DOI: 10.4329/wjr.v14.i6.114

Figure 5 Tuberculous pyo-pneumothorax. A: Sagittal high-resolution computed tomography image in lung window showing a thick-walled cavity communicating with the left pleural space. A large loculated collection in the left pleural space showing air-fluid level; B: Sagittal image in a mediastinal window showing a Right pleural effusion with partial collapse of Right lower lobe. Images courtesy Dr. Thakkar H, Prof & Head (Radiology), KEM Hospital, Mumbai.

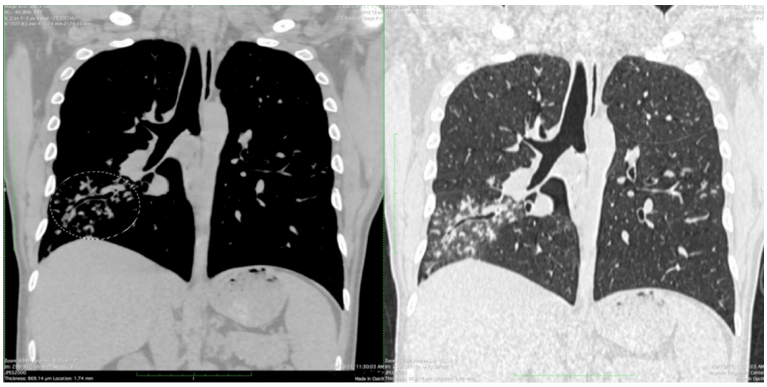

DOI: 10.4329/wjr.v14.i6.114

Figure 6 Endobronchial spread of tuberculosis. Coronal computed tomography images in mediastinal and lung windows; demonstrative of multiple discrete and confluent centrilobular nodules in the lateral basal segment of right lower lobe, some of which show V-Y branching pattern ("tree in bud appearance"- circled area). Enlarged mediastinal lymph nodes are also observed in the subcarinal region. Images courtesy Dr. Joshi A, Prof & Head (Department of Radiology), LTMMC & LTMGH, Mumbai.

abscesses and pleural effusions can easily be seen (Figure 8C). This may resolve on therapy or can undergo calcification. Myocardial TB is rare and in the presence of a myocardial mass lesion, can frequently be misdiagnosed as a neoplasm. The presence of associated diffuse or non-contiguous pericarditis in the presence of myocardial masses is a good pointer to TB etiology of the cardiac masses: The 'Myocarditis - Pericarditis Complex' sign[61] (Figure 9). In a case series of 11 Cardiac TB cases imaged on a 3 Tesla MRI scanner, myocardial lesions were seen in 6 cases (55%) and all of them had concomitant (either diffuse or non-contiguous) pericardial involvement[61]. This is in keeping with the etiopathogenesis of myopericarditis in Cardiac TB. Greater awareness about the "Myopericarditis-Pericarditis Complex" sign/when added to Cardiac AI diagnostic protocols/algorithms, can save the patient from unnecessary invasive tests / cardiac biopsies.

Additionally, novel modalities, such as MR spectroscopy (MRS), chemical exchange saturation transfer (CEST) contrast, Amide Proton transfer imaging and dynamic contrast-enhanced imaging can detect physiological or metabolic changes without the need of exogenous agents. In animal models, these novel MRI capabilities differentiated bacterial infections from sterile inflammation or oncological processes[62,63].

Low-field MRI: Though currently still under development, low-field-strength (and lower-cost) MRI (0.5 T *vs* 1.5 or 3 T for typical scanners), coupled with state-of-the-art hardware, is being evaluated for high-quality imaging lungs and heart[64].

MR spectroscopy: MR spectroscopy (MRS) allows imaging of biochemical processes using endogenous metabolites (*e.g.*, choline, creatine, lactate) or substances labelled with exogenous nuclei such as 19F and 13C. MRS can be performed with most clinical MRI scanners, but multi-voxel MRS scanners are preferred for their greater coverage and resolution. Morales *et al*[65] reported that a singlet peak at ~3.8 parts-per-million (ppm) is present in most tuberculomas and absent in most malignant tumors, allowing

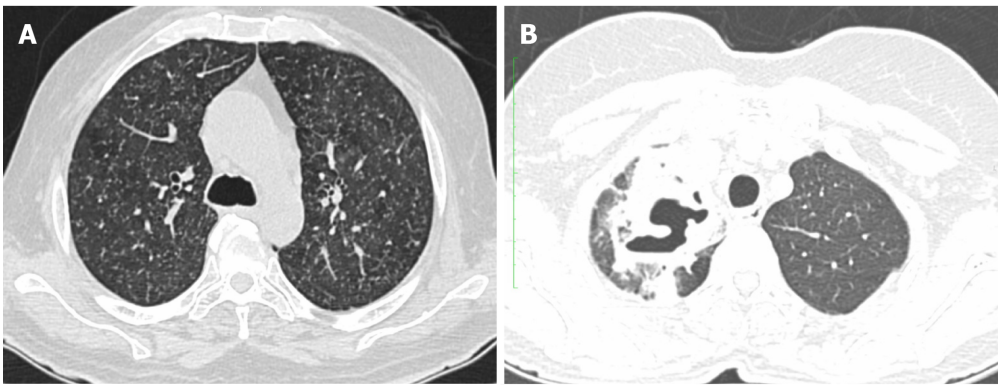

DOI: 10.4329/wjr.v14.i6.114

Figure 7 Tuberculosis sagittal computed tomography. A: Miliary tuberculosis: Axial high-resolution computed tomography (HRCT) image in lung window demonstrates miliary nodules scattered in both lungs; B: Tuberculous cavity: Axial HRCT image in lung window showing a thick-walled cavity in the apical segment of the right upper lobe. Images courtesy Dr. Joshi A, Prof & Head (Department of Radiology), LTMMC & LTMGH, Mumbai.

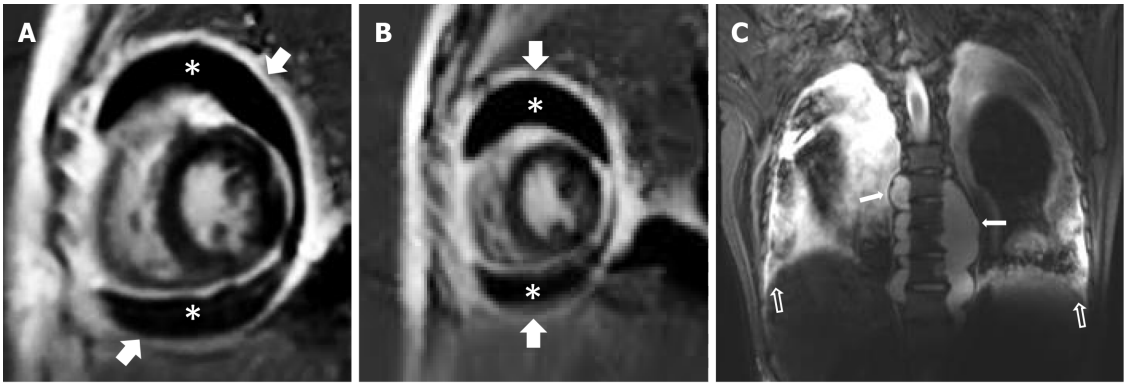

DOI: 10.4329/wjr.v14.i6.114

Figure 8 Tuberculous pericarditis and pericardial effusion: 3 Tesla Cardiac magnetic resonance imaging. A and B: PSIR (short axis view) images shows enhancing pericardial thickening (arrow) and moderate distension of pericardial space with hypointense fluid (asterisk); C: Coronal STIR dorsal spine: Paraspinal abscesses (white arrow -filled) with concomitant pleural effusions (white arrow- unfilled).

differentiation between these lesions.

CEST contrast MRI: CEST contrast MRI uses compounds containing exchangeable protons or molecules in concentrations too low to be visualized using standard MR imaging, with gadolinium substituted by alternative metals, such as manganese, lanthanides, or iron-based agents[66,67]. CEST agents can be diamagnetic or paramagnetic[68]. *Diamagnetic* agents create relatively small chemical shift differences (within 5 ppm of the water signal) that limit the observed effect per injected agent dose. *Paramagnetic* (PARACEST) ions induce much larger shifts, up to a few hundred ppm, thus allowing much shorter proton lifetimes. PARACEST can be single metal-containing chelates (*e.g.*, lanthanides), dendrimers, supramolecules, and liposomes.

Amide proton transfer: Building on the principles of CEST and Magnetization Transfer (MT), amide proton transfer (APT) imaging generates tissue contrast as a function of the mobile amide protons in the tissue's native peptides and intracellular proteins (Figure 10). Tuberculomas demonstrate lower MT ratios (MTR_{asym}) compared to High Grade Gliomas, reflective of a relative paucity of mobile amide protons in the ambient microenvironment. Elevated MTR_{asym} values in the perilesional parenchyma of tuberculomas are a unique observation that may be a clue to the inflammatory milieu[69].

MR elastography: Rapid progress has been noted in the utilisation of MR elastography (MRE), which includes the evaluation of alternatives to the expensive and invasive 'liver biopsy option' for assessing liver fibrosis in patients. Hepatic fibrosis is a known complication of TB medications (ATT) (Figure 11) [70]. Imajo *et al*[71] reported that MRE and US shear wave elastography (2D-SWE) demonstrated excellent diagnostic accuracy in detecting liver fibrosis in patients. They reported that MRE demonstrated the highest diagnostic accuracy for stage 4 fibrosis detection and intra - and inter-observer reproducibility[71]. MRE has the potential to be applied to detection of TB fibrosis in other

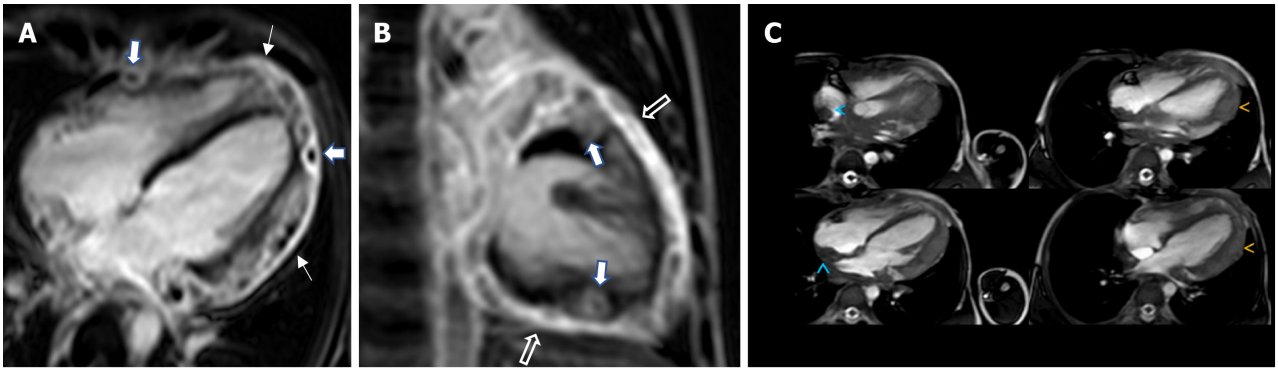

DOI: 10.4329/wjr.v14.i6.114

Figure 9 Cardiac tuberculous myo-pericarditis - 'the myocarditis-pericarditis complex - a sign of cardiac tuberculosis': 3 tesla cardiac magnetic resonance imaging. A: PSIR (4 chamber view -4CH) images shows enhancing pericardial thickening (thin arrow) and peripherally enhancing nodules in the subepicardial myocardium (thick arrow); B: PSIR (VLA view) - Thickened enhancing pericardium (unfilled arrow) with multiple nodular lesions (filled arrow) involving the myo-pericardium; C: Cine 4CH view: Diffuse pericardial thickening (<). In addition, nodular wall thickening (<) of the atria, and the interatrial septum is noted. (The patient was 10-year-old boy with a 2-mo h/o fever and chest pain and responded to anti-tuberculosis medications- regression of the lesions noted).

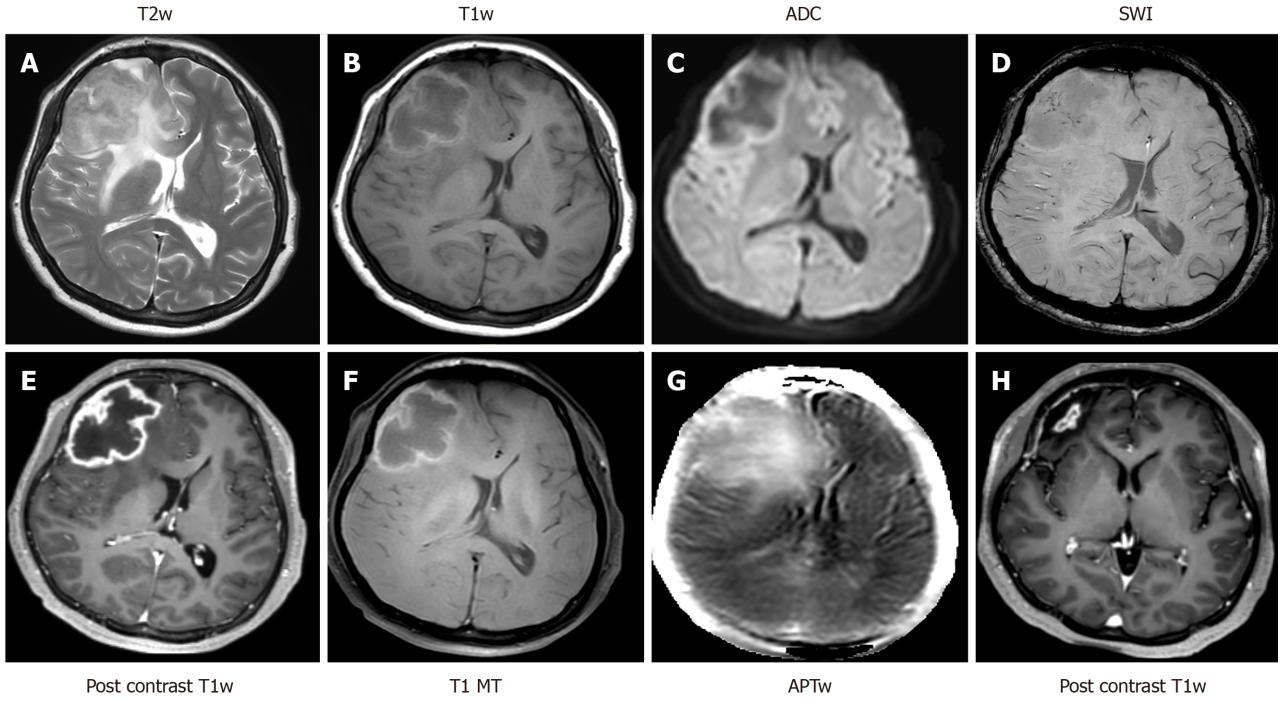

DOI: 10.4329/wjr.v14.i6.114

Figure 10 Magnetic resonance imaging - tuberculoma. A: Axial T2-weighted imaging shows a variable T2 hypointense circumscribed mass lesion in the right anterior frontal region, with surrounding perilesional edema; B: T1 weighted imaging shows a peripheral T1 hyperintense rim; C: Apparent diffusion co-efficient map shows restriction of diffusion; D: Susceptibility weighted imaging demonstrates fine punctate intralesional foci of blooming; E Post contrast T1 weighted imaging showing slightly irregular peripheral rim enhancement; F: T1 magnetization transfer images; G: Amide proton transfer weighted images show elevated magnetization transfer asymmetry in the periphery of the lesion; H: T1 post contrast imaging after completion of anti-tuberculosis treatment reveals significant reduction in the size of the previously seen ring enhancing lesion. APT: Amide proton transfer. Images courtesy Dr. Saini J, Professor, Neuroimaging & IVR, NIMHANS, Bangalore.

organs too, *e.g.* kidney: Including for treatment-response assessment and monitoring of sequelae, as fibrosis is a common manifestation in TB, including during healing[38]. This could be extremely vital in TB ureteric strictures which need to be stented, as they will heal by fibrosis (with treatment); and could result in serious damage/function loss of the affected kidney, if left unstented.

Advances in MR hardware and software: The development of sequences, arrays of coils, k-space strategies, stochastic imaging, and machine learning (ML)-based image analysis procedures will provide numerous opportunities to improve image contrast in MRI[72,73]. MRI sequences and post-processing techniques may replace or decrease the use of contrast agents (for example 4D MRI instead of MRA and CEST imaging); hybrid technologies such as positron emission tomography (PET)/MR may rely on

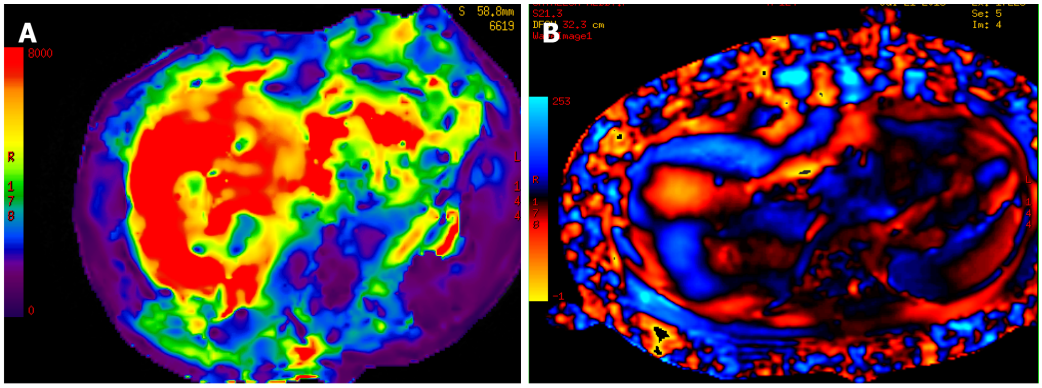

DOI: 10.4329/wjr.v14.i6.114

Figure 11 Post tuberculosis medication liver fibrosis on magnetic resonance elastography. A: Color elastogram of liver with a 0-8kPa scale shows the stiffness distribution in organs for qualitative evaluation. Red or orange regions have higher stiffness values, whereas blue and purple regions are depictive of lower stiffness values. Severe Liver fibrosis is noted - 8.1kPa; B: Wave image of liver shows excellent wave propagation anteriorly and laterally. Low amplitude waves with wave distortion observed in segment VII and II of liver. Images courtesy Dr. Bhaskar N, Vista Imaging Centre, Bangalore.

radiotracers in lieu of MR contrast agents[74].

Nuclear imaging, fusion imaging and miscellaneous

Nuclear imaging detects gamma-radiation produced by radioactive molecules administered non-invasively in micromolar quantities. If such molecules also have biological functions, one visualizes biological processes *in vivo* through functional **images** (at the cost of poorer anatomical resolution compared to CT/MRI/High-res US). Well-established for cancer management, molecular imaging may soon have potential for infectious disease[75].

PET: PET uses radionuclides that decay *via* positron emission relatively quickly (*e.g.*, 18-Fluorine and 11-Carbon have half-lives of 110 and 20 min) and require an on-site cyclotron to make the radionuclides on demand before they decay. Single-photon emission computed tomography (SPECT) uses longer-lived radionuclides (99-metastable-Technetium and 123-Iodine have half-lives of 6 and 13.2 h). In either case, gamma radiation is converted by semiconductor detectors into electrical signals which are then reconstructed as 3D tomographic images.

Pathogen-specific PET imaging agents: Pathogen-specific PET imaging agents currently in development, could provide more accurate data on bacterial burden and other longitudinal information on infection dynamics and treatment responses[76,77].

Fusion imaging: PET CT (Figure 12A and B) and PET MR (Figure 12C) combines functional imaging (PET, SPECT) for pharmacokinetic/ metabolic information with anatomic imaging (CT, MRI) for structural detail. This permits repeated studies in the same subject over time, a fundamental advantage over traditional techniques. Data thus obtained can be supplied to mathematical models of disease progression, which represents a major advance for the field that has primarily relied on snapshots to understand TB[75]. A small study in adults with MDR-TB, 18F-Fluoro-deoxyglucose (18-FDG) PET plus CT showed quantitative changes in computed abnormal volumes at 2 mo into the treatment that predicted long-term treatment success more sensitively than conventional sputum microbiology, suggesting the potential of imaging scans as possible surrogate endpoints in clinical trials of new TB drug regimens[78]. TB reactivation risk in animal models and human subjects has been accurately identified through 18F-FDG PET/CT[79-81].

Explorer total-body PET: This device's increased sensitivity (× 40) allows PET scans at extremely low radiation doses while improving the scan speed (potentially in less than a minute) and can track radiopharmaceuticals for longer periods after injection[82]. Although MDR-TB poses mortality risks comparable to those of many common cancers, radiopharmaceutical imaging, while accepted for cancer workup, is oddly avoided for infectious diseases[83]. Explorer total-body PET could allow increased PET use in both pediatric and adult patients with infectious diseases and would be very useful for assessing the extent of TB, especially when involving multiple sites, including the response to treatment [84-86].

SPECT: A rotating gamma camera captures energies from labelled molecules, which decay *via* the emission of single gamma rays. Most cameras produce 2D images, although some can perform tomographic 3D reconstructions. Foss *et al*[87] have designed a monoclonal antibody mAb 3d29 that can be used to detect and localize areas of infection with M. tuberculosis non-invasively, on SPECT, 24 h

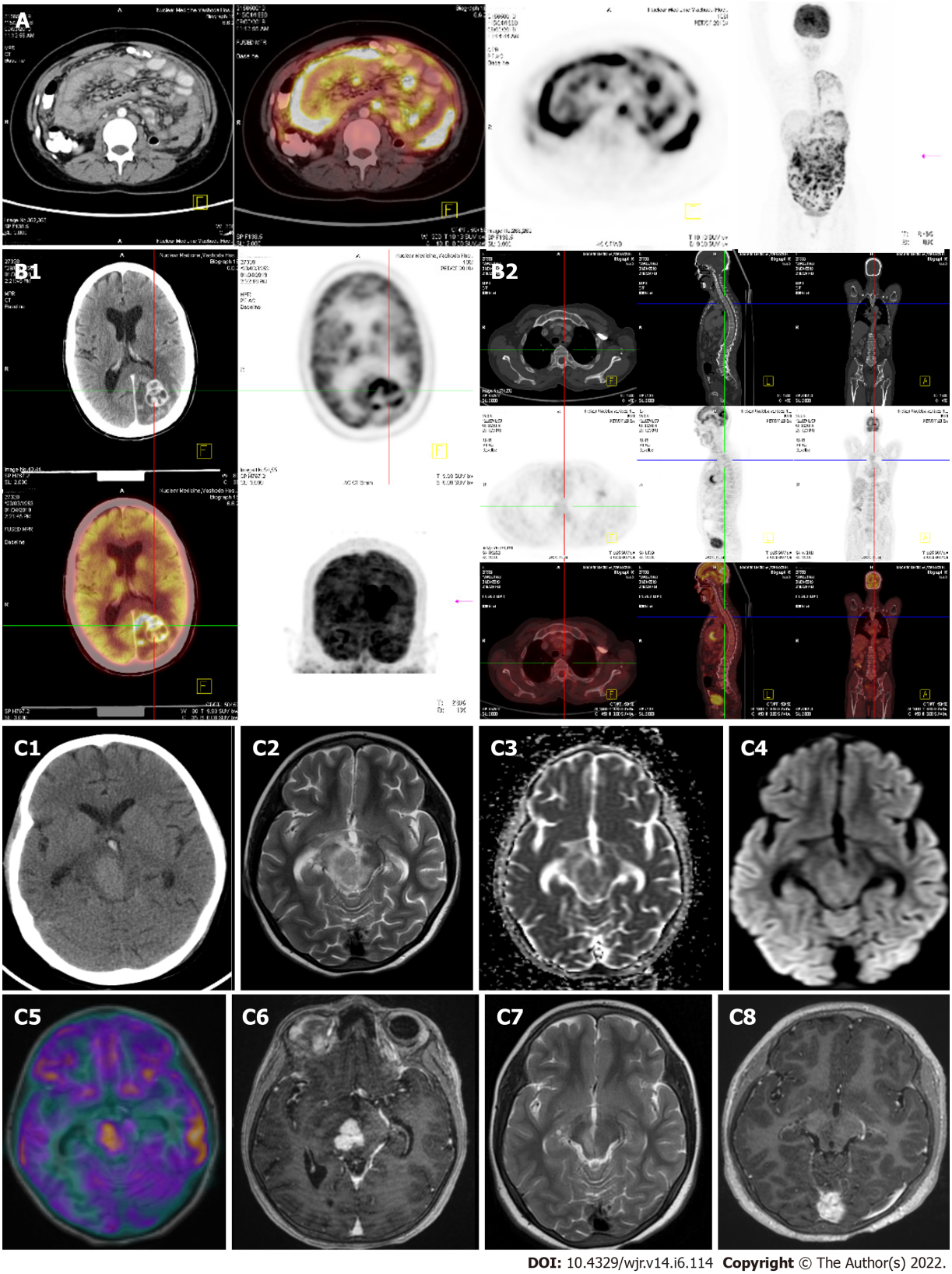

DOI: 10.4329/wjr.v14.i6.114

Figure 12 Fusion imaging. A: Fluoro-deoxyglucose (FDG) positron emission tomography (PET)/computed tomography (CT) Abdominal tuberculosis: 55-year F - h/o loss of weight with mild abdominal pain on and off gradually increasing (for 4 mo). Low grade evening rise of fever. Whole body PET CT showing irregular peritoneal thickening with nodularities and cocoon formation. PET and fused PET-CT images showing significant amount of uptake with SUV max of 12.3; B: Whole body FDG-PET/CT - Brain Tuberculomas:45 years male - h/o seizures for 5 mo, gradually increasing in frequency. PET-CT advised for the possibility of metastases; B1: Whole body FDG-PET/CT done showing irregular ring enhancing lesions in the brain with peri-lesional edema. PET and fused PET-CT images showing significant amount of uptake with SUV max of 14.8; B2: There is no other abnormal uptake in the entire body. (Normal myocardial uptake and left axillary vessel uptake is noted); C: Fusion imaging (MR-PET): Tuberculoma with Rubral tremor. 12-year-old girl presented with right 3rd and 4th cranial nerve palsy along with rhythmic to and fro left 'shoulder joint tremor' which worsened with movement; C1: Axial non-contrast CT image demonstrates a well circumscribed hyperdense mass

lesion within the right half of the midbrain; C2: T2-weighted imaging shows variable T2 hypo intensity within the lesion; C3 and C4: Diffusion weighted imaging and apparent diffusion co-efficient maps reveal restricted diffusion within the lesion; C5: Fusion imaging (T1W and PET) demonstrates avid glucose uptake within the lesion; C6: Post contrast T1 weighted imaging with fat saturation, reveals intense nodular enhancement. Stereotactic biopsy of the lesion revealed granulomatous inflammatory pathology; C7 and C8: After completion of anti-tuberculosis treatment, resolution of the granulomatous lesion with residual gliosis was observed on T2 weighted and Post contrast fat saturated T1w images. Images (A & B) courtesy Dr. Sikander Shaikh, Consultant radiologist, Yashodha Hospital, Hyderabad & Image (C) courtesy Dr. Saini J, Professor, Neuroimaging & IVR, NIMHANS, Bangalore.

after radiotracer injection.

Optical imaging: Optical Imaging provides high-resolution (*e.g.*, single-cell resolution) live imaging in small animal models and has provided very valuable insights into various biological processes (*e.g.*, TB granuloma formation)[32,88]. It is performed with highly sensitive fluorescent or bioluminescent agents. However, the use of low-energy photons means that the depth of penetration is limited to only a few centimetres. These could be used for superficial pathologies *e.g.*, cervical lymph nodes, including their complications (TB lymphadenitis, including collar-stud abscess *etc.*).

Advances in ex vivo molecular imaging and microscopy

Including autoradiography, fluorescence microscopy, fluorescence life-time imaging microscopy (FLIM), matrix assisted laser desorption/ ionization mass spectroscopy imaging (MALDI/MSI): Visualization of molecules based on mass detection. MALDI/MSI can simultaneously detect multiple compounds and provides high spatial resolution. Quantum Microscopy (improving the speed and sensitivity of Raman Scatter Microscopy (SRS); visualizing structures that would otherwise be impossible to see.

The molecular imaging techniques discussed below offer potential for cutting-edge research into the cellular mechanisms of TB. While autoradiography and Fluorescence Microscopy are long-established molecular imaging methods, the newer techniques use different modalities and/or extended study in living tissue.

FLIM: Performed *in vivo* with highly sensitive fluorescent or bioluminescent agents provides high-resolution (*e.g.*, single-cell resolution) in small animal models, allowing visualization of various biological processes (*e.g.*, TB granuloma formation)[32,88,89]. However, the use of low-energy photons limits the depth of penetration to a few centimeters. These could be used for superficial pathologies *e.g.*, cervical lymph nodes, including their complications (TB lymphadenitis, including collar-stud abscess, *etc.*).

Multiphoton intravital microscopy: Multiphoton intravital microscopy (MP-IVM) is based on the simultaneous absorption of two or more (near-) infrared photons. It allows visualization at single-cell resolution within a depth of a few millimeters. Murooka *et al*[90] used MP-IVM to monitor lymphocyte motility in lymph nodes of mice.

Matrix assisted laser desorption/ ionization mass spectroscopy imaging: This visualizes molecules based on mass detection. MALDI/MSI can simultaneously detect multiple compounds with high spatial resolution. It has been used to localize mycobacterial biomarkers and TB drugs in infected tissue[89]. MALDI-MSI can localize multiple molecules (*e.g.*, drugs, metabolites, lipids, proteins) simultaneously, overlaying them onto histologically stained sections to reveal the spatial distribution of each molecule with subcellular resolution[89,90]. MALDI-MSI can also be applied to archived tissue blocks dating back decades[91]. This would be a great boon for research, including retrospective studies.

The transition from anatomical imaging to functional/molecular imaging now allows integration of imaging data with various levels of "omics" data (genomics, metabolomics, proteomics, and pharmacogenomics). This may open new avenues for predictive, preventive, and personalized medicines[58].

Quantum microscopy: Quantum Microscopy has been utilized for improving the speed and sensitivity of SRS microscopy; visualizing structures that would otherwise be impossible to see. Casacio applied squeezed states of light in SRS, developing a quantum-enhanced-microscope[92]. This enhancement allowed for resolution of the cell membrane which could not be seen on a conventional microscope and sub-micron spatial resolution and the improved image contrast and reduced imaging time surpassed the current state-of-the-art Raman microscopes, while avoiding photodamage in the sample.

MOLECULAR MECHANISMS IN TB

Role of vitamin D

Another addition worth considering is the humble Vitamin D, which was used to treat TB in the pre-

antibiotic era[93]. Serum levels of 25-hydroxy-cholecalciferol (25-OH-D3) in TB patients have been shown to be lower than in healthy controls[94]. The vitamin D-cathelicidin pathway regulates the autophagy machinery, protective immune defenses, and inflammation; and contributes to immune cooperation between innate and adaptive immunity[95]. Vitamin D activates macrophages and restricts MTB's intracellular growth[96]. In monocytes and macrophages, MTB lipoprotein binds to the TLR2/TLR1 heterodimer (TLR = Toll-like receptor): this increases vitamin D receptor expression and processing of the pro-vitamin D precursor, which in turn increases production of a mycobactericidal peptide[94]. Vitamin D supplementation during TB treatment accelerates sputum smear conversion and hastens resolution of inflammatory responses[97].

A systematic review (Sutaria *et al*[98]) evaluated 21 randomized, controlled trials and concluded that: (1) TB patients had lower vitamin D status (lower serum levels of 25-OH-D3than healthy, age-matched, and sex-matched controls) [99]; (2) People with certain Vitamin D receptor polymorphisms (BsmI and FokI) had increased susceptibility to TB; and (3) TB patients receiving vitamin D supplementation had improved outcomes in most studies, including shortening treatment duration[98,100]. Vitamin D deficiency may adversely influence TB re-activation/ re-infection: lowered 25-OH-D3 Level leads to a fall in cell-mediated immune defenses, which can activate latent tuberculosis[101]. Hence, it would be worth checking and restoring 25-OH-D3 Levels in malnourished TB patients[102].

Epigenetics perspective

Epigenetics refers to heritable changes in DNA function caused by environmental factors, without altering the DNA sequence, through mechanisms such as DNA (de)methylation (methylation typically deactivates genes) and histone modification (DNA is inactive when tightly bound to histone proteins.) MTB is known to cause histone changes in immune cells that inactivate the defensive IL-2V gene (IL=interleukin), improving MTB's survival chances[103]. Gauba *et al*[104] review various MTB-induced epigenetic mechanisms. In their review, they have unravelled the numerous ways by which MTB re-shapes the host epigenetic landscape as a strategy to overpower the host immune system, for its survival and persistence.

The degree of methylation of key genes in the vitamin D metabolic pathway influence risk and prognosis of tuberculosis[105]. Here's where Vit D supplementation can play a vital role in protecting against TB and in complimenting Anti TB therapies. Understanding the inter-talk between MTB and epigenetic mechanisms will also play a vital role in controlling/ eliminating the scourge of TB[106]. Analysing epigenetic changes offers great potential in the diagnosis, prevention, and treatment strategies for a wide range of diseases, including TB. CRISPR interference (CRISPRi) has been utilized in mycobacteria to identify novel drug targets by the demonstration of gene essentiality. Faulkner *et al*[107] used CRISPRi to study genes involved in mycobacterial antibiotic resistance, restoring Rifampicin sensitivity in M. smegmatis with CRISPR. This offers hope for the future - for the creation of epigenetically modified Anti -TB drugs to treat MDR and XDR TB.

ADVANCES IN COMPUTING

We discuss these advances under two broad categories, software (*e.g.*, Artificial Intelligence, Augmented and Virtual Reality) as well as Hardware Innovations.

Artificial intelligence applications in TB

Increasing Internet bandwidth, coupled with transparent data security, has advanced telemedicine, so that remote diagnosis is now routine. Diagnosis can be assisted by Artificial Intelligence (AI). An important AI sub-field, ML, uses statistical techniques, rather than explicitly encoded insight from human experts, to detect patterns in (often considerable) volumes of data. ML allows classification (*e.g.*, diagnosis) or making predictions. A rapidly progressing branch of ML, called multilayer neural networks or "Deep Learning" (DL), can increase speed and accuracy of onsite and remote diagnosis. DL algorithms have already been used to detect features consistent with pulmonary TB in CXR and CT scans[108].

However, "Artificial Intelligence needs Real Intelligence to guide it!" To maximize AI applications' accuracy and utility in medical diagnosis and treatment modalities, AI must incorporate experiential wisdom accumulated over decades of clinical and radiological experience time, namely time-tested key medical 'teaching' and/or key 'clinical' parameters, including prognostic indicators.

TB is no exception. Take childhood (< 15 years) pulmonary TB, which represents 12% of new cases, but 16% of the estimated 1.4 million deaths[109]. This higher mortality highlights the urgent need to improve case detection, and to identify children without TB disease eligible for preventive treatment. One strategy is systematic screening for tuberculosis in high-risk groups[109]. Early diagnosis and prompt treatment will prevent spread to other children at school or in community settings, especially in resource-limited settings[109]. Imaging algorithms can thus play an important role in screening strategies.

The TB Primary Complex (Ghon's focus, draining lymphatics and hilar node/s) is very common in developing countries. However, inexperienced radiologists find it challenging to identify it in children on CXR, partly because the relatively prominent pulmonary arteries obscure the hila. However, co-occurrence of pleural effusion simplifies identification, because "classical" pleural effusions, especially of the lamellar type (tracking along the pleura, mimicking pleural thickening) (Figure 1) are relatively uncommon in children due to non-TB causes. A Childhood TB diagnosis algorithm using this information would gain in specificity. Similar considerations apply to Adult TB. Patients with "Open Kochs" (lung cavities or smear positive) (Figure 7B) are far more contagious and require isolation: including these factors in analysis/algorithms enables more effective screening/control/management [27].

While DL excels at recognizing individual patterns (most artificial-vision applications use it), higher-level knowledge of key imaging and clinical signs allows integrating the individual patterns into a diagnosis. Such "Holistic" algorithms that integrate all the available information-not just on a single patient, but also molecular and epidemiologic knowledge-can significantly improve not only early detection of TB, including MDR-TB, but more effective management and significant improvement in healthcare outcomes.

Augmented reality and Virtual reality

Virtual reality creates entirely synthesized 3-D environments, while augmented reality (which is technically simpler to create and often more practical) superimposes synthesized content on existing environments, typically under user control. Both are potentially valuable for teaching/simulation and in clinical practice/patient education, by providing novel visualizations. Clinicians/radiologists could walk the patient through their own body to explain the disease, intended intervention, and anticipated post-intervention changes. Such immersive experiences could likely ensure greater compliance with the treatment regimen.

Distributed computing

We introduce distributed computing (DC) because many AI problems, such as would address TB, require computing power that single computing units cannot provide; including data housed in computers at diverse geographical locations. In DC, a computational problem is tackled by multiple, communicating, computing units. It has the following characteristics: (1) The units may lie within a single organization (connected by a local area network) or be distributed geographically (connected by the Internet); (2) Typically, a subset of units (often, just one "central" unit) may operate as either "coordinators" that control/direct other "peripheral" units, or provide resources (*e.g.*, data, computing services) to them; (3) The central units typically have far more CPU power and storage capacity than the peripheral units. In the extreme case, the peripherals may be devices like smartphones, or even single-purpose sensors (*e.g.*, for continuous glucose or EKG monitoring); (4) The central units' upkeep requires skilled/expensive personnel. In Cloud Computing, the units' housing/maintenance are outsourced to a "cloud vendor" (Amazon, Microsoft, Google, *etc.*). The available services can be scaled up or down in each billing cycle based on the customer's requirements. The term "cloud" indicates that the central unit is "out there", its physical location transparent to customers: location may even change; and (5) A single central unit can pose a bottleneck if thousands of small devices connect to it, especially over a sluggish Internet. Edge Computing enhances cloud computing by interposing intermediary units between the peripherals and central units[110]. The Edge units are physically close to the peripherals at a given geographic location (*i.e.*, at the "Edge" of a network diagram). They prevent overwhelming of the central unit, reduce overall network traffic by aggregating inputs from the peripherals and also provide some computing resources.

Federated ML: ML in general, and DL specifically, need lots of data (as well as diverse data from multiple geographic locales) to achieve the desired accuracy. "Big-data" solutions naturally suggest themselves. However, the obvious solution, physical pooling of data, faces the following barriers: (1) Data privacy - which is less of an issue with all forms of digital imaging, where DICOM metadata containing identifiable information can be removed; and (2) Mistrust - a formidable hurdle when academic or commercial consortia bring rivals together.

The technique of *Federated Learning* (FL), originally pioneered by Google as an application of their well-known MapReduce algorithm allows iteratively training an ML model across geographically separated hardware: the ML algorithm is distributed, while data remains local[111,112]. It can be employed for both statistical and deep learning.

Typically, a central server coordinates computations across multiple distributed clients. At start-up, the server sends the clients initialization information. The clients commence computation. When each client is done, it sends only aggregate results back to the server, not detailed or identifiable data elements. The server collates all clients' results and sends updates to each client, which then computes again. The process continues until the ML training completes convergence.

Ng *et al*[113] provide a detailed technology overview. Sheller *et al*[114] use FL to replicate prior analysis of a 10-institution brain-tumor-image-dataset derived from The Cancer Genome Atlas (TCGA). Navia-Vasquez *et al*[115] describe an approach for Federated Logistic Regression.

Most important, many AI algorithms can run in FL mode, making them more accurate because they are based on more voluminous and diverse data. This increases the scope for Multi- Institutional/Multi-city collaborations. Dashboards augmented with these algorithms' can aid key organizational decision-makers to identify trends (including epidemiological), communicate vital information and monitor performance against strategic goals. Better information through technology-assisted developments would aid WHO, UNICEF and other such organizations counter/eliminate the scourge of TB worldwide. While FL works around institutional barriers, one pays a cost in computational speed, which is limited by Internet bandwidth. In almost all cases, this tradeoff is worthwhile.

Quantum technology

"Quantum" technology refers to a highly diverse set of technologies that leverage "quantum mechanics", the physics of sub-atomic particles. Some of these are established, such as scanning tunneling microscopy and photoionization, while others are still largely theoretical, or in the prototype stage[116]. Quantum Computers and Quantum microscopes, new quantum repeaters enabling a scalable super secure Quantum Internet (distance will no longer be a hindrance, not just IOT but 'Intelligent Edge' devices commonplace); will give a quantum boost to Medical Imaging/other health-care Algorithms/strategies, including in other related fields, improving healthcare in ways beyond the realm of dreams[117].

Quantum entanglement microscopy: Quantum entanglement (QE) occurs when a group of particles are generated and interact with each other so that each particle's sub-atomic (*i.e.*, quantum) state cannot be described independently of the others' state. Originally postulated in 1935 by Einstein, Podolsky, and Rosen, it led to seemingly bizarre predictions if true. For example, if one particle encountered an object (*e.g.*, a bacterium), the other particles would reflect this interaction instantaneously - even if the particles were at opposite ends of the universe, violating General Relativity's prediction that faster-than-light interactions are impossible. Such predictions led Einstein to believe that Quantum Theory was erroneous: However, QE was demonstrated experimentally almost eight decades later.

With QE using confocal "differential interference contrast," standard microscopy wavelengths, *e.g.*, visible light or ultraviolet (UV), provides much higher resolution than without QE, demonstrated by Ono *et al*[118]. QE achieves such detail using much less light (useful for light-sensitive micro-organisms or living tissues when UV is employed). A quantum optical counterpart has been developed to the classical Fourier-transform infrared spectrometer[119]. "Quantum ghost imaging" produced the world's first 2D image captured and reconstructed using asynchronous detection. Ghost imaging is well suited to biological and medical applications, in which light-sensitive cell samples can be observed over a long period because the new processes use less light[120]. QE microscopy may thus impact TB research and diagnosis.

Quantum computing: Quantum computing (QC) relies on the possibility of keeping a collection of "qubits" (quantum bits) stable long enough to perform computations with. While a bit (the smallest unit of information in a traditional computer, 1 Byte = 8 bits) can be either 1 or 0, a qubit can be both 1 and 0 simultaneously: thus, 32 qubits can represent 2^{32}approximately equal to 4 billion possibilities. Conceived by Nobelist Richard Feynman, QC's theoretical foundations were strengthened after Peter Shor's work ("Shor's[121] Algorithm) showed that QC could achieve exponential speedup for extremely compute-intensive problems like factorizing the product of two large prime numbers, the basis of RSA (= Rivest, Shamir, Adelman) encryption. Building a practical Quantum Computer, however, is challenging. Qubits are most stable at very low temperatures (*e.g.*, 0.025 Kelvin), and most Qubits in a computer perform error correction rather than computation. However, QC is showing remarkable progress - entangling qubits that could improve error correction in quantum computing, creation of a third state to qubits, to create 'qutrits' that allow more information to be encoded in a single element and decrease readout errors significantly, development of a high-performance source of "squeezed light" used to transmit information in optical quantum computing; all signify a quantum leap in the technology; with the last being a paradigm shift[122-124]. Optical Quantum computers can now be expected to run at room temperature, without the expensive cooling equipment needed for other quantum computers that use superconductors.

A recent simulated quantum algorithm by Case Western Reserve University and Microsoft scientists (it would have required a quantum computer with 1 million computing qubits) addressed Magnetic Resonance Fingerprinting (MRF)[125]. MRF goes beyond MRI in identifying signatures from individual tissues simultaneously.

If QC's hardware challenges are solved (there is no clear-cut timeline for this) the impact on general computing, including AI-deep learning, under the hood, performing mathematical optimization-could be extraordinary. Almost all aspects of healthcare would benefit: TB diagnosis and disease modeling would definitely be a part of it. As quantum computers are also ideally suited for solving complex optimization tasks and performing fast searches of unsorted data, this could be relevant for many applications in healthcare related to TB; medical imaging, epidemiological simulations, dashboard creation, holistic algorithm creation, targeted policy making, to a host of other applications; including the realm of Quantum Artificial Intelligence, which offers unlimited possibilities, including many

presently undreamable/unthinkable ones. Researchers have now suggested that neuromorphic or brain like computers built using memristors (these resemble neuronal synapsis) would perform well at running neural networks[126]. Scientists in Austria and Italy have already developed a quantum version of the memristor that they suggest could lead to 'quantum neuromorphic computers', which in turn could lead to an exponential growth in performance, in an ML approach known as 'reservoir computing 'that excels at learning quickly; and may have a quantum advantage over classical reservoir computing, due to the fact that the memristor, unlike any other quantum component has memory[127].

Thus, the Future looks great for QC (including QC based AI) contributing phenomenally to Medical Imaging and overall Healthcare as well. We can merely speculate at the potential applications of this yet 'Work in Progress' technology. The spectacular jump in overall computing power will enable hitherto unimaginable tasks to be done in a 'jiffy' and thus enable more complex tasks to be thought of. Quantum Artificial Intelligence Algorithms and the like will be something to look forward to. As and when QC evolves the Metaverse will give a more immersive experience both for teaching/simulation and during actual interactions; by giving visualizations/viewpoints that would otherwise not have been possible; with Augmented Reality/Virtual reality (especially for teaching/simulations *etc*.) offering tremendous potential for Medical Imaging in TB, community involvement, amongst other applications; to enable better compliance of TB guidelines and norms (refer the Augmented Reality &/Virtual Reality sectionabove).

CONCLUSION

While we have discussed numerous technologies, which operate at scales ranging from the subatomic to human populations, the primary challenge for employing these to eliminate the scourge of TB is integrating them into a holistic approach. For example, AI cannot operate in a vacuum; it needs large volumes of data at the patient and population level: incorporating data also from novel imaging modalities, or from translational applications of bench-science research (*e.g*., detection of resistance mutations through PCR, augmented optionally by CRISPR), will make it much more useful. The integration must be guided by policies developed by the coordinated actions of international consortia (including bodies like WHO, Big Pharma, national health ministries, philanthropists, *etc*.) that make use of diverse expertise around the globe, including those available through leading-edge technologies.

Below, we provide an outline for the implementation of such policies.

Prevention: In addition to current standard practices (besides the usual methods, nutrition, social norms *etc*.

Screening of vulnerable contacts/populations.

Screening for, and correction of nutritional deficiencies, including vitamin D.

Early diagnosis utilizing newer techniques/technological developments: *e.g*., Gene-Xpert, TB QUICK *etc*., for both 'regular TB' and MDR/XDR TB, including extrapulmonary samples.

Effective treatment, especially for MDR/XDR TB [including addition of recent drugs, shorter duration regimen (for better compliance)] + vitamin D for better healing as well as complimenting the action of various anti-TB drugs.

Effective monitoring including long term follow up coupled with development of large epidemiological data banks and dashboards that summarize the data therein to facilitate timely decision-making.

Enhanced Computing Infrastructure to facilitate all the above, from optimized data gathering, to more sophisticated algorithms, to more powerful hardware architectures.

The following is a useful acronym for the strategies we believe are vital to help us achieve the various targets set by the international health community for elimination of TB.

TB – REVISITED: Regular Screening / Remote patient monitoring; Early Diagnosis; Vitamin D levels/supplementation; Imaging and Investigations; Set up a Holistic Approach (Clinical/Imaging/Bacteriological); Intelligent comprehensive Holistic AI algorithms (+ wisdom *vs* knowledge); Technology – CBNAAT (GenXpert *etc*.)/National - Global Dashboards; Ensure a Global approach/Edge Computing; Do not delay the diagnosis of MDR-TB.

We believe that effective strategy implementation can help alleviate the suffering of millions of underprivileged citizens of the world.

ACKNOWLEDGEMENTS

We wish to thank Merchant N, MD, Diagnostic Radiologist, The Joint Department of Medical Imaging - Lecturer, Faculty of Medicine, University of Toronto, for assistance in preparing this manuscript.

FOOTNOTES

Author contributions: Merchant SA conceptualized the article; all authors wrote, read and approved the final manuscript.

Conflict-of-interest statement: All authors declare no conflict of interests for this article.

Country/Territory of origin: India

ORCID number: Suleman Adam Merchant 0000-0001-6513-450X; Mohd Javed Saifullah Shaikh 0000-0002-5615-4813; Prakash Nadkarni 0000-0002-9628-4700.

S-Editor: Wang LL
L-Editor: A
P-Editor: Wang LL

REFERENCES

1 **WHO**. Global tuberculosis report 2020. [cited 20 January 2022]. Available from: https://www.who.int/publications/i/item/9789240013131
2 **WHO**. Global Tuberculosis Report 2021. [cited 20 January 2022]. Available from: https://www.who.int/publications/i/item/9789240037021
3 **Centers for Disease C and Prevention**. Emergence of Mycobacterium tuberculosis with extensive resistance to second-line drugs-worldwide, 2000-2004. *MMWR Morb Mortal Wkly Rep* 2006; **55**: 301-305 [PMID: 16557213]
4 **Salazar-Austin N**, Ordonez AA, Hsu AJ. Extensively drug-resistant tuberculosis in a young child after travel to India. *Lancet Infect Dis* 2015; **15**: 1485-1491 [PMID: 26607130 DOI: 10.1016/S1473-3099(15)00356-4]
5 **Kanabus A**. TB Statistics - 2020 - deaths, case notifications. [cited 20 January 2022]. Available from: https://tbfacts.org/tb-statistics/(2021)
6 **United States AID**. [cited 20 January 2022]. Available from: https://blog.usaid.gov/2017/
7 **WHO**. Global strategy and targets for tuberculosis prevention, care and control after 2015. Sixty seventh World health Assembly: WORLD HEALTH ORGANISATION. [cited 20 January 2022]. Available from: https://apps.who.int/gb/ebwha/pdf_files/WHA67/A67_R1-en.pdf
8 **Dye C**, Glaziou P, Floyd K. Prospects for tuberculosis elimination. *Annu Rev Public Health* 2013; **34**: 271-286 [PMID: 23244049 DOI: 10.1146/annurev-publhealth-031912-114431]
9 **Lee JH**, Ammerman NC, Nolan S. Prospects for tuberculosis elimination. *Nat Commun* 2012; **3**: 753-753 [PMID: 22434196 DOI: 10.1038/ncomms1724]
10 **Comas I**, Borrell S, Roetzer A. Whole-genome sequencing of rifampicin-resistant Mycobacterium tuberculosis strains identifies compensatory mutations in RNA polymerase genes. *Nat Genet* 2011; **44**: 106-110 [PMID: 22179134 DOI: 10.1038/ng.1038]
11 **Jaleta KN**, Gizachew M, Gelaw B. Rifampicin-resistant Mycobacterium tuberculosis among tuberculosis-presumptive cases at University of Gondar Hospital, northwest Ethiopia. *Infect Drug Resist* 2017; **10**: 185-192 [PMID: 28652786 DOI: 10.2147/IDR.S135935]
12 **Piatek AS**, Van Cleeff M, Alexander H. GeneXpert for TB diagnosis: planned and purposeful implementation. *Glob Health Sci Pract* 2013; **1**: 18-23 [PMID: 25276513 DOI: 10.9745/GHSP-D-12-00004]
13 **WHO**. The shorter mdr-tb regimen. [cited 20 January 2022]. Available from: https://apps.who.int/iris/bitstream/handle/10665/250125/9789241549639-eng.pdf
14 **Mirzayev F**, Viney K, Linh NN, Gonzalez-Angulo L, Gegia M, Jaramillo E, Zignol M, Kasaeva T. World Health Organization recommendations on the treatment of drug-resistant tuberculosis, 2020 update. *Eur Respir J* 2021; **57** [PMID: 33243847 DOI: 10.1183/13993003.03300-2020]
15 **Ogwang S**, Mubiri P, Bark CM, Joloba ML, Boom WH, Johnson JL. Incubation time of Mycobacterium tuberculosis complex sputum cultures in BACTEC MGIT 960: 4weeks of negative culture is enough for physicians to consider alternative diagnoses. *Diagn Microbiol Infect Dis* 2015; **83**: 162-164 [PMID: 26239846 DOI: 10.1016/j.diagmicrobio.2015.07.002]
16 **Chavez Pachas AM**, Blank R, Smith Fawzi MC, Bayona J, Becerra MC, Mitnick CD. Identifying early treatment failure on category I therapy for pulmonary tuberculosis in Lima Ciudad, Peru. *Int J Tuberc Lung Dis* 2004; **8**: 52-58 [PMID: 14974746]
17 **Satti H**, McLaughlin MM, Seung KJ, Becerra MC, Keshavjee S. High risk of drug-resistant tuberculosis when first-line therapy fails in a high HIV prevalence setting. *Int J Tuberc Lung Dis* 2013; **17**: 100-106 [PMID: 23232009 DOI: 10.5588/ijtld.12.0344]
18 **WHO**. Multidrug and extensively drug-resistant TB (M/XDR-TB). 2010. [cited 20 January 2022]. Available from:

http://apps.who.int/iris/bitstream/handle/10665/44286/9789241599191_eng.pdf?sequence=1

19 **Osei Sekyere J**, Maphalala N, Malinga LA, Mbelle NM, Maningi NE. A Comparative Evaluation of the New Genexpert MTB/RIF Ultra and other Rapid Diagnostic Assays for Detecting Tuberculosis in Pulmonary and Extra Pulmonary Specimens. *Sci Rep* 2019; **9**: 16587 [PMID: 31719625 DOI: 10.1038/s41598-019-53086-5]

20 **Helb D**, Jones M, Story E, Boehme C, Wallace E, Ho K, Kop J, Owens MR, Rodgers R, Banada P, Safi H, Blakemore R, Lan NT, Jones-López EC, Levi M, Burday M, Ayakaka I, Mugerwa RD, McMillan B, Winn-Deen E, Christel L, Dailey P, Perkins MD, Persing DH, Alland D. Rapid detection of Mycobacterium tuberculosis and rifampin resistance by use of on-demand, near-patient technology. *J Clin Microbiol* 2010; **48**: 229-237 [PMID: 19864480 DOI: 10.1128/JCM.01463-09]

21 **Perez-Risco D**, Rodriguez-Temporal D, Valledor-Sanchez I, Alcaide F. Evaluation of the Xpert MTB/RIF Ultra Assay for Direct Detection of Mycobacterium tuberculosis Complex in Smear-Negative Extrapulmonary Samples. *J Clin Microbiol* 2018; **56** [PMID: 29950333 DOI: 10.1128/JCM.00659-18]

22 **Dorman SE**, Schumacher SG, Alland D, Nabeta P, Armstrong DT, King B, Hall SL, Chakravorty S, Cirillo DM, Tukvadze N, Bablishvili N, Stevens W, Scott L, Rodrigues C, Kazi MI, Joloba M, Nakiyingi L, Nicol MP, Ghebrekristos Y, Anyango I, Murithi W, Dietze R, Lyrio Peres R, Skrahina A, Auchynka V, Chopra KK, Hanif M, Liu X, Yuan X, Boehme CC, Ellner JJ, Denkinger CM; study team. Xpert MTB/RIF Ultra for detection of Mycobacterium tuberculosis and rifampicin resistance: a prospective multicentre diagnostic accuracy study. *Lancet Infect Dis* 2018; **18**: 76-84 [PMID: 29198911 DOI: 10.1016/S1473-3099(17)30691-6]

23 **Mechal Y**, Benaissa E, El Mrimar N, Benlahlou Y, Bssaibis F, Zegmout A, Chadli M, Malik YS, Touil N, Abid A, Maleb A, Elouennass M. Evaluation of GeneXpert MTB/RIF system performances in the diagnosis of extrapulmonary tuberculosis. *BMC Infect Dis* 2019; **19**: 1069 [PMID: 31856744 DOI: 10.1186/s12879-019-4687-7]

24 **Sam IK**, Chen YY, Ma J, Li SY, Ying RY, Li LX, Ji P, Wang SJ, Xu J, Bao YJ, Zhao GP, Zheng HJ, Wang J, Sha W, Wang Y. TB-QUICK: CRISPR-Cas12b-assisted rapid and sensitive detection of Mycobacterium tuberculosis. *J Infect* 2021; **83**: 54-60 [PMID: 33951419 DOI: 10.1016/j.jinf.2021.04.032]

25 **Churchyard GJ**, Mametja LD, Mvusi L, Ndjeka N, Hesseling AC, Reid A, Babatunde S, Pillay Y. Tuberculosis control in South Africa: successes, challenges and recommendations. *S Afr Med J* 2014; **104**: 244-248 [PMID: 24893501 DOI: 10.7196/samj.7689]

26 **Noertjojo K**, Tam CM, Chan SL, Tan J, Chan-Yeung M. Contact examination for tuberculosis in Hong Kong is useful. *Int J Tuberc Lung Dis* 2002; **6**: 19-24 [PMID: 11931396]

27 **Lee MS**, Leung CC, Kam KM, Wong MY, Leung MC, Tam CM, Leung EC. Early and late tuberculosis risks among close contacts in Hong Kong. *Int J Tuberc Lung Dis* 2008; **12**: 281-287 [PMID: 18284833]

28 **Leung EC**, Leung CC, Kam KM, Yew WW, Chang KC, Leung WM, Tam CM. Transmission of multidrug-resistant and extensively drug-resistant tuberculosis in a metropolitan city. *Eur Respir J* 2013; **41**: 901-908 [PMID: 22878878 DOI: 10.1183/09031936.00071212]

29 **Dye C**, Williams BG. Eliminating human tuberculosis in the twenty-first century. *J R Soc Interface* 2008; **5**: 653-662 [PMID: 17690054 DOI: 10.1098/rsif.2007.1138]

30 **Harisinghani MG**, McLoud TC, Shepard JA, Ko JP, Shroff MM, Mueller PR. Tuberculosis from head to toe. *Radiographics* 2000; **20**: 449-70; quiz 528 [PMID: 10715343 DOI: 10.1148/radiographics.20.2.g00mc12449]

31 **Bomanji JB**, Gupta N, Gulati P, Das CJ. Imaging in tuberculosis. *Cold Spring Harb Perspect Med* 2015; **5** [PMID: 25605754 DOI: 10.1101/cshperspect.a017814]

32 **Ordonez AA**, Tucker EW, Anderson CJ, Carter CL, Ganatra S, Kaushal D, Kramnik I, Lin PL, Madigan CA, Mendez S, Rao J, Savic RM, Tobin DM, Walzl G, Wilkinson RJ, Lacourciere KA, Via LE, Jain SK. Visualizing the dynamics of tuberculosis pathology using molecular imaging. *J Clin Invest* 2021; **131** [PMID: 33645551 DOI: 10.1172/JCI145107]

33 **WHO**. Chest radiography in tuberculosis detection. [cited 20 January 2022]. Available from: https://apps.who.int/iris/handle/10665/252424

34 **Sharma M**, Sandhu MS, Gorsi U, Gupta D, Khandelwal N. Role of digital tomosynthesis and dual energy subtraction digital radiography in detection of parenchymal lesions in active pulmonary tuberculosis. *Eur J Radiol* 2015; **84**: 1820-1827 [PMID: 26071244 DOI: 10.1016/j.ejrad.2015.05.031]

35 **Yu TZ**, Zhang Y, Zhang WZ, Yang GY. Role of ultrasound in the diagnosis of cervical tuberculous lymphadenitis in children. *World J Pediatr* 2021; **17**: 544-550 [PMID: 34472036 DOI: 10.1007/s12519-021-00453-w]

36 **Navani N**, Molyneaux PL, Breen RA, Connell DW, Jepson A, Nankivell M, Brown JM, Morris-Jones S, Ng B, Wickremasinghe M, Lalvani A, Rintoul RC, Santis G, Kon OM, Janes SM. Utility of endobronchial ultrasound-guided transbronchial needle aspiration in patients with tuberculous intrathoracic lymphadenopathy: a multicentre study. *Thorax* 2011; **66**: 889-893 [PMID: 21813622 DOI: 10.1136/thoraxjnl-2011-200063]

37 **Wang B**, Guo Q, Wang JY, Yu Y, Yi AJ, Cui XW, Dietrich CF. Ultrasound Elastography for the Evaluation of Lymph Nodes. *Front Oncol* 2021; **11**: 714660 [PMID: 34485150 DOI: 10.3389/fonc.2021.714660]

38 **Merchant S**, Bharati A, Merchant N. Tuberculosis of the genitourinary system-Urinary tract tuberculosis: Renal tuberculosis-Part II. *Indian J Radiol Imaging* 2013; **23**: 64-77 [PMID: 23986619 DOI: 10.4103/0971-3026.113617]

39 **Chaubal N**, Bam A & Khatdare K. Elastography of Lymph Nodes. In: Richard. G Barr (Ed) Elastography - A Practical Approach. First ed. New York - Stuttgart: Thieme, 2017: 100-114

40 **Dietrich CF**, Jenssen C, Arcidiacono PG, Cui XW, Giovannini M, Hocke M, Iglesias-Garcia J, Saftoiu A, Sun S, Chiorean L. Endoscopic ultrasound: Elastographic lymph node evaluation. *Endosc Ultrasound* 2015; **4**: 176-190 [PMID: 26374575 DOI: 10.4103/2303-9027.162995]

41 **Kanagaraju V**, Rakshith AVB, Devanand B, Rajakumar R. Utility of Ultrasound Elastography to Differentiate Benign from Malignant Cervical Lymph Nodes. *J Med Ultrasound* 2020; **28**: 92-98 [PMID: 32874867 DOI: 10.4103/JMU.JMU_72_19]

42 **Özel D**, Özel BD. Evaluating the role of strain ratio elastography in determining malignancy potential and calculating objective BIRADS US scores using ultrasonography and elastography features. *Pol J Radiol* 2018; **83**: e268-e274 [PMID: 30627246 DOI: 10.5114/pjr.2018.76790]

43 **Shehata RMA**, El-Sharkawy MAM, Mahmoud OM. Qualitative and quantitative strain and shear wave elastography paradigm in differentiation of breast lesions. [cited 20 January 2022]. Available from: https://ejrnm.springeropen.com/articles/10.1186/s43055-022-00697-0

44 **Wang Z**, Yang T, Wu Z, Tang S, Liang X, Qin A, Ouyang T, Liu P, Liu J. Correlation between elastography score and strain rate ratio in breast small tumor. *Zhongnan Daxue Xuebao Yixueban* 2010; **35**: 928-932 [PMID: 20871156 DOI: 10.3969/j.issn.1672-7347.2010.09.005]

45 **Chu J**, Zhang Y, Zhang W, Zhao D, Xu J, Yu T, Yang G. The value of multimodal ultrasonography in differential diagnosis of tuberculous and non-tuberculous superficial lymphadenitis. *BMC Surg* 2021; **21**: 416 [PMID: 34906107 DOI: 10.1186/s12893-021-01418-6]

46 **Lammers T**, Aime S, Hennink WE, Storm G, Kiessling F. Theranostic nanomedicine. *Acc Chem Res* 2011; **44**: 1029-1038 [PMID: 21545096 DOI: 10.1021/ar200019c]

47 **Martin KH**, Dayton PA. Current status and prospects for microbubbles in ultrasound theranostics. *Wiley Interdiscip Rev Nanomed Nanobiotechnol* 2013; **5**: 329-345 [PMID: 23504911 DOI: 10.1002/wnan.1219]

48 **Ma J**, Martin K, Dayton PA, Jiang X. A preliminary engineering design of intravascular dual-frequency transducers for contrast-enhanced acoustic angiography and molecular imaging. *IEEE Trans Ultrason Ferroelectr Freq Control* 2014; **61**: 870-880 [PMID: 24801226 DOI: 10.1109/TUFFC.2014.6805699]

49 **Duran C**, Beltrán VP, González A, Gómez C, Riego JD. Contrast-enhanced Voiding Urosonography for Vesicoureteral Reflux Diagnosis in Children. *Radiographics* 2017; **37**: 1854-1869 [PMID: 29019761 DOI: 10.1148/rg.2017170024]

50 **Kiessling F**, Fokong S, Bzyl J, Lederle W, Palmowski M, Lammers T. Recent advances in molecular, multimodal and theranostic ultrasound imaging. *Adv Drug Deliv Rev* 2014; **72**: 15-27 [PMID: 24316070 DOI: 10.1016/j.addr.2013.11.013]

51 **Palmowski M**, Morgenstern B, Hauff P, Reinhardt M, Huppert J, Maurer M, Woenne EC, Doerk S, Ladewig G, Jenne JW, Delorme S, Grenacher L, Hallscheidt P, Kauffmann GW, Semmler W, Kiessling F. Pharmacodynamics of streptavidin-coated cyanoacrylate microbubbles designed for molecular ultrasound imaging. *Invest Radiol* 2008; **43**: 162-169 [PMID: 18301312 DOI: 10.1097/RLI.0b013e31815a251b]

52 **Fei C**, Chiu CT, Chen X, Chen Z, Ma J, Zhu B, Shung KK, Zhou Q. Ultrahigh Frequency (100 MHz-300 MHz) Ultrasonic Transducers for Optical Resolution Medical Imagining. *Sci Rep* 2016; **6**: 28360 [PMID: 27329379 DOI: 10.1038/srep28360]

53 **Willer K**, Fingerle AA, Gromann LB, De Marco F, Herzen J, Achterhold K, Gleich B, Muenzel D, Scherer K, Renz M, Renger B, Kopp F, Kriner F, Fischer F, Braun C, Auweter S, Hellbach K, Reiser MF, Schroeter T, Mohr J, Yaroshenko A, Maack HI, Pralow T, van der Heijden H, Proksa R, Koehler T, Wieberneit N, Rindt K, Rummeny EJ, Pfeiffer F, Noël PB. X-ray dark-field imaging of the human lung-A feasibility study on a deceased body. *PLoS One* 2018; **13**: e0204565 [PMID: 30261038 DOI: 10.1371/journal.pone.0204565]

54 **Bech M**, Tapfer A, Velroyen A, Yaroshenko A, Pauwels B, Hostens J, Bruyndonckx P, Sasov A, Pfeiffer F. In-vivo dark-field and phase-contrast x-ray imaging. *Sci Rep* 2013; **3**: 3209 [PMID: 24220606 DOI: 10.1038/srep03209]

55 **Schleede S**, Meinel FG, Bech M, Herzen J, Achterhold K, Potdevin G, Malecki A, Adam-Neumair S, Thieme SF, Bamberg F, Nikolaou K, Bohla A, Yildirim AÖ, Loewen R, Gifford M, Ruth R, Eickelberg O, Reiser M, Pfeiffer F. Emphysema diagnosis using X-ray dark-field imaging at a laser-driven compact synchrotron light source. *Proc Natl Acad Sci U S A* 2012; **109**: 17880-17885 [PMID: 23074250 DOI: 10.1073/pnas.1206684109]

56 **Bhalla AS**, Goyal A, Guleria R, Gupta AK. Chest tuberculosis: Radiological review and imaging recommendations. *Indian J Radiol Imaging* 2015; **25**: 213-225 [PMID: 26288514]

57 **Khan AU**, Khanduri S, Tarin Z, Abbas SZ, Husain M, Singh A, Yadav P, Jain S. Dual-Energy Computed Tomography Lung in patients of Pulmonary Tuberculosis. *J Clin Imaging Sci* 2020; **10**: 39 [PMID: 32754374 DOI: 10.25259/JCIS_78_2020]

58 **Huang HM**, Shih YY. Pushing CT and MR imaging to the molecular level for studying the "omics": current challenges and advancements. *Biomed Res Int* 2014; **2014**: 365812 [PMID: 24738056 DOI: 10.1155/2014/365812]

59 **Peprah KO**, Andronikou S, Goussard P. Characteristic magnetic resonance imaging low T2 signal intensity of necrotic lung parenchyma in children with pulmonary tuberculosis. *J Thorac Imaging* 2012; **27**: 171-174 [PMID: 21516045 DOI: 10.1097/RTI.0b013e318211abfb]

60 **Sodhi KS**, Khandelwal N, Saxena AK, Singh M, Agarwal R, Bhatia A, Lee EY. Rapid lung MRI in children with pulmonary infections: Time to change our diagnostic algorithms. *J Magn Reson Imaging* 2016; **43**: 1196-1206 [PMID: 26546472 DOI: 10.1002/jmri.25082]

61 **Bharati A**, Merchant S, Nagesh C. The 'Myocarditis-Pericarditis' Complex - A CMR Sign of Cardiac Tuberculosis and The Spectrum of imaging findings of Cardiac Tuberculosis on CMR. RSNA Annual Conference. Chicago: Radiological Society of North America, 2013. [cited 20 January 2022]. Available from: https://archive.rsna.org/2013/13012394.html

62 **Liu J**, Bai R, Li Y, Staedtke V, Zhang S, van Zijl PCM, Liu G. MRI detection of bacterial brain abscesses and monitoring of antibiotic treatment using bacCEST. *Magn Reson Med* 2018; **80**: 662-671 [PMID: 29577382 DOI: 10.1002/mrm.27180]

63 **Goldenberg JM**, Berthusen AJ, Cárdenas-Rodríguez J, Pagel MD. Differentiation of Myositis-Induced Models of Bacterial Infection and Inflammation with T_2-Weighted, CEST, and DCE-MRI. *Tomography* 2019; **5**: 283-291 [PMID: 31572789 DOI: 10.18383/j.tom.2019.00009]

64 **Campbell-Washburn AE**, Ramasawmy R, Restivo MC, Bhattacharya I, Basar B, Herzka DA, Hansen MS, Rogers T, Bandettini WP, McGuirt DR, Mancini C, Grodzki D, Schneider R, Majeed W, Bhat H, Xue H, Moss J, Malayeri AA, Jones EC, Koretsky AP, Kellman P, Chen MY, Lederman RJ, Balaban RS. Opportunities in Interventional and Diagnostic Imaging by Using High-Performance Low-Field-Strength MRI. *Radiology* 2019; **293**: 384-393 [PMID: 31573398 DOI: 10.1148/radiol.2019190452]

65 **Morales H**, Alfaro D, Martinot C, Fayed N, Gaskill-Shipley M. MR spectroscopy of intracranial tuberculomas: A singlet peak at 3.8 ppm as potential marker to differentiate them from malignant tumors. *Neuroradiol J* 2015; **28**: 294-302 [PMID: 26246099 DOI: 10.1177/1971400915592077]

66 **van Zijl PC**, Yadav NN. Chemical exchange saturation transfer (CEST): what is in a name and what isn't? *Magn Reson*

Med 2011; **65**: 927-948 [PMID: 21337419 DOI: 10.1002/mrm.22761]
67 **Minton LE**, Pandit R, Willoughby WR, Porter KK. The Future of Magnetic Resonance Imaging Contrast Agents. *Appl Radiol* 2022; **51**: 7-11 [cited 20 January 2022]. Available from: https://appliedradiology.com/articles/the-future-of-magnetic-resonance-imaging-contrast-agents
68 **Hancu I**, Dixon WT, Woods M, Vinogradov E, Sherry AD, Lenkinski RE. CEST and PARACEST MR contrast agents. *Acta Radiol* 2010; **51**: 910-923 [PMID: 20828299 DOI: 10.3109/02841851.2010.502126]
69 **Kulanthaivelu K**, Jabeen S, Saini J, Raju S, Nalini A, Sadashiva N, Hegde S, Rolla NK, Saha I, M N, Vengalil S, Swaroop S, Rao S. Amide proton transfer imaging for differentiation of tuberculomas from high-grade gliomas: Preliminary experience. *Neuroradiol J* 2021; **34**: 440-448 [PMID: 33823712 DOI: 10.1177/19714009211002766]
70 **Biswas A**, Santra S, Bishnu D, Dhali GK, Chowdhury A, Santra A. Isoniazid and Rifampicin Produce Hepatic Fibrosis through an Oxidative Stress-Dependent Mechanism. *Int J Hepatol* 2020; **2020**: 6987295 [PMID: 32373368 DOI: 10.1155/2020/6987295]
71 **Imajo K**, Honda Y, Kobayashi T, Nagai K, Ozaki A, Iwaki M, Kessoku T, Ogawa Y, Takahashi H, Saigusa Y, Yoneda M, Kirikoshi H, Utsunomiya D, Aishima S, Saito S, Nakajima A. Direct Comparison of US and MR Elastography for Staging Liver Fibrosis in Patients With Nonalcoholic Fatty Liver Disease. *Clin Gastroenterol Hepatol* 2022; **20**: 908-917.e11 [PMID: 33340780]
72 **Xu C**, Howey J, Ohorodnyk P, Roth M, Zhang H, Li S. Segmentation and quantification of infarction without contrast agents *via* spatiotemporal generative adversarial learning. *Med Image Anal* 2020; **59**: 101568 [PMID: 31622838 DOI: 10.1016/j.media.2019.101568]
73 **de Figueiredo EH**, Borgonovi AF, Doring TM. Basic concepts of MR imaging, diffusion MR imaging, and diffusion tensor imaging. *Magn Reson Imaging Clin N Am* 2011; **19**: 1-22 [PMID: 21129633 DOI: 10.1016/j.mric.2010.10.005]
74 **Jadvar H**, Colletti PM. Competitive advantage of PET/MRI. *Eur J Radiol* 2014; **83**: 84-94 [PMID: 23791129 DOI: 10.1016/j.ejrad.2013.05.028]
75 **Ordonez AA**, Sellmyer MA, Gowrishankar G, Ruiz-Bedoya CA, Tucker EW, Palestro CJ, Hammoud DA, Jain SK. Molecular imaging of bacterial infections: Overcoming the barriers to clinical translation. *Sci Transl Med* 2019; **11** [PMID: 31484790 DOI: 10.1126/scitranslmed.aax8251]
76 **Ordonez AA**, Weinstein EA, Bambarger LE, Saini V, Chang YS, DeMarco VP, Klunk MH, Urbanowski ME, Moulton KL, Murawski AM, Pokkali S, Kalinda AS, Jain SK. A Systematic Approach for Developing Bacteria-Specific Imaging Tracers. *J Nucl Med* 2017; **58**: 144-150 [PMID: 27635025 DOI: 10.2967/jnumed.116.181792]
77 **Sly LM**, Hingley-Wilson SM, Reiner NE, McMaster WR. Survival of Mycobacterium tuberculosis in host macrophages involves resistance to apoptosis dependent upon induction of antiapoptotic Bcl-2 family member Mcl-1. *J Immunol* 2003; **170**: 430-437 [PMID: 12496428 DOI: 10.4049/jimmunol.170.1.430]
78 **Chen RY**, Dodd LE, Lee M, Paripati P, Hammoud DA, Mountz JM, Jeon D, Zia N, Zahiri H, Coleman MT, Carroll MW, Lee JD, Jeong YJ, Herscovitch P, Lahouar S, Tartakovsky M, Rosenthal A, Somaiyya S, Lee S, Goldfeder LC, Cai Y, Via LE, Park SK, Cho SN, Barry CE 3rd. PET/CT imaging correlates with treatment outcome in patients with multidrug-resistant tuberculosis. *Sci Transl Med* 2014; **6**: 265ra166 [PMID: 25473034 DOI: 10.1126/scitranslmed.3009501]
79 **Davis SL**, Nuermberger EL, Um PK, Vidal C, Jedynak B, Pomper MG, Bishai WR, Jain SK. Noninvasive pulmonary [18F]-2-fluoro-deoxy-D-glucose positron emission tomography correlates with bactericidal activity of tuberculosis drug treatment. *Antimicrob Agents Chemother* 2009; **53**: 4879-4884 [PMID: 19738022 DOI: 10.1128/AAC.00789-09]
80 **Lin PL**, Maiello P, Gideon HP, Coleman MT, Cadena AM, Rodgers MA, Gregg R, O'Malley M, Tomko J, Fillmore D, Frye LJ, Rutledge T, DiFazio RM, Janssen C, Klein E, Andersen PL, Fortune SM, Flynn JL. PET CT Identifies Reactivation Risk in Cynomolgus Macaques with Latent M. tuberculosis. *PLoS Pathog* 2016; **12**: e1005739 [PMID: 27379816 DOI: 10.1371/journal.ppat.1005739]
81 **Esmail H**, Lai RP, Lesosky M, Wilkinson KA, Graham CM, Coussens AK, Oni T, Warwick JM, Said-Hartley Q, Koegelenberg CF, Walzl G, Flynn JL, Young DB, Barry Iii CE, O'Garra A, Wilkinson RJ. Characterization of progressive HIV-associated tuberculosis using 2-deoxy-2-[^{18}F]fluoro-D-glucose positron emission and computed tomography. *Nat Med* 2016; **22**: 1090-1093 [PMID: 27595321 DOI: 10.1038/nm.4161]
82 **Cherry SR**, Jones T, Karp JS, Qi J, Moses WW, Badawi RD. Total-Body PET: Maximizing Sensitivity to Create New Opportunities for Clinical Research and Patient Care. *J Nucl Med* 2018; **59**: 3-12 [PMID: 28935835 DOI: 10.2967/jnumed.116.184028]
83 **Jain SK**. The Promise of Molecular Imaging in the Study and Treatment of Infectious Diseases. *Mol Imaging Biol* 2017; **19**: 341-347 [PMID: 28155078 DOI: 10.1007/s11307-017-1055-0]
84 **Cherry SR**, Badawi RD, Karp JS, Moses WW, Price P, Jones T. Total-body imaging: Transforming the role of positron emission tomography. *Sci Transl Med* 2017; **9** [PMID: 28298419 DOI: 10.1126/scitranslmed.aaf6169]
85 **Badawi RD**, Shi H, Hu P, Chen S, Xu T, Price PM, Ding Y, Spencer BA, Nardo L, Liu W, Bao J, Jones T, Li H, Cherry SR. First Human Imaging Studies with the EXPLORER Total-Body PET Scanner. *J Nucl Med* 2019; **60**: 299-303 [PMID: 30733314 DOI: 10.2967/jnumed.119.226498]
86 **Lv Y**, Lv X, Liu W, Judenhofer MS, Zwingenberger A, Wisner E, Berg E, McKenney S, Leung E, Spencer BA, Cherry SR, Badawi RD. Mini EXPLORER II: a prototype high-sensitivity PET/CT scanner for companion animal whole body and human brain scanning. *Phys Med Biol* 2019; **64**: 075004 [PMID: 30620929 DOI: 10.1088/1361-6560/aafc6c]
87 **Foss CA**, Kulik L, Ordonez AA, Jain SK, Michael Holers V, Thurman JM, Pomper MG. SPECT/CT Imaging of Mycobacterium tuberculosis Infection with [^{125}I]anti-C3d mAb. *Mol Imaging Biol* 2019; **21**: 473-481 [PMID: 29998399 DOI: 10.1007/s11307-018-1228-5]
88 **Murooka TT**, Mempel TR. Multiphoton intravital microscopy to study lymphocyte motility in lymph nodes. *Methods Mol Biol* 2012; **757**: 247-257 [PMID: 21909917 DOI: 10.1007/978-1-61779-166-6_16]
89 **Blanc L**, Lenaerts A, Dartois V, Prideaux B. Visualization of Mycobacterial Biomarkers and Tuberculosis Drugs in Infected Tissue by MALDI-MS Imaging. *Anal Chem* 2018; **90**: 6275-6282 [PMID: 29668262 DOI: 10.1021/acs.analchem.8b00985]
90 **Niehaus M**, Soltwisch J, Belov ME, Dreisewerd K. Transmission-mode MALDI-2 mass spectrometry imaging of cells

and tissues at subcellular resolution. *Nat Methods* 2019; **16**: 925-931 [PMID: 31451764 DOI: 10.1038/s41592-019-0536-2]

91 **Paine MRL**, Ellis SR, Maloney D, Heeren RMA, Verhaert PDEM. Digestion-Free Analysis of Peptides from 30-year-old Formalin-Fixed, Paraffin-Embedded Tissue by Mass Spectrometry Imaging. *Anal Chem* 2018; **90**: 9272-9280 [PMID: 29975508 DOI: 10.1021/acs.analchem.8b01838]

92 **Casacio**, Catxere and Andrade. Quantum enhanced microscopy. A thesis submitted for the degree of Doctor of Philosophy - The University of Queensland, Australia, 2020. [cited 20 January 2022]. Available from: https://espace.library.uq.edu.au/

93 **Martineau AR**, Honecker FU, Wilkinson RJ, Griffiths CJ. Vitamin D in the treatment of pulmonary tuberculosis. *J Steroid Biochem Mol Biol* 2007; **103**: 793-798 [PMID: 17223549 DOI: 10.1016/j.jsbmb.2006.12.052]

94 **Nnoaham KE**, Clarke A. Low serum vitamin D levels and tuberculosis: a systematic review and meta-analysis. *Int J Epidemiol* 2008; **37**: 113-119 [PMID: 18245055 DOI: 10.1093/ije/dym247]

95 **Chung C**, Silwal P, Kim I, Modlin RL, Jo EK. Vitamin D-Cathelicidin Axis: at the Crossroads between Protective Immunity and Pathological Inflammation during Infection. *Immune Netw* 2020; **20**: e12 [PMID: 32395364 DOI: 10.4110/in.2020.20.e12]

96 **Arora VK**, Jaiswal AK. Vitamin D receptor polymorphism and active tuberculosis. [cited 20 January 2022]. Available from: http://tbassnindia.org/images/TB_October_2013_issue.pdf

97 **Coussens AK**, Wilkinson RJ, Hanifa Y, Nikolayevskyy V, Elkington PT, Islam K, Timms PM, Venton TR, Bothamley GH, Packe GE, Darmalingam M, Davidson RN, Milburn HJ, Baker LV, Barker RD, Mein CA, Bhaw-Rosun L, Nuamah R, Young DB, Drobniewski FA, Griffiths CJ, Martineau AR. Vitamin D accelerates resolution of inflammatory responses during tuberculosis treatment. *Proc Natl Acad Sci U S A* 2012; **109**: 15449-15454 [PMID: 22949664 DOI: 10.1073/pnas.1200072109]

98 **Sutaria N**, Liu CT, Chen TC. Vitamin D Status, Receptor Gene Polymorphisms, and Supplementation on Tuberculosis: A Systematic Review of Case-Control Studies and Randomized Controlled Trials. *J Clin Transl Endocrinol* 2014; **1**: 151-160 [PMID: 25599020 DOI: 10.1016/j.jcte.2014.08.001]

99 **Lips P**. Vitamin D deficiency and secondary hyperparathyroidism in the elderly: consequences for bone loss and fractures and therapeutic implications. *Endocr Rev* 2001; **22**: 477-501 [PMID: 11493580 DOI: 10.1210/edrv.22.4.0437]

100 **Junaid K**, Rehman A. Impact of vitamin D on infectious disease-tuberculosis-a Review. [cited 20 January 2022]. Available from: https://www.clinicalnutritionopenscience.com/article/S2352-9393(19)30017-X/pdf

101 **Davies PD**. The role of vitamin D in tuberculosis. *Am Rev Respir Dis* 1989; **139**: 1571 [PMID: 2729764 DOI: 10.1164/ajrccm/139.6.1571]

102 **Merchant S**, Bharati A, Merchant N. Tuberculosis of the genitourinary system-Urinary tract tuberculosis: Renal tuberculosis-Part I. *Indian J Radiol Imaging* 2013; **23**: 46-63 [PMID: 23986618 DOI: 10.4103/0971-3026.113615]

103 **Kathirvel M**, Mahadevan S. The role of epigenetics in tuberculosis infection. *Epigenomics* 2016; **8**: 537-549 [PMID: 27035266 DOI: 10.2217/epi.16.1]

104 **Gauba K**, Gupta S, Shekhawat J, Sharma P, Yadav D, Banerjee M. Immunomodulation by epigenome alterations in Mycobacterium tuberculosis infection. *Tuberculosis (Edinb)* 2021; **128**: 102077 [PMID: 33812175 DOI: 10.1016/j.tube.2021.102077]

105 **Wang M**, Kong W, He B, Li Z, Song H, Shi P, Wang J. Vitamin D and the promoter methylation of its metabolic pathway genes in association with the risk and prognosis of tuberculosis. *Clin Epigenetics* 2018; **10**: 118 [PMID: 30208925 DOI: 10.1186/s13148-018-0552-6]

106 **Tarashi S**, Badi SA, Moshiri A, Ebrahimzadeh N, Fateh A, Vaziri F, Aazami H, Siadat SD, Fuso A. The inter-talk between *Mycobacterium tuberculosis* and the epigenetic mechanisms. *Epigenomics* 2020; **12**: 455-469 [PMID: 32267165 DOI: 10.2217/epi-2019-0187]

107 **Faulkner V**, Cox AA, Goh S, van Bohemen A, Gibson AJ, Liebster O, Wren BW, Willcocks S, Kendall SL. Re-sensitization of *Mycobacterium smegmatis* to Rifampicin Using CRISPR Interference Demonstrates Its Utility for the Study of Non-essential Drug Resistance Traits. *Front Microbiol* 2020; **11**: 619427 [PMID: 33597931 DOI: 10.3389/fmicb.2020.619427]

108 **Lakhani P**, Sundaram B. Deep Learning at Chest Radiography: Automated Classification of Pulmonary Tuberculosis by Using Convolutional Neural Networks. *Radiology* 2017; **284**: 574-582 [PMID: 28436741 DOI: 10.1148/radiol.2017162326]

109 **Vonasek B**, Ness T, Takwoingi Y, Kay AW, van Wyk SS, Ouellette L, Marais BJ, Steingart KR, Mandalakas AM. Screening tests for active pulmonary tuberculosis in children. *Cochrane Database Syst Rev* 2021; **6**: CD013693 [PMID: 34180536 DOI: 10.1002/14651858.CD013693.pub2]

110 **Shivam A**. Edge Computing vs Cloud Computing: What are the Differences. [cited 20 January 2022]. Available from: https://www.simplilearn.com/edge-computing-vs-cloud-computing-article

111 **McMahan B**, Ramage D. Federated Learning: Collaborative Machine Learning without Centralized Training Data. Google AI Blog [Internet]. Google, 2017. Introducing an additional approach: Federated Learning. [cited 20 January 2022]. Available from: https://ai.googleblog.com/2017/04/federated-learning-collaborative.html

112 **Dean JG**, Ghemawat S. MapReduce: Simplified Data Processing on Large Clusters. Sixth Symposium on Operating System Design and Implementation. San Francisco: Google Inc, 2004. [cited 20 January 2022]. Available from: https://static.googleusercontent.com/media/research.google.com/en//archive/mapreduce-osdi04.pdf

113 **Ng D**, Lan X, Yao MM, Chan WP, Feng M. Federated learning: a collaborative effort to achieve better medical imaging models for individual sites that have small labelled datasets. *Quant Imaging Med Surg* 2021; **11**: 852-857 [PMID: 33532283 DOI: 10.21037/qims-20-595]

114 **Sheller MJ**, Edwards B, Reina GA, Martin J, Pati S, Kotrotsou A, Milchenko M, Xu W, Marcus D, Colen RR, Bakas S. Federated learning in medicine: facilitating multi-institutional collaborations without sharing patient data. *Sci Rep* 2020; **10**: 12598 [PMID: 32724046 DOI: 10.1038/s41598-020-69250-1]

115 **Navia-Vazquez A**, Vazquez-Lopez M, and Cid-Sueiro J. Double Confidential Federated Machine Learning Logistic

Regression for Industrial Data Platforms. In: 37th International Conference on Machine Learning Vienna 2020, Vienna. [cited 20 January 2022]. Available from: https://www.tsc.uc3m.es/~navia/FL-ICML2020/DCFML-FL_ICML2020-A_Navia_Vazquez_et_al.pdf

116 **Wikipedia**. Quantum Microsocpy. [cited 20 January 2022]. Available from: https://en.wikipedia.org/wiki/Quantum_microscopy

117 **Studio TB**. [cited 20 January 2022]. Available from: https://techcrunch.com/sponsor/qualcomm/the-future-is-not-the-internet-of-things-it-is-the-connected-intelligent-edge/

118 **Ono T**, Okamoto R, Takeuchi S. An entanglement-enhanced microscope. *Nat Commun* 2013; **4**: 2426 [PMID: 24026165]

119 **Optics**. org. Project QUILT reveals far-reaching potential of quantum optics and imaging. [cited 20 January 2022]. Available from: https://optics.org/news/13/1/4 (2022)

120 **Fraenhofer-Gesellschaft**. Quantum imaging: Pushing the boundaries of optics. [cited 20 January 2022]. Available from: https://phys.org/news/2022-01-quantum-imaging-boundaries-optics.html

121 **Shor PW**. Algorithms for quantum computation: discrete logarithms and factoring. In: Proceedings 35th Annual Symposium on Foundations of Computer Science 1994: 124-134 [cited 20 January 2022]. Available from: https://ieeexplore.ieee.org/document/365700

122 **Sharma M**. There's been another huge quantum computing breakthrough. [cited 20 January 2022]. Available from: https://www.mckinsey.com/business-functions/mckinsey-digital/our-insights/quantum-computing-use-cases-are-getting-real-what-you-need-to-know

123 **Tung L**. Quantum computing: Forget about qubits, here come qutrits. [cited 20 January 2022]. Available from: https://www.zdnet.com/article/quantum-computing-now-rigetti-explores-qutrits-as-well-as-qubits/

124 **Oikawa A**, Ota A. Quantum computing: Japan takes step toward light-based technology. [cited 20 January 2022]. Available from: https://asia.nikkei.com/Business/Technology/Quantum-computing-Japan-takes-step-toward-light-based-technology

125 **Kahn J**. Microsoft Quantum Algorithm Boosts Medical Imaging. [cited 20 January 2022]. Available from: https://fortune.com/2019/07/15/microsoft-quantum-algorithm-boosts-medical-imaging

126 **Charles Q**, Choi AI. Fuses With Quantum Computing in Promising New Memristor Quantum device points the way toward an exponential boost in "smart" computing capabilities. [cited 20 January 2022]. Available from: https://spectrum.ieee.org/quantum-memristor

127 **Spagnolo M**, Morris J, Piacentini S. Experimental photonic quantum memristor. *Nature Photonics* 2022; **16**: 318-323 [cited 20 January 2022]. Available from: https://www.nature.com/articles/s41566

World Journal of Radiology

Submit a Manuscript: https://www.f6publishing.com

World J Radiol 2022 June 28; 14(6): 137-150

DOI: 10.4329/wjr.v14.i6.137

ISSN 1949-8470 (online)

MINIREVIEWS

Recent advances in imaging techniques of renal masses

Ankita Aggarwal, Chandan J Das, Sanjay Sharma

Specialty type: Radiology, nuclear medicine and medical imaging

Provenance and peer review: Invited article; Externally peer reviewed.

Peer-review model: Single blind

Peer-review report's scientific quality classification

Grade A (Excellent): 0
Grade B (Very good): 0
Grade C (Good): C
Grade D (Fair): D
Grade E (Poor): 0

P-Reviewer: Quartuccio N, Italy; Yang L, China
A-Editor: Liu X, China

Received: December 21, 2021
Peer-review started: December 21, 2021
First decision: February 21, 2022
Revised: March 4, 2022
Accepted: June 16, 2022
Article in press: June 16, 2022
Published online: June 28, 2022

Ankita Aggarwal, Department of Radiology, Vardhman Mahavir Medical College& Safdarjung Hospital, Delhi 110029, India

Chandan J Das, Department of Radiodiagnosis and Interventional Radiology, All India Institute of Medical Sciences, Delhi 110029, India

Sanjay Sharma, Department of Radiology (RPC), All India Institute of Medical Sciences, New Delhi 110029, India

Corresponding author: Chandan J Das, MD, Additional Professor, Department of Radiodiagnosis and Interventional Radiology, All India Institute of Medical Sciences, Ansari Nagar, Delhi, Delhi 110029, India. dascj@yahoo.com

Abstract

Multiphasic multidetector computed tomography (CT) forms the mainstay for the characterization of renal masses whereas magnetic resonance imaging (MRI) acts as a problem-solving tool in some cases. However, a few of the renal masses remain indeterminate even after evaluation by conventional imaging methods. To overcome the deficiency in current imaging techniques, advanced imaging methods have been devised and are being tested. This review will cover the role of contrast-enhanced ultrasonography, shear wave elastography, dual-energy CT, perfusion CT, MR perfusion, diffusion-weighted MRI, blood oxygen level-dependent MRI, MR spectroscopy, positron emission tomography (PET)/prostate-specific membrane antigen-PET in the characterization of renal masses.

Key Words: Advanced imaging techniques; Renal mass; Contrast-enhanced ultrasonography renal; Shear wave elastography

Core Tip: To overcome the deficiency in the existing imaging techniques for adequate characterization of renal masses, newer/advanced imaging methods have been devised and are being tested. This review will cover contrast-enhanced ultrasonography, shear wave elastography, dual-energy computed tomography (CT), perfusion CT, diffusion-weighted magnetic resonance imaging (MRI), MR perfusion, blood oxygen level-dependent MRI, MR spectroscopy, and positron emission tomography (PET)/prostate-specific membrane antigen-PET.

Citation: Aggarwal A, Das CJ, Sharma S. Recent advances in imaging techniques of renal masses. *World J Radiol* 2022; 14(6): 137-150
URL: https://www.wjgnet.com/1949-8470/full/v14/i6/137.htm
DOI: https://dx.doi.org/10.4329/wjr.v14.i6.137

INTRODUCTION

Precise characterization of any renal mass is of paramount importance for clinicians to decide the most appropriate treatment and thereby improve the survival outcome. Being safe, cost-effective, and non-invasive, ultrasound is the current screening modality for the evaluation of renal masses for malignancy with a sensitivity of 82%-83% and specificity of 98%-99%[1-3]. However, the sensitivity is low for masses less than 3cm in size[4]. Multidetector computed tomography (MDCT) forms the mainstay for diagnosis and is the imaging modality of choice for characterization of renal masses[5]. In this technique, a non-contrast scan is performed, followed by a corticomedullary phase at 25-70 s, a nephrographic phase at 80-180 s, and an excretory phase at 4-8 min[5]. A non-contrast scan is essential to detect any hemorrhage or calcification within the mass. Identification of pseudotumor is best done in the corticomedullary phase. A nephrographic phase is ideal for the detection of renal tumors. An excretory phase is acquired to detect pelvicalyceal system involvement. Conventional and dynamic contrast-enhanced magnetic resonance imaging (MRI) serves as a problem-solving tool[6]. MRI can also be done in cases when contrast-enhanced computed tomography (CT) is contraindicated.

Current imaging methods for the evaluation of renal tumors suffer from a few major drawbacks. As multiphasic MDCT involves the acquisition of multiple scans at different time intervals for the characterization of renal tumors, the risk of radiation is high with this repeated and multiple scanning. Contrast administered for CT or MRI can lead to various allergic reactions as well as impairment of renal function. Even after all these investigations, no conclusive diagnosis can be established in a few lesions like Bosniak 3 lesions and indeterminate renal masses. Masses like oncocytoma or lipopenic angiomyolipoma cannot be confidently diagnosed as they have no specific imaging criterion. Ruling out malignancy in pseudolesions at times becomes difficult. Focal pyelonephritis and evolving or resolving abscess may sometimes simulate malignancy; hence, more advanced imaging techniques are required for a definitive answer as the management would significantly differ in these groups.

To overcome the deficiency in imaging techniques, newer/advanced imaging methods have been devised and are being tested. This review will cover contrast-enhanced ultrasonography (CEUS), shear wave elastography (SWE), dual-energy CT (DECT), CT perfusion, MR perfusion, diffusion-weighted MRI, blood oxygen level-dependent (BOLD) MRI, MR spectroscopy (MRS), and positron emission tomography (PET)/prostate-specific membrane antigen (PSMA)-PET.

ADVANCED IMAGING TECHNIQUES

Contrast-enhanced ultrasound

CEUS has recently gained popularity in the last decade as it has become a problem-solving tool in many areas including renal diseases. The European Federation of Societies for Ultrasound in Medicine and Biology (EFSUMB) has incorporated renal applications of CEUS in 2012[7] and updated the recommendations in a paper published in 2017[8]. Being safe and quick, it has augmented the sensitivity and specificity of ultrasound in the characterization of renal masses. It can fairly differentiate small isoechoic or small solid lesions, better characterize complex cystic lesions, and differentiate tumors *vs* pseudotumors and renal cell carcinoma (RCC) *vs* angiomyolipoma, and can be utilized for detection and follow-up of renal infections.

Ultrasound contrast agents (USCA) are made up of microbubbles surrounded by a shell. This shell is composed of lipid, protein, or polymer. As these microbubbles are very fragile, the shell provides them with stability[9]. Two principles play a role in CEUS, one is enhancing the echogenicity of the lesion that is imaged and the other is the suppression of the background signal. Contrast agents markedly increase the backscatter due to a large difference in acoustic impedance at gas fluid/tissue surface interface. The second effect of background suppression is achieved by a technique called pulse inversion. For this, two similar signals with opposite phases which are mirror images of each other are sent through the same scan line and echoes from both are collected and added by the transducer. Normal tissues which act like linear reflectors produce no net signal due to the cancellation of echoes whereas the ones having microbubbles act like non-linear reflectors that produce some net signal which stands out against a dark background. When ultrasound waves strike these molecules (tissues with microbubbles), they strongly backscatter and increase the echoes by a factor of 500-1000, thus resulting in enhancement. Microvascular flow rate can also be calculated by calculating the rate at which microbubbles are in the imaging plane.

USCA evaluates both the macrovascular and microvascular systems. As soon as the contrast agent is injected, there is an avid and rapid enhancement of the kidney. Initially, the main renal artery and its branches are enhanced, followed by segmental, interlobular, arcuate, and intralobular branches. This is followed by enhancement of the cortex, then the outer medulla, and finally the pyramids. Only two phases are seen, cortical from 15 to 30s and parenchymal from 25 s to 4 min[10]. The point to note is that there will be no excretory phase as the contrast agents are not excreted in the kidneys, thus allowing it to use safely in patients with deranged renal function[8]. Current applications of CEUS in renal mass is as follows.

Differentiating renal tumors from pseudolesions: B-mode ultrasound and Doppler ultrasound fail to differentiate the solid renal tumors from pseudolesions. CEUS can make an apt and confident differential between the two, especially in patients with chronic kidney disease (CKD). Pseudolesions will show the same enhancement pattern as the normal renal parenchyma, whereas renal tumors will show different enhancement patterns in at least one of the phases[11]. In 5% of the cases when the tumor is isoenhancing, renal vascular anatomy should be studied in the early arterial phase which will show normal arteries passing through pseudolesions and aberrant deviation of arteries by the renal tumor[8].

Evaluation of renal cystic lesions: Several studies have shown CEUS to be better than CT in detecting any solid component, septa, and thickening in the wall within the cystic renal mass and thus can classify it according to Bosniak classification[12-16](Figure 1). Follow-up of complex renal cysts can be easily and quickly done by CEUS instead of expensive and high radiation exposure modalities like CT.

Characterization of indeterminate renal tumors: CEUS proves useful in determining even minimal vascularity in hypovascularized tumors to differentiate complex renal lesions from solid mass, which are indeterminate on cross-sectional imaging[12,17,18]. This is especially advantageous in CKD patients where both complex cysts and tumors have a high incidence[19].

Renal vein invasion: Renal vein invasion by tumor thrombus can be reliably detected by CEUS in which an enhancing thrombus can be seen within the renal vein and a diagnosis of malignancy can thus be confidently made[20].

Renal infections: Early detection of renal abscesses in a case of acute pyelonephritis can be done by CEUS which shows avascular areas in renal parenchyma in the parenchymal phase. Also, follow-up can be done by CEUS to look for progression or resolution of the disease[21].

The major advantages of CEUS are that it is extremely safe with no radiation exposure and can be done in CKD or patients with contrast allergy. It is quick and inexpensive. Major limitations are its operator dependence and poor visualization at times due to bowel gas or ribs.

SWE

SWE is a quantitative elastography technique that evaluates the stiffness of the tissue. The EFSUMB laid down guidelines and recommendations for its use in non-hepatic areas in the year 2013 and has updated it in 2018[8]. In the kidney, its use is limited to assess stiffness in CKD or transplant cases. The EFSUMB recommends its use as an additional tool for the diagnosis of chronic allograft nephropathy and does not recommend its use in native kidneys[8] as they are deep-seated and beyond 40mm depth which is usually the depth of the region of interest (ROI) box at which measurements are done. Only a few studies are available which have tried to differentiate benign from malignant renal masses based on their stiffness[22].

Shear wave propagation speed in tissues varies depending upon the tissue stiffness. Acoustic radiation force impulse transmits longitudinal forces which result in deformation of the tissue and generation of transverse waves called the shear waves. These are then captured by the transducer and their propagation speed is calculated. A color-coded, real-time SWE map is generated which shows local tissue stiffness in kilopascals (quantitative assessment). ROI is selected and values for maximum, minimum, mean stiffness, and standard deviation are produced. Less than ten studies have been published which have tried to differentiate benign from malignant renal mass based on elasticity. Amongst these, several have done strain elastography[23,24] and several shear wave elastography[22,25]. No standardized values have been obtained yet. One of the studies postulates elasticity values in the range of 4.5-4.7 ± 1.5-1.7 kPa of the normal renal cortex[22]. A study by Aydin *et al*[25] evaluated 40 renal masses and found the highest elasticity value in the malignant and benign groups to be 27.27 ± 25.66 kPa and 16.13 ± 8.89 kPa, respectively. However, more studies with a larger number of patients are required to authenticate these findings and establish a nomogram and cut-off for elasticity values of benign and malignant lesions. Figure 2 depicts a case of RCC having greater stiffness as compared to normal renal parenchyma.

This is a rapid, non-invasive, radiation-free, repeatable, and inexpensive technique that has no major side effects[22]. The only caution is advised in sensitive areas and fetuses as it can increase local temperature like Doppler ultrasound.

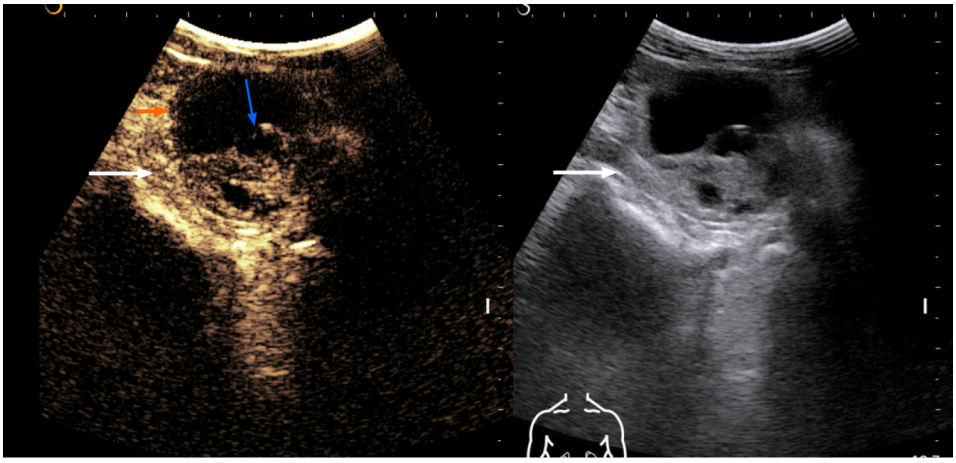

DOI: 10.4329/wjr.v14.i6.137

Figure 1 Contrast-enhanced ultrasonography images of a solid-cystic lesion in the left kidney showing thick nodular septal enhancement (blue arrow) and enhancement of solid component (long arrow). Consistent with Bosniak category 4 lesion/malignant lesion. The lesion was resected and histology revealed clear cell renal cell carcinoma.

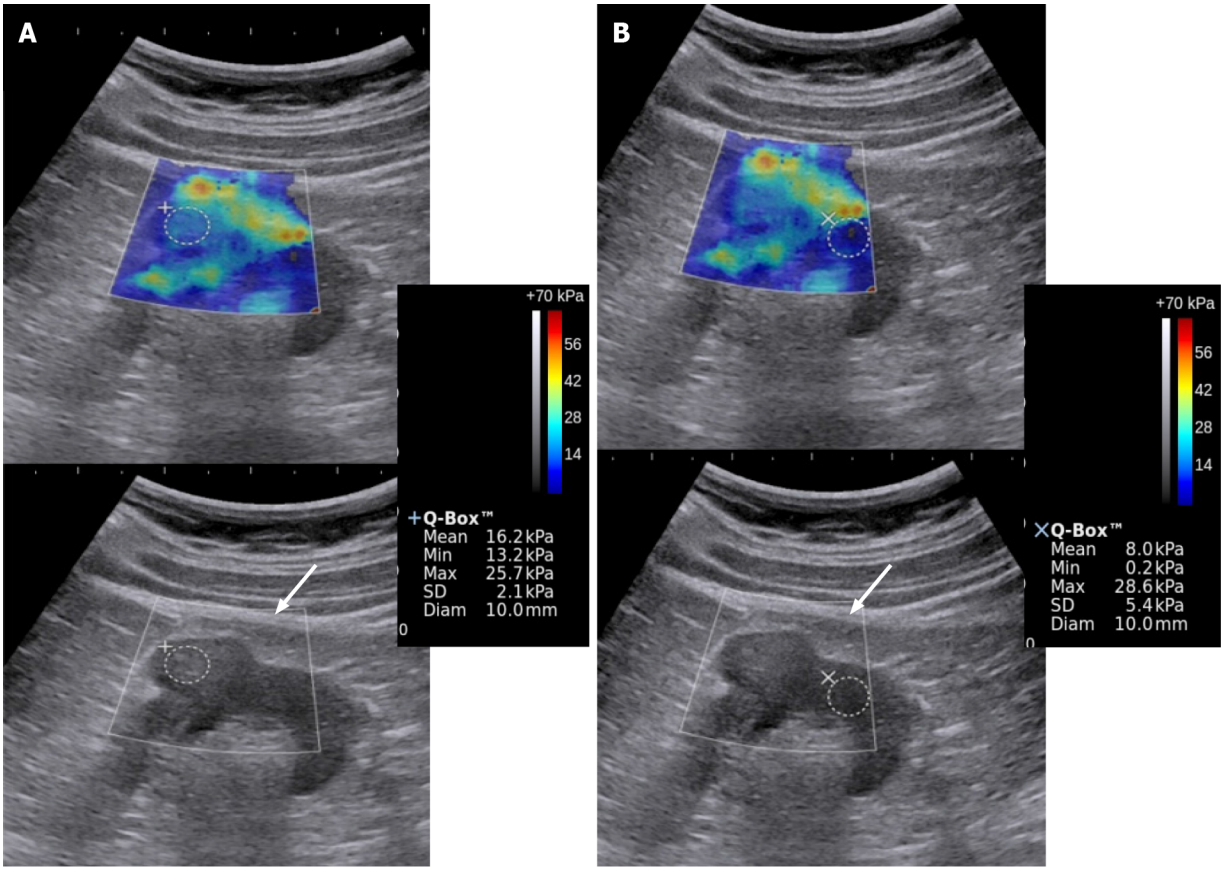

DOI: 10.4329/wjr.v14.i6.137

Figure 2 Elastography & gray-scale images of the renal mass (A) and the normal kidney (B). The mass showed greater stiffness relative to the surrounding kidney. Biopsy showed high-grade renal cell carcinoma.

DECT

DECT works on the principle of differences in absorption of photons at different photon energies which also varies with differences in material composition. Dual energy is produced either by two tubes with different peak voltages (dual-source scanner) or using a single tube with alternating peak voltage (single source)[26]. Atoms with large atomic number, like iodine, shows attenuation differences at two different peak voltages. Post-processing software is available which can subtract iodine from all images, resulting in the generation of virtual non-contrast images. Iodine overly maps can be generated which can

precisely determine areas of iodine uptake[27]. Hence, many masses which are termed indeterminate on CECT of the abdomen can be classified based on iodine uptake.

Non-contrast scans are not routinely included in abdominal CT protocol[26]. As most of the renal masses are incidentally detected, it becomes very difficult at times to detect post-contrast enhancement, hence many times the masses are labeled as indeterminate and advised for further imaging, either by multiphasic CT or MRI. If DECT is routinely done, virtual non-contrast scans can be generated and any iodine uptake can be confidently identified[28]. This will preclude the need for additional scans, thereby resulting in radiation dose reduction. Also, the cost and time of doing additional investigations can be markedly cut down.

Iodine quantification can also be done with iodine maps generated by DECT, which is given in milligram/milliliter (mg/mL). This is an indirect measure of the vascularity of the region of interest. Several studies have shown values greater than 0.5 mg/mL in tissue are indicative of enhancement[29,30]. Measurement of iodine concentration within a lesion (instead of attenuation value) solves the problem of pseudo enhancement of cysts and differentiating hyperdense cysts from hypovascular tumours[31] (Figure 3). Obtaining iodine levels from a single ROI is another advantage as it avoids the error of keeping ROI in multiple scans which can vary in position due to respiration or motion artifact [32]. Also, when the mass is large and heterogeneous, fallacious attenuation values can come if a hemorrhagic or necrotic component is included within the ROI. Measuring net total iodine concentration will not vary if such areas get included in the ROI. Hence, a large ROI covering the entire mass can be kept[33]. According to a systematic analysis and meta-analysis by Salameh, the pooled sensitivity and specificity of DECT were to be 96.6% and 95.1%, respectively, in renal masses using quantitative iodine concentration[34].

CT perfusion

CT perfusion imaging detects the temporal changes in tissue attenuation after iodinated contrast is administered intravenously. It can detect changes at the molecular level and assess tissue perfusion and vascular permeability. Both qualitative and quantitative measurements can be done. Blood flow (BF) and blood volume (BV) can be obtained from the initial intravascular phase and vascular permeability (PMB) from the second phase.

Perfusion studies are an indirect predictor of neoangiogenesis. In renal cell carcinoma, which is a highly vascular tumor, multiple factors like vascular endothelial growth factor and tyrosine kinase are recruited, which result in neoangiogenesis. This neoangiogenesis is responsible for the growth of the tumor and metastasis. Targeted chemotherapy stops the proliferation of new vessels and reduces the perfusion parameters; hence, the response to treatment can be assessed. As the size of the mass decreases much later than the reduction in vascular parameters, early response evaluation is possible with perfusion technique[35] (Figures 4 and 5).

MR perfusion

MR perfusion is the technique developed to measure perfusion or vascularity of tissue after injection of a contrast medium. Multiphasic MRI is routinely done to assess the enhancement of the tissue. However, quantitative parameters can be derived only with MR perfusion. In this signal intensity, curves are generated which are placed against time and many post-processing techniques are done to obtain perfusion parameters[36]. Tissue perfusion can also be measured without administering a contrast medium through arterial spin labeling technique[37-40]. In this technique, the red blood cells (RBCs) behave as endogenous contrast agents. They are labeled non-invasively with MR gradient and radiofrequency. Tissue perfusion is calculated by estimating the inflow of the labeled RBCs to the tissue of interest. The major advantage of non-contrast MR perfusion is as endogenous contrast is used, erroneous calculation due to vascular permeability is not problematic here. Second, it can be done in patients where MR contrast medium is contraindicated. But it has a low sensitivity in hypovascular masses.

Tumor grading of RCC is also possible by perfusion studies. Higher grade RCC shows higher perfusion values than low-grade RCC. One of the studies by Palmowski obtained mean perfusion values of high-grade RCC to be 1.59 ± 0.44 (mL/g/min) *vs* low-grade RCC 1.08 ± 0.38 (mL/g/min)[41]. Another advantage of MR perfusion is in the evaluation of antiangiogenic drug therapy commonly administered for metastatic RCC. Changes in vascularity occur much before the change in the size of the mass. Hence, for early response assessment, several studies[42-44] have demonstrated the potential role of this technique.

Diffusion-weighted imaging

Diffusion-weighted imaging (DWI) is a type of functional MR technique that quantitatively assesses the free Brownian motion of water molecules and thus derives the image contrast based on the restriction of this free motion. This in turn is dependent on the tissue cellularity, organization, cell membrane integrity, and extracellular space tortuosity[45,46]. Abundant work is available in establishing its usefulness in the central nervous system. Many studies have also come forth evaluating its role in the kidneys in the last two decades. DWI has shown promise in differentiating benign *vs* malignant renal

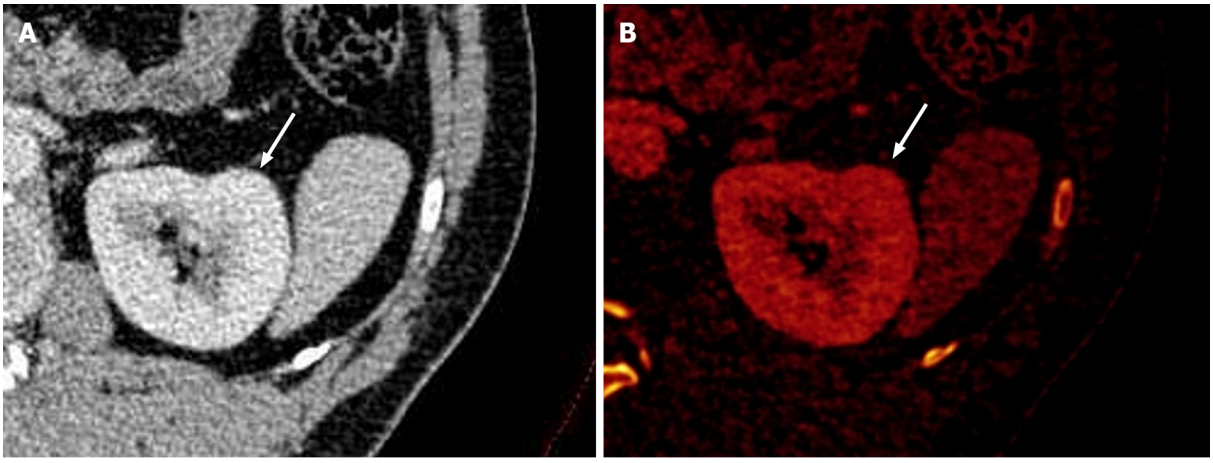

DOI: 10.4329/wjr.v14.i6.137

Figure 3 Dual-energy computed tomography images. A: Contrast-enhanced axial dual-energy computed tomography image showing contour bulge from the lateral cortex of the interpolar region of the left kidney, enhanced similar to background parenchyma; B: Iodine overlay image confirming the absence of any differential iodine distribution, suggesting the lesion to be a dromedary hump.

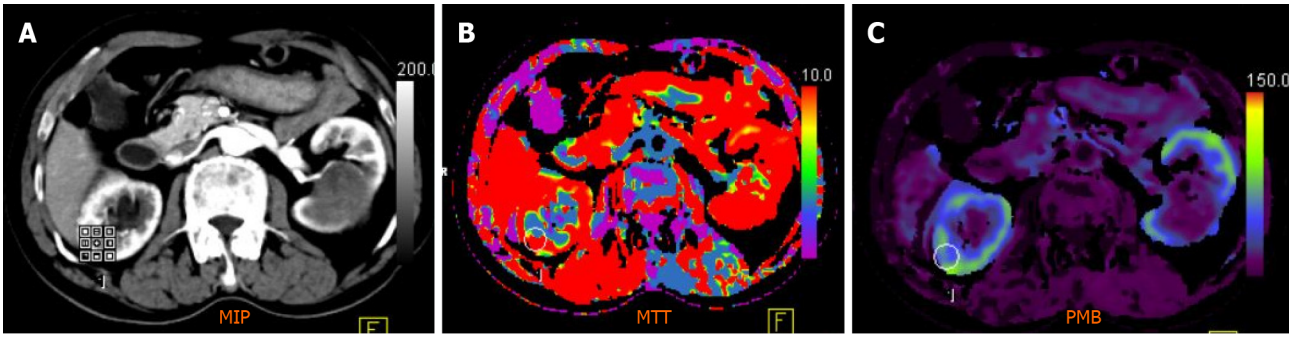

DOI: 10.4329/wjr.v14.i6.137

Figure 4 Computed tomography perfusion images (A-C) reveal a significant difference in permeability and mean transit time values between normal renal cortex and malignant lesions. Mean transit time (MTT) and permeability (PMB) in normal renal cortex were 10.48 s and 55.56 mL/100 mL/min, respectively, which were significantly different from those of renal cell carcinoma (RCC) (MTT: 9.06 s; PMB: 237.09 mL/100 mL/min). A cut-off of 2.5 mL/100 g/min yielded a 100% sensitivity and 95.92% accuracy to predict RCC.

lesions, in differentiating clear *vs* non-clear cell carcinoma, and in further subtyping the grade of RCCs [47-53].

Benign masses show higher apparent diffusion coefficient (ADC) than malignant lesions. According to a study by Sandrasegaran *et al*[53], the mean ADC of benign lesions is [mean (Standard deviation) 2.76 (0.32) × 10^{-3} mm^2/s] *vs* malignant lesions [2.02 × 10^{-3} mm^2/s]. Amongst the malignant masses, clear cell RCCs show signi-ficantly higher ADC values than papillary and chromophobe RCCs, which have a better prognosis than clear cell RCCs. Low-grade clear cell RCCs have significantly higher ADC values than high-grade RCC, *i.e.*, an inverse relation is seen, the higher the grade, the lower the ADC[46]. According to a study by Agnello *et al*[54], mean ADC was significantly different between RCC (1.2 ± 0.01 mm^2/s), angiomyolipoma(1.07 ± 0.3 mm^2/s), metastases (1.25 ± 0.04 mm^2/s), and oncocytomas (1.56 ± 0.08 mm^2/s; $P < 0.05$).

DWI is particularly helpful in patients with contrast allergy or renal impairment when the iodinated control is contraindicated. In such situations, diffusion enhances the confidence of making the distinction between benign and malignant masses on a plain scan.

As the treatment of focal renal lesions could be variable ranging from ablative procedures to complete or partial nephrectomy and radiological follow-up to chemotherapy depending upon the aggressiveness of the lesion, clear demarcation and characterization of renal mass are of utmost importance, which can be optimally done by DWI. Besides, diffusion is also done in renal parenchymal disease and renal infections. It is especially helpful in assessing the response to treatment and in follow-up scans to look for any recurrence (Figure 6). In postoperative scans due to marked post-operative/chemo inflammatory changes, it is hard to detect early recurrence in plain scans.

The main advantage of this sequence is that it is a quick sequence without much extending the total span of MRI examination and hence has been routinely incorporated in standard abdominal MRI. No

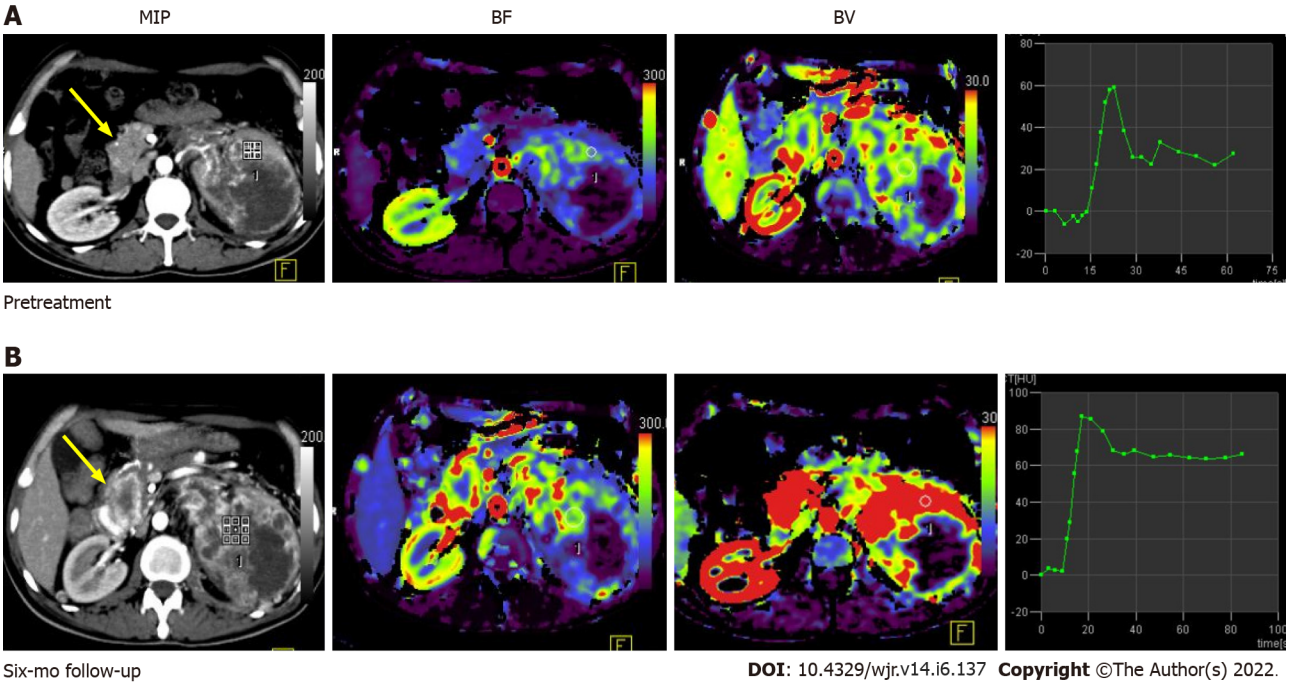

DOI: 10.4329/wjr.v14.i6.137

Figure 5 Pre-treatment (A) and post-treatment (B) computed tomography perfusion images in a case of large left renal cell carcinoma with metastasis to the uncinate process of the pancreas (yellow arrow). Comparison of perfusion parameters at the 6-mo follow-up after anti-angiogenic therapy showed that there was an increase in BF and BV, which was suggestive of progressive disease. No significant change in lesion size would have qualified this case as a stable disease as per size criteria.

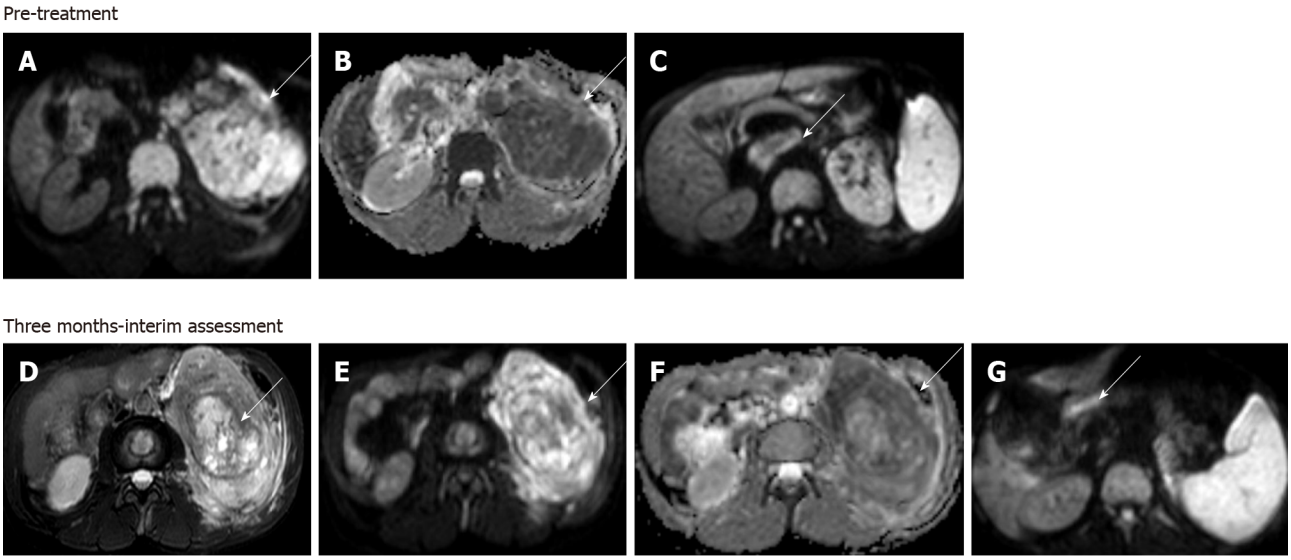

DOI: 10.4329/wjr.v14.i6.137

Figure 6 Magnetic resonance images. Diffusion-weighted imaging (DWI) at b = 800 s/mm^2 (A) and apparent diffusion coefficient (ADC) map (B) showed large clear cell renal cell carcinoma replacing the left kidney showing markedly restricted diffusion; DWI image (C) showing a malignant thrombus extending to the inferior vena cava (arrow) Axial T2W FS image (D) showing that 3 mo after treatment with sorafenib (a tyrosine kinase inhibitor), there was no significant change in the size of the lesion; however, there was increased necrosis in the mass; Resultant increase in ADC value on the corresponding DWI at b = 800 s/mm^2 (E) and ADC map (F); DWI (G) also revealed partial recanalization of the malignant thrombus (arrow)—overall features suggestive of partial response.

contrast administration is required. It is quite specific and has proved more specific when evaluated along with basic MRI than CT or MRI alone. However, caution needs to be taken with regard to the area from which the values are calculated. If ROI is kept over the hemorrhagic or necrotic component of the mass, the values can be misleading. The scanner needs to be optimized and appropriate b values (400-800) should be used to improve the accuracy of results.

Many researchers are showing interest in evaluating the role of intravoxel incoherent motion (IVIM) and diffusion kurtosis in differentiating benign from malignant renal masses and also in the grading of

renal cell carcinoma. IVIM is a biexponential model which includes both true and pseudo diffusion, which is predominantly driven by perfusion[55]. Parameters like diffusivity (D), pseudo diffusion coefficient (D*), and perfusion index (F) can be calculated. Jenson *et al*[56] in the year 2005 gave the concept of diffusion kurtosis which follows non-Gaussian diffusion, and parameters like mean diffusivity, mean kurtosis, kurtosis anisotropy, and radial kurtosis can be measured. A significant difference in Diffusion kurtosis parameters is seen in different subtypes and grades of RCC. A study by Ding *et al*[57] obtained superior results with IVIM in differentiating benign from malignant renal masses than diffusion or kurtosis parameters.

BOLD

BOLD is a quick MRI sequence that non-invasively evaluates deoxyhemoglobin levels in the kidney. In most human organs, oxygen tension is relatively constant and varies with the regional blood flow. The kidney is one of the organs where the oxygen tension varies both with the blood flow and the need for filtration. As tubular filtration is an active process requiring energy, this results in a variation of oxygen tension. The cortex of the kidney is well perfused and high in oxygen whereas the medulla is relatively less perfused with and low in oxygen tension. The medulla also has a counter-current arrangement of vessels which further contributes to lower oxygen tension in this region. This results in higher production of deoxyhemoglobin. Deoxyhaemoglobin has a paramagnetic effect and results in the rapid dephasing of protons. A higher amount of deoxyhemoglobin leads to a decrease in T2* relaxation time [58].

BOLD MRI has wide applications in the brain[59-62]. Many studies are being done on the kidneys, justifying their utility in renal pathologies. The echo-planar imaging (EPI) sequence or more sequences are used. The multiple gradient-recalled echo sequence is better than the EPI sequence in terms of SNI, spatial distortion, and spatial resolution. It calculates 1/R2* and generates various maps. After the excitation pulse, multiple gradient echoes are acquired. The higher the strength of the magnetic field, the better the results obtained. BOLD MRI proves useful in the detection of ischemia in the kidneys as in renal artery stenosis, renal artery occlusion, *etc*. as proven by a few studies[63-65]. Early initiation of treatment results in a better outcome. It is also useful in diabetics, hypertension, allograft rejection, *etc.* As various renal lesions would result in a change in perfusion of the kidney, this can be a reliable tool to differentiate benign from malignant renal lesion (Figures 7 and 8).

Proton spectroscopy

Proton spectroscopy (H1MRS) is an advanced MR technique that studies the variation in chemical metabolites in determining various pathologies. It is a powerful, non-invasive tool to quantitatively study the chemical compositions and metabolic processes *in vivo*.

Whenever there is an application of magnetic field, there is a generation of small magnetic fields by the circulating protons which interact with the main magnetic field and bring about a change in Larmor frequency. This change in frequency due to differing chemical composition is called "chemical shift [66]". Proctor and Yu, for the first time, proposed the concept of chemical shift in 1951, and the first *in vivo* proton MR spectrum was published in 1985[67].

Proton MR spectroscopy has well-known applications in the central nervous system, breast, and prostate. Its role in renal masses is the current area of interest. Promising results of a few *in vitro* and *in vivo* studies are available in the differentiation of different renal masses[68].

The first *in vivo* study was conducted by Kim *et al*[69] who recruited five patients with biopsy-proven cases of RCC and found the difference of metabolite lipid and choline as per the grade of the tumour (Figure 9).

MRS is limited by the complexity of its acquisition, processing, and data interpretation[70]. It suffers from a low sensitivity and poor spatial resolution. It can only act as a complementary tool that supplements the results of basic MRI examination.

PET scan: Fluorodeoxyglucose and PSMA PET

Fluorodeoxyglucose (FDG) PET scan plays a limited role in primary RCC due to low sensitivity[71] but can be useful in case of aggressive or advanced RCC[72], recurrent disease[73], and metastatic RCC[74], and for post-treatment evaluation[75]. As FDG is excreted by the kidneys, FDG PET is not suitable for local staging of primary RCC. However, it has a crucial role in overall staging of the disease, differentiating malignant *vs* bland thrombosis in the renal vein/inferior vena cava, detecting metastasis to distant sites, detecting recurrent/residual disease in postoperative/chemotherapy evaluation, monitoring response to therapy, and restaging of the disease. Quantitative measurement of maximum standardized uptake values(SUVs) can be done for objective assessment. The higher the SUV, the more dismal the prognosis. A cut-off of 3 is seen to be optimal to differentiate low grade *vs* high-grade RCC [75].

Although FDG is the most common tracer to be used for PET, other new tracers like ^{68}Ga-PSMA, ^{18}F-fluoroethylcholine, ^{11}C-acetate, ^{18}F-fluoromisonidazole, and ^{18}F-fluorothymidine are being investigated [76]. Prostate-specific membrane antigen (PSMA) is a molecule that is expressed in prostatic cells and has established application in the prostatic tumor. Further research showed its expression on neovasculature of renal cancer cells and hence its potential role in RCC has been explored by researchers with

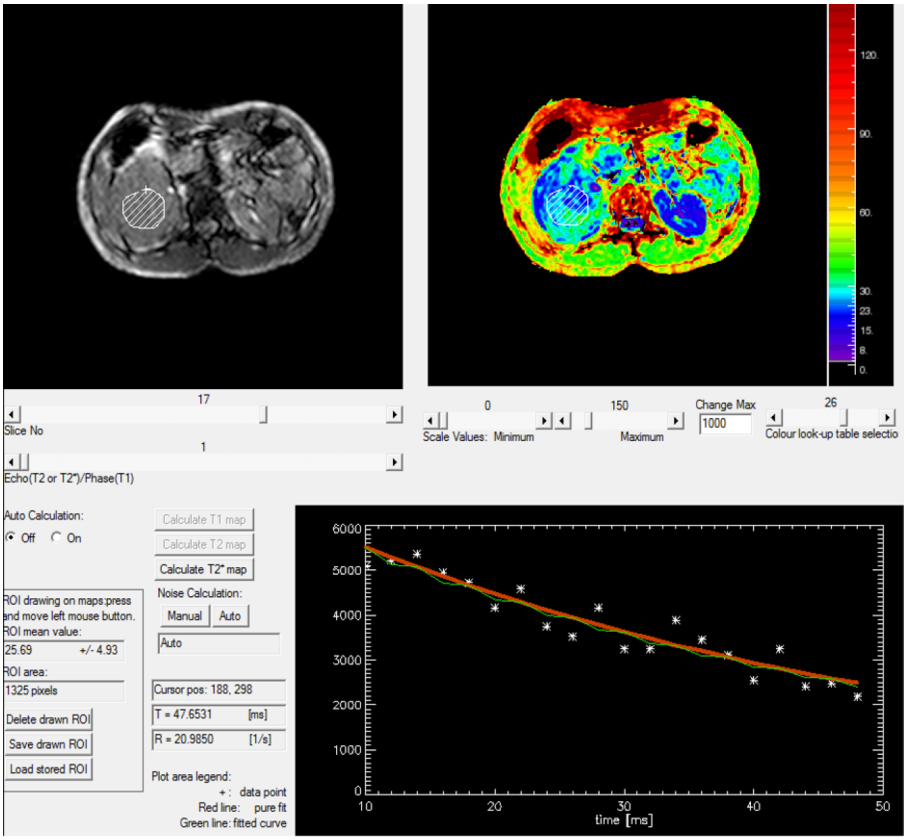

DOI: 10.4329/wjr.v14.i6.137

Figure 7 Rate of spin dephasing (R2* map) showing R2* value of right renal cell carcinoma (20.9/s), which was lower than that of a normal kidney (25.5/s).

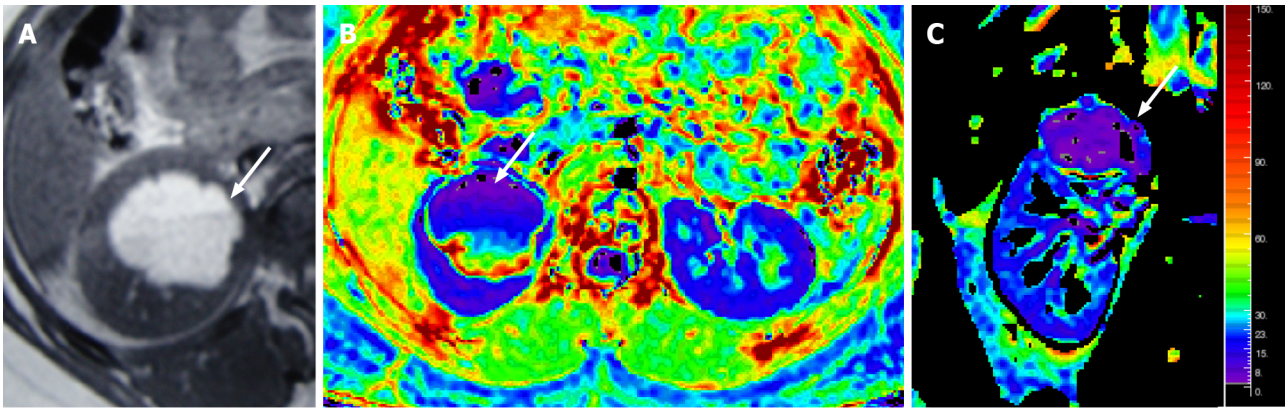

DOI: 10.4329/wjr.v14.i6.137

Figure 8 Magnetic resonance images. T1W axial MR image (A) showing a hyperintense lesion in the upper pole of the right kidney, with fluid-fluid level, suggestive of a hemorrhagic cyst; Axial & coronal R2* maps (B and C) showing an R2* value of 6.1/s.

encouraging results[77]. Several studies have shown a change in the management of RCC when gallium PSMA PET was used for primary staging compared with CECT scan due to detection of small areas of metastasis and synchronous malignancies[78]. Gallium PSMA PET is proven to be better than FDG PET for oligometastatic RCC[79].

CONCLUSION

Sonography serves as the screening modality whereas multiphasic CECT acts as the workhorse in the assessment of renal masses. MRI with DWI is a potential problem-solving adjunct technique. CEUS and

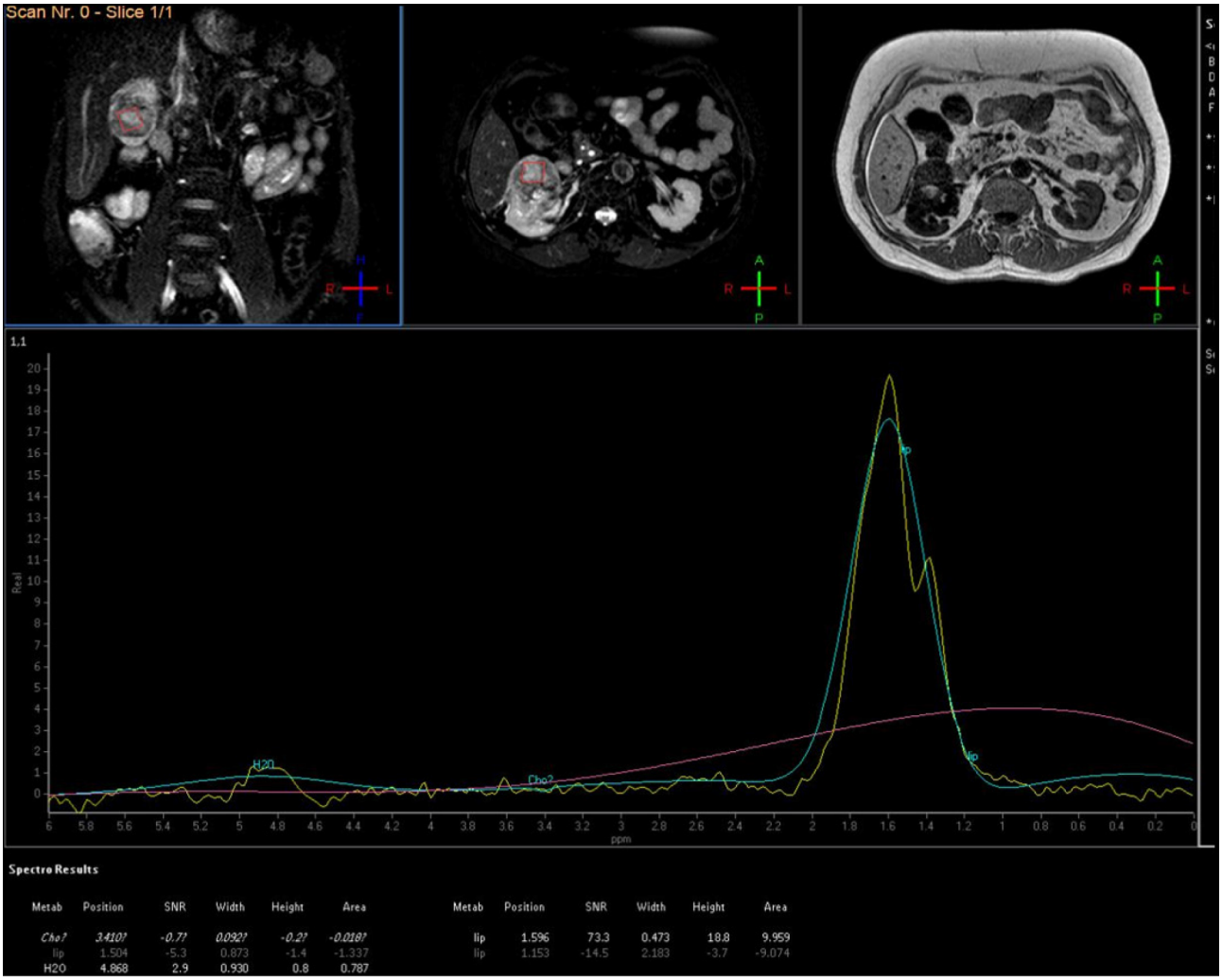

DOI: 10.4329/wjr.v14.i6.137

Figure 9 MR spectroscopy of low-grade renal cell carcinoma showed increased lipid-lactate peak.

SWE, an extension of ultrasound, provide comparable results with no added risk of nephrotoxicity or radiation-related injuries. DECT, perfusion imaging, BOLD MRI, and MR spectroscopy can be helpful in indeterminate cases. PET-CT using FDG or gallium PSMA is also finding gradual applications. The constant advancements in imaging techniques allow confident diagnosis and superior characterization of renal masses. They also serve as potential biomarkers and aid in prognostication & response assessment after chemotherapy/ablative procedures.

FOOTNOTES

Author contributions: Aggarwal A contributed to manuscript writing and original drafting; Das CJ contributed to conceptualization, and manuscript writing and editing; Sharma S contributed to supervision.

Conflict-of-interest statement: All the authors declare that they have no conflict of interest to disclose.

Country/Territory of origin: India

ORCID number: Ankita Aggarwal 0000-0003-4793-6124; Chandan J Das 0000-0001-6505-5940; Sanjay Sharma 0000-0003-0607-1611.

S-Editor: Liu JH
L-Editor: Wang TQ
P-Editor: Liu JH

REFERENCES

1 **Rossi SH**, Klatte T, Usher-Smith J, Stewart GD. Epidemiology and screening for renal cancer. *World J Urol* 2018; **36**: 1341-1353 [PMID: 29610964 DOI: 10.1007/s00345-018-2286-7]
2 **Mizuma Y**, Watanabe Y, Ozasa K, Hayashi K, Kawai K. Validity of sonographic screening for the detection of abdominal cancers. *J Clin Ultrasound* 2002; **30**: 408-415 [PMID: 12210458 DOI: 10.1002/jcu.10089]
3 **Filipas D**, Spix C, Schulz-Lampel D, Michaelis J, Hohenfellner R, Roth S, Thüroff JW. Screening for renal cell carcinoma using ultrasonography: a feasibility study. *BJU Int* 2003; **91**: 595-599 [PMID: 12699466 DOI: 10.1046/j.1464-410x.2003.04175.x]
4 **Amenta PS**, Ghobrial GM, Krespan K, Nguyen P, Ali M, Harrop JS. Cervical spondylotic myelopathy in the young adult: a review of the literature and clinical diagnostic criteria in an uncommon demographic. *Clin Neurol Neurosurg* 2014; **120**: 68-72 [PMID: 24731579 DOI: 10.1016/j.clineuro.2014.02.019]
5 **Tsili AC**, Argyropoulou MI. Advances of multidetector computed tomography in the characterization and staging of renal cell carcinoma. *World J Radiol* 2015; **7**: 110-127 [PMID: 26120380 DOI: 10.4329/wjr.v7.i6.110]
6 **Haddad MC**, Bulbul MA. Current imaging of solid renal masses. *J Med Liban* 2005; **53**: 72-79 [PMID: 16604991]
7 **Piscaglia F**, Nolsøe C, Dietrich CF, Cosgrove DO, Gilja OH, Bachmann Nielsen M, Albrecht T, Barozzi L, Bertolotto M, Catalano O, Claudon M, Clevert DA, Correas JM, D'Onofrio M, Drudi FM, Eyding J, Giovannini M, Hocke M, Ignee A, Jung EM, Klauser AS, Lassau N, Leen E, Mathis G, Saftoiu A, Seidel G, Sidhu PS, terHaar G, Timmerman D, Weskott HP. The EFSUMB Guidelines and Recommendations on the Clinical Practice of Contrast Enhanced Ultrasound (CEUS): update 2011 on non-hepatic applications. *Ultraschall Med* 2012; **33**: 33-59 [PMID: 21874631 DOI: 10.1055/s-0031-1281676]
8 **Sidhu PS**, Cantisani V, Dietrich CF, Gilja OH, Saftoiu A, Bartels E, Bertolotto M, Calliada F, Clevert DA, Cosgrove D, Deganello A, D'Onofrio M, Drudi FM, Freeman S, Harvey C, Jenssen C, Jung EM, Klauser AS, Lassau N, Meloni MF, Leen E, Nicolau C, Nolsoe C, Piscaglia F, Prada F, Prosch H, Radzina M, Savelli L, Weskott HP, Wijkstra H. The EFSUMB Guidelines and Recommendations for the Clinical Practice of Contrast-Enhanced Ultrasound (CEUS) in Non-Hepatic Applications: Update 2017 (Long Version). *Ultraschall Med* 2018; **39**: e2-e44 [PMID: 29510439 DOI: 10.1055/a-0586-1107]
9 **Cokkinos DD**, Antypa EG, Skilakaki M, Kriketou D, Tavernaraki E, Piperopoulos PN. Contrast enhanced ultrasound of the kidneys: what is it capable of? *Biomed Res Int* 2013; **2013**: 595873 [PMID: 24455707 DOI: 10.1155/2013/595873]
10 **Correas JM**, Claudon M, Tranquart F, Hélénon AO. The kidney: imaging with microbubble contrast agents. *Ultrasound Q* 2006; **22**: 53-66 [PMID: 16641794]
11 **Mazziotti S**, Zimbaro F, Pandolfo A, Racchiusa S, Settineri N, Ascenti G. Usefulness of contrast-enhanced ultrasonography in the diagnosis of renal pseudotumors. *Abdom Imaging* 2010; **35**: 241-245 [PMID: 19194642 DOI: 10.1007/s00261-008-9499-y]
12 **Barr RG**, Peterson C, Hindi A. Evaluation of indeterminate renal masses with contrast-enhanced US: a diagnostic performance study. *Radiology* 2014; **271**: 133-142 [PMID: 24475802 DOI: 10.1148/radiol.13130161]
13 **Quaia E**, Bertolotto M, Cioffi V, Rossi A, Baratella E, Pizzolato R, Cov MA. Comparison of contrast-enhanced sonography with unenhanced sonography and contrast-enhanced CT in the diagnosis of malignancy in complex cystic renal masses. *AJR Am J Roentgenol* 2008; **191**: 1239-1249 [PMID: 18806171 DOI: 10.2214/AJR.07.3546]
14 **Clevert DA**, Minaifar N, Weckbach S, Jung EM, Stock K, Reiser M, Staehler M. Multislice computed tomography versus contrast-enhanced ultrasound in evaluation of complex cystic renal masses using the Bosniak classification system. *Clin HemorheolMicrocirc* 2008; **39**: 171-178 [PMID: 18503122]
15 **Park BK**, Kim B, Kim SH, Ko K, Lee HM, Choi HY. Assessment of cystic renal masses based on Bosniak classification: comparison of CT and contrast-enhanced US. *Eur J Radiol* 2007; **61**: 310-314 [PMID: 17097844 DOI: 10.1016/j.ejrad.2006.10.004]
16 **Ascenti G**, Mazziotti S, Zimbaro G, Settineri N, Magno C, Melloni D, Caruso R, Scribano E. Complex cystic renal masses: characterization with contrast-enhanced US. *Radiology* 2007; **243**: 158-165 [PMID: 17392251 DOI: 10.1148/radiol.2431051924]
17 **Bertolotto M**, Cicero C, Perrone R, Degrassi F, Cacciato F, Cova MA. Renal Masses With Equivocal Enhancement at CT: Characterization With Contrast-Enhanced Ultrasound. *AJR Am J Roentgenol* 2015; **204**: W557-W565 [PMID: 25905962 DOI: 10.2214/AJR.14.13375]
18 **Granata A**, Zanoli L, Insalaco M, Valentino M, Pavlica P, Di Nicolò PP, Scuderi M, Fiorini F, Fatuzzo P, Bertolotto M. Contrast-enhanced ultrasound (CEUS) in nephrology: Has the time come for its widespread use? *Clin Exp Nephrol* 2015; **19**: 606-615 [PMID: 25351822 DOI: 10.1007/s10157-014-1040-8]
19 **Tickoo SK**, dePeralta-Venturina MN, Harik LR, Worcester HD, Salama ME, Young AN, Moch H, Amin MB. Spectrum of epithelial neoplasms in end-stage renal disease: an experience from 66 tumor-bearing kidneys with emphasis on histologic patterns distinct from those in sporadic adult renal neoplasia. *Am J Surg Pathol* 2006; **30**: 141-153 [PMID: 16434887 DOI: 10.1097/01.pas.0000185382.80844.b1]
20 **Ignee A**, Straub B, Brix D, Schuessler G, Ott M, Dietrich CF. The value of contrast enhanced ultrasound (CEUS) in the characterisation of patients with renal masses. *Clin HemorheolMicrocirc* 2010; **46**: 275-290 [PMID: 21187576 DOI: 10.3233/CH-2010-1352]
21 **Fontanilla T**, Minaya J, Cortés C, Hernando CG, Arangüena RP, Arriaga J, Carmona MS, Alcolado A. Acute complicated pyelonephritis: contrast-enhanced ultrasound. *Abdom Imaging* 2012; **37**: 639-646 [PMID: 21792579 DOI:

10.1007/s00261-011-9781-2]
22 **Cai Y**, Li F, Li Z, Du L, Wu R. Diagnostic Performance of Ultrasound Shear Wave Elastography in Solid Small (≤4 cm) Renal Parenchymal Masses. *Ultrasound Med Biol* 2019; **45**: 2328-2337 [PMID: 31196747 DOI: 10.1016/j.ultrasmedbio.2019.05.010]
23 **Onur MR**, Poyraz AK, Bozgeyik Z, Onur AR, Orhan I. Utility of semiquantitative strain elastography for differentiation between benign and malignant solid renal masses. *J Ultrasound Med* 2015; **34**: 639-647 [PMID: 25792579 DOI: 10.7863/ultra.34.4.639]
24 **Keskin S**, Güven S, Keskin Z, Özbiner H, Kerimoğlu Ü, Yeşildağ A. Strain elastography in the characterization of renal cell carcinoma and angiomyolipoma. *Can Urol Assoc J* 2015; **9**: e67-e71 [PMID: 25737764 DOI: 10.5489/cuaj.2349]
25 **Aydin S**, Yildiz S, Turkmen I, Sharifov R, Uysal O, Gucin Z, Armagan A, Kocakoc E. Value of Shear Wave Elastography for differentiating benign and malignant renal lesions. *Med Ultrason* 2018; **1**: 21-26 [PMID: 29400363 DOI: 10.11152/mu-1161]
26 **Graser A**, Johnson TR, Hecht EM, Becker CR, Leidecker C, Staehler M, Stief CG, Hildebrandt H, Godoy MC, Finn ME, Stepansky F, Reiser MF, Macari M. Dual-energy CT in patients suspected of having renal masses: can virtual nonenhanced images replace true nonenhanced images? *Radiology* 2009; **252**: 433-440 [PMID: 19487466 DOI: 10.1148/radiol.2522080557]
27 **Ascenti G**, Mazziotti S, Mileto A, Racchiusa S, Donato R, Settineri N, Gaeta M. Dual-source dual-energy CT evaluation of complex cystic renal masses. *AJR Am J Roentgenol* 2012; **199**: 1026-1034 [PMID: 23096175 DOI: 10.2214/AJR.11.7711]
28 **Salameh JP**, McInnes MDF, McGrath TA, Salameh G, Schieda N. Diagnostic Accuracy of Dual-Energy CT for Evaluation of Renal Masses: Systematic Review and Meta-Analysis. *AJR Am J Roentgenol* 2019; **212**: W100-W105 [PMID: 30714831 DOI: 10.2214/AJR.18.20527]
29 **Chandarana H**, Megibow AJ, Cohen BA, Srinivasan R, Kim D, Leidecker C, Macari M. Iodine quantification with dual-energy CT: phantom study and preliminary experience with renal masses. *AJR Am J Roentgenol* 2011; **196**: W693-W700 [PMID: 21606256 DOI: 10.2214/AJR.10.5541]
30 **Ascenti G**, Mileto A, Krauss B, Gaeta M, Blandino A, Scribano E, Settineri N, Mazziotti S. Distinguishing enhancing from nonenhancing renal masses with dual-source dual-energy CT: iodine quantification versus standard enhancement measurements. *EurRadiol* 2013; **23**: 2288-2295 [PMID: 23479222 DOI: 10.1007/s00330-013-2811-4]
31 **Kaza RK**, Ananthakrishnan L, Kambadakone A, Platt JF. Update of Dual-Energy CT Applications in the Genitourinary Tract. *AJR Am J Roentgenol* 2017; **208**: 1185-1192 [PMID: 28301210 DOI: 10.2214/AJR.16.17742]
32 **Mileto A**, Nelson RC, Paulson EK, Marin D. Dual-Energy MDCT for Imaging the Renal Mass. *AJR Am J Roentgenol* 2015; **204**: W640-W647 [PMID: 25730444 DOI: 10.2214/AJR.14.14094]
33 **Mileto A**, Marin D, Nelson RC, Ascenti G, Boll DT. Dual energy MDCT assessment of renal lesions: an overview. *EurRadiol* 2014; **24**: 353-362 [PMID: 24092045 DOI: 10.1007/s00330-013-3030-8]
34 **Salameh JP**, McInnes MDF, McGrath TA, Salameh G, Schieda N. Diagnostic Accuracy of Dual-Energy CT for Evaluation of Renal Masses: Systematic Review and Meta-Analysis. *AJR Am J Roentgenol* 2019; **212**: W100-W105 [PMID: 30714831 DOI: 10.2214/AJR.18.20527]
35 **Das CJ**, Thingujam U, Panda A, Sharma S, Gupta AK. Perfusion computed tomography in renal cell carcinoma. *World J Radiol* 2015; **7**: 170-179 [PMID: 26217456 DOI: 10.4329/wjr.v7.i7.170]
36 **Gilet AG**, Kang SK, Kim D, Chandarana H. Advanced renal mass imaging: diffusion and perfusion MRI. *CurrUrol Rep* 2012; **13**: 93-98 [PMID: 22081252 DOI: 10.1007/s11934-011-0227-8]
37 **Alsop DC**, Detre JA. Multisection cerebral blood flow MR imaging with continuous arterial spin labeling. *Radiology* 1998; **208**: 410-416 [PMID: 9680569 DOI: 10.1148/radiology.208.2.9680569]
38 **Martirosian P**, Klose U, Mader I, Schick F. FAIR true-FISP perfusion imaging of the kidneys. *MagnReson Med* 2004; **51**: 353-361 [PMID: 14755661 DOI: 10.1002/mrm.10709]
39 **Fenchel M**, Martirosian P, Langanke J, Giersch J, Miller S, Stauder NI, Kramer U, Claussen CD, Schick F. Perfusion MR imaging with FAIR true FISP spin labeling in patients with and without renal artery stenosis: initial experience. *Radiology* 2006; **238**: 1013-1021 [PMID: 16439565 DOI: 10.1148/radiol.2382041623]
40 **Lanzman RS**, Wittsack HJ, Martirosian P, Zgoura P, Bilk P, Kröpil P, Schick F, Voiculescu A, Blondin D. Quantification of renal allograft perfusion using arterial spin labeling MRI: initial results. *EurRadiol* 2010; **20**: 1485-1491 [PMID: 19949799 DOI: 10.1007/s00330-009-1675-0]
41 **Palmowski M**, Schifferdecker I, Zwick S, Macher-Goeppinger S, Laue H, Haferkamp A, Kauczor HU, Kiessling F, Hallscheidt P. Tumor perfusion assessed by dynamic contrast-enhanced MRI correlates to the grading of renal cell carcinoma: initial results. *Eur J Radiol* 2010; **74**: e176-e180 [PMID: 19540690 DOI: 10.1016/j.ejrad.2009.05.042]
42 **Hillman GG**, Singh-Gupta V, Al-Bashir AK, Zhang H, Yunker CK, Patel AD, Sethi S, Abrams J, Haacke EM. Dynamic contrast-enhanced magnetic resonance imaging of sunitinib-induced vascular changes to schedule chemotherapy in renal cell carcinoma xenograft tumors. *Transl Oncol* 2010; **3**: 293-306 [PMID: 20885892 DOI: 10.1593/tlo.10136]
43 **Galbraith SM**, Maxwell RJ, Lodge MA, Tozer GM, Wilson J, Taylor NJ, Stirling JJ, Sena L, Padhani AR, Rustin GJ. Combretastatin A4 phosphate has tumor antivascular activity in rat and man as demonstrated by dynamic magnetic resonance imaging. *J Clin Oncol* 2003; **21**: 2831-2842 [PMID: 12807936 DOI: 10.1200/JCO.2003.05.187]
44 **Flaherty KT**, Rosen MA, Heitjan DF, Gallagher ML, Schwartz B, Schnall MD, O'Dwyer PJ. Pilot study of DCE-MRI to predict progression-free survival with sorafenib therapy in renal cell carcinoma. *Cancer Biol Ther* 2008; **7**: 496-501 [PMID: 18219225 DOI: 10.4161/cbt.7.4.5624]
45 **Padhani AR**, Liu G, Koh DM, Chenevert TL, Thoeny HC, Takahara T, Dzik-Jurasz A, Ross BD, Van Cauteren M, Collins D, Hammoud DA, Rustin GJ, Taouli B, Choyke PL. Diffusion-weighted magnetic resonance imaging as a cancer biomarker: consensus and recommendations. *Neoplasia* 2009; **11**: 102-125 [PMID: 19186405 DOI: 10.1258/ar.2011.110415]
46 **Goyal A**, Sharma R, Bhalla AS, Gamanagatti S, Seth A, Iyer VK, Das P. Diffusion-weighted MRI in renal cell carcinoma: a surrogate marker for predicting nuclear grade and histological subtype. *Acta Radiol* 2012; **53**: 349-358 [PMID: 22496427 DOI: 10.1258/ar.2011.110415]

47 **Squillaci E**, Manenti G, Di Stefano F, Miano R, Strigari L, Simonetti G. Diffusion-weighted MR imaging in the evaluation of renal tumours. *J Exp Clin Cancer Res* 2004; **23**: 39-45 [PMID: 15149149]

48 **Cova M**, Squillaci E, Stacul F, Manenti G, Gava S, Simonetti G, Pozzi-Mucelli R. Diffusion-weighted MRI in the evaluation of renal lesions: preliminary results. *Br J Radiol* 2004; **77**: 851-857 [PMID: 15482997 DOI: 10.1259/bjr/26525081]

49 **Yoshikawa T**, Kawamitsu H, Mitchell DG, Ohno Y, Ku Y, Seo Y, Fujii M, Sugimura K. ADC measurement of abdominal organs and lesions using parallel imaging technique. *AJR Am J Roentgenol* 2006; **187**: 1521-1530 [PMID: 17114546 DOI: 10.2214/AJR.05.0778]

50 **Zhang J**, Tehrani YM, Wang L, Ishill NM, Schwartz LH, Hricak H. Renal masses: characterization with diffusion-weighted MR imaging--a preliminary experience. *Radiology* 2008; **247**: 458-464 [PMID: 18430878 DOI: 10.1148/radiol.2472070823]

51 **Taouli B**, Thakur RK, Mannelli L, Babb JS, Kim S, Hecht EM, Lee VS, Israel GM. Renal lesions: characterization with diffusion-weighted imaging versus contrast-enhanced MR imaging. *Radiology* 2009; **251**: 398-407 [PMID: 19276322 DOI: 10.1148/radiol.2512080880]

52 **Kilickesmez O**, Inci E, Atilla S, Tasdelen N, Yetimoğlu B, Yencilek F, Gurmen N. Diffusion-weighted imaging of the renal and adrenal lesions. *J Comput Assist Tomogr* 2009; **33**: 828-833 [PMID: 19940645 DOI: 10.1097/RCT.0b013e31819f1b83]

53 **Sandrasegaran K**, Sundaram CP, Ramaswamy R, Akisik FM, Rydberg MP, Lin C, Aisen AM. Usefulness of diffusion-weighted imaging in the evaluation of renal masses. *AJR Am J Roentgenol* 2010; **194**: 438-445 [PMID: 20093607 DOI: 10.2214/AJR.09.3024]

54 **Agnello F**, Roy C, Bazille G, Galia M, Midiri M, Charles T, Lang H. Small solid renal masses: characterization by diffusion-weighted MRI at 3 T. *Clin Radiol* 2013; **68**: e301-e308 [PMID: 23452876 DOI: 10.1016/j.crad.2013.01.002]

55 **Le Bihan D**, Breton E, Lallemand D, Grenier P, Cabanis E, Laval-Jeantet M. MR imaging of intravoxel incoherent motions: application to diffusion and perfusion in neurologic disorders. *Radiology* 1986; **161**: 401-407 [PMID: 3763909 DOI: 10.1148/radiology.161.2.3763909]

56 **Jensen JH**, Helpern JA, Ramani A, Lu H, Kaczynski K. Diffusional kurtosis imaging: the quantification of non-gaussian water diffusion by means of magnetic resonance imaging. *MagnReson Med* 2005; **53**: 1432-1440 [PMID: 15906300 DOI: 10.1002/mrm.20508]

57 **Ding Y**, Tan Q, Mao W, Dai C, Hu X, Hou J, Zeng M, Zhou J. Differentiating between malignant and benign renal tumors: do IVIM and diffusion kurtosis imaging perform better than DWI? *EurRadiol* 2019; **29**: 6930-6939 [PMID: 31161315 DOI: 10.1007/s00330-019-06240-6]

58 **Li LP**, Halter S, Prasad PV. Blood oxygen level-dependent MR imaging of the kidneys. *MagnReson Imaging Clin N Am* 2008; **16**: 613-625, viii [PMID: 18926426 DOI: 10.1016/j.mric.2008.07.008]

59 **Blatow M**, Nennig E, Durst A, Sartor K, Stippich C. fMRI reflects functional connectivity of human somatosensory cortex. *Neuroimage* 2007; **37**: 927-936 [PMID: 17629500 DOI: 10.1016/j.neuroimage.2007.05.038]

60 **Shen Q**, Ren H, Duong TQ. CBF, BOLD, CBV, and CMRO(2) fMRI signal temporal dynamics at 500-msec resolution. *J MagnReson Imaging* 2008; **27**: 599-606 [PMID: 18219630 DOI: 10.1002/jmri.21203]

61 **Fukunaga M**, Horovitz SG, de Zwart JA, van Gelderen P, Balkin TJ, Braun AR, Duyn JH. Metabolic origin of BOLD signal fluctuations in the absence of stimuli. *J Cereb Blood Flow Metab* 2008; **28**: 1377-1387 [PMID: 18382468 DOI: 10.1038/jcbfm.2008.25]

62 **Herrmann CS**, Debener S. Simultaneous recording of EEG and BOLD responses: a historical perspective. *Int J Psychophysiol* 2008; **67**: 161-168 [PMID: 17719112 DOI: 10.1016/j.ijpsycho.2007.06.006]

63 **Textor SC**, Glockner JF, Lerman LO, Misra S, McKusick MA, Riederer SJ, Grande JP, Gomez SI, Romero JC. The use of magnetic resonance to evaluate tissue oxygenation in renal artery stenosis. *J Am Soc Nephrol* 2008; **19**: 780-788 [PMID: 18287564 DOI: 10.1681/ASN.2007040420]

64 **Alford SK**, Sadowski EA, Unal O, Polzin JA, Consigny DW, Korosec FR, Grist TM. Detection of acute renal ischemia in swine using blood oxygen level-dependent magnetic resonance imaging. *J MagnReson Imaging* 2005; **22**: 347-353 [PMID: 16104014 DOI: 10.1002/jmri.20389]

65 **Juillard L**, Lerman LO, Kruger DG, Haas JA, Rucker BC, Polzin JA, Riederer SJ, Romero JC. Blood oxygen level-dependent measurement of acute intra-renal ischemia. *Kidney Int* 2004; **65**: 944-950 [PMID: 14871414 DOI: 10.1111/j.1523-1755.2004.00469.x]

66 **Castillo M**, Kwock L, Mukherji SK. Clinical applications of proton MR spectroscopy. *AJNR Am J Neuroradiol* 1996; **17**: 1-15 [PMID: 8770242]

67 **Bottomley PA**, Edelstein WA, Foster TH, Adams WA. In vivo solvent-suppressed localized hydrogen nuclear magnetic resonance spectroscopy: a window to metabolism? *Proc Natl Acad Sci U S A* 1985; **82**: 2148-2152 [PMID: 3856889 DOI: 10.1073/pnas.82.7.2148]

68 **Nurenberg P**, Sartoni-D'Ambrosia G, Szczepaniak LS. Magnetic resonance spectroscopy of renal and other retroperitoneal tumors. *CurrOpinUrol* 2002; **12**: 375-380 [PMID: 12172423 DOI: 10.1097/00042307-200209000-00002]

69 **Kim DY**, Kim KB, Kim OD, Kim JK. Localized in vivo proton spectroscopy of renal cell carcinoma in human kidney. *J Korean Med Sci* 1998; **13**: 49-53 [PMID: 9539319 DOI: 10.3346/jkms.1998.13.1.49]

70 **Cecil KM**. Proton magnetic resonance spectroscopy: technique for the neuroradiologist. *Neuroimaging Clin N Am* 2013; **23**: 381-392 [PMID: 23928195 DOI: 10.1016/j.nic.2012.10.003]

71 **Caldarella C**, Muoio B, Isgrò MA, Porfiri E, Treglia G, Giovanella L. The role of fluorine-18-fluorodeoxyglucose positron emission tomography in evaluating the response to tyrosine-kinase inhibitors in patients with metastatic primary renal cell carcinoma. *Radiol Oncol* 2014; **48**: 219-227 [PMID: 25177235 DOI: 10.2478/raon-2013-0067]

72 **Smaldone MC**, Uzzo RG. Balancing process and risk: standardizing posttreatment surveillance for renal cell carcinoma. *J Urol* 2013; **190**: 417-418 [PMID: 23688642 DOI: 10.1016/j.juro.2013.05.033]

73 **Alongi P**, Picchio M, Zattoni F, Spallino M, Gianolli L, Saladini G, Evangelista L. Recurrent renal cell carcinoma: clinical and prognostic value of FDG PET/CT. *Eur J Nucl Med Mol Imaging* 2016; **43**: 464-473 [PMID: 26268680 DOI:

10.1007/s00259-015-3159-6]
74 **Kang DE**, White RL Jr, Zuger JH, Sasser HC, Teigland CM. Clinical use of fluorodeoxyglucose F 18 positron emission tomography for detection of renal cell carcinoma. *J Urol* 2004; **171**: 1806-1809 [PMID: 15076281 DOI: 10.1097/01.ju.0000120241.50061.e4]
75 **Takahashi M**, Kume H, Koyama K, Nakagawa T, Fujimura T, Morikawa T, Fukayama M, Homma Y, Ohtomo K, Momose T. Preoperative evaluation of renal cell carcinoma by using 18F-FDG PET/CT. *Clin Nucl Med* 2015; **40**: 936-940 [PMID: 26164183 DOI: 10.1097/RLU.0000000000000875]
76 **Jena R**, Narain TA, Singh UP, Srivastava A. Role of positron emission tomography/computed tomography in the evaluation of renal cell carcinoma. *Indian J Urol* 2021; **37**: 125-132 [PMID: 34103794 DOI: 10.4103/iju.IJU_268_20]
77 **Evangelista L**, Zattoni F, Alongi P. ^{68}Ga-dotatoc *vs.* ^{18}F-FDG *vs.*radiolabelled PSMA PET/CT in renal cancer patients. *Ann Transl Med* 2019; **7**: S150 [PMID: 31576357 DOI: 10.21037/atm.2019.06.28]
78 **Raveenthiran S**, Esler R, Yaxley J, Kyle S. The use of ^{68}Ga-PET/CT PSMA in the staging of primary and suspected recurrent renal cell carcinoma. *Eur J Nucl Med Mol Imaging* 2019; **46**: 2280-2288 [PMID: 31332498 DOI: 10.1007/s00259-019-04432-2]
79 **Siva S**, Callahan J, Pryor D, Martin J, Lawrentschuk N, Hofman MS. Utility of ^{68} Ga prostate specific membrane antigen - positron emission tomography in diagnosis and response assessment of recurrent renal cell carcinoma. *J Med Imaging Radiat Oncol* 2017; **61**: 372-378 [PMID: 28116853 DOI: 10.1111/1754-9485.12590]

World Journal of Radiology

Submit a Manuscript: https://www.f6publishing.com

World J Radiol 2022 June 28; 14(6): 151-154

DOI: 10.4329/wjr.v14.i6.151

ISSN 1949-8470 (online)

MINIREVIEWS

Artificial intelligence technologies in nuclear medicine

Muge Oner Tamam, Muhlis Can Tamam

Specialty type: Radiology, nuclear medicine and medical imaging

Provenance and peer review: Invited article; Externally peer reviewed.

Peer-review model: Single blind

Peer-review report's scientific quality classification

Grade A (Excellent): 0
Grade B (Very good): B
Grade C (Good): C
Grade D (Fair): D
Grade E (Poor): 0

P-Reviewer: Liu J, China; Morilla I, France; Tanabe S, Japan
A-Editor: Yao QG, China

Received: January 31, 2022
Peer-review started: January 31, 2022
First decision: April 8, 2022
Revised: April 20, 2022
Accepted: June 13, 2022
Article in press: June 13, 2022
Published online: June 28, 2022

Muge Oner Tamam, Department of Nuclear Medicine, Prof. Dr. Cemil Tascioglu City Hospital, İstanbul 34381, Turkey

Muhlis Can Tamam, High School, Uskudar American Academy, İstanbul 34145, Turkey

Corresponding author: Muge Oner Tamam, MD, Associate Professor, Department of Nuclear Medicine, Prof. Dr. Cemil Tascioglu City Hospital, Darulaceze cad., İstanbul 34381, Turkey. mugeoner@yahoo.com

Abstract

The use of artificial intelligence plays a crucial role in developing precision medicine in nuclear medicine. Artificial intelligence refers to a field of computer science aimed at imitating the performance of tasks typically requiring human intelligence. From machine learning to generative adversarial networks, artificial intelligence automized the workflow of medical imaging. In this mini-review, we encapsulate artificial intelligence models and their use in nuclear medicine imaging workflow.

Key Words: Artificial intelligence; Machine learning; Deep learning; Artificial neural networks; Convolutional neural networks; Generative adversarial networks

Core Tip: Artificial intelligence is a distinguished tool for creating tailor-made medicine. Artificial intelligence (AI) consists of machine learning, deep learning, artificial neural networks, convolutional neural networks, and generative adversarial networks. These AI applications affect all phases of a routine medical imaging workflow in nuclear medicine: planning, image acquisition, and interpretation. The integration of AI into clinical workflow and protocols of medical imaging will provide the opportunity to decrease the error rate of physicians and eventually lead to improved patient management.

Citation: Tamam MO, Tamam MC. Artificial intelligence technologies in nuclear medicine. *World J Radiol* 2022; 14(6): 151-154
URL: https://www.wjgnet.com/1949-8470/full/v14/i6/151.htm
DOI: https://dx.doi.org/10.4329/wjr.v14.i6.151

INTRODUCTION

Personalized medicine (precision medicine) is a developing medical practice that develops tailor-made approaches for individual patients, leading to increased reliability and a significant impact on preventative, diagnostic, and therapeutic pathways[1]. Artificial intelligence (AI) integration plays a significant role in achieving precision medicine in nuclear medicine[2]. It refers to a field of computer science aimed at imitating the performance of tasks typically requiring human intelligence[3]. Advancements in AI have allowed for precision medicine models to be developed for individual patients (Figure 1, Table 1). The advancements in AI have been in the order of machine learning (ML), deep learning (DL), artificial neural networks (ANNs), convolutional neural networks (CNNs), and generative adversarial networks (GANs)[4,5].

AI MODELS

Machine learning is not a singular algorithm, but a subset of AI. It processes a set of training data and constructs a model that carries the associations among the variables that are relevant to a particular outcome. It usually needs handcrafted features, requiring more human intervention, for data extraction and filtration[2]. There are many ML methods, some of which are supervised learning, unsupervised learning, semi-supervised learning, and reinforcement machine learning[5,6]. DL is a subset of ML, automating many parts of input extraction, enabling less human intervention. In contrast, ML requires more human intervention for data extraction and filtration[2,5,6].

Artificial Neural Networks are a subfield of DL. ANNs are connected nodes with weighted paths. Each node has parent nodes that influence it, an activation function, firing threshold, and an output value. ANNs are analogous to neurons and their intercommunication[4,5].

Convolutional Neural Networks are made up of convoluting series of pooling layers. CNNs apply a neural-network layer to a part of an image and systematically traverse over the image. CNNs downsample and summarize features by alternating convolutional layers with pooling layers. Their computational requirements are much lower because they operate on a small subset of an image[4,5].

Generative Adversarial Networks are made up of two networks, a generator, and a discriminator, that are in a zero-sum game. Generators generate fake input data to minimize the difference between counterfeits and real inputs. The discriminator classifies the real and counterfeit inputs, attempting to maximize efficiency. Over time, the generator will be good at generating input data and the discriminator will be good at classification[5].

APPLICATIONS

AI advancements in the last decade have improved AI's application in medical imaging. The myriad of applications of AI in nuclear medicine includes all steps of a typical medical imaging workflow: planning, image acquisition, and interpretation. In the future, even patient admission and payment could be included[7-9].

For medical imaging planning, AI will automatically check for specific contraindications, such as allergies and drug interference, or eliminate needless repetition of exams by evaluating past examinations before any examination is done on a patient[10,11].

In nuclear medicine, attenuation maps and scatter correction remain relevant topics for image scanning, thus AI research focuses on these topics intensively. Hwang *et al*[10] generated attenuation maps for whole-body positron emission tomography/magnetic resonance imaging (PET/MRI) using a modified U-Net, a specialized convolutional network architecture for biomedical image segmentation. They compared the CT-derived attenuation map to the Dixon-based 4-segment technique[10,11].

Another hot topic for research is the enhancement of image quality; Hong *et al*[12] improved the picture resolution and noise properties of PET scanners using large pixelated crystals with a deep residual convolutional neural network[12,13]. Kim *et al*[14] demonstrated that Iterative PET reconstruction employing denoising CNNs and local linear fitting enhanced picture quality and robustness to noise-level disparities.

For the interpretation of images, studies on an AI-based triage system for identifying artifacts have been published recently[15]. In the near future, similar systems will be able to detect directly using raw data, such as sinograms, and issue alarms throughout the scanning process, even before reconstruction, so that technicians can adjust or prolong the scheduled scan procedure to accommodate an unexpected discovery[16]. Automated identification of pathologies provides additional intriguing potential in identifying overlooked results and secondary discoveries, saving time and effort[17].

Table 1 Artificial intelligence techniques in nuclear medicine

Machine learning (ML)
Deep learning (DL)
Artificial neural networks (ANNs)
Convolutional neural networks (CNNs)
Generative adversarial networks(GANs)

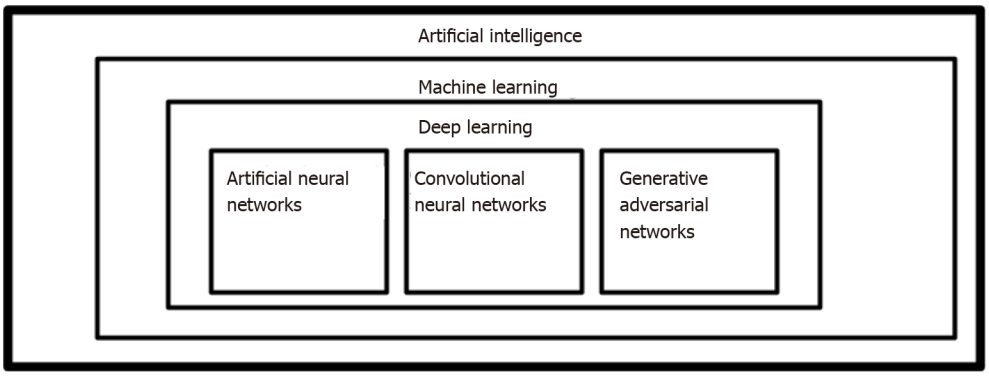

DOI: 10.4329/wjr.v14.i6.151

Figure 1 Current artificial intelligence subfields studied in the field of nuclear medicine.

ETHICAL CONSIDERATIONS, DATA PROTECTION, REGULATIONS, AND PRIVACY

Despite the improvements that the field of AI brings to nuclear medicine, there are drawbacks. Ethical considerations, data protection, legal regulations, privacy, and education are among these problems. According to Hagendorf, the ethical concerns of AI in healthcare can be summarized in the "fairness, accountability, and transparency paradigm of AI ethics"[18,19]. Moreover, AI requires considerable sensitive data in healthcare, thus standards for data protection and privacy raise issues that must be dealt with. Furthermore, for AI to generalize large numbers, large amounts of data with variability are needed. This raises more questions about consent, data anonymization, and de-identification[19]. There are promising techniques being developed on top of DL algorithms such as federative learning that might mitigate some of these issues[20]. Additionally, traditional regulatory pathways are lagging behind the recent advancements, creating difficulties regarding regulations and laws. Lastly, insufficient education about AI both from patients, physicians, and academia causes mistrust of AI applications in healthcare. Physicians and academia need familiarity with AI and the rudimentary knowledge necessary to provide patients with the necessary information[19].

CONCLUSION

The integration of AI into clinical practice will transform the medical profession and nuclear medicine imaging in particular. New abilities, such as clinical data science, computer science, and ML will be considered a necessity when AI is applied to medical imaging workflow and protocols. This could provide the opportunity to decrease the error rate of physicians and eventually lead to improved patient management.

FOOTNOTES

Author contributions: Tamam MO performed the majority of the writing, prepared the figures and tables; Tamam MC performed data accusation and writing; Tamam MC provided the input in writing the paper; Tamam MC designed the outline and coordinated the writing of the paper.

Conflict-of-interest statement: There is no conflict of interest associated with the senior author or other coauthors who contributed their efforts to this manuscript.

Country/Territory of origin: Turkey

ORCID number: Muge Oner Tamam 0000-0002-3793-0178; Muhlis Can Tamam 0000-0002-1327-8947.

S-Editor: Liu JH
L-Editor: A
P-Editor: Liu JH

REFERENCES

1 National Human Genome Research Institute. Personalized Medicine. Available from: https://www.genome.gov/genetics-glossary/Personalized-Medicine
2 **Chartrand G**, Cheng PM, Vorontsov E, Drozdzal M, Turcotte S, Pal CJ, Kadoury S, Tang A. Deep Learning: A Primer for Radiologists. *Radiographics* 2017; **37**: 2113-2131 [PMID: 29131760 DOI: 10.1148/rg.2017170077]
3 **Currie G**, Rohren E. Intelligent Imaging in Nuclear Medicine: the Principles of Artificial Intelligence, Machine Learning and Deep Learning. *Semin Nucl Med* 2021; **51**: 102-111 [PMID: 33509366 DOI: 10.1053/j.semnuclmed.2020.08.002]
4 **Herskovits EH**. Artificial intelligence in molecular imaging. *Ann Transl Med* 2021; **9**: 824 [PMID: 34268437 DOI: 10.21037/atm-20-6191]
5 **Castiglioni I**, Rundo L, Codari M, Di Leo G, Salvatore C, Interlenghi M, Gallivanone F, Cozzi A, D'Amico NC, Sardanelli F. AI applications to medical images: From machine learning to deep learning. *Phys Med* 2021; **83**: 9-24 [PMID: 33662856 DOI: 10.1016/j.ejmp.2021.02.006]
6 Machine Learning. Available from: https://www.ibm.com/cloud/Learn/machine-learning
7 **Visvikis D**, Cheze Le Rest C, Jaouen V, Hatt M. Artificial intelligence, machine (deep) learning and radio(geno)mics: definitions and nuclear medicine imaging applications. *Eur J Nucl Med Mol Imaging* 2019; **46**: 2630-2637 [PMID: 31280350 DOI: 10.1007/s00259-019-04373-w]
8 **Currie GM**. Intelligent Imaging: Artificial Intelligence Augmented Nuclear Medicine. *J Nucl Med Technol* 2019; **47**: 217-222 [PMID: 31401616 DOI: 10.2967/jnmt.119.232462]
9 **Currie G**, Hawk KE, Rohren E, Vial A, Klein R. Machine Learning and Deep Learning in Medical Imaging: Intelligent Imaging. *J Med Imaging Radiat Sci* 2019; **50**: 477-487 [PMID: 31601480 DOI: 10.1016/j.jmir.2019.09.005]
10 **Hwang D**, Kang SK, Kim KY, Seo S, Paeng JC, Lee DS, Lee JS. Generation of PET Attenuation Map for Whole-Body Time-of-Flight ^{18}F-FDG PET/MRI Using a Deep Neural Network Trained with Simultaneously Reconstructed Activity and Attenuation Maps. *J Nucl Med* 2019; **60**: 1183-1189 [PMID: 30683763 DOI: 10.2967/jnumed.118.219493]
11 **Ronneberger O**, Fischer P, Brox T. U-Net: convolutional networks for biomedical image segmentation. In: Navab N, Hornegger J, Wells WM, Frangi AF, eds. mMedical Image Computing and Computer-Assisted Intervention–MICCAI 2015.Cha, Switzerland: Springer International Publishing; 2015:234-241
12 **Hong X**, Zan Y, Weng F, Tao W, Peng Q, Huang Q. Enhancing the Image Quality *via* Transferred Deep Residual Learning of Coarse PET Sinograms. *IEEE Trans Med Imaging* 2018; **37**: 2322-2332 [PMID: 29993685 DOI: 10.1109/TMI.2018.2830381]
13 **Orlhac F**, Boughdad S, Philippe C, Stalla-Bourdillon H, Nioche C, Champion L, Soussan M, Frouin F, Frouin V, Buvat I. A Postreconstruction Harmonization Method for Multicenter Radiomic Studies in PET. *J Nucl Med* 2018; **59**: 1321-1328 [PMID: 29301932 DOI: 10.2967/jnumed.117.199935]
14 **Kim K**, Wu D, Gong K, Dutta J, Kim JH, Son YD, Kim HK, El Fakhri G, Li Q. Penalized PET Reconstruction Using Deep Learning Prior and Local Linear Fitting. *IEEE Trans Med Imaging* 2018; **37**: 1478-1487 [PMID: 29870375 DOI: 10.1109/TMI.2018.2832613]
15 **Li W**, Liu H, Cheng F, Li Y, Li S, Yan J. Artificial intelligence applications for oncological positron emission tomography imaging. *Eur J Radiol* 2021; **134**: 109448 [PMID: 33307463 DOI: 10.1016/j.ejrad.2020.109448]
16 **Noortman WA**, Vriens D, Mooij CDY, Slump CH, Aarntzen EH, van Berkel A, Timmers HJLM, Bussink J, Meijer TWH, de Geus-Oei LF, van Velden FHP. The Influence of the Exclusion of Central Necrosis on [^{18}F]FDG PET Radiomic Analysis. *Diagnostics (Basel)* 2021; **11** [PMID: 34359379 DOI: 10.3390/diagnostics]
17 **Nensa F**, Demircioglu A, Rischpler C. Artificial Intelligence in Nuclear Medicine. *J Nucl Med* 2019; **60**: 29S-37S [PMID: 31481587 DOI: 10.2967/jnumed.118.220590]
18 **Hagendorff T**. The Ethics of AI Ethics: An Evaluation of Guidelines. *Minds & Machines* 2020; 30: 99-120 [DOI: 10.1007/s11023-020-09517-8]
19 **Aktolun C**. Artificial intelligence and radiomics in nuclear medicine: potentials and challenges. *Eur J Nucl Med Mol Imaging* 2019; **46**: 2731-2736 [PMID: 31673788 DOI: 10.1007/s00259-019-04593-0]
20 **Gajera J**, Knipe H. Federated learning. Reference article, Radiopaedia.org. (accessed on 19 Apr 2022) [DOI: 10.53347/rID-81590]

World Journal of Radiology

Submit a Manuscript: https://www.f6publishing.com

World J Radiol 2022 June 28; 14(6): 155-164

DOI: 10.4329/wjr.v14.i6.155

ISSN 1949-8470 (online)

ORIGINAL ARTICLE

Prospective Study

Evaluation of the dual vascular supply patterns in ground-glass nodules with a dynamic volume computed tomography

Chao Wang, Ning Wu, Zhuang Zhang, Lai-Xing Zhang, Xiao-Dong Yuan

Specialty type: Radiology, nuclear medicine and medical imaging

Provenance and peer review: Unsolicited article; Externally peer reviewed.

Peer-review model: Single blind

Peer-review report's scientific quality classification

Grade A (Excellent): 0
Grade B (Very good): B
Grade C (Good): C
Grade D (Fair): D
Grade E (Poor): 0

P-Reviewer: Esch M, Germany; Konovalov AB, Russia

Received: December 2, 2021
Peer-review started: December 2, 2021
First decision: April 8, 2022
Revised: April 20, 2022
Accepted: June 16, 2022
Article in press: June 16, 2022
Published online: June 28, 2022

Chao Wang, Zhuang Zhang, Lai-Xing Zhang, Department of Graduate, Hebei North University, Zhangjiakou 075000, Hebei Province, China

Ning Wu, Xiao-Dong Yuan, Department of Radiology, The Eighth Medical Center of the People's Liberation Army General Hospital, Beijing 100091, China

Corresponding author: Xiao-Dong Yuan, MD, PhD, Chief Doctor, Professor, Department of Radiology, The Eighth Medical Center of the People's Liberation Army General Hospital, No. 17 Heishanhu Road, Haidian District, Beijing 100091, China. yuanxiaodongzj@163.com

Abstract

BACKGROUND

In recent years, the detection rate of ground-glass nodules (GGNs) has been improved dramatically due to the popularization of low-dose computed tomography (CT) screening with high-resolution CT technique. This presents challenges for the characterization and management of the GGNs, which depends on a thorough investigation and sufficient diagnostic knowledge of the GGNs. In most diagnostic studies of the GGNs, morphological manifestations are used to differentiate benignancy and malignancy. In contrast, few studies are dedicated to the assessment of the hemodynamics, *i.e.*, perfusion parameters of the GGNs.

AIM

To assess the dual vascular supply patterns of GGNs on different histopathology and opacities.

METHODS

Forty-seven GGNs from 47 patients were prospectively included and underwent the dynamic volume CT. Histopathologic diagnoses were obtained within two weeks after the CT examination. Blood flow from the bronchial artery [bronchial flow (BF)] and pulmonary artery [pulmonary flow (PF)] as well as the perfusion index (PI) = [PF/(PF + BF)] were obtained using first-pass dual-input CT perfusion analysis and compared respectively between different histopathology and lesion types (pure or mixed GGNs) and correlated with the attenuation values of the lesions using one-way ANOVA, student's *t* test and Pearson correlation analysis.

RESULTS

Of the 47 GGNs (mean diameter, 8.17 mm; range, 5.3-12.7 mm), 30 (64%) were

carcinoma, 6 (13%) were atypical adenomatous hyperplasia and 11 (23%) were organizing pneumonia. All perfusion parameters (BF, PF and PI) demonstrated no significant difference among the three conditions (all $P > 0.05$). The PFs were higher than the BFs in all the three conditions (all $P < 0.001$). Of the 30 GGN carcinomas, 14 showed mixed GGNs and 16 pure GGNs with a higher PI in the latter ($P < 0.01$). Of the 17 benign GGNs, 4 showed mixed GGNs and 13 pure GGNs with no significant difference of the PI between the GGN types ($P = 0.21$). A negative correlation ($r = -0.76$, $P < 0.001$) was demonstrated between the CT attenuation values and the PIs in the 30 GGN carcinomas.

CONCLUSION

The GGNs are perfused dominantly by the PF regardless of its histopathology while the weight of the BF in the GGN carcinomas increases gradually during the progress of its opacification.

Key Words: Ground-glass nodules; Tomography; X-ray computed; Lung cancer; Perfusion computed tomography; Dual blood supply

Core Tip: In this study, bronchial flow (BF) and pulmonary flow (PF) as well as perfusion index (PI) were obtained by using first-pass dual-input computed tomography perfusion analysis and compared respectively among different histopathological types and between pure and mixed ground-glass nodules (GGNs), then correlated with the attenuation values in forty-seven GGNs from 47 patients. We found that the GGNs are perfused dominantly by the PF regardless of histopathological types while the weight of the BF in the GGN carcinomas increases gradually during its opacification. Therefore, the PI may be a potentially useful biomarker for distinguishing indolent nodules from aggressive ones.

Citation: Wang C, Wu N, Zhang Z, Zhang LX, Yuan XD. Evaluation of the dual vascular supply patterns in ground-glass nodules with a dynamic volume computed tomography. *World J Radiol* 2022; 14(6): 155-164
URL: https://www.wjgnet.com/1949-8470/full/v14/i6/155.htm
DOI: https://dx.doi.org/10.4329/wjr.v14.i6.155

INTRODUCTION

In recent years, more and more ground-glass nodules (GGNs) have been detected due to the application of low-dose screening with high-resolution computed tomography (CT)[1]. The rapidly increasing GGN cases requires appropriate management which depends on a thorough investigation and sufficient knowledge of the GGNs. In most diagnostic studies of the GGNs, morphological factors or nodular characteristics are used to differentiate benignancy and malignancy[2-6]. On the other hand, studies of the solid lesions suggested that the information of CT perfusion is helpful in identification and treatment planning[7-13]. A few studies have quantitatively measured iodine concentration to assess the blood supply status of the GGNs with promising outcomes[14]. Furthermore, quantification of the dual blood supply from the pulmonary and bronchial artery, *i.e.*, the pulmonary flow (PF) and bronchial flow (BF) in lung disorders is recently achieved with the first-pass dual-input perfusion analysis at a dynamic volume CT, producing helpful information for differentiations and treatment planning[15]. Therefore, this prospective study was designed to determine the patterns of the dual vascular supply in the GGNs on different histopathology and attenuation values (HU).

MATERIALS AND METHODS

Study population

The prospective study was approved by the Institution Ethics Committee. Written informed consent was obtained from all patients. Between Jan 2014 and May 2018, 50 patients who had been previously evaluated by non-contrast CT and had GGNs with an axial diameter > 5 mm were prospectively enrolled into this study. All patients received histopathological diagnoses which were acquired by CT-guided puncture biopsy or surgical resection within 2 wk after the CT perfusion. Exclusion criteria were as follows: severe motion artifacts on the perfusion images that made it difficult to perform the perfusion analysis; patients receiving any antitumor treatment prior to the CT perfusion and contraindications to the administration of the iodinated contrast media. 1 patient with beam hardening artifacts

caused by the contrast agent in an ipsilateral subclavian vein and 2 patients who received antitumor treatment before the CT perfusion were excluded. Eventually, forty-seven patients (27 men and 20 women; mean age, 53 years; range, 35-69 years) with 47 GGNs were included in the statistical analysis.

The radiation dose of the dynamic CT was calculated from the dose–length product (DLP) listed in the exposure summary sheet generated by the CT equipment and multiplied by a k-factor of 0.014[16].

CT perfusion imaging technique

Before the CT examination, all patients performed breath training by holding their breath during the dynamic CT scan procedure and otherwise adopted regularly shallow breathing.

First, unenhanced helical CT of the entire thorax was performed to determine the location of the GGN. Then, the dynamic volume CT perfusion was performed at a 320-row multidetector CT (Aquilion ONE, Toshiba Medical Systems, Otawara, Japan). With a dual-head power injector, 50 mL of non-ionic contrast medium with an iodine concentration of 370 mgI/mL (Iopromide, Bayer Schering, Berlin, Germany) was injected at a flow rate of 5 mL/s, followed by 20 mL of saline solution at the same rate. Five seconds after the start of the bolus injection, 15 intermittent low-dose volume acquisitions were made with 2 s intervals with no table movement.

The dynamic contrast-enhanced volume CT protocol was performed with the following parameters: 80 kV tube voltage, 80 mA tube current, 0.5 s gantry rotation speed and 0.5 mm slice thickness. The 16 cm coverage included both the lung hilum and the GGN. The first two volumes were acquired before the contrast medium arrived in the pulmonary artery (PA) and served as the baseline. The duration of the breath hold was approximately 30 s. The raw data were reconstructed with adaptive iterative dose reduction and automatically produced 0.5 mm slice thickness and 0.5 mm spacing images, resulting in 320 images per volume and a total of 4800 images for the entire perfusion dataset.

Data post-processing and analysis

Post-processing was performed using perfusion software available on the CT equipment (Body Perfusion, dual-input maximum slope analysis, Toshiba Medical Systems, Otawara, Japan). The first step is volume registration. The registration is performed to correct for motion between the dynamic volumes and creates a registered volume series. The registered volumes were then loaded into the body perfusion analysis software.

Rectangular region of interests (ROIs) (mean area 1.0 cm^2) was manually placed in the pulmonary artery trunk and the aorta at the level of the hilum to generate the TDCs representing the PA input function and the bronchial artery input function, respectively. An elliptical ROI was placed in the left atrium and the peak time of the left atrium tunneled dialysis catheters (TDCs) was used to differentiate pulmonary circulation (before the peak time point) and bronchial circulation (after the peak time point) [15]. A freehand ROI was drawn to encompass the lesion to generate the TDC of the contrast medium's first-pass attenuation in the GGN. The perfusion analysis range was set from -700 HU to 50 HU to confine the perfusion analysis to the GGN or mixed GGN regions only and to ignore normal lung parenchyma. Finally, 512 × 512 matrix color-coded maps of the PF, BF and perfusion index [PI = PF/(PF + BF)] were generated automatically. For each lesion, measurements were repeated on all relevant 5.0-mm axial slices and then averaged to calculate the final value. Lesion opacity (mean HU) was measured on the non-contrast axial slice with the maximum lesion diameter using a freehand ROI closely encompassing the lesion and avoiding major vessels. This post-processing procedure was independently performed by two radiologists (**BLINDED**, with 13 and 11 years of experience, respectively in CT perfusion in the abdomen and chest). Each radiologist was blinded to the results of the other and the histopathological diagnoses. The final results were the average of the two observers. Inter-observer reproducibility was assessed for the PF, BF and PI as well as the lesion opacity (mean HU). The lesion type (pure GGN or mixed GGN) was independently determined by the two radiologists and by a third radiologist (**BLINDED**) if the results of the two radiologists were inconsistent.

The pure GGN was defined as a focal, slightly increased attenuation in lung without masking the underlying structures on the lung window images while the mixed GGN as a focal increased attenuation with solid components masking the underlying structures of pulmonary vessels[17].

Statistical analysis

Forty-seven GGNs were analyzed. The bronchial artery (BF) and pulmonary artery (PF) as well as the PI [= PF/ (PF+BF)] were compared respectively between the histopathologic types and the lesion types (pure GGNs or mixed GGNs) using one-way ANOVA and students' *t* test and correlated respectively with lesions' HU using Pearson correlation analysis. In addition, the BF and PF were compared by paired *t* test to determine the dominant blood flow in the GGNs. The inter-observer reproducibility of perfusion parameters (BF, PF and PI) and HU of GGNs were assessed using intraclass correlation coefficients (ICC). Statistical analysis was performed using commercially available software (SPSS, V13.0, IBM). A P value < 0.05 was considered to indicate a significant difference.

RESULTS

All patients showed good compliance with the CT perfusion procedure. No severe motion artifacts or adverse events occurred.

Of the 47 GGNs (mean diameter, 8.17 mm; range, 5.3-12.7 mm), 30 (64%) proved to be bronchioloalveolar cell carcinoma (BAC) (n = 24) or adenocarcinoma with predominant BAC component (n = 6), six (13%) atypical adenomatous hyperplasia and 11 (23%) organizing pneumonia. None of the three perfusion parameters demonstrated significant difference among the three histopathological types (Table 1). Of the 30 carcinomas GGNs, 14 showed mixed GGNs and 16 pure GGNs, with a greater PI in the latter (P < 0.01). Of the 17 benign GGNs, 4 showed mixed GGNs (including 1 atypical adenomatous hyperplasia and 3 organizing pneumonia) and 13 pure GGNs (including 5 atypical adenomatous hyperplasia and 8 organizing pneumonia) with no significant difference of the PI between the GGN types (P = 0.21). Of the 30 cancerous GGNs, the lesions' HU demonstrated mild negative correlation with the PF (r = -0.558, P = 0.001) while mild positive correlation with the BF (r = 0.565, P = 0.001). The PI demonstrates moderate negative correlation with the HU (r = -0.76, P < 0.001). No correlation between the perfusion parameters and the HU was revealed in the other two diseases (all P > 0.05).

Perfusion parameters were visualized by color maps and fused onto the original axial CT images. Representative perfusion color maps are shown in Figure 1 and Figure 2. Statistical results of the perfusion parameters derived from dual-input computed tomography perfusion are listed in Table 1 and shown in Figures 3-5. ICC (0.94, 95%CI: 0.93-0.95) demonstrated that the reproducibility between the two observers is good.

The dynamic volume CT perfusion protocol was identical for all 47 cases. The CT dose DLP = 324.8 mGy cm or 4.55 mSv (k = 0.014).

DISCUSSION

The PF and the BF, *i.e.*, the dual vascular supply was revealed in lung cancer through post-mortem microarteriography in the early 1970s[18]. Since then, the BF in lung cancer was confirmed by many reports and broncho angiography studies[19]. In contrast, PF in lung cancer was rarely reported until recently with an *in vivo* evaluation of the dual vascular supply in lung cancer and was achieved by using a dynamic contrast-enhanced volume CT[20] which reported a dominant BF along with a subordinate PF in solid cancerous nodules. In the present investigation, however, we revealed a dominant PF along with a subordinate BF in the GGN carcinomas. In addition, we revealed that with the increase of the lesion opacity, the weight of the PF in the total blood flow of the GGN carcinomas decreases while the weight of the BF increases. Thus, we would like to provide an interpretation of our findings combining with the findings of the previous reports as the following: During the progress of the lung adenocarcinoma from a pure GGN to a mixed GGN then to a solid nodule[21,22], the PF dominant perfusion pattern may gradually reverse to the BF dominant perfusion pattern. In contrast to solid nodular carcinoma, GGN carcinoma are supposed to be indolent, which allows long-term follow-up of their morphological changes for treatment planning[23-25]. Our findings on the increasing weight of the BF in GGNs during its opacification suggest that the PI which represents the weight of the BF in the total blood supply (BF + PF) may be a potentially useful biomarker for distinguishing indolent nodules from active ones.

Though the dual vascular supply patterns of the GGNs were determined in the current investigation, it cannot help differentiate GGNs between benignancy and malignancy because none of the three perfusion parameters (PF, BF and PI) showed significant difference between benign and malignant GGNs. Nevertheless, the feature of the PF dominant perfusion in the GGN carcinomas may have two important clinical implications: (1) Bronchial arterial chemoembolization may not be suitable for the treatment of a GGN carcinoma; and (2) radiation therapy may not be suitable for the treatment of a GGN carcinoma. The reason for the former is self-evident. The reason for the latter is because the PF dominant perfusion indicates a low level of oxygenation in the GGN carcinoma resulting in a low level of radiosensitivity[20,26].

It was reported that the pure GGNs are difficult to be distinguished morphologically between malignancy and benignancy[27]; however, the mixed GGNs tend to be a malignant one[28,29]. During a long-term CT follow-up of an adenocarcinoma in the lung, the typical case may be a pure GGN at the very beginning then gradually changing into a mixed GGN and a solid nodule at last[30,31]. Therefore, it strongly suggests an adenocarcinoma when a pure GGN gradually changed into a mixed one during follow-up. According to the current investigation, a pure GGN carcinoma is mainly perfused by the PF while the weight of the BF increases in a mixed GGN. In addition, a solid carcinoma is mainly perfused by the BF according to the previous study[15,20,32]. These adaptive changes of the perfusion patterns may bring more oxygen to feed the growth of the GGN carcinomas because of a low oxygen level in the PF and a high oxygen level in the BF. However, the mechanism behind these changes is still unknown and needs to be investigated further.

Table 1 Results of histopathologic comparisons on the three perfusion parameters

Parameters	Histopathology	*n*	mean ± SD	95% CI		One way ANOVA
				Lower	Upper	
PF (mL/min/100 mL)	Carcinoma	30	135.54 ± 46.58	118.15	152.93	$P = 0.435$
	Adenomatous hyperplasia	6	121.51 ± 40.56	78.94	164.08	
	Organizing pneumonia	11	116.06 ± 43.15	87.07	145.05	
BF (mL/min/100 mL)	Carcinoma	30	33.21 ± 12.12	28.68	37.74	$P = 0.079$
	Adenomatous hyperplasia	6	26.55 ± 4.08	22.26	30.83	
	Organizing pneumonia	11	24.96 ± 9.90	18.31	31.61	
PI (100%)	Carcinoma	30	0.79 ± 0.09	0.75	0.82	$P = 0.657$
	Adenomatous hyperplasia	6	0.80 ± 0.07	0.73	0.88	
	Organizing pneumonia	11	0.81 ± 0.69	0.76	0.86	

PF: Pulmonary flow; BF: Bronchial flow; PI: Perfusion index.

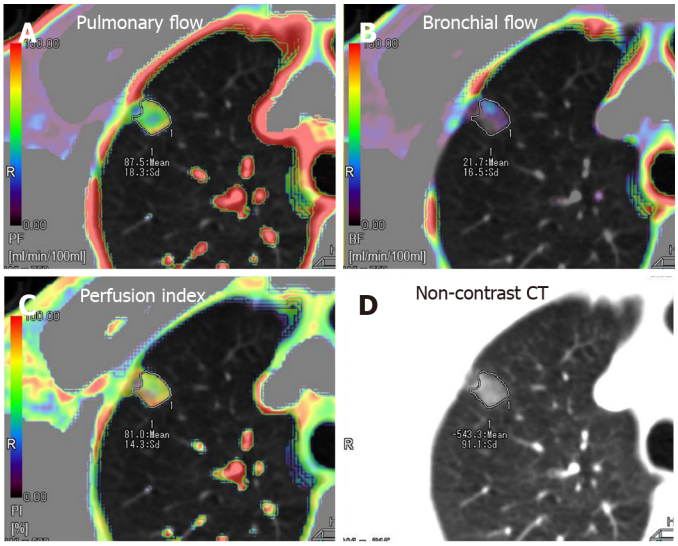

DOI: 10.4329/wjr.v14.i6.155

Figure 1 Axial colored perfusion maps in a 55-year-old male patient with pure ground-glass nodule carcinoma located in the right superior lung. Dominant pulmonary flow (PF) along with subordinate bronchial flow (BF) was observed in the pure ground-glass nodule. A: Axial colored perfusion map of PF; B: Axial colored perfusion map of BF; C: Axial colored perfusion map of perfusion index; D: Axial non-contrast computed tomography.

In this investigation, the perfusion analysis range was set from -700 HU to 50 HU to confine the perfusion analysis to the GGN or mixed GGN while ignore the normal lung parenchyma. In fact, the perfusion analysis range could be set individually according to an on-spot CT measurement of the GGN. To simplify and standardize the post-processing procedure, we adopted a fixed CT perfusion analysis range, *i.e.*, -700 HU to 50 HU in this study.

There are some limitations to this study. First, the relatively small sample size of this study will undermine the significance of our findings. Second, a relatively high radiation dose is an unavoidable limitation of perfusion CT though the total effective dose of each patient was controlled to comparable with a multiphasic CT procedure[33,34]. Third, although the difference of CT perfusion between the pure and mixed GGN carcinomas was investigated, the solid components and the pure components of the mixed GGN carcinomas were not evaluated separately because it's difficult to define the boundary of the two components. Fourth, our findings cannot help to differentiate between malignant and benign GGNs because no significant difference in perfusion parameters was revealed between them. However, the change regularity of the dual vascular supply patterns during the opacification of GGN carcinomas could help to better understand its biological behavior and therefore help to better manage it.

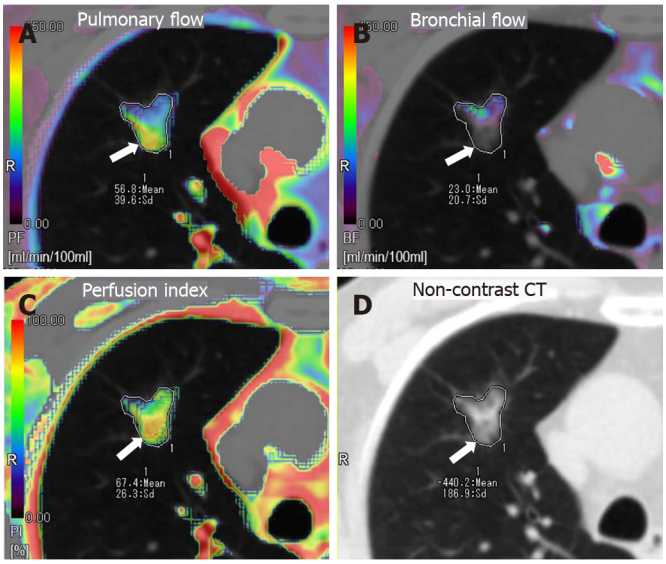

DOI: 10.4329/wjr.v14.i6.155 **Copyright** ©The Author(s) 2022.

Figure 2 Axial colored perfusion maps in a 72-year-old male patient with mixed ground-glass nodule carcinoma located in the right superior lung. The perfusion is heterogeneous throughout the lesion. Pulmonary flow (PF) is globally dominant, especially in the dorsal part of the lesion (arrow), which corresponds to the lower attenuation region of the mixed ground-glass nodule. A: Axial colored perfusion map of PF; B: Axial colored perfusion map of bronchial flow; C: Axial colored perfusion map of perfusion index; D: Axial non-contrast computed tomography.

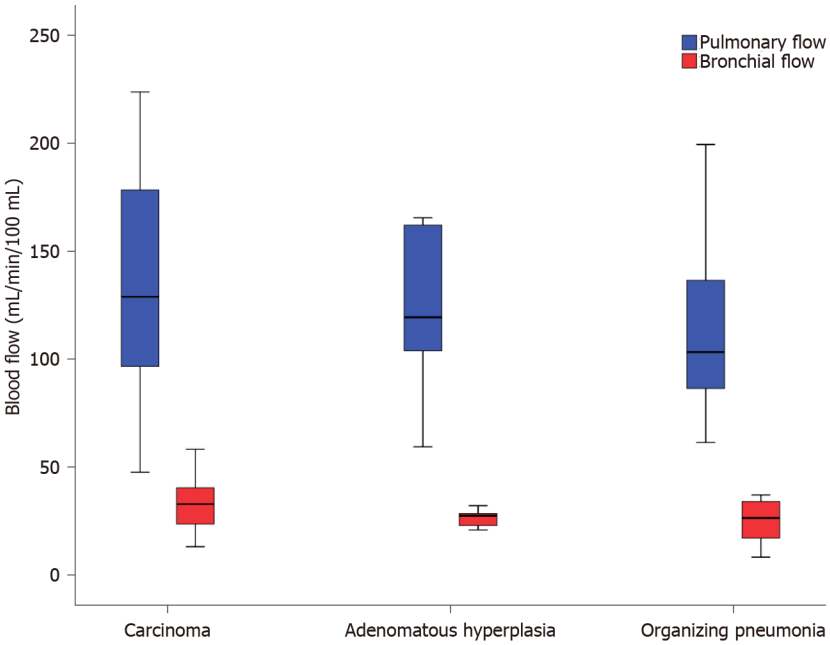

DOI: 10.4329/wjr.v14.i6.155 **Copyright** ©The Author(s) 2022.

Figure 3 Box plot of perfusion parameters demonstrates dominant Pulmonary flow (PF) along with relatively low bronchial flow (BF) in carcinoma (*n* = 30), atypical adenomatous hyperplasia (*n* = 6) and organizing pneumonia (*n* = 11).

CONCLUSION

In conclusion, the GGNs are perfused dominantly by the PF regardless of its histopathology while the weight of the BF in the GGN carcinomas increases gradually during its opacification. The PI may be a potentially useful biomarker for distinguishing indolent nodules from aggressive ones.

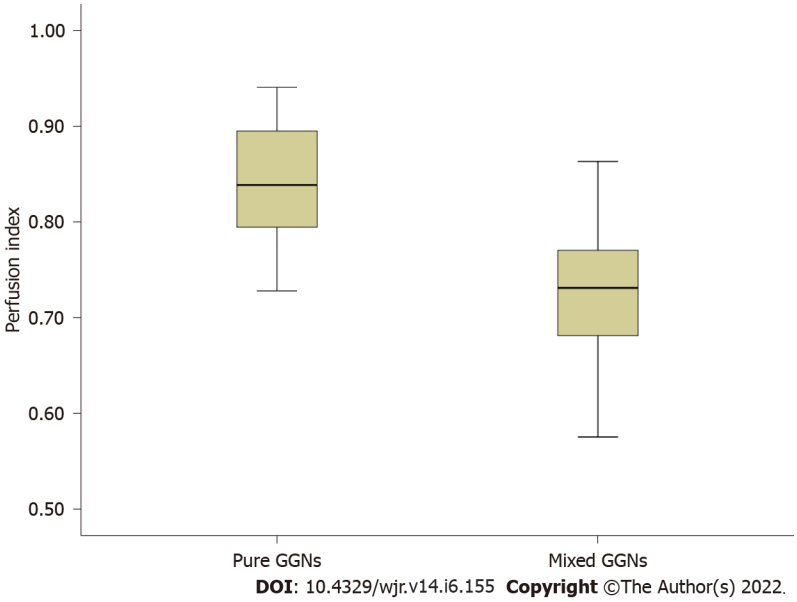

DOI: 10.4329/wjr.v14.i6.155

Figure 4 Box plot of perfusion index [= pulmonary flow/(pulmonary flow + bronchial flow)] demonstrates dominant pulmonary flow along with subordinate bronchial flow in pure ground-glass nodule carcinoma (*n* = 16) and a weakened pulmonary flow along with an enhanced bronchial flow in mixed ground-glass nodule carcinoma.

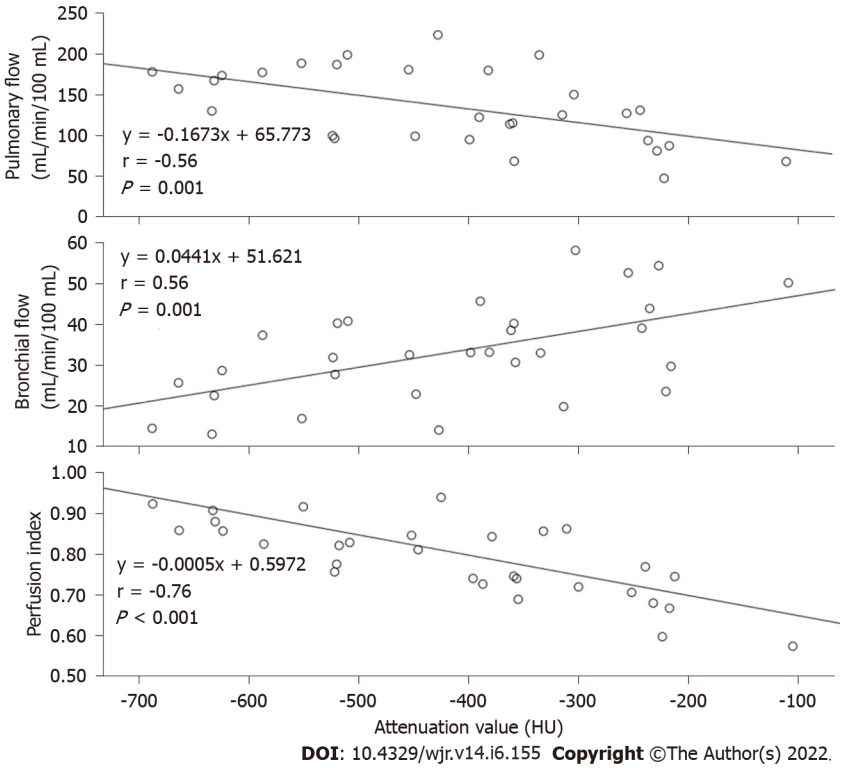

DOI: 10.4329/wjr.v14.i6.155

Figure 5 Plots of the Pearson correlation between the attenuation values of the ground-glass nodule carcinoma and the three perfusion parameters. The HU of the GGN carcinoma correlates negatively, positively and negatively with the pulmonary flow (PF), bronchial flow (BF) and the perfusion index (PI), respectively. A: Correlation between the HU of ground-glass nodule (GGN) carcinoma and PF; B: Correlation between the HU of GGN carcinoma and BF; C: Correlation between the HU of GGN carcinoma and PI.

ARTICLE HIGHLIGHTS

Research background

In recent years, the detection rate of ground-glass nodules (GGNs) has been improved dramatically due to the application of low-dose computed tomography (CT) screening and high-resolution CT. The rapidly increasing detection rate requires appropriate managements of the GGNs which depends on a thorough investigation and sufficient knowledge of the GGNs. In most diagnostic studies of the GGNs, morphological factors are used to differentiate benignancy and malignancy. However, evaluation of the dual vascular supply patterns in GGNs with a dynamic volume CT could provide more valuable information for identification and treatment planning.

Research motivation

Studies of the solid lesions suggested that the information of CT perfusion is helpful in identification and treatment planning. Furthermore, quantification of the dual blood supply from the pulmonary and bronchial artery, *i.e.*, the pulmonary flow (PF) and bronchial flow (BF) in lung disorders was recently achieved with a dynamic volume CT and the first-pass dual-input perfusion analysis producing helpful information for differentiations and treatment planning. Based on this, our study is devoted to the assessment of the dual blood supply pattern of GGNs by dynamic CT to provide more valuable information for differentiations and treatment planning.

Research objectives

To assess the dual vascular supply patterns of GGNs with regard to different histopathology and opacities using a dynamic volume CT.

Research methods

In this prospective study, 47 GGNs from 47 patients were included and underwent the dynamic volume CT. Histopathologic diagnoses were obtained within two weeks after the CT examination. BF and PF as well as the perfusion index [(PI) = PF/ (PF+BF)] were obtained using first-pass dual-input CT perfusion analysis and compared respectively between different histopathology and lesion types (pure or mixed GGN) and correlated with the attenuation values of the lesions, using one-way ANOVA, student's *t* test and Pearson correlation analysis.

Research results

Forty-seven GGNs including three histopathological types (30 carcinoma, 6 atypical adenomatous hyperplasia and 11 organizing pneumonia). All perfusion parameters (BF, PF and PI) demonstrated no significant difference among the three conditions (all $P > 0.05$). The PFs were higher than the BFs in all the three conditions (all $P < 0.001$). Of the 30 GGN carcinomas, 14 showed mixed GGNs and 16 pure GGNs, with a higher PI in the latter ($P < 0.01$). A negative correlation ($r = -0.76$, $P < 0.001$) was demonstrated between the CT attenuation values and the PIs in the 30 GGN carcinomas.

Research conclusions

In conclusion, the GGNs are perfused dominantly by the PF regardless of its histopathology while the weight of the BF in the GGN carcinomas increases gradually during the progress of its opacification.

Research perspectives

Our future study will expand the GGNs sample size to further investigate potential difference of perfusion parameters between malignant and benign GGNs and to further confirm that the PI is a useful biomarker for distinguishing indolent GGNs carcinomas from aggressive ones.

FOOTNOTES

Author contributions: Yuan XD and Wu N designed the study; Wang C wrote the first draft of the manuscript; Zhang Z and Zhang LX collected the data; Wang C performed the literature search and analysis; Yuan XD and Wang C conducted the statistical analysis and polished the language; all authors participated in and approved the final manuscript.

Supported by the National Natural Science Foundation of China, No. 81671680.

Institutional review board statement: Our prospective study was approved by our institutional review board.

Informed consent statement: Written informed consents were obtained from all patients.

Conflict-of-interest statement: The authors of this manuscript having no conflicts of interest to disclose.

Data sharing statement: No additional data are available.

Country/Territory of origin: China

ORCID number: Chao Wang 0000-0003-3446-9045; Ning Wu 0000-0002-9307-3115; Zhuang Zhang 0000-0002-9270-8342; Lai-Xing Zhang 0000-0001-7034-8043; Xiao-Dong Yuan 0000-0003-1964-5098.

S-Editor: Zhang H
L-Editor: Filipodia CL
P-Editor: Zhang H

REFERENCES

1 **Tsutsui S**, Ashizawa K, Minami K, Tagawa T, Nagayasu T, Hayashi T, Uetani M. Multiple focal pure ground-glass opacities on high-resolution CT images: Clinical significance in patients with lung cancer. *AJR Am J Roentgenol* 2010; **195**: W131-W138 [PMID: 20651172 DOI: 10.2214/AJR.09.3828]
2 **Lee HY**, Choi YL, Lee KS, Han J, Zo JI, Shim YM, Moon JW. Pure ground-glass opacity neoplastic lung nodules: histopathology, imaging, and management. *AJR Am J Roentgenol* 2014; **202**: W224-W233 [PMID: 24555618 DOI: 10.2214/AJR.13.11819]
3 **Yang J**, Wang H, Geng C, Dai Y, Ji J. Advances in intelligent diagnosis methods for pulmonary ground-glass opacity nodules. *Biomed Eng Online* 2018; **17**: 20 [PMID: 29415726 DOI: 10.1186/s12938-018-0435-2]
4 **Hu H**, Wang Q, Tang H, Xiong L, Lin Q. Multi-slice computed tomography characteristics of solitary pulmonary ground-glass nodules: Differences between malignant and benign. *Thorac Cancer* 2016; **7**: 80-87 [PMID: 26913083 DOI: 10.1111/1759-7714.12280]
5 **Jiang B**, Takashima S, Miyake C, Hakucho T, Takahashi Y, Morimoto D, Numasaki H, Nakanishi K, Tomita Y, Higashiyama M. Thin-section CT findings in peripheral lung cancer of 3 cm or smaller: are there any characteristic features for predicting tumor histology or do they depend only on tumor size? *Acta Radiol* 2014; **55**: 302-308 [PMID: 23926233 DOI: 10.1177/0284185113495834]
6 **Meng Y**, Liu CL, Cai Q, Shen YY, Chen SQ. Contrast analysis of the relationship between the HRCT sign and new pathologic classification in small ground glass nodule-like lung adenocarcinoma. *Radiol Med* 2019; **124**: 8-13 [PMID: 30191447 DOI: 10.1007/s11547-018-0936-x]
7 **Zhang M**, Kono M. Solitary pulmonary nodules: evaluation of blood flow patterns with dynamic CT. *Radiology* 1997; **205**: 471-478 [PMID: 9356631 DOI: 10.1148/radiology.205.2.9356631]
8 **Lee YH**, Kwon W, Kim MS, Kim YJ, Lee MS, Yong SJ, Jung SH, Chang SJ, Sung KJ. Lung perfusion CT: the differentiation of cavitary mass. *Eur J Radiol* 2010; **73**: 59-65 [PMID: 19481401 DOI: 10.1016/j.ejrad.2009.04.037]
9 **Boll DT**, Merkle EM. Differentiating a chronic hyperplastic mass from pancreatic cancer: a challenge remaining in multidetector CT of the pancreas. *Eur Radiol* 2003; **13** Suppl 5: M42-M49 [PMID: 14989611 DOI: 10.1007/s00330-003-2100-8]
10 **Coolen J**, Vansteenkiste J, De Keyzer F, Decaluwé H, De Wever W, Deroose C, Dooms C, Verbeken E, De Leyn P, Vandecaveye V, Van Raemdonck D, Nackaerts K, Dymarkowski S, Verschakelen J. Characterisation of solitary pulmonary lesions combining visual perfusion and quantitative diffusion MR imaging. *Eur Radiol* 2014; **24**: 531-541 [PMID: 24173597 DOI: 10.1007/s00330-013-3053-1]
11 **Bellomi M**, Petralia G, Sonzogni A, Zampino MG, Rocca A. CT perfusion for the monitoring of neoadjuvant chemotherapy and radiation therapy in rectal carcinoma: initial experience. *Radiology* 2007; **244**: 486-493 [PMID: 17641369 DOI: 10.1148/radiol.2442061189]
12 **Li XS**, Fan HX, Fang H, Huang H, Song YL, Zhou CW. Value of whole-tumor dual-input perfusion CT in predicting the effect of multiarterial infusion chemotherapy on advanced non-small cell lung cancer. *AJR Am J Roentgenol* 2014; **203**: W497-W505 [PMID: 25341164 DOI: 10.2214/AJR.13.11621]
13 **Lin G**, Sui Y, Li Y, Huang W. Diagnostic and prognostic value of CT perfusion parameters in patients with advanced NSCLC after chemotherapy. *Am J Transl Res* 2021; **13**: 13516-13523 [PMID: 35035693]
14 **Liu G**, Li M, Li G, Li Z, Liu A, Pu R, Cao H, Liu Y. Assessing the Blood Supply Status of the Focal Ground-Glass Opacity in Lungs Using Spectral Computed Tomography. *Korean J Radiol* 2018; **19**: 130-138 [PMID: 29354009 DOI: 10.3348/kjr.2018.19.1.130]
15 **Yuan X**, Zhang J, Ao G, Quan C, Tian Y, Li H. Lung cancer perfusion: can we measure pulmonary and bronchial circulation simultaneously? *Eur Radiol* 2012; **22**: 1665-1671 [PMID: 22415414 DOI: 10.1007/s00330-012-2414-5]
16 **Valentin J**; International Commission on Radiation Protection. Managing patient dose in multi-detector computed tomography(MDCT). ICRP Publication 102. *Ann ICRP* 2007; **37**: 1-79, iii [PMID: 18069128 DOI: 10.1016/j.icrp.2007.09.001]
17 **Godoy MC**, Naidich DP. Overview and strategic management of subsolid pulmonary nodules. *J Thorac Imaging* 2012; **27**: 240-248 [PMID: 22847591 DOI: 10.1097/RTI.0b013e31825d515b]

18 **Milne EN**. Circulation of primary and metastatic pulmonary neoplasms. A postmortem microarteriographic study. *Am J Roentgenol Radium Ther Nucl Med* 1967; **100**: 603-619 [PMID: 5230250 DOI: 10.2214/ajr.100.3.603]

19 **Luo L**, Wang H, Ma H, Zou H, Li D, Zhou Y. [Analysis of 41 cases of primary hypervascular non-small cell lung cancer treated with embolization of emulsion of chemotherapeutics and iodized oil]. *Zhongguo Fei Ai Za Zhi* 2010; **13**: 540-543 [PMID: 20677656 DOI: 10.3779/j.issn.1009-3419.2010.05.29]

20 **Yuan X**, Zhang J, Quan C, Cao J, Ao G, Tian Y, Li H. Differentiation of malignant and benign pulmonary nodules with first-pass dual-input perfusion CT. *Eur Radiol* 2013; **23**: 2469-2474 [PMID: 23793548 DOI: 10.1007/s00330-013-2842-x]

21 **Takashima S**, Maruyama Y, Hasegawa M, Yamanda T, Honda T, Kadoya M, Sone S. CT findings and progression of small peripheral lung neoplasms having a replacement growth pattern. *AJR Am J Roentgenol* 2003; **180**: 817-826 [PMID: 12591704 DOI: 10.2214/ajr.180.3.1800817]

22 **Min JH**, Lee HY, Lee KS, Han J, Park K, Ahn MJ, Lee SJ. Stepwise evolution from a focal pure pulmonary ground-glass opacity nodule into an invasive lung adenocarcinoma: an observation for more than 10 years. *Lung Cancer* 2010; **69**: 123-126 [PMID: 20478641 DOI: 10.1016/j.lungcan.2010.04.022]

23 **Mironova V**, Blasberg JD. Evaluation of ground glass nodules. *Curr Opin Pulm Med* 2018; **24**: 350-354 [PMID: 29634577 DOI: 10.1097/MCP.0000000000000492]

24 **Pedersen JH**, Saghir Z, Wille MM, Thomsen LH, Skov BG, Ashraf H. Ground-Glass Opacity Lung Nodules in the Era of Lung Cancer CT Screening: Radiology, Pathology, and Clinical Management. *Oncology (Williston Park)* 2016; **30**: 266-274 [PMID: 26984222]

25 **Lee GD**, Park CH, Park HS, Byun MK, Lee IJ, Kim TH, Lee S. Lung Adenocarcinoma Invasiveness Risk in Pure Ground-Glass Opacity Lung Nodules Smaller than 2 cm. *Thorac Cardiovasc Surg* 2019; **67**: 321-328 [PMID: 29359309 DOI: 10.1055/s-0037-1612615]

26 **Ohno Y**, Fujisawa Y, Koyama H, Kishida Y, Seki S, Sugihara N, Yoshikawa T. Dynamic contrast-enhanced perfusion area-detector CT assessed with various mathematical models: Its capability for therapeutic outcome prediction for non-small cell lung cancer patients with chemoradiotherapy as compared with that of FDG-PET/CT. *Eur J Radiol* 2017; **86**: 83-91 [PMID: 28027771 DOI: 10.1016/j.ejrad.2016.11.008]

27 **Kim HY**, Shim YM, Lee KS, Han J, Yi CA, Kim YK. Persistent pulmonary nodular ground-glass opacity at thin-section CT: histopathologic comparisons. *Radiology* 2007; **245**: 267-275 [PMID: 17885195 DOI: 10.1148/radiol.2451061682]

28 **Bach PB**, Silvestri GA, Hanger M, Jett JR; American College of Chest Physicians. Screening for lung cancer: ACCP evidence-based clinical practice guidelines (2nd edition). *Chest* 2007; **132**: 69S-77S [PMID: 17873161 DOI: 10.1378/chest.07-1349]

29 **Cha MJ**, Lee KS, Kim HS, Lee SW, Jeong CJ, Kim EY, Lee HY. Improvement in imaging diagnosis technique and modalities for solitary pulmonary nodules: from ground-glass opacity nodules to part-solid and solid nodules. *Expert Rev Respir Med* 2016; **10**: 261-278 [PMID: 26751340 DOI: 10.1586/17476348.2016.1141053]

30 **Sawada S**, Yamashita N, Sugimoto R, Ueno T, Yamashita M. Long-term Outcomes of Patients With Ground-Glass Opacities Detected Using CT Scanning. *Chest* 2017; **151**: 308-315 [PMID: 27435815 DOI: 10.1016/j.chest.2016.07.007]

31 **Bueno J**, Landeras L, Chung JH. Updated Fleischner Society Guidelines for Managing Incidental Pulmonary Nodules: Common Questions and Challenging Scenarios. *Radiographics* 2018; **38**: 1337-1350 [PMID: 30207935 DOI: 10.1148/rg.2018180017]

32 **Nguyen-Kim TD**, Frauenfelder T, Strobel K, Veit-Haibach P, Huellner MW. Assessment of bronchial and pulmonary blood supply in non-small cell lung cancer subtypes using computed tomography perfusion. *Invest Radiol* 2015; **50**: 179-186 [PMID: 25500892 DOI: 10.1097/RLI.0000000000000124]

33 **Tsai HY**, Tung CJ, Yu CC, Tyan YS. Survey of computed tomography scanners in Taiwan: dose descriptors, dose guidance levels, and effective doses. *Med Phys* 2007; **34**: 1234-1243 [PMID: 17500455 DOI: 10.1118/1.2712412]

34 **Galanski M**, Nagel HD, Stamm G. [Results of a federation inquiry 2005/2006: pediatric CT X-ray practice in Germany]. *Rofo* 2007; **179**: 1110-1111 [PMID: 17955412 DOI: 10.1055/s-2007-992844]

World Journal of Radiology

Submit a Manuscript: https://www.f6publishing.com

World J Radiol 2022 June 28; 14(6): 165-176

DOI: 10.4329/wjr.v14.i6.165

ISSN 1949-8470 (online)

ORIGINAL ARTICLE

Prospective Study

Do preoperative pancreatic computed tomography attenuation index and enhancement ratio predict pancreatic fistula after pancreaticoduodenectomy?

Senthil Gnanasekaran, Satish Durgesh, Ramprakash Gurram, Raja Kalayarasan, Biju Pottakkat, M Rajeswari, Bheemanathi Hanuman Srinivas, A Ramesh, Jayaprakash Sahoo

Specialty type: Radiology, nuclear medicine and medical imaging

Provenance and peer review: Invited article; Externally peer reviewed.

Peer-review model: Single blind

Peer-review report's scientific quality classification

Grade A (Excellent): 0
Grade B (Very good): B
Grade C (Good): 0
Grade D (Fair): 0
Grade E (Poor): E

P-Reviewer: Bencini L, Italy; Yang F, China
A-Editor: Morozov S

Received: January 29, 2022
Peer-review started: January 29, 2022
First decision: April 10, 2022
Revised: April 26, 2022
Accepted: June 20, 2022
Article in press: June 20, 2022
Published online: June 28, 2022

Senthil Gnanasekaran, Satish Durgesh, Ramprakash Gurram, Raja Kalayarasan, Biju Pottakkat, Department of Surgical Gastroenterology, Jawaharlal Institute of Postgraduate Medical Education and Research, Puducherry 605006, India

M Rajeswari, Department of Biostatistics, Jawaharlal Institute of Postgraduate Medical Education and Research, Puducherry 605006, India

Bheemanathi Hanuman Srinivas, Department of Pathology, Jawaharlal Institute of Postgraduate Medical Education and Research, Puducherry 605006, India

A Ramesh, Department of Radiodiagnosis, Jawaharlal Institute of Postgraduate Medical Education and Research, Puducherry 605006, India

Jayaprakash Sahoo, Department of Endocrinology, Jawaharlal Institute of Postgraduate Medical Education and Research, Puducherry 605006, India

Corresponding author: Raja Kalayarasan, DNB, MCh, MS, Additional Professor, Department of Surgical Gastroenterology, Jawaharlal Institute of Postgraduate Medical Education and Research, Room No. 5442, 4th Floor, Super Specialty Block, Puducherry-605006, India. kalayarasanraja@yahoo.com

Abstract

BACKGROUND

The commonly used predictors of clinically relevant postoperative pancreatic fistula (CR-POPF) following pancreaticoduodenectomy (PD) have subjective assessment components and can be used only in the postoperative setting. Also, the available objective predictors based on preoperative cross-sectional imaging were not prospectively studied.

AIM

To evaluate the accuracy of the pancreatic attenuation index (PAI) and pancreatic enhancement ratio (PER) for predicting CR-POPF following PD and its correlation with pancreatic fat fraction and fibrosis.

METHODS

A prospective observational study included patients who underwent PD for benign and malignant pathology of the periampullary region or pancreatic head between February 2019 and February 2021. Patients undergoing extended or total pancreatectomy and those with severe atrophy of pancreatic tissue or extensive parenchymal calcifications in the pancreatic head and neck precluding calculation of PAI and PER were excluded from the study. Preoperatively PAI was measured in the neck of the pancreas by marking regions of interest (ROI) in the non-contrast computed tomography (CT), and PER was measured during the contrast phase of the CT abdomen. Also, the fibrosis score and fat fraction of the pancreatic neck were assessed during the histopathological examination. Demographic, clinical and preoperative radiological indices (PAI, PER) were evaluated to predict CR-POPF. Preoperative pancreatic neck CT indices were correlated with the histopathological assessment of fat fraction and fibrosis.

RESULTS

Of the 70 patients who underwent PD, 61 patients fulfilling the inclusion criteria were included in the analysis. The incidence of CR-POPF was 29.5% (18/61). PAI had no association with the development of CR-POPF. Of the preoperative parameters, PER (mean ± standard deviation [SD]) was significantly lower in patients developing CR-POPF (0.58 ± 0.20 *vs* 0.81 ± 0.44, $P = 0.006$). The area under the curve for the PER was 0.661 (95%CI: 0.517-0.804), which was significant ($P = 0.049$). PER cut-off of 0.673 predicts CR-POPF with 77.8% sensitivity and 55.8% specificity. PAI and PER had a weak negative correlation (Strength-0.26, $P = 0.037$). Also, PER showed a moderately positive correlation with fibrosis (Strength 0.50, $P < 0.001$). Patients with CR-POPF had a significantly higher incidence of the intraabdominal abscess (50% *vs* 2.3%, $P < 0.001$), delayed gastric emptying (83.3% *vs* 30.2, $P < 0.001$), and prolonged mean (± SD) postoperative hospital stay (26.8 ± 13.9 *vs* 9.6 ± 3.6, $P = 0.001$).

CONCLUSION

PER exhibited good accuracy in predicting the development of CR-POPF. PER additionally showed a good correlation with PAI and fibrosis scores and may be used as an objective preoperative surrogate for assessing pancreatic texture. However, ROI-based PAI did not show any association with CR-POPF and pancreatic fat fraction.

Key Words: Pancreatic fistula; Minimally invasive; Pancreaticoduodenectomy; Pancreatic cancer; Neoplasms; Computed tomography

Core Tip: The prospective observational study evaluated the accuracy of the pancreatic computed tomography indices in predicting clinically relevant pancreatic fistula after pancreaticoduodenectomy. Though the predictive accuracy of pancreatic attenuation index (PAI) was low, pancreatic enhancement ratio (PER) exhibited good accuracy in predicting the development of clinically relevant postoperative pancreatic fistula (CR-POPF). Also, PER showed a statistically significant weak negative correlation with PAI and moderately positive correlation with fibrosis scores suggesting that PER may be an objective preoperative surrogate for assessing pancreatic texture. Preoperative quantification of PER can improve the risk stratification and management of patients at high risk of CR-POPF.

Citation: Gnanasekaran S, Durgesh S, Gurram R, Kalayarasan R, Pottakkat B, Rajeswari M, Srinivas BH, Ramesh A, Sahoo J. Do preoperative pancreatic computed tomography attenuation index and enhancement ratio predict pancreatic fistula after pancreaticoduodenectomy? *World J Radiol* 2022; 14(6): 165-176
URL: https://www.wjgnet.com/1949-8470/full/v14/i6/165.htm
DOI: https://dx.doi.org/10.4329/wjr.v14.i6.165

INTRODUCTION

Pancreaticoduodenectomy (PD) has been established as the standard surgical treatment for resectable pancreatic head cancer and periampullary tumors. Advances in surgical technology and perioperative care have reduced PD-related mortality from roughly 20% to less than 5%[1]. But the morbidity following a PD continues to remain high[2]. Hence, the focus has shifted to make PD a less morbid procedure. The most feared consequence of PD is postoperative pancreatic fistula (POPF)[1,2]. POPF is frequently linked to a lengthy and challenging hospital stay that imposes a significant social and

financial burden. Despite numerous novel perioperative therapies, there has been no substantial reduction in reported POPF rates[2,3].

The implications of identifying patients at risk of clinically relevant POPF (CR-POPF) are manifold. To begin, we can tailor surgical procedures to high-risk factors by making modifications that have been demonstrated to reduce the occurrence of CR-POPF. Second, high-risk patients can be closely assessed for the need for early intervention to avoid the disastrous consequences of POPF. Finally, it helps identify low-risk patients in whom the enhanced recovery after surgery (ERAS) pathway may be implemented confidently. Commonly used predictive models for POPF, such as the Fistula Risk Score (FRS), modified FRS, and Day 1 Drain Fluid Amylase estimation, can be used only in the postoperative setting[4-6]. Attenuation and enhancement patterns of pancreatic parenchyma on computed tomography (CT) were studied as preoperative predictors of CR-POPF[7-11]. While pancreatic attenuation index (PAI) can quantify pancreatic fat, pancreatic enhancement ratio (PER) has been correlated with pancreatic fibrosis. Therefore, the presence of a higher preoperative mean PER and lower PAI can be considered protective against the development of CR-POPF after PD[7-11]. However, the predictive accuracy of these indices for CR-POPF was not prospectively studied. Also, the distribution of fat and fibrosis within the pancreas varies, with pancreatic neck fat and fibrosis assuming relevance since it is the site of anastomosis, which previous studies have not addressed. Also, no previous research has prospectively correlated preoperative PAI and PER with histological pancreatic fat fraction and fibrosis, particularly in the neck. The present study aims to calculate the accuracy of the pancreatic neck PAI and PER in predicting CR-POPF and its correlation with histological pancreatic neck fat fraction and fibrosis scoring.

MATERIALS AND METHODS

Patient selection

Patients above 18 years of age who underwent elective PD for both benign and malignant pathology involving periampullary and pancreatic head from February 2019 to February 2021 and consented to participate were assessed for inclusion in the prospective observational study. Patients undergoing extended or total pancreatectomy and those with contraindication to undergo preoperative contrast-enhanced CT (CECT) or severe atrophy of pancreatic tissue or extensive parenchymal calcifications in the pancreatic head and neck precluding calculation of PAI and PER were excluded from the study. Also, patients who died in the immediate postoperative period (< 48 h) were excluded from the analysis. The study was approved by the Institute's scientific advisory and Ethics Committee (JIP/IEC/2018/500 dated 25-01-2019).

Preoperative CT protocol

As part of the routine evaluation, all patients underwent a pancreatic protocol CECT. Non-contrast and CECT of the abdomen and pelvis were performed using a 128 slice CT scanner (Somatom™ Definition Edge, M/s Siemens, Erlangen, Germany). Intravenous iodinated contrast media Iohexol with 300mg Iodine concentration (Contrapaque™ 300, JB chemicals and pharmaceuticals limited, India) was administered at a dose of 1.5 mL/ kg body weight at the rate of 3-4 mL/s followed by 20 mL of the saline chase at 3 mL/s. A dual head pressure injector (Medrad® Stellant D pedestal-mount with Certegra® Workstation) was used for contrast injection. Scans were triggered using the Bolus tracking technique when the threshold of 150HU was reached in the upper abdominal aorta. Contrast-enhanced scans included late arterial phase at 30-40 sec from the start of contrast injection (12-15 sec after bolus tracking), portal venous phase at 60-70 sec (25-30 secs delay after the arterial phase) and equilibrium phase at 3 min from contrast injection. The plain and contrast-enhanced images were reconstructed at 3 mm thickness and viewed in a picture archiving and communication system workstation using Centricity™ Universal Viewer Zero Footprint (GE, United States). On non-enhanced CT images, Hounsfield Units (HU) represents tissue density, while on contrast-enhanced CT images, it represents a measure of combination involving density and vascularity (18). Attenuation (HU) was measured in the neck of the pancreas and spleen, and attenuation values were calculated with regions of interest (ROI) of 0.2-0.3 cm^2. The mean of 3 ROI values obtained in the neck region divided by splenic attenuation gave the PAI of the pancreatic neck (Figure 1). PER was calculated in the neck of the pancreas as (EP-Pre)/(AP-Pre) (AP-arterial phase, pre-nonenhanced phase, EP-equilibrium phase)[11].

Surgery

All patients underwent pylorus resecting PD at the surgeon's discretion using an open, laparoscopic, or robot-assisted technique. All operations were performed by three qualified surgeons with extensive experience in pancreatobiliary surgery. Pancreaticojejunostomy (PJ) was performed using modified Blumgart or a modified invagination technique depending on the size of the pancreatic duct at the surgeon's discretion. Hepaticojejunostomy (HJ) was done 15 cm distal to PJ by Blumgart Kelly technique. Antecolic Gastrojejunostomy was done about 50 cm distal to the HJ. Two abdominal drains were placed, one in the subhepatic space near HJ and the other one adjacent to the PJ. Feeding

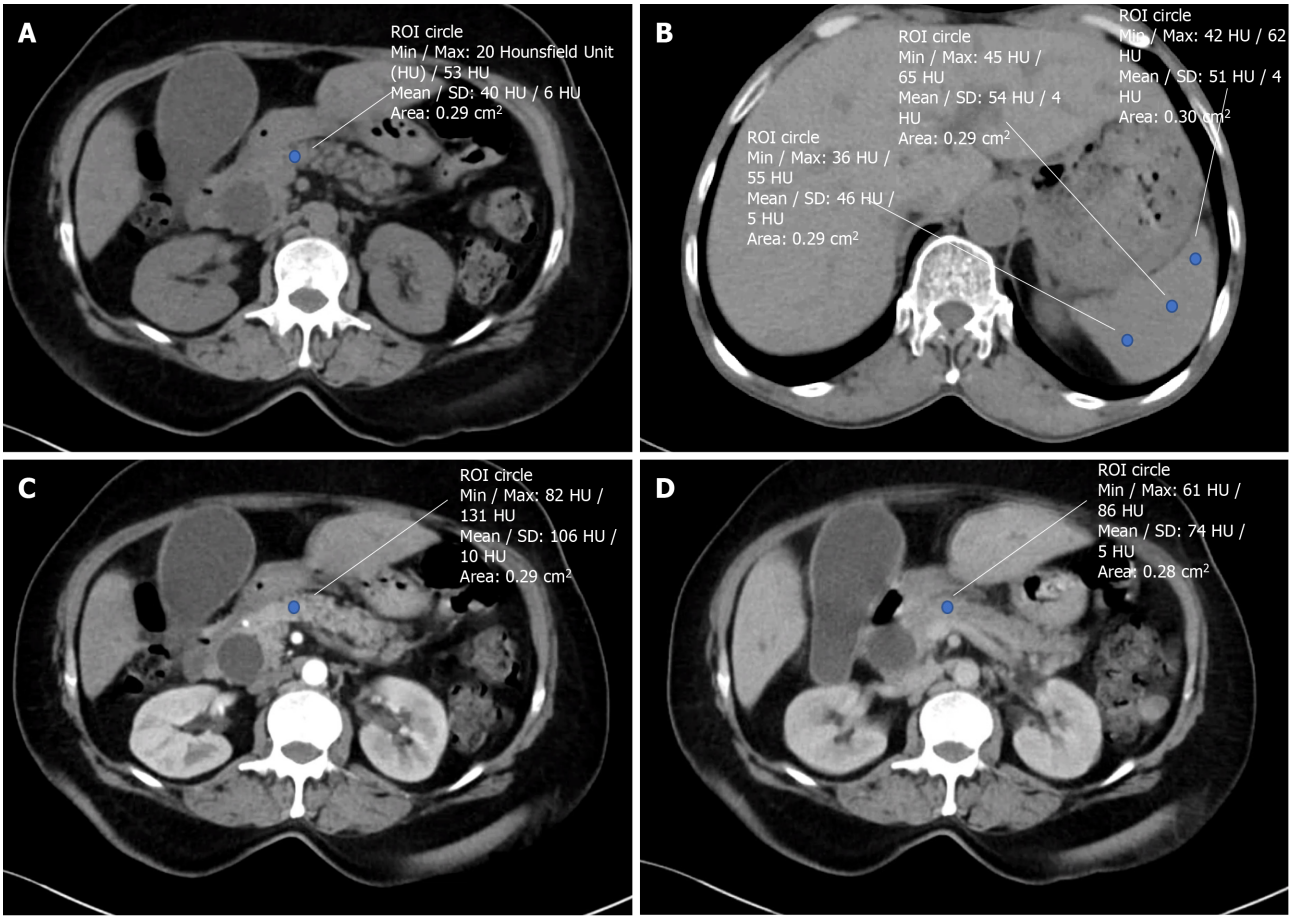

DOI: 10.4329/wjr.v14.i6.165

Figure 1 Calculation of preoperative radiological indices. A: Hounsfield unit (HU) of the pancreatic neck in plain phase; B: HU of the spleen in plain phase; C: HU of the pancreatic neck in the arterial phase; D: HU of the pancreatic neck in the equilibrium phase. ROI: Region of interest.

jejunostomy was done routinely for early postoperative enteral feeding.

Histopathological evaluation

A pancreatic neck tissue specimen was sent for histopathological evaluation. The pathologist, blinded to CT data and pancreatic texture, performed histological analysis. The existence of Langerhans' islets confirmed the Pancreatic tissue. Only tissue free of inflammatory lesions and calcifications was evaluated. The histologic pancreatic fat fraction was defined as the area ratio of pancreatic intraparenchymal fat to that of the total tissue times 100% (< 5%-mildly fatty; 5-15%-moderately fatty, > 15%-heavily fatty) using hematoxylin and eosin stain[12]. The degree of fibrosis was studied using Masson's trichome stain. The extent of intralobular and interlobular fibrosis was separately measured, and the total score (0-6) was calculated (Figure 2). According to the total score, fibrosis was classified as weak (score 0-3) and heavy (score 4-6)[13].

Outcome measures

The primary objective of this prospective observational study was to determine the predictive accuracy of PAI and PER for CR-POPF following PD. The patients' demographic and clinical data, including age, sex, body mass index, bilirubin level, preoperative biliary drainage, comorbidities (diabetes mellitus and hypertension), weight loss and radiological indices (PAI and PER) were collected to determine the preoperative factors predictive of CR-POPF. Also, the operative outcomes, including operative time, estimated blood loss, need for blood transfusion, pancreatic texture and postoperative complications, were compared between patients with and without CR-POPF. Delayed gastric emptying [DGE], Post pancreatectomy hemorrhage (PPH) and Postoperative pancreatic fistula [POPF] were graded as per the International Study Group for Pancreatic Surgery [ISGPS] definition[14-16]. To correlate preoperative CT indices (PAI and PER) with histopathological features, pancreatic neck fat fraction and fibrosis were measured in the pancreatic neck tissue specimen.

Statistical analysis

The statistical analysis was done using IBM SPSS Statistics for Windows, Version 28.0. (Armonk, NY,

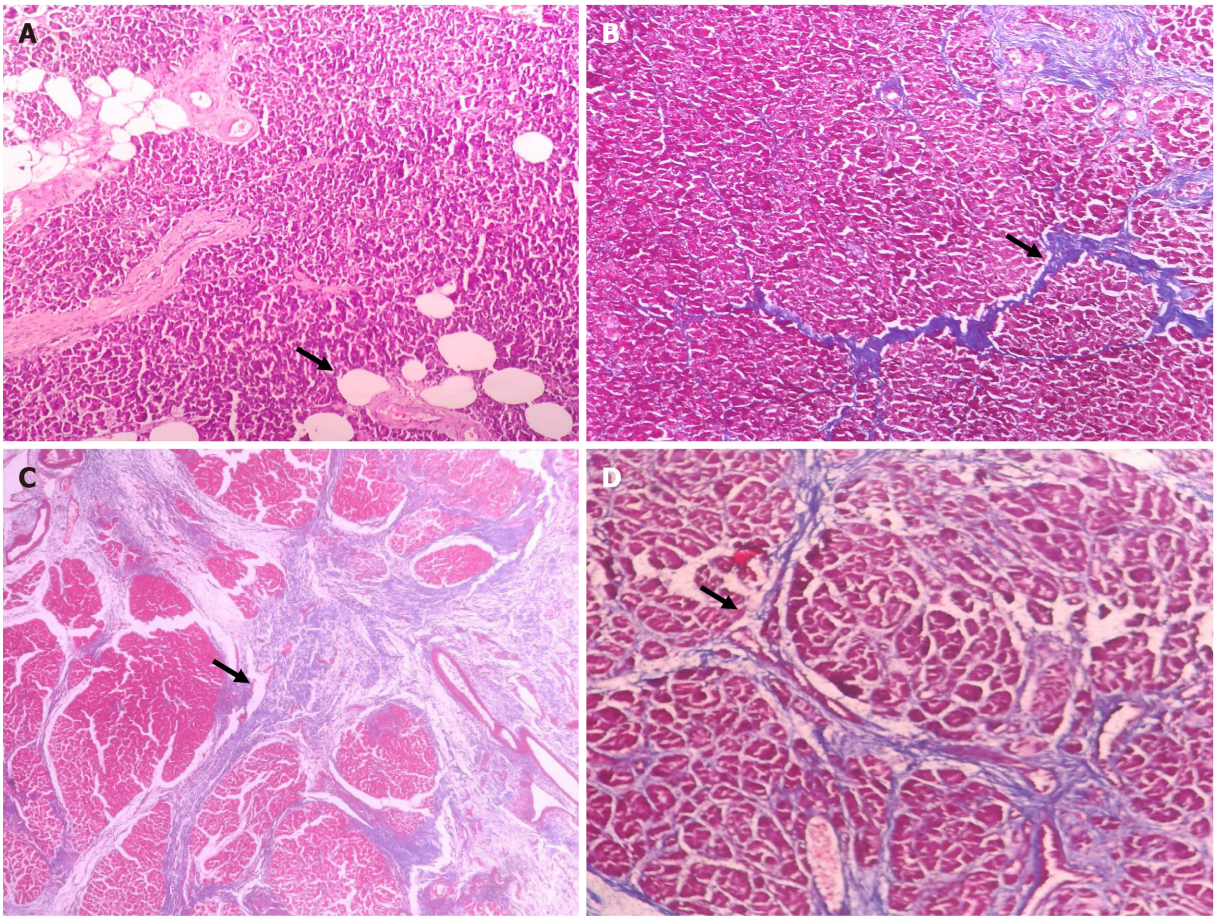

DOI: 10.4329/wjr.v14.i6.165

Figure 2 Histopathological evaluation of pancreatic neck fat fraction and fibrosis. A: Photomicrograph showing moderate fat inclusion (hematoxylin and eosin [H&E], × 100); B: Photomicrograph showing heavy intralobular fibrosis (Masson's trichome stain, H&E, × 100); C: Photomicrograph showing heavy interlobular fibrosis (Masson's trichome stain, × 40); D: Photomicrograph showing weak intra and interlobular fibrosis (Masson's trichome stain, × 200).

United States). The estimated sample size was calculated, anticipating an AUC of 0.75 for PER in predicting CR-POPF with 90% power and a 5% level of significance. The required sample size was calculated as 60. Both descriptive and inferential statistics were used to analyze the data. Baseline characteristics of the patients are presented by descriptive statistics. Categorical data (sex, clinical factors, presence or absence of DGE, CRPOPF, PPH, Intraabdominal abscess, pancreatic gland texture, pathological diagnosis) was described using percentages and frequencies and compared by using Fischer exact test or Chi-square test. The normality of continuous data was assessed by the Kolmogorov-Smirnov test. The normally distributed data were described by mean ± standard deviation (SD). Median and interquartile range was used for non-Gaussian data. Comparison of the continuous data (age, duct size, serum bilirubin) between the two groups was done by independent Student's *t*-test for parametric data and Mann-Whitney U-test for nonparametric data. The ability of PAI and PER to predict CR-POPF was assessed using receiver operating characteristic (ROC) analysis. A perfect test will have an AUC equaling 1. A 95% confidence interval was calculated and reported for the outcome measures. Statistical analysis was carried out at a 5% significance level, and $P < 0.05$ was considered statistically significant. The Pearson correlation coefficient (r) was used to examine the association of the histologic pancreatic fibrosis score and fat fraction with PAI and PER independently. A perfect positive correlation will show a value of +1, and a value of -1 indicates a perfect negative correlation.

RESULTS

Of the 70 patients who underwent PD during the study period, 61 patients fulfilling the inclusion criteria were included in the analysis. Five patients did not achieve the required ROI (0.2-0.3 cm^2), three patients who could not undergo histopathological analysis due to insufficient or other pathological changes in the sample and one patient who died during the immediate postoperative period were excluded from the analysis.

Preoperative predictive factors for CR-POPF

The overall incidence of CR-POPF in the study cohort was 29.5% (18/61). The demographic variables, history of weight loss, presence of comorbidities, preoperative hemoglobin, serum bilirubin and preoperative biliary drainage were comparable between groups with and without CR-POPF (Table 1). While PAI was similar between the two groups, the mean (± SD) PER was significantly lower in patients developing CR-POPF (0.58 ± 0.20 *vs* 0.81 ± 0.44, $P = 0.006$). The ROC analysis was done to determine the accuracy of PAI and PER in predicting CR-POPF (Figure 3). The area under the curve for the PAI was 0.461 (95%CI: 0.304-0.617), which was not significant ($P = 0.630$). At the same time, the area under the curve for the PER was 0.661 (95%CI: 0.517-0.804), which was significant ($P = 0.049$). We can predict whether a randomly chosen case will develop CR-POPF with a probability of 66.1%. With a cut-off of PER = 0.673, PER can predict those with CR-POPF with 77.8% sensitivity and 55.8% specificity (Figure 3).

Correlation between radiological indices (PAI, PER) and histopathological findings

There was no significant correlation between PAI and fat fraction or fibrosis score (Table 2). Pearson correlation coefficient between PER and fibrosis score was moderately positive and statistically significant with a strength of 0.504 and a P value of < 0.001. The positive correlation between PER and fibrosis score suggests that an increase in the intraparenchymal fibrosis results in the delayed pancreatic enhancement on CT, reflected as an increased PER. The correlation coefficient between PER and PAI was low negative and statistically significant, with a strength of -0.267 and a P-value of 0.037. The negative correlation between PER and PAI signifies that as the fibrosis increases, resulting in an increased delayed pancreatic enhancement, the fat fraction within the pancreas decreases, represented by a lower PAI.

Perioperative outcomes

The operative time, blood loss, intraoperative blood transfusion, surgical approach and pancreatic duct size was comparable between the two groups (Table 3). The proportion of patients with soft pancreas was significantly higher in the CR-POPF group. Postoperatively patients with CR-POPF had a significantly higher incidence of delayed gastric emptying (83.3% *vs* 30.2%, $P < 0.001$) and intra-abdominal abscess (50% *vs* 2.3%, $P < 0.001$). Also, Patients with CR-POPF had a prolonged postoperative hospital stay. There was no significant difference in the pancreatic fat fraction and fibrosis score between the two groups.

DISCUSSION

The present study documents the role of preoperative CT indices, especially PER, in predicting CR-POPF. Despite improved surgical techniques and perioperative management, PD remains a morbid procedure with a 30-50% estimated morbidity rate[1,2]. POPF is the critical cause of post-PD morbidity, and pancreatic texture has been reported as an important predictive parameter for POPF[17,18]. A soft pancreatic texture has been associated with an increased risk, while a firm pancreas protects against POPF. However, intraoperative assessment of gland consistency by the surgeon's digital palpation is highly subjective[18]. In recent years, laparoscopic and robotic approaches for PD have increased globally. Assessment of pancreatic texture during minimally invasive PD, especially the robotic approach, is challenging. Hence, parameters like acinar cell density and fibrosis score on histopathological examination were evaluated as objective criteria for pancreatic texture[19]. However, these parameters are not helpful for the preoperative prediction of POPF. Preoperative CR-POPF prediction using dependable parameters can assist in implementing intraoperative and postoperative measures to reduce CR-POPF-related morbidity. Hence, attempts have been made to correlate preoperative cross-sectional imaging (CECT and MRI) with pancreatic texture[7-11,20]. Most studies evaluating PAI and PER on the CECT abdomen were retrospective, which precludes assessment and correlation of pancreatic neck fat fraction and fibrosis[7-11].

PAI

The high fat fraction in the pancreas makes the pancreas softer, which might increase the risk of POPF following PD. Liver Attenuation Index is the widely used radiological index to measure liver fat fraction [21]. Similarly, Yardimci *et al*[22] proposed PAI as a simple tool to assess pancreatic fat fraction based on the study of 76 patients who underwent PD. The PAI cut-off value of 0.67 was valuable for risk calculation in their research. Other studies also reported the usefulness of PAI in assessing pancreatic fat fraction[7,8]. Although PAI was proposed as a simple tool that can be quickly evaluated, the lack of adequate external validation remains the primary impediment to its widespread adoption. In the present study, PAI was not useful for predicting CR-POPF. Also, PAI did not correlate with histological pancreatic fat fraction. On the other hand, PAI correlated negatively with PER, indicating an inverse relationship between pancreatic fat content with fibrosis and pancreatic texture. According to our analysis, PAI may not accurately reflect pancreas fat fraction and softness. However, the lack of predict-

Table 1 Comparison of demographic, clinical and preoperative radiological parameters between patients with and without clinically relevant postoperative pancreatic fistula

Parameter	CR-POPF, *n* = 18	No CR-POPF, *n* = 43	*P* value
Age in yr, mean ± SD	53.7 ± 10.8	54.7 ± 11.5	0.746
Sex, *n* (%)			
Male	10 (55.6)	28 (65.1)	0.567
Female	8 (44.4)	15 (34.9)	
BMI in kg/m^2, mean ± SD	21.1 ± 4.4	20.1 ± 3.9	0.388
Weight loss, *n* (%)	15 (83.3)	32 (74.4)	0.525
Comorbidities, *n* (%)	11 (61.1)	22 (51.2)	0.578
Hemoglobin in gm%, mean ± SD	10.7 ± 1.4	10.8 ± 1.5	0.735
Preoperative serum bilirubin (mg/dL), median (IQR)	2 (1.8-6)	3 (1-7)	0.848
Preoperative biliary drainage, *n* (%)	10 (55.6)	22 (51.2)	0.786
Pancreatic attenuation index, mean ± SD	0.8 ± 0.2	0.8 ± 0.2	0.741
Pancreatic enhancement ratio, mean ± SD	0.6 ± 0.2	0.8 ± 0.4	0.006

CR-POPF: Clinically relevant postoperative pancreatic fistula; gm: Gram; IQR: Inter quartile range; SD: Standard deviation.

Table 2 Correlation between preoperative radiological indices and histopathological pancreatic neck fat fraction and fibrosis

	Pancreatic attenuation index	Pancreatic enhancement ratio	Pancreatic fat fraction	Fibrosis score
Pancreatic attenuation index	-	-0.27 [a]	0.21	-0.20
Pancreatic enhancement ratio	-0.27[a]	-	-0.10	0.50 [b]
Pancreatic fat fraction	0.21	-0.10	-	-0.12
Fibrosis score	-0.20	0.50 [b]	-0.12	-

[a]Correlation is significant at the 0.05 level (2-tailed).
[b]Correlation is significant at the 0.01 level (2-tailed).

ability and correlation may be due to the small sample size and the underpowered study.

PER

An increase in the fibrosis of the pancreas makes the gland firmer, decreasing the incidence of POPF. It is technically straightforward to perform a pancreatoenteric anastomosis on a firmer gland. Maehira *et al* [9], in a retrospective analysis of 115 patients, reported that the pattern of pancreatic enhancement could be a reliable predictor for the development of CR-POPF. Also, Kang *et al*[11] documented that PER cut-off of 1.100 might be a valuable predictor for the risk of developing a CR-POPF following PD. In the present study, the PER cut-off value of 0.661 had a sensitivity of 78% and a specificity of 55% in predicting CR-POPF. Also, PER had a positive correlation with pancreatic fibrosis. The main drawback of using PER as a predictor for CR-POPF is that the perfusion of organs with injected contrast depends upon the patient's hemodynamic status, influencing the final indices values, unlike PAI, which is independent of contrast.

Correlation between the CT indices and Histopathological analysis

With pancreatic fibrosis known for the protection of CR-POPF and pancreatic fatty infiltration being a concern, it is prudent that radiological indices be correlated with histopathological findings to determine their predictive accuracy. While multiple studies have evaluated different CT parameters, a few have tried to link with histology. However, no previous studies have looked at both contrast and non-contrast indices and their relationship with pancreatic neck fat fraction and fibrosis. The present study results are similar to the study by Hashimoto *et al*[10], which reported a correlation between PER and pancreatic fibrosis. However, in contrast to the current study, bolus tracking was not used in their imaging protocol. Hence, the timing differences between the scan performance and arrival of injected contrast in the structures were not considered. Further, the iodine concentration of the contrast used

Table 3 Comparison of perioperative and pathological parameters between patients with and without clinically relevant postoperative pancreatic fistula

Parameter	CR-POPF, *n* = 18	No CR-POPF,*n* = 43	*P* value
Operative time in min, mean ± SD	521.9 ± 123	463.9 ± 101.2	0.275
Blood loss in mL, median (IQR)	550 (350-725)	475 (350-800)	0.830
Intraoperative blood transfusion, *n* (%)	6 (33.3)	17 (39.5)	0.775
Pancreatic texture, *n* (%)			
Firm	1 (5.6)	20 (47.6)	0.002
Soft	17 (94.4)	22 (52.4)	
Pancreatic duct size in mm, mean ± SD	2.8 ± 1.1	3.4 ± 1.6	0.169
Surgical approach, *n* (%)			
Open	9 (50)	24 (55.8)	
Laparoscopic	6 (33.3)	12 (27.9)	
Robot assisted	3 (16.7)	7 (16.3)	0.927
Delayed gastric emptying, *n* (%)	15 (83.3)	13 (30.2)	< 0.001
Postpancreatectomy hemorrhage, *n* (%)	3 (16.7)	4 (9.3)	0.662
Intra-abdominal abscess, *n* (%)	9 (50)	1 (2.3)	< 0.001
Hospital stay in d, mean ± SD	26.8 ± 13.9	9.6 ±.6	0.001
Pathology, *n* (%)			
Malignant	17 (94.4)	35 (81.4)	
Benign	1 (5.6)	8 (18.6)	0.259
Fat fraction, *n* (%)			
Absent	6 (33.3)	20 (46.5)	
Mild	9 (50.0)	17 (39.6)	0.669
Moderate	3 (16.7)	6 (13.9)	
Fibrosis score, *n* (%)			
Weak	16 (88.9)	27 (62.8)	
Heavy	2 (11.1)	16 (37.2)	0.063

CR-POPF: Clinically relevant postoperative pancreatic fistula; IQR: Inter quartile range; SD: Standard deviation.

could affect the magnitude of enhancement. Kang *et al*[11] reported that the CT enhancement ratio was a more powerful predictor of pancreatic fistula than fecal elastase-1 Levels. However, in contrast to the current study, their study was a retrospective analysis, with no reference standards of the pathological fibrosis data to correlate with the CT enhancement ratios.

Our study did not show any correlation of PAI with pancreatic fat fraction. Kim *et al*[12] reported a significant correlation between the PAI and histopathological fat fraction. However, the clinical parameter that was assessed was post PD glycemic control, unlike CR-POPF in our study. Though the study was able to show a positive correlation, it was a retrospective study, with a small sample size and lack of clarity on whether the histological fat fraction corresponded with the area of ROI. Hori *et al*[23] have recently shown that area-based assessment on unenhanced CT showed higher correlation and concordance with histopathology-based fat fraction in the pancreas than the ROI-based CT attenuation assessment. A few studies have reported the usefulness of MRI for analyzing pancreatic fat content[20]. As MRI is not widely available and routinely used for preoperative workup of patients undergoing PD, its use as a predictor tool for CR-POPF has a limited application. The different CT attenuation and enhancement values reported in the present study could be due to the calculation of CT indices precisely at the pancreatic neck. In contrast, previous studies measured randomly across the pancreas.

Limitations

Our study is limited by a few factors that require attention. Firstly, the small sample size may not

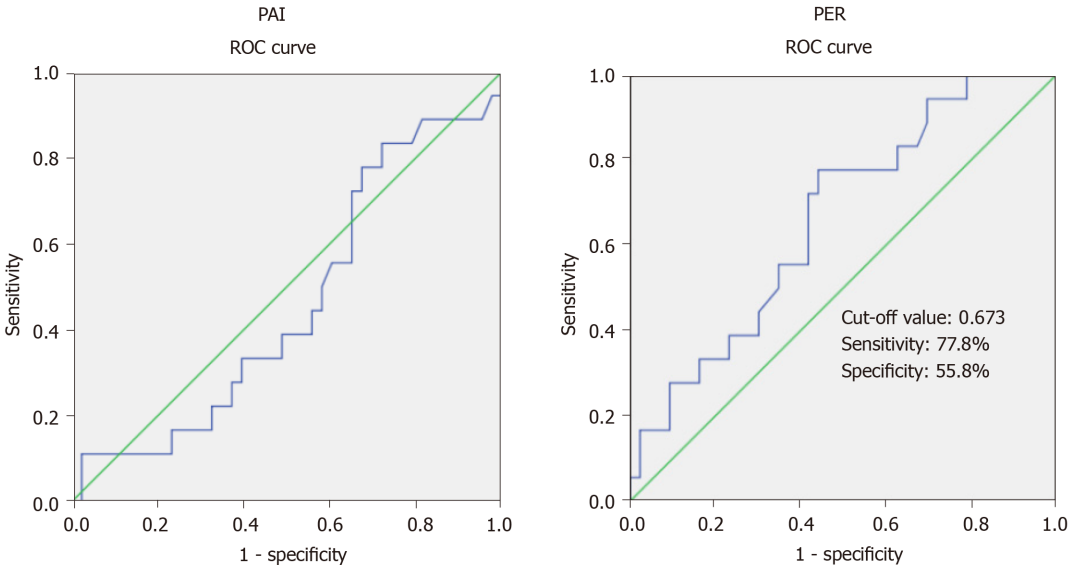

DOI: 10.4329/wjr.v14.i6.165

Figure 3 Receiver operating characteristic curve of the computed tomography indices for predicting clinically relevant postoperative fistula. The area under curve for the pancreatic attenuation index is 0.461 (95%CI: 0.304-0.617), which is not significant (P = 0.630). The area under curve for the pancreatic enhancement ratio is 0.661 (95%CI: 0.517-0.804), which is significant (P = 0.049). ROC: Receiver operating characteristic; PAI: Pancreatic attenuation index; PER: Pancreatic enhancement ratio.

represent the entire patient cohort. A future study with a larger sample size is needed to determine PAI's predictability accurately. The reliable prediction of CR-POPF preoperatively is challenging in patients undergoing PD as it is a mix of a heterogeneous population of patients subjected to different heterogeneous surgical approaches. In PD, with various reconstructive options available and each Institute and each surgeon adopting a technique of their own choice, creating a standardized operative technique is nearly impossible. A homogenous population of patients and standardized uniform surgical techniques are prerequisites for any preoperative prediction models to show good predictive ability, both of which are difficult to achieve in the case of PD. The patient characteristics, the surgeon's expertise and surgical techniques are vital in deciding the risk of a patient developing CR-POPF. With all these factors coming into play, it is expected that accurate preoperative prediction of CR-POPF is not always possible. Even if some studies show a single or group of parameters as predictors for CR-POPF, external validation might not offer the same result because of the factors mentioned above.

Nevertheless, identifying potential preoperative predictors for CR-POPF is a vital step in our journey to decrease the morbidity associated with PD. Our study failed to demonstrate any association of PAI with CR-POPF and postoperative fat fraction, which may be explained apart from the small sample size to the restrictive ROI. Area-based assessment for the pancreatic fat fraction in future studies may better correlate with histopathological fat fraction.

CONCLUSION

The PER showed good accuracy in predicting the development of CR-POPF and a PER ratio of 0.673 or below increased the likelihood of CR-POPF. The positive correlation of PER with fibrosis and negative correlation with PAI suggest that PER may be an objective surrogate for assessing pancreatic texture, especially in minimally invasive surgery, where pancreatic texture assessment could be challenging. ROI-based PAI has a poor prediction for CR-POPF and does not correlate with a pancreatic fat fraction or fibrosis scores. Preoperative quantification of PER can improve the risk stratification and management of patients at high risk of CR-POPF. A multi-center trial with a larger sample size is necessary to validate PAI and PER reliably.

ARTICLE HIGHLIGHTS

Research background

Postoperative pancreatic fistula is the critical cause of morbidity after pancreaticoduodenectomy. Identifying patients at risk of clinically relevant postoperative pancreatic fistula can potentially improve

clinical outcomes after pancreaticoduodenectomy.

Research motivation

Most of the available models to predict postoperative pancreatic fistula can be used only in the postoperative setting.

Research objectives

To calculate the accuracy of the pancreatic neck pancreatic attenuation index (PAI) and pancreatic enhancement ratio (PER) in predicting clinically relevant postoperative pancreatic fistula and its correlation with histological pancreatic neck fat fraction and fibrosis scoring.

Research methods

Patients who underwent pancreaticoduodenectomy for benign and malignant pathology of the periampullary region or pancreatic head between February 2019 and February 2021 were included in the prospective observational study. The PAI was measured in the neck of the pancreas by marking regions of interest in the preoperative non-contrast computed tomography (CT), and the PER was measured during the contrast phase of the CT abdomen. Preoperative pancreatic neck CT indices were correlated with histopathological evaluation of Fibrosis score and the fat fraction of the pancreatic neck and clinically relevant postoperative pancreatic fistula.

Research results

The PAI had no significant association with the development of clinically relevant postoperative pancreatic fistula (CR-POPF). However, PER was significantly lower in patients developing CR-POPF (0.58 ± 0.20 *vs* 0.81 ± 0.44, $P = 0.006$). Also, PER cut-off of 0.673 predicts CR-POPF with 77.8% sensitivity and 55.8% specificity. The PER showed a moderately positive correlation with fibrosis (Strength 0.50, $P < 0.001$).

Research conclusions

PER showed good accuracy in predicting CR-POPF. Also, PER showed a good correlation with fibrosis scores and may be used as an objective preoperative surrogate for assessing pancreatic texture.

Research perspectives

Quantifying PER on preoperative computed tomography can improve the risk stratification and management of patients at high risk of clinically relevant postoperative pancreatic fistula. Failure to demonstrate an association of PAI with clinically relevant postoperative pancreatic fistula and postoperative fat fraction suggests that area-based assessment for the pancreatic fat fraction may be better than the region of interest-based estimation.

FOOTNOTES

Author contributions: Gnanasekaran S and Kalayarasan R conceptualized the study; Durgesh S and Gurram R performed the research work; Rajeswari M performed the data analysis; Srinivas BH reviewed the histopathological slides for postoperative analysis; Ramesh A performed a preoperative radiological assessment of study participants; Durgesh S and Gurram R wrote the first draft of the manuscript; Gnanasekaran S, Kalayarasan R, Pottakkat B and Sahoo J gave intellectual input and critically revised the manuscript.

Institutional review board statement: The study was reviewed and approved by the institutional ethics committee (Human studies) of Jawaharlal Institute of Postgraduate Medical Education and Research (JIPMER), Puducherry, India (JIP/IEC/2018/500 dated 25-01-2019). The study protocol can be fully accessed at https://jipmer.edu.in/.

Informed consent statement: All study participants, or their legal guardian, provided written consent prior to study enrolment.

Conflict-of-interest statement: All authors of this manuscript have no financial relationships to disclose.

Data sharing statement: No additional data are available.

CONSORT 2010 statement: The authors have read the CONSORT 2010 Statement, and the manuscript was prepared and revised according to the CONSORT 2010 Statement.

Country/Territory of origin: India

ORCID number: Senthil Gnanasekaran 0000-0002-8639-5423; Satish Durgesh 0000-0001-8601-1576; Ramprakash Gurram 0000-0001-7106-2178; Raja Kalayarasan 0000-0003-4056-8672; Biju Pottakkat 0000-0002-8474-0270; M Rajeswari 0000-0003-1620-7359; BH Srinivas 0000-0002-9619-6719; A Ramesh 0000-0002-1404-6400; Jayaprakash Sahoo 0000-0002-8805-143X.

Corresponding Author's Membership in Professional Societies: Indian chapter of International Hepatopancreatobiliary Association, 563; Indian Association of Surgical Gastroenterology, K-65; International Hepatopancreatobiliary association, M02056.

S-Editor: Wang LL
L-Editor: Filipodia
P-Editor: Wang LL

REFERENCES

1 **Greenblatt DY**, Kelly KJ, Rajamanickam V, Wan Y, Hanson T, Rettammel R, Winslow ER, Cho CS, Weber SM. Preoperative factors predict perioperative morbidity and mortality after pancreaticoduodenectomy. *Ann Surg Oncol* 2011; **18**: 2126-2135 [PMID: 21336514 DOI: 10.1245/s10434-011-1594-6]

2 **Tzeng CW**, Katz MH, Fleming JB, Lee JE, Pisters PW, Holmes HM, Varadhachary GR, Wolff RA, Abbruzzese JL, Vauthey JN, Aloia TA. Morbidity and mortality after pancreaticoduodenectomy in patients with borderline resectable type C clinical classification. *J Gastrointest Surg* 2014; **18**: 146-55; discussion 155 [PMID: 24129825 DOI: 10.1007/s11605-013-2371-6]

3 **Berger AC**, Howard TJ, Kennedy EP, Sauter PK, Bower-Cherry M, Dutkevitch S, Hyslop T, Schmidt CM, Rosato EL, Lavu H, Nakeeb A, Pitt HA, Lillemoe KD, Yeo CJ. Does type of pancreaticojejunostomy after pancreaticoduodenectomy decrease rate of pancreatic fistula? *J Am Coll Surg* 2009; **208**: 738-47; discussion 747 [PMID: 19476827 DOI: 10.1016/j.jamcollsurg.2008.12.031]

4 **Callery MP**, Pratt WB, Kent TS, Chaikof EL, Vollmer CM Jr. A prospectively validated clinical risk score accurately predicts pancreatic fistula after pancreatoduodenectomy. *J Am Coll Surg* 2013; **216**: 1-14 [PMID: 23122535 DOI: 10.1016/j.jamcollsurg.2012.09.002]

5 **Kantor O**, Talamonti MS, Pitt HA, Vollmer CM, Riall TS, Hall BL, Wang CH, Baker MS. Using the NSQIP Pancreatic Demonstration Project to Derive a Modified Fistula Risk Score for Preoperative Risk Stratification in Patients Undergoing Pancreaticoduodenectomy. *J Am Coll Surg* 2017; **224**: 816-825 [PMID: 28408176 DOI: 10.1016/j.jamcollsurg.2017.01.054]

6 **Liu Y**, Li Y, Wang L, Peng CJ. Predictive value of drain pancreatic amylase concentration for postoperative pancreatic fistula on postoperative day 1 after pancreatic resection: An updated meta-analysis. *Medicine (Baltimore)* 2018; **97**: e12487 [PMID: 30235751 DOI: 10.1097/MD.0000000000012487]

7 **Tranchart H**, Gaujoux S, Rebours V, Vullierme MP, Dokmak S, Levy P, Couvelard A, Belghiti J, Sauvanet A. Preoperative CT scan helps to predict the occurrence of severe pancreatic fistula after pancreaticoduodenectomy. *Ann Surg* 2012; **256**: 139-145 [PMID: 22609844 DOI: 10.1097/SLA.0b013e318256c32c]

8 **Lim S**, Bae JH, Chun EJ, Kim H, Kim SY, Kim KM, Choi SH, Park KS, Florez JC, Jang HC. Differences in pancreatic volume, fat content, and fat density measured by multidetector-row computed tomography according to the duration of diabetes. *Acta Diabetol* 2014; **51**: 739-748 [PMID: 24671510 DOI: 10.1007/s00592-014-0581-3]

9 **Maehira H**, Iida H, Mori H, Kitamura N, Miyake T, Shimizu T, Tani M. Computed Tomography Enhancement Pattern of the Pancreatic Parenchyma Predicts Postoperative Pancreatic Fistula After Pancreaticoduodenectomy. *Pancreas* 2019; **48**: 209-215 [PMID: 30589830 DOI: 10.1097/MPA.0000000000001229]

10 **Hashimoto Y**, Sclabas GM, Takahashi N, Kirihara Y, Smyrk TC, Huebner M, Farnell MB. Dual-phase computed tomography for assessment of pancreatic fibrosis and anastomotic failure risk following pancreatoduodenectomy. *J Gastrointest Surg* 2011; **15**: 2193-2204 [PMID: 21948179 DOI: 10.1007/s11605-011-1687-3]

11 **Kang JH**, Park JS, Yu JS, Chung JJ, Kim JH, Cho ES, Yoon DS. Prediction of pancreatic fistula after pancreatoduodenectomy by preoperative dynamic CT and fecal elastase-1 Levels. *PLoS One* 2017; **12**: e0177052 [PMID: 28493949 DOI: 10.1371/journal.pone.0177052]

12 **Kim SY**, Kim H, Cho JY, Lim S, Cha K, Lee KH, Kim YH, Kim JH, Yoon YS, Han HS, Kang HS. Quantitative assessment of pancreatic fat by using unenhanced CT: pathologic correlation and clinical implications. *Radiology* 2014; **271**: 104-112 [PMID: 24475851 DOI: 10.1148/radiol.13122883]

13 **Klöppel G**, Maillet B. Pseudocysts in chronic pancreatitis: a morphological analysis of 57 resection specimens and 9 autopsy pancreata. *Pancreas* 1991; **6**: 266-274 [PMID: 1862065]

14 **Bassi C**, Marchegiani G, Dervenis C, Sarr M, Abu Hilal M, Adham M, Allen P, Andersson R, Asbun HJ, Besselink MG, Conlon K, Del Chiaro M, Falconi M, Fernandez-Cruz L, Fernandez-Del Castillo C, Fingerhut A, Friess H, Gouma DJ, Hackert T, Izbicki J, Lillemoe KD, Neoptolemos JP, Olah A, Schulick R, Shrikhande SV, Takada T, Takaori K, Traverso W, Vollmer CR, Wolfgang CL, Yeo CJ, Salvia R, Buchler M; International Study Group on Pancreatic Surgery (ISGPS). The 2016 update of the International Study Group (ISGPS) definition and grading of postoperative pancreatic fistula: 11 Years After. *Surgery* 2017; **161**: 584-591 [PMID: 28040257 DOI: 10.1016/j.surg.2016.11.014]

15 **Wente MN**, Bassi C, Dervenis C, Fingerhut A, Gouma DJ, Izbicki JR, Neoptolemos JP, Padbury RT, Sarr MG, Traverso

LW, Yeo CJ, Büchler MW. Delayed gastric emptying (DGE) after pancreatic surgery: a suggested definition by the International Study Group of Pancreatic Surgery (ISGPS). *Surgery* 2007; **142**: 761-768 [PMID: 17981197 DOI: 10.1016/j.surg.2007.05.005]

16 **Wente MN**, Veit JA, Bassi C, Dervenis C, Fingerhut A, Gouma DJ, Izbicki JR, Neoptolemos JP, Padbury RT, Sarr MG, Yeo CJ, Büchler MW. Postpancreatectomy hemorrhage (PPH): an International Study Group of Pancreatic Surgery (ISGPS) definition. *Surgery* 2007; **142**: 20-25 [PMID: 17629996 DOI: 10.1016/j.surg.2007.02.001]

17 **Lin JW**, Cameron JL, Yeo CJ, Riall TS, Lillemoe KD. Risk factors and outcomes in postpancreaticoduodenectomy pancreaticocutaneous fistula. *J Gastrointest Surg* 2004; **8**: 951-959 [PMID: 15585382 DOI: 10.1016/j.gassur.2004.09.044]

18 **Hu BY**, Wan T, Zhang WZ, Dong JH. Risk factors for postoperative pancreatic fistula: Analysis of 539 successive cases of pancreaticoduodenectomy. *World J Gastroenterol* 2016; **22**: 7797-7805 [PMID: 27678363 DOI: 10.3748/wjg.v22.i34.7797]

19 **Laaninen M**, Bläuer M, Vasama K, Jin H, Räty S, Sand J, Nordback I, Laukkarinen J. The risk for immediate postoperative complications after pancreaticoduodenectomy is increased by high frequency of acinar cells and decreased by prevalent fibrosis of the cut edge of pancreas. *Pancreas* 2012; **41**: 957-961 [PMID: 22699198 DOI: 10.1097/MPA.0b013e3182480b81]

20 **Kim Z**, Kim MJ, Kim JH, Jin SY, Kim YB, Seo D, Choi D, Hur KY, Kim JJ, Lee MH, Moon C. Prediction of post-operative pancreatic fistula in pancreaticoduodenectomy patients using pre-operative MRI: a pilot study. *HPB (Oxford)* 2009; **11**: 215-221 [PMID: 19590650 DOI: 10.1111/j.1477-2574.2009.00011.x]

21 **Adalı G**, Bozkurt B, Ceyhan Ö, Server S, Doğusoy GB, Yüzer Y, Tokat Y. Body Mass Index and Unenhanced CT as a Predictor of Hepatic Steatosis in Potential Liver Donors. *Transplant Proc* 2019; **51**: 2373-2378 [PMID: 31402250 DOI: 10.1016/j.transproceed.2019.02.047]

22 **Yardimci S**, Kara YB, Tuney D, Attaallah W, Ugurlu MU, Dulundu E, Yegen ŞC. A Simple Method to Evaluate Whether Pancreas Texture Can Be Used to Predict Pancreatic Fistula Risk After Pancreatoduodenectomy. *J Gastrointest Surg* 2015; **19**: 1625-1631 [PMID: 25982120 DOI: 10.1007/s11605-015-2855-7]

23 **Hori M**, Onaya H, Hiraoka N, Yamaji T, Kobayashi H, Takahashi M, Mutoh M, Shimada K, Nakagama H. Evaluation of the degree of pancreatic fatty infiltration by area-based assessment of CT images: comparison with histopathology-based and CT attenuation index-based assessments. *Jpn J Radiol* 2016; **34**: 667-676 [PMID: 27581428 DOI: 10.1007/s11604-016-0572-0]

World Journal of Radiology

Submit a Manuscript: https://www.f6publishing.com

World J Radiol 2022 June 28; 14(6): 177-179

DOI: 10.4329/wjr.v14.i6.177

ISSN 1949-8470 (online)

LETTER TO THE EDITOR

Comments on "Neonatal infratentorial subdural hematoma contributing to obstructive hydrocephalus in the setting of therapeutic cooling: A case report"

Ioannis Siasios, Aggeliki Fotiadou, Yulia Rud

Specialty type: Neurosciences

Provenance and peer review: Invited article; Externally peer reviewed.

Peer-review model: Single blind

Peer-review report's scientific quality classification
Grade A (Excellent): A
Grade B (Very good): 0
Grade C (Good): 0
Grade D (Fair): D
Grade E (Poor): 0

P-Reviewer: Wang Y, China; Yao W, China

Received: February 5, 2022
Peer-review started: February 5, 2022
First decision: April 8, 2022
Revised: April 17, 2022
Accepted: May 28, 2022
Article in press: May 28, 2022
Published online: June 28, 2022

Ioannis Siasios, Neurosurgery Department, Papageorgiou Hospital, Thessaloniki 56403, Greece

Aggeliki Fotiadou, Department of Neurology, General University Hospital of Alexandroupolis, Alexandroupoli 68100, Greece

Yulia Rud, Department of Anesthesiology, European Interbalkan Medical Center, Thessaloniki 57001, Greece

Corresponding author: Ioannis Siasios, MD, MSc, Neurosurgeon, Research Scientist, Department of Neurosurgery, Papageorgiou Hospital, Ring road of Thessaloniki, N. Efkarpia, Thessaloniki 56403, Greece. siasiosj@yahoo.gr

Abstract

Although therapeutic hypothermia (TH) contributes significantly in the treatment of hypoxic ischemic encephalopathy (HIE), it could result in devastating complications such as intracranial hemorrhages. Laboratory examinations for possible coagulation disorders and early brain imaging can detect all these cases that are amenable to aggravation of HIE after the initiation of TH.

Key Words: Therapeutic hypothermia; Hypoxic ischemic encephalopathy; Hemostatic disorders; Intracranial hemorrhage; Magnetic resonance imaging

Core Tip: It has not been yet elucidated if the initiation of therapeutic hypothermia (TH) contributes significantly to better outcomes in cases with already confirmed intracranial hemorrhage and hemostatic disorders. In such cases a close follow up with brain magnetic resonance imaging before and after the initiation of TH and repeated laboratory and clinical examinations may promptly identify neonates requiring emergent neurosurgical intervention.

Citation: Siasios I, Fotiadou A, Rud Y. Comments on "Neonatal infratentorial subdural hematoma contributing to obstructive hydrocephalus in the setting of therapeutic cooling: A case report". *World J Radiol* 2022; 14(6): 177-179
URL: https://www.wjgnet.com/1949-8470/full/v14/i6/177.htm
DOI: https://dx.doi.org/10.4329/wjr.v14.i6.177

TO THE EDITOR

Hypoxic ischemic encephalopathy (HIE) is thought to be a significant cause of morbidity and mortality at term and pre-term infants[1,2]. As stated in the literature, HIE is an evolving pathological process which within hours after its initiation promotes neuronal cell death through several biochemical events due to primary and secondary neuronal cell's energy crisis such as hypoperfusion, extracellular concentration of amino-acids, nitric oxide and free radicals and finally membrane depolarization[3]. Based on newborn's neurological status expressed by Sarnat scale, HIE is divided to mild, moderate and severe [4]. Diagnosis and follow up is based on patient's neurological status, laboratory monitoring as well as brain imaging studies such as cranial ultrasound and magnetic resonance imaging (MRI) of the head which is the gold standard imaging modality for intracranial lesions[5].

Therapeutic hypothermia (TH) is considered the first line treatment of HIE[6]. Several studies in the past revealed that TH can reduce neonatal mortality up to 20% in developed countries[7]. TH is widely used during the last decade for moderate to severe cases of HIE and it can be induced either as whole-body cooling or selective head cooling with a great variation in treatment protocols[8,9]. According to a published case series, hypothermia is limited to 33-34 degrees of Celsius for around 72 h under close medical surveillance and is slowly reinstated at normal body temperatures by patient rewarming with an increase rate of 0.5 Celsius degree per hour[3,5]. TH is applied only 6 h after birth in newborns with low Apgar score and a gestational age above 36 wk with evidence of moderate to severe HIE[5]. The literature describes several side effects of TH with an incidence around 20% of treated cases such as skin burns, electrolyte disturbances, low blood pressure, thrombocytopenia, prolonged prothrombin time (PT), and activated thromboplastin time[3].

We have read with great interest the case reported by Rousslang *et al*[10]. The authors eloquently highlighted the potential association between TH and increased risk of intracranial hemorrhage in neonates with HIE. They described the case of a term neonate that after an emergent C-section delivery required intubation due to cardiopulmonary instability[10]. According to the authors, the neonate fulfilled the criteria for TH which was applied from the day one. It is very interesting that the patient had from his first day of life pathological values of several parameters of coagulation mechanism such prolonged international normalized ration (INR), time of thromboplastin, activated partial thromboplastin time and low number of platelets. Authors tried to restore these pathological findings of coagulation parameters during the next four days. This is a gray zone in the literate regarding contraindications for TH. The question that has to be answered is whether a neonate with pathological laboratory findings of his coagulation mechanism is eligible for TH initiation without prior restoration of these abnormal values. We have to recognize that the time frame for such decisions is short in order to prevent a possible permanent neurological damage. It is strongly supported by the literature that TH can induce abnormalities of coagulation mechanism and indirectly favor occurrence of intracranial hemorrhages similar to the one that Rousslang *et al*[10] describe in their case report[3,11]. Obviously, this effect can be reinforced in patients with already pathological ratings of coagulation parameters.

In addition, the first screening of the neonate with head ultrasound revealed a left grade I germinal matrix hemorrhage. Although the patient already had a small intracranial hemorrhage authors applied TH. It is well known that around 38% of cases treated with TH can have an intracranial hemorrhage [12]. This is a finding that could be studied more thoroughly with an MRI scan before the application of TH as the MRI is more sensitive for the detection of any other hemorrhagic lesion, rendering it a potential first reference screening study for the neonate. Additionally, a brain MRI could be more valuable in assessing the severity of HIE and thus is a prognostic tool of great significance[12-14]. The coexistence of HIE and intracranial hemorrhages is another gray zone that requires more extensive investigation regarding the final outcome for the neonates receiving TH[13,14]. The current published case series refers to MRI scans performed usually several hours after the initiation of TH. Another issue that should be clarified in the future is whether any type of intracranial hemorrhage constitutes a contraindication for the initiation of any TH protocol.

Finally, it is well presented by the authors that any type of imaging screening combined with laboratory and clinical follow up of the neonates during TH can successfully detect any emergent intracranial hemorrhage. In these cases, prompt neurosurgical consultation can remarkably affect neurological outcome and prognosis for the neonates[15].

FOOTNOTES

Author contributions: Siasios I and Fotiadou A, Rud Y designed research; Siasios I, Fotiadou A, Rud Y performed research; Siasios I, Fotiadou A and Rud Y analyzed data; Siasios I and Fotiadou A wrote the letter; and Siasios I, Fotiadou A and Rud Y revised the letter.

Conflict-of-interest statement: All the authors declare that they have no conflict of interest.

Country/Territory of origin: Greece

ORCID number: Ioannis Siasios 0000-0001-7945-9604; Aggeliki Fotiadou 0000-0002-8614-2688; Yulia Rud 0000-0002-6063-4043.

S-Editor: Liu JH
L-Editor: A
P-Editor: Liu JH

REFERENCES

1 **Vannucci RC**. Hypoxic-ischemic encephalopathy. *Am J Perinatol* 2000; **17**: 113-120 [PMID: 11012134 DOI: 10.1055/s-2000-9293]
2 **Lee AC**, Kozuki N, Blencowe H, Vos T, Bahalim A, Darmstadt GL, Niermeyer S, Ellis M, Robertson NJ, Cousens S, Lawn JE. Intrapartum-related neonatal encephalopathy incidence and impairment at regional and global levels for 2010 with trends from 1990. *Pediatr Res* 2013; **74** Suppl 1: 50-72 [PMID: 24366463 DOI: 10.1038/pr.2013.206]
3 **Datta V**. Therapeutic Hypothermia for Birth Asphyxia in Neonates. *Indian J Pediatr* 2017; **84**: 219-226 [PMID: 27966094 DOI: 10.1007/s12098-016-2266-0]
4 **Sarnat HB**, Sarnat MS. Neonatal encephalopathy following fetal distress. A clinical and electroencephalographic study. *Arch Neurol* 1976; **33**: 696-705 [PMID: 987769 DOI: 10.1001/archneur.1976.00500100030012]
5 **Chiang MC**, Jong YJ, Lin CH. Therapeutic hypothermia for neonates with hypoxic ischemic encephalopathy. *Pediatr Neonatol* 2017; **58**: 475-483 [PMID: 28416250 DOI: 10.1016/j.pedneo.2016.11.001]
6 **Wassink G**, Davidson JO, Dhillon SK, Zhou K, Bennet L, Thoresen M, Gunn AJ. Therapeutic Hypothermia in Neonatal Hypoxic-Ischemic Encephalopathy. *Curr Neurol Neurosci Rep* 2019; **19**: 2 [PMID: 30637551 DOI: 10.1007/s11910-019-0916-0]
7 **Edwards AD**, Brocklehurst P, Gunn AJ, Halliday H, Juszczak E, Levene M, Strohm B, Thoresen M, Whitelaw A, Azzopardi D. Neurological outcomes at 18 mo of age after moderate hypothermia for perinatal hypoxic ischaemic encephalopathy: synthesis and meta-analysis of trial data. *BMJ* 2010; **340**: c363 [PMID: 20144981 DOI: 10.1136/bmj.c363]
8 **Giannakis S**, Ruhfus M, Rüdiger M, Sabir H; German Neonatal Hypothermia Network. Hospital survey showed wide variations in therapeutic hypothermia for neonates in Germany. *Acta Paediatr* 2020; **109**: 200-201 [PMID: 31432551 DOI: 10.1111/apa.14979]
9 **Gunn AJ**, Laptook AR, Robertson NJ, Barks JD, Thoresen M, Wassink G, Bennet L. Therapeutic hypothermia translates from ancient history in to practice. *Pediatr Res* 2017; **81**: 202-209 [PMID: 27673420 DOI: 10.1038/pr.2016.198]
10 **Rousslang LK**, Rooks EA, Meldrum JT, Hooten KG, Wood JR. Neonatal infratentorial subdural hematoma contributing to obstructive hydrocephalus in the setting of therapeutic cooling: A case report. *World J Radiol* 2021; **13**: 307-313 [PMID: 34630916 DOI: 10.4329/wjr.v13.i9.307]
11 **Rao R**, Trivedi S, Vesoulis Z, Liao SM, Smyser CD, Mathur AM. Safety and Short-Term Outcomes of Therapeutic Hypothermia in Preterm Neonates 34-35 Weeks Gestational Age with Hypoxic-Ischemic Encephalopathy. *J Pediatr* 2017; **183**: 37-42 [PMID: 27979578 DOI: 10.1016/j.jpeds.2016.11.019]
12 **Walas W**, Wilińska M, Bekiesińska-Figatowska M, Halaba Z, Śmigiel R. Methods for assessing the severity of perinatal asphyxia and early prognostic tools in neonates with hypoxic-ischemic encephalopathy treated with therapeutic hypothermia. *Adv Clin Exp Med* 2020; **29**: 1011-1016 [PMID: 32820870 DOI: 10.17219/acem/124437]
13 **Lakatos A**, Kolossváry M, Szabó M, Jermendy Á, Barta H, Gyebnár G, Rudas G, Kozák LR. Neurodevelopmental effect of intracranial hemorrhage observed in hypoxic ischemic brain injury in hypothermia-treated asphyxiated neonates - an MRI study. *BMC Pediatr* 2019; **19**: 430 [PMID: 31718607 DOI: 10.1186/s12887-019-1777-z]
14 **Weeke LC**, Groenendaal F, Mudigonda K, Blennow M, Lequin MH, Meiners LC, van Haastert IC, Benders MJ, Hallberg B, de Vries LS. A Novel Magnetic Resonance Imaging Score Predicts Neurodevelopmental Outcome After Perinatal Asphyxia and Therapeutic Hypothermia. *J Pediatr* 2018; **192**: 33-40.e2 [PMID: 29246356 DOI: 10.1016/j.jpeds.2017.09.043]
15 **van Steenis A**, Fumagalli M, Kruit MC, Peeters-Scholte CMPCD, de Vries LS, Steggerda SJ. Cranial Ultrasound Is an Important Tool in the Recognition of Life-Threatening Infratentorial Hemorrhage in Newborns. *Neuropediatrics* 2021; **52**: 170-178 [PMID: 33316833 DOI: 10.1055/s-0040-1716899]

Published by **Baishideng Publishing Group Inc**
7041 Koll Center Parkway, Suite 160, Pleasanton, CA 94566, USA
Telephone: +1-925-3991568
E-mail: bpgoffice@wjgnet.com
Help Desk: https://www.f6publishing.com/helpdesk
https://www.wjgnet.com

ISSN 1949-8470 (online)

World Journal of *Radiology*

World J Radiol 2022 July 28; 14(7): 180-248

Published by Baishideng Publishing Group Inc

WJR World Journal of Radiology

Contents

Monthly Volume 14 Number 7 July 28, 2022

EVIDENCE REVIEW

MINIREVIEWS

ORIGINAL ARTICLE

Retrospective Study

SYSTEMATIC REVIEWS

World Journal of Radiology

Monthly Volume 14 Number 7 July 28, 2022

Contents

ABOUT COVER

Editorial Board Member of *World Journal of Radiology*, Ying-Wei Fan, PhD, Associate Research Professor, Department of Biomedical Engineering, School of Medical Technology, Beijing Institute of Technology, Beijing 100081, China. fanyingwei@bit.edu.cn

AIMS AND SCOPE

The primary aim of *World Journal of Radiology* (*WJR*, *World J Radiol*) is to provide scholars and readers from various fields of radiology with a platform to publish high-quality basic and clinical research articles and communicate their research findings online.

WJR mainly publishes articles reporting research results and findings obtained in the field of radiology and covering a wide range of topics including state of the art information on cardiopulmonary imaging, gastrointestinal imaging, genitourinary imaging, musculoskeletal imaging, neuroradiology/head and neck imaging, nuclear medicine and molecular imaging, pediatric imaging, vascular and interventional radiology, and women's imaging.

INDEXING/ABSTRACTING

The *WJR* is now abstracted and indexed in PubMed, PubMed Central, Emerging Sources Citation Index (Web of Science), Reference Citation Analysis, China National Knowledge Infrastructure, China Science and Technology Journal Database, and Superstar Journals Database. The 2022 edition of Journal Citation Reports ® cites the 2021 Journal Citation Indicator (JCI) for *WJR* as 0.48.

RESPONSIBLE EDITORS FOR THIS ISSUE

NAME OF JOURNAL
World Journal of Radiology

ISSN
ISSN 1949-8470 (online)

LAUNCH DATE
January 31, 2009

FREQUENCY
Monthly

EDITORS-IN-CHIEF
Thomas J Vogl

EDITORIAL BOARD MEMBERS
https://www.wjgnet.com/1949-8470/editorialboard.htm

PUBLICATION DATE
July 28, 2022

INSTRUCTIONS TO AUTHORS
https://www.wjgnet.com/bpg/gerinfo/204

GUIDELINES FOR ETHICS DOCUMENTS
https://www.wjgnet.com/bpg/GerInfo/287

GUIDELINES FOR NON-NATIVE SPEAKERS OF ENGLISH
https://www.wjgnet.com/bpg/gerinfo/240

PUBLICATION ETHICS
https://www.wjgnet.com/bpg/GerInfo/288

PUBLICATION MISCONDUCT
https://www.wjgnet.com/bpg/gerinfo/208

ARTICLE PROCESSING CHARGE
https://www.wjgnet.com/bpg/gerinfo/242

STEPS FOR SUBMITTING MANUSCRIPTS
https://www.wjgnet.com/bpg/GerInfo/239

ONLINE SUBMISSION
https://www.f6publishing.com

World Journal of Radiology

Submit a Manuscript: https://www.f6publishing.com

World J Radiol 2022 July 28; 14(7): 180-193

DOI: 10.4329/wjr.v14.i7.180

ISSN 1949-8470 (online)

EVIDENCE REVIEW

Expanding utility of cardiac computed tomography in infective endocarditis: A contemporary review

Diarmaid Hughes, Richard Linchangco, Reza Reyaldeen, Bo Xu

Specialty type: Radiology, nuclear medicine and medical imaging

Provenance and peer review: Invited article; Externally peer reviewed.

Peer-review model: Single blind

Peer-review report's scientific quality classification

Grade A (Excellent): 0
Grade B (Very good): B
Grade C (Good): C
Grade D (Fair): D
Grade E (Poor): 0

P-Reviewer: Fan YW, China; Teragawa H, Japan

Received: January 5, 2022
Peer-review started: January 5, 2022
First decision: June 16, 2022
Revised: June 26, 2022
Accepted: July 6, 2022
Article in press: July 6, 2022
Published online: July 28, 2022

Diarmaid Hughes, Reza Reyaldeen, Bo Xu, Section of Cardiovascular Imaging, Robert and Suzanne Tomsich Department of Cardiovascular Medicine, Sydell and Arnold Miller Family Heart and Vascular Institute, Cleveland Clinic, Cleveland, OH 44195, United States

Richard Linchangco, Section of Cardiovascular Imaging, Imaging Institute, Cleveland Clinic, Cleveland, OH 44195, United States

Corresponding author: Bo Xu, MD, FACC, FASE, Multimodality Imaging Staff Cardiologist, Section of Cardiovascular Imaging, Robert and Suzanne Tomsich Department of Cardiovascular Medicine, Sydell and Arnold Miller Family Heart and Vascular Institute, Cleveland Clinic, 9500 Euclid Avenue, Cleveland, OH 44195, United States. xub@ccf.org

Abstract

There is increasing evidence on the utility of cardiac computed tomography (CCT) in infective endocarditis (IE) to investigate the valvular pathology, the extra-cardiac manifestations of IE and pre-operative planning. CCT can assist in the diagnosis of perivalvular complications, such as pseudoaneurysms and abscesses, and can help identify embolic events to the lungs or systemic vasculature. CCT has also been shown to be beneficial in the pre-operative planning of patients by delineating the coronary artery anatomy and the major cardiovascular structures in relation to the sternum. Finally, hybrid nuclear/computed tomography techniques have been shown to increase the diagnostic accuracy in prosthetic valve endocarditis. This manuscript aims to provide a contemporary update of the existing evidence base for the use of CCT in IE.

Key Words: Infective endocarditis; Cardiac computed tomography; Multimodality cardiac imaging; Cardiovascular structures; Hybrid nuclear

Core Tip: Cardiac computed tomography (CCT) has an expanding role in the management of infective endocarditis (IE). It has been shown to be superior to echocardiography for diagnosing perivalvular complications such as pseudoaneurysms and abscesses. CCT can also diagnose extra-cardiac manifestations of IE such as septic emboli to the lungs. It can assist in pre-operative planning by delineating the coronary anatomy and assessing vascular structures. Herein, we review the role of CCT in IE including the evidence base comparing CCT to echocardiography in diagnosing the valvular complications of IE and the use of CT in IE beyond valvular assessment.

Citation: Hughes D, Linchangco R, Reyaldeen R, Xu B. Expanding utility of cardiac computed tomography in infective endocarditis: A contemporary review. *World J Radiol* 2022; 14(7): 180-193
URL: https://www.wjgnet.com/1949-8470/full/v14/i7/180.htm
DOI: https://dx.doi.org/10.4329/wjr.v14.i7.180

INTRODUCTION

Infective endocarditis (IE) is an infection of the endocardium, heart valves or intra-cardiac devices. It remains a challenging disease to diagnose and manage with high rates of morbidity and mortality[1,2]. Echocardiography remains the main imaging modality used in IE; more recently, however, there is an increasing evidence base for a multimodality imaging approach for IE. Complementary imaging modalities including cardiac computed tomography (CCT) now play increasingly important roles in diagnosis, risk stratification and management of IE. CCT has certain advantages compared to echocardiography in being able to investigate for perivalvular extension, extra-cardiac complications of IE, including metastatic spread and planning for surgery including assessing for coronary artery disease. Advancements in CT technologies, including the use of dedicated cardiac gated four-dimensional CCT, have expanded the applications of CT in IE, demonstrating good sensitivity and specificity for diagnosing the complications of IE. This article aims to review the available evidence for the use of CCT in IE.

CLINICAL CONSIDERATIONS

The incidence of IE in the United States is estimated to be approximately 15 per 100000 persons annually [3,4], with Staphylococcus aureus (SA) being the most common pathogen followed by Viridans group Streptococci[5]. A number of risk factors have been identified for acquiring IE, including the presence of a prosthetic valve, a previous episode of IE, patients with untreated cyanotic congenital heart disease, injection drug use, poor dentition and pre-existing valvular heart disease[6]. The clinical presentation of IE can vary significantly from an acute life threatening illness to a more indolent chronic disease[7]. The most common presenting symptoms are: fever, cardiac murmur, heart failure or complications from septic emboli[8].

The Duke criteria were developed in 1994 to assist in the risk stratification of patients with suspected IE into definite, possible and rejected cases of IE[9]. These criteria have been since validated by a number of retrospective analyses, and underwent further modification in 2000 to reflect changing clinical practice and the emergence of SA as the most common pathogen encountered[10-12]. Despite the updated clinical criteria for diagnosis of IE, there often remains a delay in diagnosis for many patients, commonly due to a lack of microbiological criteria from impropriate antibiotic use, with worse outcomes seen in these patients[13,14]. Advances in CT technologies including improvements in both temporal and spatial resolution have enabled greater use of CCT for the diagnosis of IE. The European Society of Cardiology guidelines for the management of infective endocarditis reflect these advances in imaging techniques and include paravalvular lesions detected by CCT to be a major imaging criterion [15]. The 2020 American College of Cardiology/American Heart Association Guideline for the management of patients with valvular heart disease also recommend the use of CCT as an adjunctive imaging modality for IE[16].

Echocardiography

Echocardiography, including transthoracic echocardiography (TTE) and transesophageal echocardiography (TEE) where appropriate, remain the first line imaging modality for the diagnosis and monitoring of IE[17,18]. There are three main echocardiographic findings that are considered major criteria for the diagnosis of IE: vegetations, abscesses/pseudoaneurysms and new dehiscence of a prosthetic valve[15]. In native valve endocarditis, the sensitivities for the diagnosis of a vegetation are approximately 70% for TTE and 96% for TEE, respectively[17]. For prosthetic valve endocarditis (PVE),

the sensitivities for diagnosing a vegetation are approximately 50% for TTE and 92% for TEE, respectively[17]. There are many challenges in the diagnosis of IE with echocardiography, including small vegetations or embolization of the vegetation prior to imaging, difficulty visualizing the lesion in the setting of pre-existing valvular disease or with prosthetic valves. Small abscesses may also be challenging to diagnose, especially by TTE[19]. There are also many mimics of IE that could result in a false positive diagnosis, such as Lambl's excrescence, fibroelastomas, thrombus, degenerative lesions, prosthetic material/sutures or marantic lesions[20]. CCT can therefore be helpful to assist in the diagnosis of IE, when there are equivocal findings by echocardiography or in challenging cases involving prosthetic valves[21].

Dedicated cardiac CT protocol for endocarditis evaluation

For evaluation of cardiac valves, multiphase imaging using a retrospectively ECG-gated acquisition is required to obtain an isotropic data set. Images are acquired in spiral mode utilizing a low pitch of 0.16 to 0.5 during 5-10 R-R intervals with a section thickness of 0.60 mm. Thin collimation is used for optimal visualization of the valve leaflets, typically 64 mm × 0.6 mm. The tube voltage used is adapted to the patient's weight, and can vary between 100 to 120 kV. Gantry rotation time of 0.28 s to 0.35 s is used[22-27]. The scan is typically performed in a limited field of view from the level of the carina to the cardiac apex.

Timing of the iodinated contrast bolus is important to optimize visualization of the involved cardiac valves. A monophasic contrast injection is most commonly used, with timing of the contrast bolus chosen for optimal visualization of the expected involved valve and cardiac chambers. Alternatively, biphasic contrast injection may be performed, which allows evaluation of all cardiac chambers and valves[28]. Premedication with beta blockers may be used to regulate heart rate to less than 65-70 bpm if not contraindicated. This improves image quality by reducing artefacts related to cardiac motion and valvular motion.

The isotropic data set acquired from the retrospectively gated acquisition allows for reconstruction in any desired plane. In addition to static images, imaging at multiple points during the cardiac cycle also allows for creation of 4D cine images, allowing for evaluation of valve leaflet motion and planimetry.

Because images are acquired throughout the entire cardiac cycle, this results in a significantly higher radiation dose penalty compared to prospectively gated CT as used typically in CT angiography of the coronary arteries. Radiation dose may be lowered utilizing methods such as iterative reconstruction and ECG-triggered radiation dose modulation. However, ECG-triggered dose modulation may result in suboptimal evaluation during the phase of reduced tube current, typically the systolic phase[29]. There are specific protocols used for visualizing the various cardiac and extra manifestations of IE and for pre-operative planning. Herein, we group all of these into an umbrella term of CCT, referring to ECG-gated CT of the chest with contrast. There are some situations, such as during investigation for septic emboli to the visceral organs, when abdominal imaging may also be needed.

UTILITY OF CARDIAC CT IN INFECTIVE ENDOCARDITIS

CCT has the ability to assess for valvular lesions, perivalvular extension, metastatic spread/embolization, as well as aortic anatomy. CCT may also be used in appropriate cases for the assessment of coronary artery disease[30]. This is particularly relevant in patients with aortic valve IE and vegetations, whereby invasive coronary angiography may be relatively contraindicated, due to the potential risk of causing the vegetations to embolize during the procedure. CCT can detect valvular lesions, such as vegetations, prosthetic valve dehiscence in addition to perivalvular lesions such as abscesses, fistulae and pseudoaneurysms[26,31]. Table 1 compares the various definitions for IE detected on CCT *vs* TEE.

PERIVALVULAR COMPLICATIONS

Pseudoaneurysms and abscesses

Perivalvular extension of IE, which includes pseudoaneurysms, abscesses and fistulae are associated with a higher rate of operative management and mortality[32-34]. A pseudoaneurysm is a perivalvular cavity that is in communication with the cardiovascular lumen which results from an abscess rupturing into a cavity[17]. On echocardiography, this appears as a pulsatile echo-free space with detectable Doppler color flow, while on CCT, it appears as an abnormal cavity close to the valve with direct communication with the heart chambers or major blood vessel[30]. An abscess is a closed cavity with necrosis and purulent material not in communication with a cardiovascular cavity[17] . On echocardiography, this appears as a thickened perivalvular area with a homogenous echo-dense or echo-lucent appearance. On CCT, abscesses appear as perivalvular collections of fluid encased in a thick layer of inflammatory tissue enhanced by the injection of contrast medium. See Figures 1-4 for examples of

Table 1 Comparison of cardiac computed tomography *vs* transesophageal echocardiography findings in infective endocarditis[15,30]

	CCT	TEE
Vegetation	An irregular mass or thickening associated with the endocardium, native valve or prosthetic valve with low to intermediate attenuation	Mobile or non-mobile intracardiac mass on valve or other endocardial structures, including on implanted intracardiac material
Pseudoaneurysm	Perivalvular collection of contrast enhanced material usually adjacent to a valve with a visible direct communication	Abnormal perivalvular echo-free space with color-Doppler flow showing connection with the cardiovascular lumen
Abscess	Usually perivalvular collection of low attenuation material. Often has a thick layer of tissue in the wall of the collection that enhances with contrast	Usually perivalvular collection that can have an echodense or echolucent appearance without a communication to a lumen
Dehiscence of a prosthetic valve	Prosthetic valve misalignment with a tissue defect between the annulus and prosthesis	Evidence of excessive motion of a prosthetic valve. Occasionally, it is possible to see a defect between annulus and prosthesis and/or evidence of paravalvular leak on Doppler assessment
Perforation	Leaflet tissue defect that can be observed in two different views	Defect in a valve leaflet that may be seen visually as an interruption of tissue or by color flow across the defect
Fistula	An abnormal communication between two cardiac chambers that is contrast filled	An abnormal connection two neighboring lumen detected by color Doppler flow

CCT: Cardiac computed tomography; TEE: Transesophageal echocardiography.

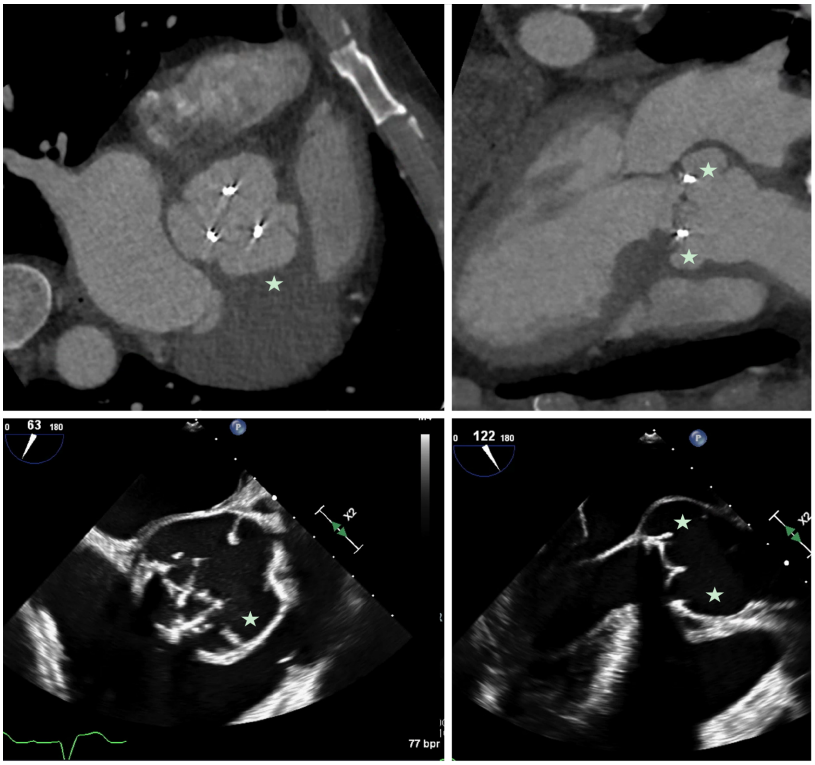

DOI: 10.4329/wjr.v14.i7.180

Figure 1 Prosthetic aortic valve infective endocarditis with valve dehiscence and pseudoaneurysm. Patient with extensive peri-aortic root abscess cavity/pseudo-aneurysm (stars) related to prosthetic valve endocarditis. Note the extensive peri-valvular space around the prosthetic aortic valve and evidence of valve dehiscence on transesophageal echocardiography. Comparable short-axis and long-axis images from cardiac computed tomography and short-axis and long-axis images from transesophageal echocardiography.

comparisons of TEE and CCT images in patients with perivalvular complications of IE (Table 2).

A 2009 study by Feuchter *et al*[24] to investigate the value of CCT for the assessment of valvular abnormalities included 37 consecutive patients (29 of whom went on to have surgery) with clinically suspected IE who underwent both CCT and TEE. CCT identified all pseudoaneurysms and abscesses in this study with sensitivity and specificity of 100%, which was superior to TEE (sensitivity of 89% and a specificity of 100%)[24]. CCT was also shown to be superior to TEE for perivalvular extension of the IE, identifying myocardial and pericardial extension more often than TEE[24]. In a 2009 prospective study,

Table 2 Strengths and limitations of various imaging modalities for assessing infective endocarditis

Modality	CCT	TTE	TEE	PET/CT
Strengths	Ability to image the entire thorax; Improved detection of perivalvular complications; CAD Assessment; Pre-Operative planning; Detection of extra-cardiac emboli	Good Spatial resolution; Availability and portable; Low cost; Lack of radiation; Lack of contrast; Chamber quantification; Assess hemodynamics	Improved spatial and temporal resolution over TTE; Availability and low cost; Lack of radiation; Lack of contrast; Better sensitivity than TTE in PVE; Assess Hemodynamics	Improved detection of perivalvular complications; Improved diagnostic accuarcy in PVE detection of embolic events
Weaknesses	Higher cost; Radiation exposure; Nephrotoxicity; Lower sensitivity for small vegetations and leaflet perforation; Availability may be limited	Limited value in PVE; No tissue characterization; Low sensitivity for peri-valvular complications	No tissue characterization; May miss some peri-valvular complications; Invasive procedure requiring sedation (cannot be performed in some patients with esophageal issues)	Limited availability; Higher cost; Radiation exposure

CCT: Cardiac computed tomography; TEE: Transesophageal echocardiography; TTE: Transthoracic echocardiography; PET: Positron emission tomography; PVE: Prosthetic valve endocarditis; CAD: Coronary artery disease.

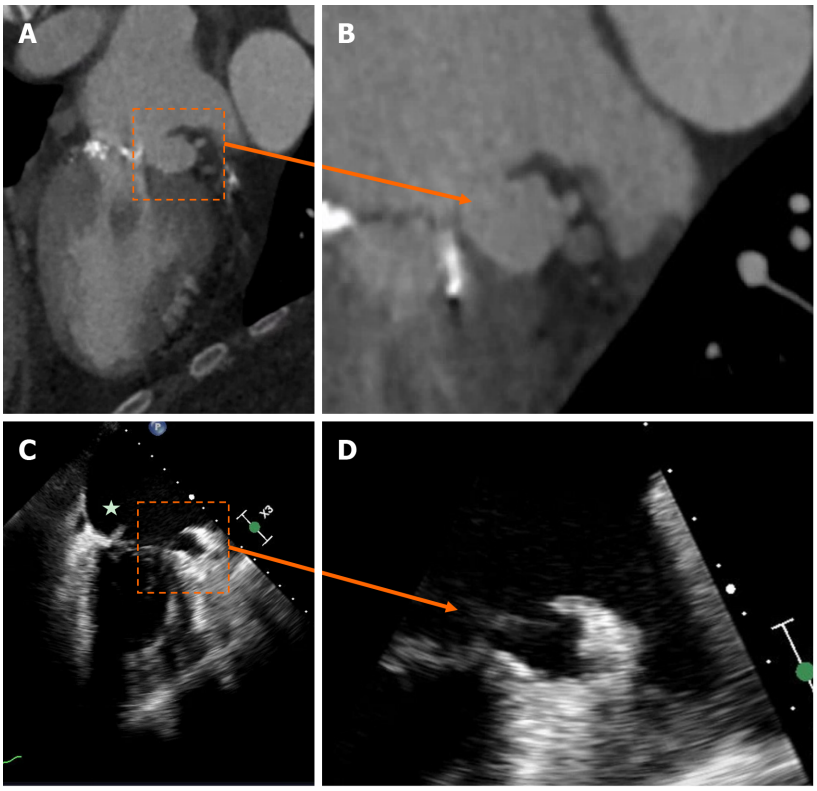

DOI: 10.4329/wjr.v14.i7.180

Figure 2 Native mitral valve infective endocarditis with pseudoaneurysm. A and B: Mitral annular pseudo-aneurysm (dotted box) detected on cardiac computed tomography; C: Cardiac computed tomography with evidence of native mitral valve endocarditis on transesophageal echocardiography (star); D: Cardiac computed tomography with a prominent peri-annular cavity, consistent with a mitral annular pseudo-aneurysm.

19 patients with aortic valve endocarditis requiring surgical intervention underwent CCT pre-operatively[25]. The majority of patients (approx. 90%) had native valve IE. This study showed that CCT had sensitivity and specificity for diagnosing pseudoaneurysms of 100% and 92%, respectively, and CCT correctly identified all cases where there was extension of IE into the intervalvular fibrosa[25]. This paper did not report the TEE findings for their participants [25].

A paper by Fagman *et al*[23] reported in 2012 on 27 consecutive patients who had TEE findings of aortic valve PVE and investigated the strength of agreement between the TEE and CT results. They found a strength of agreement compared to TEE was 0.68 for abscesses and 0.75 for dehiscence[23]. However, using surgery as the reference standard (16 patients went on to have surgery), CCT had sensitivity of 91% to detect pseudoaneurysms /abscesses compared to 82% for TEE[23]. A 2013 study investigated the additional value of CCT beyond the usual evaluation with TEE in PVE in 28 patients, with a final diagnosis being either determined clinically or at the time of surgery as reported by Habets *et al*[35]. They reported that usual evaluation had sensitivity of 68% for detecting periannular complic-

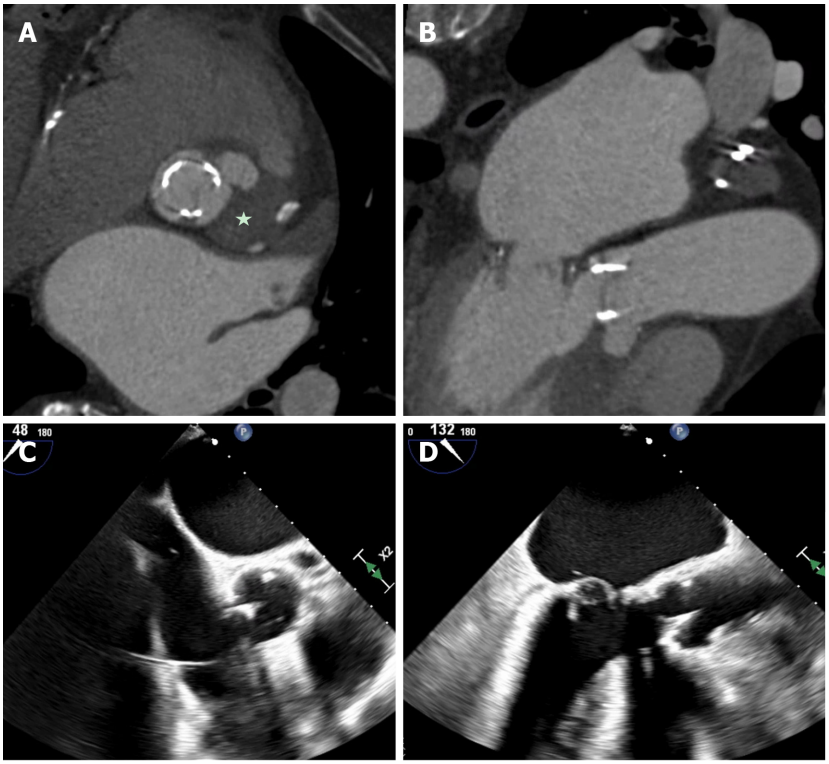

DOI: 10.4329/wjr.v14.i7.180

Figure 3 Mechanical aortic valve infective endocarditis with aortic root abscess. A and B: Patient with extensive peri-aortic root abscess, with a contrast outpouching and surrounding soft-tissue density (star) nearly encasing the left main artery; C and D: Transesophageal echocardiography demonstrated similar findings, although not as well defined due to shadowing from the aortic valve prosthesis.

ations (mycotic aneurysms and abscesses), which was increased to 100% with the use of CCT[35]. Koo *et al*[27] also compared CCT *vs* TEE using intra-operative findings as the reference standard in 2018. They enrolled 49 patients, 12 of whom had PVE[27]. The overall detection of IE by CCT was 94%, compared to 96% by TEE[27]. CCT performed better than TEE at detecting abscess/pseudoaneurysms, with sensitivities of 60% for CCT and 40% for TEE, respectively[27]. A retrospective study from 2018 by Sims *et al*[36] investigated the performance of CCT in the pre-operative evaluation of IE. In total, they had 251 patients undergoing TEE with 34 of these patients also having a CCT[36]. The sensitivity of CCT for detecting abscesses/pseudoaneurysms was 91%, which was superior to TEE at 78%[36]. CCT was reported to have a lower sensitivity for detecting fistulae at 50% *vs* 79% for TEE, and dehiscence at 57% *vs* 70% for TEE[36].

Two studies from 2018 (Ouchi *et al*[31] and Koneru *et al*[37]) retrospectively investigated the utility of CCT in IE with intra-operative findings as the reference standard. CCT performed better than TEE in detecting abscess/pseudoaneurysm in prosthetic valves with sensitivity of 81% (versus 64% for TEE) in the study by Koneru *et al*[31]. CCT had sensitivity of 100% sensitivity for detecting perivalvular complications, such as pseudoaneurysms in the paper by Ouchi *et al*[37]. A 2019 study by Hryniewiecki *et al*[26] investigated 53 consecutive patients who had perivalvular complications from IE, who also underwent CCT and TEE pre-operatively. They showed the sensitivity and specificity for detecting abscesses/pseudoaneurysms for CCT were 81% and 90%, respectively, compared to 63% and 90%, respectively for TEE[26]. A 2020 study of 68 patients reported by Sifaoui *et al* with definite left-sided IE who underwent CCT and TEE reported the comparison of CCT and TEE to detect perivalvular complications[38]. They showed again that CT had a higher sensitivity for detecting pseudoaneurysms at 100%, compared to TEE at 67%[38].

Overall, the current evidence base suggests that the diagnostic performance of CCT is likely superior to that of TEE for the detection of pseudoaneurysms and abscesses in appropriately selected cases. A recent meta-analysis reported pooled sensitivity and specificity for CCT for the detection of peri-annular complications of 88% and 93%, respectively, compared to TEE at 70% and 96%, respectively[39].

The identification of perivalvular complications is important for prognostic and management considerations. These sequelae of invasive IE, which are more common with aortic valve endocarditis and PVE, have been associated with increased rates of surgical management, and may confer an increased risk of mortality[32,33]. Therefore, a multimodality imaging strategy for IE that includes CCT would have the ability to identify more of these complications, compared to using TEE alone, and therefore impact on decision making for patients.

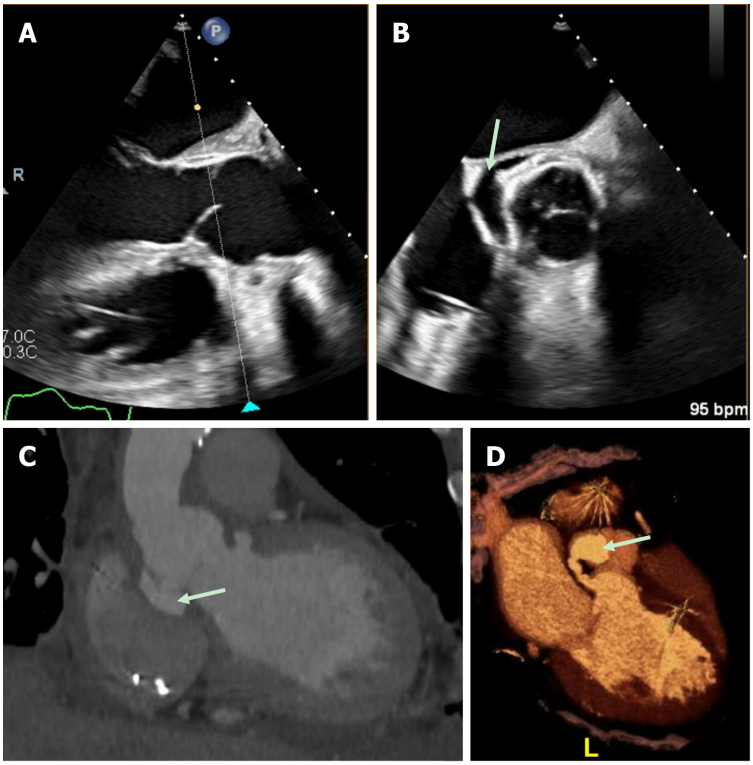

DOI: 10.4329/wjr.v14.i7.180

Figure 4 Aortic repair with left ventricular outflow tract pseudoaneurysm. A and B: This patient had a complex aortic repair with a clear peri-valvular space (arrow) on transesophageal echocardiography (TEE); however, the exact origin was difficult to define by TEE imaging; C and D: Cardiac computed tomography demonstrated multiple pseudo-aneurysms arising from the left ventricular outflow tract (LVOT) with the largest, fistulous LVOT pseudo-aneurysm (arrow) best appreciated on 3-dimensional volume-rendering.

Vegetations

A vegetation is a mass-like lesion of infected material composed of fibrin, platelets and microorganisms attached to an endocardial structure or on an implanted cardiac device (CIED)[40,41]. On echocardiography, this appears as an oscillating or non-oscillating intracardiac echodensity, which can be attached to a valve, other endocardial surface or cardiac device[15]. A vegetation tends to move with the cardiac cycle, and is more frequently found on the atrial side of the atrioventricular valves and the ventricular side of the semi-lunar valves[15]. On CT, vegetations appear as hypodense homogeneous irregular masses, which can be attached to a valve or other cardiac structures[30].

In the 2009 paper by Feuchter *et al*[24] using surgical/pathological diagnosis as the reference standard, CCT had sensitivity of 96% and specificity of 97% for the diagnosis of vegetations. 5 vegetations were missed by CCT (11%) either due to artefact or small size (≤ 4mm)[24]. The performance of TEE was similar to CCT with sensitivity of 96% and specificity of 100%[24]. CCT was found to be inferior to TEE for detecting leaflet perforations[24]. The study by Gahide *et al*[25] on aortic valve IE showed CCT had a sensitivity of 71% and a specificity of 100% for detecting vegetations, though the sensitivity was increased to 100% for large vegetations (> 10 mm). The 2012 paper by Fagman *et al*[23] found that CCT detected vegetations in 7 out of 13 cases (54%), with a lower detection rate being potentially explained by artefact from the prosthetic valves obscuring the CCT images. The 2013 study by Habets *et al*[35] found additional benefit with CCT in addition to usual work-up with TEE in PVE, with a final diagnosis being either determined clinically or at the time of surgery. They reported that usual work-up had sensitivity of 63% for detecting vegetations, which was increased to 100% with the use of CCT[35]. The 2018 study by Koo *et al*[27] reported sensitivity for CCT to detect vegetations of 91%, compared to 100% by TEE. Missed vegetations were smaller, and the authors also listed motion artefact and beam hardening from mechanical valves as reasons for the failure of CCT to detect the vegetations[27]. Sims *et al*[36] reported the sensitivity for detecting vegetations to be 70% for CCT (34 patients) and 96% for TEE (251 patients). The study by Oucho *et al*[37] reported sensitivity of 92% for detecting vegetations for CCT, correctly identifying 12 of 13 cases who had vegetations confirmed at the time of surgery. The retrospective review on 122 patients by Koneru *et al*[31] showed TEE to have a statistically significantly higher sensitivity for detecting vegetations compared to CCT at 85% *vs* 16%, though CCT did have a higher specificity at 96% compared to 69% for TEE. The lower sensitivity in detecting vegetations by CCT in this study may be related to only reviewing single-phase images, and the fact that the slice thickness used was 3 mm which was thicker than the other studies referenced above[31]. In the 2019 paper by Hryniewiecki *et al*[26] the sensitivity and specificity for detecting

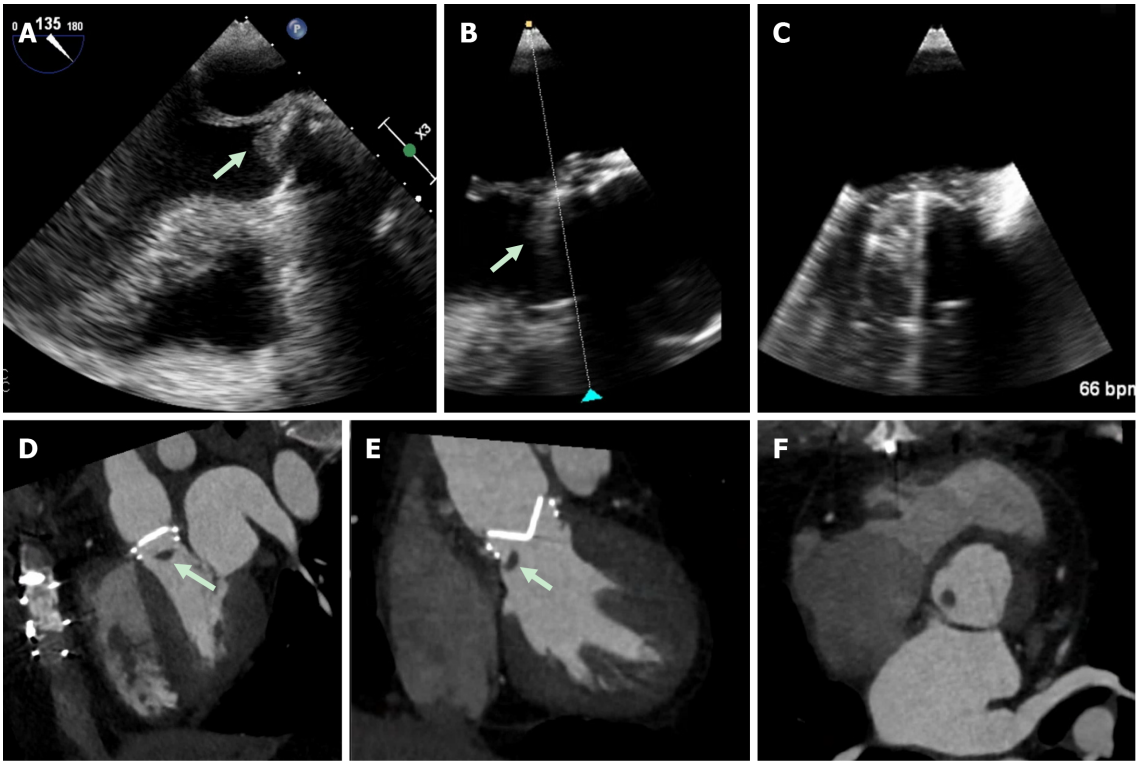

DOI: 10.4329/wjr.v14.i7.180

Figure 5 Prosthetic aortic valve with hypoattenuating lesion. A-C: This patient presented with elevated prosthetic aortic valve gradients, and although transesophageal echocardiography imaging was suspicious for an echodensity (white arrow), imaging quality was challenging due to prosthetic metallic valve shadowing; D-F: Multi-phase 4-dimensional cardiac computed tomography was utilized which clearly demonstrated a hypoattenuating mass (white arrows) attached to the prosthetic valve. Despite suspicion for infection, intra-operative pathology revealed thrombus.

vegetations by CT were 89% and 71%, respectively, compared to TEE at 97% and 42%, respectively. The 2020 study by Sifaoui *et al*[38] showed that TEE had a higher area under the curve (AUC) than CCT for detecting vegetations, with AUC for TEE of 0.86 *vs* AUC for CT of 0.69.

Overall, the current evidence base suggests that TEE is overall superior to CCT for the detection of vegetations, particular small vegetations, with pooled sensitivity for TEE from a recent meta-analysis of 94%[42]. CCT demonstrated a lower pooled sensitivity, at 64% for the detection of vegetations[42]. There was a wide range of results reported likely related to small sample sizes, differing patient populations and different protocols used for imaging. While CCT should not replace echocardiography as the first line imaging tool in the majority of patients primarily to detect vegetations, in a small subset of patients who could not undergo clinical indicated TEE (*e.g.*, esophageal pathology), CCT may add diagnostic value. CCT has also been shown to improve the diagnostic accuracy overall, when used in combination with TEE[35]. For example Figure 5 shows a hypoattenuating lesion on a mechanical aortic valve that was more clearly defined on CCT. Figures 6 and 7 shows an examples of an aortic graft and aortic stent infections that can be difficult to image with TEE.

INCREMENTAL VALUE OF CCT IN INFECTIVE ENODCARDITIS

Pre-operative assessment

In addition to the advantages related to the management of IE as outlined above, CCT can also assist in the pre-operative planning of IE surgery. In patients with prior cardiothoracic surgery, CCT can delineate the relationship of cardiovascular structures to the sternum and the location of the coronary artery bypass grafts (CABG). See Figure 8 for CCT images of a patient with a prior CABG. For all patients, CCT can identify calcification of the ascending aorta ('porcelain aorta'), which may preclude surgery as well as give precise anatomic location and extent of the degree of calcification of the subclavian, axillary and femoral arteries. The advantage of having a pre-operative CCT was described by Merlo *et al*[43] with reported lower rates of stroke and mortality in patients undergoing pre-operative CCT followed by primary cardiac surgery, *vs* those without pre-operative CCT imaging. Figure 9 shows a CCT in a patient with vascular calcification.

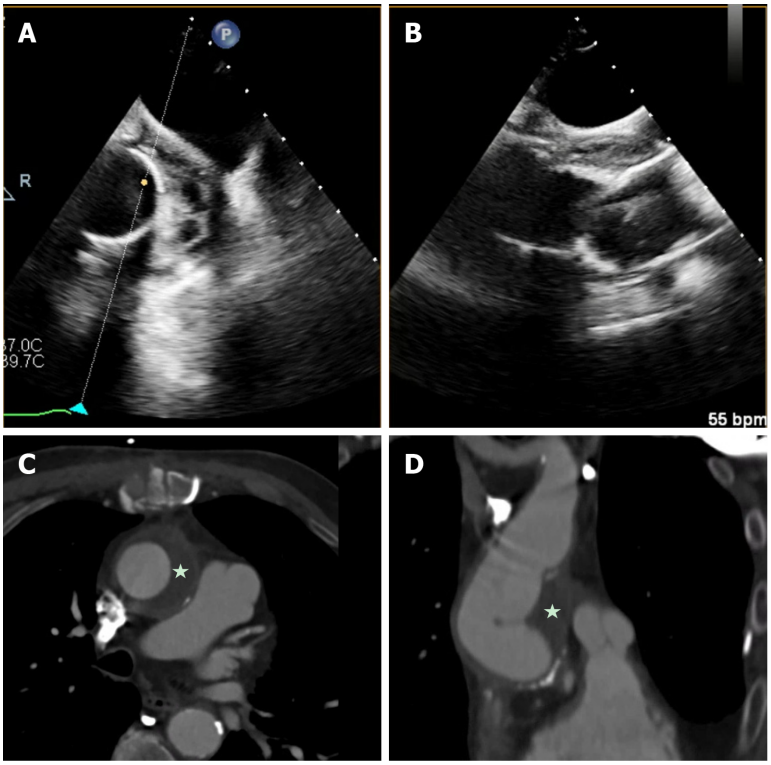

DOI: 10.4329/wjr.v14.i7.180

Figure 6 Aortic graft infection. A and B: Infection of aortic grafts can be difficult to visualize on transesophageal echocardiography (TEE); C and D: This case demonstrates evidence of a peri-aortic graft echolucent space with stranding, which was challenging to image on TEE, and further characterization with cardiac computed tomography clearly demonstrated peri-aortic graft thickening (star) consistent with infection.

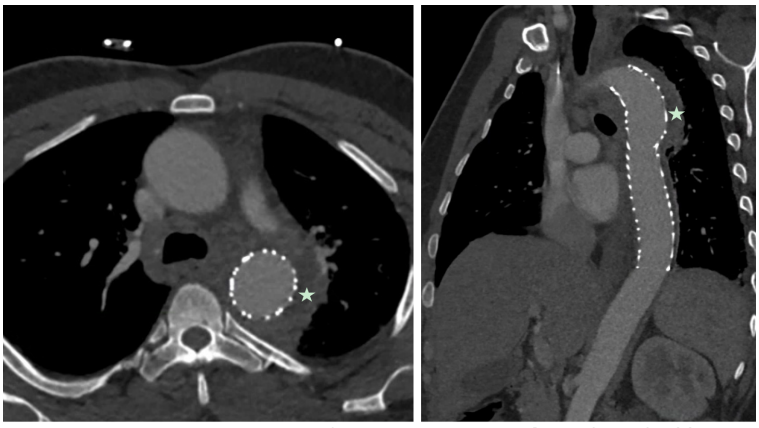

DOI: 10.4329/wjr.v14.i7.180

Figure 7 Aortic endovascular stent infection. Aortic endovascular stents are also prone to infection, and negative transesophageal echocardiography for valvular vegetations with a high suspicion should prompt consideration for other sources of infections, as in this case, which was demonstrated on cardiac computed tomography with prominent soft-tissue thickening (star) around the proximal descending thoracic aorta stent.

Pre-operative assessment

In addition to the advantages related to the management of IE as outlined above, CCT can also assist in the pre-operative planning of IE surgery[44-50]. In patients with prior cardiothoracic surgery, CCT can delineate the relationship of cardiovascular structures to the sternum and the location of the coronary artery bypass grafts (CABG). See Figure 8 for CCT images of a patient with a prior CABG[50-60]. For all patients, CCT can identify calcification of the ascending aorta ('porcelain aorta'), which may preclude surgery as well as give precise anatomic location and extent of the degree of calcification of the subclavian, axillary and femoral arteries[61,62]. The advantage of having a pre-operative CCT was described by Merlo *et al*[43] with reported lower rates of stroke and mortality in patients undergoing pre-operative CCT followed by primary cardiac surgery, *vs* those without pre-operative CCT imaging. Figures 9 and 10 shows a CCT in a patient with vascular calcification.

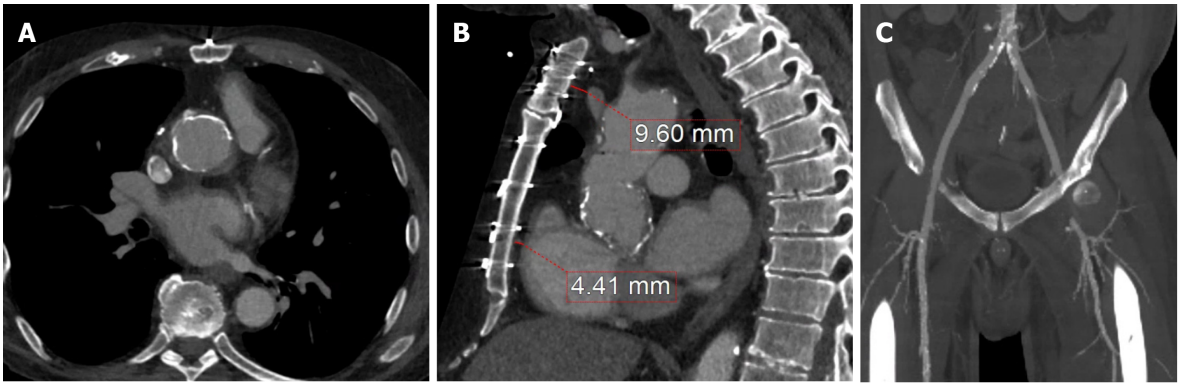

DOI: 10.4329/wjr.v14.i7.180

Figure 8 Prior coronary artery bypass graft. A: Cardiac computed tomography has added utility for pre-operative planning by identifying areas of aortic calcification (which in this case was prominent at the aortic root graft); B and C: Relevant sternal distance for cardiovascular structures, such as the left braciochephalic vein and right ventricle, as well as ilio-femoral anatomy in cases where peripheral vascular access may be needed.

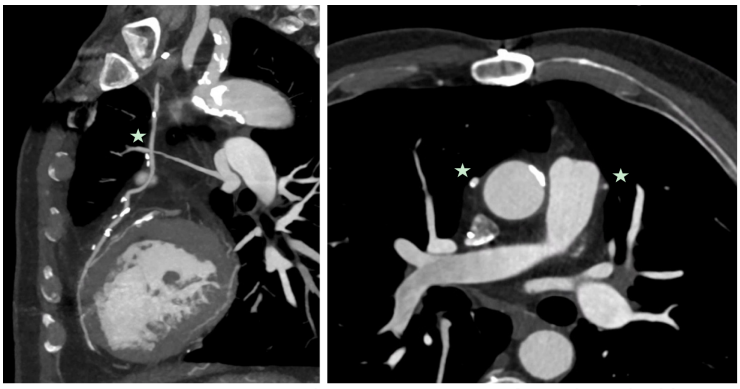

DOI: 10.4329/wjr.v14.i7.180

Figure 9 Aortic calcification and thoracic structures. Cardiac computed tomography is also important to identify prior coronary artery bypass graft locations (stars) and sternal distance to avoid complications, which can be increased in redo-surgery particularly with increased adhesions and friable structures due to infection.

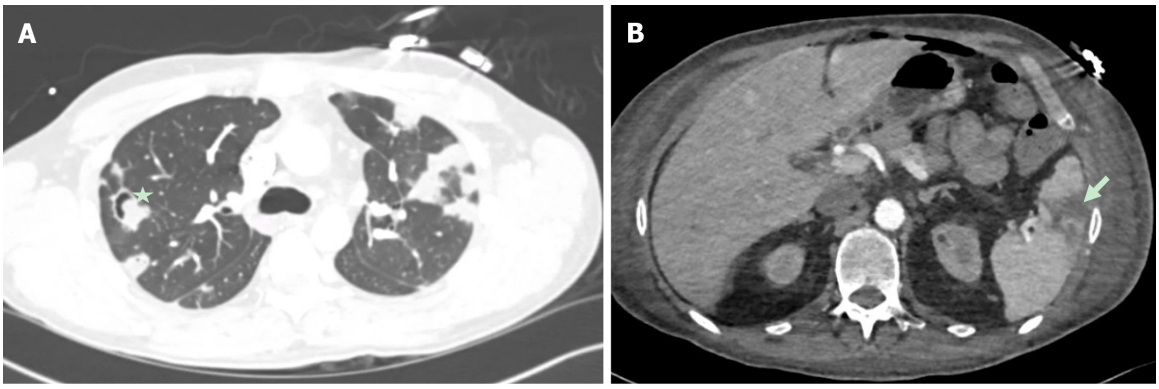

DOI: 10.4329/wjr.v14.i7.180

Figure 10 Embolic phenomena of infective endocarditis. A: It demonstrates multiple pulmonary septic emboli, including cavitary lesions (star) from tricuspid valve endocarditis. Cardiac computed tomography is also incremental in demonstrating embolic phenomena which can have implications for surgical urgency and overall prognosis; B: It demonstrates a splenic infarct (arrow) from mitral valve endocarditis).

CONCLUSION

With improvements in the temporal and spatial resolution of CCT technology, including the use of dedicated 4D CCT, there has been an expanding role of CCT imaging in IE. CCT has been shown to be superior to TEE for the identification of pseudoaneurysms and abscesses in appropriately selected cases,

while the combination of both modalities results in the greatest sensitivity for detection. TEE is superior to CCT for small vegetations; however this advantage is less marked for larger vegetations. In addition, CCT has a number of adjunctive uses in IE beyond evaluation of valvular pathology. CCT can aid in the diagnosis of embolic events, such as pulmonary complications in RSIE. It can also be used to diagnose significant CAD in low to intermediate risk patients preoperatively, or when there is a contraindication to ICA, such as when there is a large aortic valve vegetation. CCT can also be helpful for pre-operative planning to assess the relationship of the cardiovascular structures in relation to the sternum, which is particularly helpful in re-do sternotomy cases. The addition of hybrid techniques such as positron emission computed tomography or SPECT/CT, has been shown to improve the diagnostic accuracy in challenging cases of PVE. Greater awareness of the strengths, weaknesses and appropriate applications of CCT in IE will assist in its optimal use for improved diagnosis and management of this challenging condition.

FOOTNOTES

Author contributions: Hughes D, Lingchangco R, Reyaldeen R and Xu B were involved in the conceptualization, writing, revision and final approval of the manuscript.

Conflict-of-interest statement: No conflicts of interest to declare for all authors for this article.

Country/Territory of origin: United States

ORCID number: Diarmaid Hughes 0000-0003-3110-6759; Richard Linchangco 0000-0002-9265-9851; Reza Reyaldeen 0000-0001-7501-2354; Bo Xu 0000-0002-2985-7468.

S-Editor: Wang LL
L-Editor: A
P-Editor: Wang LL

REFERENCES

1 **Sy RW**, Kritharides L. Health care exposure and age in infective endocarditis: results of a contemporary population-based profile of 1536 patients in Australia. *Eur Heart J* 2010; **31**: 1890-1897 [PMID: 20453066 DOI: 10.1093/eurheartj/ehq110]
2 **Mansur AJ**, Grinberg M, da Luz PL, Bellotti G. The complications of infective endocarditis. A reappraisal in the 1980s. *Arch Intern Med* 1992; **152**: 2428-2432 [PMID: 1456853]
3 **Pant S**, Patel NJ, Deshmukh A, Golwala H, Patel N, Badheka A, Hirsch GA, Mehta JL. Trends in infective endocarditis incidence, microbiology, and valve replacement in the United States from 2000 to 2011. *J Am Coll Cardiol* 2015; **65**: 2070-2076 [PMID: 25975469 DOI: 10.1016/j.jacc.2015.03.518]
4 **Toyoda N**, Chikwe J, Itagaki S, Gelijns AC, Adams DH, Egorova NN. Trends in Infective Endocarditis in California and New York State, 1998-2013. *JAMA* 2017; **317**: 1652-1660 [PMID: 28444279 DOI: 10.1001/jama.2017.4287]
5 **Murdoch DR**, Corey GR, Hoen B, Miró JM, Fowler VG Jr, Bayer AS, Karchmer AW, Olaison L, Pappas PA, Moreillon P, Chambers ST, Chu VH, Falcó V, Holland DJ, Jones P, Klein JL, Raymond NJ, Read KM, Tripodi MF, Utili R, Wang A, Woods CW, Cabell CH; International Collaboration on Endocarditis-Prospective Cohort Study (ICE-PCS) Investigators. Clinical presentation, etiology, and outcome of infective endocarditis in the 21st century: the International Collaboration on Endocarditis-Prospective Cohort Study. *Arch Intern Med* 2009; **169**: 463-473 [PMID: 19273776 DOI: 10.1001/archinternmed.2008.603]
6 **Strom BL**, Abrutyn E, Berlin JA, Kinman JL, Feldman RS, Stolley PD, Levison ME, Korzeniowski OM, Kaye D. Risk factors for infective endocarditis: oral hygiene and nondental exposures. *Circulation* 2000; **102**: 2842-2848 [PMID: 11104742 DOI: 10.1161/01.cir.102.23.2842]
7 **Baddour LM**, Wilson WR, Bayer AS, Fowler VG Jr, Tleyjeh IM, Rybak MJ, Barsic B, Lockhart PB, Gewitz MH, Levison ME, Bolger AF, Steckelberg JM, Baltimore RS, Fink AM, O'Gara P, Taubert KA; American Heart Association Committee on Rheumatic Fever, Endocarditis, and Kawasaki Disease of the Council on Cardiovascular Disease in the Young, Council on Clinical Cardiology, Council on Cardiovascular Surgery and Anesthesia, and Stroke Council. Infective Endocarditis in Adults: Diagnosis, Antimicrobial Therapy, and Management of Complications: A Scientific Statement for Healthcare Professionals From the American Heart Association. *Circulation* 2015; **132**: 1435-1486 [PMID: 26373316 DOI: 10.1161/CIR.0000000000000296]
8 **Bayer AS**. Infective endocarditis. *Clin Infect Dis* 1993; **17**: 313-20; quiz 321 [PMID: 8218670 DOI: 10.1093/clinids/17.3.313]

9 **Durack DT**, Lukes AS, Bright DK. New criteria for diagnosis of infective endocarditis: utilization of specific echocardiographic findings. Duke Endocarditis Service. *Am J Med* 1994; **96**: 200-209 [PMID: 8154507 DOI: 10.1016/0002-9343(94)90143-0]

10 **Sekeres MA**, Abrutyn E, Berlin JA, Kaye D, Kinman JL, Korzeniowski OM, Levison ME, Feldman RS, Strom BL. An assessment of the usefulness of the Duke criteria for diagnosing active infective endocarditis. *Clin Infect Dis* 1997; **24**: 1185-1190 [PMID: 9195080 DOI: 10.1086/513657]

11 **Hoen B**, Béguinot I, Rabaud C, Jaussaud R, Selton-Suty C, May T, Canton P. The Duke criteria for diagnosing infective endocarditis are specific: analysis of 100 patients with acute fever or fever of unknown origin. *Clin Infect Dis* 1996; **23**: 298-302 [PMID: 8842267 DOI: 10.1093/clinids/23.2.298]

12 **Li JS**, Sexton DJ, Mick N, Nettles R, Fowler VG Jr, Ryan T, Bashore T, Corey GR. Proposed modifications to the Duke criteria for the diagnosis of infective endocarditis. *Clin Infect Dis* 2000; **30**: 633-638 [PMID: 10770721 DOI: 10.1086/313753]

13 **Fukuchi T**, Iwata K, Ohji G. Failure of early diagnosis of infective endocarditis in Japan--a retrospective descriptive analysis. *Medicine (Baltimore)* 2014; **93**: e237 [PMID: 25501088 DOI: 10.1097/MD.0000000000000237]

14 **Naderi HR**, Sheybani F, Erfani SS. Errors in diagnosis of infective endocarditis. *Epidemiol Infect* 2018; **146**: 394-400 [PMID: 29310727 DOI: 10.1017/S0950268817002977]

15 **Habib G**, Lancellotti P, Antunes MJ, Bongiorni MG, Casalta JP, Del Zotti F, Dulgheru R, El Khoury G, Erba PA, Iung B, Miro JM, Mulder BJ, Plonska-Gosciniak E, Price S, Roos-Hesselink J, Snygg-Martin U, Thuny F, Tornos Mas P, Vilacosta I, Zamorano JL; ESC Scientific Document Group. 2015 ESC Guidelines for the management of infective endocarditis: The Task Force for the Management of Infective Endocarditis of the European Society of Cardiology (ESC). Endorsed by: European Association for Cardio-Thoracic Surgery (EACTS), the European Association of Nuclear Medicine (EANM). *Eur Heart J* 2015; **36**: 3075-3128 [PMID: 26320109 DOI: 10.1093/eurheartj/ehv319]

16 **Otto CM**, Nishimura RA, Bonow RO, Carabello BA, Erwin JP 3rd, Gentile F, Jneid H, Krieger EV, Mack M, McLeod C, O'Gara PT, Rigolin VH, Sundt TM 3rd, Thompson A, Toly C. 2020 ACC/AHA Guideline for the Management of Patients With Valvular Heart Disease: Executive Summary: A Report of the American College of Cardiology/American Heart Association Joint Committee on Clinical Practice Guidelines. *Circulation* 2021; **143**: e35-e71 [PMID: 33332149 DOI: 10.1161/CIR.0000000000000932]

17 **Habib G**, Badano L, Tribouilloy C, Vilacosta I, Zamorano JL, Galderisi M, Voigt JU, Sicari R, Cosyns B, Fox K, Aakhus S; European Association of Echocardiography. Recommendations for the practice of echocardiography in infective endocarditis. *Eur J Echocardiogr* 2010; **11**: 202-219 [PMID: 20223755 DOI: 10.1093/ejechocard/jeq004]

18 **Haq IU**, Haq I, Griffin B, Xu B. Imaging to evaluate suspected infective endocarditis. *Cleve Clin J Med* 2021; **88**: 163-172 [PMID: 33648969 DOI: 10.3949/ccjm.88a.19142]

19 **Daniel WG**, Mügge A, Martin RP, Lindert O, Hausmann D, Nonnast-Daniel B, Laas J, Lichtlen PR. Improvement in the diagnosis of abscesses associated with endocarditis by transesophageal echocardiography. *N Engl J Med* 1991; **324**: 795-800 [PMID: 1997851 DOI: 10.1056/NEJM199103213241203]

20 **Zmaili MA**, Alzubi JM, Kocyigit D, Bansal A, Samra GS, Grimm R, Griffin BP, Xu B. A Contemporary 20-Year Cleveland Clinic Experience of Nonbacterial Thrombotic Endocarditis: Etiology, Echocardiographic Imaging, Management, and Outcomes. *Am J Med* 2021; **134**: 361-369 [PMID: 32827467 DOI: 10.1016/j.amjmed.2020.06.047]

21 **Lo Presti S**, Elajami TK, Zmaili M, Reyaldeen R, Xu B. Multimodality imaging in the diagnosis and management of prosthetic valve endocarditis: A contemporary narrative review. *World J Cardiol* 2021; **13**: 254-270 [PMID: 34589164 DOI: 10.4330/wjc.v13.i8.254]

22 **Altiok E**, Koos R, Schröder J, Brehmer K, Hamada S, Becker M, Mahnken AH, Almalla M, Dohmen G, Autschbach R, Marx N, Hoffmann R. Comparison of two-dimensional and three-dimensional imaging techniques for measurement of aortic annulus diameters before transcatheter aortic valve implantation. *Heart* 2011; **97**: 1578-1584 [PMID: 21700756 DOI: 10.1136/hrt.2011.223974]

23 **Fagman E**, Perrotta S, Bech-Hanssen O, Flinck A, Lamm C, Olaison L, Svensson G. ECG-gated computed tomography: a new role for patients with suspected aortic prosthetic valve endocarditis. *Eur Radiol* 2012; **22**: 2407-2414 [PMID: 22622348 DOI: 10.1007/s00330-012-2491-5]

24 **Feuchtner GM**, Stolzmann P, Dichtl W, Schertler T, Bonatti J, Scheffel H, Mueller S, Plass A, Mueller L, Bartel T, Wolf F, Alkadhi H. Multislice computed tomography in infective endocarditis: comparison with transesophageal echocardiography and intraoperative findings. *J Am Coll Cardiol* 2009; **53**: 436-444 [PMID: 19179202 DOI: 10.1016/j.jacc.2008.01.077]

25 **Gahide G**, Bommart S, Demaria R, Sportouch C, Dambia H, Albat B, Vernhet-Kovacsik H. Preoperative evaluation in aortic endocarditis: findings on cardiac CT. *AJR Am J Roentgenol* 2010; **194**: 574-578 [PMID: 20173130 DOI: 10.2214/AJR.08.2120]

26 **Hryniewiecki T**, Zatorska K, Abramczuk E, Zakrzewski D, Szymański P, Kuśmierczyk M, Michałowska I. The usefulness of cardiac CT in the diagnosis of perivalvular complications in patients with infective endocarditis. *Eur Radiol* 2019; **29**: 4368-4376 [PMID: 30643945 DOI: 10.1007/s00330-018-5965-2]

27 **Koo HJ**, Yang DH, Kang JW, Lee JY, Kim DH, Song JM, Kang DH, Song JK, Kim JB, Jung SH, Choo SJ, Chung CH, Lee JW, Lim TH. Demonstration of infective endocarditis by cardiac CT and transoesophageal echocardiography: comparison with intra-operative findings. *Eur Heart J Cardiovasc Imaging* 2018; **19**: 199-207 [PMID: 28329276 DOI: 10.1093/ehjci/jex010]

28 **Vrachliotis TG**, Bis KG, Haidary A, Kosuri R, Balasubramaniam M, Gallagher M, Raff G, Ross M, O'neil B, O'neill W. Atypical chest pain: coronary, aortic, and pulmonary vasculature enhancement at biphasic single-injection 64-section CT angiography. *Radiology* 2007; **243**: 368-376 [PMID: 17400761 DOI: 10.1148/radiol.2432060447]

29 **Jakobs TF**, Becker CR, Ohnesorge B, Flohr T, Suess C, Schoepf UJ, Reiser MF. Multislice helical CT of the heart with retrospective ECG gating: reduction of radiation exposure by ECG-controlled tube current modulation. *Eur Radiol* 2002; **12**: 1081-1086 [PMID: 11976849 DOI: 10.1007/s00330-001-1278-x]

30 **Grob A**, Thuny F, Villacampa C, Flavian A, Gaubert JY, Raoult D, Casalta JP, Habib G, Moulin G, Jacquier A. Cardiac

multidetector computed tomography in infective endocarditis: a pictorial essay. *Insights Imaging* 2014; **5**: 559-570 [PMID: 25225108 DOI: 10.1007/s13244-014-0353-1]

31 **Koneru S**, Huang SS, Oldan J, Betancor J, Popovic ZB, Rodriguez LL, Shrestha NK, Gordon S, Pettersson G, Bolen MA. Role of preoperative cardiac CT in the evaluation of infective endocarditis: comparison with transesophageal echocardiography and surgical findings. *Cardiovasc Diagn Ther* 2018; **8**: 439-449 [PMID: 30214859 DOI: 10.21037/cdt.2018.07.07]

32 **Baumgartner FJ**, Omari BO, Robertson JM, Nelson RJ, Pandya A, Milliken JC. Annular abscesses in surgical endocarditis: anatomic, clinical, and operative features. *Ann Thorac Surg* 2000; **70**: 442-447 [PMID: 10969660 DOI: 10.1016/s0003-4975(00)01363-1]

33 **Graupner C**, Vilacosta I, SanRomán J, Ronderos R, Sarriá C, Fernández C, Mújica R, Sanz O, Sanmartín JV, Pinto AG. Periannular extension of infective endocarditis. *J Am Coll Cardiol* 2002; **39**: 1204-1211 [PMID: 11923047 DOI: 10.1016/s0735-1097(02)01747-3]

34 **Harris WM**, Sinha S, Caputo M, Angelini GD, Ahmed EM, Rajakaruna C, Benedetto U, Vohra HA. Surgical outcomes and optimal approach to treatment of aortic valve endocarditis with aortic root abscess. *J Card Surg* 2022; **37**: 1917-1925 [PMID: 35384049 DOI: 10.1111/jocs.16464]

35 **Habets J**, Tanis W, van Herwerden LA, van den Brink RB, Mali WP, de Mol BA, Chamuleau SA, Budde RP. Cardiac computed tomography angiography results in diagnostic and therapeutic change in prosthetic heart valve endocarditis. *Int J Cardiovasc Imaging* 2014; **30**: 377-387 [PMID: 24293045 DOI: 10.1007/s10554-013-0335-2]

36 **Sims JR**, Anavekar NS, Chandrasekaran K, Steckelberg JM, Wilson WR, Gersh BJ, Baddour LM, DeSimone DC. Utility of cardiac computed tomography scanning in the diagnosis and pre-operative evaluation of patients with infective endocarditis. *Int J Cardiovasc Imaging* 2018; **34**: 1155-1163 [PMID: 29450741 DOI: 10.1007/s10554-018-1318-0]

37 **Ouchi K**, Sakuma T, Ojiri H. Cardiac computed tomography as a viable alternative to echocardiography to detect vegetations and perivalvular complications in patients with infective endocarditis. *Jpn J Radiol* 2018; **36**: 421-428 [PMID: 29713878 DOI: 10.1007/s11604-018-0740-5]

38 **Sifaoui I**, Oliver L, Tacher V, Fiore A, Lepeule R, Moussafeur A, Huguet R, Teiger E, Audureau E, Derbel H, Luciani A, Kobeiter H, Lim P, Ternacle J, Deux JF. Diagnostic Performance of Transesophageal Echocardiography and Cardiac Computed Tomography in Infective Endocarditis. *J Am Soc Echocardiogr* 2020; **33**: 1442-1453 [PMID: 32981789 DOI: 10.1016/j.echo.2020.07.017]

39 **Jain V**, Wang TKM, Bansal A, Farwati M, Gad M, Montane B, Kaur S, Bolen MA, Grimm R, Griffin B, Xu B. Diagnostic performance of cardiac computed tomography *vs* transesophageal echocardiography in infective endocarditis: A contemporary comparative meta-analysis. *J Cardiovasc Comput Tomogr* 2021; **15**: 313-321 [PMID: 33281097 DOI: 10.1016/j.jcct.2020.11.008]

40 **Habib G**, Hoen B, Tornos P, Thuny F, Prendergast B, Vilacosta I, Moreillon P, de Jesus Antunes M, Thilen U, Lekakis J, Lengyel M, Müller L, Naber CK, Nihoyannopoulos P, Moritz A, Zamorano JL; ESC Committee for Practice Guidelines. Guidelines on the prevention, diagnosis, and treatment of infective endocarditis (new version 2009): the Task Force on the Prevention, Diagnosis, and Treatment of Infective Endocarditis of the European Society of Cardiology (ESC). Endorsed by the European Society of Clinical Microbiology and Infectious Diseases (ESCMID) and the International Society of Chemotherapy (ISC) for Infection and Cancer. *Eur Heart J* 2009; **30**: 2369-2413 [PMID: 19713420 DOI: 10.1093/eurheartj/ehp285]

41 **Fava AM**, Xu B. Tricuspid valve endocarditis: Cardiovascular imaging evaluation and management. *World J Clin Cases* 2021; **9**: 8974-8984 [PMID: 34786381 DOI: 10.12998/wjcc.v9.i30.8974]

42 **Oliveira M**, Guittet L, Hamon M. Comparative Value of Cardiac CT and Transesophageal Echocardiography in Infective Endocarditis: A Systematic Review and Meta-Analysis. *Radiol Cardiothorac Imaging* 2020; **2**: e190189 [PMID: 33778583 DOI: 10.1148/ryct.2020190189]

43 **Merlo A**, Chen K, Deo S, Markowitz A. Does routine preoperative computed tomography imaging provide clinical utility in patients undergoing primary cardiac surgery? *Interact Cardiovasc Thorac Surg* 2017; **25**: 659-662 [PMID: 28962500 DOI: 10.1093/icvts/ivx098]

44 **Gulati M**, Levy PD, Mukherjee D, Amsterdam E, Bhatt DL, Birtcher KK, Blankstein R, Boyd J, Bullock-Palmer RP, Conejo T, Diercks DB, Gentile F, Greenwood JP, Hess EP, Hollenberg SM, Jaber WA, Jneid H, Joglar JA, Morrow DA, O'Connor RE, Ross MA, Shaw LJ. 2021 AHA/ACC/ASE/CHEST/SAEM/SCCT/SCMR Guideline for the Evaluation and Diagnosis of Chest Pain: Executive Summary: A Report of the American College of Cardiology/American Heart Association Joint Committee on Clinical Practice Guidelines. *Circulation* 2021; **144**: e368-e454 [PMID: 34709928 DOI: 10.1161/CIR.0000000000001030]

45 **SCOT-HEART investigators**. CT coronary angiography in patients with suspected angina due to coronary heart disease (SCOT-HEART): an open-label, parallel-group, multicentre trial. *Lancet* 2015; **385**: 2383-2391 [PMID: 25788230 DOI: 10.1016/S0140-6736(15)60291-4]

46 **SCOT-HEART Investigators**, Newby DE, Adamson PD, Berry C, Boon NA, Dweck MR, Flather M, Forbes J, Hunter A, Lewis S, MacLean S, Mills NL, Norrie J, Roditi G, Shah ASV, Timmis AD, van Beek EJR, Williams MC. Coronary CT Angiography and 5-Year Risk of Myocardial Infarction. *N Engl J Med* 2018; **379**: 924-933 [PMID: 30145934 DOI: 10.1056/NEJMoa1805971]

47 **Knuuti J**, Ballo H, Juarez-Orozco LE, Saraste A, Kolh P, Rutjes AWS, Jüni P, Windecker S, Bax JJ, Wijns W. The performance of non-invasive tests to rule-in and rule-out significant coronary artery stenosis in patients with stable angina: a meta-analysis focused on post-test disease probability. *Eur Heart J* 2018; **39**: 3322-3330 [PMID: 29850808 DOI: 10.1093/eurheartj/ehy267]

48 **Opolski MP**, Staruch AD, Jakubczyk M, Min JK, Gransar H, Staruch M, Witkowski A, Kepka C, Kim WK, Hamm CW, Möllmann H, Achenbach S. CT Angiography for the Detection of Coronary Artery Stenoses in Patients Referred for Cardiac Valve Surgery: Systematic Review and Meta-Analysis. *JACC Cardiovasc Imaging* 2016; **9**: 1059-1070 [PMID: 27344418 DOI: 10.1016/j.jcmg.2015.09.028]

49 **Vahanian A**, Beyersdorf F, Praz F, Milojevic M, Baldus S, Bauersachs J, Capodanno D, Conradi L, De Bonis M, De Paulis

R, Delgado V, Freemantle N, Gilard M, Haugaa KH, Jeppsson A, Jüni P, Pierard L, Prendergast BD, Sádaba JR, Tribouilloy C, Wojakowski W; ESC/EACTS Scientific Document Group. 2021 ESC/EACTS Guidelines for the management of valvular heart disease. *Eur Heart J* 2022; **43**: 561-632 [PMID: 34453165 DOI: 10.1093/eurheartj/ehab395]

50 **Hekimian G**, Kim M, Passefort S, Duval X, Wolff M, Leport C, Leplat C, Steg G, Iung B, Vahanian A, Messika-Zeitoun D. Preoperative use and safety of coronary angiography for acute aortic valve infective endocarditis. *Heart* 2010; **96**: 696-700 [PMID: 20424151 DOI: 10.1136/hrt.2009.183772]

51 **Saby L**, Laas O, Habib G, Cammilleri S, Mancini J, Tessonnier L, Casalta JP, Gouriet F, Riberi A, Avierinos JF, Collart F, Mundler O, Raoult D, Thuny F. Positron emission tomography/computed tomography for diagnosis of prosthetic valve endocarditis: increased valvular 18F-fluorodeoxyglucose uptake as a novel major criterion. *J Am Coll Cardiol* 2013; **61**: 2374-2382 [PMID: 23583251 DOI: 10.1016/j.jacc.2013.01.092]

52 **Wang TKM**, Sánchez-Nadales A, Igbinomwanhia E, Cremer P, Griffin B, Xu B. Diagnosis of Infective Endocarditis by Subtype Using ^{18}F-Fluorodeoxyglucose Positron Emission Tomography/Computed Tomography: A Contemporary Meta-Analysis. *Circ Cardiovasc Imaging* 2020; **13**: e010600 [PMID: 32507019 DOI: 10.1161/CIRCIMAGING.120.010600]

53 **Mahmood M**, Kendi AT, Ajmal S, Farid S, O'Horo JC, Chareonthaitawee P, Baddour LM, Sohail MR. Meta-analysis of 18F-FDG PET/CT in the diagnosis of infective endocarditis. *J Nucl Cardiol* 2019; **26**: 922-935 [PMID: 29086386 DOI: 10.1007/s12350-017-1092-8]

54 **Swart LE**, Gomes A, Scholtens AM, Sinha B, Tanis W, Lam MGEH, van der Vlugt MJ, Streukens SAF, Aarntzen EHJG, Bucerius J, van Assen S, Bleeker-Rovers CP, van Geel PP, Krestin GP, van Melle JP, Roos-Hesselink JW, Slart RHJA, Glaudemans AWJM, Budde RPJ. Improving the Diagnostic Performance of ^{18}F-Fluorodeoxyglucose Positron-Emission Tomography/Computed Tomography in Prosthetic Heart Valve Endocarditis. *Circulation* 2018; **138**: 1412-1427 [PMID: 30018167 DOI: 10.1161/CIRCULATIONAHA.118.035032]

55 **Erba PA**, Conti U, Lazzeri E, Sollini M, Doria R, De Tommasi SM, Bandera F, Tascini C, Menichetti F, Dierckx RA, Signore A, Mariani G. Added value of 99mTc-HMPAO-labeled leukocyte SPECT/CT in the characterization and management of patients with infectious endocarditis. *J Nucl Med* 2012; **53**: 1235-1243 [PMID: 22787109 DOI: 10.2967/jnumed.111.099424]

56 **Rouzet F**, Chequer R, Benali K, Lepage L, Ghodbane W, Duval X, Iung B, Vahanian A, Le Guludec D, Hyafil F. Respective performance of 18F-FDG PET and radiolabeled leukocyte scintigraphy for the diagnosis of prosthetic valve endocarditis. *J Nucl Med* 2014; **55**: 1980-1985 [PMID: 25453046 DOI: 10.2967/jnumed.114.141895]

57 **Di Salvo G**, Habib G, Pergola V, Avierinos JF, Philip E, Casalta JP, Vailloud JM, Derumeaux G, Gouvernet J, Ambrosi P, Lambert M, Ferracci A, Raoult D, Luccioni R. Echocardiography predicts embolic events in infective endocarditis. *J Am Coll Cardiol* 2001; **37**: 1069-1076 [PMID: 11263610 DOI: 10.1016/s0735-1097(00)01206-7]

58 **Rossi SE**, Goodman PC, Franquet T. Nonthrombotic pulmonary emboli. *AJR Am J Roentgenol* 2000; **174**: 1499-1508 [PMID: 10845470 DOI: 10.2214/ajr.174.6.1741499]

59 **Huang JS**, Ho AS, Ahmed A, Bhalla S, Menias CO. Borne identity: CT imaging of vascular infections. *Emerg Radiol* 2011; **18**: 335-343 [PMID: 21424803 DOI: 10.1007/s10140-011-0946-7]

60 **Thuny F**, Avierinos JF, Tribouilloy C, Giorgi R, Casalta JP, Milandre L, Brahim A, Nadji G, Riberi A, Collart F, Renard S, Raoult D, Habib G. Impact of cerebrovascular complications on mortality and neurologic outcome during infective endocarditis: a prospective multicentre study. *Eur Heart J* 2007; **28**: 1155-1161 [PMID: 17363448 DOI: 10.1093/eurheartj/ehm005]

61 **García-Cabrera E**, Fernández-Hidalgo N, Almirante B, Ivanova-Georgieva R, Noureddine M, Plata A, Lomas JM, Gálvez-Acebal J, Hidalgo-Tenorio C, Ruíz-Morales J, Martínez-Marcos FJ, Reguera JM, de la Torre-Lima J, de Alarcón González A; Group for the Study of Cardiovascular Infections of the Andalusian Society of Infectious Diseases; Spanish Network for Research in Infectious Diseases. Neurological complications of infective endocarditis: risk factors, outcome, and impact of cardiac surgery: a multicenter observational study. *Circulation* 2013; **127**: 2272-2284 [PMID: 23648777 DOI: 10.1161/CIRCULATIONAHA.112.000813]

62 **Heiro M**, Nikoskelainen J, Engblom E, Kotilainen E, Marttila R, Kotilainen P. Neurologic manifestations of infective endocarditis: a 17-year experience in a teaching hospital in Finland. *Arch Intern Med* 2000; **160**: 2781-2787 [PMID: 11025788 DOI: 10.1001/archinte.160.18.2781]

World Journal of Radiology

Submit a Manuscript: https://www.f6publishing.com

World J Radiol 2022 July 28; 14(7): 194-208

DOI: 10.4329/wjr.v14.i7.194

ISSN 1949-8470 (online)

MINIREVIEWS

Molecular imaging as a tool for evaluation of COVID-19 sequelae – A review of literature

Kunal R Chandekar, Swayamjeet Satapathy, Harmandeep Singh, Anish Bhattacharya

Specialty type: Radiology, nuclear medicine and medical imaging

Provenance and peer review: Invited article; Externally peer reviewed.

Peer-review model: Single blind

Peer-review report's scientific quality classification

Grade A (Excellent): A
Grade B (Very good): B
Grade C (Good): C, C
Grade D (Fair): 0
Grade E (Poor): 0

P-Reviewer: Kothan S, Thailand; Lanza G, Italy; Lukito AA, Indonesia; Purevjav E, United States

Received: February 22, 2022
Peer-review started: February 22, 2022
First decision: April 28, 2022
Revised: May 17, 2022
Accepted: July 11, 2022
Article in press: July 11, 2022
Published online: July 28, 2022

Kunal R Chandekar, Swayamjeet Satapathy, Harmandeep Singh, Anish Bhattacharya, Department of Nuclear Medicine, Post Graduate Institute of Medical Education and Research, Chandigarh 160012, India

Corresponding author: Swayamjeet Satapathy, MBBS, MD, Doctor, Department of Nuclear Medicine, Post Graduate Institute of Medical Education and Research, Sector-12, Chandigarh 160012, India. swayamjeet.satapathy@gmail.com

Abstract

Coronavirus disease 2019 (COVID-19) is caused by the novel viral pathogen, severe acute respiratory syndrome coronavirus 2 (SARS-CoV-2). COVID-19 primarily involves the lungs. Nucleic acid testing based on reverse-transcription polymerase chain reaction of respiratory samples is the current gold standard for the diagnosis of SARS-CoV-2 infection. Imaging modalities have an established role in triaging, diagnosis, evaluation of disease severity, monitoring disease progression, extra-pulmonary involvement, and complications. As our understanding of the disease improves, there has been substantial evidence to highlight its potential for multi-systemic involvement and development of long-term sequelae. Molecular imaging techniques are highly sensitive, allowing non-invasive visualization of physiological or pathological processes at a cellular or molecular level with potential for detection of functional changes earlier than conventional radiological imaging. The purpose of this review article is to highlight the evolving role of molecular imaging in evaluation of COVID-19 sequelae. Though not ideal for diagnosis, the various modalities of molecular imaging play an important role in assessing pulmonary and extra-pulmonary sequelae of COVID-19. Perfusion imaging using single photon emission computed tomography fused with computed tomography (CT) can be utilized as a first-line imaging modality for COVID-19 related pulmonary embolism. ^{18}F-fluorodeoxyglucose positron emission tomography (PET)/CT is a sensitive tool to detect multi-systemic inflammation, including myocardial and vascular inflammation. PET in conjunction with magnetic resonance imaging helps in better characterization of neurological sequelae of COVID-19. Despite the fact that the majority of published literature is retrospective in nature with limited sample sizes, it is clear that molecular imaging provides additional valuable information (complimentary to anatomical imaging) with semi-quantitative or quantitative parameters to define inflammatory burden and can be used to guide therapeutic strategies and assess response. However, widespread clinical applicability remains a challenge owing to longer image acquisition times and the need for adoption of infection

control protocols.

Key Words: Molecular imaging; Nuclear medicine; Functional imaging; COVID-19; SARS-CoV-2; Sequelae

Core Tip: Despite extensive global efforts, coronavirus disease 2019 (COVID-19) remains the largest public health problem of modern times. As our understanding of the disease and its manifestations improve, we must recognize and explore the potential utility of molecular imaging modalities in evaluating the long-term sequelae of COVID-19. Molecular imaging tools can be incorporated into routine clinical practice by identifying appropriate and specific indications and addressing limitations to their practical application.

Citation: Chandekar KR, Satapathy S, Singh H, Bhattacharya A. Molecular imaging as a tool for evaluation of COVID-19 sequelae – A review of literature. *World J Radiol* 2022; 14(7): 194-208
URL: https://www.wjgnet.com/1949-8470/full/v14/i7/194.htm
DOI: https://dx.doi.org/10.4329/wjr.v14.i7.194

INTRODUCTION

Coronavirus disease 2019 (COVID-19) is an infectious disease caused by the novel pathogen, severe acute respiratory syndrome coronavirus 2 (SARS-CoV-2)[1]. Having its early origins in the city of Wuhan, China, the disease was transmitted across the globe at disconcertingly rapid rates, prompting the World Health Organization (WHO) to characterize the outbreak as a pandemic in March 2020[2,3]. The resurgence of the disease in several parts of the world with identification of new mutant variants has hindered a targeted global response, owing to which, COVID-19 still remains the largest public health problem of modern times[4].

Though primarily believed to involve the lungs and the respiratory tract, the clinical spectrum of COVID-19 is diverse with potential for gastrointestinal, cardiac, renal, neurological, and hematological manifestations of varying severity[5].

SARS-CoV-2 is a single stranded RNA virus. Nucleic acid testing based on reverse-transcription polymerase chain reaction (RT-PCR) is the current gold standard for the diagnosis of SARS-CoV-2 infection. It is most commonly done with respiratory samples, such as nasopharyngeal and throat swabs [6]. Serological tests which identify antibodies to different virus proteins have also been developed. Laboratory tests, such as complete hemogram, C-reactive protein (CRP), D-dimer, prothrombin time (PT-INR), lactic dehydrogenase (LDH), ferritin, and procalcitonin, help in evaluation of disease severity and prognostication[7]. In spite of relatively low specificity and radiation exposure, imaging modalities have an established role in triaging, diagnosing, evaluating disease severity, monitoring disease progression, determining extra-pulmonary involvement, and assessing complications[8,9].

Molecular imaging modalities in current clinical practice, such as magnetic resonance imaging (MRI), single photon emission computed tomography (SPECT), and positron emission tomography (PET), have great potential in early and sensitive disease detection, accurate delineation of disease extent, and assessing therapeutic response with the ultimate aim of personalized medicine. Novel molecular targets and tracers (metabolic agents, peptides, small molecules, receptor ligands) are being rapidly identified and developed. At present, multimodality molecular imaging is most commonly used for oncological applications. However, their role in systemic inflammatory and infectious conditions is being increasingly recognized[10,11]. The utility of molecular or functional imaging for COVID-19, in particular, has been poorly defined owing to limited availability, longer imaging times, absence of clearly defined appropriate usage criteria, lack of standardized protocols, and need for infection control. In this article, we aim to review the role of molecular imaging in evaluating the sequelae of COVID-19.

METHODS

The literature search was based on three electronic databases (PubMed, Scopus, and EMBASE) using selected keywords which included, "COVID-19," "sequelae," "molecular imaging," "functional imaging," and "nuclear medicine" linked through the "AND" and "OR" Boolean operators to build specific strings for each electronic search engine. Original studies, case reports, case series, and review articles were included. No restriction was placed in terms of country or language of publication. Only

full-length articles were considered. Information from websites of different professional associations and national/international organizations was searched to retrieve relevant information.

ANATOMICAL IMAGING

Chest radiography (CXR) and computed tomography (CT) have been extensively used for imaging evaluation of COVID-19. CXR findings in COVID-19 include consolidatory changes and bilateral ground glass and peripheral air opacities. However, these findings are non-specific and are highly dependent on duration and severity of infection at the time of acquisition[12]. The advantages of CXR over CT include its near universal availability, lower ionizing radiation exposure, ability to perform multiple repeat examinations, and portability of equipment, which reduces risk of cross-infection. CXR is limited by its lower sensitivity compared to RT-PCR and CT, particularly in early stages of the disease [13,14].

Similar to CXR, the typical findings of COVID-19 on CT are multiple ground-glass opacities (GGOs) in a posterior, subpleural, and peripheral distribution, commonly showing bilateral lung involvement. Consolidatory changes, reticular opacities, intra- and inter-lobular septal thickening, and crazy paving pattern have also been described. CT abnormalities progress rapidly after symptom onset and are reported to peak between days 6 and 13 of the illness. Late stage disease shows gradual decrease in GGOs and consolidation with appearance of signs of fibrosis[15,16]. CT findings of COVID-19 are highly non-specific and may be seen with other viral pneumonias[17,18]. A recent meta-analysis of the accuracy of diagnostic tests for COVID-19 found CT to have high sensitivity (91.9%, 95%CI: 89.8%-93.7%) and low specificity (25.1%, 95%CI: 21.0%-29.5%). Hence CT findings must be interpreted in light of clinical presentation, history of exposure, and pre-test probability[6].

At present, most consensus guidelines recommend against the routine use of CT for screening and diagnosis of COVID-19 pneumonia. However, the role of chest CT as a rapid-triage tool in resource-limited facilities (*e.g.*, limited access to/longer processing time of RT-PCR) has also been acknowledged [19]. The use of CT has been deemed most appropriate in patients with moderate to severe respiratory symptoms or mild respiratory symptoms with risk factors for disease progression (such as presence of co-morbidities and advanced age)[20,21]. The major advantage of CT is the ability to stratify patients based on their risk for clinical decompensation and progression. To that end, different standard reporting and scoring systems have been proposed, such as COVID-19 Reporting and Data System (CO-RADS), Radiological Society of North America (RSNA) imaging classification for COVID-19, chest CT severity score (CT-SS), and total severity score (TSS)[22,23]. CT-SS is positively correlated with age, inflammatory biomarkers, clinical severity, and disease phases[24]. Lieveld *et al*[25] showed that the chest CT-SS was significantly positively associated with hospital and ICU admission, and in-hospital and 30 d mortality for all age groups in patients with COVID-19 and CT patterns ≥ CO-RADS 3.

MRI, owing to its lack of exposure to ionizing radiation, has been found to be useful in select patient-groups, such as pregnant women and children. Several case-reports have been published highlighting the utility of MRI in evaluation of extra-pulmonary involvement, particularly cardiac and neurological manifestations of COVID-19[26-28].

Chest ultrasonography (US) is now being advocated as a useful point-of-care (POC) imaging tool for evaluation particularly in the emergency and ICU settings. Vascular US of the limbs is useful in the diagnostic workup of patients with suspected deep vein thrombosis, a common complication of COVID-19[29,30].

WHERE DOES MOLECULAR IMAGING FIT IN?

Molecular imaging is a highly sensitive modality that allows non-invasive visualization of physiological or pathological processes at the cellular or molecular level. Pathophysiological changes in affected tissues are believed to occur earlier than anatomical changes in a variety of infectious and inflammatory conditions, and hence, molecular imaging may detect these functional changes before conventional radiologic imaging modalities[31]. Different molecular imaging modalities can help in evaluating the sequelae of COVID-19 (Figure 1).

PULMONARY VASCULAR SEQUELAE - ROLE OF VENTILATION-PERFUSION IMAGING

It is now well established that COVID-19 is associated with thrombotic complications, such as venous thromboembolism (VTE), myocardial infarction (MI), and ischemic stroke[32]. A recent meta-analysis found the overall prevalence of COVID-19 related VTE to be 14.7% (95%CI: 12.1%-17.6%), which was significantly higher in patients with severe systemic inflammation and respiratory failure[33-35]. However, these thromboembolic phenomena have also been documented in patients with milder forms

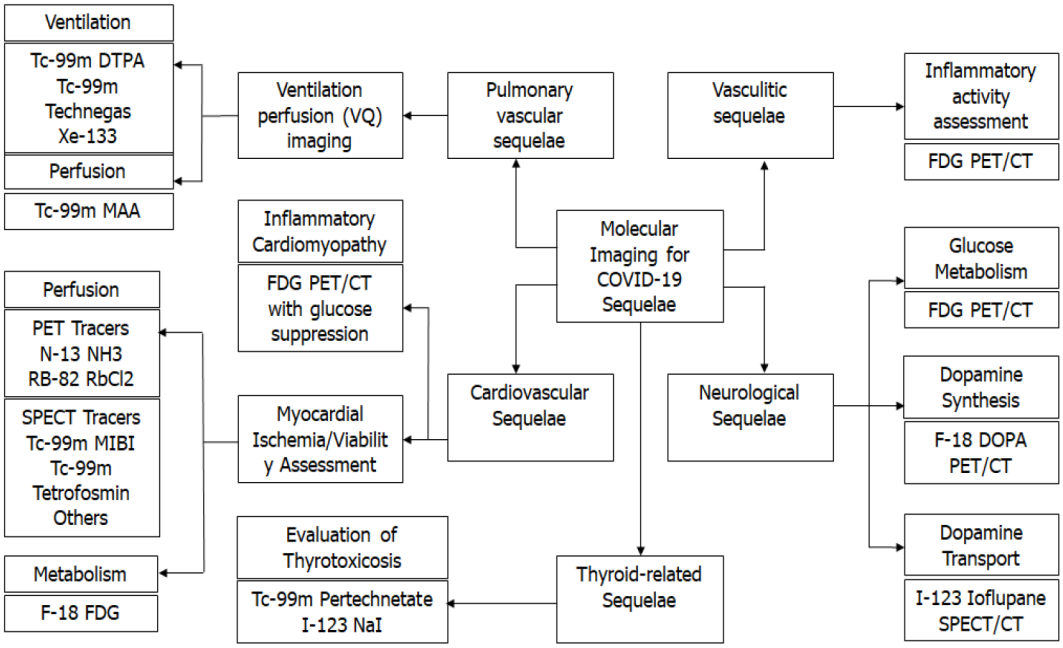

DOI: 10.4329/wjr.v14.i7.194

Figure 1 Molecular Imaging modalities for evaluating coronavirus disease 2019 sequelae. CT: Computed tomography; DOPA: L-6-fluoro-3,4-dihydroxyphenylalnine; DTPA: Diethylenetriamine pentaacetate; FDG: Fluorodeoxyglucose; MAA: Macroaggregated albumin; MIBI: Methoxy isobutyl isonitrile; PET: Positron emission tomography; SPECT: Single-photon emission computerized tomography.

of the disease[36].

From a histological stand-point, direct viral infection of endothelial cells with perivascular T-cell infiltration, thrombotic microangiopathy, and angiogenesis have been used to differentiate COVID-19 from other respiratory viruses[37]. Hence, both thromboembolic phenomena and in-situ thrombotic microangiopathy can be responsible for pulmonary vascular manifestations of COVID-19. Ventilation-Perfusion (VQ) imaging is the current gold-standard screening modality for evaluation of chronic thromboembolism[38]. Distal subsegmental small vessel thrombi can be missed on conventional CT pulmonary angiogram (CTPA), which is designed to visualize a luminal clot rather than assess how a clot affects lung perfusion, thereby underestimating the extent of micro-vascular injury[39]. Hence, VQ scintigraphy, a functional imaging modality which directly evaluates lung perfusion, can potentially help better identify vascular pathology and guide therapeutic decisions.

The possible patterns of perfusion defects seen in COVID-19 are closely related to their patho-physiology. Typically described segmental or subsegmental ventilation–perfusion mismatch defects are usually the result of large- and medium-vessel thromboembolic phenomena. Patchy, mottled peripheral pattern of ventilation-perfusion mismatch not adhering to typical segmental distribution may suggest micro-angiopathy[40,41].

Dhawan *et al*[42] recently proposed an algorithm to incorporate perfusion imaging instead of angiographic imaging as a first-line modality in the post-COVID recovery patients for follow-up of pulmonary vascular sequelae. It would serve as a triage tool to exclude or evaluate residual clot burden and small vessel injury.

A few recent publications have discouraged the use of ventilation imaging by nuclear medicine departments to reduce the risk of cross-contamination *via* aerosols[43,44]. Reporting perfusion studies without concordant ventilation imaging might hinder interpretation by increasing the likelihood of false positives. However, such limitation can be significantly overcome by the use of hybrid imaging. SPECT with CT fusion (SPECT/CT) for perfusion studies can be used as a substitute for ventilation imaging by providing corroborating anatomical information about the lung parenchyma[45-47]. Perfusion-only SPECT/CT has been shown to have practical utility in the diagnosis of pulmonary embolism in COVID-19 patients with a moderate-to-high pre-test probability. A 60-year-old male underwent perfusion-only SPECT/CT (Figure 2) in our department, 2 mo following COVID-19 infection, to rule out pulmonary thromboembolism. The study revealed subsegmental mismatched defects suggestive of pulmonary thromboembolism.

The use of VQ imaging in the setting of contraindications to iodinated contrast material also makes it preferable over CTPA as a first-line imaging modality for COVID-19 related pulmonary embolism[48].

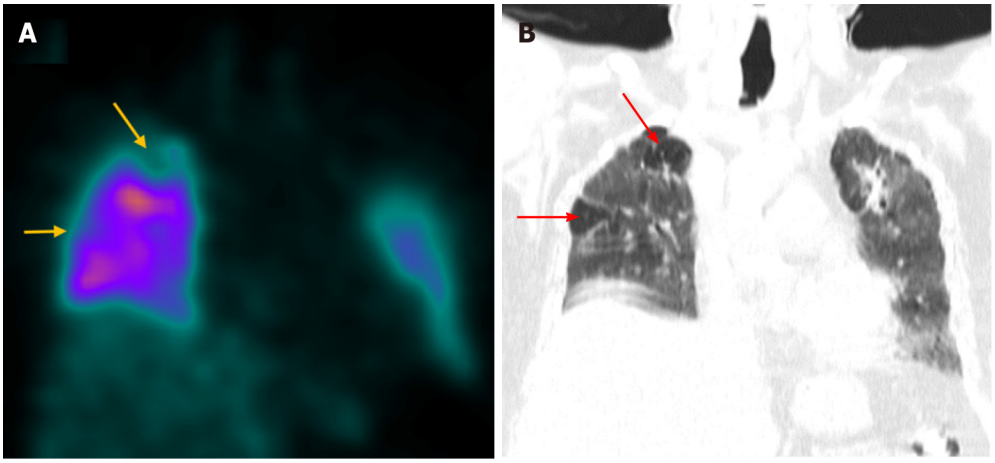

DOI: 10.4329/wjr.v14.i7.194

Figure 2 Coronavirus disease 2019 related pulmonary thromboembolism. A 60-year-old male with history of coronavirus disease 2019 (COVID-19) infection 2 mo ago underwent Tc-99m macro-aggregated albumin lung perfusion imaging to rule out pulmonary thromboembolism. A: Coronal SPECT images show reduced tracer uptake (yellow arrows) in sub-segmental defects involving the right lung apex and the lateral segment of the RML; B: Corresponding coronal CT image shows relatively normal lung parenchyma (red arrows) in the above-mentioned sites (mismatched defects) suggestive of pulmonary thromboembolism. The rest of the lung parenchyma shows ground glass changes, fibrotic bands, and bronchiectatic changes consistent with post-COVID recovery phase.

THYROID DISORDERS

SARS-CoV-2 infection has been linked to multiple thyroid disorders, including destructive thyroiditis, autoimmune thyroid disease, central hypothyroidism and euthyroid sick syndrome[49]. The binding of the viral spike protein to the angiotensin-converting-enzyme-2 (ACE2) receptors on the surface of the thyroid follicular cells has been implicated in the etiopathogenesis of the COVID-19-related destructive thyroiditis[50]. Further, an aberrant systemic inflammatory syndrome in the wake of COVID-19 can also account for the abovementioned thyroid disorders. Thyrotoxicosis, due to destructive thyroiditis or activated/relapsed Graves' disease, can exacerbate the cardiovascular complications and contribute to poor outcomes, especially in severe COVID-19 disease. Thyroid scintigraphy, with either ^{99m}Tc-pertechnetate or ^{123}I-sodium iodide, can rapidly and reliably differentiate between these etiologies of thyrotoxicosis and guide the further course of treatment[49]. A 36-year-old male had complaints of painful neck swelling and fever for 1 wk with a history of COVID-19 2 mo ago. He was found to have suppressed levels (0.013 mIU/mL) of thyroid stimulating hormone (TSH). Ultrasound neck revealed a diffusely heterogeneous thyroid parenchyma with mildly increased vascularity suggestive of thyroiditis. He was referred to our department for thyroid scintigraphy to further evaluate the cause of thyrotoxicosis. Thyroid scintigraphy revealed (Figure 3) very faint heterogeneous tracer uptake in the region of the thyroid with increased background tracer activity. With the given clinical and biochemical context, scan findings were suggestive of thyroiditis, likely related to COVID-19.

^{18}F-FLUORODEOXYGLUCOSE PET/CT

^{18}F-fluorodeoxyglucose (FDG) PET/CT is a functional imaging modality with established clinical utility in diagnosis, staging, re-staging, and therapeutic response evaluation for a variety of oncological conditions[51,52]. However, in the recent past, the role of ^{18}F-FDG PET/CT as a hybrid imaging tool for detecting and characterizing various inflammatory disorders has also been validated. ^{18}F-FDG PET/CT provides complimentary anatomical and functional information with the ability to non-invasively quantify inflammation[53,54]. SARS-CoV-2 viral infection results in a complex inflammatory cascade leading to release of pro-inflammatory cytokines and activation of cells such as neutrophils, monocytes, and effector T-cells. Activated inflammatory cells are highly glycolytic and hence, non-physiological FDG uptake can be reliably used as a surrogate marker for active inflammation[55].

Multiple studies have demonstrated incidental findings in otherwise asymptomatic or mildly symptomatic patients who underwent PET/CT for oncology/non-COVID related indications. Hence, nuclear medicine physicians must be aware of the radiological manifestations of COVID-19 and must nurture a high index of suspicion so that infection may be promptly identified at early stages and appropriate treatment may be initiated in such patient populations, the majority of whom may have a compromised immune status[56-60].

The currently accepted gold standard for diagnosing COVID-19 infection is RT-PCR to detect viral RNA[6]. Despite being fairly sensitive, multiple sources of false negative test results have been reported,

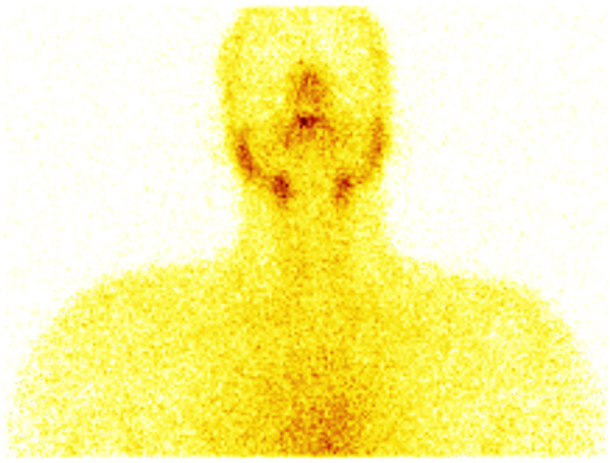

DOI: 10.4329/wjr.v14.i7.194

Figure 3 Coronavirus disease 2019 related thyroiditis. A 36-year-old male had complaints of painful neck swelling and fever for 1 wk and a past history of coronavirus disease 2019 (COVID-19) (2 mo ago). His serum TSH levels were found to be suppressed (0.013 microIU/mL). With a clinical suspicion of thyroiditis, he was referred for thyroid scintigraphy, which revealed very faint heterogeneous tracer uptake in the region of the thyroid and increased background tracer activity. In the given clinical and biochemical context, scan findings were suggestive of COVID-19 related thyroiditis.

such as insufficient viral genome, incorrect sampling technique, sampling outside the appropriate time-window for viral replication, and viral mutation. The role of ^{18}F-FDG PET/CT has been sought to be explored at early stages when clinical symptoms are not specific and differential diagnosis is challenging[61]. An early case series by Qin *et al*[62] described four patients in Wuhan with strong clinical suspicion of COVID-19 who underwent ^{18}F-FDG PET/CT during the acute phase of illness. FDG uptake was observed in regions corresponding to GGOs and/or consolidatory changes, with maximum standardized uptake (SUVmax) values ranging from 4.6 to 12.2. FDG uptake was also reported in the mediastinal and hilar lymph nodes with no obvious anatomical lymphadenopathy[62]. However, given the fact that increased FDG uptake is noted in various acute inflammatory and infectious conditions and is, hence, non-specific, ^{18}F-FDG PET/CT is not routinely recommended for the initial evaluation of patients with known or suspicious COVID-19 infection[63].

Nevertheless, data by Qin *et al*[62] also raised the possibility that higher SUVmax of pulmonary lesions on ^{18}F-FDG PET may be correlated with longer duration of healing. ^{18}F-FDG-PET/CT could, therefore, potentially be used to monitor treatment response and predict recovery. However, these trends need to be evaluated in larger populations before meaningful conclusions can be drawn.

CARDIOVASCULAR SEQUELAE

The cardiovascular manifestations of COVID-19 include arrhythmias, acute or fulminant myocarditis, acute coronary syndromes, and heart failure[64].

Different etiological mechanisms have been proposed to explain cardiac involvement in COVID-19 which include: (1) Direct myocardial cellular injury by the virus. The spike protein of the SARS-CoV2 virus binds to ACE2 receptors, which serves as an entry point to the cell. ACE2 is a membrane protein with documented expression on ciliated columnar respiratory epithelium, type II pneumocytes, and cardiomyocytes; (2) Severe systemic inflammatory response. High levels of proinflammatory cytokines and procoagulants result in endothelial dysfunction, microthombi formation within the coronary circulation, and increased plaque vulnerability; and (3) Mismatch of the myocardial oxygen supply and demand. Increased cardio-metabolic demand is the result of systemic inflammation and ongoing hypoxia due to severe pneumonia or acute respiratory distress syndrome[65].

A recent case report highlighted the role of multi-modality imaging for assessment of myocardial injury in COVID-19. ^{18}F-FDG PET/CT (with 18 h prolonged fasting protocol to suppress glucose uptake) was performed in a 69-year-old woman with COVID-19 who had complaints of dyspnea and chest pain. PET showed FDG uptake in the apex, anterior wall, and septum, and ^{99m}Tc-methoxyisobutylisonitrile (MIBI) SPECT done subsequently revealed resting perfusion defects in the same segments of the left ventricular myocardium, suggestive of an acute inflammatory response to MI precipitated by COVID-19. Severe left anterior descending artery (LAD) artery disease was found on angiography performed later, confirming anterior wall MI. Segmental FDG uptake (due to inflammation) with matching perfusion defect (due to inflammatory microvascular dysfunction), though suggestive of myocarditis, can also be seen in an acute inflammatory response to MI precipitated by COVID-19, as seen in the case described above[66].

Another case report highlighted the role of ^{18}F-FDG PET/CT in assessing myocardial inflammation in COVID-19 related multisystem inflammatory syndrome in children (MIS-C). ^{18}F-FDG PET-CT, performed after 18 h of fasting and high-fat, low-carbohydrate diet preparation in a 14-year-old child with a clinical diagnosis of COVID-19-related MIS-C, demonstrated hypermetabolism in the infero-lateral wall of the LV myocardium suggestive of active inflammation (Figure 4, attached with permission). A repeat ^{18}F-FDG PET/CT, performed 6 wk later with the same protocol, showed resolution of hypermetabolism, consistent with clinical and biochemical improvement, thus highlighting the role of ^{18}F-FDG PET/CT in the timely diagnosis and follow-up of this potentially life-threatening hyperinflammatory syndrome[67].

VASCULITIS

Recently there has been increasing recognition of the utility of ^{18}F-FDG PET/CT in inflammatory disorders and, in particular, vasculitis. The European League Against Rheumatism (EULAR) recommends ^{18}F-FDG PET/CT as an alternative imaging modality in cases of suspected large vessel vasculitis[68,69]. The advantages of ^{18}F-FDG PET/CT are its high sensitivity and the ability to non-invasively quantify inflammatory activity. Semi-quantitative methods of grading FDG uptake have been proposed. Total vascular score (TVS) and PET vascular activity score (PETVAS), have recently been suggested as PET based global inflammatory burden parameters, with potential for differentiation of active *vs* non-active inflammation, predicting relapse and treatment response monitoring in large vessel vasculitis[70,71].

Sollini *et al*[72] recently evaluated the role of ^{18}F-FDG PET/CT in assessing systemic inflammation in 10 patients who had recovered from COVID-19. Significantly higher target-to-blood pool ratio (a quantitative parameter of FDG uptake) was noted in COVID-19 patients, in comparison to controls in three arterial territories – thoracic aorta, right iliac artery, and femoral arteries. This study suggested that COVID-19 induces vascular inflammation, and FDG PET has a potential role for evaluation of whole body vascular inflammatory process[72].

Central nervous system (CNS) vasculitis can occur as a part of systemic vasculitides or as primary angiitis of CNS (PACNS). Viral infections, such as Varicella zoster, hepatitis C virus, West Nile virus, and human immunodeficiency virus (HIV), are known to trigger CNS vasculitis[73]. SARS-CoV-2 infection related vasculitis has also been proposed as a possible mechanism to explain COVID-19 related neurologic dysfunction and encephalopathy with clinical improvement post steroid administration[74]. MR angiography may reveal concentric vessel wall enhancement as a direct sign of regional mural inflammation[75]. However, the majority of the published literature on COVID-19 vasculitis is limited to case reports and case series. Further prospective studies are required to unequivocally establish a causal relationship between SARS-CoV-2 and vasculitis.

NEUROLOGICAL SEQUELAE

Neurological manifestations of COVID-19 can range from mild symptoms like headache, dizziness, and anosmia to more serious complications, such as encephalopathy, posterior reversible encephalopathy syndrome (PRES), acute demyelinating encephalomyelitis (ADEM), cerebrovascular events [including acute ischemic stroke, intracranial hemorrhage (ICH)], cortical vein and/or sinus thrombosis (CVST), and neuro-inflammatory syndromes[76].

Important neuropathological findings in COVID-19 patients include edema, gliosis with diffuse activation of microglia and astrocytes, inflammatory infiltrates, cortical and sub-cortical infarcts, hemorrhagic lesions, and arteriosclerosis. It is hypothesized that they represent a combination of direct cytopathic effects of the virus and indirect effects *via* the host immune-inflammatory response owing to ACE2 and heme dysregulation, along with release of pro-inflammatory cytokines. However, further studies are required to better understand the pathologic mechanisms which drive the neurological manifestations of COVID-19[77-79].

In COVID-19 patients with neurological manifestations, MRI neuroimaging may be performed to detect the underlying casual pathology, particularly if CT reveals no abnormality. The recommended basic MRI protocol includes pre- and post-contrast T1 weighted-images, T2-weighted, fluid-attenuated inversion recovery (FLAIR), diffusion-weighted images, and hemorrhage-sensitive sequences, such as susceptibility weighted imaging (SWI)[80]. The most common neuroimaging manifestations are acute and subacute infarcts with large clot burden, ICH, microhemorrhages, asymmetrical diffuse or tumefactive T2 and FLAIR white matter hyperintensities consistent with ADEM, mesial temporal lobe, corpus callosum, and olfactory bulb involvement, and cranial nerve enhancement[81-83].

Lu *et al*[84] explored the role of diffusion tensor imaging (DTI) and 3D high-resolution T1 weighted sequences in assessing possible disruption of micro-structural and functional brain integrity in the recovery stages of COVID-19. They reported significantly higher bilateral gray matter volumes (GMV) in olfactory cortices, hippocampi, and insulas and changes in MRI-based measures of water diffusion in

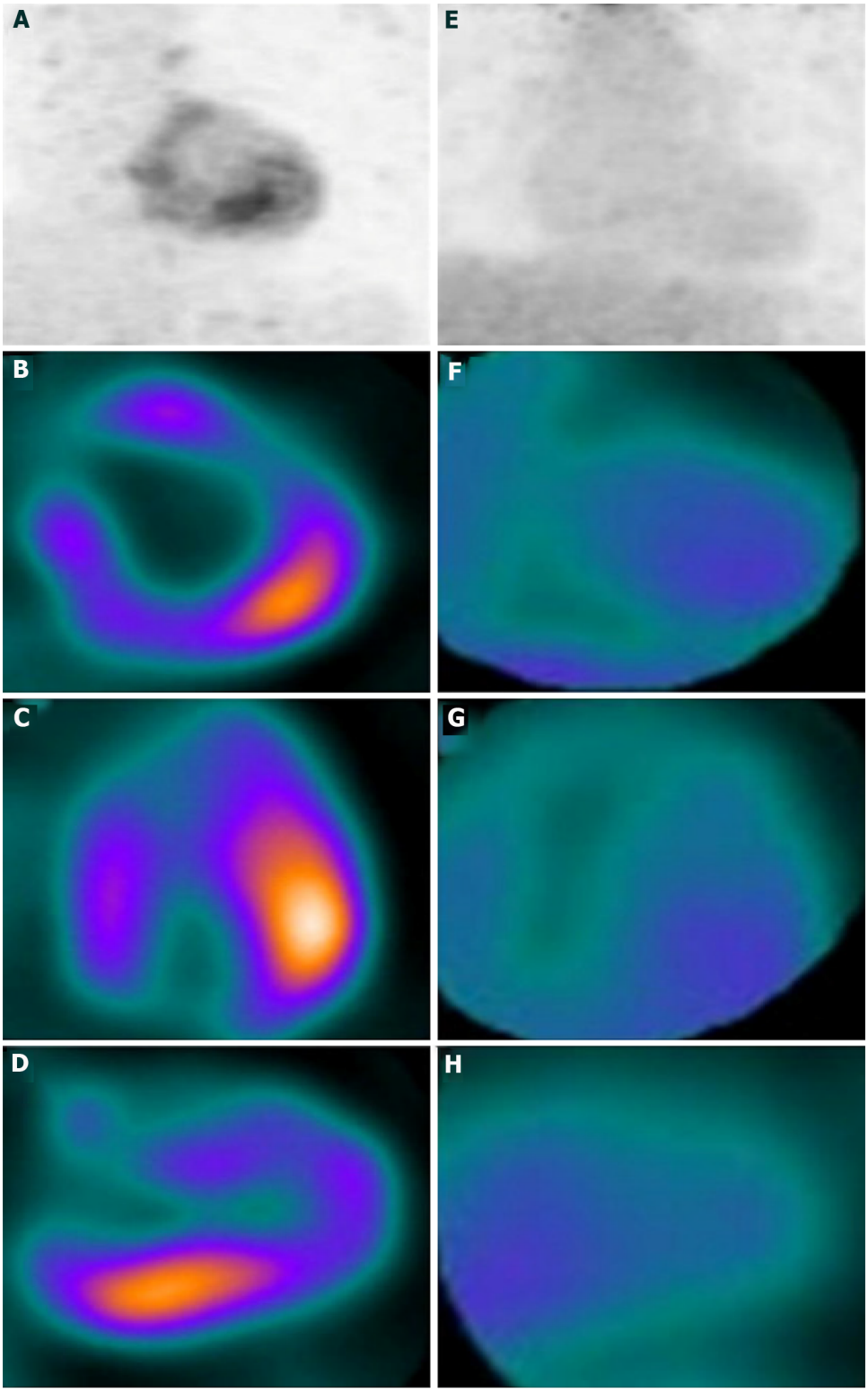

DOI: 10.4329/wjr.v14.i7.194

Figure 4 Coronavirus disease 2019 related myocarditis. A 14-year-old male child underwent regional ^{18}F-fluorodeoxyglucose (FDG) positron emission tomography (PET) to assess myocardial inflammation. Baseline maximum intensity projection (A), short axis (B), horizontal long axis (C), and vertical long axis (D) images showing increased ^{18}F-FDG uptake in the inferolateral wall of the left ventricular myocardium. Corresponding follow-up images (E to H) after 6 wk showing resolution of hypermetabolism in the inferolateral wall with no other FDG avid focus. Citation: Satapathy S, Kumar R, Kavanal AJ, Krishnaraju VS, Ramachandran A, Deo P, Dhir V, Mittal BR. COVID-19 related multisystem inflammatory syndrome in children (MIS-C): Role of ^{18}F-FDG PET/CT to assess myocardial involvement. *J Nucl Cardiol* 2021. Copyright © The Authors 2021. Published by American Society of Nuclear Cardiology.

white matter of COVID-19 patients 3 mo after acute illness compared to age and sex-matched non-COVID controls, suggesting neuro-invasion potential of SARS-CoV-2[84].

High costs, long acquisition times, limited access in developing nations, and lack of specificity of nearly all reported neuroradiological findings in COVID-19 are the major limitations of MRI[85].

Delorme *et al*[86] reported a case series with 4 COVID-19 patients suspected to have autoimmune encephalitis. ^{18}F-FDG PET/CT of the brain demonstrated prefrontal or orbito-frontal cortical hypometabolism and hypermetabolism in the cerebellar vermis. These findings were consistent in all 4 patients, with no specific MRI features nor significant cerebrospinal fluid (CSF) abnormalities, possibly suggesting a parainfectious cytokine storm or immune-mediated mechanism at play rather than direct neural invasion[86].

Similarly, Grimaldi *et al*[87] also reported diffuse cortical hypometabolism with hypermetabolism in the putamen and cerebellum in autoimmune encephalitis concomitant with SARS-CoV-2 infection. These findings, along with normal morphological data on MRI, might suggest reduced neuronal activity and functional alterations in neuro-COVID-19 patients[87]. Increased FDG uptake in the bilateral basal ganglia with T2/FLAIR hyperintensities in the bilateral hippocampi was also reported in a case of SARS-CoV-2 infection related autoimmune limbic encephalitis[88].

Further, ^{18}F-FDG PET has also been used in the evaluation of patients with persistent functional neurological symptoms after apparent recovery from COVID-19. In a retrospective series comprising 35 such patients, ^{18}F-FDG brain PET demonstrated hypometabolism in the bilateral rectal/orbital gyrus, including the olfactory gyrus, connected limbic/paralimbic regions, brainstem, and the bilateral cerebellar hemispheres. This metabolic picture was seen to be associated with the patients' symptoms and could be used to reliably identify these patients from normal controls. Brain inflammation related to the neurotropism of the SARS-CoV-2 from the olfactory bulb has been suggested as a possible mechanism underlying these findings[89].

Few case reports have also highlighted the role of molecular imaging in the evaluation of parkinsonian features post COVID-19. Cohen *et al*[90] reported a case of parkinsonism after SARS-CoV-2 infection in a 45-year-old man. Brain CT, MRI, and EEG were normal. However, ^{18}F-fluorodopa (^{18}F-FDOPA) PET scan revealed decreased radiotracer uptake in both putamina (left > right) and mild decreased uptake in the left caudate nucleus. The authors reported clinical improvement of rigidity and bradykinesia after initiation of pramipexole[90].

Morassi *et al*[91] described consistent findings of diffuse cortical hypometabolism (with relative sparing of sensorimotor areas) associated with hypermetabolism in the brainstem, mesial temporal lobes, and basal ganglia on ^{18}F-FDG PET/CT in two patients with COVID-19 related encephalopathy who developed a rapidly progressive form of atypical parkinsonism. ^{123}I-ioflupane DaT-SPECT performed in one of the two patients showed asymmetrical presynaptic dopaminergic dysfunction in the bilateral putamina, more severe on the left side consistent with a parkinsonian disorder[91].

OTHER RADIO-TRACERS

Scarlattei *et al*[59] have reported incidental findings of ^{68}Ga-labelled prostate-specific membrane antigen (^{68}Ga-PSMA) and ^{18}F-labelled choline (^{18}F-choline) radiotracer uptake in regions corresponding to subpleural GGOs in two patients who underwent PET/CT for evaluation of prostate cancer[59]. Understanding the exact mechanisms that lead to uptake of these radiotracers in acute infective/inflammatory pulmonary lesions offers an important research prospect.

There is ongoing research directed at identifying targets for molecular imaging of inflammation with several novel radiotracers being described in pre-clinical and early clinical studies, such as ^{18}F-AzaFol, ^{89}Zr-labebed Feraheme, and ^{18}F-GE180[92-94].

Further potential targets for new radiotracers include chemokine receptor CXCR4, interleukin IL-6, fibroblast activation protein inhibitors, and inhibitors of the type 1 angiotensin-II receptor ATR1 and ACE2. A radiolabeled ACE2-receptor antagonist has already been developed for autoradiography analysis, setting in motion the potential development of a PET radiotracer[95,96]. Since SARS-CoV-2 spike proteins bind to the ACE2 receptors, novel targeted radiotracers can have potential utility in the drug development process.

LIMITATIONS TO MOLECULAR IMAGING

Widespread utilization of molecular imaging in suspected or confirmed cases of COVID-19 is primarily limited by relatively longer imaging times (in comparison to anatomical imaging with CXR, CT, or USG) and the need for adopting infection control protocols. Further, there is a need for simultaneously ensuring optimal utilization of resources, such as finite amounts of radiotracer, which has economic ramifications. Nuclear medicine departments across the globe have to bear in mind these feasibility issues and ensure undisrupted services to patients with non-COVID-19 related indications, in particular oncological cases in which PET is mandated for crucial treatment decisions[97-99].

To summarize, the present review comprehensively highlights the tremendous potential utility of molecular imaging in evaluation of COVID-19 sequelae such as pulmonary thromboembolism, vasculitis, multi-systemic inflammation, and cardiovascular and neurological sequelae. Despite the fact that the majority of the published literature is retrospective in nature with limited sample sizes, it is clear that molecular imaging provides additional valuable information (complimentary to anatomical imaging) with semi-quantitative or quantitative parameters to define inflammatory burden and can be used to guide therapeutic strategies and assess response. The authors believe that clinical translation and appropriate utilization of molecular imaging and associated imaging biomarkers can greatly benefit both the diagnosis and management of COVID-19 sequelae.

CONCLUSION

The potential of molecular imaging and nuclear medicine as a whole, in contributing to this pandemic largely remains underutilized. Identifying appropriate indications, establishing standardized protocols, and developing structured clinical trials employing novel radiotracers will help in realizing that potential[100].

FOOTNOTES

Author contributions: Chandekar KR wrote the initial draft of the manuscript and prepared the figures; Satapathy S was responsible for idea conception and design of the manuscript; Singh H was in charge of editing the manuscript; and Bhattacharya A provided critical inputs and helped in the final revision.

Conflict-of-interest statement: All authors report no relevant conflicts of interest for this article.

Country/Territory of origin: India

ORCID number: Swayamjeet Satapathy 0000-0001-5318-6644.

S-Editor: Ma YJ
L-Editor: Filipodia
P-Editor: Ma YJ

REFERENCES

1 **Wang C**, Horby PW, Hayden FG, Gao GF. A novel coronavirus outbreak of global health concern. *Lancet* 2020; **395**: 470-473 [PMID: 31986257 DOI: 10.1016/S0140-6736(20)30185-9]
2 **Li Q**, Guan X, Wu P, Wang X, Zhou L, Tong Y, Ren R, Leung KSM, Lau EHY, Wong JY, Xing X, Xiang N, Wu Y, Li C, Chen Q, Li D, Liu T, Zhao J, Liu M, Tu W, Chen C, Jin L, Yang R, Wang Q, Zhou S, Wang R, Liu H, Luo Y, Liu Y, Shao G, Li H, Tao Z, Yang Y, Deng Z, Liu B, Ma Z, Zhang Y, Shi G, Lam TTY, Wu JT, Gao GF, Cowling BJ, Yang B, Leung GM, Feng Z. Early Transmission Dynamics in Wuhan, China, of Novel Coronavirus-Infected Pneumonia. *N Engl J Med* 2020; **382**: 1199-1207 [PMID: 31995857 DOI: 10.1056/NEJMoa2001316]
3 **World Health Organization**. COVID-19 Situation Report. [cited 26 December 2021] Available from: https://www.who.int/docs/default-source/coronaviruse/situation-reports/20200311-sitrep-51-covid-19.pdf?sfvrsn=1ba62e57_10
4 **World Health Organization**. COVID-19 Weekly epidemiological update- 21 December 2021. [cited 26 December 2021] Available from: https://www.who.int/publications/m/item/weekly-epidemiological-update-on-covid-19---21-december-2021
5 **Macera M**, De Angelis G, Sagnelli C, Coppola N; Vanvitelli Covid-Group. Clinical Presentation of COVID-19: Case Series and Review of the Literature. *Int J Environ Res Public Health* 2020; **17** [PMID: 32674450 DOI: 10.3390/ijerph17145062]
6 **Böger B**, Fachi MM, Vilhena RO, Cobre AF, Tonin FS, Pontarolo R. Systematic review with meta-analysis of the accuracy of diagnostic tests for COVID-19. *Am J Infect Control* 2021; **49**: 21-29 [PMID: 32659413 DOI: 10.1016/j.ajic.2020.07.011]
7 **Pourbagheri-Sigaroodi A**, Bashash D, Fateh F, Abolghasemi H. Laboratory findings in COVID-19 diagnosis and prognosis. *Clin Chim Acta* 2020; **510**: 475-482 [PMID: 32798514 DOI: 10.1016/j.cca.2020.08.019]
8 **Simpson S**, Kay FU, Abbara S, Bhalla S, Chung JH, Chung M, Henry TS, Kanne JP, Kligerman S, Ko JP, Litt H.

Radiological Society of North America Expert Consensus Statement on Reporting Chest CT Findings Related to COVID-19. Endorsed by the Society of Thoracic Radiology, the American College of Radiology, and RSNA - Secondary Publication. *J Thorac Imaging* 2020; **35**: 219-227 [PMID: 32324653 DOI: 10.1097/RTI.0000000000000524]

9 **Kooraki S**, Hosseiny M, Myers L, Gholamrezanezhad A. Coronavirus (COVID-19) Outbreak: What the Department of Radiology Should Know. *J Am Coll Radiol* 2020; **17**: 447-451 [PMID: 32092296 DOI: 10.1016/j.jacr.2020.02.008]

10 **Pysz MA**, Gambhir SS, Willmann JK. Molecular imaging: current status and emerging strategies. *Clin Radiol* 2010; **65**: 500-516 [PMID: 20541650 DOI: 10.1016/j.crad.2010.03.011]

11 **Galbán CJ**, Galbán S, Van Dort ME, Luker GD, Bhojani MS, Rehemtulla A, Ross BD. Applications of molecular imaging. *Prog Mol Biol Transl Sci* 2010; **95**: 237-298 [PMID: 21075334 DOI: 10.1016/B978-0-12-385071-3.00009-5]

12 **Wong HYF**, Lam HYS, Fong AH, Leung ST, Chin TW, Lo CSY, Lui MM, Lee JCY, Chiu KW, Chung TW, Lee EYP, Wan EYF, Hung IFN, Lam TPW, Kuo MD, Ng MY. Frequency and Distribution of Chest Radiographic Findings in Patients Positive for COVID-19. *Radiology* 2020; **296**: E72-E78 [PMID: 32216717 DOI: 10.1148/radiol.2020201160]

13 **Sadiq Z**, Rana S, Mahfoud Z, Raoof A. Systematic review and meta-analysis of chest radiograph (CXR) findings in COVID-19. *Clin Imaging* 2021; **80**: 229-238 [PMID: 34364071 DOI: 10.1016/j.clinimag.2021.06.039]

14 **Kim H**, Hong H, Yoon SH. Diagnostic Performance of CT and Reverse Transcriptase Polymerase Chain Reaction for Coronavirus Disease 2019: A Meta-Analysis. *Radiology* 2020; **296**: E145-E155 [PMID: 32301646 DOI: 10.1148/radiol.2020201343]

15 **Bernheim A**, Mei X, Huang M, Yang Y, Fayad ZA, Zhang N, Diao K, Lin B, Zhu X, Li K, Li S, Shan H, Jacobi A, Chung M. Chest CT Findings in Coronavirus Disease-19 (COVID-19): Relationship to Duration of Infection. *Radiology* 2020; **295**: 200463 [PMID: 32077789 DOI: 10.1148/radiol.2020200463]

16 **Raptis CA**, Hammer MM, Short RG, Shah A, Bhalla S, Bierhals AJ, Filev PD, Hope MD, Jeudy J, Kligerman SJ, Henry TS. Chest CT and Coronavirus Disease (COVID-19): A Critical Review of the Literature to Date. *AJR Am J Roentgenol* 2020; **215**: 839-842 [PMID: 32298149 DOI: 10.2214/AJR.20.23202]

17 **Koo HJ**, Lim S, Choe J, Choi SH, Sung H, Do KH. Radiographic and CT Features of Viral Pneumonia. *Radiographics* 2018; **38**: 719-739 [PMID: 29757717 DOI: 10.1148/rg.2018170048]

18 **Lin L**, Fu G, Chen S, Tao J, Qian A, Yang Y, Wang M. CT Manifestations of Coronavirus Disease (COVID-19) Pneumonia and Influenza Virus Pneumonia: A Comparative Study. *AJR Am J Roentgenol* 2021; **216**: 71-79 [PMID: 32755175 DOI: 10.2214/AJR.20.23304]

19 **Demirjian NL**, Fields BKK, Gholamrezanezhad A. Role of Chest CT in Resource-Driven Healthcare Systems. *AJR Am J Roentgenol* 2020; **215**: W36 [PMID: 32755173 DOI: 10.2214/AJR.20.23498]

20 **Rubin GD**, Ryerson CJ, Haramati LB, Sverzellati N, Kanne JP, Raoof S, Schluger NW, Volpi A, Yim JJ, Martin IBK, Anderson DJ, Kong C, Altes T, Bush A, Desai SR, Goldin J, Goo JM, Humbert M, Inoue Y, Kauczor HU, Luo F, Mazzone PJ, Prokop M, Remy-Jardin M, Richeldi L, Schaefer-Prokop CM, Tomiyama N, Wells AU, Leung AN. The Role of Chest Imaging in Patient Management During the COVID-19 Pandemic: A Multinational Consensus Statement From the Fleischner Society. *Chest* 2020; **158**: 106-116 [PMID: 32275978 DOI: 10.1016/j.chest.2020.04.003]

21 **American College of Radiology**. ACR Recommendations for the use of Chest Radiography and Computed Tomography (CT) for Suspected COVID-19 Infection | American College of Radiology. 2020. Available from: https://www.acr.org/Advocacy-and-Economics/ACR-Position-Statements/Recommendations-for-Chest-Radiography-and-CT-for-Suspected-COVID19-Infection

22 **Prokop M**, van Everdingen W, van Rees Vellinga T, Quarles van Ufford H, Stöger L, Beenen L, Geurts B, Gietema H, Krdzalic J, Schaefer-Prokop C, van Ginneken B, Brink M; COVID-19 Standardized Reporting Working Group of the Dutch Radiological Society. CO-RADS: A Categorical CT Assessment Scheme for Patients Suspected of Having COVID-19-Definition and Evaluation. *Radiology* 2020; **296**: E97-E104 [PMID: 32339082 DOI: 10.1148/radiol.2020201473]

23 **Yang R**, Li X, Liu H, Zhen Y, Zhang X, Xiong Q, Luo Y, Gao C, Zeng W. Chest CT Severity Score: An Imaging Tool for Assessing Severe COVID-19. *Radiol Cardiothorac Imaging* 2020; **2**: e200047 [PMID: 33778560 DOI: 10.1148/ryct.2020200047]

24 **Francone M**, Iafrate F, Masci GM, Coco S, Cilia F, Manganaro L, Panebianco V, Andreoli C, Colaiacomo MC, Zingaropoli MA, Ciardi MR, Mastroianni CM, Pugliese F, Alessandri F, Turriziani O, Ricci P, Catalano C. Chest CT score in COVID-19 patients: correlation with disease severity and short-term prognosis. *Eur Radiol* 2020; **30**: 6808-6817 [PMID: 32623505 DOI: 10.1007/s00330-020-07033-y]

25 **Lieveld AWE**, Azijli K, Teunissen BP, van Haaften RM, Kootte RS, van den Berk IAH, van der Horst SFB, de Gans C, van de Ven PM, Nanayakkara PWB. Chest CT in COVID-19 at the ED: Validation of the COVID-19 Reporting and Data System (CO-RADS) and CT Severity Score: A Prospective, Multicenter, Observational Study. *Chest* 2021; **159**: 1126-1135 [PMID: 33271157 DOI: 10.1016/j.chest.2020.11.026]

26 **Inciardi RM**, Lupi L, Zaccone G, Italia L, Raffo M, Tomasoni D, Cani DS, Cerini M, Farina D, Gavazzi E, Maroldi R, Adamo M, Ammirati E, Sinagra G, Lombardi CM, Metra M. Cardiac Involvement in a Patient With Coronavirus Disease 2019 (COVID-19). *JAMA Cardiol* 2020; **5**: 819-824 [PMID: 32219357 DOI: 10.1001/jamacardio.2020.1096]

27 **Ates OF**, Taydas O, Dheir H. Thorax Magnetic Resonance Imaging Findings in Patients with Coronavirus Disease (COVID-19). *Acad Radiol* 2020; **27**: 1373-1378 [PMID: 32830031 DOI: 10.1016/j.acra.2020.08.009]

28 **Caro-Dominguez P**, Shelmerdine SC, Toso S, Secinaro A, Toma P, Damasio MB, Navallas M, Riaza-Martin L, Gomez-Pastrana D, Ghadimi Mahani M, Desoky SM, Ugas Charcape CF, Almanza-Aranda J, Ucar ME, Lovrenski J, Gorkem SB, Alexopoulou E, Ciet P, van Schuppen J, Ducou le Pointe H, Goo HW, Kellenberger CJ, Raissaki M, Owens CM, Hirsch FW, van Rijn RR; Collaborators of the European Society of Paediatric Radiology Cardiothoracic Task Force. Thoracic imaging of coronavirus disease 2019 (COVID-19) in children: a series of 91 cases. *Pediatr Radiol* 2020; **50**: 1354-1368 [PMID: 32749530 DOI: 10.1007/s00247-020-04747-5]

29 **Peng QY**, Wang XT, Zhang LN; Chinese Critical Care Ultrasound Study Group (CCUSG). Findings of lung ultrasonography of novel corona virus pneumonia during the 2019-2020 epidemic. *Intensive Care Med* 2020; **46**: 849-850 [PMID: 32166346 DOI: 10.1007/s00134-020-05996-6]

30 **Amatya Y**, Rupp J, Russell FM, Saunders J, Bales B, House DR. Diagnostic use of lung ultrasound compared to chest

radiograph for suspected pneumonia in a resource-limited setting. *Int J Emerg Med* 2018; **11**: 8 [PMID: 29527652 DOI: 10.1186/s12245-018-0170-2]

31 **James ML**, Gambhir SS. A molecular imaging primer: modalities, imaging agents, and applications. *Physiol Rev* 2012; **92**: 897-965 [PMID: 22535898 DOI: 10.1152/physrev.00049.2010]

32 **Lodigiani C**, Iapichino G, Carenzo L, Cecconi M, Ferrazzi P, Sebastian T, Kucher N, Studt JD, Sacco C, Bertuzzi A, Sandri MT, Barco S; Humanitas COVID-19 Task Force. Venous and arterial thromboembolic complications in COVID-19 patients admitted to an academic hospital in Milan, Italy. *Thromb Res* 2020; **191**: 9-14 [PMID: 32353746 DOI: 10.1016/j.thromres.2020.04.024]

33 **Tan BK**, Mainbourg S, Friggeri A, Bertoletti L, Douplat M, Dargaud Y, Grange C, Lobbes H, Provencher S, Lega JC. Arterial and venous thromboembolism in COVID-19: a study-level meta-analysis. *Thorax* 2021; **76**: 970-979 [PMID: 33622981 DOI: 10.1136/thoraxjnl-2020-215383]

34 **Klok FA**, Kruip MJHA, van der Meer NJM, Arbous MS, Gommers DAMPJ, Kant KM, Kaptein FHJ, van Paassen J, Stals MAM, Huisman MV, Endeman H. Incidence of thrombotic complications in critically ill ICU patients with COVID-19. *Thromb Res* 2020; **191**: 145-147 [PMID: 32291094 DOI: 10.1016/j.thromres.2020.04.013]

35 **Nicolai L**, Leunig A, Brambs S, Kaiser R, Weinberger T, Weigand M, Muenchhoff M, Hellmuth JC, Ledderose S, Schulz H, Scherer C, Rudelius M, Zoller M, Höchter D, Keppler O, Teupser D, Zwißler B, von Bergwelt-Baildon M, Kääb S, Massberg S, Pekayvaz K, Stark K. Immunothrombotic Dysregulation in COVID-19 Pneumonia Is Associated With Respiratory Failure and Coagulopathy. *Circulation* 2020; **142**: 1176-1189 [PMID: 32755393 DOI: 10.1161/CIRCULATIONAHA.120.048488]

36 **Overstad S**, Tjonnfjord E, Garabet L, Fronas S, Bergan J, Aballi S, Ghanima W. Venous thromboembolism and coronavirus disease 2019 in an ambulatory care setting - A report of 4 cases. *Thromb Res* 2020; **194**: 116-118 [PMID: 32788102 DOI: 10.1016/j.thromres.2020.06.032]

37 **Wichmann D**, Sperhake JP, Lütgehetmann M, Steurer S, Edler C, Heinemann A, Heinrich F, Mushumba H, Kniep I, Schröder AS, Burdelski C, de Heer G, Nierhaus A, Frings D, Pfefferle S, Becker H, Bredereke-Wiedling H, de Weerth A, Paschen HR, Sheikhzadeh-Eggers S, Stang A, Schmiedel S, Bokemeyer C, Addo MM, Aepfelbacher M, Püschel K, Kluge S. Autopsy Findings and Venous Thromboembolism in Patients With COVID-19: A Prospective Cohort Study. *Ann Intern Med* 2020; **173**: 268-277 [PMID: 32374815 DOI: 10.7326/M20-2003]

38 **Gopalan D**, Delcroix M, Held M. Diagnosis of chronic thromboembolic pulmonary hypertension. *Eur Respir Rev* 2017; **26** [PMID: 28298387 DOI: 10.1183/16000617.0108-2016]

39 **Carrier M**, Righini M, Wells PS, Perrier A, Anderson DR, Rodger MA, Pleasance S, Le Gal G. Subsegmental pulmonary embolism diagnosed by computed tomography: incidence and clinical implications. A systematic review and meta-analysis of the management outcome studies. *J Thromb Haemost* 2010; **8**: 1716-1722 [PMID: 20546118 DOI: 10.1111/j.1538-7836.2010.03938.x]

40 **van Dam LF**, Kroft LJM, van der Wal LI, Cannegieter SC, Eikenboom J, de Jonge E, Huisman MV, Klok FA. Clinical and computed tomography characteristics of COVID-19 associated acute pulmonary embolism: A different phenotype of thrombotic disease? *Thromb Res* 2020; **193**: 86-89 [PMID: 32531548 DOI: 10.1016/j.thromres.2020.06.010]

41 **Cavagna E**, Muratore F, Ferrari F. Pulmonary Thromboembolism in COVID-19: Venous Thromboembolism or Arterial Thrombosis? *Radiol Cardiothorac Imaging* 2020; **2**: e200289 [PMID: 33778609 DOI: 10.1148/ryct.2020200289]

42 **Dhawan RT**, Gopalan D, Howard L, Vicente A, Park M, Manalan K, Wallner I, Marsden P, Dave S, Branley H, Russell G, Dharmarajah N, Kon OM. Beyond the clot: perfusion imaging of the pulmonary vasculature after COVID-19. *Lancet Respir Med* 2021; **9**: 107-116 [PMID: 33217366 DOI: 10.1016/S2213-2600(20)30407-0]

43 **Zuckier LS**, Moadel RM, Haramati LB, Freeman LM. Diagnostic Evaluation of Pulmonary Embolism During the COVID-19 Pandemic. *J Nucl Med* 2020; **61**: 630-631 [PMID: 32238427 DOI: 10.2967/jnumed.120.245571]

44 **McFarland GA**, Johnson SG. Nuclear Medicine Clinical Practice in the United States During the COVID-19 Era and Beyond. *J Nucl Med Technol* 2020; **48**: 218-226 [PMID: 32709666 DOI: 10.2967/jnmt.120.253245]

45 **Narechania S**, Renapurkar R, Heresi GA. Mimickers of chronic thromboembolic pulmonary hypertension on imaging tests: a review. *Pulm Circ* 2020; **10**: 2045894019882620 [PMID: 32257112 DOI: 10.1177/2045894019882620]

46 **Gutte H**, Mortensen J, Jensen CV, Johnbeck CB, von der Recke P, Petersen CL, Kjaergaard J, Kristoffersen US, Kjaer A. Detection of pulmonary embolism with combined ventilation-perfusion SPECT and low-dose CT: head-to-head comparison with multidetector CT angiography. *J Nucl Med* 2009; **50**: 1987-1992 [PMID: 19910421 DOI: 10.2967/jnumed.108.061606]

47 **Bhatia KD**, Ambati C, Dhaliwal R, Paschkewitz R, Hsu E, Ho B, Young A, Emmett L. SPECT-CT/VQ versus CTPA for diagnosing pulmonary embolus and other lung pathology: Pre-existing lung disease should not be a contraindication. *J Med Imaging Radiat Oncol* 2016; **60**: 492-497 [PMID: 27461384 DOI: 10.1111/1754-9485.12471]

48 **Das JP**, Yeh R, Schöder H. Clinical utility of perfusion (Q)-single-photon emission computed tomography (SPECT)/CT for diagnosing pulmonary embolus (PE) in COVID-19 patients with a moderate to high pre-test probability of PE. *Eur J Nucl Med Mol Imaging* 2021; **48**: 794-799 [PMID: 32959115 DOI: 10.1007/s00259-020-05043-y]

49 **Giovanella L**, Ruggeri RM, Petranović Ovčariček P, Campenni A, Treglia G, Deandreis D. SARS-CoV-2-related thyroid disorders: a synopsis for nuclear medicine thyroidologists. *Eur J Nucl Med Mol Imaging* 2021; **48**: 1719-1723 [PMID: 33765218 DOI: 10.1007/s00259-021-05316-0]

50 **Rotondi M**, Coperchini F, Ricci G, Denegri M, Croce L, Ngnitejeu ST, Villani L, Magri F, Latrofa F, Chiovato L. Detection of SARS-COV-2 receptor ACE-2 mRNA in thyroid cells: a clue for COVID-19-related subacute thyroiditis. *J Endocrinol Invest* 2021; **44**: 1085-1090 [PMID: 33025553 DOI: 10.1007/s40618-020-01436-w]

51 **Basu S**, Alavi A. Unparalleled contribution of 18F-FDG PET to medicine over 3 decades. *J Nucl Med* 2008; **49**: 17N-21N, 37N [PMID: 18832112]

52 **Hess S**, Blomberg BA, Zhu HJ, Høilund-Carlsen PF, Alavi A. The pivotal role of FDG-PET/CT in modern medicine. *Acad Radiol* 2014; **21**: 232-249 [PMID: 24439337 DOI: 10.1016/j.acra.2013.11.002]

53 **Basu S**, Zhuang H, Torigian DA, Rosenbaum J, Chen W, Alavi A. Functional imaging of inflammatory diseases using nuclear medicine techniques. *Semin Nucl Med* 2009; **39**: 124-145 [PMID: 19187805 DOI:

10.1053/j.semnuclmed.2008.10.006]
54 **Katal S**, Amini H, Gholamrezanezhad A. PET in the diagnostic management of infectious/inflammatory pulmonary pathologies: a revisit in the era of COVID-19. *Nucl Med Commun* 2021; **42**: 3-8 [PMID: 32991395 DOI: 10.1097/MNM.0000000000001299]
55 **Kung BT**, Seraj SM, Zadeh MZ, Rojulpote C, Kothekar E, Ayubcha C, Ng KS, Ng KK, Au-Yong TK, Werner TJ, Zhuang H, Hunt SJ, Hess S, Alavi A. An update on the role of ^{18}F-FDG-PET/CT in major infectious and inflammatory diseases. *Am J Nucl Med Mol Imaging* 2019; **9**: 255-273 [PMID: 31976156]
56 **Albano D**, Bertagna F, Bertoli M, Bosio G, Lucchini S, Motta F, Panarotto MB, Peli A, Camoni L, Bengel FM, Giubbini R. Incidental Findings Suggestive of COVID-19 in Asymptomatic Patients Undergoing Nuclear Medicine Procedures in a High-Prevalence Region. *J Nucl Med* 2020; **61**: 632-636 [PMID: 32238429 DOI: 10.2967/jnumed.120.246256]
57 **Amini H**, Divband G, Montahaei Z, Dehghani T, Kaviani H, Adinehpour Z, Akbarian Aghdam R, Rezaee A, Vali R. A case of COVID-19 lung infection first detected by [18F]FDG PET-CT. *Eur J Nucl Med Mol Imaging* 2020; **47**: 1771-1772 [PMID: 32333071 DOI: 10.1007/s00259-020-04821-y]
58 **Setti L**, Kirienko M, Dalto SC, Bonacina M, Bombardieri E. FDG-PET/CT findings highly suspicious for COVID-19 in an Italian case series of asymptomatic patients. *Eur J Nucl Med Mol Imaging* 2020; **47**: 1649-1656 [PMID: 32342191 DOI: 10.1007/s00259-020-04819-6]
59 **Scarlattei M**, Baldari G, Silva M, Bola S, Sammartano A, Migliari S, Graziani T, Cidda C, Sverzellati N, Ruffini L. Unknown SARS-CoV-2 pneumonia detected by PET/CT in patients with cancer. *Tumori* 2020; **106**: 325-332 [PMID: 32567505 DOI: 10.1177/0300891620935983]
60 **Mattoli MV**, Taralli S, Pennese E, D'Angelo C, Angrilli F, Villano C. Atypical Presentation of COVID-19 Incidentally Detected at 18F-FDG PET/CT in an Asymptomatic Oncological Patient. *Clin Nucl Med* 2020; **45**: e383-e385 [PMID: 32520513 DOI: 10.1097/RLU.0000000000003175]
61 **Tang YW**, Schmitz JE, Persing DH, Stratton CW. Laboratory Diagnosis of COVID-19: Current Issues and Challenges. *J Clin Microbiol* 2020; **58** [PMID: 32245835 DOI: 10.1128/JCM.00512-20]
62 **Qin C**, Liu F, Yen TC, Lan X. ^{18}F-FDG PET/CT findings of COVID-19: a series of four highly suspected cases. *Eur J Nucl Med Mol Imaging* 2020; **47**: 1281-1286 [PMID: 32088847 DOI: 10.1007/s00259-020-04734-w]
63 **Treglia G**. The role of ^{18}F-FDG PET for COVID-19 infection: myth versus reality. *Clin Transl Imaging* 2020; **8**: 125-126 [PMID: 32355659 DOI: 10.1007/s40336-020-00367-z]
64 **Kang Y**, Chen T, Mui D, Ferrari V, Jagasia D, Scherrer-Crosbie M, Chen Y, Han Y. Cardiovascular manifestations and treatment considerations in COVID-19. *Heart* 2020; **106**: 1132-1141 [PMID: 32354800 DOI: 10.1136/heartjnl-2020-317056]
65 **Nishiga M**, Wang DW, Han Y, Lewis DB, Wu JC. COVID-19 and cardiovascular disease: from basic mechanisms to clinical perspectives. *Nat Rev Cardiol* 2020; **17**: 543-558 [PMID: 32690910 DOI: 10.1038/s41569-020-0413-9]
66 **Yousefi-Koma A**, Naghashzadeh F, Figtree GA, Patel S, Karimi Galougahi K. Multi-modality imaging of inflammation and ischemia for assessment of myocardial injury in Covid-19. *J Nucl Cardiol* 2021; **28**: 3100-3103 [PMID: 32562192 DOI: 10.1007/s12350-020-02233-x]
67 **Satapathy S**, Kumar R, Kavanal AJ, Krishnaraju VS, Ramachandran A, Deo P, Dhir V, Mittal BR. COVID-19 related multisystem inflammatory syndrome in children (MIS-C): Role of ^{18}F-FDG PET/CT to assess myocardial involvement. *J Nucl Cardiol* 2021 [PMID: 33624189 DOI: 10.1007/s12350-021-02540-x]
68 **Slart RHJA**; Writing group; Reviewer group; Members of EANM Cardiovascular; Members of EANM Infection & Inflammation; Members of Committees, SNMMI Cardiovascular; Members of Council, PET Interest Group; Members of ASNC; EANM Committee Coordinator. FDG-PET/CT(A) imaging in large vessel vasculitis and polymyalgia rheumatica: joint procedural recommendation of the EANM, SNMMI, and the PET Interest Group (PIG), and endorsed by the ASNC. *Eur J Nucl Med Mol Imaging* 2018; **45**: 1250-1269 [PMID: 29637252 DOI: 10.1007/s00259-018-3973-8]
69 **Dejaco C**, Ramiro S, Duftner C, Besson FL, Bley TA, Blockmans D, Brouwer E, Cimmino MA, Clark E, Dasgupta B, Diamantopoulos AP, Direskeneli H, Iagnocco A, Klink T, Neill L, Ponte C, Salvarani C, Slart RHJA, Whitlock M, Schmidt WA. EULAR recommendations for the use of imaging in large vessel vasculitis in clinical practice. *Ann Rheum Dis* 2018; **77**: 636-643 [PMID: 29358285 DOI: 10.1136/annrheumdis-2017-212649]
70 **Kang F**, Han Q, Zhou X, Zheng Z, Wang S, Ma W, Zhang K, Quan Z, Yang W, Wang J, Zhu P. Performance of the PET vascular activity score (PETVAS) for qualitative and quantitative assessment of inflammatory activity in Takayasu's arteritis patients. *Eur J Nucl Med Mol Imaging* 2020; **47**: 3107-3117 [PMID: 32567005 DOI: 10.1007/s00259-020-04871-2]
71 **Blockmans D**, de Ceuninck L, Vanderschueren S, Knockaert D, Mortelmans L, Bobbaers H. Repetitive 18F-fluorodeoxyglucose positron emission tomography in giant cell arteritis: a prospective study of 35 patients. *Arthritis Rheum* 2006; **55**: 131-137 [PMID: 16463425 DOI: 10.1002/art.21699]
72 **Sollini M**, Ciccarelli M, Cecconi M, Aghemo A, Morelli P, Gelardi F, Chiti A. Vasculitis changes in COVID-19 survivors with persistent symptoms: an [^{18}F]FDG-PET/CT study. *Eur J Nucl Med Mol Imaging* 2021; **48**: 1460-1466 [PMID: 33123760 DOI: 10.1007/s00259-020-05084-3]
73 **Mansueto G**, Lanza G, Fisicaro F, Alaouieh D, Hong E, Girolami S, Montella M, Feola A, Di Napoli M. Central and Peripheral Nervous System Complications of Vasculitis Syndromes From Pathology to Bedside: Part 1-Central Nervous System. *Curr Neurol Neurosci Rep* 2022; **22**: 47-69 [PMID: 35138587 DOI: 10.1007/s11910-022-01172-z]
74 **Vaschetto R**, Cena T, Sainaghi PP, Meneghetti G, Bazzano S, Vecchio D, Pirisi M, Brustia D, Barini M, Cammarota G, Castello L, Della Corte F. Cerebral nervous system vasculitis in a Covid-19 patient with pneumonia. *J Clin Neurosci* 2020; **79**: 71-73 [PMID: 33070922 DOI: 10.1016/j.jocn.2020.07.032]
75 **Lersy F**, Anheim M, Willaume T, Chammas A, Brisset JC, Cotton F, Kremer S. Cerebral vasculitis of medium-sized vessels as a possible mechanism of brain damage in COVID-19 patients. *J Neuroradiol* 2021; **48**: 141-146 [PMID: 33340640 DOI: 10.1016/j.neurad.2020.11.004]
76 **Whittaker A**, Anson M, Harky A. Neurological Manifestations of COVID-19: A systematic review and current update. *Acta Neurol Scand* 2020; **142**: 14-22 [PMID: 32412088 DOI: 10.1111/ane.13266]

77 **Fisicaro F**, Di Napoli M, Liberto A, Fanella M, Di Stasio F, Pennisi M, Bella R, Lanza G, Mansueto G. Neurological Sequelae in Patients with COVID-19: A Histopathological Perspective. *Int J Environ Res Public Health* 2021; **18** [PMID: 33546463 DOI: 10.3390/ijerph18041415]

78 **Pajo AT**, Espiritu AI, Apor ADAO, Jamora RDG. Neuropathologic findings of patients with COVID-19: a systematic review. *Neurol Sci* 2021; **42**: 1255-1266 [PMID: 33483885 DOI: 10.1007/s10072-021-05068-7]

79 **Cosentino G**, Todisco M, Hota N, Della Porta G, Morbini P, Tassorelli C, Pisani A. Neuropathological findings from COVID-19 patients with neurological symptoms argue against a direct brain invasion of SARS-CoV-2: A critical systematic review. *Eur J Neurol* 2021; **28**: 3856-3865 [PMID: 34339563 DOI: 10.1111/ene.15045]

80 **Kremer S**, Gerevini S, Ramos A, Lersy F, Yousry T, Vernooij MW, Anzalone N, Jäger HR. Neuroimaging in patients with COVID-19: a neuroradiology expert group consensus. *Eur Radiol* 2022; **32**: 3716-3725 [PMID: 35044509 DOI: 10.1007/s00330-021-08499-0]

81 **Kremer S**, Lersy F, de Sèze J, Ferré JC, Maamar A, Carsin-Nicol B, Collange O, Bonneville F, Adam G, Martin-Blondel G, Rafiq M, Geeraerts T, Delamarre L, Grand S, Krainik A, Caillard S, Constans JM, Metanbou S, Heintz A, Helms J, Schenck M, Lefèbvre N, Boutet C, Fabre X, Forestier G, de Beaurepaire I, Bornet G, Lacalm A, Oesterlé H, Bolognini F, Messié J, Hmeydia G, Benzakoun J, Oppenheim C, Bapst B, Megdiche I, Henry Feugeas MC, Khalil A, Gaudemer A, Jager L, Nesser P, Talla Mba Y, Hemmert C, Feuerstein P, Sebag N, Carré S, Alleg M, Lecocq C, Schmitt E, Anxionnat R, Zhu F, Comby PO, Ricolfi F, Thouant P, Desal H, Boulouis G, Berge J, Kazémi A, Pyatigorskaya N, Lecler A, Saleme S, Edjlali-Goujon M, Kerleroux B, Zorn PE, Matthieu M, Baloglu S, Ardellier FD, Willaume T, Brisset JC, Boulay C, Mutschler V, Hansmann Y, Mertes PM, Schneider F, Fafi-Kremer S, Ohana M, Meziani F, David JS, Meyer N, Anheim M, Cotton F. Brain MRI Findings in Severe COVID-19: A Retrospective Observational Study. *Radiology* 2020; **297**: E242-E251 [PMID: 32544034 DOI: 10.1148/radiol.2020202222]

82 **Gulko E**, Oleksk ML, Gomes W, Ali S, Mehta H, Overby P, Al-Mufti F, Rozenshtein A. MRI Brain Findings in 126 Patients with COVID-19: Initial Observations from a Descriptive Literature Review. *AJNR Am J Neuroradiol* 2020; **41**: 2199-2203 [PMID: 32883670 DOI: 10.3174/ajnr.A6805]

83 **Moonis G**, Filippi CG, Kirsch CFE, Mohan S, Stein EG, Hirsch JA, Mahajan A. The Spectrum of Neuroimaging Findings on CT and MRI in Adults With COVID-19. *AJR Am J Roentgenol* 2021; **217**: 959-974 [PMID: 33236647 DOI: 10.2214/AJR.20.24839]

84 **Lu Y**, Li X, Geng D, Mei N, Wu PY, Huang CC, Jia T, Zhao Y, Wang D, Xiao A, Yin B. Cerebral Micro-Structural Changes in COVID-19 Patients - An MRI-based 3-month Follow-up Study. *EClinicalMedicine* 2020; **25**: 100484 [PMID: 32838240 DOI: 10.1016/j.eclinm.2020.100484]

85 **Sklinda K**, Dorobek M, Wasilewski PG, Drężewski K, Dębicka M, Walecki J, Mruk B. Radiological Manifestation of Neurological Complications in the Course of SARS-CoV-2 Infection. *Front Neurol* 2021; **12**: 711026 [PMID: 34744963 DOI: 10.3389/fneur.2021.711026]

86 **Delorme C**, Paccoud O, Kas A, Hesters A, Bombois S, Shambrook P, Boullet A, Doukhi D, Le Guennec L, Godefroy N, Maatoug R, Fossati P, Millet B, Navarro V, Bruneteau G, Demeret S, Pourcher V; CoCo-Neurosciences study group and COVID SMIT PSL study group. COVID-19-related encephalopathy: a case series with brain FDG-positron-emission tomography/computed tomography findings. *Eur J Neurol* 2020; **27**: 2651-2657 [PMID: 32881133 DOI: 10.1111/ene.14478]

87 **Grimaldi S**, Lagarde S, Harlé JR, Boucraut J, Guedj E. Autoimmune Encephalitis Concomitant with SARS-CoV-2 Infection: Insight from ^{18}F-FDG PET Imaging and Neuronal Autoantibodies. *J Nucl Med* 2020; **61**: 1726-1729 [PMID: 32709734 DOI: 10.2967/jnumed.120.249292]

88 **Pizzanelli C**, Milano C, Canovetti S, Tagliaferri E, Turco F, Verdenelli S, Nesti L, Franchi M, Bonanni E, Menichetti F, Volterrani D, Cosottini M, Siciliano G. Autoimmune limbic encephalitis related to SARS-CoV-2 infection: Case-report and review of the literature. *Brain Behav Immun Health* 2021; **12**: 100210 [PMID: 33521691 DOI: 10.1016/j.bbih.2021.100210]

89 **Guedj E**, Campion JY, Dudouet P, Kaphan E, Bregeon F, Tissot-Dupont H, Guis S, Barthelemy F, Habert P, Ceccaldi M, Million M, Raoult D, Cammilleri S, Eldin C. ^{18}F-FDG brain PET hypometabolism in patients with long COVID. *Eur J Nucl Med Mol Imaging* 2021; **48**: 2823-2833 [PMID: 33501506 DOI: 10.1007/s00259-021-05215-4]

90 **Cohen ME**, Eichel R, Steiner-Birmanns B, Janah A, Ioshpa M, Bar-Shalom R, Paul JJ, Gaber H, Skrahina V, Bornstein NM, Yahalom G. A case of probable Parkinson's disease after SARS-CoV-2 infection. *Lancet Neurol* 2020; **19**: 804-805 [PMID: 32949534 DOI: 10.1016/S1474-4422(20)30305-7]

91 **Morassi M**, Palmerini F, Nici S, Magni E, Savelli G, Guerra UP, Chieregato M, Morbelli S, Vogrig A. SARS-CoV-2-related encephalitis with prominent parkinsonism: clinical and FDG-PET correlates in two patients. *J Neurol* 2021; **268**: 3980-3987 [PMID: 33884450 DOI: 10.1007/s00415-021-10560-3]

92 **Müller C**, Schibli R, Maurer B. Can Nuclear Imaging of Activated Macrophages with Folic Acid-Based Radiotracers Serve as a Prognostic Means to Identify COVID-19 Patients at Risk? *Pharmaceuticals (Basel)* 2020; **13** [PMID: 32916949 DOI: 10.3390/ph13090238]

93 **Iking J**, Staniszewska M, Kessler L, Klose JM, Lückerath K, Fendler WP, Herrmann K, Rischpler C. Imaging Inflammation with Positron Emission Tomography. *Biomedicines* 2021; **9** [PMID: 33669804 DOI: 10.3390/biomedicines9020212]

94 **Fan Z**, Calsolaro V, Atkinson RA, Femminella GD, Waldman A, Buckley C, Trigg W, Brooks DJ, Hinz R, Edison P. Flutriciclamide (18F-GE180) PET: First-in-Human PET Study of Novel Third-Generation In Vivo Marker of Human Translocator Protein. *J Nucl Med* 2016; **57**: 1753-1759 [PMID: 27261523 DOI: 10.2967/jnumed.115.169078]

95 **Fung SY**, Yuen KS, Ye ZW, Chan CP, Jin DY. A tug-of-war between severe acute respiratory syndrome coronavirus 2 and host antiviral defence: lessons from other pathogenic viruses. *Emerg Microbes Infect* 2020; **9**: 558-570 [PMID: 32172672 DOI: 10.1080/22221751.2020.1736644]

96 **Linares A**, Couling LE, Carrera EJ, Speth RC. Receptor Autoradiography Protocol for the Localized Visualization of Angiotensin II Receptors. *J Vis Exp* 2016 [PMID: 27341008 DOI: 10.3791/53866]

97 **Czernin J**, Fanti S, Meyer PT, Allen-Auerbach M, Hacker M, Sathekge M, Hicks R, Scott AM, Hatazawa J, Yun M,

Schöder H, Bartenstein P, Herrmann K. Nuclear Medicine Operations in the Times of COVID-19: Strategies, Precautions, and Experiences. *J Nucl Med* 2020; **61**: 626-629 [PMID: 32238430 DOI: 10.2967/jnumed.120.245738]

98 **Azam SA**, Myers L, Fields BKK, Demirjian NL, Patel D, Roberge E, Gholamrezanezhad A, Reddy S. Coronavirus disease 2019 (COVID-19) pandemic: Review of guidelines for resuming non-urgent imaging and procedures in radiology during Phase II. *Clin Imaging* 2020; **67**: 30-36 [PMID: 32512479 DOI: 10.1016/j.clinimag.2020.05.032]

99 **Nakajima K**, Kato H, Yamashiro T, Izumi T, Takeuchi I, Nakajima H, Utsunomiya D. COVID-19 pneumonia: infection control protocol inside computed tomography suites. *Jpn J Radiol* 2020; **38**: 391-393 [PMID: 32185669 DOI: 10.1007/s11604-020-00948-y]

100 **Juengling FD**, Maldonado A, Wuest F, Schindler TH. The Role of Nuclear Medicine for COVID-19: Time to Act Now. *J Nucl Med* 2020; **61**: 781-782 [PMID: 32303597 DOI: 10.2967/jnumed.120.246611]

World Journal of Radiology

Submit a Manuscript: https://www.f6publishing.com

World J Radiol 2022 July 28; 14(7): 209-218

DOI: 10.4329/wjr.v14.i7.209

ISSN 1949-8470 (online)

MINIREVIEWS

Radiological review of rhinocerebral mucormycosis cases during the COVID-19 Pandemic: A single-center experience

P S Saneesh, Satya Chowdary Morampudi, Raghav Yelamanchi

Specialty type: Radiology, nuclear medicine and medical imaging

Provenance and peer review: Invited article; Externally peer reviewed.

Peer-review model: Single blind

Peer-review report's scientific quality classification

Grade A (Excellent): A
Grade B (Very good): 0
Grade C (Good): C
Grade D (Fair): D
Grade E (Poor): 0

P-Reviewer: Chavan RP, India; Fan YW, China; Roushdy TM, Egypt

Received: March 28, 2022
Peer-review started: March 28, 2022
First decision: May 12, 2022
Revised: June 9, 2022
Accepted: July 18, 2022
Article in press: July 18, 2022
Published online: July 28, 2022

P S Saneesh, Department of Radiology, Aster MIMS, Kannur 670007, Kerala, India

Satya Chowdary Morampudi, Department of Radiodiagnosis, Pinnamaneni Siddhartha Institute of Medical Sciences & Research Foundation, Gannavaram 521101, Andhra Pradesh, India

Raghav Yelamanchi, Department of Surgery, Atal Bihari Vajpayee Institute of Medical Sciences and Dr. Ram Manohar Lohia Hospital, Delhi 110001, Delhi, India

Corresponding author: Raghav Yelamanchi, DNB, MS, Surgeon, Surgical Oncologist, Department of Surgery, Atal Bihari Vajpayee Institute of Medical Sciences and Dr. Ram Manohar Lohia Hospital, Delhi 110001, Delhi, India. raghavyelamanchi@gmail.com

Abstract

Mucormycosis is caused by the fungi belonging to the order *Mucorales* and class *Zygomycetes*. The incidence of mucormycosis has increased with the onset of the severe acute respiratory syndrome coronavirus 2 infections leading to the coronavirus disease 2019 (COVID-19) pandemic. This rise is attributed to the use of immunosuppressive medication to treat COVID-19 infections. Authors have retrospectively collected data of our cases of mucormycosis diagnosed from April 2020 to April 2021 at our institute. A total of 20 patients with rhinocerebral mucormycosis were studied. Most of the study subjects were male patients (90%) and were of the age group 41-50 years. Most patients in the review had comorbidities (85%) with diabetes being the most common comorbidity. Para nasal sinuses were involved in all the cases. Involvement of the neck spaces was present in 60% of the cases. Involvement of the central nervous system was present in 80% of the cases. Orbital involvement was present in 90% of the cases. The authors reviewed the various imaging findings of mucormycosis on computed tomography and magnetic resonance imaging in this article.

Key Words: Mucormycosis; Rhinocerebral infections; Fungal sinusitis; Medical imaging; Radiodiagnosis; COVID-19 pandemic

Core Tip: Rhinocerebral mucormycosis constituted the aftermath of the coronavirus disease 2019 pandemic, leading to rapid increase in the number of cases, which were previously restricted only to few susceptible groups of patients. Rhinocerebral mucormycosis is associated with high mortality and morbidity. After clinical examination, imaging is the backbone for the diagnosis of this severe disease. Computed tomography helps in the preliminary diagnosis and helps to stage the disease. However, when orbital and intracranial extension is present, magnetic resonance imaging (MRI) is preferred because it delineates the involvement of these structures better. MRI can also delineate vascular involvement better. This article reviews the various imaging findings of mucormycosis.

Citation: Saneesh PS, Morampudi SC, Yelamanchi R. Radiological review of rhinocerebral mucormycosis cases during the COVID-19 Pandemic: A single-center experience. *World J Radiol* 2022; 14(7): 209-218
URL: https://www.wjgnet.com/1949-8470/full/v14/i7/209.htm
DOI: https://dx.doi.org/10.4329/wjr.v14.i7.209

INTRODUCTION

Mucormycosis is caused by fungi belonging to the order *Mucorales* and class *Zygomycetes*[1]. Fungal spores that are present in the air constitute a source of infection. However, these fungi rarely infect healthy individuals, as normal host defense mechanisms prevent invasion by these organisms. However, when host defense mechanisms are weakened due to several factors, such as congenital disorders, acquired immunodeficiency syndrome, hematological malignancies, uncontrolled systemic illnesses, and the use of immunosuppressive medication, these organisms invade and proliferate in human tissues. The incidence of mucormycosis has increased over the past few years due to the aging population, medical comorbidities, the increase in the incidence of malignancies, and the pandemic of human immunodeficiency virus infection[2].

The situation has worsened with the onset of the severe acute respiratory syndrome coronavirus 2 infections, which has led to the coronavirus disease 2019 (COVID-19) pandemic that began in late 2019 and has continued till the present. The main pathogenesis of the complications of this viral infection is due to the excessive immunological response that leads to damage to host's own tissues[3]. This has resulted in the use of immunosuppressive medication in the form of corticosteroids, interleukin antagonists, and various antibodies to counter the inflammatory cytokines. These drugs have proved to be efficacious in dealing with the complications and cytokine storm of COVID-19. However, they come with serious side effects of immunosuppression.

The number of cases of mucormycosis has rapidly increased in the last few months. This rise is attributed to the use of immunosuppressive medication to treat COVID-19 infections[4]. The paranasal sinuses and lungs, being the first spaces to come in contact with the fungus, are most commonly affected. Once the disease is established, it spreads to the surrounding structures, such as the orbit, brain, mediastinum, *etc*. The overall mortality of mucormycosis is more than 50%, and the mortality rate for disseminated disease reaches 100%[5]. The infection responds to only a few antifungals, such as amphotericin B, which are very toxic[5].

The authors of the present study have also come across many cases of mucormycosis in the last few months during the times of the COVID-19 pandemic. The following is a mini-review of the radiological findings of the rhinocerebral mucormycosis cases recorded by us in the last few months.

MATERIALS AND METHODS

We have retrospectively collected data on cases of mucormycosis diagnosed from April 2020 to April 2021 at our institute, which is a tertiary care center located in the state of Kerala, India.

All adult patients above the age of 18 years who were diagnosed with mucormycosis by imaging post–COVID-19 infection and confirmed by histopathological examination were studied. Patients with an unknown medical history, absent hospital records, and unknown outcomes were excluded from the review.

Hospital databases in the radiology department of our hospital were searched with the keyword "mucormycosis," and results were obtained. A list of cases was obtained, which was filtered to include only those cases from April 2020 to April 2021. Hospital identification numbers were then used to trace the clinical details and outcomes of the patients. The demographic details of the patients were recorded, and the COVID-19 infection history and treatment history were noted. History of various comorbidities, including malignancies, was obtained from the hospital records. The findings of the CECT scans,which were obtained using a 128-slice dual-energy CT scanner (SOMATOM Definition Flash, Siemens, Germany), were reviewed by the same radiologist to ensure uniformity in reporting. Images were

acquired with 1–3 mm collimation and a pitch of up to 2:1 to allow for coverage of the area of interest in a single breath-hold.

Imaging was repeated at one-month follow-up to study the lesions.

RESULTS

A total of 20 patients with rhinocerebral mucormycosis were studied. Eighteen patients had isolated rhino-cerebral mucormycosis, and two patients had combined pulmonary and rhino-cerebral mucormycosis (Table 1). Most study subjects were male patients (90%). The age distribution of the subjects is as follows: 10% were between 20–30 years of age, 20% were between 31–40 years of age, 30% were between 41–50 years of age, 5% were between 51–60 years of age,20% were between 61–70 years of age, and 15% were between 71–80 years of age. Most patients in the review had comorbidities (85%): 20% had hematological malignancy, 40% had diabetes, 10% had acquired immunodeficiency syndrome, and 15% were transplant recipients on immunosuppressive medication.

Sinuses were involved in all the cases. Unilateral involvement of the sinuses was more common than bilateral involvement. In most cases (35%), all four sinuses (maxillary, frontal, ethmoid, and sphenoid) were involved. The isolated maxillary sinus was involved in 20% of the cases. The isolated frontal sinus was involved in 5% of the cases. The ethmoid and sphenoid sinuses combined were involved in 10% of the cases. The frontal, ethmoid, and sphenoid sinuses combined were involved in 5% of the cases.

Involvement of the neck spaces was present in 60% of the cases (Table 2). The pterygopalatine space was involved in 50% of the cases. The infratemporal fossa was involved in 40% of the cases. The masticator space, retropharyngeal space, and parapharyngeal spaces were each involved in 10% of the cases.

At one month follow-up, only 50% of the patients survived, 25% had progression of the lesions, 20% had improvement in the lesions, and 5% had static lesions.

There were no cases of isolated cerebral mucormycosis. Involvement of the central nervous system (CNS) was present in 80% of the cases. The involvement of CNS included the following: leptomeningeal enhancement, meningoencephalitis, brain infarcts, brain abscesses, internal carotid artery thrombosis, cavernous sinus thrombosis, dural venous sinus thrombosis, and epidural abscesses.

The involvement of various structures of the CNS is listed in Table 2. Vascular involvement was present in 60% of the patients in our study, with the most common lesion being cavernous sinus thrombosis. Orbital involvement, which included orbital fat involvement, extraocular muscle involvement, and orbital cellulitis, was present in 90% of the cases (Table 2).

DISCUSSION

Most cases of rhinocerebral mucormycosis occurred in males in the present review as in other previous case series and reviews[6,7]. Most patients had comorbidities, with diabetes being the predominant comorbidity as in other previous studies. In the study by Dubey *et al*[8], all post–COVID-19 patients diagnosed with rhinocerebral mucormycosis were diabetic. This also includes new-onset diabetes due to the usage of corticosteroids during the treatment of COVID-19, which is as high as 38.18%[8].

In the present study, similar to the study by Therakathu *et al*[9], unilateral involvement of the sinuses was more common. The ethmoid sinus was the most common sinus to be involved in the present study, followed by the maxillary sinus, as in the studies by Therakathu *et al*[9] and Patel *et al*[10]. In the study by Therakathu *et al*[9], the most common site to be involved other than the sinuses was the orbit (76%) and the face (57%), followed by the orbital apex, masticator space, pterygopalatine fossa, bone, skull base, cavernous sinus, brain, and internal carotid artery.Orbital involvement was also very common in the present study, accounting for 90% of the cases. However, in the study by Patel *et al*[10], orbital involvement was present in only 60% of the cases.

Infection by fungi of the order *Mucorales* begins in the nasal cavity mostly in the middle turbinate and starts spreading, mostly invading the sphenoethmoidal complex[11,12]. As the fungi have the ability to invade the blood vessels and the bony walls, they spread rapidly in immunocompromised hosts and those with chronic debilitating illnesses, to reach the sinus cavity[13]. The necrotic tissue formed due to vascular occlusion acts as a rich niche for the further growth of the organism. Further invasion of the orbits and brain occurs through the foramen and through the sphenopalatine and internal maxillary arteries[14].

The invasion in mucormycosis can be divided into three stages as per Rupa *et al*[15]:

Stage 1: The infection is localized to the nasal cavity and paranasal sinuses.

Stage 2: The infection begins to spread to the peri-sinus areas, which are completely resectable.

Stage 3: The infection spreads into the intracranial cavity and to the surrounding areas of the sinuses, which are partially resectable.

Table 1 Table showing the demographic data and findings of the patients under study

Serial No.	Age	Sex	Co-morbidities	Primary location	Cerebral involvement	Orbital involvement	Involvement of neck spaces
1	34	Male	Acute myeloid leukemia	Right nasal cavity, Right ethmoid, Sphenoid	ICA thrombosis, Cavernous sinus thrombosis, Leptomeningeal enhancement	No	Right pterygopalatine, Right infra temporal, Bilateral parapharangeal, Retropharyngeal space
2	64	Male	Renal transplant	Pan sinusitis	> Meningoencephalitis, > infiltration into left basifrontal and gangliocapsular region along olfactory fossa	Extra ocular muscles, Orbital cellulitis	No
3	72	Male	Diabetes	Left maxillary, Ethmoid, Frontal, Sphenoid	Ganglio-capsular infarctcavernous sinus thrombosis	Retro- orbitalfat and extra ocular muscles and orbital apex	No
4	50	Male	No	Right maxillary	Cavernous sinus, Subdural abscess	Orbital apex, Orbital abscess	Temporal, pterygopalatine, masticator space
5	40	Male	Post renal transplant	Pan sinus	Cavernous sinus thrombosis, Temporal lobe involvement	Extra conal extension, Right extra ocular muscles, Orbital floor	Infratemporal fossa, pterygopalatine
6	45	Male	Acquired immunodeficiency syndrome	Frontal	ICA thrombosis cavernous sinus thrombosis, Cerebral infarct epidural abscess	Left orbit, Extra ocular muscles	Left pterygopalatine
7	67F	Female	Diabetes	Pan-sinus	Basifrontal brain parenchyma involvement, meningoencephalitis	Orbital apex, extra ocular muscles Subperiosteal abscess	Right infra temporal fossa, retropharyngeal space
8	75	Male	Diabetes	Pan-sinusitis	No cerebral involvement	Extraconal fat involvement	No
9	22	Male	ALL	Right maxillary sinus	ICA thrombosis, Cavernous sinus involvement, Cerebral infarct	Extra ocular muscle, Orbital apex, Subperiosteal abscess	Right Infratemporal fossa, Right pterygopalatine fossa
10	50	Male	Diabetes	Left maxillary sinus	No cerebral involvement	Left extraconal space	No
11	50	Male	Acquired immunodeficiency syndrome	Pan sinusitis	Cavernous sinus, Epidural abscess	Orbital Apex, Extra ocular muscles involvement, Subperiosteal abscess	Pterygopalatine fossa
12	40	Male	Kidney transplant	Frontal, Ethmoid, sphenoid	ICA thrombosis, Temporal lobe abscess	Orbital apex, Extra ocular muscles, Subperiosteal abscess, Cellulitis	No
13	21	Female	Acute lymphocytic leukemia	Right maxillary sinus and nasal cavity	ICA thrombosis, Frontal lobe abscess, Infarct	Extra ocular muscles, Intraconal fat	Pterygopalatine fossa and infratemporal fossa
14	64	Male	Diabetes	Pan sinusitis	Cavernous sinus, Subdural abscess	Orbital apex, Extraocular muscles, Subperiosteal abscess	No
15	48	Male	No	Pan sinusitis	Cavernous sinus, ICA thrombosis	Orbital apex, Extra ocular muscles, Orbital abscess	Pterygopalatine fossa, Infra temporal fossa
16	68	Male	Diabetes	Pan sinusitis	Not involved	Extraconal fat	Pterygopalatine fossa
17	57	Male	Diabetes	Pan sinusitis	Subdural abscess	Extraconal orbital fat, Extra ocular muscles, Orbital cellulitis	Infratemporal fossa
18	71	Male	Diabetes	Sphenoid, Ethmoid, Nasal cavity	Frontal lobe	Orbital apex, Extra ocular muscles	Para pharyngeal space, Pterygopalatine fossa
19	48	Male	No	Right pan sinusitis, Nasal cavity	Frontal lobe, Cavernous sinus	Extraconal fat, extra ocular muscles	No

20	37	Male	Lymphoma	Right sinusitis	Not involved	Extraconal orbital fat	No

ICA: Internal carotid artery.

Table 2 Table showing the summary of central nervous system involvement, orbital involvement and neck space involvement

Complication/local invasion	N = 20
Cerebral	16/20
Arterial involvement (ICA thrombosis)	6
Cavernous sinus thrombosis	10
Brain Parenchymal involvement	11
Meninges and Dural/epidural involvement	7
Orbit	18/20
Extraocular muscles	14
Orbital apex	9
Orbital fat only/orbital cellulitis/abscess	16
Neck spaces	12/20
Pterygopalatine foramen and fossa	10
Infratemporal fossa	8
Masticator space	2
Retropharyngeal space	2
Parapharyngeal space	2

ICA: Internal carotid artery.

Computed tomography appearance of the lesions in the sinuses

Computed tomography (CT) is usually the first investigation to be performed whenever invasive rhinocerebral mucormycosis is suspected based on clinical history and examination. The CT findings are nonspecific and include inflammatory changes in the sinuses. Early changes include mucosal thickening due to inflammation, bony erosions, and the formation of a mass lesion inside the sinuses, leading to the opacification of the sinuses. Hyperattenuation of the secretions on CT is suggestive of fungal sinusitis. The hyperdense areas seen in the sinuses are due to the presence of fungal hyphae and debris. Early changes suggestive of the spread of the infection outside the sinus include loss of normal fat density in the periantral fat (anterior, premaxillary, or retroantral) and orbit owing to edemafrom vascular congestion[16]. Superficial cellulitis is another early sign of invasion, which is not common in nonfungal sinusitis[10]. Late stages are characterized by signs suggestive of gross invasion of the structures of the orbit and the cranial cavity, which are more specific (Figure 1). Bone changes are also better visualized on CT.

The enhancement pattern of the lesions on contrast-enhanced computed tomography (CECT) varies from none to mild to heterogeneous enhancement, which was also seen in the cases in the present study [9,10]. The mild form was the most common type of enhancement observed by Therakathu *et al*[9]. Mucosal involvement may appear as a diffuse thickening or nodular thickening. Bone involvement was seen in the form of bone rarefaction, erosion, and permeative destruction in 40% of the cases in the study by Therakathu *et al*[9]. Middlebrooks *et al*[17]designed a CT-based model based on seven variables; this model can be used to suspect acute invasive fungal sinusitis. The variables are periantral fatinvolvement, bone dehiscence, orbital invasion, septal ulceration, pterygopalatine fossa, nasolacrimal duct, and lacrimal sac. In a study by Silverman *et al*[16], most cases of extra sinus invasion occurred without bony invasion, suggesting that perivascular or perineural invasion plays an important role in the spread of mucormycosis. In the same study, Silverman *et al*[16] noted that the presence of retroantral, facial, and orbital fat stranding was associated with a more aggressive infection.

Magnetic resonance imaging appearance of the sinus lesions

Orbital and intracranial invasions are best seen by magnetic resonance imaging (MRI). Early changes are nonspecific. These include mucosal thickening, which appears hypointense on T1-weighted images and

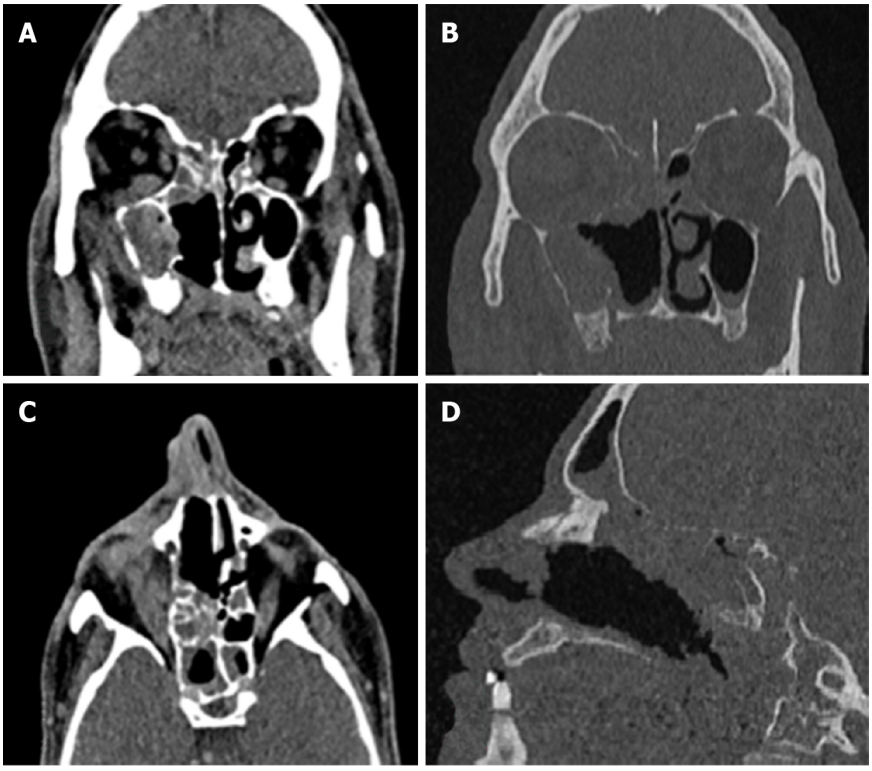

DOI: 10.4329/wjr.v14.i7.209

Figure 1 Non contrast computed tomography image of a 40 year old male post renal transplant patient showing. A: Soft tissue density in maxillary, ethmoidal, sphenoidal and frontal sinus; B: Rarefaction of ethmoidal lamella, lamina papyracea and floor of anterior cranial fossa and erosion of maxillary walls; C: Section showing orbital involvement; D: Section showing erosions of the cribriform plate.

hyperintense on T2-weighted images. In the study by Therakathu *et al*[9], on a T2-weighted sequence, 37% of the lesions were isointense to mildly hypointense, 32% were heterogeneous, and 32% were hyperintense. Fungal elements are hypointense on T2-weighted images (Figure 2). The enhancement pattern is best studied on fat-suppressed post-gadolinium images and is different for different lesions. Of all the cases in the study by Therakathu *et al*[9], 29% showed intense homogenous enhancement, 36% showed heterogeneous enhancement, and 36% showed no enhancement.

Because of the angioinvasive nature of mucormycosis, the vessels get thrombosed. Upon injection of the contrast, the normal expected pattern of mucosal enhancement in case of inflammatory lesions may not be visible. Instead, there will be a low-signal intensity of the affected mucosa of the nasal turbinate on T2-weighted MRI images associated with an increased signal on diffusion-weighted images. This was referred to as the black turbinate sign by Safder *et al*[18].

Differential diagnosis on imaging for mucormycosis includes the following: Acute rhinosinusitis with complications, Wegener's granulomatosis, and squamous cell carcinoma.

However, in the COVID-19pandemic, mucormycosis should be considered the first differential diagnosis.

Imaging features of intracranial mucormycosis

Most of the imaging features correlate with the angioinvasive pattern of the mucormycosis infection. The imaging findings are nonspecific, but early diagnosis is of paramount importance because of the associated morbidity and mortality. Sen *et al*[19] found that cavernous sinus thrombosis and cribriform plate erosion were the commonest pathways of spread into the cranium and were present in 76% and 22% of the patients, respectively[19]. The involvement may appear as leptomeningeal inflammation, which appears as leptomeningeal enhancement and involvement of the cranial nerves with signs of meningism.This may be accompanied by cerebritis. Cerebritis appears as T2-FLAIR hyperintensity with variable enhancement and heterogeneous diffusion restriction on diffusion-weighted imaging. Invasion of the parenchyma may appear as granuloma formation or abscess formation. Fungal granulomas may show faint enhancement and surrounding edema.

In contrast to the pyogenic abscess, fungal abscesses are frequently multiple and form at the corticomedullary junction and in the basal ganglia. Isolated fungal abscesses are rare, and one should suspect intravenous drug abuse if encountered with such a situation. Fungal abscesses have crenated borders and non-enhancing, diffusion-restricting intracavitary projections[20].They are hypointense on T1 and hyperintense on T2 and show rim enhancement[20]. On diffusion-weighted imaging, Luthra *et al*

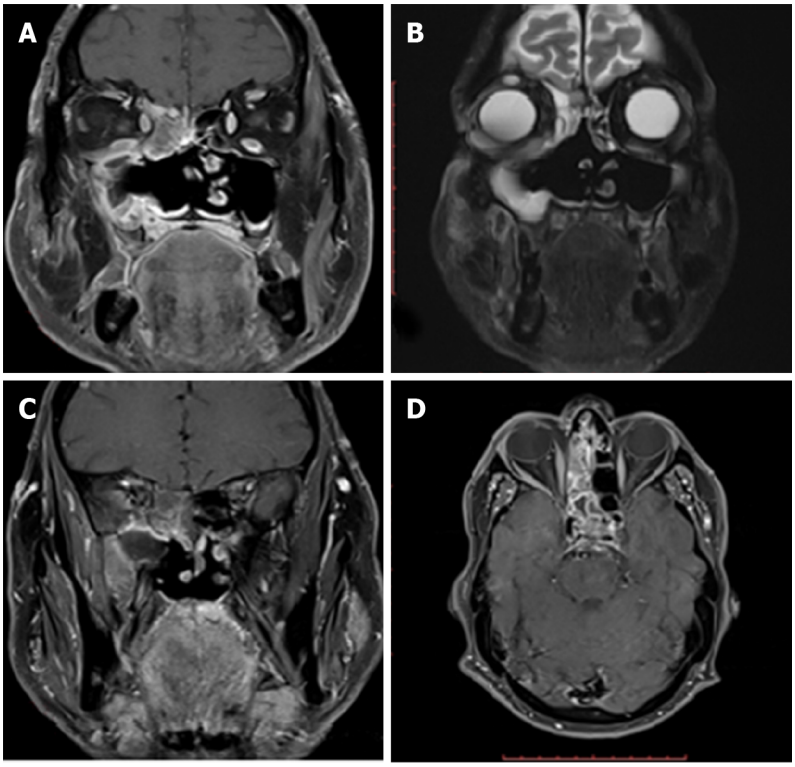

DOI: 10.4329/wjr.v14.i7.209

Figure 2 Magnetic resonance imaging of the patient of Figure 1 showing. A: T1 image showing orbital involvement; B: T2 image showing orbital and infratemporal fossa involvement; C: T1+C showing infratemporal fossa involvement; D: T1+C showing cavernous sinus thrombosis.

[20] found that fungal abscesses showed restriction of diffusion in the projections and the wall, and the core of the abscess had no restriction of diffusion. In the same study, the authors found that the apparent diffusion coefficient was higher for the wall of the abscess when compared to the intracavitary projections for the fungal abscess, and it was statistically significant[20].

Vascular complications are observed in the late stages. They include both venous and arterial complications such as cavernous sinus thrombosis, arterial thrombosis, and aneurysmal dilatation (Figure 3). In the study by Mohindra *et al*[21], the role of MRI in the detection of vascular lesions was studied. In the study by Razek *et al*[22], cavernous sinus involvement in mucormycosis appears hypointense on T1 and T2 sequences with intense, inhomogeneous post-contrast enhancement. Cavernous sinus thrombosis is the most common complication in the present study, as in certain published studies.

Cause of the increased incidence and severity of mucormycosis during the COVID-19 pandemic

Diabetes was one of the major predisposing factors for mucormycosis during the COVID-19 pandemic. Prakash *et al*[23] highlighted that rhinocerebral mucormycosis cases were predominantly present in those with uncontrolled diabetes and diabetic ketoacidosis, and few were present in immunosuppressed hosts. The findings were similar to those in other studies by Sen *et al*[18], John *et al*[24], and Hoenigl *et al*[25]. In the afore mentioned studies, the prevalence of diabetes was 78%-94% among patients with mucormycosis post–COVID-19 infection. In Patel *et al*'s study, patients with mucormycosis with poor glycemic control had a more invasive disease, which was statistically significant (P value = 0.040)[10]. The rampant use of corticosteroids and other immunomodulatory drugs to control the severity of the COVID-19 infection has further led to the increased predisposition[26]. During the peak of the pandemic, when healthcare facilities were functioning beyond their capacities, there were instances of unsupervised treatment with these immunomodulatory agents, leading to further escalation of the problem.

CONCLUSION

Rhinocerebral mucormycosis constituted the aftermath of the COVID-19 pandemic, leading to a rapid increase in the number of cases, which were previously restricted to only a few susceptible groups of patients. Rhinocerebral mucormycosis is associated with high mortality and morbidity. Hence, it should be suspected in any patient who presents symptoms of sinusitis, facial swelling, or CNS symptoms.

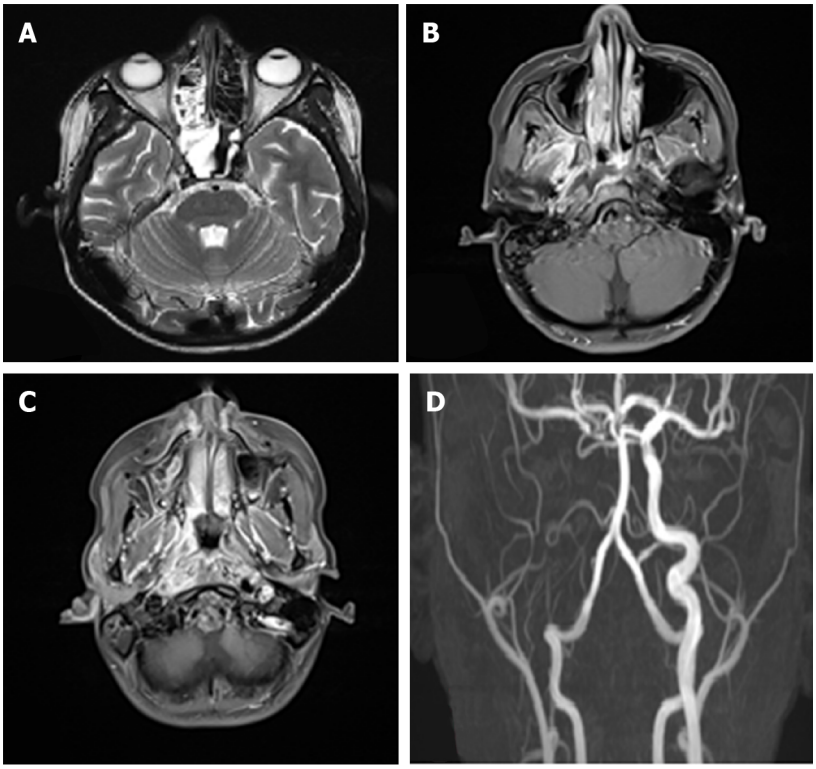

DOI: 10.4329/wjr.v14.i7.209

Figure 3 Magnetic resonance imaging images of a patient of rhinocerebral mucormycosis showing. A: Enhancing soft tissue thickening in right nasal cavity involving right maxillary, ethmoid and sphenoid sinus; B: T1+C showing right infratemporal fossa involvement; C: T1+C showing right parapharangeal space involvement; D: Angiogram showing right internal carotid artery thrombosis.

After clinical examination, imaging is the backbone of the diagnosis of this severe disease. CT helps in the preliminary diagnosis and helps stage the disease. CT detects bony erosion better. However, when an orbital and intracranial extension is present, MRI is preferred, as it delineates the involvement of these structures better. MRI can also delineate vascular involvement better. In accessible sites, biopsy and potassium hydroxide mount help clinch the diagnosis. The treatment of rhinocerebral mucormycosis consists of debridement of the necrotic tissue along with intravenous antifungals for a prolonged duration. Control of diabetes and judicious use of corticosteroids and immunomodulatory drugs can decrease the incidence of this life-threatening disease.

FOOTNOTES

Author contributions: Saneesh PS analyzed the data; Morampudi SC analyzed the data and wrote the manuscript; Yelamanchi R analyzed the data and wrote the manuscript; All authors have read and approved the final manuscript.

Conflict-of-interest statement: None of the authors in the study have any conflict of interest.

Country/Territory of origin: India

ORCID number: P S Saneesh 0000-0003-1492-7395; Satya Chowdary Morampudi 0000-0002-4061-5363; Raghav Yelamanchi 0000-0001-6786-8056.

S-Editor: Liu JH
L-Editor: A
P-Editor: Liu JH

REFERENCES

1 **Ibrahim AS**, Spellberg B, Walsh TJ, Kontoyiannis DP. Pathogenesis of mucormycosis. *Clin Infect Dis* 2012; **54** Suppl 1: S16-S22 [PMID: 22247441 DOI: 10.1093/cid/cir865]

2 **Camara-Lemarroy CR**, González-Moreno EI, Rodríguez-Gutiérrez R, Rendón-Ramírez EJ, Ayala-Cortés AS, Fraga-Hernández ML, García-Labastida L, Galarza-Delgado DÁ. Clinical features and outcome of mucormycosis. *Interdiscip Perspect Infect Dis* 2014; **2014**: 562610 [PMID: 25210515 DOI: 10.1155/2014/562610]

3 **Sweeney RM**, McAuley DF. Acute respiratory distress syndrome. *Lancet* 2016; **388**: 2416-2430 [PMID: 27133972 DOI: 10.1016/S0140-6736(16)00578-X]

4 **Song G**, Liang G, Liu W. Fungal Co-infections Associated with Global COVID-19 Pandemic: A Clinical and Diagnostic Perspective from China. *Mycopathologia* 2020; **185**: 599-606 [PMID: 32737747 DOI: 10.1007/s11046-020-00462-9]

5 **Roden MM**, Zaoutis TE, Buchanan WL, Knudsen TA, Sarkisova TA, Schaufele RL, Sein M, Sein T, Chiou CC, Chu JH, Kontoyiannis DP, Walsh TJ. Epidemiology and outcome of zygomycosis: a review of 929 reported cases. *Clin Infect Dis* 2005; **41**: 634-653 [PMID: 16080086 DOI: 10.1086/432579]

6 **Herrera DA**, Dublin AB, Ormsby EL, Aminpour S, Howell LP. Imaging findings of rhinocerebral mucormycosis. *Skull Base* 2009; **19**: 117-125 [PMID: 19721767 DOI: 10.1055/s-0028-1096209]

7 **Gupta N**, Dembla S. Cranial nerve involvement in mucormycosis in post-COVID patients: a case series. *Egypt J Radiol Nucl Med* 2022; **53**: 28 [DOI: 10.1186/s43055-022-00700-8]

8 **Dubey S**, Mukherjee D, Sarkar P, Mukhopadhyay P, Barman D, Bandopadhyay M, Pandit A, Sengupta A, Das S, Ghosh S, Adhikari S, Biswas PS, Pal P, Roy H, Patra N, Das A, Sinha P, Mondal MK, Shrivastava SR, Bhattacharya K, Mukhopadhyay M, Ahmed K, Halder TK, Saha M, Maity S, Mandal A, Chatterjee D, Saha S, Chunakar A, Saha A, Ray BK. COVID-19 associated rhino-orbital-cerebral mucormycosis: An observational study from Eastern India, with special emphasis on neurological spectrum. *Diabetes Metab Syndr* 2021; **15**: 102267 [PMID: 34509790 DOI: 10.1016/j.dsx.2021.102267]

9 **Therakathu J**, Prabhu S, Irodi A, Sudhakar SV, Yadav VK, Rupa V. Imaging features of rhinocerebral mucormycosis: a study of 43 patients. *Egypt J Radiol Nucl Med* 2018; **49**: 447-452 [DOI: 10.1016/j.ejrnm.2018.01.001]

10 **Patel DD**, Adke S, Badhe PV, Lamture S, Marfatia H, Mhatre P. COVID-19 associated Rhino-Orbito-Cerebral Mucormycosis: Imaging spectrum and Clinico-radiological correlation- a single Centre experience. *Clin Imaging* 2022; **82**: 172-178 [PMID: 34864270 DOI: 10.1016/j.clinimag.2021.10.014]

11 **Gillespie MB**, Huchton DM, O'Malley BW. Role of middle turbinate biopsy in the diagnosis of fulminant invasive fungal rhinosinusitis. *Laryngoscope* 2000; **110**: 1832-1836 [PMID: 11081595 DOI: 10.1097/00005537-200011000-00013]

12 **Gillespie MB**, O'Malley BW Jr, Francis HW. An approach to fulminant invasive fungal rhinosinusitis in the immunocompromised host. *Arch Otolaryngol Head Neck Surg* 1998; **124**: 520-526 [PMID: 9604977 DOI: 10.1001/archotol.124.5.520]

13 **Skiada A**, Pavleas I, Drogari-Apiranthitou M. Epidemiology and Diagnosis of Mucormycosis: An Update. *J Fungi (Basel)* 2020; **6** [PMID: 33147877 DOI: 10.3390/jof6040265]

14 **Bhandari J**, Thada PK, Nagalli S. Rhinocerebral Mucormycosis. [Updated 2021 Nov 25]. In: StatPearls [Internet]. Treasure Island (FL): StatPearls Publishing; 2022 Jan. Available from: https://www.ncbi.nlm.nih.gov/books/NBK559288/

15 **Rupa V**, Maheswaran S, Ebenezer J, Mathews SS. Current therapeutic protocols for chronic granulomatous fungal sinusitis. *Rhinology* 2015; **53**: 181-186 [PMID: 26030043 DOI: 10.4193/Rhino14.183]

16 **Silverman CS**, Mancuso AA. Periantral soft-tissue infiltration and its relevance to the early detection of invasive fungal sinusitis: CT and MR findings. *AJNR Am J Neuroradiol* 1998; **19**: 321-325 [PMID: 9504486]

17 **Middlebrooks EH**, Frost CJ, De Jesus RO, Massini TC, Schmalfuss IM, Mancuso AA. Acute Invasive Fungal Rhinosinusitis: A Comprehensive Update of CT Findings and Design of an Effective Diagnostic Imaging Model. *AJNR Am J Neuroradiol* 2015; **36**: 1529-1535 [PMID: 25882281 DOI: 10.3174/ajnr.A4298]

18 **Safder S**, Carpenter JS, Roberts TD, Bailey N. The "Black Turbinate" sign: An early MR imaging finding of nasal mucormycosis. *AJNR Am J Neuroradiol* 2010; **31**: 771-774 [PMID: 19942703 DOI: 10.3174/ajnr.A1808]

19 **Sen M**, Honavar SG, Bansal R, Sengupta S, Rao R, Kim U, Sharma M, Sachdev M, Grover AK, Surve A, Budharapu A, Ramadhin AK, Tripathi AK, Gupta A, Bhargava A, Sahu A, Khairnar A, Kochar A, Madhavani A, Shrivastava AK, Desai AK, Paul A, Ayyar A, Bhatnagar A, Singhal A, Nikose AS, Tenagi AL, Kamble A, Nariani A, Patel B, Kashyap B, Dhawan B, Vohra B, Mandke C, Thrishulamurthy C, Sambare C, Sarkar D, Mankad DS, Maheshwari D, Lalwani D, Kanani D, Patel D, Manjandavida FP, Godhani F, Agarwal GA, Ravulaparthi G, Shilpa GV, Deshpande G, Thakkar H, Shah H, Ojha HR, Jani H, Gontia J, Mishrikotkar JP, Likhari K, Prajapati K, Porwal K, Koka K, Dharawat KS, Ramamurthy LB, Bhattacharyya M, Saini M, Christy MC, Das M, Hada M, Panchal M, Pandharpurkar M, Ali MO, Porwal M, Gangashetappa N, Mehrotra N, Bijlani N, Gajendragadkar N, Nagarkar NM, Modi P, Rewri P, Sao P, Patil PS, Giri P, Kapadia P, Yadav P, Bhagat P, Parekh R, Dyaberi R, Chauhan RS, Kaur R, Duvesh RK, Murthy R, Dandu RV, Kathiara R, Beri R, Pandit R, Rani RH, Gupta R, Pherwani R, Sapkal R, Mehta R, Tadepalli S, Fatima S, Karmarkar S, Patil SS, Shah S, Dubey S, Gandhi S, Kanakpur S, Mohan S, Bhomaj S, Kerkar S, Jariwala S, Sahu S, Tara S, Maru SK, Jhavar S, Sharma S, Gupta S, Kumari S, Das S, Menon S, Burkule S, Nisar SP, Kaliaperumal S, Rao S, Pakrasi S, Rathod S, Biradar SG, Kumar S, Dutt S, Bansal S, Ravani SA, Lohiya S, Ali Rizvi SW, Gokhale T, Lahane TP, Vukkadala T, Grover T, Bhesaniya T, Chawla U, Singh U, Une VL, Nandedkar V, Subramaniam V, Eswaran V, Chaudhry VN, Rangarajan V, Dehane V, Sahasrabudhe VM, Sowjanya Y, Tupkary Y, Phadke Y; members of the Collaborative OPAI-IJO Study on Mucormycosis in COVID-19 (COSMIC) Study Group. Epidemiology, clinical profile, management, and outcome of COVID-19-associated rhino-orbital-cerebral mucormycosis in 2826 patients in India - Collaborative OPAI-IJO Study on Mucormycosis in COVID-19 (COSMIC), Report 1. *Indian J Ophthalmol* 2021; **69**: 1670-1692 [PMID: 34156034 DOI: 10.4103/ijo.IJO_1565_21]

20 **Luthra G**, Parihar A, Nath K, Jaiswal S, Prasad KN, Husain N, Husain M, Singh S, Behari S, Gupta RK. Comparative evaluation of fungal, tubercular, and pyogenic brain abscesses with conventional and diffusion MR imaging and proton MR spectroscopy. *AJNR Am J Neuroradiol* 2007; **28**: 1332-1338 [PMID: 17698537 DOI: 10.3174/ajnr.A0548]

21 **Mohindra S**, Mohindra S, Gupta R, Bakshi J, Gupta SK. Rhinocerebral mucormycosis: the disease spectrum in 27 patients. *Mycoses* 2007; **50**: 290-296 [PMID: 17576322 DOI: 10.1111/j.1439-0507.2007.01364.x]

22 **Razek AA**, Castillo M. Imaging lesions of the cavernous sinus. *AJNR Am J Neuroradiol* 2009; **30**: 444-452 [PMID: 19095789 DOI: 10.3174/ajnr.A1398]

23 **Prakash H**, Chakrabarti A. Global Epidemiology of Mucormycosis. *J Fungi (Basel)* 2019; **5** [PMID: 30901907 DOI: 10.3390/jof5010026]

24 **John TM**, Jacob CN, Kontoyiannis DP. When Uncontrolled Diabetes Mellitus and Severe COVID-19 Converge: The Perfect Storm for Mucormycosis. *J Fungi (Basel)* 2021; **7** [PMID: 33920755 DOI: 10.3390/jof7040298]

25 **Hoenigl M**, Seidel D, Carvalho A, Rudramurthy SM, Arastehfar A, Gangneux JP, Nasir N, Bonifaz A, Araiza J, Klimko N, Serris A, Lagrou K, Meis JF, Cornely OA, Perfect JR, White PL, Chakrabarti A; ECMM and ISHAM collaborators. The emergence of COVID-19 associated mucormycosis: a review of cases from 18 countries. *Lancet Microbe* 2022; **3**: e543-e552 [PMID: 35098179 DOI: 10.1016/S2666-5247(21)00237-8]

26 **Al-Tawfiq JA**, Alhumaid S, Alshukairi AN, Temsah MH, Barry M, Al Mutair A, Rabaan AA, Al-Omari A, Tirupathi R, AlQahtani M, AlBahrani S, Dhama K. COVID-19 and mucormycosis superinfection: the perfect storm. *Infection* 2021; **49**: 833-853 [PMID: 34302291 DOI: 10.1007/s15010-021-01670-1]

World Journal of Radiology

Submit a Manuscript: https://www.f6publishing.com

World J Radiol 2022 July 28; 14(7): 219-228

DOI: 10.4329/wjr.v14.i7.219

ISSN 1949-8470 (online)

MINIREVIEWS

Impact of X-radiation in the management of COVID-19 disease

Aishwarya T A, Divya K Mohan, K Nandhini, Venkateswarlu Raavi, Venkatachalam Perumal

Specialty type: Health care sciences and services

Provenance and peer review: Invited article; Externally peer reviewed.

Peer-review model: Single blind

Peer-review report's scientific quality classification

Grade A (Excellent): 0
Grade B (Very good): 0
Grade C (Good): C, C, C
Grade D (Fair): D
Grade E (Poor): 0

P-Reviewer: Konovalov AB, Russia; Liu J, China; Wang D, Thailand

Received: March 27, 2022
Peer-review started: March 27, 2022
First decision: June 8, 2022
Revised: June 16, 2022
Accepted: July 18, 2022
Article in press: July 18, 2022
Published online: July 28, 2022

Aishwarya T A, Divya K Mohan, K Nandhini, Venkatachalam Perumal, Department of Human Genetics, Sri Ramachandra Institute of Higher Education and Research (Deemed to be University), Porur, Chennai 600 116, Tamil Nadu, India

Venkateswarlu Raavi, Department of Cell Biology and Molecular Genetics, Sri Devaraj Urs Academy of Higher Education and Research (Deemed to be University), Tamaka, Kolar 563 103, Karnataka, India

Corresponding author: Venkatachalam Perumal, DSc, PhD, Professor, Department of Human Genetics, Sri Ramachandra Institute of Higher Education and Research (Deemed to be University), Porur, Chennai 600116, Tamil Nadu, India. venkip@yahoo.com

Abstract

Coronaviruses are a diverse group of viruses that infect both animals and humans. Even though the existence of coronavirus and its infection to humans is not new, the 2019-novel coronavirus (nCoV) caused a major burden to individuals and society *i.e.*, anxiety, fear of infection, extreme competition for hospitalization, and more importantly financial liability. The nCoV infection/disease diagnosis was based on non-specific signs and symptoms, biochemical parameters, detection of the virus using reverse-transcription polymerase chain reaction (RT-PCR), and X-ray-based imaging. This review focuses on the consolidation of potentials of X-ray-based imaging modality [chest-X radiography (CXR) and chest computed tomography (CT)] and low-dose radiation therapy (LDRT) for screening, severity, and management of COVID-19 disease. Reported studies suggest that CXR contributed significantly toward initial rapid screening/diagnosis and CT- imaging to monitor the disease severity. The chest CT has high sensitivity up to 98% and low specificity for diagnosis and severity of COVID-19 disease compared to RT-PCR. Similarly, LDRT compliments drug therapy in the early recovery/Less hospital stays by maintaining the physiological parameters better than the drug therapy alone. All the results undoubtedly demonstrated the evidence that X-ray-based technology continues to evolve and play a significant role in human health care even during the pandemic.

Key Words: Corona virus; COVID-19 infection; COVID-19 disease; X-rays; Computed tomography; Low dose radiotherapy

Core Tip: Majority of asymptomatic individuals with coronavirus disease 2019 (COVID-19) disease, an early diagnosis was a challenge despite the gold standard reverse-transcription polymerase chain reaction measures the viral nucleic acid with a turnaround period of reporting for 5-6 h. This ultimately led to the usage of chest-X radiography with sensitivity up to 80%, which served as a screening tool for COVID-19. X-radiation-based computed tomography imaging served as another modality to monitor the severity of COVID-19 disease with sensitivity up to 98%. Low-dose radiation therapy with a limited setting showed that it can complement drug therapies in the management of COVID-19. Therefore, X-rays on a whole are been widely used for both diagnostic and therapeutic management of COVID-19 disease.

Citation: Aishwarya T A, Mohan DK, Nandhini K, Raavi V, Perumal V. Impact of X-radiation in the management of COVID-19 disease. *World J Radiol* 2022; 14(7): 219-228
URL: https://www.wjgnet.com/1949-8470/full/v14/i7/219.htm
DOI: https://dx.doi.org/10.4329/wjr.v14.i7.219

INTRODUCTION

Coronaviruses are a diverse group of viruses that infect both animals and humans. The existence of coronavirus and its infection to humans is not new; since the beginning of this century, severe acute respiratory syndrome coronavirus (SARS-CoV) and Middle East respiratory syndrome coronavirus are infecting humans and are of concern to public health[1]. The coronavirus infection is majorly associated with an array of clinical symptoms, which range from upper respiratory tract infection of moderate clinical concern to lower respiratory tract including bronchiolitis and pneumonia leading to fatality, especially in the elderly, and individuals with compromised immunity. The 2019-novel coronavirus (nCoV) outbreak leads to a lower respiratory tract disease called novel coronavirus pneumonia and renamed this beta-corona virus SARS-CoV-2, the established etiology for COVID-19 disease.

COVID-19 disease

The World Health Organization (WHO) has declared 2019-nCoV infection as a global health emergency, because, within a few months not only did several thousand individuals test positive for the virus infection but also resulted in a significant number of deaths worldwide. That was because of the disease burden, the WHO officially characterized the global COVID-19 flare-up as a pandemic on 11 March 2020. Important clinical features of COVID-19 spread documented were: (1) An infection rate of 83% within the family; (2) Mild to moderate with more systematic symptoms and severe radiological abnormalities as clinical manifestations seen in older patients; and (3) Transmission of SARS-CoV-2 from asymptomatic carriers to others[2]. Given the rapid spread of the disease and asymptomatic carriers, it remains a major health problem throughout the world. Although genetic evidence suggests that SARS-CoV-2 is a natural virus that likely originated in animals, there is no conclusion yet about when and where the virus first entered humans. However, these viruses are known to constantly change through mutation and result in a new variant of the virus; such a new variant is known to affect the virus properties, such as infection rate, the severity of disease, the performance of vaccines, therapeutic medicines, diagnostic tools, or other public health and social measures. Of late many variants form of the virus has been reported with a higher infection rate (Omicron) despite the severity of the disease and the need for hospitalization is less when compared to that of earlier variants (beta and delta coronavirus as SARS-CoV-2) and COVID 19 disease[3]. Even the variant reported causing less severe disease, in general, an increase in the total number of cases could lead to an upsurge in hospitalizations, laying more strain on healthcare resources.

Symptoms and Pathogenesis of the disease

The most common symptoms after COVID-19 infection are fever, fatigue, and dry cough. Less common symptoms include sputum production, headache, hemoptysis, diarrhea, anorexia, sore throat, chest pain, chills, nausea, and vomiting[2,4-7] olfactory and taste disorders[8]. The majority of infected people showed signs of disease for about fourteen days (frequently around five days), and dyspnea and pneumonia developed within a median time of eight days from illness onset[9,10]. The pathogenesis of SARS-CoV-2 infection in humans manifests itself as mild symptoms to severe respiratory failure. Upon entry of the virus in the nasal route, the virus binds to epithelial cells in the respiratory tract, starts replicating and migrating down to the airways, and goes into alveolar epithelial cells in the lungs. Owing to the hasty replication of SARS-CoV-2 in the lungs, activate a strong immune response, and cascade into a cytokine storm, resulting in acute respiratory distress syndrome and then respiratory failure, which is considered the notable cause of death in patients with COVID-19 infection[2,5]. Even multiple organ failure has also been reported in some COVID-19 cases. Despite the range and severity of the disease, clinical manifestations differ with age; men >60 years with co-morbidities are more

prospective to develop a severe respiratory disease that required hospitalization or even death, whereas most young people and children had only mild diseases and/or are asymptomatic[7,11]. Moreover, regardless of evidence of trans-placental transmission of SARS-CoV-2 from an infected mother to a neonate, the risk of disease was not higher for pregnant women[4,12]. Thus, the disease caused a major burden on the individual and society i.e., anxiety, fear of infection, struggle and extreme competition for hospitalization, and more importantly financial liability.

Diagnosis of COVID-19

Given the rapid spread of infection, early diagnosis is crucial for controlling the spread of COVID-19. Choice of diagnosis options is: (1) detection of SARS-CoV-2 nucleic acid; (2) detecting antibodies to N or S protein; and (3) imaging by simple chest X-ray and high-resolution computed tomography (CT) with X-rays. The detection time ranges from several minutes to hours depending on the technology used for the diagnosis[13-18]. Among those tools, a quantitative reverse-transcription polymerase chain reaction (RT-PCR) test is the current standard of test and remains the "gold standard" to confirm the COVID-19 infection. RT-PCR has also its challenges such as delays in result turnaround time and interpretation of the results. Another major hurdle is the dynamic conversion of RT-PCR results from either negative to positive or vice-versa. Serology tests detecting antibodies to N or S protein could complement molecular diagnosis, particularly in late phases after disease onset or for retrospective studies[19-21].

In alternate, imaging using X-rays such as conventional chest X-rays (CXR) and high-resolution CT was used to quickly identify a patient when the capacity of molecular detection was overloaded as well as to identify the disease severity. CXR examination after two days of RT-PCR tests revealed that the yield of improved heatmaps of influential regions contributed to deep learning prediction scores *via* machine learning[22]. CT, a routine imaging modality is being performed for immediate diagnosis which is even effective in asymptomatic patients whose RT-PCR test results reveal to be negative as the CT scores give better disease findings and long-term follow-up with 29% increased sensitivity in comparison with chest radiography[23]. CT scanning combined with repeated swab tests was used for individuals with high clinical suspicion of COVID-19. Thus, combining RT-PCR with CT of the chest in an appropriate clinical setting is considered the best modality to investigate any patient. Ai *et al*[24], 2020 suggested a higher sensitivity of CT chest (98%) than RT-PCR (71%) in diagnosing COVID-19. In addition to CXR and CT, Infrared thermography has been useful in the identification of asymptomatic carriers *via* the detection of true core body temperature but its thermal cameras are insufficient for screening the disease[25]. The single-photon emission computerized tomography, and *in vivo* molecular imaging allows the observation of patient-specific and disease-specific characteristics for physiological models of COVID-19 patients[26,27].

Therapy and management of COVID-19 infection

Until the introduction of vaccines, test-positive subjects were isolated/ quarantined and provided with medication and supplements to boost their immune mechanism to overcome the disease. Initially, in the absence of proven effective therapies for COVID-19 or antivirals against SARS-CoV-2, researchers and manufacturers are conducting large-scale clinical trials to evaluate various therapies for COVID-19. Some of the existing options are to prevent viral entry, inhibition of virus replication, immunomodulatory agents, immunoglobulin therapy, vaccines, and potential control measures using ultraviolet radiation, and low-dose ionizing radiation[28]. The illustration of the use of X-rays in the diagnosis and therapy for COVID-19 has been provided in Figure 1. Absence of knowledge on the COVID-19 disease, screening, and specific treatment regimes, multiple approaches were tried to contain the spread of infection in the early time of the pandemic. Thus, the X-radiation technology was used in the early diagnosis, management, and containment of COVID-19 disease. The present review focused on consolidating the role of X-radiation in various stages of COVID-19 infection and disease manifestations: Screening, diagnosis, and management. Also, concerns associated with the use of X-rays in those phases of disease management were discussed.

CXR AND CT IMAGING OF COVID-19 PATIENTS

X-ray-based imaging is being used for the diagnosis of numerous health conditions for several decades. In the sudden outbreak of COVID-19, X-ray-based imaging was considered a relevant and rapid modality in the diagnosis of patients with COVID-19 disease, especially if the availability of other diagnostic methods like RT-PCR becomes limited due to a large number of infected patients and the time required for the reporting. CXR and high-resolution chest CT are the two important non-invasive examinations for the diagnosis of lung damage caused by COVID-19 infection[29]. Because of its intense resolution capacity and also clarity of organizational structures, these two X-ray imaging modalities have been used for the diagnosis of COVID infection and severity of disease in several countries. The prominent chest CT imaging findings of COVID-19 patients were found to be bilateral lung involvement and Ground Glass Opacities (GGO). Since then, many hospitals from different countries used both chest X-ray and chest CT imaging for the initial diagnosis of lung damage and published at a rapid pace. An

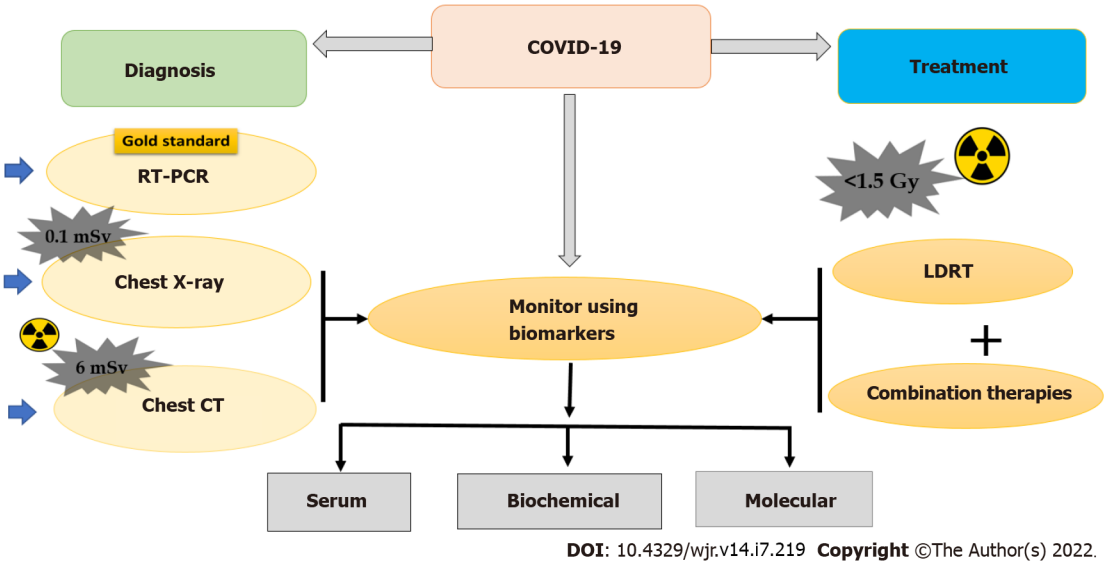

Figure 1 The use of X-rays in the diagnosis and therapy for coronavirus disease 2019 disease. COVID-19: Coronavirus disease 2019; CT: Computed tomography; LDRT: Low-dose radiation therapy; RT-PCR: Reverse-transcription polymerase chain reaction.

overview of the published articles on the diagnosis of COVID-19 infection using chest X-ray and chest CT imaging were shown in Supplementary Table 1. The finding from all those studies suggests that the radiographic findings seem to be good predictors for assessing the progress of COVID-19 disease. It was found that the chest CT has high sensitivity and lower specificity for diagnosis and severity of COVID-19 disease. CXR was used as a primary imaging technique for the initial screening of COVID-19 in many hospitals[30,31]. However, few studies sounded controversial that chest CT detected a combination of lung abnormalities that were not observed in CXR[32]. The enhanced use of CT substantially improved diagnostic performance over CXR in COVID-19 infections and diseases. Age-dependent variations on CT features were associated with clinical manifestation and also with patient prognosis[33]. Therefore, CT was considered for the initial assessment of suspected COVID-19 infections compared to CXR. In general, the CT features and scores ranging between, mild (0-7), moderate (8-17), and severe (18 or more) are usually associated with clinical manifestation and COVID-19 disease prognosis[34]. CT imaging had good diagnostic value in symptomatic infections and was insufficient to justify its use as a first-line screening approach in asymptomatic infections[35]. CXR severity was correlated with known laboratory markers of disease such as higher lactate dehydrogenase (LDH), higher C-reactive protein (CRP), and lower lymphocyte count[36]. In a similar study, CT findings showed characteristics of GGO, which were correlated with biochemical markers such as CRP, erythrocyte sedimentation rate, and LDH to the severity of COVID-19 infection[37]. Although the gold standard RT-PCR has been the primary source of diagnosis of COVID-19 infection, chest CT imaging has a high sensitivity for diagnosis and finding the severity of COVID-19 disease when compared to RT-PCR[24]. Both RT-PCR and X-ray-based imaging has been used extensively throughout the world to contain the spread of COVID-19 infection and disease severity in COVID-19 patients.

LOW DOSE X-RADIATION THERAPY (LDRT) FOR THE MANAGEMENT OF COVID-19 PATIENTS

The sudden outbreak of SARS-CoV-2 infections results in COVID-19 disease, which is associated with compromised immunological defense and lung damage[38]. Therefore, the COVID-19 patients were isolated/quarantined and provided with medication and supplements to boost their immune mechanism to overcome the disease[39]. In addition to the boosters to immune mechanisms, several therapy strategies were tested to prevent viral entry, inhibition of virus replication, immunomodulatory agents, immunoglobulin therapy, vaccines, and potential control measures[28]. The schematic representation of the possible therapy has been provided in Figure 2. One of those therapy strategies is the use of LDRT for COVID-19-infected patients because it has been proven to cure pneumonia in the early 20th century[40]. The treatment with low-dose X-rays complements other treatment modalities and has a profound role in minimizing COVID-19 infection severity[39]. Low dose comprises doses below 100 mGy as defined by UNSCEAR and has the characteristics such as accelerated immune senescence, altered immune fitness, a shift in peripheral lymphocyte, balance in favor of B-cells, and pro-inflammatory responses[39]. The first attempt on the use of LDRT for COVID-19-related pneumonia was made

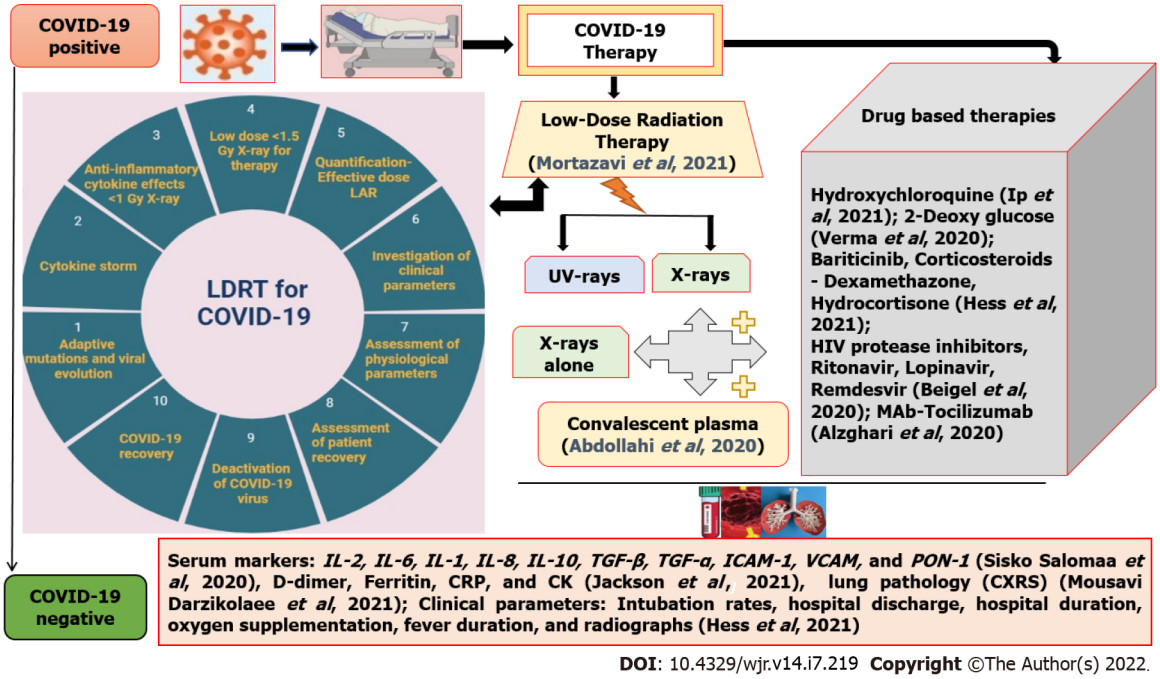

DOI: 10.4329/wjr.v14.i7.219

Figure 2 Overview of the therapy strategies to treat coronavirus disease 2019 disease. COVID-19: Coronavirus disease 2019; CT: Computed tomography; LDRT: Low-dose radiation therapy; RT-PCR: Reverse-transcription polymerase chain reaction.

by Italian and American scientists for which the patients received a single dose of either 0.10, 0.18 or 0.25 Gy[38]. Since then, many studies have attempted to exploit the potential of radiation in the management of COVID-19 disease. The list of major studies (animal models, isolated studies, and multi-centric clinical trials) related to LDRT and their salient findings are presented in Supplementary Table 2.

The range of doses employed in the LDRT among the published literature varies between 0.5-1.5 Gy of X-rays[39]. Whole lung LDRT may serve as a better option as it presents a low-risk treatment for COVID-19 pneumonia patients[38]. The LDRT is possible by using LINAC equipment that can deliver an appropriately low dose[39]. A recent study with nine clinical trials used the dose range between 0.5-1 Gy in a single fraction to investigate the effect of whole-lung irradiation of COVID-19 patients by analyzing the parameters such as CRP, IL-6, D- dimer, and ferritin as it can affect the lung macrophages at these doses[39]. The therapeutic benefits of LDRT for pneumonitis were evaluated based on the percentage of recovery and the extent of severity[41]. The most commonly evaluated outcome parameters were ventilator-free numerous hematologic, cardiac, hepatic, and inflammatory markers. Few parameters such as the probability of intubation rates, hospital discharge, hospital duration, oxygen supplementation, fever duration, radiographs, clinical recovery , SatO2/FiO2 index, and lung inflammation [42,43]. The radiation toxicity effects had also been studied apart from other parameters [44]. Physiological parameters such as blood oxygen level, clinical recovery rate, mean oxygen saturation, improvement in oxygenation SF ratio, and demand for supplemental oxygen in post-radiotherapy[45]. Clinical parameters such as overall survival, response rate, and X-ray severity score were mainly considered[46]. The level of serum biomarkers such as CRP, CK, and inflammatory cytokines such as IL-2, IL-6, IL-1, IL-8, IL-10, TGF-beta, TGF-alpha, ICAM-1, VCAM, and oxidative marker (PON-1) had been evaluated in previous studies[42]. LDRT can increase interferon-γ production, activates natural killer cells, stimulates antigen processing and antigen presentation to T- cells and activates natural killer T-cells (NKT), γδ T cells, and αβ CD8+ T-cells[47]. The results of these initial studies highlight that the LDRT can be used as one of the treatment options to treat pneumonia in COVID-19 patients.

The inclusion criteria for LDRT adopted in recent studies were COVID-19 +ve patients, age > 18 years, both genders, and national early warning score of ≥ 5, and the exclusion criteria were healthy volunteers, patients on mechanical ventilatory support, and hemodynamically unstable patients[48]. The mechanisms proposed in these recent studies are that the LDRT could inhibit the cytokine storm, activation of immune and endothelial cells, and inhibition of subsequent virus-induced pulmonary dysfunction in COVID-19 patients[49]. Despite many clinical trials being ongoing, three studies reported the prognosis of COVID-19 patients treated with LDRT as 80% to 90%[45,46,48]. The guidelines routinely used for whole-lung-irradiation of patients undergoing radiotherapy have been applied for COVID-19 patients treated using LDRT[49].

COVID-19 patients are associated with mucormycosis, shortly referred to as CAM, being one notifiable disease in India with a 50% fatality rate for which administering anti-fungal drugs (amphotericin-B) is the treatment[50]. This CAM condition had been observed in 79% of males, either

with 59% active COVID-19 or with 41% COVID-19 recovered status[44]. Further CAM studies were inquisitive for COVID-19 variants with mucor-immunity-associated disturbances, population-associated genetic susceptibilities, and the presence of virulent strains or influence of environmental factors. In such cases, LDRT is a hope in reducing CAM as it can increase CD3, CD4, and CD8 cells thereby transforming them to CD8 cells that can destroy acute respiratory syndrome-infected cells. An example of this LDRT was its implementation in treating tinea captitis till the discovery of griseofulvin[44].

Radiation as the choice of COVID-19 infection containment

LDRT also regulates lymphocyte counts, and bacterial co-infections in COVID-19 patients by modulating excess inflammatory responses[5]. The use of UV or γ-rays for sanitization will effectively kill viral particles[51]. Thus, deactivating COVID-19 viral cells and not allowing the infection to recur by implicating minimal dose radiation therapy by assessing the patient's condition can cure COVID-19[52]. The LDRT was also tested by combining with 2-deoxy glucose (2-DG), which has a potential adjuvant to enhance the efficacy of LDRT in the treatment of COVID-19 pneumonia[53]. Anti-inflammatory effects in LDRT are found to be associated with anti-viral or anti-bacterial effects[53]. Targeting the glycolytic pathway by 2-DG has been well established for its radio- and chemo-sensitizing effects in both *in vitro* and *in vivo* conditions. The 2-DG has been suggested as a therapeutic for the management of COVID-19 patients[53]. The 2-DG in combination with LDRT may also protect other virus-sensitive tissues and organs leading to a reduction in mortality and morbidity[53]. Azido-2-DG will produce the electron-mediated formation of oxidizing aminyl radicals, thus an adjuvant to LDRT[53].

BIOMARKERS FOR DIAGNOSIS OF COVID-19 INFECTION AND DISEASE

The biomarkers for the diagnosis of COVID-19 disease have been categorized into hematological [lymphocyte count, neutrophil count, and neutrophil-lymphocyte ratio (NLR)], inflammatory (CRP, Erythrocyte Sedimentation Rate, and procalcitonin), immunological (cytokines), and biochemical (D-dimer, troponin, creatine kinase, and aspartate aminotransferase), coagulation cascades in disseminated intravascular coagulation in most of the studies[54]. Retrospective studies conducted in COVID-19 patients admitted in intensive care unit (ICU) and post-recovery had been assessed for levels of several biomarkers wherein interleukins (IL)-2, IL7, IL10, GCSF, IP10, MCP1, MIP1A, and TNFα were higher in ICU patients than non-ICU patients[2]. Elevation of glomerular filtration function markers such as serum urea, CREA, and Cys C had been observed in severe COVID-19 patients more than in mild COVID-19 patients[55]. In comparison with the recovered group, the deceased group had an elevation in levels of leukocytes, neutrophils, high-sensitivity C-reactive protein (hsCRP), prothrombin, D-dimer, serum ferritin, IL-2, and IL-6[56]. Elevated levels of LDH, CRP, ferritin, and D-dimer had been found in most of the cases. IL-6 significantly increased in severe type, also IL-6, CRP, LDH, and ferritin were the most commonly elevated biomarkers and were associated with the severity of COVID-19[57]. On the other hand, a decrease in the density of natural killer cells and CD3+ T cells, including all T cell subsets had been observed in patients. Multiplex gene expression analysis showed an up-regulation of genes involved in type-I IFN signaling (*IFNAR1*, *JAK1*, and *TYK2*) contrasting with a striking down-regulation of *IFN*-stimulated genes (*MX1*, *IFITM1*, and *IFIT2*) in critical SARS-CoV-2 patients[58]. Lymphocytopenia was found to be the most common marker of infection in most critically ill COVID-19 patients [59]. These biomarkers are thus significant in the early identification of COVID-19 disease; hence disease prognosis can be improved and also helpful to monitor the LDRT.

LIMITATIONS/ FUTURE IMPROVEMENTS ON USING X-RAYS FOR THE DIAGNOSIS AND THERAPY OF COVID-19 DISEASE

Although, exposure to radiation from these X-ray imaging is a concern, due to its wide application in delivering intense structures of the organs which are been reliably used for the diagnosis of COVID-19 disease. However, the use of this X-ray-based imaging should be done with the most precaution since it might result in stochastic effects later in the life span of the exposed individual. Also, the concerns associated with the use of radiation in terms of risk for carcinogenesis were evaluated using phantom models[60]. The stochastic effects are seen with low doses in LDRT and thus quantifying the effective dose and Lifetime Attributable Risk will help in the effective treatment of COVID-19 pneumonia[41]. Delivering radiotherapy by giving quality assurance is impossible as the system conditions of portable X-ray machines delivering low-dose radiation therapy are not compatible. The concept of being as low as reasonably achievable is the basis of the radiation protection approach[61]. Targeting the whole lung requires vast knowledge about the biological mechanisms and hence deliverance of a low dose for an appropriate target volume is highly challenging. Examining LDRT in a trial setting in the case of COVID-19 treatment can be beneficial for patients and can be taken to the next level for scientific scrutiny. Shortening overall therapy time by giving multiple fractions/weeks may enhance COVID-19

management[62]. Based on the previous clinical trials, the effectiveness of LDRT in treating COVID-19 was up to 80%; therefore, the Food and Drug Administration recommended LDRT (by irradiating 0.5 Gy) as a treatment for COVID-19[63]. Thus, the contribution of X-ray-based imaging is enormous and its use is inevitable in modern-day health care including the COVID-19 pandemic. Despite the beneficial effects, the ethical concerns to use LDRT in the management of COVID-19 were the risk of spread of infection, time frame for a patient, and inconvenience in treating an intubated patient[64]. Even though medical imaging is widely used, divergent thoughts existed on the health effects of low-dose IR in scientific communities/stakeholders[65,66]. An "enhanced risk of stochastic effects due to radiation dose received by the patients during CT imaging" and "clarifications" from professional associations and regulatory authorities during this COVID-19 pandemic raised the anxiety among the public at the national level[67,68]. Any technology is not devoid of risk/side effects. Nevertheless, the improvements/advancements in technology contribute to minimizing the risk while enhancing the benefits. The same is the case for CT imaging; a recent low-dose chest CT protocol has been proposed to reduce the dose up to 89% when compared to the standard-dose protocol without compromising the diagnostic accuracy of COVID-19-induced pneumonia in CT images[69]. Despite those developments, the medical uses of IR are not devoid of criticism owing to the projected risk for different health effects. The reported studies suggest that CXR contributed significantly toward initial rapid diagnosis and CT- imaging to monitor the disease.

CONCLUSION

Overall the review of the literature suggests that the chest CT has high sensitivity (98%) and less specificity for COVID-19 disease diagnosis compared to RT-PCR. The LDRT therapy for COVID-19 patients compliments the drug therapy in the early recovery stage by maintaining the physiological parameters better than the drug therapy alone. All the recent studies results demonstrated that X-ray-based technology continues to evolve and play a significant role even during the COVID-19 pandemic.

FOOTNOTES

Author contributions: Aishwarya T A, Mohan DK, Nandhini K contributed to review of literature and preparation of the draft; Raavi V contributed to conceptualization and design of the work, revision, and editing; Perumal V contributed to conceptualization and approval of the final version of the manuscript.

Conflict-of-interest statement: All the authors declared that there is no conflict of interest.

Country/Territory of origin: India

ORCID number: Aishwarya T A 0000-0001-7818-3386; Divya K Mohan 0000-0001-8283-6343; Nandhini K 0000-0002-6066-1826; Venkateswarlu Raavi 0000-0002-7858-1664; Venkatachalam Perumal 0000-0003-2152-2003.

S-Editor: Liu JH
L-Editor: A
P-Editor: Liu JH

REFERENCES

1 **Cui J**, Li F, Shi ZL. Origin and evolution of pathogenic coronaviruses. *Nat Rev Microbiol* 2019; **17**: 181-192 [PMID: 30531947 DOI: 10.1038/s41579-018-0118-9]

2 **Huang C**, Wang Y, Li X, Ren L, Zhao J, Hu Y, Zhang L, Fan G, Xu J, Gu X, Cheng Z, Yu T, Xia J, Wei Y, Wu W, Xie X, Yin W, Li H, Liu M, Xiao Y, Gao H, Guo L, Xie J, Wang G, Jiang R, Gao Z, Jin Q, Wang J, Cao B. Clinical features of patients infected with 2019 novel coronavirus in Wuhan, China. *Lancet* 2020; **395**: 497-506 [PMID: 31986264 DOI: 10.1016/S0140-6736(20)30183-5]

3 **Na W**, Moon H, Song D. A comprehensive review of SARS-CoV-2 genetic mutations and lessons from animal coronavirus recombination in one health perspective. *J Microbiol* 2021; **59**: 332-340 [PMID: 33624270 DOI: 10.1007/s12275-021-0660-4]

4 **Chen H**, Guo J, Wang C, Luo F, Yu X, Zhang W, Li J, Zhao D, Xu D, Gong Q, Liao J, Yang H, Hou W, Zhang Y. Clinical

characteristics and intrauterine vertical transmission potential of COVID-19 infection in nine pregnant women: a retrospective review of medical records. *Lancet* 2020; **395**: 809-815 [PMID: 32151335 DOI: 10.1016/S0140-6736(20)30360-3]

5 **Mehta P**, McAuley DF, Brown M, Sanchez E, Tattersall RS, Manson JJ; HLH Across Speciality Collaboration, UK. COVID-19: consider cytokine storm syndromes and immunosuppression. *Lancet* 2020; **395**: 1033-1034 [PMID: 32192578 DOI: 10.1016/S0140-6736(20)30628-0]

6 **Wang D**, Hu B, Hu C, Zhu F, Liu X, Zhang J, Wang B, Xiang H, Cheng Z, Xiong Y, Zhao Y, Li Y, Wang X, Peng Z. Clinical Characteristics of 138 Hospitalized Patients With 2019 Novel Coronavirus-Infected Pneumonia in Wuhan, China. *JAMA* 2020; **323**: 1061-1069 [PMID: 32031570 DOI: 10.1001/jama.2020.1585]

7 **Guan WJ**, Ni ZY, Hu Y, Liang WH, Ou CQ, He JX, Liu L, Shan H, Lei CL, Hui DSC, Du B, Li LJ, Zeng G, Yuen KY, Chen RC, Tang CL, Wang T, Chen PY, Xiang J, Li SY, Wang JL, Liang ZJ, Peng YX, Wei L, Liu Y, Hu YH, Peng P, Wang JM, Liu JY, Chen Z, Li G, Zheng ZJ, Qiu SQ, Luo J, Ye CJ, Zhu SY, Zhong NS; China Medical Treatment Expert Group for Covid-19. Clinical Characteristics of Coronavirus Disease 2019 in China. *N Engl J Med* 2020; **382**: 1708-1720 [PMID: 32109013 DOI: 10.1056/NEJMoa2002032]

8 **Giacomelli A**, Pezzati L, Conti F, Bernacchia D, Siano M, Oreni L, Rusconi S, Gervasoni C, Ridolfo AL, Rizzardini G, Antinori S, Galli M. Self-reported Olfactory and Taste Disorders in Patients With Severe Acute Respiratory Coronavirus 2 Infection: A Cross-sectional Study. *Clin Infect Dis* 2020; **71**: 889-890 [PMID: 32215618 DOI: 10.1093/cid/ciaa330]

9 **Lauer SA**, Grantz KH, Bi Q, Jones FK, Zheng Q, Meredith HR, Azman AS, Reich NG, Lessler J. The Incubation Period of Coronavirus Disease 2019 (COVID-19) From Publicly Reported Confirmed Cases: Estimation and Application. *Ann Intern Med* 2020; **172**: 577-582 [PMID: 32150748 DOI: 10.7326/M20-0504]

10 **Wu Z**, McGoogan JM. Characteristics of and Important Lessons From the Coronavirus Disease 2019 (COVID-19) Outbreak in China: Summary of a Report of 72 314 Cases From the Chinese Center for Disease Control and Prevention. *JAMA* 2020; **323**: 1239-1242 [PMID: 32091533 DOI: 10.1001/jama.2020.2648]

11 **Lu X**, Zhang L, Du H, Zhang J, Li YY, Qu J, Zhang W, Wang Y, Bao S, Li Y, Wu C, Liu H, Liu D, Shao J, Peng X, Yang Y, Liu Z, Xiang Y, Zhang F, Silva RM, Pinkerton KE, Shen K, Xiao H, Xu S, Wong GWK; Chinese Pediatric Novel Coronavirus Study Team. SARS-CoV-2 Infection in Children. *N Engl J Med* 2020; **382**: 1663-1665 [PMID: 32187458 DOI: 10.1056/NEJMc2005073]

12 **Vivanti AJ**, Vauloup-Fellous C, Prevot S, Zupan V, Suffee C, Do Cao J, Benachi A, De Luca D. Transplacental transmission of SARS-CoV-2 infection. *Nat Commun* 2020; **11**: 3572 [PMID: 32665677 DOI: 10.1038/s41467-020-17436-6]

13 **Bordi L**, Nicastri E, Scorzolini L, Di Caro A, Capobianchi MR, Castilletti C, Lalle E; On Behalf Of Inmi Covid-Study Group And Collaborating Centers. Differential diagnosis of illness in patients under investigation for the novel coronavirus (SARS-CoV-2), Italy, February 2020. *Euro Surveill* 2020; **25** [PMID: 32127123 DOI: 10.2807/1560-7917.ES.2020.25.8.2000170]

14 **Chan JF**, Yip CC, To KK, Tang TH, Wong SC, Leung KH, Fung AY, Ng AC, Zou Z, Tsoi HW, Choi GK, Tam AR, Cheng VC, Chan KH, Tsang OT, Yuen KY. Improved Molecular Diagnosis of COVID-19 by the Novel, Highly Sensitive and Specific COVID-19-RdRp/Hel Real-Time Reverse Transcription-PCR Assay Validated *In Vitro* and with Clinical Specimens. *J Clin Microbiol* 2020; **58** [PMID: 32132196 DOI: 10.1128/JCM.00310-20]

15 **Corman VM**, Landt O, Kaiser M, Molenkamp R, Meijer A, Chu DK, Bleicker T, Brünink S, Schneider J, Schmidt ML, Mulders DG, Haagmans BL, van der Veer B, van den Brink S, Wijsman L, Goderski G, Romette JL, Ellis J, Zambon M, Peiris M, Goossens H, Reusken C, Koopmans MP, Drosten C. Detection of 2019 novel coronavirus (2019-nCoV) by real-time RT-PCR. *Euro Surveill* 2020; **25** [PMID: 31992387 DOI: 10.2807/1560-7917.ES.2020.25.3.2000045]

16 **Konrad R**, Eberle U, Dangel A, Treis B, Berger A, Bengs K, Fingerle V, Liebl B, Ackermann N, Sing A. Rapid establishment of laboratory diagnostics for the novel coronavirus SARS-CoV-2 in Bavaria, Germany, February 2020. *Euro Surveill* 2020; **25** [PMID: 32156330 DOI: 10.2807/1560-7917.ES.2020.25.9.2000173]

17 **Lu R**, Wu X, Wan Z, Li Y, Zuo L, Qin J, Jin X, Zhang C. Development of a Novel Reverse Transcription Loop-Mediated Isothermal Amplification Method for Rapid Detection of SARS-CoV-2. *Virol Sin* 2020; **35**: 344-347 [PMID: 32239445 DOI: 10.1007/s12250-020-00218-1]

18 **Cordes AK**, Heim A. Rapid random access detection of the novel SARS-coronavirus-2 (SARS-CoV-2, previously 2019-nCoV) using an open access protocol for the Panther Fusion. *J Clin Virol* 2020; **125**: 104305 [PMID: 32143123 DOI: 10.1016/j.jcv.2020.104305]

19 **Zhang W**, Du RH, Li B, Zheng XS, Yang XL, Hu B, Wang YY, Xiao GF, Yan B, Shi ZL, Zhou P. Molecular and serological investigation of 2019-nCoV infected patients: implication of multiple shedding routes. *Emerg Microbes Infect* 2020; **9**: 386-389 [PMID: 32065057 DOI: 10.1080/22221751.2020.1729071]

20 **Guo L**, Ren L, Yang S, Xiao M, Chang, Yang F, Dela Cruz CS, Wang Y, Wu C, Xiao Y, Zhang L, Han L, Dang S, Xu Y, Yang QW, Xu SY, Zhu HD, Xu YC, Jin Q, Sharma L, Wang L, Wang J. Profiling Early Humoral Response to Diagnose Novel Coronavirus Disease (COVID-19). *Clin Infect Dis* 2020; **71**: 778-785 [PMID: 32198501 DOI: 10.1093/cid/ciaa310]

21 **To KK**, Tsang OT, Leung WS, Tam AR, Wu TC, Lung DC, Yip CC, Cai JP, Chan JM, Chik TS, Lau DP, Choi CY, Chen LL, Chan WM, Chan KH, Ip JD, Ng AC, Poon RW, Luo CT, Cheng VC, Chan JF, Hung IF, Chen Z, Chen H, Yuen KY. Temporal profiles of viral load in posterior oropharyngeal saliva samples and serum antibody responses during infection by SARS-CoV-2: an observational cohort study. *Lancet Infect Dis* 2020; **20**: 565-574 [PMID: 32213337 DOI: 10.1016/S1473-3099(20)30196-1]

22 **Hu Q**, Drukker K, Giger ML. Role of standard and soft tissue chest radiography images in deep-learning-based early diagnosis of COVID-19. *J Med Imaging (Bellingham)* 2021; **8**: 014503 [PMID: 34595245 DOI: 10.1117/1.JMI.8.S1.014503]

23 **Pal A**, Ali A, Young TR, Oostenbrink J, Prabhakar A, Deacon N, Arnold A, Eltayeb A, Yap C, Young DM, Tang A, Lakshmanan S, Lim YY, Pokarowski M, Kakodkar P. Comprehensive literature review on the radiographic findings, imaging modalities, and the role of radiology in the COVID-19 pandemic. *World J Radiol* 2021; **13**: 258-282 [PMID: 34630913 DOI: 10.4329/wjr.v13.i9.258]

24 **Ai T**, Yang Z, Hou H, Zhan C, Chen C, Lv W, Tao Q, Sun Z, Xia L. Correlation of Chest CT and RT-PCR Testing for Coronavirus Disease 2019 (COVID-19) in China: A Report of 1014 Cases. *Radiology* 2020; **296**: E32-E40 [PMID: 32101510 DOI: 10.1148/radiol.2020200642]

25 **Khaksari K**, Nguyen T, Hill B, Quang T, Perreault J, Gorti V, Malpani R, Blick E, González Cano T, Shadgan B, Gandjbakhche AH. Review of the efficacy of infrared thermography for screening infectious diseases with applications to COVID-19. *J Med Imaging (Bellingham)* 2021; **8**: 010901 [PMID: 33786335 DOI: 10.1117/1.JMI.8.S1.010901]

26 **Barrett HH**, Caucci L. Stochastic models for objects and images in oncology and virology: application to PI3K-Akt-mTOR signaling and COVID-19 disease. *J Med Imaging (Bellingham)* 2021; **8**: S16001 [PMID: 33313340 DOI: 10.1117/1.JMI.8.S1.S16001]

27 **Giger M**. Medical imaging of COVID-19. *J Med Imaging (Bellingham)* 2021; **8**: 010101 [PMID: 34754885 DOI: 10.1117/1.JMI.8.S1.010101]

28 **Hu B**, Guo H, Zhou P, Shi ZL. Characteristics of SARS-CoV-2 and COVID-19. *Nat Rev Microbiol* 2021; **19**: 141-154 [PMID: 33024307 DOI: 10.1038/s41579-020-00459-7]

29 **Benmalek E**, Elmhamdi J, Jilbab A. Comparing CT scan and chest X-ray imaging for COVID-19 diagnosis. *Biomed Eng Adv* 2021; **1**: 100003 [PMID: 34786568 DOI: 10.1016/j.bea.2021.100003]

30 **Rousan LA**, Elobeid E, Karrar M, Khader Y. Chest x-ray findings and temporal lung changes in patients with COVID-19 pneumonia. *BMC Pulm Med* 2020; **20**: 245 [PMID: 32933519 DOI: 10.1186/s12890-020-01286-5]

31 **Stephanie S**, Shum T, Cleveland H, Challa SR, Herring A, Jacobson FL, Hatabu H, Byrne SC, Shashi K, Araki T, Hernandez JA, White CS, Hossain R, Hunsaker AR, Hammer MM. Determinants of Chest X-Ray Sensitivity for COVID-19: A Multi-Institutional Study in the United States. *Radiol Cardiothorac Imaging* 2020; **2**: e200337 [PMID: 33778628 DOI: 10.1148/ryct.2020200337]

32 **Das KM**, Alkoteesh JA, Al Kaabi J, Al Mansoori T, Winant AJ, Singh R, Paraswani R, Syed R, Sharif EM, Balhaj GB, Lee EY. Comparison of chest radiography and chest CT for evaluation of pediatric COVID-19 pneumonia: Does CT add diagnostic value? *Pediatr Pulmonol* 2021; **56**: 1409-1418 [PMID: 33631061 DOI: 10.1002/ppul.25313]

33 **Niu R**, Ye S, Li Y, Ma H, Xie X, Hu S, Huang X, Ou Y, Chen J. Chest CT features associated with the clinical characteristics of patients with COVID-19 pneumonia. *Ann Med* 2021; **53**: 169-180 [PMID: 33426973 DOI: 10.1080/07853890.2020.1851044]

34 **Hefeda MM**, Elsharawy DE, Dawoud TM. Correlation between the initial CT chest findings and short-term prognosis in Egyptian patients with COVID-19 pneumonia. *ESRNM* 2022; 1-17 [DOI: 10.1186/s43055-021-00685-w]

35 **De Smet K**, De Smet D, Ryckaert T, Laridon E, Heremans B, Vandenbulcke R, Demedts I, Bouckaert B, Gryspeerdt S, Martens GA. Diagnostic Performance of Chest CT for SARS-CoV-2 Infection in Individuals with or without COVID-19 Symptoms. *Radiology* 2021; **298**: E30-E37 [PMID: 32776832 DOI: 10.1148/radiol.2020202708]

36 **Hui TCH**, Khoo HW, Young BE, Haja Mohideen SM, Lee YS, Lim CJ, Leo YS, Kaw GJL, Lye DC, Tan CH. Clinical utility of chest radiography for severe COVID-19. *Quant Imaging Med Surg* 2020; **10**: 1540-1550 [PMID: 32676371 DOI: 10.21037/qims-20-642]

37 **Xiong Y**, Sun D, Liu Y, Fan Y, Zhao L, Li X, Zhu W. Clinical and High-Resolution CT Features of the COVID-19 Infection: Comparison of the Initial and Follow-up Changes. *Invest Radiol* 2020; **55**: 332-339 [PMID: 32134800 DOI: 10.1097/RLI.0000000000000674]

38 **Mehdizadeh A R**, Bevelacqua J J, Mortazavi S A R, Mortazavi S M J. COVID-19: Introducing Low Dose Radiation as an Effective Treatment for Pneumonia that Shouldn't Induce Selective Pressure and New Mutations. *J Biomed Phys Eng* 2020; **10**: 247-250 [PMID: 32637368 DOI: 10.31661/jbpe.v0i0.2005-1114]

39 **Mortazavi SMJ**, Shams SF, Mohammadi S, Mortazavi SAR, Sihver L. Low-Dose Radiation Therapy for COVID-19: A Systematic Review. *Radiation* 2021; 234-249 [DOI: 10.3390/radiation1030020]

40 **Lara PC**, Burgos J, Macias D. Low dose lung radiotherapy for COVID-19 pneumonia. The rationale for a cost-effective anti-inflammatory treatment. *Clin Transl Radiat Oncol* 2020; **23**: 27-29 [PMID: 32373721 DOI: 10.1016/j.ctro.2020.04.006]

41 **Jackson MR**, Stevenson K, Chahal SK, Curley E, Finney GE, Gutierrez-Quintana R, Onwubiko E, Rupp A, Strathdee K, Williams K, MacLeod MKL, McSharry C, Chalmers AJ. Low-Dose Lung Radiation Therapy for COVID-19 Lung Disease: A Preclinical Efficacy Study in a Bleomycin Model of Pneumonitis. *Int J Radiat Oncol Biol Phys* 2022; **112**: 197-211 [PMID: 34478832 DOI: 10.1016/j.ijrobp.2021.08.029]

42 **Hess CB**, Nasti TH, Dhere VR, Kleber TJ, Switchenko JM, Buchwald ZS, Stokes WA, Weinberg BD, Rouphael N, Steinberg JP, Godette KD, Murphy DJ, Ahmed R, Curran WJ Jr, Khan MK. Immunomodulatory Low-Dose Whole-Lung Radiation for Patients with Coronavirus Disease 2019-Related Pneumonia. *Int J Radiat Oncol Biol Phys* 2021; **109**: 867-879 [PMID: 33340603 DOI: 10.1016/j.ijrobp.2020.12.011]

43 **Ganesan G**, Ponniah S, Sundaram V, Marimuthu PK, Pitchaikannu V, Chandrasekaran M, Thangarasu J, Kannupaiyan G, Ramamoorthy P, Thangaraj B, Shree Vaishnavi R. Whole lung irradiation as a novel treatment for COVID-19: Interim results of an ongoing phase 2 trial in India. *Radiother Oncol* 2021; **163**: 83-90 [PMID: 34391759 DOI: 10.1016/j.radonc.2021.08.001]

44 **Sharma DN**, Welsh J, Kumar R. Can low-dose radiation therapy reduce the risk of mucormycosis in COVID-19 patients? *J Cancer Res Ther* 2021; **17**: 1294-1296 [PMID: 34916356 DOI: 10.4103/jcrt.JCRT_2011_21]

45 **Ameri A**, Rahnama N, Bozorgmehr R, Mokhtari M, Farahbakhsh M, Nabavi M, Shoaei SD, Izadi H, Yousefi Kashi AS, Dehbaneh HS, Taghizadeh-Hesary F. Low-Dose Whole-Lung Irradiation for COVID-19 Pneumonia: Short Course Results. *Int J Radiat Oncol Biol Phys* 2020; **108**: 1134-1139 [PMID: 32707264 DOI: 10.1016/j.ijrobp.2020.07.026]

46 **Hess CB**, Eng TY, Nasti TH, Dhere VR, Kleber TJ, Switchenko JM, Weinberg BD, Rouphael N, Tian S, Rudra S, Taverna LS, Daisson AP, Ahmed R, Khan MK. Whole-lung low-dose radiation therapy (LD-RT) for non-intubated oxygen-dependent patients with COVID-19-related pneumonia receiving dexamethasone and/or remdesevir. *Radiother Oncol* 2021; **165**: 20-31 [PMID: 34653525 DOI: 10.1016/j.radonc.2021.10.003]

47 **Abdollahi H**, Shiri I, Bevelacqua J J, Jafarzadeh A, Rahmim A, Zaidi H, Mortazavi S A R, Mortazavi S M J. Low Dose Radiation Therapy and Convalescent Plasma: How a Hybrid Method May Maximize Benefits for COVID-19 Patients. *J*

Biomed Phys Eng 2020; **10**: 387-394 [PMID: 32802787 DOI: 10.31661/jbpe.v0i0.2006-1125]

48 **Sharma DN**, Guleria R, Wig N, Mohan A, Rath G, Subramani V, Bhatnagar S, Mallick S, Sharma A, Patil P, Madan K, Soneja M, Thulkar S, Singh A, Singh S. Low-dose radiation therapy for COVID-19 pneumonia: a pilot study. *Br J Radiol* 2021; **94**: 20210187 [PMID: 34545760 DOI: 10.1259/bjr.20210187]

49 **Prasanna PG**, Woloschak GE, DiCarlo AL, Buchsbaum JC, Schaue D, Chakravarti A, Cucinotta FA, Formenti SC, Guha C, Hu DJ, Khan MK, Kirsch DG, Krishnan S, Leitner WW, Marples B, McBride W, Mehta MP, Rafii S, Sharon E, Sullivan JM, Weichselbaum RR, Ahmed MM, Vikram B, Coleman CN, Held KD. Low-Dose Radiation Therapy (LDRT) for COVID-19: Benefits or Risks? *Radiat Res* 2020; **194**: 452-464 [PMID: 33045077 DOI: 10.1667/RADE-20-00211.1]

50 **Aranjani JM**, Manuel A, Abdul Razack HI, Mathew ST. COVID-19-associated mucormycosis: Evidence-based critical review of an emerging infection burden during the pandemic's second wave in India. *PLoS Negl Trop Dis* 2021; **15**: e0009921 [PMID: 34793455 DOI: 10.1371/journal.pntd.0009921]

51 **Dua V**, Shishir V. Effect of ultraviolet c radiation, radiation & heat treatment on disinfection rate of SARS-COVID virus-2. *IJSDR* 2021; 206-213 Available from: https://www.ijsdr.org/papers/IJSDR2105035.pdf

52 **Venkatraman P**, Sahay JJ, Maidili T, Rajan R, Pooja S. Breakthrough of COVID-19 using radiotherapy treatment modalities. *Radiother Oncol* 2020; **148**: 225-226 [PMID: 32342867 DOI: 10.1016/j.radonc.2020.04.024]

53 **Verma A**, Adhikary A, Woloschak G, Dwarakanath BS, Papineni RVL. A combinatorial approach of a polypharmacological adjuvant 2-deoxy-D-glucose with low dose radiation therapy to quell the cytokine storm in COVID-19 management. *Int J Radiat Biol* 2020; **96**: 1323-1328 [PMID: 32910699 DOI: 10.1080/09553002.2020.1818865]

54 **Ponti G**, Maccaferri M, Ruini C, Tomasi A, Ozben T. Biomarkers associated with COVID-19 disease progression. *Crit Rev Clin Lab Sci* 2020; **57**: 389-399 [PMID: 32503382 DOI: 10.1080/10408363.2020.1770685]

55 **Xiang J**, Wen J, Yuan X, Xiong S, Zhou X, Liu C, Min X. Potential biochemical markers to identify severe cases among COVID-19 patients. *MedRxiv* 2020 [DOI: 10.1101/2020.03.19.20034447]

56 **Zhou S**, Chen C, Hu Y, Lv W, Ai T, Xia L. Chest CT imaging features and severity scores as biomarkers for prognostic prediction in patients with COVID-19. *Ann Transl Med* 2020; **8**: 1449 [PMID: 33313194 DOI: 10.21037/atm-20-3421]

57 **Liu T**, Zhang J, Yang Y, Zhang L, Ma H, Li Z, Cheng J, Zhang X, Wu G. The potential role of IL-6 in monitoring coronavirus disease 2019. SSRN 3548761: 2020 [DOI: 10.2139/ssrn.3548761]

58 **Hadjadj J**, Yatim N, Barnabei L, Corneau A, Boussier J, Smith N, Péré H, Charbit B, Bondet V, Chenevier-Gobeaux C, Breillat P, Carlier N, Gauzit R, Morbieu C, Pène F, Marin N, Roche N, Szwebel TA, Merkling SH, Treluyer JM, Veyer D, Mouthon L, Blanc C, Tharaux PL, Rozenberg F, Fischer A, Duffy D, Rieux-Laucat F, Kernéis S, Terrier B. Impaired type I interferon activity and inflammatory responses in severe COVID-19 patients. *Science* 2020; **369**: 718-724 [PMID: 32661059 DOI: 10.1126/science.abc6027]

59 **Yang X**, Yu Y, Xu J, Shu H, Xia J, Liu H, Wu Y, Zhang L, Yu Z, Fang M, Yu T, Wang Y, Pan S, Zou X, Yuan S, Shang Y. Clinical course and outcomes of critically ill patients with SARS-CoV-2 pneumonia in Wuhan, China: a single-centered, retrospective, observational study. *Lancet Respir Med* 2020; **8**: 475-481 [PMID: 32105632 DOI: 10.1016/S2213-2600(20)30079-5]

60 **García-Hernández T**, Romero-Expósito M, Sánchez-Nieto B. Low dose radiation therapy for COVID-19: Effective dose and estimation of cancer risk. *Radiother Oncol* 2020; **153**: 289-295 [PMID: 33065184 DOI: 10.1016/j.radonc.2020.09.051]

61 **Boon IS**, Au Yong TPT, Boon CS. Radiotherapy for COVID-19: Primum non nocere. *Radiother Oncol* 2020; **149**: 236-237 [PMID: 32505723 DOI: 10.1016/j.radonc.2020.05.046]

62 **Lancia A**, Bonzano E, Bottero M, Camici M, Catellani F, Ingrosso G. Radiotherapy in the era of COVID-19. *Expert Rev Anticancer Ther* 2020; **20**: 625-627 [PMID: 32552073 DOI: 10.1080/14737140.2020.1785290]

63 **Hahn SM**, Hahn DD. Low-dose radiotherapy, 0.5 Gy to the lungs, for COVID-19 pneumonia. 2020 [DOI: 10.13140/RG.2.2.27967.33441]

64 **Venkatesulu BP**, Lester S, Hsieh CE, Verma V, Sharon E, Ahmed M, Krishnan S. Low-Dose Radiation Therapy for COVID-19: Promises and Pitfalls. *JNCI Cancer Spectr* 2021; **5**: pkaa103 [PMID: 33437924 DOI: 10.1093/jncics/pkaa103]

65 **Oakley PA**, Harrison DE. Are Continued Efforts to Reduce Radiation Exposures from X-Rays Warranted? *Dose Response* 2021; **19**: 1559325821995653 [PMID: 33746654 DOI: 10.1177/1559325821995653]

66 **Rühm W**, Harrison RM. High CT doses return to the agenda. *Radiat Environ Biophys* 2020; **59**: 3-7 [PMID: 31844985 DOI: 10.1007/s00411-019-00827-9]

67 **Randeep Guleria**. (2021, May3). *"CT Scan Being Misused, Can't Detect Mild Covid Cases": AIIMS Director.* Randeep Guleria said asymptomatic patients with normal oxygen saturation should not go for CT scans. All India. Available from: https://www.ndtv.com/india-news/aiims-director-randeep-guleria-says-ct-scan-being-misused-cant-detect-mild-covid-cases-2427262

68 **A R Sundararajan**. (2021, May 13). “How safe are CT, X-Rays as first-line tools to screen for Covid-19?”. Unlike the swab tests which can diagnose Covid-19 accurately, imaging findings are not specific enough to confirm Covid-19. Deccan Herald. Available from: www.deccanherald.com/opinion/how-safe-are-ct-x-rays-as-first-line-tools-to-screen-for-covid-19-985344

69 **Azadbakht J**, Khoramian D, Lajevardi ZS, Elikaii F, Aflatoonian AH, Farhood B, Najafi M, Bagheri H. A review on chest CT scanning parameters implemented in COVID-19 patients: bringing low-dose CT protocols into play. *EJRNM* 2021; 1-10 [DOI: 10.1186/s43055-020-00400-1]

World Journal of Radiology

Submit a Manuscript: https://www.f6publishing.com

World J Radiol 2022 July 28; 14(7): 229-237

DOI: 10.4329/wjr.v14.i7.229

ISSN 1949-8470 (online)

ORIGINAL ARTICLE

Retrospective Study

Type 2 dynamic curves: A diagnostic dilemma

Erdal Karavas, Bunyamin Ece, Sonay Aydın

Specialty type: Radiology, nuclear medicine and medical imaging

Provenance and peer review: Invited article; Externally peer reviewed.

Peer-review model: Single blind

Peer-review report's scientific quality classification

Grade A (Excellent): 0
Grade B (Very good): B
Grade C (Good): 0
Grade D (Fair): D
Grade E (Poor): 0

P-Reviewer: Chrcanovic BR, Sweden; Ma C, China

Received: February 19, 2022
Peer-review started: February 19, 2022
First decision: April 8, 2022
Revised: April 16, 2022
Accepted: July 6, 2022
Article in press: July 6, 2022
Published online: July 28, 2022

Erdal Karavas, Sonay Aydın, Department of Radiology, Erzincan University, Erzincan 24142, Turkey

Bunyamin Ece, Department of Radiology, Kastamonu University, Kastamonu 37150, Turkey

Corresponding author: Bunyamin Ece, MD, Associate Professor, Doctor, Department of Radiology, Kastamonu University, Kuzeykent 57, Alay Street No. 4, Kastamonu 37150, Turkey. bunyaminece@hotmail.com

Abstract

BACKGROUND

Magnetic resonance imaging (MRI) with multiparametric dynamic contrast plays a critical role in the assessment of breast lesions. Dynamic curves are a critical parameter in determining the benign or malignant nature of lesions. Dynamic curves of type 1 are known to represent benign masses, while dynamic curves of type 3 are known to identify malignant masses. Type 2 dynamic curves have a sensitivity of 42.6% and specificity of 75% for malignancy detection.

AIM

To investigate the pathological diagnosis of lesions with type 2 dynamic curves.

METHODS

We evaluated breast MRI examinations performed between 2020 and 2021 retrospectively and included lesions with type 2 dynamic curves. We included 38 lesions from 33 patients. The lesions were evaluated for their pathological diagnosis and morphological characteristics.

RESULTS

Twenty-six lesions were malignant, while twelve were benign. The most frequently encountered benign lesion (7/12, 58.3%) was sclerosing adenosis, while the most frequently encountered malignant diagnosis was invasive ductal cancer. The presence of a type 2 dynamic curve had a sensitivity of 40.2% and specificity of 73.4% for predicting malignancy. By combining type 2 curves and morphological features, the sensitivity and specificity were increased.

CONCLUSION

The high rates of malignancy detected histopathologically among patients with type 2 dynamic curves in our study are remarkable. Type 2 dynamic curves can be detected in benign breast masses, especially in sclerosing adenosis cases. Considering morphological features can increase the diagnostic accuracy in cases

with type 2 dynamic curves.

Key Words: Type 2; Dynamic curve; Benign; Malignant; Breast; Magnetic resonance imaging

Core Tip: Dynamic contrast-enhanced magnetic resonance imaging (MRI) plays a critical role in the evaluation of breast lesions. The sensitivity and specificity of dynamic curves acquired using MRI are variable. While type 1 curves indicate more benign pathologies and type 3 curves indicate more malignant pathologies, there is a significant overlap in type 2 dynamic curves. We examined the histopathological outcomes of lesions with type 2 curves retrospectively. The histopathology results of lesions with type 2 curves were malignant at a rate of 68.4%. The presence of a type 2 dynamic curve had a sensitivity of 40.2% and specificity of 73.4% for predicting malignancy. By combining type 2 curves and morphological features, the area under the curve, sensitivity, and specificity were increased.

Citation: Karavas E, Ece B, Aydın S. Type 2 dynamic curves: A diagnostic dilemma. *World J Radiol* 2022; 14(7): 229-237
URL: https://www.wjgnet.com/1949-8470/full/v14/i7/229.htm
DOI: https://dx.doi.org/10.4329/wjr.v14.i7.229

INTRODUCTION

Breast magnetic resonance imaging (MRI) is a noninvasive technique that is highly sensitive for detecting breast cancer. Breast MRI can be used in situations where mammography is insufficient, in patients with dense breast structure, for preoperative planning in breast cancer, in multifocal and multicentric cases, for detecting contralateral malignancy, for evaluating response to neoadjuvant chemotherapy, and for postoperative control[1-5]. Breast MRI provides morphological information about lesions as well as kinetic features such as perfusion and enhancement of the lesion. Additionally, breast MR imaging is less affected by dense breast tissue than other imaging modalities, allowing for a higher sensitivity in detecting lesions[6-10].

The most frequently used MRI technique for evaluating breast cancer is dynamic contrast-enhanced magnetic resonance imaging (DCE-MR). A low molecular weight contrast agent (gadolinium) is injected intravenously for DCE-MR imaging. Gadolinium uptake and washout, and thus the detection of signal changes on T1-weighted images and the differentiation of cancerous from normal breast tissue, are the foundations of DCE-MR imaging of breast cancer[11].

The enhancement properties are determined by examining changes in signal intensity across multiple images acquired by pre- and post-contrast repeat MRI scans. The time-signal intensity curve, also known as the kinetic curve, can be classified into three types: Type 1 (persistence), type 2 (plateau), and type 3 (washout). Dynamic curve of type 1 (persistent) exhibits a persistent increase in signal intensity following contrast agent injection. Dynamic curve of type 2 (plateau) exhibits an initial slow or rapid increase followed by a flattening. Dynamic curve of type 3 (washout) involves an initial increase and subsequent decrease in signal intensity. Between benign and malignant lesions, there is considerable overlap in dynamic curves. Various noninvasive cancers may lack washout or plateau kinetics, but various benign entities, such as fibroadenomas, fibrocystic changes, scars, sclerosing adenosis, lobular carcinoma *in situ*, focal fibrosis, and atypical ductal hyperplasia, may show malignant curves[9,12,13]. Therefore, dynamic curves should not be evaluated alone without considering lesion morphology.

The aim of this study was to examine the histopathological outcomes of lesions with type 2 dynamic curves, in which there is a high degree of overlap between benign and malignant entities in the kinetic analysis performed using dynamic contrast MR imaging.

MATERIALS AND METHODS

Between January 2020 and January 2021, dynamic contrast enhanced breast MRI scans were evaluated retrospectively. In the research conducted from the hospital information system, there were 560 patients who underwent dynamic contrast MR examinations between January 2020 and January 2021. In the results of these patients, type 2 dynamic curve was detected in 48 lesions of 41 patients. Ten lesions in eight patients were excluded from the study due to a history of radiotherapy within the previous 6 mo, previous surgery or tru-cut biopsy, lack of histopathological results, and imaging artifacts. As a result,

38 lesions in 33 patients were included in the study.

Dynamic contrast enhanced breast MR images of the lesions included in the study were reviewed retrospectively with a consensus formed by two radiology specialists. The evaluators had more than 8 years of experience in interpreting breast MRI images. The patients' anamnesis, previous mammography, and ultrasonography examinations were re-examined using the hospital information system. The radiologists who performed the retrospective evaluation were blinded to the lesions' histopathological findings. Enhancement dynamic curves were calculated using the region of interest (ROI) method. Evaluators checked for type 2 dynamic curves by reconstructing dynamic curves from high temporal resolution dynamic images of the included lesions. Additionally, the evaluators classified the lesions according to their morphological characteristics using the American College of Radiology (ACR)'s Breast Imaging Reporting and Data System (BI-RADS) classification[14], which ranges from 0 to 5. Additionally, the histopathological findings of the patients were retrieved and recorded retrospectively from the hospital information system.

The data used for this study were collected anonymously and local ethics committee approval was obtained for this study (ethics committee number: 34336249-604.01.02-E.30236). This study adhered to the Declaration of Helsinki. Because the study was retrospective, informed consent was not obtained.

The same device and protocol were used for dynamic contrast-enhanced breast MRI examinations. One 1.5-T whole-body MRI scanner was used for breast MRI with dynamic contrast (Magnetom Avanto; Siemens Healthineers). The vendor-supplied receive-only 4-channel circularly polarized breast array coil was used. A standard protocol includes a T2-weighted rapid (fast or turbo) spin-echo (TR: 4000 ms; TE: 90 ms; ≤ 4 mm thickness) acquisition and 3D T1-weighted GRE (20/4.5; flip angle, 30°–45°; ≤ 3 mm thickness) acquisitions before and after the administration of gadolinium, with the usual dose of 0.1 mmol/kg injected as a bolus and followed by a 10–20-mL saline flush. For sagittal plane, an image matrix of 256 × 192 can be used with zero-filled interpolation to 512 × 512, a small field of view (16–18 cm), and chemical fat suppression. For bilateral axial imaging, the field of view is increased to approximately 30 cm, and high-resolution matrices (between 256 and 512) are used.

Statistical analysis

The sample size was calculated using G power analysis (alpha error: 0.05; power: 80%); the minimum number of patients was thus defined as 31. The Statistical Package for Social Sciences (SPSS) for Windows 20 software was used to analyze the data (IBM SPSS Inc., Chicago, IL, United States). The Kolmogorov-Smirnov test was used to determine whether the age data conformed to a normal distribution. Age is represented as the mean ± SD and categorical variables as number (n) and percentage values (%). To define the diagnostic efficacy of type 2 dynamic curves alone and along with morphological characteristics, receiver operating characteristic analysis was used. The chi-square test was used to compare two groups of categorical variables. Statistical significance was defined as a two-tailed value of $P < 0.050$.

RESULTS

A total of 38 lesions in 33 patients were included in the study. The mean age of the patients was 53.7 ± 10.1 years (range, 43-87 years).

The 38 lesions included in the study showed a dynamic contrast enhancement curve of type 2 (plateau) on their dynamic contrast imaging (Figures 1 and 2). The histopathological diagnoses of these lesions are shown in Table 1. As a result, 12 lesions were determined to be benign, while 26 lesions were determined to be malignant. While sclerosing adenosis was the most frequently encountered benign pathology, invasive ductal carcinoma was the most frequently encountered malignant pathology (Table 1).

The morphological evaluation results obtained using the ACR BI-RADS classification system for the lesions are given in Table 2. Histopathological examinations of eight lesions classified as BI-RADS 3 revealed that the vast majority (5 of them) were sclerosing adenosis. One lesion in the BI-RADS 3 category was histopathologically diagnosed as invasive ductal carcinoma. The remaining two lesions were benign. Sixteen of the 18 BI-RADS 4 lesions with type 2 dynamic curve were malignant, while two were benign. All 12 lesions classified as BI-RADS 5 were found to be malignant on histopathology (Table 2).

The presence of a type 2 dynamic curve had a sensitivity of 40.2% and specificity of 73.4% for predicting malignancy. By combining type 2 curves and morphological features, the area under the curve, sensitivity, and specificity were increased (Table 3, Figure 3).

DISCUSSION

In our study, we investigated the histopathological results of type 2 dynamic curves obtained from dynamic contrast magnetic resonance imaging, which plays a critical role in the evaluation of breast

Table 1 Histopathological results of lesions with type 2 curves

	Histopathological diagnosis	*n* (%)
Benign 12/38 (31.6%)	Sclerosing adenosis	7 (18.4)
	Fibroadenoma	3 (7.9)
	Intraductal papilloma	1 (2.6)
	Usual ductal hyperplasia	1 (2.6)
Malignant 26/38 (68.4%)	Ductal carcinoma in situ	7 (18.4)
	Invasive ductal carcinoma	15 (39.5)
	Invasive lobular carcinoma	4 (10.5)
Total		38 (100)

Table 2 Breast Imaging Reporting and Data System categories of lesions

BI-RADS category	*n* (%)
BI-RADS-0	0
BI-RADS-1	0
BI-RADS-2	0
BI-RADS-3	8 (21)
BI-RADS-4	18 (47.4)
BI-RADS-5	12 (31.6)
Total	38 (100)

BI-RADS: Breast Imaging Reporting and Data System.

Table 3 Sensitivity and specificity values obtained by combining type 2 curves and morphological features for predicting malignancy

	Sensitivity	Specificity
Type 2 dynamic curve	40.2	73.4
Type 2 dynamic curve + BI-RADS 3 category	41.9	75.8
Type 2 dynamic curve + BI-RADS 4 category	95.3	97.7
Type 2 dynamic curve + BI-RADS 5 category	100	100

BI-RADS: Breast Imaging Reporting and Data System.

lesions. We found that the type 2 dynamic curve had a sensitivity of 40.2% and specificity of 73.4% in predicting malignancy. Additionally, we found that combining type 2 dynamic curve with morphological findings increased the sensitivity and specificity.

The type 1 (persistent) dynamic curve obtained from breast MRI with dynamic contrast indicates a higher rate of benign pathologies, while the type 3 (washout) dynamic curve indicates a higher rate of malignant pathologies according to the literature[9,11]. However, it has been reported in the literature that time-signal intensity curves have a high sensitivity but relatively low specificity for breast cancer diagnosis[15-20]. It is critical to keep in mind when evaluating these kinetic images that there is considerable overlap between benign and malignant lesions[9,12,13,21]. Schnall *et al*[20] reported in a multicenter study of evaluating 995 breast lesions that a lesion with type 3 curve has a five times higher relative risk of cancer than a lesion with type 1 curve. According to the same study, 76% of lesions with type 3 curves were associated with malignancy. In other studies in the literature, a significant correlation was reported between malignancy and type 3 washout dynamic curve[15,16,22,23]. Durhan *et al*[24] in their study on young women under 40 years of age, stated that 25 of 27 malignant lesions had type 2 and type 3 dynamic curves. In contrary to the majority in the literature, Williams *et al*[25] found no significant difference between dynamic curves and benign and malignant lesions in their study with

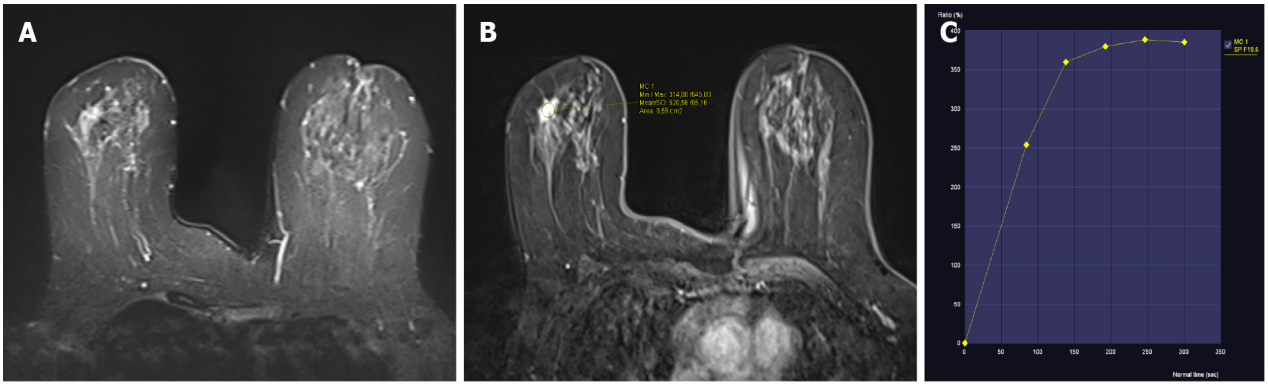

DOI: 10.4329/wjr.v14.i7.229 **Copyright** ©The Author(s) 2022.

Figure 1 A 63-year-old patient. A: Hyperintense lesion on T2 weighted image (WI) in the right breast; B: The lesion is enhanced on post-contrast T1WI; C: The dynamic curve of the lesion is type 2. Pathological diagnosis is invasive ductal carcinoma.

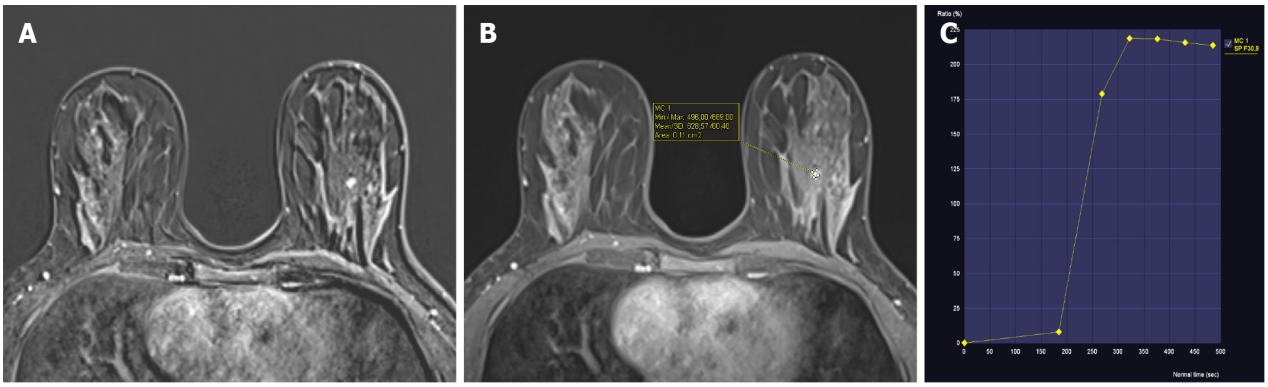

DOI: 10.4329/wjr.v14.i7.229 **Copyright** ©The Author(s) 2022.

Figure 2 A 37-year-old patient. A: Hyperintense lesion on T2 weighted image (WI) in the right breast; B: The lesion is enhanced on post-contrast T1WI; C: The dynamic curve of the lesion is type 2. Pathological diagnosis is fibroadenoma.

41 malignant and 113 benign lesions. They stated that the reason for lack of significant difference may be due to the lower temporal resolution in their study and the different MR imaging protocols compared to other studies. Macura *et al*[26] stated in support of this in the literature that due to the low temporal resolution, washout may not be visible in the signal intensity-time curve because the first contrast images are acquired too late after peak formation. When these data in the literature are reviewed, it is understood that the results of dynamic curves, especially type 2 dynamic curves, may be contradictory. For this reason, we conducted a study investigating the histopathological results of type 2 curves. Our findings show that type 2 dynamic curve can be an important finding in demonstrating malignancy and supports other data in the literature in contrary to the study of Williams *et al*[25].

In our study, we evaluated lesions with a type 2 (plateau) dynamic curve and discovered that approximately 68% of these lesions were malignant. According to the literature, Kuhl *et al*[15] in their study including 101 malignant and 165 benign cases, found that the type 1 dynamic curve was observed in 83% of benign lesions and 9% of malignant lesions, type 2 dynamic curve was observed in 13% of benign lesions and 34% of malignant lesions, and type 3 dynamic curve was observed in 6% of benign lesions and 57% of malignant lesions. Bluemke *et al*[16] in their study including 404 malignant and 366 benign cases, found that the type 3 dynamic curve had a 20.5% sensitivity and 90.4% specificity, type 2 dynamic curve had a 42.6% sensitivity and 75% specificity, and type 1 dynamic curve had a 52.2% sensitivity and 71% specificity for detecting benignity. According to these results[15,16], our study's malignancy rate was higher than those reported in the literature, but the sensitivity and specificity rates were similar. As supported by our findings and the literature, the type 2 dynamic curve indicates an increased risk of malignant lesions. These results led us to believe that in the presence of a type 2 dynamic curve, we should exercise caution in terms of suspicion of malignancy.

Numerous studies have demonstrated that combining use of both morphological and enhancement kinetics improves the sensitivity and specificity of MRI[27-29]. Lee *et al*[21] stated in their study that as a reasonable strategy, the morphological features of the lesion should be evaluated before evaluating the enhancement kinetics, and in case of suspicious morphological features, further evaluation including histopathological diagnosis should be made. They also stated that if the lesion is morphologically

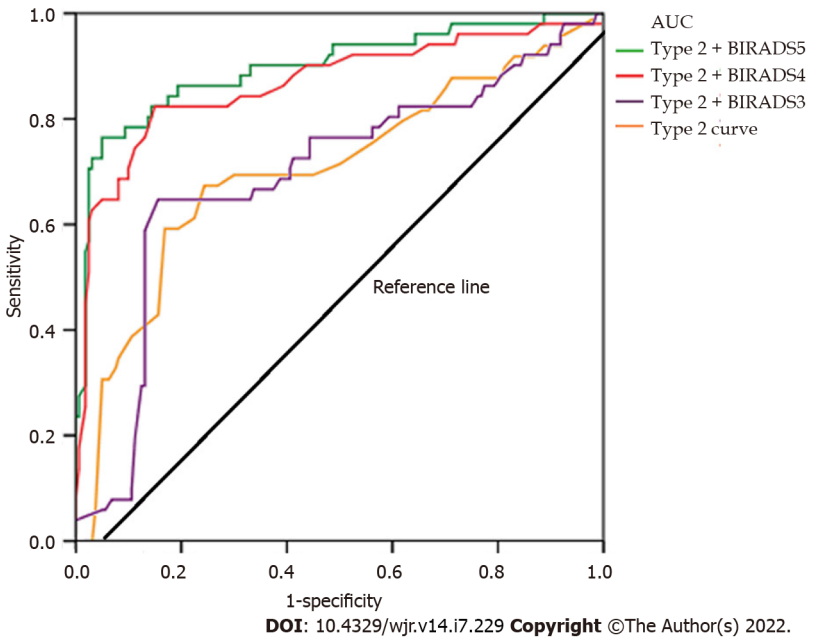

DOI: 10.4329/wjr.v14.i7.229

Figure 3 Receiver operating characteristic analysis graph by combining type 2 curves and morphological features for predicting malignancy. AUC: Area under the curve.

benign or indeterminate, evaluation of the enhancement kinetics can help differentiate lesions that may require biopsy. Additionally, it should be emphasized at this point that the MR examination should be correlated with mammographic and sonographic findings to increase the accuracy of the result. According to these data, we also examined the sensitivity and specificity of type 2 dynamic curves for detecting malignancy both alone and in combination with the BI-RADS classification. Accordingly, while the sensitivity and specificity values of the type 2 dynamic curve increased significantly when combined with BI-RADS 4 and 5, no significant increase was observed when combined with BI-RADS 3. According to the ACR, radiological follow-up is recommended instead of histopathological correlation in BI-RADS 3 lesions[14]. In our study, histopathological correlation was performed on eight lesions with type 2 dynamic curves in BI-RADS 3 lesions, and one of them was found to be malignant. At this point, although there is a possibility of unnecessary histopathological correlation to BI-RADS 3 lesions, the fact that even one malignancy was detected in our results suggests that histopathological correlation may provide additional benefit in the presence of type 2 dynamic curve in BI-RADS 3 lesions. There is a need for studies examining the type 2 dynamic curve and BI-RADS 3 classification in a larger patient population.

There are some limitations to our study. The most significant limitations are the study's retrospective design and small patient population. Additionally, when the ROI method is used to create a dynamic curve, inter-rater variability may occur. In our study, two radiologists evaluated the images retrospectively with a consensus and there was no assessment of interobserver variability. Finally, the study was designed to assess only the type 2 dynamic curve in contrast-enhanced dynamic series; lesions with type 1 or type 3 dynamic curves were not included and early phase (initial) enhancement was not assessed.

CONCLUSION

In conclusion, the high rates of malignancy detected histopathologically among patients with type 2 curves in our study are remarkable. However, it is possible to detect type 2 dynamic curves in benign lesions as well. Compared to the evaluation made with only the type 2 dynamic curve, the combined evaluation with the BI-RADS categories increases the sensitivity and specificity of the type 2 dynamic curve.

ARTICLE HIGHLIGHTS

Research background

Dynamic contrast-enhanced magnetic resonance imaging (MRI) is the most frequently used MRI

technique for evaluating breast cancer. Changes in signal intensity across multiple images acquired by pre- and post-contrast repeat MRI scans are used to determine the enhancement patterns. The time-signal intensity curve, also known as the kinetic curve, can be classified into three types: Type 1 (persistence), type 2 (plateau), and type 3 (washout). A higher rate of benign pathologies is indicated by the type 1 dynamic curve, while a higher rate of malignant pathologies is indicated by the type 3 dynamic curve. However, there is a dilemma with the type 2 curve. The aim of this study was to investigate the histopathological outcomes of lesions with type 2 dynamic curves, which have much overlap in the kinetic analysis between benign and malignant entities.

Research motivation

There have been several studies on type 3 and type 1 dynamic curves, but studies on type 2 dynamic curves are not sufficient. More research on type 2 dynamic curves, which have much overlap in kinetic analysis between benign and malignant entities, is needed.

Research objectives

The aim of this study was to examine the histopathological outcomes of lesions with type 2 dynamic curves, in which there is a high degree of overlap between benign and malignant entities in the kinetic analysis performed using dynamic contrast MRI.

Research methods

Two experienced radiologists retrospectively re-evaluated lesions with type 2 dynamic curves. The included lesions were re-examined for type 2 dynamic curves by the evaluators. Additionally, the evaluators classified the lesions according to their morphological characteristics using the American College of Radiology's Breast Imaging Reporting and Data System classification. The histopathological findings of the patients were retrieved and recorded retrospectively from the hospital information system. Receiver operating characteristic analysis was done to determine the diagnostic efficacy of type 2 dynamic curves alone and in combination with morphological characteristics.

Research results

Thirty-eight lesions in 33 patients were included in the study. As a result, 12 lesions were determined to be benign, while 26 lesions were determined to be malignant. While sclerosing adenosis was the most frequently encountered benign pathology, invasive ductal carcinoma was the most frequently encountered malignant pathology. The presence of a type 2 dynamic curve had a sensitivity of 40.2% and specificity of 73.4% for predicting malignancy. By combining type 2 curves and morphological features, the area under the curve, sensitivity, and specificity were increased.

Research conclusions

In our investigation, the significant rates of malignancy discovered histopathologically among patients with type 2 curves are remarkable. In the presence of a type 2 dynamic curve, we should exercise caution in terms of suspicion of malignancy.

Research perspectives

Studies with larger patient populations focusing on the histopathological results of lesions with type 2 dynamic curves are needed.

FOOTNOTES

Author contributions: Karavas E participated in design and oversight of the study, and drafted the manuscript; Ece B participated in design of the study and drafted the manuscript; and Aydin S participated in design of the study, drafted the manuscript, and performed statistical analysis.

Institutional review board statement: The study was reviewed and approved by the Erzincan University Institutional Review Board (ethics committee number: 34336249-604.01.02-E.30236).

Conflict-of-interest statement: All authors report no relevant conflicts of interest for this article.

Data sharing statement: Technical appendix, statistical code, and dataset available from the corresponding author at bunyaminece@hotmail.com. Informed consent was not obtained since the presented data are anonymized and risk of identification is low.

Country/Territory of origin: Turkey

ORCID number: Erdal Karavas 0000-0001-6649-3256; Bunyamin Ece 0000-0001-6288-8410; Sonay Aydın 0000-0002-3812-6333.

S-Editor: Ma YJ
L-Editor: Wang TQ
P-Editor: Ma YJ

REFERENCES

1 **Peters NH**, Borel Rinkes IH, Zuithoff NP, Mali WP, Moons KG, Peeters PH. Meta-analysis of MR imaging in the diagnosis of breast lesions. *Radiology* 2008; **246**: 116-124 [PMID: 18024435 DOI: 10.1148/radiol.2461061298]
2 **Bedrosian I**, Mick R, Orel SG, Schnall M, Reynolds C, Spitz FR, Callans LS, Buzby GP, Rosato EF, Fraker DL, Czerniecki BJ. Changes in the surgical management of patients with breast carcinoma based on preoperative magnetic resonance imaging. *Cancer* 2003; **98**: 468-473 [PMID: 12879462 DOI: 10.1002/cncr.11490]
3 **Fischer U**, Kopka L, Grabbe E. Breast carcinoma: effect of preoperative contrast-enhanced MR imaging on the therapeutic approach. *Radiology* 1999; **213**: 881-888 [PMID: 10580970 DOI: 10.1148/radiology.213.3.r99dc01881]
4 **Liberman L**, Morris EA, Kim CM, Kaplan JB, Abramson AF, Menell JH, Van Zee KJ, Dershaw DD. MR imaging findings in the contralateral breast of women with recently diagnosed breast cancer. *AJR Am J Roentgenol* 2003; **180**: 333-341 [PMID: 12540428 DOI: 10.2214/ajr.180.2.1800333]
5 **Lehman CD**, Gatsonis C, Kuhl CK, Hendrick RE, Pisano ED, Hanna L, Peacock S, Smazal SF, Maki DD, Julian TB, DePeri ER, Bluemke DA, Schnall MD; ACRIN Trial 6667 Investigators Group. MRI evaluation of the contralateral breast in women with recently diagnosed breast cancer. *N Engl J Med* 2007; **356**: 1295-1303 [PMID: 17392300 DOI: 10.1056/NEJMoa065447]
6 **DeMartini W**, Lehman C. A review of current evidence-based clinical applications for breast magnetic resonance imaging. *Top Magn Reson Imaging* 2008; **19**: 143-150 [PMID: 18941394 DOI: 10.1097/RMR.0b013e31818a40a5]
7 **Kriege M**, Brekelmans CT, Boetes C, Besnard PE, Zonderland HM, Obdeijn IM, Manoliu RA, Kok T, Peterse H, Tilanus-Linthorst MM, Muller SH, Meijer S, Oosterwijk JC, Beex LV, Tollenaar RA, de Koning HJ, Rutgers EJ, Klijn JG; Magnetic Resonance Imaging Screening Study Group. Efficacy of MRI and mammography for breast-cancer screening in women with a familial or genetic predisposition. *N Engl J Med* 2004; **351**: 427-437 [PMID: 15282350 DOI: 10.1056/NEJMoa031759]
8 **Orel SG**, Schnall MD. MR imaging of the breast for the detection, diagnosis, and staging of breast cancer. *Radiology* 2001; **220**: 13-30 [PMID: 11425968 DOI: 10.1148/radiology.220.1.r01jl3113]
9 **Kuhl C**. The current status of breast MR imaging. Part I. Choice of technique, image interpretation, diagnostic accuracy, and transfer to clinical practice. *Radiology* 2007; **244**: 356-378 [PMID: 17641361 DOI: 10.1148/radiol.2442051620]
10 **Boetes C**, Veltman J. Screening women at increased risk with MRI. *Cancer Imaging* 2005; **5** Spec No A: S10-S15 [PMID: 16361123 DOI: 10.1102/1470-7330.2005.0040]
11 **Moon M**, Cornfeld D, Weinreb J. Dynamic contrast-enhanced breast MR imaging. *Magn Reson Imaging Clin N Am* 2009; **17**: 351-362 [PMID: 19406363 DOI: 10.1016/j.mric.2009.01.010]
12 **Rausch DR**, Hendrick RE. How to optimize clinical breast MR imaging practices and techniques on Your 1.5-T system. *Radiographics* 2006; **26**: 1469-1484 [PMID: 16973776 DOI: 10.1148/rg.265055176]
13 **Jansen SA**, Fan X, Karczmar GS, Abe H, Schmidt RA, Newstead GM. Differentiation between benign and malignant breast lesions detected by bilateral dynamic contrast-enhanced MRI: a sensitivity and specificity study. *Magn Reson Med* 2008; **59**: 747-754 [PMID: 18383287 DOI: 10.1002/mrm.21530]
14 **D'Orsi C**, Morris E, Mendelson E. ACR BI-RADS® Atlas, Breast Imaging Reporting and Data System. American College of Radiology; 2013. Available from: https://www.scienceopen.com/document?vid=ddb508dc-e150-4b1c-aad8-1be1c031edd8
15 **Kuhl CK**, Mielcareck P, Klaschik S, Leutner C, Wardelmann E, Gieseke J, Schild HH. Dynamic breast MR imaging: are signal intensity time course data useful for differential diagnosis of enhancing lesions? *Radiology* 1999; **211**: 101-110 [PMID: 10189459 DOI: 10.1148/radiology.211.1.r99ap38101]
16 **Bluemke DA**, Gatsonis CA, Chen MH, DeAngelis GA, DeBruhl N, Harms S, Heywang-Köbrunner SH, Hylton N, Kuhl CK, Lehman C, Pisano ED, Causer P, Schnitt SJ, Smazal SF, Stelling CB, Weatherall PT, Schnall MD. Magnetic resonance imaging of the breast prior to biopsy. *JAMA* 2004; **292**: 2735-2742 [PMID: 15585733 DOI: 10.1001/jama.292.22.2735]
17 **Kinkel K**, Helbich TH, Esserman LJ, Barclay J, Schwerin EH, Sickles EA, Hylton NM. Dynamic high-spatial-resolution MR imaging of suspicious breast lesions: diagnostic criteria and interobserver variability. *AJR Am J Roentgenol* 2000; **175**: 35-43 [PMID: 10882243 DOI: 10.2214/ajr.175.1.1750035]
18 **El Khouli RH**, Macura KJ, Jacobs MA, Khalil TH, Kamel IR, Dwyer A, Bluemke DA. Dynamic contrast-enhanced MRI of the breast: quantitative method for kinetic curve type assessment. *AJR Am J Roentgenol* 2009; **193**: W295-W300 [PMID: 19770298 DOI: 10.2214/AJR.09.2483]
19 **Baltzer PA**, Benndorf M, Dietzel M, Gajda M, Runnebaum IB, Kaiser WA. False-positive findings at contrast-enhanced breast MRI: a BI-RADS descriptor study. *AJR Am J Roentgenol* 2010; **194**: 1658-1663 [PMID: 20489110 DOI: 10.2214/AJR.09.3486]
20 **Schnall MD**, Blume J, Bluemke DA, DeAngelis GA, DeBruhl N, Harms S, Heywang-Köbrunner SH, Hylton N, Kuhl CK,

Pisano ED, Causer P, Schnitt SJ, Thickman D, Stelling CB, Weatherall PT, Lehman C, Gatsonis CA. Diagnostic architectural and dynamic features at breast MR imaging: multicenter study. *Radiology* 2006; **238**: 42-53 [PMID: 16373758 DOI: 10.1148/radiol.2381042117]

21 **Lee CH**. Problem solving MR imaging of the breast. *Radiol Clin North Am* 2004; **42**: 919-934, vii [PMID: 15337425 DOI: 10.1016/j.rcl.2004.05.001]

22 **Chen W**, Giger ML, Lan L, Bick U. Computerized interpretation of breast MRI: investigation of enhancement-variance dynamics. *Med Phys* 2004; **31**: 1076-1082 [PMID: 15191295 DOI: 10.1118/1.1695652]

23 **Gilhuijs KG**, Deurloo EE, Muller SH, Peterse JL, Schultze Kool LJ. Breast MR imaging in women at increased lifetime risk of breast cancer: clinical system for computerized assessment of breast lesions initial results. *Radiology* 2002; **225**: 907-916 [PMID: 12461278 DOI: 10.1148/radiol.2253011582]

24 **Durhan G**, Azizova A, Önder Ö, Kösemehmetoğlu K, Karakaya J, Akpınar MG, Demirkazık F, Üner A. Imaging Findings and Clinicopathological Correlation of Breast Cancer in Women under 40 Years Old. *Eur J Breast Health* 2019; **15**: 147-152 [PMID: 31312789 DOI: 10.5152/ejbh.2019.4606]

25 **Williams TC**, DeMartini WB, Partridge SC, Peacock S, Lehman CD. Breast MR imaging: computer-aided evaluation program for discriminating benign from malignant lesions. *Radiology* 2007; **244**: 94-103 [PMID: 17507720 DOI: 10.1148/radiol.2441060634]

26 **Macura KJ**, Ouwerkerk R, Jacobs MA, Bluemke DA. Patterns of enhancement on breast MR images: interpretation and imaging pitfalls. *Radiographics* 2006; **26**: 1719-34; quiz 1719 [PMID: 17102046 DOI: 10.1148/rg.266065025]

27 **Liu PF**, Debatin JF, Caduff RF, Kacl G, Garzoli E, Krestin GP. Improved diagnostic accuracy in dynamic contrast enhanced MRI of the breast by combined quantitative and qualitative analysis. *Br J Radiol* 1998; **71**: 501-509 [PMID: 9691895 DOI: 10.1259/bjr.71.845.9691895]

28 **Schnall MD**, Rosten S, Englander S, Orel SG, Nunes LW. A combined architectural and kinetic interpretation model for breast MR images. *Acad Radiol* 2001; **8**: 591-597 [PMID: 11450959 DOI: 10.1016/S1076-6332(03)80683-9]

29 **Szabó BK**, Aspelin P, Wiberg MK, Boné B. Dynamic MR imaging of the breast. Analysis of kinetic and morphologic diagnostic criteria. *Acta Radiol* 2003; **44**: 379-386 [PMID: 12846687 DOI: 10.1080/j.1600-0455.2003.00084.x]

World Journal of Radiology

Submit a Manuscript: https://www.f6publishing.com

World J Radiol 2022 July 28; 14(7): 238-248

DOI: 10.4329/wjr.v14.i7.238

ISSN 1949-8470 (online)

SYSTEMATIC REVIEWS

Catheter-based renal sympathetic nerve denervation on hypertension management outcomes

Som P Singh, Kevin J Varghese, Fahad M Qureshi, Macy C Anderson, John Foxworth, Mark M Knuepfer

Specialty type: Cardiac and cardiovascular systems

Provenance and peer review: Unsolicited article; Externally peer reviewed.

Peer-review model: Single blind

Peer-review report's scientific quality classification

Grade A (Excellent): A
Grade B (Very good): 0
Grade C (Good): C
Grade D (Fair): 0
Grade E (Poor): 0

P-Reviewer: Manrai M, India; Prkacin I, Croatia

Received: February 14, 2022
Peer-review started: February 14, 2022
First decision: April 8, 2022
Revised: May 6, 2022
Accepted: July 5, 2022
Article in press: July 5, 2022
Published online: July 28, 2022

Som P Singh, Kevin J Varghese, Fahad M Qureshi, Macy C Anderson, John Foxworth, Department of Internal Medicine, University of Missouri Kansas City School of Medicine, Kansas City, MO 64106, United States

Mark M Knuepfer, Department of Pharmacological and Physiological Science, Saint Louis University School of Medicine, Saint Louis, MO 63104, United States

Corresponding author: Som P Singh, Academic Research, Department of Internal Medicine, University of Missouri Kansas City School of Medicine, 2411 Holmes Street, Kansas City, MO 64106, United States. somsingh@mail.umkc.edu

Abstract

BACKGROUND

Renal sympathetic denervation (RSD) provides a minimally invasive interventional treatment modality for patients with resistant hypertension. However, the post-operative outcomes remain a key area of investigation since its earliest clinical trials.

AIM

To evaluate patient outcomes after RSD intervention among peer-reviewed patient cases.

METHODS

A systematic review of literature on MEDLINE, Google Scholar, and the Cochrane Database of Systematic Reviews for RSD case studies to assess post-operative hypertension readings and medical management.

RESULTS

Among 51 RSD cases, the post-operative RSD patients report an apparent reduction with a mean number of 3.1 antihypertensive medications. The mean systolic arterial blood pressure 1 year following RSD was 136.0 mmHg (95%CI: 118.7-153.3).

CONCLUSION

The apparent improvements in office systolic blood pressure after 12 month post-operative RSD can support the therapeutic potential of this intervention for blood pressure reduction. Additional studies which utilized a uniform methodology for blood pressure measurement can further support the findings of this systematic review.

Key Words: Renal denervation; Hypertension; Systematic review; Interventional radiology; Outcomes

Core Tip: This is the first systematic review focused on peer-reviewed clinical case reports in the topic area of renal sympathetic denervation in hypertension outcomes. In addition, this study has noted the changes in blood pressure medication regimens for the management of resistant hypertension.

Citation: Singh SP, Varghese KJ, Qureshi FM, Anderson MC, Foxworth J, Knuepfer MM. Catheter-based renal sympathetic nerve denervation on hypertension management outcomes. *World J Radiol* 2022; 14(7): 238-248
URL: https://www.wjgnet.com/1949-8470/full/v14/i7/238.htm
DOI: https://dx.doi.org/10.4329/wjr.v14.i7.238

INTRODUCTION

Hypertension continues to be a pressing health condition worldwide. Despite widespread use of antihypertensive medications, it is estimated that only 24% of the patients who are prescribed these medications currently have their blood pressures controlled[1,2]. It is estimated that between 10% and 15% of patients with hypertension do not achieve adequate blood pressure control, despite the use of at least three antihypertensive agents[1,2]. Moreover, this group of patients is designated as having resistant hypertension[2]. Let alone, patients with true resistant hypertension bear a greater risk for mortality compared to the general population[3-5]. In fact, rates of cardiovascular events correlate with mean 24-hour ambulatory blood pressures, which further justifies the pressing need to innovate medical management of this condition[5]. Similarly, non-adherence to anti-hypertensive therapy is a significant problem that limits the success of drug therapies[6]. As such, the need for additional intervention beyond medication in patients with resistant hypertension is apparent.

Renal sympathetic denervation (RSD) has been proposed as a potential solution to control arterial pressure. Moreover, RSD is a catheter-based renal denervation which employs transvascular ablation of the renal sympathetic nerves using radiofrequency energy to interrupt both sensory and motor nerves through the renal arterial wall. The earliest clinical studies on RSD demonstrated a significant reduction in arterial pressure in most patients[7-9]. However, the body of evidence has largely been in dispute as to what the true postoperative outcomes are regarding this novel procedure. In fact, the SYMPLICITY HTN-3 clinical trial did not show a benefit for patients treated with the procedure compared to the sham group[10]. This has prompted the numerous additional studies of the effects of RSD. Most of these studies have reported reductions of ambulatory blood pressure, but the extent and location of ablation sites have varied considerably[10-12]. The efficacy of this procedure is difficult to evaluate due to widely varying levels of denervation and often the lack of appropriate control groups[11]. Despite this paucity in evidence, there have been a number of clinical cases reported in peer-reviewed literature which showcase the utilization of catheter-based renal denervation. However, there has not been a systematic review of these cases to consolidate the findings. Therefore, the aim of this study is to assess the efficacy of RSD treatment in attenuating systolic blood pressures and reducing antihypertensive agents among patients with resistant hypertension.

MATERIALS AND METHODS

Study design and inclusion

A systematic review of literature was performed on MEDLINE, Google Scholar, and the Cochrane Database of Systematic Reviews for renal denervation case studies. This study methodology was registered by PROSPERO International prospective register of systematic reviews (National Institute for Health Research). The search was performed following the Preferred Reporting Items for Systematic Reviews and Meta-Analyses (PRISMA) guidelines and checklist.3 Contingent valuation studies within renal denervation procedures were identified using search terminologies that combined the following epidemiological terms: renal sympathetic denervation, renal sympathetic ablation, hypertension renal denervation, renal denervation case studies, renal denervation case reports. Variations of the terms were also used when deemed necessary by the reviewers (*e.g.*, "study" *vs* "studies").

The initial search yielded 368 articles. Duplicates were removed, and then each article was reviewed for the following inclusion criteria: English language, case reports, full-text, pertinence to renal denervation procedures, and peer-reviewed (Figure 1). In addition, the reference list of each identified

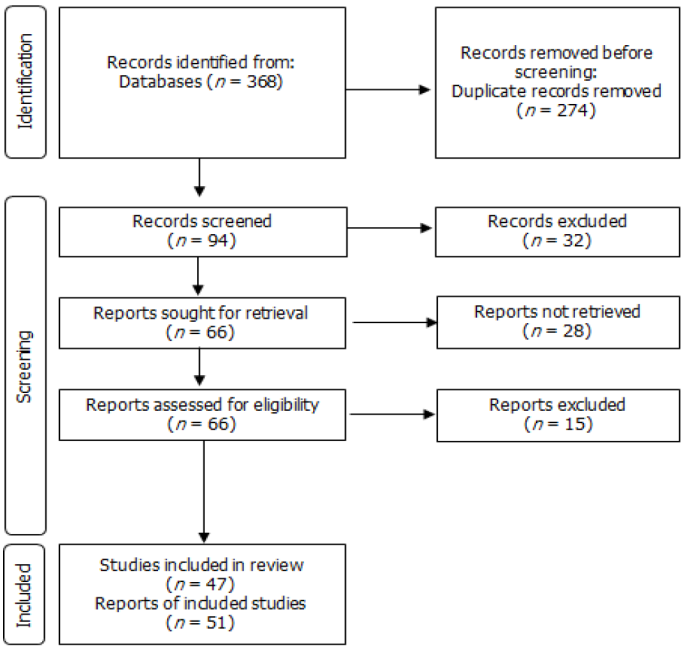

DOI: 10.4329/wjr.v14.i7.238

Figure 1 Flow diagram of study selection process.

study was also reviewed to further ensure that all appropriate studies were identified. No further articles met the inclusion criteria. This qualitative synthesis yielded 62 articles.

Data extraction and evaluation

Each study included was independently appraised by three reviewers (Singh SP, Varghese KJ, Qureshi FM) for literature quality and categorical data including: patient age, sex, ethnicity, height, weight, hypertension diagnosis, years hypertensive, blood pressure reading prior to renal denervation, presentation to emergency department, medications prior to renal denervation procedure, previous treatments related to hypertension, past medical/social/family history, renal denervation approach, number of lesions, duration of lesion/ablation, brand name of ablation catheter, bilateral (Y/N), renal artery length/diameter(s), days until discharge, blood pressure readings on follow-up, post-treatment medications, success in attenuating hypertension, and complications post-procedure. If there was any discrepancy between the three reviewers, discussion was conducted, and final determination was made by Singh SP. Meta-analyses were not performed due to a heterogeneity in reporting methodologies.

Statistical analysis

Statistical analysis was performed using Stata 14 Statistical Package (StataCorp, College Station, TX, United States) for descriptive statistics on the variables of interest including counts, percentages, means and standard deviations where appropriate. ANOVA calculations were performed to determine significance between variable groups of interest. The level of significance was set at $P < 0.05$.

RESULTS

The systematic review identified 368 records through the search methodology (Figure 1). After duplicates were removed, 94 records remained and 66 of those records were then screened and assessed for eligibility. This left a total of 43 complete studies to be included in the qualitative synthesis. Three of these studies included multiple patients. In total, 51 patient cases involving renal denervation procedures for hypertension were extracted from the 43 studies examined. The articles included in this study were published between 2012 and 2021. The peak year for case study reports was 2015 (n = 12), followed by 2013 (n = 11), 2012 (n = 7), 2014 (n = 6), 2017 and 2018 (n = 4), 2021 (n = 3), 2019 and 2020 (n = 1), respectively.

Among patients treated with RSD, 24 were female, 27 were male. The mean age of the patient population was 49.9 years (95%CI: 44.9-55.0) with the youngest being 6 years and the oldest being 83 years. Among sexes, the mean age of females was 50.1 (95%CI: 41.7-58.5) and for males was 49.5 (95%CI: 43.3-55.8). The mean body mass index (BMI) of the patient population was 31.3 (95%CI: 27.4-35.2). Among sexes, the mean BMI of females was 31.6 (95%CI: 25.3-37.9) and males was 31.0 (95%CI: 24.7-37.3).

The reviewers identified the terminology used for diagnosis of hypertension for each of the 51 patients studied and stratified these to identify 40 patients with resistant hypertension. Additionally, not all studies reported the number of years patients were hypertensive prior to RSD. Among those that did, the total patient population had a mean duration of diagnosed hypertension of 10.1 years (95%CI: 4.5-15.8), with the mean for males being 8.1 years (95%CI: -1.2-17.4) and females being 11.8 years (95%CI: 2.4-21.2). Additionally, of the patients diagnosed with resistant hypertension, the mean decreases to 7.8 years (95%CI: 3.4-12.1).

Two patients underwent RSD treatment following a presentation of hypertensive crisis in the Emergency Department. Six patients reported a history of diabetes (type 1: n = 1; type 2: n = 5). Another 4 patients reported polycystic kidney disease. One patient reported fibromuscular dysplasia. Histories of myocardial infarctions, hypercholesterolemia and hyperlipidemia were not compiled due to variations in reporting these potential contributing factors. No patient underwent RSD before the case report. Prior to RSD treatment, patient histories reported a mean number of 4.7 antihypertensive medications (95%CI: 4.1-5.4) as shown in Table 1.

The mean standard office blood pressure of patients prior to RSD treatment was assessed. The mean systolic blood pressure was 172.7 mmHg (95%CI: 165.1-180.3) among the entire patient population, and 171.4 mmHg (95%CI: 162.3-180.4) among those with resistant hypertension. Females had a mean systolic blood pressure of 170.2 mmHg (95%CI: 158.2-183.3), and males had a mean of 175.5 mmHg (95%CI: 164.7 – 186.3).

The first-generation SYMPLICITY renal denervation catheter® (Medtronic, Dublin, Ireland) was the most commonly used, being identified in 57.5% of cases (n = 40). This frequency was greater than EnligHTN renal artery ablation catheter® (St. Jude Medical, Inc., Saint Paul Minnesota) at 15%. The remaining cases used other available treatments. The mean number of ablations on the left renal artery was 5.0 (95%CI: 3.2-6.8), and the right renal artery was 5.3 (95%CI: 3.5-7.2). The reported duration of an ablation varied among each study, noting the shortest duration at 10 s, and longest duration at 120 s. Four studies reported discharge from the hospital within 24 h of treatment.

Three studies reported renal artery stenosis in at least 1 artery during follow up appointments. One study noted progression into aortic stenosis. Two studies reported aortic dissection, one occurring during the operation, and the second reported the dissection twenty-two months post-operatively. In both cases, the dissection was deemed unrelated to the RSD procedure. Episodes of hypertensive crises post-treatment were not reported in any of the case studies. In addition, the mean standard office blood pressure (BP) of patients post-RSD treatment was assessed. The mean post-operative systolic blood pressure of reported cases was reported at 24 h, 1 mo, 3 mo, 6 mo and 1 year after surgery (Table 2). The arterial pressure appeared to be significantly reduced although all measurements were not done at all time points in all these studies. After RSD treatment, patient follow-up histories in some reports described an apparent reduction with a mean number of 3.1 antihypertensive medications (95%CI: 2.3-3.9) in all patients (Table 3).

DISCUSSION

The aim of this systematic review of case reports was to examine the postoperative efficacy of RSD on blood pressure reduction in patients with resistant hypertension and evaluate the change in antihypertensive medication regimen. Overall, the therapeutic potential that this catheter-based procedure provides in attenuating hypertension merits its exploration. This search for contemporary case studies published in English medical journals yielded 48 patient cases which reviewers utilized to draw conclusions. The focus of this study is to determine the effect of RSD on blood pressure attenuation in hypertensive patients. Based on the most recent European Society of Cardiology (ESC) and the European Society of Hypertension (ESH) guidelines for the management of arterial hypertension, which classifies arterial blood pressures into grades[12], the mean standard office systolic blood pressure of patients prior to RSD treatment was between 160-179, or grade 2 hypertension, and ≥ 180, or grade 3 hypertension, among the patient population as a whole. The mean 24 h post-operative systolic blood pressure of reported cases was in grade 2 hypertension. At 1, 3, 6, and 12 month follow-up, the mean systolic arterial pressure of reported cases remained in grade 1 hypertension (systolic blood pressure between 140-159). For the majority of patients, the severity of hypertension declined from borderline-malignant hypertension to grade I hypertension. The resulting reduction in arterial pressure during these follow up visits are consistent with the results of larger renal denervation trials[7-9,12].

Regarding the current body of literature, the SYMPLICITY HTN-3 clinical trial which was performed in the United States reported the lack of a sustained reduction in arterial pressure after RSD[10]. Despite the observations in other studies showing reductions maintained for at least three years, the consistency of arterial pressure reduction has been controversial. There were similar observations in the case reports reviewed here, but the overall findings note a net reduction in blood pressure at one year follow up. In addition, the intention to evaluate the office systolic blood pressure readings is further supported by contemporary literature as a modality to objectively evaluate blood pressure reduction effects[13].

Table 1 Case reports used in this study

Ref.	Patients, *n*	Age (yr)	Sex	Brand
Aksu *et al*[21]	1	46	M	MARINER
Alegria-Barrero *et al*[22]	1	53	M	SYMPLICITY
Armaganijan *et al*[23]	1	29	F	
Atas *et al*[24]	1	42	F	SYMPLICTY, ARDIAN
Berra *et al*[25]	1	54	M	SYMPLICITY
Bilge *et al*[26]	1,1	41, 51	F, M	.
Yap *et al*[27]	2	44, 69	M, M	
Bonanni *et al*[28]	1	6	F	SYMPLICITY
Bortolotto *et al*[29]	1	39	F	MARINER
Celik *et al*[30]	1	59	M	SYMPLICITY
Chandra *et al*[31]	1	51	F	SYMPLICITY
Chiarito *et al*[32]	1	47	F	ARDIAN
Daemen *et al*[33]	1	55	M	RADIANCE
Ewen *et al*[34]	1	61	M	.
de Araújo Gonçalves *et al*[35]	1	67	F	SYMPLICITY
Gziut *et al*[36]	1	62	.	ENLIGHTN
Heradien *et al*[37]	1	62	F	SYMPLICITY
Himmel *et al*[38]	1	83	F	SYMPLICITY
Ho *et al*[39]	1	58	M	.
Jaguszewski *et al*[40]	1	72	F	ENLIGHTN
Kelle *et al*[41]	1	62	F	SYMPLICITY
Kiuchi *et al*[42]	1	15, 16, 32	F, F, M	ENLIGHTN
Koppelstaetter *et al*[43]	1	68	F	SYMPLICITY
Kostka-Jeziorny *et al*[44]	1	52	F	SYMPLICITY
Lee *et al*[45]	1	31	F	SYMPLICITY
Lee *et al*[46]	1	16	M	
Luo *et al*[47]	1	80	F	
Miller *et al*[48]	1	54	M	
Możeńska *et al*[49]	1	60	M	
Ott *et al*[50]	1	29	F	SYMPLICITY
Papademetriou *et al*[51]	1	59	F	ENLIGHTN
Pietilä-Effati *et al*[52]	4	24, 55, 56, 72	M, F, F, M	SYMPLICITY
Prejbisz *et al*[53]	1	26	M	SYMPLICITY
Pucci *et al*[54]	1	73	F	SYMPLICITY
Raju *et al*[55]	1	19	M	STOCKERT
Shah *et al*[56]	1	74	M	SYMPLICITY
Spinelli *et al*[57]	1	39	M	SYMPLICITY
Sridhar *et al*[58]	1	67	F	SYMPLICITY
Stefanadis *et al*[59]	1	74	M	SYMPLICITY
Tsioufis *et al*[60]	1	58	M	
Versaci *et al*[61]	1	49	M	VESSIX

Wang *et al*[62]	1	49	M	
Wu *et al*[63]	1	62	M	CORDIS

Table 2 Summary of arterial blood pressure measurements at different time points before and after renal sympathetic denervation

	Mean systolic blood pressure					
	Prior to RSD	Time post-RSD				
		24 h	1 mo	3 mo	6 mo	1 yr
All subjects	172.7 mmHg (95%CI: 165.1-180.3)	146.2 mmHg (95%CI: 131.4-161.1)	139.2 mmHg (95%CI: 124.8-153.6)	132.9 mmHg (95%CI: 114.8-151.1)	133.0 mmHg (95%CI: 120.7-145.31)	136.0 mmHg (95%CI: 118.7-153.3)
Females	170.2 mmHg (95%CI: 158.2-183.3)	147.2 mmHg (95%CI: 125.7-168.7)	137.0 mmHg (95%CI: 102.8-171.2)	136.7 mmHg (95%CI: 105.3-168.7)	130.0 mmHg (95%CI: 118.0-142.0)	134.2 mmHg (95%CI: 107.4-161.0)
Males	175.5 mmHg (95%CI: 164.7– 186.3)	144.4 mmHg (95%CI: 114.0-174.8)	137.0 mmHg (95%CI: 102.8-171.2)	126.3 mmHg (95%CI: 117.2-135.3)	[1]160.0 mmHg	[1]131.0 mmHg

[1]One reported observation.
RSD: Renal sympathetic denervation.

Table 3 Comparison of quantity of antihypertensive medications used before and after renal sympathetic denervation

	Mean number of antihypertensive medications	
	Pre-RSD	Post-RSD
All subjects	4.7 (95%CI: 4.1-5.4),	3.1 (95%CI: 2.3-3.9),
Females	4.9 (95%CI: 3.8-6.0)	3.0 (95%CI: 1.0–5.0)
Males	4.6 (95%CI: 3.7-5.5)	3.0 (95%CI: 1.96-4.0)

RSD: Renal sympathetic denervation.

The most common instrument used in these studies was the first generation, radiofrequency device (Symplicity, Medtronic®). During the initial studies with this instrument, it was recommended that the device be advanced to the first bifurcation of the renal artery allowing for 3-6 RF lesions on each renal artery. Subsequent studies have shown that this has highly variable effects on depletion of renal catecholamines[14]. Additionally, it has been shown that the renal nerves are more closely apposed to the renal artery in the distal segments[15]. This has led to the development of smaller catheters with multiple electrode sites that can be advanced farther into the renal artery and are able to make many more focal lesions[16]. This has likely improved the success of the actual denervation making the second-generation devices more effective in RSD.

Contemporary clinical guidelines encourage a stepwise approach, involving combination therapy, in order to increase the number and doses of medications when treating hypertension. Additionally, this is also with the understanding that every drug has a limited capacity for blood pressure reduction[17,18]. Therefore, patients described in these reports with grade 2 or 3 hypertension were typically on several medications. Since it is known that adherence to antihypertensive drug therapy is poor[6], the permanence of the RSD treatment offers a significant advantage, including reducing drug therapies in some patients and thereby improving compliance. These case reports were encouraging in this regard, as this study reported an average reduction by one-to-two medications from the patient's regimen. Furthermore, chronic administration of common antihypertensives can lead to adverse effects such as impotence with beta-blockers or angioedema with ACE inhibitors. Therefore, a desirable characteristic of RSD is a corresponding reduction in pharmacotherapy leading to improved compliance and reduced side effects.

Several case studies detailed complications of RSD, particularly associated with renal artery stenosis. While these were not deemed a major risk, the outcome can exacerbate hypertension. Furthermore, renal artery stenosis is a contraindication for medications such as ACE inhibitors or angiotensin receptor blockers. The combination of drug therapy and inhibiting Angiotensin II can significantly reduce renal function, particularly in the context of kidney disease. This study proposes the close monitoring of the renal arteries at the follow-up visits post-RSD treatment to track and quickly counter the occurrence of renal artery stenosis.

While the first United States-based trial (SYMPLICITY HTN-3) reported a reduction in arterial pressure in treated patients that was the same as the reduction observed in control patients[10], RSD has not been approved in the United States. Clinicians in the United States have a wealth of data because practitioners in other countries have been using RSD to treat resistant hypertension for nearly a decade. The International Sympathetic Nervous System Summit evaluated the future of RSD. The author's conclusions include an expected 10 mmHg decrease in blood pressure and 25% decrease in overall cardiovascular events[19]. Furthermore, a large meta-analysis comparable to this review established similar findings. Warchoł-Celińska *et al*[7] included 613815 patients from 122 studies to find a reduction of office systolic blood pressure by 10 mmHg, cardiovascular events by 20%, and overall mortality by 13%. Adding our study to the current conversation supports the notion that RSD is an intervention with significant advantages[18,19]. It would be most beneficial to perform additional randomized control trials to acquire definitive evidence of the antihypertensive effects of RSD treatment.

CONCLUSION

Renal sympathetic denervation is a procedure that can manage resistant hypertension while avoiding the complications of drug adherence. Benefits of the procedure include sustainable attenuation of arterial pressure, reduced dependence on medications leading to fewer side effects, and to a reduction in the inherent diseases associated with hypertension. One limitation encountered in this analysis is that the antihypertensive medications detailed were only evaluated based on the quantity, dose or number that a patient was taking, not based on the class or mechanism of action. Furthermore, as all included articles were case studies, which can affect the validity of these results to translate into clinical reasoning and practice. Moreover, the use of case reports in a systematic review make the structure of this review require further investigation through larger systematic reviews in order to have more rigor in translational reasoning. Another area of development which would benefit future studies is through use of a artificial intelligence-controlled databases which can provide greater accuracy of citation retrieval in a systematic review (*e.g.*, Reference Citation Analysis)[20]. Overall, this study recognizes that there is a need for more randomized control trials to establish the benefits of RSD, duration of effectiveness, incidence of complications, and improvement in all-cause mortality. Finally, findings of irregular attenuation of arterial pressure are likely confounded by improved quality of denervation afforded by newer devices. This procedure offers a viable option to control blood pressure with significant advantages over current treatments that could improve the effectiveness of the treatment of hypertension.

ARTICLE HIGHLIGHTS

Research background

The background behind this literature is the initial collaboration between SPS and MMK who explored the effects of renal afferent denervation from a basic science perspective. Of note, MMK has contributed to a number of early literatures regarding renal sympathetic denervation.

Research motivation

The utilization of thermal radiofrequency ablation in medical practice has grown tremendously over the past decade alone. We are motivated to contribute to the potential direction of bringing this therapeutic modality to greater avenues of evaluation compared to the past. Of note, renal sympathetic denervation (RSD) is not used in the United States yet.

Research objectives

The objective was to utilize current peer-reviewed case report data to gain a current understanding of the climate regarding RSD interventions.

Research methods

Systematic Review of the literature.

Research results

RSD intervention has shown, in these case reports, to mainly lower office systolic blood pressure and lessen the patient burden on medication regimens.

Research conclusions

The promising results of RSD can simplify therapeutic regimens in patients with resistant hypertension. There is a significant amount of area which can be explored in clinical trials in the future.

Research perspectives

The study team believes this therapeutic intervention needs to be brought under greater attention among the interventional radiology community for it future usage.

FOOTNOTES

Author contributions: Singh SP, Varghese KJ, Qureshi FQ, and Knuepfer MM designed the research study; Singh SP, Varghese KJ, and Qureshi FQ performed the research; Anderson MA and Foxworth J contributed critical revision; Varghese KV and Qureshi FQ analyzed the data; and All authors wrote the manuscript. All authors have read and approve the final manuscript.

Conflict-of-interest statement: All authors report no relevant conflicts of interest for this article.

PRISMA 2009 Checklist statement: The authors have read the PRISMA 2009 Checklist, and the manuscript was prepared and revised according to the PRISMA 2009 Checklist.

Country/Territory of origin: United States

ORCID number: Som P Singh 000-0001-7553-8487.

S-Editor: Ma YJ
L-Editor: A
P-Editor: Ma YJ

REFERENCES

1 **Elliott WJ**. Systemic hypertension. *Curr Probl Cardiol* 2007; **32**: 201-259 [PMID: 17398315 DOI: 10.1016/j.cpcardiol.2007.01.002]
2 **Ritchey MD**, Gillespie C, Wozniak G, Shay CM, Thompson-Paul AM, Loustalot F, Hong Y. Potential need for expanded pharmacologic treatment and lifestyle modification services under the 2017 ACC/AHA Hypertension Guideline. *J Clin Hypertens (Greenwich)* 2018; **20**: 1377-1391 [PMID: 30194806 DOI: 10.1111/jch.13364]
3 **American Heart Association**. Hypertension Guideline Resources. [cited August 3, 2020] Available from: https://www.heart.org/en/health-topics/high-blood-pressure/high-blood-pressure-toolkit-resources
4 **Oliveras A**, de la Sierra A. Resistant hypertension: patient characteristics, risk factors, co-morbidities and outcomes. *J Hum Hypertens* 2014; **28**: 213-217 [PMID: 23985879 DOI: 10.1038/jhh.2013.77]
5 **Judd E**, Calhoun DA. Apparent and true resistant hypertension: definition, prevalence and outcomes. *J Hum Hypertens* 2014; **28**: 463-468 [PMID: 24430707 DOI: 10.1038/jhh.2013.140]
6 **Chang TE**, Ritchey MD, Park S, Chang A, Odom EC, Durthaler J, Jackson SL, Loustalot F. National Rates of Nonadherence to Antihypertensive Medications Among Insured Adults With Hypertension, 2015. *Hypertension* 2019; **74**: 1324-1332 [PMID: 31679429 DOI: 10.1161/HYPERTENSIONAHA.119.13616]
7 **Warchoł-Celińska E**, Prejbisz A, Florczak E, Kądziela J, Witkowski A, Januszewicz A. Renal denervation - current evidence and perspectives. *Postepy Kardiol Interwencyjnej* 2013; **9**: 362-368 [PMID: 24570754 DOI: 10.5114/pwki.2013.38866]
8 **Esler MD**, Böhm M, Sievert H, Rump CL, Schmieder RE, Krum H, Mahfoud F, Schlaich MP. Catheter-based renal denervation for treatment of patients with treatment-resistant hypertension: 36 month results from the SYMPLICITY HTN-2 randomized clinical trial. *Eur Heart J* 2014; **35**: 1752-1759 [PMID: 24898552 DOI: 10.1093/eurheartj/ehu209]
9 **Krum H**, Schlaich MP, Sobotka PA, Böhm M, Mahfoud F, Rocha-Singh K, Katholi R, Esler MD. Percutaneous renal denervation in patients with treatment-resistant hypertension: final 3-year report of the Symplicity HTN-1 study. *Lancet* 2014; **383**: 622-629 [PMID: 24210779 DOI: 10.1016/S0140-6736(13)62192-3]
10 **Bhatt DL**, Kandzari DE, O'Neill WW, D'Agostino R, Flack JM, Katzen BT, Leon MB, Liu M, Mauri L, Negoita M, Cohen SA, Oparil S, Rocha-Singh K, Townsend RR, Bakris GL; SYMPLICITY HTN-3 Investigators. A controlled trial of renal denervation for resistant hypertension. *N Engl J Med* 2014; **370**: 1393-1401 [PMID: 24678939 DOI: 10.1056/NEJMoa1402670]
11 **Esler M**. Renal denervation for treatment of drug-resistant hypertension. *Trends Cardiovasc Med* 2015; **25**: 107-115 [PMID: 25467242 DOI: 10.1016/j.tcm.2014.09.014]
12 **Williams B**, Mancia G, Spiering W, Agabiti Rosei E, Azizi M, Burnier M, Clement DL, Coca A, de Simone G, Dominiczak A, Kahan T, Mahfoud F, Redon J, Ruilope L, Zanchetti A, Kerins M, Kjeldsen SE, Kreutz R, Laurent S, Lip GYH, McManus R, Narkiewicz K, Ruschitzka F, Schmieder RE, Shlyakhto E, Tsioufis C, Aboyans V, Desormais I; ESC

Scientific Document Group. 2018 ESC/ESH Guidelines for the management of arterial hypertension. *Eur Heart J* 2018; **39**: 3021-3104 [PMID: 30165516]

13 **Liang B**, Liang Y, Li R, Gu N. Effect of renal denervation on long-term outcomes in patients with resistant hypertension. *Cardiovasc Diabetol* 2021; **20**: 117 [PMID: 34090434 DOI: 10.1186/s12933-021-01309-3]

14 **Feyz L**, van den Berg S, Zietse R, Kardys I, Versmissen J, Daemen J. Effect of renal denervation on catecholamines and the renin-angiotensin-aldosterone system. *J Renin Angiotensin Aldosterone Syst* 2020; **21**: 1470320320943095 [PMID: 32862760 DOI: 10.1177/1470320320943095]

15 **van Amsterdam WA**, Blankestijn PJ, Goldschmeding R, Bleys RL. The morphological substrate for Renal Denervation: Nerve distribution patterns and parasympathetic nerves. A post-mortem histological study. *Ann Anat* 2016; **204**: 71-79 [PMID: 26617159 DOI: 10.1016/j.aanat.2015.11.004]

16 **Wolf M**, Hubbard B, Sakaoka A, Rousselle S, Tellez A, Jiang X, Kario K, Hohl M, Böhm M, Mahfoud F. Procedural and anatomical predictors of renal denervation efficacy using two radiofrequency renal denervation catheters in a porcine model. *J Hypertens* 2018; **36**: 2453-2459 [PMID: 30005030 DOI: 10.1097/HJH.0000000000001840]

17 **Paz MA**, de-La-Sierra A, Sáez M, Barceló MA, Rodríguez JJ, Castro S, Lagarón C, Garrido JM, Vera P, Coll-de-Tuero G. Treatment efficacy of anti-hypertensive drugs in monotherapy or combination: ATOM systematic review and meta-analysis of randomized clinical trials according to PRISMA statement. *Medicine (Baltimore)* 2016; **95**: e4071 [PMID: 27472680 DOI: 10.1097/MD.0000000000004071]

18 **Guirguis-Blake JM**, Evans CV, Webber EM, Coppola EL, Perdue LA, Weyrich MS. Screening for Hypertension in Adults: Updated Evidence Report and Systematic Review for the US Preventive Services Task Force. *JAMA* 2021; **325**: 1657-1669 [PMID: 33904862 DOI: 10.1001/jama.2020.21669]

19 **Kiuchi MG**, Esler MD, Fink GD, Osborn JW, Banek CT, Böhm M, Denton KM, DiBona GF, Everett TH 4th, Grassi G, Katholi RE, Knuepfer MM, Kopp UC, Lefer DJ, Lohmeier TE, May CN, Mahfoud F, Paton JFR, Schmieder RE, Pellegrino PR, Sharabi Y, Schlaich MP. Renal Denervation Update From the International Sympathetic Nervous System Summit: JACC State-of-the-Art Review. *J Am Coll Cardiol* 2019; **73**: 3006-3017 [PMID: 31196459 DOI: 10.1016/j.jacc.2019.04.015]

20 **Baishideng Publishing Group Inc**. Reference Citation Analysis.[cited June 29, 2022] Available from: https://www.referencecitationanalysis.com/

21 **Aksu T**, Güler TE, Özcan KS, Bozyel S, Yalın K. Renal sympathetic denervation assisted treatment of electrical storm due to polymorphic ventricular tachycardia in a patient with cathecolaminergic polymorphic ventricular tachycardia. *Turk Kardiyol Dern Ars* 2017; **45**: 441-449 [PMID: 28694398 DOI: 10.5543/tkda.2017.72773]

22 **Alegria-Barrero E**, Teijeiro R, Casares M, Vega M, Blazquez MA, Martos R, De Diego C, Moreno R, Martin MA. Treating Refractory Hypertension: Renal Denervation With High-Resolution 3D-Angiography. *Res Cardiovasc Med* 2013; **2**: 106-108 [PMID: 25478504 DOI: 10.5812/cardiovascmed.9700]

23 **Armaganijan L**, Staico R, Abizaid A, Moraes A, Moreira D, Amodeo C, Sousa M, Sousa JE. Unilateral renal artery sympathetic denervation may reduce blood pressure in patients with resistant hypertension. *J Clin Hypertens (Greenwich)* 2013; **15**: 606 [PMID: 23889725 DOI: 10.1111/jch.12121]

24 **Atas H**, Durmus E, Sunbul M, Mutlu B. Successful accessory renal artery denervation in a patient with resistant hypertension. *Heart Views* 2014; **15**: 19-21 [PMID: 24949184 DOI: 10.4103/1995-705X.132142]

25 **Berra E**, Rabbia F, Rossato D, Covella M, Totaro S, Chiara F, Di Monaco S, Veglio F. Renal sympathetic denervation in a previously stented renal artery. *J Clin Hypertens (Greenwich)* 2014; **16**: 238-239 [PMID: 24387740 DOI: 10.1111/jch.12251]

26 **Bilge M**, Tolunay H, Kurmuş O, Köseoğlu C, Alemdar R, Ali S. Percutaneous renal denervation in patients with resistant hypertension-first experiences in Turkey. *Anadolu Kardiyol Derg* 2012; **12**: 79-80 [PMID: 22231942 DOI: 10.5152/akd.2012.020]

27 **Yap LB**, Balachandran K. Renal Denervation in the treatment of Resistant Hypertension. *Med J Malaysia* 2021; **76**: 893-897 [PMID: 34806679 DOI: 10.30824/2110-3]

28 **Bonanni A**, Pasetti F, Ghiggeri GM, Gandolfo C. Renal denervation for severe hypertension in a small child with Turner syndrome: miniaturisation of the procedure and results. *BMJ Case Rep* 2015; **2015** [PMID: 25759273 DOI: 10.1136/bcr-2014-208777]

29 **Bortolotto LA**, Midlej-Brito T, Pisani C, Costa-Hong V, Scanavacca M. Renal denervation by ablation with innovative technique in resistant hypertension. *Arq Bras Cardiol* 2013; **101**: e77-e79 [PMID: 24217435 DOI: 10.5935/abc.20130194]

30 **Celik IE**, Acar B, Kurtul A, Murat SN. De novo renal artery stenosis after renal sympathetic denervation. *J Clin Hypertens (Greenwich)* 2015; **17**: 242-243 [PMID: 25625526 DOI: 10.1111/jch.12482]

31 **Chandra AP**, Marron CD, Puckridge P, Spark JI. Severe bilateral renal artery stenosis after transluminal radiofrequency ablation of renal sympathetic nerve plexus. *J Vasc Surg* 2015; **62**: 222-225 [PMID: 24468285 DOI: 10.1016/j.jvs.2013.11.005]

32 **Chiarito M**, Scotti A, A Pivato C, Cottone G, Ballarotto C, Godino C, Margonato A. A Complicated Case of Resistant Hypertension. *Acta Med Iran* 2017; **55**: 525-529 [PMID: 29034650]

33 **Daemen J**, Van Mieghem N. First-in-man radial access renal denervation with the ReCor Radiance™ catheter. *EuroIntervention* 2015; **10**: 1209-1212 [PMID: 25493912 DOI: 10.4244/EIJY14M12_03]

34 **Ewen S**, Mahfoud F, Böhm M. First-in-human experience: percutaneous renal denervation through a false lumen fenestration in aortic dissection type B. *EuroIntervention* 2013; **8**: 1110 [PMID: 23339818 DOI: 10.4244/EIJV8I9A170]

35 **de Araújo Gonçalves P**, Teles RC, Raposo L. Catheter-based renal denervation for resistant hypertension performed by radial access. *J Invasive Cardiol* 2013; **25**: 147-149 [PMID: 23468446]

36 **Gziut AI**, Gil RJ. Denervation of three equivalent right renal arteries in a patient with resistant hypertension after left-sided nephrectomy: five-year follow-up. *Postepy Kardiol Interwencyjnej* 2020; **16**: 114-115 [PMID: 32368247 DOI: 10.5114/aic.2020.93920]

37 **Heradien MJ**, Augustyn J, Saaiman A, Brink PA. First reported cases: renal denervation with second-generation multi-electrode catheter *via* brachial and radial access. *Cardiovasc J Afr* 2016; **27**: 53-55 [PMID: 26956499 DOI:

10.5830/CVJA-2015-089]
38 **Himmel F**, Bode F, Mortensen K, Reppel M, Franzen K, Schunkert H, Weil J. Successful single-sided renal denervation approach in a patient with stenosis of an accessory renal artery. *J Clin Hypertens (Greenwich)* 2012; **14**: 187-188 [PMID: 22372780 DOI: 10.1111/j.1751-7176.2011.00585.x]
39 **Ho HH**, Foo D, Ong PJ. Successful preoperative treatment of a patient with resistant hypertension who had percutaneous renal denervation therapy before bariatric surgery. *J Clin Hypertens (Greenwich)* 2012; **14**: 569-570 [PMID: 22863167 DOI: 10.1111/j.1751-7176.2012.00623.x]
40 **Jaguszewski M**, Ghadri JR, Lüscher TF, Templin C. Optical coherence tomography to reveal vascular lesions after catheter-based renal nerve ablation with a novel multi-electrode EnligHTN™ system. *Kardiol Pol* 2013; **71**: 775 [PMID: 23907918 DOI: 10.5603/KP.2013.0172]
41 **Kelle S**, Teller DC, Fleck E, Stawowy P. Renal denervation in fibromuscular dysplasia. *BMJ Case Rep* 2013; **2013** [PMID: 23960148 DOI: 10.1136/bcr-2013-010204]
42 **Kiuchi MG**, Souto HB, Kiuchi T, Chen S. Case Report: Renal Sympathetic Denervation as a Tool for the Treatment of Refractory Inappropriate Sinus Tachycardia. *Medicine (Baltimore)* 2015; **94**: e2094 [PMID: 26579823 DOI: 10.1097/MD.0000000000002094]
43 **Koppelstaetter C**, Kerschbaum J, Lenzhofer M, Glodny B, Esterhammer R, Frick M, Alber H, Mayer G. Distal renal artery stenosis after percutaneous renal denervation leading to renal impairment but normotension. *J Clin Hypertens (Greenwich)* 2015; **17**: 162-164 [PMID: 25545297 DOI: 10.1111/jch.12456]
44 **Kostka-Jeziorny K**, Radziemski A, Tykarski A, Niklas A, Grajek S. Effect of unilateral catheter-based renal sympathetic denervation in a patient with resistant hypertension. *Kardiol Pol* 2015; **73**: 132 [PMID: 25706782 DOI: 10.5603/KP.2015.0021]
45 **Lee CJ**, Kim BK, Yoon KB, Lee HY, Dominiczak AF, Touyz RM, Jennings GLR, Cho EJ, Hering D, Park S. Case of Refractory Hypertension Controlled by Repeated Renal Denervation and Celiac Plexus Block: A Case of Refractory Sympathetic Overload. *Hypertension* 2017; **69**: 978-984 [PMID: 28416585 DOI: 10.1161/HYPERTENSIONAHA.117.09260]
46 **Lee SH**, Lim DH, Lee JH, Chang K, Koo JM, Park HJ. Long-Term Blood Pressure Control Effect of Celiac Plexus Block with Botulinum Toxin. *Toxins (Basel)* 2016; **8**: 51 [PMID: 26907344 DOI: 10.3390/toxins8020051]
47 **Luo G**, Zhu JJ, Yao M, Xie KY. Computed tomography-guided chemical renal sympathetic nerve modulation in the treatment of resistant hypertension: A case report. *World J Clin Cases* 2021; **9**: 9970-9976 [PMID: 34877338 DOI: 10.12998/wjcc.v9.i32.9970]
48 **Miller MA**, Gangireddy SR, Dukkipati SR, Koruth JS, d'Avila A, Reddy VY. Renal sympathetic denervation using an electroanatomic mapping system. *J Am Coll Cardiol* 2014; **63**: 1697 [PMID: 24613336 DOI: 10.1016/j.jacc.2013.11.065]
49 **Możeńska O**, Rosiak M, Gziut A, Gil RJ, Kosior DA. Firstinman experience with renal denervation of multiple renal arteries in a patient with solitary kidney and resistant hypertension. *Pol Arch Intern Med* 2017; **127**: 60-62 [PMID: 28146462 DOI: 10.20452/pamw.3912]
50 **Ott C**, Schmid A, Ditting T, Sobotka PA, Veelken R, Uder M, Schmieder RE. Renal denervation in a hypertensive patient with end-stage renal disease and small arteries: a direction for future research. *J Clin Hypertens (Greenwich)* 2012; **14**: 799-801 [PMID: 23126353 DOI: 10.1111/jch.12017]
51 **Papademetriou V**, Tsioufis C, Stefanadis C. Impressive blood pressure and heart rate response after percutaneous renal denervation in a woman with morbid obesity and severe drug-resistant hypertension. *J Clin Hypertens (Greenwich)* 2013; **15**: 852-855 [PMID: 24283599 DOI: 10.1111/jch.12189]
52 **Pietilä-Effati PM**, Salmela AK, Koistinen MJ. Intravascular Renal Denervation in Renal Dialysis Patients with Uncontrolled Hypertension: A Case Series of Four Patients. *Am J Case Rep* 2018; **19**: 985-991 [PMID: 30127334 DOI: 10.12659/AJCR.909820]
53 **Prejbisz A**, Kądziela J, Lewandowski J, Florczak E, Zylińska E, Kłopotowski M, Witkowski A, Januszewicz A. Effect of percutaneous renal denervation on blood pressure level and sympathetic activity in a patient with polycystic kidney disease. *Clin Res Cardiol* 2014; **103**: 251-253 [PMID: 24322784 DOI: 10.1007/s00392-013-0647-1]
54 **Pucci G**, Battista F, Lazzari L, Dominici M, Boschetti E, Schillaci G. Progression of renal artery stenosis after renal denervation. Impact on 24-hour blood pressure. *Circ J* 2014; **78**: 767-768 [PMID: 24284919 DOI: 10.1253/circj.cj-13-0997]
55 **Raju N**, Lloyd V, Yalagudri S, Das B, Ravikishore AG. Renal denervation in a patient with Alport syndrome and rejected renal allograft. *Indian Heart J* 2015; **67** Suppl 3: S71-S73 [PMID: 26995439 DOI: 10.1016/j.ihj.2015.12.004]
56 **Shah S**, Jimenez MA, Fishel RS. Irrigated radiofrequency ablation catheter and electro-anatomical mapping with computerized tomography integration for renal artery sympathetic denervation. *J Invasive Cardiol* 2012; **24**: E308-E310 [PMID: 23220990]
57 **Spinelli A**, Da Ros V, Morosetti D, Onofrio SD, Rovella V, Di Daniele N, Simonetti G. Technical aspects of renal denervation in end-stage renal disease patients with challenging anatomy. *Diagn Interv Radiol* 2014; **20**: 267-270 [PMID: 24378992 DOI: 10.5152/dir.2013.13408]
58 **Sridhar GS**, Watson T, Han CK, Ahmad WA. Profound sustained hypotension following renal denervation: a dramatic success? *Arq Bras Cardiol* 2015; **105**: 202-204 [PMID: 26352181 DOI: 10.5935/abc.20150100]
59 **Stefanadis C**, Toutouzas K, Vlachopoulos C, Tsioufis C, Synetos A, Pietri P, Tousoulis D, Tsiamis E. Chemical denervation of the renal artery with vincristine for the treatment of resistant arterial hypertension: first-in-man application. *Hellenic J Cardiol* 2013; **54**: 318-321 [PMID: 23912924 DOI: 10.1016/j.jcin.2016.03.041]
60 **Tsioufis C**, Dimitriadis K, Tsiachris D, Thomopoulos C, Kasiakogias A, Kordalis A, Kefala A, Kallikazaros I, Stefanadis C. Catheter-based renal sympathetic denervation for the treatment of resistant hypertension: first experience in Greece with significant ambulatory blood pressure reduction. *Hellenic J Cardiol* 2012; **53**: 237-241 [PMID: 22653249 DOI: 10.1016/s0735-1097(13)60736-6]
61 **Versaci F**, Andò G, Chiocchi M, Romeo F. Long-term benefit of renal denervation on blood pressure control in a patient with hemorrhagic stroke. *SAGE Open Med Case Rep* 2019; **7**: 2050313X19870972 [PMID: 31489195 DOI:

10.1177/2050313X19870972]

62 **Wang P**, Wan J, Hou J, Liu S, Ran F. Renal denervation in a patient with a highly tortuous renal artery using a guide extension catheter: a case report. *BMC Cardiovasc Disord* 2021; **21**: 388 [PMID: 34376149 DOI: 10.1186/s12872-021-02199-9]

63 **Wu Y**, Duan S, Qiang X, Ning Z, Xing C, Zhang B. Sympathetic renal denervation in hypertension with chronic kidney disease: a case report and review of literature. *Int J Clin Exp Med* 2015; **8**: 16858-16862 [PMID: 26629235 DOI: 10.1007/978-1-4939-1982-6_7]

Published by **Baishideng Publishing Group Inc**
7041 Koll Center Parkway, Suite 160, Pleasanton, CA 94566, USA
Telephone: +1-925-3991568
E-mail: bpgoffice@wjgnet.com
Help Desk: https://www.f6publishing.com/helpdesk
https://www.wjgnet.com

ISSN 1949-8470 (online)

World Journal of *Radiology*

World J Radiol 2022 August 28; 14(8): 249-318

Published by Baishideng Publishing Group Inc

World Journal of Radiology

Contents

Monthly Volume 14 Number 8 August 28, 2022

OPINION REVIEW

MINIREVIEWS

ORIGINAL ARTICLE

Retrospective Study

World Journal of Radiology

Monthly Volume 14 Number 8 August 28, 2022

Contents

ABOUT COVER

Editorial Board Member of *World Journal of Radiology*, Alexander B Konovalov, PhD, Associate Professor, Leading Scientist, Russian Federal Nuclear Center - Zababakhin Institute of Applied Physics, Snezninsk 456770, Russia. a_konov@mail.vega-int.ru

AIMS AND SCOPE

The primary aim of *World Journal of Radiology* (*WJR*, *World J Radiol*) is to provide scholars and readers from various fields of radiology with a platform to publish high-quality basic and clinical research articles and communicate their research findings online.

WJR mainly publishes articles reporting research results and findings obtained in the field of radiology and covering a wide range of topics including state of the art information on cardiopulmonary imaging, gastrointestinal imaging, genitourinary imaging, musculoskeletal imaging, neuroradiology/head and neck imaging, nuclear medicine and molecular imaging, pediatric imaging, vascular and interventional radiology, and women's imaging.

INDEXING/ABSTRACTING

The *WJR* is now abstracted and indexed in PubMed, PubMed Central, Emerging Sources Citation Index (Web of Science), Reference Citation Analysis, China National Knowledge Infrastructure, China Science and Technology Journal Database, and Superstar Journals Database. The 2022 edition of Journal Citation Reports ® cites the 2021 Journal Citation Indicator (JCI) for *WJR* as 0.48.

RESPONSIBLE EDITORS FOR THIS ISSUE

NAME OF JOURNAL
World Journal of Radiology

ISSN
ISSN 1949-8470 (online)

LAUNCH DATE
January 31, 2009

FREQUENCY
Monthly

EDITORS-IN-CHIEF
Thomas J Vogl

EDITORIAL BOARD MEMBERS
https://www.wjgnet.com/1949-8470/editorialboard.htm

PUBLICATION DATE
August 28, 2022

INSTRUCTIONS TO AUTHORS
https://www.wjgnet.com/bpg/gerinfo/204

GUIDELINES FOR ETHICS DOCUMENTS
https://www.wjgnet.com/bpg/GerInfo/287

GUIDELINES FOR NON-NATIVE SPEAKERS OF ENGLISH
https://www.wjgnet.com/bpg/gerinfo/240

PUBLICATION ETHICS
https://www.wjgnet.com/bpg/GerInfo/288

PUBLICATION MISCONDUCT
https://www.wjgnet.com/bpg/gerinfo/208

ARTICLE PROCESSING CHARGE
https://www.wjgnet.com/bpg/gerinfo/242

STEPS FOR SUBMITTING MANUSCRIPTS
https://www.wjgnet.com/bpg/GerInfo/239

ONLINE SUBMISSION
https://www.f6publishing.com

World Journal of Radiology

Submit a Manuscript: https://www.f6publishing.com

World J Radiol 2022 August 28; 14(8): 249-255

DOI: 10.4329/wjr.v14.i8.249

ISSN 1949-8470 (online)

OPINION REVIEW

Augmenting prostate magnetic resonance imaging reporting to incorporate diagnostic recommendations based upon clinical risk calculators

Karisma Gupta, Jordan D Perchik, Andrew M Fang, Kristin K Porter, Soroush Rais-Bahrami

Specialty type: Radiology, nuclear medicine and medical imaging

Provenance and peer review: Invited article; Externally peer reviewed.

Peer-review model: Single blind

Peer-review report's scientific quality classification

Grade A (Excellent): 0
Grade B (Very good): 0
Grade C (Good): C, C
Grade D (Fair): 0
Grade E (Poor): 0

P-Reviewer: Andrejic-Visnjic B, Serbia; Liang L, China

Received: March 22, 2022
Peer-review started: March 22, 2022
First decision: June 16, 2022
Revised: June 27, 2022
Accepted: July 25, 2022
Article in press: July 25, 2022
Published online: August 28, 2022

Karisma Gupta, Department of Radiology, University of Washington, Seattle, WA 98195, United States

Jordan D Perchik, Kristin K Porter, Soroush Rais-Bahrami, Department of Radiology, University of Alabama at Birmingham, Birmingham, AL 35233, United States

Andrew M Fang, Soroush Rais-Bahrami, Department of Urology, University of Alabama at Birmingham, Birmingham, AL 35233, United States

Soroush Rais-Bahrami, O'Neal Comprehensive Cancer Center, University of Alabama at Birmingham, Birmingham, AL 35233, United States

Corresponding author: Soroush Rais-Bahrami, MD, Associate Professor, Departments of Urology and Radiology, University of Alabama at Birmingham, Faculty Office Tower 1107 510 20th Street South, Birmingham, AL 35233, United States. soroushraisbahrami@gmail.com

Abstract

Risk calculators have offered a viable tool for clinicians to stratify patients at risk of prostate cancer (PCa) and to mitigate the low sensitivity and specificity of screening prostate specific antigen (PSA). While initially based on clinical and demographic data, incorporation of multiparametric magnetic resonance imaging (MRI) and the validated prostate imaging reporting and data system suspicion scoring system has standardized and improved risk stratification beyond the use of PSA and patient parameters alone. Biopsy-naïve patients with lower risk profiles for harboring clinically significant PCa are often subjected to uncomfortable, invasive, and potentially unnecessary prostate biopsy procedures. Incorporating risk calculator data into prostate MRI reports can broaden the role of radiologists, improve communication with clinicians primarily managing these patients, and help guide clinical care in directing the screening, detection, and risk stratification of PCa.

Key Words: Prostatic adenocarcinoma; Multiparametric magnetic resonance imaging; Nomograms; Risk calculators; Biopsy

Core Tip: Incorporating risk calculator data into prostate magnetic resonance imaging reports can broaden the role of radiologists, improve communication with clinicians primarily managing these patients, and help guide clinical care in directing the screening, detection, and risk stratification of prostate cancer.

Citation: Gupta K, Perchik JD, Fang AM, Porter KK, Rais-Bahrami S. Augmenting prostate magnetic resonance imaging reporting to incorporate diagnostic recommendations based upon clinical risk calculators. *World J Radiol* 2022; 14(8): 249-255
URL: https://www.wjgnet.com/1949-8470/full/v14/i8/249.htm
DOI: https://dx.doi.org/10.4329/wjr.v14.i8.249

INTRODUCTION

Prostate cancer (PCa) is the most common solid organ malignancy in American men and the second cause of cancer-related death in the United States[1]. Due to increased awareness, nearly 20 million men in the United States engage in screening and early detection discussions (National Comprehensive Cancer Network). Prostate specific antigen (PSA) made large-scale screening for PCa feasible, but lacked accuracy, with 15%-25% false negatives and 60% false positives[2,3]. Since PSA has proven to be an unreliable biomarker for clinically significant prostate cancer [csPCa; Grade Group (GG) ≥ 2], a large percentage of patients continue to undergo prostate biopsies with either benign or clinically indolent PCa (GG 1). Prostate biopsies are an invasive diagnostic procedure with well-established risks, such as hematuria, hematospermia, rectal bleeding, urinary tract infections, and recognized risk of sepsis[4-7]. Furthermore, potentially unnecessary biopsies and over treatment of low-risk prostate cancer has placed an undue psychological burden on patients[8].

The role of multiparametric magnetic resonance imaging (mpMRI) in prostate cancer diagnosis, surveillance, and treatment has significantly evolved and is growing in popularity as a tool to potentially avoid unnecessary biopsies in biopsy-naive patients. Controversy remains due to significant variability across patient cohorts and institutions. Risk calculators combining mpMRI with clinical variables can limit this variation and have been shown to improve predictive models[9,10]. An individualized screening algorithm using a patient's clinical history can result in a considerable reduction in unnecessary biopsy sessions. A validated clinical risk calculator that could be incorporated into MRI reporting and aid in the decision to pursue prostate biopsies in biopsy-naive patients is needed[11]. However, such a risk calculator must be carefully validated to ensure its reliable performance and applicability to a broad population of patients undergoing prostate cancer screening when including MRI in the screening algorithm.

OVERVIEW OF RISK CALCULATORS

Historical perspective

One of the first algorithms to predict the risk of prostate cancer on prostate biopsy was the European Randomized Study for Screening of Prostate Cancer (ERSPC) risk calculator. The ERSPC has six calculators, two of which are used by patients and the remaining four used by physicians. The RC3/RC4 combined calculator uses PSA levels, digital rectal exam (DRE) exam, previous prostate biopsy history, prostate volume, and now incorporates MRI prostate imaging reporting and data system (PI-RADS) v 1.0 score to predict the detectable risk of prostate cancer on biopsy. The calculator stratifies the risk of detecting cancer to assist clinicians with the decision to pursue biopsy (https://www.prostatecancer-riskcalculator.com/). Several external validation studies have been performed for these RCs. The discriminative ability of detecting positive prostate biopsy (PBx) in biopsy-naive or previously biopsied patients using the ERSPC RC3 or RC4 was assessed, showing area under the curve (AUC) values in the range of 0.71-0.88[12-16].

Thompson *et al*[17] developed one of the first online individualized predictive assessments of prostate cancer before prostate biopsy extrapolated from the 5519 patients in the Prostate Cancer Prevention Trial (PCPT). It was found that PSA, family history, DRE findings, African American race, and history of a prior negative prostate biopsy provided independent predictive value to the calculation of risk of a biopsy that showed presence of cancer. The first calculator became known as the Prostate Cancer Prevention Trial Risk Calculator (PCPTRC) and has been used widely online at https://riskcalc.org/PCPTRC/. In 2012, an updated PCPTRC 2.0 was released with the added capability to provide prediction of indolent low-grade (Gleason grade < 7) *vs* high-grade (GG ≥ 2) PCa. Both versions of the online PCPT risk calculator were externally validated in 2014.

Independent validation and comparisons between the ERSPC and PCPTRC calculators demonstrated comparable calibration in their agreement between predicted and observed risks of prostate cancer. However, the AUC for predicting clinically significant sPCa was higher for the ERSPC risk calculator compared with the PCPTRC (0.73 *vs* 0.70; $P = 0.043$)[18]. The PCPTRC has been replaced by a more contemporary risk calculator developed by the Prostate Biopsy Collaborative Group (PBCG) that incorporates age, PSA level, DRE results, family history, race, and a history of negative biopsy along with more contemporary biopsy schemes[19]. The study demonstrates a greater inclusion of patients with diverse backgrounds and PBCG model outperformed the PCPTRC in predicting csPCa on both internal (AUC, 75.5% *vs* 72.3%; $P < 0.0001$) and external validation (AUC, 72.9% *vs* 69.7%; $P < 0.0001$). Furthermore, the PBCG model was found to be well calibrated and offered a higher net clinical benefit than the PCPT risk calculator: it led to 2.7% fewer biopsies without missing any csPCa.

Advent of imaging

Prior to 2017, mpMRI of the prostate was not commonly used in the PCa workup worldwide due to the high cost and limited availability of prostate MRI. In 2019, Alberts *et al*[20] published a study on the use of risk calculators and biopsy results to avoid unnecessary prostate MRI. Alberts *et al*[20] suggested that mpMRI of the prostate provided an opportunity to enhance the non-invasive portion of the PCa workup and introduced a nomogram integrating PI-RADS data into the ERSPC risk calculator. Alberts *et al*[20] demonstrated a superior nomogram compared to the ERSPC standard, achieving an AUC of 0.84, which was significantly increased compared to ERSPC calculators that did not incorporate imaging data.

As mpMRI of the prostate became more widely available and the Urology community became more aware of the potential impact of PI-RADS score on risk calculator development, prostate MRI data was more widely incorporated into PCa risk nomograms. PI-RADS data, scored on a zero to five Likert scale, is easily incorporated into nomograms due to its objective, defined numerical values. In 2019, Alberts *et al*[20] refined the ERSPC-RC-3/4 risk calculators, developing MRI-ERSPC-RC-3/4 by adding mpMRI examination results. The addition of MRI to the ERSPC calculators increased the discriminative ability for high-grade PCa [AUC of 0.84 (95%CI 0.81-0.88) and 0.85 (95%CI 0.81-0.89) for the MRI-ERSPC-RC3 and MRI-ERSPC-RC4, respectively][20]. Beyond the established clinical based calculators like the ERSPC and the PBCG, novel risk calculators were developed across the globe, with several large multicenter trials occurring in North America, the United Kingdom, and Australia, such as the Stanford Prostate Cancer Calculator (SPCC)[21], the PLUM cohort[22], the PCRC-MRI[23], MRI study by Chau *et al*[24], and the study done by van Leeuwen *et al*[25] PI-RADS integrated clinical calculators consistently demonstrated superior performance to calculators using clinical data alone[23-27]. Of note, due to the wide variety in study location, practice type, and timing of data collection, some of these risk calculators use data from PI-RADS v1.0 and PI-RADS 2.0. The SPCC notes that its calculator is validated for both PI-RADS v1.0 and v2.0[21].

For biopsy-naive patients, the superior performance of imaging integrated risk calculators represents a possibility to avoid invasive biopsy for low risk PCa. Trials specific to the biopsy-naive population have demonstrated promising results with high sensitivity and specificity and high net benefit. Radtke *et al*[27] and Chau *et al*[24] attained high AUC values, both in excess of 0.8, and both were trained on patient populations from the United Kingdom. The van Leeuwen *et al*'s risk calculator has an AUC of 0.90 and demonstrates one of the most substantial net benefits, avoiding 28.6% of biopsies at 10% risk tolerance, missing only 2.6% of PCa[25]. Additional external validation studies have demonstrated high AUC for the van Leeuwen and ERSPC based models, however both studies conclude that the use of MRI integrated risk calculators to avoid biopsy remains controversial[28,29].

DISCUSSION

Risk calculators and nomograms provide a valuable tool in risk stratification of patients with abnormal screening PSA levels potentially allowing selection of cases to avoid biopsy in patients at low risk for harboring csPCa. Incorporation of risk calculator data into radiology reports could represent an opportunity for radiologists to add value to the patient evaluation and mitigate ambiguity of borderline results, especially PI-RADS 3 Lesions found on prostate indication MRI studies (Figures 1 and 2). In collaboration with the referring clinician, the radiologist could incorporate patient clinic and demographic information, along with the lesion PI-RADS score, calculate the percent risk of csPCa, and include this information in the final diagnostic imaging report.

Three PI-RADS integrated calculators, the SPCC[21], the PLUM Prostate cancer risk calculator, and the MRI-ERSPC-R-3/4 published open access online calculators, allowing a more streamlined integration into workflow. For biopsy-naive patients, the PLUM calculator demonstrated the highest sensitivity and specificity with an AUC value of 0.87 and a net benefit of avoiding 18.1% of biopsies without missing any csPCa in biopsy-naive patients at a 15% tolerance. The MRI-ERSPC-R-3/4 calculator reported an AUC of 0.84 in its initial study from Alberts *et al*'s net benefit for biopsy-naive patients was not reported in the Alberts *et al*'s study[20], but in Petersmann *et al*[29], which compared the MRI-ERSPC-R-3/4 calculator to the calculator described in van Leeuwen *et al*[25], the MRI/ERSPC-

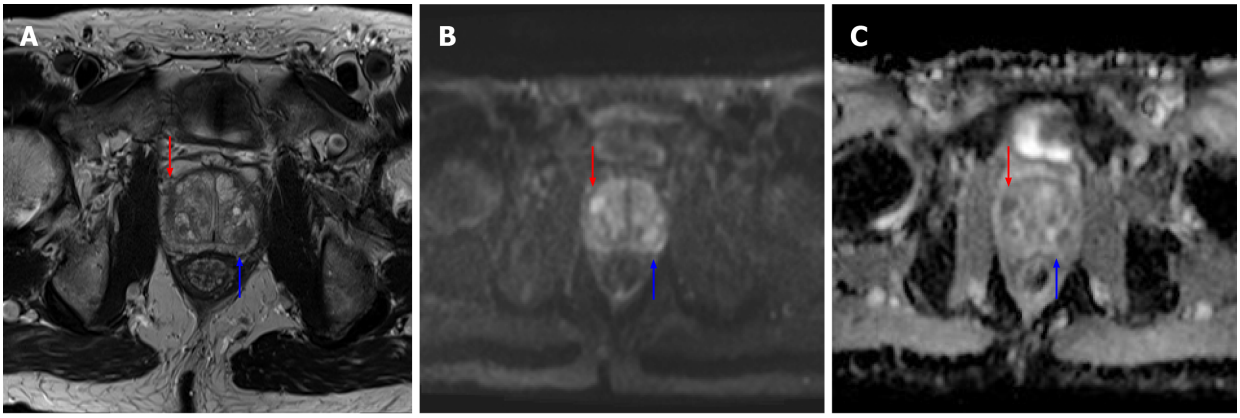

DOI: 10.4329/wjr.v14.i8.249 **Copyright** ©The Author(s) 2022.

Figure 1 Axial magnetic resonance imaging images of the prostate. A: T2 weighted image; B: b1200 diffusion weighted imaging (DWI) image; C: Calculated apparent dispersion coefficient (ADC) image. A mostly encapsulated T2-hypointense transitional zone lesion is demonstrated in the left posterior central gland, measuring 10 mm (blue arrows) with focal moderate low ADC, high DWI signal, designated prostate imaging reporting and data system (PI-RADS) 3 per PI-RADS version 2.1. An additional 8 mm PI-RADS 4 Lesion of the anterior right transitional zone is present (red arrow), demonstrating non-circumscribed moderate T2 hypointensity and marked focal ADC hypointensity and DWI hyperintensity.

PROSTATE:

Focal lesion(s): [ ]
Lesion # 1 (index lesion):
Key image: image [ ] series [ ]
Size: [ ] mm
Location: [ ] [ ] [ ]
T2WI: [ ] [ ] DWI: [ ] DCE (early and focal enhancement): [ ]
PI-RADS v2.1 score: [ ]
Likelihood of extraprostatic extension: [ ] [ ]
Likelihood of seminal vesicle invasion: [ ] [ ]
Diffuse prostate abnormalities: [ ]
Other prostate findings: [None]

RISK CALCULATOR:
Prostate Volume: [ ]
PSA: [ ]
PSA density: [ ]
Clinical data (DRE, family history, prior biopsy, etc): [ ] [ ]
Demographic information: [ ]
PIRADS v2.1 score: [ ]

% risk of csPCa: [ ]
Recommendation: [ ]

DOI: 10.4329/wjr.v14.i8.249 **Copyright** ©The Author(s) 2022.

Figure 2 Sample structured report for prostate lesion reporting with integrated risk calculator reporting. The calculated percent risk of clinically significant prostate cancer is included in the lesion evaluation findings with recommendations for biopsy or observation in the conclusion. csPCa: Clinically significant prostate cancer; DRE: Digital rectal exam; DWI: Diffusion weighted imaging; PI-RADS: Prostate imaging reporting and data system; PSA: Prostate specific antigen.

R-3/4 nomogram avoids only 9% of biopsies in biopsy-naive patients while missing 3% at a 15% risk threshold. The SPCC trial did not report a specific AUC or net benefit for biopsy-naive patients but reported AUC values ranging from 0.78-0.83 and a net benefit of avoiding 10.3% of biopsies while missing csPCa in 0.8% of patients with a risk tolerance of 20%[21].

Additional notable nomograms have demonstrated promising results for biopsy-naive patients that outperform some of the larger and more established risk calculators. The van Leeuwen *et al*[25] nomogram demonstrated the highest AUC of all evaluated risk calculators and reported one of the highest net benefits, avoiding 28.6% of biopsies while missing only 2.6% of csPCa, but was developed on a smaller and more homogenous patient population (393 patients from Australia) than many of the other noted calculators. However in the external validation study by Petersmann *et al*[29], the van Leeuwen nomogram was demonstrated to maintain high performance, and even outperformed the ERSPC in net benefit. Petersmann *et al*[29] compared ERSPC and van Leeuwen risk calculator. This study showed comparable AUC values between the two studies, 0.81 for ERSPC and 0.82 for van Leeuwen, however the van Leeuwen calculator demonstrated a greater net benefit from a risk threshold

of 10%-15%, avoiding 24% of biopsies while missing 6% of csPCa, compared to 14% and 5% for the MRI-ERSP-RC-3/4, respectively. Notably the ERSPC calculator had a near perfect calibration, with a calibration slope of 0.94 compared to the van Leeuwen model, 0.70. The Petersmann *et al*'s study population came from a hospital system in Nuremberg, Germany and likely reflected a similar demographic to the ERSPC training population, whereas the van Leeuwen study was performed in Australia[29]. The gaps in calibration between these two studies may indicate future pitfalls in generalizability, and clinicians need to be aware of the training data and population demographics when applying these calculators to their own patient population.

Novel imaging technologies such as prostate cancer directed PET imaging may further aid in refining these risk calculators, allowing for additional improvements in pre-biopsy patient risk stratification. Radiomics, a subset of clinical artificial intelligence (AI), is a promising tool on the horizon of prostate imaging and prostate cancer classification. Prostate MRI has represented a prolific area of AI research in the past decade, with algorithms demonstrating improved prostate cancer detection, classification, and upstream applications, such as deep learning reconstruction and its role in instituting abbreviated protocols. In a systematic review, Ferro *et al*[30] discuss 21 manuscripts related to radiomics and the detection of csPCa. These publications have demonstrated the capability of radiomics to extract salient features and develop models that predict csPCa that significantly outperform clinical models[31] and combined clinical and imaging models[32]. While these results are encouraging, the algorithms to date are often trained at a single institution and are limited by a lack of external validation and heterogeneity of the extracted radiomics features. Although further refinement and broader, multi-institution testing is needed, early successes of radiomics models suggest a promising future for AI in the evaluation, diagnosis, risk stratification, and treatment decision making in the management of csPCa.

CONCLUSION

Risk calculators have enabled physicians and patients to make a more informed decision when considering pursuit of a prostate biopsy. When evaluating biopsy-naïve patients, multiple risk calculators can be applied, each with their own strengths. The role of imaging using MRI in the diagnosis of csPCa has significantly evolved and is growing in popularity. The PI-RADS system has become a component of many currently available pre-biopsy prostate cancer risk calculators. Artificial intelligence shows promise in further advancing the role of imaging in csPCa risk assessment. Further incorporation of imaging in clinical risk calculators shows promise in aiding the decision to pursue prostate biopsies with improved confidence and patient-centric goals.

FOOTNOTES

Author contributions: Porter KK and Rais-Bahrami S contributed equally to this work; Porter KK and Rais-Bahrami S designed the study; Gupta K, Perchik JD, Fang AM, Porter KK, and Rais-Bahrami S contributed to authoring the manuscript and critically reviewing and revising the manuscript; all authors have read and approved the final manuscript.

Conflict-of-interest statement: Rais-Bahrami S serves as a consultant to Philips/InVivo Corp, Genomic Health Inc, Blue Earth Diagnostics, Bayer Healthcare, UroViu Corp, and Intuitive Surgical.

Country/Territory of origin: United States

ORCID number: Andrew M Fang 0000-0002-2390-7575; Soroush Rais-Bahrami 0000-0001-9466-9925.

S-Editor: Gong ZM
L-Editor: A
P-Editor: Gong ZM

REFERENCES

1 **Siegel RL**, Miller KD, Fuchs HE, Jemal A. Cancer Statistics, 2021. *CA Cancer J Clin* 2021; **71**: 7-33 [PMID: 33433946 DOI: 10.3322/caac.21654]

2 **Gambert SR**. Screening for prostate cancer. *Int Urol Nephrol* 2001; **33**: 249-257 [PMID: 12092637 DOI: 10.1023/a:1015290429403]

3 **Thompson IM**, Pauler DK, Goodman PJ, Tangen CM, Lucia MS, Parnes HL, Minasian LM, Ford LG, Lippman SM, Crawford ED, Crowley JJ, Coltman CA Jr. Prevalence of prostate cancer among men with a prostate-specific antigen level < or =4.0 ng per milliliter. *N Engl J Med* 2004; **350**: 2239-2246 [PMID: 15163773 DOI: 10.1056/NEJMoa031918]

4 **Halpern JA**, Sedrakyan A, Dinerman B, Hsu WC, Mao J, Hu JC. Indications, Utilization and Complications Following Prostate Biopsy: New York State Analysis. *J Urol* 2017; **197**: 1020-1025 [PMID: 27856226 DOI: 10.1016/j.juro.2016.11.081]

5 **Loeb S**, Carter HB, Berndt SI, Ricker W, Schaeffer EM. Complications after prostate biopsy: data from SEER-Medicare. *J Urol* 2011; **186**: 1830-1834 [PMID: 21944136 DOI: 10.1016/j.juro.2011.06.057]

6 **Loeb S**, Vellekoop A, Ahmed HU, Catto J, Emberton M, Nam R, Rosario DJ, Scattoni V, Lotan Y. Systematic review of complications of prostate biopsy. *Eur Urol* 2013; **64**: 876-892 [PMID: 23787356 DOI: 10.1016/j.eururo.2013.05.049]

7 **Ravi P**, Sammon J, Meskawi M, Sun M, Karakiewicz PI, Trinh QD. Re: Complications after prostate biopsy: data from SEER-Medicare: S. Loeb, H. B. Carter, S. I. Berndt, W. Ricker and E. M. Schaeffer J Urol 2011; 186: 1830-1834. *J Urol* 2012; **188**: 677-678 [PMID: 22704450 DOI: 10.1016/j.juro.2012.04.021]

8 **Loeb S**, Bjurlin MA, Nicholson J, Tammela TL, Penson DF, Carter HB, Carroll P, Etzioni R. Overdiagnosis and overtreatment of prostate cancer. *Eur Urol* 2014; **65**: 1046-1055 [PMID: 24439788 DOI: 10.1016/j.eururo.2013.12.062]

9 **Bjurlin MA**, Rosenkrantz AB, Sarkar S, Lepor H, Huang WC, Huang R, Venkataraman R, Taneja SS. Prediction of Prostate Cancer Risk Among Men Undergoing Combined MRI-targeted and Systematic Biopsy Using Novel Pre-biopsy Nomograms That Incorporate MRI Findings. *Urology* 2018; **112**: 112-120 [PMID: 29155186 DOI: 10.1016/j.urology.2017.09.035]

10 **Radtke JP**, Wiesenfarth M, Kesch C, Freitag MT, Alt CD, Celik K, Distler F, Roth W, Wieczorek K, Stock C, Duensing S, Roethke MC, Teber D, Schlemmer HP, Hohenfellner M, Bonekamp D, Hadaschik BA. Combined Clinical Parameters and Multiparametric Magnetic Resonance Imaging for Advanced Risk Modeling of Prostate Cancer-Patient-tailored Risk Stratification Can Reduce Unnecessary Biopsies. *Eur Urol* 2017; **72**: 888-896 [PMID: 28400169 DOI: 10.1016/j.eururo.2017.03.039]

11 **Fang AM**, Rais-Bahrami S. Magnetic resonance imaging-based risk calculators optimize selection for prostate biopsy among biopsy-naive men. *Cancer* 2022; **128**: 25-27 [PMID: 34427940 DOI: 10.1002/cncr.33872]

12 **Cavadas V**, Osório L, Sabell F, Teves F, Branco F, Silva-Ramos M. Prostate cancer prevention trial and European randomized study of screening for prostate cancer risk calculators: a performance comparison in a contemporary screened cohort. *Eur Urol* 2010; **58**: 551-558 [PMID: 20580483 DOI: 10.1016/j.eururo.2010.06.023]

13 **Gayet M**, Mannaerts CK, Nieboer D, Beerlage HP, Wijkstra H, Mulders PFA, Roobol MJ. Prediction of Prostate Cancer: External Validation of the ERSPC Risk Calculator in a Contemporary Dutch Clinical Cohort. *Eur Urol Focus* 2018; **4**: 228-234 [PMID: 28753781 DOI: 10.1016/j.euf.2016.07.007]

14 **Trottier G**, Roobol MJ, Lawrentschuk N, Boström PJ, Fernandes KA, Finelli A, Chadwick K, Evans A, van der Kwast TH, Toi A, Zlotta AR, Fleshner NE. Comparison of risk calculators from the Prostate Cancer Prevention Trial and the European Randomized Study of Screening for Prostate Cancer in a contemporary Canadian cohort. *BJU Int* 2011; **108**: E237-E244 [PMID: 21507190 DOI: 10.1111/j.1464-410X.2011.10207.x]

15 **van Vugt HA**, Roobol MJ, Kranse R, Määttänen L, Finne P, Hugosson J, Bangma CH, Schröder FH, Steyerberg EW. Prediction of prostate cancer in unscreened men: external validation of a risk calculator. *Eur J Cancer* 2011; **47**: 903-909 [PMID: 21163642 DOI: 10.1016/j.ejca.2010.11.012]

16 **Yoon DK**, Park JY, Yoon S, Park MS, Moon du G, Lee JG, Schröder FH. Can the prostate risk calculator based on Western population be applied to Asian population? *Prostate* 2012; **72**: 721-729 [PMID: 21837777 DOI: 10.1002/pros.21475]

17 **Thompson IM**, Ankerst DP, Chi C, Goodman PJ, Tangen CM, Lucia MS, Feng Z, Parnes HL, Coltman CA Jr. Assessing prostate cancer risk: results from the Prostate Cancer Prevention Trial. *J Natl Cancer Inst* 2006; **98**: 529-534 [PMID: 16622122 DOI: 10.1093/jnci/djj131]

18 **Poyet C**, Nieboer D, Bhindi B, Kulkarni GS, Wiederkehr C, Wettstein MS, Largo R, Wild P, Sulser T, Hermanns T. Prostate cancer risk prediction using the novel versions of the European Randomised Study for Screening of Prostate Cancer (ERSPC) and Prostate Cancer Prevention Trial (PCPT) risk calculators: independent validation and comparison in a contemporary European cohort. *BJU Int* 2016; **117**: 401-408 [PMID: 26332503 DOI: 10.1111/bju.13314]

19 **Ankerst DP**, Straubinger J, Selig K, Guerrios L, De Hoedt A, Hernandez J, Liss MA, Leach RJ, Freedland SJ, Kattan MW, Nam R, Haese A, Montorsi F, Boorjian SA, Cooperberg MR, Poyet C, Vertosick E, Vickers AJ. A Contemporary Prostate Biopsy Risk Calculator Based on Multiple Heterogeneous Cohorts. *Eur Urol* 2018; **74**: 197-203 [PMID: 29778349 DOI: 10.1016/j.eururo.2018.05.003]

20 **Alberts AR**, Roobol MJ, Verbeek JFM, Schoots IG, Chiu PK, Osses DF, Tijsterman JD, Beerlage HP, Mannaerts CK, Schimmöller L, Albers P, Arsov C. Prediction of High-grade Prostate Cancer Following Multiparametric Magnetic Resonance Imaging: Improving the Rotterdam European Randomized Study of Screening for Prostate Cancer Risk Calculators. *Eur Urol* 2019; **75**: 310-318 [PMID: 30082150 DOI: 10.1016/j.eururo.2018.07.031]

21 **Wang NN**, Zhou SR, Chen L, Tibshirani R, Fan RE, Ghanouni P, Thong AE, To'o KJ, Ghabili K, Nix JW, Gordetsky JB, Sprenkle P, Rais-Bahrami S, Sonn GA. The stanford prostate cancer calculator: Development and external validation of online nomograms incorporating PIRADS scores to predict clinically significant prostate cancer. *Urol Oncol* 2021; **39**: 831.e19-831.e27 [PMID: 34247909 DOI: 10.1016/j.urolonc.2021.06.004]

22 **Patel HD**, Koehne EL, Shea SM, Bhanji Y, Gerena M, Gorbonos A, Quek ML, Flanigan RC, Goldberg A, Gupta GN. Risk of prostate cancer for men with prior negative biopsies undergoing magnetic resonance imaging compared with biopsy-naive men: A prospective evaluation of the PLUM cohort. *Cancer* 2022; **128**: 75-84 [PMID: 34427930 DOI: 10.1002/cncr.33875]

23 **Kinnaird A**, Brisbane W, Kwan L, Priester A, Chuang R, Barsa DE, Delfin M, Sisk A, Margolis D, Felker E, Hu J, Marks LS. A prostate cancer risk calculator: Use of clinical and magnetic resonance imaging data to predict biopsy outcome in North American men. *Can Urol Assoc J* 2022; **16**: E161-E166 [PMID: 34672937 DOI: 10.5489/cuaj.7380]

24 **Chau EM**, Russell B, Santaolalla A, van Hemelrijck M, McCracken S, Page T, Liyanage SH, Aning J, Gnanapragasam VJ, Acher P. MRI-based nomogram for the prediction of prostate cancer diagnosis: A multi-centre validated patient-physician decision tool. *J Clin Urol* 2022; E-Pub ahead of Print [DOI: 10.1177/20514158211065949]

25 **van Leeuwen PJ**, Hayen A, Thompson JE, Moses D, Shnier R, Böhm M, Abuodha M, Haynes AM, Ting F, Barentsz J, Roobol M, Vass J, Rasiah K, Delprado W, Stricker PD. A multiparametric magnetic resonance imaging-based risk model to determine the risk of significant prostate cancer prior to biopsy. *BJU Int* 2017; **120**: 774-781 [PMID: 28207981 DOI: 10.1111/bju.13814]

26 **Mehralivand S**, Shih JH, Rais-Bahrami S, Oto A, Bednarova S, Nix JW, Thomas JV, Gordetsky JB, Gaur S, Harmon SA, Siddiqui MM, Merino MJ, Parnes HL, Wood BJ, Pinto PA, Choyke PL, Turkbey B. A Magnetic Resonance Imaging-Based Prediction Model for Prostate Biopsy Risk Stratification. *JAMA Oncol* 2018; **4**: 678-685 [PMID: 29470570 DOI: 10.1001/jamaoncol.2017.5667]

27 **Radtke JP**, Giganti F, Wiesenfarth M, Stabile A, Marenco J, Orczyk C, Kasivisvanathan V, Nyarangi-Dix JN, Schütz V, Dieffenbacher S, Görtz M, Stenzinger A, Roth W, Freeman A, Punwani S, Bonekamp D, Schlemmer HP, Hohenfellner M, Emberton M, Moore CM. Prediction of significant prostate cancer in biopsy-naïve men: Validation of a novel risk model combining MRI and clinical parameters and comparison to an ERSPC risk calculator and PI-RADS. *PLoS One* 2019; **14**: e0221350 [PMID: 31450235 DOI: 10.1371/journal.pone.0221350]

28 **Mannaerts CK**, Gayet M, Verbeek JF, Engelbrecht MRW, Savci-Heijink CD, Jager GJ, Gielens MPM, van der Linden H, Beerlage HP, de Reijke TM, Wijkstra H, Roobol MJ. Prostate Cancer Risk Assessment in Biopsy-naïve Patients: The Rotterdam Prostate Cancer Risk Calculator in Multiparametric Magnetic Resonance Imaging-Transrectal Ultrasound (TRUS) Fusion Biopsy and Systematic TRUS Biopsy. *Eur Urol Oncol* 2018; **1**: 109-117 [PMID: 31100233 DOI: 10.1016/j.euo.2018.02.010]

29 **Petersmann AL**, Remmers S, Klein T, Manava P, Huettenbrink C, Pahernik SA, Distler FA. External validation of two MRI-based risk calculators in prostate cancer diagnosis. *World J Urol* 2021; **39**: 4109-4116 [PMID: 34169337 DOI: 10.1007/s00345-021-03770-x]

30 **Ferro M**, de Cobelli O, Vartolomei MD, Lucarelli G, Crocetto F, Barone B, Sciarra A, Del Giudice F, Muto M, Maggi M, Carrieri G, Busetto GM, Falagario U, Terracciano D, Cormio L, Musi G, Tataru OS. Prostate Cancer Radiogenomics-From Imaging to Molecular Characterization. *Int J Mol Sci* 2021; **22** [PMID: 34576134 DOI: 10.3390/ijms22189971]

31 **Li M**, Chen T, Zhao W, Wei C, Li X, Duan S, Ji L, Lu Z, Shen J. Radiomics prediction model for the improved diagnosis of clinically significant prostate cancer on biparametric MRI. *Quant Imaging Med Surg* 2020; **10**: 368-379 [PMID: 32190563 DOI: 10.21037/qims.2019.12.06]

32 **Deniffel D**, Abraham N, Namdar K, Dong X, Salinas E, Milot L, Khalvati F, Haider MA. Using decision curve analysis to benchmark performance of a magnetic resonance imaging-based deep learning model for prostate cancer risk assessment. *Eur Radiol* 2020; **30**: 6867-6876 [PMID: 32591889 DOI: 10.1007/s00330-020-07030-1]

World Journal of Radiology

Submit a Manuscript: https://www.f6publishing.com

World J Radiol 2022 August 28; 14(8): 256-271

DOI: 10.4329/wjr.v14.i8.256

ISSN 1949-8470 (online)

MINIREVIEWS

Advanced magnetic resonance imaging findings in salivary gland tumors

Erkan Gökçe, Murat Beyhan

Specialty type: Radiology, nuclear medicine and medical imaging

Provenance and peer review: Invited article; Externally peer reviewed.

Peer-review model: Single blind

Peer-review report's scientific quality classification

Grade A (Excellent): 0
Grade B (Very good): B
Grade C (Good): C
Grade D (Fair): 0
Grade E (Poor): 0

P-Reviewer: Kurokawa R, Japan; Wang WCY, Taiwan

Received: January 12, 2022
Peer-review started: January 12, 2022
First decision: March 16, 2022
Revised: March 22, 2022
Accepted: August 7, 2022
Article in press: August 7, 2022
Published online: August 28, 2022

Erkan Gökçe, Murat Beyhan, Department of Radiology, Faculty of Medicine, Tokat Gaziosmanpasa University, Tokat 60100, Turkey

Corresponding author: Erkan Gökçe, MD, Professor, Department of Radiology, Faculty of Medicine, Tokat Gaziosmanpasa University, Kaleardı Neighborhood, Muhittin Fisunoglu Street, Tokat 60100, Turkey. drerkangokce@gmail.com

Abstract

Salivary gland tumors (SGTs) make up a small portion (approximately 5%) of all head and neck tumors. Most of them are located in the parotid glands, while they are less frequently located in the submandibular glands, minor salivary glands or sublingual gland. The incidence of malignant or benign tumors (BTs) in the salivary glands varies according to the salivary gland from which they originate. While most of those detected in the parotid gland tend to be benign, the incidence of malignancy increases in other glands. The use of magnetic resonance imaging (MRI) in the diagnosis of SGTs is increasing every day. While conventional sequences provide sufficient data on the presence, localization, extent and number of the tumor, they are insufficient for tumor specification. With the widespread use of advanced techniques such as diffusion-weighted imaging, semi-quantitative and quantitative perfusion MRI, studies and data have been published on the differentiation of malignant or BTs and the specificity of their subtypes. With diffusion MRI, differentiation can be made by utilizing the cellularity and microstructural properties of tumors. For example, SGTs such as high cellular Warthin's tumor (WT) or lymphoma on diffusion MRI have been reported to have significantly lower apparent diffusion values than other tumors. Contrast agent uptake and wash-out levels of tumors can be detected with semi-quantitative perfusion MRI. For example, it is reported that almost all of the pleomorphic adenomas show an increasing enhancement time intensity curve and do not wash-out. On quantitative perfusion MRI studies using perfusion parameters such as Ktrans, Kep, and Ve, it is reported that WTs can show higher Kep and lower Ve values than other tumors. In this study, the contribution of advanced MRI to the diagnosis and differential diagnosis of SGTs will be reviewed.

Key Words: Salivary gland tumors; Magnetic resonance imaging; Diffusion-weighted imaging; Dynamic contrast-enhanced imaging; Perfusion-weighted magnetic resonance imaging

Core Tip: Conventional magnetic resonance imaging (MRI) provides more data than other radiological modalities in determining the extent of tumor extension and evaluating its relationship with vascular and neural structures in salivary gland tumors (SGTs). Advanced MRI techniques, which have been increasingly used in the radiological evaluation of SGTs in recent years, contribute to obtaining more information about the nature of the lesion compared to conventional sequences. Different features such as cellularity, microstructural features and vascularity of tumors can be evaluated by diffusion MRI or perfusion MRI techniques, and they can contribute to the differentiation of benign or malignant tumors.

Citation: Gökçe E, Beyhan M. Advanced magnetic resonance imaging findings in salivary gland tumors. *World J Radiol* 2022; 14(8): 256-271
URL: https://www.wjgnet.com/1949-8470/full/v14/i8/256.htm
DOI: https://dx.doi.org/10.4329/wjr.v14.i8.256

INTRODUCTION

Salivary gland tumors (SGTs) account for approximately 3%-5% of all head and neck tumors[1-3]. The majority of SGTs occur in the parotid glands, followed by those arising from the submandibular glands, minor salivary glands, and sublingual glands[3-6]. While the majority of those developing from the parotid glands are benign, the incidence of malignancy increases in tumors in other glands. In SGTs for which operation is planned, it is essential to determine the preoperative characterization of the tumor, its number, location (localization in the superficial or deep lobe for the parotid gland), extension to the surrounding tissues and lymphatic involvement[7]. The most effective radiological method in operative planning is magnetic resonance imaging (MRI). Conventional sequences may be insufficient to characterize SGTs. For this reason, in recent years, it has been tried to characterize tumors with advanced MRI applications [diffusion-weighted imaging (DWI) MRI, dynamic contrast-enhanced (semi-quantitative) MRI, perfusion (quantitative) MRI, diffusion tensor imaging (DTI), MR spectroscopy (MRS) *etc.*][1-5]. In this review, it is aimed to evaluate the imaging findings detected in advanced MRI applications of SGTs.

DWI

DWI is an imaging method that detects the motion of water molecules and allows calculation with the apparent diffusion coefficient (ADC). DWI, which can determine the cellularity and microstructural properties of tissues, can contribute to the differentiation of tumors[8-11]. When the studies on SGT were reviewed, some studies stated that the ADC values of malignant and benign tumors (BTs) were significantly different[12-16], while in some studies no significant difference was found[17,18], but in most of these studies, it was reported that ADC values were more effective in separating subgroups [pleomorphic adenomas (PMAs), Warthin's tumors (WTs) and lymphoma]. In the literature, mean ADC values of malignant SGTs are (0.8-1.53) × 10^{-3} mm^2/s that of benign SGTs is (1.04-1.72) × 10^{-3} mm^2/s reported in the range[16-21]. Although ADC values overlap in some SGTs due to the nature of the components they contain, we can generalize the mean ADC values of SGTs as malignant lymphomas < WTs < carcinomatous malignant tumors (MTs) < PMAs.

SEMI-QUANTITATIVE DYNAMIC CONTRAST-ENHANCED MRI

Dynamic contrast-enhanced (DCE) MRI in tumoral lesions is the acquisition of multiple T1-weighted images (T1WI) within a few minutes following contrast material administration to monitor contrast agent uptake and wash-out. On DCE MRI, the time intensity curve (TIC) is obtained in connection with the signal changes that occur with the passage of the contrast material through the tissues and the wash-out processes from the tissues. Slope, signal intensity (SI) peak, time to peak (Tpeak), enhancement ratio and wash-out ratio (WR) values can be obtained semi-quantitatively from the TIC curve. In the literature, different TIC patterns have been defined based on the Tpeak and wash-out values of SGTs[14,22-27]. The most preferred TIC patterns were those described by Yabuuchi *et al*[24]. Tumor cellularity and vascularity are correlated with TIC patterns. Tpeak is related to the microvessel number and tends to be short when the microvessel count is high. Wash-out is dependent on the cellularity and stromal grade, with cellular tumors being wash-out more rapidly[3,24]. When we evaluate the TIC patterns of

SGTs, in general, PMAs tend to demonstrate progressive enhancement due to low microvessel content and cellularity-stromal grade. WTs and lymphomas show rapid enhancement and wash-out because of their high microvessel content and cellularity-stromal grade. MTs show rapid enhancement and wash-out due to high microvessel count and lower cellularity-stromal grade, but they tend to have a lower and slower wash-out compared to WTs[3]. TIC analysis can reveal physiological characterizations of different tissues using the blood flow properties of SGTs[26,28]. Despite overlapping TIC patterns in some SGTs, semi-quantitative DCE MRI is an imaging modality that can help differentiate subtypes of SGTs.

QUANTITATIVE DCE PERFUSION MRI

On DCE MRI, in addition to semi-quantitative examination with TIC parameters, quantitative perfusion MRI can be performed. In the literature, perfusion parameters such as Ktrans [volume transfer constant between blood plasma and extracellular extravascular space (EES)], Kep (flux rate constant between the EES and plasma), and Ve (EES fractional volume) have been studied in SGTs on quantitative DCE perfusion MRI[29]. In the literature, the Ktrans values of PMAs were found to be lower than the Ktrans values of other SGTs. However, while some studies stated that the Ktrans values of PMAs differ significantly from those of other SGTs[29,30], some studies could not detect a significant difference[31]. In studies in the literature, Kep values were found to be lowest in PMAs and highest in WTs. In some studies[29,31], the Kep values of PMAs, WTs and MTs differed significantly, while in some studies only the Kep values of WTs differed significantly from the other SGTs[30]. In the literature, it was found that mean Ve values of WTs were significantly lower than the Ve values of other SGTs[29-31].

DYNAMIC SUSCEPTIBILITY CONTRAST PERFUSION-WEIGHTED MRI

Dynamic susceptibility contrast (DSC) perfusion-weighted MRI measures signal loss during passage of a non-invasive contrast bolus through a tumor and can be performed using the bolus tracking technique that follows the first passage of contrast material through a capillary bed. DSC perfusion-weighted MRI is increasingly used as a diagnostic and research tool and to assess the extent of capillaries and microvasculature, mostly in central nervous system tumors. DSC perfusion-weighted MRI contributes to the assessment of tumor angiogenesis as the degree of signal loss depends on the volume of the intravascular space within a tumor and the concentration of injected contrast material in the blood[32]. There is a limited number of studies in the literature that have performed DSC perfusion-weighted MRI for SGTs and differing results have been obtained. In the study of Abdel Razek and Mukherji[33] on parotid tumors, it was reported that the mean DSC % values of both MTs and all BTs as well as PMAs, WTs and MTs were significantly different. Park *et al*[32] found that WTs tended to have higher DSC % values than malignant parotid tumors, although there was no significant difference. The parameters used in the evaluation of SGTs on some advanced MRI techniques are shown in Table 1.

PSEUDO/PULSED CONTINUOUS ARTERIAL SPIN LABELING PERFUSION MRI

Arterial spin labeling (ASL) provides measurement of tumor blood flow (TBF) using the magnetization of protons in arterial blood as an intrinsic tracer without the use of contrast material[34,35]. High vascularity, increased tumor blood volume, arterio-venous shunt formation, altered capillary transit time and increased the capillary permeability may lead to high TBF values in MTs. There is a limited number of studies in the literature that have performed ASL perfusion-weighted MRI for SGTs[35]. Razek[35] reported that TBF values of malignant SGTs were significantly higher than benign SGTs.

DTI

DTI provides the ability to distinguish between different tissue compartments at the cellular level, with different matrices that reflect the micromovement of water molecules. The most common DTI metrics used are fractional anisotropy (FA) and mean diffusivity (MD). MD is the average diffusivity along three orthogonal planes in the x, y, z directions of the tensor, equal to the mean of the three eigenvalues and equal to the ADC value. As the cellularity of the tumor increases, the MD value decreases. FA indicates the level of directionality of tissue microstructure in water diffusion and correlates with structural tissue orientations. FA correlates linearly with tumor cellularity and grade of malignancy. Abdel Razek *et al*[33] found a significant difference between the MD values of malignant and benign SGTs. At the same time, significant differences were found between the FA values of MTs and BTs in

Table 1 Evaluation on advance magnetic resonance imaging techniques of salivary gland tumors

	Advance magnetic resonance imaging techniques			
	Lymphoma	**Warthin's tumor**	**Malign tumor**	**Pleomorphic adenoma**
Diffusion weighted imaging (ADC values)	< 0.8 × 10^{-3} mm^2/s	(0.8-1.0) × 10^{-3} mm^2/s	(1.0-1.2) × 10^{-3} mm^2/s	> 1.2 × 10^{-3} mm^2/s
Dynamic contrast-enhanced MRI	50 s < Tpeak < 90 s, WR < 30%	Tpeak < 50 s, WR ≥ 30%	Tpeak < 120 s, WR < 30%	Tpeak > 120 s, WR: Non-washout
Quantitative dynamic contrast-enhanced perfusion MRI		Ktrans < 0.8 min^{-1}, Kep > 1 min^{-1}, Ve < 0.2	Ktrans < 0.5 min^{-1}, Kep < 1 min^{-1}, Ve > 0.3	Ktrans < 0.3 min^{-1}, Kep < 0.6 min^{-1}, Ve < 0.9

ADC: Apparent diffusion coefficient; MRI: Magnetic resonance imaging; Tpeak: Time to peak; WR: Wash-out ratio; Ktrans: Volume transfer constant between blood plasma and extracellular extravascular space; Kep: Flux rate constant between the extracellular extravascular space and plasma; Ve: Extracellular extravascular space fractional volume.

DTI studies performed for SGTs[20]. WTs, which are rich in lymphoid content and have high anisotropy, have the highest FA levels among benign SGTs[20,33].

DIFFUSION KURTOSIS IMAGING

Diffusion kurtosis imaging (DKI) is a complex method that uses the non-Gaussian movement of water molecules in tissues. The MRIs are obtained based on the diffusion and microstructural features resulting from the organization of water molecules. A minimum of three *b* values are required on the DKI[36]. In the literature, some authors reported that DKI is useful in defining benign and malign SGTs, while some authors reported that no significant difference was found in distinguishing BTs and MTs. However, some of these authors reported that DKI parameters [ADC (D_{app}) and apparent kurtosis coefficient (K_{app})] differ significantly in PMAs compared to other SGTs[30,37].

INTRAVOXEL INCOHERENT MOTION MRI

Intravoxel incoherent motion (IVIM) provides both true molecular diffusion and motion of water molecules in the capillary network can be estimated with a single diffusion-weighted acquisition technique. Microvascular volume fraction (f), pure diffusion coefficient (D), and perfusion-related incoherent microcirculation (D*) parameters are used on IVIM. Single-shot spin-echo echo-planar imaging with multiple *b* values usually ranging from 0-800 s/mm^2 is used to generate IVIM MRI. Sumi and Nakamura[26] reported that WTs had significantly higher *f* values than PMAs. In addition, Sumi and Nakamura[26] reported that *D* and *D** values contribute to the differentiation of WTs, PMAs, and MTs, and even the use of these parameters together provides 100% diagnostic accuracy.

PROTON MRS

Metabolite concentration in tissues and organs is measured in Proton MRS (1H-MRS) and used to characterize metabolic changes associated with tumors. Proton MRS in neoplasms uses a diagnostic algorithm based predominantly on the detection of high levels of choline compounds. Choline is an indicator of cellular proliferation and cell membrane transformation[38]. A limited number of studies have been conducted in the literature with MRS in SGTs[39]. King *et al*[39] reported that Cho/Cr ratios were significantly different between PMAs and WTs, and between BTs and MTs.

SGTS

According to the 4th edition of the World Health Organization (WHO)'s head and neck tumors classification published in 2017, SGTs are classified as MTs, BTs, non-neoplastic epithelial lesions, benign soft tissue lesions and haematolymphoid tumors[40]. WHO's head and neck tumors classification version 4 is given in Table 2. Despite efforts to simplify this classification, there are still more than 30 entities. MTs were divided into 20, BTs 11, non-neoplastic epithelial lesions 4, benign soft tissue lesions 3 subgroups. Two new entities have been added to this classification: Secretory carcinoma [known as mammary

Table 2 World Health Organization classification of salivary gland tumors 2017

Salivary gland tumors	
Malignant tumors	**Benign tumors**
Mucoepidermold carcinoma	Pleomorphic adenoma
Adenoid cystic carcinoma	Myoepithelioma
Acinic cell carcinoma	Basal cell adenoma
Polymorphous adenocarcinoma	Warthin's tumor
Clear cell carcinoma	Oncocytoma
Basal cell adenocarcinoma	Lymphadenoma
Intraductal carcinoma	Cystadenoma
Adenocarcinoma, NOS	Sialadenoma papilliferum
Salivary duct carcinoma	Ductal papillomas
Myoepithelial carcinoma	Sebaceous adenoma
Epithelial-myoepithelial carcinoma	Canalicular adenoma and other ductal adenomas
Carcinoma ex pleomorphic adenoma	**Non-neoplastic epithelial lesions**
Secretory carcinoma	Sclerosing polycystic adenosis
Sebaceous adenocarcinoma	Nodular oncocytic hyperplasia
Carcinosarcoma	Lymphoepithelial sialadenitis
Poorly differentiated carcinoma	Haemangioma
Lymphoepithelial carcinoma	Lipoma/sialolipoma
Squamous cell carcinoma	Nodular fasciitis
Oncocytic carcinoma	**Haematolymphoid tumors**
Sialoblastoma	Extranodal marginal zone lymphoma of mucosa-associated lymphoid tissue

NOS: Not otherwise specified.

analogue secretory carcinoma (MASC)] and sclerosing polycystic adenosis to non-neoplastic epithelial lesions[41].

SALIVARY GLAND BTS

Pleomorphic adenoma (benign mixed tumor)

Pleomorphic adenoma is the most frequently observed SGT. Great majority of them are located in the parotid gland, and about 80%-90% is found on the surface of the gland[42-44]. PMAs are slowly growing, painless masses observed in 30-60 years of age and more frequently in women (ratio 2:1)[43, 44]. Multicentricity of PMAs is less than 1%[43]. At cellular level, morphological diversity characterized by a mixture of both epithelial and mesenchymal components is a characteristic feature of PMAs[44,45]. Ratio of these components varies greatly in PMAs, and MRI features vary based on the distribution of these components[44,46]. Stromal components in PMAs could be myxomatous, chondromatous, lipomatous, hyalinized, fibrous, calcified, or osseous, myxoid stroma being the most frequent (94.2%) [44,45]. Tsushima *et al*[47] mentioned that high intensity signals on T2WI represented myxoid histology. Classical appearance on T2WI of MRI is generally well bordered, microlobule contoured masses with prominently high signal confined by hypointense fibrous capsule[10,44,46-48]. Zaghi *et al*[49] evaluated the diagnostic efficiency of conventional MRI in differentiating PMAs using five different criteria. They found that masses with bright T2 signal, sharp borders, heterogeneous nodular enhancement, lobulated contours and a T2 dark rim were predictive of PMAs with a sensitivity of 43.9% and a specificity of 95%. Cellular variants of PMAs featured intermediate SI on T2WI due to their epithelial components, while the ones with fibrous stroma were hypointense. PMAs with hypointense signals on T2WI could represent malignity, but the presence of complete capsule and lobulated contour are good indications of PMAs[44]. Cystic degeneration was observed in 29%-40% of parotid gland PMAs[50]. Due to their heterogeneous composition of epithelial, myoepithelial and stromal cells with fluid areas within

epithelial glandular regions, PMAs have unrestricted diffusion and high ADC values. ADC values of PMAs were reported to vary between (0.66-2.86) × 10^{-3} mm^2/s[19-21,51], while ADC_{mean} values varied from (1.35-2.15) × 10^{-3} mm^2/s[19,20,51-53]. Cellular variants of PMAs could have lower ADC values in the range of (1.0-1.3) × 10^{-3} mm^2/s[44,54]. Average Dapp value of (1.525 ± 0.396) × 10^{-3} mm^2/s and average Kapp value of 0.394 ± 0.172 were reported for PMAs on DKI[37]. Huang *et al*[30] reported the mean *D* value as 1.81 × 10^{-3} mm^2/s and the *K* value as 0.51 on DKI. Zheng *et al*[52] reported that a great majority of PMAs featured type A TIC pattern (persistent and Tpeak > 120 s) because of unbroken capillary endothelial cells and more complex nature of stroma in tumor (Figure 1). They also mentioned slow flow of contrast medium into extracellular space. However, cellular variants of PMAs showed atypical gradual wash-out pattern on DCE MR due to their high epithelium content and low myxoid stroma[52]. Frequency of this atypical pattern in all PMA TIC patterns was reported to be about 17%-18%[24,44,55].

Regarding Tpeak values of PMAs on DCE MRI, Tsushima *et al*[23] observed Tpeak was equal to or greater than 260 s while Sumi and Nakamura[26] found Tpeak values of 120 s or longer in 92.9% of the cases and less than 120 s in 7.1% of them. Similarly, Zheng *et al*[52] measured 120 s or over in 88.9% of the cases and less than 120 s in 11.1%. Tao *et al*[14], on the other hand, found 58 s or longer Tpeak values in 82.0% of the cases whereas in 18% it was less than 58 s. For WR values of PMAs, Tsushima *et al*[23] reported no wash-out while Zheng *et al*[52] reported no wash-out in 88.9% of the patients and less than 30% WR in 11.1% of the cases. The literature contains a few studies on quantitative DCE perfusion MRI parameters (Ktrans, Kep and Ve) in SGTs. In these studies, mean Ktrans value of PMAs was 0.101 ± 0.069 to 0.217 ± 0.036; mean Kep values 0.245 ± 0.160 to 0.567 ± 0.048; mean and values were determined as 0.380 ± 0.192 to 0.590 ± 0.478[3,7,30].

WT

WT is the second most commonly observed benign SGT[43,48]. It is mostly observed in middle-age or older men in the parotid gland or periparotid region and more commonly in the inferior pole of the parotid gland[56,57]. Smoking, autoimmune disease and radiation exposure were reported to increase WT risk[43,48,56]. About 20% of WTs tend to be bilateral and multicentric[43,56]. They generally have a spherical to ovoid shape of 2-4 cm diameter, and their surface is smooth. WT is basically an adenoma with mucoid or brown fluid filled cysts of variable number. The cysts are made of two layered papillary proliferations of oncocytic epithelium and supporting stroma made of an abundant follicle carrying lymphoid tissue. They may have focal hemorrhage and necrosis[57]. Transformation of WTs to malignancy is extremely rare (0.3%)[43,56]. Intermediate or hypointense areas on short tau inversion recovery and T2WI, and hyperintense area on T1WI on MRI suggest WTs[48,57,58]. Solid WT components result in iso-intensity or hypo-intensity on T2WI because histopathologically WT is made of epithelial cells and lymphoid stroma with fibrovascular tissue[56]. About 30%-60% of WTs are partly or predominantly cystic[50,56,58]. WTs may resemble other less frequently observed benign lesions such as myoepitheliomas and basal cell adenomas (BCAs) which may also carry cystic components and tend to involve superficial lobe of parotid gland[48,59,60]. WTs were reported to have low ADC values (Figure 2) due to their epithelial and lymphoid stroma contents which have microscopic slit-like cysts containing proteinous fluid[56,57]. In different studies, ADC values of WTs ranged from (0.69-1.36) × 10^{-3} mm^2/s and ADC_{mean} was about (0.74-1.02) × 10^{-3} mm^2/s[19,52,53,56,57]. Only two studies in the literature reported ADC_{mean} values higher than 1.0 × 10^{-3} mm^2/s, while others had lower values. A study reported that mean D_{app} and mean K_{app} values of WTs on DKI were (0.808 ± 0.227) × 10^{-3} mm^2/s and 0.999 ± 0.228, respectively[37]. Huang *et al*[30] reported the mean *D* value of WTs as 0.97 × 10^{-3} mm^2/s and the mean *K* value as 0.99 on DKI.

In terms of Tpeak values of WT in studies on the literature dealing with DCE MRI, Tsushima *et al*[23] reported < 20 s, Hisatomi *et al*[61] in the range of 30-45 s, Sumi and Nakamura[26] < 120 s, while Tao *et al*[14] found that in 97.6% of the cases Tpeak was less than 58 s and in 2.4% of the cases Tpeak was equal to or greater than 58 s. For WR values of WTs, Hisatomi *et al*[61] mentioned that WR was prominent in the first 30 s after Tmax. On the other hand, Sumi and Nakamura[26] found that WR ranged from 30%-70%, while Zheng *et al*[52] found WR values equal to or larger than 30%. Tao *et al*[14] found that WR values were 22.6% or over in 85.4% of the cases, less than 22.6% in 12.2% and no wash-out was observed in 2.4% of the cases. In the literature, quantitative DCE perfusion MRI values in WTs mean Ktrans values 0.105 ± 0.064 to 0.464 ± 0.036; mean Kep values 0.729 ± 0.112 to 2.299 ± 1.312; mean Ve values are reported in the range of 0.1439 ± 0.093 to 0.272 ± 0.013[29-31].

Oncocytoma

Oncocytomas are well bordered, benign epithelial neoplasms of homogeneous solid structure consisting of mitochondria-rich oncocytes[48,60]. They constitute about 1% of parotid tumors, but about 80% of them are observed in the parotid gland[48,56,60]. They are commonly observed in people in their 60 s and 80 s, and are slightly more common in women. Because they have high cellularity and low free water content, conventional MRI findings of oncocytomas resemble those of WTs[62]. In addition, with their lower ADC content, fast enhancement and wash-out on dynamic MRI, findings of DWI and DCE MRI could overlap. However, oncocytomas usually have higher ADC values than WTs[56]. Oncocytomas were reported to have ADC values ranging from (0.8-1.16) ×10^{-3} mm^2/s[56,63]. Hisatomi *et*

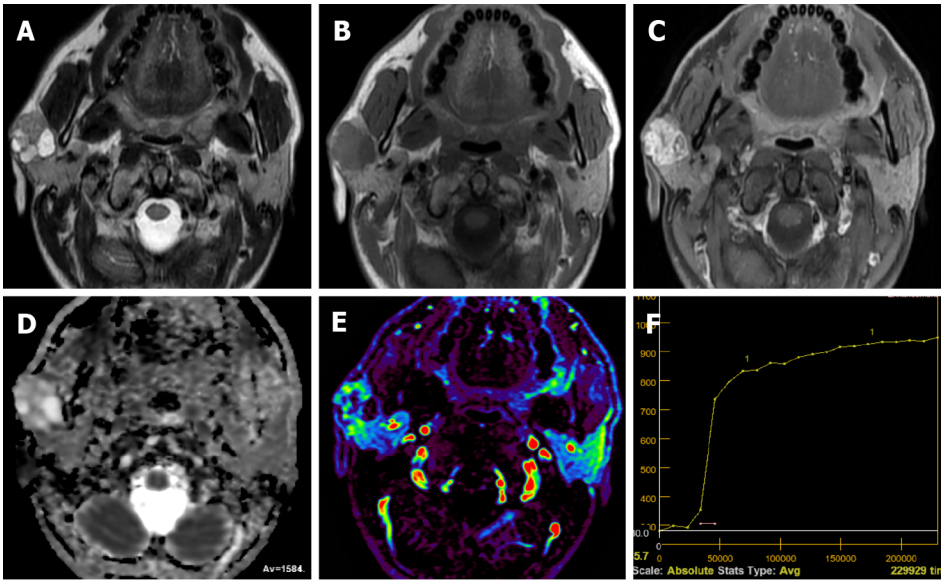

DOI: 10.4329/wjr.v14.i8.256 **Copyright** ©The Author(s) 2022.

Figure 1 Twenty-nine years old male patient with smooth lobule contoured pleomorphic adenoma located on the superficial lobe of right parotid gland. A: The lesion contains prominent hyperintense components and mixed signals on T2-weighted image; B: The lesion contains heterogeneous hypointense signal on T1-weighted image; C: The lesion appears to have marked heterogeneous enhancement on the contrast-enhanced image; D: The apparent diffusion coefficient (ADC) value of mass was 1.58 × 10^{-3} mm^2/s on ADC map; E: Hypo-hyper perfused areas on perfusion magnetic resonance imaging color map; F: The time intensity curve of mass is seen increasing contrast-enhancement towards late phases.

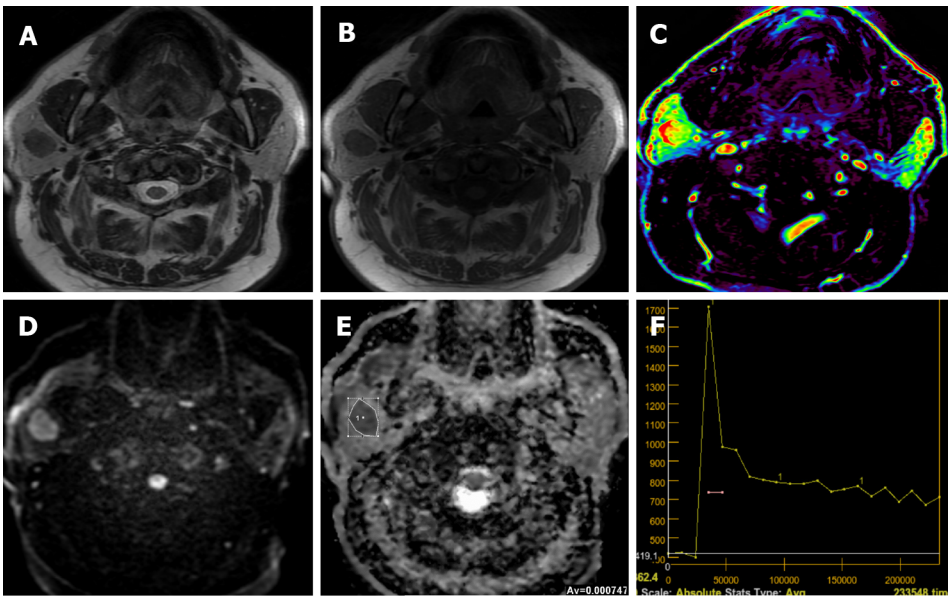

DOI: 10.4329/wjr.v14.i8.256 **Copyright** ©The Author(s) 2022.

Figure 2 Sixty-five years old male patient with smooth lobule contoured Warthin's tumor located on the superficial lobe of right parotid gland. A and B: Hypointense signal of the lesion compared to the gland on T2-weighted image and T1-weighted image; C: The mass is hyperperfused on the color-coded perfusion image; D: The mass appears to be slightly heterogenous hyperintense on the diffusion-weighted image, E: The apparent diffusion coefficient (ADC) value of mass was 0.74 × 10^{-3} mm^2/s on the ADC map; F: The time intensity curve of mass has a wash-out ratio of 50%.

al[61] found that oncocytomas have similar contrasting dynamics to WT, and consequently, they cannot be differentiated from WTs using DCE MRI alone.

BCA

BCAs are made of basaloid cells carrying eosinophilic cytoplasm, and they have no clear cell borders. Their nuclei are round-to-oval. They have solid, trabecular, tubular and membranous distribution patterns. Although most tumors carry one of these patterns predominantly, some of them may have more than one pattern. Membranous BCAs have different biological characteristics from other BCA

variants because they carry microfocal adenomas, incomplete capsules or no capsule. Besides, they may recur after operation and they have malignant transformation characteristics. Their frequency is higher after 50 years of age, and women have a slightly higher prevalence[51]. BCAs most frequently arise from the parotid gland and are more frequently located in the superficial lobe[31,51]. They tend to have clearly defined borders[3,31,51]. BCAs may have cystic or hemorrhagic components[51]. In MRI of BCAs, signal intensities on T1WIs are relatively low while on T2WIs intensity varies between hypointense to slightly intense. In studies in the literature, mean ADC values of BCAs were found to be [(1.21 ± 0.20)-(1.24 ± 0.18)] × 10^{-3} mm^2/s[31,51]. On dynamic MRI, on the other hand, they feature rapid and prolonged enhancement[51]. Mukai *et al*[51] found that on DCE MRI, 12 of 14 BCAs (85.7%) had TIC patterns of either Tpeak > 120 s or Tpeak < 120 s and wash-out < 30%. Yabuuchi *et al*[31] reported Tpeak < 120 s and wash-out < 30% in 61.5% of BCAs in DCE MRI, and Tpeak > 120 s and no wash-out in 15.3% of them.

Myoepithelioma

Myoepitheliomas are responsible only for about 1%-1.5% of all salivary neoplasms. Their primary location is parotid gland (about 40%) but they may also appear on other salivary gland parts (about 21%)[59,64]. Differentiated myoepithelial cells in the form of spindle, plasmacytoid, epithelioid, or clear cells constitute most of myoepithelioma[59]. Myoepithelial cells were proposed to have contractile units helping to excrete glandular secretions. Myoepitheliomas need to be differentiated from parotid cyst, abscess, mucocele, schwannoma, leiomyoma, neurofibroma, rhabdomyosarcoma, smooth muscle neoplasms, extramedullary plasmacytoma, benign fibrous histiocytoma, PMA, mucoepidermoid carcinoma (MEC) and myoepithelial carcinoma[64]. They feature homogeneous isointense signal based on muscle tissue on T1WI and homogeneous iso-hyperintense signals on T2WI. In the majority of them (about 80%), hypointense capsule formation and homogeneous contrasting could be observed on T2WI and contrast-enhanced series[59]. ADC_{mean} values of myoepithelioma in different studies varied from 1.31 ± 0.9 to 1.86 ± 0.18 (range 1.18-1.91) × 10^{-3} mm^2/s[19].

Schwannoma and neurofibroma

Intraparotid neurofibromas or schwannomas could be associated with neurofibromatosis, but they may also arise sporadically[48]. Frequency of parotid tumors which originate in the facial nerve was estimated to be between 0.2%-1.55%[65]. A fusiform tumor appearance extending into intratemporal facial nerve canal could be a distinguishing feature in diagnosis. However, this appearance also resembles perineural extension of malignant neoplasms. Peripheral nerve sheath tumors could easily be distinguished by their target and fascicular signs on MRI[48]. The target sign refers to the appearance of central T2 hypointensity and enhancement and peripheral T2 hyperintensity and non-enhancement[48,65]. The fascicular sign corresponds to multiple ring-like T2 hypointense foci within a relatively T2 hyperintense and enhancing background[48]. On DWI, neurofibromas were reported to have ADC_{mean} values in the range of (1.41-1.91) × 10-3 mm^2/s[13,17].

Lipoma or sialolipoma

Lipomas are neoplasms consisting of mature adipose tissue. For salivary gland involvement, they may be intraglandular or extraglandular[48]. Lipomas have similar signal intensities to subcutaneous adipose tissue on T1WI and T2WI[66]. Fat-suppression is useful on MRI of salivary gland lipomas. These tumors may have septations when they surround vessels[48]. Some rare variants of lipomas with a biphasic pattern where serous tissue is diffusely scattered among fat is termed sialolipoma and their appearance closely resemble normal parotid tissue[48,67]. They are encapsulated but tend to be heterogeneous in appearance due to their soft salivary gland tissue and fat tissue[48]. DWI studies showed that lipomas had ADC_{mean} values of (0.09-0.62) ± 0.21 [range (0.08-0.76) × 10^{-3} mm^2/s] [19].

Hemangioma

Hemangiomas refer to vascular abnormalities involving increased proliferation and endothelial cell renewal. They are more common in childhood. About 60%-65% of hemangiomas are observed in the head and neck area, and 81%-85% of them are found in the parotid gland. Hemangiomas constitute 0.4%-0.6% of all tumors in the parotid gland and the ADC value of the hemangioma was found to be 0.8 × 10^{-3} mm^2/s[68]. On MRI, they have homogeneously hyperintense appearance on T2WI and strong enhancement, but they are devoid of prominent flow. These tumors often affect the whole gland and could have additional lesions elsewhere in the head and neck or in other regions[48,68].

SALIVARY GLAND MTS

MEC

MEC refers to the most common salivary gland malignancy and 60% of these lesions involve the parotid gland. MEC develops in epithelium tissue of salivary gland ducts. It is made of mucus secreting cells,

epidermoid cells and intermediate cells[46]. They may have low, intermediate or high-grade subtypes with different radiological appearances. Low grade tumors have smooth borders and cystic components containing mucin, and have hyperintense signals on T1WI and T2WI. High-grade tumors, on the other hand, are quite solid with undefined borders due to extension into neighboring structures. They often appear on T2WI as hypointense or isointense lesions due to their high cellularity[33]. ADC values of MECs on DWI is low in poorly differentiated lesions. ADC_{mean} values of MECs on DWI studies were reported to vary from [(0.81 ± 0.06)-(1.05 ± 0.03)] × 10^{-3} mm^2/s [range (0.65-1.14) × 10^{-3} mm^2/s][13,19,20,69]. Zheng *et al*[52] reported Tpeak value of 120 s or lower for MECs on DCE MRI. WR of a case was reported to be less than 30% while that of another was 30% or over.

Adenoid cystic carcinoma

Adenoid cystic carcinoma (ACCa) is made of ductal epithelial and myoepithelial cells. It may be in solid, cribriform or tubular forms, cribriform being most common. It is more frequent in middle-aged or elderly patients. Perineural spreading and invasion capacity of ACCa is very high[46]. They can result in distant metastases and local invasions. ACCa is frequently observed as ill-defined masses with perineural spreading in imaging. ACCa has intermediate to low signal on T1WI and T2WI MRI. The parotid gland is the most common location for ACCa (about 25%), which often involves perineurium of cranial nerve VII during the diagnosis[46]. On DWI studies, ACCas were found to have ADC_{mean} values varying from [(0.84 ± 0.07)-(1.46 ± 0.03)] × 10^{-3} mm^2/s[9,13,17,19,69]. Tsushima *et al*[23] detected PMA-like TIC pattern (Figure 3) in two ACCa cases using DCE MR (Tpeak > 260 s and no wash-out). It was suggested that this pattern could be due to increased interstitial space of ACCa which contains extracellular mucin and low microvessel count[3,23]. Zheng *et al*[52] reported that one ACCa they studied had the TIC pattern most commonly observed in MTs (type C, T_{peak} ≤ 120 s and WR < 30%).

Acinic cell carcinoma

Acinic cell carcinoma is a low-grade malignant lesion, and about 90% of these lesions are located in the parotid gland[46]. Its characteristic feature is serous acinar differentiation and basophilic granules in cytoplasm[8]. No specific finding is observed in imaging, but most acinic cell carcinomas are homogeneously enhanced, well-bordered, slowly growing masses like other benign or low grade malignant lesions[33,46]. Most of the malignancies which were previously considered acinic cell carcinomas are now identified as MASCs[46]. Kashiwagi *et al*[70] revealed that acinic cell carcinomas tended to be solid while MASCs were predominantly cystic masses with solid papillary extensions. The authors mentioned that intermediate-high SI of acinic cell carcinomas on T1WI could help in differential diagnosis. DWI studies in the literature showed ADC_{mean} values from [(0.79 ± 0.33)-(1.76 ± 0.11)] × 10^{-3} mm^2/s for acinic cell carcinomas[69,70]. Zheng *et al*[52] studied three acinic cell carcinoma cases on DCE MRI and observed a Tpeak value of 120 s or less. WR was over 30% in two cases and equal to or larger than 30% in the other.

MASC

MASC was first described in 2010 as a rare salivary carcinoma mimicking acinar cell carcinoma and was released to the World Health Organization classification of head and neck tumors in 2017[71,72]. MASC has morphological and genetic similarities with secretory carcinoma of the breast. The majority of MASCs (approximately 70%-80%) are located in the parotid gland, while a smaller number are located in other minor salivary gland areas or major salivary gland glands[72,73]. MASCs are often tumors of "papillary and cystic" or "non-papillary and cystic" morphology. The cystic and solid components of these tumors have high signal on T1WIs on MRI, more often in the cystic component. On contrast-enhanced MRI series, solid components may show different forms of enhancement (homogeneous, heterogeneous, or scarce)[72]. DWI has been applied in a limited number of cases in MASCs, and ADC values in the solid components of the tumor vary between (0.5-1.7) × 10^{-3} mm^2/s[70,72].

Carcinoma ex pleomorphic adenoma

Carcinoma ex pleomorphic adenoma arises in connection with a primary or repeating benign PMA. About 1.5% of pleomorphic adenoma cases develop carcinoma ex pleomorphic adenoma in five years, and 10% of them in 15 years. In this condition, a painless mass still for many years starts growing. They appear in MRI as masses with ill-defined borders extending into surrounding tissues, discontinuous hypointense rim and mediate to low heterogeneous SI on T2WI[74]. On DWI studies, carcinoma ex PMAs were reported to have ADC_{mean} values in the range of [(0.82 ± 0.01)-(1.32 ± 0.035)] × 10^{-3} mm^2/s[9,13,17]. Zheng *et al*[52] found that Tpeak of carcinoma ex PMA was 120 s or less while their WR was less than 30% on DCE MRI.

Lymphoma

Primary lymphoma of salivary glands is rare and in 75%-80% of the cases parotid gland is involved. Most commonly encountered Non-Hodgkin lymphoma types of salivary glands are extranodal marginal zone B-cell lymphoma in mucosa-associated lymphoid tissue (MALT), follicular B-cell lymphoma and diffuse large B-cell lymphoma. Follicular type and MALT lymphomas are low-grade

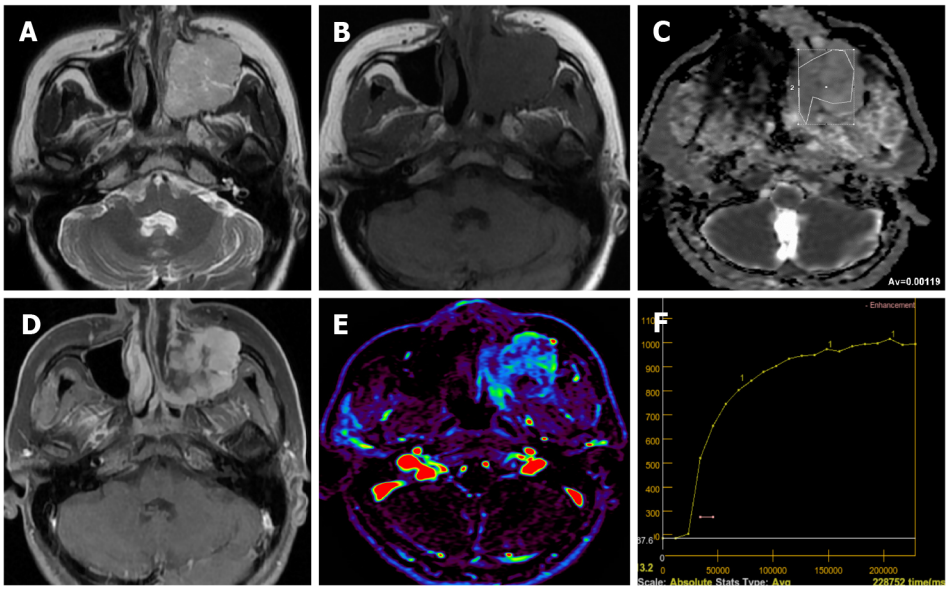

DOI: 10.4329/wjr.v14.i8.256 **Copyright** ©The Author(s) 2022.

Figure 3 Fourty-four years old female patient with adenoid cystic carcinoma infiltrating into the left maxiller sinus. A: T2-weighted image shows a hyperintense mass in the left maxillary sinus; B: T1-weighted image shows a hypointense mass in the left maxillary sinus; C: The apparent diffusion coefficient (ADC) value of mass was 1.19 × 10^{-3} mm^2/s on the ADC map; D: There was intense contrast enhancement on the contrast-enhanced image of the mass; E: On the color-coded perfusion magnetic resonance imaging, hyper and hypoperfused areas are seen in the mass; F: On the time intensity curve of mass, progressive enhancement is seen towards the late phases.

lesions characterized by slow growth, which sometimes regress spontaneously. In cases with autoimmune conditions such as Sjogren's syndrome MALT lymphoma risk is 44 times higher. Parotid MALT lymphomas are mostly solid-cystic lesions which may have a solitary or diffused pattern. In non-MALT lymphomas, on the other hand, multiple or solitary homogeneous internal structure is more common. A diffuse large B-cell lymphoma is the most common high-grade lymphoma involving the parotid gland. Some of them arise from an underlying low-grade lesion. They manifest themselves with an asymptomatic mass in the parotid gland which grows in a period of four to six months[75]. The ADC values of lymphomas on DWI were generally lower than other solitary tumors (Figure 4), which helps in their differential diagnosis. DWI studies found ADC_{mean} values from 0.55 to 0.98 [range (0.4-1.21) × 10^{-3} mm^2/s] for parotid gland lymphomas[15,20,21,58,76].

It has been known that malignant lymphomas have higher cellularity and less extracellular space than head and neck carcinomas[27,76]. Therefore, malignant lymphomas show rapid enhancing and wash-out TIC patterns[19,26,28]. Since TIC patterns of malignant lymphomas and WTs are similar, differentiation of WTs and malignant lymphomas cannot be done using DCE MRI alone[27]. However, Tpeak of lymphomas are somewhat longer and their WR is lower compared to WTs. In their study dealing with head and neck lymphomas, Asaumi *et al*[77] measured average maximum duration for lymphomas to reach contrast index as 78.5 ± 29.1 s. Tao *et al*[14], on the other hand, found that in all of seven lymphomas they studied Tpeak was less than 58 s while WR was less than 22.6% in six of them (85.7%) but equal to or greater than 22.6% in one (14.3%). Wang *et al*[76] evaluated 20 MALToma cases and reported that parotid MALTomas were usually (94.1% of the patients) in early ascending type (*i.e.*, type I, with a Tpeak of less than 79.65 s and an initial slope of increase less than 0.807). They mentioned that Tpeak values could be used to distinguish between parotid tumor-like benign lymphoepithelial lesion (BLEL) and MALToma because Tpeak value was at least twice higher in tumor-like BLEL cases compared to MALToma cases[76].

Salivary duct carcinoma

Salivary duct carcinoma (SDC) refers to tumors of different sizes characterized by duct structures which contain eosinophilic tumor cells. They often have a cribriform structure. SDC constitutes the most commonly encountered malignant component of carcinoma ex pleomorphic adenoma. Majority of SDCs originate from PMAs[78]. On DWI studies, ADC_{mean} values of SDCs were reported to vary from (0.88-1.28) ± 0.16 [range (0.87-1.47) × 10^{-3} mm^2/s][26,27,30,31,79]. Motoori *et al*[79] reported that on DCE MRI 78% of SDCs appeared as type B (Tpeak < 120 s and WR < 30%), and 67% of had areas of type C TIC pattern (Tpeak > 120 s) due to their abundant fibrotic tissue.

Epithelial-myoepithelial carcinoma

Epithelial-myoepithelial carcinoma (EMC) is a rare subtype of malignant salivary gland tumor.

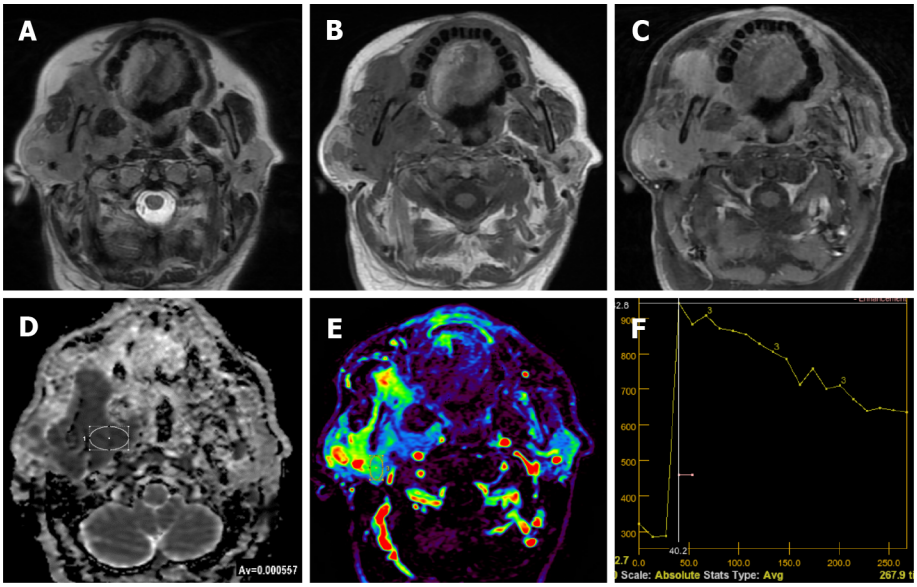

DOI: 10.4329/wjr.v14.i8.256 **Copyright** ©The Author(s) 2022.

Figure 4 Sixty-one years old male patient with non-Hodgkin lymphoma infiltrating into the right parotid gland. A and B: Hypointense signal of the lesion compared to the gland on T2-weighted image and T1-weighted image; C: Contrast enhancement components of different intensities are seen on contrast-enhanced image in the lesion; D: The apparent diffusion coefficient (ADC) value of mass was 0.55 × 10^{-3} mm^2/s on the ADC map; E: The mass is hyperperfused on the color-coded perfusion image; F: The time intensity curve of mass has a wash-out ratio of 43%.

Histopathologically, it consists of a biphasic array of inner lumen ductal cells and outer myoepithelial cells. On conventional MRI, EMCs are well-contoured, may contain mostly solid or cystic components, septa or multi-nodularity can be detected, solid components are isointense or hypointense on T1WIs, hyperintense or isointense on T2WIs, contrast-enhancement with different forms (homogeneous or heterogeneous; moderate, mild or none) can be seen as masses. On DWI studies, ADCmean values of EMCs were reported to vary from (0.96-1.05) ± 0.03 [range (0.789-1.14) × 10^{-3} mm^2/s][80].

Secondary malignancies of the salivary glands (metastases)

Secondary malignancies of the salivary glands may develop either by distant metastasis or by direct infiltration of tumors from adjacent tissues. Secondary malignancies of the salivary glands may involve the parenchyma of the salivary glands or the intraglandular and/or periglandular lymph nodes. Secondary malignancies most commonly involve the parotid gland, followed by the submandibular gland. Metastases in other salivary glands are less common. Metastases to the salivary glands most commonly arise from squamous cell carcinomas of the head and neck region and the upper aerodigestive tract[81,82] (Figure 5). Various hematopoietic and lymphoid malignancies, including lymphomas, but not as much as squamous cell carcinomas, constitute a significant portion of secondary malignancies of the salivary glands[81]. Metastases may originate less frequently from distant organs such as malignant melanoma, breast, lung, kidney, thyroid, pancreatobiliary, prostate, and bladder[81,82].

Cystic lesions of parotid gland and its tumors which may have cystic component

Parotid gland could have pure cystic benign lesions such as lymphoepithelial cysts, lymphangiomas, dermoid cysts, first branchial cleft cysts and mucocele, but they could be BTs and MTs which contain cystic components of different size[50]. Kato *et al*[50] found cystic components of different size scattered over different areas which might have different T1 and T2 signal characteristics in 40% of PMAs, 60% of WTs, 67% of BCAs, 86% of SDCs, 80% of MECs, 75% of epithelial myoepithelial cell carcinomas, 50% of acinic cell carcinomas, 100% of carcinoma ex PMA, 100% of adenocarcinomas and 100% of ACCs. In order to avoid erroneous ADC measurements in tumors with cystic or necrotic components using DWI and in measurements to determine TIC pattern in DCI, region of interest should be placed in solid sections of the lesions[24,62,83].

CONCLUSION

In addition to the morphological data of conventional MRI, advanced MRI techniques allow us to obtain information about the cellularity, microstructural features or vascularity of tumors and thus to interpret the nature and subtypes of tumors. For example, while high cellular tumors such as WTs or lymphomas

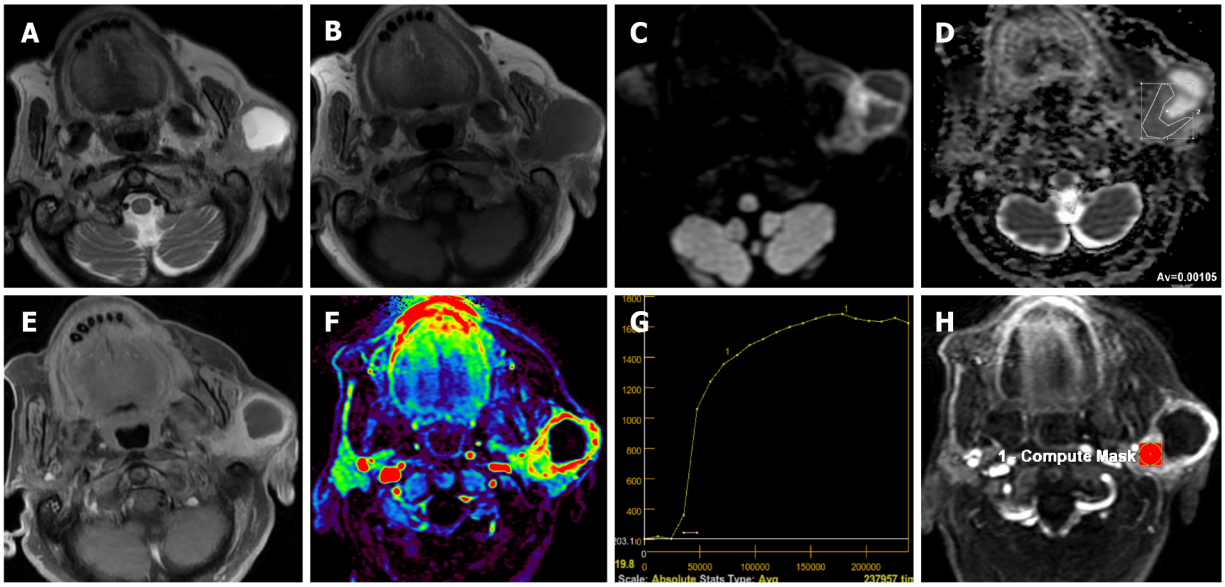

DOI: 10.4329/wjr.v14.i8.256

Figure 5 Eighty-seven years old female patient with squamous cell carcinoma infiltrating into the left parotid gland. A: T2-weighted image shows a mass with a large cystic component; B: The lesion is hypointense on T1-weighted image; C: Solid component of the mass appears to be slightly hyperintens on the diffusion-weighted image; D: The apparent diffusion coefficient (ADC) value of the solid component of mass was 1.05 × 10^{-3} mm^2/sec on the ADC; E: There was intense contrast enhancement of the solid component of mass on the contrast-enhanced image; F: On the color-coded perfusion magnetic resonance imaging, hyperperfused areas are seen in the solid component of the mass; G: On the time intensity curve of mass, progressive enhancement is seen towards the late phases. H: Ktrans was measured on quantitative dynamic contrast-enhanced magnetic resonance imaging.

show low ADC values on diffusion MRI, they cause rapid contrast enhancement and significant wash-out on dynamic contrast MRI series. Except for their cellular variants, PMAs show high ADC values and an increasing TIC pattern on dynamic MR series. High cellular MTs show diffusion restrictions and WRs not as much as WTs or lymphomas. Quantitative perfusion MRI values (such as Ktrans, Kep, Ve) can be measured in accordance with the structural features of the tumors. With the increase in data and studies on the nature and subtypes of SGTs in the literature, threshold values or acceptance intervals for quantitative measurements have begun to emerge, although there are overlaps.

FOOTNOTES

Author contributions: Gökçe E designed the study; Beyhan M supervised the study. Gökçe E and Beyhan M participated in literature research and manuscript preparation, and read and approved the final version.

Conflict-of-interest statement: All the authors report no relevant conflicts of interest for this article.

Country/Territory of origin: Turkey

ORCID number: Erkan Gökçe 0000-0003-3947-2972; Murat Beyhan 0000-0002-8630-4632.

S-Editor: Wang JJ
L-Editor: A
P-Editor: Wang JJ

REFERENCES

1 **Gao M**, Hao Y, Huang MX, Ma DQ, Chen Y, Luo HY, Gao Y, Cao ZQ, Peng X, Yu GY. Salivary gland tumours in a northern Chinese population: a 50-year retrospective study of 7190 cases. *Int J Oral Maxillofac Surg* 2017; **46**: 343-349

[PMID: 27769738 DOI: 10.1016/j.ijom.2016.09.021]
2 **Del Signore AG**, Megwalu UC. The rising incidence of major salivary gland cancer in the United States. *Ear Nose Throat J* 2017; **96**: E13-E16 [PMID: 28346649 DOI: 10.1177/014556131709600319]
3 **Abdel Razek AAK**, Mukherji SK. State-of-the-Art Imaging of Salivary Gland Tumors. *Neuroimaging Clin N Am* 2018; **28**: 303-317 [PMID: 29622121 DOI: 10.1016/j.nic.2018.01.009]
4 **Carlson ER**. Management of Parotid Tumors. *J Oral Maxillofac Surg* 2017; **75**: 247-248 [PMID: 28328430 DOI: 10.1016/j.joms.2016.12.001]
5 **Kuan EC**, Mallen-St Clair J, St John MA. Evaluation of Parotid Lesions. *Otolaryngol Clin North Am* 2016; **49**: 313-325 [PMID: 26902978 DOI: 10.1016/j.otc.2015.10.004]
6 **Eveson JW**, Cawson RA. Salivary gland tumours. A review of 2410 cases with particular reference to histological types, site, age and sex distribution. *J Pathol* 1985; **146**: 51-58 [PMID: 4009321 DOI: 10.1002/path.1711460106]
7 **Mansour N**, Hofauer B, Knopf A. Ultrasound Elastography in Diffuse and Focal Parotid Gland Lesions. *ORL J Otorhinolaryngol Relat Spec* 2017; **79**: 54-64 [PMID: 28231589 DOI: 10.1159/000455727]
8 **Munhoz L**, Abdala Júnior R, Abdala R, Arita ES. Diffusion-weighted magnetic resonance imaging of the paranasal sinuses: A systematic review. *Oral Surg Oral Med Oral Pathol Oral Radiol* 2018; **126**: 521-536 [PMID: 30143461 DOI: 10.1016/j.oooo.2018.07.004]
9 **Inci E**, Hocaoglu E, Kilickesmez O, Aydin S, Cimilli T. Quantitative Diffusion-Weighted MR Imaging in the Differential Diagnosis of Parotid Gland Tumors: Is it a Useful Technique? *Turkiye Klinikleri J Med Sci* 2010; **30**: 1339-1345 [DOI: 10.5336/medsci.2009-14994]
10 **Lechner Goyault J**, Riehm S, Neuville A, Gentine A, Veillon F. Interest of diffusion-weighted and gadolinium-enhanced dynamic MR sequences for the diagnosis of parotid gland tumors. *J Neuroradiol* 2011; **38**: 77-89 [PMID: 20542568 DOI: 10.1016/j.neurad.2009.10.005]
11 **Celebi I**, Mahmutoglu AS, Ucgul A, Ulusay SM, Basak T, Basak M. Quantitative diffusion-weighted magnetic resonance imaging in the evaluation of parotid gland masses: a study with histopathological correlation. *Clin Imaging* 2013; **37**: 232-238 [PMID: 23465973 DOI: 10.1016/j.clinimag.2012.04.025]
12 **Milad P**, Elbegiermy M, Shokry T, Mahmoud H, Kamal I, Taha MS, Keriakos N. The added value of pretreatment DW MRI in characterization of salivary glands pathologies. *Am J Otolaryngol* 2017; **38**: 13-20 [PMID: 27806890 DOI: 10.1016/j.amjoto.2016.09.002]
13 **Abdel Razek AA**, Samir S, Ashmalla GA. Characterization of Parotid Tumors With Dynamic Susceptibility Contrast Perfusion-Weighted Magnetic Resonance Imaging and Diffusion-Weighted MR Imaging. *J Comput Assist Tomogr* 2017; **41**: 131-136 [PMID: 27636248 DOI: 10.1097/RCT.0000000000000486]
14 **Tao X**, Yang G, Wang P, Wu Y, Zhu W, Shi H, Gong X, Gao W, Yu Q. The value of combining conventional, diffusion-weighted and dynamic contrast-enhanced MR imaging for the diagnosis of parotid gland tumours. *Dentomaxillofac Radiol* 2017; **46**: 20160434 [PMID: 28299943 DOI: 10.1259/dmfr.20160434]
15 **Elmokadem AH**, Abdel Khalek AM, Abdel Wahab RM, Tharwat N, Gaballa GM, Elata MA, Amer T. Diagnostic Accuracy of Multiparametric Magnetic Resonance Imaging for Differentiation Between Parotid Neoplasms. *Can Assoc Radiol J* 2019; **70**: 264-272 [PMID: 30922790 DOI: 10.1016/j.carj.2018.10.010]
16 **Zhang W**, Zuo Z, Luo N, Liu L, Jin G, Liu J, Su D. Non-enhanced MRI in combination with color Doppler flow imaging for improving diagnostic accuracy of parotid gland lesions. *Eur Arch Otorhinolaryngol* 2018; **275**: 987-995 [PMID: 29430614 DOI: 10.1007/s00405-018-4895-6]
17 **Matsushima N**, Maeda M, Takamura M, Takeda K. Apparent diffusion coefficients of benign and malignant salivary gland tumors. Comparison to histopathological findings. *J Neuroradiol* 2007; **34**: 183-189 [PMID: 17568674 DOI: 10.1016/j.neurad.2007.04.002]
18 **Faheem MH**, Shady S, Refaat MM. Role of magnetic resonance imaging (MRI) including diffusion weighted images (DWIs) in assessment of parotid gland masses with histopathological correlation. *Egypt J Radiol Nucl Med* 2018; **49**: 368-373 [DOI: 10.1016/j.ejrnm.2018.03.001]
19 **Habermann CR**, Gossrau P, Graessner J, Arndt C, Cramer MC, Reitmeier F, Jaehne M, Adam G. Diffusion-weighted echo-planar MRI: a valuable tool for differentiating primary parotid gland tumors? *Rofo* 2005; **177**: 940-945 [PMID: 15973595 DOI: 10.1055/s-2005-858297]
20 **Takumi K**, Fukukura Y, Hakamada H, Ideue J, Kumagae Y, Yoshiura T. Value of diffusion tensor imaging in differentiating malignant from benign parotid gland tumors. *Eur J Radiol* 2017; **95**: 249-256 [PMID: 28987676 DOI: 10.1016/j.ejrad.2017.08.013]
21 **Matsusue E**, Fujihara Y, Matsuda E, Tokuyasu Y, Nakamoto S, Nakamura K, Ogawa T. Differentiating parotid tumors by quantitative signal intensity evaluation on MR imaging. *Clin Imaging* 2017; **46**: 37-43 [PMID: 28704680 DOI: 10.1016/j.clinimag.2017.06.009]
22 **Ogawa T**, Kojima I, Ishii R, Sakamoto M, Murata T, Suzuki T, Kato K, Nakanome A, Ohkoshi A, Ishida E, Kakehata S, Shiga K, Katori Y. Clinical utility of dynamic-enhanced MRI in salivary gland tumors: retrospective study and literature review. *Eur Arch Otorhinolaryngol* 2018; **275**: 1613-1621 [PMID: 29623392 DOI: 10.1007/s00405-018-4965-9]
23 **Tsushima Y**, Matsumoto M, Endo K. Parotid and parapharyngeal tumours: tissue characterization with dynamic magnetic resonance imaging. *Br J Radiol* 1994; **67**: 342-345 [PMID: 8173873 DOI: 10.1259/0007-1285-67-796-342]
24 **Yabuuchi H**, Fukuya T, Tajima T, Hachitanda Y, Tomita K, Koga M. Salivary gland tumors: diagnostic value of gadolinium-enhanced dynamic MR imaging with histopathologic correlation. *Radiology* 2003; **226**: 345-354 [PMID: 12563124 DOI: 10.1148/radiol.2262011486]
25 **Hisatomi M**, Asaumi J, Yanagi Y, Unetsubo T, Maki Y, Murakami J, Matsuzaki H, Honda Y, Konouchi H. Diagnostic value of dynamic contrast-enhanced MRI in the salivary gland tumors. *Oral Oncol* 2007; **43**: 940-947 [PMID: 17257881 DOI: 10.1016/j.oraloncology.2006.11.009]
26 **Sumi M**, Nakamura T. Head and neck tumours: combined MRI assessment based on IVIM and TIC analyses for the differentiation of tumors of different histological types. *Eur Radiol* 2014; **24**: 223-231 [PMID: 24013848 DOI: 10.1007/s00330-013-3002-z]

27 **Lam PD**, Kuribayashi A, Imaizumi A, Sakamoto J, Sumi Y, Yoshino N, Kurabayashi T. Differentiating benign and malignant salivary gland tumours: diagnostic criteria and the accuracy of dynamic contrast-enhanced MRI with high temporal resolution. *Br J Radiol* 2015; **88**: 20140685 [PMID: 25791568 DOI: 10.1259/bjr.20140685]

28 **Eida S**, Ohki M, Sumi M, Yamada T, Nakamura T. MR factor analysis: improved technology for the assessment of 2D dynamic structures of benign and malignant salivary gland tumors. *J Magn Reson Imaging* 2008; **27**: 1256-1262 [PMID: 18504743 DOI: 10.1002/jmri.21349]

29 **Xu Z**, Zheng S, Pan A, Cheng X, Gao M. A multiparametric analysis based on DCE-MRI to improve the accuracy of parotid tumor discrimination. *Eur J Nucl Med Mol Imaging* 2019; **46**: 2228-2234 [PMID: 31372671 DOI: 10.1007/s00259-019-04447-9]

30 **Huang N**, Xiao Z, Chen Y, She D, Guo W, Yang X, Chen Q, Cao D, Chen T. Quantitative dynamic contrast-enhanced MRI and readout segmentation of long variable echo-trains diffusion-weighted imaging in differentiating parotid gland tumors. *Neuroradiology* 2021; **63**: 1709-1719 [PMID: 34241661 DOI: 10.1007/s00234-021-02758-z]

31 **Yabuuchi H**, Kamitani T, Sagiyama K, Yamasaki Y, Hida T, Matsuura Y, Hino T, Murayama Y, Yasumatsu R, Yamamoto H. Characterization of parotid gland tumors: added value of permeability MR imaging to DWI and DCE-MRI. *Eur Radiol* 2020; **30**: 6402-6412 [PMID: 32613285 DOI: 10.1007/s00330-020-07004-3]

32 **Park SY**, Kim HJ, Cha W. Comparative Study of Dynamic Susceptibility Contrast Perfusion MR Images between Warthin's Tumor and Malignant Parotid Tumors. *Kosin Med J* 2019; **34**: 38 [DOI: 10.7180/kmj.2019.34.1.38]

33 **Abdel Razek AAK**, Mukherji SK. Imaging of Minor Salivary Glands. *Neuroimaging Clin N Am* 2018; **28**: 295-302 [PMID: 29622120 DOI: 10.1016/j.nic.2018.01.008]

34 **Fujima N**, Kudo K, Tsukahara A, Yoshida D, Sakashita T, Homma A, Tha KK, Shirato H. Measurement of tumor blood flow in head and neck squamous cell carcinoma by pseudo-continuous arterial spin labeling: comparison with dynamic contrast-enhanced MRI. *J Magn Reson Imaging* 2015; **41**: 983-991 [PMID: 25787123 DOI: 10.1002/jmri.24885]

35 **Razek AAKA**. Multi-parametric MR imaging using pseudo-continuous arterial-spin labeling and diffusion-weighted MR imaging in differentiating subtypes of parotid tumors. *Magn Reson Imaging* 2019; **63**: 55-59 [PMID: 31422165 DOI: 10.1016/j.mri.2019.08.005]

36 **Rosenkrantz AB**, Padhani AR, Chenevert TL, Koh DM, De Keyzer F, Taouli B, Le Bihan D. Body diffusion kurtosis imaging: Basic principles, applications, and considerations for clinical practice. *J Magn Reson Imaging* 2015; **42**: 1190-1202 [PMID: 26119267 DOI: 10.1002/jmri.24985]

37 **Qian W**, Xu XQ, Zhu LN, Ma G, Su GY, Bu SS, Wu FY. Preliminary study of using diffusion kurtosis imaging for characterizing parotid gland tumors. *Acta Radiol* 2019; **60**: 887-894 [PMID: 30259752 DOI: 10.1177/0284185118803784]

38 **Abdel Razek AA**, Poptani H. MR spectroscopy of head and neck cancer. *Eur J Radiol* 2013; **82**: 982-989 [PMID: 23485098 DOI: 10.1016/j.ejrad.2013.01.025]

39 **King AD**, Yeung DK, Ahuja AT, Tse GM, Yuen HY, Wong KT, van Hasselt AC. Salivary gland tumors at *in vivo* proton MR spectroscopy. *Radiology* 2005; **237**: 563-569 [PMID: 16244265 DOI: 10.1148/radiol.2372041309]

40 **El-Naggar AK**, Chan JKC, Grandis JR, Takata T, Slootweg PJ. WHO classification of head and neck tumours. 4th ed. Lyon: International Agency for Research on Cancer, 2017: 159-201

41 **Speight PM**, Barrett AW. Salivary gland tumours: diagnostic challenges and an update on the latest WHO classification. *Diagn Histopathol* 2020; **26**: 147-158 [DOI: 10.1016/j.mpdhp.2020.01.001]

42 **Speight PM**, Barrett AW. Salivary gland tumours. *Oral Dis* 2002; **8**: 229-240 [PMID: 12363107 DOI: 10.1034/j.1601-0825.2002.02870.x]

43 **Branstetter BF**. Benign tumors. Parotid space. In: Hansberger HR. Diagnostic Imaging: Head and Neck. 2nd ed. Canada: Amirsys, 2011; 5: 5-28

44 **Kato H**, Kawaguchi M, Ando T, Mizuta K, Aoki M, Matsuo M. Pleomorphic adenoma of salivary glands: common and uncommon CT and MR imaging features. *Jpn J Radiol* 2018; **36**: 463-471 [PMID: 29845358 DOI: 10.1007/s11604-018-0747-y]

45 **Ito FA**, Jorge J, Vargas PA, Lopes MA. Histopathological findings of pleomorphic adenomas of the salivary glands. *Med Oral Patol Oral Cir Bucal* 2009; **14**: E57-E61 [PMID: 19179950]

46 **Kessler AT**, Bhatt AA. Review of the Major and Minor Salivary Glands, Part 2: Neoplasms and Tumor-like Lesions. *J Clin Imaging Sci* 2018; **8**: 48 [PMID: 30546932 DOI: 10.4103/jcis.JCIS_46_18]

47 **Tsushima Y**, Matsumoto M, Endo K, Aihara T, Nakajima T. Characteristic bright signal of parotid pleomorphic adenomas on T2-weighted MR images with pathological correlation. *Clin Radiol* 1994; **49**: 485-489 [PMID: 8088045 DOI: 10.1016/s0009-9260(05)81748-9]

48 **Ginat DT**. Imaging of Benign Neoplastic and Nonneoplastic Salivary Gland Tumors. *Neuroimaging Clin N Am* 2018; **28**: 159-169 [PMID: 29622111 DOI: 10.1016/j.nic.2018.01.002]

49 **Zaghi S**, Hendizadeh L, Hung T, Farahvar S, Abemayor E, Sepahdari AR. MRI criteria for the diagnosis of pleomorphic adenoma: a validation study. *Am J Otolaryngol* 2014; **35**: 713-718 [PMID: 25128908 DOI: 10.1016/j.amjoto.2014.07.013]

50 **Kato H**, Kanematsu M, Watanabe H, Mizuta K, Aoki M. Salivary gland tumors of the parotid gland: CT and MR imaging findings with emphasis on intratumoral cystic components. *Neuroradiology* 2014; **56**: 789-795 [PMID: 24948426 DOI: 10.1007/s00234-014-1386-3]

51 **Mukai H**, Motoori K, Horikoshi T, Takishima H, Nagai Y, Okamoto Y, Uno T. Basal cell adenoma of the parotid gland; MR features and differentiation from pleomorphic adenoma. *Dentomaxillofac Radiol* 2016; **45**: 20150322 [PMID: 26837669 DOI: 10.1259/dmfr.20150322]

52 **Zheng N**, Li R, Liu W, Shao S, Jiang S. The diagnostic value of combining conventional, diffusion-weighted imaging and dynamic contrast-enhanced MRI for salivary gland tumors. *Br J Radiol* 2018; **91**: 20170707 [PMID: 29902075 DOI: 10.1259/bjr.20170707]

53 **Khamis MEM**, Ahmed AF, Ismail EI, Bayomy MF, El-Anwarc MW. The diagnostic efficacy of apparent diffusion coefficient value and Choline/Creatine ratio in differentiation between parotid gland tumors. *Egypt J Radiol Nucl Med* 2018; **49**: 358-367 [DOI: 10.1016/j.ejrnm.2018.02.004]

54 **Espinoza S**, Halimi P. Interpretation pearls for MR imaging of parotid gland tumor. *Eur Ann Otorhinolaryngol Head Neck*

Dis 2013; **130**: 30-35 [PMID: 22819222 DOI: 10.1016/j.anorl.2011.12.006]
55 **Hisatomi M**, Asaumi J, Yanagi Y, Konouchi H, Matsuzaki H, Honda Y, Kishi K. Assessment of pleomorphic adenomas using MRI and dynamic contrast enhanced MRI. *Oral Oncol* 2003; **39**: 574-579 [PMID: 12798400 DOI: 10.1016/s1368-8375(03)00040-x]
56 **Kato H**, Fujimoto K, Matsuo M, Mizuta K, Aoki M. Usefulness of diffusion-weighted MR imaging for differentiating between Warthin's tumor and oncocytoma of the parotid gland. *Jpn J Radiol* 2017; **35**: 78-85 [PMID: 28074380 DOI: 10.1007/s11604-016-0608-5]
57 **Ikeda M**, Motoori K, Hanazawa T, Nagai Y, Yamamoto S, Ueda T, Funatsu H, Ito H. Warthin tumor of the parotid gland: diagnostic value of MR imaging with histopathologic correlation. *AJNR Am J Neuroradiol* 2004; **25**: 1256-1262 [PMID: 15313720]
58 **Minami M**, Tanioka H, Oyama K, Itai Y, Eguchi M, Yoshikawa K, Murakami T, Sasaki Y. Warthin tumor of the parotid gland: MR-pathologic correlation. *AJNR Am J Neuroradiol* 1993; **14**: 209-214 [PMID: 8427092]
59 **Ding J**, Wang W, Peng W, Zhou X, Chen T. MRI and CT imaging characteristics of myoepithelioma of the parotid gland. *Acta Radiol* 2016; **57**: 837-843 [PMID: 26508793 DOI: 10.1177/0284185115609364]
60 **Sepúlveda I**, Platín E, Spencer ML, Mucientes P, Frelinghuysen M, Ortega P, Ulloa D. Oncocytoma of the parotid gland: a case report and review of the literature. *Case Rep Oncol* 2014; **7**: 109-116 [PMID: 24707257 DOI: 10.1159/000359998]
61 **Hisatomi M**, Asaumi J, Konouchi H, Yanagi Y, Matsuzaki H, Kishi K. Assessment of dynamic MRI of Warthin's tumors arising as multiple lesions in the parotid glands. *Oral Oncol* 2002; **38**: 369-372 [PMID: 12076701 DOI: 10.1016/s1368-8375(01)00073-2]
62 **Sakai E**, Yoda T, Shimamoto H, Hirano Y, Kusama M, Enomoto S. Pathologic and imaging findings of an oncocytoma in the deep lobe of the left parotid gland. *Int J Oral Maxillofac Surg* 2003; **32**: 563-565 [PMID: 14759120]
63 **Iida E**, Wiggins RH 3rd, Anzai Y. Bilateral parotid oncocytoma with spontaneous intratumoral hemorrhage: a rare hypervascular parotid tumor with ASL perfusion. *Clin Imaging* 2016; **40**: 357-360 [PMID: 27133667 DOI: 10.1016/j.clinimag.2016.02.003]
64 **Weitzel M**, Cohn JE, Spector H. Myoepithelioma of the Parotid Gland: A Case Report with Review of the Literature and Classic Histopathology. *Case Rep Otolaryngol* 2017; **2017**: 6036179 [PMID: 28900549 DOI: 10.1155/2017/6036179]
65 **Shimizu K**, Iwai H, Ikeda K, Sakaida N, Sawada S. Intraparotid facial nerve schwannoma: a report of five cases and an analysis of MR imaging results. *AJNR Am J Neuroradiol* 2005; **26**: 1328-1330 [PMID: 15956491]
66 **Chikui T**, Yonetsu K, Yoshiura K, Miwa K, Kanda S, Ozeki S, Shinohara M. Imaging findings of lipomas in the orofacial region with CT, US, and MRI. *Oral Surg Oral Med Oral Pathol Oral Radiol Endod* 1997; **84**: 88-95 [PMID: 9247958 DOI: 10.1016/s1079-2104(97)90302-4]
67 **Agaimy A**, Ihrler S, Märkl B, Lell M, Zenk J, Hartmann A, Michal M, Skalova A. Lipomatous salivary gland tumors: a series of 31 cases spanning their morphologic spectrum with emphasis on sialolipoma and oncocytic lipoadenoma. *Am J Surg Pathol* 2013; **37**: 128-137 [PMID: 23232852 DOI: 10.1097/PAS.0b013e31826731e0]
68 **Lara-Sánchez H**, Peral-Cagigal B, Madrigal-Rubiales B, Verrier-Hernández A. Cavernous hemangioma of the parotid gland in adults. *J Clin Exp Dent* 2014; **6**: e592-e594 [PMID: 25674332 DOI: 10.4317/jced.51750]
69 **Salama AA**, El-Barbary AH, Mlees MA, Esheba GES. Value of apparent diffusion coefficient and magnetic resonance spectroscopy in the identification of various pathological subtypes of parotid gland tumors. *Egypt J Radiol Nucl Med* 2015; **46**: 45-52 [DOI: 10.1016/j.ejrnm.2014.09.005]
70 **Kashiwagi N**, Nakatsuka SI, Murakami T, Enoki E, Yamamoto K, Nakanishi K, Chikugo T, Kurisu Y, Kimura M, Hyodo T, Tsukabe A, Kakigi T, Tomita Y, Ishii K, Narumi Y, Yagyu Y, Tomiyama N. MR imaging features of mammary analogue secretory carcinoma and acinic cell carcinoma of the salivary gland: a preliminary report. *Dentomaxillofac Radiol* 2018; **47**: 20170218 [PMID: 29493279 DOI: 10.1259/dmfr.20170218]
71 **Skálová A**, Vanecek T, Sima R, Laco J, Weinreb I, Perez-Ordonez B, Starek I, Geierova M, Simpson RH, Passador-Santos F, Ryska A, Leivo I, Kinkor Z, Michal M. Mammary analogue secretory carcinoma of salivary glands, containing the ETV6-NTRK3 fusion gene: a hitherto undescribed salivary gland tumor entity. *Am J Surg Pathol* 2010; **34**: 599-608 [PMID: 20410810 DOI: 10.1097/PAS.0b013e3181d9efcc]
72 **Kurokawa R**, Kurokawa M, Baba A, Ota Y, Moritani T, Srinivasan A. Radiological features of head and neck mammary analogue secretory carcinoma: 11 new cases with a systematic review of 29 cases reported in 28 publications. *Neuroradiology* 2021; **63**: 1901-1911 [PMID: 34427706 DOI: 10.1007/s00234-021-02796-7]
73 **Khalele BA**. Systematic review of mammary analog secretory carcinoma of salivary glands at 7 years after description. *Head Neck* 2017; **39**: 1243-1248 [PMID: 28370824 DOI: 10.1002/hed.24755]
74 **Kashiwagi N**, Murakami T, Chikugo T, Tomita Y, Kawano K, Nakanishi K, Mori K, Tomiyama N. Carcinoma ex pleomorphic adenoma of the parotid gland. *Acta Radiol* 2012; **53**: 303-306 [PMID: 22287150 DOI: 10.1258/ar.2011.110389]
75 **Shum JW**, Emmerling M, Lubek JE, Ord RA. Parotid lymphoma: a review of clinical presentation and management. *Oral Surg Oral Med Oral Pathol Oral Radiol* 2014; **118**: e1-e5 [PMID: 24405648 DOI: 10.1016/j.oooo.2013.10.013]
76 **Wang J**, Takashima S, Takayama F, Kawakami S, Saito A, Matsushita T, Momose M, Ishiyama T. Head and neck lesions: characterization with diffusion-weighted echo-planar MR imaging. *Radiology* 2001; **220**: 621-630 [PMID: 11526259 DOI: 10.1148/radiol.2202010063]
77 **Asaumi J**, Yanagi Y, Hisatomi M, Matsuzaki H, Konouchi H, Kishi K. The value of dynamic contrast-enhanced MRI in diagnosis of malignant lymphoma of the head and neck. *Eur J Radiol* 2003; **48**: 183-187 [PMID: 14680911 DOI: 10.1016/S0720-048x(02)00347-9]
78 **Andreasen S**, Kiss K, Mikkelsen LH, Channir HI, Plaschke CC, Melchior LC, Eriksen JG, Wessel I. An update on head and neck cancer: new entities and their histopathology, molecular background, treatment, and outcome. *APMIS* 2019; **127**: 240-264 [PMID: 30811708 DOI: 10.1111/apm.12901]
79 **Motoori K**, Iida Y, Nagai Y, Yamamoto S, Ueda T, Funatsu H, Ito H, Yoshitaka O. MR imaging of salivary duct carcinoma. *AJNR Am J Neuroradiol* 2005; **26**: 1201-1206 [PMID: 15891184]
80 **Suto T**, Kato H, Kawaguchi M, Kobayashi K, Miyazaki T, Ando T, Noda Y, Hyodo F, Matsuo M, Ishihara H, Ogawa T.

MRI findings of epithelial-myoepithelial carcinoma of the parotid gland with radiologic-pathologic correlation. *Jpn J Radiol* 2022; **40**: 578-585 [PMID: 34982376 DOI: 10.1007/s11604-021-01243-0]

81 **Wang H**, Hoda RS, Faquin W, Rossi ED, Hotchandani N, Sun T, Pusztaszeri M, Bizzarro T, Bongiovanni M, Patel V, Jhala N, Fadda G, Gong Y. FNA biopsy of secondary nonlymphomatous malignancies in salivary glands: A multi-institutional study of 184 cases. *Cancer Cytopathol* 2017; **125**: 91-103 [PMID: 28001329 DOI: 10.1002/cncy.21798]

82 **Horáková M**, Porre S, Tommola S, Baněčková M, Skálová A, Kholová I. FNA diagnostics of secondary malignancies in the salivary gland: Bi-institutional experience of 36 cases. *Diagn Cytopathol* 2021; **49**: 241-251 [PMID: 33017519 DOI: 10.1002/dc.24629]

83 **Mikaszewski B**, Markiet K, Smugała A, Stodulski D, Szurowska E, Stankiewicz C. Diffusion- and Perfusion-Weighted Magnetic Resonance Imaging-An Alternative to Fine Needle Biopsy or Only an Adjunct Test in Preoperative Differential Diagnostics of Malignant and Benign Parotid Tumors? *J Oral Maxillofac Surg* 2017; **75**: 2248-2253 [PMID: 28412261 DOI: 10.1016/j.joms.2017.03.018]

World Journal of Radiology

Submit a Manuscript: https://www.f6publishing.com

World J Radiol 2022 August 28; 14(8): 272-285

DOI: 10.4329/wjr.v14.i8.272

ISSN 1949-8470 (online)

MINIREVIEWS

Amebic liver abscess: Clinico-radiological findings and interventional management

Rajeev Nayan Priyadarshi, Ramesh Kumar, Utpal Anand

Specialty type: Radiology, nuclear medicine and medical imaging

Provenance and peer review: Invited article; Externally peer reviewed.

Peer-review model: Single blind

Peer-review report's scientific quality classification

Grade A (Excellent): A
Grade B (Very good): 0
Grade C (Good): C
Grade D (Fair): D, D
Grade E (Poor): 0

P-Reviewer: Cerwenka H, Austria; Parzen-Johnson S, United States; Shelat VG, Singapore

Received: February 28, 2022
Peer-review started: February 28, 2022
First decision: May 9, 2022
Revised: May 30, 2022
Accepted: June 20, 2022
Article in press: June 20, 2022
Published online: August 28, 2022

Rajeev Nayan Priyadarshi, Department of Radiodiagnosis, All India Institute of Medical Sciences, Patna, Patna 801507, Bihar, India

Ramesh Kumar, Department of Gastroenterology, All India Institute of Medical Sciences, Patna, Patna 801507, Bihar, India

Utpal Anand, Department of Surgical Gastroenterology, All India Institute of Medical Sciences, Patna, Patna 801507, Bihar, India

Corresponding author: Ramesh Kumar, MD, Associate Professor, Department of Gastroenterology, All India Institute of Medical Sciences, Patna, Phulwari Sharif, Patna 801507, Bihar, India. docrameshkr@gmail.com

Abstract

In its classic form, amebic liver abscess (ALA) is a mild disease, which responds dramatically to antibiotics and rarely requires drainage. However, the two other forms of the disease, *i.e.*, acute aggressive and chronic indolent usually require drainage. These forms of ALA are frequently reported in endemic areas. The acute aggressive disease is particularly associated with serious complications, such as ruptures, secondary infections, and biliary communications. Laboratory parameters are deranged, with signs of organ failure often present. This form of disease is also associated with a high mortality rate, and early drainage is often required to control the disease severity. In the chronic form, the disease is characterized by low-grade symptoms, mainly pain in the right upper quadrant. Ultrasound and computed tomography (CT) play an important role not only in the diagnosis but also in the assessment of disease severity and identification of the associated complications. Recently, it has been shown that CT imaging morphology can be classified into three patterns, which seem to correlate with the clinical subtypes. Each pattern depicts its own set of distinctive imaging features. In this review, we briefly outline the clinical and imaging features of the three distinct forms of ALA, and discuss the role of percutaneous drainage in the management of ALA.

Key Words: Amebic liver abscess; Complicated liver abscess; Refractory liver abscess; Ruptured amebic liver abscess; Pleuropulmonary complication; Biliary communication; Needle aspiration; Catheter drainage

Core Tip: The clinical presentation and imaging findings of amebic liver abscess (ALA) can be classified into three forms: subacute mild, acute aggressive and chronic indolent. The latter two forms are particularly associated with most complications of ALA. Despite this, prior literature primarily focused on the mild form of the disease, which responds well to antibiotics. To the best of our knowledge, there is no research on the types of ALA. In this review, the distinct clinical and imaging characteristics of each type are discussed in detail. With this understanding, the therapeutic strategy, medical or interventional, can be employed more efficiently for patients with ALA.

Citation: Priyadarshi RN, Kumar R, Anand U. Amebic liver abscess: Clinico-radiological findings and interventional management. *World J Radiol* 2022; 14(8): 272-285
URL: https://www.wjgnet.com/1949-8470/full/v14/i8/272.htm
DOI: https://dx.doi.org/10.4329/wjr.v14.i8.272

INTRODUCTION

Amebic liver abscess (ALA) is an infection caused by the protozoan *Entamoeba histolytica* (EH), an intestinal parasite. The infection is acquired by ingestion of water or food contaminated by EH cysts (the infective stage of the parasite). The cysts resist gastric juice and reach the distal ileum, where they undergo excystation producing trophozoites (the feeding stage of the parasite). In > 90% patients, the trophozoites feed on intestinal tissue and bacteria without producing symptoms. In less than 1% of cases, however, the trophozoites penetrate the mucosa and, through the portal route, reach the liver causing liver abscess[1]. ALA is the most common and has the highest mortality of amebiasis manifestations. It continues to remain the most common cause of liver abscess in developing and underdeveloped countries[2-6].

ALA was known as a progressive and deadly disease a century ago; however, since the introduction of modern antibiotics, the mortality has drastically reduced to between 1% and 3%[7]. Metronidazole is the most effective agent, with cure rates of approximately 90%. Most patients become asymptomatic within 72 to 96 h of treatment, and drainage adds no benefit to uncomplicated cases[7,8]. This fact seems to be more relevant for a typical case where the patient presents the classic and the most common form of the disease, *i.e.*, subacute mild disease. Reports from endemic areas have shown that a greater percentage of cases require drainage through either a needle or catheter. The reported prevalence of such cases varies from 44% to 80%[3-5,7,9-14]. A thorough literature search shows that two distinct clinical settings usually require drainage. In the first, the patients present acutely with severe and fulminant disease, and drainage is performed to control disease progression and prevent organ failure. Such abscesses, by different authors, have been denoted by different terms that indicate the aggressive nature of the disease, such as "acute aggressive ALA", "severe ALA" or "fulminant ALA"[10,15-17]. In the second clinical setting of the disease, the patients present late with mild symptoms, usually tenderness; they usually have a large persistent abscess despite medical therapy. Various terms are used to describe such abscesses, such as "drug-resistant ALA", "refractory ALA" or "chronic indolent ALA" [18-22]. Regardless of the presentations, most cases are usually associated with a few complications, such as rupture, secondary infection or biliary communication. Considering this fact, a few authors prefer referring to it as "complicated ALA"[13,14]. Therefore, ALA can be classified into three clinical subtypes: subacute mild, acute aggressive and chronic indolent. Not only do the ALAs have varied clinical presentations, but they are also associated with distinct imaging patterns[10].

This review describes the three major types of clinical presentations as well as three types of imaging patterns (correlating with clinical subtypes). Special emphasis has been placed on the two clinical types — acute aggressive and chronic indolent. This paper also discusses the complications of ALA and their percutaneous management.

OVERVIEW OF EPIDEMIOLOGY, RISK FACTORS AND PATHOGENESIS OF COMPLICATED ALA

Epidemiology

Although ALA occurs globally, most reports emerge from endemic countries, such as India, Sri Lanka, Bangladesh, Mexico, East and South Africa or parts of Central and South America[23]. A high endemicity in these countries is related to poor hygiene and sanitation since the parasite is transmitted *via* the fecal-oral route. Even in endemic countries, ALA occurs primarily in rural areas where defecation in the open air is a common practice[11,24-26]. The lack of adequate sewage disposal results in contamination of drinking water with EH cysts. Using polymerase chain reaction (PCR), a

population-based study from India detected the prevalence of EH in 14% of stool samples[27]. In developed countries, ALA occurs mostly in travelers or immigrants from endemic areas[28]. Apart from endemicity, several other epidemiological factors also increase the risk of developing complicated disease.

Risk factors

The disease is found almost exclusively in men (male: female > 10:1)[11]. The reason for this is unknown but several investigators have speculated that it might be related to alcohol, particularly those prepared locally from the sap of palm trees (toddy)[11,24,25,29]. Not only is the toddy a risk factor for ALA, but in many studies it has been linked to severe disease[13,30]. The exact mechanism by which it contributes to the pathogenesis of ALA is unclear. It has been proposed that alcohol may alter the gut mucosa or convert the pathogen to a more virulent strain or render the liver more susceptible to the infection[23,24,29]. Most cases occur in middle age ranging from 20 to 50 years[30]. In older patients, the disease tends to be more severe possibly due to their poor immunity, whereas it is rare in children[31]. Another factor contributing to the pathogenesis of ALA is malnutrition[11,13,23]. For centuries, the disease has been a symbol of poverty. A typical patient with ALA, as we have observed, is a thin emaciated villager of low socioeconomic status. Their poor nutritional status is evidenced by low albumin, BMI and hemoglobin [11]. ALA has also been shown to be severe in diabetic patients[16,32].

Pathogenesis

The term "amebic liver abscess" is a misnomer as the cavity formation or liquefaction is not due to suppuration; rather, it is the result of a unique type of necrosis[33,34]. The necrotic area appears as if it has been dissolved by chemical or toxin. Considering this morphological pattern, it was believed that the parasite possesses a toxin that lyses the hepatocytes, and therefore the parasite was named "histolytica"[35]. It is now known that several proteolytic enzymes released by the inflammatory cells are responsible for tissue destruction[7,36,37].

Understanding the gross morphology is important because it is characteristic and, to a large extent, can be extrapolated to imaging findings[35,38,39]. The gross appearance varies depending on the severity and the duration of the disease. In the early stage, it is that of a necrotic area where the center has liquefied necrotic tissue (chocolate-colored sterile "pus"); however, the periphery has more solid tissue[10,35,38-40]. The peripheral solid and partially liquified tissue is responsible for the shaggy or ragged appearance on the abscess wall[10,40]. A mature wall is absent and the tissue surrounding the abscess is congested, compressed and edematous[41]. There may be pressure over the surrounding liver parenchyma or the hepatic capsule. Venous thrombosis and ischemic infarction are commonly observed in fatal cases[42]. As the abscess heals, a fibrous wall forms and the cavity becomes more sharply defined[38,43]. The edema and congestion regress and the abscess wall is surrounded only by a thin rim of edema. The peripheral solid tissue becomes more liquefied, the content is gradually resorbed, and the lesion heals completely without scar. However, a complicated or a very large abscess can persist in the form of a residual abscess with a thick fibrous wall. A mature wall, as opposed to the ragged wall, indicates chronicity or secondary infection[42].

ALA is usually solitary, located in the right lobe of the liver. The size varies from a few centimeters to 20 cm[35]. However, the risk of complications increases with the number and size. In autopsy series, unlike successfully treated series, 60% of cases show multiple abscesses varying in size from 10 to 15 cm [35]. Literature shows a higher incidence of large (> 5 to 10 cm) and multiple abscesses (occurring in about 50% of cases) among the Southeast Asian population compared to other studied populations[8-11,43-47].

CLINICAL PRESENTATION

The clinical presentation varies from mild to severe. Based on the duration and the severity, ALA can be classified into three main types: subacute mild, acute aggressive, and chronic indolent[10,15,23,28,48].

Subacute mild ALA

Most patients (approximately 80%) have a subacute course characterized by mild symptoms that develop in less than 2 to 4 wk[23,28,30,49-51]. The disease typically begins with fever and chills, right upper quadrant pain and tender hepatomegaly. Other symptoms include anorexia, weakness, nausea and diarrhea. There may be right shoulder pain when an abscess located in the posterosuperior segments irritates the diaphragm. The typical finding on physical examination is point tenderness in the intercostal spaces[31]. The disease is associated with no or minimal organ dysfunction; the laboratory parameters are near normal except mild to moderate leukocytosis. Dramatic improvement is observed after medical therapy and no further complications occur. This pattern of presentation has also been referred to as "acute benign ALA" by a few authors; however, the term "subacute mild" may be preferable as it correctly defines the clinical course of the disease[15,48]. Additionally, the term also differentiates it from the two other forms of the disease, *i.e.*, acute aggressive ALA and chronic indolent

ALA.

Acute aggressive ALA

Acute aggressive ALA is characterized by a more severe and rapidly progressive course. Considering the acuteness and severity of this form, Katzenstein *et al*[15] named it "acute aggressive ALA". The prevalence of this type of ALA may be high in endemic areas[10]. In a study of 317 patients with ALA, Balasegaram reported acute fulminating infection in 13% of cases[17]. The patients often present more acutely (< 10 d) with signs of severe disease including systemic toxicity, high fevers and chills, and an exquisitely tender hepatomegaly[15]. Signs related to rupture and other complications may be present. In fact, rupture is a common presenting manifestation of aggressive ALA, occurring in up to 57% of patients[10]. The patients with free intraperitoneal rupture often have features of generalized peritonitis. Sepsis-like features can occur in more severely affected patients. Up to 90% of patients require hospitalization and about 13% require intensive care unit management[10]. Signs of organ dysfunction, such as jaundice, may also be observed in most patients[9,12,32]. Renal dysfunction can occur in 5% to 12% of cases[6,10]. Hepatic failure and encephalopathy may also occur. Approximately, one-third to one-half of the patients will have gross fluid derangements including ascites, pleural effusion and edema[5,9,10,13,52]. Patients with aggressive ALA are often misdiagnosed as having acute cholecystitis, appendicitis or bowel perforation[30,53-55].

Most patients with aggressive ALA will have markedly deranged laboratory parameters, such as severe leukocytosis, hyperbilirubinemia, hypoalbuminemia, elevated liver enzymes, and elevated alkaline phosphatase[10]. A high mortality has been recorded in this group of patients. Most deaths are usually related to intraperitoneal rupture, which is followed by sepsis and multiorgan failure. Many findings of aggressive disease have been identified as poor prognostic markers in different studies, such as multiple abscesses, large (> 500 cc) volume abscesses, presence of encephalopathy, hypoalbuminemia, and hyperbilirubinemia (> 3.5 mg/dL)[3,9,13,32]. Medical therapy alone is often suboptimal to control the disease and the laboratory tests do not return to near normal following treatment. Therefore, drainage with either a needle or catheter is usually required[10,15].

Chronic indolent ALA

Chronic presentation can occur in approximately 10 to 20% of cases[10,15,23,49,56,57]. This presentation has been designated in most studies as "chronic indolent ALA". In this form, patients present late with mild symptoms for more than four weeks. Most patients complain of pain over the right lower chest or upper abdomen. Fever is usually absent or of low grade. However, a history of fever with chills at the onset of the disease may be obtained in most cases. Additionally, many patients will have a history of prior medical treatment or sometimes prior needle aspirations. On examination, right upper quadrant tenderness is usually present. Other low-grade symptoms include weight loss, anorexia, or malaise[10,15]. Laboratory tests are usually normal except elevated alkaline phosphatase level and low serum albumin. Leukocytosis in chronic abscesses suggests the presence of secondary infection, which is the most common complication in this form of the disease. In contrast to acute aggressive ALA, chronic ALA is rarely associated with intraperitoneal rupture.

LABORATORY EVALUATION

The diagnosis of ALA is based on recognition of the typical clinical features, imaging studies and serological tests. Serological tests are considered confirmatory (sensitivity > 94%; specificity > 95%)[7]. However, their usefulness in the diagnosis of acute ALA is limited in endemic areas because the tests remain positive for several months to years after resolution of infection. Moreover, the serological tests may be negative in the first seven to ten days of the infection, limiting their diagnostic use for acute ALA[7].

Routine laboratory tests in ALA are nonspecific and do not differ from those in pyogenic abscess[58,59]. However, these tests are useful in assessing the severity and monitoring the treatment response. In most patients with acute benign ALA, mild to moderate leukocytosis is found with an average WBC count of 16000/μL. However, a high WBC count above 20000/μL should suggest either aggressive, or secondarily infected abscesses[9,56,60]. In our series, a mean of 24000/μL was found in patients with aggressive abscesses. Serum bilirubin and liver enzyme (AST/ALT) levels are normal or minimally elevated in mild cases. When elevated, the AST/ALT levels return to normal following medical therapy. However, the alkaline phosphatase level is elevated in 70 to 80% of cases, regardless of the severity of the disease and the duration of presentation[56,60]. A very high value of bilirubin (> 3.5 mg/dL) and liver enzymes indicates complications or aggressive disease. A low serum albumin (< 2 g/dL) is found in almost all patients; however, an exceedingly low value is a poor prognostic marker[34]. Inflammatory biomarkers, such as C-reactive protein and procalcitonin have been found to be nonspecifically raised in most patients with ALA[34,59,61].

IMAGING EVALUATION: IMAGING CLASSIFICATION AND CLINICORADIOLOGICAL CORRELATION

Chest radiographs, ultrasound, computed tomography (CT), and magnetic resonance imaging (MRI) are the most employed modalities for diagnosis of ALA. Radiographs are insensitive, non-specific and are abnormal in only half of cases[23]. They can reveal elevated diaphragm, pleural effusion and basal consolidation or atelectasis. MRI seems to offer no advantage over CT[33,62]. Of all radiological tests, ultrasound and CT are the most employed tools; in fact, they are complementary to one another in many ways. For example, ultrasound can detect the degrees of liquefaction, differentiating solid necrotic tissue from more liquefied tissue; this information is not provided by CT. Ultrasound, however, can fail to detect an early abscess when the lesion is not liquid enough to be visible[63]. CT is more sensitive in this regard. Another concern with ultrasound may be that early aggressive abscesses might be mistaken for necrotic malignant masses because they often contain solid (non-liquefied) necrotic material[8,38,39,47]. Due to its ability to differentiate viable tissue from necrotic tissue, contrast-enhanced CT can distinguish between necrotic mass and aggressive abscesses. Additionally, CT is useful in the identification of various complications associated with ALA. Although both ultrasound and CT are highly sensitive (ultrasound, 85%-95%; CT, 100%)[64], their specificity is low for differentiating ALA from other infective abscesses or necrotic masses[45].

The imaging features of ALA on CT have been described as round oval hypodense lesions with a rim enhancing wall and on sonography as hypoechoic or anechoic lesions with internal echoes. This classic description of ALA, however, does not take into account the entire spectrum of the imaging findings, which are known to vary considerably. The varied morphology has largely been shown to reflect the underlying pathological changes, which occur as ALA evolves through the different phases of maturation. Acute abscesses consist mainly of solid necrotic tissue and their edges are irregular or ragged. As the abscesses heal, there is formation of a distinct wall, edges become smooth, and the contents become more liquefied[10,38,43]. This morphologic variation has prompted several investigators to classify the imaging features of ALA into distinct types[46,65,66]. Most investigators have classified ALA into three types based on sonographic appearance. In 1987, Léonetti *et al*[65] divided the sonographic morphology into three stages: pre-suppurative stage (phase I), suppurative stage (phase II), and scarring stage (phase III). Subsequently, N'Gbesso *et al*[66] proposed a similar sonographic classification: non-collected ALA (type I), collected ALA (type II), and healed ALA (type III).

On MRI, a variable degree of wall formation and edema surrounding ALA have been reported according to the status of abscess healing. Elizondo *et al*[43], who examined 29 ALAs with MRI, reported that untreated ALAs are associated with an incomplete ring (corresponding to incomplete wall) and diffuse or wedge-shaped perilesional edema. Following successful treatment, the ring formation is complete and the edema regresses to form concentric rings around the abscess. Matching with the MRI findings, a double-target sign has been described on contrast-enhanced CT; the inner ring corresponds to the enhancing wall and the outer ring to the perilesional edema[10,67].

Our recent experience suggests that the latest generation CT can effectively evaluate several imaging characteristics, such as wall formation, degree of liquefaction, enhancement patterns, septa, or perilesional hypodensity[10]. These characteristics can provide considerable information on the patient's clinical status. It appears that imaging findings of ALA can be classified into three distinct but overlapping patterns (type I, II and III) that correlate well with the clinical subtypes (Table 1)[10]. This classification may be useful for identifying those abscesses that would require more aggressive treatment.

Type I: ALA with ragged edges

Type I pattern is observed in patients with acute aggressive ALA. It is characterized by incomplete or absent walls and ragged edges (Figure 1A). This pattern is observed in patients with acute aggressive ALA. Type I pattern indicates an early and progressive abscess, with no sign of healing. Surrounding the abscess, there is a diffuse or wedge-shaped hypodensity, which is usually due to the combined effect of hypoperfusion and edema[10,68]. Most cases show irregular and interrupted enhancement at the edges. Multiple irregular septa may be observed at the periphery, indicating the viable parenchyma that is yet to be necrotic[10]. On sonography, they appear heterogeneous due to the presence of both solid and liquefied necrotic tissue[38,47]. The heterogeneity accounts for the frequent misdiagnosis of aggressive ALA as malignant lesions[10,38,47,67]. Other imaging features often associated with type I morphology are large size, multiplicity, and irregular shape (due to coalescence of multiple lesions)[10].

Type II: ALA with a complete rim enhancing wall

Type II pattern indicates subacute mild ALA. It is characterized by a well-defined enhancing wall (Figure 1B). The rim enhancement of the wall indicates active granulation tissue, a pathological sign of inflammation and beginning of healing[43]. A thin rim of edema surrounding the wall (in contrast to the more widespread edema of type I pattern) may be observed to form a perilesional "halo" on contrast CT. In many cases, a double-target sign (the inner ring of wall enhancement and outer ring of hypodense edema) is identified. The content is more liquefied and homogeneous compared to those

Table 1 Distinguishing clinical findings, imaging features and treatment strategy of the three forms of amebic liver abscesses

	Acute aggressive	Subacute mild	Chronic indolent
Presentation	Acute (< 10 d)	Subacute (< 2-4 wk)	Chronic (> 4 wk)
Symptoms	Severe symptoms (RUQ pain, fever, toxicity, abdominal distention, leg edema, shock-like syndrome resembling sepsis, jaundice, signs of intraperitoneal or intrathoracic rupture)	Moderate symptoms(usually intermittent fever and RUQ tenderness)	Mild (usually RUQ tenderness, fever if secondary infection)
Laboratory tests	Marked leukocytosis (> 20000/μL), abnormal LFT, features of organ failure (hyperbilirubinemia, renal dysfunction)	Transient leukocytosis and transient elevation of LFT (returns to normal after treatment)	Usually normal
Imaging features	Incomplete or absent wall, ragged edge, interrupted or no enhancement, septations, heterogeneous content, widespread or wedge-shaped perilesional hypodensity	Relatively smooth outline, rim-enhancing wall with perilesional hypodense "halo" (double-target sign)	Smooth outline, thick non-enhancing wall, faint or no perilesional "halo"
Size and number	> 5-10 cm, multiple in over 50% of cases	< 5-10 cm, usually single	> 5-10 cm, usually single
Treatment	Antibiotics; Early drainage is often required to control severity	Antibiotic alone suffices in most cases; rapid recovery, drainage when symptoms persist	Mostly pre-treated with antibiotics, drainage not required unless pressure symptoms or secondary infection present

RUQ: Right upper quadrant; LFT: Liver function test.

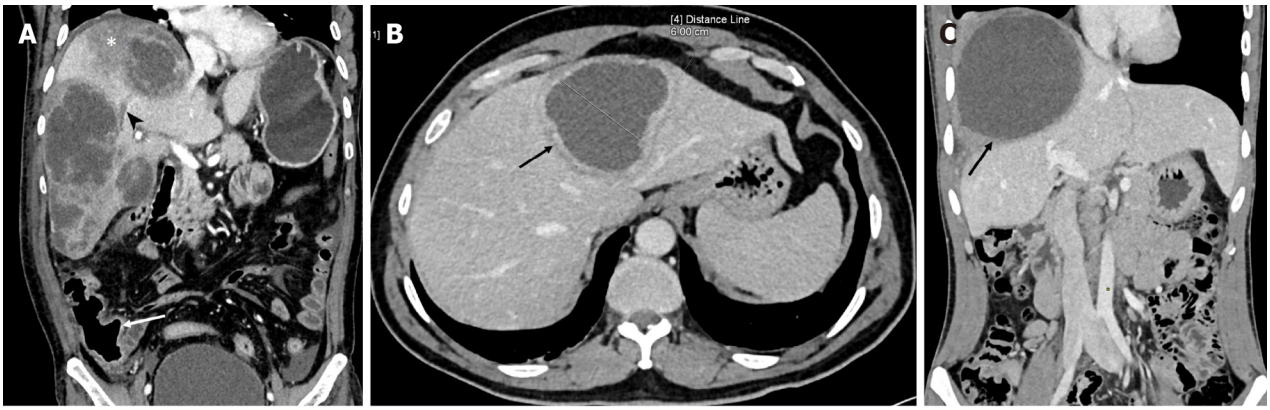

DOI: 10.4329/wjr.v14.i8.272 **Copyright** ©The Author(s) 2022.

Figure 1 Computed tomography images. A: Computed tomography (CT) (coronal image) demonstrating the characteristic imaging findings of an acute aggressive abscess (type I pattern) in a 60-year-old man who presented with sepsis-like features and markedly deranged laboratory parameters. There are multiple abscesses in the right lobe with irregular ragged edges, multiple septa and heterogeneous densities indicating partially liquefied tissue. Also, note the presence of a hypodense area in the surrounding parenchyma (asterisk) and right hepatic vein thrombosis (arrowhead). The thickened cecal wall (arrow) and mild ascites are also evident; B: CT of a typical case of subacute mild disease. The laboratory profile was near normal. The axial image shows an abscess in the left lobe with a well-defined wall showing rim enhancement (type II pattern). This patient presented with mild abdominal pain after 20 d of symptoms; C: CT image of a chronic indolent abscess (type III pattern). Coronal image of a 24-year-old man showing a large abscess with a thick non-enhancing wall in the right lobe. He had persistent pain in the right upper quadrant for two months despite complete resolution of fever and normalization of laboratory tests after metronidazole therapy.

presenting acutely. This pattern is nonspecific and resembles pyogenic abscesses[43,69,70].

Type III: ALA with a nonenhancing wall

Type III pattern represents chronic indolent ALA. It is characterized by a thick fibrotic wall that is much smoother and does not enhance with contrast (Figure 1C). The absence of contrast enhancement excludes active inflammation. This pattern, in fact, represents persistence of amebic pus (usually more than four weeks), in which the liver fails to clear the necrotic tissue. The abscesses in this form are usually asymptomatic; however, when they are large enough to cause capsular stretching, they can cause right upper quadrant pain. Clinicians should be aware that healed ALAs in this pattern often resemble cysts and can persist for months or years following successful treatment[46,66,71,72].

COMPLICATIONS: CLINICO-RADIOLOGICAL FINDINGS

Rupture

The most feared complication of ALA is rupture. The overall incidence ranges from 6 to 40%[10,44,52,73]. ALA generally ruptures into the thoracic cavity or intraperitoneal space. Occasionally, the abscess can rupture into hollow viscera, such as the stomach, duodenum, or colon[20,60,74,75]. Of all ruptures, the gravest, but fortunately rare, is rupture into the pericardium[49]. In our experience, the risk of free intraperitoneal ruptures is high when the abscesses present acutely (type I pattern). However, intrathoracic ruptures, particularly the intrapulmonary ones, are noted more frequently in chronic cases (type II or III pattern). This may be due to development of adhesion between the diaphragm and pleura in older abscesses[10].

Intrathoracic rupture: Pleural empyema, lung abscess, hepatobronchial fistula

Pleuropulmonary rupture occurs in 7% to 20% of patients[7,56,57]. The abscesses located inferior to the diaphragm can perforate it to enter the pleural space causing amebic empyema, which is the most common intrathoracic complication. It is important that pleural empyema be differentiated from sterile pleural effusion, which occurs more frequently than empyema. The sterile effusion is reactionary and resolves spontaneously, and therefore, it requires no drainage[57]. The presence of loculations and septations on ultrasound indicate amebic empyema[11]. The next intrathoracic complication is the development of lung consolidation or lung abscess, which occurs when an abscess directly ruptures into lung parenchyma invading through both the diaphragm and pleura. The lung abscess may, in turn, communicate with the bronchi to cause hepatobronchial fistula or with pleura to cause bronchopleural fistula. Bronchial communication has been reported to occur in over one-third of thoracic complications [76]. The presence of air in the lung abscess or liver abscess or in the pleural collections indicates these fistulous complications (Figure 2)[11]. Clinically, the patients complain of productive cough, often expectoration of amebic pus-like material. The pleuropulmonary rupture is considered less severe than the intraperitoneal rupture because of spontaneous drainage of the abscesses following the hepatobronchial fistula.

Intraperitoneal rupture: Contained rupture versus free rupture

Intraperitoneal rupture has been said to occur in only 7% of cases[7,56,57]. However, we found an incidence of intraperitoneal rupture of 33% in our series[10]. In fact, several series from endemic countries have reported similar findings[6,13,17]. Based on imaging findings, intraperitoneal ruptures can be divided into two types: contained rupture and free rupture[11,60]. The contained rupture is characterized by accumulation of the localized fluid collection around the liver, usually in the subphrenic or subhepatic space (Figure 3A)[11]. The localized fluid from the contained rupture may occasionally be palpable on abdominal examination. This type of rupture carries a good prognosis and fortunately, is more common than its counterpart — the free rupture. The free rupture is characterized by fluid collection that diffusely involves the entire peritoneal cavity; it can cause generalized peritonitis and carry a poor prognosis (Figure 3B). The differentiation between these two types is significant as more aggressive treatment for longer duration is required for free ruptures[11,21].

Biliary complication: Communication versus compression

A common cause of drug failure is the presence of biliary complications, which has been reported to occur in up to 27% of refractory cases[12,22,77]. This occurs either from ductal communication with the abscess or from external compression by a large abscess[12,41]. When the liver parenchyma is destroyed by an aggressive abscess, the bile ducts are also damaged, producing ductal communications[12]. Usually, the communication is subtle, and therefore, ductal dilatation may not be evident on imaging. In several cases, the diagnosis is made only during percutaneous drainage when the initial aspirated fluid is bilious or when bile (usually persistent) appears thereafter[11,22,77]. Uncommonly, an abscess, particularly when large and aggressive, can rupture into the central bile ducts, causing duct dilation (Figure 4). In such cases, the diagnosis may be confirmed when endoscopic retrograde cholangiopancreatography (ERCP) or cavitogram demonstrates contrast extravasation into the abscess cavity[22,55]. Usually, the bile ducts are compressed by a large abscess, resulting in biliary duct dilation; these cases are evident on ultrasound or CT. The size and location of an abscess on imaging can provide anatomic clues to the presence of a biliary complication. The large (> 5 to 10 cm) and centrally located abscesses (near porta hepatis) are more likely to have biliary compilations than those smaller and with subcapsular locations[12]. Clinically, the presence of high jaundice may indicate biliary complications. Agarwal *et al*[22] compared the abscesses with and without biliary communications and found that total bilirubin levels > 2 mg/dL were present only in the patients with biliary complications.

Secondary bacterial infection

ALA is typically sterile. However, in 10% to 20% of cases, it can be complicated by secondary bacterial infections[58,78,79]. The incidence may be higher than generally recognized. Recently, in a PCR based study from liver aspirates, Singh *et al*[2] found bacterial infection in 37% of cases, mostly anaerobes of

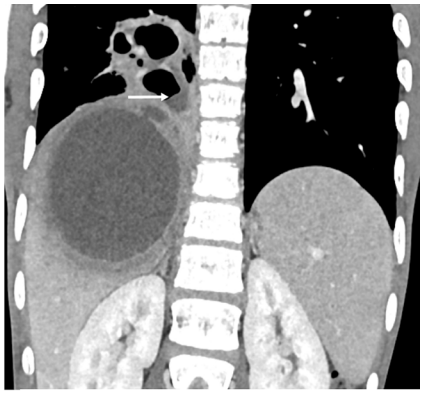

DOI: 10.4329/wjr.v14.i8.272 **Copyright** ©The Author(s) 2022.

Figure 2 Computed tomography image (coronal view) of a patient who presented with productive cough and mild upper abdominal pain for more than four weeks. Note the rupture of a subdiaphragmatic abscess into the lung resulting in the formation of a lung abscess. The air-fluid level in the lung abscess (arrow) indicates fistulous communication between the lung abscess and the bronchus.

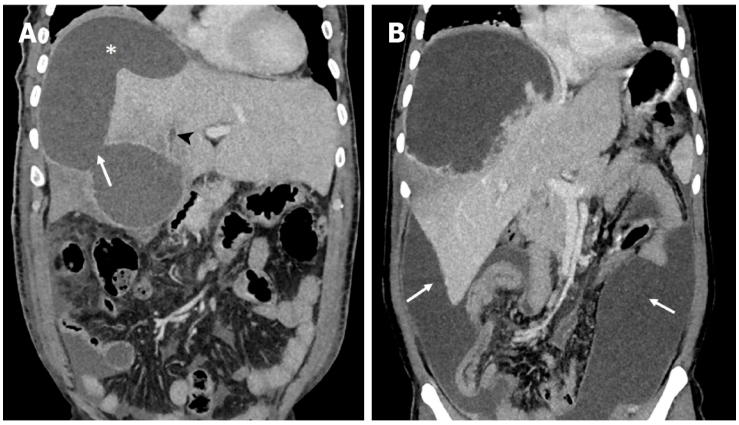

DOI: 10.4329/wjr.v14.i8.272 **Copyright** ©The Author(s) 2022.

Figure 3 Computed tomography image. A: Computed tomography image (coronal view) demonstrating a contained rupture. A fluid collection that is localized in the subphrenic space (asterisk). Note the wide rent in the abscess (arrow). Additional imaging features of an aggressive disease in this image are the presence of ascites and thrombus in a segment of the hepatic vein (arrowhead); B: Free intraperitoneal rupture in a 40-year-old man who presented with features of generalized peritonitis. Coronal computed tomography image showing a large amebic abscess with an irregular edge in the right lobe and diffuse intraperitoneal fluid collection (arrows).

intestinal microbiota. The authors suggested that intestinal bacteria reach the liver along with the trophozoites through the portal route, that is, concurrent or coinfection with bacteria. When secondary bacterial infection occurs as coinfection, the disease may take an aggressive course. This complication should be suspected in refractory cases, particularly those associated with persistent high fever and marked leukocytosis (> 20000/μL)[56]. Another mechanism of secondary infection is bacterial superinfection, which usually occurs in the stagnant fluid following unsuccessful needle aspiration or inadequate catheter drainage[18]. Since most of the abscesses are walled off at this point, symptoms are of chronic indolent disease. In contrast to sterile amebic aspirate, cultures of pus from secondarily infected ALA usually yield positive results. Blood cultures, however, may be negative because most patients are generally pretreated with antibiotics[80].

Vascular complication: Venous thrombosis, venous compression and arterial aneurysm

Venous thrombosis is a common phenomenon in this disease. Autopsy studies have shown that venous thrombosis occurs in up to 30% of cases; however, we have identified venous thrombus in 70% of cases with the use of the latest multidetector CT[42,68]. Venous thrombosis may involve the portal or hepatic vein, but usually both are involved. Thrombus typically occurs in the smaller segmental or subsegmental branches. The hepatic vein thrombosis can extend into the inferior vena cava (IVC) or even into the right atrium[68]. Rarely, it can cause a Budd-Chiari like syndrome[81]. Detection of thrombus in large veins may be indicative of severe ALA[68,82]. The diagnosis of thrombosis on CT can be suggested by the presence of a wedge-shaped hypoattenuating area surrounding the abscess, which might be due to thrombosis led hypoperfusion[68]. Another vascular complication is compression of the intrahepatic veins and the IVC. Venous compression may be a clue to the presence of a high intracavitary pressure in

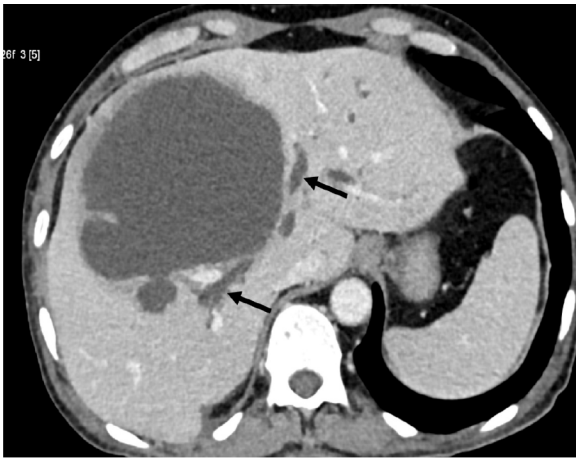

DOI: 10.4329/wjr.v14.i8.272 **Copyright** ©The Author(s) 2022.

Figure 4 Axial computed tomography of a 60-year-old man showing a large abscess in segment IV of the liver near the porta hepatis. Note the duct dilation (arrows) that resulted from rupture of the abscess into the central bile ducts. He was managed with catheter drainage. Bilious fluid draining through the catheter was observed for several weeks in this patient.

the abscess, which in turn indicates aggressive abscesses. IVC compression occurs when a large abscess located in the caudate lobe compresses the IVC, causing leg edema[48]. Additionally, portal vein compression near the porta hepatis has been reported to cause splenomegaly and portal hypertension [41]. Hepatic artery pseudoaneurysm is a rare, but serious complication of ALA that results from erosion of the arterial wall by an aggressive abscess[83].

Concurrent colitis and perforations

Although diarrhea is found in only 15% to 30% of patients with ALA, concurrent colonic ulcers are detected in approximately 50% of patients with ALA on colonoscopy[17,57,84,85]. The colonic lesions on colonoscopy appear as small discrete ulcers in the cecum or ascending colon. Approximately 70% of the ulcers are localized to cecum and contiguous involvement of the appendix (amebic typhlo-appendicitis) is common[10]. As the ulcers are usually small and localized, symptoms related to colitis are mild. In severe cases, however, other segments may also be involved or there may be cecal perforations. Furthermore, the severity of colitis seems to parallel the severity of abscesses. Recently, Premkumar *et al* [85], in a study of 52 patients with ALA, reported bleeding and large ileocecal ulcers in the majority of their patients; most synchronous ALAs in this series had aggressive clinical and imaging features. In an autopsy study of 76 patients with fatal ALA, Aikat *et al*[42] found that the incidence of colonic ulcers was 62%. With multidetector CT, we have observed concurrent colitis in 28% of patients, more frequently and possibly more severe in the patients with aggressive ALA than those with mild ALA. On CT, colitis generally manifests as nonspecific bowel wall thickening (Figure 1A)[10].

MANAGEMENT: ROLE OF IMAGE-GUIDED PERCUTANEOUS DRAINAGE

ALA, in most patients, is mild and responds promptly to medical therapy. The drug of choice for the treatment of ALA is metronidazole, a nitroimidazole, which is given at a dose of 750 mg orally or intravenously three times daily for seven to ten days[31]. This regime results in resolution of fever, toxemia, and pain in 80% to 90% of patients with uncomplicated ALA within 72 to 96 h of treatment[7]. The disease resolves without complications or without the need for any invasive procedures. This treatment is followed by a luminal agent (paromomycin or diloxanide furoate) to clear the luminal parasites.

The decision to perform drainage is based largely on the clinical grounds. Any symptomatic patient with persistent symptoms after four days of treatment requires drainage, regardless of the imaging findings. In the most common scenario of percutaneous drainage, the patients continue to have symptoms, primarily pain or tenderness in the right upper quadrant, despite completed medical therapy. In another clinical setting, early drainage is performed for acute aggressive abscesses to control the disease severity[10]. The third clinical setting may be the patients in whom there is diagnostic uncertainty between ALA and pyogenic abscess. In such cases, most physicians prefer to drain the amebic abscesses considering them as a pyogenic abscess.

In addition to clinical criteria, imaging-based criteria for the use of drainage was formulated by de la Rey Nel *et al*[86]. They recommended that abscesses with the following risk factors should be drained: abscesses > 10 cm (because of their long healing time), abscesses located in the left lobe (because of the

risk of rupture into the pericardium), and large superficial abscesses with a thin rim (because of the risk of rupture). In this context, it must be emphasized that lack of a mature wall is also an important risk factor that must be considered while assessing rupture risk. Most intraperitoneal ruptures in our series occurred when the abscesses lacked a mature wall[10].

Needle aspiration vs catheter drainage

Percutaneous drainage can be performed either by needle aspiration or catheter drainage under image guidance. Usually, sonographic guidance suffices for the placement of the catheter or needle into the abscess cavity[11]. CT guidance may be required in some cases, particularly in thoracic complications. Success of the procedure is dependent on its effectiveness in evacuation of the amebic pus. Needle aspiration is a simple, less invasive technique and requires less expertise. However, it is not as effective as catheter drainage, and presents several disadvantages. It fails to evacuate the solid necrotic tissue, which usually blocks the needle lumen during aspiration. Since tissue necrosis and its liquefaction is a dynamic process, not all tissue is completely liquid at the time of aspiration, and therefore, multiple sessions are generally needed to achieve complete drainage. This practice is perhaps related to the most serious drawback of needle aspiration, *i.e.*, bacterial superinfections. The reported rate of superinfections following needle aspirations is 15%[18]. Nevertheless, needle aspirations may be useful in the appropriate settings, such as when the abscesses are small (< 5 cm) and the content is completely liquefied. Another common scenario includes multiple abscesses, where smaller and more liquefied abscesses are aspirated using an 18G spinal needle, whereas the larger and partially necrotic abscesses are drained using catheters[11]. Several randomized controlled studies have demonstrated that catheter drainage offers a higher success rate (up to 100%) compared to needle aspiration, particularly when abscesses are larger than 5 cm[78,87-89]. Due to its obvious advantage of having a large bore, it evacuates the necrotic tissue efficiently. It has an additional advantage of being indwelling, which makes it more effective in clearing those abscesses that liquefy over a period of time.

Percutaneous drainage in the management of complications

Although aspirations have been useful in the management of refractory abscesses for several decades, free rupture with peritonitis was typically considered an indication for surgery. The reported mortality rate in surgically treated patients was as high as 50%[90,91]. In the last three decades, a paradigm shift has been seen from surgical drainage to catheter drainage. All complications related to ALA are currently managed with percutaneous catheter drainage[11,19-21,92-94]. By using catheter drainage, we have achieved a success rate of 97%, without significant mortality[11]. Only the placement of multiple catheters, usually in multiple sessions, is required to drain intraperitoneal fluid collections. As the collections are sterile, the peritonitis is not as severe as that seen in cases of bowel perforation. Not only is catheter drainage curative for the intraperitoneal rupture, it also effectively treats pleuropulmonary ruptures[11]. The drainage of pleural fluid collections may require CT guidance as ultrasound has low sensitivity for pleuropulmonary pathology. Lung abscesses usually do not require drainage due to the presence of bronchial fistula, which provides natural drainage in most patients. Catheter drainage has also been proved to be excellent in the management of biliary communications. Agarwal *et al*[22] evaluated 33 patients with refractory abscesses, nine of the patients were found to have an abscess with intrabiliary communication, and all patients were successfully treated with prolonged catheter drainage (12 to 50 d). None of the patients required endoscopic placement of stents. Endoscopic stenting or sphincterotomy, however, may be required to control bile leak prior to catheter removal when fistulous communication persists despite prolonged catheter drainage. Catheter drainage has also been shown to facilitate spontaneous healing of small arterial aneurysms resulting from ALA[83].

Surgical management

The role of surgical drainage in the management of ALA has been reassessed due to the widespread use of radiologically guided drainage[95]. However, open drainage may be warranted in some cases where percutaneous drainage may fail to evacuate abscess content. Surgery may also be indicated in selected cases of intraperitoneal rupture with generalized peritonitis[96]. As an alternative to open surgical drainage, laparoscopic drainage can result in less morbidity and mortality[97].

CONCLUSION

Clinical and imaging features of ALA are variable and parallel to each other. Although the mild form of the disease is cured easily with antibiotics alone, the other two forms of the disease-acute aggressive and chronic indolent-often require percutaneous drainage. Most complications and mortality in ALA occur when it presents in its acute aggressive form. Imaging studies play a key role in identifying the different forms of the disease and assessing the complications. All complications, including free intraperitoneal ruptures, can be managed with percutaneous catheter drainage.

FOOTNOTES

Author contributions: Priyadarshi RN contributed to the concept and design of the manuscript, data collection and manuscript writing; Kumar R and Anand U contributed to the literature search, critical inputs and manuscript revision.

Conflict-of-interest statement: All the authors declare that they have no conflict of interest related to this article.

Country/Territory of origin: India

ORCID number: Rajeev Nayan Priyadarshi 0000-0003-2890-8910; Ramesh Kumar 0000-0001-5136-4865; Utpal Anand 0000-0003-0653-4129.

S-Editor: Liu JH
L-Editor: Webster JR
P-Editor: Liu JH

REFERENCES

1 **Walsh JA**. Problems in recognition and diagnosis of amebiasis: estimation of the global magnitude of morbidity and mortality. *Rev Infect Dis* 1986; **8**: 228-238 [PMID: 2871619 DOI: 10.1093/clinids/8.2.228]
2 **Singh A**, Banerjee T, Kumar R, Shukla SK. Prevalence of cases of amebic liver abscess in a tertiary care centre in India: A study on risk factors, associated microflora and strain variation of Entamoeba histolytica. *PLoS One* 2019; **14**: e0214880 [PMID: 30943253 DOI: 10.1371/journal.pone.0214880]
3 **Khan R**, Hamid S, Abid S, Jafri W, Abbas Z, Islam M, Shah H, Beg S. Predictive factors for early aspiration in liver abscess. *World J Gastroenterol* 2008; **14**: 2089-2093 [PMID: 18395912 DOI: 10.3748/wjg.14.2089]
4 **Ghosh S**, Sharma S, Gadpayle AK, Gupta HK, Mahajan RK, Sahoo R, Kumar N. Clinical, laboratory, and management profile in patients of liver abscess from northern India. *J Trop Med* 2014; **2014**: 142382 [PMID: 25002869 DOI: 10.1155/2014/142382]
5 **Khanna S**, Chaudhary D, Kumar A, Vij JC. Experience with aspiration in cases of amebic liver abscess in an endemic area. *Eur J Clin Microbiol Infect Dis* 2005; **24**: 428-430 [PMID: 15928909 DOI: 10.1007/s10096-005-1338-2]
6 **Jindal A**, Pandey A, Sharma MK, Mukund A, Vijayaraghavan R, Arora V, Shasthry SM, Choudhary A, Sarin SK. Management Practices and Predictors of Outcome of Liver Abscess in Adults: A Series of 1630 Patients from a Liver Unit. *J Clin Exp Hepatol* 2021; **11**: 312-320 [PMID: 33994714 DOI: 10.1016/j.jceh.2020.10.002]
7 **Stanley SL Jr**. Amoebiasis. *Lancet* 2003; **361**: 1025-1034 [PMID: 12660071 DOI: 10.1016/S0140-6736(03)12830-9]
8 **Ralls PW**, Barnes PF, Johnson MB, De Cock KM, Radin DR, Halls J. Medical treatment of hepatic amebic abscess: rare need for percutaneous drainage. *Radiology* 1987; **165**: 805-807 [PMID: 3317505 DOI: 10.1148/radiology.165.3.3317505]
9 **Nigam P**, Gupta AK, Kapoor KK, Sharan GR, Goyal BM, Joshi LD. Cholestasis in amoebic liver abscess. *Gut* 1985; **26**: 140-145 [PMID: 3967831 DOI: 10.1136/gut.26.2.140]
10 **Priyadarshi RN**, Sherin L, Kumar R, Anand U, Kumar P. CT of amebic liver abscess: different morphological types with different clinical features. *Abdom Radiol (NY)* 2021; **46**: 4148-4158 [PMID: 33893854 DOI: 10.1007/s00261-021-03093-w]
11 **Priyadarshi RN**, Prakash V, Anand U, Kumar P, Jha AK, Kumar R. Ultrasound-guided percutaneous catheter drainage of various types of ruptured amebic liver abscess: a report of 117 cases from a highly endemic zone of India. *Abdom Radiol (NY)* 2019; **44**: 877-885 [PMID: 30361869 DOI: 10.1007/s00261-018-1810-y]
12 **Datta DV**, Saha S, Singh SA, Aikat BK, Chhuttani PN. The clinical pattern and prognosis of patients with amebic liver abscess and jaundice. *Am J Dig Dis* 1973; **18**: 887-898 [PMID: 4355077 DOI: 10.1007/BF01073340]
13 **Jha AK**, Jha P, Chaudhary M, Purkayastha S, Jha SK, Ranjan R, Priyadarshi RN, Kumar R. Evaluation of factors associated with complications in amoebic liver abscess in a predominantly toddy-drinking population: A retrospective study of 198 cases. *JGH Open* 2019; **3**: 474-479 [PMID: 31832547 DOI: 10.1002/jgh3.12183]
14 **Sharma N**, Sharma A, Varma S, Lal A, Singh V. Amoebic liver abscess in the medical emergency of a North Indian hospital. *BMC Res Notes* 2010; **3**: 21 [PMID: 20181006 DOI: 10.1186/1756-0500-3-21]
15 **Katzenstein D**, Rickerson V, Braude A. New concepts of amebic liver abscess derived from hepatic imaging, serodiagnosis, and hepatic enzymes in 67 consecutive cases in San Diego. *Medicine (Baltimore)* 1982; **61**: 237-246 [PMID: 6806561 DOI: 10.1097/00005792-198207000-00003]
16 **Chuah SK**, Chang-Chien CS, Sheen IS, Lin HH, Chiou SS, Chiu CT, Kuo CH, Chen JJ, Chiu KW. The prognostic factors of severe amebic liver abscess: a retrospective study of 125 cases. *Am J Trop Med Hyg* 1992; **46**: 398-402 [PMID: 1575285 DOI: 10.4269/ajtmh.1992.46.398]
17 **Balasegaram M**. Management of hepatic abscess. *Curr Probl Surg* 1981; **18**: 282-340 [PMID: 6263552]
18 **Singh JP**, Kashyap A. A comparative evaluation of percutaneous catheter drainage for resistant amebic liver abscesses. *Am*

J Surg 1989; **158**: 58-62 [PMID: 2662790 DOI: 10.1016/0002-9610(89)90316-4]
19 **Hanna RM**, Dahniya MH, Badr SS, El-Betagy A. Percutaneous catheter drainage in drug-resistant amoebic liver abscess. *Trop Med Int Health* 2000; **5**: 578-581 [PMID: 10995100 DOI: 10.1046/j.1365-3156.2000.00586.x]
20 **Ken JG**, vanSonnenberg E, Casola G, Christensen R, Polansky AM. Perforated amebic liver abscesses: successful percutaneous treatment. *Radiology* 1989; **170**: 195-197 [PMID: 2909097 DOI: 10.1148/radiology.170.1.2909097]
21 **Baijal SS**, Agarwal DK, Roy S, Choudhuri G. Complex ruptured amebic liver abscesses: the role of percutaneous catheter drainage. *Eur J Radiol* 1995; **20**: 65-67 [PMID: 7556258 DOI: 10.1016/0720-048x(95)00613-u]
22 **Agarwal DK**, Baijal SS, Roy S, Mittal BR, Gupta R, Choudhuri G. Percutaneous catheter drainage of amebic liver abscesses with and without intrahepatic biliary communication: a comparative study. *Eur J Radiol* 1995; **20**: 61-64 [PMID: 7556257 DOI: 10.1016/0720-048x(95)00603-n]
23 **Hughes MA**, Petri WA Jr. Amebic liver abscess. *Infect Dis Clin North Am* 2000; **14**: 565-582, viii [PMID: 10987110 DOI: 10.1016/s0891-5520(05)70121-5]
24 **Kumanan T**, Sujanitha V, Sreeharan N. Amoebic liver abscess: a neglected tropical disease. *Lancet Infect Dis* 2020; **20**: 160-162 [PMID: 32006496 DOI: 10.1016/S1473-3099(19)30696-6]
25 **Kannathasan S**, Murugananthan A, Kumanan T, de Silva NR, Rajeshkannan N, Haque R, Iddawela D. Epidemiology and factors associated with amoebic liver abscess in northern Sri Lanka. *BMC Public Health* 2018; **18**: 118 [PMID: 29316900 DOI: 10.1186/s12889-018-5036-2]
26 Ray G. Sociodemographic and Clinical Profile of Amoebic Liver Abscess observed at a Tertiary Referral Hospital over 10 Years. *Trop Gastroenterol* 2021; **42**: 126-33
27 **Nath J**, Ghosh SK, Singha B, Paul J. Molecular Epidemiology of Amoebiasis: A Cross-Sectional Study among North East Indian Population. *PLoS Negl Trop Dis* 2015; **9**: e0004225 [PMID: 26633890 DOI: 10.1371/journal.pntd.0004225]
28 **Wuerz T**, Kane JB, Boggild AK, Krajden S, Keystone JS, Fuksa M, Kain KC, Warren R, Kempston J, Anderson J. A review of amoebic liver abscess for clinicians in a nonendemic setting. *Can J Gastroenterol* 2012; **26**: 729-733 [PMID: 23061067 DOI: 10.1155/2012/852835]
29 **Kumar R**, Priyadarshi RN, Anand U. Toddy consumption and amoebic liver abscess in India: An unexplored link. *Indian J Public Health* 2019; **63**: 89-90 [PMID: 30880745 DOI: 10.4103/ijph.IJPH_192_18]
30 **Mukhopadhyay M**, Saha AK, Sarkar A, Mukherjee S. Amoebic liver abscess: presentation and complications. *Indian J Surg* 2010; **72**: 37-41 [PMID: 23133202 DOI: 10.1007/s12262-010-0007-6]
31 **Haque R**, Huston CD, Hughes M, Houpt E, Petri WA Jr. Amebiasis. *N Engl J Med* 2003; **348**: 1565-1573 [PMID: 12700377 DOI: 10.1056/NEJMra022710]
32 **Sharma MP**, Dasarathy S, Verma N, Saksena S, Shukla DK. Prognostic markers in amebic liver abscess: a prospective study. *Am J Gastroenterol* 1996; **91**: 2584-2588 [PMID: 8946991]
33 **Singh R**, Adhikari DR, Patil BP, Talathi NR, Hanamshetti SR, Joshi RM. Amoebic liver abscess: an appraisal. *Int Surg* 2011; **96**: 305-309 [PMID: 22808611 DOI: 10.9738/cc9.1]
34 **Khim G**, Em S, Mo S, Townell N. Liver abscess: diagnostic and management issues found in the low resource setting. *Br Med Bull* 2019; **132**: 45-52 [PMID: 31836890 DOI: 10.1093/bmb/ldz032]
35 **Brandt H**, Tamayo RP. Pathology of human amebiasis. *Hum Pathol* 1970; **1**: 351-385 [PMID: 4330002 DOI: 10.1016/s0046-8177(70)80072-7]
36 **Martínez-Palomo A**. The pathogenesis of amoebiasis. *Parasitol Today* 1987; **3**: 111-118 [PMID: 15462926 DOI: 10.1016/0169-4758(87)90048-2]
37 **Tsutsumi V**, Mena-Lopez R, Anaya-Velazquez F, Martinez-Palomo A. Cellular bases of experimental amebic liver abscess formation. *Am J Pathol* 1984; **117**: 81-91 [PMID: 6385728]
38 **Simjee AE**, Patel A, Gathiram V, Engelbrecht HE, Singh K, Rooknoodeen F. Serial ultrasound in amoebic liver abscess. *Clin Radiol* 1985; **36**: 61-68 [PMID: 3905191 DOI: 10.1016/s0009-9260(85)80027-1]
39 **Missalek W**. Ultrasonography in the diagnosis of amoebic liver abscess and its complications. *Trop Doct* 1992; **22**: 59-64 [PMID: 1318595 DOI: 10.1177/004947559202200205]
40 **Jimenez F**. Pathology of amebiasis. *Bull N Y Acad Med* 1981; **57**: 217-223 [PMID: 6938282]
41 **Knight R**. Hepatic amebiasis. *Semin Liver Dis* 1984; **4**: 277-292 [PMID: 6098014 DOI: 10.1055/s-2008-1040657]
42 **Aikat BK**, Bhusnurmath SR, Pal AK, Chhuttani PN, Datta DV. The pathology and pathogenesis of fatal hepatic amoebiasis--A study based on 79 autopsy cases. *Trans R Soc Trop Med Hyg* 1979; **73**: 188-192 [PMID: 473308 DOI: 10.1016/0035-9203(79)90209-8]
43 **Elizondo G**, Weissleder R, Stark DD, Todd LE, Compton C, Wittenberg J, Ferrucci JT Jr. Amebic liver abscess: diagnosis and treatment evaluation with MR imaging. *Radiology* 1987; **165**: 795-800 [PMID: 2891154 DOI: 10.1148/radiology.165.3.2891154]
44 **Basile JA**, Klein SR, Worthen NJ, Wilson SE, Hiatt JR. Amebic liver abscess. The surgeon's role in management. *Am J Surg* 1983; **146**: 67-71 [PMID: 6869681 DOI: 10.1016/0002-9610(83)90261-1]
45 **Radin DR**, Ralls PW, Colletti PM, Halls JM. CT of amebic liver abscess. *AJR Am J Roentgenol* 1988; **150**: 1297-1301 [PMID: 3259367 DOI: 10.2214/ajr.150.6.1297]
46 **Nari GA**, Ceballos Espinosa R, Carrera Ladrón de Guevara S, Preciado Vargas J, Cruz Valenciano JL, Briones Rivas JL, Moreno Hernández F, Góngora Ortega J. [Amebic liver abscess. Three years experience]. *Rev Esp Enferm Dig* 2008; **100**: 268-272 [PMID: 18662078 DOI: 10.4321/s1130-01082008000500004]
47 **Boultbee JE**, Simjee AE, Rooknoodeen F, Engelbrecht HE. Experiences with grey scale ultrasonography in hepatic amoebiasis. *Clin Radiol* 1979; **30**: 683-689 [PMID: 509870 DOI: 10.1016/s0009-9260(79)80020-3]
48 **Sharma MP**, Ahuja V. Amoebic liver abscess. *J Indian Acad Clin Med* 2003; **4**: 107-11
49 **Adams EB**, MacLeod IN. Invasive amebiasis. II. Amebic liver abscess and its complications. *Medicine (Baltimore)* 1977; **56**: 325-334 [PMID: 875719 DOI: 10.1097/00005792-197707000-00004]
50 **Wells CD**, Arguedas M. Amebic liver abscess. *South Med J* 2004; **97**: 673-682 [PMID: 15301125 DOI: 10.1097/00007611-200407000-00013]

51 **Anesi JA**, Gluckman S. Amebic liver abscess. *Clin Liver Dis (Hoboken)* 2015; **6**: 41-43 [PMID: 31040985 DOI: 10.1002/cld.488]

52 **Alam F**, Salam MA, Hassan P, Mahmood I, Kabir M, Haque R. Amebic liver abscess in northern region of Bangladesh: sociodemographic determinants and clinical outcomes. *BMC Res Notes* 2014; **7**: 625 [PMID: 25204395 DOI: 10.1186/1756-0500-7-625]

53 **Wallace RJ Jr**, Greenberg SB, Lau JM, Kalchoff WP, Mangold DE, Martin R. Amebic peritonitis following rupture of an amebic liver abscess. Successful treatment of two patients. *Arch Surg* 1978; **113**: 322-325 [PMID: 205190 DOI: 10.1001/archsurg.1978.01370150094024]

54 **Ajao OG**, Adebo OA. Unruptured amoebic liver abscess presenting as acute abdomen. *Trop Doct* 1983; **13**: 109-111 [PMID: 6879689 DOI: 10.1177/004947558301300305]

55 **Ibrarullah M**, Agarwal DK, Baijal SS, Mittal BR, Kapoor VK. Amebic liver abscess with intra-biliary rupture. *HPB Surg* 1994; **7**: 305-10; discussion 310 [PMID: 8204550 DOI: 10.1155/1994/36160]

56 **Peters RS**, Gitlin N, Libke RD. Amebic liver abscess. *Annu Rev Med* 1981; **32**: 161-174 [PMID: 7013659 DOI: 10.1146/annurev.me.32.020181.001113]

57 **Reed SL**. Amebiasis: an update. *Clin Infect Dis* 1992; **14**: 385-393 [PMID: 1554822 DOI: 10.1093/clinids/14.2.385]

58 **Barnes PF**, De Cock KM, Reynolds TN, Ralls PW. A comparison of amebic and pyogenic abscess of the liver. *Medicine (Baltimore)* 1987; **66**: 472-483 [PMID: 3316923 DOI: 10.1097/00005792-198711000-00005]

59 **Neill L**, Edwards F, Collin SM, Harrington D, Wakerley D, Rao GG, McGregor AC. Clinical characteristics and treatment outcomes in a cohort of patients with pyogenic and amoebic liver abscess. *BMC Infect Dis* 2019; **19**: 490 [PMID: 31159769 DOI: 10.1186/s12879-019-4127-8]

60 **Greaney GC**, Reynolds TB, Donovan AJ. Ruptured amebic liver abscess. *Arch Surg* 1985; **120**: 555-561 [PMID: 3885916 DOI: 10.1001/archsurg.1985.01390290037006]

61 **Recipon G**, Piver É, Caille A, Le Pape P, Pihet M, Pagès JC, Chandenier J, Desoubeaux G. Is procalcitonin increased in cases of invasive amoebiasis? *Diagn Microbiol Infect Dis* 2015; **83**: 395-399 [PMID: 26388549 DOI: 10.1016/j.diagmicrobio.2015.08.014]

62 **Ralls PW**, Henley DS, Colletti PM, Benson R, Raval JK, Radin DR, Boswell WD Jr, Halls JM. Amebic liver abscess: MR imaging. *Radiology* 1987; **165**: 801-804 [PMID: 3317504 DOI: 10.1148/radiology.165.3.3317504]

63 **Elzi L**, Laifer G, Sendi P, Ledermann HP, Fluckiger U, Bassetti S. Low sensitivity of ultrasonography for the early diagnosis of amebic liver abscess. *Am J Med* 2004; **117**: 519-522 [PMID: 15464710 DOI: 10.1016/j.amjmed.2004.01.031]

64 **Seeto RK**, Rockey DC. Amebic liver abscess: epidemiology, clinical features, and outcome. *West J Med* 1999; **170**: 104-109 [PMID: 10063397]

65 **Léonetti P**, Moncany G, Soubeyrand J. [Amebic abscess of the liver. Contribution of ultrasonics to developmental diagnosis apropos of 983 cases]. *J Radiol* 1987; **68**: 259-264 [PMID: 3295224]

66 **N'Gbesso RD**, Kéita AK. [Ultrasonography of amebic liver abscesses. Proposal of a new classification]. *J Radiol* 1997; **78**: 569-576 [PMID: 9537173]

67 **Terrier F**, Becker CD, Triller JK. Morphologic aspects of hepatic abscesses at computed tomography and ultrasound. *Acta Radiol Diagn (Stockh)* 1983; **24**: 129-137 [PMID: 6624514]

68 **Priyadarshi RN**, Kumar P, Kumar R, Anand U, Shyama. Venous thrombosis and segmental hypoperfusion in amebic liver abscess: MDCT demonstration and its implications. *Abdom Radiol (NY)* 2020; **45**: 652-660 [PMID: 31955219 DOI: 10.1007/s00261-020-02409-6]

69 **Qian LJ**, Zhu J, Zhuang ZG, Xia Q, Liu Q, Xu JR. Spectrum of multilocular cystic hepatic lesions: CT and MR imaging findings with pathologic correlation. *Radiographics* 2013; **33**: 1419-1433 [PMID: 24025933 DOI: 10.1148/rg.335125063]

70 **Mathieu D**, Vasile N, Fagniez PL, Segui S, Grably D, Lardé D. Dynamic CT features of hepatic abscesses. *Radiology* 1985; **154**: 749-752 [PMID: 3969480 DOI: 10.1148/radiology.154.3.3969480]

71 **Ralls PW**, Quinn MF, Boswell WD Jr, Colletti PM, Radin DR, Halls J. Patterns of resolution in successfully treated hepatic amebic abscess: sonographic evaluation. *Radiology* 1983; **149**: 541-543 [PMID: 6622702 DOI: 10.1148/radiology.149.2.6622702]

72 **Berry M**, Bazaz R, Bhargava S. Amebic liver abscess: sonographic diagnosis and management. *J Clin Ultrasound* 1986; **14**: 239-242 [PMID: 3084579 DOI: 10.1002/jcu.1870140402]

73 **Sarda AK**, Bal S, Sharma AK, Kapur MM. Intraperitoneal rupture of amoebic liver abscess. *Br J Surg* 1989; **76**: 202-203 [PMID: 2702459 DOI: 10.1002/bjs.1800760231]

74 **Pawar SV**, Zanwar VG, Gambhire PA, Mohite AR, Choksey AS, Rathi PM, Asgaonkar DS. Unusual complication of amebic liver abscess: Hepatogastric fistula. *World J Gastrointest Endosc* 2015; **7**: 916-919 [PMID: 26240693 DOI: 10.4253/wjge.v7.i9.916]

75 **Mowji PJ**, Cohen AJ, Potkin B, Viltuznik J. Amebic liver abscess with hepatoduodenal fistula. *Am J Gastroenterol* 1987; **82**: 558-559 [PMID: 3578237]

76 **Ibarra-Pérez C**. Thoracic complications of amebic abscess of the liver: report of 501 cases. *Chest* 1981; **79**: 672-677 [PMID: 7226956 DOI: 10.1378/chest.79.6.672]

77 **Sandeep SM**, Banait VS, Thakur SK, Bapat MR, Rathi PM, Abraham P. Endoscopic biliary drainage in patients with amebic liver abscess and biliary communication. *Indian J Gastroenterol* 2006; **25**: 125-127 [PMID: 16877823]

78 **Singh S**, Chaudhary P, Saxena N, Khandelwal S, Poddar DD, Biswal UC. Treatment of liver abscess: prospective randomized comparison of catheter drainage and needle aspiration. *Ann Gastroenterol* 2013; **26**: 332-339 [PMID: 24714320]

79 **Ochsner A**, DeBakey M. Liver abscess part I. *Am J Surg* 1935; **29**: 173-194 [DOI: 10.1016/s0002-9610(35)91120-5]

80 **Chemaly RF**, Hall GS, Keys TF, Procop GW. Microbiology of liver abscesses and the predictive value of abscess gram stain and associated blood cultures. *Diagn Microbiol Infect Dis* 2003; **46**: 245-248 [PMID: 12944014 DOI: 10.1016/s0732-8893(03)00088-9]

81 **Méchaï F**, Aoun O, Ficko C, Barruet R, Imbert P, Rapp C. Budd-Chiari syndrome as a vascular complication of amebic liver abscess. *Am J Trop Med Hyg* 2009; **81**: 768-769 [PMID: 19861608 DOI: 10.4269/ajtmh.2009.09-0230]

82 **Yadav T**, Patel RK, Bansal A, Chatterjee N, Patidar Y, Mukund A. Caudate lobe amebic abscesses: percutaneous image-guided aspiration or drainage. *Abdom Radiol (NY)* 2022; **47**: 1157-1166 [PMID: 34964910 DOI: 10.1007/s00261-021-03395-z]

83 **Priyadarshi RN**, Kumar R, Anand U. Case Report: Spontaneous Resolution of Intracavitary Hepatic Artery Pseudoaneurysm Caused by Amebic Liver Abscess following Percutaneous Drainage. *Am J Trop Med Hyg* 2019; **101**: 157-159 [PMID: 31162010 DOI: 10.4269/ajtmh.19-0103]

84 **Sachdev GK**, Dhol P. Colonic involvement in patients with amebic liver abscess: endoscopic findings. *Gastrointest Endosc* 1997; **46**: 37-39 [PMID: 9260703 DOI: 10.1016/s0016-5107(97)70207-4]

85 **Premkumar M**, Devurgowda D, Dudha S, Kulkarni A, Joshi YK. Clinical and Endoscopic Management of Synchronous Amoebic Liver Abscess and Bleeding Colonic Ulcers. *J Assoc Physicians India* 2019; **67**: 14-18 [PMID: 31304698]

86 **de la Rey Nel J**, Simjee AE, Patel A. Indications for aspiration of amoebic liver abscess. *S Afr Med J* 1989; **75**: 373-376 [PMID: 2711266]

87 **Rajak CL**, Gupta S, Jain S, Chawla Y, Gulati M, Suri S. Percutaneous treatment of liver abscesses: needle aspiration versus catheter drainage. *AJR Am J Roentgenol* 1998; **170**: 1035-1039 [PMID: 9530055 DOI: 10.2214/ajr.170.4.9530055]

88 **Cai YL**, Xiong XZ, Lu J, Cheng Y, Yang C, Lin YX, Zhang J, Cheng NS. Percutaneous needle aspiration versus catheter drainage in the management of liver abscess: a systematic review and meta-analysis. *HPB (Oxford)* 2015; **17**: 195-201 [PMID: 25209740 DOI: 10.1111/hpb.12332]

89 **Ramani A**, Ramani R, Kumar MS, Lakhkar BN, Kundaje GN. Ultrasound-guided needle aspiration of amoebic liver abscess. *Postgrad Med J* 1993; **69**: 381-383 [PMID: 8346134 DOI: 10.1136/pgmj.69.811.381]

90 **Kumar R**, Anand U, Priyadarshi RN, Mohan S, Parasar K. Management of amoebic peritonitis due to ruptured amoebic liver abscess: It's time for a paradigm shift. *JGH Open* 2019; **3**: 268-269 [PMID: 31276048 DOI: 10.1002/jgh3.12144]

91 **Eggleston FC**, Handa AK, Verghese M. Amebic peritonitis secondary to amebic liver abscess. *Surgery* 1982; **91**: 46-48 [PMID: 7054906]

92 **Saraswat VA**, Agarwal DK, Baijal SS, Roy S, Choudhuri G, Dhiman RK, Bhandari L, Naik SR. Percutaneous catheter drainage of amoebic liver abscess. *Clin Radiol* 1992; **45**: 187-189 [PMID: 1555372 DOI: 10.1016/s0009-9260(05)80639-7]

93 **vanSonnenberg E**, Ferrucci JT Jr, Mueller PR, Wittenberg J, Simeone JF. Percutaneous drainage of abscesses and fluid collections: technique, results, and applications. *Radiology* 1982; **142**: 1-10 [PMID: 7053517 DOI: 10.1148/radiology.142.1.7053517]

94 **vanSonnenberg E**, Mueller PR, Schiffman HR, Ferrucci JT Jr, Casola G, Simeone JF, Cabrera OA, Gosink BB. Intrahepatic amebic abscesses: indications for and results of percutaneous catheter drainage. *Radiology* 1985; **156**: 631-635 [PMID: 4023220 DOI: 10.1148/radiology.156.3.4023220]

95 **Gibney EJ**. Amoebic liver abscess. *Br J Surg* 1990; **77**: 843-844 [PMID: 2203504 DOI: 10.1002/bjs.1800770803]

96 **Akgun Y**, Tacyildiz IH, Celik Y. Amebic liver abscess: changing trends over 20 years. *World J Surg* 1999; **23**: 102-106 [PMID: 9841772 DOI: 10.1007/s002689900573]

97 **Tay KH**, Ravintharan T, Hoe MN, See AC, Chng HC. Laparoscopic drainage of liver abscesses. *Br J Surg* 1998; **85**: 330-332 [PMID: 9529485 DOI: 10.1046/j.1365-2168.1998.00617.x]

World Journal of Radiology

Submit a Manuscript: https://www.f6publishing.com

World J Radiol 2022 August 28; 14(8): 286-292

DOI: 10.4329/wjr.v14.i8.286

ISSN 1949-8470 (online)

MINIREVIEWS

Progress in interventional radiology treatment of pulmonary embolism: A brief review

Alessandro Posa, Pierluigi Barbieri, Giulia Mazza, Alessandro Tanzilli, Roberto Iezzi, Riccardo Manfredi, Cesare Colosimo

Specialty type: Radiology, nuclear medicine and medical imaging

Provenance and peer review: Invited article; Externally peer reviewed.

Peer-review model: Single blind

Peer-review report's scientific quality classification

Grade A (Excellent): A
Grade B (Very good): 0
Grade C (Good): C
Grade D (Fair): 0
Grade E (Poor): 0

P-Reviewer: Lv XL, China; Schoenhagen P, United States

Received: March 20, 2022
Peer-review started: March 20, 2022
First decision: May 31, 2022
Revised: June 14, 2022
Accepted: August 6, 2022
Article in press: August 6, 2022
Published online: August 28, 2022

Alessandro Posa, Pierluigi Barbieri, Giulia Mazza, Alessandro Tanzilli, Roberto Iezzi, Riccardo Manfredi, Cesare Colosimo, Department of Diagnostic Imaging, Oncologic Radiotherapy and Hematology, Fondazione Policlinico Universitario A. Gemelli IRCCS, Rome 00168, Italy

Corresponding author: Alessandro Posa, MD, Doctor, Department of Diagnostic Imaging, Oncologic Radiotherapy and Hematology, Fondazione Policlinico Universitario A. Gemelli IRCCS, L.go A. Gemelli 8, Rome 00168, Italy. alessandro.posa@gmail.com

Abstract

Pulmonary embolism represents a common life-threatening condition. Prompt identification and treatment of this pathological condition are mandatory. In cases of massive pulmonary embolism and hemodynamic instability or right heart failure, interventional radiology treatment for pulmonary embolism is emerging as an alternative to medical treatment (systemic thrombolysis) and surgical treatment. Interventional radiology techniques include percutaneous endovascular catheter directed therapies as selective thrombolysis and thrombus aspiration, which can prove useful in cases of failure or infeasibility of medical and surgical approaches.

Key Words: Pulmonary embolism; Interventional radiology; Thrombolysis; Thrombectomy; Catheter directed therapy; Endovascular

Core Tip: Endovascular treatment of massive pulmonary embolism can be a life-saving intervention in hemodynamically unstable patients.

Citation: Posa A, Barbieri P, Mazza G, Tanzilli A, Iezzi R, Manfredi R, Colosimo C. Progress in interventional radiology treatment of pulmonary embolism: A brief review. *World J Radiol* 2022; 14(8): 286-292

URL: https://www.wjgnet.com/1949-8470/full/v14/i8/286.htm

DOI: https://dx.doi.org/10.4329/wjr.v14.i8.286

INTRODUCTION

Venous thromboembolism, clinically presenting as deep vein thrombosis or pulmonary embolism (PE), is the third most frequent acute cardiovascular syndrome globally, after myocardial infarction and stroke[1]. Approximately one-third of all patients with a new diagnosis of venous thromboembolism have PE, with or without deep vein thrombosis[2]. PE can be defined as the occlusion of the pulmonary arteries or its branches with embolic material (thrombus, air, fat or amniotic fluid) that originates elsewhere in the body. Most commonly, the cause is a thrombus arising from the deep veins of the lower extremities, which travels to the pulmonary circulation.

Diagnosis of PE can be subtle, as there are no specific symptoms, and clinical presentation varies widely, ranging from asymptomatic to sudden cardiac death, which is seen in 25%-30% of patients[3]. There have been many advances in the field of PE in the recent decades. The development of new diagnostic and therapeutic strategies, including medical and surgical treatment as well as endovascular therapy, has led to an increasing complexity of patient treatment and, consequently, to the need of optimizing the management of this serious condition.

PHYSIOPATHOLOGY

PE, by definition, is characterized by the presence of emboli in the pulmonary arterial circulation. Most emboli originate as thrombi in the deep veins of the lower extremities; the most common site of thrombosis is represented by the calf veins, followed by femoro-popliteal veins and iliac veins. Less frequently, emboli arise from upper extremity veins and are typically associated with central venous catheters, intracardiac devices, malignancy or venous trauma. A smaller percentage of PE is caused by pelvic deep vein thrombosis, but they are generally associated with a predisposing factor such as pelvic infection, pelvic surgery or pregnancy[4]. When 25%-30% of the pulmonary vasculature is obliterated by a thrombo-embolus, pulmonary artery pressure begins to increase. However, the mechanical obstruction is not the only element leading to pulmonary hypertension: the disruption of the alveolar-capillary membrane by the thrombi results in a decrease of oxygen diffusion, with subsequent hypoxia and release of vasoconstrictors that contribute to the acute development of pulmonary hypertension[5]. The increase of pression in the pulmonary artery determines heterogeneity of pulmonary perfusion, leading to the simultaneous presence of hypo- and hyperperfused areas; there will be an imbalance between ventilation and perfusion, generating hypoxemia[6].

Moreover, PE can have significant cardiac and hemodynamic consequences, related to the size of emboli and the presence or absence of underlying cardiopulmonary disease. In healthy patients, the mean pulmonary artery pressure can be up to 40 mmHg acutely; right ventricle (RV) failure ensues when 50%-75% of pulmonary arteries are obstructed[7]. When the degree of pulmonary artery obstruction exceeds 50%-75%, the right heart dilates and the combination of the increased wall stress and cardiac ischemia impair RV function and left ventricular (LV) output, leading to hypotension[8]. The presence of pre-existing cardiopulmonary disease results in diminished pulmonary vascular reserve and hemodynamic compromise at a lower level of pulmonary arterial obstruction.

PULMONARY EMBOLISM RISK STRATIFICATION

The American Heart Association (AHA) and the European Society of Cardiology (ESC) classified PE according to its severity, identifying three main categories[1,9].

Patients with massive (AHA) or high risk (ESC) PE present with hypotension, defined as a systolic blood pressure lower than 90 mmHg, or a drop of > 40 mmHg for at least 15 min or need for vasopressor support.

Submassive (AHA) or intermediate risk (ESC) classifications slightly differ as, according to AHA, patients with submassive PE present with an RV strain with no hypotension. RV strain is defined as: RV dysfunction on echocardiography or computed tomography pulmonary angiography, and RV injury identified by an increase in cardiac biomarkers as troponins or brain natriuretic hormone. On the other side, the ESC criteria for intermediate-risk PE include patients with a simplified Pulmonary Embolism Severity Index score ≥ 1, regardless of RV strain. The Pulmonary Embolism Severity Index score is based on the patient's age, comorbidities, heart rate, blood pressure and oxygen saturation. Moreover, the ESC subclassifies intermediate-risk patients in two groups based on RV dysfunction and RV injury (intermediate risk–high) or only one or neither of these findings (intermediate risk–low).

Low risk patients, according to both AHA and ESC, do not meet criteria for the abovementioned risk categories.

MEDICAL AND SURGICAL TREATMENT

Severe PE leads to hypoxaemia due to the ventilation-perfusion mismatch. Therefore, it is advised to use oxygen in patients with oxygen saturation < 90%. High-flow oxygen and mechanical ventilation should be taken in consideration when extreme hemodynamic instability is present (*i.e.* cardiac arrest), even though obtaining a good hypoxemia correction is not completely possible without PE reperfusion techniques[10,11]. Intubation should be considered in patients who are not manageable with noninvasive ventilation[1].

Acute RV failure is a cause of death in high-risk PE patients due to the reduction of cardiac output. When low central venous pressure is present, modest fluid challenge (< 500 mL) could be an option, increasing cardiac index in these patients[12]. On the other hand, fluid challenge could also over-distend the RV, leading to a reduction of cardiac output. Therefore, it is recommended to use it wisely[13]. If signs of elevated central venous pressure are present, no volume loading is advised. Vasopressors are often necessary in association with reperfusion treatment (medical, surgical or interventional). Norepinephrine leads to an improvement in coronary perfusion and ventricular systolic interaction, without changing pulmonary vascular resistance[14]; the use of norepinephrine should be limited in patients with cardiogenic shock.

Temporary extracorporeal membrane oxygenation could be used in patients with a high-risk PE, cardiac arrest and circulatory collapse, but its use needs to be further tested with clinical trials[15,16].

Acute PE may lead to cardiac arrest, in which case the current advanced life support guidelines have to be followed[17].

Moreover, in patients with intermediate to high risk of PE, it is advised to start subcutaneous anticoagulation while waiting for diagnostic tests, usually with low-molecular weight heparin, fondaparinux or unfractionated heparin[18]. Clinical trials with non-vitamin K antagonist oral anticoagulants are ongoing.

Vitamin K antagonists are vastly used for oral anticoagulation in recent years; when vitamin K antagonists are used, low-molecular weight heparin or unfractionated heparin should be continued along with oral anticoagulants for more than 5 d until the International Normalized Ratio value reaches 2-3 for 2 d[19].

Regarding reperfusion treatment, systemic thrombolysis leads to fast improvement of the pulmonary obstruction and cardiovascular parameters in patients with PE compared to medical treatment alone[20,21]. The best results are obtained when reperfusion treatment starts 48 h after symptoms onset; however thrombolysis could be useful even after 6-14 d[22]. Intravenous administration of recombinant tissue-type plasminogen activator is preferred to first generation thrombolytic agents (*i.e.* urokinase)[23].

Surgical embolectomy in patients with acute PE is performed through cardiopulmonary bypass, with incision of the pulmonary arteries and clots removal. This approach is advised in high-risk PE and in selected intermediate-risk patients[1,24].

ENDOVASCULAR TREATMENTS: CURRENT EVIDENCE AND FUTURE PERSPECTIVES

Catheter directed thrombolysis

Catheter directed thrombolysis (CDT) gives the advantage of locally delivering a high concentration of fibrinolytic agent to a great clot surface. This way, fibrinolytic dose can be greatly reduced compared to the systemic one, and side effects are therefore lower. A routine use diagnostic angiography catheter with multiple holes can be used to deliver the fibrinolytic agent and increase its local blood concentration. This could enhance the efficiency of fibrinolysis, reducing the risk of bleeding. Each pulmonary artery is catheterized with a multihole catheter, and a fibrinolytic agent such as tissue plasminogen activator is injected through the clot at a rate of 1 mg/h for 24 h in case of a unilateral PE (single device) and 1 mg/h for 12 h if bilateral PE (double device) (SEATTLE II Trial)[25]. A more recent trial, the OPTALYSE PE trial, analyzed the possibility to further lower the dose of tissue plasminogen activator with shorter infusions. The total dose was significantly lower, ranging from 4 to 12 mg per lung, and shorter infusion times (2 to 6 h)[26].

Efficient systemic administration of heparin is continued throughout the endovascular fibrinolysis procedure. Despite the lack of randomized trial studies comparing endovascular and systemic thrombolytic therapy, several comparative studies have been carried out. In a meta-analysis of Bloomer *et al*[27], the rate of intracranial hemorrhage with CDT was 0.35%, which is significantly lower than that reported with systemic thrombolytics in other randomized trials (1.46%). Bloomer *et al*[27] also found that the rate of major bleeding or vascular complication was 4.65%, and the observed mortality rate was 3.4% (12.9% in the massive PE group, 0.74% in the submassive PE group).

In addition, results of an American national registry enrolling 3107 patients who underwent systemic fibrinolytic treatment and 1319 patients undergoing CDT showed that the systemic thrombolysis group had increased rates of bleeding-related mortality (18.1% *vs* 8.4%), general mortality (14.9% *vs* 6.12%) and rehospitalization (10.6% *vs* 7.6%)[28]. According to these data, the risk of fatal bleeding is lower during CDT than in cases of systemic thrombolysis. This can be due to the higher (approximately four-fold)

Table 1 Main mechanical thrombectomy devices

Rheolytic	Rotational	Aspiration +/- retriever	Fragmentation	Ultrasound
Angiojet (*Boston Scientific*)	Aspirex (*Straub Medical*)	Indigo CAT8 (*Penumbra Inc.*); Flowtriever (*Inari*)	Fogarty arterial balloon embolectomy catheter (*Edwards*); Pig-Tail Catheters	Ekos endovascular system (*Boston Scientific*)

dose of fibrinolytic agent used in systemic thrombolysis. However, as these data are extracted from a national registry and not from randomized studies, they should cautiously be taken in consideration. The ongoing PE-TRACT and HI-PEITHO studies are designed to overcome this issue.

Mechanical thrombectomy

In cases of massive PE, the first aim should be to quickly declot the affected pulmonary artery to decrease pulmonary hypertension and the risk of RV failure. Initial fragmentation or thrombectomy by different devices (Table 1) can help reduce the thrombotic load and improve reperfusion. In addition, fragmentation of the clot exposes a greater surface of the thrombus, increasing the efficacy of local or systemic therapies[29].

Current catheters for mechanical thrombectomy or endovascular aspiration are classified based on the mechanism of action.

Rheolytic: AngioJet (Boston Scientific, Massachusetts, United States) working mechanism is determined by aspiration of the thrombus using the Venturi-Bernoulli effect. It creates a suction effect with high-pressure jets in the catheter's distal holes. Various complications (*e.g.*, bradycardia and heart attack, severe hemoptysis, kidney failure as well as intra- and periprocedural deaths) were reported during the use of this device[30]; hence, the use of AngioJet as a first-approach treatment should be avoided. Currently the main indication of this product remains treatment of peripheral venous districts.

Rotational: A relatively new device for treatment of PE is Aspirex (Straub, Wangs, Switzerland). Launched in mid-2010, the Aspirex catheter acts as an Archimedean screw that rotates inside the catheter lumen; this spiral mechanism provides an aspiration supplied by an active motor. Clinical results are promising; however, only recent studies with small cohorts of patients demonstrated its safety and efficacy, and there is a lack of randomized studies supporting this evidence[31]. Two European case series have been reported, with complete thrombus clearance observed in 83% to 88% of patients with intermediate- and high-risk PE[31,32].

Aspiration: The Indigo mechanical aspiration system (Penumbra, Alameda, United States) is an aspiration thrombectomy catheter system. A large caliber (8 French) catheter with a directional soft tip, allows easy aspiration of the clots in the pulmonary arteries due to the great suction power of a suction pump. Several studies are being performed to evaluate safety and efficacy of this device. The recent Indigo Aspiration System for Treatment of Pulmonary Embolism Trial (EXTRACT-PE), a prospective multicenter study on 119 patients demonstrated a significant reduction in the RV/LV ratio and a low major adverse event rate in submassive PE patients treated with the Indigo CAT8 aspiration system, with a reduction of administered intraprocedural thrombolytic drugs, which were avoided in 98.3% of patients[33]. The Indigo CAT8 received Food and Drug Administration approval for PE treatment in December 2019. The system is being monitored to assess its safety even in real-world clinical practice, showing a low incidence of reports linked to the product[34].

FlowTriever® System (Inari Medical) is another aspiration device. Its mechanism features three self-expanding nitinol mesh disks designed to engage, disrupt and deliver the clot to the Triever Aspiration Catheter for extraction. It has been evaluated in a recent single-arm multicenter trial involving 106 patients (FLARE Study) and appears safe and effective in patients with acute intermediate-risk PE, with significant improvement in RV/LV ratio and minimal major bleeding[35]. In 2021 Inari Medical, Inc. announced enrollment of the PEERLESS randomized controlled trial comparing the clinical outcomes of patients with intermediate-high risk PE treated with the company's FlowTriever system *vs* CDT (NCT05111613). PEERLESS is a prospective, multicenter trial that will include up to 700 patients and 60 centers in the United States and Europe. It will be the first ever randomized controlled trial to compare mechanical thrombectomy to catheter-directed thrombolysis for the treatment of PE and aims to provide definitive data on interventional treatment options for these patients.

Fragmentation: The EKOSonic system (Boston Scientific, Massachusetts, United States) is an ultrasound-assisted catheter-directed thrombolysis system, which was specifically indicated for treatment of PE. The ultrasound waves that depart from the interior of the 5.4 French catheter can reach and treat the whole thrombus; in addition, fibrinolytic agent infusion can be performed from the catheter, combining the two treatment modalities. The functioning tip of the catheter can be of different lengths, with a range from 6 to 50 cm. Although it has been associated with a relatively safe and effective profile, the clinical benefits of this treatment when compared to classical CDT has yet to be proven[25]. Ultrasound-assisted thrombolysis was shown in a randomized trial named ULTIMA to determine faster decreases of the

RV/LV ratio in patients with acute onset of intermediate-risk PE when compared to medical treatment, with no occurrence of major bleeding. However, the authors did not observe variations in 90-d patient mortality[36].

CONCLUSION

Actual ESC guidelines indicate that in high-risk or intermediate/high-risk patients (with RV dysfunction at transthoracic ultrasonography or at computed tomography pulmonary angiography or Pulmonary Embolism Severity Index greater than 1 and positive troponin test), reperfusion treatments should be performed, in association with prompt hemodynamic support[1]. However, systemic thrombolysis is actually considered as the first indication, and as literature evidence states surgical pulmonary embolectomy is recommended in patients with high-risk PE in whom systemic thrombolysis is contraindicated or has failed (level of evidence I). Percutaneous catheter-directed treatment has level of evidence IIa and therefore should be conditionally considered after failure or infeasibility of the abovementioned medical and surgical therapies[2].

Set up of a multidisciplinary team and of management protocols for high-risk and intermediate/high-risk patients with PE should be considered, to promptly and correctly address every PE case.

New perspectives

The 2021 announcement of the multicentric prospective PEERLESS randomized controlled trial comparing aspiration thrombectomy *vs* catheter-directed thrombolysis in up to 700 patients will provide real-life data on interventional radiology treatments for patients with intermediate/high-risk PE. At the same time, ultrasonography-assisted thrombolysis is proving valuable in intermediate/high-risk PE patients with good results and low complication rates[36]. However, more prospective studies are needed to shed light on the best interventional radiology treatment for this critical condition as well as to give the right place in the guidelines to these endovascular and mini-invasive techniques, on par to medical and surgical treatments.

FOOTNOTES

Author contributions: Posa A designed the research study; Posa A, Barbieri P, Tanzilli A and Mazza G performed the research and wrote the manuscript; Posa A, Iezzi R, Manfredi R and Colosimo C revised the manuscript; All authors have read and approved the final manuscript.

Conflict-of-interest statement: All the Authors have no conflict of interest to disclose.

Country/Territory of origin: Italy

ORCID number: Alessandro Posa 0000-0001-9617-3413; Roberto Iezzi 0000-0002-2791-481X; Riccardo Manfredi 0000-0002-4972-9500.

S-Editor: Liu JH
L-Editor: Filipodia
P-Editor: Liu JH

REFERENCES

1 **Konstantinides SV**, Meyer G, Becattini C, Bueno H, Geersing GJ, Harjola VP, Huisman MV, Humbert M, Jennings CS, Jiménez D, Kucher N, Lang IM, Lankeit M, Lorusso R, Mazzolai L, Meneveau N, Ní Áinle F, Prandoni P, Pruszczyk P, Righini M, Torbicki A, Van Belle E, Zamorano JL; ESC Scientific Document Group. 2019 ESC Guidelines for the diagnosis and management of acute pulmonary embolism developed in collaboration with the European Respiratory Society (ERS). *Eur Heart J* 2020; **41**: 543-603 [PMID: 31504429 DOI: 10.1093/eurheartj/ehz405]

2 **Ortel TL**, Neumann I, Ageno W, Beyth R, Clark NP, Cuker A, Hutten BA, Jaff MR, Manja V, Schulman S, Thurston C, Vedantham S, Verhamme P, Witt DM, D Florez I, Izcovich A, Nieuwlaat R, Ross S, J Schünemann H, Wiercioch W, Zhang Y. American Society of Hematology 2020 guidelines for management of venous thromboembolism: treatment of

deep vein thrombosis and pulmonary embolism. *Blood Adv* 2020; **4**: 4693-4738 [PMID: 33007077 DOI: 10.1182/bloodadvances.2020001830]

3 **Morrone D**, Morrone V. Acute Pulmonary Embolism: Focus on the Clinical Picture. *Korean Circ J* 2018; **48**: 365-381 [PMID: 29737640 DOI: 10.4070/kcj.2017.0314]

4 **Turetz M**, Sideris AT, Friedman OA, Triphathi N, Horowitz JM. Epidemiology, Pathophysiology, and Natural History of Pulmonary Embolism. *Semin Intervent Radiol* 2018; **35**: 92-98 [PMID: 29872243 DOI: 10.1055/s-0038-1642036]

5 **Stratmann G**, Gregory GA. Neurogenic and humoral vasoconstriction in acute pulmonary thromboembolism. *Anesth Analg* 2003; **97**: 341-354 [PMID: 12873915 DOI: 10.1213/01.ANE.0000068983.18131.F0]

6 **Fernandes CJ**, Luppino Assad AP, Alves-Jr JL, Jardim C, de Souza R. Pulmonary Embolism and Gas Exchange. *Respiration* 2019; **98**: 253-262 [PMID: 31390642 DOI: 10.1159/000501342]

7 **Matthews JC**, McLaughlin V. Acute right ventricular failure in the setting of acute pulmonary embolism or chronic pulmonary hypertension: a detailed review of the pathophysiology, diagnosis, and management. *Curr Cardiol Rev* 2008; **4**: 49-59 [PMID: 19924277 DOI: 10.2174/157340308783565384]

8 **Wood KE**. Major pulmonary embolism: review of a pathophysiologic approach to the golden hour of hemodynamically significant pulmonary embolism. *Chest* 2002; **121**: 877-905 [PMID: 11888976 DOI: 10.1378/chest.121.3.877]

9 **Giri J**, Sista AK, Weinberg I, Kearon C, Kumbhani DJ, Desai ND, Piazza G, Gladwin MT, Chatterjee S, Kobayashi T, Kabrhel C, Barnes GD. Interventional Therapies for Acute Pulmonary Embolism: Current Status and Principles for the Development of Novel Evidence: A Scientific Statement From the American Heart Association. *Circulation* 2019; **140**: e774-e801 [PMID: 31585051 DOI: 10.1161/CIR.0000000000000707]

10 **Messika J**, Goutorbe P, Hajage D, Ricard JD. Severe pulmonary embolism managed with high-flow nasal cannula oxygen therapy. *Eur J Emerg Med* 2017; **24**: 230-232 [PMID: 28452810 DOI: 10.1097/MEJ.0000000000000420]

11 **Lacroix G**, Pons F, D'Aranda E, Legodec J, Romanat PE, Goutorbe P. High-flow oxygen, a therapeutic bridge while awaiting thrombolysis in pulmonary embolism? *Am J Emerg Med* 2013; **31**: 463.e1-463.e2 [PMID: 23159426 DOI: 10.1016/j.ajem.2012.08.030]

12 **Mercat A**, Diehl JL, Meyer G, Teboul JL, Sors H. Hemodynamic effects of fluid loading in acute massive pulmonary embolism. *Crit Care Med* 1999; **27**: 540-544 [PMID: 10199533 DOI: 10.1097/00003246-199903000-00032]

13 **Green EM**, Givertz MM. Management of acute right ventricular failure in the intensive care unit. *Curr Heart Fail Rep* 2012; **9**: 228-235 [PMID: 22805893 DOI: 10.1007/s11897-012-0104-x]

14 **Ghignone M**, Girling L, Prewitt RM. Volume expansion *vs* norepinephrine in treatment of a low cardiac output complicating an acute increase in right ventricular afterload in dogs. *Anesthesiology* 1984; **60**: 132-135 [PMID: 6198941 DOI: 10.1097/00000542-198402000-00009]

15 **Corsi F**, Lebreton G, Bréchot N, Hekimian G, Nieszkowska A, Trouillet JL, Luyt CE, Leprince P, Chastre J, Combes A, Schmidt M. Life-threatening massive pulmonary embolism rescued by venoarterial-extracorporeal membrane oxygenation. *Crit Care* 2017; **21**: 76 [PMID: 28347320 DOI: 10.1186/s13054-017-1655-8]

16 **Meneveau N**, Guillon B, Planquette B, Piton G, Kimmoun A, Gaide-Chevronnay L, Aissaoui N, Neuschwander A, Zogheib E, Dupont H, Pili-Floury S, Ecarnot F, Schiele F, Deye N, de Prost N, Favory R, Girard P, Cristinar M, Ferré A, Meyer G, Capellier G, Sanchez O. Outcomes after extracorporeal membrane oxygenation for the treatment of high-risk pulmonary embolism: a multicentre series of 52 cases. *Eur Heart J* 2018; **39**: 4196-4204 [PMID: 30137303 DOI: 10.1093/eurheartj/ehy464]

17 **Perkins GD**, Olasveengen TM, Maconochie I, Soar J, Wyllie J, Greif R, Lockey A, Semeraro F, Van de Voorde P, Lott C, Monsieurs KG, Nolan JP; European Resuscitation Council. European Resuscitation Council Guidelines for Resuscitation: 2017 update. *Resuscitation* 2018; **123**: 43-50 [PMID: 29233740 DOI: 10.1016/j.resuscitation.2017.12.007]

18 **Soar J**, Nolan JP, Böttiger BW, Perkins GD, Lott C, Carli P, Pellis T, Sandroni C, Skrifvars MB, Smith GB, Sunde K, Deakin CD; Adult advanced life support section Collaborators. European Resuscitation Council Guidelines for Resuscitation 2015: Section 3. Adult advanced life support. *Resuscitation* 2015; **95**: 100-147 [PMID: 26477701 DOI: 10.1016/j.resuscitation.2015.07.016]

19 **Witt DM**, Clark NP, Kaatz S, Schnurr T, Ansell JE. Guidance for the practical management of warfarin therapy in the treatment of venous thromboembolism. *J Thromb Thrombolysis* 2016; **41**: 187-205 [PMID: 26780746 DOI: 10.1007/s11239-015-1319-y]

20 **Goldhaber SZ**, Haire WD, Feldstein ML, Miller M, Toltzis R, Smith JL, Taveira da Silva AM, Come PC, Lee RT, Parker JA. Alteplase *vs* heparin in acute pulmonary embolism: randomised trial assessing right-ventricular function and pulmonary perfusion. *Lancet* 1993; **341**: 507-511 [PMID: 8094768 DOI: 10.1016/0140-6736(93)90274-k]

21 **Kline JA**, Nordenholz KE, Courtney DM, Kabrhel C, Jones AE, Rondina MT, Diercks DB, Klinger JR, Hernandez J. Treatment of submassive pulmonary embolism with tenecteplase or placebo: cardiopulmonary outcomes at 3 mo: multicenter double-blind, placebo-controlled randomized trial. *J Thromb Haemost* 2014; **12**: 459-468 [PMID: 24484241 DOI: 10.1111/jth.12521]

22 **Daniels LB**, Parker JA, Patel SR, Grodstein F, Goldhaber SZ. Relation of duration of symptoms with response to thrombolytic therapy in pulmonary embolism. *Am J Cardiol* 1997; **80**: 184-188 [PMID: 9230156 DOI: 10.1016/s0002-9149(97)00315-9]

23 **Sharifi M**, Bay C, Skrocki L, Rahimi F, Mehdipour M; "MOPETT" Investigators. Moderate pulmonary embolism treated with thrombolysis (from the "MOPETT" Trial). *Am J Cardiol* 2013; **111**: 273-277 [PMID: 23102885 DOI: 10.1016/j.amjcard.2012.09.027]

24 **Lee T**, Itagaki S, Chiang YP, Egorova NN, Adams DH, Chikwe J. Survival and recurrence after acute pulmonary embolism treated with pulmonary embolectomy or thrombolysis in New York State, 1999 to 2013. *J Thorac Cardiovasc Surg* 2018; **155**: 1084-1090.e12 [PMID: 28942971 DOI: 10.1016/j.jtcvs.2017.07.074]

25 **Piazza G**, Hohlfelder B, Jaff MR, Ouriel K, Engelhardt TC, Sterling KM, Jones NJ, Gurley JC, Bhatheja R, Kennedy RJ, Goswami N, Natarajan K, Rundback J, Sadiq IR, Liu SK, Bhalla N, Raja ML, Weinstock BS, Cynamon J, Elmasri FF, Garcia MJ, Kumar M, Ayerdi J, Soukas P, Kuo W, Liu PY, Goldhaber SZ; SEATTLE II Investigators. A Prospective, Single-Arm, Multicenter Trial of Ultrasound-Facilitated, Catheter-Directed, Low-Dose Fibrinolysis for Acute Massive and

Submassive Pulmonary Embolism: The SEATTLE II Study. *JACC Cardiovasc Interv* 2015; **8**: 1382-1392 [PMID: 26315743 DOI: 10.1016/j.jcin.2015.04.020]

26 **Tapson VF**, Sterling K, Jones N, Elder M, Tripathy U, Brower J, Maholic RL, Ross CB, Natarajan K, Fong P, Greenspon L, Tamaddon H, Piracha AR, Engelhardt T, Katopodis J, Marques V, Sharp ASP, Piazza G, Goldhaber SZ. A Randomized Trial of the Optimum Duration of Acoustic Pulse Thrombolysis Procedure in Acute Intermediate-Risk Pulmonary Embolism: The OPTALYSE PE Trial. *JACC Cardiovasc Interv* 2018; **11**: 1401-1410 [PMID: 30025734 DOI: 10.1016/j.jcin.2018.04.008]

27 **Bloomer TL**, El-Hayek GE, McDaniel MC, Sandvall BC, Liberman HA, Devireddy CM, Kumar G, Fong PP, Jaber WA. Safety of catheter-directed thrombolysis for massive and submassive pulmonary embolism: Results of a multicenter registry and meta-analysis. *Catheter Cardiovasc Interv* 2017; **89**: 754-760 [PMID: 28145042 DOI: 10.1002/ccd.26900]

28 **Arora S**, Panaich SS, Ainani N, Kumar V, Patel NJ, Tripathi B, Shah P, Patel N, Lahewala S, Deshmukh A, Badheka A, Grines C. Comparison of In-Hospital Outcomes and Readmission Rates in Acute Pulmonary Embolism Between Systemic and Catheter-Directed Thrombolysis (from the National Readmission Database). *Am J Cardiol* 2017; **120**: 1653-1661 [PMID: 28882336 DOI: 10.1016/j.amjcard.2017.07.066]

29 **Patel N**, Patel NJ, Agnihotri K, Panaich SS, Thakkar B, Patel A, Savani C, Patel N, Arora S, Deshmukh A, Bhatt P, Alfonso C, Cohen M, Tafur A, Elder M, Mohamed T, Attaran R, Schreiber T, Grines C, Badheka AO. Utilization of catheter-directed thrombolysis in pulmonary embolism and outcome difference between systemic thrombolysis and catheter-directed thrombolysis. *Catheter Cardiovasc Interv* 2015; **86**: 1219-1227 [PMID: 26308961 DOI: 10.1002/ccd.26108]

30 **Kuo WT**, Gould MK, Louie JD, Rosenberg JK, Sze DY, Hofmann LV. Catheter-directed therapy for the treatment of massive pulmonary embolism: systematic review and meta-analysis of modern techniques. *J Vasc Interv Radiol* 2009; **20**: 1431-1440 [PMID: 19875060 DOI: 10.1016/j.jvir.2009.08.002]

31 **Dumantepe M**, Teymen B, Akturk U, Seren M. Efficacy of rotational thrombectomy on the mortality of patients with massive and submassive pulmonary embolism. *J Card Surg* 2015; **30**: 324-332 [PMID: 25683156 DOI: 10.1111/jocs.12521]

32 **Bayiz H**, Dumantepe M, Teymen B, Uyar I. Percutaneous aspiration thrombectomy in treatment of massive pulmonary embolism. *Heart Lung Circ* 2015; **24**: 46-54 [PMID: 25060976 DOI: 10.1016/j.hlc.2014.06.014]

33 **Sista AK**, Horowitz JM, Tapson VF, Rosenberg M, Elder MD, Schiro BJ, Dohad S, Amoroso NE, Dexter DJ, Loh CT, Leung DA, Bieneman BK, Perkowski PE, Chuang ML, Benenati JF; EXTRACT-PE Investigators. Indigo Aspiration System for Treatment of Pulmonary Embolism: Results of the EXTRACT-PE Trial. *JACC Cardiovasc Interv* 2021; **14**: 319-329 [PMID: 33454291 DOI: 10.1016/j.jcin.2020.09.053]

34 **Sedhom R**, Abdelmaseeh P, Haroun M, Megaly M, Narayanan MA, Syed M, Ambrosia AM, Kalra S, George JC, Jaber WA. Complications of Penumbra Indigo Aspiration Device in Pulmonary Embolism: Insights From MAUDE Database. *Cardiovasc Revasc Med* 2022; **39**: 97-100 [PMID: 34706845 DOI: 10.1016/j.carrev.2021.10.009]

35 **Tu T**, Toma C, Tapson VF, Adams C, Jaber WA, Silver M, Khandhar S, Amin R, Weinberg M, Engelhardt T, Hunter M, Holmes D, Hoots G, Hamdalla H, Maholic RL, Lilly SM, Ouriel K, Rosenfield K; FLARE Investigators. A Prospective, Single-Arm, Multicenter Trial of Catheter-Directed Mechanical Thrombectomy for Intermediate-Risk Acute Pulmonary Embolism: The FLARE Study. *JACC Cardiovasc Interv* 2019; **12**: 859-869 [PMID: 31072507 DOI: 10.1016/j.jcin.2018.12.022]

36 **Kucher N**, Boekstegers P, Müller OJ, Kupatt C, Beyer-Westendorf J, Heitzer T, Tebbe U, Horstkotte J, Müller R, Blessing E, Greif M, Lange P, Hoffmann RT, Werth S, Barmeyer A, Härtel D, Grünwald H, Empen K, Baumgartner I. Randomized, controlled trial of ultrasound-assisted catheter-directed thrombolysis for acute intermediate-risk pulmonary embolism. *Circulation* 2014; **129**: 479-486 [PMID: 24226805 DOI: 10.1161/CIRCULATIONAHA.113.005544]

World Journal of Radiology

Submit a Manuscript: https://www.f6publishing.com

World J Radiol 2022 August 28; 14(8): 293-310

DOI: 10.4329/wjr.v14.i8.293

ISSN 1949-8470 (online)

ORIGINAL ARTICLE

Retrospective Study

Imaging volumes during COVID-19: A Victorian health service experience

Jo-Anne Pinson, My Linh Diep, Vinay Krishnan, Caroline Aird, Cassie Cooper, Christopher Leong, Jeff Chen, Nicholas Ardley, Eldho Paul, Mohamed Khaldoun Badawy

Specialty type: Radiology, nuclear medicine and medical imaging

Provenance and peer review: Unsolicited article; Externally peer reviewed.

Peer-review model: Single blind

Peer-review report's scientific quality classification

Grade A (Excellent): A
Grade B (Very good): 0
Grade C (Good): C
Grade D (Fair): 0
Grade E (Poor): 0

P-Reviewer: Chen Q, China; Verde F, Italy

Received: March 16, 2022
Peer-review started: March 16, 2022
First decision: June 16, 2022
Revised: July 7, 2022
Accepted: July 20, 2022
Article in press: July 20, 2022
Published online: August 28, 2022

Jo-Anne Pinson, My Linh Diep, Vinay Krishnan, Caroline Aird, Cassie Cooper, Christopher Leong, Jeff Chen, Nicholas Ardley, Mohamed Khaldoun Badawy, Monash Health Imaging, Monash Health, Clayton, Victoria 3168, Australia

Jo-Anne Pinson, Department of Medical Imaging, Peninsula Health, Melbourne, Victoria 3099, Australia

Jo-Anne Pinson, Mohamed Khaldoun Badawy, Department of Medical Imaging and Radiation Sciences, School of Allied Health Care, Faculty of Medicine, Nursing and Health Sciences, Monash University, Clayton, Victoria 3800, Australia

Eldho Paul, Department of Epidemiology and Preventive Medicine, School of Public Health and Preventive Medicine, Monash University, Melbourne, Victoria 3800, Australia

Corresponding author: Mohamed Khaldoun Badawy, BSc, MSc, PhD, Senior Lecturer, Senior Scientist, Monash Health Imaging, Monash Health, 246 Clayton Road, Clayton, Victoria 3168, Australia. mohamed.badawy@monashhealth.org

Abstract

BACKGROUND

The World Health Organisation declared the coronavirus disease 2019 (COVID-19) a pandemic on March 11, 2020. While globally, the relative caseload has been high, Australia's has been relatively low. During the pandemic, radiology services have seen significant changes in workflow across modalities and a reduction in imaging volumes.

AIM

To investigate differences in modality imaging volumes during the COVID-19 pandemic across a large Victorian public health network.

METHODS

A retrospective analysis from January 2019 to December 2020 compared imaging volumes across two periods corresponding to the pandemic's first and second waves. Weekly volumes across patient class, modality and mobile imaging were summed for periods: wave 1 (weeks 11 to 16 for 2019; weeks 63 to 68 for 2020) and wave 2 (weeks 28 to 43 for 2019; weeks 80 to 95 for 2020). Microsoft Power Business Intelligence linked to the radiology information system was used to mine

all completed examinations.

RESULTS

Summed weekly data during the pandemic's first wave showed the greatest decrease of 29.8% in adult outpatient imaging volumes and 46.3% in paediatric emergency department imaging volumes. Adult nuclear medicine demonstrated the greatest decrease of 37.1% for the same period. Paediatric nuclear medicine showed the greatest decrease of 47.8%, with angiography increasing by 50%. The pandemic's second wave demonstrated the greatest decrease of 23.5% in adult outpatient imaging volumes, with an increase of 18.2% in inpatient imaging volumes. The greatest decrease was 28.5% in paediatric emergency department imaging volumes. Nuclear medicine showed the greatest decrease of 37.1% for the same period. Paediatric nuclear medicine showed the greatest decrease of 36.7%. Mobile imaging utilisation increased between 57.8% and 135.1% during the first and second waves. A strong correlation was observed between mobile and non-mobile imaging in the emergency setting (Spearman's correlation coefficient = -0.743, P = 0.000). No correlation was observed in the inpatient setting (Spearman's correlation coefficient = -0.059, P = 0.554).

CONCLUSION

Nuclear medicine was most impacted, while computed tomography and angiography were the least affected by the pandemic. The impact was less during the pandemic's second wave. Mobile imaging shows continuous growth during both waves.

Key Words: COVID-19; Pandemic; Radiology; Imaging volume; Modality; Mobile imaging

Core Tip: Analysis of weekly imaging modality volumes provides an overview of changes in service demand over time. We describe the changes in imaging modality and mobile imaging volumes during Victoria's first and second waves of the coronavirus disease 2019 pandemic.

Citation: Pinson JA, Diep ML, Krishnan V, Aird C, Cooper C, Leong C, Chen J, Ardley N, Paul E, Badawy MK. Imaging volumes during COVID-19: A Victorian health service experience. *World J Radiol* 2022; 14(8): 293-310
URL: https://www.wjgnet.com/1949-8470/full/v14/i8/293.htm
DOI: https://dx.doi.org/10.4329/wjr.v14.i8.293

INTRODUCTION

The World Health Organisation declared the coronavirus disease 2019 (COVID-19) a pandemic on March 11, 2020[1]. Healthcare facilities implemented strict infection control, social distancing protocols, and other measures in the interest of public health and safety[2]. In preparation for the surge in hospitalisations across the globe, overall elective surgical services decreased by approximately 72%[3]. In comparison, in Australia, this fell by about 69%. Others utilised computational modelling to help predict the health services saturation point for ICU beds and ventilators[4]. While globally, the relative caseload has been high, Australia's has been relatively low. In this context, during 2020, Victoria has experienced most of Australia's cases, with the new daily caseloads shown in Figure 1.

Due to the overwhelming prevalence of COVID-19 in various countries, for example, Italy, some radiology departments were dedicated to imaging COVID-19 patients only[5]. Radiology services have also seen significant changes in workflow across modalities and a reduction in imaging volumes[6-8]. For example, departments were re-configured to separate COVID-19 patients from non-infected patients, segregation of staff to reduce infection transmission, increased demand for PPE, radiologists reporting from home, and expansion of video conferencing use[5,9]. For patients presenting to the emergency department, general radiography was primarily used due to its accessibility, availability and low radiation levels. The chest X-ray was an ideal first choice for patients with typical symptoms of COVID-19, such as shortness of breath on exertion, persistent cough and chest pain [8]. To minimise the transmission risk of suspected COVID-19 (sCOVID) patients in hospital, mobile imaging became particularly important to manage workflow[10,11]. Imaging in the ward wearing PPE could reduce staff exposure, with effective cleaning of mobile units possible between imaging patients, without compromising patient care.

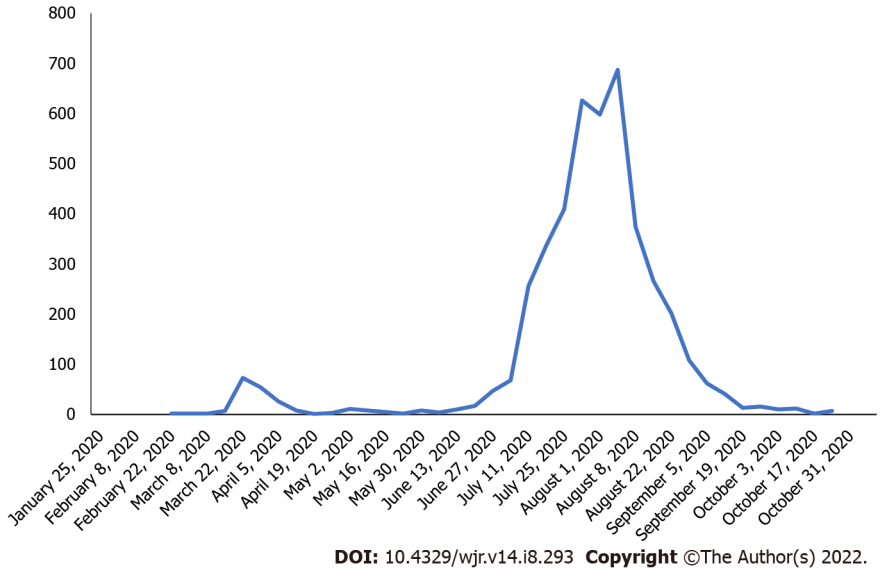

DOI: 10.4329/wjr.v14.i8.293

Figure 1 Victorian new the coronavirus disease 2019 case numbers by date from January 2020-November 2020.

While it has been reported, there was a decrease in patients presenting with stroke to our institution during the pandemic[7]. To our knowledge, little is known about the severity of impact on radiology volumes in Australia. While overall Australian imaging volumes were analysed through Medicare, no institutional experience has been presented[12].

Objectives

This study investigates the imaging volume changes during the pandemic across the network at a large Victorian public health service provider. A secondary aim was to study changes in mobile imaging utilisation and whether that impacted the use of fixed (non-mobile) X-ray imaging systems. This data will help inform radiology practices for service adaptation with subsequent pandemic phases or other "once in a lifetime" events.

MATERIALS AND METHODS

This health network has 98 imaging systems across eight imaging modalities analysed according to Table 1.

Study setting

Our network provided over three million episodes of care from 2019 to 2020. Three of our five hospitals provide accident and emergency services, and one is a geriatric centre, and the other is an oncology centre that did not service COVID-19-positive patients ('clean site'). Data from the geriatric and oncology centre were excluded due to heterogeneity in these sites. Significant federal, state and local health policy and guideline changes were implemented and updated during the pandemic that impacted the imaging pathway, including: patients with typical respiratory symptoms (fever, chest tightness, dyspnoea, cough) were classified as sCOVID-19 (suspected COVID-19); recommendation for all eligible sCOVID-19 patients to have computed tomography (CT) pulmonary angiography (CTPA) instead of V/Q scans[13]; rescheduling of non-urgent cases as discussed with referring clinicians; use of mobile X-ray to reduce infection transmission; social distancing guidelines restricting patient waiting room numbers and minimum area of 4 m^2 per person in shared spaces.

Data collection

Microsoft Power Business Intelligence, linked to the radiology information system, was used to mine all completed examinations between January 1, 2019 and December 31, 2020 across three sites. Imaging modality was defined as the device or technology used in medical imaging (general X-ray, mammography, nuclear medicine, CT, magnetic resonance imaging (MRI), fluoroscopy, angiography, ultrasound, with mobile X-ray being a subset of X-ray). Fixed or non-mobile imaging was an X-ray system permanently secured in an X-ray room. Mobile imaging was defined as using a portable X-ray imaging system capable of moving to different locations. Patient classes were defined by location (inpatient (IP), outpatient (OP) or emergency department (ED)). Adult patients were ≥ 16 years, while paediatric patients were aged < 16 years. Examinations were filtered by modality and patient class.

Table 1 List of equipment number across all modalities

Modality	MRI	NM	BMD	CT	X-ray	Fluoro	US	Angio
Equip No.	5	6	2	7	26	4	45	3

MRI: Magnetic resonance imaging; NM: Nanometer; BMD: Bone mineral densitometry; CT: Computed tomography; Fluoro: Fluoroscopy; US: Ultrasound; Angio: Angiography.

March 2020 and April 2020 [week 63 (March 11 to March 17) to week 68 (April 15 to April 21)] corresponded to Victoria's first wave of the pandemic; July 2020 to October 2020 [week 80 (July 9 to July 14) to week 95 (October 21 to October 26)] corresponded to the second wave of the pandemic. Figure 2 provides the timeline of the first and second waves for considering the impact on departmental caseloads. The outcome measure was total weekly completed imaging case numbers from Wednesday to Tuesday commencing Wednesday January 2 to Tuesday January 8, 2019 (week 1) for direct day matched weekly comparisons between 2019 and 2020, allowing for any periodic variability observed. Weekly modality data were summed to reflect the first and second waves of the pandemic.

Statistical analysis

Weekly volumes across patient class, modality and mobile imaging were summed for defined periods: wave 1 (weeks 11 to 16 for 2019; weeks 63 to 68 for 2020) and wave 2 (weeks 28 to 43 for 2019; weeks 80 to 95 for 2020). This was to evaluate the impact of COVID-19 on patient class, modality and mobile imaging case volumes during each COVID-19 wave. For analysis of mean weekly case numbers, pre-COVID data were defined as weeks 1 to 60 (*i.e.,* January 2, 2019 to February 29, 2020), while COVID-19 data were defined as the mean of weeks 61 to 104 (*i.e.,* March 1, 2020 to December 31, 2020). Independent sample *t*-tests were performed comparing the mean weekly imaging case volumes in the years 2020 and 2019 for each imaging modality type stratified by patient service locations for the pre-COVID-19 and post-COVID-19 periods with results presented as means and 95% confidence intervals (95%CI). The relationship between mobile and non-mobile imaging volumes was assessed using Spearman rank correlation. Statistical significance was considered for p values < 0.05. All analyses were performed using SAS version 9.4 (SAS Institute, Cary, NC, United States). Dr Eldho Paul reviewed the statistical methods of this study from Monash University.

This study was approved by the Monash Health Human Research Ethics Committee.

RESULTS

Adults

Total volume (all modalities): During the pandemic's first wave in Victoria, total adult imaging volume across all modalities declined by 20.7% between March 11 and April 21, 2020 (weeks 63 to 68) compared to the same time in 2019 (March 13 and April 23, 2019, weeks 11 to 16). During the pandemic's second wave, adult imaging volume across all modalities declined by 6.6% between July 8, and October 27, 2020 (weeks 80 to 95) compared to the same time in 2019 (July 10, and October 29, 2019, weeks 28 to 43).

Volume by patient class

Table 2 shows the summed weekly imaging volumes for the defined periods and the percentage of adult image volume change across all included modalities by patient class for weeks 11 to 16 (March 13 and April 23) and 28 to 43 (July 10 and October 29) in 2019 and weeks 63 to 68 (March 11 and April 21) and 80 to 95 (July 8 and 2October 27) in 2020.

Volume by modality: During the pandemic's first wave between March 11 and April 21, 2020 (weeks 63 to 68), adult angiography, bone mineral densitometry, computed tomography, fluoroscopy, general radiography, magnetic resonance imaging, mammography, nuclear medicine and ultrasound imaging volumes declined between 10.3% and 37.1% when compared to the same time in 2019 (March 13 and April 23, 2019, weeks 11 to 16) shown in Table 3.

During the pandemic's second wave between July 8 and October 27, 2020 (weeks 80 to 95), adult angiography, bone mineral densitometry, fluoroscopy, general radiography, magnetic resonance imaging, mammography, nuclear medicine and ultrasound services declined between 1.6% and 31.6%, while computed tomography increased by 1.7% when compared to the same time in 2019 (July 10 and October 29, 2019, weeks 28 to 43) shown in Table 4.

Figure 3 highlights the weekly adult modality imaging volumes.

Comparison of the adult mean weekly 2019 (pre-COVID-19, January 1, 2019 to February 29, 2020, weeks 1 to 61) with 2020 (March 1 to December 31, 2020 weeks 61 to 104) imaging volumes by modality, categorised by inpatient, outpatient and emergency services (Table 5) shows statistically significant

Table 2 Summed imaging volumes and percentage change in adult imaging volume across patient class in waves 1 and 2

Wave 1	2020 (weeks 63-68)	2019 (weeks 11-16)	% change	Wave 2	2020 (weeks 80-95)	2019 (weeks 28-43)	% change
ED	9521	12783	-25.5	ED	29454	32262	-8.7
IP	9210	9395	-2.0	IP	31424	26576	18.2
OP	8874	12636	-29.8	OP	26967	35236	-23.5
Overall	27605	34814	-20.7	Overall	87845	94074	-6.6

ED: Emergency department; IP: Inpatient; OP: Outpatient.

Table 3 Summed imaging volumes and percentage change in adult imaging volumes across modalities in wave 1

Wave 1	2020 (weeks 63-68)	2019 (weeks 11-16)	%
Angiography	269	300	-10.3
Bone Mineral Densitometry	185	239	-22.6
Computed Tomography	5883	6688	-12.0
Fluoroscopy	766	968	-20.9
General Radiography	11668	15311	-23.8
Magnetic Resonance Imaging	2013	2709	-25.7
Mammography	82	123	-33.3
Nuclear Medicine	394	626	-37.1
Ultrasound	6345	7850	-19.2
Total	27605	34814	-20.7

Table 4 Summed imaging volumes and percentage change in adult imaging volume across modalities in wave 2

Wave 2	2020 (weeks 80-95)	2019 (weeks 28-43)	%
Angiography	822	835	-1.6
Bone mineral densitometry	690	892	-22.6
Computed tomography	19316	18997	1.7
Fluoroscopy	2313	2550	-9.3
General radiography	36845	40592	-9.2
Magnetic resonance imaging	6685	7539	-11.3
Mammography	303	334	-9.3
Nuclear medicine	1149	1679	-31.6
Ultrasound	19722	20656	-4.5
Total	87845	94074	-6.6

declines in six imaging modalities ($P = 0.042$ to $P < 0.0001$). There were statistically significant declines in one inpatient imaging modality ($P = 0.002$) and nine outpatient imaging modalities ($P = 0.027$ to $P < 0.0001$). Statistically significant increases were observed in five inpatient modalities ($P = 0.0003$ to $P < 0.0001$). All patient classes observed overall declines across seven imaging modalities ($P = 0.027$ to $P < 0.0001$).

Mobile and non-mobile X-ray imaging: During the pandemic's first wave in Victoria, total adult mobile imaging volume increased by 57.8% between March 11 and April 21, 2020 (weeks 63 to 68) compared to the same time in 2019 (March 13 and April 23, 2019, weeks 11 to 16). During the pandemic's second wave, adult mobile imaging volume increased by 135.1% between July 8 and October 27, 2020 (weeks 80 to 95) compared to the same time in 2019 (July 10 and October 29, 2019, weeks 28 to 43). Table 6 highlights the mobile imaging changes across inpatient and emergency patient classes during the first

Table 5 Comparison of mean adult weekly imaging volumes for 2019 and 2020 including 95%CIs, by imaging modality categorised by patient setting

Adult Setting	Modality	2020			2019			*P* value
		Mean	Min-max	95%CI	Mean	Min-max	95%CI	
Emergency	Angiography	4.05	1-10	3.38-4.71	5.03	2-12	4.51-5.56	0.02
	Computed tomography	541.2	384-663	520-562.4	548.68	473-606	541.7-555.7	0.453
	Fluoroscopy	5.18	1-12	4.31-6.05	4.15	0-11	3.58-4.72	0.042
	Radiography	1162.64	925-1309	1133.02-1192.25	1299.03	1156-1446	1281.05-1317.02	< 0.0001
	Magnetic resonance imaging	12.11	3-27	10.35-13.87	18.55	9-30	17.09-20.01	< 0.0001
	Nuclear Medicine	3.27	0-8	2.66-3.88	7.55	0-21	6.43-8.67	< 0.0001
	Ultrasound	122.98	85-157	117.52-128.43	172.13	116-255	163.72-180.55	< 0.0001
	Mammography	0	0-0	0-0	0.02	-0.02-0.05	0-0.1	0.394
Inpatient	Angiography	38.8	23-53	36.25-41.34	29.48	17-43	27.94-31.02	< 0.0001
	Computed tomography	408.05	277-498	392.38-423.71	298.87	210-416	285.57-312.16	< 0.0001
	Fluoroscopy	125.98	82-162	120.33-131.63	129.25	80-155	125.39-133.11	0.325
	Radiography	855.64	557-1015	824.02-887.25	794.77	685-968	779.87-809.67	0.0003
	Magnetic resonance imaging	123.09	74-158	117.84-128.34	100.65	67-132	97.32-103.98	< 0.0001
	Nuclear Medicine	21.64	8-37	19.76-23.52	20.92	12-35	19.68-22.15	0.507
	Ultrasound	325.82	215-395	314.29-337.35	264.22	192- 323	256.97-271.46	< 0.0001
	Mammography	0.7	0-7	0.3-1.1	1.87	0-10	1.3-2.43	0.002
	Bone mineral densitometry	1.41	0-5	0.97-1.85	1.6	0-5	1.27-1.93	0.479
Outpatient	Angiography	9.0	2-26	7.47-10.53	17.08	5-30	15.86-18.31	< 0.0001
	Computed tomography	249.86	107-333	234.48-265.25	313.7	139-367	302.61-324.79	< 0.0001
	Fluoroscopy	17.61	6-37	15.2-20.03	24.78	5-43	22.97-26.59	< 0.0001
	Radiography	268.02	120-473	246.82-289.23	427.12	147-507	410.57-443.66	< 0.0001
	Magnetic resonance imaging	268.09	98-414	249.76-286.43	347.6	108-401	335.36- 359.84	< 0.0001
	Nuclear medicine	50.84	19-88	46.88-54.8	71.72	31-112	68.14-75.3	< 0.0001
	Ultrasound	768.48	492-943	741.33-795.62	855.27	554-931	836.21-874.32	< 0.0001
	Mammography	15.82	2-24	14.2-17.44	17.75	8-23	16.87-18.63	0.027
	Bone mineral densitometry	36.77	4-72	301.13-42.42	50.9	0-72	47.57-54.23	< 0.0001
All classes	Angiography	51.84	30-70	48.58-55.11	51.6	30-63	49.76-53.44	0.892
	Computed tomography	1199.11	768-1458	1154.65-1243.58	1161.25	962-1339	1141.96-1180.54	0.090
	Fluoroscopy	148.77	96-205	141.2-145.35	158.18	92-184	153.59-162.78	0.027
	Radiography	2286.3	1602-2603	2214.97-2357.62	2520.92	2310-2718	2498.03-2543.80	< 0.0001
	Magnetic resonance imaging	403.30	175-556	380.71-425.88	466.8	200-526	452.6-481.0	< 0.0001
	Nuclear medicine	75.75	29-128	70.65-80.85	100.18	46-134	96.21-104.15	< 0.0001
	Ultrasound	1217.27	808-1491	1178.47-1256.08	1291.62	918-1429	1268.35-1314.88	.001
	Mammography	16.52	2-24	14.87-18.17	19.63	10-30	18.61-20.66	0.001
	Bone mineral densitometry	38.18	5-74	32.33-44.03	52.5	0-72	49.13-55.87	< 0.0001
	Total	5437.05	3520-6441	5250.9-5623.8	5822.68	4645-6175	5750.97- 5894.4	< 0.0001

and second waves.

Comparison of the adult mean weekly 2019 (pre-COVID-19, January 2, 2019 to February 29, 2020, weeks 1 to 61) with 2020 (March 1 to December 31, 2020, weeks 61 to 104) mobile and non-mobile X-ray

Table 6 Summed imaging volumes and percentage change in adult mobile imaging volume across patient class in waves 1 and 2

Wave 1	2020 (weeks 63-68)	2019 (weeks 11-16)	% change	Wave 2	2020 (weeks 80-95)	2019 (weeks 28-43)	% change
ED	1952	372	424.7	ED	7526	1037	625.7
IP	2008	2138	-6.1	IP	8654	5845	48.1
Overall	3960	2510	57.8	Overall	16180	6882	135.1

ED: Emergency department; IP: Inpatient.

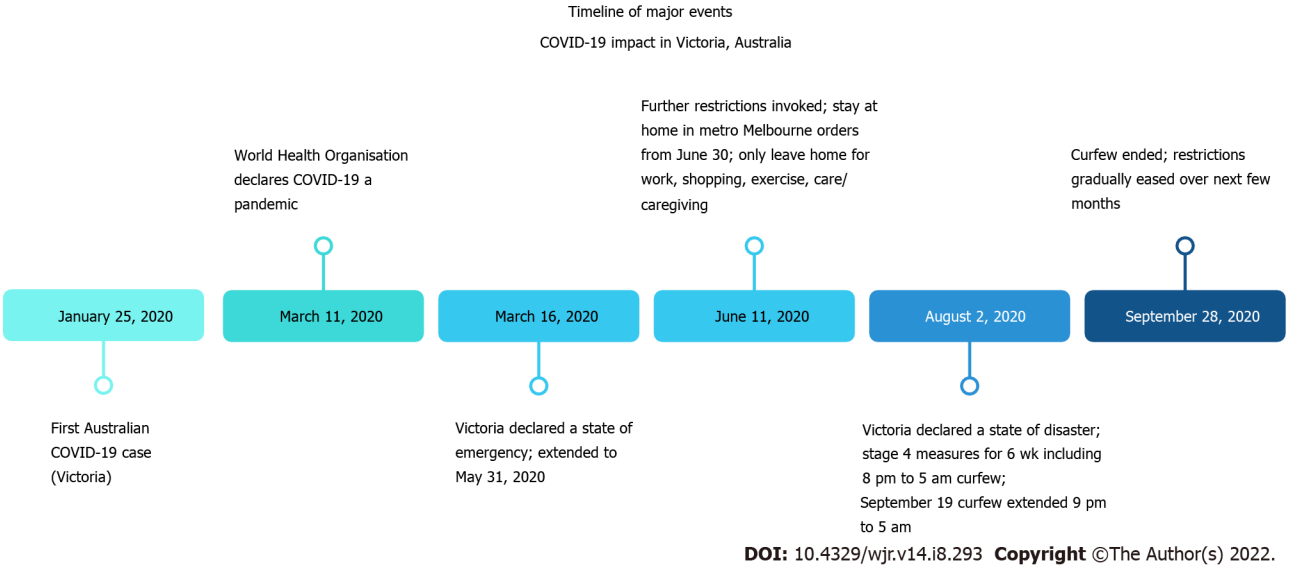

Figure 2 Timeline of significant events in Victoria, Australia during the first and second waves of the coronavirus disease 2019 pandemic. COVID-19: The coronavirus disease 2019.

imaging volumes, categorised by inpatient and emergency services (Table 7) shows statistically significant changes across all mobile and non-mobile imaging (P = 0.001 to < 0.0001). A strong correlation was observed between mobile and non-mobile imaging in the emergency setting (Spearman's correlation coefficient = -0.743, P = 0.000). No correlation was observed in the inpatient setting (Spearman's correlation coefficient = -0.059, P = 0.554). Figure 4 shows the weekly adult X-ray mobile and non-mobile imaging volumes.

Paediatrics

Total volume (all modalities): Total paediatric imaging volume across all modalities declined by 28.6% between March 11 and April 21, 2020 (weeks 63 to 68) compared to the same time in 2019 (March 13 and April 23, 2019, weeks 11 to 16). During the pandemic's second wave, paediatric imaging volume across all modalities declined by 6.6% between July 8 and October 27, 2020 (weeks 80 to 95) compared to the same time in 2019 (July 10 and October 29, 2019, weeks 28 to 43).

Volume by patient class: Table 8 shows the percentage of paediatric image volume change across all included modalities by patient class for weeks 11 to 16 and 28 to 43 in 2019 and weeks 63 to 68 and 80 to 95 in 2020.

During the pandemic's first wave between March 11 and April 21, 2020 (weeks 63-68), paediatric IP, OP and ED services declined by between 3.7% and 46.3% when compared to the same time in 2019 (March 13 and April 23 2019, weeks 11 to 16).

During the pandemic's second wave between July 8 and October 27, 2020 (weeks 80 to 95), paediatric IP, OP and ED services declined by between 16.1% and 28.5% when compared to the same time in 2019 (July 10 and October 29, 2019, weeks 28 to 43).

Volume by modality: During the pandemic's first wave between March 11 and April 21, 2020 (weeks 63 to 68), paediatric imaging modality services declined by between 18.6% and 47.8% and 18.6%, while angiography increased by 50% when compared to the same time in 2019 (March 13 and 23th April 2019, weeks 11 to 16 shown in Table 9.

Table 7 Comparison of mean adult weekly imaging volumes for 2019 and 2020 including 95%CIs, by mobile and non-mobile imaging categorised by patient setting

Adult Setting	Modality	2020			2019			*P* value
		Mean	Min-max	95%CI	Mean	Min-max	95%CI	
Emergency	Mobile	366.64	63- 550	330.11-403.17	63.23	45-85	60.86-65.61	< 0.0001
	Non-mobile	783.59	574-1190	739.11-828.08	1234.33	1095-1385	1216.54-1252.13	< 0.0001
Inpatient	Mobile	451.25	240-614	420.38-482.12	355.65	298-417	348.44-362.86	< 0.0001
	Non-mobile	404.00	310-514	386.64-421.36	438.93	339-564	428.10-449.77	0.001

Table 8 Summed imaging volumes and percentage change in paediatric imaging volume across patient class in waves 1 and 2

Wave 1	2020 (weeks 63-68)	2019 (weeks 11-16)	% change	Wave 2	2020 (weeks 80-95)	2019 (weeks 28-43)	% change
ED	804	1498	-46.3	ED	2780	3887	-28.5
IP	1799	2571	-30.0	IP	5818	6938	-16.1
OP	1162	1207	-3.7	OP	3041	3776	-19.5
Overall	3765	5276	-28.6	Overall	11639	14601	-20.3

ED: Emergency department; IP: Inpatient; OP: Outpatient.

Table 9 Summed imaging volumes and percentage change in paediatric imaging volume across modalities in wave 1

Wave 1	2020 (weeks 63-68)	2019 (weeks 11-16)	%
Angiography	9	6	50
Bone mineral densitometry	16	22	-27.3
Computed tomography	71	96	-26.0
Fluoroscopy	120	148	-18.9
General radiography	1896	2936	-35.4
Magnetic resonance imaging	253	340	-25.6
Nuclear medicine	12	23	-47.8
Ultrasound	1388	1705	-18.6

During the pandemic's second wave between July 8 and October 27, 2020 (weeks 80 to 95), paediatric imaging modality services declined by between 5.2% and 36.7% when compared to the same time in 2019 (July 10 and October 29, 2019, weeks 28 to 43), shown in Table 10. Figure 5 highlights the weekly paediatric modality imaging volumes.

Comparison of the paediatric mean weekly 2019 (pre-COVID-19, Jan 2nd 2019 to 29th Feb 2020, weeks 1 to 61) with 2020 (March 1st to Dec 31st 2020 weeks 61 to 104) imaging volumes by modality, categorised by inpatient, outpatient and emergency services (Table 11) shows statistically significant changes in two emergency imaging modalities ($P = 0.0001$ to $P < 0.0001$), two inpatient imaging modalities ($P = 0.0003$ to $P < 0.0001$), and four outpatient imaging modalities ($P = 0.019$ to $P < 0.0001$). Overall changes across all patient classes were observed in five imaging modalities ($P = 0.037$ to $P < 0.0001$).

Mobile and non-mobile X-ray imaging: During the pandemic's first wave in Victoria, total paediatric mobile imaging volume decreased by 0.7% between March 11 and April 21, 2020 (weeks 63 to 68) compared to the same time in 2019 (March 13 and April 23 2019, weeks 11 to 16). During the pandemic's second wave, paediatric mobile imaging volume decreased by 6.7% between July 8 and October 27, 2020 (weeks 80 to 95) compared to the same time in 2019 (July 10 and October 29, 2019, weeks 28 to 43). Table 12 highlights the mobile imaging changes across inpatient and emergency patient classes during the first and second waves.

Comparison of the paediatric mean weekly 2019 (pre-COVID-19, Jan 2nd 2019 to 29th Feb 2020, weeks 1 to 61) with 2020 (March 1st to Dec 31st 2020 weeks 61 to 104) mobile and non-mobile X-ray imaging volumes, categorised by inpatient and emergency services (Table 13) shows statistically significant

Table 10 Summed imaging volumes and percentage change in paediatric imaging volume across modalities in wave 2

Wave 2	2020 (weeks 80-95)	2019 (weeks 28-43)	%
Angiography	19	23	-17.4
Bone mineral densitometry	56	68	-17.6
Computed tomography	226	241	-6.2
Fluoroscopy	314	397	-20.9
General radiography	5472	7938	-31.1
Magnetic resonance imaging	874	922	-5.2
Nuclear medicine	38	60	-36.7
Ultrasound	4640	4952	-6.3

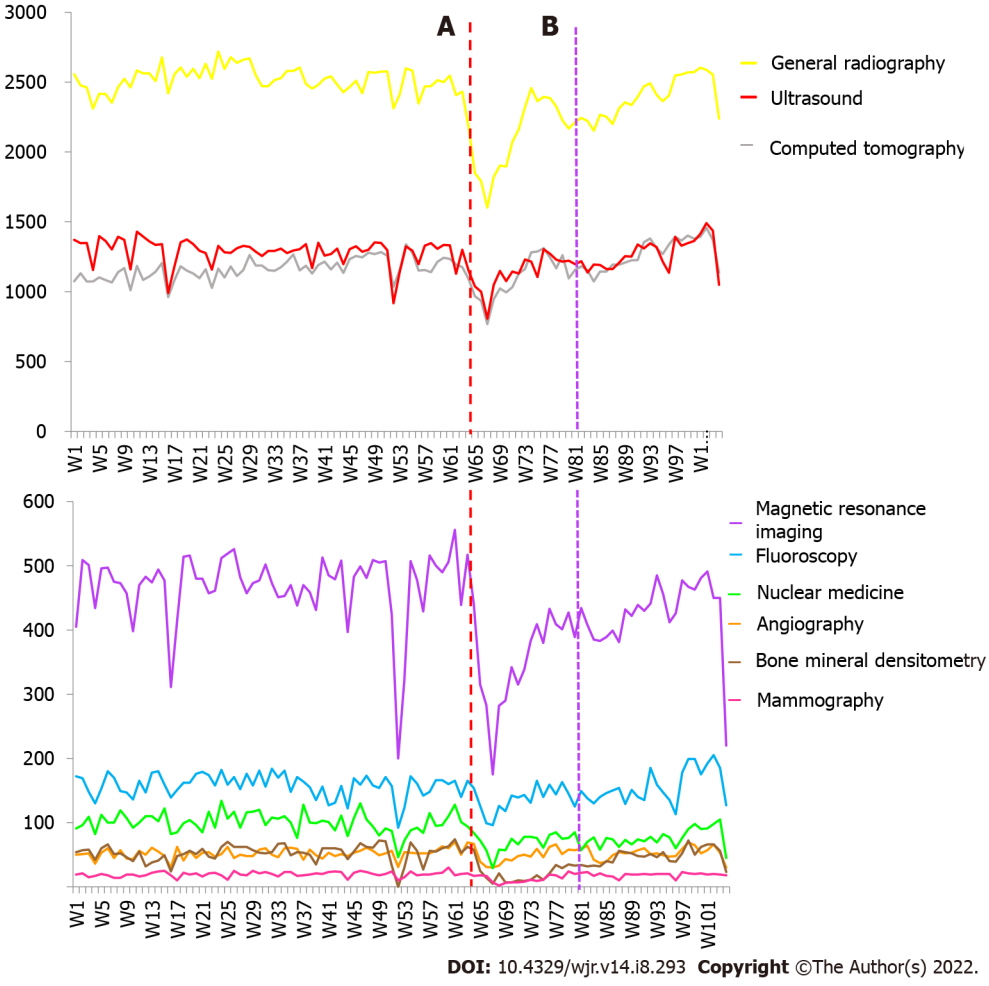

DOI: 10.4329/wjr.v14.i8.293

Figure 3 Weekly adult imaging volumes by modality from January 2019 to December 2020 (Weeks 1 to 104). A: Week 63-commencement of first wave; B: Week 80-commencement of second wave.

changes across all mobile and non-mobile imaging (P = 0.025 to < 0.0001). The correlation between mobile and non-mobile imaging was -0.29 (P = 0.003) in the emergency setting, while no correlation was observed in the inpatient setting (Spearman correlation coefficient 0.044, P = 0.656). Figure 6 highlights the weekly paediatric X-ray mobile and non-mobile imaging volumes.

DISCUSSION

We found a reduction in the imaging volume between 2% and 30% across all adult patient classes and

Table 11 Comparison of mean paediatric weekly imaging volumes for 2019 and 2020 including 95%CIs, by imaging modality categorised by patient setting

Paediatric Setting	Modality	2020			2019			*P* value
		Mean	Min-max	95%CI	Mean	Min-max	95%CI	
Emergency	Angiography	0.02	0-1	-0.02-0.07	0.02	0-1	-0.02-0.05	-0.83
	Computed tomography	4.3	0-11	3.54-5.05	5.0	0-12	4.33-5.67	0.17
	Fluoroscopy	2.27	0-6	1.68-2.86	2.53	0-7	2.08-2.99	0.48
	Radiography	160.77	75-281	144.44 -177.11	206.58	123-268	198.64-214.52	< 0.0001
	Magnetic resonance imaging	1.7	0-5	1.33-2.08	1.87	0-5	1.49-2.24	0.55
	Nuclear Medicine	0.07	0-1	-0.01-0.15	0.05	0-1	-0.01-0.11	0.70
	Ultrasound	14.41	6-25	13.16-15.65	17.67	8-26	16.59-18.74	0.0001
Inpatient	Angiography	1.18	0-4	0.83-1.53	1.17	0-6	0.85-1.48	0.95
	Computed tomography	5.66	1-14	4.92-6.4	5.66	0-11	5.0-6.27	0.96
	Fluoroscopy	17.8	7-38	15.86-19.73	19.98	7-30	18.61-21.36	0.061
	Radiography	85.84	56-120	81.74-89.94	97.97	70-143	93.99- 101.95	< 0.0001
	Magnetic resonance imaging	25.73	11-41	23.6-27.86	25.05	8-41	23.41-26.69	0.61
	Nuclear Medicine	0.55	0-3	0.28-0.81	0.98	0-5	0.72-1.25	0.025
	Ultrasound	58.36	33-76	55.51-61.21	65.33	40-84	62.9-67.77	0.0003
	Bone mineral densitometry	0.82	0-4	0.47-1.17	1.27	0-4	1.01-1.53	0.038
Outpatient	Angiography	0.05	0-1	-0.02-0.11	0.38	0-3	0.20-0.57	0.003
	Computed tomography	4.43	1-9	3.82-5.04	4.28	0-10	3.75-4.82	0.72
	Fluoroscopy	2.25	0-7	1.7-2.8	2.72	0-9	2.22-3.22	0.22
	Radiography	121.2	66-197	110.62-131.79	167.88	87-215	161.21-174.55	< 0.0001
	Magnetic resonance imaging	25.48	10-37	23.49-27.46	28.82	11-47	26.92-30.72	0.019
	Nuclear medicine	2	0-6	1.54-2.46	2.47	0-6	2.08-2.86	0.13
	Ultrasound	198.77	92-266	186.88-210.66	208.77	117-260	201.54-215.99	0.13
	Bone mineral densitometry	1.86	0-8	1.37-2.35	2.8	0-7	2.35-3.25	0.007
All classes	Angiography	1.25	0-4	0.89-1.61	1.57	0-6	1.22-1.91	0.22
	Computed tomography	14.39	8-23	13.10-15.67	14.92	5-21	14.01-15.83	0.49
	Fluoroscopy	22.32	11-44	20.04-24.60	25.23	8-40	3.59-4.54	0.037
	Radiography	367.82	239-538	340.73-394.90	472.43	331-581	458.91-485.96	< 0.0001
	Magnetic resonance imaging	52.91	23-78	49.27-56.55	55.73	22-84	52.78-58.68	0.23
	Nuclear Medicine	2.61	0-8	2.01-3.21	3.5	0-7	3.05-3.95	0.017
	Ultrasound	271.55	149-346	258.11-284.98	291.77	184-350	283.07-300.46	0.010
	Bone mineral densitometry	2.68	0-9	2.03-3.33	4.07	0-8	3.59-4.54	0.001
	Total	735.52	476-1024	693.13-777.91	869.22	553-1016	845.88-892.55	< 0.0001

10% and 37% in adult imaging volumes by modality during the first wave of the pandemic. Nuclear Medicine was the modality most impacted, and angiography the least impacted. While periods analysed may differ slightly, the findings for adult imaging volumes were less than those reported in Germany (41%, all modalities)[14], New York (14% to 53%)[15], California, Florida, Michigan, Massachusetts and New York (40% to 70%)[16], and Ohio (53%)[17]. During the second wave of the pandemic, all adult radiology modalities reported a reduction of between 2% and 32% in imaging volumes and between 9% and 24% in imaging volumes across all patient classes. Adult computed tomography imaging volumes experienced a 2% increase. Nuclear medicine was the modality most impacted. This is less than the data obtained from Medicare reported by Sreedharan *et al*[12], who found that general radiography and ultrasound were most impacted, while computed tomography and nuclear medicine services were less

Table 12 Summed imaging volumes and percentage change in paediatric mobile imaging volume across patient class in waves 1 and 2

Wave 1	2020 (weeks63-68)	2019 (weeks 11-16)	% change	Wave 2	2020 (weeks 80-95)	2019 (weeks 28-43)	% change
ED	44	32	37.5	ED	370	151	145.0
IP	400	415	-3.6	IP	1021	1340	-23.8
Overall	444	447	-0.7	Overall	1391	1491	-6.7

ED: Emergency department; IP: Inpatient.

Table 13 Comparison of mean paediatric weekly imaging volumes for 2019 and 2020 including 95%CIs, by mobile and non-mobile imaging categorised by patient setting

Paediatric Setting	Modality	2020			2019			*P* value
		Mean	Min-max	95%CI	Mean	Min-max	95%CI	
Emergency	Mobile	18.70	1-38	16.08-21.33	6.62	1-17	5.69-7.54	< 0.0001
	Non-mobile	142.07	63-251	126.62 – 157.52	199.97	121-261	192.12 – 207.81	< 0.0001
Inpatient	Mobile	66.89	44-95	63.13-70.64	72.95	46-102	69.31- 76.59	0.025
	Non-mobile	18.95	7-33	17.22-20.69	25.00	9-42	23.24-26.76	< 0.0001

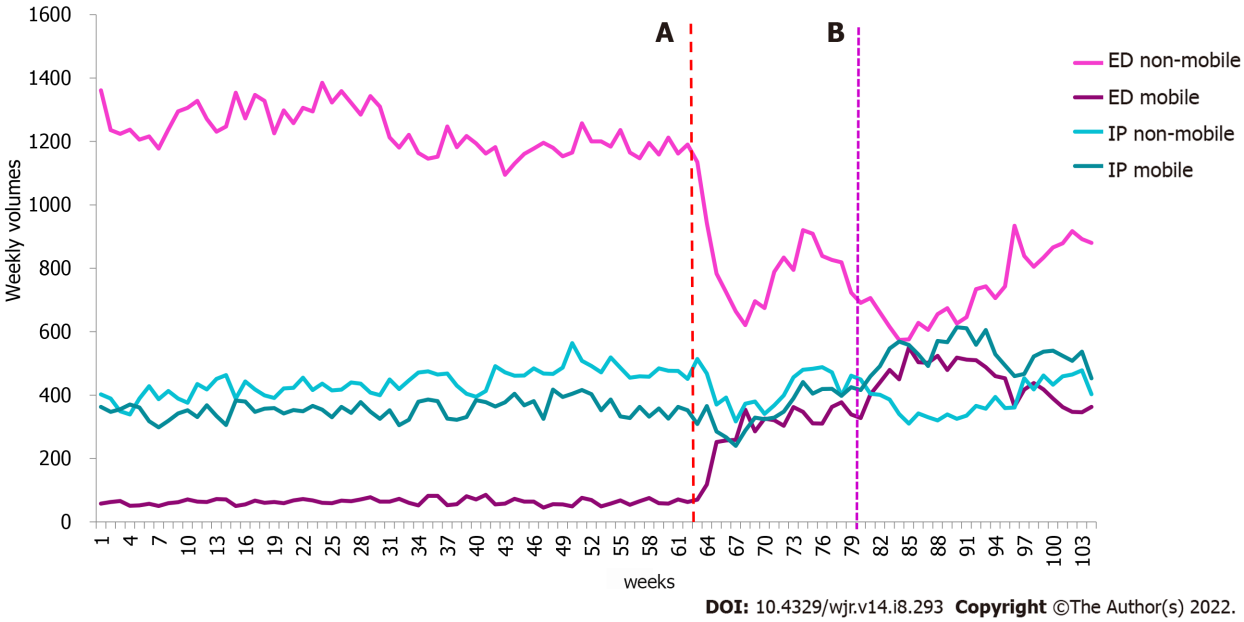

DOI: 10.4329/wjr.v14.i8.293

Figure 4 Weekly adult X-ray mobile and non-mobile imaging volumes from January 2019 to December 2020 (Weeks 1 to 104). A: Week 63-commencement of first wave; B: Week 80 commencement of second wave. ED: Emergency department; IP: Inpatient.

affected. It was unclear whether paediatric data were included in their analysis[12].

Similarly, during the first wave of the pandemic, there was a reduction in paediatric imaging volumes of between 19% and 48% across all modalities except for angiography reporting a 50% increase in the imaging volume. There was a 4%-46% reduction across all paediatric patient classes. Nuclear Medicine was the modality most impacted, with ultrasound being the least impacted. While paediatric emergency patient presentations decreased by 25% in one Sydney health service, we observed a larger decrease in paediatric imaging service utilisation in the emergency department and inpatient settings[18].

During the second wave of the pandemic, there was a reduction of between 5% and 37% in paediatric modality cases and between 16% and 28% across paediatric patient classes. Nuclear Medicine was most impacted, while magnetic resonance imaging was least affected.

Decline in adult services (2% IP, 30% OP, 26% ED) were generally less to those reported by Naidich *et al*[15] (ED (27%), OP (57%), IP (14%)). Furthermore, outpatient services were reported in South Africa (40% over six months)[5]. outpatient imaging (58%, 72%[14,17], inpatient imaging (41%, 43%)[14,17],

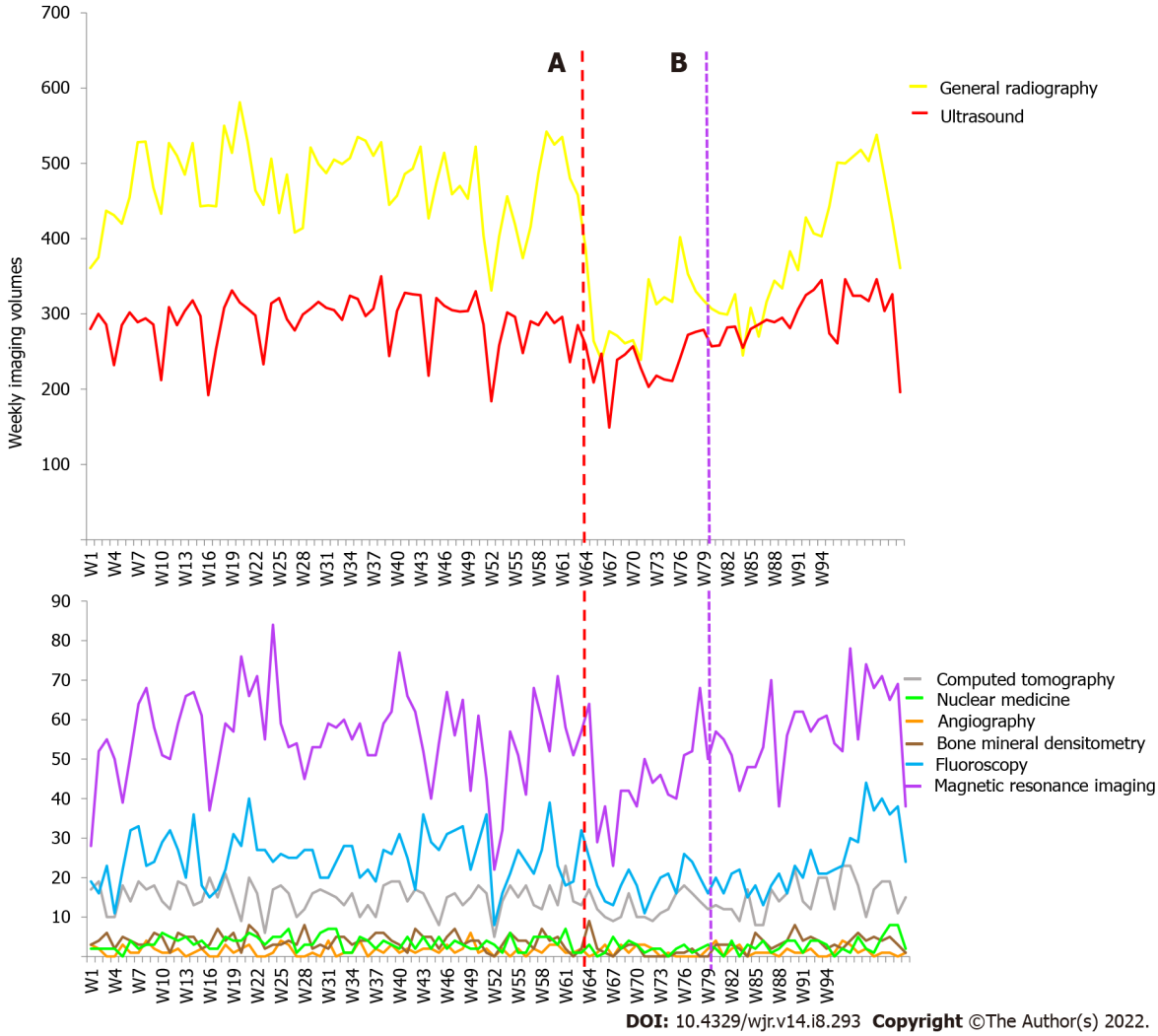

Figure 5 Weekly paediatric imaging volumes by modality from January 2019 to December 2020 (Weeks 1 to 104). A: Week 63-commencement of first wave; B: Week 80 commencement of second wave.

and emergency department imaging (39%, 49%)[14,17] in Ohio and Berlin highlighted greater declines in demands than we observed. Australia utilised the experience of other nations in preparation for COVID-19. For example, Australia reduced elective medical procedures in line with other countries and implemented PPE measures, social distancing, and stay-at-home measures for non-essential workers[5]. We found that most of our outpatient imaging services were severely impacted (19%-50% loss in imaging volume) by new social distancing and appropriate cleaning measures. Inpatient services were also affected by the decline in elective surgeries, while emergency patient volume was reduced due to more people isolating at home.

From July to September 2020, Australia experienced the pandemic's second wave. This was most prevalent in Victoria. The government implemented border closures, curfews, limiting movement to a five-kilometre radius, working from home for non-essential workers, business and education closures, wearing masks indoors and outdoors, and physical distancing measures to reduce COVID-19 cases[5]. During this phase of the pandemic, we observed a minor reduction in patient volume across all modalities at our institution compared to the first wave's impact. This could be due to health services becoming better equipped, informed and organised to manage pandemic outbreaks[5]; earlier diagnosis of COVID-19 *via* more rigorous PCR testing[5,20]; patients were better informed about the risks of contracting COVID-19, thus more likely to seek medical care. Earlier in the pandemic, it had been reported that patients were afraid to come to the hospital, potentially compromising their health[21,22].

Angiography

Our angiography statistics represented interventional radiology procedures performed in the angiography suite primarily guided by fluoroscopy or ultrasound. Like other modalities, the angiography suite was substantially impacted in outpatient volume when the Department of Health and Human Services ruled that only Category 1 patients could attend. In April and August 2020, there was a decrease in inpatient studies. However, recovery in this patient class was swift, with patient

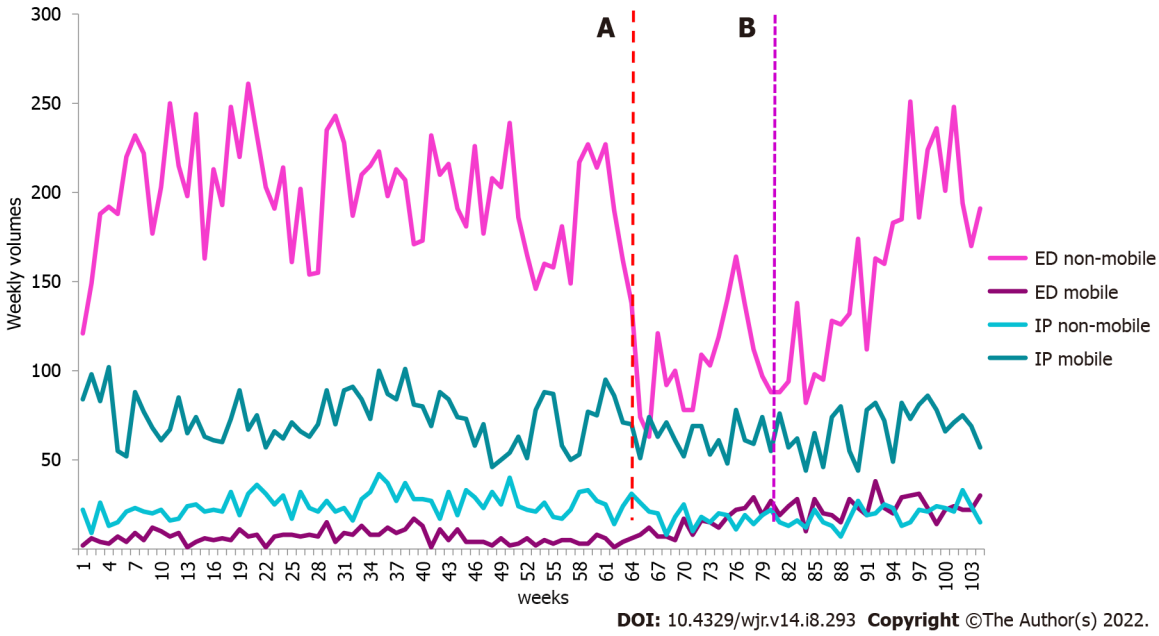

DOI: 10.4329/wjr.v14.i8.293

Figure 6 Weekly paediatric X-ray mobile and non-mobile imaging volumes from January 2019 to December 2020 (Weeks 1 to 104). A: Week 63-commencement of first wave; B: Week 80 commencement of second wave. ED: Emergency department; IP: Inpatient.

volume surpassing pre-COVID attendances. Patients delayed procedures during the first wave of COVID-19 for fear of contracting the virus while in hospital.[7] This increased unplanned hospital admissions with patients requiring procedures, leading to increased service demand. Some patients may have also been scheduled to relieve burgeoning waitlist times.

Bone mineral densitometry

United Kingdom bone mineral densitometry (BMD) wait lists increased during the pandemic, resulting in treatment delays for osteoporosis[23]. We observed the same relative reduction in imaging volumes during the first and second waves of the pandemic, likely determined by clinic closures[24], use of telehealth to minimise hospital visits[5], staff redeployment[25], or delaying medical treatment[26].

CT

CT was one of the modalities least impacted by new policies and guidelines implemented during the pandemic. This is not surprising given the importance of CTPA for early contribution to patient diagnosis[5]. While early in the pandemic, CT was the modality of choice for assisting in COVID-19 diagnosis[5], this changed due to the high radiation doses and availability of PCR testing[5]. While there was a reduction in CT demand during the peak waves of the pandemic, we observed an increase in CT utilisation during the second wave of the pandemic, consistent with other reports[27]. During the pandemic, outpatient CT studies for malignancy staging were delayed based on criteria set by senior management due to the risk of cross-contamination between inpatients and outpatients. Access to an independent CT scanner within the hospital at an onsite research facility improved workflow for this patient cohort. During the pandemic, elderly Victorians in aged care died from the virus as transmission rates among staff members in certain aged care facilities increased. The government intervened by placing aged care residents into Victorian hospitals as a safety measure for our most vulnerable. The increase in inpatient CT scans during this period can likely be attributed to this mandate.

Fluoroscopy

Many non-clinically urgent fluoroscopy studies, such as barium swallows for outpatient studies, were placed on hold or rescheduled during the pandemic. Following Victoria's second wave, there was a resurgence of patient bookings from October 2020. The end of September 2020 marked the easing of stage 4 restrictions, with COVID-19 infections decreasing significantly. Thus outpatient and inpatient bookings were rescheduled over the coming months to cope with demand. A significant change in imaging volume was observed between June and July, with a below-average patient number in July (Figure S2). This can be likely attributed to the similar timing of outbreaks in COVID-19 at aged care centres, prompting the Victorian government to move aged care residents to hospitals to prevent further COVID-19-related deaths.

General radiography

While adult general X-ray was particularly impacted during the pandemic's first wave, likely due to the cancellation of elective surgery and outpatient clinics, less impact was observed during the second wave. Conversely, paediatric general X-ray imaging volumes significantly reduced during both pandemic waves. In 2020, the utilisation of mobile imaging saw significant growth. This can be attributed to workflow changes such as infection control measures to reduce patient movement[28]. Senior management purchased extra mobile imaging systems to manage the increased demand, contributing to the observed changes. Other imaging protocol modifications to reduce the risk of contracting COVID-19, such as imaging through glass, were performed but not used routinely at our institution[8]. The utilisation of mobile imaging more than doubled during the peak of the pandemic at our institution, particularly in the emergency setting. This is comparable with the findings of others. Surveyed Western Australian medical imaging professionals perceived increased mobile chest imaging, particularly in the public hospital setting[29]. At the same time, in Singapore, there was a three-fold increase in emergency department mobile imaging usage[30]. Although mobile imaging utilisation increased, there was little change in radiographer-reported doses[31]. There was a slight shift in imaging regions other than the chest (data not shown)[31]. We also observed that fixed X-ray imaging decreased when adult mobile imaging increased in the emergency setting. This was likely to reduce transmission risk and manage potential increased demand[8,32]. The greatest impact on adult mobile imaging usage was observed during the pandemic's second wave, when the risk of cold and influenza was heightened (July-September 2020)[33].

MRI

We observed appreciable declines due to work practice changes implemented in adult and paediatric MRI services during the pandemic contributed to long waiting lists across our network. Elective general anaesthetic cases were placed "on hold" as per Victorian Government recommendations and aerosol-generating procedure policies to allow room resting and cleaning that extended the total examination time, particularly impacted paediatric services[3,34,35].

Mammography

As with other imaging modalities, our mammography service also experienced a reduction in imaging volumes during the first and second waves of the pandemic. This is consistent with other findings, though to a lesser extent, in our health service[15,36,37]. In Australia, breast screening services were temporarily suspended, with services reopening based upon government recommendations. Similarly, changes in workflow required stricter patient management protocols and cleaning protocols to minimise transmission risk[28,37,38].

Nuclear medicine

We found that nuclear medicine, then mammography were the modalities most impacted by the pandemic and consistent with the findings of others[15,16,36,37]. This could, in part, be due to logistical changes to isotope supply. From March to July and October to November 2020, there were significant issues with isotope transportation locally and overseas, particularly during the first wave of the pandemic. Due to unforeseen mechanical problems at the Australian Nuclear Science and Technology Organisation manufacturing site, there were also supply interruptions. These included a broken conveyer belt, storm causing electrical faults, production failure, isotope refinement and contamination issues. Other challenges included scheduled reactor shutdown, with difficulty in alternate isotope sourcing to meet demand. These interruptions could have contributed to the significant changes observed.

Ultrasound

At our institution, ultrasound was less impacted than other modalities, which is consistent with other experiences[16,19]. However, data from Germany found ultrasound was the most significantly affected imaging modality, though not all modalities were included in their analysis[14]. Ultrasound services were transformed considerably in the early weeks of the outbreak, with the expansion of ambulatory centres to provide 'clean' sites. In the main hospital centres, there was a substantive need for mobile ultrasound examination both in ED and in the wards. In the lead-up to the pandemic, we observed a decrease in ED patients. ED patient imaging volume stabilised during the pandemic, with some growth observed. The reason for this surge was thought to be multi-factorial. There seemed to be a tendency for patients to attend an ED rather than their local GP. It was also believed that patients' examinations were initially delayed, and the surge compensated for this. There was no obvious change in the referral patterns for the types of examinations requested. Anecdotally, point of care ultrasound (PoCUS) examinations decreased across this period. This seemed to be related to clinicians minimising patient contact and deciding to suspend PoCUS training.

Inpatient services overall increased, but there were small reductions in patient volumes during the first and second waves. While other services reported some value for lung ultrasound, this was not used in evaluating COVID-19-positive patients at our institution[10]. Consistent with the other modalities, we

did see a decrease in outpatient attendances, which returned relatively quickly. This is likely due to outpatient clinic closures, halting non-essential ultrasound intervention, and patients' choice to delay their scans. As with other modalities, ultrasound was less impacted during the second wave. Obstetric cases throughout this period were deemed an essential service and did not change. Sonographers were activated to perform blood pressures as part of a third-trimester pathway as many women were seen *via* telehealth. The Early Pregnancy Bleeding pathway and clinic were also relocated to ultrasound. Minor changes were made to scan protocols. Targeted scans were introduced for high-risk patients. The timing of paediatric hip screening was adjusted to minimise the risk of repeat examinations.

Paediatrics

Overall, there was a decrease of approximately 55% from April to October 2020 compared to 2019. Recovery of paediatric imaging, particularly after the second wave (September to December 2020), was more rapid, coinciding with the gradual reduction in Melbourne's COVID-19 case numbers and the subsequent easing of restrictions. Many patients and families deferred non-urgent imaging during the lockdown. Moreover, lockdown, home-schooling and suspension of group sports further reduced paediatric cases from sporting injuries[39]. We did observe a slight increase in some services, such as MRI, during 2020 despite COVID-19 disruption, as services returned to pre-COVID-19 demand. This was due to the new software and hardware upgrade in February 2020, reducing the total scan time and potentially increasing patient throughput while providing additional time for cleaning. As observed with adult modality data, following lockdowns in April and July-September 2020 and elective surgery deferral, there was a dramatic decrease in paediatric imaging across all modalities, except for angiography (minimal imaging volume). Recovery was observed between the first and second waves. However, it did not reach the pre-COVID-19 Levels. We also observed an increase in mobile usage in emergencies to help reduce the transmission risk.

Study limitations

While our health service cared for the first Australian COVID-19 patient, other health services across Melbourne, particularly in the north and west, experienced higher caseloads. Consequently, these health services may have experienced more significant declines in radiology services than we observed across our health services. Our institution purchased additional mobile X-ray units to prepare for the pandemic, contributing to the increased use. Of note, the MRI software and hardware upgrades did not significantly increase the imaging volume. However, they did provide additional time for practice changes, such as improved infection control measures. Nuclear medicine experienced even more significant challenges during the pandemic due to unforeseen interruptions to isotope supplies as a confounding variable. This required additional patient rescheduling, often at short notice. Given that data was analysed between 2019 and 2020, some underlying baseline year-to-year variability may be contributing to the findings. Timeframes defining COVID-19 may vary worldwide, making data comparison somewhat difficult.

This work represents one large Victorian health service; however, it may not be generalisable to other health services.

Lessons learned: (1) Once-in-a-lifetime events such as a global pandemic can significantly impact workflow across imaging modalities, with the need to implement new processes; (2) Our experience during the pandemic was not the same as those experiences described by other nations due to the variation in severity and (3) Modalities across our health network were impacted differently due to changes in service demands, closures of outpatient clinics, and rescheduling elective surgeries.

CONCLUSION

Collected data provides an evidence-based insight into changing imaging volume related to COVID-19. This information will allow the network to predict the dynamic demands in imaging more accurately and promptly adapt its policies. We found that adult CT, angiography and ultrasound recovery following the first and second waves of the pandemic recovered faster than nuclear medicine, BMD and MRI. Paediatric MRI and ultrasound recovered faster than nuclear medicine and general radiography following the first and second waves of the pandemic. Modalities were less impacted during the second wave (July-September 2020) than during the first wave (April 2020), except for angiography outpatients. At our health network, nuclear medicine was the imaging modality most impacted by COVID-19 in adult and paediatric settings. There may have been other factors, however, influencing these results. Adult CT imaging increased during the second wave, while paediatric ultrasound was the least affected. Radiology departments can minimise the impact of future COVID-19/public health outbreaks on imaging volumes by ensuring each modality is appropriately resourced to continue providing safe and patient-centred care.

ARTICLE HIGHLIGHTS

Research background

Medical imaging modalities worldwide were significantly impacted by the the coronavirus disease 2019 (COVID-19) pandemic; however, each country's experience differed. This study provides an in-depth analysis of the impact on adult, paediatric, inpatient, outpatient, emergency and mobile services across the first and second waves of the COVID-19 pandemic in a large public health network in Victoria, Australia.

Research motivation

This work provides evidence for managing and redeploying resources during "once in a lifetime" events such as a pandemic and impact duration. Using this work, modelling and forecasting anticipated changes to imaging demand can be performed, allowing optimal utilisation of departmental staffing to manage workloads.

Research objectives

To identify adult and paediatric imaging volume changes, including mobile imaging across a large Victorian public hospital network. We realised our objectives, and the findings highlighted significant differences across the modalities analysed. Future research could monitor the long-term impacts of such events, such as staff burnout or opportunities for additional training to address deficiencies identified.

Research methods

The use of statistical methods in data analysis highlighted the modalities, patient classes and differences between adult and paediatric imaging. Particularly, methods to identify any correlation between mobile and non-mobile imaging volumes were novel.

Research results

We identified that the greatest impact occurred in Nuclear Medicine during the first and second waves, with all modalities less affected during the second wave; other modalities such as computed tomography were less impacted, requiring greater resources to manage service demand. We observed a shift in regions imaged using mobile imaging. It would be essential to understand this impact regarding image quality, workflow and patient radiation dose.

Research conclusions

Medical imaging modality services across a large Victorian public health network were significantly affected during the COVID-19 pandemic; however, the impact on different modalities varied relative to studies performed in other countries. It is essential to have a broad perspective of the impact to each imaging modality in both the adult and paediatric context to help better address the need for workflow changes. It is essential to consider whether imaging services are inversely correlated to manage optimal departmental resourcing.

Research perspectives

Future research could further investigate the long-term impact of lockdowns and the pandemic on imaging modality volumes and their recovery. This can help inform future budgeting requirements regarding the need for additional equipment and staffing to manage continuous workflow demands.

FOOTNOTES

Author contributions: Pinson JA, Badawy MK, designed and coordinated the study; Pinson JA, Badawy MK, Diep ML, Krishnan V, Aird C, Cooper C, Leong C, Chen J, Paul E and Ardley N performed the data collection, analysed and interpreted the data; Pinson JA, Badawy MK, Diep ML, Krishnan V, Aird C, Cooper C, Leong C, Chen J, Paul E and Ardley N wrote the manuscript; all authors have read, edited and approved the final version of the manuscript.

Institutional review board statement: The study was reviewed and approved by the Monash Health Human Research Ethics Committee Institutional Review Board [(Approval No. QA/69362/MonH-2020-235260(v1))].

Informed consent statement: Patients were not required to give informed consent to the study because the analysis used anonymous clinical data that were obtained after each patient agreed to treatment by written consent. For full disclosure, the details of the study are published on the home page of Fukushima Medical University.

Conflict-of-interest statement: We have no financial relationships to disclose.

Data sharing statement: Technical appendix, statistical code, and dataset available from the corresponding author at

mohamed.badawy@monashhealth.org.

Country/Territory of origin: Australia

ORCID number: Jo-Anne Pinson 0000-0001-6654-0278; My Linh Diep 0000-0001-5007-3046; Vinay Krishnan 0000-0002-0062-5348; Caroline Aird 0000-0002-3942-4375; Cassie Cooper 0000-0001-8504-8086; Christopher Leong 0000-0001-9496-799X; Jeff Chen 0000-0003-4553-9221; Nicholas Ardley 0000-0002-2251-8754; Eldho Paul 0000-0003-1263-7255; Mohamed Khaldoun Badawy 0000-0001-8029-9951.

Corresponding Author's Membership in Professional Societies: The Australasian Radiation Protection, 63506470.

S-Editor: Wang LL
L-Editor: A
P-Editor: Wang LL

REFERENCES

1 **Cucinotta D**, Vanelli M. WHO Declares COVID-19 a Pandemic. *Acta Biomed* 2020; **91**: 157-160 [PMID: 32191675 DOI: 10.23750/abm.v91i1.9397]
2 **Islam MS**, Rahman KM, Sun Y, Qureshi MO, Abdi I, Chughtai AA, Seale H. Current knowledge of COVID-19 and infection prevention and control strategies in healthcare settings: A global analysis. *Infect Control Hosp Epidemiol* 2020; **41**: 1196-1206 [PMID: 32408911 DOI: 10.1017/ice.2020.237]
3 **COVIDSurg Collaborative**. Elective surgery cancellations due to the COVID-19 pandemic: global predictive modelling to inform surgical recovery plans. *Br J Surg* 2020; **107**: 1440-1449 [PMID: 32395848 DOI: 10.1002/bjs.11746]
4 **Weissman GE**, Crane-Droesch A, Chivers C, Luong T, Hanish A, Levy MZ, Lubken J, Becker M, Draugelis ME, Anesi GL, Brennan PJ, Christie JD, Hanson CW 3rd, Mikkelsen ME, Halpern SD. Locally Informed Simulation to Predict Hospital Capacity Needs During the COVID-19 Pandemic. *Ann Intern Med* 2020; **173**: 21-28 [PMID: 32259197 DOI: 10.7326/M20-1260]
5 **Tan BS**, Dunnick RN, Gangi A, Goergen S, Jin Z-Y, Neri E, Nomura CH, Pitcher RD, Yee J, Mahmood U. RSNA International Trends: A Global Perspective on the COVID-19 Pandemic and Radiology in Late 2020. *Radiology* 2021; **299**: E193-E203 [DOI: 10.1148/radiol.2020204267]
6 **Currie G**. COVID19 impact on nuclear medicine: an Australian perspective. *Eur J Nucl Med Mol Imaging* 2020; **47**: 1623-1627 [PMID: 32296883 DOI: 10.1007/s00259-020-04812-z]
7 **Amukotuwa SA**, Bammer R, Maingard J. Where have our patients gone? *J Med Imaging Radiat Oncol* 2020; **64**: 607-614 [DOI: 10.1111/1754-9485.13093]
8 **Brady Z**, Scoullar H, Grinsted B, Ewert K, Kavnoudias H, Jarema A, Crocker J, Wills R, Houston G, Law M, Varma D. Technique, radiation safety and image quality for chest X-ray imaging through glass and in mobile settings during the COVID-19 pandemic. *Phys Eng Sci Med* 2020; **43**: 765-779 [PMID: 32662037 DOI: 10.1007/s13246-020-00899-8]
9 **Seghers MC**, Seghers VJ, Sher AC, Jadhav SP, States LJ, Trout AT, Alazraki AL, Sammer MBK. Working from home during the COVID-19 pandemic: surveys of the Society for Pediatric Radiology and the Society of Chiefs of Radiology at Children's Hospitals. *Pediatr Radiol* 2022; **52**: 1242-1254 [PMID: 35229184 DOI: 10.1007/s00247-022-05299-6]
10 **Blažić I**, Brkljačić B, Frija G. The use of imaging in COVID-19-results of a global survey by the International Society of Radiology. *Eur Radiol* 2021; **31**: 1185-1193 [PMID: 32939620 DOI: 10.1007/s00330-020-07252-3]
11 **Eastgate P**, Neep MJ, Steffens T, Westerink A. COVID-19 Pandemic-considerations and challenges for the management of medical imaging departments in Queensland. *J Med Radiat Sci* 2020; **67**: 345-351 [PMID: 32827241 DOI: 10.1002/jmrs.423]
12 **Sreedharan S**, Mian M, McArdle DJT, Rhodes A. The impact of the COVID-19 pandemic on diagnostic imaging services in Australia. *J Med Imaging Radiat Oncol* 2022; **66**: 377-384 [PMID: 34288493 DOI: 10.1111/1754-9485.13291]
13 **Vöö S**, Dizdarevic S. Single photon emission computed tomography lung perfusion imaging during the COVID-19 pandemic: does nuclear medicine need to reconsider its guidelines? *Nucl Med Commun* 2020; **41**: 991-993 [PMID: 32796489 DOI: 10.1097/MNM.0000000000001246]
14 **Fleckenstein FN**, Maleitzke T, Böning G, Kahn J, Büttner L, Gebauer B, Aigner A, Hamm B. Decreased Medical Care During the COVID-19 Pandemic-A Comprehensive Analysis of Radiological Examinations. *Rofo* 2021; **193**: 937-946 [PMID: 33735933 DOI: 10.1055/a-1368-5047]
15 **Naidich JJ**, Boltyenkov A, Wang JJ, Chusid J, Hughes D, Sanelli PC. Impact of the Coronavirus Disease 2019 (COVID-19) Pandemic on Imaging Case Volumes. *J Am Coll Radiol* 2020; **17**: 865-872 [PMID: 32425710 DOI: 10.1016/j.jacr.2020.05.004]
16 **Norbash AM**, Moore AV Jr, Recht MP, Brink JA, Hess CP, Won JJ, Jain S, Sun X, Brown M, Enzmann D. Early-Stage Radiology Volume Effects and Considerations with the Coronavirus Disease 2019 (COVID-19) Pandemic: Adaptations, Risks, and Lessons Learned. *J Am Coll Radiol* 2020; **17**: 1086-1095 [PMID: 32717183 DOI: 10.1016/j.jacr.2020.07.001]

17 **Vagal A**, Mahoney M, Allen B, Kapur S, Udstuen G, Wang L, Braley S, Makramalla A, Chadalavada S, Choe KA, Scheler J, Brown A, England E, Hudepohl J, Rybicki FJ. Rescheduling Nonurgent Care in Radiology: Implementation During the Coronavirus Disease 2019 (COVID-19) Pandemic. *J Am Coll Radiol* 2020; **17**: 882-889 [PMID: 32473108 DOI: 10.1016/j.jacr.2020.05.010]

18 **Kam AW**, Chaudhry SG, Gunasekaran N, White AJ, Vukasovic M, Fung AT. Fewer presentations to metropolitan emergency departments during the COVID-19 pandemic. *Med J Aust* 2020; **213**: 370-371 [PMID: 32946589 DOI: 10.5694/mja2.50769]

19 **Naidich JJ**, Boltyenkov A, Wang JJ, Chusid J, Hughes D, Sanelli PC. Coronavirus Disease 2019 (COVID-19) Pandemic Shifts Inpatient Imaging Utilization. *J Am Coll Radiol* 2020; **17**: 1289-1298 [PMID: 32622817 DOI: 10.1016/j.jacr.2020.06.011]

20 **Wang C**, Horby PW, Hayden FG, Gao GF. A novel coronavirus outbreak of global health concern. *Lancet* 2020; **395**: 470-473 [PMID: 31986257 DOI: 10.1016/S0140-6736(20)30185-9]

21 **Iezzi R**, Valente I, Cina A, Posa A, Contegiacomo A, Alexandre A, D'Argento F, Lozupone E, Barone M, Giubbolini F, Milonia L, Romi A, Scrofani AR, Pedicelli A, Manfredi R, Colosimo C. Longitudinal study of interventional radiology activity in a large metropolitan Italian tertiary care hospital: how the COVID-19 pandemic emergency has changed our activity. *Eur Radiol* 2020; **30**: 6940-6949 [PMID: 32607633 DOI: 10.1007/s00330-020-07041-y]

22 **Wong LE**, Hawkins JE, Langness S, L. MK, Iris P, Sammann A. Where Are All the Patients? *N Engl J Med Catalyst Innovations in Care Delivery* 2020; **1**: 12. [DOI: 10.1056/CAT.20.0193]

23 **Sapkota HR**, Nune A, Bateman J, Venkatachalam S. A pragmatic proposal for triaging DXA testing during the COVID-19 global pandemic. *Osteoporos Int* 2021; **32**: 1-6 [PMID: 33146750 DOI: 10.1007/s00198-020-05722-4]

24 **Andrikopoulos S**, Johnson G. The Australian response to the COVID-19 pandemic and diabetes-Lessons learned. *Diabetes Res Clin Pract* 2020; **165**: 108246 [PMID: 32502693 DOI: 10.1016/j.diabres.2020.108246]

25 **Shi J**, Giess CS, Martin T, Lemaire KA, Curley PJ, Bay C, Mayo-Smith WW, Boland GW, Khorasani R. Radiology Workload Changes During the COVID-19 Pandemic: Implications for Staff Redeployment. *Acad Radiol* 2021; **28**: 1-7 [PMID: 33036897 DOI: 10.1016/j.acra.2020.09.008]

26 **Czeisler MÉ**, Kennedy JL, Wiley JF, Facer-Childs ER, Robbins R, Barger LK, Czeisler CA, Rajaratnam SMW, Howard ME. Delay or avoidance of routine, urgent and emergency medical care due to concerns about COVID-19 in a region with low COVID-19 prevalence: Victoria, Australia. *Respirology* 2021; **26**: 707-712 [PMID: 34081819 DOI: 10.1111/resp.14094]

27 **Garg M**, Prabhakar N, Bhalla AS. Cancer risk of CT scan in COVID-19: Resolving the dilemma. *Indian J Med Res* 2021; **153**: 568-571 [PMID: 34596597 DOI: 10.4103/ijmr.ijmr_1476_21]

28 **ACR Recommendations for the use of Chest Radiography and Computed Tomography (CT) for Suspected COVID-19 Infection**. Am Coll Radiol 2020, March 11. [cited 15 July 2021]. Available from: https://psnet.ahrq.gov/issue/acr-recommendations-use-chest-radiography-and-computed-tomography-ct-suspected-covid-19

29 **Dann C**, Sun Z. The impact of COVID-19 on Western Australian medical imaging clinical practice and workplace. *J Med Radiat Sci* 2022 [PMID: 35555866 DOI: 10.1002/jmrs.594]

30 **Goh Y**, Chua W, Lee JKT, Ang BWL, Liang CR, Tan CA, Choong DAW, Hoon HX, Ong MKL, Quek ST. Operational Strategies to Prevent Coronavirus Disease 2019 (COVID-19) Spread in Radiology: Experience From a Singapore Radiology Department After Severe Acute Respiratory Syndrome. *J Am Coll Radiol* 2020; **17**: 717-723 [PMID: 32298643 DOI: 10.1016/j.jacr.2020.03.027]

31 **Yeung P**, Pinson JA, Lawson M, Leong C, Badawy MK. COVID-19 pandemic and the effect of increased utilisation of mobile X-ray examinations on radiation dose to radiographers. *J Med Radiat Sci* 2022; **69**: 147-155 [PMID: 35180810 DOI: 10.1002/jmrs.570]

32 **Koehler D**, Ozga AK, Molwitz I, May P, Görich HM, Keller S, Adam G, Yamamura J. Time series analysis of the demand for COVID-19 related chest imaging during the first wave of the SARS-CoV-2 pandemic: An explorative study. *PLoS One* 2021; **16**: e0247686 [PMID: 33657140 DOI: 10.1371/journal.pone.02476867]

33 **Reichert TA**, Simonsen L, Sharma A, Pardo SA, Fedson DS, Miller MA. Influenza and the winter increase in mortality in the United States, 1959-1999. *Am J Epidemiol* 2004; **160**: 492-502 [PMID: 15321847 DOI: 10.1093/aje/kwh227]

34 **van Doremalen N**, Bushmaker T, Morris DH, Holbrook MG, Gamble A, Williamson BN, Tamin A, Harcourt JL, Thornburg NJ, Gerber SI, Lloyd-Smith JO, de Wit E, Munster VJ. Aerosol and Surface Stability of SARS-CoV-2 as Compared with SARS-CoV-1. *N Engl J Med* 2020; **382**: 1564-1567 [PMID: 32182409 DOI: 10.1056/NEJMc2004973]

35 **Raissaki M**, Shelmerdine SC, Damasio MB, Toso S, Kvist O, Lovrenski J, Hirsch FW, Görkem SB, Paterson A, Arthurs OJ, Rossi A, van Schuppen J, Petit P, Argyropoulou MI, Offiah AC, Rosendahl K, Caro-Domínguez P. Management strategies for children with COVID-19: ESPR practical recommendations. *Pediatr Radiol* 2020; **50**: 1313-1323 [PMID: 32621013 DOI: 10.1007/s00247-020-04749-3]

36 **Parikh KD**, Ramaiya NH, Kikano EG, Tirumani SH, Pandya H, Stovicek B, Sunshine JL, Plecha DM. COVID-19 Pandemic Impact on Decreased Imaging Utilization: A Single Institutional Experience. *Acad Radiol* 2020; **27**: 1204-1213 [PMID: 32665091 DOI: 10.1016/j.acra.2020.06.024]

37 **Sprague BL**, O'Meara ES, Lee CI, Lee JM, Henderson LM, Buist DSM, Alsheik N, Macarol T, Perry H, Tosteson ANA, Onega T, Kerlikowske K, Miglioretti DL. Prioritizing breast imaging services during the COVID pandemic: A survey of breast imaging facilities within the Breast Cancer Surveillance Consortium. *Prev Med* 2021; **151**: 106540 [PMID: 34217424 DOI: 10.1016/j.ypmed.2021.106540]

38 **Spuur KM**. The COVID-19 BreastScreen Department-beyond the pandemic. *J Med Radiat Sci* 2020; **67**: 352-355 [PMID: 33026711 DOI: 10.1002/jmrs.430]

39 **Johnson MA**, Halloran K, Carpenter C, Pascual-Leone N, Parambath A, Sharma J, Seltzer R, Ellis HB, Shea KG, Ganley TJ. Changes in Pediatric Sports Injury Presentation During the COVID-19 Pandemic: A Multicenter Analysis. *Orthop J Sports Med* 2021; **9**: 23259671211010826 [PMID: 33997072 DOI: 10.1177/23259671211010826]

World Journal of Radiology

Submit a Manuscript: https://www.f6publishing.com

World J Radiol 2022 August 28; 14(8): 311-318

DOI: 10.4329/wjr.v14.i8.311

ISSN 1949-8470 (online)

ORIGINAL ARTICLE

Retrospective Study

Triple rule-out computed tomography angiography: Evaluation of acute chest pain in COVID-19 patients in the emergency department

Suzan Bahadir, Sonay Aydın, Mecit Kantarci, Edhem Unver, Erdal Karavas, Düzgün Can Şenbil

Specialty type: Radiology, nuclear medicine and medical imaging

Provenance and peer review: Invited article; Externally peer reviewed.

Peer-review model: Single blind

Peer-review report's scientific quality classification

Grade A (Excellent): 0
Grade B (Very good): 0
Grade C (Good): C, C
Grade D (Fair): D
Grade E (Poor): 0

P-Reviewer: Luo W, China; Ren S, China
A-Editor: Ferreira GSA, Brazil

Received: April 11, 2022
Peer-review started: April 11, 2022
First decision: May 30, 2022
Revised: May 30, 2022
Accepted: August 5, 2022
Article in press: August 5, 2022
Published online: August 28, 2022

Suzan Bahadir, Department of Radiology, Baskent University, Antalya 07000, Turkey

Sonay Aydın, Erdal Karavas, Düzgün Can Şenbil, Department of Radiology, Erzincan Binali Yıldırım University, Erzincan 24100, Turkey

Mecit Kantarci, Department of Radiology, Ataturk University, Erzurum 25100, Turkey

Edhem Unver, Department of Chest Disease, Erzincan Binali Yildirim University, Erzincan 24100, Turkey

Corresponding author: Düzgün Can Şenbil, MD, Academic Research, Doctor, Department of Radiology, Erzincan Binali Yıldırım University, Hacı Ali Akın Street, Erzincan 24100, Turkey. can.senbil@erzincan.edu.tr

Abstract

BACKGROUND

The aim of this study was to define clinical evidence supporting that triple rule-out computed tomography angiography (TRO CTA) is a comprehensive and feasible diagnostic tool in patients with novel coronavirus disease 2019 (COVID-19) who were admitted to the emergency department (ED) for acute chest pain. Optimizing diagnostic imaging strategies in COVID-19 related thromboembolic events, will help for rapid and noninvasive diagnoses and results will be effective for patients and healthcare systems in all aspects.

AIM

To define clinical evidence supporting that TRO CTA is a comprehensive and feasible diagnostic tool in COVID-19 patients who were admitted to the ED for acute chest pain, and to assess outcomes of optimizing diagnostic imaging strategies, particularly TRO CTA use, in COVID-19 related thromboembolic events.

METHODS

TRO CTA images were evaluated for the presence of coronary artery disease, pulmonary thromboembolism (PTE), or acute aortic syndromes. Statistical analyses were used for evaluation of significant association between the variables. A two tailed *P*-value < 0.05 was considered statistically significant.

RESULTS

Fifty-three patients were included into the study. In 31 patients (65.9%), there was

not any pathology, while PTE was diagnosed in 11 patients. There was no significant relationship between the rates of pathology on CTA and history of hypertension. On the other hand, the diabetes mellitus rate was much higher in the acute coronary syndrome group, particularly in the PTE group (8/31 = 25.8% *vs* 6/16 = 37.5%, $P = 0.001$). The rate of dyslipidemia was significantly higher in the group with pathology on CTA while compared to those without pathology apart from imaging findings of the pneumonia group (62.5% *vs* 38.7%, $P < 0.001$). Smoking history rates were similar in the groups. Platelets, D-dimer, fibrinogen, C-reactive protein, and erythrocyte sedimentation rate values were higher in COVID-19 cases with additional pathologies.

CONCLUSION

TRO CTA is an effective imaging method in evaluation of all thoracic vascular systems at once and gives accurate results in COVID-19 patients.

Key Words: COVID-19; Pulmonary thromboembolism; Coronary artery disease; Acute aortic syndromes; Triple rule-out computed tomography angiography

Core Tip: Acute chest pain might be due to pneumonia itself or accompanying vascular events in novel coronavirus disease 2019 (COVID-19) cases. Triple rule-out computed tomography angiography (TRO CTA) is an effective and non-invasive diagnostic method in COVID-19 patients who were admitted to the emergency department with acute chest pain. TRO CTA is an imaging method that evaluates all thoracic vascular systems at once and gives accurate results in the COVID-19 patient group with acute chest pain, which has been proven to be susceptible to thrombotic events.

Citation: Bahadir S, Aydın S, Kantarci M, Unver E, Karavas E, Şenbil DC. Triple rule-out computed tomography angiography: Evaluation of acute chest pain in COVID-19 patients in the emergency department. *World J Radiol* 2022; 14(8): 311-318

URL: https://www.wjgnet.com/1949-8470/full/v14/i8/311.htm

DOI: https://dx.doi.org/10.4329/wjr.v14.i8.311

INTRODUCTION

Acute chest pain is one of the major complaints among the admissions to the emergency department (ED)[1,2]. In some patients, diagnoses can be made by electrocardiographic (ECG) changes, elevated cardiac laboratory biomarkers, and typical symptoms. However, a normal ECG or cardiac biomarkers do not rule out acute cardiovascular disease and symptoms might be atypical[3]. Moreover, after the novel coronavirus disease 2019 (COVID-19) pandemic, it has been more complicated to make a differential diagnosis list of acute chest pain in the ED. To date, many studies have presented that COVID-19 causes hypercoagulability[4]. Hypercoagulability is attributed to endothelial cell dysfunction, hypoxia-induced pathways, and increased blood viscosity[5]. Therefore, to make a rapid and accurate diagnosis in COVID-19 patients presenting with acute chest pain is of utmost importance.

Triple rule-out computed tomography angiography (TRO CTA) covers all thoracic vascular systems and has advantages in the detection of coronary artery disease, pulmonary thromboembolism (PTE), or acute aortic syndromes[6]. TRO CTA has ability to rule out pathology in all three vascular systems, particularly in COVID-19 patients who have already increased risk of thrombosis and myocardial injury [7].

The aim of this study was to define clinical evidence supporting that TRO CTA is a comprehensive and feasible diagnostic tool in patients with COVID-19 who were admitted to the ED for acute chest pain. Optimizing diagnostic imaging strategies in COVID-19 related thromboembolic events, will help for rapid and noninvasive diagnoses and results will be effective for patients and healthcare systems in all aspects.

MATERIALS AND METHODS

This study was approved by our Institutional Review Board and as it was a retrospective study, written informed consent was waived. No author has any conflict of interest to declare in this study. Our radiology archiving system was searched for patients who applied to the ED for acute chest pain and

underwent TRO CTA between September 2020 and January 2021. Patients older than 18 years, who had COVID-19 pneumonia and applied to the emergency department for acute chest pain, and underwent TRO CTA for further evaluation were included in this study. The exclusion criteria were as follows: Unreachable clinical or laboratory data and incomplete documentation of imaging data or inadequate imaging quality. Six of the patients were excluded from the study and the remaining 47 patients fulfilled the inclusion criteria. Medical records were used for the collection of demographics and clinical and laboratory findings. TRO CTA images were evaluated for the presence of the coronary artery disease, PTE, or acute aortic syndromes.

In our center, TRO CTA examination is performed according to the eligibility criteria in the article of Eltabbakh AR *et al*[8].

TRO-CTA protocol

All TRO CTA scans were acquired using a third-generation dual-source CT scanner (Somatom Force, Siemens Healthineers). The protocol begins with a noncontrast prospectively ECG-triggered acquisition between the levels of the carina and the base of the diaphragm for coronary artery calcium scoring. After this, CTA was acquired from the lung apices to the diaphragm after the administration of intravenous contrast. According to patients' condition, prospectively ECG-triggered, retrospectively ECG-gated, or prospectively ECG-triggered high pitch spiral acquisition was used. An intravenous iodinated contrast material of 60 to 90 mL was administered at an injection rate of 4 to 6 mL/s, followed by a saline chaser of 50 mL. Nitroglycerin or beta-blocker administration was not used. Primarily, the coronary arteries were opacified during image acquisition, while homogeneous enhancement of the pulmonary arteries happened. For the evaluation of the maximum intensity projection of the aorta, coronary and pulmonary arteries, curved planar and volume-rendered reconstructions were obtained; findings were then confirmed on the axial CT source images.

Statistical analysis

Data were analyzed using the Statistical Package for Social Sciences (SPSS) for Windows 20 software (IBM SPSS Inc., Chicago, IL, United States). Normal distribution of the data was evaluated using the Kolmogorov-Smirnov test. Numerical variables with a normal distribution are shown as minimum-maximum values. Categorical variables are shown as percentages. Differences in normally distributed variables between groups were evaluated using Student's *t*-test. Categorical variables were evaluated by the chi-square test between groups.

A two tailed *P*-value < 0.05 was considered statistically significant.

RESULTS

In this study, 53 patients who were previously diagnosed with laboratory-proven (real-time PCR) COVID-19 pneumonia and underwent triple rule-out computed tomography angiography due to sudden chest pain between September 2020-January 2021, were retrospectively searched. Six of these patients were excluded from the study because of insufficient quality of the images or because the necessary laboratory and/or clinical data could not be reached. The study population consisted of 47 patients. The creatinine values of 47 patients included in the study were within the physiological range.

Twenty-nine (61.7%) of 47 patients were men and 18 (38.3%) of them were women. Mean age was 61.7 ± 13.6 years and median age was 59 years (min-max: 47-84 years).

In 31 patients (65.9%), there was not any pathology except for parenchymal findings of COVID-19 pneumonia. PTE was diagnosed in 11 patients (Figure 1), significant stenosis in the coronary arteries diagnosed in 4 (Figures 2 and 3), and dissection in the descending aorta diagnosed in 1 (Figure 4). All coronary artery stenoses were observed in the left anterior descending artery and its branches. The patient with thoracic aortic dissection had a history of previous abdominal aortic dissection.

Forty-one (41/47, 87.2%) of the patients included in this study had a history of hypertension. All patients with hypertension were using antihypertensive drugs and blood pressures were under control. There was no significant relationship between the rates of pathology on CTA and history of hypertension. When patients with findings on CTA and those without findings other than COVID-19 pneumonia on CTA were compared, HT rates were similar (normal group 14/16, 87.5% *vs* pathologic group 27/31, 87%, $P = 0.09$).

Fourteen patients had a history of diabetes mellitus (DM) (14/47, 29.7%). Eight of these 14 patients were in the group with no imaging findings other than pneumonia, 5 of them were in the PTE group, and 1 was in the acute coronary syndrome group. When compared with those without any imaging findings other than pneumonia on CTA, the DM rate was much higher in the acute coronary syndrome group, particularly in the PTE group (8/31 = 25.8% *vs* 6/16 = 37.5%, $P = 0.001$).

Dyslipidemia was detected in the blood test taken just before (1-3 d) the CTA examination in 22 (22/47, 46.8%) patients. Nine of these patients also had a history of DM. Fourteen of these patients were previously aware of the history of hypercholesterolemia and were using statin derivatives.

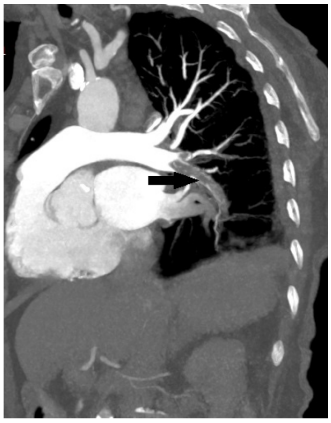

DOI: 10.4329/wjr.v14.i8.311 **Copyright** ©The Author(s) 2022.

Figure 1 A 77-year-old male patient. Curved multiplanar reformatted image shows embolus in the right lung lower lobe artery (arrow).

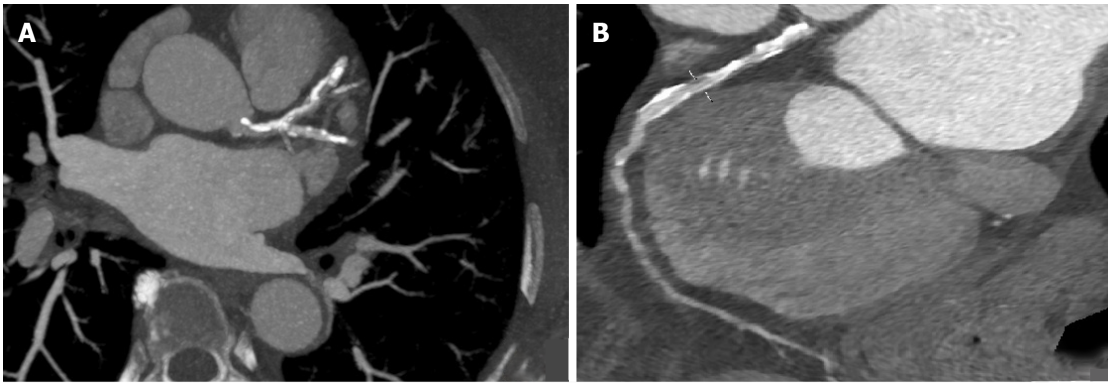

DOI: 10.4329/wjr.v14.i8.311 **Copyright** ©The Author(s) 2022.

Figure 2 A 73-year-old male patient. A: Diffuse calcific and soft plaque formations are seen in the left main, left anterior descending (LAD), and left circumflex arteries on axial maximum intensity projection image; B: Moderate stenosis (50% to 69%) is present (linear marker) in the proximal segment of LAD on curved multiplanar reformatted image.

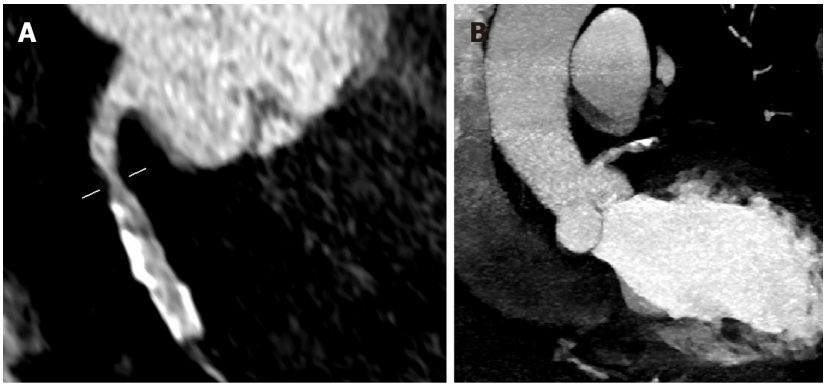

DOI: 10.4329/wjr.v14.i8.311 **Copyright** ©The Author(s) 2022.

Figure 3 A 63-year-old female patient. A: Moderate stenosis (50% to 69%; linear marker); B: Calcific plaque formations are seen in the right coronary artery on coronal maximum intensity projection images.

The mean total cholesterol level of these patients was 243.9 ± 71.2 mg/dL, and the low-density lipoprotein cholesterol level was 171.5 ± 42.6 mg/dL. All of the patients with significant findings on TRO CTA had a total cholesterol level above 240 mg/dL and low-density lipoprotein cholesterol level above 175 mg/dL. Twelve of these 22 patients were in the group without imaging findings other than pneumonia, 7 were in the PTE detected group, 2 were in the acute coronary syndrome group, and 1 was in the group with aortic dissection. The rate of dyslipidemia was significantly higher in the group with pathology on CTA while compared to those without pathology apart from imaging findings of the

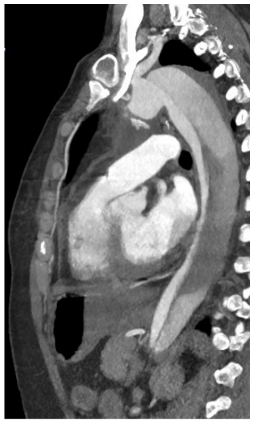

DOI: 10.4329/wjr.v14.i8.311

Figure 4 A 78-year-old male patient. Sagittal maximum intensity projection image depicts Stanford type B dissection.

pneumonia group (10/16 = 62.5% *vs* 12/31 = 38.7%, $P < 0.001$).

Nine of the patients included in this study (9/47, 19.1%) had a smoking history. There was not any significant relationship between smoking history and the rate of pathology detected using TRO CTA. Smoking history rates were similar in the group who had pathology on CTA, compared to those without pathology apart from imaging findings of the pneumonia group (3/16 = 18.7%, 6/31 = 19.3%, $P < 0.08$).

Two patients (2/47, 4.2%) had a history of cancer (breast cancer and lymphoma). There was not any pathology except for imaging findings of pneumonia detected on CTA in these patients.

The mean PLT value of the whole population was 231.99 ± 64.15 (x 10^9/L), the D-dimer value was 854.75 ± 347.65 μg/L , the fibrinogen value was 333.05 ± 66.3 mg/dL, the C-reactive protein (CRP) value was 37.31 ± 2.01 mg/dL, and the erythrocyte sedimentation rate (ESR) value was 55.9 ± 8.2 mm/h (Table 1).

DISCUSSION

Our study revealed that TRO CTA is an effective and non-invasive diagnostic method in COVID-19 patients who were admitted to the ED with acute chest pain. Acute chest pain might be due to pneumonia itself or accompanying vascular events which are related to an increased risk of thrombosis, endothelial dysfunction, and myocardial injury in COVID-19 cases[5,7,8].

TRO CTA accelerates the precise diagnosis and utilizes the evaluation of the aorta, coronary arteries, and pulmonary vascular systems with a single examination for safe and rapid decisions[9]. However, it requires a larger amount of contrast medium and higher radiation dose, and might not be easily reachable in all centers[10]. But still instead of separate examinations, it is plausible to choose TRO CTA not only for acute thoracic vascular emergencies but for parenchymal pathologies in COVID-19 patients. Because the correct diagnosis of PTE, acute coronary syndrome, and aortic dissection, influences early treatment and thus, it is life-saving[11].

It has been previously emphasized that COVID-19 increases the risk for pulmonary thromboembolic events, so the thromboprophylaxis is suggested to prevent PTE[12]. Being a common cause of acute chest pain, coronary vascular pathologies can be encountered as a potential differential diagnosis for COVID-19. In addition to being an alternative diagnosis, coronary vascular pathologies can also increase the mortality of COVID-19 cases[13]. The results of the current study demonstrated that pathologies that can be easily diagnosed *via* the TRO CTA method, such as PTE and coronary vascular pathologies, were also frequently encountered in COVID-19 cases. Therefore, easy, accurate, and rapid diagnosis of accompanying pathologies can help guide treatment and reduce mortality/morbidity rates. Moreover, the effective use of TRO CTA in the ED can enable clinicians to both detect comorbidities and eliminate the mimickers of COVID-19 pneumonia.

Performing TRO CTA in every patient with acute chest pain might be challenging and it will not be a cost-effective method. According to our results, accompanying pathologies were mostly seen in COVID-19 patients with DM and dyslipidemia. These data can help the clinicians to select the more eligible patients for TRO CTA examinations. In addition to clinical properties, laboratory parameters can also help to define suitable patients. We showed that PLT, D-dimer, fibrinogen, CRP, and ESR values were higher in COVID-19 cases with additional pathologies other than pneumonia. The relationship between D-dimer and fibrinogen levels with thromboembolic events, and the relationship between CRP/ESR levels with severity of inflammation and the course of disease were previously studied for COVID-19 cases[14]. Hence, it would be a wise choice to prefer TRO CTA examinations in cases with severe

Table 1 Mean values and statistical significance according to subgroups

	Normal group	Pathological group	*P* value
PLT (× 109/L)	202.18 ± 45.59	289.75 ± 109.68	0.003
D-Dimer (μg/L)	651.53 ± 167.71	1248.49 ± 520.11	0.001
Fibrinogen (mg/dL)	307.49 ± 61	382.59 ± 80.1	0.002
CRP (mg/dL)	28.75 ± 3.02	53.91 ± 2.2	0.001
ESR (mm/hr)	43.1 ± 7.3	81.23 ± 12.2	0.003

inflammation and who are prone to thromboembolic events.

To the best of our knowledge, there is no research to date that has examined the TRO CTA findings in COVID-19 cases and related them to the clinical features. By examining the TRO CTA findings, performed in the emergency setting of COVID-19 cases, the current study might increase the awareness about the diagnostic utility and effectiveness of the technique, and increase its use.

The limitations of this study are that it is a retrospective single-center study with a small sample size. Although our center is a third-level university hospital and has a wide variety of facilities, future studies in larger populations are required to support the use of TRO CTA in COVID-19 patients with acute chest pain. Subsequently in times to come, our findings should be confirmed in well-powered clinical studies in multicenter hospitals. Since our study was retrospective, ECG data of some patients could not be accessed.

CONCLUSION

Our study has shown that TRO CTA is an imaging method that evaluates all thoracic vascular systems at once and gives accurate results in the COVID-19 patient group with acute chest pain, which has been proven to be susceptible to thrombotic events.

ARTICLE HIGHLIGHTS

Research background

The aim of this study was to define clinical evidence supporting that triple rule-out computed tomography angiography (TRO CTA) is a comprehensive and feasible diagnostic tool in patients with novel coronavirus disease 2019 (COVID-19) who were admitted to the emergency department for acute chest pain. Optimizing diagnostic imaging strategies in COVID-19 related thromboembolic events, will help for rapid and noninvasive diagnoses and results will be effective for patients and healthcare systems in all aspects.

Research motivation

Acute chest pain in COVID 19 patients becomes more difficult due to increasing differential diagnosis. TRO CTA helps diagnosis by excluding pulmonary thromboembolism (PTE), coronary artery disease, and acute aortic syndrome at the same time.

Research objectives

To decrease the morbidity and mortality rates in patients.

Research methods

Our study is a retrospective study.

Research results

No pathology was detected in 31 of 57 patients included in the study. PTE was detected in 11 patients. The diabetes mellitus rate was much higher in the acute coronary syndrome group, particularly in the PTE group. The rate of dyslipidemia was significantly higher in the group with pathology on CTA while compared to those without pathology apart from imaging findings of the pneumonia group

Research conclusions

TRO CTA can be a useful method in the differential diagnosis of COVID-19 patients who present to the emergency department with chest pain.

Research perspectives

The use of TRO CTA will reduce mortality and morbidity as it will accelerate the diagnosis and treatment process in the future. Studies will proceed in this direction.

FOOTNOTES

Author contributions: Aydın S, Bahadır S, Kantarcı M, and Karavas E designed the research study; Bahadır S, Ünver E, Şenbil DC, and Karavas E performed the research; Aydın S and Bahadır S contributed new reagents and analytic tools; Aydın S, Karavas E, and Şenbil DC analyzed the data and wrote the manuscript; all authors have read and approved the final manuscript.

Institutional review board statement: This study was approved by our Institutional Review Board (Erzincan Binali Yıldırım University Faculty of Medicine protocol number kaek-ebyu-2020/03/14) and as it was a retrospective study, written informed consent was waived.

Informed consent statement: Patients were not required to give informed consent to the study because the analysis used anonymous clinical data that were obtained after each patient agreed to treatment by written consent.

Conflict-of-interest statement: No author has any conflict of interest to declare in this study.

Data sharing statement: No additional data are available.

Country/Territory of origin: Turkey

ORCID number: Suzan Bahadir 0000-0002-0019-5851; Sonay Aydın 0000-0002-3812-6333; Mecit Kantarci 0000-0002-1043-6719; Edhem Unver 0000-0002-0322-8102; Erdal Karavas 0000-0001-6649-3256; Düzgün Can Şenbil 0000-0003-0233-7371.

S-Editor: Wang LL
L-Editor: Wang TQ
P-Editor: Wang LL

REFERENCES

1 **Backus BE**, Six AJ, Kelder JH, Gibler WB, Moll FL, Doevendans PA. Risk scores for patients with chest pain: evaluation in the emergency department. *Curr Cardiol Rev* 2011; **7**: 2-8 [PMID: 22294968 DOI: 10.2174/157340311795677662]
2 **Lee TH**, Goldman L. Evaluation of the patient with acute chest pain. *N Engl J Med* 2000; **342**: 1187-1195 [PMID: 10770985 DOI: 10.1056/NEJM200004203421607]
3 **Pope JH**, Aufderheide TP, Ruthazer R, Woolard RH, Feldman JA, Beshansky JR, Griffith JL, Selker HP. Missed diagnoses of acute cardiac ischemia in the emergency department. *N Engl J Med* 2000; **342**: 1163-1170 [PMID: 10770981 DOI: 10.1056/NEJM200004203421603]
4 **Tang N**, Li D, Wang X, Sun Z. Abnormal coagulation parameters are associated with poor prognosis in patients with novel coronavirus pneumonia. *J Thromb Haemost* 2020; **18**: 844-847 [PMID: 32073213 DOI: 10.1111/jth.14768]
5 **Gupta N**, Zhao YY, Evans CE. The stimulation of thrombosis by hypoxia. *Thromb Res* 2019; **181**: 77-83 [PMID: 31376606 DOI: 10.1016/j.thromres.2019.07.013]
6 **Lee HY**, Yoo SM, White CS. Coronary CT angiography in emergency department patients with acute chest pain: triple rule-out protocol *vs* dedicated coronary CT angiography. *Int J Cardiovasc Imaging* 2009; **25**: 319-326 [PMID: 18853277 DOI: 10.1007/s10554-008-9375-4]
7 **Zhou F**, Yu T, Du R, Fan G, Liu Y, Liu Z, Xiang J, Wang Y, Song B, Gu X, Guan L, Wei Y, Li H, Wu X, Xu J, Tu S, Zhang Y, Chen H, Cao B. Clinical course and risk factors for mortality of adult inpatients with COVID-19 in Wuhan, China: a retrospective cohort study. *Lancet* 2020; **395**: 1054-1062 [PMID: 32171076 DOI: 10.1016/S0140-6736]
8 **Eltabbakh AR**, Dawoud MA, Langer M, Moharm MA, Hamdy EA, Hamisa MF. 'Triple-rule-out'CT angiography for clinical decision making and early triage of acute chest pain patients: use of 320-multislice CT angiography. *Egypt J Radiol Nuc M* 2019; **50**: 1-10 [DOI: 10.1186/s43055-019-0003-1]
9 **Chae MK**, Kim EK, Jung KY, Shin TG, Sim MS, Jo IJ, Song KJ, Chang SA, Song YB, Hahn JY, Choi SH, Gwon HC, Lee SH, Kim SM, Eo H, Choe YH, Choi JH. Triple rule-out computed tomography for risk stratification of patients with acute chest pain. *J Cardiovasc Comput Tomogr* 2016; **10**: 291-300 [PMID: 27375202 DOI: 10.1016/j.jcct.2016.06.002]
10 **Yoon YE**, Wann S. Evaluation of acute chest pain in the emergency department: "triple rule-out" computed tomography angiography. *Cardiol Rev* 2011; **19**: 115-121 [PMID: 21464639 DOI: 10.1097/CRD.0b013e31820f1501]

11 **Takx RAP**, Wichmann JL, Otani K, De Cecco CN, Tesche C, Baumann S, Mastrodicasa D, Litwin SE, Bayer RR 2nd, Nance JW, Suranyi P, Jacobs BE, Duguay TM, Vogl TJ, Carr CM, Schoepf UJ. In-Hospital Cost Comparison of Triple-Rule-Out Computed Tomography Angiography Versus Standard of Care in Patients With Acute Chest Pain. *J Thorac Imaging* 2020; **35**: 198-203 [PMID: 32032251 DOI: 10.1097/RTI.0000000000000474]

12 **Sakr Y**, Giovini M, Leone M, Pizzilli G, Kortgen A, Bauer M, Tonetti T, Duclos G, Zieleskiewicz L, Buschbeck S, Ranieri VM, Antonucci E. Pulmonary embolism in patients with coronavirus disease-2019 (COVID-19) pneumonia: a narrative review. *Ann Intensive Care* 2020; **10**: 124 [PMID: 32953201 DOI: 10.1186/s13613-020-00741-0]

13 **Dan S**, Pant M, Upadhyay SK. The Case Fatality Rate in COVID-19 Patients With Cardiovascular Disease: Global Health Challenge and Paradigm in the Current Pandemic. *Curr Pharmacol Rep* 2020; 1-10 [PMID: 32953401 DOI: 10.1007/s40495-020-00239-0]

14 **Eljilany I**, Elzouki AN. D-Dimer, Fibrinogen, and IL-6 in COVID-19 Patients with Suspected Venous Thromboembolism: A Narrative Review. *Vasc Health Risk Manag* 2020; **16**: 455-462 [PMID: 33223833 DOI: 10.2147/VHRM.S280962]

Published by **Baishideng Publishing Group Inc**
7041 Koll Center Parkway, Suite 160, Pleasanton, CA 94566, USA
Telephone: +1-925-3991568
E-mail: bpgoffice@wjgnet.com
Help Desk: https://www.f6publishing.com/helpdesk
https://www.wjgnet.com

ISSN 1949-8470 (online)

World Journal of *Radiology*

World J Radiol 2022 September 28; 14(9): 319-351

Published by Baishideng Publishing Group Inc

World Journal of Radiology

Contents

Monthly Volume 14 Number 9 September 28, 2022

ORIGINAL ARTICLE

Retrospective Study

LETTER TO THE EDITOR

World Journal of Radiology

Monthly Volume 14 Number 9 September 28, 2022

Contents

ABOUT COVER

Peer Reviewer of *Word Journal of Radiology*, Suleman A Merchant, MD, DMRD, MBBS, Professor, LTM General Hospital & Medical College, Sion, Mumbai 400022, India. suleman.a.merchant@gmail.com

AIMS AND SCOPE

The primary aim of *World Journal of Radiology* (*WJR*, *World J Radiol*) is to provide scholars and readers from various fields of radiology with a platform to publish high-quality basic and clinical research articles and communicate their research findings online.

WJR mainly publishes articles reporting research results and findings obtained in the field of radiology and covering a wide range of topics including state of the art information on cardiopulmonary imaging, gastrointestinal imaging, genitourinary imaging, musculoskeletal imaging, neuroradiology/head and neck imaging, nuclear medicine and molecular imaging, pediatric imaging, vascular and interventional radiology, and women's imaging.

INDEXING/ABSTRACTING

The *WJR* is now abstracted and indexed in PubMed, PubMed Central, Emerging Sources Citation Index (Web of Science), Reference Citation Analysis, China National Knowledge Infrastructure, China Science and Technology Journal Database, and Superstar Journals Database. The 2022 edition of Journal Citation Reports ® cites the 2021 Journal Citation Indicator (JCI) for *WJR* as 0.48.

RESPONSIBLE EDITORS FOR THIS ISSUE

NAME OF JOURNAL
World Journal of Radiology

ISSN
ISSN 1949-8470 (online)

LAUNCH DATE
January 31, 2009

FREQUENCY
Monthly

EDITORS-IN-CHIEF
Thomas J Vogl

EDITORIAL BOARD MEMBERS
https://www.wjgnet.com/1949-8470/editorialboard.htm

PUBLICATION DATE
September 28, 2022

INSTRUCTIONS TO AUTHORS
https://www.wjgnet.com/bpg/gerinfo/204

GUIDELINES FOR ETHICS DOCUMENTS
https://www.wjgnet.com/bpg/GerInfo/287

GUIDELINES FOR NON-NATIVE SPEAKERS OF ENGLISH
https://www.wjgnet.com/bpg/gerinfo/240

PUBLICATION ETHICS
https://www.wjgnet.com/bpg/GerInfo/288

PUBLICATION MISCONDUCT
https://www.wjgnet.com/bpg/gerinfo/208

ARTICLE PROCESSING CHARGE
https://www.wjgnet.com/bpg/gerinfo/242

STEPS FOR SUBMITTING MANUSCRIPTS
https://www.wjgnet.com/bpg/GerInfo/239

ONLINE SUBMISSION
https://www.f6publishing.com

World Journal of Radiology

Submit a Manuscript: https://www.f6publishing.com

World J Radiol 2022 September 28; 14(9): 319-328

DOI: 10.4329/wjr.v14.i9.319

ISSN 1949-8470 (online)

ORIGINAL ARTICLE

Retrospective Study

Reliability of ultrasound ovarian-adnexal reporting and data system amongst less experienced readers before and after training

Prayash Katlariwala, Mitchell P Wilson, Yeli Pi, Baljot S Chahal, Roger Croutze, Deelan Patel, Vimal Patel, Gavin Low

Specialty type: Radiology, nuclear medicine and medical imaging

Provenance and peer review: Unsolicited article; Externally peer reviewed.

Peer-review model: Single blind

Peer-review report's scientific quality classification

Grade A (Excellent): 0
Grade B (Very good): B
Grade C (Good): C, C
Grade D (Fair): 0
Grade E (Poor): 0

P-Reviewer: Aydin S, Turkey; Sahin H, Turkey

Received: March 12, 2022
Peer-review started: March 12, 2022
First decision: May 31, 2022
Revised: June 14, 2022
Accepted: September 13, 2022
Article in press: September 13, 2022
Published online: September 28, 2022

Prayash Katlariwala, Mitchell P Wilson, Yeli Pi, Baljot S Chahal, Roger Croutze, Deelan Patel, Vimal Patel, Gavin Low, Department of Radiology and Diagnostic Imaging, University of Alberta, Edmonton T6G 2B7, AB, Canada

Corresponding author: Prayash Katlariwala, BSc, Department of Radiology and Diagnostic Imaging, University of Alberta, 8440-112 Street NW, Edmonton T6G 2B7, AB, Canada. prayashvk@gmail.com

Abstract

BACKGROUND

The 2018 ovarian-adnexal reporting and data system (O-RADS) guidelines are aimed at providing a system for consistent reports and risk stratification for ovarian lesions found on ultrasound. It provides key characteristics and findings for lesions, a lexicon of descriptors to communicate findings, and risk characterization and associated follow-up recommendation guidelines. However, the O-RADS guidelines have not been validated in North American institutions or amongst less experienced readers.

AIM

To evaluate the diagnostic accuracy and inter-reader reliability of ultrasound O-RADS risk stratification amongst less experienced readers in a North American institution with and without pre-test training.

METHODS

A single-center retrospective study was performed using 100 ovarian/adnexal lesions of varying O-RADS scores. Of these cases, 50 were allotted to a training cohort and 50 to a testing cohort *via* a non-randomized group selection process in order to approximately equal distribution of O-RADS categories both within and between groups. Reference standard O-RADS scores were established through consensus of three fellowship-trained body imaging radiologists. Three PGY-4 residents were independently evaluated for diagnostic accuracy and inter-reader reliability with and without pre-test O-RADS training. Sensitivity, specificity, positive predictive value, negative predictive value (NPV), and area under the curve (AUC) were used to measure accuracy. Fleiss kappa and weighted quadratic (pairwise) kappa values were used to measure inter-reader reliability. Statistical significance was $P < 0.05$.

RESULTS
Mean patient age was 40 ± 16 years with lesions ranging from 1.2 to 22.5 cm. Readers demonstrated excellent specificities (85%-100% pre-training and 91%-100% post-training) and NPVs (89%-100% pre-training and 91-100% post-training) across the O-RADS categories. Sensitivities were variable (55%-100% pre-training and 64%-100% post-training) with malignant O-RADS 4 and 5 Lesions pre-training and post-training AUC values of 0.87-0.95 and 0.94-098, respectively ($P < 0.001$). Nineteen of 22 (86%) misclassified cases in pre-training were related to mischaracterization of dermoid features or wall/septation morphology. Fifteen of 17 (88%) of post-training misclassified cases were related to one of these two errors. Fleiss kappa inter-reader reliability was 'good' and pairwise inter-reader reliability was 'very good' with pre-training and post-training assessment (k = 0.76 and 0.77; and k = 0.77-0.87 and 0.85-0.89, respectively).

CONCLUSION
Less experienced readers in North America achieved excellent specificities and AUC values with very good pairwise inter-reader reliability. They may be subject to misclassification of potentially malignant lesions, and specific training around dermoid features and smooth *vs* irregular inner wall/septation morphology may improve sensitivity.

Key Words: Ovarian-adnexal reporting and data system; Ovary; Malignancy; Accuracy; Reliability; Ultrasound

Core Tip: This study supports the applied utilization of the ovarian-adnexal reporting and data system (O-RADS) ultrasound risk stratification tool by less experienced readers in North America. KEY RESULTS: The O-RADS ultrasound risk stratification requires validation in less experienced North American readers; Excellent specificities (85%-100%), area under the curve values (0.87-0.98) and very good pairwise reliability can be achieved by trainees in North America regardless of formal pre-test training; Less experienced readers may be subject to down-grade misclassification of potentially malignant lesions and specific training about typical dermoid features and smooth *vs* irregular margins of ovarian lesions may help improve sensitivity.

Citation: Katlariwala P, Wilson MP, Pi Y, Chahal BS, Croutze R, Patel D, Patel V, Low G. Reliability of ultrasound ovarian-adnexal reporting and data system amongst less experienced readers before and after training. *World J Radiol* 2022; 14(9): 319-328
URL: https://www.wjgnet.com/1949-8470/full/v14/i9/319.htm
DOI: https://dx.doi.org/10.4329/wjr.v14.i9.319

INTRODUCTION

Building on the original ovarian-adnexal reporting and data system (O-RADS) publication in 2018, the American College of Radiology (ACR) O-RADS working group has recently introduced risk stratification and management recommendations to supplement the detailed reporting lexicon for this classification system[1,2]. These guidelines aim to provide consistent language, accurate characterization, and standardized recommendations for ovarian/adnexal lesions identified on ultrasound, ultimately improving the quality of communication between ultrasound examiners, referring clinicians and patients. A couple of recent papers have validated the use of the O-RADS system as an effective tool for the detection of ovarian malignancies, possessing high diagnostic accuracy and robust inter-reader reliability even without formalized training[3,4] For its future directions, the O-RADS working group specifically calls for additional studies validating this system in North American institutions and amongst less experienced readers[1]. Thus, the primary objective of the present study is to assess the inter-reader reliability of O-RADS classification amongst North American Radiology trainees using the O-RADS system, before and after training.

MATERIALS AND METHODS

This is a single center retrospective study performed at the University of Alberta Institutional Health

Research Ethics Board (HREB) approval was acquired prior to the study (Pro00097690). Patient consent for individual test cases was waived by the HREB as cases were retrospectively retrieved from the institutional Picture Archiving and Communication System (PACS) and de-identified prior to review by individual readers.

Patient selection

The University of Alberta institutional PACS was reviewed between May 2017 and July 2020 for all pelvic ultrasounds in adult female patients that demonstrated at least 1 ovarian/adnexal lesion with adequate diagnostic quality, including the presence of transvaginal 2D and Doppler sonographic image of the lesion(s) of interest. Studies were excluded if limited by technical factors such as bowel gas, large size of lesion, location of the adnexa, or inability to tolerate transvaginal ultrasound (O-RADS 0)[1].

A total of 100 diagnostic non-consecutive cases were selected by a Steering Committee of three authors including the senior author (Wilson MP, Patel V, Low G). In patients with more than one ovarian lesion, only different ipsilateral lesions were used with each individual lesion extracted as an independent blinded case when presented to study readers and the lesion of interest was designated with an arrow in each respective case. No concurrent contralateral lesions were used within the same patient. Cases were selected non-consecutively to acquire an approximately equal range of O-RADS 1 to O-RADS 5 Lesions. From these 100 cases, 50 cases were selected into separate 'Training' and 'Testing' groups. All cases were then de-identified leaving only the age, with 50 years of age used as a threshold for menopausal status. The cases were then listed as a teaching file in our institutional PACS (IMPAX 6 AGFA Healthcare) with a randomly assigned case number. All available static and cine imaging for the case were included in the teaching case file, with the additional inclusion of a 'key image' identifying the lesion intended for risk stratification with an arrow.

Training and testing

Three PGY-4 Diagnostic Radiology residents from a single institution volunteered as readers for the present study, henceforth referred to as R1, R2 and R3. The residents did not have prior formal experience with the O-RADS, SRU or IOTA systems for adnexal lesions, but have been exposed to ultrasonography in routine clinical practice totaling up to 12 wk. The residents were provided a copy of the O-RADS US Risk Stratification and Management System publication for independent review[1], and subsequently were asked to independently analyze all 50 'Testing' cases assigning the best O-RADS risk stratification score and lexicon descriptor. Answers were collected using an online Google Forms survey. Following completion of the testing file, an interval of six weeks was selected to prevent case recall. The senior author (Low G) then provided residents with a presentation reviewing the O-RADS system including lexicon descriptors, differentiating nuances for scoring, and separate examples of lesions in each O-RADS category (no overlap with cases used in the study design). The residents were then provided access to the 50 'Training' cases together with an answer key, for practice purposes and to establish familiarity with using the O-RADS system. Following the training session, and after the readers had reviewed the 'Training Cases,' the 50 "Testing" cases were then re-randomized, and independently scored again by all 3 readers in similar fashion to the pre-training format.

For both pre and post-training assessment, the reference gold standard was determined by independent consensus reading of three fellowship-trained body imaging radiologists with experience in gynaecologic ultrasound with 5, 13, and > 25 years of ultrasound experience (Wilson MP, Patel V, Low G).

Statistical analysis

The diagnostic accuracy of each individual reader and inter-observer variability between each reader both pre-training and post-training was evaluated. Continuous variables were expressed as the mean ± standard deviation. Statistical tests included: Fleiss kappa (overall agreement) and weighted quadratic kappa (pairwise agreement) was used to calculate the inter-reader agreement. The kappa (k) value interpretation as suggested by Cohen was used: κ < 0.20 (poor agreement), κ = 0.21–0.40 (fair agreement), 0.41–0.60 (moderate agreement), 0.61–0.80 (good agreement), and 0.81–1.00 (very good agreement)[5]. Diagnostic accuracy measurements including sensitivity, specificity, positive predictive value (PPV) and negative predictive value (NPV) were calculated per O-RADS category for each individual reader. Receiver operating characteristic (ROC) analysis was used to evaluate the area under the receiver operating curve (AUC) for each reader. All statistical analyses were conducted using IBM SPSS (version 26) and MedCalc (version 19.6.1). A P value of < 0.05 was considered as statistically significant.

RESULTS

Cumulatively, the testing portion of the study was comprised of 50 cases. The average age of the patients in the test cohort was 40.1 ± 16.2 years and a range from 17 to 85 years. According to the reference standard, there were 10 cases (20%) of O-RADS 1, 10 cases (20%) of O-RADS 2, 7 cases (14%) of

Table 1 Sensitivity, specificity, positive predictive value and negative predictive value per ovarian-adnexal reporting and data system category for each reader on the pre-training assessment

Pre training	ORADS 1, %	ORADS 2, %	ORADS 3, %	ORADS 4, %	ORADS 5, %
Sensitivity					
R1	90 (55.5 to 99.8)	100 (69.5 to 100)	100 (59.0 to 100)	92 (61.5 to 99.8)	55 (23.4 to 83.3)
R2	90% (55.5 to 99.8)	100% (69.2 to 100)	71 (29.0 to 96.3)	92 (61.5 to 99.8)	82 (48.2 to 97.7)
R3	90 (55.5 to 99.8)	100 (69.2 to 100)	100 (59.0 to 100)	75 (42.8 to 94.5)	55 (23.4 to 83.3)
Specificity					
R1	100 (91.2 to 100)	85 (70.2 to 94.3)	98 (87.7 to 99.4)	100 (90.8 to 100)	100 (91.0 to 100)
R2	100 (91.2 to 100)	90 (76.3 to 97.2)	98 (87.7 to 99.4)	97 (86.2 to 99.9)	100 (91.0 to 100)
R3	98 (86.8 to 99.9)	90 (76.3 to 97.2)	95 (84.2 to 99.4)	95 (82.3 to 99.4)	100 (91.0 to 100)
PPV					
R1	100	63 (44.4 to 77.7)	88 (50.2 to 98.0)	100	100
R2	100	71 (49.7 to 86.4)	83 (40.5 to 97.4)	92 (61.2 to 98.7)	100
R3	90 (56.2 to 98.4)	71 (49.7 to 86.4)	78 (47.5 to 93.1)	82 (52.9 to 94.8)	100
NPV					
R1	98 (86.2 to 99.6)	100	100	97 (85.3 to 99.6)	89 (80.3 to 93.7)
R2	98 (86.2 to 99.6)	100	96 (86.7 to 98.6)	97 (85.0 to 99.6)	95 (84.8 to 98.6)
R3	98 (85.9 to 99.6)	100	100	93 (81.8 to 97.0)	89 (80.3 to 93.7)

O-RADS: Ovarian-Adnexal Reporting and Data System; PPV: Positive predictive value; NPV: Negative predictive value.

O-RADS 3, 12 cases (24%) of O-RADS 4 and 11 cases (22%) of O-RADS 5. Of the complete test cohort, 24 lesions (48%) were lateralized to the left and right with 2 lesions (4%) being located centrally in the pelvis and with an indeterminate origin site.

Overall, the lesion sizes ranged from 1.2 cm to 22.5 cm with an average size of 6.9 ± 4.7. Mean lesion size by O-RADS category was: 2.1 ± 0.5 cm for O-RADS 1, 5.1 ± 1.4 cm for O-RADS 2, 10.6 ± 5.8 cm for O-RADS 3, 7.8 ± 4.6 cm for O-RADS 4 and 9.4 ± 4.4 cm for O-RADS 5 ($P < 0.001$).

Inter-reader reliability

The overall inter-reader agreement for the 3 readers as a group on the pre-training assessment was considered '*good*' (k = 0.76 [0.68 to 0.84, 95% Confidence Interval {CI}], p < 0.001). Kappa values for agreement on individual 0-RADS categories were '*good*' or '*very good*', as follows: O-RADS 1, k = 0.82 (0.66 to 0.98), $P < 0.001$; O-RADS 2, k = 0.78 (0.62 to 0.94), $P < 0.001$; O-RADS 3, k = 0.74 (0.58 to 0.90), $P < 0.001$; O-RADS 4, k = 0.73 (0.57 to 0.89), $P < 0.001$; O-RADS 5, k = 0.72 (0.56 to 0.88), $P < 0.001$.

The overall inter-reader agreement for the 3 readers as a group on the post-training assessment was considered '*good*' (k = 0.77 [0.69 to 0.86, 95%CI], $P < 0.001$). Kappa values for agreement on individual O-RADS categories were '*good*' or '*very good*', as follows: O-RADS 1, k = 0.96 (0.80 to 1), $P < 0.001$; O-RADS 2, k = 0.81 (0.65 to 0.97), $P < 0.001$; O-RADS 3, k = 0.65 (0.49 to 0.81), $P < 0.001$; O-RADS 4, k = 0.74 (0.58 to 0.90), $P < 0.001$; O-RADS 5, k = 0.70 (0.54 to 0.86), $P < 0.001$.

Pairwise inter-reader agreement, as evaluated using weighted kappa, was '*very good*', as follows: Pre-training: R1 and R2, k = 0.79 (0.62 to 0.96), $P < 0.001$; R1 and R3, k = 0.77 (0.59 to 0.95) $P < 0.001$; R2 and R3, k = 0.87 (0.73 to 1.00) $P < 0.001$. Post-training: R1 and R2, k = 0.86 (0.73 to 0.99), $P < 0.001$; R1 and R3, k = 0.85 (0.71 to 0.99) $P < 0.001$; R2 and R3, k = 0.89 (0.78 to 0.99) $P < 0.001$.

Diagnostic accuracy

The respective sensitivity, specificity, NPV, and PPV for each reader per O-RADS category are included in Table 1 for the pre-training assessment and Table 2 for the post-training assessment. All readers showed excellent specificities (85%-100% pre-training and 91%-100% post-training) and NPVs (89%-100% pre-training and 91%-100% post-training) across the O-RADS categories. Sensitivities range from 90%-100% in both pre-training and post-training for O-RADS 1 and O-RADS 2, 71%-100% pre-training and 86%-100% post-training for O-RADS 3, 75-92% in both pre-training and post-training for O-RADS 4, and 55%-82% pre-training and 64%-82% post-training for O-RADS 5. Readers misclassified 22 (14.7%) of 150 cases on pre-training assessment and 17 (11.3%) on post-training assessment. Misclassified cases and their respective lexicon descriptors are included in Table 3.

Table 2 The sensitivity, specificity, positive predictive value and negative predictive value per Ovarian-Adnexal Reporting and Data System category for each reader on the post-training assessment

Post training	ORADS 1, %	ORADS 2, %	ORADS 3, %	ORADS 4, %	ORADS 5, %
Sensitivity					
R1	100 (69.2 to 100)	100 (69.2 to 100)	100 (59 to 100)	92 (61.5 to 99.8)	73 (39 to 94)
R2	90 (55.5 to 99.8)	90 (55.5 to 99.8)	86 (42.1 to 99.6)	92 (61.5 to 99.8)	82 (48.2 to 97.7)
R3	100 (69.2 to 100)	100 (69.2 to 100)	100 (59 to 100)	75 (42.8 to 94.5)	64 (30.8 to 89.1)
Specificity					
R1	100 (91.2 to 100)	95 (83.1 to 99.4)	98 (87.7 to 99.9)	97 (86.2 to 99.9)	100 (91 to 100)
R2	100 (91.2 to 100)	98 (86.8 to 99.9)	93 (80.9 to 98.5)	95 (82.3 to 99.4)	100 (91 to 100)
R3	100 (91.2 to 100)	95 (83.1 to 99.4)	91 (77.9 to 97.4)	97 (86.2 to 99.9)	100 (91 to 100)
PPV					
R1	100	83 (56.4 to 95.1)	88 (50.2 to 98)	92 (61.2 to 98.7)	100
R2	100	90 (56.2 to 98.4)	67 (39.2 to 86.1)	85 (58.5 to 95.5)	100
R3	100	83 (56.4 to 95.1)	64 (40.8 to 81.7)	90 (55.9 to 98.5)	100
NPV					
R1	100	100	100	97 (85 to 99.6)	93 (83.2 to 97.2)
R2	98 (86.2 to 99.6)	98 (85.9 to 99.6)	98 (86.7 to 99.6)	97 (84.6 to 99.6)	95 (84.8 to 98.6)
R3	100	100	100	93 (82.2 to 97.1)	91 (81.7 to 95.5)

O-RADS: Ovarian-adnexal reporting and data system; PPV: Positive predictive value; NPV: Negative predictive value.

The ROC analysis evaluated diagnostic accuracy of the readers are included in Figure 1A for the pre-training assessment and Figure 1B for the post-training assessment. Given that higher O-RADS score (*i.e.* O-RADS 4 and O-RADS 5) are predictors of malignancy, reader AUC values are as follows: Pre-training: R1, AUC of 0.87 (0.75 to 0.95), $P < 0.001$; R2, AUC of 0.95 (0.84 to 0.99), $P < 0.001$; R3, AUC of 0.89 (0.77 to 0.96), $P < 0.001$. Post-training: R1, AUC of 0.96 (0.86 to 0.99), $P < 0.001$; R2, AUC of 0.98 (0.89 to 1.00), $P < 0.001$; R3, AUC of 0.94 (0.83 to 0.99), $P < 0.001$.

Pairwise comparison of the ROC curves showed a significant improvement post-training *vs* pre-training for R1 ($P = 0.04$) but not for R2 ($P = 0.29$) and R3 ($P = 0.21$).

DISCUSSION

This study demonstrates 'good' to 'very good' inter-reader agreement amongst less experienced readers in a North American institution, with pairwise and overall kappa values between spanning 0.76 and 0.89 ($P < 0.001$). The high degree of reliability is concordant with the findings of a prior study by Cao *et al*[4]. In their study performed at a tertiary care hospital and a cancer hospital in China, the pair-wise inter-reader agreement between a first-year radiology resident and a staff radiologist with 9 years experience in gynaecologic ultrasound was assessed. The authors found a kappa of 0.714 for the O-RADS system and a kappa of 0.77 for classifying lesion categories ($P < 0.001$).

Our study also highlights excellent diagnostic accuracies of resident readers when compared to a reference standard of three body-fellowship trained radiologists with experience in gynaecologic ultrasound. Solely with self-review of the O-RADS guidelines, the readers achieved high specificities greater than 0.85 and NPV greater than 0.89. These results persisted post-training, showing significant improvement in 1 resident ($P = 0.04$) and a trend towards improved accuracy amongst the other readers. The otherwise non-significant differences are due in part to excellent overall diagnostic accuracy without pre-test training as well as inadequate power to detect small differences. The study suggests that individual review of the O-RADS risk stratification is sufficient in less experienced readers with respect to specificity and AUC values. In this regard, this study validates the use of O-RADS risk classification amongst less experienced readers in a North American institution; a cohort specifically requiring validation by the ACR O-RADS committee[1].

An important risk amongst less experienced readers is the potential to misclassify potentially malignant lesions as benign. The sensitivity results in this study were variable in both pre-training and post-training assessment, particularly in higher O-RADS categories. In their respective pre-training and

Table 3 Misclassified ovarian-adnexal reporting and data system categories by readers in pre-training and post-training assessment

ORADS category	Reference standard lexicon descriptor	Misclassification category	Reader lexicon descriptor	Frequency of error in pre-training	Frequency of error in post-training
ORADS 1	Follicle defined as a simple cyst ≤ 3 cm	ORADS 2	Follicle defined as a simple cyst ≤ 3 cm	1	1
	Follicle defined as a simple cyst ≤ 3 cm	ORADS 2	Simple cyst > 5 cm but < 10 cm	1	0
	Follicle defined as a simple cyst ≤ 3 cm	ORADS 3	Multilocular cyst with smooth inner walls/septations < 10 cm, CS1-3	1	0
ORADS 2	simple cyst > 3 cm to 5 cm	ORADS 3	Unilocular cyst with irregular inner wall < 3mm height, any size	0	1
ORADS 3	Multilocular cyst with smooth inner walls/septations, < 10 cm, CS1-3	ORADS 2	Simple cyst > 5 cm but < 10 cm	1	0
	Multilocular cyst with smooth inner walls/septations, < 10 cm, CS1-3	ORADS 4	Multilocular cyst, irregular inner wall ± irregular septation	0	1
	Unilocular cyst (simple or non-simple) ≥ 10 cm	ORADS 4	Unilocular cyst with 1-3 papillary projections	1	0
ORADS 4	Multilocular cyst, irregular inner wall ± irregular septation	ORADS 1	Follicle defined as a simple cyst ≤ 3 cm	1	0
	Multilocular cyst, irregular inner wall ± irregular septation	ORADS 2	Classic benign lesion (hemorrhagic cyst < 10 cm)	1	0
	Multilocular cyst, irregular inner wall ± irregular septation	ORADS 3	Typical dermoid cyst, endometrioma, hemorrhagic cyst ≥ 10 cm	0	1
	Multilocular cyst, irregular inner wall ± irregular septation	ORADS 3	Multilocular cyst with smooth inner walls/septations < 10 cm, CS1-3	3	4
ORADS 5	Solid lesion with irregular outer contour	ORADS 2	Classic benign lesion (dermoid cyst < 10 cm)	10	4
	Solid lesion with irregular outer contour	ORADS 3	Solid lesion with smooth outer contour, any size, CS = 1	0	1
	Solid lesion with irregular outer contour	ORADS 3	Typical dermoid cyst, endometrioma, hemorrhagic cyst ≥ 10 cm	0	1
	Solid lesion with irregular outer contour	ORADS 4	Unilocular cyst with solid component	1	1
	Solid lesion with irregular outer contour	ORADS 4	Solid lesion with smooth outer contour, any size, CS = 2-3	0	2
	Multilocular cyst with solid component, CS3-4	ORADS 4	Multilocular cyst with solid component, CS1-2	1	0

O-RADS: Ovarian-adnexal reporting and data system; CS: Color scor.

post-training assessments, sensitivities were 64%-82% and 75%-92% for O-RADS 4 and 55%-82% and 64%-82% for O-RADS 5. The most frequent error on pre-training assessment was classifying a solid lesion as O-RADS 2 with a "typical dermoid cyst < 10 cm" lexicon descriptor. This error accounted for 45% (10/22) of misclassified cases in the pre-training assessment, with a reduction to 27% (4/17) of misclassified cases following training. This pitfall may be mitigated by comparing the hyperechoic component of a solid ovarian lesion to the surrounding pelvic and subcutaneous fat. The lesion should be classified as a dermoid only if it is isoechoic to the internal reference, and/or demonstrates one of three typical features including: (1) hyperechoic component with shadowing; (2) hyperechoic lines and dots; or (3) floating echogenic spherical structures[1,2]. In reviewing the test cases, all the solid lesions misclassified as dermoid had echogenicity lower than the intrapelvic fat. An example of this misclassification is shown in Figure 2.

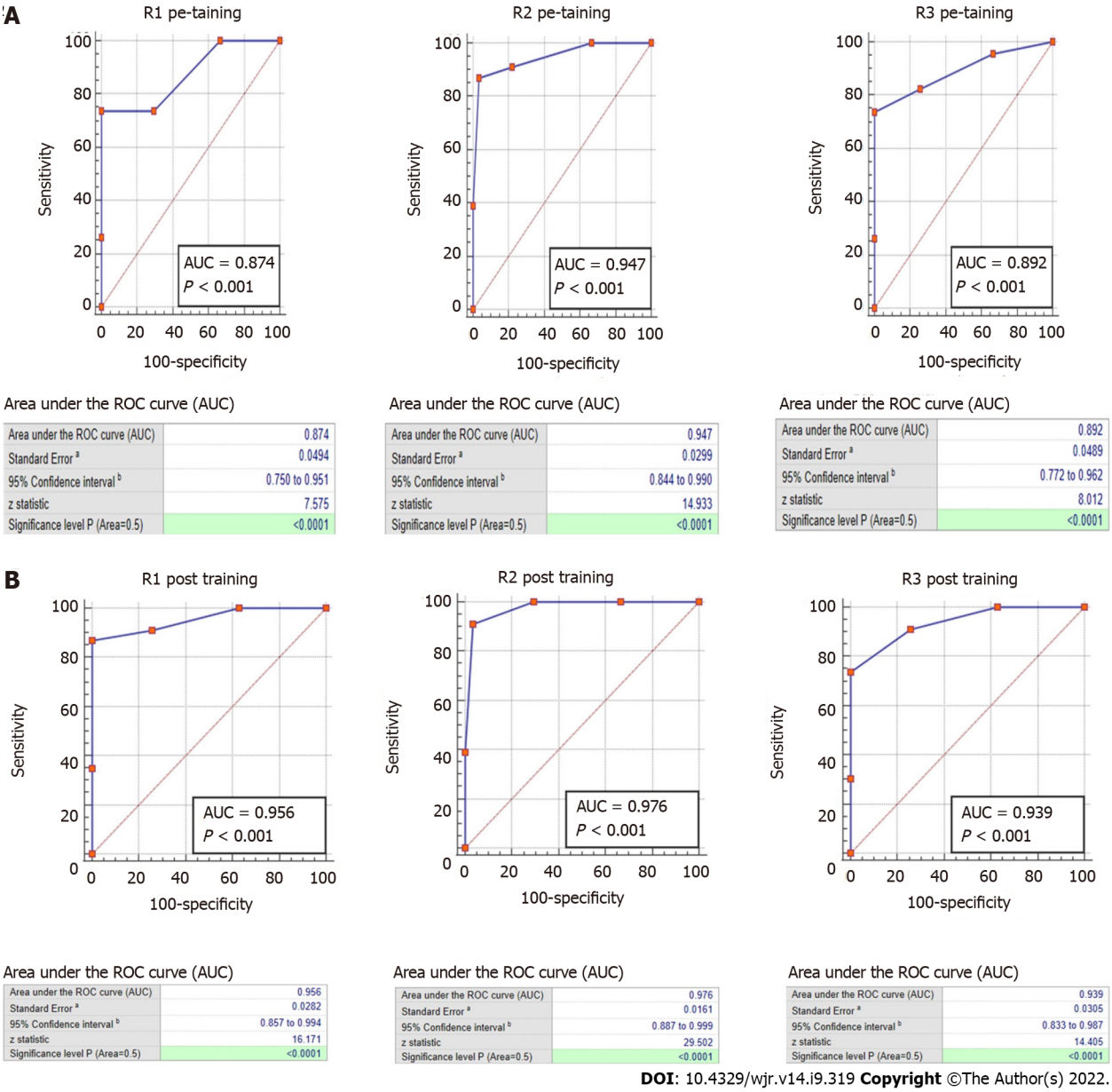

DOI: 10.4329/wjr.v14.i9.319

Figure 1 Receiver operating characteristic curve. A: Receiver operating characteristic (ROC) curve of each reader on the pre-training assessment; B: ROC curve of each reader on the post-training assessment. AUC: Area under the curve.

A second frequent error occurred in multilocular lesions with an irregular inner wall and/or irregular septation (O-RADS 4). These lesions were downgraded to O-RADS 1 through O-RADS 3 Lesions with variable lexicon descriptors used. Most commonly, these were characterized as a multilocular lesion with a smooth inner wall (O-RADS 3) in both pre-training and post-training assessment, suggesting that specific training on this finding was not sufficient in the current study. In this scenario, it is important that readers comprehensively evaluate the entire lesion on the cine clips, as irregularity in the inner wall/septation may be a subtle finding only seen in a small area within the lesion. An example of this misclassification is shown in Figure 3. Unlike the dermoid misclassification, however, this downgrade still results in a recommendation for evaluation by an ultrasound specialist or MRI and gynecology referral, reducing the risk for adverse potential complication of this misclassification. Despite these misclassifications, the negative predictive value in O-RADS 4 and O-RADS 5 Lesions remains high in both pre-training and post-training assessment (89%-97% and 91%-97%).

This study is subject to several limitations Firstly, this was a retrospective non-consecutive review. As the menopausal status was often not provided in the clinical information, an arbitrary age cut-off of 50 years was used to differentiate pre-menopausal (< 50 years) *vs* post-menopausal patients (≥ 50 years), an approach has also been used in previous epidemiologic studies[6-8]. Secondly, we did not use a pathological reference standard. Our reference standard was an expert panel of 3 three fellowship-trained radiologists with experience in gynaecologic ultrasound. However, as O-RADS is a risk stratification system that is designed to be applied universally in the clinical setting and as our study is

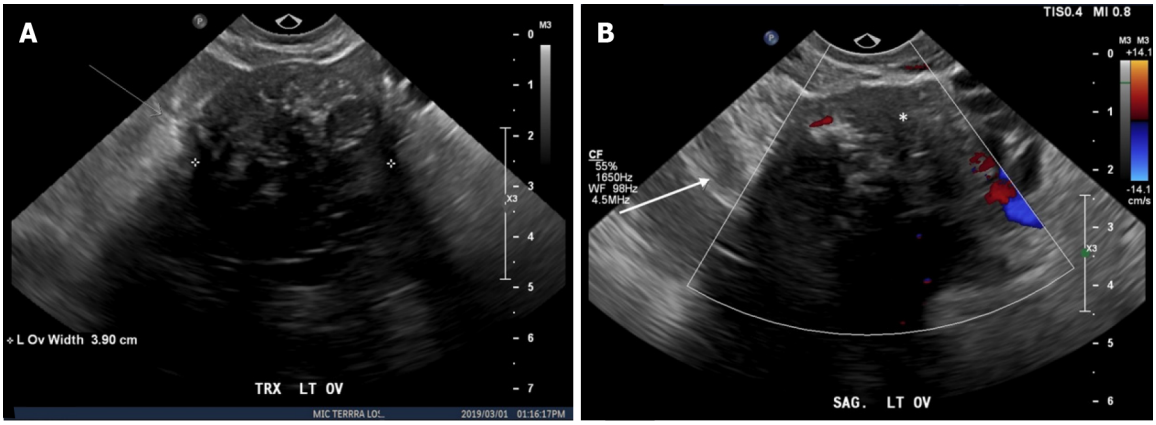

DOI: 10.4329/wjr.v14.i9.319 **Copyright** ©The Author(s) 2022.

Figure 2 An example of a left ovarian solid lesion misclassified as a typical ovarian dermoid. A: Static gray-scale images; B: Static color Doppler ultrasound images. Static gray-scale and color Doppler ultrasound images shows a solid hypoechoic lesion with a non-uniform (irregular) margin demonstrated on the color Doppler image (Ovarian-Adnexal Reporting and Data System 5). The lesion demonstrates punctate echogenic areas (white asterisk) which are less echogenic than the surrounding pelvic fat (white arrow). Further, the echogenic areas do not fulfill one of the three descriptors required to characterize as a "typical dermoid cyst < 10 cm" according to ovarian-adnexal reporting and data system criteria (2). The hypoechoic lesion with posterior shadowing suggests a fibrous lesion.

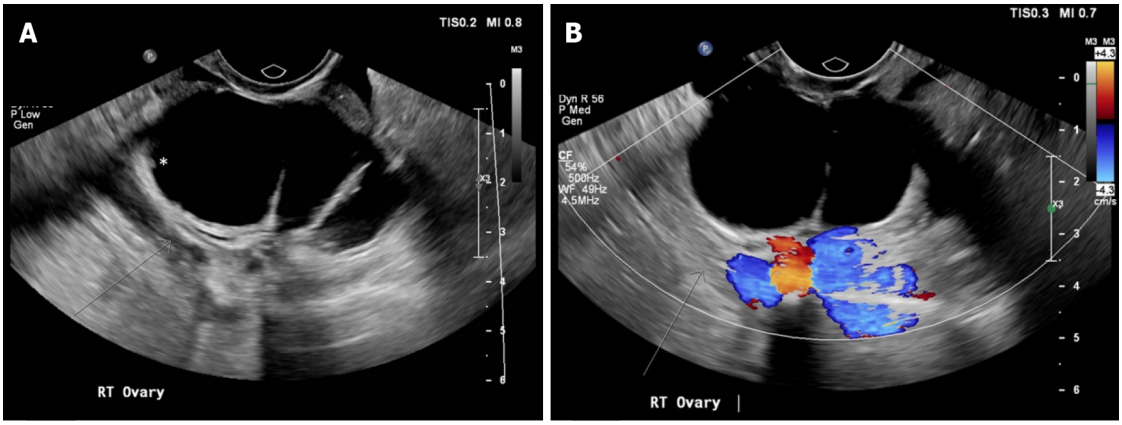

DOI: 10.4329/wjr.v14.i9.319 **Copyright** ©The Author(s) 2022.

Figure 3 An example of a right ovarian cystic lesion misclassified as a "multilocular cyst < 10 cm, smooth inner wall, color score 1-3" (Ovarian-Adnexal Reporting and Data System 3). A: Static gray-scale images; B: Static color Doppler ultrasound images. Static gray-scale and color Doppler ultrasound images show a multilocular cyst with a subtle non-uniform (irregular) inner wall with solid components < 3 mm in height (white asterisk) (ovarian-adnexal reporting and data system 4) (2).

designed primarily to evaluate inter-reader agreement, an expert consensus panel is arguably a reasonable reference standard, and one that simulates 'real world' clinical practice. A similar approach has been taken in previous O-RADS accuracy studies[3,9]. Thirdly, our sample size of 50 training cases was fairly small. A large multi-center inter-observer variability study in North America would be useful to evaluate the generalizability of our findings. Despite these limitations, we believe that the rigorous study design and specific reader cohort provide valuable insight into a needed area of validation identified by the ACR O-RADS committee.

CONCLUSION

In summary, the study validated the use of the ACR-ORADS risk stratification system in less experienced readers, showing excellent specificities and AUC values when compared to a consensus reference standard and high pairwise inter-reader reliability. Less experienced readers may be at risk for misclassification of potentially malignant lesions, and specific training around common pitfalls may help improve sensitivity.

ARTICLE HIGHLIGHTS

Research background

The 2018 Ovarian-Adnexal Reporting and Data System (O-RADS) guidelines are aimed at providing a system for consistent reports and risk stratification for ovarian lesions found on ultrasound. It provides key characteristics and findings for lesions, a lexicon of descriptors to communicate findings, and risk characterization and associated follow-up recommendation guidelines. However, the O-RADS guidelines have not been validated in North American institutions.

Research motivation

The O-RADS ultrasound risk stratification requires validation in less experienced North American readers.

Research objectives

Evaluate the diagnostic accuracy and inter-reader reliability of ultrasound O-RADS risk stratification amongst less experienced readers in a North American institution without and with pre-test training.

Research methods

A single-center retrospective study was performed using 100 ovarian/adnexal lesions of varying O-RADS scores. Of these cases, 50 were allotted to a training cohort and 50 to a testing cohort *via* a non-randomized group selection process in order to approximately equal distribution of O-RADS categories both within and between groups. Reference standard O-RADS scores were established through consensus of three fellowship-trained body imaging radiologists. Three PGY-4 residents were independently evaluated for diagnostic accuracy and inter-reader reliability without and with pre-test O-RADS training. Sensitivity, specificity, positive predictive value, negative predictive value, and area under the curve (AUC) were used to measure accuracy. Fleiss kappa and weighted quadratic (pairwise) kappa values were used to measure inter-reader reliability.

Research results

Excellent specificities (85%-100%), AUC values (0.87-0.98) and very good pairwise reliability can be achieved by trainees in North America regardless of formal pre-test training. Less experienced readers may be subject to down-grade misclassification of potentially malignant lesions and specific training about typical dermoid features and smooth *vs* irregular margins of ovarian lesions may help improve sensitivity.

Research conclusions

Less experienced readers in North America achieved excellent specificities and AUC values with very good pairwise inter-reader reliability though they may be subject to misclassification of potentially malignant lesions. Training around dermoid features and smooth *vs* irregular inner wall/septation morphology may improve sensitivity.

Research perspectives

This study supports the applied utilization of the O-RADS ultrasound risk stratification tool by less experienced readers in North America.

FOOTNOTES

Author contributions: All authors contributed equally to the paper.

Supported by RSNA Research & Education Foundation Medical Student Grant #RMS2020.

Institutional review board statement: Institutional Health Research Ethics Board (HREB) approval was acquired from the University of Alberta prior to the study (Pro00097690).

Informed consent statement: Institutional ethics approval was obtained for this study which also waived the requirement for the informed consent. Please see institutional HREB approval document for details.

Conflict-of-interest statement: All authors have no conflicts of interest.

Data sharing statement: No additional data available.

Country/Territory of origin: Canada

ORCID number: Prayash Katlariwala 0000-0002-5822-1071; Mitchell P Wilson 0000-0002-1630-5138; Vimal Patel 0000-0003-2972-5980; Gavin Low 0000-0002-4959-8934.

S-Editor: Liu JH
L-Editor: A
P-Editor: Liu JH

REFERENCES

1 **Andreotti RF**, Timmerman D, Strachowski LM, Froyman W, Benacerraf BR, Bennett GL, Bourne T, Brown DL, Coleman BG, Frates MC, Goldstein SR, Hamper UM, Horrow MM, Hernanz-Schulman M, Reinhold C, Rose SL, Whitcomb BP, Wolfman WL, Glanc P. O-RADS US Risk Stratification and Management System: A Consensus Guideline from the ACR Ovarian-Adnexal Reporting and Data System Committee. *Radiology* 2020; **294**: 168-185 [PMID: 31687921 DOI: 10.1148/radiol.2019191150]

2 **Andreotti RF**, Timmerman D, Benacerraf BR, Bennett GL, Bourne T, Brown DL, Coleman BG, Frates MC, Froyman W, Goldstein SR, Hamper UM, Horrow MM, Hernanz-Schulman M, Reinhold C, Strachowski LM, Glanc P. Ovarian-Adnexal Reporting Lexicon for Ultrasound: A White Paper of the ACR Ovarian-Adnexal Reporting and Data System Committee. *J Am Coll Radiol* 2018; **15**: 1415-1429 [PMID: 30149950 DOI: 10.1016/j.jacr.2018.07.004]

3 **Pi Y**, Wilson MP, Katlariwala P, Sam M, Ackerman T, Paskar L, Patel V, Low G. Diagnostic accuracy and inter-observer reliability of the O-RADS scoring system among staff radiologists in a North American academic clinical setting. *Abdom Radiol (NY)* 2021; **46**: 4967-4973 [PMID: 34185128 DOI: 10.1007/s00261-021-03193-7]

4 **Cao L**, Wei M, Liu Y, Fu J, Zhang H, Huang J, Pei X, Zhou J. Validation of American College of Radiology Ovarian-Adnexal Reporting and Data System Ultrasound (O-RADS US): Analysis on 1054 adnexal masses. *Gynecol Oncol* 2021; **162**: 107-112 [PMID: 33966893 DOI: 10.1016/j.ygyno.2021.04.031]

5 **Landis JR**, Koch GG. The measurement of observer agreement for categorical data. *Biometrics* 1977; **33**: 159-174 [PMID: 843571]

6 **Phipps AI**, Ichikawa L, Bowles EJ, Carney PA, Kerlikowske K, Miglioretti DL, Buist DS. Defining menopausal status in epidemiologic studies: A comparison of multiple approaches and their effects on breast cancer rates. *Maturitas* 2010; **67**: 60-66 [PMID: 20494530 DOI: 10.1016/j.maturitas.2010.04.015]

7 **Hill K**. The demography of menopause. *Maturitas* 1996; **23**: 113-127 [PMID: 8735350 DOI: 10.1016/0378-5122(95)00968-x]

8 **Im SS**, Gordon AN, Buttin BM, Leath CA 3rd, Gostout BS, Shah C, Hatch KD, Wang J, Berman ML. Validation of referral guidelines for women with pelvic masses. *Obstet Gynecol* 2005; **105**: 35-41 [PMID: 15625139 DOI: 10.1097/01.AOG.0000149159.69560.ef]

9 **Basha MAA**, Metwally MI, Gamil SA, Khater HM, Aly SA, El Sammak AA, Zaitoun MMA, Khattab EM, Azmy TM, Alayouty NA, Mohey N, Almassry HN, Yousef HY, Ibrahim SA, Mohamed EA, Mohamed AEM, Afifi AHM, Harb OA, Algazzar HY. Comparison of O-RADS, GI-RADS, and IOTA simple rules regarding malignancy rate, validity, and reliability for diagnosis of adnexal masses. *Eur Radiol* 2021; **31**: 674-684 [PMID: 32809166 DOI: 10.1007/s00330-020-07143-7]

World Journal of Radiology

Submit a Manuscript: https://www.f6publishing.com

World J Radiol 2022 September 28; 14(9): 329-341

DOI: 10.4329/wjr.v14.i9.329

ISSN 1949-8470 (online)

ORIGINAL ARTICLE

Retrospective Study

Contrast-enhanced multidetector computed tomography features and histogram analysis can differentiate ameloblastomas from central giant cell granulomas

Adarsh Ghosh, Meyyappan Lakshmanan, Smita Manchanda, Ashu Seith Bhalla, Prem Kumar, Ongkila Bhutia, Asit Ranjan Mridha

Specialty type: Radiology, nuclear medicine and medical imaging

Provenance and peer review: Invited article; Externally peer reviewed.

Peer-review model: Single blind

Peer-review report's scientific quality classification

Grade A (Excellent): 0
Grade B (Very good): 0
Grade C (Good): C, C
Grade D (Fair): 0
Grade E (Poor): 0

P-Reviewer: Chen Q, China; Xie Q, China

Received: March 19, 2022
Peer-review started: March 19, 2022
First decision: June 16, 2022
Revised: July 5, 2022
Accepted: September 2, 2022
Article in press: September 2, 2022
Published online: September 28, 2022

Adarsh Ghosh, Department of Radiology, Children's Hospital of Philadelphia, Philadelphia, PA 19104, United States

Meyyappan Lakshmanan, Smita Manchanda, Department of Radiology, All India Institute of Medical Sciences, New Delhi 110029, India

Ashu Seith Bhalla, Department of Radiodiagnosis, All India Institute of Medical Sciences, New Delhi 110029, India

Prem Kumar, Ongkila Bhutia, Department of Oral & Maxillofacial Surgery, All India Institute of Medical Sciences, New Delhi 110029, India

Asit Ranjan Mridha, Department of Pathology, All India Institute of Medical Sciences, Ansari Nagar, New Delhi 110029, India

Corresponding author: Ashu Seith Bhalla, MD, Professor, Department of Radiodiagnosis, All India Institute of Medical Sciences, New Delhi 110029, India. ashubhalla1@yahoo.com

Abstract

BACKGROUND

No qualitative or quantitative analysis of contrast-enhanced computed tomography (CT) images has been reported for the differentiation between ameloblastomas and central giant cell granulomas (CGCGs).

AIM

To describe differentiating multidetector CT (MDCT) features in CGCGs and ameloblastomas and to compare differences in enhancement of these lesions qualitatively and using histogram analysis.

METHODS

MDCT of CGCGs and ameloblastomas was retrospectively reviewed to evaluate qualitative imaging descriptors. Histogram analysis was used to compare the extent of enhancement of the soft tissue. Fisher's exact tests and Mann–Whitney *U* test were used for statistical analysis ($P < 0.05$).

RESULTS

Twelve CGCGs and 33 ameloblastomas were reviewed. Ameloblastomas had a predilection for the posterior mandible with none of the CGCGs involving the angle. CGCGs were multilocular (58.3%), with a mixed lytic sclerotic appearance (75%). Soft tissue component was present in 91% of CGCGs, which showed hyperenhancement (compared to surrounding muscles) in 50% of cases, while the remaining showed isoenhancement. Matrix mineralization was present in 83.3% of cases. Ameloblastomas presented as a unilocular (66.7%), lytic (60.6%) masses with solid components present in 81.8% of cases. However, the solid component showed isoenhancement in 63%. No matrix mineralization was present in 69.7% of cases. Quantitatively, the enhancement of soft tissue in CGCG was significantly higher than in ameloblastoma on histogram analysis ($P < 0.05$), with a minimum enhancement of > 49.05 HU in the tumour providing 100% sensitivity and 85% specificity in identifying a CGCG.

CONCLUSION

A multilocular, lytic sclerotic lesion with significant hyperenhancement in soft tissue, which spares the angle of the mandible and has matrix mineralization, should indicate prospective diagnosis of CGCG.

Key Words: Ameloblastoma; Granuloma; Giant cell; Multidetector CT

Core Tip: Central giant cell granulomas (CGCGs) are rare tumours of the jaw. This study evaluated the findings of CGCGs on contrast-enhanced computed tomography in contrast with ameloblastomas, which are the most common tumours of the jaw in the developing world.

Citation: Ghosh A, Lakshmanan M, Manchanda S, Bhalla AS, Kumar P, Bhutia O, Mridha AR. Contrast-enhanced multidetector computed tomography features and histogram analysis can differentiate ameloblastomas from central giant cell granulomas. *World J Radiol* 2022; 14(9): 329-341
URL: https://www.wjgnet.com/1949-8470/full/v14/i9/329.htm
DOI: https://dx.doi.org/10.4329/wjr.v14.i9.329

INTRODUCTION

The most current World Health Organization classification of jaw tumours places giant cell granulomas under "giant cell lesions and simple bone cyst". These include both central and peripheral giant cell granulomas[1]. Central giant cell granuloma (CGCG) usually appears as an expansile, multiloculated lesion with post-contrast enhancement and soft tissue extension[2-4]. Histologically it is characterized by focally distributed giant cells, spindle cells and possible areas of haemorrhage. A similar radiological and histopathological appearance may also be seen in brown tumours of hyperparathyroidism, and further clinical and laboratory correlation is required whenever aggressive, atypical or multiple CGCGs are seen[1,5]. CGCGs are slow-growing and insidious, although, increased rates of growth, presence of pain, tooth resorption or cortical erosions are considered signs of aggressive behaviour[2,3,6]. CGCGs are rare and tend to occur with a female preponderance in the second decade of life. Accelerated growth during pregnancy or following childbirth suggests hormone responsiveness of CGCGs. Although the exact pathophysiology of the tumour is yet to be elucidated: a reparative response to trauma, haemorrhagic products and inflammation is presumed to result in tumorigenesis. The classical lytic multilocular appearance of CGCGs on radiographs makes difficult their differentiation from ameloblastomas, odontogenic cyst, aneurysmal bone cysts, and odontogenic fibromas[3,7]. This differentiation is, however, vital because CGCGs are treated less aggressively (curettage, intralesional interferon, steroids or calcitonin injections[8]) as compared to other lesions with a similar radiological appearance. Ameloblastomas are by far is the most prevalent odontogenic tumour in the developing world[9], constituting about 14% of all jaw lesions[10]. Although benign, ameloblastomas exhibit an aggressive growth pattern, with up to 70% of cases[11] undergoing malignant transformation. It presents most frequently in males, in their third to fifth decades of life, as a slowly progressive swelling. The lesion favours the posterior mandible (63.15% of all cases as per one study[12]) and on imaging is a close differential of CGCGs with its unilocular or multilocular, lytic, expansive appearance[13]. Ameloblastomas are treated more radically and aggressively (with block resection, radiotherapy and vemurafenib[14]) vis-à-vis CGCGs making differentiation between the two crucial clinically.

Contrast-enhanced computed tomography (CT) can help characterise tumour biology better than noncontrast scans[15]. Although tumour location, appearance, contour and mass effect of the lesion on surrounding structures and teeth can be easily evaluated on noncontrast multidetector CT (MDCT)[4,7,16,17] or on cone beam CT (CBCT), the presence of enhancing soft tissue and the extent of enhancement in the tumour can provide significant insight into tumour biology and can differentiate tumour types and pathological processes. For example, contrast-enhanced CT (CECT) helps differentiate purely cystic lesions of the jaw from cyst like lesions[18], a task relatively difficult on noncontrast MDCT or CBCT. Similarly, contrast-enhanced dynamic MDCT can help differentiate ameloblastomas[19] from other cystic jaw lesions, including keratocystic odontogenic tumours. Further quantification of the extent of tumour enhancement using histogram and texture analysis[20] can also characterise these tumours. However, to our knowledge, no qualitative or quantitative analysis of CECT images has been reported for the differentiation between ameloblastomas and CGCGs.

Given this background, we undertook this study to compare the MDCT features of CGCGs and ameloblastomas. More specifically we compared the utility of quantitative and qualitative evaluation of extent of tumour enhancement in differentiation of these two tumours.

MATERIALS AND METHODS

Subjects

The electronic records available from the Department of Pathology were searched to identify cases of CGCGs and ameloblastomas, between December 2016 and January 2019. All cases with MDCT images were included in the study, and six patients who did not have MDCT images were excluded. A total of 12 CGCGs and 33 ameloblastomas were identified and used in this study. The study was approved by the Institutional Ethics Committee (Ref No: IEC-622/03.07.2020, RP-31/2020).

Imaging technique

All MDCT acquisitions were performed either on a 64-MDCT scanner (Siemens SOMATOM Sensation, Erlangen, Germany) or 128-MDCT scanner (Siemens SOMATOM Definition Flash) available in our department. The images were acquired using 120 kV with automated tube current modulation, and a quality reference mAs of 80. A slice thickness of 0.6 mm was used. A 16-cm field of view, 512 × 512 matrix, was used to reconstruct data with routine 1mm sections being obtained using standard soft tissue and bone window kernels. CECT images were available for 38 of these 45 scans. Among these 38, venous phase images acquired at 60–70 s after intravenous injection were available in 35 patients (8 CGCGs and 27 ameloblastomas) [1–1.5 mL/kg of nonionic iodinated contrast (Iohexol 350 mg iodine/mL)]. Only arterial phase images were available as part of a head and neck angiography protocol in three patients. Noncontrast MDCT was available in seven patients.

Imaging interpretation

Two radiologists with 16 and 6 years' experience in head and neck imaging, blinded to clinical and pathological data reviewed all the MDCT scans in consensus. Nonconsensus was resolved by reviewing with a third radiologist. Zone-wise mapping of each lesion was done, as explained in Figure 1. Location of the lesion (mandible or maxilla); density (mixed, lytic or sclerotic as characterized on the bone window); multilocularity (unilocular with 1 or 2 thin septae; multilocular, honeycombing pattern); presence or absence of solid components; and erosion or thinning of the surrounding cortex were recorded. In mandibular lesions, the involvement of the angle (yes/no), and the status of the inferior alveolar canal was recorded (involvement/erosion) as well. The status of the overlying teeth (missing or root resorbed/present/adjoining roots displaced), and adjacent fat stranding and muscle thickening (present or absent) were noted. Venous phase images were evaluated (n = 35) to quantify the amount of soft tissue in each lesion (0–10%, 10%–25%, 25%–50%, 50%–75% and > 75%) and the type of enhancement of the solid component in the lesion were also characterised (purely cystic, hypoenhancing, isoenhancing, or hyperenhancing – the enhancement in these cases was compared to that of the surrounding muscles). Mineralisation of the tumour was recorded (absent, mineralised osteoid, thin bony septa, or thick septa with associated matrix). The three largest diameters of each lesion were recorded (along and perpendicular to the axis of mandible, and craniocaudal). These measurements were then used to derive the lesion's volume using the volume formula for an ellipsoid (0.523 × AP × TR × CC).

Quantitative analysis of enhancement

The venous phase MDCT images were evaluated to compare the degree of enhancement between the tumours. Specifically, the contrast-enhanced MDCT images were opened on 3D Slicer 4.11.0 (https://download.slicer.org/). A freehand oval region of interest (ROI) measuring at least 1 cm in diameter was drawn on the largest bulk of the tumour, ensuring that the ROI was placed on soft tissue only, avoiding bony septa (Supplementary Figure 1). This was done by AG with 6 years' experience in

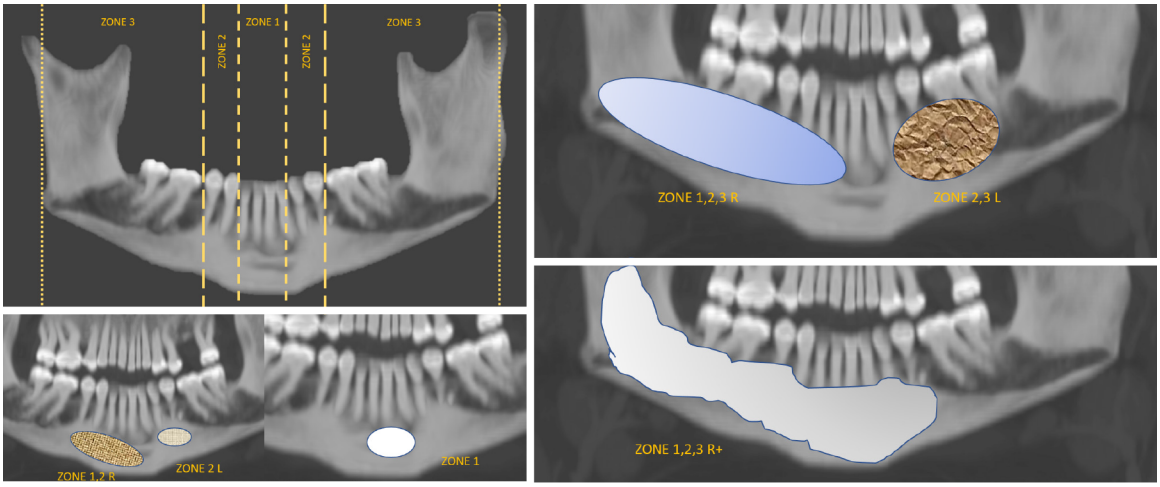

DOI: 10.4329/wjr.v14.i9.329 **Copyright** ©The Author(s) 2022.

Figure 1 Location of every lesion was classified into the following zones: 1, limited to the incisors; 2, limited to the canine and premolars; and 3, limited to the molars and posterior mandible. A similar classification was applied to the maxilla. Lesions extending over multiple zones were classified as such, and a suffix of R or L was used to denote right or left-sided location. When the lesion crossed the midline across multiple zones, + was used to denote the same.

head and neck imaging and ROI placement was reviewed by SM. The pyRadiomics plugin (https://pyradiomics.readthedocs.io/en/Latest/index.html) was used to evaluate the histogram of the distribution of the HUs in the ROIs. Skewness, uniformity, entropy, kurtosis, and mean, median, maximum, minimum, 10th and 90th percentiles of the HU values in the histogram were evaluated. Purely cystic lesions (n = 6) were excluded from this analysis.

Statistical analysis

All data were tabulated and tested for normality when indicated. Continuous data were compared between the two data sets using the Mann–Whitney U test, while Fisher's exact test was used to compare categorical data. $P < 0.05$ was considered statistically significant. Receiver operating characteristic (ROC) curve analysis was used to obtain the area under the curve (AUC) for texture parameters found to be significantly different between the two groups. Optimal cutoffs were obtained using bootstrapped Youden index. A leave-one-out cross-validation of the various enhancement parameters was done to evaluate generalisability.

RESULTS

A total of 12 CGCGs and 33 ameloblastomas were included in our study. The median age of patients with ameloblastoma was higher [35 years [95%confidence interval (CI) 28–48 years] as compared to patients with CGCG [29 years (95%CI 18–42 years)]; however, this was not significant (P = 0.26). Of the patients having ameloblastomas, 27.30% (n = 9) were female and 72.70% (n = 24) were male. The prevalence of CGCGs was nearly equal between the sexes: 41.70% (n = 5) in females *versus* 58.30% (n = 7) in males. This difference was again not significant.

Location

Both the pathologies favoured the mandible, with five ameloblastomas and four CGCGs appearing in the maxilla. CGCGs favoured a more central location with six lesions being located in zone 1 (50.00%), three in zone 2 (25.00%) and two in zone 3 (16.70%) (Table 1 and Figure 1). Only a single CGCG was large enough to involve zones 1, 2 and 3 simultaneously. This was significantly ($P < 0.0001$) different from ameloblastomas, which had a more varied distribution. Fourteen (42.40%) ameloblastomas were located exclusively in zone 3. Simultaneously, nine ameloblastomas were large enough to involve all three zones and two were large enough to cross the midline. Fifty per cent (n = 14 out of 28) of ameloblastomas had involvement of the angle of the mandible. In contrast, none of the CGCGs had this feature (P = 0.013).

Volume and size

Lesion volume was determined using the ellipsoid formula. CGCGs were significantly smaller in volume (median 10.31 cm^3) as compared to ameloblastomas (median 35.9 cm^3) (P = 0.027) (Table 2). ROC curve analysis and the associated cutoff are provided in Table 3. While there was considerable overlap

Table 1 Comparison of the various multidetector computed tomography imaging features between ameloblastoma and central giant cell granuloma

MDCT features		Pathology				Fisher's exact test (exact sig. two-sided)
		Ameloblastoma		CGCG		
		Count	% of all cases	Count	% of all cases	
Zone wise location (figure × for reference)	1, 2, 3	9	27.3 (14.4–43.9)	1	8.3 (0.9–32.8)	< 0.0001[a]
	1	0	0.00%	6	50 (24.3–75.7)	
	1, 2	4	12.1 (4.2–26.3)	0	0.00%	
	2	0	0.00%	3	25 (7.6–52.9)	
	2,3	6	18.2 (8–33.7)	0	0.00%	
	3	14	42.4 (26.8–59.3)	2	16.7 (3.6–43.6)	
Density	Mixed	13	39.4 (24.2–56.4)	9	75 (47.1–92.4)	0.036[a]
	Lytic	20	60.6 (43.6–75.8)	3	25 (7.6–52.9)	
Multilocularity; 1-Unilocular with 1 or 2 thin septae/2-Multilocular/3-Honeycombing	1	22	66.7 (49.7–80.8)	3	25 (7.6–52.9)	0.047[a]
	2	8	24.2 (12.2–40.6)	7	58.3 (31.2–82)	
	3	3	9.1 (2.6–22.3)	2	16.7 (3.6–43.6)	
Bucco-lingual expansion	1	33	100.00%	12	100.00%	-
Solid component	Absent	6	18.2 (8–33.7)	1	8.3 (0.9–32.8)	0.309
	Present	27	81.8 (66.3–92)	11	91.7 (67.2–99.1)	
Cortical erosion	Thinning	1	3 (0.3–13.3)	1	8.3 (0.9–32.8)	1.000
	Erosion	32	97 86.7–99.7)	11	91.7 (67.2–99.1)	
Angle involved (of lesions in mandible)	No	14	50 (32.2–67.8)	8	100.00%	0.013[a]
	Yes	14	50 (32.2–67.8)	0	0.00%	
Inferior alveolar canal displacement	No	3	14.3 (4.2–33.4)	2	25 (5.6–59.2)	0.597
	Yes	18	85.7 (66.6–95.8)	6	75 (40.8–94.4)	
Status of overlying teeth; Missing-0/Adjoining roots-1/Present-2	0	19	57.6 (40.7–73.2)	8	72.7 (43.5–91.7)	0.152
	1	12	36.4 21.6–53.4)	1	9.1 (1–35.3)	
	2	2	6.1 (1.3–18.1)	2	18.2 (4–46.7)	
Inferior alveolar canal erosion	No	2	9.5 (2–27.2)	3	37.5 (11.9–70.5)	0.112
	Yes	19	90.5 (72.8–98)	5	62.5 (29.5–88.1)	
Adjacent fat stranding	Absent	27	81.8 (66.3–92)	10	83.3 (56.4–96.4)	1.000
	Present	6	18.2 (8–33.7)	2	16.7 (3.6–43.6)	
Adjacent muscle thickening	Absent	26	78.8 (62.8–90)	11	91.7 (67.2–99.1)	0.419
	Present	7	21.2 (10–37.2)	1	8.3 (0.9–32.8)	
Extent of enhancement of soft tissue component in venous phase;	0	6	22.2 (9.8–40.2)	0	0.00%	

0-cystic/1- hypoenhancing/2- isoenhancing/3- hyperenhancing	2	17	63 (44.2–79.1)	4	50 (19.9–80.1)	0.013[a]
	3	1	3.7 (0.4–16)	4	50 (19.9–80.1)	
	1	3	11.1 (3.2–26.8)	0	0.00%	
Amount of solid component	> 75%	9	33.3 (17.9–52.1)	6	75 (40.8–94.4)	0.061
	0- < 10%	8	29.6 (15.1–48.2)	0	0.00%	
	10%-25%	3	11.1 (3.2–26.8)	0	0.00%	
	25%-50%	5	18.5 (7.4–35.9)	0	0.00%	
	50%-75%	2	7.4 (1.6–21.7)	2	25 (5.6–59.2)	
Matrix mineralisation; Mineralised osteoid-1; Absent- 2; Thick septae with associated matrix-3; Thin bony septa- 4	1	1	3 (0.3–13.3)	3	25 (7.6–52.9)	0.004[a]
	2	23	69.7 (52.9–83.2)	2	16.7 (3.6–43.6)	
	3	4	12.1 (4.2–26.3)	3	25 (7.6–52.9)	
	4	5	15.2 (6–30.1)	4	33.3 (12.5–61.2)	
Diameter		33	5.1(4.5–6)	12	3.7(2.1–4.8)	0.011[a]
Volume		33	35.9 (23.05–47.59)	12	10.31 (3.67–59.37)	0.027[a]

[a]Statistically significant.

CGCG: Central giant cell granulomas; MDCT: Multidetector computed tomography.

Table 2 First-order histogram parameters comparing the extent of enhancement seen in the soft tissue component of ameloblastomas and central giant cell granulomas

		Ameloblastoma (*n* = 21); median (95%CI)	CGCG (*n* = 8); median(95%CI)	*P* value
Histogram parameter (*n* = 29)	Skewness	0.1 (-0.23–0.22)	0.07 (-0.51–0.47)	0.981
	Median (HU)	74.91 (56.97–93.24)	106.21 (95.1–134.52)	0.002
	Maximum (HU)	121.01 (100.11–150.05)	154.2 (133.42–183.09)	0.013
	90 percentile (HU)	95.32 (75.72–113.71)	137.43 (113.91–150.17)	0.001
	Entropy	1.62 (1.57–1.8)	1.5 (1.34–1.98)	0.487
	10 percentile (HU)	53.32 (34.2–71.13)	82.65 (74.86–116.64)	0.002
	Kurtosis	3.11 (2.71–3.54)	3.25 (2.69–4.08)	0.83
	Mean (HU)	74.06 (58.58–91.92)	106.95 (97.48–132.39)	0.002

CGCG: Central giant cell granulomas; CI: Confidence interval; MDCT: Multidetector computed tomography.

between the two volumes, a cutoff ≤ 13.04 cm^3 obtained 84.85% (68.1%–94.9%) specificity in identifying CGCG. Similarly, the diameter of ameloblastomas (measured along the long axis of the mandible) was higher than that of CGCGs with a cut off of ≤ 3.5 cm (95%CI ≤ 2.1 cm to ≤ 4.4 cm) providing 50% (95%CI 21.1%–78.9%) sensitivity and 90.91% (95%CI 75.7%–98.1%) specificity in identifying the latter.

Lesion appearance on bone window

60.6% of ameloblastomas were purely lytic (*n* = 20), as compared to only 25% of CGCGs (*n* = 3) (*P* = 0.047). A majority of all CGCGs (75%; *n* = 9) were predominantly mixed in appearance with both lytic and sclerotic components being present in the lesion. However, only 39.4% of ameloblastomas were mixed in appearance (*n* = 13). Neither of the tumours was purely sclerotic. Ameloblastomas (*n* = 22) were predominantly unilocular (66.7%) compared to 58.3% of CGCGs, which were multilocular. Matrix mineralisation in the form of osteoid, thin septa, or thick septa and associated dense matrix, was more common in CGCGs than ameloblastomas, where 70% showed no matrix mineralisation.

Table 3 Area under the curve of the various statistically significant histogram parameters of tumours in differentiating central giant cell granulomas from ameloblastomas

Variable	10 percentile	90 percentile	Mean	Median	Minimum
Area under the ROC curve (AUC)	0.863	0.875	0.863	0.869	0.887
5, 95%CI	0.685 to 0.962	0.699 to 0.968	0.685 to 0.962	0.692 to 0.965	0.714 to 0.974
Associated criterion (HU)	> 71.13	> 106.33	> 91.92	> 93.24	> 49.05
95%CI	> 66.43 to > 96.63	> 82.80 to > 113.71	> 88.68 to > 114.75	> 93.15 to > 110.22	> 48.51 to > 49.05
Sensitivity %	100 (63.1-100.0)	100 (63.1-100.0)	100 (63.1-100.0)	100 (63.1-100.0)	100 (63.1-100.0)
Specificity %	76.19 (52.8-91.8)	66.67 (43.0-85.4)	76.19 (52.8-91.8)	76.19 (52.8-91.8)	85.71 (63.7-97.0)
Leave-one out sensitivity %	100 (63.06–100)	100 (63.06–100)	100 (63.06–100)	100 (63.06–100)	100 (63.06–100)
Leave-one out specificity %	71.43 (47.82–88.72)	47.62 (25.71–70.22)	71.43 (47.82–88.72)	71.43 (47.82–88.72)	80.95 (58.09–94.55)

AUC: Area under the curve; CI: Confidence interval; ROC: Receiver operating characteristic.

Qualitative evaluation of contrast enhancement

Evaluation of the degree of enhancement of solid component on venous phase images (8 CGCGs and 27 ameloblastomas) showed that six ameloblastomas were purely cystic with no solid component, and 17 (62.9%) ameloblastomas showed enhancement that was similar to the surrounding muscles. In comparison, four (50%) CGCGs showed enhancement higher than the surrounding muscles. This was significantly different (P = 0.013) from ameloblastomas, with only one ameloblastoma (3.7%) showing enhancement higher than muscles. These above findings are summarised in Table 1 and Figure 2.

Quantitative evaluation of enhancement

Histogram analysis (8 CGCGs and 21 ameloblastomas) of the enhancement of the solid component in the venous phase image was carried out after excluding the purely cystic lesions (n = 6). CGCGs had higher minimum, median, mean and maximum enhancement as compared to ameloblastomas (P < 0.05) on venous imaging (Table 2). A boot-strapped ROC curve analysis provided the AUC of the individual parameters as well as the optimum cutoffs. Minimum enhancement of > 49.0538, had a sensitivity of 100% and a specificity of 85.71% in identifying a CGCC over ameloblastoma. The cutoffs, their associated sensitivity and specificity, and accuracy metrics of a leave-one-out cross-validation are provided in Table 3.

DISCUSSION

We described the MDCT imaging features of CGCGs and contrasted them with ameloblastomas. Morphologically, both CGCGs and ameloblastomas had several overlapping features – making their differentiation difficult. Both ameloblastomas and CGCGs can be either unilocular or multilocular. Cortical expansion, cortical perforation, root displacement and root resorption are features suggestive of an aggressive variant of CGCG; however, these features are also present in ameloblastomas. MDCT or CBCT is preferred over radiography because it allows better evaluation of the bony anatomy, especially the integrity of the buccal and lingual cortex. MDCT with intravenous contrast allows better evaluation of the soft tissue component in these lesions. Location wise, we found that, although the CGCGs favoured the central jaw, up to 25% of the lesions were also found in the ramus[21,22]. Because of the small size of CGCGs, only one lesion was large enough to involve all the three zones. Ameloblastomas because of their larger sizes tended to involve more than one zone, with the most predominant preference for zone 3 (ramus of the mandible). This varied distribution is similar to that described in the literature[14,15]; involvement of the angle when present was highly specific for ameloblastoma. None of the CGCGs demonstrated the involvement of the angle. CGCGs were considerably smaller (28.82 ± 40.75 cm^3) in volume as compared to ameloblastomas (66.18 ± 84.33 cm^3) (Tables 2 and 3). Ameloblastomas are locally aggressive tumours, while CGCGs are slow-growing insidious masses that are sometimes known to regress spontaneously. Thus, the smaller volume of CGCG may be in keeping with the natural history of CGCGs (Table 2). Cortical expansion, cortical perforation, root displacement and root resorption as previously stated, can occur in both tumours[19,24-26]. Even in our series, there was no difference in the prevalence of root resorption, tooth displacement, cortical expansion or cortical perforation between the two entities (Table 1). CGCGs were predominantly multilocular (58.3%) with a unilocular appearance in only 25% of cases. In contrast, 67% of ameloblastomas were unilocular. Seventy-five percent of CGCGs

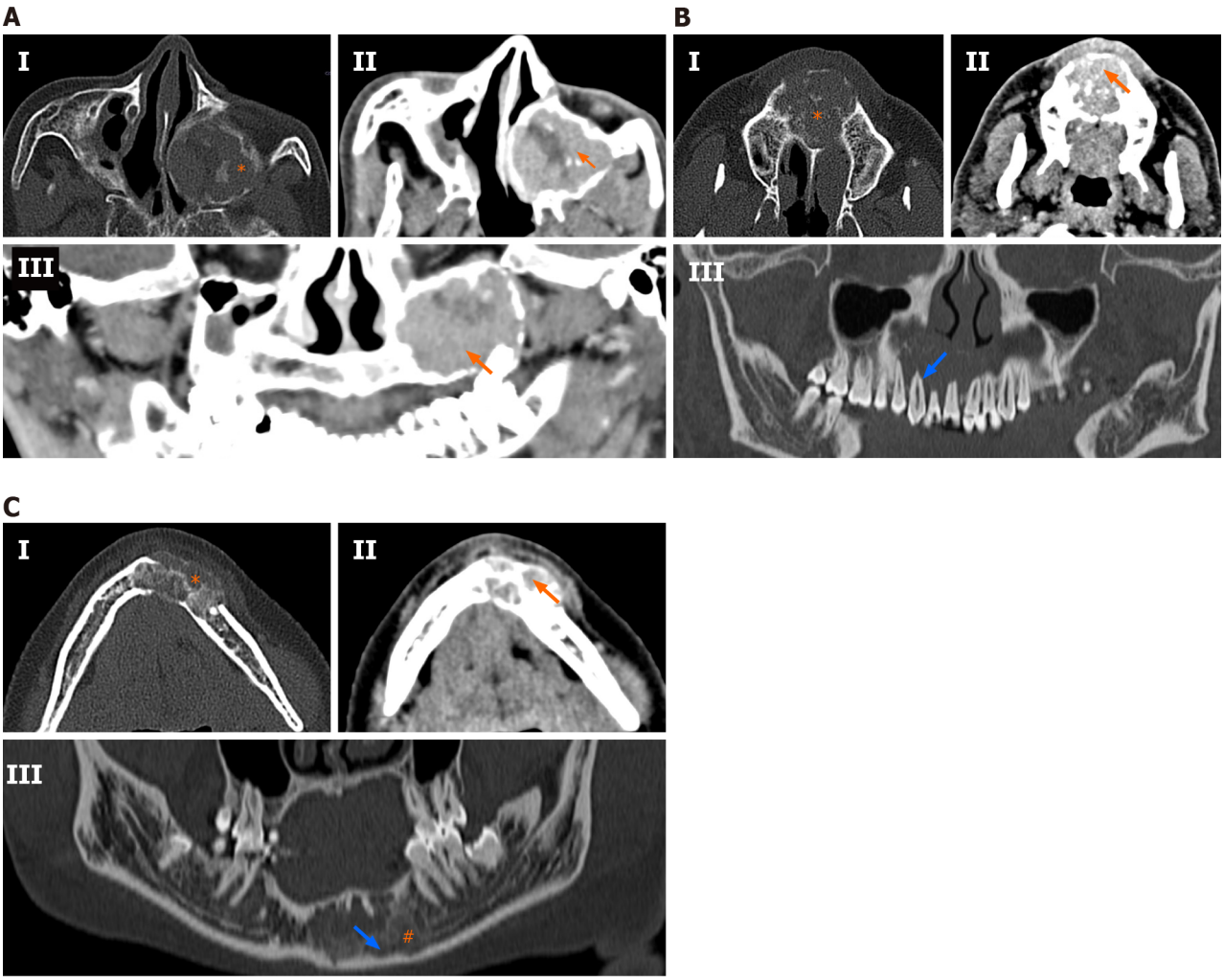

DOI: 10.4329/wjr.v14.i9.329 **Copyright** ©The Author(s) 2022.

Figure 2 Spectrum of multidetector computed tomography findings in central giant cell granulomas. A: 35-year-old woman presented with upper facial pain and nasal obstruction. Cone beam computed tomography (CBCT) shows a left-sided unilocular lytic lesion arising from the left maxilla (Panel I: Bone window) with compression of the maxillary sinus. Mineralised matrix was scattered in the substance of the tumour (asterisk). The lesion showed a significant soft tissue component, which enhanced to an extent greater than the surrounding muscles [arrow, Panel II and III: Axial and curved multiplanar reconstructed (MPR) coronal soft tissue images]. Hyperenhancement of the soft tissue tumour component was highly suggestive of a prospective central giant cell granuloma (CGCG) diagnosis; B: A 30-year-old man presented with pain and upper jaw swelling, contrast-enhanced computed tomography (CECT) showed a lytic sclerotic, multilocular mass arising from the maxilla with the presence of incomplete septae (asterisk) with mineralised matrix (Panel I: Axial bone window). Significant solid soft tissue component with enhancement greater (arrow) than the surrounding muscles was also noted (Panel II: Axial soft tissue window images). Curved MPR images (Panel III: Bone window) showed resorption of the roots (empty arrow) and floor of the nasal cavity; C: A 24-year-old woman presented with progressive jaw swelling over the last 6 mo, with intermittent pain. CECT showed a sclerotic lytic lesion with a honeycomb appearance (Panel I: Axial bone window) arising from the mandible. The lesion showed thick bony septae with mineralised matrix (asterisk). The associated soft tissue component showed enhancement similar to the surrounding muscles (orange arrow: Panel II: Axial soft tissue window). The tumour (blue arrow) can be seen encroaching onto the distal end (#) of the left inferior alveolar canal (Panel III: Curved MPR bone window).

showed both sclerotic and lytic components on the bone window, while 60% of ameloblastomas had a predominant lytic appearance (Figures 2 and 3). Additionally, the presence of osteoid either in the form of a mineralised matrix, thin bony septa or thick bony septa with dense mineralised matrix was a significant feature, and was present in 83% of CGCGs. In comparison, 70% of ameloblastomas had no mineralisation. Imaging features of ameloblastomas as contrasted with CGCGs are presented in Table 4 and Figures 2 and 3. Solid soft tissue was present in > 90% of all CGCGs, while 18% of ameloblastomas were purely lytic. The solid component of CGCGs showed avid enhancement in 50% of cases, while in the rest it showed enhancement similar to surrounding muscles, and only 4% of ameloblastomas showed hyperenhancement. On quantitative evaluation, we found that the solid components in CGCGs enhanced significantly greater than the solid tissue in ameloblastomas. Nackos *et al*[4] in their case series of seven CGCGs reported that the soft tissue in all the CGCGs showed avid contrast enhancement. Similarly, in our series, 50% of CGCGs showed enhancement greater than surrounding muscles, while the rest showed similar enhancement. While a mathematical discussion of each of the parameters used is beyond this paper's scope, briefly, entropy characterises the randomness of the distribution of the HU

Table 4 Summary of radiographic, multidetector computed tomography and magnetic resonance imaging findings in central giant cell granulomas and ameloblastomas

	Ameloblastoma	CGCG
Radiography	Posterior mandible; unilocular or multilocular; scalloped margins; root resorption, root displacement and bone expansion- may erode the cortex	Central mandible; multilocular sclerotic; root resorption, root displacement and bony expansion and cortical erosion
CBCT or MDCT	Mixed solid and cystic or purely cystic with thick enhancing rim or enhancing nodule (in unicystic variant)	Avid enhancement of soft tissue; mineralised matrix; better bony details
Our findings	Unilocular 66.7%; lytic 60.6%; solid component shows isoenhancement compared to surrounding muscles 63%; no matrix mineralisation in 69.7%	Multilocular 58.3%; mixed lytic sclerotic 75%; solid component shows hyperenhancement compared to surrounding muscles 50%; matrix mineralisation in 83.3%
MRI	T1 weighted – isointense; T2 weighted – hyperintense- cystic component; Heterogenous solid component	T1 weighted isointense; T2 weighted hyperintense to heterogeneous solid component

CBCT: Cone beam computed tomography; CGCG: Central giant cell granulomas; MDCT: Multidetector computed tomography; MRI: Magnetic resonance imaging.

values in the ROI. Skewness quantifies the asymmetry in the distribution of the HU values; meanwhile, kurtosis measures the histogram's peak obtained from the HU values. A more detailed description can be read in the review by Lubner *et al*[23]. Histogram analysis showed that the mean, minimum and maximum enhancement of CGCGs was significantly higher than that of ameloblastomas (Tables 2 and 3). A cutoff > 49.05 HU for minimum enhancement in the tumour allowed 100% (63.1%–100.0%) sensitivity and 85.71% (63.7%–97.0%) specificity in differentiating CGCG from ameloblastoma.

The difference in enhancement patterns may be explained based on microvascular density (MVD) of these two tumours. While there are no studies directly comparing MVD of these two entities, separate studies have shown that ameloblastomas had an MVD of 14.9 ± 6[27] compared to 24.5 ± 5.8 in CGCGs [28]. This difference, we hypothesise, would result in a faster and a more considerable peak enhancement in CGCGs than in ameloblastomas, which would then translate to differences in the maximum and minimum venous phase-contrast enhancement of CGCGs. Orthopantomography and CBCT only evaluate the morphology of tumours. Tumour vascularity, enhancement and MVD are important components of radiological tumour assessment and can be evaluated using contrast-enhanced MDCTs. Since in an index case, morphological imaging feature may overlap, the marked differences in enhancement may allow a confident prospective distinction between CGCGs and ameloblastomas.

CGCGs are rare tumours of the jaw making their prospective diagnosis difficult. The classical lytic multilocular appearance of CGCGs on radiographs makes their differentiation difficult from odontogenic cysts, aneurysmal bone cysts, odontogenic fibromas and ameloblastomas[3,7] (the most prevalent odontogenic tumours in the developing world[9]). However, this differentiation is vital because CGCGs are treated less aggressively (curettage, intralesional interferon, steroids or calcitonin injections[8]) compared to other lesions with a similar radiological appearance. We believe this is the unique value of our study, demonstrating the utility of CECT. We acknowledge that imaging alone cannot distinguish these lesions from their other mimics, including giant cell tumours and aneurysmal bone cysts. Moreover, because CGCGs are rare, prospective radiological diagnosis is often difficult and histopathological correlation is thus needed for definitive diagnosis. Sometimes, however, a pathological diagnosis may not be forthcoming[29], and in such cases, the radiological–pathological correlation becomes essential. We believe our findings would add value in such complex cases. Moreover, in patients due to multiple concurrent CGCGs[30] in patients with a mutation of the RAS/MAPK pathway[31], or underlying systemic illnesses, not all lesions undergo biopsy. In such patients, imaging would be valuable in follow-up and diagnosis. We believe contrast-enhanced MDCT would be invaluable in work-up and management of such cases.

This study had several limitations. Of a broad potential range of lytic lesions of the jaw, we compared only ameloblastomas and CGCGs. In our routine practice, we have seen that ameloblastomas have several overlapping imaging features with CGCGs. This, compounded with the rarity of CGCGs, makes their prospective identification difficult. Given the rarity of CGCGs, we decided to contrast the imaging and enhancement characteristics of CGCGs with its most common mimic in the jaw. The retrospective design of the study, with an asymmetric dataset, might have prevented the demonstration of more variations in the imaging features of CGCGs. Because of these limitations, further prospective studies are required to investigate the imaging characteristics and enhancement features of CGCGs, ameloblastomas and their various mimics.

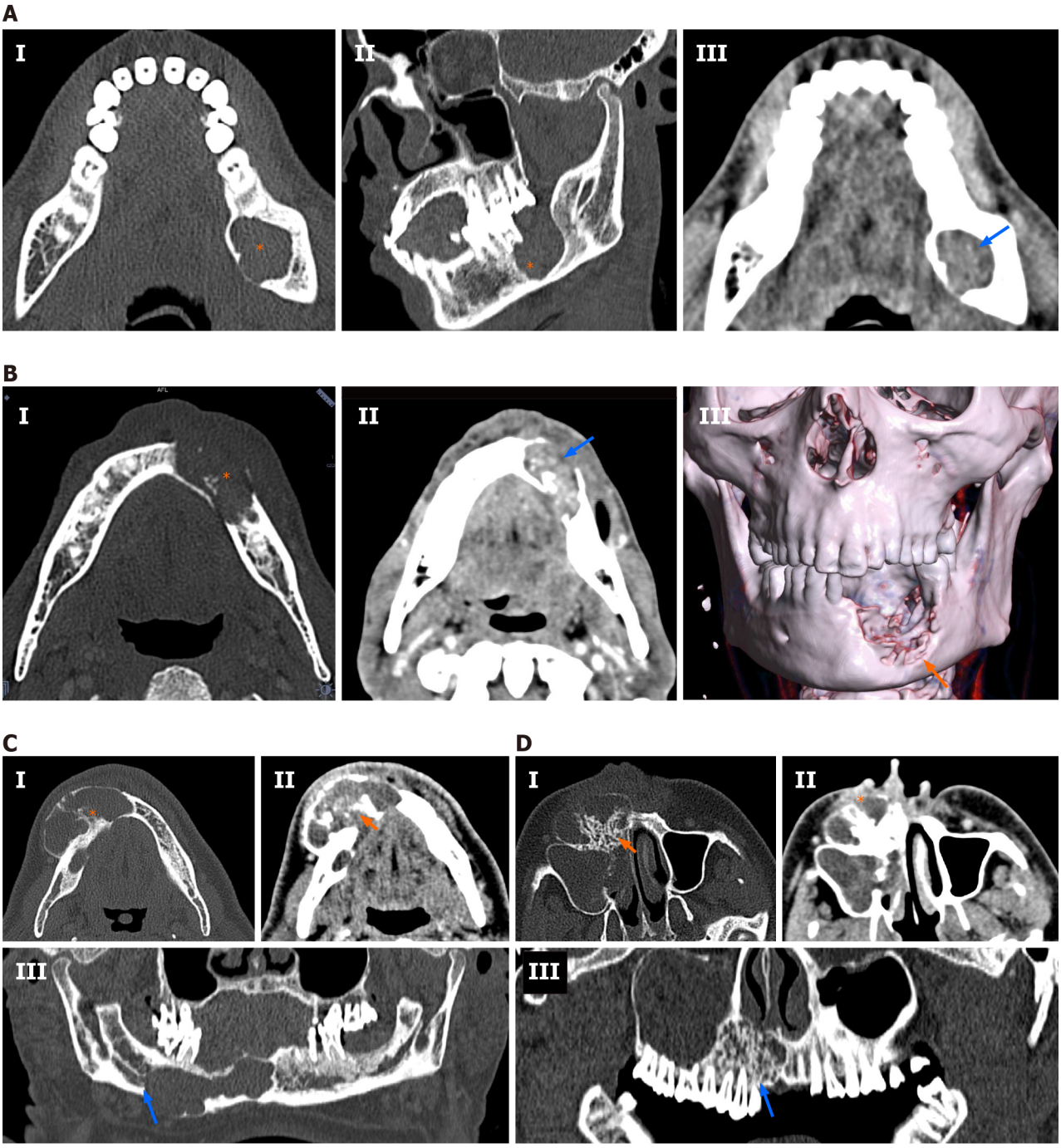

DOI: 10.4329/wjr.v14.i9.329

Figure 3 Spectrum of multidetector computed tomography findings in ameloblastoma. A: A 30-year-old man presented with progressive left lower jaw swelling. Cone beam computed tomography (CBCT) showed a unilocular, lytic lesion (asterisk) with no septae involving the left angle of the mandible (Panel I and II: Axial and coronal bone window). The soft tissue component showed enhancement similar (blue arrow) to the surrounding muscles (Panel III: Axial soft tissue window); B: A 52-year-old man with lower mid jaw pain and swelling; contrast-enhanced computed tomography (CECT) showed a sclerotic, lytic multilocular lesion with thin incomplete septae (asterisk) and associated mineralised matrix (Panel I: Axial bone window). There was a significant soft tissue component showing enhancement (blue arrow) similar to the surrounding muscles (Panel II: Axial soft tissue window). Erosion of the buccal cortex was seen in three-dimensional volume-rendered images (Panel III); C: A 53-year-old man with painful progressive lower jaw swelling of 7 mo duration. CECT showed a lytic sclerotic multilocular mandibular mass with multiple thick septae (asterisk), cortical expansion and breach (Panel I: Axial bone window). The solid component present in the tumour showed hypoenhancement (arrow) compared to the surrounding muscles (Panel II: Axial soft tissue window). Hypoenhancing soft tissue was characteristically not seen in central giant cell granulomas, allowing a prospective diagnosis of ameloblastoma. Erosion of the right canal of the inferior alveolar nerve (blue arrow) was clearly seen [Panel III: Curved multiplanar coronal reconstruction (MPR), bone window]; D: A 42-year-old man with upper maxillary swelling and significant malar pain. CECT showed a lytic sclerotic mass with honeycombing (orange arrow) and thick bony septae (Panel I: Axial bone window). There was significant cortical expansion with extension into the right maxillary sinus. The mass was predominantly lytic with minimal solid component (asterisk) seen in the mass, hypoenhancing compared to the surrounding muscles (Panel II: Axial soft tissue window). Erosion of the roots (blue arrow) with honeycomb appearance was visible (Panel III: Curved MPR coronal bone window).

CONCLUSION

Significant hyperenhancement of the soft tissue component on CECT in a jaw tumour may allow a prospective diagnosis of CGCG, especially in a multilocular lytic sclerotic centrally located jaw tumour with matrix mineralisation.

ARTICLE HIGHLIGHTS

Research background

Contrast-enhanced multidetector computed tomography (MDCT) can provide unique information about ameloblastomas and central giant cell granulomas (CGCGs).

Research motivation

To evaluate contrast-enhanced multidetector computed tomography (MDCT) features of ameloblastomas and CGCGs.

Research objectives

To describe differentiating MDCT features in CGCGs and ameloblastomas and to compare the differences in the enhancement of these two lesions qualitatively and using histogram analysis.

Research methods

MDCTs of CGCGs and ameloblastomas were retrospectively reviewed to evaluate qualitative imaging descriptors. Histogram analysis was used to compare the extent of enhancement of the soft tissue. Fisher's exact test and Mann–Whitney *U* test were used for statistical analysis ($P < 0.05$).

Research results

Twelve CGCGs and 33 ameloblastomas were reviewed. Ameloblastomas had a predilection for the posterior mandible with none of the CGCGs involving the angle. CGCGs were multilocular (58.3%), with a mixed lytic sclerotic appearance (75%). Soft tissue component was present in 91% of CGCGs, which showed hyperenhancement (compared to surrounding muscles) in 50% of cases, while the remaining showed isoenhancement. Matrix mineralisation was present in 83.3% of cases. Ameloblastomas presented as a unilocular (66.7%), lytic (60.6%) masses with solid components present in 81.8% of cases. However, the solid component showed isoenhancement in 63%. No matrix mineralisation was present in 69.7% of cases. Quantitatively, the enhancement of soft tissue in CGCGs was significantly higher than in ameloblastomas on histogram analysis ($P < 0.05$), with a minimum enhancement of > 49.05 HU in the tumour, providing 100% sensitivity and 85% specificity in identifying CGCG.

Research conclusions

A multilocular, lytic sclerotic lesion with significant hyperenhancing soft tissue component, which spares the angle of the mandible and has matrix mineralisation, should indicate a prospective diagnosis of CGCG.

Research perspectives

Future studies can evaluate the role of perfusion imaging for differentiating these two tumour types.

FOOTNOTES

Author contributions: Ghosh A contributed to methodology, software; Ghosh A and Lakshmanan M contributed to writing - original draft; Lakshmanan M contributed to investigation; Bhalla AS and Manchanda S contributed to conceptualization; Bhalla AS, Manchanda S, Kumar P, Bhutia O, and Mridha AR contributed to writing - review & editing, supervision; Kumar P, Bhutia O, and Mridha AR contributed to resources.

Institutional review board statement: The study was reviewed and approved by the All India Institute of Medical Science, New Delhi Institutional Review Board [(Approval No.IEC-622/03.07.2020, RP-31/2020)].

Informed consent statement: The requirement of signed consent forms was waived by the Institutional Ethics Board.

Conflict-of-interest statement: All the authors declare that they have no conflict of interest.

Data sharing statement: No additional data are available.

Country/Territory of origin: India

ORCID number: Ashu Seith Bhalla 0000-0003-2200-2544.

S-Editor: Liu JH
L-Editor: Kerr C
P-Editor: Liu JH

REFERENCES

1 WHO histological classification of tumours of the oral cavity and oropharynx [DOI: 10.1007/978-2-287-92246-6_11]
2 **Flanagan AM**, Speight PM. Giant cell lesions of the craniofacial bones. *Head Neck Pathol* 2014; **8**: 445-453 [PMID: 25409853 DOI: 10.1007/s12105-014-0589-6]
3 **Etoz M**, Asantogrol F, Akyol R. Central giant cell granulomas of the jaws: retrospective radiographic analysis of 13 patients. *Oral Radiol* 2020; **36**: 60-68 [PMID: 30825099 DOI: 10.1007/s11282-019-00380-7]
4 **Nackos JS**, Wiggins RH 3rd, Harnsberger HR. CT and MR imaging of giant cell granuloma of the craniofacial bones. *AJNR Am J Neuroradiol* 2006; **27**: 1651-1653 [PMID: 16971606]
5 **Abdel Razek AA**. Computed tomography and magnetic resonance imaging of maxillofacial lesions in renal osteodystrophy. *J Craniofac Surg* 2014; **25**: 1354-1357 [PMID: 24902107 DOI: 10.1097/SCS.0000000000000819]
6 **Triantafillidou K**, Venetis G, Karakinaris G, Iordanidis F. Central giant cell granuloma of the jaws: a clinical study of 17 cases and a review of the literature. *Ann Otol Rhinol Laryngol* 2011; **120**: 167-174 [PMID: 21510142 DOI: 10.1177/000348941112000305]
7 **Dunfee BL**, Sakai O, Pistey R, Gohel A. Radiologic and pathologic characteristics of benign and malignant lesions of the mandible. *Radiographics* 2006; **26**: 1751-1768 [PMID: 17102048 DOI: 10.1148/rg.266055189]
8 **Pogrel AM**. The diagnosis and management of giant cell lesions of the jaws. *Ann Maxillofac Surg* 2012; **2**: 102-106 [PMID: 23482697 DOI: 10.4103/2231-0746.101325]
9 **Lasisi TJ**, Adisa AO, Olusanya AA. Appraisal of jaw swellings in a Nigerian tertiary healthcare facility. *J Clin Exp Dent* 2013; **5**: e42-e47 [PMID: 24455050 DOI: 10.4317/jced.51011]
10 **Brown NA**, Betz BL. Ameloblastoma: A Review of Recent Molecular Pathogenetic Discoveries. *Biomark Cancer* 2015; **7**: 19-24 [PMID: 26483612 DOI: 10.4137/BIC.S29329]
11 **Odukoya O**, Effiom OA. Clinicopathological study of 100 Nigerian cases of ameloblastoma. *Niger Postgrad Med J* 2008; **15**: 1-5 [PMID: 18408774]
12 **Agbaje JO**, Olumuyiwa Adisa A, Ivanova Petrova M, Adenike Olusanya A, Osayomi T, Ajibola Effiom O, Oladele Soyele O, Gbenga Omitola O, Babajide Olawuyi A, Obos Okiti R, Eziafa Saiki T, Fomete B, Aremu Ibikunle A, Okwuosa C, Abimbola Olajide M, Mofoluwake Ladeji A, Emmanuel Adebiyi K, Mobola Emmanuel M, Sikiru Lawal H, Uwadia E, Oludare Fakuade B, Mohammed Abdullahi Y, Politis C. Biological profile of ameloblastoma and its location in the jaw in 1246 Nigerians. *Oral Surg Oral Med Oral Pathol Oral Radiol* 2018; **126**: 424-431 [PMID: 30126803 DOI: 10.1016/j.oooo.2018.06.014]
13 **Cadavid AMH**, Araujo JP, Coutinho-Camillo CM, Bologna S, Junior CAL, Lourenço SV. Ameloblastomas: current aspects of the new WHO classification in an analysis of 136 cases. *Surg Exp Pathol* 2019 [DOI: 10.1186/s42047-019-0041-z]
14 **Effiom OA**, Ogundana OM, Akinshipo AO, Akintoye SO. Ameloblastoma: current etiopathological concepts and management. *Oral Dis* 2018; **24**: 307-316 [PMID: 28142213 DOI: 10.1111/odi.12646]
15 **Malignant Tumours Involving the Jaws**. In: Atlas of Oral and Maxillofacial Radiology [Internet]. Chichester, UK: John Wiley & Sons, Ltd; 2017 [DOI: 10.1002/9781118939604.ch11]
16 **Meyer KA**, Bancroft LW, Dietrich TJ, Kransdorf MJ, Peterson JJ. Imaging characteristics of benign, malignant, and infectious jaw lesions: a pictorial review. *AJR Am J Roentgenol* 2011; **197**: W412-W421 [PMID: 21862767 DOI: 10.2214/AJR.10.7225]
17 **Özgür A**, Kara E, Arpacı R, Arpacı T, Esen K, Kara T, Duce MN, Apaydın FD. Nonodontogenic mandibular lesions: differentiation based on CT attenuation. *Diagn Interv Radiol* 2014; **20**: 475-480 [PMID: 25297390 DOI: 10.5152/dir.2014.14143]
18 **Hayashi K**, Tozaki M, Sugisaki M, Yoshida N, Fukuda K, Tanabe H. Dynamic multislice helical CT of ameloblastoma and odontogenic keratocyst: correlation between contrast enhancement and angiogenesis. *J Comput Assist Tomogr* 2002; **26**: 922-926 [PMID: 12488736 DOI: 10.1097/00004728-200211000-00011]
19 **Apajalahti S**, Kelppe J, Kontio R, Hagström J. Imaging characteristics of ameloblastomas and diagnostic value of computed tomography and magnetic resonance imaging in a series of 26 patients. *Oral Surg Oral Med Oral Pathol Oral Radiol* 2015; **120**: e118-e130 [PMID: 26166034 DOI: 10.1016/j.oooo.2015.05.002]
20 **Oda M**, Staziaki PV, Qureshi MM, Andreu-Arasa VC, Li B, Takumi K, Chapman MN, Wang A, Salama AR, Sakai O. Using CT texture analysis to differentiate cystic and cystic-appearing odontogenic lesions. *Eur J Radiol* 2019; **120**: 108654

[PMID: 31539792 DOI: 10.1016/j.ejrad.2019.108654]

21 **Jadu FM**, Pharoah MJ, Lee L, Baker GI, Allidina A. Central giant cell granuloma of the mandibular condyle: a case report and review of the literature. *Dentomaxillofac Radiol* 2011; **40**: 60-64 [PMID: 21159917 DOI: 10.1259/dmfr/85668294]

22 **Hosur MB**, Puranik RS, Vanaki SS, Puranik SR, Ingaleshwar PS. Clinicopathological profile of central giant cell granulomas: An institutional experience and study of immunohistochemistry expression of p63 in central giant cell granuloma. *J Oral Maxillofac Pathol* 2018; **22**: 173-179 [PMID: 30158768 DOI: 10.4103/jomfp.JOMFP_260_17]

23 **Lubner MG**, Smith AD, Sandrasegaran K, Sahani DV, Pickhardt PJ. CT Texture Analysis: Definitions, Applications, Biologic Correlates, and Challenges. *Radiographics* 2017; **37**: 1483-1503 [PMID: 28898189 DOI: 10.1148/rg.2017170056]

24 **Meng Y**, Zhao YN, Zhang YQ, Liu DG, Gao Y. Three-dimensional radiographic features of ameloblastoma and cystic lesions in the maxilla. *Dentomaxillofac Radiol* 2019; **48**: 20190066 [PMID: 31124699 DOI: 10.1259/dmfr.20190066]

25 **Ariji Y**, Morita M, Katsumata A, Sugita Y, Naitoh M, Goto M, Izumi M, Kise Y, Shimozato K, Kurita K, Maeda H, Ariji E. Imaging features contributing to the diagnosis of ameloblastomas and keratocystic odontogenic tumours: logistic regression analysis. *Dentomaxillofac Radiol* 2011; **40**: 133-140 [PMID: 21346078 DOI: 10.1259/dmfr/24726112]

26 **Stavropoulos F**, Katz J. Central giant cell granulomas: a systematic review of the radiographic characteristics with the addition of 20 new cases. *Dentomaxillofac Radiol* 2002; **31**: 213-217 [PMID: 12087437 DOI: 10.1038/sj.dmfr.4600700]

27 **ArabSheibani M**, Seifi S, Salehinejad J, Bijani A. Expression of CD34, VEGFR3 and eosinophil density in selected odontogenic tumors- a pilot study. *J Oral Biol Craniofac Res* 2020; **10**: 367-371 [PMID: 31687323 DOI: 10.1016/j.jobcr.2019.09.003]

28 **Sadri D**, Shahsavari F, Hezarkhani M, Shafizadeh M. Expression of CD34 and CD31 in Central and Peripheral Giant Cell Granulomas. *J Dent (Shiraz)* 2019; **20**: 10-15 [PMID: 30937331 DOI: 10.30476/DENTJODS.2019.44557]

29 **Upadhyaya JD**, Cohen DM, Islam MN, Bhattacharyya I. Hybrid Central Odontogenic Fibroma with Giant Cell Granuloma like Lesion: A Report of Three Additional Cases and Review of the Literature. *Head Neck Pathol* 2018; **12**: 166-174 [PMID: 28785965 DOI: 10.1007/s12105-017-0845-7]

30 **Edwards PC**, Fox J, Fantasia JE, Goldberg J, Kelsch RD. Bilateral central giant cell granulomas of the mandible in an 8-year-old girl with Noonan syndrome (Noonan-like/multiple giant cell lesion syndrome). *Oral Surg Oral Med Oral Pathol Oral Radiol Endod* 2005; **99**: 334-340 [PMID: 15716842 DOI: 10.1016/j.tripleo.2004.08.021]

31 **van den Berg H**, Schreuder WH, de Lange J. Multiple central giant cell tumour lesions are exclusively linked to syndromes related to RAS/MAPK pathway anomalies. *Int J Oral Maxillofac Surg* 2017; **46**: 1354-1355 [PMID: 28499505 DOI: 10.1016/j.ijom.2017.04.013]

World Journal of Radiology

Submit a Manuscript: https://www.f6publishing.com

World J Radiol 2022 September 28; 14(9): 342-351

DOI: 10.4329/wjr.v14.i9.342

ISSN 1949-8470 (online)

LETTER TO THE EDITOR

Augmentation of literature review of COVID-19 radiology

Suleman Adam Merchant, Prakash Nadkarni, Mohd Javed Saifullah Shaikh

Specialty type: Radiology, nuclear medicine and medical imaging

Provenance and peer review: Unsolicited article; Externally peer reviewed.

Peer-review model: Single blind

Peer-review report's scientific quality classification

Grade A (Excellent): 0
Grade B (Very good): B, B
Grade C (Good): C, C, C
Grade D (Fair): 0
Grade E (Poor): 0

P-Reviewer: Konovalov AB, Russia; Schoenhagen P, United States; Taydas O, Turkey; Zhu JB, China

Received: December 14, 2021
Peer-review started: December 14, 2021
First decision: March 7, 2022
Revised: March 26, 2022
Accepted: August 21, 2022
Article in press: August 21, 2022
Published online: September 28, 2022

Suleman Adam Merchant, LTM Medical College & LTM General Hospital, Mumbai 400022, Maharashtra, India

Prakash Nadkarni, College of Nursing, University of Iowa, Iowa City, IA 52242, United States

Mohd Javed Saifullah Shaikh, Department of Radiology, North Bengal Neuro Centre - Jupiter MRI & Diagnostic Centre, Siliguri 734003, West Bengal, India

Corresponding author: Suleman Adam Merchant, MBBS, MD, Chairman, LTM Medical College & LTM General Hospital, Sion Hospital, Mumbai 400022, Maharashtra, India.
suleman.a.merchant@gmail.com

Abstract

We suggest an augmentation of the excellent comprehensive review article titled "Comprehensive literature review on the radiographic findings, imaging modalities, and the role of radiology in the coronavirus disease 2019 (COVID-19) pandemic" under the following categories: (1) "Inclusion of additional radiological features, related to pulmonary infarcts and to COVID-19 pneumonia"; (2) "Amplified discussion of cardiovascular COVID-19 manifestations and the role of cardiac magnetic resonance imaging in monitoring and prognosis"; (3) "Imaging findings related to fluorodeoxyglucose positron emission tomography, optical, thermal and other imaging modalities/devices, including 'intelligent edge' and other remote monitoring devices"; (4) "Artificial intelligence in COVID-19 imaging"; (5) "Additional annotations to the radiological images in the manuscript to illustrate the additional signs discussed"; and (6) "A minor correction to a passage on pulmonary destruction".

Key Words: COVID-19 radiological findings; Chest radiographs; Hamptons hump; Westermark sign; Computed tomography; Cardiac magnetic resonance imaging; COVID-19-associated coagulopathy; COVID-19 imaging; Artificial intelligence in COVID-19

Core Tip: Utility of classical radiographic findings suggestive of coronavirus disease 2019 (COVID-19) mediated pulmonary infarction (Hampton's hump, Westermark sign, subpleural sparing and reversed halo sign) should improve the diagnostic accuracy of identification of COVID-19 pulmonary complications. This gain in accuracy would apply whether these findings are seen on plain chest X-ray or computed tomography. The former is important in financially constrained locales with limited medical technology infrastructure. Distinctive COVID-19-associated coagulopathy is more frequent with worsening disease severity in COVID-19. Cardiac magnetic resonance imaging can play an important role in monitoring and prognosis. "Artificial intelligence in COVID-19" and "'Intelligent edge' and other remote monitoring devices" are also discussed.

Citation: Merchant SA, Nadkarni P, Shaikh MJS. Augmentation of literature review of COVID-19 radiology. *World J Radiol* 2022; 14(9): 342-351
URL: https://www.wjgnet.com/1949-8470/full/v14/i9/342.htm
DOI: https://dx.doi.org/10.4329/wjr.v14.i9.342

TO THE EDITOR

We compliment Pal *et al*[1] for their excellent review. It is a comprehensive review indeed. An excellent effort with great details, including in depth pathophysiology, detailed illustrations, *etc.* Their coverage of imaging modalities is quite extensive too and includes a detailed look into the role of ultrasound in coronavirus disease 2019 (COVID-19), including point-of-care ultrasound, an invaluable addition. For the benefit of your readers, we wish to augment their excellent work and submit the following suggestions for the benefit of your readers.

INCLUSION OF ADDITIONAL RADIOLOGIC FEATURES

We are involved in an ongoing multicentric international study on COVID-19 chest imaging and developing artificial intelligence (AI) algorithms for diagnosis, risk stratification, monitoring, prognostication, *etc.* Our 2020 publication has described additional important and distinctive COVID-19 chest-imaging features[2]. These include the following, seen on both plain chest radiographs and computed tomography (CT).

Classic signs of pulmonary infarcts

Hampton's hump: Triangular/wedge shaped opacities with their bases towards the periphery of the lung/lobe/lobule. This sign has sensitivity and specificity of 22% and 82%, respectively[3,4].

Westermark sign: Oligemia, a rarefied area due to blood vessel collapse, distal to the site of occlusion by a pulmonary embolus. This sign has sensitivity and specificity of 14% and 92%, respectively[3,5].

Palla's sign: An enlarged right pulmonary artery, suggesting embolism of segmental/subsegmental pulmonary arteries when seen together with Westermark sign. Sensitivity is reported to be "low" and specificity unknown. These findings are likely due to the microvascular thrombosis propensity in COVID-19[6-8], as discussed below, leading to a relatively increased incidence of pulmonary thromboembolism in COVID-19 pneumonia patients[9].

It is time to revisit these time-tested radiological signs for pulmonary infarcts[2]. Utilizing classic signs of infarcts and pneumonia will increase diagnostic accuracy and help raise awareness about the utility of chest radiographs, even in the current era; especially in cost-constrained locales lacking sophisticated infrastructure. It will also help develop more accurate AI algorithms for diagnosis/prognosis of COVID-19. Co-occurrences of these signs are uncommon across COVID-19 patients: When seen in tandem, however, they may constitute a highly specific diagnostic signature. This speculation, of course, needs validation by larger studies.

SIGNS ASSOCIATED WITH COVID-19 PNEUMONIA

Subpleural sparing

Reported in 23% of COVID-19 cases in an Iranian study[10], subpleural sparing is commonly associated with nonspecific interstitial pneumonia and is described with lung contusions, pulmonary alveolar proteinosis, severe acute respiratory syndrome (SARS) and *pneumocystis jirovecii* infection[11]. The

specificity of this finding depends on the prior probability of COVID-19 based on molecular detection *via* polymerase chain reaction (PCR).

Reversed halo sign

The reversed halo sign is a focal ring-shaped area of ground-glass opacity within a peripheral rim of consolidation, suggesting an organizing/healing pneumonia[12]. It offers prognostic potential in COVID-19[13,14]. Data on sensitivity/specificity are not currently available. Utilizing classic signs of infarcts and pneumonia will increase diagnostic accuracy, and also help raise awareness about chest radiographs' utility, even in the current era, especially in cost-constrained locales lacking sophisticated infrastructure. It will also help develop more accurate AI algorithms for diagnosis/prognosis of COVID-19. Co-occurrences of these signs are uncommon across COVID-19 patients: When seen in tandem, however, they may constitute a highly specific diagnostic signature. This speculation, of course, needs validation by larger studies.

ADDITIONAL ANNOTATION TO IMAGES

The paper's images[1] show the following (currently unannotated) features: Subpleural sparing, figures 4B just under arrow marked as ground glass opacities, 7C and 7F; Hampton's humps, figures 2E, 2F, 4B (marked as consolidation), 4C and 7A (larger, but fewer, in the right lung than left lung); Westermark sign, figure 2F; and pericardial air, figure 2C.

AMPLIFIED DISCUSSION OF CARDIOVASCULAR EFFECTS FROM COVID-19

Distribution of cardiovascular angiotensin-converting enzyme 2 receptors and pathophysiology impact

While correctly noting the ability of the severe acute respiratory syndrome coronavirus 2 (SARS-CoV-2), the causative agent of COVID-19, to invade cells by binding with high affinity to angiotensin-converting enzyme 2 and transmembrane protease serine 2 receptors, the authors have not discussed the cardiovascular system, where COVID-19's impact has been reviewed widely[6,15-17]. The angiotensin-converting enzyme 2 receptor is also expressed in the cardiovascular system in the endothelium of coronary arteries, cardiomyocytes, cardiac fibroblasts, epicardial adipocytes, vascular endothelial and smooth muscle cells[18-20].

Binding of SARS-CoV-2 to the endothelium predisposes to microthrombosis *via* endothelial inflammation, complement activation, thrombin generation, platelet and leukocyte recruitment and initiation of innate and adaptive immune responses with complications such as deep vein thrombosis, pulmonary embolism, cortical venous thrombosis, stroke, cardiac inflammation and injury, arrhythmias, blood clots [18] and acute/chronic myocardial injury[21]. An assay of the fibrin degradation product D-dimer (a thrombosis marker) on admission for prognostication of in-hospital mortality is now mandated in most clinical protocols to differentiate mild from severe COVID-19[7,22], especially when coupled with thrombocytopenia[8]. In infants and children reports of coronary artery aneurysms (CAA), including giant CAAs are gathering momentum as a part of multisystem inflammatory syndrome in post COVID-19 children[23-26].

ROLE OF CARDIAC AND THORACIC MAGNETIC RESONANCE IMAGING

While the authors correctly note that cardiac magnetic resonance imaging (MRI) may be useful in the future to detect complications in patients with abnormal echocardiography, this is a current need too. Up to 60% of hospitalized COVID-19 patients have been reported to have evidence of myocardial injury [21] (Figure 1A). Among post-discharge patients, approximately 10% complain of palpitations, with half of these having ongoing chest pain 6 mo after discharge[15]. Dilated cardiomyopathy is a known complication of COVID-19 cardiac injury[27] (Figures 1B and C). In post-COVID-vaccination patients, distinct self-limited myocarditis and pericarditis have appeared. While myocarditis developed rapidly in younger patients, mostly after the second vaccination, pericarditis affected older patients later, after either the first or second dose[28].

A recent report implicates the booster dose of the COVID-19 vaccine for acute myocarditis too[29]. In infants and children with COVID-19 reports of CAAs, including giant CAAs are gathering momentum [23-26], and cardiac MRI/CT can be an invaluable in diagnosing these too. This is particularly important as these aneurysms (and their catastrophic consequences) are potentially regressible with 'steroid therapy'. In addition these aneurysms would need to be monitored and managed, including for their potential to develop thrombosis[24]. Management includes cardiac support, immunomodulatory agents

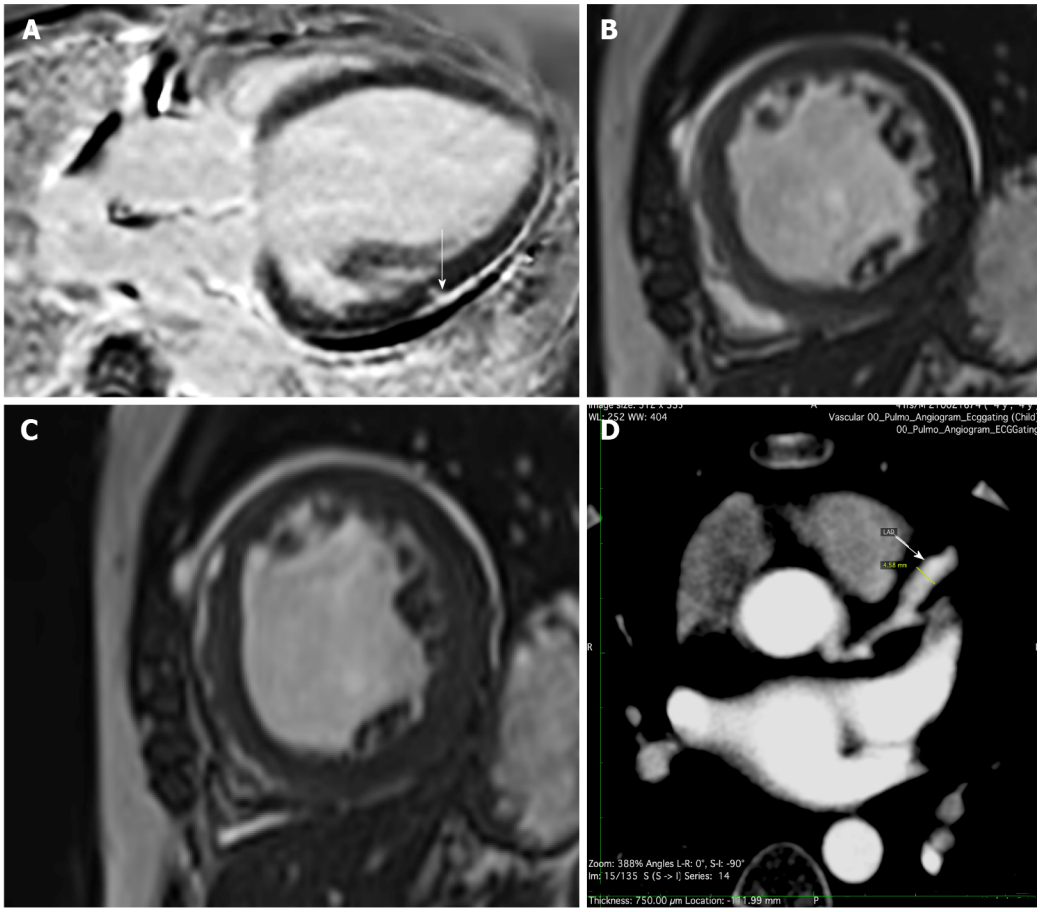

DOI: 10.4329/wjr.v14.i9.342

Figure 1 Post coronavirus disease 2019 imaging. A: Myocarditis: Magnetic resonance late gadolinium enhancement imaging, 4 chamber view. Subepicardial scar with focal myocardial extension (arrow) in the mid anterolateral segment of the left ventricle; B and C: Dilated cardiomyopathy: Bright blood T2 weighted cine imaging in short-axis 2 chamber view showing a dilated left ventricle. Patient had a history of coronavirus disease 2019 (COVID-19) infection a year ago followed by increasing dyspnea. Magnetic resonance imaging revealed severe left ventricular dysfunction and asynchronous left ventricle contractions, B: End diastole; C: End systole; D: Coronary artery aneurysm: Computed tomography angiography in a 4-year-old child reveals a fusiform aneurysm of the left anterior descending coronary artery (arrow). The patient had a history of COVID-19 8 mo ago and was following up for the same.

and anticoagulation[26]. Richardson *et al*[24] stated that in infants rapidly progressing CAAs are noted post COVID-19 infection. They also stated that as opposed to published reports these may be seen even in the absence of hemodynamic instability, ventricular dysfunction, myocardial ischemia or myopericarditis. In view of the risk of progression of cardiac signs and symptoms, Sperotto *et al*[26] recommended long-term follow-up of these patients. Coronary arteries should therefore be thoroughly assessed in patients presenting with multisystem inflammatory syndrome in children symptoms[25]. For its non-ionizing radiation nature MRI would be the first choice in children. However, CT on account of its speed (and current low radiation protocols) can be utilized effectively too (Figure 1D).

In their Radiology 2021 editorial, Lima *et al*[30] stated that prolonged symptoms due to "long-haul" COVID-19 portend the potential for chronic cardiac sequelae, whose duration and severity remain unknown. They introduced the work of Kravchenko *et al*[31], which demonstrated the value of cardiac MRI in identifying inflammation, adverse patterns of hypertrophy, fibrosis and myocardial injury due to myocarditis, pericarditis, cardiomyopathy and healing.

Although thoracic CT is widely used for imaging of COVID-19 infection, thoracic MRI can also be used as an alternative diagnostic tool because of its advantages[32]. This is particularly important in patients requiring avoidance of exposure to ionizing radiation, *e.g.*, in children and during pregnancy where pulmonary MRI may be preferred over pulmonary CT[33]. Pulmonary abnormalities caused by COVID-19 pneumonia can be detected on True FISP MRI sequences and correspond to the patterns known from CT. Spiro *et al*[34] made a useful suggestion for the current pandemic: Following MRI of the abdomen or heart, there should be careful evaluation of the visualized parts of the lungs for COVID-19 findings. This would enable the identification and isolation of undetected cases of COVID-19.

Necker *et al*[35] reported a cinematic rendering of SARS-CoV-2 pneumonia. Cinematic rendering is a digital three-dimensional visualization technique that converts grayscale slices from CT or MRI into colored three-dimensional volumes *via* transfer functions illuminating the reconstruction with physical light simulation. They have stated that this type of rendering produces a natural, photorealistic image

that is intuitively understandable and can be well applied for clinical purposes. Cinematic rendering of CT images is a new way to show the three dimensionality of the various densities contained in volumetric CT/MRI data. We agree with them and feel that such cinematic rendering can make complicated volume rendered CT/MRI images easy to understand for other clinicians, administrators, policy makers as well as patients alike.

ROLE OF 18-FLUORODEOXYGLUCOSE POSITRON EMISSION TOMOGRAPHY

The authors' suggestion of using fluorodeoxyglucose-positron emission tomography (PET) in the future for prognosis and monitoring is wonderful. We wish to add that the "rim sign", a slight and continuous fluorodeoxyglucose uptake at the border of a peripheral lung consolidation[36], is easily recognizable on fluorodeoxyglucose PET/CT (though data on sensitivity/specificity are not available). When present, it strongly suggests pulmonary infarction and is observable even without suggestive finding of pulmonary infarction. The reverse halo sign would also be seen. Though highly sensitive, use of PET/CT for primary detection of COVID-19 is constrained by poor specificity as well as considerations of cost, radiation burden and prolonged exposure times for imaging staff. However, in patients who may require nuclear medicine studies for other clinical indications, PET imaging may yield the earliest detection of nascent infection in otherwise asymptomatic individuals. This may be extremely vital for immunocompromised patients, including those with coexistent malignancies, where the early diagnosis of infection and subsequent initiation of care needed will contribute vitally to improving outcomes and reducing morbidity and mortality[33].

Role of optical thermal imaging and other remote patient monitoring devices

Lukose *et al*[37] stated that the currently popular method of collecting samples using the nasopharyngeal swab and subsequent detection of RNA using real-time PCR has false-positive results and a longer diagnostic time frame. Various optical techniques such as optical sensing, spectroscopy and imaging show great promise in virus detection, and the progress in the field of optical techniques for virus detection unambiguously show great promise in the development of rapid photonics-based devices for COVID-19 detection. They also provided a comprehensive review of the various photonics technologies employed for virus detection, especially the SARS-CoV family, such as near-infrared spectroscopy, fourier transform infrared spectroscopy, raman spectroscopy, fluorescence-based techniques, super-resolution microscopy and surface plasmon resonance-based detection.

Gomez-Gonzalez *et al*[38] reported a proof of concept of optical imaging spectroscopy for rapid, primary screening of SARS-CoV-2. A study by Shah *et al*[39] found that home pulse oximetry monitoring identified the need for hospitalization in initially non-severe COVID-19 patients when a cutoff SpO_2 of 92% was used and that home SpO_2 monitoring also reduced unnecessary emergency department revisits. McKay *et al*[40] stated that due to its portability, affordability and potential to serve as a screening tool for a conventionally lab-based invasive test, the mobile phone capillaroscope could serve as an important point-of-care tool and that the simplicity and portability of their technique may enable the development of an effective non-invasive tool for white blood cell screening in point-of-care and global health settings. This would be extremely useful in the COVID-19 pandemic scenario as white blood cell monitoring forms an essential part of COVID-19 management and follow-up[41,42].

Infrared thermography has been considered a gold standard method for screening febrile individuals during pandemics since the SARS outbreak in 2003. Khaksari *et al*[43] showed that in addition to an elevated body temperature a patient with COVID-19 will exhibit changes in other parameters such as oxygenation of tissues and cardiovascular and respiratory system functions. They also promulgated a compelling need to develop a new technique that would have the ability to screen all these signals and utilize the same for early detection of viral infections. In their opinion, keeping the advent of wireless technologies in mind, the development of such sensors that have point-of-care home-accessible capabilities will go a long way in better managing the increasing numbers of patients with COVID-19 who are opting for home quarantine and that this will eventually reduce the burden on the healthcare system.

The COVID-19 pandemic is changing the landscape of healthcare delivery worldwide. There is a discernible shift toward remote patient monitoring. It is pertinent to note that a large number of remote patient monitoring platforms are already utilizing optical technologies[44]. This area of research has great potential for growth, and the biomedical optics community has great prospects in the development, testing and commodification of new wearable remote patient monitoring technologies to add to the available healthcare armamentarium and contribute to the rapidly changing healthcare and research environment, not just for the COVID-19 era but far beyond[44].

Various other ingenious methods/modalities have been used for early detection/screening for COVID-19. These include smartwatches[45], smart phones and other intelligent edge devices. Mishra *et al*[45] developed a method utilizing data from smartwatches to detect the onset of COVID-19 infection in real-time that detected 67% of infection cases at or before symptom onset. They stated that their study provided a roadmap to a rapid and universal diagnostic method for the large-scale detection of

respiratory viral infections in advance of symptoms, highlighting a useful approach for managing epidemics using digital tracking and health monitoring. Seshadri *et al*[46] stated that when used in conjunction with predictive platforms, wearable device users could receive alerts when changes in their metrics match those related to COVID-19 and that such anonymous data localized to regions such as neighborhoods or zip codes could provide public health officials and researchers a valuable tool to track and mitigate the spread of the virus. Their manuscript describes clinically relevant physiological metrics that can be measured from commercial devices today and highlights their role in tracking the health, stability, and recovery of COVID-19 + individuals and front-line workers.

Schuller *et al*[47] in their paper tilted 'COVID-19 and Computer Audition: An Overview on What Speech & Sound Analysis Could Contribute in the SARS-CoV-2 Corona Crisis' provided an overview on the potential for computer audition, *i.e.*, the usage of speech and sound analysis by AI, to help in the COVID-19 pandemic scenario and concluded that computer audition appears ready for implementation of (pre-)diagnosis and monitoring tools and more generally provides rich and significant, yet so far untapped, potential in the fight against COVID-19 spread.

AI in COVID-19 imaging. Telemedicine has advanced by leaps and bounds. AI algorithms enable faster diagnosis (including remote diagnosis), with a fair degree of accuracy[48]. While the application of AI to medical imaging of cancers and other diseases is being developed over the past decades, the recent COVID-19 pandemic hastened the: (1) Need; (2) Development; (3) Training; and (4) Testing of AI algorithms, within a relatively shorter time-span of less than 2 years[49]. This was extremely beneficial for radiologists and other physicians involved in performing rapid diagnosis, keeping in mind this was a time when there was immense overloading of the healthcare system[50]. The benefits including for management were obvious. However limitations such as: (1) Limited datasets; (2) Inaccurate execution of training and testing procedures; and (3) Use of incorrect performance criteria needed to be dealt with. The above limitations can be overcome by the utilization of federated learning[48,51,52].

The technique of federated learning was originally pioneered by Google[53] as an application of their well-known MapReduce algorithm[54] and allows for iteratively training a machine learning model across geographically separated hardware, including mobile devices. The machine learning algorithm is distributed, while data remains local. It can be employed for both statistical and deep learning. Despite its drawbacks, specifically wide-area network bandwidth limits computation speed, federated learning appears to be a great way forward, especially for multicenter collaborations, getting around the 'tricky' data privacy issue and enabling algorithms/outcomes with much more accuracy than otherwise possible[51].

If AI is to make an even greater impact, Merchant *et al*[48] suggested getting down to the basics and incorporating time tested key medical 'teaching' and/or key 'clinical' parameters, including prognostic indicators, for more effective AI algorithms and their better clinical utility. They also stated that "Artificial Intelligence needs real Intelligence to guide it!". Combining the wisdom gained over the years with the immense versatility of AI algorithms will maximize the accuracy and utility of AI applications in medical diagnosis and treatment modalities. We have gained wisdom regarding COVID-19 imaging over the past few years and should utilize the same for creation of better algorithms for screening/detection/prognostication and management.

El Naqa *et al*[55], as part of a Medical Imaging Data and Resource Center initiative, noted that the pandemic has led to the coupling of interdisciplinary experts that include: (1) Clinicians; (2) Medical physicists; (3) Imaging scientists; (4) Computer scientists; and (5) Informatics experts, all of whom are working towards solving the challenges of the COVID-19 pandemic, specifically AI methods applied to medical imaging. They stated that the lessons learned during the transitioning to AI in the medical imaging of COVID-19 can inform and enhance future AI applications, making the entire transition more than every discipline combined to respond to emergencies like the COVID-19 pandemic. AI has been used in multiple imaging fields for COVID-19 imaging.

The model by Manokaran *et al*[56] could achieve an accuracy of 94.00% in detecting COVID-19 and an overall accuracy of 92.19%, which was based on DenseNet-201. The model can achieve an area under receiver operating characteristic curve of 0.99 for COVID-19, 0.97 for normal and 0.97 for pneumonia. Their automated diagnostic model yielded an accuracy of 94.00% in the initial screening of COVID-19 patients and an overall accuracy of 92.19% using chest X-ray images.

Kusakunniran *et al*[57] proposed a solution to automatically classify COVID-19 cases in chest X-ray images using the ResNet-101 architecture, which was adopted as the main network with over 44 million parameters. A heatmap was constructed under the region of interest of the lung segment to visualize and emphasize signals of COVID-19. Their method achieved a sensitivity, specificity and accuracy of 97%, 98% and 98%, respectively. Rao *et al*[58] stated that separable SVRNet and separable SVDNet models greatly reduced the number of parameters while improving the accuracy and increasing the operating speed.

Yi *et al*[50] utilized a large CT database (1112 patients) provided by the China Consortium of Chest CT Image Investigation and investigated multiple solutions in detecting COVID-19 and distinguishing it from other common pneumonia and normal controls. They compared the performance of different models for complete and segmented CT slices, in particular studying the effects of CT-superimposition depths into volumes, on the performance of their models and showed that an optimal model could identify COVID-19 slices with 99.76% accuracy (99.96% recall, 99.35% precision and 99.65% F1-score).

Chaddad *et al*[59] investigated the potential of deep transfer learning to predict COVID-19 infection using chest CT and X-ray images. They opined that combining chest CT and X-ray images with DarkNet architecture achieved the highest accuracy of 99.09% and area under receiver operating characteristic curve of 99.89% in classifying COVID-19 from non-COVID-19 and that their results confirmed the ability of deep convolutional neural networks with transfer learning to predict COVID-19 in both chest CT and X-ray images. They concluded that this approach could help radiologists improve the accuracy of their diagnosis and improve overall efficiency of COVID-19 management.

Cho *et al*[60] performed quantitative CT analysis on chest CT images using supervised machine learning to measure regional ground glass opacities and inspiratory and expiratory image matching to measure regional air trapping in survivors of COVID-19. They summarized that quantitative analysis of expiratory chest CT images demonstrated that small airway disease with the presence of air trapping is a long-lasting sequelae of SARS-CoV-2 infection.

Fuhrman *et al*[61] developed a cascaded transfer learning approach to extract quantitative features from thoracic CT sections using a fine-tuned VGG19 network where a CT-scan-level representation of thoracic characteristics and a support vector machine was trained to distinguish between patients who required steroid administration and those who did not. They demonstrated significant differences between patients who received steroids and those who did not and concluded that their 'cascade deep learning method' has great potential in clinical decision-making and for monitoring patient treatment.

THE FUTURE

Quantum computers and quantum microscopes, new quantum repeaters enabling a scalable super secure quantum internet (distance will no longer be a hindrance, not just internet of things but 'intelligent edge' devices commonplace[62]) will give a quantum boost to COVID-19 and other health care algorithms/strategies, including in other related fields, improving healthcare in ways beyond the realm of dreams[51]. Cloud computing could be complemented by edge computing, taking advantage of the burgeoning intelligent edge devices (smartphones are commonplace in the remotest of locations). Besides latency, edge computing is preferred over cloud computing in remote locations, where there is limited or no connectivity to a centralized location (a requirement of cloud computing), which requires local storage, similar to a mini data center at their location[63]. Medical imaging including COVID-19/other pandemic imaging and AI will never be the same again, in the era of quantum computing and quantum AI imaging and health care will reach stratospheric levels and beyond[47].

Correction of "pulmonary destruction". The author's state: "The migration of fluid into the alveolar sacs is governed by the imbalance in Starling forces. The diffuse alveolar damage caused by the viral particles results in an increased capillary wall permeability (high *k* value), thereby increasing the force at which fluid migrates from the capillaries to the alveolar space." emphasis added. Surely the authors mean "rate" instead of "force". Permeability is the inverse of resistance. By analogy with Ohm's Law for electricity (current = voltage/resistance) or its equivalent for blood pressure (cardiac output = blood pressure/peripheral resistance), capillary outflow will increase under fixed/constant pressure if permeability increases.

We hope that this augmentation of the excellent review by Pal *et al*[1] will enhance your readers' ability to evaluate COVID-19 patients on imaging. COVID-19 is here to stay. Each effort at adding to the information available in the literature will go a long way in improving patient care overall.

FOOTNOTES

Author contributions: All authors contributed equally.

Conflict-of-interest statement: All the authors report no relevant conflicts of interest for this article.

Country/Territory of origin: India

ORCID number: Suleman Adam Merchant 0000-0001-6513-450X; Prakash Nadkarni 0000-0002-9628-4700; Mohd Javed Saifullah Shaikh 0000-0002-5615-4813.

S-Editor: Wang JJ
L-Editor: Filipodia

P-Editor: Wang JJ

REFERENCES

1 **Pal A**, Ali A, Young TR, Oostenbrink J, Prabhakar A, Deacon N, Arnold A, Eltayeb A, Yap C, Young DM, Tang A, Lakshmanan S, Lim YY, Pokarowski M, Kakodkar P. Comprehensive literature review on the radiographic findings, imaging modalities, and the role of radiology in the COVID-19 pandemic. *World J Radiol* 2021; **13**: 258-282 [PMID: 34630913 DOI: 10.4329/wjr.v13.i9.258]

2 **Merchant SA**, Ansari SMS, Merchant N. Additional Chest Imaging Signs That Have the Potential of Being COVID-19 Imaging Markers. *AJR Am J Roentgenol* 2020; **215**: W57-W58 [PMID: 32762540 DOI: 10.2214/AJR.20.24170]

3 **Worsley DF**, Alavi A, Aronchick JM, Chen JT, Greenspan RH, Ravin CE. Chest radiographic findings in patients with acute pulmonary embolism: observations from the PIOPED Study. *Radiology* 1993; **189**: 133-136 [PMID: 8372182 DOI: 10.1148/radiology.189.1.8372182]

4 **Han D**, Lee KS, Franquet T, Müller NL, Kim TS, Kim H, Kwon OJ, Byun HS. Thrombotic and nonthrombotic pulmonary arterial embolism: spectrum of imaging findings. *Radiographics* 2003; **23**: 1521-1539 [PMID: 14615562 DOI: 10.1148/rg.1103035043]

5 **Stein PD**, Beemath A, Matta F, Weg JG, Yusen RD, Hales CA, Hull RD, Leeper KV Jr, Sostman HD, Tapson VF, Buckley JD, Gottschalk A, Goodman LR, Wakefied TW, Woodard PK. Clinical characteristics of patients with acute pulmonary embolism: data from PIOPED II. *Am J Med* 2007; **120**: 871-879 [PMID: 17904458 DOI: 10.1016/j.amjmed.2007.03.024]

6 **Madjid M**, Safavi-Naeini P, Solomon SD, Vardeny O. Potential Effects of Coronaviruses on the Cardiovascular System: A Review. *JAMA Cardiol* 2020; **5**: 831-840 [PMID: 32219363 DOI: 10.1001/jamacardio.2020.1286]

7 **Zhang L**, Yan X, Fan Q, Liu H, Liu X, Liu Z, Zhang Z. D-dimer levels on admission to predict in-hospital mortality in patients with Covid-19. *J Thromb Haemost* 2020; **18**: 1324-1329 [PMID: 32306492 DOI: 10.1111/jth.14859]

8 **McFadyen JD**, Stevens H, Peter K. The Emerging Threat of (Micro)Thrombosis in COVID-19 and Its Therapeutic Implications. *Circ Res* 2020; **127**: 571-587 [PMID: 32586214 DOI: 10.1161/CIRCRESAHA.120.317447]

9 **Léonard-Lorant I**, Delabranche X, Séverac F, Helms J, Pauzet C, Collange O, Schneider F, Labani A, Bilbault P, Molière S, Leyendecker P, Roy C, Ohana M. Acute Pulmonary Embolism in Patients with COVID-19 at CT Angiography and Relationship to d-Dimer Levels. *Radiology* 2020; **296**: E189-E191 [PMID: 32324102 DOI: 10.1148/radiol.2020201561]

10 **Tabatabaei SMH**, Talari H, Moghaddas F, Rajebi H. CT Features and Short-term Prognosis of COVID-19 Pneumonia: A Single-Center Study from Kashan, Iran. *Radiol Cardiothorac Imaging* 2020; **2**: e200130 [PMID: 33778569 DOI: 10.1148/ryct.2020200130]

11 **Chong WH**, Saha BK, Austin A, Chopra A. The Significance of Subpleural Sparing in CT Chest: A State-of-the-Art Review. *Am J Med Sci* 2021; **361**: 427-435 [PMID: 33487401 DOI: 10.1016/j.amjms.2021.01.008]

12 **Maturu VN**, Agarwal R. Reversed halo sign: a systematic review. *Respir Care* 2014; **59**: 1440-1449 [PMID: 24782557 DOI: 10.4187/respcare.03020]

13 **Sales AR**, Casagrande EM, Hochhegger B, Zanetti G, Marchiori E. The Reversed Halo Sign and COVID-19: Possible Histopathological Mechanisms Related to the Appearance of This Imaging Finding. *Arch Bronconeumol* 2021; **57**: 73-75 [PMID: 34629671 DOI: 10.1016/j.arbres.2020.06.029]

14 **Marchiori E**, Nobre LF, Hochhegger B, Zanetti G. CT characteristics of COVID-19: reversed halo sign or target sign? *Diagn Interv Radiol* 2021; **27**: 306-307 [PMID: 33290240 DOI: 10.5152/dir.2020.20734]

15 **Huang C**, Huang L, Wang Y, Li X, Ren L, Gu X, Kang L, Guo L, Liu M, Zhou X, Luo J, Huang Z, Tu S, Zhao Y, Chen L, Xu D, Li Y, Li C, Peng L, Xie W, Cui D, Shang L, Fan G, Xu J, Wang G, Zhong J, Wang C, Wang J, Zhang D, Cao B. 6-month consequences of COVID-19 in patients discharged from hospital: a cohort study. *Lancet* 2021; **397**: 220-232 [PMID: 33428867 DOI: 10.1016/S0140-6736(20)32656-8]

16 **Hamming I**, Timens W, Bulthuis ML, Lely AT, Navis G, van Goor H. Tissue distribution of ACE2 protein, the functional receptor for SARS coronavirus. A first step in understanding SARS pathogenesis. *J Pathol* 2004; **203**: 631-637 [PMID: 15141377 DOI: 10.1002/path.1570]

17 **Zheng YY**, Ma YT, Zhang JY, Xie X. COVID-19 and the cardiovascular system. *Nat Rev Cardiol* 2020; **17**: 259-260 [PMID: 32139904 DOI: 10.1038/s41569-020-0360-5]

18 **Salamanna F**, Maglio M, Landini MP, Fini M. Body Localization of ACE-2: On the Trail of the Keyhole of SARS-CoV-2. *Front Med (Lausanne)* 2020; **7**: 594495 [PMID: 33344479 DOI: 10.3389/fmed.2020.594495]

19 **Gheblawi M**, Wang K, Viveiros A, Nguyen Q, Zhong JC, Turner AJ, Raizada MK, Grant MB, Oudit GY. Response by Gheblawi *et al* to Letter Regarding Article, "Angiotensin-Converting Enzyme 2: SARS-CoV-2 Receptor and Regulator of the Renin-Angiotensin System: Celebrating the 20th Anniversary of the Discovery of ACE2". *Circ Res* 2020; **127**: e46-e47 [PMID: 32614719 DOI: 10.1161/CIRCRESAHA.120.317332]

20 **Patel VB**, Zhong JC, Grant MB, Oudit GY. Role of the ACE2/Angiotensin 1-7 Axis of the Renin-Angiotensin System in Heart Failure. *Circ Res* 2016; **118**: 1313-1326 [PMID: 27081112 DOI: 10.1161/CIRCRESAHA.116.307708]

21 **Giustino G**, Croft LB, Stefanini GG, Bragato R, Silbiger JJ, Vicenzi M, Danilov T, Kukar N, Shaban N, Kini A, Camaj A, Bienstock SW, Rashed ER, Rahman K, Oates CP, Buckley S, Elbaum LS, Arkonac D, Fiter R, Singh R, Li E, Razuk V, Robinson SE, Miller M, Bier B, Donghi V, Pisaniello M, Mantovani R, Pinto G, Rota I, Baggio S, Chiarito M, Fazzari F, Cusmano I, Curzi M, Ro R, Malick W, Kamran M, Kohli-Seth R, Bassily-Marcus AM, Neibart E, Serrao G, Perk G, Mancini D, Reddy VY, Pinney SP, Dangas G, Blasi F, Sharma SK, Mehran R, Condorelli G, Stone GW, Fuster V, Lerakis S, Goldman ME. Characterization of Myocardial Injury in Patients With COVID-19. *J Am Coll Cardiol* 2020; **76**: 2043-2055 [PMID: 33121710 DOI: 10.1016/j.jacc.2020.08.069]

22 **Velavan TP**, Meyer CG. Mild versus severe COVID-19: Laboratory markers. *Int J Infect Dis* 2020; **95**: 304-307 [PMID: 32344011 DOI: 10.1016/j.ijid.2020.04.061]

23 **Navaeifar MR**, Shahbaznejad L, Sadeghi Lotfabadi A, Rezai MS. COVID-19-Associated Multisystem Inflammatory Syndrome Complicated with Giant Coronary Artery Aneurysm. *Case Rep Pediatr* 2021; **2021**: 8836403 [PMID: 33505752 DOI: 10.1155/2021/8836403]

24 **Richardson KL**, Jain A, Evans J, Uzun O. Giant coronary artery aneurysm as a feature of coronavirus-related inflammatory syndrome. *BMJ Case Rep* 2021; **14** [PMID: 34210694 DOI: 10.1136/bcr-2020-238740]

25 **Pick JM**, Wang S, Wagner-Lees S, Badran S, Szmuszkovicz JR, Wong P, Votava-Smith J. Abstract 17092: Coronary Artery Aneurysms Are More Common in Post-COVID-19 Multisystem Inflammatory Syndrome in Children (MIS-C) Than Pre-Pandemic Kawasaki Disease. *Circulation* 2020; **142**: A17092 [DOI: 10.1161/circ.142.suppl_3.17092]

26 **Sperotto F**, Friedman KG, Son MBF, VanderPluym CJ, Newburger JW, Dionne A. Cardiac manifestations in SARS-CoV-2-associated multisystem inflammatory syndrome in children: a comprehensive review and proposed clinical approach. *Eur J Pediatr* 2021; **180**: 307-322 [PMID: 32803422 DOI: 10.1007/s00431-020-03766-6]

27 **Omidi F**, Hajikhani B, Kazemi SN, Tajbakhsh A, Riazi S, Mirsaeidi M, Ansari A, Ghanbari Boroujeni M, Khalili F, Hadadi S, Nasiri MJ. COVID-19 and Cardiomyopathy: A Systematic Review. *Front Cardiovasc Med* 2021; **8**: 695206 [PMID: 34222385 DOI: 10.3389/fcvm.2021.695206]

28 **Diaz GA**, Parsons GT, Gering SK, Meier AR, Hutchinson IV, Robicsek A. Myocarditis and Pericarditis After Vaccination for COVID-19. *JAMA* 2021; **326**: 1210-1212 [PMID: 34347001 DOI: 10.1001/jama.2021.13443]

29 **Sanchez Tijmes F**, Zamorano A, Thavendiranathan P, Hanneman K. Imaging of Myocarditis Following mRNA COVID-19 Booster Vaccination. *Radiol Cardiothorac Imaging* 2022; **4**: e220019 [PMID: 35506135 DOI: 10.1148/ryct.220019]

30 **Lima JAC**, Bluemke DA. Myocardial Scar in COVID-19: Innocent Marker versus Harbinger of Clinical Disease. *Radiology* 2021; **301**: E434-E435 [PMID: 34374597 DOI: 10.1148/radiol.2021211710]

31 **Kravchenko D**, Isaak A, Zimmer S, Mesropyan N, Reinert M, Faron A, Pieper CC, Heine A, Velten M, Nattermann J, Kuetting D, Duerr GD, Attenberger UI, Luetkens JA. Cardiac MRI in Patients with Prolonged Cardiorespiratory Symptoms after Mild to Moderate COVID-19. *Radiology* 2021; **301**: E419-E425 [PMID: 34374593 DOI: 10.1148/radiol.2021211162]

32 **Ates OF**, Taydas O, Dheir H. Thorax Magnetic Resonance Imaging Findings in Patients with Coronavirus Disease (COVID-19). *Acad Radiol* 2020; **27**: 1373-1378 [PMID: 32830031 DOI: 10.1016/j.acra.2020.08.009]

33 **Fields BKK**, Demirjian NL, Dadgar H, Gholamrezanezhad A. Imaging of COVID-19: CT, MRI, and PET. *Semin Nucl Med* 2021; **51**: 312-320 [PMID: 33288215 DOI: 10.1053/j.semnuclmed.2020.11.003]

34 **Spiro JE**, Curta A, Mansournia S, Marschner CA, Maurus S, Weckbach LT, Hedderich DM, Dinkel J. Appearance of COVID-19 pneumonia on 1.5 T TrueFISP MRI. *Radiol Bras* 2021; **54**: 211-218 [PMID: 34393286 DOI: 10.1590/0100-3984.2021.0028]

35 **Necker FN**, Scholz M. Chest CT Cinematic Rendering of SARS-CoV-2 Pneumonia. *Radiology* 2022; **303**: 501 [PMID: 34935512 DOI: 10.1148/radiol.212902]

36 **Soussan M**, Rust E, Pop G, Morère JF, Brillet PY, Eder V. The rim sign: FDG-PET/CT pattern of pulmonary infarction. *Insights Imaging* 2012; **3**: 629-633 [PMID: 22903456 DOI: 10.1007/s13244-012-0189-5]

37 **Lukose J**, Chidangil S, George SD. Optical technologies for the detection of viruses like COVID-19: Progress and prospects. *Biosens Bioelectron* 2021; **178**: 113004 [PMID: 33497877 DOI: 10.1016/j.bios.2021.113004]

38 **Gomez-Gonzalez E**, Barriga-Rivera A, Fernandez-Muñoz B, Navas-Garcia JM, Fernandez-Lizaranzu I, Munoz-Gonzalez FJ, Parrilla-Giraldez R, Requena-Lancharro D, Gil-Gamboa P, Rosell-Valle C, Gomez-Gonzalez C, Mayorga-Buiza MJ, Martin-Lopez M, Muñoz O, Gomez-Martin JC, Relimpio-Lopez MI, Aceituno-Castro J, Perales-Esteve MA, Puppo-Moreno A, Garcia-Cozar FJ, Olvera-Collantes L, Gomez-Diaz R, de Los Santos-Trigo S, Huguet-Carrasco M, Rey M, Gomez E, Sanchez-Pernaute R, Padillo-Ruiz J, Marquez-Rivas J. Optical imaging spectroscopy for rapid, primary screening of SARS-CoV-2: a proof of concept. *Sci Rep* 2022; **12**: 2356 [PMID: 35181702 DOI: 10.1038/s41598-022-06393-3]

39 **Shah S**, Majmudar K, Stein A, Gupta N, Suppes S, Karamanis M, Capannari J, Sethi S, Patte C. Novel Use of Home Pulse Oximetry Monitoring in COVID-19 Patients Discharged From the Emergency Department Identifies Need for Hospitalization. *Acad Emerg Med* 2020; **27**: 681-692 [PMID: 32779828 DOI: 10.1111/acem.14053]

40 **McKay GN**, Mohan N, Butterworth I, Bourquard A, Sánchez-Ferro Á, Castro-González C, Durr NJ. Visualization of blood cell contrast in nailfold capillaries with high-speed reverse lens mobile phone microscopy. *Biomed Opt Express* 2020; **11**: 2268-2276 [PMID: 32341882 DOI: 10.1364/BOE.382376]

41 **Pirsalehi A**, Salari S, Baghestani A, Sanadgol G, Shirini D, Baerz MM, Abdi S, Akbari ME, Bashash D. Differential alteration trend of white blood cells (WBCs) and monocytes count in severe and non-severe COVID-19 patients within a 7-day follow-up. *Iran J Microbiol* 2021; **13**: 8-16 [PMID: 33889357 DOI: 10.18502/ijm.v13i1.5486]

42 **Leulseged TW**, Hassen IS, Ayele BT, Tsegay YG, Abebe DS, Edo MG, Maru EH, Zewde WC, Naylor LK, Semane DF, Dresse MT, Tezera BB. Laboratory biomarkers of COVID-19 disease severity and outcome: Findings from a developing country. *PLoS One* 2021; **16**: e0246087 [PMID: 33720944 DOI: 10.1371/journal.pone.0246087]

43 **Khaksari K**, Nguyen T, Hill B, Quang T, Perreault J, Gorti V, Malpani R, Blick E, González Cano T, Shadgan B, Gandjbakhche AH. Review of the efficacy of infrared thermography for screening infectious diseases with applications to COVID-19. *J Med Imaging (Bellingham)* 2021; **8**: 010901 [PMID: 33786335 DOI: 10.1117/1.JMI.8.S1.010901]

44 **Roblyer D**. Perspective on the increasing role of optical wearables and remote patient monitoring in the COVID-19 era and beyond. *J Biomed Opt* 2020; **25** [PMID: 33089674 DOI: 10.1117/1.JBO.25.10.102703]

45 **Mishra T**, Wang M, Metwally AA, Bogu GK, Brooks AW, Bahmani A, Alavi A, Celli A, Higgs E, Dagan-Rosenfeld O, Fay B, Kirkpatrick S, Kellogg R, Gibson M, Wang T, Rolnik B, Ganz AB, Li X, Snyder MP. Early Detection Of COVID-19 Using A Smartwatch. 2020 Preprint. Available from: medRxiv: 2020.07.06.20147512 [DOI: 10.1101/2020.07.06.20147512]

46 **Seshadri DR**, Davies EV, Harlow ER, Hsu JJ, Knighton SC, Walker TA, Voos JE, Drummond CK. Wearable Sensors for COVID-19: A Call to Action to Harness Our Digital Infrastructure for Remote Patient Monitoring and Virtual Assessments. *Front Digit Health* 2020; **2**: 8 [PMID: 34713021 DOI: 10.3389/fdgth.2020.00008]

47 **Schuller BW**, Schuller DM, Qian K, Liu J, Zheng H, Li X. COVID-19 and Computer Audition: An Overview on What Speech & Sound Analysis Could Contribute in the SARS-CoV-2 Corona Crisis. *Front Digit Health* 2021; **3**: 564906

[PMID: 34713079 DOI: 10.3389/fdgth.2021.564906]

48 **Merchant SA**, Shaikh MJS, Nadkarni P. Tuberculosis conundrum - current and future scenarios: A proposed comprehensive approach combining laboratory, imaging, and computing advances. *World J Radiol* 2022; **14**: 114-136 [DOI: 10.4329/wjr.v14.i6.114]

49 **Giger M**. Medical imaging of COVID-19. *J Med Imaging (Bellingham)* 2021; **8**: 010101 [PMID: 34754885 DOI: 10.1117/1.JMI.8.S1.010101]

50 **Li Y**, Pei X, Guo Y. 3D CNN classification model for accurate diagnosis of coronavirus disease 2019 using computed tomography images. *J Med Imaging (Bellingham)* 2021; **8**: 017502 [PMID: 34322573 DOI: 10.1117/1.JMI.8.S1.017502]

51 **Nadkarni P**, Merchant SA. Enhancing medical-imaging artificial intelligence through holistic use of time-tested key imaging and clinical parameters: Future insights. *Artif Intell Med Imaging* 2022; **3**: 55-69 [DOI: 10.35711/aimi.v3.i3.55]

52 **Rieke N**, Hancox J, Li W, Milletarì F, Roth HR, Albarqouni S, Bakas S, Galtier MN, Landman BA, Maier-Hein K, Ourselin S, Sheller M, Summers RM, Trask A, Xu D, Baust M, Cardoso MJ. The future of digital health with federated learning. *NPJ Digit Med* 2020; **3**: 119 [PMID: 33015372 DOI: 10.1038/s41746-020-00323-1]

53 **McMahan B**, Ramage D. Federated Learning: Collaborative Machine Learning without Centralized Training Data. Google AI Blog. 6 Apr 2017. [cited 14 November 2021]. Available from: https://starrymind.tistory.com/180

54 **Dean J**, Ghemawat S. MapReduce: Simplified Data Processing on Large Clusters. *Commun ACM* 2008; **51**: 107-113 [DOI: 10.1145/1327452.1327492]

55 **El Naqa I**, Li H, Fuhrman J, Hu Q, Gorre N, Chen W, Giger ML. Lessons learned in transitioning to AI in the medical imaging of COVID-19. *J Med Imaging (Bellingham)* 2021; **8**: 010902-010902 [PMID: 34646912 DOI: 10.1117/1.JMI.8.S1.010902]

56 **Manokaran J**, Zabihollahy F, Hamilton-Wright A, Ukwatta E. Detection of COVID-19 from chest x-ray images using transfer learning. *J Med Imaging (Bellingham)* 2021; **8**: 017503 [PMID: 34435075 DOI: 10.1117/1.JMI.8.S1.017503]

57 **Kusakunniran W**, Karnjanapreechakorn S, Siriapisith T, Borwarnginn P, Sutassananon K, Tongdee T, Saiviroonporn P. COVID-19 detection and heatmap generation in chest x-ray images. *J Med Imaging (Bellingham)* 2021; **8**: 014001 [PMID: 33457446 DOI: 10.1117/1.JMI.8.S1.014001]

58 **Rao K**, Xie K, Hu Z, Guo X, Wen C, He J. COVID-19 detection method based on SVRNet and SVDNet in lung x-rays. *J Med Imaging (Bellingham)* 2021; **8**: 017504 [PMID: 34471647 DOI: 10.1117/1.JMI.8.S1.017504]

59 **Chaddad A**, Hassan L, Desrosiers C. Deep CNN models for predicting COVID-19 in CT and x-ray images. *J Med Imaging (Bellingham)* 2021; **8**: 014502 [PMID: 33912622 DOI: 10.1117/1.JMI.8.S1.014502]

60 **Cho JL**, Villacreses R, Nagpal P, Guo J, Pezzulo AA, Thurman AL, Hamzeh NY, Blount RJ, Fortis S, Hoffman EA, Zabner J, Comellas AP. Quantitative Chest CT Assessment of Small Airways Disease in Post-Acute SARS-CoV-2 Infection. *Radiology* 2022; **304**: 185-192 [PMID: 35289657 DOI: 10.1148/radiol.212170]

61 **Fuhrman JD**, Chen J, Dong Z, Lure FYM, Luo Z, Giger ML. Cascaded deep transfer learning on thoracic CT in COVID-19 patients treated with steroids. *J Med Imaging (Bellingham)* 2021; **8**: 014501 [PMID: 33415179 DOI: 10.1117/1.JMI.8.S1.014501]

62 **TechCrunch BS**. The future is not the Internet of Things… it is the Connected Intelligent Edge. Dec 21, 2021. [cited 22 December 2021]. Available from: https://www.nastel.com/the-future-is-not-the-internet-of-things-it-is-the-connected-intelligent-edge/

63 **Arora S**. Edge Computing Vs. Cloud Computing: What are the Differences. Jun 30, 2022. [cited 8 March 2022]. Available from: https://www.simplilearn.com/edge-computing-vs-cloud-computing-article

Published by **Baishideng Publishing Group Inc**
7041 Koll Center Parkway, Suite 160, Pleasanton, CA 94566, USA
Telephone: +1-925-3991568
E-mail: bpgoffice@wjgnet.com
Help Desk: https://www.f6publishing.com/helpdesk
https://www.wjgnet.com

ISSN 1949-8470 (online)

World Journal of *Radiology*

World J Radiol 2022 October 28; 14(10): 352-366

Published by Baishideng Publishing Group Inc

WJR

World Journal of Radiology

Contents

Monthly Volume 14 Number 10 October 28, 2022

ORIGINAL ARTICLE

Retrospective Study

World Journal of Radiology

Monthly Volume 14 Number 10 October 28, 2022

Contents

AIMS AND SCOPE

The primary aim of *World Journal of Radiology* (*WJR*, *World J Radiol*) is to provide scholars and readers from various fields of radiology with a platform to publish high-quality basic and clinical research articles and communicate their research findings online.

WJR mainly publishes articles reporting research results and findings obtained in the field of radiology and covering a wide range of topics including state of the art information on cardiopulmonary imaging, gastrointestinal imaging, genitourinary imaging, musculoskeletal imaging, neuroradiology/head and neck imaging, nuclear medicine and molecular imaging, pediatric imaging, vascular and interventional radiology, and women's imaging.

INDEXING/ABSTRACTING

The *WJR* is now abstracted and indexed in PubMed, PubMed Central, Emerging Sources Citation Index (Web of Science), Reference Citation Analysis, China National Knowledge Infrastructure, China Science and Technology Journal Database, and Superstar Journals Database. The 2022 edition of Journal Citation Reports ® cites the 2021 Journal Citation Indicator (JCI) for *WJR* as 0.48.

NAME OF JOURNAL
World Journal of Radiology

ISSN
ISSN 1949-8470 (online)

LAUNCH DATE
January 31, 2009

FREQUENCY
Monthly

EDITORS-IN-CHIEF
Thomas J Vogl

EDITORIAL BOARD MEMBERS
https://www.wjgnet.com/1949-8470/editorialboard.htm

PUBLICATION DATE
October 28, 2022

INSTRUCTIONS TO AUTHORS
https://www.wjgnet.com/bpg/gerinfo/204

GUIDELINES FOR ETHICS DOCUMENTS
https://www.wjgnet.com/bpg/GerInfo/287

GUIDELINES FOR NON-NATIVE SPEAKERS OF ENGLISH
https://www.wjgnet.com/bpg/gerinfo/240

PUBLICATION ETHICS
https://www.wjgnet.com/bpg/GerInfo/288

PUBLICATION MISCONDUCT
https://www.wjgnet.com/bpg/gerinfo/208

ARTICLE PROCESSING CHARGE
https://www.wjgnet.com/bpg/gerinfo/242

STEPS FOR SUBMITTING MANUSCRIPTS
https://www.wjgnet.com/bpg/GerInfo/239

ONLINE SUBMISSION
https://www.f6publishing.com

World Journal of Radiology

Submit a Manuscript: https://www.f6publishing.com

World J Radiol 2022 October 28; 14(10): 352-366

DOI: 10.4329/wjr.v14.i10.352

ISSN 1949-8470 (online)

ORIGINAL ARTICLE

Retrospective Study

Diagnostic performance of abbreviated gadoxetic acid-enhanced magnetic resonance protocols with contrast-enhanced computed tomography for detection of colorectal liver metastases

Kumi Ozaki, Shota Ishida, Shohei Higuchi, Toyohiko Sakai, Ayaki Kitano, Kenji Takata, Kazuyuki Kinoshita, Yuki Matta, Takashi Ohtani, Hirohiko Kimura, Toshifumi Gabata

Specialty type: Gastroenterology and hepatology

Provenance and peer review: Invited article; Externally peer reviewed.

Peer-review model: Single blind

Peer-review report's scientific quality classification

Grade A (Excellent): 0
Grade B (Very good): B
Grade C (Good): 0
Grade D (Fair): D
Grade E (Poor): 0

P-Reviewer: Gao L, China; Liao W, China

Received: August 14, 2022
Peer-review started: August 14, 2022
First decision: August 29, 2022
Revised: September 5, 2022
Accepted: October 5, 2022
Article in press: October 5, 2022
Published online: October 28, 2022

Kumi Ozaki, Shohei Higuchi, Toyohiko Sakai, Ayaki Kitano, Kenji Takata, Kazuyuki Kinoshita, Yuki Matta, Takashi Ohtani, Hirohiko Kimura, Department of Radiology, University of Fukui, Fukui 9101193, Japan

Shota Ishida, Department of Radiological Technology, Faculty of Medical Science, Kyoto College of Medical Science, Kyoto 6220041, Japan

Toshifumi Gabata, Department of Radiology, Kanazawa University Graduate School of Medical Science, Kanazawa 9208641, Japan

Corresponding author: Kumi Ozaki, MD, PhD, Lecturer, Department of Radiology, University of Fukui, 23-3 Matsuoka-Shimoaizuki, Fukui 9101193, Japan. ozakik-rad@umin.org

Abstract

BACKGROUND

Although contrast-enhanced magnetic resonance imaging (MRI) using gadoxetic acid has been shown to have higher accuracy, sensitivity, and specificity for the detection and characterization of hepatic metastases compared with other modalities, the long examination time would limit the broad indication. Several abbreviated enhanced MRI (Ab-MRI) protocols without dynamic phases have been proposed to achieve equivalent diagnostic performance for the detection of colorectal liver metastases. However, an optimal protocol has not been established, and no studies have assessed the diagnostic performance of Ab-MRI combined with contrast-enhanced computed tomography (CE-CT), which is the preoperative imaging of colorectal cancer staging in clinical settings, to determine the best therapeutic strategy.

AIM

To compare the diagnostic performance of two kinds of Ab-MRI protocol with the standard MRI protocol and a combination of the Ab-MRI protocol and CE-CT for the detection of colorectal liver metastases.

METHODS

Study participants comprised 87 patients (51 males, 36 females; mean age, 67.2 ± 10.8 years) who had undergone gadoxetic acid-enhanced MRI and CE-CT during

the initial work-up for colorectal cancer from 2010 to 2021. Each exam was independently reviewed by two readers in three reading sessions: (1) Only single-shot fast spin echo (FSE) T2-weighted or fat-suppressed-FSE-T2-weighted, diffusion-weighted, and hepatobiliary-phase images (Ab-MRI protocol 1 or 2); (2) all acquired MRI sequences (standard protocol); and (3) a combination of an Ab-MRI protocol (1 or 2) and CE-CT. Diagnostic performance was then statistically analyzed.

RESULTS

A total of 380 Lesions were analyzed, including 195 metastases (51.4%). Results from the two Ab-MRI protocols were similar. The sensitivity, specificity, and positive and negative predictive values from Ab-MRI were non-inferior to those from standard MRI ($P > 0.05$), while those from the combination of Ab-MRI protocol and CE-CT tended to be higher than those from Ab-MRI alone, although the difference was not significant ($P > 0.05$), and were quite similar to those from standard MRI ($P > 0.05$).

CONCLUSION

The diagnostic performances of two Ab-MRI protocols were non-inferior to that of the standard protocol. Combining Ab-MRI with CE-CT provided better diagnostic performance than Ab-MRI alone.

Key Words: Colorectal liver metastases; Gadoxetic acid; Magnetic resonance imaging; Hepatobiliary phase; Contrast-enhanced computed tomography; Diagnostic performance

Core Tip: For the detection of colorectal liver metastases, the diagnostic performance of two kinds of abbreviated enhanced magnetic resonance imaging (Ab-MRI) protocols was non-inferior to that of the standard protocol. The combination of Ab-MRI and contrast-enhanced computed tomography provided better diagnostic performance than that of Ab-MRI alone.

Citation: Ozaki K, Ishida S, Higuchi S, Sakai T, Kitano A, Takata K, Kinoshita K, Matta Y, Ohtani T, Kimura H, Gabata T. Diagnostic performance of abbreviated gadoxetic acid-enhanced magnetic resonance protocols with contrast-enhanced computed tomography for detection of colorectal liver metastases. *World J Radiol* 2022; 14(10): 352-366

URL: https://www.wjgnet.com/1949-8470/full/v14/i10/352.htm

DOI: https://dx.doi.org/10.4329/wjr.v14.i10.352

INTRODUCTION

Metastatic disease is the most frequent malignant condition in the liver, and colorectal cancer (CRC), which is the third most common cancer[1], is the most frequent primary cancer causing hepatic metastases. Synchronous and metachronous liver metastases are found in 20%-25% and 35%-55%, respectively, of patients with advanced CRC[2,3]. Accurate detection of metastases is therefore essential for optimizing patient management and guiding therapeutic strategies.

Although several imaging modalities have been adopted to assess hepatic metastases, contrast-enhanced magnetic resonance imaging (MRI) using gadoxetic acid has been shown to offer higher accuracy, sensitivity, and specificity for the detection and characterization of hepatic metastases compared with other modalities such as ultrasound, contrast-enhanced computed tomography (CE-CT), and ^{18}F-fluoro-2-deoxy-D-glucose positron emission tomography/CT[4-7]. Nevertheless, the long examination time and relatively high cost of the standard MRI protocol with gadoxetic acid limit its use for the routine surveillance of liver metastases in patients with CRC, whereas CE-CT is routinely used for primary staging and metastatic surveillance.

Most previous reports on the detection of liver metastases, including dynamic contrast studies, have assessed acquired sequences[4-7]; however, high sensitivity for the detection of liver metastases is mainly provided by diffusion-weighted imaging (DWI) and hepatobiliary phase (HBP) imaging with gadoxetic acid obtained 20 min after injection[8-10], and no definitive evidence has shown that T1-weighted images with or without fat suppression or dynamic contrast study are essential for accurate detection.

Recently, several selected MRI protocols without dynamic phases [*e.g.*, abbreviated enhanced MRI (Ab-MRI)] have been proposed to achieve equivalent diagnostic performance for the detection of colorectal liver metastases to standard MRI protocols[11-13]. However, the number of reports is still small, and the sequences included in the protocols have been slightly different. As a result, no optimal protocol has been established. Furthermore, while MRI with gadoxetic acid is regularly performed after CE-CT for preoperative CRC staging in clinical settings, no studies appear to have assessed the diagnostic performance of Ab-MRI in combination with CE-CT to determine the best therapeutic strategy.

The purpose of the present study was therefore to compare the diagnostic performance of two Ab-MRI protocols with those of the standard MRI protocol and a combination of an Ab-MRI protocol and CE-CT in the detection of colorectal liver metastases.

MATERIALS AND METHODS

This single-center retrospective study was approved by our institutional review board. Given the retrospective design of the study, the need to obtain written informed consent was waived.

Study population

We identified all patients with CRC pathologically confirmed from surgically resected specimens who had undergone gadoxetic acid-enhanced MRI and CE-CT for cancer staging during the initial work-up between October 2010 and April 2021. In our institution, hepatic MRI using gadoxetic acid and CE-CT are routinely performed during the initial work-up of patients with CRC. The inclusion criteria for the study population were as follows: (1) Pathologically proven primary CRC; (2) performance of CE-CT within 2 wk of an MRI; and (3) previous abdominal CT or MRI performed ≥ 12 mo earlier. Among 386 patients seen in our facility during the study period, 105 patients with CRC confirmed at pathological analysis satisfied the inclusion criteria; 118 patients with CRC had no colorectal liver metastases, and 163 with colorectal liver metastases underwent chemotherapy without surgical resection. Patients with the following conditions were then excluded: motion artifacts or missing part of the MRI acquisition (n = 5); history of other malignancy (n = 4); missing part of a CT examination due to iodine allergy (n = 4); chronic live disease or cirrhosis (n = 3); and cancer other than adenocarcinoma, such as neuroendocrine tumor (n = 2). A final total of 87 patients was included in this study (Figure 1). The demographic and clinical-biological data of these patients were obtained from the medical records.

MRI examinations

Gadoxetic acid-enhanced MRI was performed using a 3-T system (Discovery 750 DV 25.1; GE Healthcare, Waukesha, WI, United States) with an 8-channel body phased-array coil. All patients included in the study had undergone scans using a standard liver MRI protocol including the following sequences: in- and opposed-phase T1-weighted imaging, and 3-dimensional T1-weighted fat-suppressed spoiled gradient-recalled echo sequences [liver acquisition with volume acceleration (LAVA); GE Medical Systems] as pre-contrast sequences. After gadoxetic acid (Primovist; Bayer Schering Pharma, Osaka, Japan) was administered at a rate of 1 mL/s followed by a 20-mL saline flush using a power injector and a bolus tracking technique, late arterial-, portal venous-, and transitional-phase images were acquired using LAVA. Single-shot fast spin echo (SSFSE) T2-weighted imaging, fat-suppressed fast spin echo (FSE) T2-weighted imaging, DWI (b = 0 s/mm^2, b = 800 s/mm^2), and HBP imaging were acquired at least 20 min after contrast administration using the same sequences as applied pre-contrast (Figure 2). Details of the MRI protocols are provided in Table 1.

CT examinations

All CT examinations were conducted using a CT system (SOMATOM Force; Siemens Healthcare, Forchheim, Germany). Following non-enhanced CT, contrast material-enhanced study was performed at 60-70 s (portal phase) and 180 s (equilibrium phase) after completing intravenous injection of non-ionic contrast material (Iopamiron 370; Bayer Health Care, Osaka, Japan) (500 mg of iodine per kilogram body weight) for 30 s. Images were acquired in the craniocaudal direction, including the whole abdomen and pelvis. The following imaging parameters were used: tube current, 250 mAs; tube voltages, 100 kVp; collimation, 0.6´192 mm; pitch factor, 0.8; rotation time, 0.5 s; matrix, 512´512; field of view, 300-500 mm; and reconstruction interval (slice thickness), 3 mm.

Image analysis

All MRI and CT examinations were pooled after anonymization by a radiologist (K.O.) with 20 years of experience in the field of abdominal imaging who did not participate in the readings. Two different Ab-MRI protocols were arranged, including only SSFSE T2-weighted or fat-suppressed FSE-T2-weighted, DWI and HBP images (Ab-MRI protocol 1 or 2) (Figure 2). Four radiologists (T.S., K.K., K.T., A.K., with 30, 22, 10, and 8 years of experience in oncology imaging, respectively) randomized into two groups retrospectively and independently reviewed the following three reading sessions: (1) Ab-MRI protocol 1

Table 1 Magnetic resonance imaging acquisition parameters

Sequence	Orientation	Respiratory compensation	Repetition/echo time (ms)	Flip angle (degrees)	Section thickness (mm)	Intersection gap (mm)	Field-of-view (mm^2)	Matrix	Acquisition time (s)
T1-weighted in and opposed phases (SPGR)	Axial	Breath-hold	6.9/4.5	12	4	1	350´280	320´224	20
Dynamic study (LAVA)[1]	Axial	Breath-hold	6.5/3.1	15	4	1	350´280	320´192	20
Single-shot FSE T2-weighted imaging	Axial	Breath-hold	520/82	90	5	1	350´350	384´256	20
Diffusion-weighted imaging	Axial	Respiration trigger	8000-12000/68	90	5	1	350´350	128´128	210
Fat-suppressed FSE T2-weighted imaging	Axial	Respiration trigger	520/82	160	5	1	350´350	320´320	230
Hepatobiliary phase	Axial	Breath-hold	6.5/3.1	30	4	1	350´280	320´224	20

[1]Dynamic study consists of pre-contrast, late arterial, portal venous, and transitional phases.
SPGR: Spoiled gradient-recalled echo; LAVA: Liver acquisition with volume acceleration; FSE: Fast spin echo.

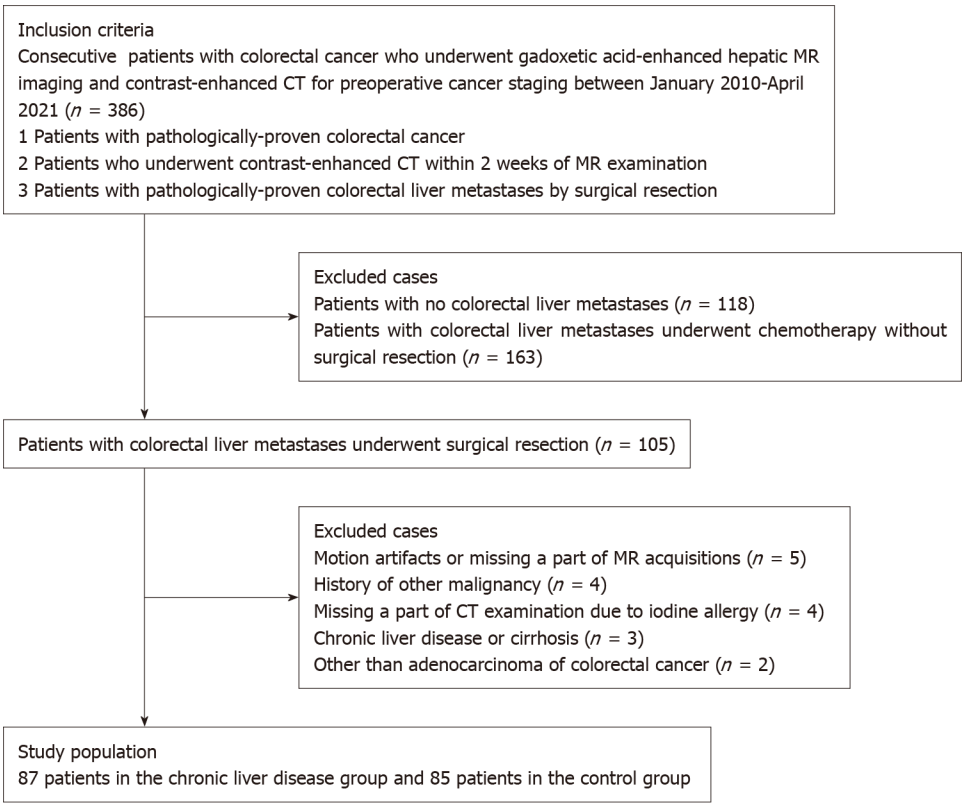

DOI: 10.4329/wjr.v14.i10.352

Figure 1 Flowchart of the study population. MR: Magnetic resonance; CT: Computed tomography.

or 2; (2) the standard MRI protocol including all acquired sequences; and (3) a combination of Ab-MRI protocol 1 or 2 and CE-CT. The reader who performed the Ab-MRI in the first reading session used the same abbreviated protocol in the third reading session. All interpretation of images from MRI and CT was blinded to clinical-biological and follow-up data. The reader at the second or third reading was blinded to results from the prior session, which had been held at least 2 mo earlier.

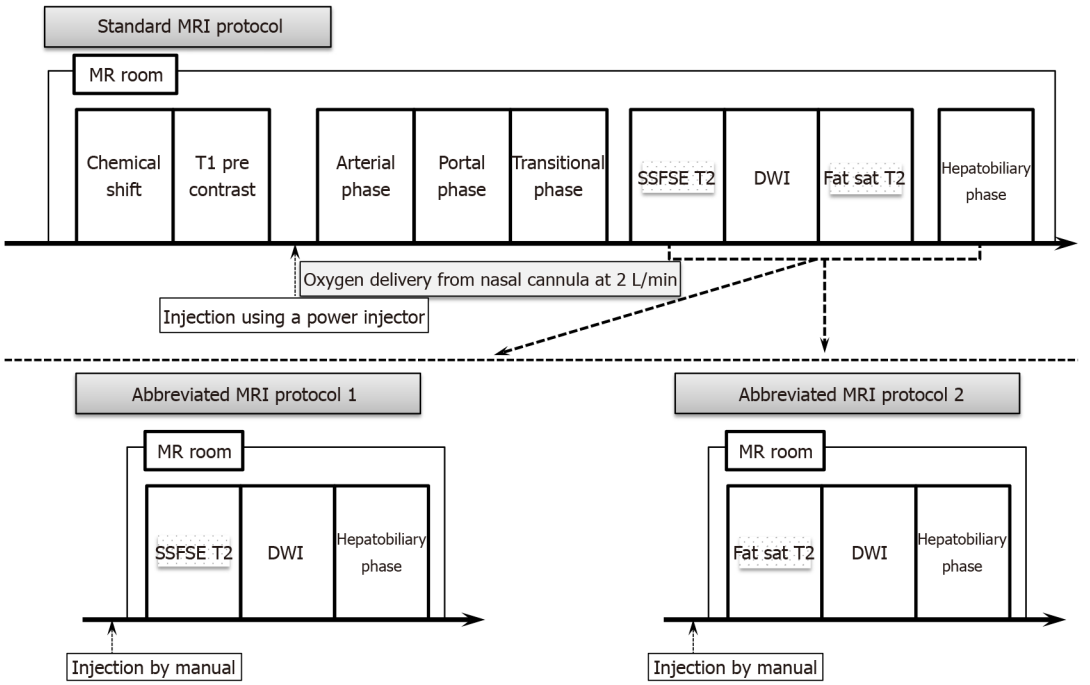

DOI: 10.4329/wjr.v14.i10.352

Figure 2 Schematic diagrams of the standard magnetic resonance imaging protocol (upper diagram) and both kinds of simulated abbreviated magnetic resonance imaging protocol (lower diagram). SSFSE T2: Single-shot fast spin echo T2-weighted imaging; Fat-sat T2: Fat-suppressed T2-weighted imaging; DWI: Diffusion-weighted imaging; MR: Magnetic resonance.

Reviewers were asked to report all focal liver lesions detected. Lesion locations were defined according to the Couinaud classification. Maximal diameter on the axial plane was measured in millimeters. Readers characterized the detected lesions using a 5-point scale (1, definitely not liver metastasis; 2, probably not liver metastasis; 3, indeterminate; 4, probably liver metastasis; and 5, definitely liver metastasis). Lesions were considered liver metastases for scores of 4 or 5, whereas lesions were considered to not represent liver metastases for scores ≤ 3.

Standard of reference

All metastases were pathologically confirmed from surgically resected specimens. The MRI of each metastasis was pathologically checked in the cut sections of the resected specimens by a radiologist (K.O.) and a pathologist (S.H., 7 years of experience) who did not participate in the readings.

Benign lesions such as simple hepatic cysts and hemangiomas were diagnosed on the basis of typical imaging findings and by the fact that the lesions demonstrated no change in size on previous contrast-enhanced CT or MRI performed over a period of ≥ 12 mo (range, 12-38 mo). Typical imaging findings of hepatic cysts and hemangiomas are as follows: hepatic cysts are diagnosed on the basis of marked hyperintensity on T2-weighted imaging and the absence of contrast enhancement. Hemangiomas are diagnosed on the basis of moderate to marked hyperintensity on T2-weighted imaging and expanding globular peripheral enhancement approximately paralleling that of the blood pool. Tiny hepatic cysts (diameter < 2 mm) detected only on SSFSE T2-weighted imaging were not subjected to analysis. Other benign lesions (such as focal nodular hyperplasia) were also recorded if found. Examples of colorectal liver metastases, hemangiomas, and hepatic cysts are shown in Figures 3-6.

Statistical analysis

Continuous variables are reported as mean and standard or median deviation and extreme values, depending on the distribution. Sensitivity, specificity, positive predictive value (PPV), negative predictive values (NPV), accuracy of each session, and 95%CIs were calculated. A false positive was a lesion considered by radiologists to be malignant but not confirmed as a metastasis according to the reference standard. A false negative was a lesion considered to be benign by radiologists but identified as a metastasis according to the reference standard. McNemar's test or Fisher's exact test was used to compare sensitivity, specificity, PPV, NPV, and accuracy between each reading session. Areas under the receiver operating characteristic curve (AUROCs) were computed and compared using the DeLong test. Inter-reader variability for the characterization of detected lesions was assessed using Cohen's kappa statistics. Kappa values of 0.01-0.20, 0.21-0.40, 0.41-0.60, 0.61-0.80, and 0.81-1.0 were considered to indicate "poor", "fair", "moderate", "good", and "excellent" agreement, respectively. A bilateral value

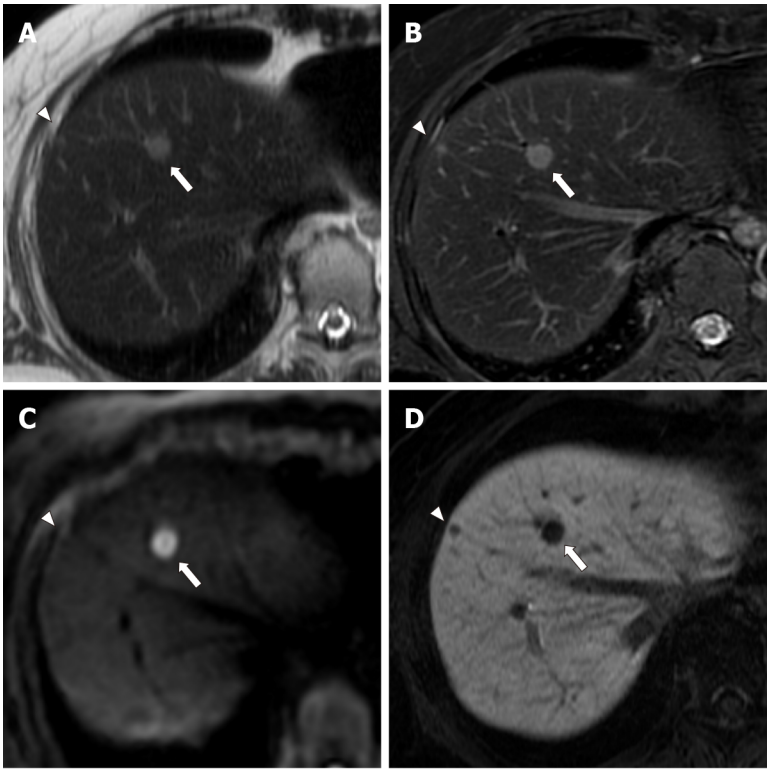

DOI: 10.4329/wjr.v14.i10.352

Figure 3 A 54-year-old woman with two colorectal liver metastases in segment 8, with diameters of 9 mm (arrows) and 4 mm (arrowheads). A: The lager metastasis (arrow) is clearly depicted as an area of hyperintensity, and the smaller metastasis (arrowhead) shows indistinct hyperintensity on single-shot fast spin echo (SSFSE) imaging; B: Lager (arrow) and smaller (arrowhead) metastases are clearly depicted as an area of hyperintensity on fat-suppressed fast spin echo (FSE) T2-weighted imaging; C: The lager metastasis (arrow) is clearly depicted as an area of hyperintensity, and the smaller metastasis (arrowhead) is not depicted on diffusion-weighted imaging (DWI); D: Lager (arrow) and smaller (arrowhead) metastases are clearly depicted as an area of hypointensity on hepatobiliary-phase imaging. Abbreviated magnetic resonance imaging (Ab-MRI) protocol 1 included SSFSE T2-weighted imaging (A), DWI (C), and hepatobiliary-phase imaging (D), whereas abbreviated MRI protocol 2 included fat-suppressed FSE T2-weighted imaging (B), DWI (C), and hepatobiliary phase imaging (D). The lager metastasis (arrows) were scored as 5 by all four readers. The smaller metastasis (arrowheads) was incorrectly scored as 3 or 4 by one of the two readers in Ab-MRI protocols 1 and 2, respectively, and was missed by one reader in Ab-MRI protocol 1.

of $P < 0.05$ was considered statistically significant. All statistical analyses were performed using SPSS software version 21.0 (SPSS, IBM; Armonk, NY, United States).

RESULTS

Patient and tumor characteristics

The 87 patients had 195 metastases (51.4%) and 175 benign lesions (49.6%) (15 hemangiomas/160 cysts; no other benign lesions were observed). The mean sizes of metastases and benign lesions were 28.2 ± 13.6 mm and 4.8 ± 2.8 mm, and median numbers per patient were 2.2 (range, 1-8) and 3.1 (range, 0-12), respectively. Patient and tumor characteristics are shown in Table 2.

Lesion detection

A total of 352 (95.1%) and 349 (94.3%) of the 370 Lesions were detected by Readers 1 and 2, respectively, using Ab-MRI protocol 1, including 182 (93.3%) and 178 (91.3%) of the 195 metastases and 170 (97.1%) and 171 (97.7%) of the 175 benign lesions, respectively. A total of 350 (94.6%) and 355 (95.9%) of the 370 Lesions were detected by Readers 3 and 4, respectively, using Ab-MRI protocol 2, including 185 (94.9%) and 184 (94.4%) of the 195 metastases and 168 (96.0%) and 171 (97.7%) of the 175 benign lesions, respectively.

All performance indices (sensitivity, specificity, PPV, NPV, accuracy, and AUROC) for the two Ab-MRI protocols were similar. Sensitivity, specificity, PPV, and NPV of the two Ab-MRI protocols were non-inferior to that of standard MRI for all readers ($P > 0.05$), whereas significant differences in accuracy and AUROC were observed ($P < 0.05$).

All performance indices for the combination of Ab-MRI and CE-CT were higher than that of Ab-MRI alone for all four readers, although only accuracy or AUROC differed significantly ($P < 0.05$). All performance indices for the combination of Ab-MRI and CE-CT were similar to that of standard MRI for

Table 2 Patient and tumor characteristics

Characteristics	
Number of cases	87
Gender (male/female)	51 (58.6%)/36 (41.4%)
Age (yr)[1] overall	67.2 ± 10.8
Male	67.5 ± 9.6
Female	66.8 ± 12.4
Location of colorectal cancer colon/rectum	31/56
Total number of lesions; metastases/benign	370
Metastases	195 (51.4%)
Benign lesions	175 (49.6%) (15 hemangiomas/160 cysts)
Number of lesions per patient with liver metastases	2.2 (1-8)
Size of metastatic lesion (mm)[1]	28.2 ± 13.6
Number of benign lesions per patient	3.1 (0-12)
Size of benign lesions (mm)[1]	4.8 ± 2.8

[1]Data are expressed as means ± SD. Other data represent numbers of lesions and range.

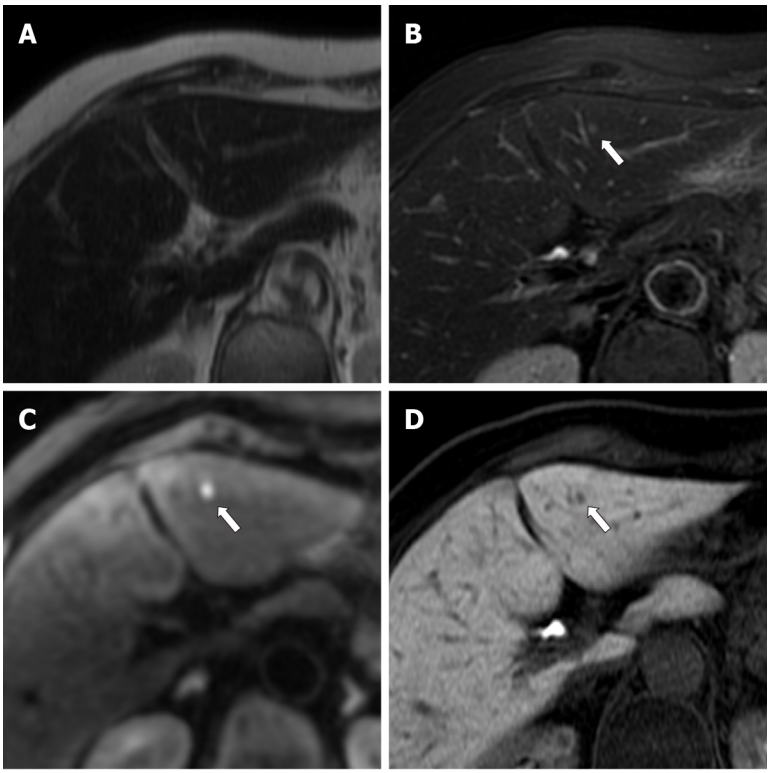

DOI: 10.4329/wjr.v14.i10.352

Figure 4 An 86-year-old woman with a colorectal liver metastasis in segment 3, measuring 2.8 mm in diameter (arrows). A: The metastasis (arrow) appears indistinct on single-shot fast spin echo T2-weighted imaging; B: The metastasis (arrow) appears indistinct on fat-suppressed fast spin echo T2-weighted imaging; C: The metastasis (arrow) is clearly depicted as an area of hyperintensity on diffusion-weighted imaging; D: The metastasis (arrow) is clearly depicted as an area of hypointensity on hepatobiliary-phase imaging. The lesion was scored 4 or 5 by one reader in each abbreviated enhanced magnetic resonance imaging (Ab-MRI) protocol, and was missed by the other reader in Ab-MRI protocol 1 and 2.

all four readers ($P > 0.05$). The details and results of a comparison of all performance indices between the three reading sessions by each reader are shown in Tables 3 and 4.

Table 3 Comparison of diagnostic performance of three reading sessions including abbreviated magnetic resonance imaging protocol 1

	Reader 1						Reader 2					
	Ab-MRI	Standard MRI	Ab-MRI + CE-CT	*P* value (Ab-MRI *vs* standard)	*P* value (Ab-MRI *vs* Ab-MRI + CE-CT)	*P* value (standard *vs* Ab-MRI + CE-CT)	Ab-MRI	Standard MRI	Ab-MRI + CE-CT	*P* value (Ab-MRI *vs* standard)	*P* value (Ab-MRI *vs* Ab-MRI + CE-CT)	*P* value (standard *vs* Ab-MRI + CE-CT)
Sensitivity	93.3 (88.9-96.4)	94.4 (92.3-95.1)	93.8 (91.8-94.6)	0.5	> 0.99	> 0.99	91.3 (88.9-92.5)	93.8 (91.7-94.8)	93.3 (91.1-94.3)	0.063	0.125	> 0.99
Specificity	97.1 (93.5-99.1)	98.9 (96.6-99.7)	98.9 (96.6-99.7)	0.125	0.25	> 0.99	97.7 (95.0-99.1)	98.3 (95.8-99.4)	98.3 (95.8-99.4)	> 0.99	> 0.99	> 0.99
PPV	97.3 (93.9-99.1)	98.9 (96.8-99.7)	98.9 (96.8-99.7)	0.25	0.25	> 0.99	97.8 (95.2-99.1)	98.4 (96.1-99.4)	98.4 (96.0-99.4)	0.25	0.25	> 0.99
NPV	92.9 (88.2-96.2)	94 (91.9-94.8)	93.5 (91.4-94.3)	0.5	> 0.99	> 0.99	91 (85.9-94.6)	93.5 (91.2-94.5)	93 (90.6-94.0)	0.063	0.125	> 0.99
Accuracy	95.1 (92.4-97.1)	96.5 (94.4-97.3)	96.2 (94.1-97.0)	0.063	0.125	> 0.99	94.3 (91.8-95.6)	95.9 (93.6-97.0)	95.7 (93.3-96.7)	0.031	0.063	> 0.99
AUROC	0.952 (0.931-0.974)	0.966 (0.948-0.984)	0.964 (0.945-0.982)	0.025	0.045	0.317	0.945 (0.922-0.968)	0.961 (0.941-0.980)	0.958 (0.938-0.978)	0.014	0.025	0.317

Abbreviated magnetic resonance imaging protocol 2 consisting of fat-suppressed fast spin echo T2-weighted, diffusion-weighted, and hepatobiliary phase images. Numbers in square brackets represent 95%CIs. PPV: Positive predictive value; NPV: Negative predictive value; AUROC: Area under the receiver operating characteristic curve; Ab-MRI: Abbreviated magnetic resonance imaging; CE-CT: Contrast-enhanced computed tomography.

More specifically, with regard to false-negative lesions in the Ab-MRI protocols, 11 metastases of the 13 false-negative lesions for reader 1, 12 of 17 for reader 2, 8 of 13 for reader 3, and 6 of 11 for reader 4 were not detected on any of the three reading sessions by each reader, respectively (all were < 1 cm). Among these false-negative lesions, seven metastases were detected by at least one reader using the combination of Ab-MRI and CE-CT or the standard MRI protocol. On the other hand, five small metastases were not detected on any reading sessions by any reader (all were < 1 cm) (Figures 3 and 4). Three of these small metastases were located on the peripheral edge of the liver. The mean diameter of metastases detected using Ab-MRI protocols was 12 ± 10 mm, compared to 2.3 ± 1.7 mm for undetected metastases. With regard to the false-positive lesions, three hemangiomas were misdiagnosed as liver metastases on both Ab-MRI protocols by all four readers and correctly diagnosed on standard MRI and the combination of Ab-MRI and CE-CT (Figure 5).

Inter-reader agreement for tumor classification

In Ab-MRI protocol 1, the kappa value for the two readers was 0.891 (95%CI: 0.846-0.938) for the combination of Ab-MRI and CE-CT, which was slightly higher than that for Ab-MRI (0.849; 95%CI: 0.795-0.903) and standard MRI (0.887; 95%CI: 0.839-0.9334). In Ab-MRI protocol 2, the kappa value for the two readers was 0.935 (95%CI: 0.899-0.971) for the combination of Ab-MRI and CE-CT, which was

Table 4 Comparison of diagnostic performance of three reading sessions including abbreviated magnetic resonance imaging protocol 2

	Reader 3						Reader 4					
	Ab-MRI	Standard MRI	Ab-MRI + CE-CT	*P* value (Ab-MRI *vs* standard)	*P* value (Ab-MRI *vs* Ab-MRI + CE-CT)	*P* value (standard *vs* Ab-MRI + CE-CT)	Ab-MRI	Standard MRI	Ab-MRI + CE-CT	*P* value (Ab-MRI *vs* standard)	*P* value (Ab-MRI *vs* Ab-MRI + CE-CT)	*P* value (standard *vs* Ab-MRI + CE-CT)
Sensitivity	93.3 (90.7-95.0)	94.9 (92.7-95.9)	95.9 (93.8-96.9)	0.25	0.063	0.5	94.4 (90.1-97.2)	95.9 (93.8-96.9)	96.9 (95.1-97.6)	0.25	0.063	0.5
Specificity	96 (93.1-97.8)	98.3 (95.9-99.4)	98.3 (96.0-99.4)	0.125	0.125	> 0.99	97.7 (94.3-99.4)	98.3 (96.0-99.4)	98.9 (96.8-99.7)	> 0.99	0.5	> 0.99
PPV	96.3 (93.6-98.0)	98.4 (96.2-99.4)	98.4 (96.3-99.4)	0.125	0.125	> 0.99	97.9 (94.6-99.4)	98.4 (96.3-99.4)	99 (97.1-99.7)	> 0.99	0.5	> 0.99
NPV	92.8 (90.0-94.6)	94.5 (92.2-95.6)	95.6 (93.3-96.6)	0.5	0.125	0.5	94 (89.4-96.9)	95.6 (93.3-96.6)	96.7 (94.7-97.5)	0.25	0.063	0.5
Accuracy	94.6 (91.9-96.3)	96.5 (94.2-97.5)	97 (94.9-98.0)	0.016	0.004	0.5	95.9 (93.4-97.7)	97 (94.9-98.0)	97.8 (95.9-98.6)	0.125	0.063	0.5
AUROC	0.947 (0.924-0.969)	0.943 (0.919-0.967)	0.948 (0.925-0.971)	0.603	0.862	0.156	0.960 (0.941-0.980)	0.971 (0.954-0.988)	0.979 (0.964-0.993)	0.045	0.007	0.083

Abbreviated magnetic resonance imaging protocol 2 consisting of fat-suppressed fast spin echo T2-weighted, diffusion-weighted, and hepatobiliary phase images. Numbers in square brackets represent 95%CIs. PPV: Positive predictive value; NPV: Negative predictive value; AUROC: Area under the receiver operating characteristic curve; Ab-MRI: Abbreviated magnetic resonance imaging; CE-CT: Contrast-enhanced computed tomography.

similar to that for standard MRI (0.942; 95%CI: 0.885-0.963) and slightly higher than that for Ab-MRI (0.827; 95%CI: 0.770-0.885). All kappa values indicated excellent inter-reader agreement with regard to the presence of liver metastases.

DISCUSSION

The results of this study revealed that the overall diagnostic performances of both Ab-MRI protocols 1 and 2 were non-inferior to that of the standard MRI protocol, and that of the combination of Ab-MRI and CE-CT were higher than that of Ab-MRI alone and similar to that of the standard MRI protocol. These findings indicate that Ab-MRI protocols could provide a viable alternative to conventional MRI protocols for evaluating colorectal liver metastases, and that parallel assessment with CE-CT appears more useful.

Our results are similar to those from other recently published articles[11,12]. In retrospective studies of patients with CRC and using a similar design, Ghorra *et al*[11] and Canellas *et al*[12] assessed similar Ab-MRI protocols and reported high sensitivity for lesion detection (88.5% and 93.5%, respectively) and

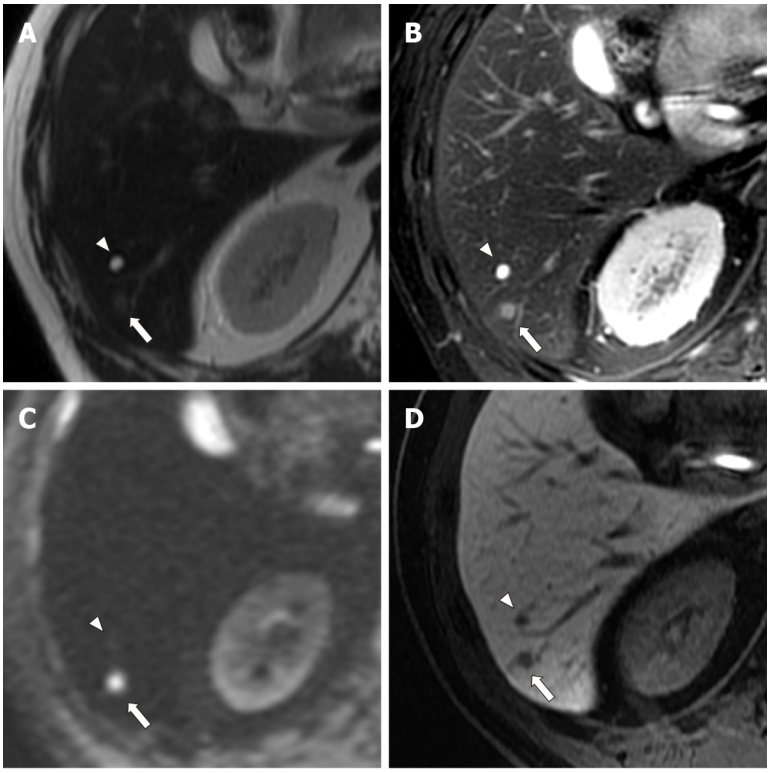

DOI: 10.4329/wjr.v14.i10.352 **Copyright** ©The Author(s) 2022.

Figure 5 A 59-year-old man with a colorectal small liver metastasis (arrows) and a small simple hepatic cyst (arrowheads) that were 4.1 mm and 5.5 mm, respectively. A: The metastasis (arrow) appears indistinct, whereas the cyst (arrowhead) is clearly depicted as an area of hyperintensity on single-shot fast spin echo T2-weighted imaging; B: The metastasis (arrow) is depicted as mild hyperintensity, and the cyst (arrowhead) is clearly depicted as an area of hyperintensity on fat-suppressed fast spin echo T2-weighted imaging; C: The metastasis (arrow) is clearly depicted as an area of hyperintensity, and the cyst (arrowhead) is not depicted on diffusion-weighted imaging; D: The metastasis (arrow) and the cyst (arrowhead) are clearly depicted as an area of hypointensity on hepatobiliary-phase imaging. The metastasis (arrows) was scored 5 by all four readers. The cyst (arrowheads was scored 1 or 2 by all four readers.

high PPV for lesion characterization (91.9% and 98.3%, respectively). The high diagnostic performance of Ab-MRI protocols could be preserved with DWI and HBP images[8-10]. Because of the background suppression of normal parenchyma and intrahepatic vessels, DWI shows high sensitivity for detecting liver metastases, especially small lesions < 2 cm in diameter, compared with T2-weighted imaging, and discriminates between metastases and benign lesions more effectively because of its excellent contrast-to-noise ratio (CNR) and signal-to-noise ratio (SNR)[14,15]. Gadoxetic acid-enhanced MRI also shows high sensitivity (92%), particularly for small lesions (≤ 1 cm), even compared with enhanced MRI using superparamagnetic iron oxide (63%)[16]. The higher detection sensitivity of gadoxetic acid-enhanced MRI can be explained by the HBP images, which provide higher SNR, CNR, and spatial resolution, improving the conspicuity and detectability of liver metastases[17,18]. The combination of DWI and HBP images yield excellent performance for lesion detection compared with each sequence alone[9,10]. However, these two sequences are insufficient for the accurate detection and diagnosis of liver metastases.

DWI characterization of focal liver lesions offers several potential pitfalls and limitations. First, the DWI signal intensity for metastases shows significant overlap between those of benign and other malignant lesions[19], and cannot accurately distinguish between each focal liver lesion. In addition, DWI in the upper abdomen is limited by susceptibility and ghosting artifacts in relation to the presence of gas in the nearby bowel and physiologic movements, respectively, which can hide lesions located on the upper edge or in the left lobe, respectively[15,20,21]. The excellent detectability of HBP images can compensate for these limitations but because many types of lesions show the same hypointensity, HBP images without dynamic contrast also show a potential drawback in regard to the difficulty of characterizing focal hepatic lesions.

Lesion characterization requires additional sequences, mainly for differentiating between metastases and benign lesions such as cysts or hemangiomas. We therefore adopted T2-weighted images in the present study, as with previous reports[11-13]. On T2-weighted imaging, liver metastases tend to show mild hyperintensity compared with cysts and hemangiomas, both of which show marked hyperintensity[22]. SSFSE T2-weighted imaging is more useful than FSE T2-weighted imaging for characterizing cysts and hemangiomas[23], whereas liver metastases (particularly small lesions) remain indistinct. On the other hand, FSE T2-weighted imaging with fat suppression might be more helpful for differentiating metastases from hemangiomas[24]. As both SSFSE and FSE T2-weighted imaging have specific

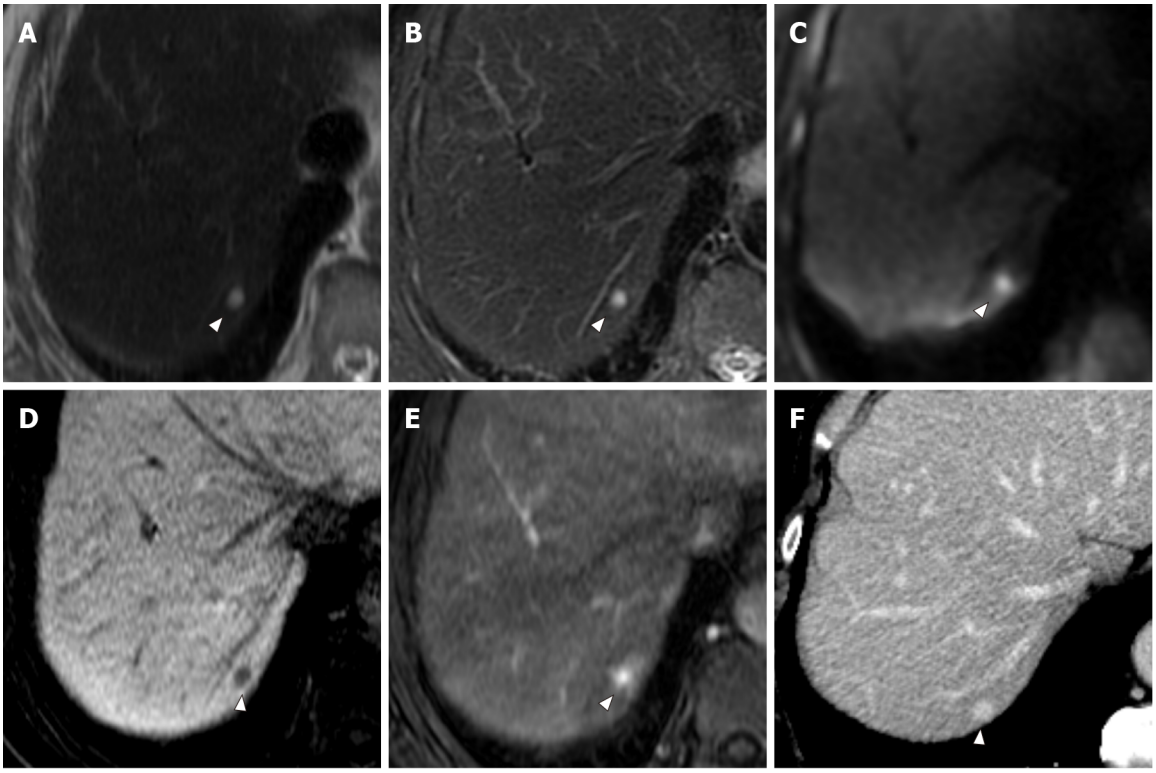

DOI: 10.4329/wjr.v14.i10.352

Figure 6 A 70-year-old man with colorectal liver metastasis (not shown) and a hepatic hemangioma in segment 7, which is 4 mm in diameter (arrowheads). A: The hemangioma (arrowhead) is clearly depicted as an area of hyperintensity on single-shot fast spin echo T2-weighted imaging; B: The hemangioma (arrowhead) is clearly depicted as an area of hyperintensity on fat-suppressed fast spin echo T2-weighted imaging; C: The hemangioma (arrowhead) is clearly depicted as an area of hyperintensity on diffusion-weighted imaging; D: The hemangioma (arrowhead) is clearly depicted as an area of hypointensity on hepatobiliary-phase imaging; E: The characteristic early enhancement accompanying arterio-portal shunt of hemangioma (arrowhead) is depicted on arterial phase magnetic resonance (MR) image; F: The characteristic prolonged enhancement of hemangioma (arrowhead) is depicted on equilibrium phase computed tomography (CT) image. The lesion was incorrectly scored 4 by two readers in abbreviated enhanced magnetic resonance imaging (Ab-MRI) protocol 1, and was scored 4 or 5 by two readers in Ab-MRI protocol 2. The lesion was scored 1 by all four readers in standard MR protocol and the combination of each Ab-MRI and contrast-enhanced CT.

advantages and disadvantages, we used two kinds of Ab-MRI protocol including T2-weighted imaging. Consequently, our results showed little difference between both kinds of Ab-MRI protocols with SSFSE or FSE T2-weighted images.

The difficulties in discriminating between metastases and hemangiomas, particularly for small lesions, may be a potential drawback of even gadoxetic acid-enhanced MRI, including dynamic contrast study, which is the standard protocol, because of the lack of an equilibrium phase in the real sense of the term[25,26]. The shortcomings of gadoxetic acid-enhanced MRI can be overcome by CE-CT, as supported by Sofue's report[27] that the PPV with the combination of CE-CT and gadoxetic acid-enhanced MRI was superior to that of gadoxetic acid-enhanced MRI alone[4,17,28]. To the best of our knowledge, this study provides the first assessment of the diagnostic performance of combination CE-CT and Ab-MRI for liver metastases. CT examinations are required to determine the therapeutic strategy for CRC. The use of CT examinations in Ab-MRI reading sessions is thus quite reasonable. Our results revealed that the combination of CE-CT and Ab-MRI achieved superior detection and characterization performance compared with Ab-MRI alone, and were quite similar to standard MRI alone[4,17,28].

Ab-MRI protocols should enable a reduction in imaging acquisition time, as noted by Canellas *et al*[12], who reported that Ab-MRI protocols may be performed in less than 15 min, while standard liver MRI takes up to 30 min. The implementation of Ab-MRI protocols can be expected because they have shown no significant influence on gadoxetic acid administration on T2-weighted imaging and diffusion sequences in regard to acquisition and image interpretation[29,30], suggesting that patients could undergo contrast administration without a bolus injection before entering the MRI suite. This would not only reduce the imaging acquisition time, but also provide several other advantages. First, a smaller intravenous route could be used because of the absence of a bolus injection, and this could reduce complications such as the leakage of contrast materials. Second, avoiding the use of a power injector could allow tangled procedures to be limited. Third, saline solution would not be needed after administration of gadoxetic acid, which would cut costs. Fourth, oxygen administration, which is used in selected patients to obtain appropriate arterial-phase images, would be unnecessary, resulting in

additional cost-cutting. Fifth, fewer imaging sequences would be needed, which would save time.

This study has several limitations that need to be considered. First, the study used a retrospective design and included a relatively small number of patients from a single center. Second, selection bias was possible because the patients selected for our series all had a high probability of metastases being detected, owing to our aim to achieve histologic diagnostic confirmation. Third, despite their availability as additional data, we did not assess apparent diffusion coefficient maps or values. Fourth, given the retrospective nature of this study, we could not measure the true acquisition time or cost of the Ab-MRI protocols. Fifth, unexpected malignant lesions other than colorectal liver metastases, such as hepatocellular carcinoma, could not be accurately diagnosed. Sixth, no other metastatic sites were assessed, because this study focused only on liver tumors. Finally, we did not assess the influence of the MRI protocol on surgical management or patient survival. Overall, further analyses are warranted before deciding whether to adapt Ab-MRI protocols for the initial surveillance of liver metastases in patients with CRC.

CONCLUSION

The diagnostic performances of two kinds of Ab-MRI protocol, including SSFSE or FSE T2-weighted images, were non-inferior to that of the standard protocol. The combination of Ab-MRI and CE-CT provided better diagnostic performance than Ab-MRI alone, nearly equivalent to that of the standard protocol.

ARTICLE HIGHLIGHTS

Research background

Although contrast-enhanced magnetic resonance imaging (MRI) using gadoxetic acid has been shown to have higher accuracy, sensitivity, and specificity for the detection and characterization of hepatic metastases compared with other modalities, the long examination time would limit the broad indication. Several abbreviated MRI protocols without dynamic phases (Ab-MRI) have been proposed to achieve equivalent diagnostic performance for the detection of colorectal liver metastases. However, an optimal protocol has not been established, and no studies have assessed the diagnostic performance of Ab-MRI combined with contrast-enhanced computed tomography (CE-CT), which is the preoperative imaging of colorectal cancer staging in clinical settings, to determine the best therapeutic strategy.

Research motivation

The long examination time and relatively high cost of the standard MRI protocol with gadoxetic acid limit its use for the routine surveillance of liver metastases in patients with colorectal cancer. In order to further expand use of the MRI examination with gadoxetic acid with maintaining the diagnostic performance of liver metastases in patients with colorectal cancer, the diagnostic performance of Ab-MRI combined with or without CE-CT, which is the preoperative imaging of colorectal cancer should be estimated.

Research objectives

To compare the diagnostic performance of two kinds of Ab-MRI protocol with the standard MRI protocol and a combination of the Ab-MRI protocol and CE-CT for the detection of colorectal liver metastases.

Research methods

Study participants comprised 87 patients (51 males, 36 females; mean age, 67.2 ± 10.8 years) who had undergone gadoxetic acid-enhanced MRI and CE-CT during the initial work-up for colorectal cancer from 2010 to 2021. Each exam was independently reviewed by two readers in three reading sessions: (1) Only single-shot fast spin echo (FSE) T2-weighted or fat-suppressed-FSE-T2-weighted, diffusion-weighted, and hepatobiliary-phase images (Ab-MRI protocol 1 or 2); (2) all acquired MRI sequences (standard protocol); and (3) a combination of an Ab-MRI protocol (1 or 2) and CE-CT. Diagnostic performance was then statistically analyzed.

Research results

A total of 380 Lesions were analyzed, including 195 metastases (51.4%). Results from the two Ab-MRI protocols were similar. The sensitivity, specificity, and positive and negative predictive values from Ab-MRI were non-inferior to those from standard MRI ($P > 0.05$), while those from the combination of Ab-MRI protocol and CE-CT tended to be higher than those from Ab-MRI alone, although the difference was not significant ($P > 0.05$), and were quite similar to those from standard MRI ($P > 0.05$).

Research conclusions

The diagnostic performances of two kinds of Ab-MRI protocol, including SSFSE or FSE T2-weighted images, were non-inferior to that of the standard protocol. The combination of Ab-MRI and CE-CT provided better diagnostic performance than Ab-MRI alone, nearly equivalent to that of the standard protocol.

Research perspectives

The combination of Ab-MRI and CE-CT can provide a sufficient diagnostic performance for the detection of colorectal liver metastases, and enable a reduction in imaging acquisition time.

FOOTNOTES

Author contributions: Ozaki K contributed to the methodology and data curation; Ishida S contributed to the conceptualization; Higuchi S, Sakai T, Kitano A, Takata K and Kinoshita K contributed to the investigation; Ozaki K, Matta Y and Ohtani T contributed to the writing-original draft; Kimura H contributed to the methodology, writing-review and editing; Gabata T contributed to the supervision and project administration.

Institutional review board statement: This single-center retrospective study was approved by our institutional review board (No. 20210035).

Informed consent statement: The written informed consent was waived.

Conflict-of-interest statement: The authors declare that they have no conflicts of interest.

Data sharing statement: The authors share all data.

Country/Territory of origin: Japan

ORCID number: Kumi Ozaki 0000-0002-1454-7512; Shota Ishida 0000-0002-0728-8057; Shohei Higuchi 0000-0002-5301-1390; Ayaki Kitano 0000-0001-8704-3465; Yuki Matta 0000-0003-4338-0771; Takashi Ohtani 0000-0002-7318-4571; Hirohiko Kimura 0000-0003-1649-2030; Toshifumi Gabata 0000-0002-9413-3431.

S-Editor: Zhang H
L-Editor: A
P-Editor: Zhang H

REFERENCES

1 **Haggar FA**, Boushey RP. Colorectal cancer epidemiology: incidence, mortality, survival, and risk factors. *Clin Colon Rectal Surg* 2009; **22**: 191-197 [PMID: 21037809 DOI: 10.1055/s-0029-1242458]
2 **Siegel R**, Ma J, Zou Z, Jemal A. Cancer statistics, 2014. *CA Cancer J Clin* 2014; **64**: 9-29 [PMID: 24399786 DOI: 10.3322/caac.21208]
3 **Seront E**, Van den Eynde M. Liver-directed therapies: does it make sense in the current therapeutic strategy for patients with confined liver colorectal metastases? *Clin Colorectal Cancer* 2012; **11**: 177-184 [PMID: 22306027 DOI: 10.1016/j.clcc.2011.12.004]
4 **Scharitzer M**, Ba-Ssalamah A, Ringl H, Kölblinger C, Grünberger T, Weber M, Schima W. Preoperative evaluation of colorectal liver metastases: comparison between gadoxetic acid-enhanced 3.0-T MRI and contrast-enhanced MDCT with histopathological correlation. *Eur Radiol* 2013; **23**: 2187-2196 [PMID: 23519439 DOI: 10.1007/s00330-013-2824-z]
5 **Cho JY**, Lee YJ, Han HS, Yoon YS, Kim J, Choi Y, Shin HK, Lee W. Role of gadoxetic acid-enhanced magnetic resonance imaging in the preoperative evaluation of small hepatic lesions in patients with colorectal cancer. *World J Surg* 2015; **39**: 1161-1166 [PMID: 25609116 DOI: 10.1007/s00268-015-2944-5]
6 **Kim HJ**, Lee SS, Byun JH, Kim JC, Yu CS, Park SH, Kim AY, Ha HK. Incremental value of liver MR imaging in patients with potentially curable colorectal hepatic metastasis detected at CT: a prospective comparison of diffusion-weighted imaging, gadoxetic acid-enhanced MR imaging, and a combination of both MR techniques. *Radiology* 2015; **274**: 712-722 [PMID: 25286324 DOI: 10.1148/radiol.14140390]
7 **Floriani I**, Torri V, Rulli E, Garavaglia D, Compagnoni A, Salvolini L, Giovagnoni A. Performance of imaging modalities in diagnosis of liver metastases from colorectal cancer: a systematic review and meta-analysis. *J Magn Reson Imaging* 2010; **31**: 19-31 [PMID: 20027569 DOI: 10.1002/jmri.22010]

8 **Colagrande S**, Castellani A, Nardi C, Lorini C, Calistri L, Filippone A. The role of diffusion-weighted imaging in the detection of hepatic metastases from colorectal cancer: A comparison with unenhanced and Gd-EOB-DTPA enhanced MRI. *Eur J Radiol* 2016; **85**: 1027-1034 [PMID: 27130067 DOI: 10.1016/j.ejrad.2016.02.011]

9 **Vilgrain V**, Esvan M, Ronot M, Caumont-Prim A, Aubé C, Chatellier G. A meta-analysis of diffusion-weighted and gadoxetic acid-enhanced MR imaging for the detection of liver metastases. *Eur Radiol* 2016; **26**: 4595-4615 [PMID: 26883327 DOI: 10.1007/s00330-016-4250-5]

10 **Koh DM**, Collins DJ, Wallace T, Chau I, Riddell AM. Combining diffusion-weighted MRI with Gd-EOB-DTPA-enhanced MRI improves the detection of colorectal liver metastases. *Br J Radiol* 2012; **85**: 980-989 [PMID: 22167501 DOI: 10.1259/bjr/91771639]

11 **Ghorra C**, Pommier R, Piveteau A, Rubbia-Brandt L, Vilgrain V, Terraz S, Ronot M. The diagnostic performance of a simulated "short" gadoxetic acid-enhanced MRI protocol is similar to that of a conventional protocol for the detection of colorectal liver metastases. *Eur Radiol* 2021; **31**: 2451-2460 [PMID: 33025173 DOI: 10.1007/s00330-020-07344-0]

12 **Canellas R**, Patel MJ, Agarwal S, Sahani DV. Lesion detection performance of an abbreviated gadoxetic acid-enhanced MRI protocol for colorectal liver metastasis surveillance. *Eur Radiol* 2019; **29**: 5852-5860 [PMID: 30888485 DOI: 10.1007/s00330-019-06113-y]

13 **Granata V**, Fusco R, Avallone A, Cassata A, Palaia R, Delrio P, Grassi R, Tatangelo F, Grazzini G, Izzo F, Petrillo A. Abbreviated MRI protocol for colorectal liver metastases: How the radiologist could work in pre surgical setting. *PLoS One* 2020; **15**: e0241431 [PMID: 33211702 DOI: 10.1371/journal.pone.0241431]

14 **Parikh T**, Drew SJ, Lee VS, Wong S, Hecht EM, Babb JS, Taouli B. Focal liver lesion detection and characterization with diffusion-weighted MR imaging: comparison with standard breath-hold T2-weighted imaging. *Radiology* 2008; **246**: 812-822 [PMID: 18223123 DOI: 10.1148/radiol.2463070432]

15 **Coenegrachts K**, Delanote J, Ter Beek L, Haspeslagh M, Bipat S, Stoker J, Van Kerkhove F, Steyaert L, Rigauts H, Casselman JW. Improved focal liver lesion detection: comparison of single-shot diffusion-weighted echoplanar and single-shot T2 weighted turbo spin echo techniques. *Br J Radiol* 2007; **80**: 524-531 [PMID: 17510250 DOI: 10.1259/bjr/33156643]

16 **Muhi A**, Ichikawa T, Motosugi U, Sou H, Nakajima H, Sano K, Sano M, Kato S, Kitamura T, Fatima Z, Fukushima K, Iino H, Mori Y, Fujii H, Araki T. Diagnosis of colorectal hepatic metastases: comparison of contrast-enhanced CT, contrast-enhanced US, superparamagnetic iron oxide-enhanced MRI, and gadoxetic acid-enhanced MRI. *J Magn Reson Imaging* 2011; **34**: 326-335 [PMID: 21780227 DOI: 10.1002/jmri.22613]

17 **Sofue K**, Tsurusaki M, Tokue H, Arai Y, Sugimura K. Gd-EOB-DTPA-enhanced 3.0 T MR imaging: quantitative and qualitative comparison of hepatocyte-phase images obtained 10 min and 20 min after injection for the detection of liver metastases from colorectal carcinoma. *Eur Radiol* 2011; **21**: 2336-2343 [PMID: 21748389 DOI: 10.1007/s00330-011-2197-0]

18 **Chang KJ**, Kamel IR, Macura KJ, Bluemke DA. 3.0-T MR imaging of the abdomen: comparison with 1.5 T. *Radiographics* 2008; **28**: 1983-1998 [PMID: 19001653 DOI: 10.1148/rg.287075154]

19 **Wei C**, Tan J, Xu L, Juan L, Zhang SW, Wang L, Wang Q. Differential diagnosis between hepatic metastases and benign focal lesions using DWI with parallel acquisition technique: a meta-analysis. *Tumour Biol* 2015; **36**: 983-990 [PMID: 25318600 DOI: 10.1007/s13277-014-2663-9]

20 **Chen ZG**, Xu L, Zhang SW, Huang Y, Pan RH. Lesion discrimination with breath-hold hepatic diffusion-weighted imaging: a meta-analysis. *World J Gastroenterol* 2015; **21**: 1621-1627 [PMID: 25663782 DOI: 10.3748/wjg.v21.i5.1621]

21 **Xiong H**, Zeng YL. Standard-b-Value Versus Low-b-Value Diffusion-Weighted Imaging in Hepatic Lesion Discrimination: A Meta-analysis. *J Comput Assist Tomogr* 2016; **40**: 498-504 [PMID: 26938696 DOI: 10.1097/RCT.0000000000000377]

22 **Danet IM**, Semelka RC, Braga L, Armao D, Woosley JT. Giant hemangioma of the liver: MR imaging characteristics in 24 patients. *Magn Reson Imaging* 2003; **21**: 95-101 [PMID: 12670595 DOI: 10.1016/s0730-725x(02)00641-0]

23 **Kiryu S**, Okada Y, Ohtomo K. Differentiation between hemangiomas and cysts of the liver with single-shot fast-spin echo image using short and long TE. *J Comput Assist Tomogr* 2002; **26**: 687-690 [PMID: 12439299 DOI: 10.1097/00004728-200209000-00004]

24 **Takayama Y**, Nishie A, Okamoto D, Fujita N, Asayama Y, Ushijima Y, Yoshizumi T, Yoneyama M, Ishigami K. Differentiating Liver Hemangioma from Metastatic Tumor Using T2-enhanced Spin-echo Imaging with a Time-reversed Gradient-echo Sequence in the Hepatobiliary Phase of Gadoxetic Acid-enhanced MR Imaging. *Magn Reson Med Sci* 2022; **21**: 445-457 [PMID: 33883364 DOI: 10.2463/mrms.mp.2020-0151]

25 **Tateyama A**, Fukukura Y, Takumi K, Shindo T, Kumagae Y, Kamimura K, Nakajo M. Gd-EOB-DTPA-enhanced magnetic resonance imaging features of hepatic hemangioma compared with enhanced computed tomography. *World J Gastroenterol* 2012; **18**: 6269-6276 [PMID: 23180948 DOI: 10.3748/wjg.v18.i43.6269]

26 **Goshima S**, Kanematsu M, Watanabe H, Kondo H, Shiratori Y, Onozuka M, Moriyama N. Hepatic hemangioma and metastasis: differentiation with gadoxetate disodium-enhanced 3-T MRI. *AJR Am J Roentgenol* 2010; **195**: 941-946 [PMID: 20858822 DOI: 10.2214/AJR.09.3730]

27 **Sofue K**, Tsurusaki M, Murakami T, Onoe S, Tokue H, Shibamoto K, Arai Y, Sugimura K. Does Gadoxetic acid-enhanced 3.0T MRI in addition to 64-detector-row contrast-enhanced CT provide better diagnostic performance and change the therapeutic strategy for the preoperative evaluation of colorectal liver metastases? *Eur Radiol* 2014; **24**: 2532-2539 [PMID: 24865698 DOI: 10.1007/s00330-014-3233-7]

28 **Berger-Kulemann V**, Schima W, Baroud S, Koelblinger C, Kaczirek K, Gruenberger T, Schindl M, Maresch J, Weber M, Ba-Ssalamah A. Gadoxetic acid-enhanced 3.0 T MR imaging versus multidetector-row CT in the detection of colorectal metastases in fatty liver using intraoperative ultrasound and histopathology as a standard of reference. *Eur J Surg Oncol* 2012; **38**: 670-676 [PMID: 22652037 DOI: 10.1016/j.ejso.2012.05.004]

29 **Choi SA**, Lee SS, Jung IH, Kim HA, Byun JH, Lee MG. The effect of gadoxetic acid enhancement on lesion detection and characterisation using T_2 weighted imaging and diffusion weighted imaging of the liver. *Br J Radiol* 2012; **85**: 29-36 [PMID: 21123305 DOI: 10.1259/bjr/12929687]

30 **Cieszanowski A**, Podgórska J, Rosiak G, Maj E, Grudziński IP, Kaczyński B, Szeszkowski W, Milczarek K, Rowiński O. Gd-EOB-DTPA-Enhanced MR Imaging of the Liver: The Effect on T2 Relaxation Times and Apparent Diffusion Coefficient (ADC). *Pol J Radiol* 2016; **81**: 103-109 [PMID: 27026795 DOI: 10.12659/PJR.895701]

Published by **Baishideng Publishing Group Inc**
7041 Koll Center Parkway, Suite 160, Pleasanton, CA 94566, USA
Telephone: +1-925-3991568
E-mail: bpgoffice@wjgnet.com
Help Desk: https://www.f6publishing.com/helpdesk
https://www.wjgnet.com

ISSN 1949-8470 (online)

World Journal of *Radiology*

World J Radiol 2022 November 28; 14(11): 367-374

Published by Baishideng Publishing Group Inc

WJR

World Journal of Radiology

Contents

Monthly Volume 14 Number 11 November 28, 2022

ORIGINAL ARTICLE

Observational Study

World Journal of Radiology

Monthly Volume 14 Number 11 November 28, 2022

Contents

ABOUT COVER

Editorial Board Member of *World Journal of Radiology*, Si-Ze Wu, MD, Chief Doctor, Professor, Department of Ultrasound, Dept Ultrasound, The First Affiliated Hosp, Hainan Med University, Haikou 570102, Hainan Province, China. wsz074@aliyun.com

AIMS AND SCOPE

The primary aim of *World Journal of Radiology* (*WJR*, *World J Radiol*) is to provide scholars and readers from various fields of radiology with a platform to publish high-quality basic and clinical research articles and communicate their research findings online.

WJR mainly publishes articles reporting research results and findings obtained in the field of radiology and covering a wide range of topics including state of the art information on cardiopulmonary imaging, gastrointestinal imaging, genitourinary imaging, musculoskeletal imaging, neuroradiology/head and neck imaging, nuclear medicine and molecular imaging, pediatric imaging, vascular and interventional radiology, and women's imaging.

INDEXING/ABSTRACTING

The *WJR* is now abstracted and indexed in PubMed, PubMed Central, Emerging Sources Citation Index (Web of Science), Reference Citation Analysis, China National Knowledge Infrastructure, China Science and Technology Journal Database, and Superstar Journals Database. The 2022 edition of Journal Citation Reports ® cites the 2021 Journal Citation Indicator (JCI) for *WJR* as 0.48.

RESPONSIBLE EDITORS FOR THIS ISSUE

NAME OF JOURNAL
World Journal of Radiology

ISSN
ISSN 1949-8470 (online)

LAUNCH DATE
January 31, 2009

FREQUENCY
Monthly

EDITORS-IN-CHIEF
Thomas J Vogl

EDITORIAL BOARD MEMBERS
https://www.wjgnet.com/1949-8470/editorialboard.htm

PUBLICATION DATE
November 28, 2022

COPYRIGHT
© 2022 Baishideng Publishing Group Inc

INSTRUCTIONS TO AUTHORS
https://www.wjgnet.com/bpg/gerinfo/204

GUIDELINES FOR ETHICS DOCUMENTS
https://www.wjgnet.com/bpg/GerInfo/287

GUIDELINES FOR NON-NATIVE SPEAKERS OF ENGLISH
https://www.wjgnet.com/bpg/gerinfo/240

PUBLICATION ETHICS
https://www.wjgnet.com/bpg/GerInfo/288

PUBLICATION MISCONDUCT
https://www.wjgnet.com/bpg/gerinfo/208

ARTICLE PROCESSING CHARGE
https://www.wjgnet.com/bpg/gerinfo/242

STEPS FOR SUBMITTING MANUSCRIPTS
https://www.wjgnet.com/bpg/GerInfo/239

ONLINE SUBMISSION
https://www.f6publishing.com

World Journal of Radiology

Submit a Manuscript: https://www.f6publishing.com

World J Radiol 2022 November 28; 14(11): 367-374

DOI: 10.4329/wjr.v14.i11.367

ISSN 1949-8470 (online)

ORIGINAL ARTICLE

Observational Study

Interobserver reliability between pediatric radiologists and residents in ultrasound evaluation of intraventricular hemorrhage in premature infants

Muhammad Danish Barakzai, Ayimen Khalid, Zara Za Sheer, Faheemullah Khan, Naila Nadeem, Noman Khan, Kiran Hilal

Specialty type: Radiology, nuclear medicine and medical imaging

Provenance and peer review: Invited article; Externally peer reviewed.

Peer-review model: Single blind

Peer-review report's scientific quality classification

Grade A (Excellent): A
Grade B (Very good): B
Grade C (Good): C
Grade D (Fair): 0
Grade E (Poor): 0

P-Reviewer: Aydin S, Turkey; Moshref RH, Saudi Arabia; Schoenhagen P, United States

Received: March 13, 2022
Peer-review started: March 13, 2022
First decision: May 12, 2022
Revised: May 25, 2022
Accepted: September 21, 2022
Article in press: September 21, 2022
Published online: November 28, 2022

Muhammad Danish Barakzai, Department of Radiology, The Hospital for Sick Children, Toronto 555, Canada

Muhammad Danish Barakzai, Ayimen Khalid, Faheemullah Khan, Naila Nadeem, Noman Khan, Kiran Hilal, Department of Radiology, Aga Khan University Hospital, Karachi 74800, Pakistan

Zara Za Sheer, Community Health Sciences, Aga Khan University Hospital, Karachi 74800, Pakistan

Corresponding author: Kiran Hilal, FCPS, MBBS, Assistant Professor, Department of Radiology, Aga Khan University Hospital, Stadium Road, Karachi 74800, Pakistan.
kiran.hilal@aku.edu

Abstract

BACKGROUND

Germinal matrix intraventricular hemorrhage (IVH) may contribute to significant morbidity and mortality in premature infants. Timely identification and grading of IVH affect decision-making and clinical outcomes. There is possibility of misinterpretation of the ultrasound appearances, and the interobserver variability has not been investigated between radiology resident and board-certified radiologist.

AIM

To assess interobserver reliability between senior radiology residents performing bedside cranial ultrasound during on-call hours and pediatric radiologists.

METHODS

From June 2018 to June 2020, neonatal cranial ultrasound examinations were performed in neonatal intensive care unit. Ultrasound findings were recorded by the residents performing the ultrasound and the pediatric attending radiologists.

RESULTS

In total, 200 neonates were included in the study, with a mean gestational age of 30.9 wk. Interobserver agreement for higher grade (Grade III & IV) IVH was excellent. There was substantial agreement for lower grade (Grade I & II) IVH.

CONCLUSION
There is strong agreement between radiology residents and pediatric radiologists, which is higher for high grade IVHs.

Key Words: Ultrasound head; Neonatal cranial ultrasound; Cranial ultrasound; Intraventricular hemorrhage; Neonatal intraventricular hemorrhage

Core Tip: While possibility of interobserver variability exists in all imaging modalities, it is the highest in ultrasound. Interobserver variability in ultrasound may result from technical errors such as inadequate gain/depth settings, incomplete anatomic interrogation, or error in misinterpretation. During ultrasound examination, both the image acquisition and interpretive skills improve with increasing experience. Differences in identification and grading of intraventricular hemorrhage may affect the clinical outcome, and the subsequent management options.

Citation: Barakzai MD, Khalid A, Sheer ZZ, Khan F, Nadeem N, Khan N, Hilal K. Interobserver reliability between pediatric radiologists and residents in ultrasound evaluation of intraventricular hemorrhage in premature infants. *World J Radiol* 2022; 14(11): 367-374
URL: https://www.wjgnet.com/1949-8470/full/v14/i11/367.htm
DOI: https://dx.doi.org/10.4329/wjr.v14.i11.367

INTRODUCTION

Intraventricular hemorrhage (IVH) is a major neurological complication of prematurity. In neonates weighing less than 1500 g, the incidence of IVH reaches up to 27% whereas, in extremely preterm infants weighing 500-750 g, the prevalence is about 45%[1]. A substantial subgroup of premature infants with moderate to severe IVH develops neurologic sequelae including an elevated risk of post-hemorrhagic hydrocephalus, cerebral palsy, and mental retardation, while infants with mild IVH are at risk of developmental disabilities[2-4]. IVH and its neurologic and psychiatric sequelae are a major public health concern worldwide[5].

The multifaceted etiology of IVH is primarily attributed to the intrinsic fragility of the germinal matrix vasculature and the disturbance in the cerebral blood flow. The germinal matrix exhibits rapid angiogenesis in contrast to other brain regions causing its high vascular density. Hemorrhages occurring in the germinal matrix often rupture through the ependyma into the lateral ventricle and are then referred to as IVH[6].

The development of IVH is attributable to a number of risk factors including vaginal delivery, low Apgar score, severe respiratory distress syndrome, pneumothorax, hypoxia, hypercapnia, seizures, patent ductus arteriosus, thrombocytopenia, infection, and others[7-9]. Dysregulation of cerebral blood flow by these risk factors induces IVH.

While the possibility of interobserver variability exists in all imaging modalities, it is the highest in ultrasound. Interobserver variability in ultrasound may result from technical errors such as inadequate gain/depth settings, incomplete anatomic interrogation, or misinterpretation errors[10]. During ultrasound examination, both the image acquisition and interpretive skills improve with increasing experience.

Few studies have examined the reliability of cranial ultrasound interpretation, despite the ostensibly important role of accurate interpretation. Variations in the identification and grading of IVH may affect the morbidity, clinical outcomes, and subsequent treatment options. This study aims to assess interobserver reliability between senior residents performing bedside cranial ultrasounds during on-call hours and board-certified pediatric radiologists.

MATERIALS AND METHODS

This cross-sectional study was carried out in the Department of Radiology at Aga Khan University Hospital, Karachi, Pakistan. The Institutional Ethical Review Committee approved the study with a waiver for informed consent. The study period was two years, from June 2016 to June 2018. All premature infants (less than 37 wk of gestational age) or infants with very low birth weight (birth weight equal to or less than 1500 g) and infants in the Neonatal Intensive Care Unit who underwent a

cranial ultrasound were included in the study. Patients who were born at term, and had prior brain computed tomography (CT) or brain magnetic resonance imaging (MRI) , or patients with known cerebral malformations were excluded. To prevent potential selection bias, patients with prior neuroimaging were excluded.

Prematurity was defined as infants born alive before 37 wk of gestation with further subcategorization as: (1) Extremely preterm (less than 28 wk); (2) very preterm (28 - 32 wk); and (3) moderate to late preterm (32 - 37 wk).

The gestational age of all infants was determined from a chart review of the mother. The weight of all infants included in the study was measured with a digital weighing scale.

Cranial ultrasound in all cases was performed through the anterior fontanelle in both coronal and sagittal planes using the Mindray M7 Diagnostic Ultrasound System with a 5- to 10-MHz transducer. All ultrasound examinations were performed by a senior resident (Year III and year IV) and reviewed by an attending board-certified radiologist with at least five years' experience in pediatric imaging. The findings of both the resident and the pediatric radiologist with regards to the presence and absence of intraventricular hemorrhage and its grading were recorded on a structured proforma by a year III resident, blinded to additional clinical information. In addition to IVH, all scans were recorded for the presence or absence of hydrocephalus, periventricular leukomalacia, and brain malformations. If hydrocephalus was noted to be present, it was graded as mild, moderate, or severe based on the measurement of transverse atrial width.

The Volpe grading system was used for sonographic grading of IVH/germinal matrix hemorrhage [11]. (1) Grade I: Bleeding confined to the periventricular area (germinal matrix). An example of grade I IVH is shown in Figure 1, in which abnormal echogenicity is apparent in caudothalamic groove on parasagittal view; (2) Grade II: Intraventricular bleeding (10%-50% of the ventricular area on sagittal view). An example of grade II IVH is shown in Figure 2, in which abnormal echogenicity is seen extending into left lateral ventricle on coronal view; (3) Grade III: Intraventricular bleeding (> 50% of the ventricular area or distends ventricle. An example of grade III IVH is shown in Figure 3, in which hemorrhage in right lateral ventricle is seen on coronal view, with mild associated ventricular dilatation; and (4) Grade IV: Germinal matrix hemorrhage grade I, II or III with extension into brain parenchyma. An example of grade IV IVH is seen in Figure 4, in which the hemorrhage in bilateral lateral ventricles is seen extending into periventricular region bilaterally on coronal view.

Interobserver agreement was calculated using Kappa statistics (Table 1). Data was entered and analyzed using Statistical Package for Social Sciences version 20 software.

RESULTS

The study included 200 neonates with a gestational age of 30.9 wk (range 20-36, SD ± 3.8). There were 120 (60%) male neonates and 80 (40%) female neonates. A total of 78 (39%) babies were delivered vaginally while 122 (61%) were delivered *via* lower segment cesarean section. The mean weight was 1.2 kg (range 0.5-1.5, SD ± 0.3). Based on the clinical indication on the radiology slip, 83 (41%) of the neonates had sepsis, 60 (30%) had respiratory distress, and 5 (2.5%) had a pneumothorax. The mean duration of hospital stay was 9 days (range 1-46).

The radiology resident reported 136 (68%) cases as normal and 64 (32%) as abnormal. The pediatric radiologist reported 148 (74%) cases as normal and 52 (26%) as abnormal. Twenty-four patients had IVH on the right side, 13 patients had IVH on the left side, and 27 had bilateral IVH according to resident interpretations. Fourteen patients had IVH on the right side, 11 patients had IVH on the left side, and 27 patients had bilateral IVH according to the pediatric radiologist. The presence of IVH and its grading by the resident and attending along with the Kappa values are shown in Table 1. We did not measure the interobserver agreement on additional findings encountered in the study.

DISCUSSION

On making the diagnosis of rheumatic fever by auscultation, Alvan Feinstein wrote in his book Clinical Judgment "The main problems of observer variability were neither in the eyes nor the ears of the observers. We all saw and heard essentially the same things, but each observer used different ingredients in his criteria for description and interpretation of the observations"[12]. The same can be said about medical imaging in which interobserver variability remains a critical issue[13].

Bedside cranial ultrasound is the neuroimaging standard of care for the detection of IVH[14]. Cranial sonography is cost-effective, does not require sedation, and is portable, allowing for the evaluation of critical patients at the bedside. In a study by Maalouf *et al*[15], ultrasound has a predictive probability of 0.85 (0.76-0.94) for the presence of IVH on MRI.

The interobserver agreement for findings on neonatal head ultrasound varies from poor to excellent among radiologists[16]. Although there is a possibility of intra-observer agreement, this is quite low. While numerous studies have explored interobserver variability in neonatal cranial ultrasonography,

Table 1 Interobserver agreement with Kappa values in cranial ultrasound interpretation between radiology residents and attending pediatric radiologists

Findings	Senior resident, %	Attending radiologist, %	Kappa value
Normal ultrasound	68	74	0.94
Abnormal ultrasound	32	26	0.94
Grade I IVH	72	62	0.82
Grade II IVH	12	12	0.86
Grade III IVH	6	7	0.90
Grade IV IVH	10	19	0.92
Right-sided IVH	38	27	0.92
Left-sided IVH	20	21	
Bilateral IVH	42	52	

IVH: Intraventricular hemorrhage.

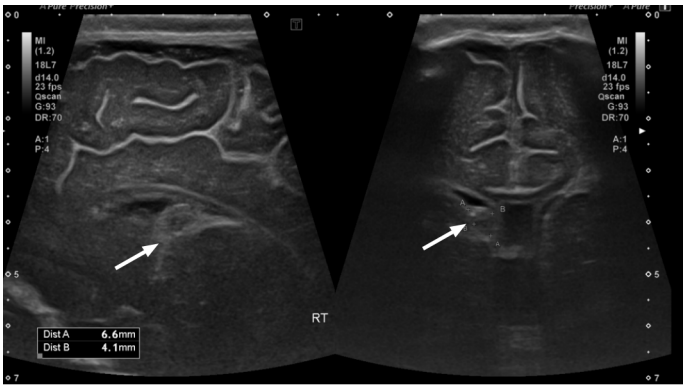

DOI: 10.4329/wjr.v14.i11.367 **Copyright** ©The Author(s) 2022.

Figure 1 Grade I germinal matrix hemorrhage. Parasagittal and cornal views of the right lateral ventricle, in which abnormal echogenicity in caudothalamic groove was consistent with grade I intraventricular hemorrhage/germinal matrix hemorrhage as indicated by arrows.

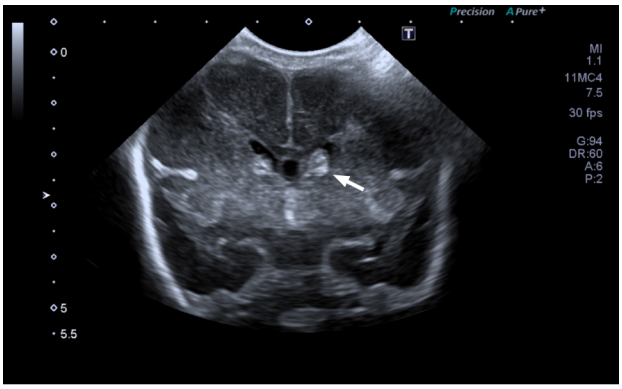

DOI: 10.4329/wjr.v14.i11.367 **Copyright** ©The Author(s) 2022.

Figure 2 Grade II intraventricular hemorrhage. Coronal view ultrasound image reveals abnormal echogenicity in the left caudothalamic groove extending into left lateral ventricle. There was no associated ventricular dilatation (white arrow).

ours is the first to study the differences in interpretation between senior residents and board-certified pediatric radiologists.

In our study, there was excellent agreement between the senior resident and the attending for intracranial hemorrhage. There was substantial agreement on grade I and grade II intraventricular hemorrhage, whilst agreement on grade III and grade IV intraventricular hemorrhage was almost

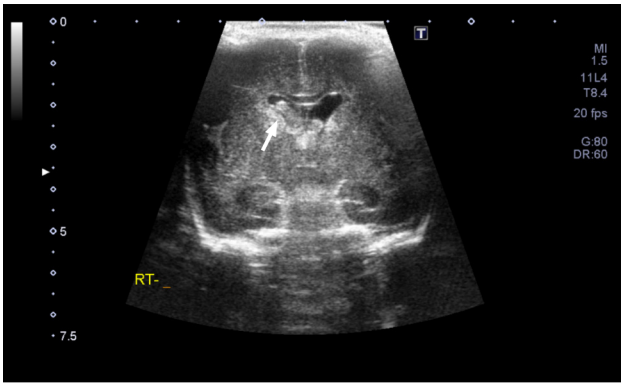

DOI: 10.4329/wjr.v14.i11.367 **Copyright** ©The Author(s) 2022.

Figure 3 Grade III intraventricular hemorrhage. Coronal view ultrasound image reveals right-sided intraventricular hemorrhage with associated ventricular dilatation (white arrow).

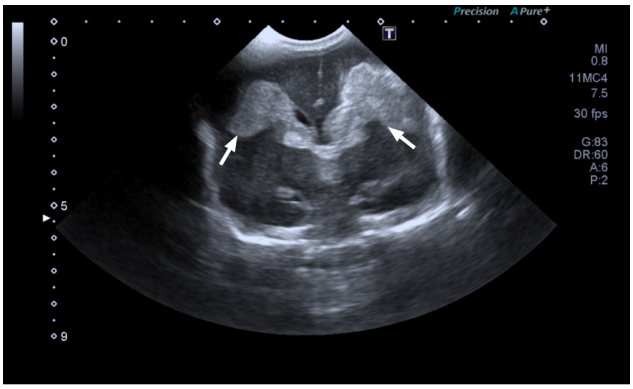

DOI: 10.4329/wjr.v14.i11.367 **Copyright** ©The Author(s) 2022.

Figure 4 Grade IV bilateral intraventricular hemorrhage. Coronal view ultrasound image reveals bilateral intraventricular hemorrhage filling the dilated bilateral lateral ventricles, and extending into adjacent parenchyma (white arrows).

perfect.

Among radiologists, experienced neonatologists, and less experienced neonatologists involved in a study by Hagmann *et al*[17], the interobserver agreement in the interpretation of cranial ultrasound ranged from poor to good. Hintz *et al*[18] found excellent interobserver agreement on severe intraventricular hemorrhage, but poor agreement on periventricular leukomalacia between experienced board-certified radiologists with special expertise in cranial ultrasound. Among radiologists, pediatric neurologists, and neonatologists experienced in neonatal ultrasounds, Pinto *et al*[19] obtained excellent interobserver agreement for major findings such as parenchymal hemorrhage, but rather poor agreement for less severe pathologies such as germinal matrix hemorrhage. A study by Corbett *et al*[16] found excellent agreement on high-grade hemorrhage but poor agreement on interpretation of ventricular size.

Even though we did not find any prior studies on interobserver variability between senior residents and radiologists, our results are comparable to previous studies in that there is excellent agreement on major abnormalities such as grade III and IVH.

The board-certified radiologist's experience is most likely to be responsible for the study's relatively low interobserver agreements for grade I and II IVH. Because of greater image gain/depth, improved probe handling, and knowledge of pertinent anatomy, experience with doing cranial ultrasonography can result in better imaging quality.

This experience also manifests itself in improved ultrasound interpretation performed by others. Due to inexperience, the resident in our study initially missed the additional findings of hydrocephalus, choroid plexus abnormalities, and periventricular echogenicity as indicated in Table 2. We plan to conduct a follow-up study to investigate abnormalities other than IVH on neonatal cranial ultrasound which can have significant impact on disease prognosis.

This study has some limitations. The residents and pediatric radiologists were compared for interobserver agreement only on one variable, *i.e.*, IVH, but no cross-sectional neuroimaging such as CT or MRI was performed for confirmation. The interobserver agreement was not calculated for additional findings such as parenchymal hemorrhage, hydrocephalus, and venous infarctions, which also have implications

Table 2 Additional ultrasound examination findings initially missed by the resident

Additional findings on neonatal cranial ultrasound (%)	
Ventricular abnormalities	12 (6)
Mild hydrocephalus	11 (5.5)
Severe hydrocephalus	1 (0.5)
Choroid plexus abnormalities	4 (2)
Increased periventricular echogenicity	4 (2)

for neonatal neurodevelopment.

CONCLUSION

Interobserver agreement regarding detection of intraventricular hemorrhage is high for low-grade hemorrhage and almost perfect for high-grade hemorrhage between residents and board-certified pediatric radiologists.

ARTICLE HIGHLIGHTS

Research background

Neonatal cranial ultrasound examinations were evaluated in neonatal intensive care unit (NICU) patients. Ultrasound findings were recorded for the resident performing the ultrasound and the pediatric attending radiologist.

Research motivation

Despite the ostensibly important role of accurate cranial ultrasound interpretation, few studies have investigated the reliability of interpretation of cranial ultrasound. Differences in the identification and grading of intraventricular hemorrhage (IVH) may affect the clinical outcome and the subsequent management options. This is the reason the study was undertaken.

Research objectives

To assess interobserver reliability between senior radiology residents performing bedside cranial ultrasounds during on-call hours and board-certified pediatric radiologists.

Research methods

A total of 200 neonatal cranial ultrasound examinations were evaluated in NICU patients. Ultrasound findings were recorded for both the resident performing the ultrasound and the pediatric attending radiologist. Interobserver agreement was calculated.

Research results

The mean gestational age was 30.9 wk. Interobserver agreement for higher grade (Grade III & IV) IVH was excellent. There was substantial agreement for lower grade (Grade I & II) IVH.

Research conclusions

Interobserver agreement for detection of IVH is high for low-grade hemorrhage and almost perfect for high-grade hemorrhage between radiology residents and board certified pediatricians.

Research perspectives

Our study results are limited by the cross sectional nature of the study. Additionally, we did not compare agreement on the interpretation of periventricular leukomalacia, incidental findings, and degree of ventriculomegaly if it was present which can have significant impact on disease prognosis. This may be explored in a future study.

FOOTNOTES

Author contributions: Barakzai MD, Khalid A, Sheer ZZ, Nadeem N and Hilal K designed the research study; Barakzai MD, Nadeem N, Khan N and Khan F performed the research; Khalid A, Sheer ZZ, Khan N and Hilal K contributed new reagents and analytic tools; Khalid A, Sheer ZZ, Khan F and Khan N analyzed the data and wrote the manuscript; All authors have read and approve the final manuscript.

Institutional review board statement: Exemption from ethical approval was granted by Ethics Review Committee.

Informed consent statement: Individual informed consent was waived off by the Institutional Review Committee due to minimal risk to the subjects, observational nature of the study and anonymized imaging review.

Conflict-of-interest statement: All authors of this manuscript have no conflict of interest to disclose.

Data sharing statement: Technical appendix, statistical code, and dataset available from the corresponding author at kiran.hilal@aku.edu. Participants gave informed consent for anonymized data sharing.

STROBE statement: The authors have read the STROBE Statement—checklist of items, and the manuscript was prepared and revised according to the STROBE Statement—checklist of items.

Country/Territory of origin: Pakistan

ORCID number: Muhammad Danish Barakzai 0000-0001-8867-2124; Faheemullah Khan 0000-0001-6369-743X; Noman Khan 0000-0002-8343-6445; Kiran Hilal 0000-0003-0737-3419.

S-Editor: Liu JH
L-Editor: Ma JY
P-Editor: Liu JH

REFERENCES

1 **Allen KA**. Treatment of intraventricular hemorrhages in premature infants: where is the evidence? *Adv Neonatal Care* 2013; **13**: 127-130 [PMID: 23532032 DOI: 10.1097/ANC.0b013e31828ac82e]
2 **Sherlock RL**, Anderson PJ, Doyle LW; Victorian Infant Collaborative Study Group. Neurodevelopmental sequelae of intraventricular haemorrhage at 8 years of age in a regional cohort of ELBW/very preterm infants. *Early Hum Dev* 2005; **81**: 909-916 [PMID: 16126353 DOI: 10.1016/j.earlhumdev.2005.07.007]
3 **Murphy BP**, Inder TE, Rooks V, Taylor GA, Anderson NJ, Mogridge N, Horwood LJ, Volpe JJ. Posthaemorrhagic ventricular dilatation in the premature infant: natural history and predictors of outcome. *Arch Dis Child Fetal Neonatal Ed* 2002; **87**: F37-F41 [PMID: 12091289 DOI: 10.1136/fn.87.1.f37]
4 **Pinto-Martin JA**, Whitaker AH, Feldman JF, Van Rossem R, Paneth N. Relation of cranial ultrasound abnormalities in low-birthweight infants to motor or cognitive performance at ages 2, 6, and 9 years. *Dev Med Child Neurol* 1999; **41**: 826-833 [PMID: 10619281 DOI: 10.1017/s0012162299001644]
5 **Wilson-Costello D**, Friedman H, Minich N, Fanaroff AA, Hack M. Improved survival rates with increased neurodevelopmental disability for extremely low birth weight infants in the 1990s. *Pediatrics* 2005; **115**: 997-1003 [PMID: 15805376 DOI: 10.1542/peds.2004-0221]
6 **Ballabh P**, Xu H, Hu F, Braun A, Smith K, Rivera A, Lou N, Ungvari Z, Goldman SA, Csiszar A, Nedergaard M. Angiogenic inhibition reduces germinal matrix hemorrhage. *Nat Med* 2007; **13**: 477-485 [PMID: 17401377 DOI: 10.1038/nm1558]
7 **Osborn DA**, Evans N, Kluckow M. Hemodynamic and antecedent risk factors of early and late periventricular/intraventricular hemorrhage in premature infants. *Pediatrics* 2003; **112**: 33-39 [PMID: 12837865 DOI: 10.1542/peds.112.1.33]
8 **Babnik J**, Stucin-Gantar I, Kornhauser-Cerar L, Sinkovec J, Wraber B, Derganc M. Intrauterine inflammation and the onset of peri-intraventricular hemorrhage in premature infants. *Biol Neonate* 2006; **90**: 113-121 [PMID: 16549908 DOI: 10.1159/000092070]
9 **Vural M**, Yilmaz I, Ilikkan B, Erginoz E, Perk Y. Intraventricular hemorrhage in preterm newborns: risk factors and results from a University Hospital in Istanbul, 8 years after. *Pediatr Int* 2007; **49**: 341-344 [PMID: 17532832 DOI: 10.1111/j.1442-200X.2007.02381.x]
10 **Muhammad A**, Waheed AA, Alvi MI, Khan N, Sayani R. Interobserver Agreement on Focused Assessment with Sonography for Trauma in Blunt Abdominal Injury. *Cureus* 2018; **10**: e2592 [PMID: 31501719 DOI: 10.7759/cureus.2592]
11 **Volpe JJ**. Intraventricular hemorrhage and brain injury in the premature infant. Diagnosis, prognosis, and prevention. *Clin Perinatol* 1989; **16**: 387-411 [PMID: 2663308]

12 **Feinstein AR**. Clinical Judgement. 1976 [DOI: 10.1002/cpt197619178]

13 **Benchoufi M**, Matzner-Lober E, Molinari N, Jannot AS, Soyer P. Interobserver agreement issues in radiology. *Diagn Interv Imaging* 2020; **101**: 639-641 [PMID: 32958434 DOI: 10.1016/j.diii.2020.09.001]

14 **Lowe LH**, Bailey Z. State-of-the-art cranial sonography: Part 1, modern techniques and image interpretation. *AJR Am J Roentgenol* 2011; **196**: 1028-1033 [PMID: 21512067 DOI: 10.2214/AJR.10.6160]

15 **Maalouf EF**, Duggan PJ, Counsell SJ, Rutherford MA, Cowan F, Azzopardi D, Edwards AD. Comparison of findings on cranial ultrasound and magnetic resonance imaging in preterm infants. *Pediatrics* 2001; **107**: 719-727 [PMID: 11335750 DOI: 10.1542/peds.107.4.719]

16 **Corbett SS**, Rosenfeld CR, Laptook AR, Risser R, Maravilla AM, Dowling S, Lasky R. Intraobserver and interobserver reliability in assessment of neonatal cranial ultrasounds. *Early Hum Dev* 1991; **27**: 9-17 [PMID: 1802667 DOI: 10.1016/0378-3782(91)90023-v]

17 **Hagmann CF**, Halbherr M, Koller B, Wintermark P, Huisman T, Bucher HU; Swiss Neonatal Network. Interobserver variability in assessment of cranial ultrasound in very preterm infants. *J Neuroradiol* 2011; **38**: 291-297 [PMID: 21396715 DOI: 10.1016/j.neurad.2010.12.008]

18 **Hintz SR**, Slovis T, Bulas D, Van Meurs KP, Perritt R, Stevenson DK, Poole WK, Das A, Higgins RD; NICHD Neonatal Research Network. Interobserver reliability and accuracy of cranial ultrasound scanning interpretation in premature infants. *J Pediatr* 2007; **150**: 592-596, 596.e1 [PMID: 17517240 DOI: 10.1016/j.jpeds.2007.02.012]

19 **Pinto J**, Paneth N, Kazam E, Kairam R, Wallenstein S, Rose W, Rosenfeld D, Schonfeld S, Stein I, Witomski T. Interobserver variability in neonatal cranial ultrasonography. *Paediatr Perinat Epidemiol* 1988; **2**: 43-58 [PMID: 3070483 DOI: 10.1111/j.1365-3016.1988.tb00179.x]

Published by **Baishideng Publishing Group Inc**
7041 Koll Center Parkway, Suite 160, Pleasanton, CA 94566, USA
Telephone: +1-925-3991568
E-mail: bpgoffice@wjgnet.com
Help Desk: https://www.f6publishing.com/helpdesk
https://www.wjgnet.com

ISSN 1949-8470 (online)

World Journal of *Radiology*

World J Radiol 2022 December 28; 14(12): 375-383

Published by Baishideng Publishing Group Inc

World Journal of Radiology

Contents

Monthly Volume 14 Number 12 December 28, 2022

ORIGINAL ARTICLE

Retrospective Study

World Journal of Radiology

Monthly Volume 14 Number 12 December 28, 2022

Contents

ABOUT COVER

Editorial Board Member of *World Journal of Radiology*, Roberto Grassi, MD, Professor, Researcher - University of Campania "Luigi Vanvitelli", Piazza Miraglia, Naples, Italy. roberto.grassi@unicampania.it

AIMS AND SCOPE

The primary aim of *World Journal of Radiology* (*WJR*, *World J Radiol*) is to provide scholars and readers from various fields of radiology with a platform to publish high-quality basic and clinical research articles and communicate their research findings online.

WJR mainly publishes articles reporting research results and findings obtained in the field of radiology and covering a wide range of topics including state of the art information on cardiopulmonary imaging, gastrointestinal imaging, genitourinary imaging, musculoskeletal imaging, neuroradiology/head and neck imaging, nuclear medicine and molecular imaging, pediatric imaging, vascular and interventional radiology, and women's imaging.

INDEXING/ABSTRACTING

The *WJR* is now abstracted and indexed in PubMed, PubMed Central, Emerging Sources Citation Index (Web of Science), Reference Citation Analysis, China National Knowledge Infrastructure, China Science and Technology Journal Database, and Superstar Journals Database. The 2022 edition of Journal Citation Reports ® cites the 2021 Journal Citation Indicator (JCI) for *WJR* as 0.48.

RESPONSIBLE EDITORS FOR THIS ISSUE

NAME OF JOURNAL
World Journal of Radiology

ISSN
ISSN 1949-8470 (online)

LAUNCH DATE
January 31, 2009

FREQUENCY
Monthly

EDITORS-IN-CHIEF
Thomas J Vogl

EDITORIAL BOARD MEMBERS
https://www.wjgnet.com/1949-8470/editorialboard.htm

PUBLICATION DATE
December 28, 2022

INSTRUCTIONS TO AUTHORS
https://www.wjgnet.com/bpg/gerinfo/204

GUIDELINES FOR ETHICS DOCUMENTS
https://www.wjgnet.com/bpg/GerInfo/287

GUIDELINES FOR NON-NATIVE SPEAKERS OF ENGLISH
https://www.wjgnet.com/bpg/gerinfo/240

PUBLICATION ETHICS
https://www.wjgnet.com/bpg/GerInfo/288

PUBLICATION MISCONDUCT
https://www.wjgnet.com/bpg/gerinfo/208

ARTICLE PROCESSING CHARGE
https://www.wjgnet.com/bpg/gerinfo/242

STEPS FOR SUBMITTING MANUSCRIPTS
https://www.wjgnet.com/bpg/GerInfo/239

ONLINE SUBMISSION
https://www.f6publishing.com

World Journal of Radiology

Submit a Manuscript: https://www.f6publishing.com

World J Radiol 2022 December 28; 14(12): 375-383

DOI: 10.4329/wjr.v14.i12.375

ISSN 1949-8470 (online)

ORIGINAL ARTICLE

Retrospective Study

Unmasking lower gastrointestinal bleeding under administration of norepinephrine

David John Werner, Nicolai Wenzel, Nael Abusalim, Ralf Kiesslich, Till Baar, Achim Tresch, Johannes Wilhelm Rey

Specialty type: Radiology, nuclear medicine and medical imaging

Provenance and peer review: Unsolicited article; Externally peer reviewed.

Peer-review model: Single blind

Peer-review report's scientific quality classification

Grade A (Excellent): 0
Grade B (Very good): B
Grade C (Good): C, C
Grade D (Fair): 0
Grade E (Poor): 0

P-Reviewer: Farid K, Egypt; Govindarajan KK, India; Liang HL, Taiwan

Received: September 9, 2022
Peer-review started: September 9, 2022
First decision: October 12, 2022
Revised: October 24, 2022
Accepted: December 1, 2022
Article in press: December 1, 2022
Published online: December 28, 2022

David John Werner, Nicolai Wenzel, Nael Abusalim, Department of Radiology, Helios Dr. Horst-Schmidt-Clinic, Wiesbaden 65199, Hessen, Germany

David John Werner, Radiologie Rhein-Nahe, Krankenhaus St. Marienwörth, Bad Kreuznach 55543, Rheinland-Pfalz, Germany

Nael Abusalim, Department of Diagnostic and Interventional Radiology, Medical Center Hanau, Hanau 63450, Hessen, Germany

Ralf Kiesslich, Johannes Wilhelm Rey, Department of Internal Medicine II, Helios Dr. Horst-Schmidt-Clinic, Wiesbaden 65199, Hessen, Germany

Till Baar, Achim Tresch, Institute for Medical Statistics and Computational Biology, Faculty of Medicine, University of Cologne, Cologne 50923, Nordrhein-Westfalen, Germany

Johannes Wilhelm Rey, Department of Gastroenterology and Endoscopy, Medical Center Osnabrueck, Osnabrueck 49076, Niedersachsen, Germany

Corresponding author: Johannes Wilhelm Rey, MD, PhD, Chief Doctor, Department of Gastroenterology and Endoscopy, Medical Center Osnabrueck, Am Finkenhügel 1, Osnabrueck 49076, Niedersachsen, Germany. johannes.wilhelm.rey@t-online.de

Abstract

BACKGROUND

Bleeding in the gastrointestinal tract is common and transarterial embolization enables the clinician to control gastrointestinal bleeding. Contrast extravasation is a prerequisite for successful embolization. Provocative angiography is helpful in the detection of elusive bleeding.

AIM

We performed a retrospective analysis of angiographic treatment in patients with lower gastrointestinal hemorrhage and initially negative angiographies, as well as the role of norepinephrine (NE) in unmasking bleeding.

METHODS

We analyzed 41 patients with lower gastrointestinal bleeding after angiography who had undergone treatment over a period of 10 years. All patients had a

positive shock index and needed intensive care.

RESULTS
In three of four patients, angiography disclosed the site of bleeding when NE was used during the procedure for hemodynamic stabilization.

CONCLUSION
We suggest that angiography performed after the administration of NE in unstable patients with gastrointestinal bleeding and an initially negative angiography has the potential to unmask bleeding sites for successful embolization. However, this statement must be confirmed in prospective studies.

Key Words: Lower gastrointestinal bleeding; Endoscopy; Provocative angiography; Norepinephrine; Radiology; Gastrointestinal bleeding

Core Tip: Bleeding in the gastrointestinal tract is common in hospital emergency settings. Gastrointestinal endoscopy is currently the undisputed method of choice for achieving hemostasis. Provocative angiography has been reported to help in the detection of elusive bleeding. We performed a retrospective analysis of angiographic management of bleeding in the lower gastrointestinal tract (LGIB). In a small number of patients, hemodynamic stabilization with norepinephrine (NE) disclosed LGIB which had escaped detection until this time. Angiography after administration of NE unmasked bleeding in three of four patients. We saw no complications in two of three patients after embolization. It may be assumed that this method can detect bleeding successfully and help to achieve hemostasis by angiography.

Citation: Werner DJ, Wenzel N, Abusalim N, Kiesslich R, Baar T, Tresch A, Rey JW. Unmasking lower gastrointestinal bleeding under administration of norepinephrine. *World J Radiol* 2022; 14(12): 375-383
URL: https://www.wjgnet.com/1949-8470/full/v14/i12/375.htm
DOI: https://dx.doi.org/10.4329/wjr.v14.i12.375

INTRODUCTION

Bleeding in the gastrointestinal tract may occur at various sites and is frequently encountered in the preclinical and in-hospital emergency setting. Gastrointestinal endoscopy is currently the undisputed method of choice for achieving hemostasis at the bleeding site in the gastrointestinal tract[1]. Bleeding occurs in the upper gastrointestinal tract four to five times more frequently than it does in the lower gastrointestinal tract (LGIB)[2]. The estimated incidence of LGIB is 25 *per* 100000 adults *per* year[3]. LGIB is strongly dependent on aging; a 200-fold increase was observed between the third and the ninth decade of life[4]. Diverticular bleeding is the most common cause of LGIB. Endoscopy reveals the bleeding site in a mere 20%-30% of cases. Some patients require surgical or angiographic treatment. Although endoscopic hemostasis is effective and the treatment of choice for LGIB, the optimal technique remains to be determined[5,6]. A bleeding site may not be evident in some patients despite endoscopic evaluation. In fact, the bleeding may cease and thus make it difficult to identify the site.

Provocative angiography with vasodilators, anticoagulants or thrombolytics has been reported to help in the detection of elusive bleeding[7-11]. Bloomfeld *et al*[8,12] identified bleeding in 37.5% of their patients using intra-arterial urokinase, tolazoline, and heparin during angiography procedures. In a retrospective analysis of 34 patients, provocative mesenteric angiography using systemic anticoagulation with heparin and selective transcatheter injection of a vasodilator disclosed the bleeding site in 31% of cases. Ten patients received embolization[9]. In a recently published case series of pharmacologic provocation combined with endoscopy, the source of bleeding was discovered in 15 of 27 patients with a regimen of antiplatelet/anticoagulant medication[13]. In 2020, Kokoroskos *et al*[14] described a regimen for stepwise provocation of bleeding with anticoagulants, vasodilators and thrombolytic agents. Twenty-three patients were included in the study; provocation was successful in seven patients, and four of the seven patients were successfully treated by interventional radiological procedures. No complications occurred. The role of vasopressors, such as norepinephrine (NE) in hemorrhagic shock has been reported elsewhere and is well-documented[15-17].

We performed a retrospective analysis of angiographic management of LGIB. In a small number of patients, hemodynamic stabilization with NE disclosed LGIB which had escaped detection until this time. We suspect that, after administering NE, occult bleeding and the concomitant short-term increase

in systolic blood pressure become visible on angiography. We retrospectively identified four patients with LGIB who needed NE in the intensive care setting and whose initial angiography had been negative. To the best of our knowledge, provocative challenges with intravenous NE in unstable patients with LGIB have not been reported so far.

Future prospective studies should address the usefulness of inducing blood pressure peaks in patients on NE treatment during angiography in order to disclose occult gastrointestinal bleeding. It may be assumed that this method, when used in eligible patients, may disclose bleeding successfully and help to achieve hemostasis by angiography. However, this assumption should be confirmed in prospective randomized multicenter studies.

MATERIALS AND METHODS

All patients who had undergone catheter angiography for gastrointestinal bleeding at our maximum-care hospital between 1 January, 2007 and 31 March, 2018 were included in the study[6]. Predictors of complicated angiographic treatment and the role of specific laboratory parameters and scores in predicting the likelihood of a successful intervention were identified. The study protocol conformed to the 1975 Declaration of Helsinki and was approved by the ethics committee of the Regional Medical Society of Hessen (Landesärztekammer Hessen), approval number FF 95/2017, on 31 August 2017. Written informed consent was obtained from each patient. In three of 41 patients, intravenous administration of NE was followed by contrast media extravasation, although the patients had experienced no extravasation during the initial procedure. In one patient, intravenous administration of NE did not disclose the bleeding. The maximal individual dose of NE was 10 μg. A specific time interval was not applied. For the accompanying anesthetists, the application of NE depended on their observations during monitoring and achieving a mean pressure higher than 60 mmHg. The maximum dose *per* patient during an angiography was 40 μg.

From our previous retrospective analysis, we identified a new subgroup of patients with the following common features: LGIB, intensive care, the need for NE, intra-arterial blood pressure measurement, and an intravenous NE bolus of 10-40 μg during angiography (Table 1).

RESULTS

In a retrospective analysis, we studied 41 consecutive patients with LGIB between 2007 and 2018. Twenty-six of 41 patients had diverticular bleeding. The primary endoscopy failed to achieve hemostasis in any patient (Figure 1). Sixteen of 41 patients underwent pre-interventional computed tomography (CT). The mean systolic blood pressure on the day of angiography was 104 mmHg, and the mean shock index was 0.91 (heart rate *per* minute/systolic blood pressure). Twenty-five of 41 patients were monitored by an anesthetist. Of these patients, 16 were intubated. Angiography demonstrated the bleeding in 18 of 41 patients, and 20 patients underwent embolization (2 prophylactic embolizations). The angiography was technically successful in 16/18 cases, and clinically successful in 10/18 cases[6].

Patients who needed catecholamines were documented separately. Three patients presented with severe hematochezia and signs of hemorrhagic shock, and a further patient with chronic sigmoid diverticulitis. Only one patient was female. The mean age was 75.8 years. All patients had a positive shock index, and all had at least one notable comorbid condition. The mean Glasgow-Blatchford bleeding score was 10 or higher in all cases (mean score 12). The mean interval from the time of hospitalization and the endoscopic investigation was 14.1 h. All patients received an emergency colonoscopy. Three of four colonoscopies revealed the stigmata of hemorrhage with no evidence of manageable bleeding. Only one case of diverticular bleeding was classified as active bleeding that could not be managed by endoscopy, and was directly treated by radiological procedures. Two of four patients underwent pre-interventional CT. In patient 1 we performed a triphasic CT scan and found no contrast medium extravasation on the CT, but did observe signs of previous hemorrhage in the colon. Patient 4 also underwent a triphasic CT scan and revealed contrast medium extravasation in the lower gastrointestinal tract as evidence of active bleeding.

The mean period of time until angiography was 3.5 d. The primary angiography failed to reveal active contrast media extravasation in any patient. In three of four cases (75%), the bleeding was seen after the application of noradrenaline for cardiovascular stabilization (Figures 2 and 3). In all cases, microcoils (Tornado® Embolization Coil, Cook Medical) were used for embolization. Superselective embolization failed in one patient; multiple feeding vessels were embolized using a front-door and back-door technique, which resulted in confirmed hemostasis. It should be noted that extended dearterialization caused mesenteric ischemia and necessitated a right-sided hemicolectomy the following day. The mean duration of the hospital stay for patients in the NE population was 18 d.

Table 1 Clinical, endoscopic and angiographic characteristics of patients

	Case 1	Case 2	Case 3	Case 4
Age (yr)	66	79	94	64
Sex	Male	Male	Female	Male
Reasons for admission	GI bleeding	Amputation	GI bleeding	Inflammatory disease
Shock index > 1	Yes	Yes	Yes	Yes
Heart rate (bpm)	112	106	84	120
Blood pressure (mmHg)	75/50	90/50	80/40	90/60
Comorbidities	PE, AA, Hypertension	DM, Hypertension, PAOD IV	CHD, DM, Hypertension	Hypertension
Glasgow-Blatchford score	12	13	10	13
Packed red cells	17	1	0	2
Time to endoscopy (h)	6.5	6	36	8
Source of bleeding	Diverticular	No bleeding	Diverticular	Diverticular
Location	Cecum	Not located	Sigmoid colon	Cecum
Number of endoscopic interventions	2	0	2	1
Types of intervention	1. Clipping2. Injection	None	1. Injection2. Clipping	1. Clipping
Number of endoscopies(Before/After angiography)	7 (6/1)	4 (2/2)	4 (2/2)	3 (3/0)
Time to angiography (d)	6	4	2	2
CTA	Yes	No	No	Yes
Artery with extravasation	A colica dextra	None	AMI	Ileocolic artery
Side of embolization	End arteries	None	Sigmoid artery	Marginal arteries
Material for embolization	Microcoils	-	Microcoils	Microcoils
Type of embolization (mm)	Ø 3/2	-	Ø 10/5	Ø 3/2
Baseline blood pressure (mmHg)	70/40	90/50	80/50	90/60
Dose of norepinephrine	20 μg	20 μg	40 μg	30 μg
Blood pressure (mmHg) at the time the bleeding was identified	155/8	-	170/90	160/90
Bleeding on provocation	Yes	No	Yes	Yes
Early complications	No	No	No	Ischemia
Endoscopy after coiling	Yes	No	No	No
Late complications	No	No	No	No
Duration of hospital stay (d)	18	16	8	30

AA: Aortic aneurysm; AF: Atrial fibrillation; AMI: Inferior mesenteric artery; CHD: Coronary heart disease; CTA: Computed tomography angiography; DM: Diabetes mellitus; Microcoils: Tornado® Embolization Coil, Cook Medical; MM: Malignant melanoma; PAOD: Peripheral arterial occlusive disease; PE: Pulmonary embolism.

DISCUSSION

The fact that NE is able to unmask LGIB in unstable patients has not been reported so far in the published literature. The pharmacological basis is alpha1-induced global vasoconstriction with an increase in peripheral vascular resistance and a resulting increase in systolic and mean arterial blood pressure, provoking a morphologically visible contrast media extravasation.

Our case series must be viewed in the context of other scientific investigations on bleeding site provocation in patients with GIB, using established endoscopic or angiographic procedures[6]. Permissive hypotension under sedation is a common phenomenon in patients with GIB and hemorrhagic shock. These conditions are usually treated effectively by intravenous volume substitution

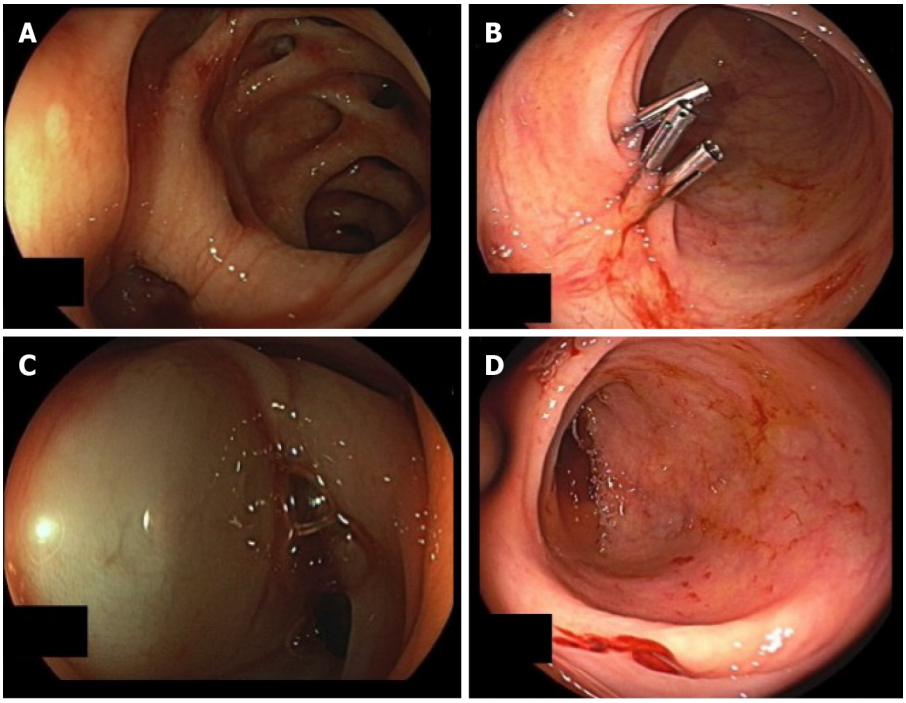

DOI: 10.4329/wjr.v14.i12.375 **Copyright** ©The Author(s) 2022.

Figure 1 Urgent colonoscopy in case 3. A: Revealed diverticular bleeding in the sigmoid colon; B: The endoscopic procedure was performed with three hemoclips; no further signs of bleeding; C: Injection therapy was used; D: Diverticular bleeding of the right colon was detected in case 4.

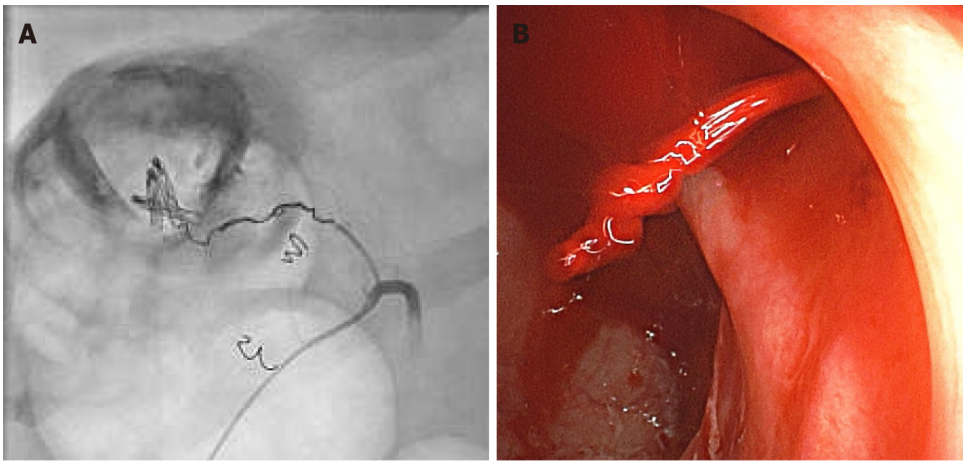

DOI: 10.4329/wjr.v14.i12.375 **Copyright** ©The Author(s) 2022.

Figure 2 Final colonoscopy in case 1, which revealed a spurt of bleeding at the right colon during norepinephrine treatment of hemorrhagic shock. A: The bleeding site was clip-marked before the patient was transferred for angiographic treatment; B: Superselective view of the right colic artery after norepinephrine application and coiling (the cumulative dose of norepinephrine was 20 μg).

and intravenous NE. In our analysis, this treatment disclosed the source of bleeding in patient 1.

The bleeding site is rarely detected by endoscopy, especially in patients with LGIB[18]. Previously, bleeding provocation procedures were usually performed in conjunction with an intervention in the coagulation system[8,9,11,13]. Although safe and uncomplicated provocation has been reported in all publications, we believe that the use of an anticoagulant as provocation in patients with GIB is a critical measure and is associated with a potential risk of bleeding complications.

All patients were in a state of hemorrhagic shock and had to be treated in an intensive care unit. Blood pressure was measured invasively. The shock index was elevated in 3/4 patients. A previously undetectable extravasation appeared in three of four cases after the administration of a cumulative dose of NE. Two of three patients had no complications after embolization. Nevertheless, the use of NE requires thorough knowledge of its pharmacological properties, especially in unstable patients. NE has a number of potential side effects, such as dizziness, headache, angina, ischemia, necrosis, and vasospasm[17]. Vasospasms occurred in one of our cases (Figure 3).

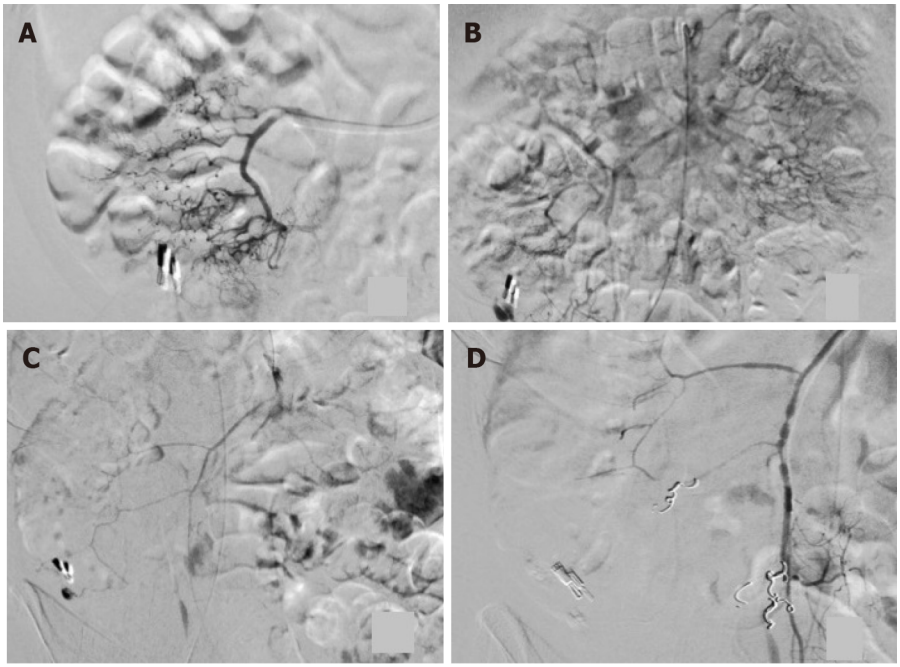

DOI: 10.4329/wjr.v14.i12.375 **Copyright** ©The Author(s) 2022.

Figure 3 Angiographic procedure in case 4. A: The ileocolic artery after application of 10 μg of norepinephrine is shown; no sign of extravasation; B: Selective view of the superior mesenteric artery, showing bleeding next to the hemoclip after repeated administration of a cumulative dose of 20 μg of norepinephrine; C: Arterial vasospasm was observed during an ongoing extravasation in the cecum; D: Following extensive embolization, no further bleeding was seen after a cumulative dose of 30 μg of norepinephrine.

In view of the high re-bleeding rates reported under NE, its use as a means of provocation calls for further investigation[19]. Other measures, such as the administration of at least three erythrocyte concentrates, may also improve the detection of bleeding[20]. However, transfusions with concentrates are known to cause side effects, and contrast extravasation after transfusion takes longer than it does after the administration of NE. Liang *et al*[21] used an intra-arterial epinephrine bolus with a small dose of vasopressin to induce vasospasm in the intra-arterial treatment of acute LGIB. The technical success rate in 21 procedures (16 patients) was 100%.

Bowel ischemia is a complication of embolization. In retrospective analyses, 10% of patients who underwent treatment for LGIB required surgical intervention 24 h after the procedure. Long-term survival rates were 70.6% (1 year), 56.6% (3 years) and 50.8% (5 years)[22]. This complication has also been reported in other studies[23-25]. We believe that the case of intestinal ischemia and subsequent hemicolectomy in the present study was not caused by provocation but by unsuccessful superselective embolization. However, this notion cannot be proved conclusively. Bowel ischemia may also have been induced by the administration of NE, which was a clinical necessity.

In view of this ischemic complication, patients with LGIB who have received interventional radiological treatment with provocation must be monitored closely in terms of laboratory parameters as well as follow-up endoscopies, although some authors do not advocate routine colonoscopy after angiography[23]. The need for a standard follow-up colonoscopy and its ideal timing must be investigated further.

We are aware of the crucial importance of patients being monitored by qualified intensive care specialists, including the administration of fluids, as well as the need to monitor other organ functions such as the kidneys, bowel and extremities by specialists and experienced physicians. In the future it may be meaningful to perform an angiography at the time when NE is administered, in order to identify an accidentally provoked contrast media extravasation. In the present investigation, NE was administered for the purpose of cardiovascular stabilization and the extravasation of contrast medium was a positive additional effect.

Limitations: This was a retrospective investigation and was accompanied by the known difficulties incumbent upon a study of this nature. If further investigations show that the suggested approach might be successful, the outcomes will have to be validated prospectively under controlled conditions. Furthermore, the data were not obtained for the purpose of the study and data collection may have been subject to structural inaccuracies. NE is a highly potent substance and should only be used by experienced clinicians. In one of our cases, the complication of bowel ischemia may have been an effect of NE. Further prospective studies are needed to address this problem. The limitations of the previously published study[6] also apply. Many crucial points such as the fluctuating nature of GIB, the time point of endoscopy, the number of endoscopies to be performed, the role of CT diagnosis, and the optimal

time point of angiography have not yet been clearly specified, and must be clarified in future investigations[6].

CONCLUSION

In summary, bleeding was discovered by the administration of NE in three of four patients with LGIB. NE was needed in all cases as a means of cardiovascular support.

Future prospective studies should address the usefulness of inducing blood pressure peaks in patients on NE treatment during angiography in order to disclose occult gastrointestinal bleeding. It may be assumed that this method, when used in eligible patients, may disclose bleeding successfully and help to achieve hemostasis by angiography. However, this assumption should be confirmed in prospective randomized multicenter studies.

ARTICLE HIGHLIGHTS

Research background

Gastrointestinal endoscopy is the undisputed method of choice for achieving hemostasis in the gastrointestinal tract. Provocative angiography has been reported to help in the detection of elusive bleeding.

Research motivation

We discovered contrast extravasation following the application of norepinephrine (NE) in angiographic procedures. Our purpose was to investigate the detection of masked bleeding during NE therapy.

Research objectives

The aim was to describe the procedure for the detection of elusive bleeding under the administration of NE and intensive care therapy.

Research methods

We performed a retrospective analysis of 41 patients with lower gastrointestinal tract bleeding treated by radiological procedures. Four patients received NE during angiography.

Research results

A previously undetected bleed was found in three patients. The bleeding was embolized without complications in two of four patients. In one patient we observed no bleeding after the administration of NE. One patient experienced bowel ischemia and had to be treated surgically.

Research conclusions

Bleeding was discovered in three of four cases. No complications were observed in two of three cases of embolization. Our results suggest that the use of NE may have the potential to improve the angiographic therapy of lower gastrointestinal bleeding in critically ill patients.

Research perspectives

Future studies should be focused on a prospective validation of the procedures described here but with a larger number of patients.

FOOTNOTES

Author contributions: Rey JW and Werner DJ designed the topic and wrote the paper; Wenzel N collected the data and edited the text; Baar T and Tresch A performed data analysis; Kiesslich R performed endoscopy and Abusalim N performed interventional angiography.

Institutional review board statement: The study was reviewed and approved by the Ethik-Komission bei der Landesärztekammer Hessen Institutional Review Board (Approval No. FF95/2017).

Informed consent statement: Patients were not required to give informed consent to the study as the analysis used anonymous clinical data that were obtained after each patient agreed to treatment by written consent.

Conflict-of-interest statement: All authors declare that they have no conflicts of interest.

Data sharing statement: If there is a need, you can contact the corresponding author to share data at any time.

Country/Territory of origin: Germany

ORCID number: David John Werner 0000-0003-1828-2969; Nicolai Wenzel 0000-0002-8820-2461; Nael Abusalim 0000-0003-3594-6050; Ralf Kiesslich 0000-0003-0199-6412; Till Baar 0000-0002-6744-1463; Achim Tresch 0000-0002-4146-6371; Johannes Wilhelm Rey 0000-0001-9905-4444.

S-Editor: Liu GL
L-Editor: Webster JR
P-Editor: Liu GL

REFERENCES

1 **Cook DJ**, Guyatt GH, Salena BJ, Laine LA. Endoscopic therapy for acute nonvariceal upper gastrointestinal hemorrhage: a meta-analysis. *Gastroenterology* 1992; **102**: 139-148 [PMID: 1530782 DOI: 10.1016/0016-5085(92)91793-4]
2 **van Leerdam ME**. Epidemiology of acute upper gastrointestinal bleeding. *Best Pract Res Clin Gastroenterol* 2008; **22**: 209-224 [PMID: 18346679 DOI: 10.1016/j.bpg.2007.10.011]
3 **Vernava AM 3rd**, Moore BA, Longo WE, Johnson FE. Lower gastrointestinal bleeding. *Dis Colon Rectum* 1997; **40**: 846-858 [PMID: 9221865 DOI: 10.1007/BF02055445]
4 **Longstreth GF**. Epidemiology and outcome of patients hospitalized with acute lower gastrointestinal hemorrhage: a population-based study. *Am J Gastroenterol* 1997; **92**: 419-424 [PMID: 9068461]
5 **Yamada A**, Niikura R, Yoshida S, Hirata Y, Koike K. Endoscopic management of colonic diverticular bleeding. *Dig Endosc* 2015; **27**: 720-725 [PMID: 26258405 DOI: 10.1111/den.12534]
6 **Werner DJ**, Baar T, Kiesslich R, Wenzel N, Abusalim N, Tresch A, Rey JW. Endoscopic hemostasis makes the difference: Angiographic treatment in patients with lower gastrointestinal bleeding. *World J Gastrointest Endosc* 2021; **13**: 221-232 [PMID: 34326943 DOI: 10.4253/wjge.v13.i7.221]
7 **ASGE Technology Committee**, DiSario JA, Petersen BT, Tierney WM, Adler DG, Chand B, Conway JD, Coffie JM, Mishkin DS, Shah RJ, Somogyi L, Wong Kee Song LM. Enteroscopes. *Gastrointest Endosc* 2007; **66**: 872-880 [PMID: 17904135 DOI: 10.1016/j.gie.2007.07.032]
8 **Bloomfeld RS**, Smith TP, Schneider AM, Rockey DC. Provocative angiography in patients with gastrointestinal hemorrhage of obscure origin. *Am J Gastroenterol* 2000; **95**: 2807-2812 [PMID: 11051352 DOI: 10.1111/j.1572-0241.2000.03191.x]
9 **Kim CY**, Suhocki PV, Miller MJ Jr, Khan M, Janus G, Smith TP. Provocative mesenteric angiography for lower gastrointestinal hemorrhage: results from a single-institution study. *J Vasc Interv Radiol* 2010; **21**: 477-483 [PMID: 20171902 DOI: 10.1016/j.jvir.2009.11.021]
10 **Malden ES**, Hicks ME, Royal HD, Aliperti G, Allen BT, Picus D. Recurrent gastrointestinal bleeding: use of thrombolysis with anticoagulation in diagnosis. *Radiology* 1998; **207**: 147-151 [PMID: 9530310 DOI: 10.1148/radiology.207.1.9530310]
11 **Rösch J**, Keller FS, Wawrukiewicz AS, Krippaehne WW, Dotter CT. Pharmacoangiography in the diagnosis of recurrent massive lower gastrointestinal bleeding. *Radiology* 1982; **145**: 615-619 [PMID: 6983087 DOI: 10.1148/radiology.145.3.6983087]
12 **Bloomfeld RS**, Rockey DC, Shetzline MA. Endoscopic therapy of acute diverticular hemorrhage. *Am J Gastroenterol* 2001; **96**: 2367-2372 [PMID: 11513176 DOI: 10.1111/j.1572-0241.2001.04048.x]
13 **Raines DL**, Jex KT, Nicaud MJ, Adler DG. Pharmacologic provocation combined with endoscopy in refractory cases of GI bleeding. *Gastrointest Endosc* 2017; **85**: 112-120 [PMID: 27343413 DOI: 10.1016/j.gie.2016.06.030]
14 **Kokoroskos N**, Naar L, Peponis T, Martinez M, El Moheb M, El Hechi M, Alser O, Fuentes E, Velmahos G. Provocative Angiography, Followed by Therapeutic Interventions, in the Management of Hard-To-Diagnose Gastrointestinal Bleeding. *World J Surg* 2020; **44**: 2944-2949 [PMID: 32405731 DOI: 10.1007/s00268-020-05545-8]
15 **Gupta B**, Garg N, Ramachandran R. Vasopressors: Do they have any role in hemorrhagic shock? *J Anaesthesiol Clin Pharmacol* 2017; **33**: 3-8 [PMID: 28413267 DOI: 10.4103/0970-9185.202185]
16 **Meier J**, Pape A, Loniewska D, Lauscher P, Kertscho H, Zwissler B, Habler O. Norepinephrine increases tolerance to acute anemia. *Crit Care Med* 2007; **35**: 1484-1492 [PMID: 17452931 DOI: 10.1097/01.CCM.0000265740.62130.1C]
17 **Hoellein L**, Holzgrabe U. Ficts and facts of epinephrine and norepinephrine stability in injectable solutions. *Int J Pharm* 2012; **434**: 468-480 [PMID: 22613065 DOI: 10.1016/j.ijpharm.2012.05.017]
18 **Rey JW**, Fischbach A, Teubner D, Dieroff M, Heuberger D, Nguyen-Tat M, Manner H, Kiesslich R, Hoffman A. Acute gastrointestinal bleeding - a new approach to clinical and endoscopic management. *Eur J Gastroenterol Hepatol* 2015; **27**: 483-491 [PMID: 25822855 DOI: 10.1097/MEG.0000000000000343]
19 **Travis AC**, Wasan SK, Saltzman JR. Model to predict rebleeding following endoscopic therapy for non-variceal upper gastrointestinal hemorrhage. *J Gastroenterol Hepatol* 2008; **23**: 1505-1510 [PMID: 18823441 DOI:

10.1111/j.1440-1746.2008.05594.x]

20 **Koval G**, Benner KG, Rösch J, Kozak BE. Aggressive angiographic diagnosis in acute lower gastrointestinal hemorrhage. *Dig Dis Sci* 1987; **32**: 248-253 [PMID: 3493124 DOI: 10.1007/BF01297049]

21 **Liang HL**, Chiang CL, Chen MC, Lin YH, Huang JS, Pan HB. Pharmaco-induced vasospasm therapy for acute lower gastrointestinal bleeding: a preliminary report. *Eur J Radiol* 2014; **83**: 1811-1815 [PMID: 25043985 DOI: 10.1016/j.ejrad.2014.06.032]

22 **Maleux G**, Roeflaer F, Heye S, Vandersmissen J, Vliegen AS, Demedts I, Wilmer A. Long-term outcome of transcatheter embolotherapy for acute lower gastrointestinal hemorrhage. *Am J Gastroenterol* 2009; **104**: 2042-2046 [PMID: 19455109 DOI: 10.1038/ajg.2009.186]

23 **Teng HC**, Liang HL, Lin YH, Huang JS, Chen CY, Lee SC, Pan HB. The efficacy and long-term outcome of microcoil embolotherapy for acute lower gastrointestinal bleeding. *Korean J Radiol* 2013; **14**: 259-268 [PMID: 23483780 DOI: 10.3348/kjr.2013.14.2.259]

24 **Mejaddam AY**, Cropano CM, Kalva S, Walker TG, Imam AM, Velmahos GC, de Moya MA, King DR. Outcomes following "rescue" superselective angioembolization for gastrointestinal hemorrhage in hemodynamically unstable patients. *J Trauma Acute Care Surg* 2013; **75**: 398-403 [PMID: 23928742 DOI: 10.1097/TA.0b013e31829a8b7a]

25 **Werner DJ**, Manner H, Nguyen-Tat M, Kloeckner R, Kiesslich R, Abusalim N, Rey JW. Endoscopic and angiographic management of lower gastrointestinal bleeding: Review of the published literature. *United European Gastroenterol J* 2018; **6**: 337-342 [PMID: 29774146 DOI: 10.1177/2050640617746299]

Published by **Baishideng Publishing Group Inc**
7041 Koll Center Parkway, Suite 160, Pleasanton, CA 94566, USA
Telephone: +1-925-3991568
E-mail: bpgoffice@wjgnet.com
Help Desk: https://www.f6publishing.com/helpdesk
https://www.wjgnet.com